

UC Berkeley

UC Berkeley Previously Published Works

Title

State of the Art and Prospects for Halide Perovskite Nanocrystals

Permalink

<https://escholarship.org/uc/item/1dh1q8zz>

Journal

ACS Nano, 15(7)

ISSN

1936-0851

Authors

Dey, Amrita
Ye, Junzhi
De, Apurba
et al.

Publication Date

2021-07-27

DOI

10.1021/acsnano.0c08903

Peer reviewed

1 State of the Art and Prospects of Halide Perovskite 2 Nanocrystals

3 Amrita Dey,[†] Junzhi Ye,[‡] Apurba De,[§] Elke Debroye,^{||} Seung Kyun Ha,[#] Eva Bladt,^{⊥,7} Anuraj S.
4 Kshirsagar,⁸ Ziyu Wang,⁹ Jun Yin,¹⁰ Yue Wang,^{11,12} Li Na Quan,^{13,14} Yan Fei,¹⁵ Mengyu Gao,^{14,16}
5 Xiaoming Li,¹¹ Javad Shamsi,[‡] Tushar Debnath,[†] Muhan Cao,¹⁷ Manuel A. Scheel,¹⁸ Sudhir
6 Kumar,¹⁹ Julian A. Steele,²⁰ Marina Gerhard,²¹ Lata Chouhan,²² Ke Xu,²³ Xian-gang Wu,²⁴ Yanxiu
7 Li,²⁵ Yangning Zhang,²⁶ Anirban Dutta,²⁷ Chuang Han,²⁸ Ilka Vincon,[†] Andrey L. Rogach,²⁵
8 Angshuman Nag,⁸ Anunay Samanta,[§] Brian A. Korgel,²⁶ Chih-Jen Shih,¹⁹ Daniel R. Gamelin,²⁹
9 Dong Hee Son,³⁰ Haibo Zeng,¹¹ Haizheng Zhong,²⁴ Handong Sun,^{12,31} Hilmi Volkan Demir,^{15,32,33}
10 Ivan G. Scheblykin,²¹ Iván Mora-Seró,³⁴ Jacek K. Stolarczyk,[†] Jin Z. Zhang,²³ Jochen Feldmann,[†]
11 Johan Hofkens,^{||,35} Joseph M. Luther,³⁶ Julia Pérez-Prieto,³⁷ Liang Li,³⁸ Liberato Manna,³⁹ Maryna
12 I. Bodnarchuk,^{40,41} Maksym V. Kovalenko,^{40,41} Maarten B.J. Roeloffs,²⁰ Narayan Pradhan,²⁷
13 Omar F. Mohammed,¹⁰ Osman M. Bakr,¹⁰ Peidong Yang,^{13, 14, 16, 42} Peter Müller-Buschbaum,^{18,43}
14 Prashant V Kamat,⁴⁴ Qialiang Bao,⁴⁵ Qiao Zhang,¹⁷ Roman Krahne,⁴⁶ Raquel E. Galian,³⁸ Samuel
15 D Stranks,^{‡, 47} Sara Bals,^{⊥,7} Vasudevanpillai Biju,²² William A. Tisdale,[#] Yong Yan,²⁸ Robert LZ
16 Hoye^{48*} and Lakshminarayana Polavarapu^{†,49*}

17
18 [†] Chair for Photonics and Optoelectronics, Nano-Institute Munich, Department of Physics,
19 Ludwig-Maximilians-Universität (LMU), Königinstrasse 10, 80539 Munich, Germany

20 [‡] Cavendish Laboratory, University of Cambridge, 19 JJ Thomson Avenue, Cambridge CB3 0HE,
21 United Kingdom

22 [§]School of Chemistry, University of Hyderabad, Hyderabad 500 046, India

23 ^{||}Department of Chemistry, KU Leuven, 3001 Leuven, Belgium

24 [#]Department of Chemical Engineering, Massachusetts Institute of Technology, Cambridge,
25 Massachusetts 02139, United States

1 ⁴EMAT, University of Antwerp, Groenenborgerlaan 171, 2020 Antwerp, Belgium
2 ⁷NANOLab Center of Excellence, University of Antwerp, Antwerp, Belgium.
3 ⁸Department of Chemistry, Indian Institute of Science Education and Research (IISER), Pune
4 411008, India
5 ⁹School of Science and Technology for Optoelectronic Information, Yantai University, Yantai,
6 Shandong Province 264005, P. R. China
7 ¹⁰Division of Physical Science and Engineering, King Abdullah University of Science and
8 Technology, Thuwal 23955-6900, Kingdom of Saudi Arabia
9 ¹¹MIT Key Laboratory of Advanced Display Materials and Devices, Institute of Optoelectronics
10 & Nanomaterials, College of Materials Science and Engineering, Nanjing University of Science
11 and Technology, Nanjing 210094, China
12 ¹²Division of Physics and Applied Physics, School of Physical and Mathematical Sciences,
13 Nanyang Technological University, Singapore 637371, Singapore
14 ¹³Department of Chemistry, University of California, Berkeley, Berkeley, California 94720,
15 United States
16 ¹⁴Materials Sciences Division, Lawrence Berkeley National Laboratory, Berkeley, California
17 ¹⁵LUMINOUS! Center of Excellence for Semiconductor Lighting and Displays, TPI-The
18 Photonics Institute, School of Electrical and Electronic Engineering, Nanyang Technological
19 University, Singapore, 639798 Singapore
20 ¹⁶Department of Materials Science and Engineering, University of California, Berkeley, Berkeley,
21 California 94720, United States
22 ¹⁷Institute of Functional Nano & Soft Materials (FUNSOM), Jiangsu Key Laboratory for Carbon-
23 Based Functional Materials and Devices, Soochow University, 215123, Suzhou, China
24 ¹⁸Institute for Functional Materials, Department of Physics, Technical University Munich, James-
25 Franck-Str. 1, 85748 Garching, Germany
26 ¹⁹Heinz Maier-Leibnitz Zentrum (MLZ), Technische Universität München, Lichtenbergstr. 1, D-
27 85748 Garching, Germany
28 ²⁰MACS Department of Microbial and Molecular Systems, KU Leuven, 3001 Leuven, Belgium

1 ²¹Chemical Physics and NanoLund, PO Box 124, Lund University, 22100 Lund, Sweden
2 ²²Graduate School of Environmental Science and Research Institute for Electronic Science,
3 Hokkaido University, Sapporo, Hokkaido 001-0020, Japan
4 ²³Department of Chemistry and Biochemistry, University of California, Santa Cruz, CA 95064,
5 United States of America
6 ²⁴Beijing Key Laboratory of Nanophotonics and Ultrafine Optoelectronic Systems, School of
7 Materials Science & Engineering, Beijing Institute of Technology, 5 Zhongguancun South Street,
8 Haidian District, Beijing 100081, China
9 ²⁵Department of Materials Science and Engineering, and Centre for Functional Photonics (CFP),
10 City University of Hong Kong, 83 Tat Chee Avenue, Kowloon, Hong Kong S.A.R.
11 ²⁶McKetta Department of Chemical Engineering and Texas Materials Institute, The University of
12 Texas at Austin, Austin, TX 78712-1062, USA
13 ²⁷School of Materials Sciences, Indian Association for the Cultivation of Science, Kolkata, India
14 700032
15 ²⁸Department of Chemistry and Biochemistry, San Diego State University, San Diego, California,
16 92182 USA
17 ²⁹Department of Chemistry, University of Washington, Seattle, Washington 98195, United States
18 ³⁰Department of Chemistry, Texas A&M University, College Station, Texas 77843, United States
19 ³¹Centre for Disruptive Photonic Technologies (CDPT), Nanyang Technological University,
20 Singapore 637371, Singapore
21 ³²Division of Physics and Applied Physics, School of Physical and Mathematical Sciences,
22 Nanyang Technological University, Singapore, 639798 Singapore
23 ³³Department of Electrical and Electronics Engineering, Department of Physics, UNAM-Institute
24 of Materials Science and Nanotechnology, Bilkent University, Ankara, 06800 Turkey
25 ³⁴Institute of Advanced Materials (INAM), Universitat Jaume I, 12071 Castelló, Spain.
26 ³⁵Max Planck Institute for Polymer Research, 55128 Mainz, Germany
27 ³⁶National Renewable Energy Laboratory, Golden, Colorado 80401, United States.
28 ³⁷Institute of Molecular Science, University of Valencia, c/ Catedrático José Beltrán 2, Paterna,
29 46980, Valencia, Spain

1 ³⁸School of Environmental Science and Engineering, Shanghai Jiao Tong University, Shanghai
2 200240, China

3 ³⁹Nanochemistry Department, cPhotonic Nanomaterials Lab, eAnalytical Chemistry Lab

4 ⁴⁰Institute of Inorganic Chemistry and § Institute of Chemical and Bioengineering, Department of
5 Chemistry and Applied Bioscience, ETH Zurich, Vladimir Prelog Weg 1, CH-8093 Zürich,
6 Switzerland

7 ⁴¹Laboratory for Thin Films and Photovoltaics, Empa–Swiss Federal Laboratories for Materials
8 Science and Technology, Überlandstrasse 129, CH-8600 Dübendorf, Switzerland

9 ⁴²Kavli Energy NanoScience Institute, Berkeley, California 94720, United States

10 ⁴³Institute for Chemical and Bioengineering, Department of Chemistry and Applied Biosciences,
11 ETH-Zurich, CH-8093 Zürich, Switzerland

12 ⁴⁴Notre Dame Radiation Laboratory, Department of Chemistry and Biochemistry, University of
13 Notre Dame, Notre Dame, IN, 46556, USA

14 ⁴⁵Department of Materials Science and Engineering and ARC Centre of Excellence in Future Low-
15 Energy Electronics Technologies (FLEET), Monash University, Clayton, Victoria 3800, Australia

16 ⁴⁶Istituto Italiano di Tecnologia, Via Morego 30, 16163 Genova, Italy

17 ⁴⁷Department of Chemical Engineering and Biotechnology, University of Cambridge, Cambridge,
18 UK

19 ⁴⁸Department of Materials, Imperial College London, Exhibition Road, London SW7 2AZ, UK

20 ⁴⁹Materials Chemistry and Physics group, CINBIO, Universidade de Vigo, Departamento de
21 Química Física, Campus Universitario As Lagoas, Marcosende, 36310 Vigo, Spain

22

23 **KEYWORDS** Metal-halide perovskite, nanocrystals, nanoplatelets, nanotubes, nanowires,
24 synthesis, lead-free perovskite-inspired materials, light-emitting devices, photovoltaics, lasers,
25 photocatalysts, photodetectors

26

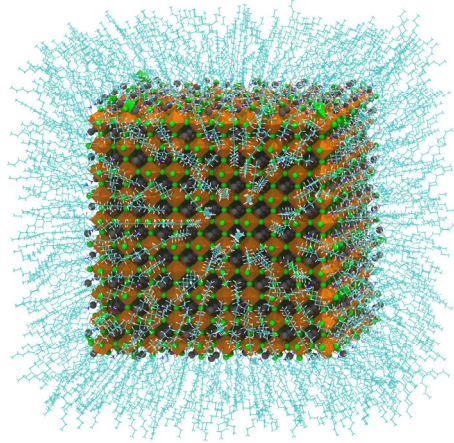
27

28

1

2

ABSTRACT



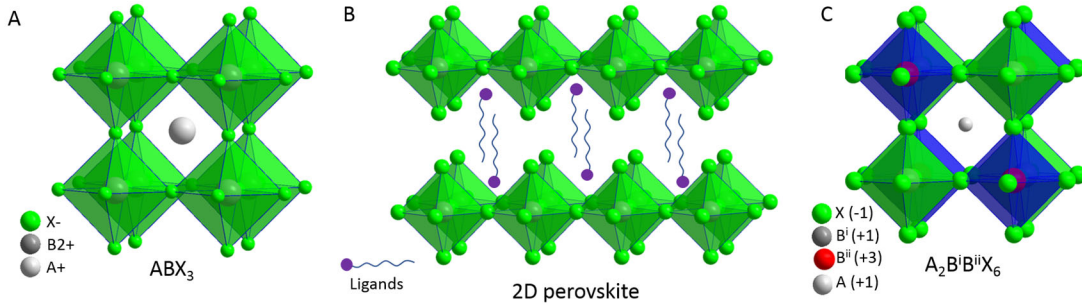
3

4 Metal-halide perovskites have rapidly emerged as one of the most promising materials of the
5 twenty-first century, with many exciting properties and great potential for a broad range of
6 applications, from photovoltaics to optoelectronics and photocatalysis. The ease with which metal-
7 halide perovskites can be synthesized in the form of brightly luminescent colloidal nanocrystals,
8 as well as their tunable and intriguing optical and electronic properties, have attracted researchers
9 from different disciplines of science and technology. In the last few years, there has been a
10 remarkable progress in the shape-controlled synthesis of perovskite nanocrystals, understanding
11 of their properties and applications. In this comprehensive review, researchers having expertise in
12 different fields (chemistry, physics and device engineering) of metal-halide perovskite
13 nanocrystals have joined together to provide a state of the art overview and future prospects of
14 metal-halide perovskite nanocrystal research.

1 INTRODUCTION

2 The earliest research work on metal halide perovskites (MHPs) was conducted in the late 1800s
3 by Wells,¹ while the detailed structural characterization was carried out by Weber in the 1900s.²⁻⁴
4 Their potential applications in electronic and optical devices first attracted attention in the late
5 1990s and the early 2000s, long before captivating the broad scientific community.⁵⁻⁶ In 2009,
6 Kojima et al.⁷ first demonstrated the use of lead halide perovskites (LHPs) as visible-light
7 sensitizers in solar cells, but it took another three years to fully grasp their potential for highly
8 efficient photovoltaics.⁸⁻⁹ Since then, the number of researchers working on MHPs has been
9 increasing significantly over the years, accompanied by a substantial increase in research output
10 in this area. The high efficiency of LHP photovoltaic cells is attributed to long charge carrier
11 diffusion lengths along with low Urbach energies, high photoluminescence quantum yields and
12 high absorption coefficients.¹⁰⁻¹¹ These remarkable features are of interest not only for the device
13 communities, but also for the chemistry, physics and materials research communities. Over the
14 last decade, numerous advances have been made towards the fundamental understanding as well
15 as potential applications of MHPs. The certified power conversion efficiency (PCE) of single-
16 junction perovskite-based solar cells has surpassed 25% in a short span of time, demonstrating an
17 order of magnitude higher rate of improvement compared to other photovoltaic technologies.¹²
18 MHPs have recently emerged at the forefront of materials research not only because of their
19 impressive photovoltaic performance but also due to their attractive optical and electronic
20 properties.^{10, 13-30} Over the years, they have already shown great promise in a wide range of
21 technological applications encompassing photovoltaics (PVs), light emitting diodes (LEDs),
22 lasers, transistors, photodetectors and photocatalysts.^{28, 31-47} The optical and electronic properties

1 of MHPs were shown to be strongly dependent on their dimensionality (both structural and
 2 morphological).^{6, 15, 17, 19, 23, 48-51}



3
 4 **Figure 1.** Illustrations of cubic crystal structure of (a) 3D perovskites, (b) 2D layered perovskites
 5 and (c) cubic crystal structure of 3D double perovskite.

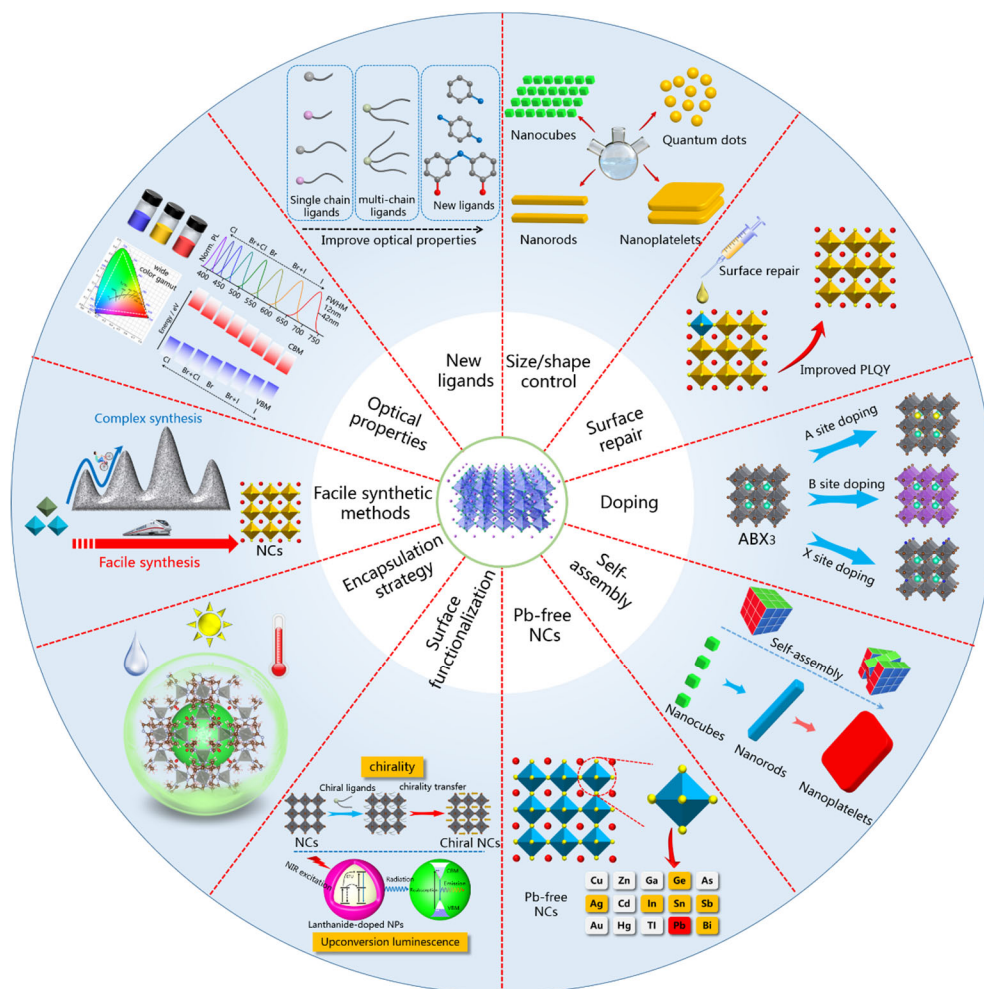
6
 7 Three-dimensional (3D) MHPs refer to a class of crystalline compounds adopting the generic
 8 chemical formula ABX_3 , where the cation “B” has six nearest-neighbor anions “X”, while the
 9 cation “A” sits in a cavity formed by eight corner-shared BX_6 octahedra.^{10, 52-53} MHPs are
 10 generally classified into either organic-inorganic hybrid (OIH) or inorganic perovskites depending
 11 on whether the A-site cation is organic or inorganic. OIH perovskites generally have
 12 methylammonium (MA) or formamidinium (FA)) as the monovalent A-site cation, lead, tin, or
 13 germanium as the divalent B cation, chlorine, bromine, iodine, or their combinations as the halide
 14 ion (X). On the other hand, inorganic perovskites have cesium (Cs) or rubidium (Rb) as the A
 15 cation. The ideal structure of the perovskite, which is illustrated in Figure 1a, is based on a cubic
 16 lattice. However, the deviation from the ideal perovskite structure in ABX_3 materials can be
 17 predicted through the Goldschmidt tolerance factor t ($t = (r_A + r_X) / [\sqrt{2}(r_B + r_X)]$), where r_A , r_B
 18 and r_X are the ionic radii of the corresponding ions, t is defined as the ratio of the distance A-X to
 19 the distance B-X). Unlike classical semiconductors (such as Ge, Si, GaAs, CdS, CdSe, InP), high-

1 quality MHPs can be prepared by simply mixing the corresponding precursor solutions at room
2 temperature (RT) under ambient conditions due to their inherent ionic character.^{30, 54-55} The optical
3 properties of MHPs are easily tunable across the visible spectrum of light by simply varying the
4 halide composition.⁵⁶⁻⁵⁹ While the bulk properties of MHP are remarkable, decreasing the size of
5 the crystals to the nanoscale reveals new features and opens further avenues for controlling the
6 properties. For instance, nanosized crystals (nanocrystals, NCs) of MHP exhibit quantum
7 confinement effects that can be exploited to tune the optical properties,^{15, 17, 20, 23} much like in other
8 semiconductors.⁶⁰⁻⁶¹ The structural dimensionality of MHPs is easily tunable from 3D to 2D using
9 long-chain alkylammonium cations in their synthesis (Figure 1b). The emission wavelength and
10 exciton binding energies of these layered perovskites are controllable by the number of octahedral
11 layers between the long-chain organic layers ($n = 1$ to ∞).^{50, 62-63} The tunable emission wavelength,
12 narrow emission, and low nonradiative losses of MHPs make them potential candidates for LEDs.
13 In addition, the long charge carrier diffusion lengths in MHPs facilitate efficient recombination of
14 electrically injected charge carriers. Bulk perovskites suffer from low photoluminescence quantum
15 yields (PLQYs) due to inherent defects, particularly those present at grain boundaries, surfaces
16 and interfaces.^{16, 64-65} On the other hand, MHP NCs emerged as extremely efficient light emitters
17 with near-unity PLQY. The early reports on colloidal halide perovskite NCs emerged in 2012-
18 2014.⁶⁶⁻⁶⁸ Despite limited control over the size, shape and colloidal stability, those early papers
19 showed that such fine perovskite particles exhibit much enhanced emissivity, as evidenced by a
20 PLQY of ~20% for MAPbBr₃ colloids.⁶⁸ In late 2014, Gonzalez-Carrero *et al.*²⁶ reported the
21 optimized synthesis of highly luminescent, well-dispersed and stable MAPbBr₃ colloids in toluene.
22 Although the particles appeared to be polydisperse and irregularly shaped, as seen from the TEM
23 images, they exhibited an impressive PLQY of 80% and stood in drastic contrast to classical

1 colloidal quantum dots (QDs), such as those made of CdSe and InP, which must be epitaxially
2 overcoated with wider-bandgap inorganic shells, such as CdS or ZnS, for imparting high PLQY
3 values.⁶⁹ The most relevant colloidal synthesis of well-defined colloidal LHP NCs, which enabled
4 exquisite control over the size and size distribution and thermodynamic stability of colloids, was
5 the one by Protesescu *et al.* in January 2015 using the hot-injection (HI) method, which delivered
6 monodisperse CsPbX₃ NCs.¹⁵ These CsPbX₃ NCs exhibited not only PLQY values up to 100%,
7 but also showed quantum-size effects similar to classical QDs. In March 2015, Zhong *et al.* first
8 introduced the ligand-assisted reprecipitation (LARP) approach for the room-temperature
9 synthesis of MAPbX₃ NCs with color tunable emission and PLQY up 70%.³⁰ In the same year,
10 Tyagi *et al.*²⁰ and Sichert *et al.*¹⁷ simultaneously reported the preparation of MAPbBr₃ perovskite
11 nanoplatelets (NPLs). The precise control of the number of monolayers in the platelets, down to
12 monolayer, demonstrated in the latter report and achieved by changing the ratio of the organic
13 cations in LARP, enabled a careful assessment of the quantum confinement effects in the
14 platelets.¹⁷ Later, the synthesis methodology initially proposed for CsPbX₃ NCs in Ref. 15 was
15 used also in the first reports on FAPbX₃ (X=Br, I) and CsFAPbI₃ NCs.⁷⁰⁻⁷¹ After these seminal
16 reports on uniform perovskite NCs, there has been a surge in MHP NC research. Over the years,
17 numerous efforts have been devoted to control the size and shape of MHP NCs by varying the
18 ligands, reaction temperatures and precursors. A wide range of morphologies such as nanocubes,
19 nanowires (NWs), nanorods (NRs), nanoplatelets (NPLs), nanosheets (NSs), multi-faced
20 nanocrystals,⁷²⁻⁷⁴ and QDs (nanocubes with sized in the strong quantum confinement regime) have
21 been reported.^{19, 24, 36, 49, 53, 57, 75-78} These NCs exhibit either bulk-like (3D) or quantum confined
22 (2D or 0D) properties depending on their dimensions. For instance, the thickness of the NPLs is
23 precisely tunable down to a single layer of edge-sharing octahedra (Figure 1B, strongly quantum

1 confined region). Over the years, the syntheses of LHP NCs have been optimized toward
2 monodispersity, with near unity PLQY and colloidal stability.⁷⁹⁻⁸⁰ Their size/shape and
3 composition (A, B and X) is also tunable by post-synthetic shape transformations and ion-
4 exchange, respectively.^{53, 58, 75, 81} Furthermore, their optical properties are tunable by self-assembly
5 into superlattices.⁸²⁻⁸⁴ Although low-bandgap, iodine-based MHPs are also defect tolerant, surface
6 defects caused by the detachment of ligands and surface atoms (B and X) can strongly affect their
7 PLQYs.^{62, 85} To overcome these effects, post-synthetic surface treatment methods have been
8 developed.^{53, 62, 86} In general, a post-synthetic treatment of LHP NCs with ligand molecules or
9 metal halides leads to a significant improvement in their PLQY.^{62, 85, 87-88} In addition, new
10 properties could be achieved in perovskite NCs by post-synthetic treatments with functional
11 molecules. The controlled synthesis of LHP NCs makes it easy for the researchers to test these
12 fascinating NCs as active materials in a wide range of applications, including LEDs,⁴⁰ lasers,⁸⁹
13 solar cells,⁹⁰⁻⁹¹ photodetectors,³⁷ transistors⁹²⁻⁹³ and for photocatalysis.⁴⁵ On the other hand, despite
14 the rapid progress in various aspects of LHP NCs, their stability is one of the major roadblocks in
15 advancing the field toward real-world applications. To address this issue, researchers have
16 implemented both *in-situ* synthesis as well as post-synthetic surface coating strategies,^{41, 94} but by
17 these approaches, the perovskite NCs are often protected with a layer of organic ligands, acting as
18 a dielectric surface coating, which is a major concern for the injection and transport of charge
19 carriers. Therefore, perovskite NCs coating with dielectric shells can only be used as down-
20 converters in LEDs. Another major obstacle for applying LHP NCs in consumer products such as
21 LEDs and solar cells is the toxicity of lead. Therefore, researchers have been testing various other
22 metals to replace this lead with less toxic alternatives. The replacement of divalent Pb^{2+} with
23 trivalent Bi^{3+} or Sb^{3+} leads to the formation of vacancy ordered triple perovskites ($\text{A}_3\text{B}_2\text{X}_9$), which

1 have a 0D or 2D structure, with higher exciton binding energies than the 3D perovskites.⁹⁵⁻⁹⁷ On
 2 the other hand, the perovskite crystal structure can be preserved by adding a monovalent B-site
 3 cation as well (e.g., Ag), which leads to the formation of double perovskites, as illustrated in Figure
 4 1c, which have been facing their own challenges in terms of wide bandgaps and low PLQYs thus
 5 far.



6
 7 **Figure 2.** Schematic overview of the current research directions on chemistry of colloidal MHP
 8 NCs.

9
 10 As illustrated in Figure 2, currently, MHP NCs are undergoing further chemical engineering in
 11 connection with shape-controlled synthesis using different precursors and ligands, surface

1 functionalization for inducing new functionality (for example, chirality), metal-ion doping, search
2 for Pb-free NCs alternatives, phase stability (thermal and moisture) and self-assembly. All these
3 research lines are aimed toward improving and stabilizing their optical properties. Over the years,
4 numerous excellent reviews have been published on MHP NCs, regarding their colloidal
5 chemistry, optical properties (linear and nonlinear) and potential applications.<sup>22-24, 36-37, 41, 47, 53, 92-
6 94, 98-116</sup> However, there is no extensive literature review covering the entire spectrum of research
7 into aspects of MHP NCs, from synthesis and fundamental properties to device applications and
8 related challenges. It has already been over five years since MHP NC research has started, and it
9 has quickly emerged as an important field in contemporary nanoscience and nanotechnology, a
10 field that is still rapidly growing. We have therefore identified the need for a comprehensive
11 literature review on current research lines and future prospects of MHP NCs, not only to guide
12 currently active researchers of this field, but also to inspire a younger generation of researchers to
13 join this exciting research field. To realize this, we have put together our expertise and experience
14 to provide a broad overview of currently available knowledge on various aspects of MHP NCs.
15 This review article provides comprehensive and up-to-date developments in the synthetic methods
16 for the shape-controlled synthesis of MHP NCs (both Pb and Pb-free), their surface chemistry,
17 post-synthetic surface passivation, surface-functionalization, self-assembly and optical properties
18 along with potential applications.

19 We have organized this review into eleven main sections: (1) colloidal synthesis of LHP NCs.
20 This section includes a brief history of colloidal synthesis of LHP NCs and a discussion on general
21 approaches developed over the years for their shape/size-controlled (nanocubes, nanoplatelets and
22 nanowires) synthesis and post-synthetic ion exchange for compositional tuning, along with post-
23 synthetic shape-transformations. We also discuss in situ synthesis approaches to obtain LHP NCs

1 on a substrate. (2) Surface chemistry and post-synthetic surface treatment of LHP NCs to improve
2 their optical properties. Our objective is to provide our current understanding of ligand chemistry
3 on LHP NC surface and passivation. (3) We discuss recent advances on 0D Cs₄PbBr₆ NCs,
4 regarding their syntheses, phase transformations and origin of their green photoluminescence. (4)
5 surface coating strategies to enhance the stability of LHP NCs toward humidity, heat and harsh
6 environments. (5) We then discuss various possible metal combinations to synthesize Pb-free
7 perovskite NCs. (6) We provide a summary of LHP NCs doped with various other metal ions to
8 improve their optical properties as well as their phase-stability. Special emphasis is paid to Mn-
9 doped HLP NCs. (7) We provide a summary of self-assembly strategies employed for the
10 fabrication of LHP nanocube superlattices. (8) We discuss the characterization of LHP NCs and
11 their assembly by transmission electron microscopy (TEM) and X-ray scattering techniques. In
12 this section, we describe the challenges associated with characterization of LHP NCs by TEM due
13 to electron-beam induced degradation. In addition, we discuss X-Ray scattering analysis of LHP
14 NC degradation. (9) We discuss the optical properties of MHP NCs, such as their PL, quantum
15 confinement effects, chirality and ultrafast charge carrier dynamics. (10) We also discuss the
16 optical studies of quantum dots and nano- and microcrystals at the single-particle level. (11) In the
17 last section, we offer an up-to-date research progress on various potential applications of MHP
18 NCs, including lasers, LEDs, photodetectors, FETs, photovoltaics and photocatalysis. In addition,
19 an outlook is provided at the end of each section, along with an overall outlook at the end of the
20 article.

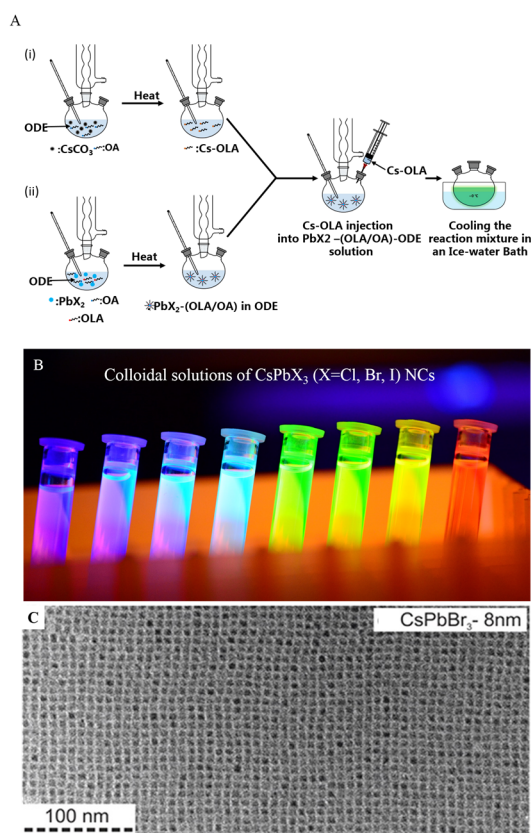
21

1 1. SHAPE-CONTROLLED SYNTHESIS OF MHP NCs

2 1.1 EVOLUTION OF DIFFERENT SYNTHESIS METHODS

3 The success of colloidal MHP NCs has resided mainly in the ability to synthesize them with
4 excellent control over their shape, size and composition, as well as with high quality.^{15, 23-24, 36, 48,}
5 ^{53, 86, 105, 117-118} Part of this success stems from the fact that these systems, as soon as they were
6 approached, have largely benefited from the knowledge on conventional colloidal nanocrystals
7 that had accumulated over the past few decades, especially on their synthesis, the study of their
8 fundamental properties and their device applications.^{60, 119-125} On the other hand, MHPs have been
9 known for a very long time, but their connection with the NC world has come only in relatively
10 recent times. As a matter of fact, the fabrication and optical properties of layered MHPs were
11 reported long before (in the 1990s) the realization of their great potential for applications in
12 devices, especially for photovoltaics.¹²⁶⁻¹²⁹ Along the line of conventional colloidal QD
13 photovoltaics (PVs), Im *et al.* first explored MAPbI₃ NCs in a TiO₂ matrix as a potential sensitizer
14 for PVs in 2011.¹³⁰ In their work, the NCs were synthesized on a nanocrystalline TiO₂ surface by
15 spin-coating the perovskite precursor solution. This work was probably one of the first to inspire
16 the colloidal chemistry research community to investigate the solution-phase synthesis of colloidal
17 MHP NCs. In 2014, Schmidt *et al.* reported the synthesis of MAPbBr₃ perovskite nano/micro
18 crystals.⁶⁸ Their synthesis relied on the use of medium-length alkyl chain organic ammonium
19 cations (octylammonium bromide and octadecylammonium bromide) as capping ligands to obtain
20 colloidal MAPbBr₃ NCs *via* the solvent (acetone)-induced reprecipitation of MABr and PbBr₂
21 precursors. The prepared MAPbBr₃ nano/micro crystals exhibited green emission with a PLQY of
22 ~20%. The ligands played a critical role in limiting the crystallization to obtain colloidal NCs, as
23 otherwise the precursors would precipitate out to form non-emissive or (weakly emissive) large

1 bulk crystals. Interestingly, a similar concept had been employed previously to obtain 2D layered
 2 halide perovskites on substrates and perovskite colloidal dispersions.¹³¹ In a subsequent work,
 3 Gonzalez-Carrero et al.²⁶ further improved the PLQY of these NCs to 83% by optimizing the
 4 ligand concentration. However, the morphology of the perovskite colloids was unclear until the
 5 first colloidal synthesis of well-defined CsPbX₃ NCs reported by Protesescu et al. in 2015.¹⁵ They
 6 synthesized the CsPbX₃ NCs by adapting a hot-injection (HI) strategy (Figure 3). Interestingly, HI
 7 has been used for more than two decades for CdSe⁶⁰ and since then also for other conventional
 8 colloidal NCs (Pb chalcogenides, In pnictides, *etc.*).



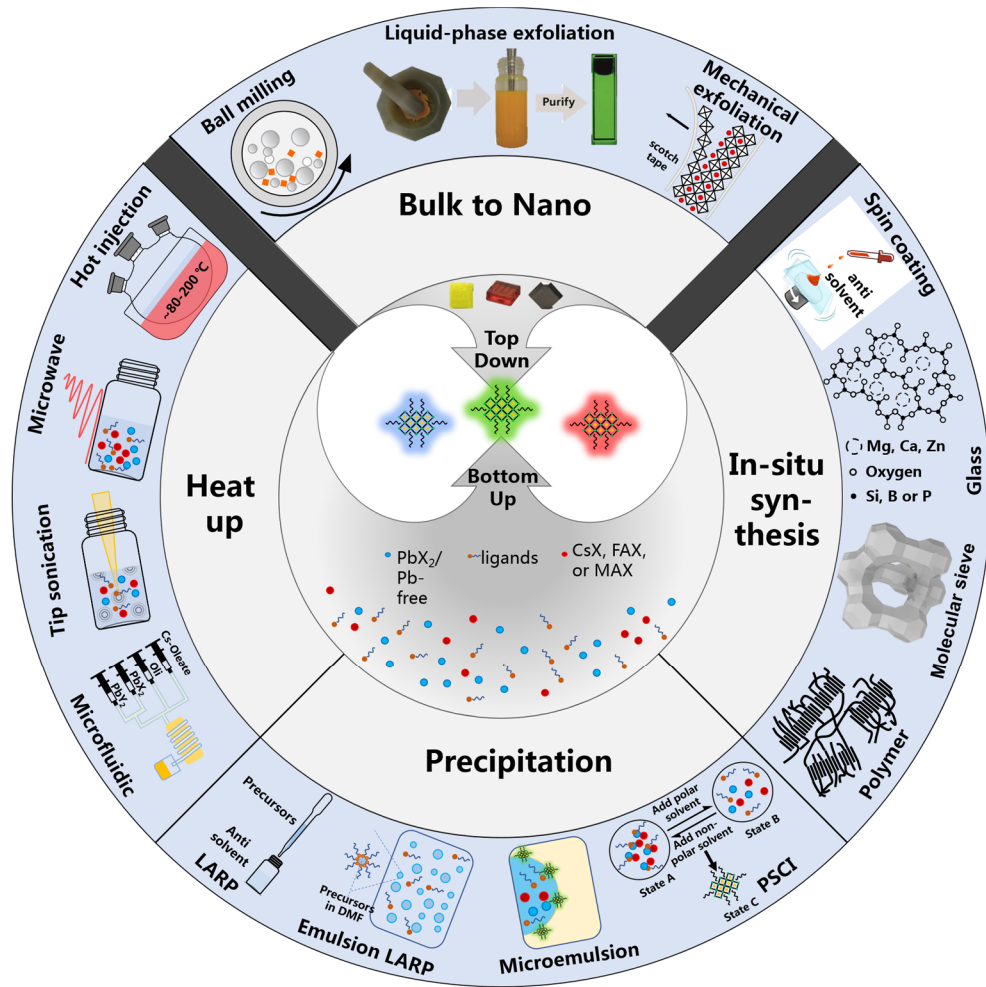
20 **Figure 3.** (A) Schematic illustrations of HI synthesis of colloidal CsPbX₃ NCs. The synthesis relies
 21 on the injection of pre-synthesized Cs-oleate into a reaction solution (PbX₂ dissolved in 1-
 22 octadecene using oleylamine and oleic acid) at high temperature. (B) Photographs of the colloidal

1 solutions of CsPbX₃ NCs synthesized by the HI method. (C) TEM images of the corresponding
2 CsPbBr₃ NCs. Reprinted with permission from Ref.¹⁵ Copyright American Chemical Society 2015.

3
4 Protesescu *et al.* were able to tune the size of the NCs by varying the reaction temperature, and
5 thus explored the quantum size effects in this class of NCs. This work lays the foundation for the
6 shape-controlled synthesis of MHP NCs. This pioneering work clearly highlighted that LHP NCs
7 have narrow emission spectra width with high PLQYs (up to 90%) and the PL peak position is
8 precisely tunable across the visible spectrum (400-700 nm) of light by varying the halide (Cl, Br,
9 I) composition and NC size (Figure 3). It is remarkable that LHP NCs, unlike conventional
10 colloidal semiconductor QDs, exhibit such high PLQYs without any surface passivation. Later in
11 2015, Sichert *et al.*¹⁷ demonstrated the synthesis of organic-inorganic hybrid perovskite NPLs with
12 thickness control down to a monolayer by varying the ratio of long and short-chain ligands in the
13 reprecipitation reaction. For such thin NPLs the quantum confinement effects clearly strongly
14 affected their absorption and PL properties. The outstanding optical properties of both organic-
15 inorganic and all-inorganic LHPs unveiled by these initial reports have greatly attracted the interest
16 of researchers from various disciplines.

17 Over the last few years, significant efforts have been devoted to developing facile and reliable
18 synthesis methods for MHPs. As schematically illustrated in Figure 4, these methods can be mainly
19 classified into either ‘bottom up’ or ‘top down’ approaches based on the growth process.¹³²⁻¹³³ The
20 bottom-up approaches can be further sub-classified into three different categories based on the
21 nature of the synthesis: (1) heat-up, (2) reprecipitation and (3) in-situ synthesis. Among all the
22 strategies illustrated in Figure 2, HI and LARP have been the most frequently used methods for
23 the synthesis of MHP NCs. As illustrated in Figure 3A, the HI synthesis of CsPbX₃ NCs generally
24 relies on the injection of pre-synthesized Cs-oleate into a reaction mixture containing PbX₂-ligands

- 1 in 1-octadecene at high temperatures and inert atmospheres, followed by immediate quenching of
- 2 the reaction with an ice-bath.



3

4 **Figure 4.** Schematic overview of various synthetic methods for MHP NCs. These methods can be

5 generally classified into either “top-down” or “bottom-up”. The bottom-up methods can be further

6 classified into three different sub-categories (heat up, precipitation, and in-situ synthesis)

7 depending on the type of reaction. PSCI: polar solvent controlled ionization, LARP: Ligand-

8 assisted reprecipitation.

9

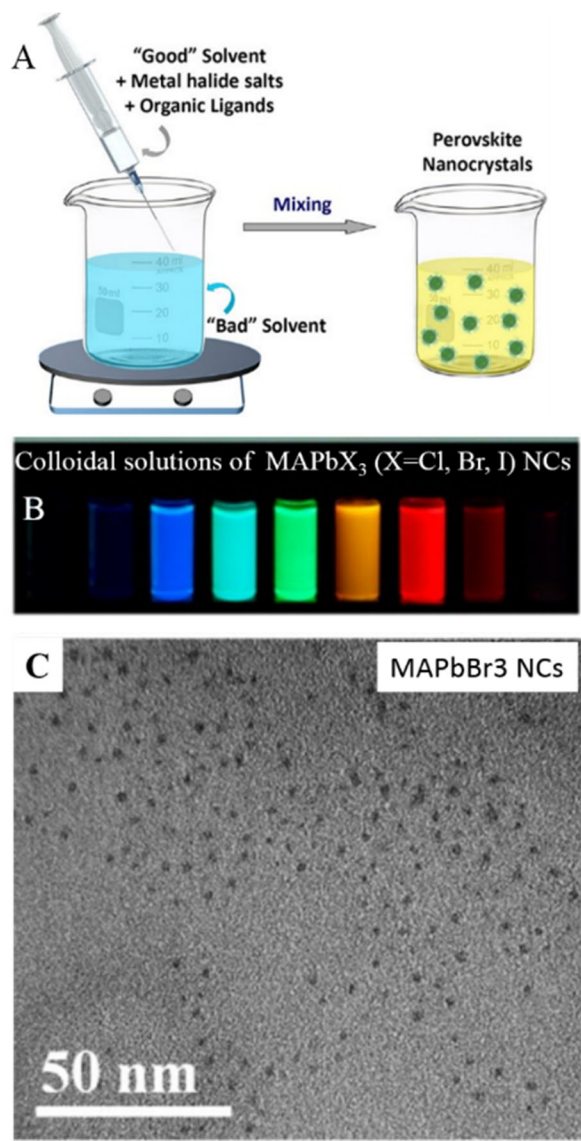
10 This method generally produces high-quality monodisperse CsPbX₃ NCs with high PLQY, and

11 this can also be adapted to the synthesis of Pb-free perovskite NCs using suitable precursors (refer

1 to Section 7). Over the years, the HI synthesis of MHP NCs has undergone further optimization
2 with different precursors and ligands to achieve better stability and shape control. However, this
3 method is tedious and requires high temperatures and inert atmospheres, which limits cost-
4 effective mass production. Alternatively, researchers have adapted a few other methods such as
5 tip-sonication,⁵⁹ microwave irradiation,¹³⁴ ball-milling,¹³² and solvothermal methods¹³⁵ for the
6 synthesis of MHP NCs at atmospheric conditions. These are single-step synthesis approaches, in
7 which all the precursors and ligands are mixed in a solvent, and then reacted by applying heat
8 (solvothermal synthesis, which is very similar to HI) or by tip-sonication or microwave irradiation
9 at atmospheric conditions. Nevertheless, the temperature in the reaction medium increases during
10 ultrasonication or microwave irradiation, promoting the reaction.

11 The inherent ionic nature of perovskites has enabled the synthesis of high-quality MHP NCs by
12 the LARP approach in ambient atmosphere at room temperature. The reprecipitation approach has
13 been known for centuries, and it has been used to prepare organic nanoparticles.¹³⁶⁻¹³⁸ This
14 approach relies on the spontaneous crystallization of substances upon reaching a supersaturated
15 state, which can be achieved by lowering the temperature, by solvent evaporation, or by the
16 addition of a poor solvent in which the solubility of the substance is low. If this is carried out in
17 the presence of ligands, nucleation and growth of the precipitate can be controlled, and this is
18 called the LARP process. In early 2015, Zhang *et al.*³⁰ first employed this LARP approach to
19 synthesize strongly luminescent colloidal MAPbX₃ (X=Cl, Br, I) NCs at room temperature (RT).
20 In this approach, a solution of perovskite precursors (such as MAX, FAX, CsX along with PbX₂)
21 ligands (alkylamines and alkyl carboxylic acids) dissolved in a good solvent such as
22 dimethylformamide (DMF), dimethylsulfoxide (DMSO) is dropped into a poor solvent (such as
23 toluene or hexane), inducing the instantaneous formation of ligand capped colloidal perovskite

1 NCs (Figure 5A & see movie S1). The LARP approach generally yields either spherical NCs
2 (Figure 5C) or nanoplatelets.^{17, 20} The size of the MAPbBr₃ NCs is tunable by varying the
3 temperature at which LARP is carried out, as shown by Huang *et al.*¹³⁹ Yet, there is still a debate
4 on whether the spherical NCs are perovskites or Pb clusters that result from electron-beam induced
5 degradation of perovskite NCs (movie S2).^{17, 59, 140} The LARP approach has been further updated
6 into emulsion synthesis, which enabled the purification of MAPbBr₃ NCs by precipitation into
7 solid-state light-emitting powder form.¹³⁹ This can be redissolved into solvents for processing thin-
8 film devices.¹⁴¹⁻¹⁴² This LARP approach has also been extended to all-inorganic MHP NCs.^{54, 79}
9 However, the level of shape control achieved by LARP is still lagging far behind that of the HI
10 synthesis. As illustrated in Figure 2, currently, the synthesis of MHP NCs is undergoing further
11 fine-tuning in connection with shape control using different precursors and ligands, surface
12 functionalization for inducing new functionalities (for example, chirality), metal-ion doping,
13 moving the focus towards Pb-free NCs, phase stability (thermal and moisture) and self-assembly.
14 All these research lines are aimed toward improving the optical properties of NCs or finding
15 alternative, less toxic compositions while keeping optical performances high. Despite significant
16 advances in the synthesis of MHP NCs, only limited shape-control has been achieved, as mainly
17 nanocubes, nanoplatelets (NPIs) and nanowires (NWs) have been frequently reported. In the
18 following, we discuss the state of the art synthesis of these three morphologies.



1
 2 **Figure 5.** (A) Schematic illustrations of the synthesis of colloidal MAPbX₃ NCs by the LARP
 3 approach. Reprinted with permission from Ref.¹⁴³ Copyright American Chemical Society 2019.
 4 The synthesis relies on dropping precursor powders and ligands dissolved in a good solvent (such
 5 as DMF or DMSO) into a poor solvent (such as toluene or hexane). (B) Photographs of the
 6 colloidal solutions of MAPbX₃ NCs synthesized by the HI method. (C) TEM images of the

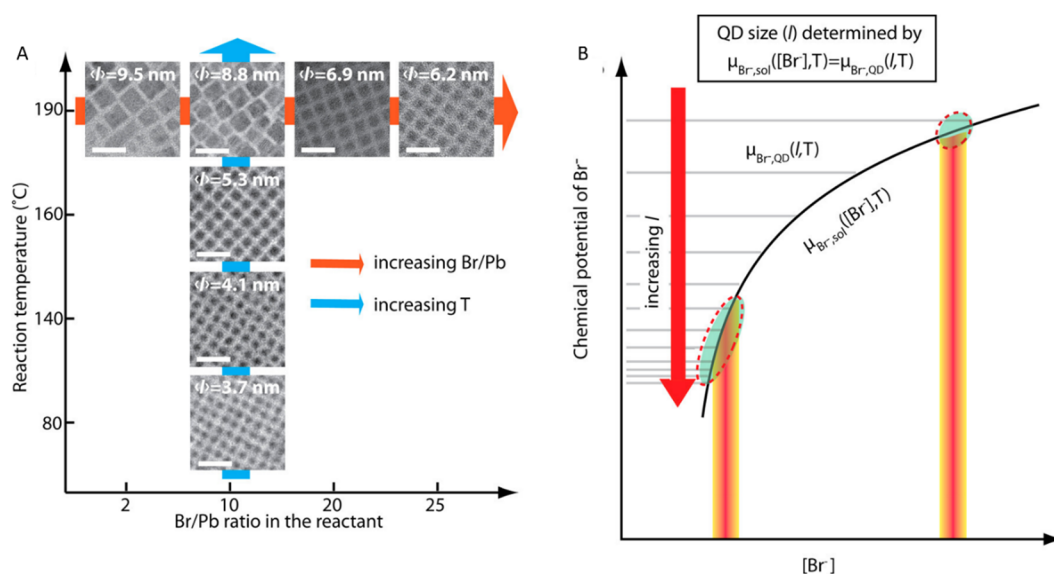
1 corresponding MAPbX₃ NCs. Panels b and c are reprinted with permission from Ref.³⁰ Copyright
2 American Chemical Society 2015.

3

4 **1.2 NANOCUBES**

5 Nanocubes are the most explored MHP NCs in terms of their synthesis, characterization, and
6 investigation for potential applications.^{15, 53, 89, 144-145} Over the last five years, there has been
7 remarkable progress towards the development of reliable and scalable synthetic approaches for
8 MHP nanocubes with tunable composition and high PLQY.^{15, 59, 135, 144, 146-147} As a result, these
9 nanocubes have already shown great promise for LEDs, lasers and solar cells, as compared with
10 other MHP morphologies and nanostructures.^{43, 89-90, 145} In general, perovskite precursors often
11 tend to precipitate to form NCs with cubic shapes at high reaction temperatures, while they tend
12 to crystallize into nanoplatelet morphologies at relatively low reaction temperatures. This
13 temperature dependence is now better understood in terms of acid/base equilibria regulating the
14 protonation/deprotonation of the alkylamine ligands used in the synthesis competing with Cs⁺ ions
15 for their inclusion to the facets of the growing NCs.¹⁴⁸ In fact, CsPbX₃ perovskite nanocubes were
16 first synthesized using a well-known HI method, and it is still the most frequently used method to
17 synthesize MHP NCs (Figure 3 & movie S3: large-scale synthesis of CsPbBr₃ nanocubes. The hot
18 injection is realized here by creating a reduced pressure in flask, and opening the valve of the
19 dropping funnel).¹⁵ In this method, PbX₂ precursors were first dissolved in octadecene, followed
20 by the injection of Cs-oleate at high temperature and inert atmosphere. It is worth mentioning that
21 the reaction has to be quickly quenched with an ice bath upon the injection of Cs-oleate, otherwise
22 a prolonged reaction time lead to the formation of nanowires as side products (the reader should
23 consult the nanowires section for additional details).⁷⁷ This method generally yields monodisperse

1 CsPbX₃ nanocubes, and the halide composition of the nanocubes is easily tunable by varying the
 2 ratio of PbX₂ precursors in the reaction medium. Although the initial studies suggested that these
 3 CsPbX₃ nanocubes exhibit cubic structures,^{15, 59, 144} CsPbBr₃ nanocubes were later found to have
 4 an orthorhombic crystal structure.^{146, 149-150} The Br- and I-based perovskite NCs generally feature
 5 high PLQY (near unity has been reported), while the Cl-based NCs suffer from lower PLQYs.^{15,}
 6 ⁵⁸⁻⁵⁹ Nevertheless, recent studies have shown that postsynthetic treatment with metal chloride salts
 7 can significantly improve the PLQY of CsPbCl₃ nanocubes up to near unity.^{87, 151} However, it is
 8 still unclear whether metal ion doping or the chloride passivation leads to the observed PLQY
 9 enhancement.¹⁵²

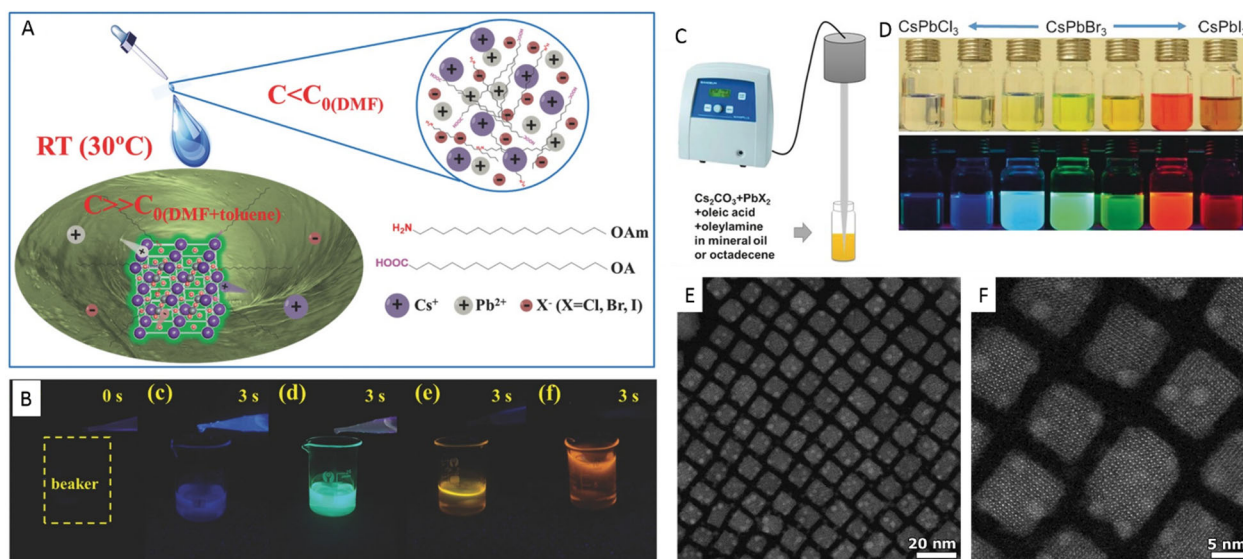


10
 11 **Figure 6.** Size control of CsPbBr₃ perovskite nanocubes via thermodynamic equilibrium in hot-
 12 injection synthesis: (A) Dependence of the size of CsPbBr₃ nanocube on the Br-to-Pb ratio in the
 13 reaction medium and the reaction temperature. (B) A proposed model illustrating the determination
 14 of the nanocube size via equilibrium of Br⁻ in between the nanocube lattice and the reaction
 15 medium. The nanocube size for a given concentration of Br⁻ ([Br⁻]) and temperature (T) is
 16 determined at which the chemical potentials (μ_{Br^-}) of Br⁻ in the and in the reaction medium become

1 equal. The inverse correlation between the nanocube size and the concentration of Br^- at a given
2 temperature (T) can be clearly seen from the two marked (dotted circles) areas. Reprinted with
3 permission from Ref.¹⁵³ Copyright American Chemical Society 2018.

4
5 In addition, the size of the CsPbX_3 perovskite nanocubes is also tunable over a limited range via
6 hot-injection synthesis. However, unlike conventional colloidal NCs, the size of the perovskite
7 NCs is tunable by controlling the reaction temperature, rather than the growth kinetics because of
8 their fast (1-3 s) nucleation and growth. In general, the size of the perovskite nanocubes decreases
9 with decreasing reaction temperature. For instance, Protesescu *et al.* synthesized monodisperse
10 nanocubes of size range 4-15 nm by hot-injection synthesis via temperature control (140–200
11 °C).¹⁵ Nevertheless, it should be noted that precursors crystallize into nanoplatelets at low reaction
12 temperatures (<130 °C).¹⁹ For precise control over the size of quantum-confined CsPbX_3
13 nanocubes, Dong *et al.*¹⁵³ proposed a strategy based on the halide ion equilibrium in between the
14 nanocubes and the reaction medium, along with temperature control (Figure 6). In principle, the
15 halide (X)-to-Pb ratio should be higher for small (strongly quantum-confined) CsPbX_3 nanocubes.
16 Since the Br^- ions diffuses in and out of the crystal lattice with a low kinetic barrier, the size of the
17 resulting nanocube depends on the variation of the Br^- equilibrium between the nanocube and the
18 reaction medium. Therefore, at a given temperature, the increase in the Br/Pb ratio for a fixed
19 amount of Cs^+ and Pb^{2+} in the reaction medium leads to a decrease in the nanocube size (Figure
20 6A). Similarly, for a fixed Br/Pb ratio, the size of the nanocube decreases with decreasing reaction
21 temperature (Figure 6A). This model was proposed based on the Br^- equilibrium between the
22 nanocube lattice and the reaction medium, and is consistent with the experimentally observed
23 (from TEM analysis shown figure 6A) correlation between nanocube size and Br/Pb ratio (Figure
24 6B). This method has received considerable attention regarding the preparation and study of the

1 optical properties of size controlled quantum-confined nanocubes.¹⁵⁴⁻¹⁵⁷ In addition, several other
2 potential methods have also been reported for the growth of size-controlled quantum-confined
3 CsPbBr₃ nanocubes.^{81, 148, 158} For instance, Pradhan and co-workers showed that the size of the
4 CsPbBr₃ nanocubes can be reduced down to ~3.5 nm by increasing the amount of
5 oleylamine-HBr (OLA-HBr) in the reaction medium at a fixed temperature (160 °C).⁸¹ To achieve
6 a better understanding of the role of ligands (OLA and OA) in controlling the shape and size of
7 perovskite NCs, Almeida and co-workers performed a systematic synthetic study by varying the
8 ratio between OLA and OA, and correlated with the size, shape and distribution of the resultant
9 CsPbBr₃ NCs.¹⁴⁸ They found that a high concentration of oleylammonium species in the reaction
10 medium leads to the formation of nanoplatelets, whereas a low concentration results in nanocubes.
11 In addition, they were able to prepare monodisperse CsPbBr₃ nanocubes with sizes ranging from
12 4.0 to 16.4 nm by varying the OLA/OA ratio along with reaction temperature. Despite the
13 successful synthesis of small nanocubes (<20 nm), precise control over the size of CsPbX₃
14 nanocubes with sizes above 20 nm is still challenging.



1

2 **Figure 7.** Highly luminescent CsPbX_3 ($X=\text{Cl}$, Br and I) nanocubes via supersaturated

3 recrystallization at RT and single-step ultrasonication approaches. (A) Schematic illustration of

4 the RT synthesis of CsPbX_3 nanocubes. The precursors (Cs^+ , Pb^{2+} and X^- ions) crystallize into

5 perovskite nanocubes under ambient conditions within 10s after having been transferred from a

6 good solvent (DMF) to a bad solvent (Toluene). (B) Photographs of pure toluene (0s) and the

7 colloidal solutions of CsPbX_3 nanocubes with different halide compositions formed within 3s after

8 the injection of corresponding DMF-precursors into pure toluene under UV illumination in

9 darkness. Panels A-B are reprinted with permission from Ref.⁵⁴ Copyright John Wiley & Sons, Inc.

10 2016. (C) Schematic illustration of the single-step synthesis of CsPbX_3 perovskite nanocubes. (D)

11 Photograph of the colloidal dispersions of CsPbX_3 NCs with different halide ($X=\text{Cl}$, Br , and I)

12 compositions under room light (top) and UV light (bottom). (E-F). (D) Different magnification

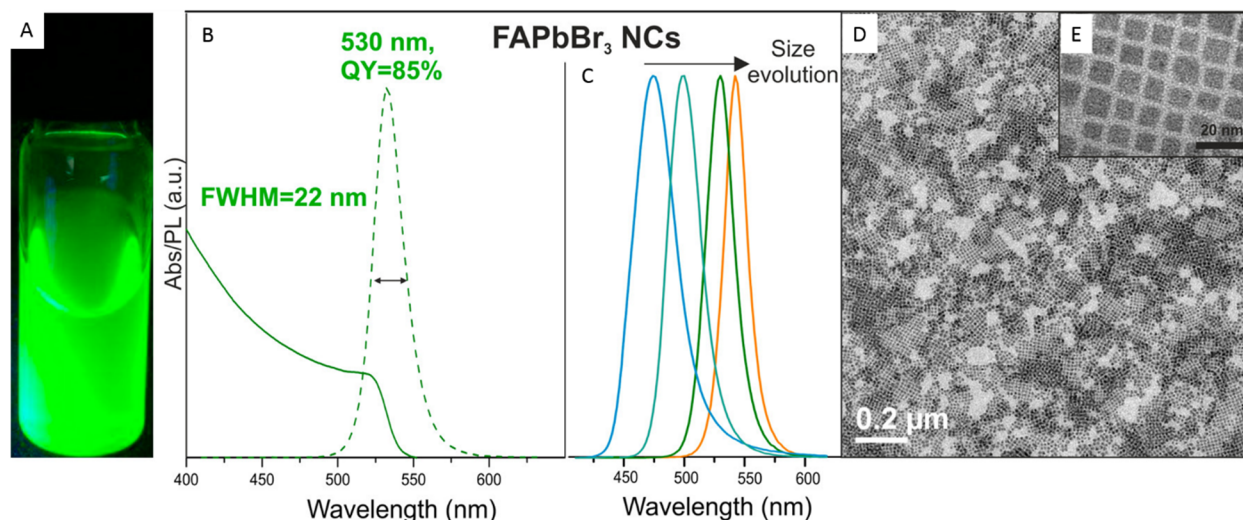
13 HAADF - STEM images of CsPbBr_3 nanocubes obtained by ultrasonication approach. Panels C-

14 D are adapted from Ref.⁵⁹ Copyright John Wiley & Sons, Inc. 2016.

15

1 Although the hot-injection method has been extensively used for the synthesis of inorganic
2 perovskite nanocubes, it is tedious, and generally carried out under inert conditions. Moreover, it
3 requires an additional synthesis step for the Cs-oleate precursor. To overcome these limitations,
4 several alternative methods, such as microwave irradiation,¹³⁴ ultrasonication,⁵⁹ solvothermal
5 synthesis¹³⁵ and LARP¹⁴⁴ have been reported. For instance, Zeng and co-workers first reported the
6 room temperature (RT) synthesis of highly luminescent CsPbX₃ perovskite nanocubes by using
7 the LARP method (Figure 7A-B).⁵⁴ In this method, CsBr and PbBr₂ precursors were first dissolved
8 in DMF or DMSO along with OLA and OA ligands. The precursor solution was then added to
9 toluene at RT to trigger the precipitation of brightly luminescent perovskite nanocubes within a
10 few seconds, as shown in Figure 7B. The authors reported a PLQY of 95% for CsPbBr₃ nanocubes
11 prepared by this method. The emission color was easily tunable by the halide composition in the
12 precursor solution in *N,N* – dimethylformamide (DMF). Nevertheless, this method required the
13 use of polar solvents that can influence the stability of the prepared NCs. In 2016, Tong *et al.*⁵⁹
14 reported the polar-solvent-free single-step synthesis of CsPbX₃ nanocubes with controllable halide
15 composition by ultrasonication of the precursor salts in the presence of ligands (Figure 7C-D). This
16 is one of the easiest and fastest methods to obtain perovskite NCs. The emission color of the
17 prepared nanocubes is easily tunable by varying the ratio of different halide precursors in the
18 reaction medium. The nanocubes prepared by this approach are nearly monodisperse and exhibit
19 high PLQY. This method was further extended to the preparation of perovskite nanowires²³ and
20 nanorods.¹⁵⁹ In 2017, Chen *et al.* reported the solvothermal synthesis CsPbX₃ NCs. In this method,
21 the precursors and ligands were loaded into a Teflon-lined autoclave and then heated
22 at 160 °C for 30 min. The obtained nanocubes appeared to be rather monodisperse with a PLQY

1 up to 80%. Zhai *et al.* further extended this method to CsPbBr₃ nanoplatelets using pre-synthesized
2 Cs-oleate as precursor.¹⁶⁰



3
4 **Figure 8.** Synthesis of FAPbBr₃ nanocubes by hot-injection (HI). (A) Photograph of colloidal
5 solution of FAPbBr₃ nanocubes in toluene under UV light illumination. (B) UV-vis absorption and
6 PL spectra of FAPbBr₃ nanocubes with a PL peak maximum at 530 nm. (c) PL spectra for FAPbBr₃
7 NCs of different sizes. The emission peak redshifts with increasing size from 5 to >50 nm, (D,E)
8 TEM images of FAPbBr₃ nanocubes at two different magnifications. Reprinted with permission
9 from Ref.⁷⁰ Copyright American Chemical Society 2016.

10
11 In comparison to the many studies on inorganic perovskite NCs, organic-inorganic hybrid
12 perovskite nanocubes have been rarely reported.^{70, 161-165} In 2016, Vybornyi *et al.*¹⁶² demonstrated
13 a polar-solvent-free colloidal synthesis of MAPbBr₃ perovskite NCs by the HI method. They were
14 able to tune the morphology from nanocubes to nanoplatelets and nanowires by varying the
15 reaction parameters. In 2019, Korgel and co-workers extended this method to the synthesis of
16 monodisperse MAPbI₃ nanocubes.¹⁶⁴ The main problem associated with these MA-based
17 perovskites is their chemical decomposition, which limits their applications. Alternatively,

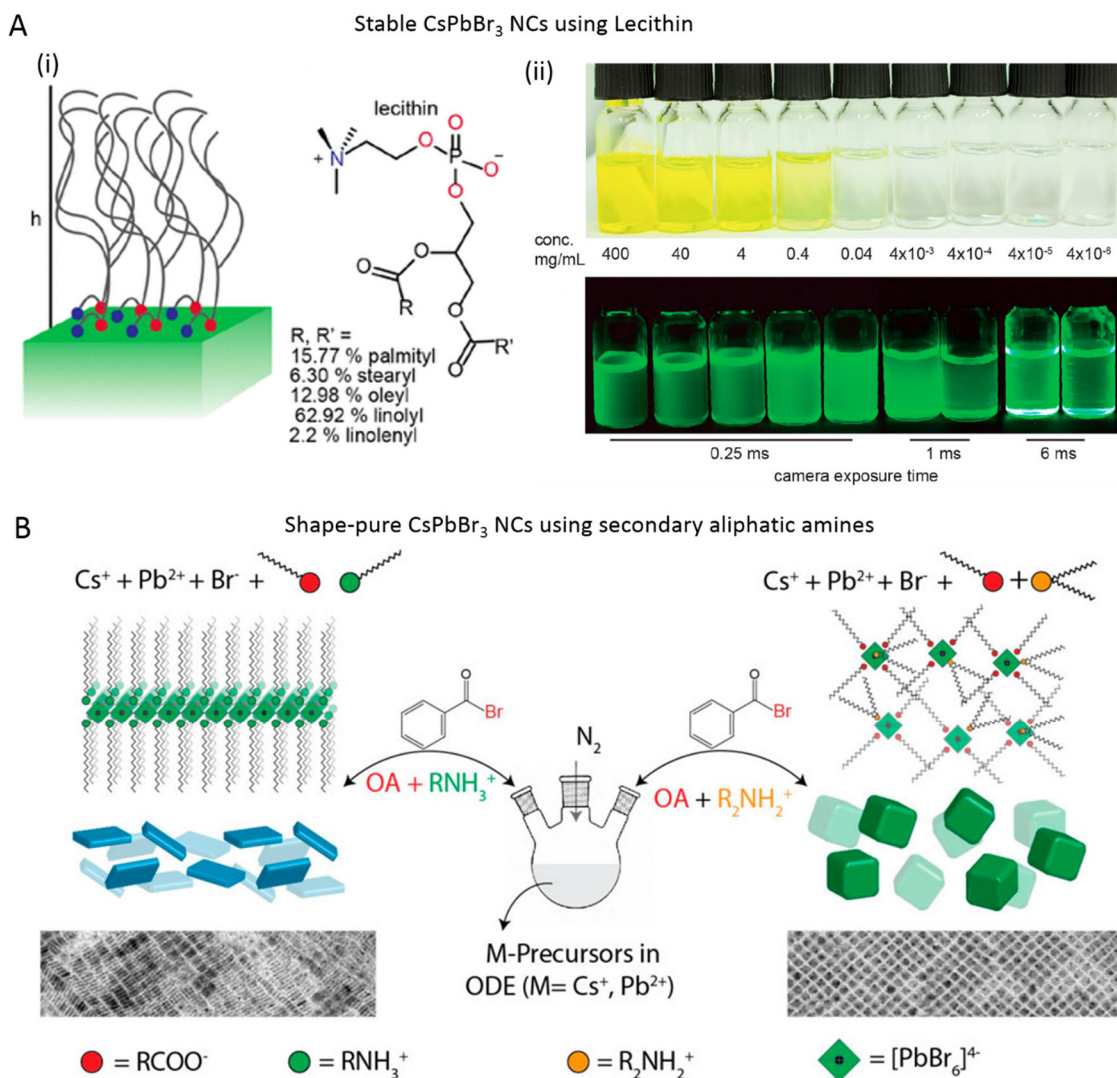
1 Protesescu *et al.*⁷⁰ reported stable and bright green emissive FAPbBr₃ nanocubes by the hot-
2 injection method (Figure 8). In this method, FA and Pb acetate precursors were first dissolved in
3 octadecene in the presence of OA, followed by the injection of pre-synthesized oleylammonium
4 bromide (OAmBr) at 130 °C. This method is slightly different from the typical hot-injection
5 method used for the synthesis of CsPbX₃ NCs, where PbBr₂ was used as precursor for both Pb and
6 Br. This hot-injection method, in which FA-oleate was injected into PbBr₂-OA-OLA solution,
7 produced FAPbBr₃ nanocubes with a much broader size distribution. The nanocubes prepared by
8 this method are rather monodisperse (12 nm) with the PL peak at 530 nm and QY of 85% (Figure
9 4B). In addition, the authors demonstrated that the size of the FAPbBr₃ nanocubes can be tuned
10 from 5 to 50 nm by adjusting either the amount of OAmBr or the reaction temperature, and thus
11 the emission peak is tunable from 470 to 545 nm (Figure 8C).⁷⁰ The purification process after the
12 synthesis of perovskite NCs is critical in order to recover monodisperse NCs. Very recently, Li *et*
13 *al.*⁹¹ proposed size-selective precipitation using a mixture of ethyl acetate and methyl acetate (2:1
14 volume ratio) to obtain strongly-confined nanocubes of different sizes. The precipitation process
15 can be repeated multiple times to obtain FAPbBr₃ nanocubes of different sizes. Hybrid perovskite
16 NCs have also often been prepared by the LARP method and the resulting NCs possess either
17 spherical or nanoplatelet morphology.^{30, 68} However, there is still debate on whether the spherical
18 particles obtained by the LARP method are perovskites or they are the e-beam induced degradation
19 product of perovskite NPLs (see electron microscopy section). In 2017, Levchuk *et al.*¹⁶³ first
20 reported the RT synthesis of brightly luminescent FAPbX₃ nanocubes by the LARP method. The
21 synthesis relies on the rapid injection of a precursor solution (PbX₂ and FAX dissolved in DMF
22 along with OA and OLA) into chloroform. The obtained nanocubes exhibit PLQYs up to 85%.
23 They were able to tune the morphology from nanocubes to NPLs of different thicknesses by varying

1 the OLA/OA ratio. However, the cubic morphology of the particles obtained in this approach is
2 not as perfect as that of the nanocubes synthesized by the hot-injection method. A few months
3 later, Minh *et al.*¹⁶⁶ reported a RT synthesis of FAPbX₃ nanocubes by LARP method, in which
4 pre-synthesized PbX₂-DMSO complexes were used as precursors. In this approach, the precursors
5 (FAX and PbX₂-DMSO complex) were first dissolved in DMF along with OLA, followed by
6 injection of the precursor solution into a mixture of toluene and OA. They were able to tune the
7 size distribution of the nanocubes by varying the amount of OLA used in the reprecipitation
8 reaction. The quality of the nanocubes prepared by this approach appeared to be as good as that of
9 the nanocubes prepared by hot injection. Such a purification approach is also useful for the size-
10 selective separation of inorganic perovskite nanocubes, as demonstrated by Forde *et al.*¹⁵⁸ Very
11 recently, Zu *et al.* reported the synthesis of FAPbBr₃ NCs by the LARP approach using
12 sulfobetaine-18 (SBE-18) as the capping ligand. The authors claimed that the FAPbBr₃ nanocubes
13 prepared using SBE-18 ligands (PLQY≈90.6%, fwhm≈20.5 nm) exhibited higher PLQYs (as well
14 as green color purity) than OLA/OA-capped FAPbBr₃ nanocubes (PLQY≈83.2%, fwhm≈24 nm)
15 prepared under similar conditions.

16 In general, capping agents play a critical role in controlling the shape of NCs during colloidal
17 synthesis, the properties of the NCs, as well as their colloidal stability.¹⁶⁷⁻¹⁶⁹ Recently, there has
18 been a growing interest in the exploration of different ligands for shape-controlled synthesis and
19 stability of perovskite NCs with high PLQYs.¹⁷⁰⁻¹⁷⁷ For instance, in 2017, Liu *et al.*¹⁷³ reported the
20 use of trioctylphosphine-PbI₂ (TOP-PbI₂) as a precursor for the synthesis of phase-stable CsPbI₃
21 nanocubes with near-unity PLQY. Their approach relies on the injection of pre-synthesized
22 TOP-PbI₂ precursor into a reaction mixture containing Cs₂CO₃, OA and OLA in ODE at different
23 temperatures that are set to achieve a desired size for nanocubes. The authors found that these

1 CsPbI₃ nanocubes exhibited higher stability as well higher PLQY compared to the nanocubes
2 prepared without the use of the TOP ligand. The higher PLQY was attributed to the removal of
3 nonradiative traps upon strong binding of TOP to the nanocube surface. Around the same time,
4 Wu *et al.*¹⁷¹ further showed that the incorporation of a highly branched capping ligand,
5 trioctylphosphine oxide (TOPO), along with traditional oleic acid/oleylamine ligand, leads to
6 monodisperse CsPbX₃ nanocubes at high temperature (260 °C). Otherwise, the reaction led to
7 large aggregates at such temperatures in the absence of TOPO. More importantly, the authors
8 found that the TOPO-protected CsPbBr₃ nanocubes exhibited superior stability in ethanol as
9 compared to that of OA/OLA capped CsPbBr₃ nanocubes, regardless of the reaction temperatures
10 at which they were synthesized. The most important factor in the selection of ligands is that they
11 should bind strongly to the NC surface so that they do not detach during the washing process.
12 However, this is not the case for OA/OLA capped perovskite NCs, as their optical properties and
13 applications are often hampered by the colloidal and structural instability caused by the desorption
14 of ligands. To address this issue, Krieg *et al.*¹⁷⁴ proposed zwitterionic capping ligands to enhance
15 the stability and durability of CsPbBr₃ nanocubes, and the authors named the corresponding NCs
16 as “CsPbX₃ (X = Cl, Br, I) nanocrystals 2.0”. The Cs and Pb precursors used in their synthesis are
17 different from the ones used in the hot injection synthesis of OA/OLA capped CsPbX₃ NCs. The
18 synthesis used by Krieg *et al.* is based on the injection of pre-synthesized TOP-X₂ into a mixture
19 of pre-synthesized Cs-2-ethylhexanoate solution, Pb(II)-ethylhexanoate solution and zwitterionic
20 ligand (3-N,N-(dimethyloctadecylammonio)propanesulfonate) at 160 °C. Interestingly, the
21 authors claimed that the morphology and optical properties of these nanocubes were preserved
22 after several washing cycles. The enhanced stability of zwitterionic ligand capped CsPbX₃ NCs
23 was attributed to the simultaneous coordination of each ligand molecule to the surface cations and

1 anions of NC. In a subsequent work, the same group introduced another zwitterionic capping
2 ligand, namely soy lecithin, a mass-produced natural phospholipid, to protect the surface of
3 CsPbX₃ (X = Cl, Br) nanocubes through tight binding to the cations and anions at the surface
4 (Figure 9A-i).¹⁷² The ligand enabled the high yield synthesis of CsPbX₃ nanocubes with a long-
5 term colloidal and structural stability in a broad range of colloidal concentrations (from a few
6 mg mL⁻¹ to >400 mg mL⁻¹), as shown in Figure 9A-ii. They attributed such high colloidal stability
7 to an increased particle–particle repulsion caused by branched chains and ligand polydispersity.
8 In addition, the authors demonstrated the fabrication of micrometer-thick and homogeneous dense
9 CsPbBr₃ nanocube films in a single spin-coating step using ultra-concentrated colloidal solutions.
10 Very recently, Wang *at al.*¹⁷⁶ demonstrated the potential application of polyzwitterionic ligands
11 for phase transfer of CsPbBr₃ nanocubes from a non-polar solvent to a polar solvent through ligand
12 exchange. Such polyzwitterionic ligands on the NC surface enabled the stabilization of CsPbBr₃
13 NCs in a wide range of solvents. These studies suggest that the long chain molecules with multiple
14 functional groups can serve as potential ligands for perovskite NCs with long-term colloidal
15 stability. A similar ligand binding strategy was applied to obtain stable CsPbI₃ NCs with near unity
16 PLQY using 2,2'-iminodibenzoic acid as the bidentate ligand.¹⁷⁵

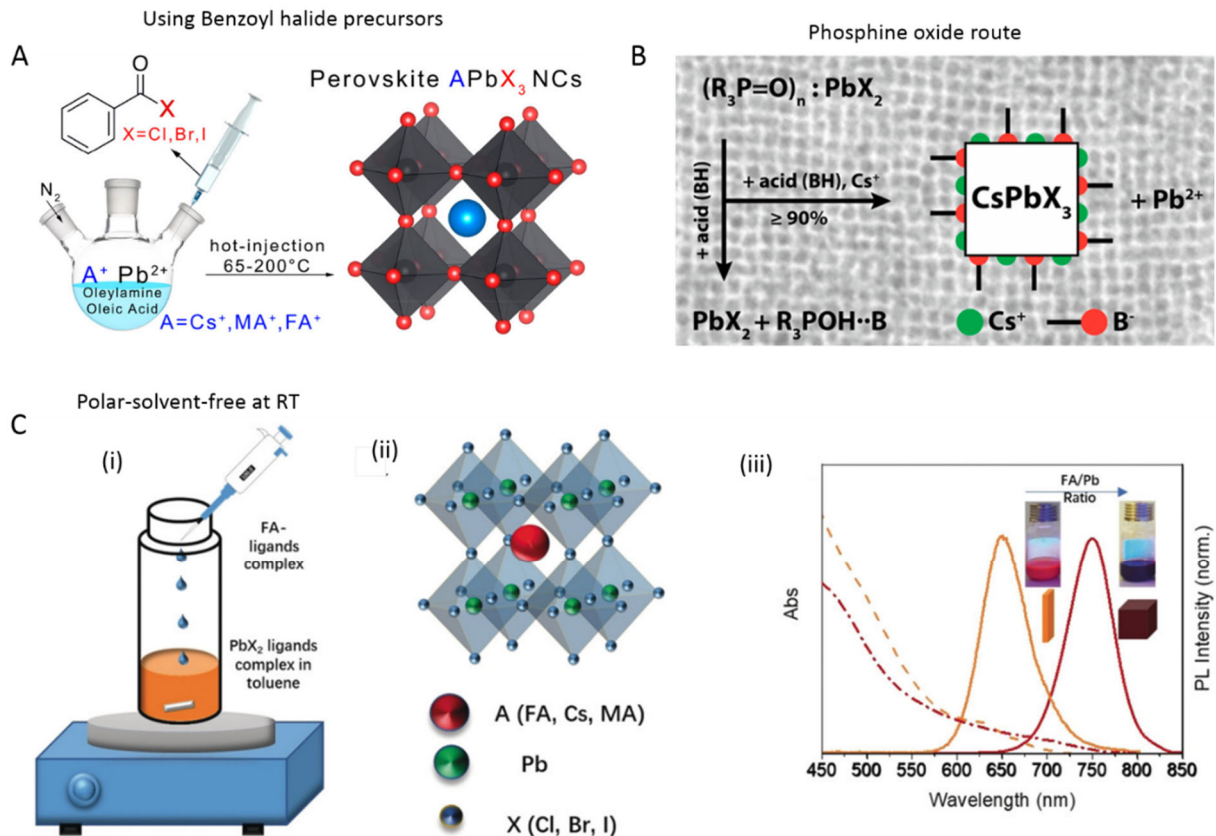


1
2 **Figure 9.** (A) Schematic illustration showing the synthesis of CsPbBr₃ NCs using primary (left)
3 and secondary (right) aliphatic amines. The TEM images showing the resultant products in the
4 respective reactions. Reprinted with permission from Ref.¹⁴⁶ Copyright 2016 American Chemical
5 Society. (B) (i) Schematic of lecithin-ligands forming brush like structure on NC surface and the
6 'h' indicates the brush height (left), and chemical structure of lecithin and statistical occurrence of
7 side chains (R, R') in soy lecithin (right), (ii) Photographs of the colloidal solutions of lecithin-

1 capped CsPbBr₃ NCs at various concentrations under day light (top) and UV light (bottom).

2 Reprinted with permission from Ref.¹⁷² Copyright 2016 American Chemical Society.

3
4 In addition, several groups showed that the chain length of alkylamines and carboxylic acids
5 ligands play an important role in the morphology of perovskite NCs.^{146, 178-179} For instance, Pan *et*
6 *al.* systematically studied the influence of the chain length of alkyl amine and carboxylic acid
7 ligands used in hot injection.¹⁷⁹ They found an increase in the size of the CsPbBr₃ nanocubes
8 when the chain length of the carboxylic acid was shortened at high reaction temperatures. On the
9 other hand, the replacement of OLA with a short-chain amine leads to a change in the morphology
10 from nanocubes to nanoplatelets. However, it is not uncommon to have a small percentage of
11 nanoplatelets in nanocube samples or vice versa. Very recently, Imran and co-workers reported
12 the synthesis of shape-pure, nearly monodisperse nanocubes using secondary aliphatic amine
13 ligands (Figure 9B).¹⁴⁶ Interestingly, their synthesis yielded only nanocubes, regardless of the
14 length of the alkyl chains, oleic acid concentration and reaction temperature. As illustrated in
15 Figure 5B, they proposed that the secondary ammonium ions do not bind to the surface of CsPbBr₃
16 NCs as effectively as primary ammonium ions (oleylammonium in this case) due to steric
17 hindrance, which limits the formation of nanoplatelets. This was further supported by the fact that
18 the surface coverage (6–8%) of secondary ammonium cations is much lower than that of oleate
19 molecules (92–94%), as revealed by nuclear magnetic resonance (NMR) measurements and X-ray
20 photoelectron spectroscopy (XPS).



1

2 **Figure 10.** Reaction schemes of the colloidal synthesis of halide perovskite NCs using: (A)

3 benzoyl halide precursors (Reprinted with permission from Ref.¹⁸⁰ Copyright American Chemical

4 Society 2018), (B) trioctylphosphine oxide (TOPO) instead of aliphatic amines (Reprinted with

5 permission from Ref.¹⁸¹ Copyright American Chemical Society 2018). (C) Schematic illustration

6 of the polar-solvent-free synthesis of halide perovskite NCs at room temperature by spontaneous

7 crystallization (i) and perovskite crystal structure (ii). The shape of the NCs depends on the

8 precursor ratio (iii). Reprinted with permission from Ref.⁵⁵ Copyright John Wiley & Sons, Inc. 2019.

9

10 Currently, colloidal syntheses of $CsPbX_3$ NCs are undergoing further optimization using a

11 variety of precursors and ligands, and many general methods are being developed for better control

12 over their shape, composition and polydispersity.^{55, 165, 169, 180-184} In most synthesis methods that

1 are in use for perovskite NCs, PbX_2 salts are employed as precursors for both Pb and halide ions.
2 This limits the precise control over the reactant species and thus the final chemical composition of
3 colloidal perovskite NCs. To overcome this, Imran *et al.* reported the use of benzoyl halides as the
4 halide precursors for monodisperse $APbX_3$ NCs (in which $A = Cs^+$, $CH_3NH_3^+$, or $CH(NH_2)_2^+$).
5 Their method relied on the injection of benzoyl halide precursor into the reaction medium
6 containing cesium carbonate (organic cation for hybrid perovskite NCs) and lead acetate trihydrate
7 along with ligands at high temperature (Figure 10A, also note that, a similar approach, using
8 instead tris-trimethylsilyl bromide or chloride as halide precursor, was employed by Creutz *et al.*
9 in the synthesis of double halide perovskite NCs).¹⁸⁵ This approach enabled to independently tune
10 the amount of both cations (A^+ and Pb^{2+}) and halide (X^-) precursors in the synthesis. Interestingly,
11 this method produced nearly monodisperse $MAPbX_3$ nanocubes, which seems difficult to obtain
12 using other synthesis methods. In addition, the same group developed an amine-free synthesis of
13 $CsPbBr_3$ nanocubes by complete replacement of the routinely used aliphatic amines with TOPO
14 (Figure 10B). Their synthesis relied on the injection of Cs-oleate into a reaction mixture containing
15 $PbBr_2$ along with TOPO and OA. This reaction yielded only nanocubes regardless of the tested
16 reaction conditions. This was attributed to the absence of primary amines in the reaction medium.
17 The TOPO helped to dissolve the $PbBr_2$ in the reaction medium as well as to establish an acid-
18 base equilibrium with OA in a way similar to the OA-OLA system (Figure 10B). Therefore, the
19 acidity of the reaction environment controlled the reactivity of the PbX_2 precursor, and thus
20 regulated the size of the NCs. Interestingly, only Cs-oleate ligands were present on the surface of
21 the NCs and they were bound dynamically to the NC surface, and therefore an optimum
22 concentration of ligands was necessary to achieve high PLQY. Despite achieving excellent control
23 over the shape purity and polydispersity of ABX_3 perovskite NCs, most discussed synthesis

1 methods require inert atmosphere and high temperature. In contrast, Polavarapu and co-workers
2 demonstrated a polar-solvent-free synthesis for ABX_3 NCs at ambient conditions through
3 spontaneous crystallization of precursor-ligand complexes in a nonpolar organic medium (Figure
4 10C-i).⁵⁵ Furthermore, the shape of perovskite NCs was controllable from nanocubes to
5 nanoplatelets by varying the ratio of monovalent (e.g. formamidinium (FA^+) and Cs^+) to divalent
6 (Pb^{2+}) cation–ligand complexes. (Figure 10C-iii). The authors demonstrated the versatility of this
7 method by applying it to perovskite NCs of different compositions.

8

9 **Isolation and purification of colloidal MHP nanocubes**

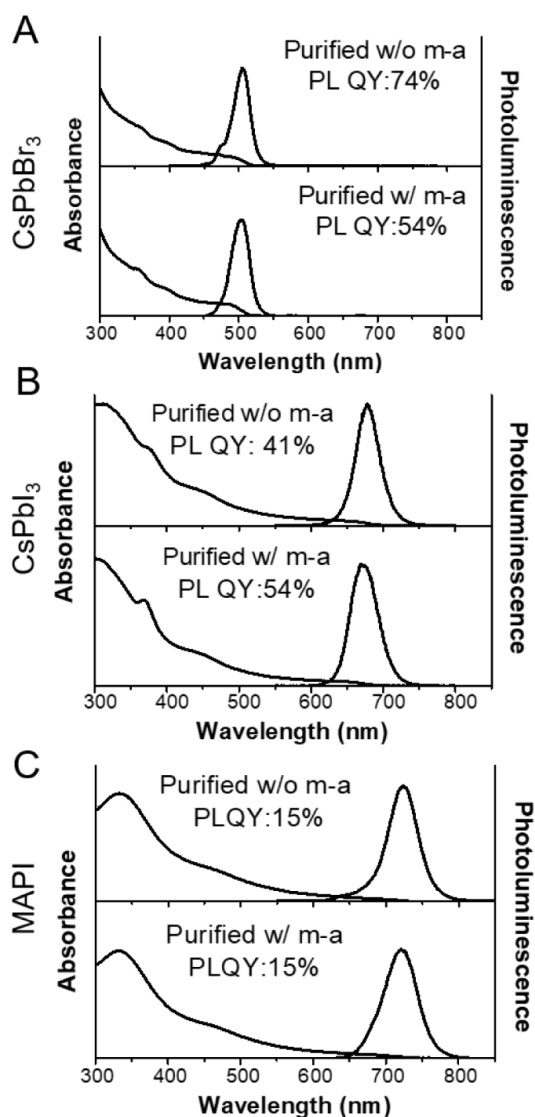
10 Colloidal ligand-stabilized NCs are usually extracted from crude reaction mixtures and purified
11 by antisolvent precipitation.⁶⁰ When the capping ligand layer is hydrophobic, a miscible polar
12 solvent is used to flocculate the NCs, which are then isolated by centrifugation. This precipitative
13 washing procedure removes excess ligand, residual reactants, and molecular byproducts, and is an
14 important step when the NCs are to be used in devices, such solar cells or light-emitting diodes
15 that require charge transport through a deposited layer of nanocrystals.

16 Metal halide perovskite nanocubes can degrade during the purification process. Bound ligands
17 are in dynamic equilibrium with free ligands, and polar solvents can lower the kinetic barrier to
18 ligand exchange and enhance ligand desorption.⁸⁵ “Over-washing” can lead to irreversible
19 aggregation, changes in morphology, a significant drop in photoluminescence (PL), or even more
20 significantly, changes in crystal phase or composition.¹⁸⁶⁻¹⁸⁷ For example, perovskite $CsPbI_3$
21 nanocubes often transform to the yellow non-perovskite phase,¹⁸⁷⁻¹⁸⁸ and $CH_3NH_3PbI_3$ (MAPI)
22 nanocubes decompose into PbI_2 .¹⁸⁹

1 Of course, one way to minimize degradation is to avoid the use of polar solvents, hence simply
2 allowing the nanocubes to settle by centrifuging the crude reaction mixture at high speeds.^{162, 180,}
3 ¹⁹⁰ This mostly works, but it often leaves a significant amount of nanocubes suspended in the
4 supernatant, which are then discarded. A considerable residue of unbound ligand and low volatility
5 reaction solvent (i.e., octadecene) is also retained in the nanocube precipitate.^{85, 191} This residue is
6 a problem for device applications. It also creates challenges during characterization. Transmission
7 electron microscopy (TEM) is difficult with so much excess hydrocarbon impurity, and free ligand
8 contamination strongly interferes with the signal from bound ligand in analytical techniques like
9 Fourier-transform infrared (FTIR) spectroscopy and nuclear magnetic resonance (NMR)
10 spectroscopy.

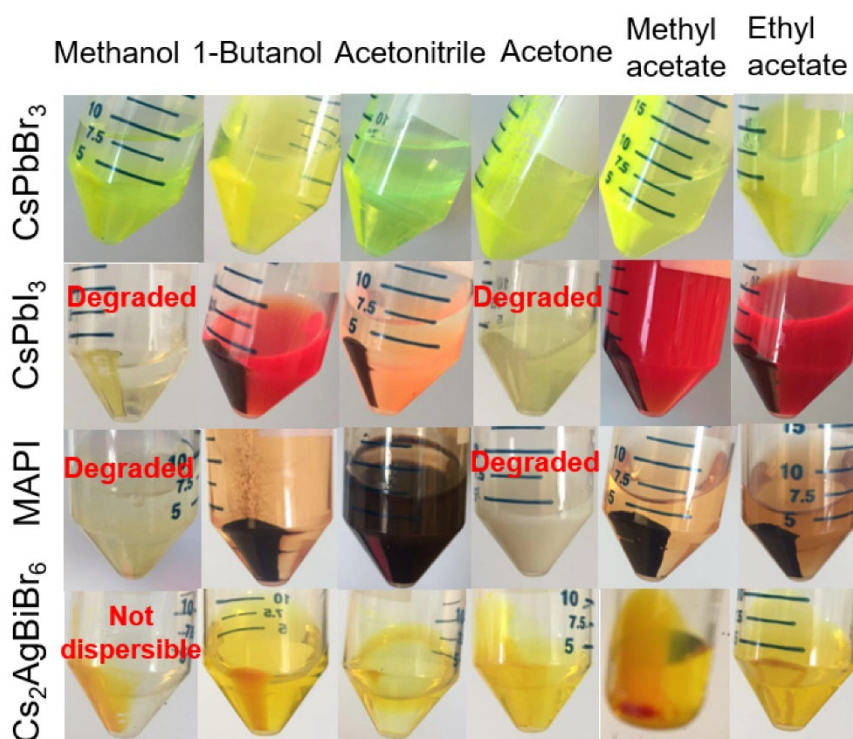
11 With some care, a variety of polar antisolvents can be used to precipitate and purify metal halide
12 perovskite nanocubes without degradation.^{186-187, 192} Methyl acetate has been widely used.^{164, 187,}
13 ¹⁹³⁻¹⁹⁵ Figure 11 shows absorbance and PL spectra of CsPbBr₃, CsPbI₃ and MAPI nanocubes
14 isolated from reaction mixtures by antisolvent precipitation with methyl acetate. The optical
15 properties of these nanocubes are comparable to those of the nanocubes isolated without methyl
16 acetate. Figure 12 shows images of CsPbBr₃, CsPbI₃, MAPI, and Cs₂AgBiBr₆ nanocubes that were
17 precipitated with methanol, 1-butanol, acetonitrile, acetone, methyl acetate and ethyl acetate. A
18 clear and colorless supernatant indicates that all the nanocubes had been precipitated. There are a
19 few situations where nanocubes are still retained in the supernatant, even with the use of the
20 antisolvent. The expected colors of CsPbBr₃, CsPbI₃, MAPI, and Cs₂AgBiBr₆ nanocubes are
21 yellow-green, dark red, dark brown, and golden-orange, respectively. Precipitation of CsPbI₃ and
22 MAPI nanocubes with methanol and acetone turned the color of the precipitate into pale yellow or
23 milky white. Methanol and acetone are not compatible with CsPbI₃ and MAPI nanocubes, and in

1 general, methanol and acetone should be avoided when purifying iodide-containing nanocubes,
2 including FAPbI₃. Methanol and acetonitrile are also not completely miscible with octadecene,
3 and a liquid-liquid phase separation results that retains some nanocubes in the supernatant, which
4 cannot be isolated. CsPbBr₃ nanocubes are the most stable of these metal halide perovskite NCs
5 and were found to be compatible with all of the polar antisolvents shown in Figure 12. Cs₂AgBiBr₆
6 nanocubes are also relatively stable, although methanol does lead to irreversible aggregation and
7 should be avoided.



8

1 **Figure 11.** UV-vis absorbance and PL emission spectra of (A) CsPbBr₃, (B) CsPbI₃ and (C)
 2 MAPbI₃ (MAPI) nanocubes in hexane that were isolated from crude reaction mixtures by
 3 centrifugation with or without the addition of methyl acetate (m-a). The nanocubes were isolated
 4 using an equal volume of m-a added to the crude reaction mixtures, followed by centrifugation at
 5 8000 rpm (8228 × g) for 5 min. Poorly capped nanocubes were removed from the sample by
 6 dispersing the nanocubes in hexane and centrifuging again at 8500 rpm (9289 × g) for 5 min. The
 7 excitation wavelength was 350 nm for CsPbBr₃ and 470 nm for CsPbI₃ and MAPbI₃ nanocubes,
 8 and PL QYs were determined relative to Rhodamine B. Reproduced from Ref.¹⁸⁹. Copyright 2020
 9 American Chemical Society.

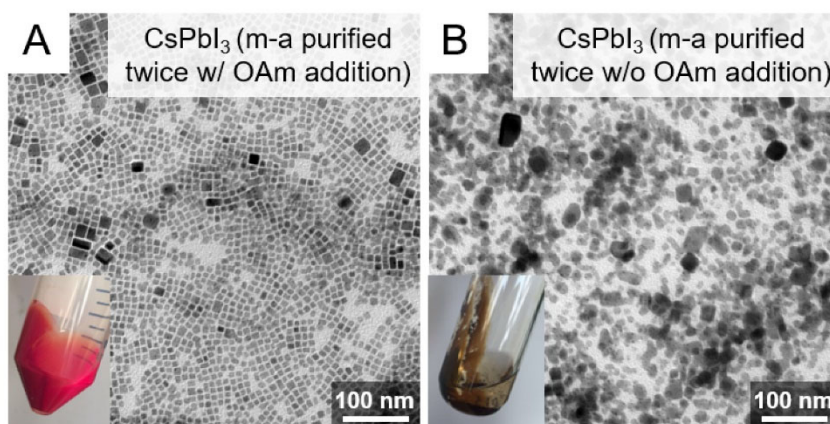


10
 11 **Figure 12.** Photographs of centrifuge tubes with CsPbBr₃, CsPbI₃, MAPI and Cs₂AgBiBr₆ (see
 12 lead-free section for synthesis of Cs₂AgBiBr₆ nanocubes) nanocubes precipitated by
 13 centrifugation (8000 rpm (8228 × g) for 5 min) from crude reaction mixtures with six different

1 polar solvents using equivalent volumes of polar solvent and crude reaction mixture. Nanocube
2 concentrations were about 5-10 mg/mL. Some variation in nanocube concentration occurs because
3 of the differences in reaction yields. Based on measured product yields, the concentrations were
4 4.3 mg/mL for Cs₂AgBiBr₆, 9 mg/mL for CsPbI₃, and 7 mg/mL for CsPbBr₃ and MAPbI₃. Images
5 are reproduced from Ref.¹⁸⁹. Copyright 2020 American Chemical Society.

6
7 In addition to the antisolvent chemistry, the conditions used to precipitate the nanocubes are
8 important. Some of these conditions may seem trivial, like centrifugation time for example.^{186-187,}
9 ¹⁹⁶⁻¹⁹⁷ For CsPbI₃ nanocubes, 5-10 min of centrifugation at 8000 rpm (8228 × g) works well.
10 Longer centrifugation times can result in drastically different results, yielding CsPbI₃ nanocubes
11 with very poor dispersibility, low PL QYs, and nanocubes largely transformed to the yellow phase.
12 The precipitate should be separated from the supernatant immediately after centrifugation.
13 Degradation of the sample can continue to occur when the nanocubes remain in the presence of
14 the large volume of polar solvent. The volume ratio of antisolvent to solvent is important. For
15 example, when CsPbI₃ nanocubes are dispersed in a crude reaction mixture of octadecene or
16 redispersed in hexane at a concentration of about 10 mg/mL, an antisolvent to solvent volume ratio
17 in the range of 1-2 is usually appropriate. This is not quite enough antisolvent to precipitate all of
18 the nanocubes in the sample, but more antisolvent can end up degrading the nanocubes. An
19 antisolvent:solvent ratio of 3, for example, will precipitate nearly all of the nanocubes, but the
20 nanocubes will not be able to be redispersed easily and the PL QYs will be significantly reduced.
21 Anhydrous solvents should be used to minimize degradation induced by water. Although not
22 always necessary, the purification can be carried out in a glovebox under inert conditions. Using
23 that procedure tends to provide nanocubes with longer shelf-life. There is a risk, however, that the

1 sample starts degrading because the extra time spent transferring samples in and out of a glovebox
2 prolongs the exposure of the nanocubes to antisolvent, which can induce such degradation. In
3 general, the purification process should be optimized for each type of nanocube and the synthetic
4 approach that is used. Differences in capping ligand chemistry and concentrations of the crude
5 reaction mixture due to variations in the yields of alternative reactions can all lead to changes in
6 the optimized antisolvent precipitation conditions.



7
8 **Figure 13.** TEM images of CsPbI₃ nanocubes that were precipitated twice with methyl acetate
9 (A) with and (B) without the addition of oleylamine before the second precipitative washing step.
10 The insets show photographs of the products obtained after centrifugation. The nanocubes in (A)
11 were isolated after adding 10 μ L of oleylamine to 3 mL of CsPbI₃ nanocubes in hexane at a
12 concentration of 10 mg/mL. Both samples in (A) and (B) were centrifuged at 8000 rpm ($8228 \times$
13 g) for 3 min after adding 3 mL of methyl acetate (1:1 v:v methyl acetate: hexane). Reproduced
14 from Ref.¹⁸⁹. Copyright 2020 American Chemical Society.

15
16 The use of antisolvents to purify metal halide perovskite nanocubes is essential in some cases.
17 Analytical techniques, like NMR spectroscopy, require samples that are nearly completely free of
18 unbound ligand and other organic impurities. One precipitative washing step is not enough to

1 achieve the necessary level of purity required for these measurements. At least two cycles of
2 precipitative washing are needed.⁸⁵ A second precipitative washing step with antisolvent can
3 degrade metal halide perovskite nanocubes. To prevent degradation, a small amount of excess
4 ligand (i.e., oleylamine) must be added before the second precipitative wash.¹⁸⁹ Figure 13 shows
5 TEM images and photographs of CsPbI₃ nanocubes after a second precipitation with methyl
6 acetate. Without additional oleylamine, the CsPbI₃ nanocube product ends up with a dull brown
7 color. X-ray diffraction (XRD) showed that the nanocubes are still mostly in the perovskite
8 phase,¹⁸⁹ but have lost most of their luminescence and their distinct cubic shape. They do not
9 redisperse in hexane. In contrast, the nanocubes in Fig. 13A that were precipitated after an addition
10 of oleylamine (10 μL) retain their luminescence and cubic shape, and disperse readily in hexane.
11 The NMR spectra of these nanocubes also do not show the presence of any free unbound ligand.^{85,}
12 ^{148, 189} For some nanocubes, however, the addition of oleylamine before a second precipitative
13 wash can lead to degradation, as in the case of Cs₂AgBiBr₆ nanocubes.¹⁹⁸ Each sample requires
14 optimization of the best purification conditions, but in general, precipitation with polar antisolvents
15 is an effective way to isolate and purify metal halide perovskite nanocubes.

16 **Summary and outlook of perovskite nanocubes**

17 A wide range of synthetic methods has been reported for monodisperse CsPbX₃ (X = Cl, Br, and
18 I) nanocubes with 80-100% PLQY (for X = Br and I) under optimized conditions. Every method
19 has its own advantages and disadvantages. To date, HI and LARP methods have been extensively
20 explored for the synthesis of inorganic perovskite NCs.^{15, 199} In particular, HI synthesis is being
21 heavily explored for shape-controlled synthesis of CsPbX₃ NCs using different kinds of precursors
22 and ligands. The role of acid-base equilibria of ligands, precursor types, and the chain length of
23 amines in the shape control of CsPbBr₃ nanocubes have been explored.^{178-179, 200 201} In most

1 synthesis methods, long-chain alkylamines have been used as ligands for stabilization of
2 perovskite nanocubes. However, they are problematic for device applications as they block the
3 transport of charge carriers. Therefore, it is important to explore short-chain ligands in future
4 studies for the stabilization of perovskite nanocubes. Although perovskite nanocubes exhibit
5 extremely high PLQYs right after synthesis, their purification leads to a significant reduction in
6 PLQY (~20-40%) due to the removal of ligands from the NC surface. To overcome this problem,
7 bidentate ligands (or chelating ligands) have been proposed for enhanced stability and to retain
8 high PLQY even after purification of nanocubes.^{202 203} While CsPbBr₃ nanocubes have been found
9 to be relatively stable over a long time, it is still challenging to obtain strongly luminescent, phase-
10 stable CsPbI₃ nanocubes. Various ligands have been proposed for improving their cubic phase
11 stability, however, the stability is still not comparable to that of CsPbBr₃ nanocubes. On the other
12 hand, despite great progress in the synthesis of inorganic perovskite nanocubes, organic-inorganic
13 hybrid nanocubes have been less explored regarding their shape-controlled synthesis, and future
14 studies could be focused in this direction. In addition, more studies are needed in the future to
15 obtain highly luminescent and stable lead-free perovskite nanocubes (see later sections on lead-
16 free NCs).²⁰⁴

17

18 **1.3 NANOPATELETS**

19 **Origins of perovskite nanoplatelets**

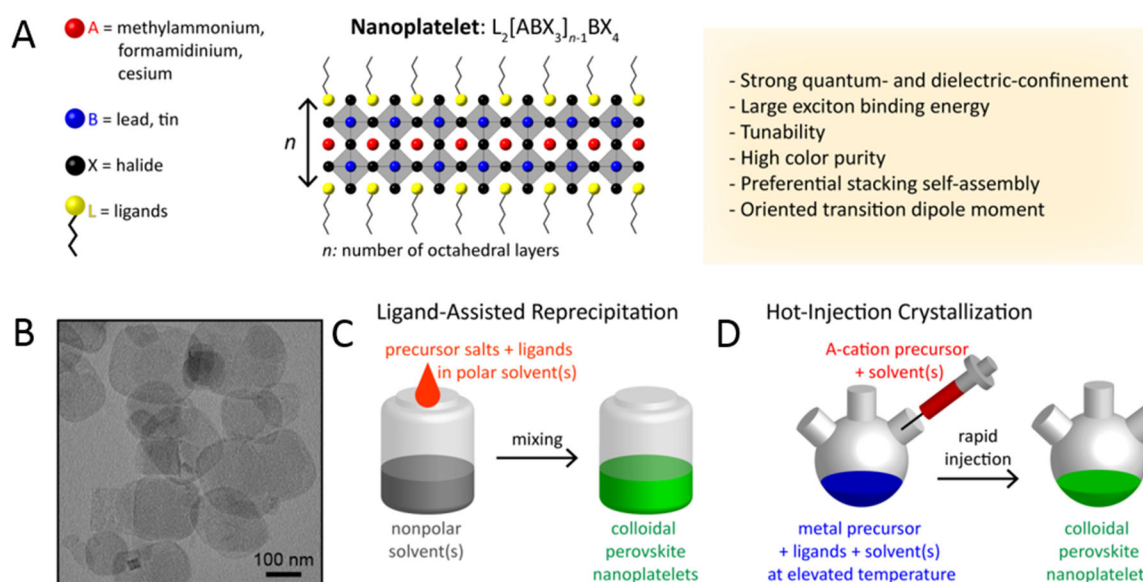
20 Two-dimensional (2D) metal halide perovskite nanoplatelets (NPLs) trace their origin to the
21 synthesis of Ruddlesden-Popper (R.-P.) phase layered perovskite crystals. In the 1990s, it was
22 discovered that substituting the usual small A-site cations (e.g. methylammonium (MA), FA, Cs)
23 for larger organic cations (e.g. butylammonium) could induce the crystallization of layered

1 structures.^{6, 128, 205-209} These layered perovskite crystals consist of alternating inorganic layers of
2 lead halide octahedra and organic cations; the inorganic metal halide layer primarily determines
3 the optoelectronic properties and the large organic cation layer electronically isolates the inorganic
4 layers. Because of quantum-confinement effects, layered perovskites exhibit drastically different
5 properties compared to the bulk 3D phase.²¹⁰ Also, layered perovskites showed enhanced stability
6 compared to 3D counterparts due to a negative enthalpy of formation²¹¹⁻²¹³ as well as the presence
7 of organic spacer layers that protect inorganic layers from external factors such as oxygen and
8 moisture.¹²

9 Around 2015, multiple groups reported the synthesis of colloidal perovskite nanoplatelets
10 (NPLs)^{17, 19, 49, 214} – 2D perovskite crystals much like their R.-P. predecessors, but dispersed in
11 solution. Colloidal perovskite NPLs are generally characterized by the chemical formula of
12 $L_2[ABX_3]_{n-1}BX_4$ (Figure 14A & B) where n indicates the number of inorganic metal halide
13 octahedral layers in thickness. Thicknesses of NPLs are confined to a few unit cells and NPLs can
14 tolerate lateral dimension dispersity as long as thickness homogeneity is ensured.⁴⁸ Surface ligands
15 act as surfactants, entropically stabilizing the 2D crystals in solution, but their role in 2D NC
16 formation is debated.²¹⁵⁻²¹⁶ Since layered R.-P. perovskites can be thought as a crystal of stacked
17 NPLs with electronically decoupled inorganic layers, there are many parallels between layered
18 perovskites and perovskite NPLs. They seem to be tunable over the same range and composition
19 with identical bandgap and optical properties,^{19, 48, 210, 217-219} which implies that previous studies on
20 layered perovskites can also shed light on the properties of colloidal perovskite NPLs.

21 Colloidal perovskite NPLs were first identified as a side product of MAPbBr₃ NC synthesis,²¹⁴
22 but very quickly the ability to precisely control thickness was reported.^{17, 19, 49, 162} Following these
23 initial works, subsequent efforts focused on developing refined synthetic protocols for NPLs with

1 well-controlled thicknesses and improved material properties. For instance, the color of emission
 2 can be tuned by varying thickness and composition.^{17, 19, 49, 219-222} Also, reports on the tunability of
 3 surface-capping ligands, ranging from short ligands for optimal charge transport behavior to long
 4 and functionalized ligands for enhanced stability, have highlighted the possibility of optimizing
 5 surface properties of NPLs for specific applications.²²²⁻²²⁴ It has also been reported that the lateral
 6 dimension of NPLs, which may affect electronic transport in NPL optoelectronic devices, can be
 7 tuned from tens of nanometers^{19, 49, 162, 220, 225-227} to several micrometers^{48, 219, 228-229} without loss of
 8 quantum confinement in the vertical direction.



9
 10 **Figure 14.** Structure of colloidal perovskite nanoplatelets and synthetic approaches. (a) Perovskite
 11 nanoplatelet structure and its unique properties. (b) Transmission Electron Microscopy (TEM)
 12 image of nanoplatelets. Reprinted with permission from Ref. ²¹⁹. Copyright 2016 American

1 Chemical Society. (c) Schematic illustration of ligand-assisted reprecipitation method. (d)
2 Schematic illustration of hot-injection crystallization method.

3

4 **Unique properties of nanoplatelets**

5 2D nanoplatelets possess unique characteristics specific to their 2D shape (Figure 14A). The
6 exciton Bohr radius of lead halide perovskite materials has been reported to be ~ 3 nm or larger,
7 depending on composition.^{15, 17, 48-49, 129} It is synthetically challenging to prepare 0D NCs with such
8 small dimensions, however, perovskite NPLs as thin as 0.6 nm in thickness^{219, 223, 230-231} exhibiting
9 strong quantum- and dielectric-confinement can be easily fabricated. This strong confinement
10 induces excitonic absorption and emission features to be blue-shifted from those of the bulk
11 perovskite phase by up to 0.7 eV,^{219, 232} which enables the synthesis of bluer light-emitting NCs.
12 Spatial confinement of excitons in 2D structures also yields large exciton binding energies,
13 reaching up to several hundred meV,^{100, 208-209, 232} which can facilitate efficient recombination of
14 excitons. Moreover, monodisperse NPLs exhibit superior emission color purity due to atomically
15 precise thickness homogeneity. Achieving monodispersity is of great importance for NPLs since
16 bandgaps of strongly-confined NPLs show significantly larger shifts when the thickness
17 changes,^{48, 219, 221} compared to other weakly confined NCs.^{15, 233} Nonetheless, monodisperse
18 nanoplatelets have been widely demonstrated.^{19, 49, 62, 162, 219-220, 224, 226, 228-229, 231, 234-235}

19 A 2D structure is ideal for integration into optoelectronic devices. A key feature of 2D NPLs
20 is the tendency for the transition dipole moment to preferentially orient within the 2D plane,²³⁶⁻²³⁷
21 which is advantageous for optical coupling. Additionally, NPLs exhibit face-to-face stacking^{19, 226,}
22 ²³⁴ and preferential face-down assembly on a given substrate.^{219, 223, 229, 238} This tendency –
23 combined with transition dipole anisotropy – leads to preferential emission in the out-of-plane

1 direction.²³⁷ Moreover, large lateral dimensions of NPLs^{17, 219, 228-229} can potentially be utilized to
2 minimize grain boundaries in-plane and lower the percolation threshold for charge transport.²³⁹

3 **Synthesis of nanoplatelets**

4 Numerous synthetic approaches to perovskite NPLs have been developed. In this review, we
5 will first discuss the two most widely used techniques – LARP (Figure 14C) and hot-injection
6 crystallization (Figure 14D) – and then introduce other synthetic approaches. The ligand-assisted
7 reprecipitation (LARP) method usually consists of dissolving perovskite NPL precursor salts in
8 relatively polar solvent(s) (e.g. N,N-Dimethylformamide (DMF), Dimethyl sulfoxide (DMSO))
9 and then mixing it with less polar solvent(s) (e.g. Toluene, hexane) to induce crystallization at
10 room-temperature. In 2015, Sichert *et al.* published the first synthesis of thickness-controlled
11 MAPbBr₃ NPLs via LARP (Figure 15A).¹⁷ They dissolved NPL precursors (MABr, PbBr₂ and
12 OABr) in DMF and NPs were then crystallized upon mixing the solution with excess toluene.
13 Precise tuning of NPL thickness was achieved by varying the methylammonium-to-
14 octylammonium ratio in the precursor solution. Soon after, Akkerman *et al.* reported the synthesis
15 of $n = 3 - 5$ CsPbBr₃ NPLs with modified LARP process where the addition of acetone into the
16 precursor solution mixture induced destabilization of precursor complexes and initiated NPL
17 crystallization under ambient conditions (Figure 15B).⁴⁹ They also showed that the bandgap of the
18 NPLs can be continuously tuned by an anion exchange reaction. Later, Weidman *et al.* published
19 $n = 1$ and $n = 2$ perovskite NPLs with wide ranging composition (A = MA/FA/Cs, B = Pb/Sn, X =
20 Cl/Br/I, ligand = butylammonium/octylammonium) via LARP by simply varying the
21 stoichiometric ratios of precursor solutions (Figure 15C).²¹⁹ Tong *et al.* demonstrated the breakup
22 of large MAPbX₃ NCs synthesized via LARP into NPLs by diluting the solution, which triggered
23 osmotic swelling by solvent (Figure 15D).²⁴⁰ In addition, Sun *et al.* carried out a systematic study

1 and showed that choosing the right combination of ligand species plays crucial role in determining
2 the shape of the NCs synthesized via LARP.²⁴¹

3 In general, LARP enables facile synthesis of colloidal perovskite NPLs with easily tunable
4 composition and ligands. Moreover, LARP can be highly cost-effective as it delivers colloidal
5 perovskite NPLs in ambient atmosphere at room-temperature. However, thinner NPLs synthesized
6 via LARP tend to exhibit lower photoluminescence quantum yield (PLQY)^{17, 219, 223} and it is
7 difficult to target thicker ($n \geq 3$) dispersions with good thickness control.^{223, 242-243} Recent works
8 have focused on refining the synthesis and improving material properties – expanding synthetic
9 capability,^{62, 222, 230} improving thickness selectivity,^{223, 230} modulating surface properties by
10 incorporating new ligand species,²²²⁻²²³ boosting photoluminescence quantum yield (PLQY)^{62, 221,}
11 ²³⁵ and enhancing material stability.²³⁸ Although significant advancements have been made in the
12 past few years, there is still ample room for further development.

13 Another widely used synthetic approach is hot-injection (HI) crystallization, as described in
14 section 1. The HI approach is based on the rapid injection of a precursor solution into a solution
15 containing the other precursors, ligands and solvent(s), at elevated temperature. The HI synthesis
16 enables the separation of nucleation and growth of NCs so that it can deliver high-quality NCs.⁵³
17 Also, it does not involve any polar solvent which could potentially be detrimental to colloidal
18 perovskites. First reports of perovskite NPL synthesis via the HI protocol^{19, 162} came out a few
19 months after Protesescu et al. published the synthesis of CsPbX₃ quantum dots via HI.¹⁵ Bekenstein
20 et al. found that lowering the temperature of cesium precursor injection into lead halide precursor
21 solution results in the formation of $n = 1 - 5$ CsPbBr₃ NPLs (Figure 15E).¹⁹ They also
22 demonstrated NPL bandgap tuning via halide exchange reaction. Around the same time, Vybornyi
23 et al. reported the HI synthesis of $n = 3$ MAPbBr₃ NPLs (Figure 15F).¹⁶² Along with the previous

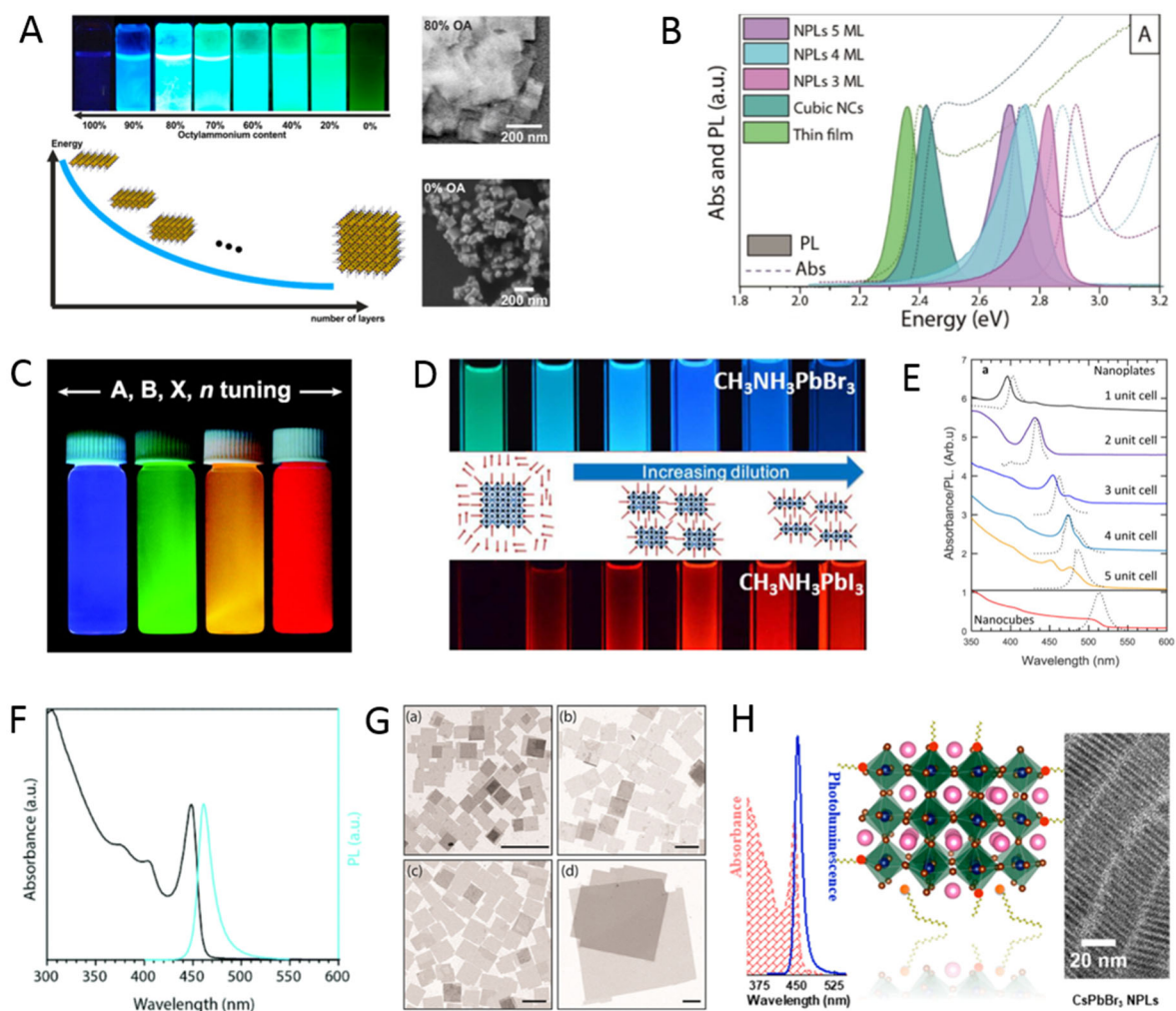
1 report from Sichert et al. on the synthesis of MAPbBr₃ NPLs via LARP,¹⁷ those reports opened up
2 the field of thickness-controlled colloidal perovskite NPL synthesis. However, it was pointed out
3 that lateral dimensions of perovskite NPLs synthesized via HI (10 – 100 nm)^{19, 162, 220} are generally
4 smaller than those of NPLs synthesized via LARP (100 – 1000 nm).^{17, 219, 223} In response to it,
5 Shamsi et al. showed that the lateral dimension of CsPbBr₃ NPLs can be increased to several
6 microns by adjusting the ratio of shorter ligands to longer ligands in the synthetic mixture during
7 the HI synthesis (Figure 15G).²²⁸ Similarly, Zhang et al. published the synthesis of micron-sized *n*
8 = 2 FAPbBr₃ NPLs.²²⁹ Furthermore, Pan et al. provided deeper insight into HI synthesis by
9 identifying the key factors that control the shape of the NCs in HI synthesis – reaction temperature
10 and choice of ligands.²⁴⁴

11 Recent works on NPL synthesis via HI have focused on refining the synthesis of NPLs
12 accompanied by detailed structural characterizations²²⁰ and understanding the complex dynamics
13 of the HI reaction.^{148, 225} However, the HI synthesis is still highly focused on Cs-based NPLs^{19, 148,}
14 ^{220, 225, 228, 244} and there is only a limited number of reports on organic cation-based NPLs.^{162, 229}
15 Compared to LARP-synthesized NPLs, HI-synthesized NPLs are generally smaller in lateral
16 dimensions^{19, 162, 220} and usually capped by longer ligands,^{17, 19, 219-220} which could undermine
17 electronic transport properties. Since the HI method requires high temperature and inert
18 atmosphere, scalability and cost-effectiveness could be greater barriers to eventual
19 commercialization for HI than for LARP. Historically, HI-synthesized NPLs have shown higher
20 PLQY,^{19, 49} though the PLQY of LARP-synthesized NPLs has recently become comparable.^{62, 221,}
21 ^{235, 240} Thus, more efforts on further developing HI synthesis of perovskite NPLs are needed.

22 Apart from LARP and HI, other creative approaches to perovskite NPL synthesis have been
23 demonstrated. Shamsi et al. showed that quantum-confined CsPbBr₃ NPLs can be synthesized by

1 mixing of cesium oleate solution with PbBr₂-ligands complex solution, adding isopropanol to
2 initiate nucleation and then heating the solution to grow NPLs.²⁴⁵ A few years later, Shamsi et al.
3 slightly modified this heat-up method and demonstrated the synthesis of hexylphosphonate-capped
4 NPLs (Figure 15H).²²⁴ They observed that stronger binding of phosphonate ions compared to
5 conventional alkylammonium ions to NPL surface^{224, 244} greatly improved the stability of NPLs
6 and suppressed transformation of NPLs into thicker, less-confined structures which can result in
7 the loss of desirable optical properties.^{238, 245-246} Huang et al. reported the scalable synthesis of $n =$
8 4 FAPbI₃ NPLs by mixing FA-ligands complex solution with PbX₂-ligands complex solution in
9 toluene.²²⁶ This approach was a hybrid of HI and LARP in that it was done under ambient
10 conditions at room temperature but no polar solvent was involved. Another interesting approach
11 is ultrasonication-assisted synthesis; Tong et al.²⁴⁷ and Hintermayr et al.²⁴⁸ reported the synthesis
12 of perovskite NPLs by sonicating the dispersion of perovskite precursors in the presence of
13 coordinating ligands. Lastly, Dou et al. demonstrated the direct synthesis of atomically-thin
14 monolayer of L₂BX₄ perovskite on the substrate by dropcasting the solution of precursor salts
15 dissolved in DMF/chlorobenzene co-solvent.²⁴⁹ Even though this was not a ‘colloidal nanoplatelet’
16 synthesis, it introduces another promising route to deposit a thin layer of 2D perovskites.

17



1
2 **Figure 15.** Advancements of colloidal perovskite nanoplatelet synthesis. (A) Synthesis of
3 thickness-controlled MAPbBr₃ nanoplatelets via ligand-assisted reprecipitation (LARP). (B)
4 Synthesis of CsPbBr₃ nanoplatelets via LARP. (C) Thickness and compositional tunability of
5 nanoplatelets via LARP. (D) Dilution-induced nanoplatelet formation via LARP. (E) Thickness-
6 controlled CsPbBr₃ nanoplatelet synthesis via hot-injection crystallization (HI). (F) $n = 3$
7 MAPbBr₃ NPL synthesis via HI. (G) NPL lateral dimension control through HI synthesis. (h)
8 Synthesis of hexylphosphonate-capped NPLs with enhanced stability via heat-up approach.
9 Reprinted with permission from (A) Ref.¹⁷. Copyright 2015 American Chemical Society (B) Ref.
10 ⁴⁹. Copyright 2016 American Chemical Society (C) Ref.²¹⁹. Copyright 2016 American Chemical

1 Society. (D) Ref. ²⁴⁰. Copyright 2016 American Chemical Society (E) Ref. ¹⁹. Copyright 2015
2 American Chemical Society (F) Ref. ¹⁶². Published by The Royal Society of Chemistry (G) Ref.
3 ²²⁸. Copyright 2016 American Chemical Society. (H) Ref. ²²⁴. Copyright 2020 American Chemical
4 Society.

6 **Outstanding questions and future opportunities**

7 Although various synthetic techniques have been developed for colloidal perovskite NPLs, a
8 complete understanding of anisotropic perovskite NPL growth is lacking. How can thin 2D
9 structures grow from an isotropic crystal lattice and homogeneous solvent environment? An in-
10 depth study carried out by Riedinger et al. on the formation of 2D CdSe NPLs from isotropic
11 materials²¹⁵ provides some interesting insight. In that paper, the authors started with
12 experimentally verifying that CdSe NPLs can be formed in an isotropic environment in the absence
13 of any molecular mesophases, and then formulated a growth model based on experimental results.
14 General theory of nucleation and growth predicts the growth of a NC to occur through the
15 nucleation of a new island on one of the facets; when this island reaches a critical size, expansion
16 of the island becomes thermodynamically favorable and leads to the formation of a complete new
17 layer on that facet. Riedinger et al. showed that when specific criteria are met – namely, 1) NC
18 formation occurs through nucleation-limited growth, 2) initial small crystallites can adopt
19 anisotropic 2D shapes due to the random fluctuations in the reaction mixture, and 3) the thickness
20 of this initial crystallite is smaller than the critical island size – certain combinations of volume,
21 surface and edge formation energies of NCs in the system can lead to a lower nucleation barrier
22 for narrower facets compared to large planar facets. This lower nucleation barrier results in the
23 faster growth on the narrower facet, which can eventually yield anisotropic 2D NPLs. Their model

1 also predicts higher narrow-facet nucleation barrier for thicker NPLs than thinner NPLs, and it is
2 consistent with the observations by Bekenstein et al.¹⁹ and Pan et al.²⁴⁴ that thicker perovskite
3 NPLs were formed at higher reaction temperatures. Although Riedinger et al. studied the CdSe
4 NPL system, their theoretical model is generalizable to any isotropic materials system, including
5 perovskite NPLs. It should also be noted that, along with reaction temperature, previous reports
6 listed a careful choice of ligands, precise control of perovskite precursor composition and
7 concentration of precursor solution as other key factors in the shape-controlled synthesis of
8 perovskite NPLs.^{148, 241, 244} We speculate that optimized synthetic conditions in those reports may
9 in fact reflect precisely tuned volume, surface and edge formation energies of the NC in the system
10 where the formation of anisotropic 2D NPLs is favored. And more recently, Burlakov and
11 coworkers proposed a CsPbBr₃ NPL formation mechanism based on the competitive nucleation of
12 an inorganic perovskite layer and an organic ligand layer.²¹⁶ Being consistent with the discussion
13 above, their work also focused on temperature and interaction energies between constituents as
14 primary factors that determine nucleation kinetics. Through a combination of theoretical and
15 experimental work, they showed that, under certain conditions, narrower facets can favor crystal
16 layer nucleation while wider facets are more effectively passivated by ligand layer formation,
17 which can lead to anisotropic two-dimensional crystal growth. Their theoretical prediction of
18 preferential formation of thinner NPLs at low reaction temperature was experimentally verified,
19 and is also consistent with the observations by Bekenstein et al.¹⁹ and Pan et al.¹⁷⁹ But still, this
20 picture is far from complete and we do not yet have a firm grasp on the mechanism of how
21 anisotropic NPL are formed from isotropic environments.

22 In addition to open questions regarding nucleation and growth, a detailed understanding of
23 electronic structure in 2D NPLs is still lacking. Furthermore, it is unclear to what extent perovskite

1 NPLs actually exist as isolated sheets in solution rather than small crystallites of RP phase.²⁵⁰
2 Spontaneous stacking^{162, 234} and slow precipitation of NPLs²²³ in concentrated solutions have been
3 observed, which may indicate the existence of large RP phase crystallites with poor colloidal
4 stability. Thus, a systematic study on the behavior of NPLs in colloidal solution is needed for a
5 better solution processability. In addition, efforts are underway to tackle the main drawbacks of
6 perovskite NPLs, namely improving their low PLQY^{62, 235} and enhancing the stability.²³⁸
7 Additional goals include the synthesis of stable lead-free NPLs,²¹⁹ doping NPLs to expand their
8 functionality,²⁵¹ and integrating NPLs into state-of-the-art optoelectronic devices (see also later
9 sections on these various topics).²²¹

10 **1.4 NANOWIRES**

11 Semiconductor nanowires (NWs) are fundamental nanoscale building blocks for nanophotonic
12 platforms such as interconnects, waveguides, and optical cavities. Due to the single-crystallinity
13 and well-controlled interfacial engineering, individual NWs or their assemblies are also ideal
14 model systems for the fundamental study of charge transfer and carrier dynamics at the nanoscale.
15 Metal halide perovskites have demonstrated a remarkable level of defect tolerance. The ionic
16 nature of halide perovskites makes them interesting systems to understand charge dynamics in
17 defect tolerant materials compared with covalent inorganic semiconductors. In addition, low-
18 temperature synthesis and facile ion exchange chemistry provide new opportunities for
19 understanding alloy and heterostructure formation to explore nanoscale properties. In this section,
20 we review the synthetic approaches of inorganic halide perovskite NWs, their self-assembly, anion
21 exchange, phase transition and their various applications, especially in photonics and
22 thermoelectrics.

1 **Synthesis of inorganic perovskite nanowires**

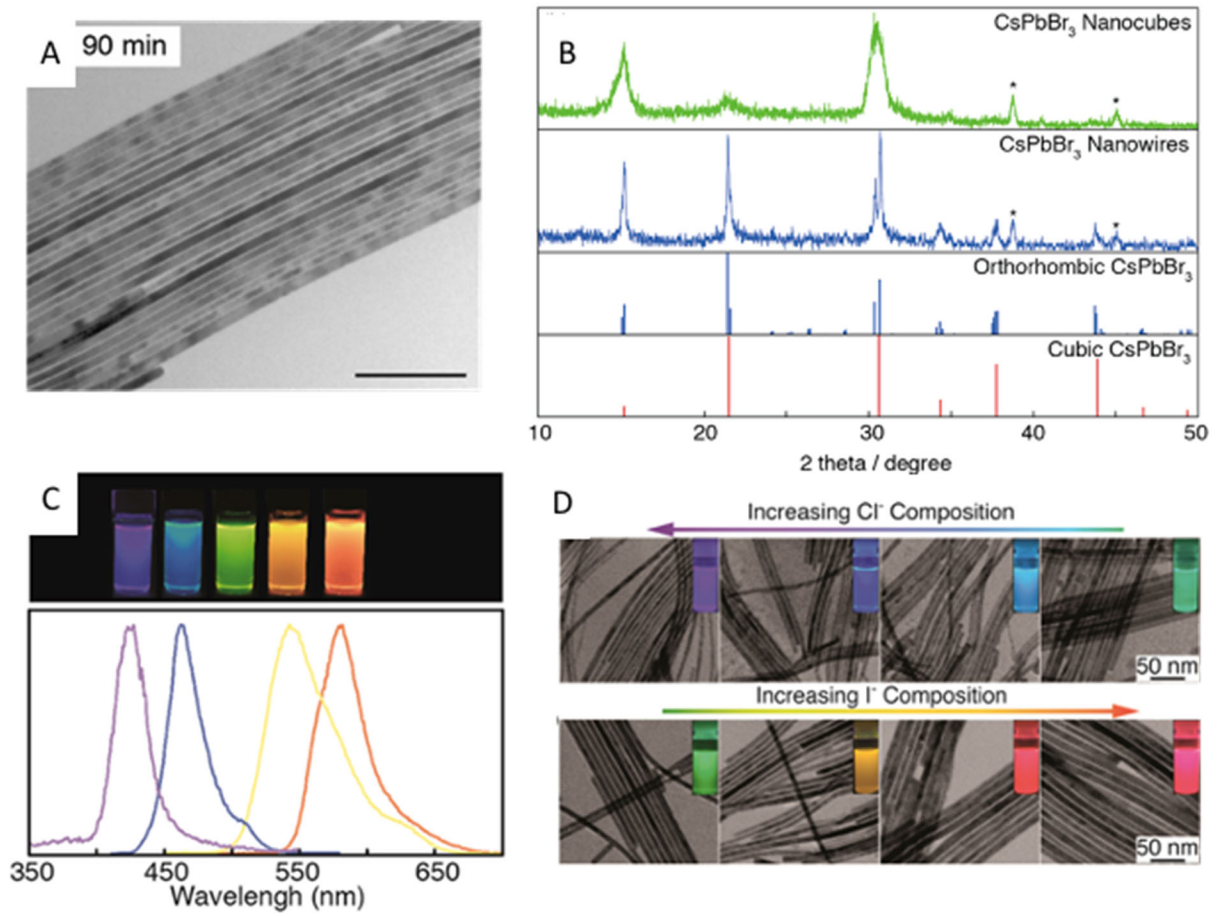
2 *Colloidal synthesis.* One-dimensional (1D) perovskite NWs have been attracting the attention
3 because of their large morphology anisotropy and quantum mechanical effects associated with the
4 two confined dimensions. Shortly after the successful synthesis of perovskite NCs,¹⁵ halide
5 perovskite NWs has been synthesized by controlling the reaction condition to achieve different
6 aspect ratios, chemical compositions and phases. In the synthesis of NWs, the formation of
7 “isotropic” perovskite NCs typically dominates in the early stage of reaction, which is triggered
8 by the rapid injection of cesium precursor (Cs-oleate) into a hot solution of lead precursor (Pb-
9 halide) with the proper choice of organic ligands such as oleic acid, oleylamine, and octylamine^{76,}
10 ²⁵². The morphology evolution of CsPbBr₃ NWs can be seen in Figure 16 A-B: through a linear
11 growth, their aspect ratio quickly increases over time, and NW lengths up to 5 μm are easily
12 reached.²⁵³ Inspired by this approach, Tong et al.²³ reported the synthesis of CsPbBr₃ NWs by
13 ultrasonication of precursor powders and ligands. They found that the initially formed nanocubes
14 gradually transform into nanowires through the oriented attachment mechanism. These methods
15 seem to work quite well for CsPbBr₃ NWs. However, the growth of CsPbI₃ NWs was found to be
16 characterized by much faster kinetics and less controllable size and phase: although the cubic phase
17 of CsPbI₃ can be stabilized at high temperature (above 360 °C), especially at the nanoscale it
18 spontaneously transforms into the room-temperature stable orthorhombic phase characterized by
19 1D chains of edge-sharing octahedra. A recent study suggested that at the initial growth stage of
20 orthorhombic CsPbI₃ NWs, the cubic phase CsPbI₃ nanocubes show lattice distortion induced by
21 the polar solvent molecules, which triggers hierarchical self-assembly of CsPbI₃ nanocubes into
22 single crystalline nanowires through an orientated attachment process¹⁸⁸. This distinct crystal
23 structure of the CsPbI₃ nanowires leads to their unique optical behaviors at room temperature.

1 Unlike the narrow and strong excitonic emission from CsPbBr₃ NWs, the CsPbI₃ NWs show a
2 broad and low-energy emission that is attributed to the indirect bandgap transition of the
3 orthorhombic phase.²⁵⁴

4 Ultrathin perovskite NWs with a diameter less than the exciton Bohr radius down to atomic level
5 (<3 nm) are additionally interesting due to their potential quantum confinement effects⁷⁸. Zhang
6 *et. al.*, developed a method to improve both purity and yields of ultrathin nanowires from colloidal
7 synthesis⁷⁸. The ultrathin CsPbBr₃ NWs showed a strong photoluminescence at around 465 nm,
8 which is significantly blue-shifted compared to the emission wavelength for bulk CsPbBr₃ (~ 530
9 nm) (Figure 16 C-D). A surface treatment with PbBr₂ precursor led to an increase in both PLQY
10 and stability of the NWs by retarding the ripening process. Similarly Imran *et. al.*, developed a
11 method to grow CsPbBr₃ NWs with a width that could be tuned down to the quantum confinement
12 regime (3.4 ± 0.5 nm), by using short carboxylic acids and long alkyl amines as the growth
13 medium.⁷⁶ From their study, the increased concentration of short carboxylic acid over the long
14 ligand led to a reduction in the NW width.

15 To achieve the composition tunability in colloiddally synthesized halide perovskites, the facile
16 anion exchange process has been applied to perovskites with different morphologies, and is
17 disussed extensively in the ion-exchange section of this review.^{56, 255} Halide anion exchange
18 chemistry in CsPbX₃ NWs represents a powerful strategy for attaining bandgap tunability across
19 the blue to near-IR wavelength region.⁵⁷ Post-synthetic chemical transformations have been used
20 in halide perovskites to obtain broad compositional tunability. CsPbBr₃ NWs were used as the
21 starting materials and the CsPbX₃ alloy NWs with a wide range of halide compositions can be
22 achieved through anion-exchange reactions using organic or inorganic halide precursors. The
23 anion-exchange reaction in perovskite NCs typically happens at the nanocrystal-solvent interface

1 and at room temperature. The PL of CsPbX₃ nanowires is easily tunable across the entire visible
2 range by varying the halide composition in a similar way to CsPbX₃ nanocubes.

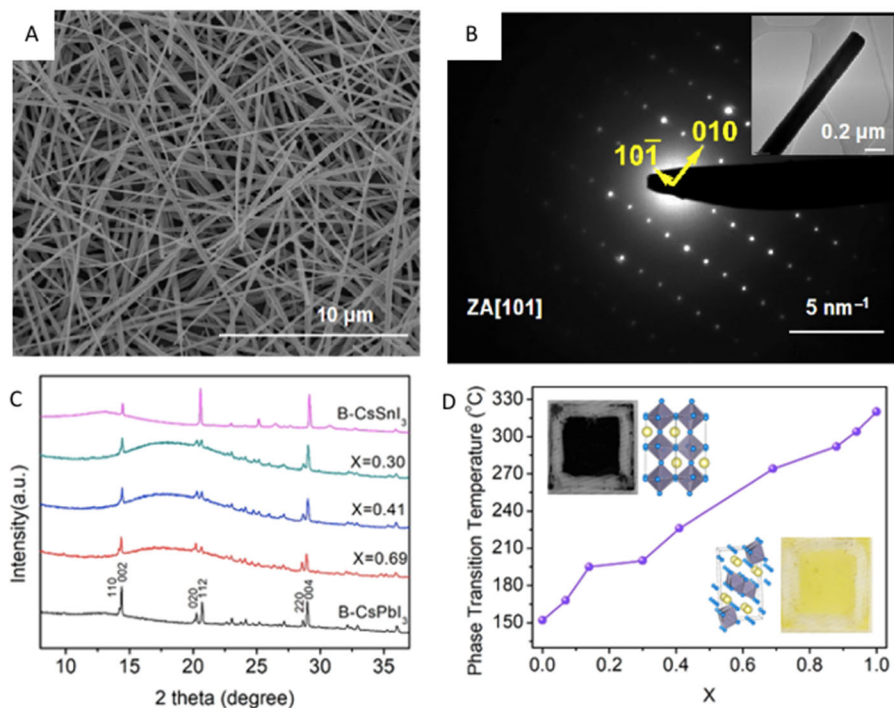


3
4 **Figure 16.** A) TEM image of CsPbBr₃ nanowire synthesized from colloidal method. B) XRD
5 spectrum of CsPbBr₃ nanocubes and nanowires²⁵². C) Photoluminescence properties of ultrathin
6 CsPbBr₃ nanowires with different diameters⁷⁸. D) TEM images of anion exchange in CsPbX₃
7 perovskite nanowires with various halide contents⁵⁷. Copyright American Chemical Society.

8
9 **Solvent evaporation induced nanowire growth**

10 In addition to the inorganic perovskite NW synthesis using colloidal methods, single crystalline
11 micrometer-sized perovskite NWs can be synthesized by using the surfactant-free, substrate

1 assisted dissolution-recrystallization growth method²⁵⁶⁻²⁵⁸. Here, the polycrystalline thin film of
2 PbX_2 acts as the seed to initiate the perovskite NW growth, by immersing it into a diluted cesium
3 halide precursor solution. The lead precursor slowly dissolves and recrystallizes with the
4 surrounding cesium precursor to form one-dimensional perovskite single crystals (Figure 17A-B).
5 The appropriate balance between the choice of high halide salt solubility and low perovskite
6 solubility is the key to achieve effective transformation of perovskite NWs from the seeding layer.
7 This method has been applied to perovskites with different phases and compositions.²⁵⁸ For
8 example, and as already state earlier, the $CsPbI_3$ system can adopt either the non-perovskite yellow
9 phase (double chain orthorhombic structure) or the black perovskite phase through the rapid
10 thermal quenching process²⁵⁷. The synthesis of single crystalline perovskite alloys with mixed “B”
11 site cation has been challenging due to the thermodynamically favorable phase separation in
12 solution. Lei *et. al.*, successfully synthesized single crystalline $CsPb_xSn_{1-x}I_3$ NWs (Figure 17C)
13 with the substrate based solvent evaporation method.²⁵⁹ Especially the yellow phase and the black
14 phase $CsPb_xSn_{1-x}I_3$ NWs can easily be interconverted by carefully tuning of the quenching
15 temperature. The transition temperature increases from 152 to 320 °C as the Pb concentration
16 increases in $CsPb_xSn_{1-x}I_3$ NWs (Figure 17D). The electrical conductivity of direct bandgap black
17 phase $CsPb_xSn_{1-x}I_3$ is 3-4 orders of magnitude higher than that of the yellow phase $CsPb_xSn_{1-x}I_3$
18 NWs. In addition to the mixed “B” cite cation perovskites, mixed alloyed NWs can also be
19 prepared by adjusting the ratios of halides (I, Br, Cl) or A cite cations (MA, FA, Cs).²⁶⁰⁻²⁶¹

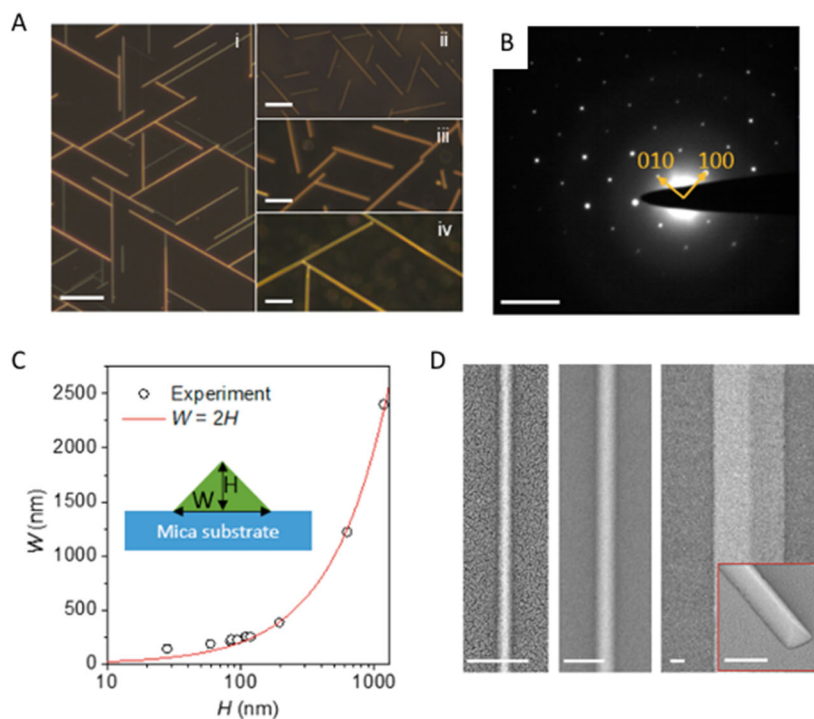


1
 2 **Figure 17.** A) SEM images of CsPbI₃ nanowires grown on a glass substrate from solvent
 3 evaporation method and B) SAED pattern of a single nanowire to confirm the single crystalline
 4 orthorhombic CsPbI₃ phase²⁵⁷. Copyright from Springer Nature. C) XRD patterns of black phase
 5 CsPb_xSn_{1-x}I₃ nanowire mesh. D) Phase transition temperature of CsPb_xSn_{1-x}I₃ nanowires as a
 6 function of Pb content in alloy composition²⁵⁹. Copyright American Chemical Society.

7
 8 **Vapor phase transport and growth**

9 For hybrid organic-inorganic perovskites, direct vapor-phase growth is challenging due to the
 10 decomposition of the organic cation from the perovskite before vaporization. However, this is not
 11 a problem for all-inorganic CsPbX₃ perovskite systems and they can be easily obtained at ~450
 12 °C. By precise control of reactant transport and epitaxial substrate selection (mica, sapphire etc.),
 13 the perovskite NWs can achieve controlled alignment and orientation with tunable
 14 compositions²⁶²⁻²⁶⁵. For example, the CsPbBr₃ NWs can be grown such that they are horizontally

1 aligned on the mica substrate, and the size distribution spans from less than 200 nm to a few
2 microns (Figure 18)²⁶⁵. With the same synthetic approach, the growth of perovskite NWs can be
3 controlled in the in-plane direction by the graphoepitaxial effect on sapphire substrate.²⁶⁶ A
4 comparative study of epitaxial and graphoepitaxial growth has been conducted with CsPbBr₃
5 nanowires²⁶⁷. The graphoepitaxial growth of CsPbBr₃ nanowires results in the bidirectional growth
6 and horizontally alignment on a faceted sapphire substrate. The CsPbBr₃ nanowires grown
7 epitaxially on the flat sapphire plane show six isoperiodic directions. Such facile synthesis and
8 controllability of large scale nanowire networks could potentially facilitate their integration in
9 electronic devices. These single crystals are highly photoluminescent with tunable emission
10 wavelengths, making it possible to observe phase transitions and physical property evolution
11 through an optical approach. Vapor-phase grown single-crystal perovskites can provide an
12 excellent platform for fundamental understanding of the lattice dynamics and transport properties,
13 considering their high crystalline quality, low defect density, and controllable morphologies.



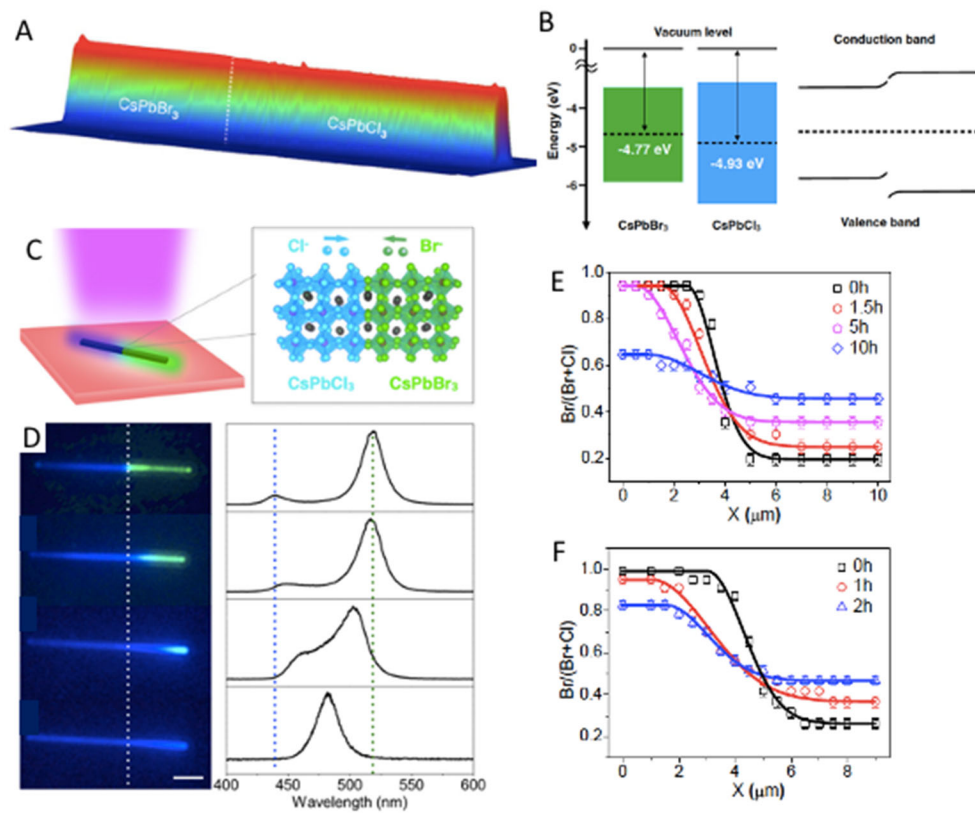
1
 2 **Figure 18.** A) Optical dark field images of CsPbBr₃ nanowires grown on the mica substrate from
 3 chemical vapor transport method and B) SAED patterns from CsPbBr₃ nanowires with a high
 4 single crystallinity. C) The mapping of nanowire geometry on the mica substrate for the width and
 5 height. D) SEM images of individual CsPbBr₃ nanowire with different lateral widths from left to
 6 right (Scale bar, 500 nm)²⁶⁵. Copyright American Chemical Society.

8 Anion Exchange and Phase Transition in Perovskite Nanowires

9 Compared to many of traditional covalent semiconductors, the soft nature of the crystal lattice
 10 and the weak ionic bonding enable higher reconfigurability in halide perovskites. Consequently, a
 11 significant ionic migration is expected in the perovskite lattice, which is considered as a possible
 12 origin for anomalous hysteresis, light-induced phase segregation and photo-instability. A
 13 fundamental understandings of the ionic behavior in halide perovskites has been primarily based
 14 on conventional charge transport studies, which only revealed long-range diffusion on average at

1 the macroscopic level. By combining anion exchange chemistry with nanofabrication techniques,
2 single-crystalline halide perovskite NW heterostructures have been synthesized.²⁶⁸⁻²⁶⁹ The
3 spatially resolved multicolor CsPbX₃ (X=I, Br, Cl or alloy of two halides) NWs show a sharp
4 electronic interface of the heterojunctions, which enables a quantitative study of ion interdiffusion
5 and migration dynamics. Unlike the single crystalline nanostructured perovskite, ionic
6 migrations/diffusions across the grain boundary in polycrystalline thin film are usually faster than
7 inside the lattice.²⁷⁰⁻²⁷¹ Thus, the high ionic conductivity from polycrystalline thin films may not
8 truly represents the intrinsic properties.

9 Heterostructures of single crystalline CsPbX₃ perovskite NWs with two different halide species
10 (CsPbBr₃-CsPbCl₃) have been used as a model system to understand ionic diffusion in halide
11 perovskites (Figure 19 A-B)²⁷². The heterostructures exhibit two-color PL emission with a sharp
12 interface. The sharp interface, with one-dimensional control, makes these highly crystalline
13 heterojunctions ideal systems to study the intrinsic halide anion inter-diffusion because of the well-
14 defined morphology and absence of grain boundary. The changes in surface potential between two
15 components show distinctive electronic properties across the heterostructure NW. The single
16 crystalline CsPbX₃ nanowires that were grown on epitaxial substrates were also used to study the
17 kinetics of ion exchange²⁷³. For example, CsPbCl₃, MAPbBr₃ or MAPbI₃ microplates were grown
18 from the solution-based approaches and transferred on top of aligned CsPbBr₃ nanowires on
19 fluorinated-mica substrates. The corresponding solid-state anion interdiffusion could be studied
20 using time-dependent confocal PL microscopy (Figure 19 C-F). The temperature-dependent
21 measurements revealed the interdiffusion coefficient of chloride to bromide, along with an
22 activation energy of 0.44 eV.

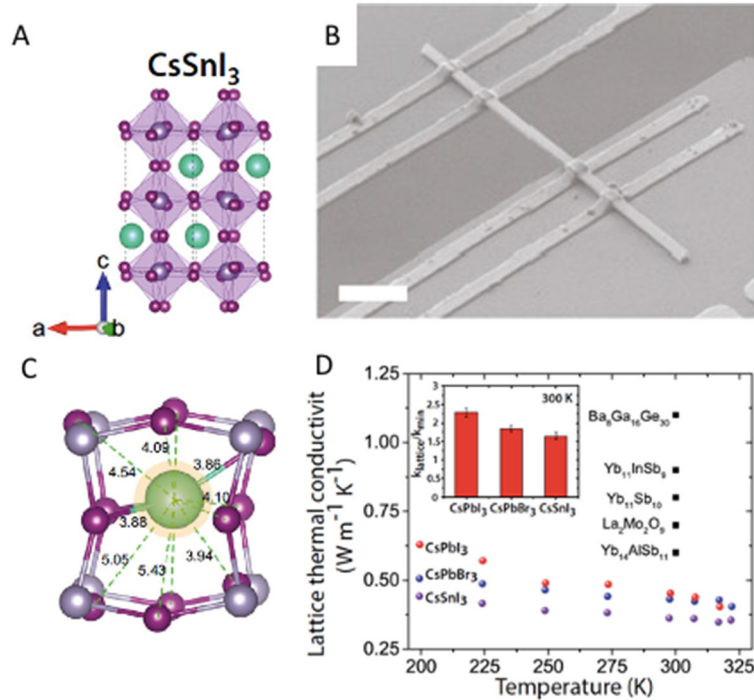


1
 2 **Figure 19.** A) Three-dimensional Atomic Force Microscopy image of CsPbCl₃-CsPbBr₃ nanowire
 3 heterostructure, B) Corresponding electronic work functions determined by Kelvin Probe Force
 4 Microscopy and the electronic band alignment of CsPbBr₃-CsPbCl₃ nanowire²⁶⁸. C) Schematic
 5 illustration of perovskite nanowire heterostructure of CsPbBr₃-CsPbCl₃ nanowire, D) PL evolution
 6 of nanowire heterostructure as a function of anion interdiffusion time due to the heat treatment. E-
 7 F) Halide concentration profiles of perovskite nanowire heterostructure that measured from
 8 confocal PL²⁷². Copyright National Academy of Sciences of the United States of America.

9
 10 The variation in photoluminescence can be exploited to monitor not only the ion migration, but
 11 also solid-state phase transition dynamics. In-situ characterization of the phase transition dynamics
 12 (from perovskite phase [α or γ phase] to non-perovskite phase [β phase]) in CsPbIBr₂ nanowires

1 has been probed in microscopic pathways with high spatial resolution, providing an opportunity
2 to determine the underlying relationships between physical crystal structures and their
3 thermal/electronic properties.²⁷⁴ To observe the thermally induced phase transition dynamics,
4 cathodoluminescence (CL) (luminescence induced by an electron beam) and secondary electron
5 images were simultaneously collected at high frame rates with low electron dose, using a
6 customized scanning electron microscope. The non-perovskite phase of CsPbIBr₂ shows an
7 indirect bandgap, with a low PL emission intensity, and the perovskite phase of CsPbIBr₂ shows
8 instead direct bandgap with a bright PL emission. The difference in emission intensity yields
9 distinctive contrast in CL imaging which allows to track the phase transition dynamics. The phase
10 propagation rates along the nanowires were measured by increasing the temperature from 163 to
11 182 °C. An activation energy of 210±60 kJ/mol was extracted, pointing towards an Arrhenius-like
12 behavior. The microscopic mechanism of phase propagation dynamics was studied from the
13 molecular dynamics simulations, revealing the structurally disordered, liquid-like interface as the
14 origin of the increase in entropy for interphase boundary propagation.

15 Additionally, p-n junction formation can be fabricated with the single-crystalline CsSnI₃ NWs
16 by utilizing a localized, thermally driven phase transition²⁷⁵. CsSnI₃ undergoes a thermally driven
17 phase transition from the double-chain non-perovskite yellow phase to the orthorhombic black
18 perovskite phase at around 150 °C, and the formation energies of cation and anion vacancies in
19 these two phases are significantly different, which leads to n- and p-type electrical characteristics
20 for yellow and black phases. The carrier mobility of black phase CsSnI₃ is ~400 cm²V⁻¹S⁻¹, while
21 that of the yellow phase CsPbSnI₃ is two orders of magnitude lower (~0.9 cm²V⁻¹S⁻¹). Also, using
22 the CL microscopy technique, the interface formation and propagation between two phases could
23 be directly monitored.



1
2 **Figure 20.** A) Crystal structures of CsSnI₃ perovskite. B) SEM images of single nanowire on
3 micro-island device. C) Inhomogeneous bonding structure of atomic cluster rattling mechanism in
4 CsSnI₃. D) comparison of thermal conductivity in perovskites and other crystals²⁷⁶. Copyright
5 National Academy of Sciences of the United States of America.

6
7 Perovskite NWs have received considerable attention in lasing (see lasing section) and
8 optoelectronic devices. Therefore, exploring the thermal transport properties of single-crystalline
9 solids is crucial for developing microelectronic devices. One of the unique characteristics of halide
10 perovskite NWs is the coupling between inorganic crystal lattice and the confining one dimensional
11 geometry. Combined with the heavy elements (Pb, Sn) in the halide perovskite structure, thermal
12 conductivity in halide perovskites can be greatly reduced, which may significantly boost the
13 thermoelectric performance (Figure 20)²⁷⁶, especially when the diameter of NW is smaller than
14 the length of phonon mean free path. The thermal conductivity has been shown to be ultralow

1 (~0.5 Wm⁻¹K⁻¹ at room temperature) in CsPbI₃, CsPbBr₃ and CsSnI₃ perovskite NWs. Interestingly,
2 these NWs exhibit crystal-like thermal conductivity in which the lattice thermal conductivity
3 initially increases and then decreases as the temperature rises. The ultralow thermal conductivity
4 of inorganic perovskite NWs was attributed to the cluster rattling mechanism based on phonon-
5 phonon scattering measurements.²⁷⁶ Compared to the inorganic perovskites, a large reduction of
6 thermal conductivity (0.22 Wm⁻¹K⁻¹) was observed in the organic-inorganic hybrid MAPbBr₃
7 NWs²⁷⁷. In addition, temperature-dependent measurements revealed the dynamic disorder of the
8 organic cations in MAPbBr₃ nanowires, which affects the thermal conductivity at low
9 temperature.²⁷⁸ On the other hand, the effects of phonon group velocity and the high Umklapp
10 scattering rate are dominant in MAPbI₃ NWs at high temperatures.²⁷⁸

11

12 **Synthesis of organic-inorganic hybrid (OIH) perovskite nanowires**

13 Unlike in the case of colloidal inorganic CsPbX₃ perovskite NWs, only limited research progress
14 has been made regarding the controlled synthesis and applications of colloidal OIH perovskite
15 nanowires. Most of the studies on OIH perovskite NWs have been focused on growing them on
16 substrates for optoelectronic and photovoltaic applications.²⁷⁹⁻²⁸⁴ In 2014, Horváth et al.²⁸⁴
17 reported the fabrication of methylammonium lead iodide (CH₃NH₃PbI₃: MAPI) perovskite NWs
18 by a slip-coating method. This method relies on drying a saturated solution of MAPI dissolved in
19 DMF in a confined volume between two glass plates. However, the NWs were rather thick, with a
20 diameter in the range of 50 and 400 nm. In a subsequent work, Grätzel and co-workers
21 demonstrated the fabrication of dense MAPI NWs films for solar cell applications. The NWs were
22 grown on a TiO₂ layer substrate by two-step spin-coating using a DMF-isopropanol (IPA) solution
23 of MAPI precursor. It was found that the amount of DMF and the concentration of MAPI in the

1 precursor solution is critical for NW formation, and the thickness and length of the NWs can be
2 controlled by varying the amount of DMF. In a follow-up work, the same group carried out a
3 detailed analysis of the intermediate structures during the crystallization of NWs and they found
4 that the intermediate phase MAI-PbI₂-DMF acts as a structure-directing agent.²⁸⁵ Interestingly, it
5 was found that the treatment of perovskite thin films with a mixture of DMF: IPA could also lead
6 to the formation of perovskite NWs through dissolution and recrystallization.²⁷⁹ In addition, pre-
7 designed templates could also be used to guide the crystallization of perovskite into NWs. For
8 instance, Spina et al.²⁸⁶ demonstrated the fabrication of MAPI NW arrays in open nanofluidic
9 channels, by which it was possible to control the thickness, length, cross-sectional shape, and
10 orientation of the NWs. Similarly, anodized aluminum oxide (AAO) templates were used for the
11 fabrication of uniform perovskite (CH₃NH₃PbI₃ and CH₃NH₃PbBr₃) NW arrays with a controlled
12 diameter (50–200 nm) on ITO substrates.²⁸⁷ The NWs prepared by these template-approaches
13 appear to have rather rough surfaces. Similar to the case of inorganic perovskite NWs, it has been
14 shown that high-quality HOI perovskite NWs with smooth surfaces and a rectangular cross-section
15 can be prepared on silicon substrates by vapor-phase synthesis.²⁸⁸ This is a two-step fabrication
16 process. First, chemical vapor disposition of PbX₂ precursor powders at high-temperature leads to
17 the formation of PbX₂ NWs, which then convert into MAPbX₃ by chemical evaporation of MAX
18 in the same reaction chamber.²⁸⁸ These OIH perovskite NWs exhibit room-temperature lasing
19 characteristics upon optical pumping.

20 A few attempts have been made toward the solution-phase synthesis of high-quality OIH
21 perovskite NWs by the LARP approach.²⁸⁹⁻²⁹¹ This approach was initially applied to obtain
22 brightly luminescent small NCs. However, this reaction generally yields a side product consisting
23 of larger nanocubes and NWs in the sediment. Zhang et al.²⁸⁹ showed that this LARP reaction

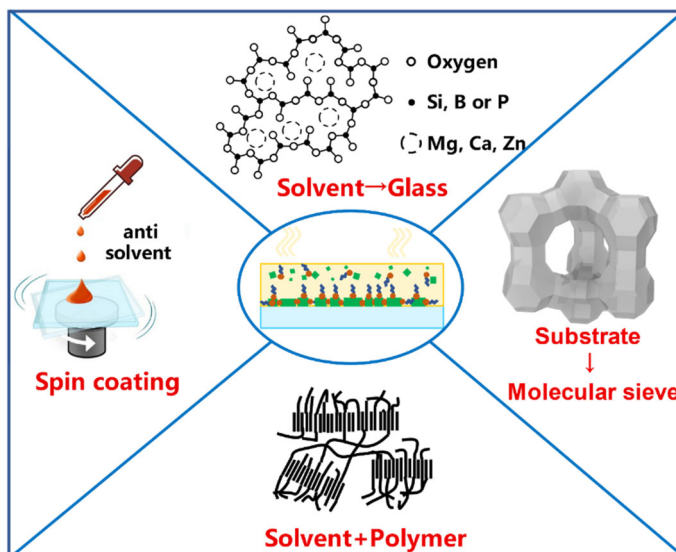
1 produces either high-quality larger MAPbBr nanocubes or NWs upon stirring the reaction mixture
2 for longer times (24 hrs). The morphology is controllable from nanocubes to NWs by adjusting
3 the amount of ligand solution (octylamine). Debroye et al.²⁹⁰ further extended this approach to
4 MAPI NWs. They used both oleylamine (OLA) and oleic acid (OA) as ligands and found that the
5 length of the NWs increases with increasing the amount of OLA in the reaction medium with a
6 fixed amount of OA. This was attributed to the differences in surface binding kinetic of two
7 different ligands to specific crystal facets.²⁹⁰ The NWs were found to be single crystalline and they
8 exhibit longer PL lifetimes. However, the exact mechanism behind the morphology control is still
9 unexplored.

10

11 **1.5 SYNTHESIS OF MHP NCs ON SUBSTRATE (IN-SITU SYNTHESIS)**

12 Despite the great success of HT and LARP methods in the shape-controlled synthesis of high
13 quality perovskite NCs, they also suffer from their fragile surface chemistry and instability. In
14 particular, preserving their superior optical properties when processing them into thin films or
15 embedding them into solid matrix has been challenging. To overcome such problems, an in-situ
16 synthesis strategy (i.e., synthesis on a substrate) has been employed to colloidal synthesis since
17 1990s²⁹². Because of the high formation enthalpy of II-VI semiconductors, the in-situ fabrication of
18 conventional quantum dots usually requires high reaction temperature, which affects their optical
19 properties with large FWHM and low PLQY²⁹³. On the other hand, perovskites are ionic
20 semiconductors with low formation enthalpy and are defect-tolerant^{117, 294}. These two features
21 make the in-situ synthesis strategy well suitable for fabrication of high quality MHP NC based
22 nanocomposites for color conversion applications²⁹⁵ or MHP NC thin films for
23 electroluminescence devices²²⁹. Through this approach, MHP NCs can be directly synthesized in

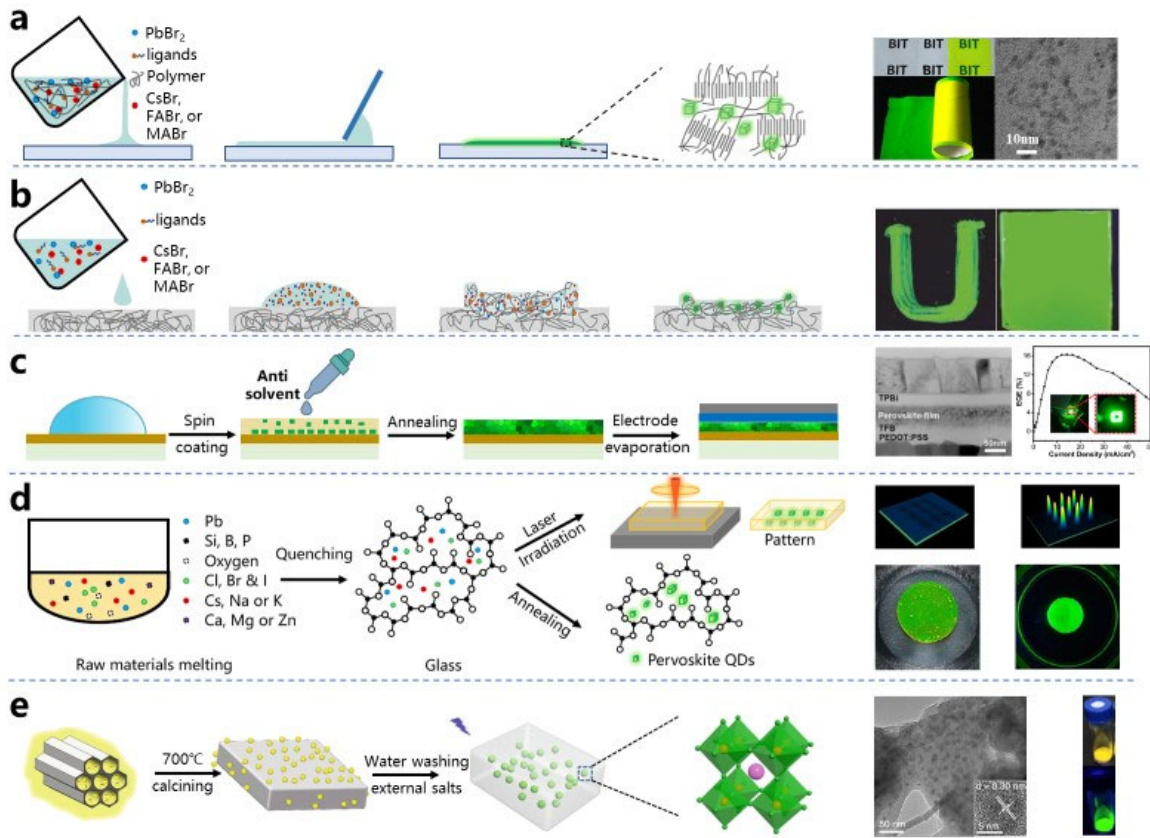
1 a hard matrix such as porous aluminum oxides²⁹⁶, glasses²⁹⁷⁻²⁹⁹, molecular sieve³⁰⁰, or in a soft
 2 polymeric matrix²⁹⁵. It is worth mentioning that the in-situ fabricated perovskite NC-polymer
 3 composite films have been successfully applied in TCL TV products.²⁷³ Using polymerizable
 4 monomers as antisolvent, one can overcome the complexity of purifying perovskite NCs and then
 5 combining them with polymers for the preparation of composites.³⁰¹



6
 7 **Figure 21.** Schematic illustration of four types substrates used in in-situ synthesis for perovskite
 8 NC-composites.

9
 10 Recently, there has been a growing interest in in-situ synthesis of perovskite NCs directly on a
 11 substrate or in a matrix. As illustrated in Figure 21, mainly four types of substrates have been
 12 reported for in-situ synthesis of perovskite NC-composites: 1) glass matrix (for NC-doped glasses,
 13 only suitable for inorganic perovskite NCs due to high reaction temperature), 2) molecular sieves,
 14 3) polymer matrix, 4) glass surface (for obtaining perovskite NC films by in-situ LARP approach).
 15 The first three substrates offer a constrained space for perovskites to crystallize it, which can be
 16 called Nano-confined crystallization. However, unlike solution phase colloidal synthesis, the
 17 shape of the NCs cannot be controlled with these in-situ synthesis strategies.

1



2

3 **Figure 22.** (a) Schematic illustration of the fabrication of perovskite NC-composite by blade

4 coating of precursor solution. The insets are the photographs of the luminescent film under sunlight

5 and UV light, and the TEM images of sliced films (right side). Reprinted with permission from

6 Ref.²⁹⁵ Copyright John Wiley & Sons, Inc. 2016 (b) Schematic illustration showing the fabrication

7 of nanocomposites preparation with swelling–deswelling microencapsulation strategy. The insets

8 are the images of the luminescent nanocomposite prepared by swab painting and spin coating

9 under UV light (right side). Reprinted with permission from Ref.²⁴⁶ Copyright John Wiley & Sons,

10 Inc. 2016 (c) Schematic illustration of the fabrication of LED device based on NCs film prepared

11 by in-situ LARP progress. The insets are the TEM image of a device cross-section and the plot of

12 EQE vs current density of the device. Reprinted with permission from Ref.²²⁹ Copyright American

1 Chemical Society 2018. (d) Schematic illustration of the fabrication of perovskite NC-glass
2 composite and, the photographs of glass substrates having patterned NCs in the glass matrix (by
3 either laser irradiation) and uniformly distributed NCs (by uniform annealing). Reprinted with
4 permission from Ref.²⁹⁹ Nature Publishing Group 2020 (e) Schematic illustration of perovskite
5 NCs embedded molecular sieve phosphors. The insets are the TEM images and the photos of the
6 phosphors under sunlight and UV light (right side). Reprinted with permission from Ref.³⁰⁰ Nature
7 Publishing Group 2019

8
9 As shown in Figure 22a, Zhong and co-workers developed the in-situ fabrication strategy to
10 obtain flexible and free-standing perovskite NC-polymer composite films.²⁹⁵ The fabrication
11 process exploited the solubility difference between polymer and perovskites, enabling the
12 formation of small size NCs in the polymeric matrix. The as-prepared composite films exhibit
13 improved stability and enhanced PL emission, along with excellent mechanical and also
14 piezoelectric properties. Furthermore, the authors demonstrated the first liquid crystal display
15 (LCD) backlights based on perovskites. Meanwhile, Wang et al.²⁴⁶ demonstrated a swelling–
16 deswelling microencapsulation strategy for the fabrication of MAPbBr₃-polymer composite
17 (figure 22b). In this approach, the introduction of the perovskite precursor solution into the
18 polymer matrix leads to solvent-induced polymer swelling, which then deswell after the removal
19 of the solvent by annealing. In 2018, Zhong’s group demonstrated the in-situ synthesis of highly
20 luminescent FAPbBr₃ NC films on ITO-coated glass substrates.²²⁹ Their approach relies on the
21 crystallization of smooth NC film directly on a substrate by LARP (Figure 22c). The prepared
22 films exhibited bright luminescence with a PLQY up to 78%. They demonstrated that the green
23 LEDs made out of these films exhibit external quantum efficiency up to 16.3%. Figure 22d

1 illustrates a synthesis route for the preparation of a perovskite NC-glass composite. This method
2 relies on heating (at 1300 °C) and then quenching a mixture of perovskite precursors (PbO, CsCO₃,
3 KX, and so on) and glass melt (SiO₂, B₂O₃, and P₂O₅, and so on) to obtain a transparent glass
4 substrate embedded with perovskite precursor.²⁹⁹ The precursors in glass matrix can be
5 transformed into perovskite NCs either by laser irradiation or by thermal annealing. By precisely
6 controlling the laser focal point, one can draw reversible fine patterns of perovskite NCs in the
7 glass matrix (inset of figure 2d). On the other hand, a uniformly doped luminescent glass substrate
8 can be produced by thermal annealing at 400 to 600 °C (Figure 2d, right side).²⁹⁸ A similar strategy
9 could be applied to obtain perovskite NC-doped phosphors using a mixture of perovskite
10 precursors and a molecular sieve, as shown in Figure 22e.³⁰⁰ In this approach, highly luminescent
11 perovskite NC doped phosphor with ultra-high stability can be achieved by washing away the
12 unbound perovskite NCs.

13

14 **1.6. COMPOSITION CONTROL BY ION EXCHANGE AND SUPPRESSION OF** 15 **EXCHANGE**

16 **Anion exchange**

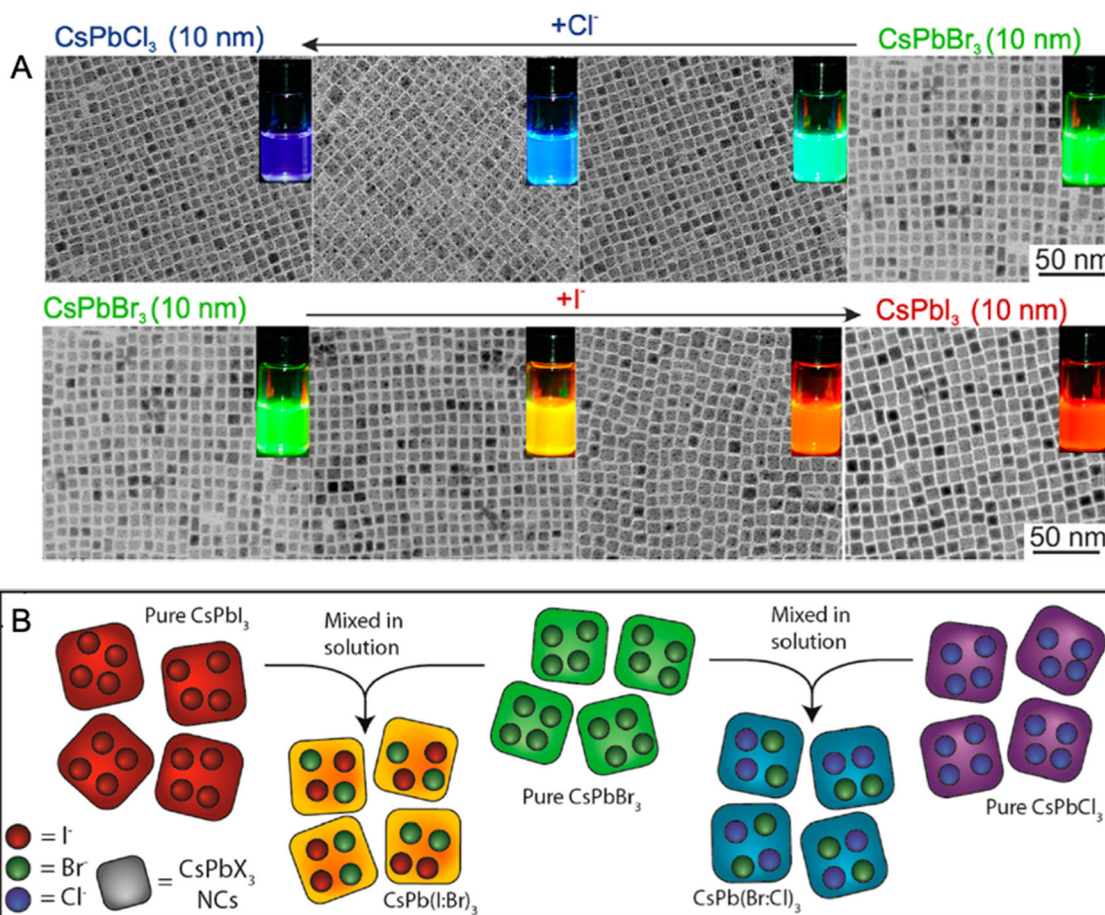
17 *Halide exchange and mixed halide NCs.* The bandgap and therefore the color of the emission
18 in lead halide perovskite NCs is mainly defined by halide atom, with CsPbCl₃ NCs emitting in the
19 blue, CsPbBr₃ in the green, and CsPbI₃ in the red visible spectral range. Mixing of the halide
20 composition (Br_x,Cl_{1-x}; Br_x, I_{1-x}) provides the possibility of fine-tuning the emission wavelength
21 across the visible range. Mixed halide composition was already reported in the first report on
22 colloidal lead halide perovskite NC by Protesescu et al.¹⁵ through direct synthesis. This work was
23 quickly followed up by reports on post-synthesis exchange of the halide anions by Kovalenko's

1 and Manna's groups. Nedelcu et al.³⁰² and Akkerman et al.⁵⁸ showed that fast anion exchange
2 between Cl and Br, and Br and I could be reversibly achieved by providing the halide sources to
3 the already synthesized NCs in dry octadecene. This reaction worked for all tested halide sources,
4 from organometallic Grignard reagents (MeMgX) to oleylammonium halides (OAmX) and simple
5 PbX₂ salts, without affecting the cationic sublattice, and by maintaining the cubic crystals structure
6 and the size of the parent NCs. In this way, the anion exchange provided a synthesis strategy for
7 mixed halide CsPbBr/I and CsPb Br/Cl NCs with good size monodispersity, which translated to
8 improved optical properties such as emission line width and intensity. Gradual halide exchange
9 from Cl to I or vice versa was not achieved, in these attempts the NCs were either shattered,⁵⁸ or
10 quickly converted to single halide crystals,³⁰² which was attributed to the large difference between
11 the ionic radii of Cl and I atoms. Furthermore, anion exchange was also observed without the use
12 of additional halide sources by direct mixing of CsPbBr₃ NCs with CsPbI₃ or CsPbBr₃ NCs in
13 colloidal solutions. Here the NCs themselves can serve as halide sources and fast shuttling of halide
14 anions in between NCs occurs until a homogeneous distribution within the sample is reached.

15 Towards the fabrication of perovskite NCs with tunable emission for lighting application, the
16 anion exchange process was integrated in a microfluidic reactor system for the synthesis of
17 CsPbX/Y NCs with mixed halide composition by Kang et al.³⁰³ Here the CsPbBr₃ NCs were
18 fabricated in a first microreactor stage, and then the anion exchange with I and Cl occurred in a
19 second reactor, where the respective halide precursors were added to the flow of the CsPbBr₃ NCs
20 that were formed in the first reactor. In situ control of the flow parameters of the precursors and
21 monitoring of the PL emission enabled fine control of NC size and composition.

22 Anion exchange reactions also allowed to extend the range of Pb-free double perovskite NC
23 materials. Gamelin and coworkers¹⁸⁵ fabricated elpasolite Cs₂AgBiX₆ (X=Cl, Br) NCs and then

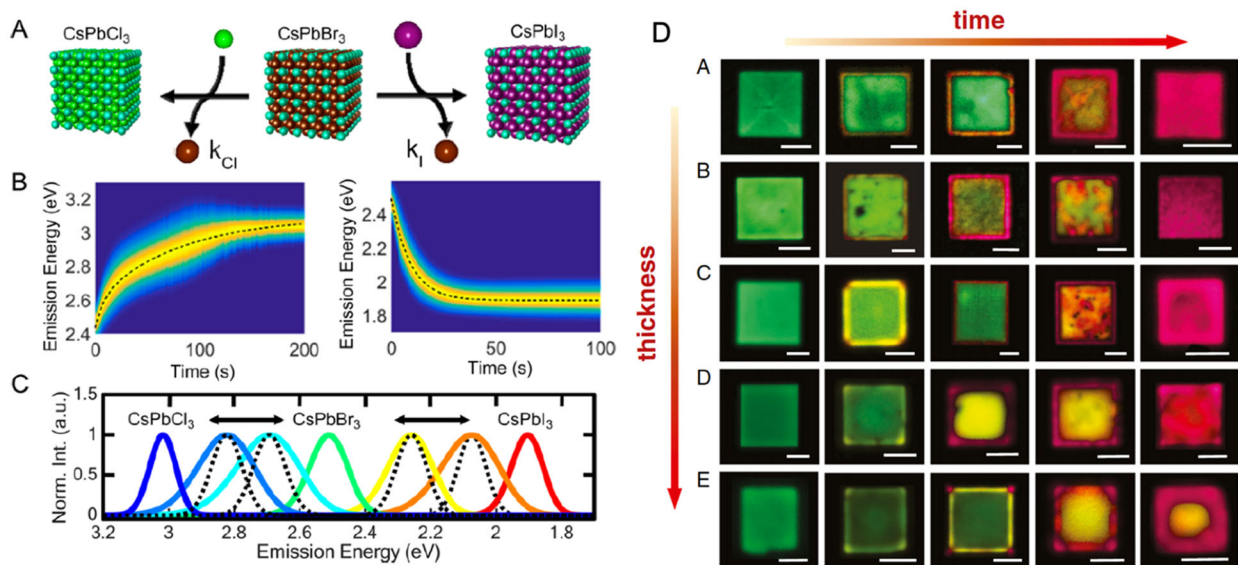
1 used the anion exchange with I to obtain $\text{Cs}_2\text{AgBiI}_6$ NCs, which could not be prepared by a direct
 2 synthesis route. This Pb-free material is a strong photoabsorber across the visible range and is
 3 therefore attractive for photovoltaic applications.



4
 5 **Figure 23.** Post-synthesis halide exchange. (A) TEM images of CsPbX₃ nanocubes with mixed
 6 halide composition. The insets show photographs of the colloidal solutions under ultraviolet light
 7 illumination. Reproduced with permission from Ref. ³⁰² Copyright American Chemical Society.
 8 (B) Schematic illustration of the anion exchange reaction that occurs upon mixing NC solutions

1 with different halides. Reproduced with permission from Ref. ⁵⁸ Copyright American Chemical
2 Society.

3 ***In situ monitoring of anion exchange.*** The bright photoluminescence of the mixed cesium lead
4 halides enabled in situ monitoring of the anion exchange dynamics in the NCl samples. Alivisatos
5 and coworkers measured the PL spectra over time during the anion exchange reaction from
6 CsPbBr₃ to CsPbCl₃ and CsPbI₃ NCs in solution ensuring fast injection by a stopped-flow
7 injector.³⁰⁴ The reaction kinetics were analyzed via the bandgap and PL line width change during
8 the chlorine and iodine exchange. These experiments allowed them to draw a kinetic model for
9 the exchange reaction process, in which distinctly different behaviors were observed for the two
10 reactions. The red shift of the bandgap in the exchange from CsPbBr₃ to CsPbI₃ followed a
11 monoexponential trend, and this rapid initial alloying was attributed to a surface limited process.
12 The more complex kinetics for the exchange with chlorine, that manifested with different time
13 intervals with nearly constant bandgap change, could be assigned to a diffusion limited dynamics.
14 Such different behavior was rationalized by the differences in ion sizes and mobilities. The anion
15 exchange reaction in single crystals perovskite nanoplates (with tens of micrometer lateral size)
16 could be monitored by following the change in PL of individual platelets with a confocal
17 microscope.³⁰⁵ Since this study was not done in situ, vapor phase anion exchange reaction on dry
18 CsPbBr₃ nanoplates was used that ensured rapid quenching of the reaction. At the intermediate
19 stages of the anion exchange from CsPbBr₃ to CsPbI₃, a coexistence of red and green emission
20 peaks was observed in the PL spectra. Confocal PL maps recorded on nanoplates with different
21 thicknesses and at different reaction times evidenced a gradual transformation from the edges
22 toward the center of the plate, with dynamics that correspond to a diffusion-controlled mechanism.

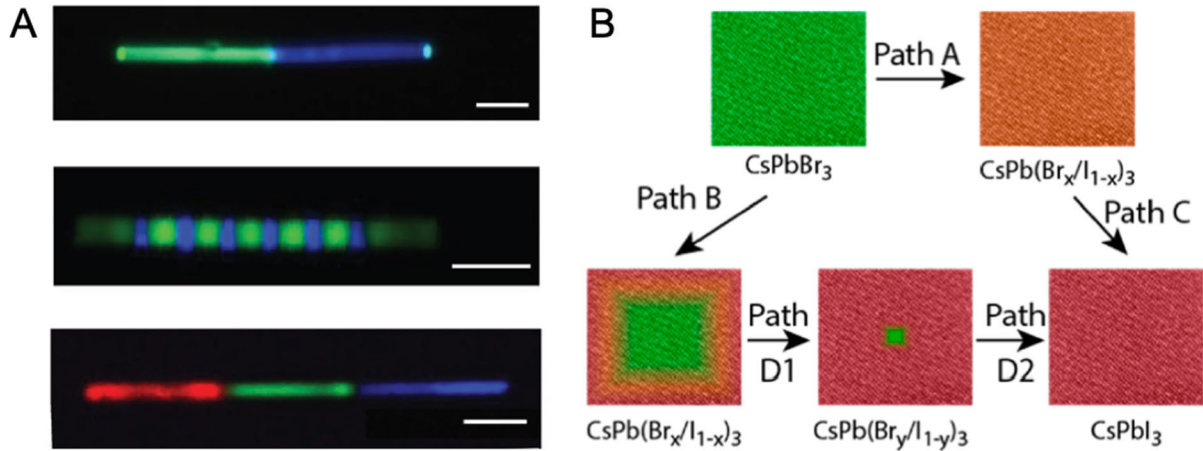


1
 2 **Figure 24.** In situ photoluminescence monitoring during halide exchange reactions. (A) Schematic
 3 illustration of the exchange reaction. (B) PL spectra recorded from colloidal solutions during the
 4 anion exchange reactions. (C) PL spectra for the starting CsPbBr₃ NCs (green) and ending CsPbCl₃
 5 (dark blue) or CsPbI₃ (red) along with spectra for mixed halide compositions (CsPbBr_{3-y}X_y) in the
 6 both the kinetic (solid) and equilibrium (dashed) regime for each bandgap shown. A-C are
 7 reproduced with permission from Ref. ³⁰⁴ Copyright American Chemical Society. (D) Confocal
 8 PL mapping of individual nanoplates for different thicknesses and reaction times.³⁰⁵ Copyright
 9 National Academy of Sciences of the United States of America.

10
 11 The reversible reaction from CsPbCl₃ to CsPbBr₃ nanoplatelets was investigated by in situ PL
 12 spectroscopy by Sadtler and coworkers³⁰⁶, revealing heterogeneity in the reaction kinetics that
 13 depend on the density of the exchanged ions in the crystals. By selecting different fields of view
 14 in the micro-PL measurements, the time traces of the emission of individual NCs were recorded,
 15 which manifested a strong dependence for the switching times on the concentration of
 16 substitutional halide ions used to induce anion exchange.

1 ***Heterostructure fabrication via anion exchange.*** Anion exchange can be exploited to fabricate
2 heterojunctions in lead halide perovskite NCs. Yang and coworkers have shown in their progress
3 report¹⁰⁶ a variety of lateral heterostructures in perovskite nanowires. CsPbBr₃ nanowires with
4 different diameters were fabricated by wet chemistry, coated with PMMA, and selected regions
5 were exposed by electron beam lithography. By applying anion exchange with chlorine and iodine
6 precursor solutions, lateral heterojunctions with spatial resolution down to 500 nm were achieved,
7 and imaged by confocal fluorescence microscopy (Figure 25). Mixed halide heterojunctions were
8 also fabricated starting from CsPbBr₃ nanocubes with an anion exchange to CsPbI₃, and imaged
9 by variable energy hard X-ray photoelectron spectroscopy.³⁰⁷ These measurements elucidate, in
10 contrast to a homogeneous alloy, that the anion exchange progresses via the formation of a
11 heterojunction from the outer regions to inner regions of the nanowires, where the surface is rich
12 with the exchanged anions, and the core with the native ones. Even in fully exchanged nanocubes
13 a small core region containing the native (Br) anions was observed.

14 Colloidal atomic layer deposition (c-ALD) has been employed to fabricate perovskite/metal
15 oxide heterojunctions in NCs.³⁰⁸ Here, for the case of alumina coated CsPbBr₃ nanocubes, the
16 oxide shell protected the perovskite NC core from anion exchange reactions, which significantly
17 increased the photoluminescence quantum yield, and slowed down the kinetics of the anion
18 exchange, which made monitoring by X-ray diffraction possible.

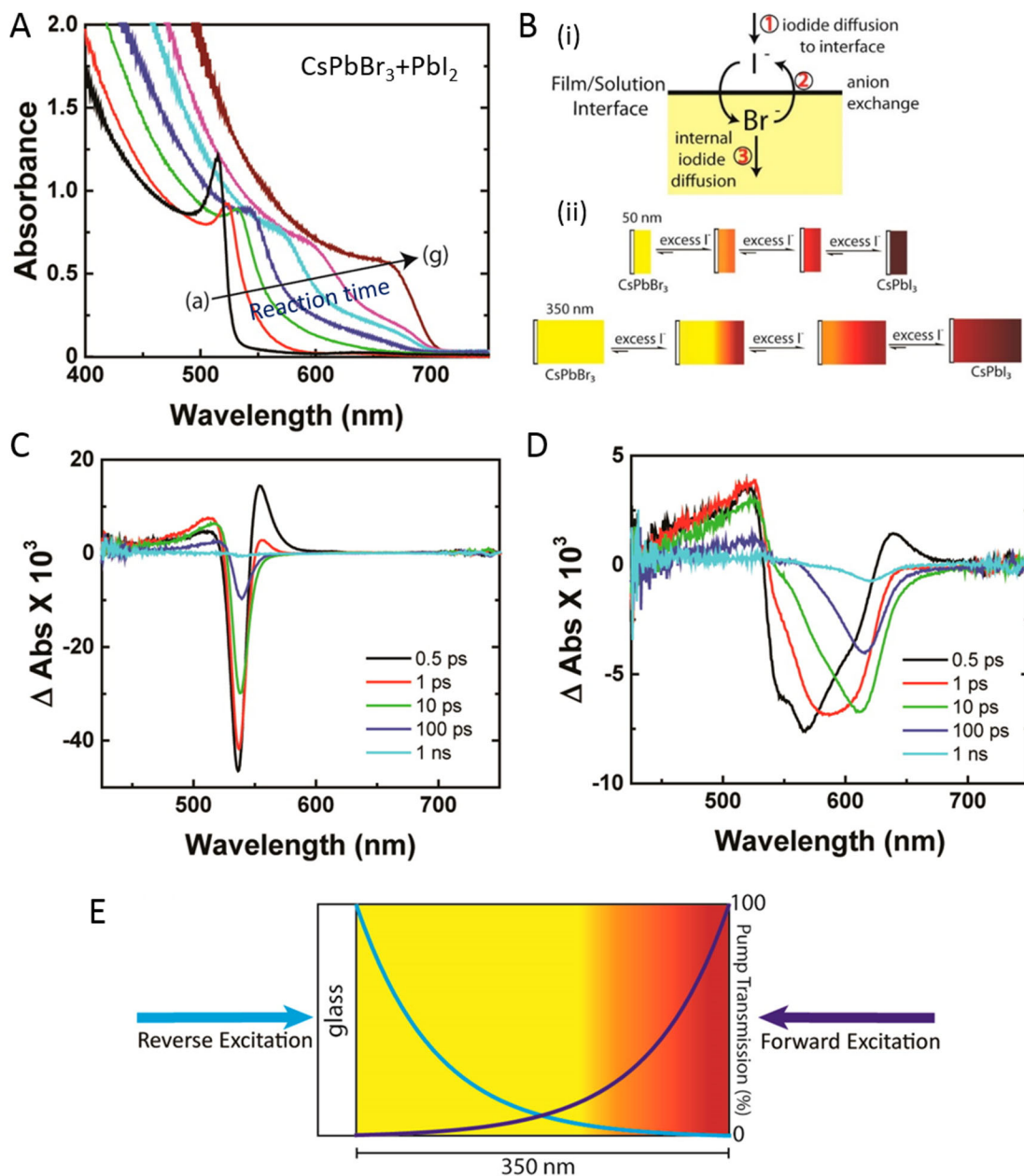


1
 2 **Figure 25.** Heterojunctions fabricated by anion exchange reactions. (A) Heterojunctions obtained
 3 by masked anion exchange in a CsPbX_3 nanowire, leading to different halide compositions.
 4 Reproduced with permission from Ref.¹⁰⁶ Copyright Wiley. (B) Schematic illustration of core-
 5 shell structures obtained by post-synthesis halide exchange. Reproduced with permission from
 6 Ref.³⁰⁷ Copyright American Chemical Society.

7
 8 In another study, a sintered CsPbBr_3 nanocrystalline film was converted into a cubic CsPbI_3 film
 9 by exchanging bromide with iodide ions (Figure 26A). This approach enabled to create a gradient
 10 structure with CsPbBr_3 at one side and CsPbI_3 on the other side of the film.³⁰⁹ The exchange
 11 reaction proceeds through three steps, as illustrated in Figure 26B(i). The halide anion exchange
 12 rate is most likely governed by the anion exchange at the interface and the internal diffusion of
 13 newly formed iodide domain. In thinner films, the iodide ions can diffuse throughout the film,
 14 leading to a near-uniform film composition (Figure 26B(ii)). However, in the case of thick films,
 15 iodide ions cannot diffuse as fast as the new iodide ions enter at the interface, causing a
 16 compositional gradient across the film (Figure 26B(ii)). Time resolved transient absorption studies
 17 confirmed the migration of charge carriers from the high bandgap CsPbBr_3 and $\text{CsPbBr}_x\text{I}_{3-x}$ regions

1 to the iodide rich region near the film surface with in few ps after excitation (Figure 26 C-E). The
2 transient absorption spectra exhibited a narrow bleach upon reverse excitation (Figure 26C), which
3 is consistent with steady state absorption spectra (Figure 26A). However, the bleach peak became
4 broad when the excitation was switched to the forward side, and the peak shifted to lower energies
5 with increasing time delay (Figure 26D). A time constant of 0.5 ps was estimated from the growth
6 of bleaching of the iodide region. These differences in the transient absorption spectra were
7 attributed to the inhomogeneous distribution of anions in thick films as compared to that of thin
8 films after halide ion exchange (Figure 26E). Thus, the gradient films prepared through the halide
9 ion exchange can direct charge carrier-funneling behavior and could improve charge separation
10 and transportation in optoelectronic devices. Because of the miscibility of different halides such
11 gradient structures are extremely sensitive to temperature and can quickly homogenize at higher
12 temperatures.³¹⁰⁻³¹¹

13

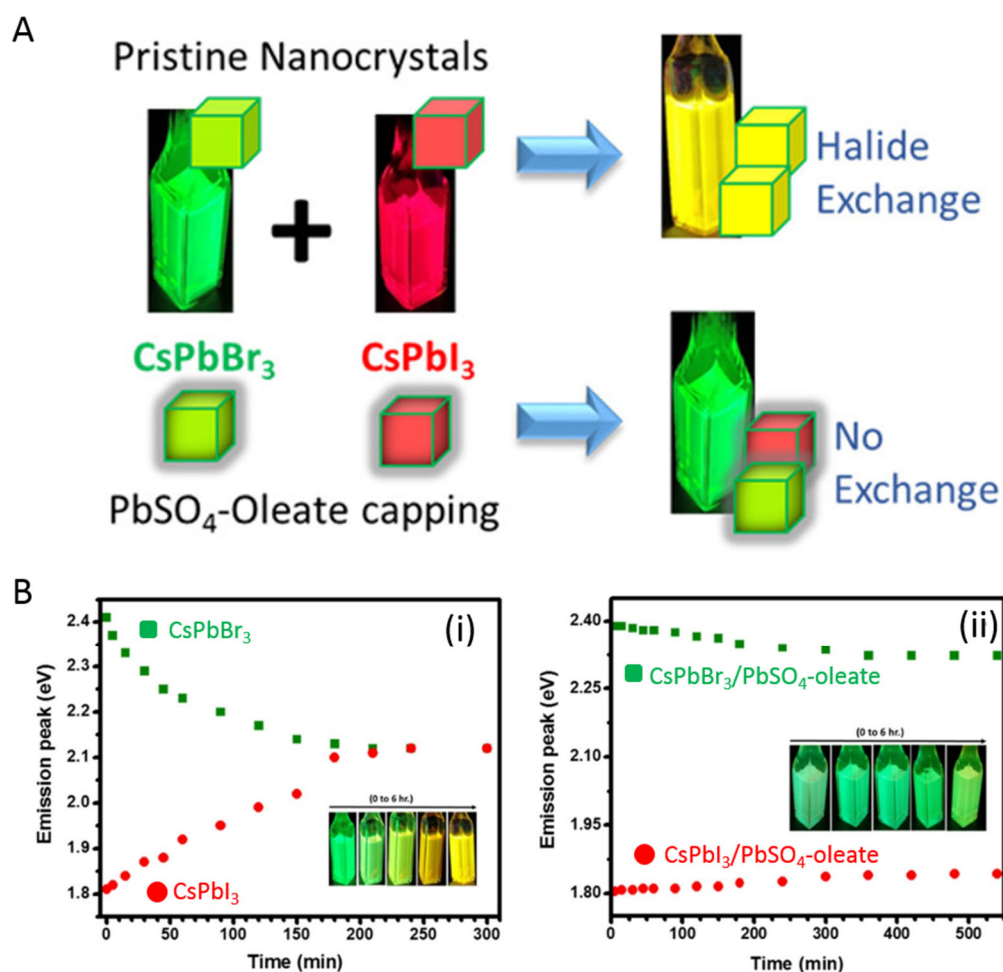


1
2 **Figure 26.** (A) UV-visible extinction spectra of CsPbBr₃ films (350 nm thick) soaked in PbI₂
3 solution at 120 °C for (a) 0, (b) 5, (c) 15, (d) 30, (e) 60, (f) 150, and (g) 480 min. (B) Schematic
4 illustrations showing (i) three-step halide exchange reaction: Iodide ions diffuses to the film-
5 solution interface and exchanges with bromide, and the internal iodide diffuses away from the
6 interface; (ii) Differences in internal film structure of exchanged films of thickness 75 nm and 350
7 nm. (C, D) Transient absorption spectra (TA) of the 15 min soaked 350 nm thick film, acquired

1 upon reverse (C) and forward (D) excitation. The TA spectra acquired under reverse excitation
2 matches well with the steady-state absorption peak (Figure 26A(d)), indicating that the signals
3 originates from within the minimally exchanged portion of the thick film. Forward excitation gives
4 rise a broad bleach spectra moving across the visible spectrum, indicating the excitation of the film
5 surface at the compositional gradient. (E) Schematic representation showing the transient
6 absorption experimental setup for study of thick film. The 387 nm pump can be completely
7 absorbed by the film with an estimated penetration depth of 67 nm. Thus leading to the significant
8 differences in the position of the film where the pump is absorbed when exciting from the forward
9 or reverse direction. Reproduced with permission from Ref. ³⁰⁹. Copyright American Chemical
10 Society 2016.

11
12 **Suppression of Anion Exchange.** In many device applications it is important that the anion
13 exchange be suppressed between different layers of metal halide perovskites. For example, in an
14 all-perovskite tandem solar cell one would like to maintain the individual mixed halide
15 compositions, in order to retain the aligned band structure of the films. The ease of halide exchange
16 between different lead halide perovskite films³¹⁰⁻³¹¹ requires therefore the suppression of anion
17 exchange. One such effective strategy is to cap $\text{CsPbBr}_{x\text{I}_{3-x}}$ NCs with PbSO_4 -Oleate (figure
18 27A).³¹²⁻³¹³ These capped NCs align linearly and can be deposited as films with a hierarchical
19 nanotube architecture. The suppression of halide ion can be seen in both NC suspension as well as
20 multilayered films. For example, Figure 27B shows the emission changes during anion exchange
21 and suppression of anion exchange with PbSO_4 -Oleate capping of CsPbBr_3 and CsPbI_3 NCs.
22 Similarly, a silica shell coating strategy has also been used for suppression of halide anion
23 exchange in perovskite NCs.³¹⁴ Besides, Palazon and co-workers found that the CsPbX_3 NC films

1 exposed to low flux of X-rays do not undergo halide anion exchange.³¹⁵ This is because of the
 2 organic shell formed on the surface of NCs through intermolecular C=C bonding within ligands
 3 upon exposure to x-rays. This approach enabled the fabrication of fluorescent patterns over
 4 millimeter scales with greater stability. By suppressing halide ion exchange it was possible to mix
 5 lead halide perovskite NCs and have a broader emission in the visible region of the spectrum,
 6 including white emission.³¹³ Significantly suppressed ion migration has also been achieved in
 7 layered perovskites.³¹⁶



8 **Figure 27.** (A) Schematic illustration showing the halide exchange and no exchange with and
 9 without PbSO₄-oleatecapping. (B) Changes in photoluminescence peak energy with time of (i)
 10 pure CsPbBr₃ and CsPbI₃ NCs and (ii) PbSO₄-oleate-capped CsPbBr₃ and CsPbI₃ NCs after
 11

1 mixing them in hexane solution. The insets show photographs of the colloidal NC mixture under
2 UV light at various mixing times. Reproduced with permission from Ref. ³¹³, Copyright American
3 Chemical Society 2018.

4

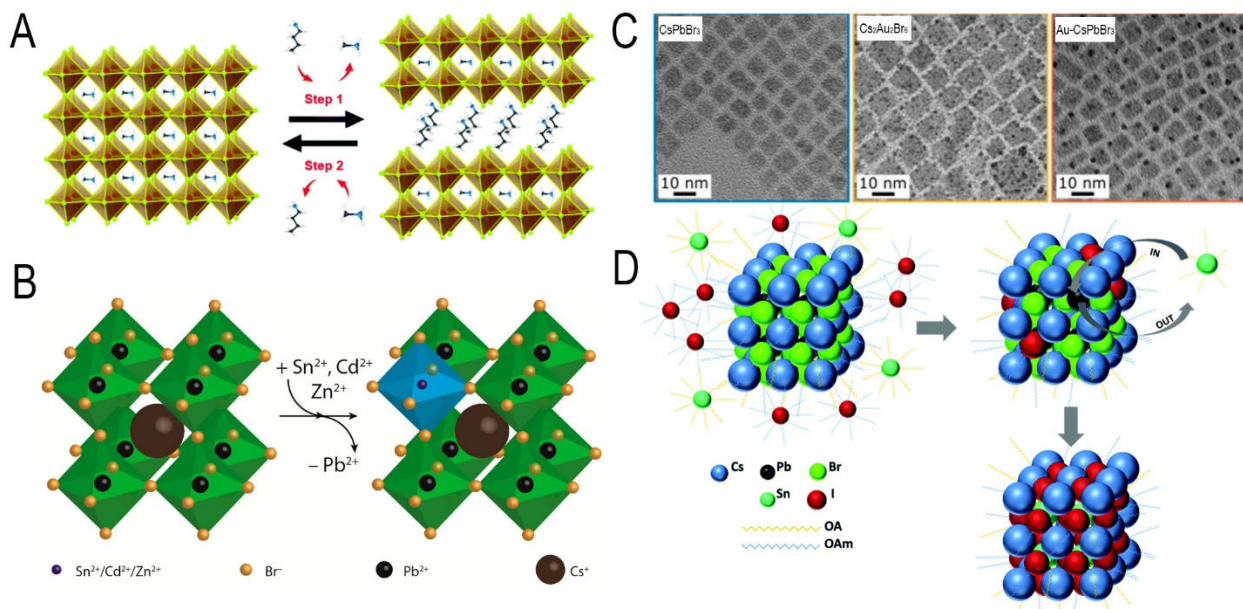
5 **Cation exchange**

6 **“A” cation exchange.** One of the first observations of “A” cation exchange on halide
7 perovskites was reported in a work describing halide anion exchange reactions in CsPbX₃ NCs by
8 Akkerman *et al.*⁵⁸ In that work, various halide sources were explored to elicit anion exchange,
9 starting from CsPbBr₃ NCs, and going to CsPbCl₃ and CsPbI₃ (and back). On the other hand,
10 exposing the CsPbBr₃ NCs to methyl ammonium (MA) bromide caused their PL to red shift from
11 2.43 to 2.36 eV, a value in line with that observed from MAPbBr₃ NCs. The exchange of Cs⁺ with
12 MA⁺ was corroborated by the XRD pattern of the sample after the reaction, which indicated a
13 lattice expansion, compatible with the larger size of the MA⁺ cation compared to Cs⁺. It is
14 interesting to note that that exchange of the Cs⁺ cation with smaller cations (Rb⁺, K⁺) attempted
15 by Nedelcu *et al.*³⁰² led instead to the decomposition of the NCs. This was rationalized by
16 hypothesizing that the cation sub-lattice in halide perovskites is much more rigid than in other
17 compounds, for example metal chalcogenides, where instead cation exchange occurs easily.³¹⁷ A
18 partial methylammonium (MA⁺) to formamidinium (FA⁺) cation exchange was also observed by
19 Xie *et al.*³¹⁸ during the deposition of a film of MaPbI₃ from a solution containing both MA⁺ and
20 FA⁺ cations: even though MaPbI₃ was formed first, it evolved in 2 minutes to FA_{0.85}MA_{0.15}PbI₃, a
21 composition that was observed to stabilize the α -phase.

22 Partial “A” exchange, followed by a phase transformation, was reported by Wang *et al.*,³¹⁹ who
23 treated CsPbBr₃ NCs with rubidium oleate. The exchange of Cs⁺ with Rb⁺ ions was limited to the

1 surface of the NCs. Also, it was accompanied by a phase transition to the Rb_4PbBr_6 structure,
 2 leading to the formation of core/shell $\text{CsPbBr}_3/\text{Rb}_4\text{PbBr}_6$ NCs with improved stability and
 3 enhanced PLQY compared to the core “only” CsPbBr_3 NCs. Another example of “A” exchange
 4 triggering a phase transformation is the one provided by Huang *et al.*,³²⁰ who started from
 5 MAPbBr_3 NCs and reacted them with phenethylammonium bromide (PEABr). The large size of
 6 the PEA^+ cations makes the 3D perovskite phase unstable, hence their introduction in the lattice
 7 causes a transition to the layered phase, accompanied by a blue shift of the emission to 411 nm, as
 8 the layered material has a higher bandgap than MAPbBr_3 (Figure 28A). The reverse reaction took
 9 place when MA^+ ions were added to the 2D NC solution (Figure 28A).³²⁰ Partial exchange of MA^+
 10 ions with Cs^+ ions in films of MAPbI_3 was found to be essential to preserve the black γ phase, and
 11 therefore to avoid the detrimental transition to the higher bandgap δ phase, which is undesirable
 12 for photovoltaic applications.³²¹ In addition, the resulting films were compact and pin-hole free
 13 and the solar cells fabricated from such films had a power conversion efficiency of 14.1%.

14



15

1 **Figure 28.** A) A sketch of the “A” cation induced transformation of 3D to 2D perovskite structures,
2 and back. Reprinted with permission from Ref.³²⁰ Copyright Royal Society of Chemistry. B)
3 Partial “B” cation exchange in CsPbBr₃ NCs. Reprinted with permission from Ref. ³²² Copyright
4 American Chemical Society. C) Competition between Au metal deposition and Pb²⁺ for Au³⁺
5 cation exchange in CsPbBr₃ NCs. From left to right: TEM images of starting CsPbBr₃ NCs,
6 CsPbBr₃ NCs after Pb²⁺ for Au³⁺ cation exchange, CsPbBr₃-Au heterostructures. Reprinted with
7 permission from Ref.³²³ Copyright American Chemical Society. D) I⁻ anion driven Sn²⁺ cation
8 exchange in in CsPbBr₃ NCs. Reprinted with permission from Ref.³²⁴ Copyright Royal Society of
9 Chemistry.

10

11 **“B” cation exchange, “partial” versus “full”.** Initial attempts by Nedelcu *et al.*³⁰² to exchange
12 the “B” cation in NCs were unsuccessful (Ba²⁺, Sn²⁺, Ge²⁺, etc), as the NCs were dissolved. The
13 first report on successful “B” cation exchange is by van der Stam *et al.*,³²² who could partially
14 replace Pb²⁺ ions with various bivalent M²⁺ cations (Sn²⁺, Cd²⁺, Zn²⁺), with no major changes in
15 the size and shape of the NCs, except for a small shrinkage due to the contraction of the unit cell,
16 as all these cations have smaller ionic radii compared to Pb²⁺ (Figure 28B). The lattice contraction
17 was also invoked as an explanation for the blue shift in the optical spectra (with preservation of
18 PLQY at values over 50%) following the partial “B” cation exchange. Extensive analysis of the
19 samples showed that the guest cations were homogeneously distributed in the NCs. The extent of
20 the exchange was such that roughly up to 10% of the Pb²⁺ cations could be replaced. These
21 reactions are limited by the low diffusion rate of the cations in the perovskite lattice, especially for
22 the “B” cation.³²⁵ Although the reaction should be favored by the increase in entropy arising from
23 the formation of a CsPb_{1-x}M_xBr₃ solid solution, van der Stam *et al.* argued that the replacement of

1 Pb^{2+} ions with smaller cations progressively builds up compressive strain in the lattice, which tends
2 to counter any further exchange,³²² thus making the overall process self-limited. Another
3 interesting point made by van der Stam *et al.* is that the cation exchange should be promoted by
4 the presence of halide vacancies (which have low formation energies), so that any exogenous factor
5 limiting the formation of such vacancies should also limit the exchange.³²² In this regard, the
6 authors considered alkylamine molecules, with their binding ability to Br^- ions, as being
7 responsible for preserving a high density of Br vacancies in the NCs, through their ability to
8 remove Br^- ions from the NCs. However, when working at large a concentration of MBr_2 in
9 solution (in the attempt to further promote Pb^{2+} for M^{2+} exchange), the amines lose this
10 “extracting” capability (as there are already too many Br^- ions in solution), and the exchange slows
11 down considerably.

12 Reversible partial “B” cation exchange was observed by Gao *et al.* when reacting CsPbCl_3 NCs
13 with Mn^{2+} ions, leading to $\text{CsPb}_{1-x}\text{Mn}_x\text{Cl}_3$ NCs, or even starting from CsMnCl_3 NCs and reacting
14 them with Pb^{2+} ions.³²⁶ This latter case is similar to that of Fang *et al.*,³²⁷ who also started from
15 rhombohedral CsMnCl_3 NCs and reacted them with PbCl_2 , thus forming hexagonal $\text{Cs}_4\text{Pb}_x\text{Mn}_{1-x}\text{Cl}_6$
16 NCs as intermediated and then cubic $\text{CsPb}_x\text{Mn}_{1-x}\text{Cl}_3$, hence undergoing through successive
17 phase transitions during the exchange.

18 The hypothesis that only partial “B” cation exchange is possible in halide perovskites was
19 actually challenged by Eperon *et al.*³²⁸ who started from films of formamidinium tin triiodide
20 $(\text{CH}(\text{NH}_2)_2\text{SnI}_3$, i.e. FASnI_3) which could be either partially or fully converted to FAPbI_3 . The
21 preservation of the morphology of the films proved that this conversion did not proceed through
22 dissolution-recrystallization, but was indeed a topotactic exchange reaction. In the same work, the
23 reverse exchange (from Pb to Sn) was demonstrated as well, and the same processes were extended

1 to colloidal NCs.³²⁸ The work demonstrated that the “B” cations, at least in selected cases, are
2 actually mobile, thus providing a starting point for possible studies in which transient effects
3 stemming from such B cation mobility may be identified by appropriate experimental tools.

4 Another notable report on “B” cation exchange is the work of Roman *et al.*³²³ (Figure 28C). In
5 their case, the exchange was actually an undesired reaction, as they were attempting to deposit an
6 Au metal domain on top of CsPbBr₃ NCs by adding Au³⁺ ions, in a reducing environment provided
7 by the surfactant molecules (oleic acid and oleyl amine). The exclusive formation of Au-CsPbBr₃
8 heterostructures was possible only if PbBr₂ was added together with the Au³⁺ ions, so that Pb²⁺
9 could efficiently outcompete the Au³⁺ and Au⁺ ions in the exchange with the Pb²⁺ ions already
10 present in the NCs. Indeed, when no PbBr₂ was added, a significant side reaction was the
11 replacement of Pb²⁺ ions by couples of Au(I) and Au(III) ions, leading to the formation of double
12 perovskite Cs₂Au^IAu^{III}Br₆ NCs with tetragonal crystal structure, decorated by Au domains.

13 ***Simultaneous anion-cation exchange.*** There are several reports on concomitant anion-cation
14 exchange. In one of the first works in this topic, Li *et al.*³²⁹ started from Mn doped CsPbCl₃ NCs
15 (written as CsPb_{1-x}Cl₃:xMn²⁺), which were reacted with ZnBr₂, such that CsPb_{1-x-z}Zn_z(Cl_yBr₁₋
16 _y)₃:xMn²⁺ NCs were obtained. Hence, in this type of reaction the Pb²⁺ (and indeed also Mn²⁺) ions
17 were partially exchanged with Zn²⁺, and the Cl⁻ ions with Br⁻. The motivation in that work was to
18 fabricate a system in which the concentration of Mn²⁺ dopants is still high (so that there is strong
19 emission from Mn²⁺ derived states), and that at the same time the lattice is rich in Br⁻ ions.
20 Apparently, it is not possible to reach high Mn²⁺ doping levels in Br⁻-dominant CsPbX₃ hosts, but
21 the additional presence of Zn²⁺ ions made it possible.

22 Various groups have actually observed that the rate of cation exchange is significantly
23 accelerated if also anions are simultaneously exchanged, a process that has been named as “anion-

1 driven cation exchange”. In one of the first observations of this type, CsPbBr₃ NCs were reacted
2 with SnI₂ and they quickly transformed to CsSnI₃ (a process which however broadened the size
3 distribution), going through intermediate CsPb_xSn_{1-x}(Br_yI_{1-y})₃ compositions (Figure 28D).³²⁴ A
4 much lower reactivity was observed instead towards SnBr₂. An interesting case of anion-driven
5 cation exchange is the one described by Qiao *et al.*³³⁰ who used light to trigger the degradation of
6 dihalomethane in a solution containing CsPbX₃ NCs (X = Cl, Br) and a sub-micromolar
7 concentration of Mn acetate. The photodegradation reaction released halide ions, which triggered
8 halide and Pb²⁺ to Mn²⁺ exchange at the same time. This process was named as “photoinduced
9 doping”.

10 A different approach, which can be nonetheless still considered as a sort of anion-assisted
11 exchange, is the one described by Zhou *et al.*,²³⁸ in which CsPbCl₃ NCs were effectively doped
12 with Mn²⁺ ions, when in the one-pot synthesis of the NCs trimethylchlorosilane (TMS-Cl) was
13 present in addition to Mn acetate. The authors of the work argued that the high bond dissociation
14 energy of the Mn-O bond in Mn acetate severely limits the availability of Mn²⁺ ions in solution,
15 hence their possibility to be incorporated in the CsPbBr₃ NCs. On the other hand, the rapid
16 degradation of TMS-Cl frees a large amount of Cl⁻ ions, and as a consequence octahedral [MnCl₆]⁴⁻
17 complexes are formed in solution (in addition to [PbCl₆]⁴⁻ complexes). These units are then directly
18 inserted in the NCs as they nucleate and grow. The general applicability of this reaction scheme
19 was demonstrated by extending the doping to other divalent transition metal cations (Ni²⁺, Cu²⁺,
20 and Zn²⁺).²³⁸

21 Doping strategies aim at conferring new physical properties to the perovskite materials, but they
22 can also impart higher structural, chemical and photochemical stability (including improved
23 PLQY). A recent case was disclosed by Shapiro *et al.*,³³¹ who also exploited an anion-driven cation

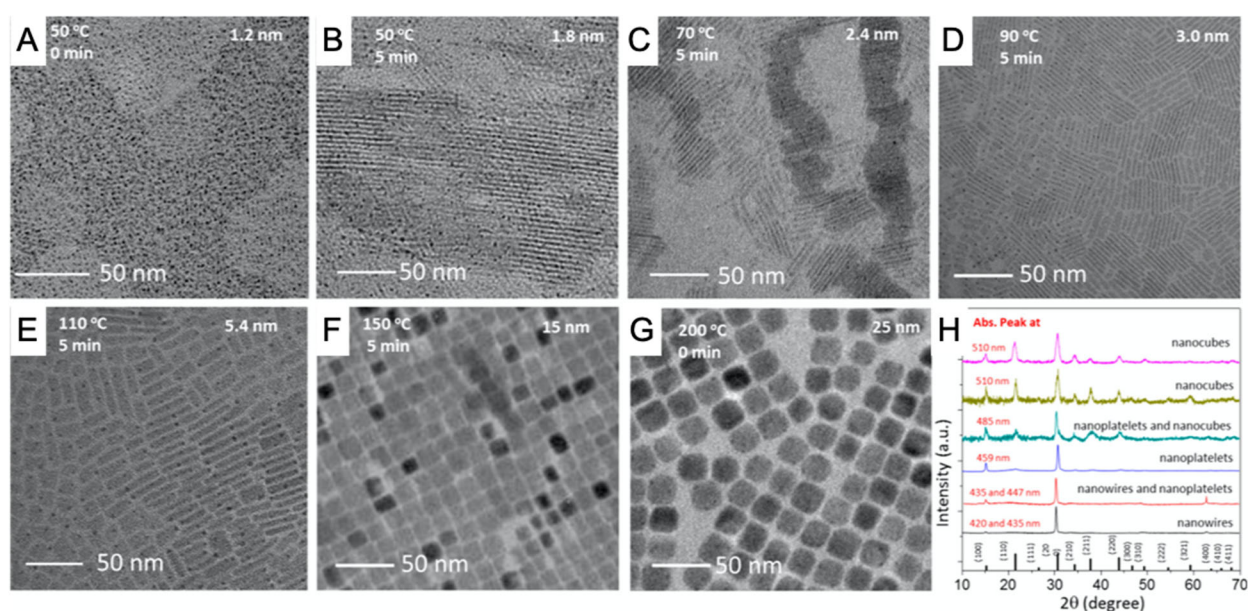
1 exchange on CsPbBr₃ NCs, using NiCl₂ (or NiBr₂), and were able to prepare Ni-doped
2 CsPb(BrCl)₃ NCs, with Ni concentrations tunable from below 1% up to 12% and higher PLQY
3 than that of the starting NCs. When using NiCl₂, compositional analysis showed that the extent of
4 halide exchange was much higher than that of cation exchange. For example, to a Ni doping of
5 5.6% corresponded a 50:50 ratio of Br:Cl. This evidenced that, although halide ions are key to
6 ensure the Pb²⁺ to Ni²⁺ exchange, the latter reaction still proceeds at a much lower rate than the
7 concomitant anion exchange.

8

9 **1.7 POST-SYNTHETIC NANOCRYSTAL SHAPE TRANSFORMATION**

10 Post-synthetic shape-transformations provide access to colloidal NCs that are difficult to obtain
11 by direct synthesis. In addition, they help to understand the growth mechanism and the properties
12 of the corresponding NCs. Attempts to improve the properties of nanocube-shaped perovskite NCs
13 by post-synthesis annealing revealed that such heat treatments can lead to changes in the NC shape
14 and size. Yuan et al.³³² observed a red shift of the photoluminescence wavelength accompanied
15 by a degradation in intensity upon thermal annealing under vacuum at a temperature of 400 K.
16 TEM imaging revealed an increase in NC size of up to a factor of 2 to 3, and compositional analysis
17 showed that the Pb/Br ratio decreased, thus pointing to more Br rich surfaces after annealing. The
18 impact of the temperature on the NC growth and shape transformations was elucidated in detail by
19 Pradhan and coworkers (Figure 29).²⁶⁵ By step-wise increasing the temperature in their reactions,
20 they demonstrated highly accurate size control, and observed shape transformations from thin
21 nanowires to nanoplatelets in the early stages of the reaction, that evolved into nanocubes with
22 dimensions up to 25 nm for longer reaction times. Tong et al.²³ found that CsPbBr₃ nanocubes
23 could gradually transform into nanowires through oriented attachment mechanism under specific

1 reaction conditions. A similar shape transformation was reported by Sun et al.¹⁸⁸, who showed that
 2 cubic crystalline CsPbI₃ nanocubes transform into nanowires upon their treatment with polar
 3 solvents. The authors attributed this to polar solvent induced lattice distortions in cubic crystalline
 4 CsPbI₃ nanocubes, followed by dipole moment triggered their self-assembly into single crystalline
 5 NWs. Similarly, Pradhan et al.³³³ showed that post-synthetic aging of colloidal solutions leads to
 6 the transformation of CsPb(Br_xI_{1-x})₃ into the corresponding NWs with length up to several
 7 micrometers. Such shape transformation can also be triggered by halide-vacancy-driven, ligand-
 8 directed self-assembly process, as demonstrated by Bakr and co-workers.³³⁴ They have shown that
 9 the halide vacancy CsPbBr₃ nanocubes transform into millimeter long NWs upon ligand exchange
 10 with didodecyldimethylammonium sulfide (DDAS).

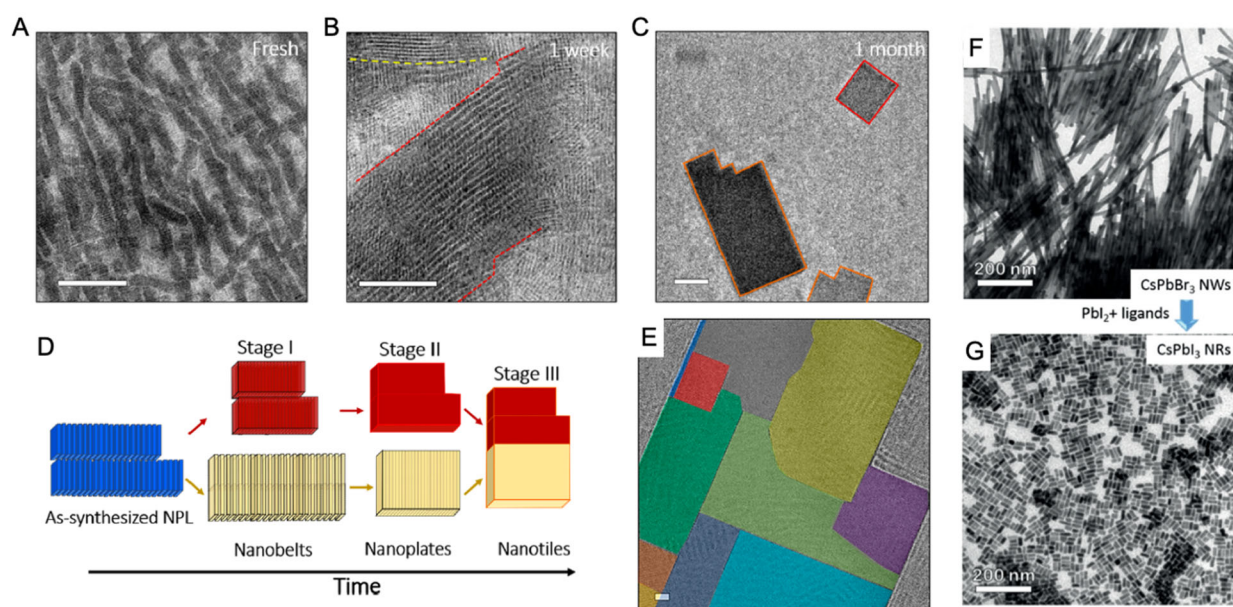


11
 12 **Figure 29.** Shape transformations occurring during CsPbBr₃ NC synthesis for different
 13 temperatures and reaction times. (A-G) TEM images. (H) X-ray diffraction data. Reproduced with
 14 permission from Ref. ²⁶⁵ Copyright American Chemical Society.

15

1 The evolution of CsPbBr₃ nanoplatelets into nanobelts, nanoplates and nanotiles over time in
2 solution and in films was investigated in detail by Dang *et al.*³³⁵ (Figure 30A-E), who evidenced
3 the formation of nearly defect free nanobelts at the early stage by oriented attachment and fusion
4 of the nanoplatelets, while at later stages the nanobelts and nanoplates assembled into mosaic-like
5 nanotiles. The interfaces in such nanotiles were characterized by Ruddlesden-Popper stacking
6 faults due to the presence of CsBr bilayers. This transformation, which occurred in solution at
7 room temperature over several weeks, was also observed in thin NC films and could be accelerated
8 to time frames of less than one hour by increasing the temperature. Around the same time, Pradhan
9 and co-workers reported a similar shape transformation on a TEM grid at RT.³³⁶ They found that
10 the polyhedral nanocubes transform into either zigzag-shaped 1D nanostructures by oriented
11 attachment of corners or nanotiles by side-wise fusion, depending on their composition.
12 Interestingly, these transformations could be ceased at any point of time either by applying heat or
13 by addition of sufficient ligands. A similar transformation had been reported earlier by Shamsi *et*
14 *al.*,²⁴⁵ who found that the exposure of CsPbBr₃ nanoplatelet films to intense ultraviolet light lead
15 to the transformation into nanobelts. Since the initial nanoplatelets were blue emitting due to
16 quantum confinement effects, while the larger nanobelts emitted green light, the use of shadow
17 masks in such transformation could lead to color patterned films. The high brightness and stability
18 of the films that were exposed to ultraviolet light enabled the fabrication of solution-processed
19 light emitting diodes. Such light-induced shape transformations strongly depend on the type of
20 surface ligands. Li *et al.*²⁰² showed that individual CsPbBr₃ perovskite NCs capped with 1-alkynyl
21 acids could readily transform either into large cuboid- or peanut-shaped micro crystals under UV-
22 irradiation. The shape of the resultant microcrystals depend on the chain length of the 1-alkynyl
23 acid used as surface ligand. The authors proposed that the shape transformation was caused by

1 self-assembly of CsPbBr₃ nanocubes through ligand-induced homocoupling of surface ligands. In
 2 addition, the transformation of nanocubes to nanoplates has also achieved by applying pressure in
 3 the GPa range (in a diamond anvil cell) to superlattices of CsPbBr₃ nanocubes.³³⁷ The pressure
 4 treatment lead to the formation of nanoplates with edge length that were 2-3 times larger than those
 5 of the initial nanocubes, and to a blue shifted emission after pressure release, pointing to quantum
 6 confinement in the out-of-plane direction.



7
 8 **Figure 30.** Temperature and chemically induced transformations in shape of CsPbBr₃ NC
 9 structures. (A-C) TEM images recorded from aliquot taken from CsPbBr₃ nanoplatelet solution at
 10 different times. (D) Illustration of the oriented assembly process and transformation from
 11 nanoplatelets to nanobelts, nanoplates and nanotiles. (E) False colored TEM image of a nanotile.
 12 Reproduced with permission from Ref. ³³⁵. Copyright American Chemical Society. (F-G)

1 Chemical cutting of CsPbBr₃ NWs into CsPbI₃ nanorods. Reproduced with permission from Ref.
2 ⁷⁵. Copyright Wiley.

3
4 Transformations via fragmentation of perovskite NCs, instead of assembly, is another possible
5 mechanism. Polavarapu and coworkers⁷⁵ demonstrated the chemical cutting of CsPbBr₃ by a
6 ligand induced fragmentation into CsPbX₃ nanorods (X= Cl, Br, I) that was triggered by a halide
7 anion exchange reaction (Figure 30F-G). The emission of the resulting perovskite nanorods could
8 be tuned across the visible range, and photon antibunching experiments revealed single photon
9 emission from such nanorods. Other ligand-induced post synthesis transformations include the
10 evolution of CsPbBr₃ nanocubes to NWs and 0D structures, or to nanoplates.³³⁸ In this latter work,
11 the transformation could be controlled by the choice of the ligands: alkyl carboxylic acids lead to
12 emitting nanoplates, while oleyl amine and octyl amine initiated the formation of NWs and 0D
13 structures. On the other hand, shape transformations have been rarely reported for OIHP NCs. For
14 instance, Tong et al.³³⁹ demonstrated the ligand-induced transformation of 3D nanocubes into 2D
15 NPLs upon dilution of colloidal solution. They showed that the thickness of the NPLs is tunable by
16 both the ligand concentration as well as the dilution level. In addition, nanoplatelets could be
17 obtained by bottom-up shape transformation of spherical nanodots, as reported by Liu et al.³⁴⁰
18 They showed that the nanodots obtained by LARP gradually transform into square shape NPLs
19 upon aging the nanodot solution for 3 days. They attributed this transformation to dipole–dipole
20 interactions along with realignment of dipolar vectors of nanodots.

1
2
3
4
5
6
7
8
9
10
11
12
13
14
15
16
17
18
19
20
21
22
23

Summary and outlook of shape and composition-controlled synthesis of LHP NCs

Numerous methods have been reported for the shape-controlled synthesis of both OIH and inorganic colloidal LHP NCs. Most of the reported methods generally yield either nanocubes, nanoplatelets or nanowires.¹⁴³ Recent studies have demonstrated the synthesis of non-cubic LHP NCs at relatively high reaction temperature.⁷²⁻⁷³ However, these methods are yet to be standardized for the routine synthesis of non-cubic LHP NCs. The shape of the LHP NCs is controllable from nanocubes to NPI of different thicknesses by varying several parameters, such as reaction temperature,¹⁹ precursor ratio,⁶² long-chain to short-chain ligands ratio,¹⁷ acid-base equilibrium of ligands.¹⁴⁸ In general, lower reaction temperatures lead to anisotropic growth of NCs, and this results in the formation of LHP NPI at reaction temperatures below 100 °C, and the thickness of NPIs decreases with decreasing the reaction temperature.¹⁹ On the other hand, LHP nanocubes transform into nanowires under prolonged reaction times in both the HI synthesis and the ultrasonication-assisted synthesis.^{23, 77} It was demonstrated that the transformation of nanocubes into nanowires occurs through an oriented attachment mechanism.^{23 188, 334} Furthermore, it was shown that the thickness of the nanowires is tunable down to the strong quantum-confinement regime using short-chain ligands.^{76, 78} In addition, shape-control is achieved through post-synthetic transformations. For example, it was shown that NPIs could be transformed into nanosheets,³³⁵ and nanowires could be transformed into nanorods.⁷⁵ Despite significant advances in the synthesis of LHP NCs, their growth mechanism is still not well understood due to the fast nucleation and growth processes, which are therefore hard to follow. This is critical for further advancing the synthesis of LHP NCs of desired shapes through controlled growth rate and directionality using specific ligands. The optical band gap of LPH NCs mainly depends on the extent of the quantum-

1 confinement that the NCs exhibit and this is discussed in detail in the optical properties section
2 (see section 9.1). The optical properties of LHP NCs are easily tunable across the visible spectrum
3 of light by halide (Cl, Br, and I) composition, and they can be prepared either by direct synthesis
4 or by applying halide ion exchange reactions. The unique feature of LHP NCs is that the halide
5 ion exchange is spontaneous and reversible, and it takes place at room temperature. This means
6 LHP NCs with any halide composition can be easily achieved using pre-synthesized LHP NCs
7 made of any one of the halide types. For some applications, such a spontaneous halide exchange
8 can be problematic. However, it was demonstrated that the halide exchange could be suppressed
9 by coating LHP NCs with lead sulfates.³¹³ In addition, good progress has been made regarding the
10 cation (A and B-site) exchange of LHP NCs for enhancement of their stability, for the sake of
11 introducing new optical properties and replacing Pb with nontoxic metal ions.

12

13 **2. SURFACE CHEMISTRY OF COLLOIDAL HALIDE PEROVSKITE NCs**

14 With the decrease of particle size down to several nanometers, the fraction of surface atoms in
15 NCs can be higher than 30%. The incomplete coordination of surface atoms usually contributes to
16 the appearance of defect energy levels in the bandgap that behave as exciton traps and lead to
17 nonradiative recombination.³⁴¹⁻³⁴² Therefore, in the past decades, researchers from the field of II-
18 VI semiconductor NCs (mainly the cadmium-based NCs) have made great efforts to solve this
19 problem. Finally, photoluminescence quantum yield (PLQY) of 100% and perfect
20 monoexponential PL decay were achieved by an elaborate design of synthesis procedures and shell
21 structures.³⁴³⁻³⁴⁴ However, lead halide perovskite (LHP) NCs with a high QY (ca. 100%) can be
22 prepared directly and easily even without shells.^{15, 345-346} This phenomenon is related to the high
23 defect tolerance of these materials.^{117, 347} Theoretical calculations have suggested that the defects

1 with low formation energies are the ones that contribute to shallow states. A detailed discussion
2 on defect tolerance and the unique emission properties of lead halide perovskite NCs are provided
3 in the optical properties section.

4 After several years of research, it was found that the surface defects, especially the halide
5 vacancies (V_X), still make great contributions to nonradiative recombination. Then, various
6 passivation strategies have been developed to enable a PLQY for perovskite NCs close to 100%.
7 As a whole, these passivation approaches can be divided into two types: post-synthesis passivation
8 and in-situ passivation, that is, during the synthesis (see below). It should be noted that crystal
9 defects in NCs can be eliminated by a self-purification mechanism.³⁴⁸

10

11 **2.1 SURFACE LIGANDS**

12 Lead halide perovskite nanomaterials typically consist of an all-inorganic or organic-inorganic
13 core, such as $CsPbX_3$ and $CH_3NH_3PbX_3$ ($X = Cl, Br, I$) NCs, capped with organic ligands and we
14 will refer to them as LHP@capping NCs. The interest of focusing on surface chemistry of LHP
15 NCs is to better understand the interaction between the ligand anchoring group(s) and the NC
16 surface in LHP@capping NCs with a view to finding the most suitable ligands for surface
17 passivation, thereby manifesting the best of the unique properties of the perovskite, thus enhancing
18 their applicability.

19 Ligands play a crucial role during the synthesis of the NCs, such as in the kinetics of the crystal
20 growth and in regulating the final NC size and shape.^{53, 349} In addition, the capping ligands can be
21 designed to prevent the agglomeration of the NCs and determine the extent of the NC-solvent
22 interaction and consequently, their dispersibility in the medium.^{53, 349, 113} However, the high
23 dynamic bonding between the NC surface and the capping ligands is at the origin of the chemical

1 instability of LHP@capping NCs; this has become patent during the purification of these
2 nanomaterials.^{53, 179} Therefore, enhancing the strength of the ligand coordination to the NC surface
3 can have a positive impact on the colloidal and chemical stability of the NCs, and consequently on
4 the conservation of their optical properties. Nevertheless, another important feature of the ligand
5 that has to be taken into account is its electrical conductivity, as efficient charge carrier transport
6 is required in NC thin film-based optoelectronic devices. Lately, this matter has attracted a great
7 deal of interest.³⁵⁰⁻³⁵¹

8 Techniques to visualize the dissociation of the ligands from the NC surface, as well as the nature
9 of the ligand anchoring group, are providing relevant information to find the most adequate ligand,
10 or combination of ligands, to exploit the unique properties of these materials at the nanoscale.^{85,}
11 ³⁵² The combination of spectroscopic techniques, such as nuclear magnetic resonance (NMR),
12 Fourier-transform infrared (FT-IR), and X-ray photoelectron spectroscopy (XPS) are useful to
13 determine the eventual ligand(s) on the NC surface and the nature of the ligand anchoring group(s).
14 In addition, the combination of NMR spectroscopy and thermogravimetric analysis (TGA) is a
15 suitable strategy to study the composition of LHP@capping.²⁶ The ionic nature of these NCs
16 makes them revert back to the NC precursors in a polar solvent, such as deuterated
17 dimethylsulfoxide (DMSO), thus making it possible to know the structure of the ligand(s) bonded
18 to the surface and to determine the ratio between the LHP@capping components easily by ¹H-
19 NMR.²⁶ In addition, the combination of NMR, nuclear Overhauser effect spectroscopy (NOESY)
20 and diffusion ordered spectroscopy (DOSY) makes it possible to determine if the organic ligand
21 is loosely or tightly bound at the NC surface.⁸⁵ Moreover, the NMR line broadening technique is
22 also of interest for surface chemistry analysis, and has been related to poor ligand solvation, a
23 feature of bound ligands.³⁵³ The broad line has a homogeneous and a heterogeneous component.

1 Solvation of the ligand shell contributes mainly to the heterogeneous line broadening as was
2 confirmed by dynamic simulations, while the homogeneous contribution depends on the NC size
3 (the bigger the size, the broader the line).³⁵⁴

4 Although the knowledge about ligand-NC interaction in colloids has increased remarkably in
5 the last years, there are still some issues to be overcome to improve the potential of colloidal
6 perovskite NCs in different technologies. Several contributions will be discussed below.

7

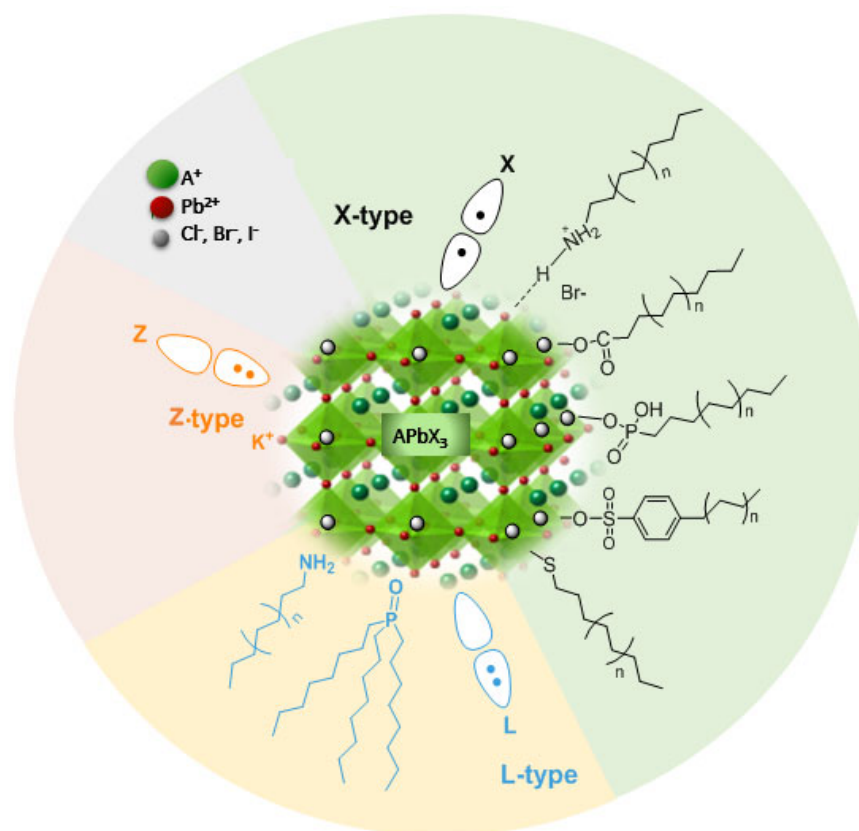
8 **2.2 PASSIVATION OF SURFACE DEFECTS WITH LIGANDS**

9 **The type of ligand binding** to the surface of common semiconductor NCs has been analyzed
10 using the covalent bond classification introduced by Green et al. for organometallic compounds.³⁵⁵⁻

11 ³⁵⁶ In this model, the covalent bond of any element is classified according to the total number of
12 electrons involved in the primary bonding in the valence shell of the element (M) and the number
13 of electrons the ligand used to form the bond.

14 Three types of binding ligands were reported: a) X-type, which involves a single occupied orbital
15 of the ligand anchoring group and one electron from M (the ligands are neutral species that are
16 radicals, such as H, COR, CR₃, C₆H₅, CN, OCN, ONO; X ligands can derive from anionic
17 precursors, such as halides, hydroxide, alkoxide alkyl species that are one-electron as neutral
18 ligands, but two electron donors as anionic ligands); b) L-type, which involves an orbital of the
19 ligand filled with two electrons and acts as a donor to the empty orbital of M (the ligands are
20 neutral molecules that are Lewis bases, such as NH₃, NR₃, OH₂, OR₂, PR₃, SR₃); and c) Z-type,
21 whose anchoring group orbital is empty and can accept an electron pair from M (the ligands are
22 neutral molecules that are Lewis acids, such as BH₃, BF₃, BCl₃).³⁵⁵⁻³⁵⁶

1 Regarding the type of ligands in LHP@capping NCs, the most common ligands used are of X-
 2 and L-type (see Scheme 1). The binding of ligands to the surface of these NCs is usually highly
 3 dynamic and therefore ligands can be lost during the isolation and the subsequent purification
 4 steps. Highly emissive LHP@capping NCs are the consequence of an efficient passivation of their
 5 surface defects with ligands that anchor to the NC surface with a high binding constant, which are
 6 mainly of the X- and L-types, thus providing colloidal and chemical stability.



7
 8 **Scheme 1.** Binding ligands (X, L, and Z-type, according to the covalent bond classification) used
 9 as capping agents of colloidal APbX₃ perovskite NCs.

10
 11 According to Table 1, the binding mechanism of the ligands ranked by the covalent bond
 12 classification can be summarized as: i) *X-type ligand*: covalent bond created after one electron

1 donation from the halide anion to the ammonium, or from the carboxylate, phosphate, sulphonate
2 or thiol/thiolate to the perovskite cations (Pb^{2+} , A^+), or between the charged groups of a
3 zwitterionic molecule and X^- and Pb^{2+} ; ii) *L-type ligand*: dative covalent bond created by sharing
4 a lone electron pair from the ligand with the metal center, and iii) *Z-type ligand*: dative covalent
5 bond by sharing a lone electron pair from the halide with a Lewis acid, such as the interaction
6 between K^+ and the perovskite and X^- .

7 In 2012, Papavassiliou et. al. described the preparation of nanocrystalline/microcrystalline
8 materials based on $\text{Pb}(\text{Br}_x\text{Cl}_{1-x})_3$, $\text{Pb}(\text{Br}_x\text{I}_{1-x})_3$, $\text{Pb}(\text{Cl}_x\text{I}_{1-x})_3$ units with $x=0-1$, which exhibit tunable
9 emission from 400-700 nm, from the corresponding quasi-two-dimensional compounds.⁶⁶
10 Suspensions based on lead bromides materials were obtained using a titration-like method, in
11 which the solutions of $(\text{CH}_3\text{NH}_3)(\text{CH}_3\text{C}_6\text{H}_4\text{CH}_2\text{NH}_3)_2\text{Pb}_2\text{Br}_7$, $(\text{CH}_3\text{NH}_3)(\text{C}_4\text{H}_9\text{NH}_3)_2\text{Pb}_2\text{Br}_7$ or
12 their precursors in dimethylformamide were injected into toluene, or toluene containing
13 polymethyl methacrylate (PMMA), at room temperature. The crystalline particles presented sizes
14 ranging in between 30-160 nm and green emission in the 531-510 nm range with PL quantum yield
15 from 0.13 to 16 %. These values were improved up to 25% by using $(\text{CH}_3\text{NH}_3)(\text{C}_4\text{H}_9\text{NH}_3)_2\text{Pb}_2\text{Br}_7$
16 as precursor. The particles prepared in a PMMA matrix increased their stability upon aging for at
17 least one year compared with a few hours for the suspension in toluene.

18 Galian and Pérez-Prieto et al. reported the preparation of colloidal hybrid perovskite NCs by
19 using a non-template strategy consisting of adding a mixture of **a long chain ammonium**
20 **bromide**, such as octylammonium bromide (OAmBr) and methylammonium bromide (MABr), to
21 an 80 °C solution of oleic acid (OA) in octadecene (ODE), followed by the consecutive addition
22 of PbBr_2 , and immediately afterwards the addition of acetone to induce the crystallization of the
23 perovskite (yellow solid) with a PLQY of 20% in toluene.⁶⁸ The electroluminescence of a thin-

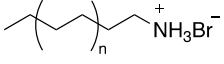
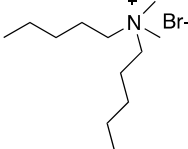
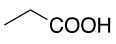
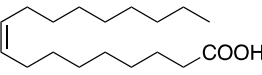
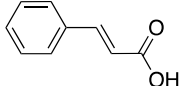
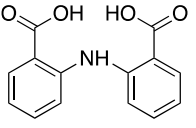
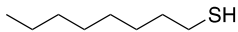
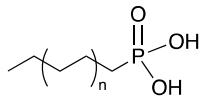
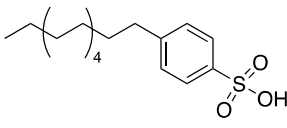
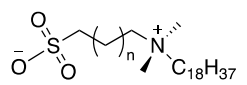
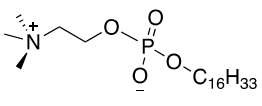
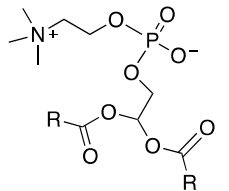
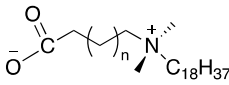
1 film light-emitting device prepared with these colloidal hybrid perovskite NCs showed a
2 noticeable improvement compared with that of bulk film, thus evidencing their potential for
3 optoelectronic applications. A year later, it was demonstrated that more emissive and stable
4 colloidal MAPbBr₃ NCs (PLQY of 83%) can be obtained in the absence of OA. ¹H-NMR studies
5 of the NCs, by reverting the perovskite back to its precursors in deuterated-DMSO, combined with
6 TGA made it possible to determine the presence of OAmBr (X₂ ligand) on the NC surface, as well
7 as the composition of the nanomaterial (NC plus ligand).²⁶ The N1s XPS spectrum of the NC
8 showed only a band with maximum at 402.6 eV, thus corroborating the presence of
9 alkylammonium to passivate the under-coordinated bromide of the NC surface. Then, bright lead
10 bromide perovskite NCs (PLQY of about 100%) were prepared by following the ligand-assisted
11 reprecipitation (LARP) technique (see below), using the quasi-spherical shaped 2-
12 adamantylammonium bromide as the only capping ligand.³⁵⁷ Though extraordinarily luminescent,
13 these NCs showed a trend to aggregate due to the high interaction between the adamantyl moieties;
14 in fact, they exhibited an average lifetime in the microsecond scale. The high affinity of the
15 adamantyl moiety for the cavity of cucurbit[7]uril (CB) enabled the preparation of perovskite NCs
16 with a host-guest complex as capping ligand, which showed a higher photostability under contact
17 with water than the NC passivated with 2-adamantylammonium bromide.³⁵⁷ Among various
18 ligands, **primary amine/carboxylic acid ligand** pairs became the most commonly used pairs of
19 organic ligands for the synthesis of bright colloidal perovskite NCs.^{15, 142} The LARP strategy,
20 introduced by Zhong et al., consisted of a dropwise addition of the capping ligands (octylamine
21 and oleic acid) and the MAPbBr₃ perovskite precursor solutions into a low polar solvent, followed
22 by centrifugation at room temperature to remove bulk material.¹⁵ The PLQY of MAPbBr₃ was
23 high and well-preserved after purification (PLQY ~80%). Similarly, Protesescu et al. prepared

1 highly luminescent and monodispersed colloidal CsPbBr₃ (PLQY of 90%) by a hot injection
2 methodology using oleylamine and oleic acid as organic ligands.¹⁵

3 Table 1 shows the chemical structure of the organic ligands mentioned in this section,
4 including acids, such as alkylcarboxylic, alkylphosphonic, alkylsulphonic and alkylphosphonic
5 acids, alkylamines, alkylammonium salts, alkylthiols and zwitterionic species. De Roo et al.
6 performed ¹H-NMR spectroscopic studies to determine the eventual ligand(s) at the NC surface
7 and also to gain insight into the surface chemistry of CsPbBr₃ NCs synthesized using oleylamine,
8 oleic acid, a Cs-oleate solution, octadecene and PbBr₂. NOESY experiments demonstrated that
9 octadecene and oleic acid did not bind to the NC surface, while oleylammonium bromide was
10 proposed as the capping ligand. It was suggested that the oleylammonium cation might have bound
11 to the surface bromide atoms via a hydrogen bridge and the bromide anion might have bound to
12 cesium or lead atoms located on the surface, in agreement with the ionic character of the CsPbBr₃
13 NCs.³⁵³ However, the data were not conclusive as to whether the NCs were stabilized by
14 oleylammonium bromide or oleylammonium oleate, both with a pair of X-type ligands, which
15 corresponds to an NC(X)₂ binding motif. Three possible combinations of these ligands were then
16 proposed: **oleylammonium bromide, oleylammonium oleate, and the unprotonated amine (L-**
17 **type ligand)**. As a consequence of the fast exchange between the ligands, it was difficult to
18 determine their individual contribution on the surface of the NCs. The addition of small amounts
19 of excess oleic acid and oleylamine before precipitation preserved the colloidal integrity and PL
20 of the NCs. They corroborated the presence of a tightly bound fraction of oleic acid by means of
21 NMR spectroscopy using dodecylamine/oleic acid as the ligand pair.

22

- 1 Table 1: Chemical structure of organic ligands used to prepare colloidal LHP NCs, categorized
- 2 according to the functional group and covalent bond classification (Part I)

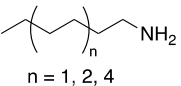
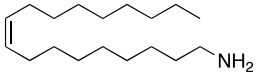
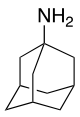
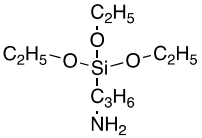
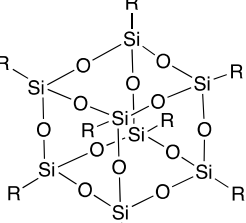
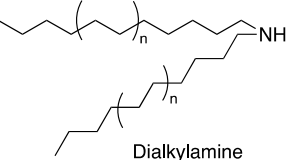
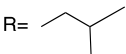
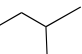
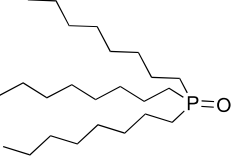
Type of Ligands	Classification of the ligands by Functional group & chemical structure			
X-type	Alkylammonium salt			
	 <p style="text-align: center;">$n = 1, 2, 4$</p> <p style="text-align: center;">hexyl-, octyl- or dodecylammonium bromide</p>	 <p style="text-align: center;">Didodecyltrimethylammonium bromide</p>		
	Alkylcarboxylic acid			
	 <p style="text-align: center;">propionic acid</p>	 <p style="text-align: center;">oleic acid</p>	 <p style="text-align: center;">cinnamic acid</p>	 <p style="text-align: center;">2,2'-iminodibenzoic acid</p>
	Alkylthiols	Alkylphosphonic acids	Alkylsulfonic acids	
	 <p style="text-align: center;">octanethiol</p>	 <p style="text-align: center;">$n = 1, 6, 8, 14, 18$</p>	 <p style="text-align: center;">dodecylbenzene sulfonic acid</p>	
	Zwitterionic compounds			
 <p style="text-align: center;">Sulfobetaine</p>	 <p style="text-align: center;">N-hexadecylphosphocholine</p>	 <p style="text-align: center;">Lecithin</p> <p style="text-align: center;">$R, R' = \text{palmityl, stearyl, oleyl, linolyl, linolenyl}$</p>		
 <p style="text-align: center;">γ-aminoacid</p> <p style="text-align: center;">N,N-dimethyldodecylammonium butyrate</p>				

3

4

5

- Table 1: Chemical structure of organic ligands used to prepare colloidal LHP NCs, categorized
- according to the functional group and covalent bond classification (Part II)

Type of Ligands	Classification of the ligands by Functional group & chemical structure
L-type	<p style="text-align: center;">Alkylamine</p> <div style="display: flex; justify-content: space-around;"> <div style="text-align: center;"> <p>primary amine</p> <p>Linear and small primary amine</p>  <p>n = 1, 2, 4 hexyl- octyl- or dodecylamine</p>  <p>oleylamine</p>  <p>adamantylamine</p> </div> <div style="text-align: center;"> <p>Bulky primary amine</p>  <p>(3-aminopropyl)triethoxysilane (APTES)</p>  <p>polyhedral oligomeric silsesquioxane (POOS) PSS-[3-(2-aminoethyl)amino]propyl-heptaisobutyl substituted</p> </div> <div style="text-align: center;"> <p>Secondary amine</p>  <p>Dialkylamine</p>  <p>R = </p> </div> </div> <p style="text-align: center;">Alkylphosphine oxide</p>  <p>trioctylphosphine oxide</p>
Z-type	<p>Cation K^+</p>

3

4

1 It was reasoned that oleic acid cannot bind by itself, but it binds as an ion pair with amine, the
2 actual tightly bound ligand pair being oleylammonium oleate. Rogach et al.³⁵⁸ have suggested
3 that **oleylamine** i) acts as an L-type coordinating agent binding to Pb^{2+} to form a Pb^{2+} -oleylamine
4 complex and ii) reacts with oleic acid to form the **oleylammonium oleate** salt, and then oleate
5 coordinates to Pb^{2+} due to the high coordination number of the metal cation (between 2 and 10).³⁵⁹
6 Consequently, the N1s XPS spectrum showed two peaks, at 398.6 eV and 400 eV, which can be
7 ascribed to the oleylamine and methylammonium/oleylammonium, respectively, while the O 1s
8 XPS showed two peaks at 532.3 eV and 533.7 eV, which can be attributed to two nonequivalent
9 oxygen atoms of carboxylic acid and to the two chemically equivalent oxygen atoms of oleate,
10 respectively.

11 Galian and Pérez-Prieto et al. combined a **short primary amine and a short carboxylic acid**,
12 such as 2-adamantylamine and propanoic acid, as ligand pairs to produce highly photoluminescent
13 (PLQY ca. 100%) colloidal $CH_3NH_3PbBr_3$ perovskites.³⁴⁶ The N1s XPS spectrum deconvoluted
14 into two peaks centered at 399.8 eV and 401.5 eV with an area ratio of 0.3; these peaks can be
15 ascribed to 2-adamantylamine and the methylammonium salt, respectively. Both O1s and C1s XPS
16 spectra confirmed the presence of carboxylic acid and carboxylate species. The quantification of
17 the perovskite components by XPS showed an atomic ratio of 2.7 and 1.1 for Br/Pb and N/Pb,
18 respectively. This can be considered as a presence of bromide vacancies (V_{Br}) in the perovskite
19 more than an excess of lead atoms, as was observed by other researchers.¹⁹⁶ These LHP@capping
20 nanomaterials showed a low tendency to aggregate in solution due to the reduction of the ligand-
21 ligand interaction between the NCs while preserving the high QY. Those NCs assembled in solid
22 films with thicknesses of hundreds of nanometers also retained a high PLQY, specifically ca.
23 80%.³⁴⁶

1 **Primary amines with a branched structure** have been used as an L-type ligand, but their
2 use has led to perovskites with a low PLQY. Examples of this type of ligands³⁶⁰ are 3-
3 aminopropyl)-triethoxysilane, (APTES) and polyhedral oligomeric silsesquioxane (POSS) PSS-
4 [3-(2-aminoethyl)amino]propyl-heptaisobutyl substituted, which have enabled a good control over
5 the size of $\text{CH}_3\text{NH}_3\text{PbBr}_3$ NCs. Their low PLQY of $< 20\%$ has been attributed to an inadequate
6 passivation of the nanoparticle surface due to the steric effect of the branched ligands. In addition,
7 $\text{CH}_3\text{NH}_3\text{PbBr}_3$ NCs have been passivated with a commercial cyclic peptide cyclo(RGDFK),
8 containing 5 amino acids (arginine, glycine, aspartic acid, phenylalanine and lysine).³⁶¹ Modeling
9 of $\text{PbBr}_3^-/\text{Cyclo(RGDFK)}$ precursor complexes suggested the preferential coordination of the
10 peptide to the PbBr_3^- via the amine vs the guanidine group, which is consistent with the broadening
11 of the $-\text{NH}_3^+$ moiety peak (3200 cm^{-1}) in the FTIR spectrum of the complex. The low PLQY (ca.
12 20%) of the perovskite NCs passivated with cyclo(RGDFK) has been ascribed to charge transfer
13 from the perovskite core to the peptide shell.

14 **Secondary amines** of different length, such as dihexyl-, dioctyl-, dodecyl-, didodecyl and
15 dioctadecylamine have been used to prepare, in combination with oleic acid, CsPbBr_3 nanocubes
16 with good emissive properties ($48\text{-}80\%$) and a uniform cubic shape that allows their self-assembly
17 in $50\text{ }\mu\text{m}$ -sized superlattices.¹⁴⁶ Interestingly, the pure shaped NCs were obtained irrespectively
18 of the length of the amine, oleic acid concentration and temperature. Density functional theoretical
19 (DFT) calculations suggested that the binding of the dialkylammonium molecules to the [100]
20 facets of CsPbBr_3 is weak and secondary to that of oleate, otherwise it would cause a drastic
21 distortion to the lattice.¹⁴⁶

22 Different capping agents, such as acids (oleic, phosphonic and sulphonic acids) and thiols, have
23 been proposed to avoid the labile binding of amines (L-type ligand), ammonium/halide and

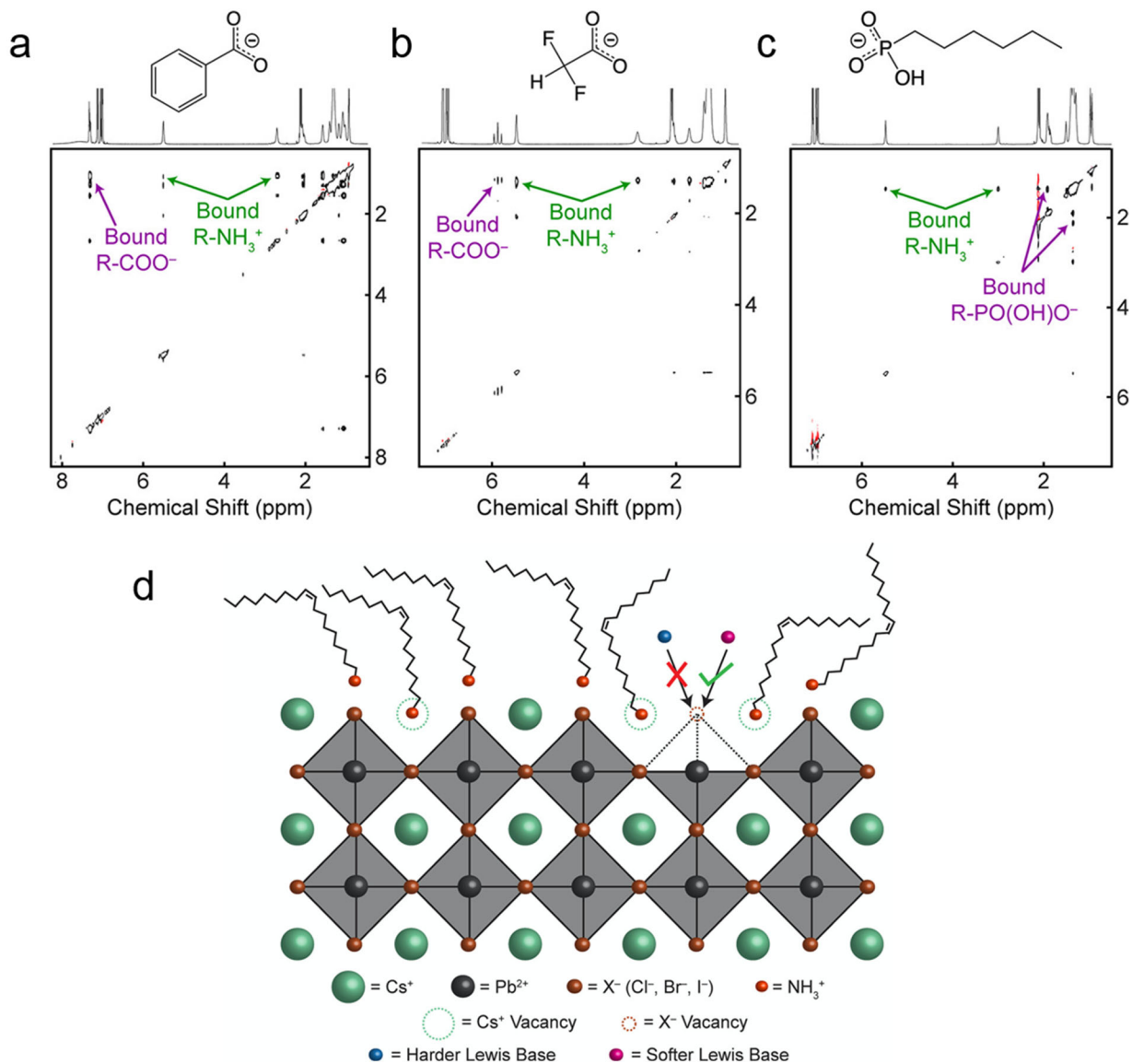
1 ammonium/oleate pairs (X₂-type ligands) to the NC surface. There is some controversy regarding
2 the performance of oleic acid as the CsPbX₃ NC surface ligand. Yassitepe et al. developed an
3 amine-free method to prepare CsPbX₃ NCs passivated by only oleic acid,³⁶² which exhibits strong
4 interaction with the surface and as a result, the NCs can be washed several times. However, oleic
5 acid does not seem to be a good candidate to provide CsPbX₃ NCs with a high PLQY. By contrast,
6 Lu et al. built colloidal CsPbBr₃ with **oleate as the only ligand** (X-type ligand) and produced
7 nanocubes of 11.2 nm with a PLQY of 70 %. They showed a colloidal stability over at least two
8 months, which is considerably higher than that reported for LHP@amine-oleate passivated NCs.³⁶³
9 ¹H-NMR spectroscopy corroborated oleate as the surface ligand, which was then effectively
10 replaced by cinnamic acid derivatives, namely *trans*-cinnamate and *trans*-3,5-difluorocinnamate,
11 as demonstrated by FT-IR spectra of the new NCs (quantitative removal of the native oleate), as
12 well as by ¹⁹F NMR and XPS measurements of the difluoro-compound (observation of a broad
13 signal and the presence of F signals, respectively). The easy replacement enabled the tuning of the
14 NC optical/electronic properties but decreased its PLQY. Interestingly, LHP@cinnamate NCs
15 showed enhanced photocatalytic activity for α -alkylation of aldehydes. The positive effects of the
16 ligands in terms of the NC photocatalytic response might be due to a) an increase of the NC
17 photoredox potential, b) a change in the ligand shell permeability, and c) a good passivation of the
18 surface defects, thus increasing the lifetime of the photocarriers and/or reducing surface catalytic
19 sites.³⁶³ Another important factor can be the synergy between the NC surface and its organic ligand
20 to lead to a high substrate pre-concentration near the NC surface (for further details see section 20
21 “Photocatalysis using perovskite NCs”).³⁶⁴ More studies are required to determine the contribution
22 of these factors on the performance of the NCs in photocatalysis.

1 The combination of trioctylphosphine and oleic acid has been used to prepare nanocubes of
2 CsPbBr₃ NCs (PLQY of ca. 60%) with oleate as the only capping ligand;¹⁸¹ this synthetic route
3 can be extended to *n*-tetradecylphosphonic acid and diisooctylphosphonic acid. ³¹P-NMR
4 spectroscopic studies were performed to determine the role of trioctylphosphine and oleic acid in
5 PbBr₂ solubility; these studies indicate a competing interaction between the protic acid and PbBr₂
6 for the oxygen of TOPO. ¹H-NMR studies give information on the dynamics of the Cs-oleate
7 capping agent by focusing on the broadening and shift of the signals compared to those of the free
8 acid. Negative cross-peaks in the NOESY spectrum corresponded to species with long correlation
9 times with a movement that was slower in solution compared to small free molecules. A diffusion
10 coefficient of 242 μm²/s, calculated by DOSY spectroscopy, was highly reduced compared to 725
11 μm²/s in the free acid and corresponded to a 76% of bounded oleate species on the NC surface.¹⁸¹

12 **Sulfur-containing X-type ligands**, alkyl-thiol and thiocyanates, were proposed to replace the
13 oleylamine/oleic acid pair of ligands and to act as better passivation agents, by reducing the surface
14 defects and leading to NCs with a monoexponential PL lifetime and a better PLQY.³⁶⁵ A
15 combination of alkyl-thiols with alkyl-amines or alkyl acids was used as a novel strategy to control
16 the crystal structure from orthorhombic CsPbBr₃ towards tetragonal CsPb₂Br₅ nanowires and
17 nanosheets, which exhibited a high stability at high-temperature and under humid conditions.

18 An exhaustive and systematic surface chemistry study has been reported by Alivisatos et. al. in
19 2018 to draw together the observations from several reports on this subject.¹⁹⁶ A methodology to
20 obtain trap-free lead halide NCs was proposed based on the combination of different techniques,
21 such as NMR, NOESY and fluorescence spectroscopies, with Ab initio calculations that evidenced
22 that a soft X-type ligand can properly passivate the uncoordinated lead atoms, created by the halide
23 vacancies on the NC surface. A cesium vacancy on the surface can be replaced by the

1 oleylammonium cation. The lower the NC concentration (high dilution), the greater number of
2 surface V_x , due to low binding of the oleylammonium halide pair. NMR line width was used to
3 determine the number of trap-states, related to V_x , which combined with the PLQY gave the ratio
4 between the radiative and non-radiative rate constant (k_r/k_{nr}). The k_r/k_{nr} ratio value was related to
5 the defect tolerance of the different halide perovskites (9500, 390 and 53 for CsPbI₃, CsPbBr₃ and
6 CsPbCl₃, respectively). Soft Lewis bases that can substitute halide vacancies and coordinate to
7 lead (which is a relatively soft Lewis acid) can be a neutral molecule such as a pyridine and
8 thiophene or an anionic X-type ligand, such as alkylphosphonate, S^{2-} , benzoate, fluoroacetate,
9 methane sulphonate or trioctylphosphine. A ligand exchange strategy was used to introduce
10 different alkyl carboxylate for the oleylammonium-R-COOH ligand pair, such as benzoate,
11 fluoroacetate, and difluoroacetate. Nuclear Overhauser effect NMR spectroscopy was used to
12 confirm the binding of the ligands to the NC surface supported by the negative cross peaks (Figure
13 31A-B). A good affinity of softer X-type ligands for the NC surface was also confirmed by the
14 negative (black) NOE of oleylammonium-hexylphosphonate (Figure 31C). These anionic ligands,
15 X-type Lewis bases, could bind to cesium atoms on the surface, but this is not thermodynamically
16 favorable³⁶⁶, indicating they are binding to the surface lead atoms eliminating the V_x . By contrast,
17 hard Lewis X-type ligands, such as alkylcarboxylates, carbonates and nitrates are inefficient
18 passivating ligands (Figure 31D).
19



1
2 **Figure 31.** ¹H-NOESY NMR spectra of CsPbBr₃ NC samples exchanged to ligand pairs of
3 oleylammonium and (a) benzoate, (b) difluoroacetate, and (c) hexylphosphonate. All ligand pairs
4 feature negative (black) NOE signals rather than positive (red) NOE signals, thereby corroborating
5 their interaction with the NC surface. (d) Schematic representation of a cesium- and halide-

1 deficient surface terminated by CsX facets, consistent with experimental results. Reprinted with
2 permission from *Ref.*¹⁹⁶ Copyright (2020) American Chemical Society.

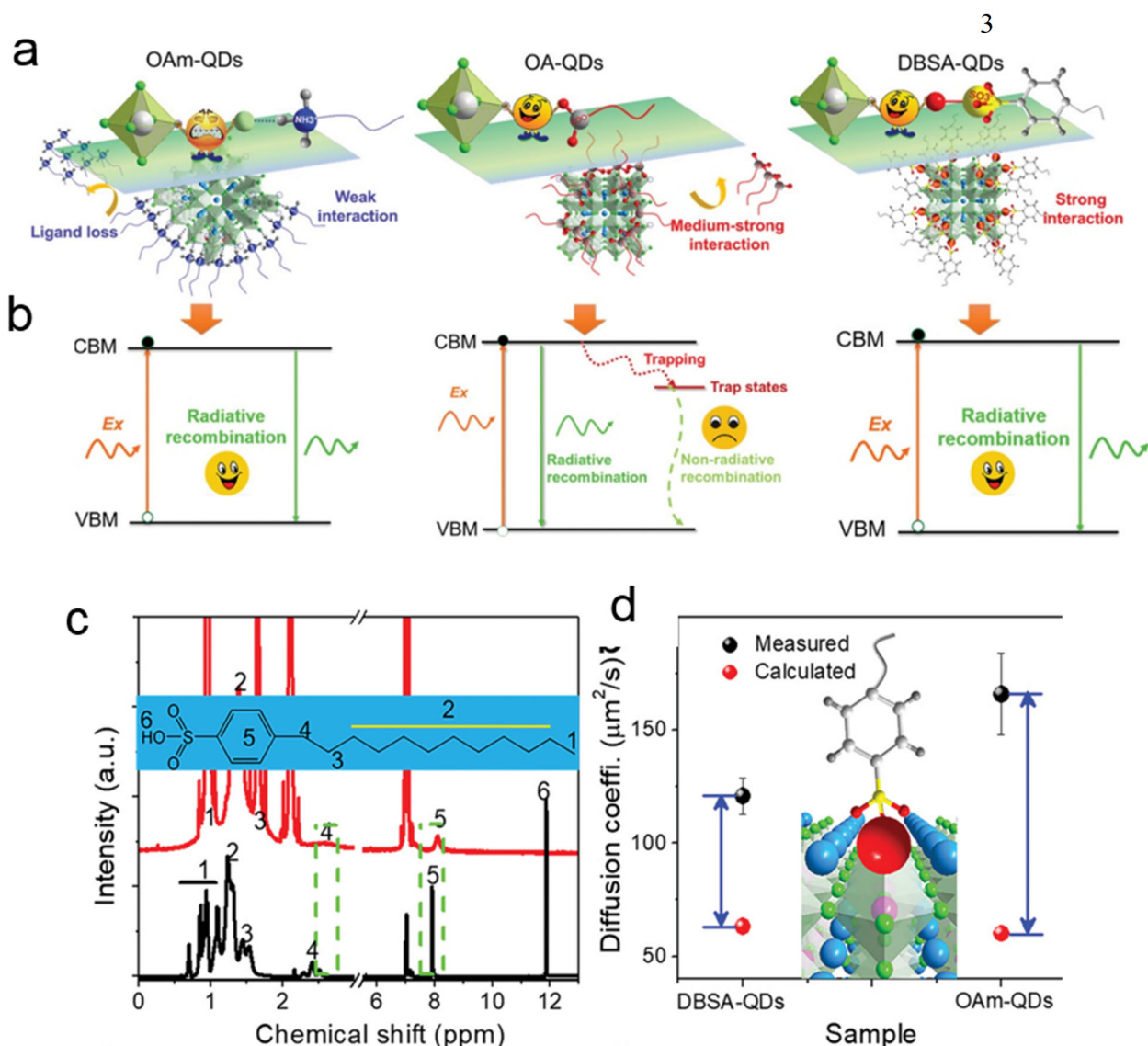
3
4 **Alkylphosphonates as the only organic ligand** were first introduced by Xuan. et al.²⁹¹ CsPbBr₃
5 NCs passivated with 1-tetradecylphosphonate were prepared at room temperature with good
6 emissive properties (PLQY of 68 %) and extraordinary water and thermal stability by using 1-
7 tetradecylphosphonic acid. FTIR showed the replacement of the P=O band at 1230 cm⁻¹, belonging
8 to the 1-tetradecylphosphonic acid, by a broad band at 1000-900 cm⁻¹, ascribed to Pb-O-P, thus
9 corroborating the anchoring of the alkylphosphonate. Consequently, the O1s XPS spectrum
10 evidenced the presence of peaks at 530.8 eV and 530.2 eV corresponding to P-O-Pb and P-O
11 bonds, respectively, confirming the FTIR analysis. Increasing the concentration of the phosphonic
12 acid caused a blue shift in the absorption spectrum, which is consistent with the formation of
13 smaller NCs due to a decrease in the rate of ligand release through the organic shell. The use of a
14 phosphonic acid concentration higher than 7.5 mg. mL⁻¹ caused the decrease of NC PLQY, which
15 can be associated to the steric hindrance resulting in a high number of uncoordinated surface atoms.
16 Likewise, Zhang et al. prepared colloidal CsPbBr₃ NCs by employing alkyl phosphonic acids as
17 the only surfactant. NMR analysis revealed the presence of both phosphonic acid anhydride and
18 hydrogen phosphonate species on the NCs surface. Theoretical calculations indicated a high
19 affinity of phosphonate ligands for the NC surface, and similar stabilization energy of the [001]
20 and [110] facets, thus resulting in the formation of NCs with a truncated octahedron shape, that
21 exhibited a nearly 100% PLQY.³⁶⁷ A follow-up of this work, by the same group, reported the
22 synthesis of CsPbBr₃ NCs using custom-made oleylphosphonic acid (OLPA). The lower
23 temperature at which OLPA was soluble in the reaction mixture, compared to phosphonic acids

1 with linear chains, allowed the synthesis of NCs (at 100°C) with sizes down to 5 nm. These NCs
2 were also more colloiddally stable upon exposure to air than thos of ref. ³⁶⁷, and againg this was
3 traced back to the higher solubility of OLPA.

4 **Alkylthiols** were used to induce the transformation of CsPbBr₃ NCs to CsPb₂Br₅ nanostructures,
5 CsPb₂Br₅ nanosheets and nanowires were obtained by controlling the ratio between alkyl thiols
6 and alkyl amine or alkyl acids.³⁶⁵ The presence of thiols in the system increased the tolerance to a
7 high-temperature and a high humid environment favored by the good affinity of sulfur to lead
8 atoms. The strong affinity of thiols for the Pb²⁺ sites reduced considerably the densisty of surface
9 defects, leading to a PLQY close to unity and a monoexponential PL decay kinetics.

10 **Long chain benzene sulfonic acid**, such as dodecylbenzene sulfonic acid, was chosen as an
11 excellent candidate to replace the bromide vacancy on the NC surface (Figure 32a).³⁶⁸ In order to
12 eliminate the defect energy levels, ligands with anionic heads with similar electronic features to
13 those of bromide ions should be favorable. A good interaction of alkylsulfonic acid with lead is
14 expected as the calculated binding energy of 1.64 eV in sulfonate-Pb is comparable with 1.47 eV
15 in CH₃NH₃Br-Pb. The interaction strength between the ligand and the NC surface was estimated
16 by diffusion ordered spectroscopy (Figure 32d); the registered diffusion coefficient was smaller
17 than for oleylamine capped NCs, which is consistent with a stronger interaction between the
18 sulfonate and the NC surface. Such ligand interacts with lead atoms and eliminates the defect
19 energy level successfully, leading to CsPbBr₃ NCs with a PLQY higher than 90%. This binding
20 was strong enough to resist a washing treatment, as shown by NMR (Figure 32c), keeping the
21 PLQY up to 90% (Figure 32b). The high long-term colloidal stability and photostability under 400
22 nm irradiation of sulfonate-capped NCs compared to oleylammonium halide-capped NCs is a

- 1 further evidence of the strong interaction between the sulfonate ligands and the NC surface, which
- 2 makes these NCs appealing in thin-film technologies.³⁶⁸



6 **Figure 32.** Comparison of different ligand strategies. (a) Binding motif on CsPbBr₃ QD surface
 7 and interaction strength of oleylammonium (OAm), oleic acid (OA), and dodecylbenzene sulfonic
 8 acid (DBSA) ligands. (b) The effect of different ligands on exciton recombination dynamics.
 9 Evidence of strong DBSA-QD interaction. (c) ¹H NMR full spectra of pure DBSA and perovskite

1 capped with DBSA after three purification cycles. (d) Diffusion coefficients of DBSA and
2 perovskites capped with oleylammonium capped NCs. Reprint with permission of Ref.³⁶⁸

3
4 **Zwitterionic long-chain molecules**, such as commercially available sulfobetaines,
5 phosphocholines and γ -aminoacids, bind tightly to the CsPbBr₃ surface due to the fact that i) they
6 can coordinate simultaneously to the surface cations and anions on the NC surface and ii) the
7 cationic and anionic groups of their structure cannot be neutralized. The presence of the
8 zwitterionic ligand as the sole ligand at the NC surface was evidenced by complete ionic
9 dissolution of purified NCs in deuterated-DMSO, which freed the surface-bound ligands.¹⁷⁴ In
10 addition, DOSY NMR spectroscopy of the NCs evidenced that the diffusion coefficient related to
11 the broad resonances (corresponding to the zwitterionic ligands anchored to the NC surface) was
12 consistent with that estimated by the Stokes-Einstein equation (2 orders of magnitude slower than
13 that of the free ligand). These NCs can be thoroughly purified, while preserving a PLQY above
14 90%, and can be densely packed in films, which exhibit high PLQY and good charge transport
15 characteristics.

16 Inspired by these results, natural lecithin (a zwitterionic phospholipid with branched chains) was
17 proposed as an effective ligand due to its branched chains that increase interparticle repulsion, thus
18 enabling a high effective recovery of the NCs as well as single nanoparticle spectroscopy when
19 using diluted samples.¹⁷² In addition to these X-type acid ligands, L-type ligands which possess
20 lone electron pairs can also interact with lead ions with an unoccupied orbital.⁷⁹ However, from
21 the synthesis viewpoint, it is difficult to introduce L-type ligands since many of them cannot
22 dissolve the precursors. Interestingly, Zhang et al. prepared CsPbBr₃ NCs following the room-
23 temperature anti-solvent strategy, using only oleylamine (OAm) as the ligand. In this strategy, the

1 polar solvent dissolved the precursors efficiently, thereby enabling the direct interaction of OAm
2 with the NC surface; both theoretical and experimental results confirmed the significant
3 passivation effect and strong binding energy of OAm. As a consequence, the NCs exhibited a
4 PLQY close to unity and dramatically improved their stability when undergoing purification
5 processes and in the presence of water.

6 To our knowledge, there are hardly any examples of surface passivation of lead halide NCs with
7 Z-type ligands; namely, the K^+ cation and the K-oleate complex were used as passivating ligands.
8 Galian and Pérez-Prieto et al. prepared **K^+ -capped** $CH_3NH_3PbBr_3$ NCs by adding KPF_6 to the
9 perovskite precursor dimethylformamide solution following the reprecipitation strategy.³⁴⁶ The K^+
10 counterion is more lipophilic and less coordinating than bromide ions and replaced the excess of
11 methylammonium cation at the NC surface. The NCs effectively self-assembled on a substrate to
12 produce homogeneous solid films. On the contrary, Huang et al. added **K-oleate** to a toluene
13 dispersion of previously prepared $CsPbBr_3$ NCs by following a hot-injection protocol; the post-
14 synthetic treatment of the $CsPbBr_3$ NCs with K-oleate enhanced their photoluminescence and
15 photostability.³⁶⁹

16 Remarkably, the high dynamic bonding between the NC surface and some capping ligands can
17 be used advantageously to assemble perovskite NCs into two-dimensional superstructures. Yang
18 and Dong et al.³⁷⁰ have reported on the linear assembly of $CsPbBr_3$ NCs within $PbSO_4$ -oleate
19 polymers, resembling the morphology of a peapod. The capping pod mostly preserved the NC
20 optical properties. In addition, Hofkens and Pérez-Prieto et al.³⁷¹ reported on the linear assembly
21 of $CH_3NH_3PbBr_3$ NCs in lead(II) polymers by simply mixing the precursors of both the NC and
22 the polymer. Correlative single-particle fluorescence and AFM evidenced the formation of ordered

1 and non-connected $\text{CH}_3\text{NH}_3\text{PbBr}_3$ NC polymers, which were emissive and showed PL
2 intermittency.

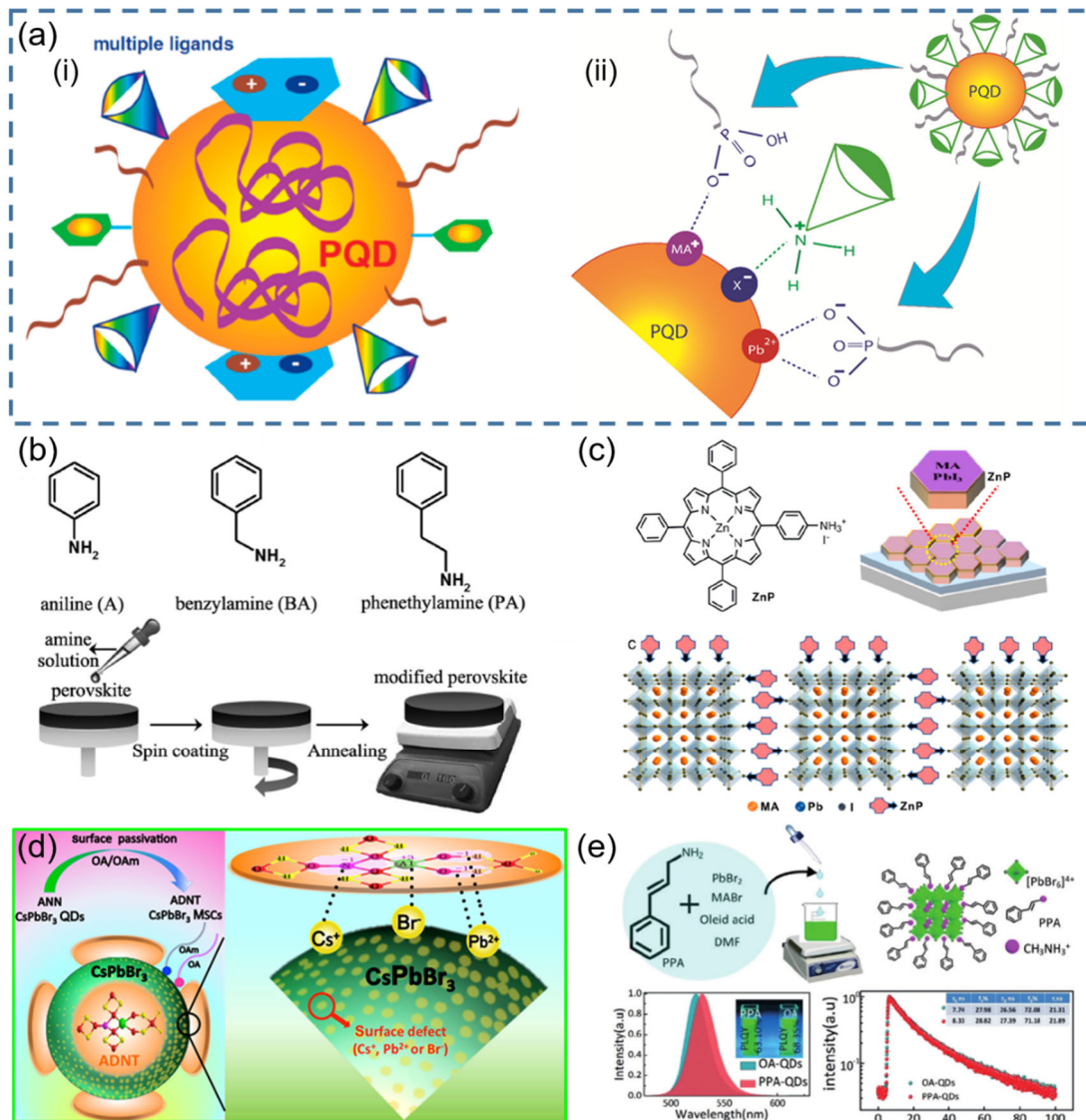
3 **Simultaneous passivation** of both cationic and anionic defects with anionic and cationic ligands
4 is usually required for efficient stabilization of LHP NCs, and this essentially demands a “cocktail”
5 approach, as illustrated in Figure 33a-i.³⁷² The **degree of acidity and basicity of the ligands** is
6 also important for effective passivation, as the defects can have a varying degree of acidity or
7 basicity. Over the years, a wide range of organic acids and amines (e.g. oleylamine/oleic acid,
8 octylamine, phosphonic acids (PAs), aminopropyl)triethoxysilane (APTES), L-cysteine,
9 aniline/benzylamine, phenerhylamine and n-trioctylphosphine (TOP)) have been tested as ligands
10 for LHP NCs.^{15, 139, 348, 373-382} For instance, in the case of CsPbI_3 , Cs^+ is considered as a weak acid,
11 Pb^{2+} a weak acid as well, and I^- a weak base,³⁸³ while in the case of MAPbBr_3 , MA^+ is a weak acid
12 and Br^- is a weak base (though stronger than I^-).³⁷⁷ Based on the Pearson acid/base case concept,
13 weak acid defects require weak base ligands, while weak base defects require weak acid ligand for
14 optimal passivation.³⁷⁷ For example, short chain organic phosphoric acids (PAs) have stronger
15 acidity and thus their conjugate base has stronger basicity than their longer chain counterparts.³⁷⁷
16 Four different linear alkyl PAs [PAs with the straight chain from short to long: MPA, n-
17 hexylphosphonic acid (HPA), 1-tetradecylphosphonic acid (TDPA), and n-octadecylphosphonic
18 acid (ODPA)] have been used in conjunction with APTES as capping ligands to synthesize
19 MAPbBr_3 perovskite NCs.⁶ As illustrated in Figure 33a-ii, the protonated APTES and
20 deprotonated PAs produce weak acidic R-NH_3^+ , weak basic $\text{R-PO}_2(\text{OH})^-$, and even weaker basic
21 R-PO_3^{2-} . These ions likely passivate the surface weak basic Br^- , weak acidic MA^+ , and even weaker
22 acidic Pb^{2+} cations, respectively. In addition, MPA-APTES has larger acid-base equilibrium
23 constant (K_{eq}) compared with that of HLA-APTES, TDPA-APTES and ODPA-APTES, thereby

1 producing of a higher concentration of $R-NH_3^+$, $R-PO_2(OH)^-$, and $R-PO_3^{2-}$. Therefore, better
2 passivation is achieved with the most acidic and shortest chain MPA.⁶ Similarly, a change in
3 basicity of amines can also affect the passivation. As shown in Figure 33 b, FAPbI₃ (FA for
4 formamidinium) films have been prepared using amines with different basicity: aniline (pKa 4.87),
5 benzylamine (pKa 9.34), and phenethylamine (pKa 9.83). The basicity of these amines follows the
6 order of phenethylamine > benzylamine > aniline, therefore, protonated phenylalkylamine should
7 be the weakest acid, which should provide the most effective passivation by interacting with the
8 weak base I⁻.³⁷⁵

9 If the acidity and basicity of both the acidic and basic ligands with the same anchoring groups
10 are changed in the precursor solution during synthesis, the passivation outcome can also change.
11 For instance, Pan et al.¹⁷⁹ systematically varied the hydrocarbon chain of carboxylic acids and
12 amines, from 18 carbons (18C) down to 2 carbons (2C), including carboxylic acids including
13 C18A (OA), C12A (dodecanoic acid), C8A (octanoic acid), and C6A (hexanoic acid) and amines
14 including C18B (OAm), C12B (dodecylamine), and C6B (hexylamine), to understand their effect
15 on the surface properties of CsPbBr₃ PNCs. These organic surfactant molecules affect the
16 nucleation and crystallization processes, with the C18A-C18B sample showing the highest PLQY
17 indicative of the best passivation. This is attributed to the longer chain length C18A-C18B with
18 larger K_{eq} , which producing higher concentrations of $-COO^-$ and $-NH_3^+$ ligands that are stronger
19 bases and acids than that of the short-chain molecules to passivate Cs^+ , Pb^{2+} , and Br^- defects,
20 respectively.

21

22



1
 2 **Figure 33.** (a-i) Structural model for surface passivation of LHP NCs with multiple defects using
 3 a combination of ligands in a “cocktail” approach. Reproduced with permission from Ref.³⁷².
 4 Copyright 2019 American Chemical Society. (a-ii) Schematic illustration of the major surface
 5 passivation mechanism of $\text{CH}_3\text{NH}_3\text{PbBr}_3$ perovskite NCs surface defects. Reproduced with
 6 permission from Ref.⁹. Copyright 2019 Wiley. (b) The chemical structures of aniline, benzylamine,
 7 and phenethylamine, and schematic illustration of amine treatment of perovskite films through a
 8 spin-coating method, followed by an annealing process. Reproduced with permission from Ref.
 9 ³⁷⁵. Copyright 2016 Wiley. (c) Structure of Zn-porphyrin (ZnP), scheme illustration of MAPbI_3

1 film with ZnP “doping”, and structure of perovskite encapsulated by ZnP. Reproduced with
2 permission from Ref.³⁸⁴. Copyright 2019 American Chemical Society. (d) Schematic illustration
3 of the major surface passivation mechanism of CsPbBr₃ magic sized clusters or perovskite NCs
4 surface defects. Reproduced with permission from Ref. ³⁸⁵. Copyright 2019 American Chemical
5 Society. (e) Illustration of the MAPbBr₃ NCs processing progress, the structural representation of
6 PAA- perovskite NCs (PAA: 3-phenyl-2-propen-1-amine) in which PAA instead of OA (oleic
7 acid) acts as capping ligands, steady-state PL spectra and representative photograph and PLQY
8 (photoluminescence quantum yield) values of PPA-perovskite NCs and OA-perovskite NCs
9 colloidal solution under 365 nm UV light, TRPL (Time-resolved photoluminescence) spectra of
10 PPA- perovskite NCs and OA- perovskite NCs colloidal solution, and color-tunable MAPbX₃
11 perovskite NCs with PPA as capping ligand. Reproduced with permission from Ref. ³⁸⁶. Copyright
12 2018 Wiley.

13
14 **The size and shape of molecular ligands** can also strongly influence the effectiveness of
15 passivation of MHPs, partly due to different steric hindrance, which in turn affect the morphology,
16 crystalline phase, and optical and electronic properties of MHPs.^{378, 387-388} On the other hand,
17 MHPs of different sizes and shapes can create different combinations and types of defects, and
18 therefore demand molecular ligands with different sizes and shapes for optimal passivation.
19 Besides passivating the surface defects through the anchoring groups, the size and shape of the
20 ligands are particularly important in stabilizing MHPs by preventing reaction with external
21 environmental species such as O₂ and moisture.³⁶² In particular, large ligands can afford multiple
22 functional groups in one molecule. For example, butylphosphonic acid 4-ammonium chloride with
23 a combination of phosphate and amino functional groups can simultaneously passivate MA⁺, Pb²⁺

1 and I⁻ defects.³⁸⁹ Additionally, suarine, polyaniline, and quaternary ammonium salts have been
2 shown to be good capping ligands for MAPbI₃ bulk, MAPbI₃ film, and MAPbBr₃ bulk,
3 respectively.^{320, 374} Peptides containing both -NH₃⁺ and -COO⁻ in one molecule have been used to
4 passivate MA⁺, Pb²⁺, and Br⁻ of MAPbBr₃ perovskite NCs.³⁸⁰ Similarly, trifunctional L-cysteine
5 has been used to passivate MAPbBr₃ perovskite NCs and induced self-assembly of perovskite
6 NCs, based on synergistic effects among -NH₃⁺, -COO⁻, and -SH groups.³⁷³ Therefore, the key
7 choice of the size of molecular ligands not only depends on the size and surface defects distribution
8 of perovskites but also relates to the synergistic effects of the functional groups of the used ligands.

9 **Regarding the ligand shape**, this can be linear, branched, umbrella-shaped, planar, or spherical.
10 Most studies to date have used linear shaped molecules, such as OA and OLA as capping
11 ligands.³⁹⁰⁻³⁹¹ In addition, a few attempts were made with branched ligands. For instance, Zhu et
12 al.³⁹² used protonated (3-Aminopropyl)trimethoxysilane (APTMS, umbrella shaped) ligands in the
13 synthesis of CsPbBr₃ perovskite NCs. The authors found that the resulting NCs exhibit improved
14 PLQY and stability in polar solvents. Similarly, umbrella shaped APTES and polyhedral
15 oligomeric silsesquioxane (POSS) PSS-(3-(2-aminoethyl)amino)propyl-heptaisobutyl substituted
16 (NH₂-POSS) have been used along with OA to passivate MAPbBr₃ perovskite NCs for enhanced
17 stability.³⁹³ This is attributed to the strong steric hindrance and propensity for hydrolysis of
18 APTMS, APTES, and NH₂-POSS, which prevent molecules such as H₂O and O₂ from reaching
19 and reacting with the core of perovskites.

20 The combination of the umbrella shaped APTES and liner OA does not appear to improve the
21 stability of bulk MAPbI₃ films, an effect that can be attributed to the higher steric hindrance among
22 APTES molecules.³⁹⁴ However, interestingly, liner OA alone is highly effective in passivating
23 bulk films, but not perovskite NCs. This is likely because the liner OAs can form a self-assembled

1 monolayer on the bulk film surface, which is less likely for perovskite NCs due to their large
2 curvature.³⁹⁴ For bulk MHP films, some planar and spherical molecular ligands also show good
3 passivating ability. As shown in Figure 33c, when the planar molecular ligand of monoammonium
4 ZnP is used as a molecular ligand for MAPbI₃ film, the interaction between NH₃⁺ and I⁻ leads to
5 effective passivation.³⁸⁴ Another interesting planar molecular ligand is ADNT, along with OA and
6 OAm, was found to passivate CsPbBr₃ surface very efficiently to the point that perovskite magic
7 sized clusters (PMSCs) were generated besides perovskite NCs (see the section below).³⁸⁵ This
8 was attributed to the ADNT being planar on the surface of the PMSCs or perovskite NCs with its
9 NO₃⁻ and OH⁻ groups binding to the Cs⁺ and Pb²⁺ defect sites, and Al³⁺ binding to the Br⁻ defect
10 sites of the PMSCs or perovskite NCs (Figure 33d). In addition, the spherical-shaped molecular
11 ligand of mesostructured [6,6]-phenyl-C61-butyric acid methyl ester (ms-PCBM) has been used
12 to passivate MAPbI₃ films owing to the hydrophobic and high-performance mesostructured of ms-
13 PCBM.³⁹⁵ It would be interesting to test such ligands for perovskite NCs as well.

14 Although long alkyl-chain and alkoxy-silanes molecular ligands are effective in passivating MHP
15 NCs to improve their optical properties and stability, their insulating nature limits electronic
16 coupling among MHP NCs and thereby impede charge transfer and transport important for device
17 application.^{351,386} One way to improve inter-NC coupling and charge transport is to use conjugated
18 or conductive molecular ligands, such as aromatic, alkene, and alkyne compounds with an
19 unhindered positive or negative terminal ion that will interact strongly with the surface defects.^{351,}
20 ³⁸⁶ For instance, as shown in Figure 33e, the conjugated amine containing a C=C group of aromatic
21 molecule ligand of 3-phenyl-2-propen-1-amine (PPA) has been used to prepare MAPbBr₃ NCs.³⁸⁶
22 Compared with OA, the carrier mobility of bulk PPA-MAPbBr₃ film increase almost 22 times over
23 that of PA-MAPbBr₃ films without compromising stability and optical properties. The

1 conductivity of PPA-MAPbBr₃ perovskite NCs films was improved due to enhanced coupling
2 between perovskite NCs.³⁸⁶ Similarly, conjugated PPA with both “quasi-coplanar” rigid
3 geometrical configuration and distinct electron delocalization characteristics has also been used to
4 modify MAPbI₃ films. The conjugated cation coordinating to the surface of the perovskite
5 grains/units provides a network for charge exchange.³⁹⁶ In addition, short conductive aromatic
6 capping ligands such as benzylamine (BZA) and benzoic acid (BA) have also been used to
7 synthesize MAPbBr₃ perovskite NCs with high PLQY (86%), indicative of a well-passivated
8 surface. The perovskite NCs synthesized using BZA/BA capping ligands exhibit higher
9 conductivity and longer charge carrier lifetime as compared to MAPbBr₃ perovskite NCs with
10 insulating OA and APTES capping ligands. This was attributed to the delocalization of the
11 excitonic wave function of the perovskite NCs by the aromatic ligands.³⁵¹

12 **The valency or oxidation state of the ligand** and the charge density and distribution in the
13 ligand can critically affect how effective it can passivate the MHPs. For monovalent and divalent
14 cationic surface defects, it would be ideal to use corresponding oppositely charged monovalent
15 and divalent ligands for their passivation. With some weak acid ligands such as PAs, multiple
16 conjugate bases with different valency or charges can be produced upon deprotonation, which can
17 passivate differently charged cations, such as MA⁺, Cs⁺ or Pb²⁺ defects.³⁸⁸ Specifically, for the PA-
18 APTES MAPbBr₃ perovskite NCs discussed earlier, the APTES are protonated and can produce a
19 charged functional groups of R-NH₃⁺ to passivate Br⁻. On the other hand, the two proton transfers
20 of R-PO₂(OH)⁻, PA can produce two charged functional groups of R-PO₂(OH)⁻ and R-PO₃²⁻ that
21 could passivate MA⁺ and Pb²⁺, respectively.³⁷⁷ The above example is in contrast to OA-APTES
22 MAPbBr₃ perovskite NCs that have two charged functional groups of R-NH₃⁺ and R-COO⁻, with

1 the latter passivating both MA^+ and Pb^{2+} .³⁷⁷ Therefore, the valence state of the molecular ligands
2 should ideally be consistent with the valence state of the surface defects for optimal passivation.

3

4 **Passivation of perovskite magic sized clusters**

5 Perovskite magic sized clusters (PMSCs) are ultrasmall (usually < 2 nm) nanoparticles with a
6 narrow size distribution and strong quantum confinement. Recently, it has been found that the
7 ligands play a key role on the preparation and passivation of perovskite “magic sized” clusters
8 (PMSCs), that is, clusters that have a single size or in any case an extremely narrow size
9 distribution.^{385, 397} Compared to perovskite NCs, PMSC are smaller and less stable and thereby
10 they require better protection or passivation. As a result, strong ligands and high concentrations of
11 ligands favor PMSCs over perovskite NCs.^{385, 397} Because of their highly uniform size distribution
12 and narrow optical bandwidth, PMSCs are attractive for studying fundamental issues and as
13 potential building blocks for creating larger PNCs.³⁹⁸⁻⁴⁰⁰ It was found that one of the key factors
14 in producing PMSCs is the amount of Lewis acid ligands used, with more acids leading to more
15 PMSCs.³⁹⁷ However, not all the type of Lewis acids can produce pure PMSCs, the PMSCs only
16 exist in organic solvent owing to their small size (< 2 nm).³⁸⁵

17 To date, there have been a few reports on PMSCs and their ensembles. Single sized (~ 2 – 4 nm)
18 APbX_3 (where $\text{A} = \text{CH}_3\text{NH}_3^+$ or Cs^+) nanocrystalline phosphors have been synthesized using OA
19 and OAm as capping ligands, showing a high PLQY ($\sim 80\%$).⁴⁰¹ CsPbBr_3 nanoclusters with ~ 2 nm
20 size and a sharp absorption peak at ~ 398 nm have been synthesized using OA and OAm as capping
21 ligands and converted into highly deep blue-emitting nanoribbons.⁴⁰² In addition, smaller size
22 clusters (~ 0.6 nm) of CsPbBr_3 (nearly equal to the CsPbBr_3 unit cell length of 0.59 nm) have been
23 synthesized using OA and OAm ligands.²⁶⁵ Zhang et. al. found that the single size of MAPbBr_3

1 and CsPbBr₃ PMSCs are strongly dependent on the ligands used.^{385, 397} As shown in Figure 36d, a
2 unique inorganic capping ligand based on a trivalent metal hydrated nitrate coordination complex,
3 Al(NO₃)₃·9H₂O), together with OA and OAm, has been used to control the synthesis of CsPbBr₃
4 PMSCs and CsPbBr₃ perovskite NCs. By changing the amount of metal complex ligand used, the
5 final product can be tuned from perovskite NCs to PMSCs or to a mixture of both NCs and PMSCs,
6 with excess ligands favoring PMSCs.³⁸⁵ The conversion from CsPbBr₃ perovskite NCs to PMSCs
7 is mainly related to the concentration of CAs. The concentration of CAs affects the excitonic
8 absorption of the CsPbBr₃ PMSCs ($\lambda = 430\text{--}441$ nm) and CsPbBr₃ perovskite NCs ($\lambda = 447\text{--}518$
9 nm), with more CA favoring CsPbBr₃ PMSCs over perovskite NCs.³⁸⁵ Due to the ultra-small size
10 and extremely large surface to volume ratio of PMSCs, a higher concentration of molecular ligands
11 are necessary compared to perovskite NCs.

12

13 **2.3 STRATEGIES TO GAIN INSIGHT INTO THE LIGAND-SURFACE INTERACTION**

14 Alivisatos et al.¹⁷⁹ have studied how to gain information on the ligand-surface interaction in
15 CsPbBr₃ NCs from their purification step. The as-synthesized NCs were purified using hexane and
16 a hexane/acetone mixture. NMR and FTIR measurements demonstrated that ammonium ligands
17 can be preferentially removed from the NC surface compared to carboxylate; this is consistent with
18 the weaker strength of the H-bonding interaction of alkylammonium with the surface bromide
19 atoms [Br...H-N⁺] compared to the lead-carboxylate coordination. The treatment of the NCs with
20 a polar solvent destabilizes the hydrogen bond interaction producing a detachment of the
21 ammonium from the NC surface, as was evidenced by the decrease and disappearance of the N-H
22 bending vibration band in the FTIR spectrum (1575 cm⁻¹), while alkene protons (5.50 ppm) from
23 oleate remained unchanged. Solvent-dependent ligand surface interactions were clearly

1 demonstrated, and this finding should be considered when ligands and washing solvents are used
2 in the synthesis and purification steps.

3 **Washing treatment with an anti-solvent** reduces the colloidal stability of the NCs due to a
4 decrease of the ligand density on the NC surface. The addition of didodecyldimethylammonium
5 bromide (DDABr), a branched ligand, can promote the exchange of the pristine ligands
6 (oleylamine and oleic acid) on the NC surface with DDABr, thereby enhancing their photostability.
7 However, this strategy has not proved successful enough in protecting the NC surface, since the
8 obtained NCs deteriorated unavoidably after the washing step. The unwashed NCs were then
9 sealed into a resin to fabricate a blue-LED, which exhibited a higher photostability than that
10 prepared with pure NCs.⁴⁰³ We recommend to read section I (purification and isolation), subsection
11 Isolation and purification of colloidal MHP nanocubes, for specific examples on metal halide
12 perovskite nanocubes.

13 In addition, **post-synthesis ligand exchange** allows to estimate the binding constant of the added
14 ligands to get thermodynamically stable coordination of organic ligands to the NC surface. Thus,
15 two different surface CsPbBr₃ NCs were prepared using the hot injection method: i) NC terminated
16 with oleylammonium bromide (PLQY of 92%) and ii) NC terminated with Cs-oleate species
17 (PLQY of 69%).⁴⁰⁴ Interestingly, the reduction of scattering was associated with the saturation of
18 the NC binding energy. It has been demonstrated that primary alkyl ammonium and
19 benzylammonium bromides bind to the NC surface with a binding constant $> 10^5 \text{ M}^{-1}$, but the
20 constant is reduced to 10^4 M^{-1} with short length ligands, sterically hindered ligands (e.g.,
21 triethylammonium and oleylammonium), and weak acid ligands (such as phenylammonium). The
22 higher the binding constant of the ligands to the NC surface, the better the long-term stability and
23 emissive properties due to a complete surface passivation. However, the excess of ammonium

1 ligands could transform the core of the NCs by substitution of cesium and reconstruction of the
2 NCs inducing a blue shift in the emission.

3 Post-synthetic treatment of CsPbI₃ NCs with a dicarboxylic acid, namely 2,2'-iminodibenzoic
4 acid, enhanced their PL from 80% to 95 %. NMR, XPS and FTIR measurements confirmed the
5 bidentate binding of the ligand by the carboxylic groups. DFT calculations are consistent with the
6 anchoring of the bifunctional ligand to two lead atoms at the NC surface with a binding energy of
7 1.4 eV, compared to a binding energy of 1.14 eV for oleic acid. The dicarboxylic ligand stabilizes
8 the NC surface, with low structural distortion and phase transformation, leading to high PLQY.¹⁷⁵

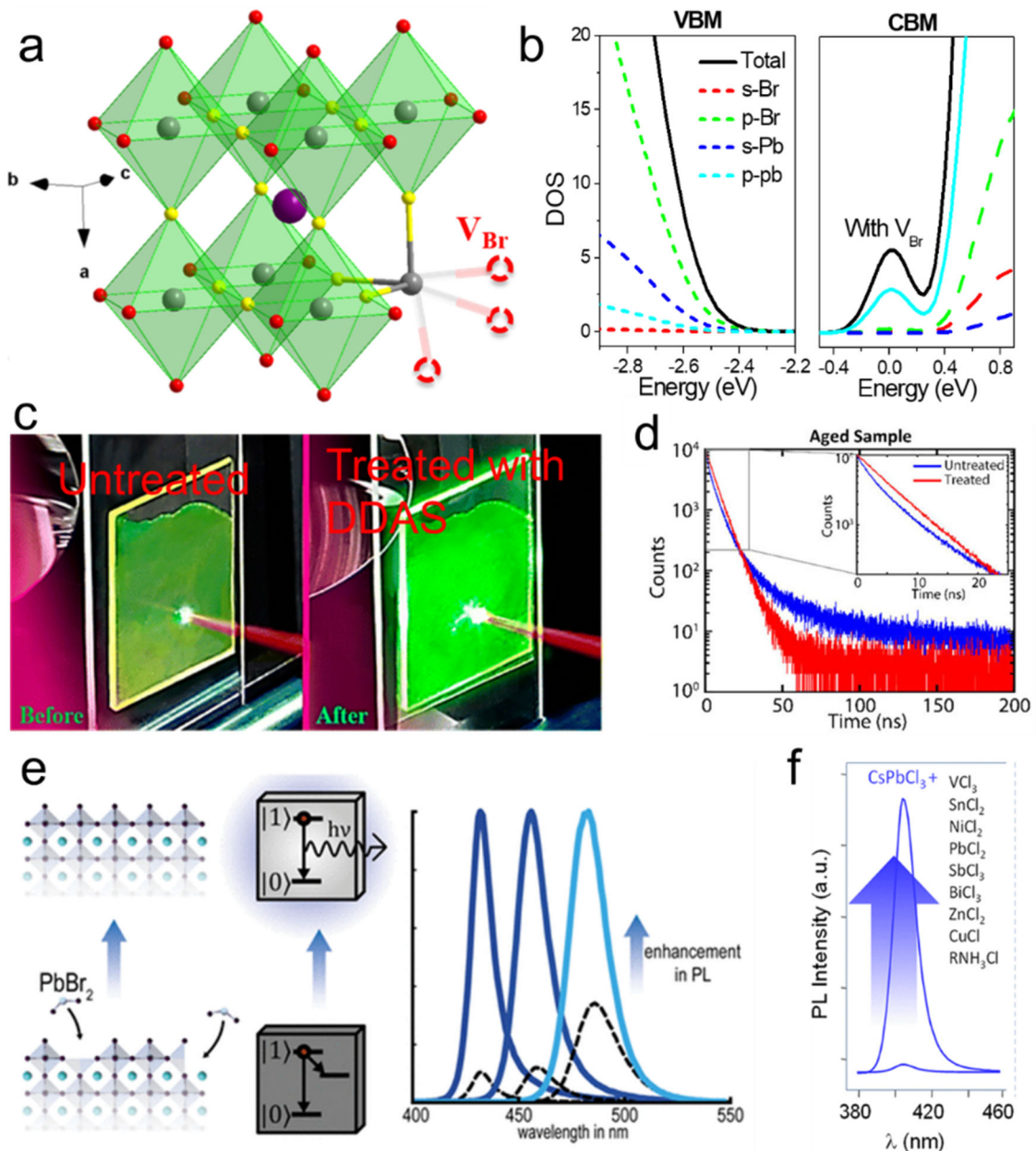
9

10 **2.4 POST-SYNTHETIC PASSIVATION OF CsPBX₃ NCs**

11 The performance of LHP@capping NCs by following a post-treatment of the NCs has focused
12 on all-inorganic CsPbX₃. Defect energy levels result from the crystal discontinuity on the surface
13 and the role of passivation is mainly to reduce (ideally eliminate) the resulting surface defects. It
14 is widely acknowledged that surface cesium atoms of CsPbX₃ NCs are replaced with protonated
15 amine ligands, which interact with halide atoms through hydrogen bonding (Figure 34a).^{18, 366, 405}
16 Since only the orbitals of Pb and X atoms contribute to the band edge, exciton recombination
17 seems to take place primarily within the Pb-X octahedrons. The symmetric crystal structure makes
18 lead vacancy (V_{Pb}) hardly affect the exciton recombination while V_X considerably influences the
19 recombination process (Figure 34b).^{382, 406-407} Therefore, the main purpose of both the post- and
20 in-situ passivation strategies is to fill the V_X on the surface. Furthermore, if the ligands possess
21 similar physicochemical properties to halide ions, they can passivate the V_X directly. Pan et al.
22 initiated the post-treatment of perovskite NCs in late 2015. CsPbBr₃ NCs were first treated with
23 oleic acid and then with didodecyl dimethylammonium bromide (DDAB) or didodecyl

1 dimethylammonium sulfide DDAS (here S means S^{2-} ; Figure 34c).⁴⁰⁸⁻⁴⁰⁹ The treatment
2 significantly improved the PLQY and the stability of the CsPbBr₃ NCs and enabled stable
3 stimulated emission from the NCs after 1.2×10^8 laser shots. The pretreatment of the NCs with
4 oleic acid before the adsorption of DDAB is an indication of the complexity of the ligand-NC
5 interaction. After that, Alivisatos' group treated CsPbBr₃ NCs with thiocyanate salts (NH₄SCN,
6 NaSCN) and NH₄Br⁸⁸ by adding the salt powder into the NC dispersion directly and stirring the
7 mixture at room temperature. They reported a PLQY value close to unity, with an obvious
8 monoexponential PL decay (Figure 34d). The key point of this method is repairing a lead-rich
9 surface (surface with V_X) with pseudohalogen ions, which open the window of post-treating
10 CsPbBr₃ NCs with bromides or related chemicals. For example, tetrafluoroborate salts, ZnX₂, and
11 PbBr₂ were used as the post-treating agents to improve the PLQY of green CsPbBr₃ NCs^{197, 382, 410}
12 to close to 100%. In addition to these inorganic salts, organic salts with bromides were also applied
13 to repair the surface V_{Br} to provide NCs with a PLQY of 100%.¹⁶⁵ Such ligands endow CsPbBr₃
14 NCs with strong endurance against polar solvent washing and ambient storage, indicating their
15 better potentials in future optoelectronic devices. The post-treatment of blue-emitting perovskite
16 NCs is generally difficult. There are mainly two types of three-dimensional, blue LHPs: mixed-
17 halide perovskites and CsPbBr₃ nanoplatelets (NPLs). It is difficult to accurately passivate surface
18 V_X of mixed halides since ion exchange occurs easily³⁰² and it is challenging to ensure the stability
19 of the emission wavelength during the surface treatment. For CsPbBr₃ NPLs, poor stability is the
20 main obstacle during post-passivation.⁴¹¹ In spite of these difficulties, some interesting studies
21 have been reported. For instance, the treatment of CsPbBr₃ NPLs of different thicknesses with a
22 PbBr₂-ligand solution led to an overall enhancement of their low PLQY (Figure 34e).⁶²
23 Considering NCs with a shorter emission wavelength, such as CsPbCl₃ NCs, Pradhan's and others'

1 groups conducted comprehensive experiments and demonstrated giant PL enhancement when
 2 CsPbCl₃ NCs were treated with various types of metal chlorides (Figure 34f).^{87, 151, 412} It should be
 3 noted that no doping was detected. Considering the similarity of these inorganic salts, there is no
 4 doubt that repairing surface V_{Cl} contributes greatly to the enhanced PLQY; in fact, Wang et al.
 5 demonstrated that the treatment of CsPbCl_xBr_{3-x} NCs with several nitrates highly enhanced the NC
 6 PL (PLQY of 85%).⁹⁶



7

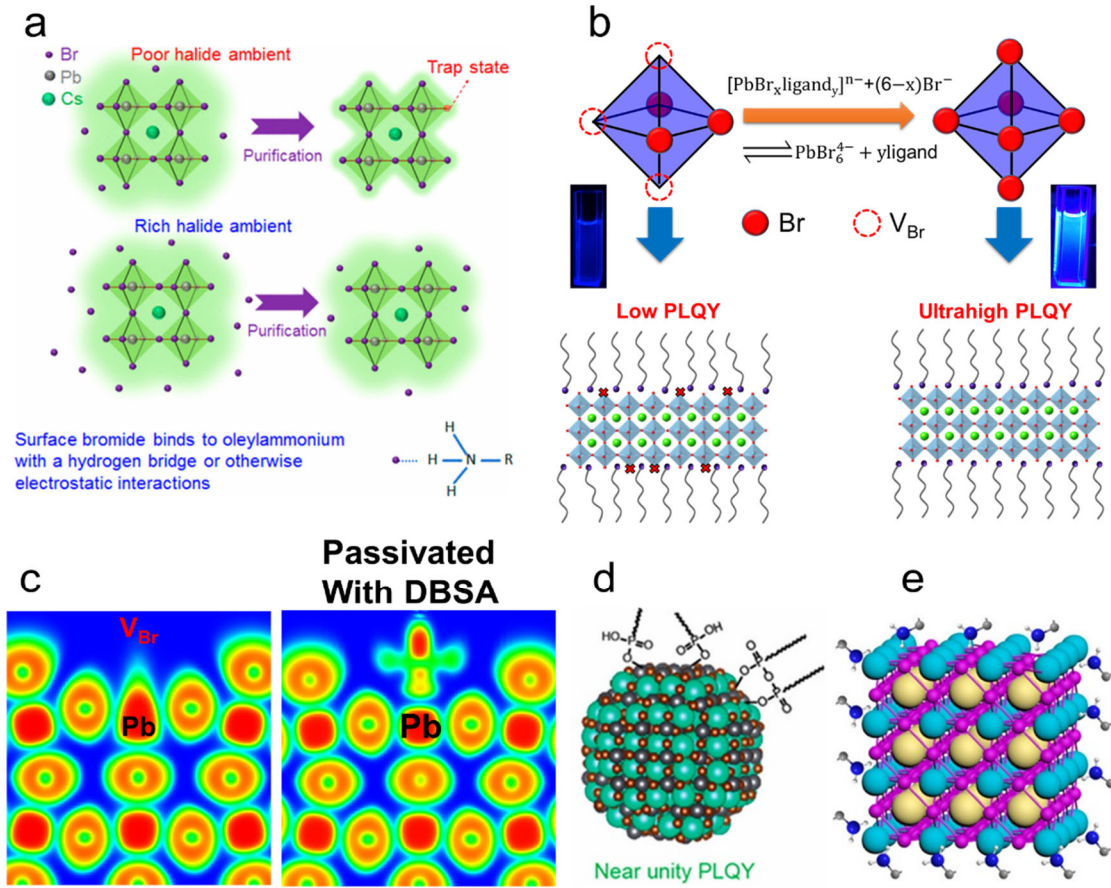
1 **Figure 34.** (a) Crystal structure of CsPbBr₃ NC, with the presence of a surface V_{Br}. Reprinted with
2 permission from Ref.⁴⁰⁶ (b) Electronic density of states (DOS) curves of valence band maximum
3 (VBM) and conduction band minimum (CBM) of CsPbBr₃ with V_{Br}. Reprinted with permission
4 from Ref.³⁶⁸ (c) CsPbBr₃ NC films before and after being treated with DDAS. Reprinted with
5 permission from Ref.⁴⁰⁹ (d) The PL decay of treated and untreated CsPbBr₃ NC with NH₄SCN.
6 Reprinted with permission from Ref.⁸⁸ (e) CsPbBr₃ NPLs with post-treatment of PbBr₂. Reprinted
7 with permission from Ref.⁶² (f) Greatly improved PL of CsPbCl₃ NCs after being treated with
8 metal chlorides. Reprinted with permission from Ref.⁸⁷

9

10 **2.5 POST-SYNTHESIS PASSIVATION VERSUS IN-SITU PASSIVATION OF LHP NCs**

11 The post-passivation strategy is a widely accepted strategy in the field of common-
12 semiconductor and perovskite NCs. However, additional impurities are unavoidable in such
13 strategy and this might be detrimental for their optoelectronic properties. Further purification is
14 often necessary to remove the unreacted chemicals, which is challenging for perovskite NCs.
15 Eliminating the surface defects during synthesis, i.e., in-situ passivation, via surface stoichiometric
16 control, ligand design, and precursor engineering may be more favorable as no further treatment
17 and purification steps are needed.^{343, 413-415} As mentioned above, the main task of perovskite NC
18 passivation is to compensate the halide vacancies (V_x) on the surface. According to this principle,
19 Liu et al. added ammonium halide in the precursors to construct halide-rich NCs (Figure 35a).⁴¹⁶
20 During and after growth, the excessive halide ions in the solution can fill the surface vacancy
21 efficiently, contributing to reduce the non-radiative process and consequently enhancing the NC
22 PLQY. This strategy was further modified by several other groups by using metal bromides
23 (ZnBr₂, MnBr₂, PbBr₂, among others)^{324, 348, 417} to passivate the surface defects and consequently

1 a PLQY close to unity was achieved. Although these metal bromides were added together with the
 2 precursors, no NC doping was observed.



3
 4 **Figure 35.** (a) Schematics for conventional and in-situ passivation under halide-rich circumstances
 5 with inorganic ammonium bromides. Reprinted with permission from Ref.⁴¹⁶ (b) Schematic for
 6 ionic-equilibrium based in-situ passivation strategy for highly efficient CsPbBr₃ NPLs. Reprinted
 7 with permission from Ref.⁴¹⁸ Direct in-situ passivation with (c) X-type DBSA, (d) X-type alkyl
 8 phosphonic acids, and (e) L-type oleylamine. Reprinted with permission from Ref.^{79, 367-368}

9
 10 LEDs fabricated with the these NCs exhibited a record EQE value of 16.8%, indicating the
 11 superiority of the in-situ passivation strategy; further studies are needed to gain insight into how

1 these metal bromides work. By contrast, the addition of NiCl₂ during the preparation of CsPbCl₃
2 NCs resulted in NC Ni-doping as well as a decrease in the surface chloride vacancy density,⁴¹⁹
3 thus leading to NCs with a PLQY close to 100%. Therefore, more investigations are needed to
4 identify the significance of the halide salts during synthesis.

5 Very recently, Yang et al. prepared highly efficient and stable CsPbBr_xI_{3-x} NCs with emission
6 wavelength at the pure red region (637 nm) through the addition of potassium oleate.⁴²⁰ Potassium
7 bromide was detected on the surface, which passivated the V_X and inhibited the halide segregation
8 simultaneously. The final LED exhibited high EQE and especially stable emission peak. Usually,
9 the addition of inorganic halides also introduces impurities to some extent. Then, Wu et al.
10 developed an in-situ passivation strategy with organic halides (oleylammonium bromide)
11 obtaining a record PLQY of 96% for CsPbBr₃ nanoplatelets (NPLs) emitting in the blue (Figure
12 35b).⁴¹⁸ According to their approach, PbBr₆⁴⁻ complexes could be formed before nucleation of the
13 NCs by controlling the amount of HBr. The formation of single-layered hybrid perovskites capped
14 with oleylammonium bromide after injection of PbBr₂ precursor was followed by the
15 disconnection between PbBr₂ and ligands after the addition of HBr, thus shifting the ionic
16 equilibrium towards the formation of isolated PbBr₆⁴⁻ octahedral complexes, due to the increased
17 Br⁻ concentration. The process was monitored by absorption spectroscopy. LEDs based on these
18 NPLs exhibited an ultra-narrow electroluminescence emission with a full width at high maximum
19 of 12 nm.

20 Direct in situ-passivation was carried out with organic ligands of different natures and presenting
21 strong affinity to Pb²⁺ ions: i) X-type ligands, such as dodecylbenzene sulfonic acid³⁶⁸ and
22 alkylphosphonic,³⁶⁷ and ii) L-type ligand such as oleylamine⁷⁹. The groups of Zhang and Pradhan
23 prepared CsPbX₃ NCs with ultrahigh PLQY by adding organic halides with long chains.⁴²¹⁻⁴²³

1 Moreover, organic halides with multi-alkyl chains can participate in the in-situ passivation of the
2 NCs, but they are not detected on the surface due to their large steric hindrance.⁴⁰⁶ These organic
3 halides play a role during the growth stage by enabling the formation of complete Pb-Br
4 octahedrons and therefore a low surface V_X density. The surface is eventually capped by other
5 long-chain ligands, such as oleic acid or oleylamine. This method provides more possibilities for
6 tuning optical and structural features. The above-discussed in-situ passivation methods were all
7 based on the consideration of filling surface V_X . In a sense, if the ligands can passivate the exposed
8 lead atoms directly, we would achieve efficient perovskite NCs by using simply one kind of ligand.

9 On the whole, since most of the results confirmed that surface V_X is at the origin of carrier
10 trapping and non-radiative recombination,^{196, 406, 419} the passivation strategy design for trap-free
11 perovskite NCs should focus on the elimination of surface V_X . In fact, researchers have been
12 succeeding in doing this and PLQY close to 100% have been achieved for almost all the visible
13 emission wavelengths.

14 Perovskite QDs relevant for optoelectronic devices require not only capping ligands that
15 stabilize NCs and enhance their luminescence, but also that promote charge injection and transport
16 at the interface. Long-chain saturated amines and carboxylic acids, such as oleylamine (OLA) and
17 oleic acid (OA), have been commonly used as passivating ligands of perovskite NCs surface to
18 enhance their stability and optical properties. However, their insulating nature creates an electronic
19 energy barrier and impedes interparticle electronic coupling, thereby limiting the application of
20 the NCs in optoelectronic devices. Thereby, different strategies have been tested to overcome this
21 issue. Control of the surface ligand density on the NC surface has been devised as a way to
22 improve the stability and PL QY, as well as the uniformity and carrier-injection efficiency of

1 perovskite thin films, and it has been attained via treatment with a mixture of polar/non-polar
2 solvents.¹⁸⁶

3 Shorter-chain saturated amines and acids have been used to enhance the performance of light-
4 emitting diodes, such as those based on colloidal FAPbBr₃ NCs capped with n-butylamine⁴²⁴ and
5 CsPbBr₃/CH₃NH₃Br quasi-core/shell structures⁴²⁵ to provide green LEDs with EQE of up to
6 2.05% and 20.3%, respectively. Moreover, CsPbI₃ NC LEDs with EQE of 12.6% have been
7 fabricated by using octylphosphonic acid (OPA).⁴²⁶ In addition, relatively short-chain quaternary
8 ammonium bromide salts, such as didodecyldimethylammonium bromide and didecyldimethyl
9 ammonium bromide has enabled the preparation of LEDs based on CsPbBr₃ NCs with an EQE of
10 9.71%.⁴²⁷ Remarkably, long-chain ligands, such as 3-(*N,N*-dimethyloctadecylammonio)-
11 propanesulfonate, capable of coordinating simultaneously to the cation and anion of CsPbBr₃ NC
12 surface, have led to densely packed NC films in which the charge transport is not severely
13 impeded.¹⁷⁴

14 Ligand shortening combined with conductive capabilities has proved to be a promising
15 strategy to facilitate charge transport between perovskite NCs by lowering the energy barrier.³⁵¹
16 The passivation of MAPbBr₃ QDs with benzylamine and benzoic acid enhance the conductivity
17 and carrier lifetime as well as the charge extraction efficiency, while preserving the high chemical
18 stability and PL QY of the perovskite. In this regard, Yan et al. have recently proposed the use 3,4-
19 ethylenedioxythiophene to passivate CsPbBr₃ NCs to provide photodetectors with enhanced
20 performance by exploiting the ligand capacity to be polymerized on the NC surface under the
21 photocurrent of the photodetector, thus enhancing the device performance in up to 178% while
22 exhibiting high stability in air.⁴²⁸ This molecular engineering strategy can be of great interest for
23 the development of high performance and stable optoelectronic devices based on perovskite NCs.

1 Somewhat related, Hassan et al.⁴²⁹ have shown the beneficial effect of multidentate ligands to
2 passivate effectively perovskite NCs, thus preventing halide segregation in I/Br mixed-halide
3 perovskite LEDs under electroluminescent operation. Moreover, Han et al.⁴³⁰ have recently
4 applied the Lewis base cyclam (1,4,8,11-tetraazacyclotetradecane) as effective, self-sufficient
5 passivation, multichelating ligand of perovskite NCs, thus boosting the performance of light-
6 emitting diodes (EQE of 16.24%). These results are encouraging and give clues on the nature of
7 the ligands needed to enhance the charge injection and transport at the interface of the passivated
8 of perovskite surfaces. Identifying ideal ligands which enable even more efficient optoelectronic
9 devices, which combine enhanced chemical stability and high efficiency in charge injection and
10 transport at the interface, requires further experimental investigations, as well as, state-of-art
11 theoretical calculations on surface chemistry.

12 Future development of passivation strategies should take into consideration electrical and optical
13 properties, colloidal stability, and operation stability, simultaneously.¹⁷² But, achieving these
14 advantages together cannot be more challenging and mixed passivation strategies with both
15 organic and inorganic chemicals may be a better solution. Besides, a new in-situ passivation ligand
16 systems are urgently needed to further promote the optoelectronic properties and stabilities.

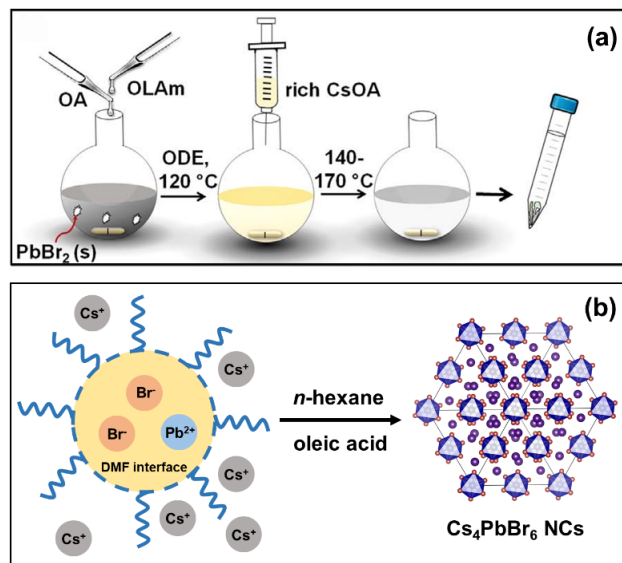
17

1 3. 0D NONPEROVSKITES (PEROVSKITE DERIVATIVES)

2 The 2016-2017 reports^{402, 431-433} on so-called “zero-dimensional” (0D) Cs₄PbX₆ (X = Cl, Br,
3 or I) materials and NCs inspired many research works on the synthesis and device applications of
4 Cs₄PbX₆ colloidal nanocrystals.⁴³⁴ Compared to their CsPbX₃ counterparts (also referred to as 3D
5 perovskites), Cs₄PbX₆ NCs were shown to have improved thermal and optical stability, especially
6 with respect to their high photoluminescence quantum yield (PLQY) of green emission in the solid
7 state. From a crystal structure point of view, 0D Cs₄PbX₆ exhibit isolated [PbX₆]⁴⁻ octahedral units
8 – in contrast to the corner-sharing [PbX₆]⁴⁻ octahedra of 3D CsPbX₃ – surrounded by Cs⁺ cations
9 that are completely decoupled in all directions. The reduction of dimensionality from 3D to a
10 strongly quantum-confined 0D gives rise to the molecular-like electronic properties of Cs₄PbX₆,
11 such as a widened bandgap and an increased exciton binding energy, a reduced charge carrier
12 mobility, and a lower conductivity. Meanwhile, it brings several interesting photophysical features
13 into play, like small polaron absorption and broadband ultraviolet (UV) emissions. In the following
14 we will review the recent work on the 0D perovskites NCs, particularly Cs₄PbBr₆, by covering
15 their syntheses and phase transformations; optical properties and molecular features; the origin of
16 green emission; and optoelectronic applications.

17

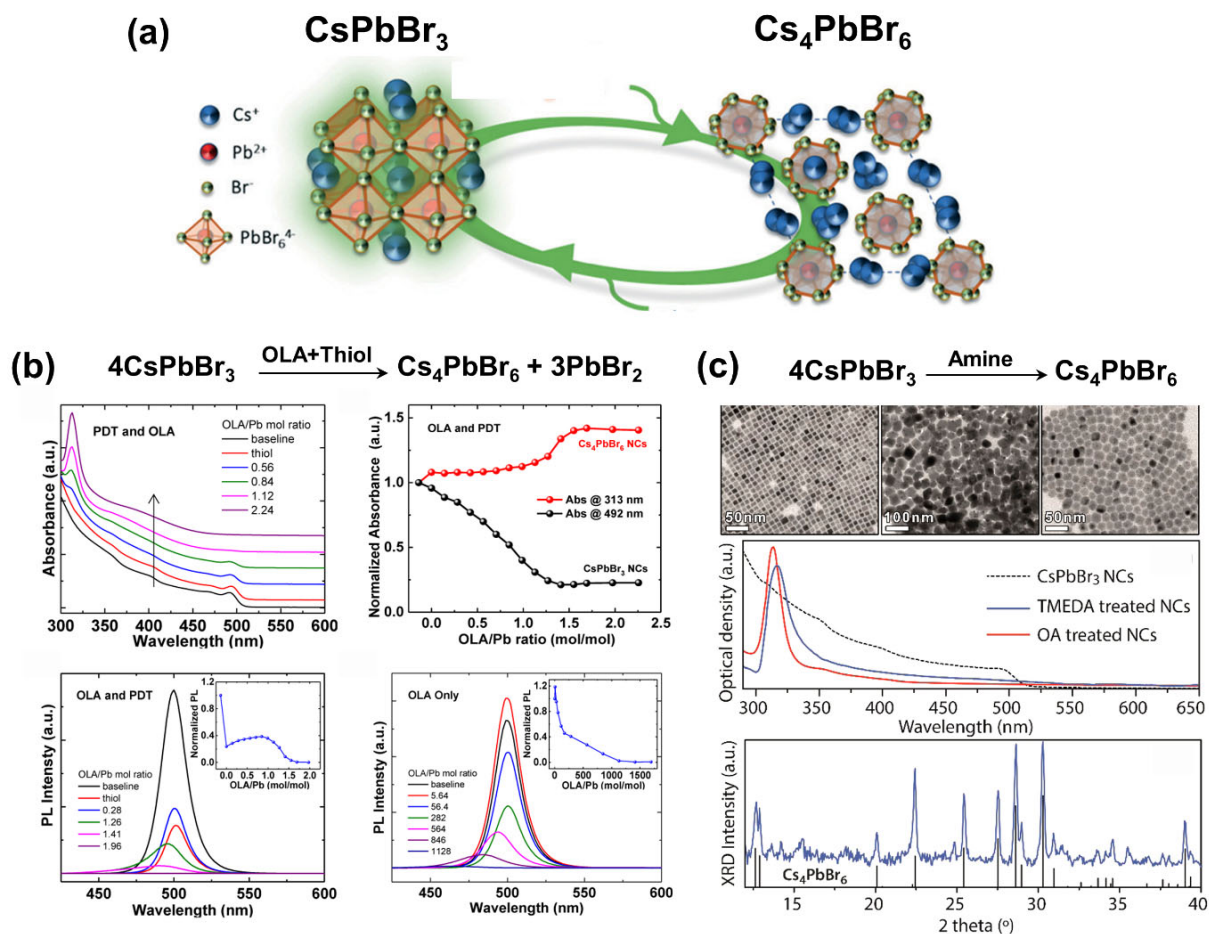
1 3.1 SYNTHESIS AND PHASE TRANSFORMATION OF Cs_4PbBr_6 NCs



2
3 **Figure 36.** (a) Schematic illustration of the hot-injection method of synthesizing Cs_4PbBr_6 NCs at
4 the rich Cs-oleate environment. Reproduced from Ref. ⁴³⁵. Copyright 2019 ELSEVIER. (b)
5 Schematic illustration of low-temperature reverse microemulsion method of synthesizing
6 Cs_4PbBr_6 NCs formed at the interface between an “oil” phase (*n*-hexane) and an “aqueous” phase
7 (DMF). Redrawn from Ref. ⁴⁰². Copyright 2017 American Chemical Society.

8
9 Hot-injection and low-temperature reverse microemulsion methods are two popular methods to
10 obtain highly monodisperse Cs_4PbX_6 NCs. The former method is also best known for synthesizing
11 highly luminescent CsPbX_3 NCs, as shown by Protesescu et al.¹⁵ In their developed method, the
12 precursor PbBr_2 was dissolved in a nonpolar solvent with a combination of oleic acid (OA) and
13 oleylamine (OLA) and then Cs-oleate complex was injected (Figure 36a). Based on this,
14 Akkerman *et al.* utilized a similar hot-injection strategy, but under Cs-rich conditions, to obtain
15 nearly monodisperse Cs_4PbX_6 NCs with the size distribution of 10-36 nm.⁴³² After that,
16 Udayabhaskararao *et al.* developed another hot-injection method by mediating the excess ligands

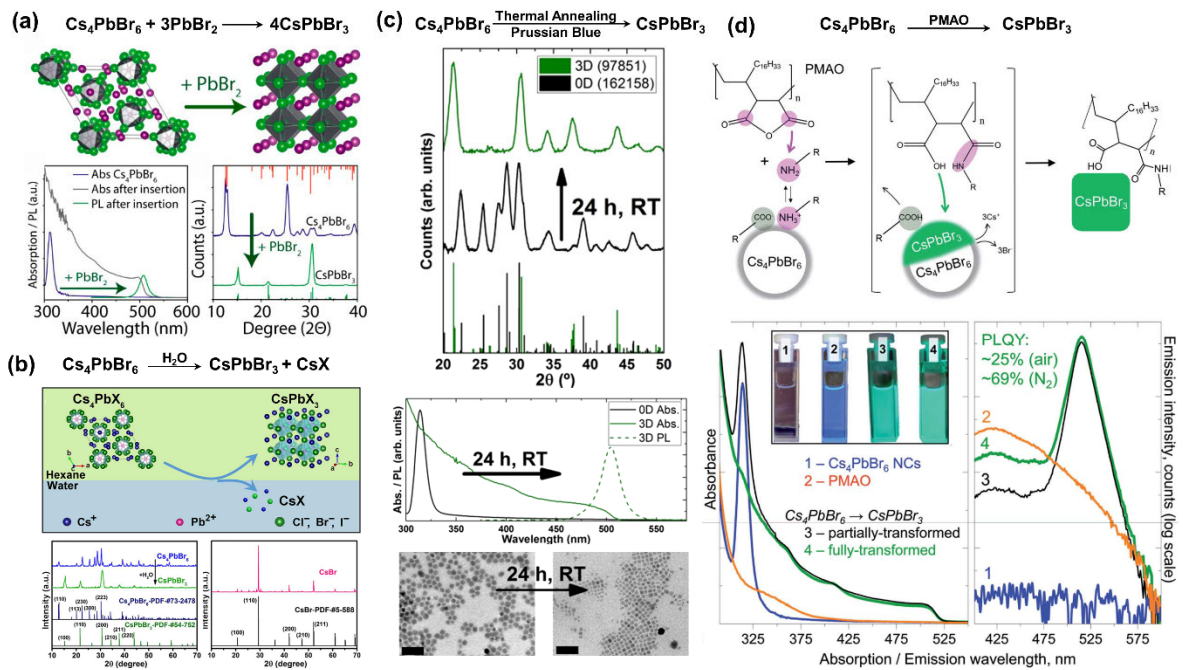
1 and they found that the size of Cs₄PbX₆ NCs can be tuned by controlling the ratio of OA/OLA and
2 also by the temperature.⁴³⁶ Meanwhile, Zhang *et al.* reported the synthesis of Cs₄PbBr₆ NCs (size
3 distribution: 26 ± 4 nm) using a low-temperature reverse microemulsion method.⁴⁰² As illustrated
4 in Figure 36b, the precursors PbBr₂ and Cs-oleate were dissolved in DMF and hexane,
5 respectively. These two solvents are immiscible and, thus, the NC nucleation rate was controlled
6 by the slow release of Cs⁺ ions from Cs-oleate complex when the solvents were mixed. The
7 microemulsion method has been used to obtain other inorganic perovskite NCs with different
8 dimensionalities (CsPbBr₃ and CsPb₂Br₅),⁴³⁷ as well as the ligand-free highly emissive Cs₄PbBr₆
9 NCs.⁴³⁸ Recently, Hui *et al.* reported a one-step method for the synthesis of Cs₄PbBr₆ NCs by
10 mixing three independent precursors of Cs, Pb, and Br in a cuvette.⁴³⁹ They proposed a two-step
11 pathway for forming Cs₄PbBr₆ NCs. First, Pb and Br precursors immediately react to form
12 intermediates (*i.e.*, [PbBr₄]²⁻, [PbBr₃]⁻, and [PbBr₆]⁴⁻), and then the Cs precursor (CaOA) induces
13 the assembly of the intermediates into Cs₄PbBr₆ NCs.



1
 2 **Figure 37.** (a) Schematic illustration of structural transformation between CsPbBr_3 and Cs_4PbBr_6
 3 NCs. Reproduced with permission from Ref. ⁴⁴⁰. Copyright 2018 Royal Society of Chemistry. (b)
 4 Absorbance spectra, normalized absorbance at two spectral features, and PL spectra of CsPbBr_3
 5 NCs solution before and after adding different amount of oleylamine with and without PDT.
 6 Reproduced from Ref. ⁴⁴¹. Copyright 2017 American Chemical Society. (c) TEM micrographs,
 7 absorption spectra and X-ray diffraction (XRD) patterns of CsPbBr_3 NCs before and after the
 8 treatment with either TMEDA or OA. Reproduced from Ref. ⁴⁴². Copyright 2017 American
 9 Chemical Society.

10

1 In addition to the direct synthesis methods mentioned above, Cs₄PbBr₆ NCs can be obtained *via*
2 the phase transformation from CsPbBr₃ to Cs₄PbBr₆ NCs by adding different amines (Figure 37a).
3 For example, Liu *et al.* showed that after adding OLA into the solution of CsPbBr₃ NCs, the
4 absorption around 492 nm from CsPbBr₃ NCs decreased while the absorption around 313 nm from
5 Cs₄PbBr₆ NCs increased (Figure 37b).⁴⁴¹ The evolution of the normalized absorbance at these two
6 spectral positions had the inverse dependence on the OLA concentration. They found that
7 including large amounts of 1,3-propanedithiol (PDT) had almost no effect on the absorption
8 spectrum without adding OLA, indicating that the PDT cannot trigger the transformation.
9 Therefore, such transformation was triggered by adding oleylamine and the size uniformity and
10 chemical stability of the Cs₄PbBr₆ NCs can be improved by adding PDT. Palazon and co-workers
11 provided another method to realize this transformation through adding the different amines at room
12 temperature.⁴⁴² They found the optical properties measured after tetramethylethylenediamine
13 (TMEDA) treatment were different from those of the starting solution of CsPbBr₃ NCs. The
14 spectral features (a sharp absorption peak at 317 nm, no absorption in the visible range and no
15 significant green emission) together with XRD patterns indicate the transformation from CsPbBr₃
16 to Cs₄PbBr₆ NCs (see Figure 37c).



1
2 **Figure 38.** (a) Schematic illustration of phase transformation of the Cs₄PbBr₆ to CsPbBr₃ after
3 insertion of additional PbBr₂ with the optical absorption, PL spectra and XRD patterns of Cs₄PbBr₆
4 NCs before and after the insertion of additional PbBr₂. Reproduced from Ref. ⁴³². Copyright 2017 American
5 Chemical Society. (b) Schematic illustration of crystal structure change and transformation process
6 from Cs₄PbBr₆ to CsPbBr₃ after water treatment, together with the XRD patterns of Cs₄PbBr₆ NCs
7 before and after adding water. Reproduced from Ref. ⁴⁴³. Copyright 2017 American Chemical
8 Society. (c) XRD patterns, absorption spectra, and TEM images of Cs₄PbBr₆ NCs transformed to
9 CsPbBr₃ by adding prussian blue. Reproduced from Ref. ⁴⁴⁴. Copyright 2017 American Chemical
10 Society. (d) Schematic illustration of the transformation of Cs₄PbBr₆ into CsPbBr₃ NCs induced
11 by PMAO, together with optical absorption and emission spectra of initial Cs₄PbBr₆ NCs, PMAO,

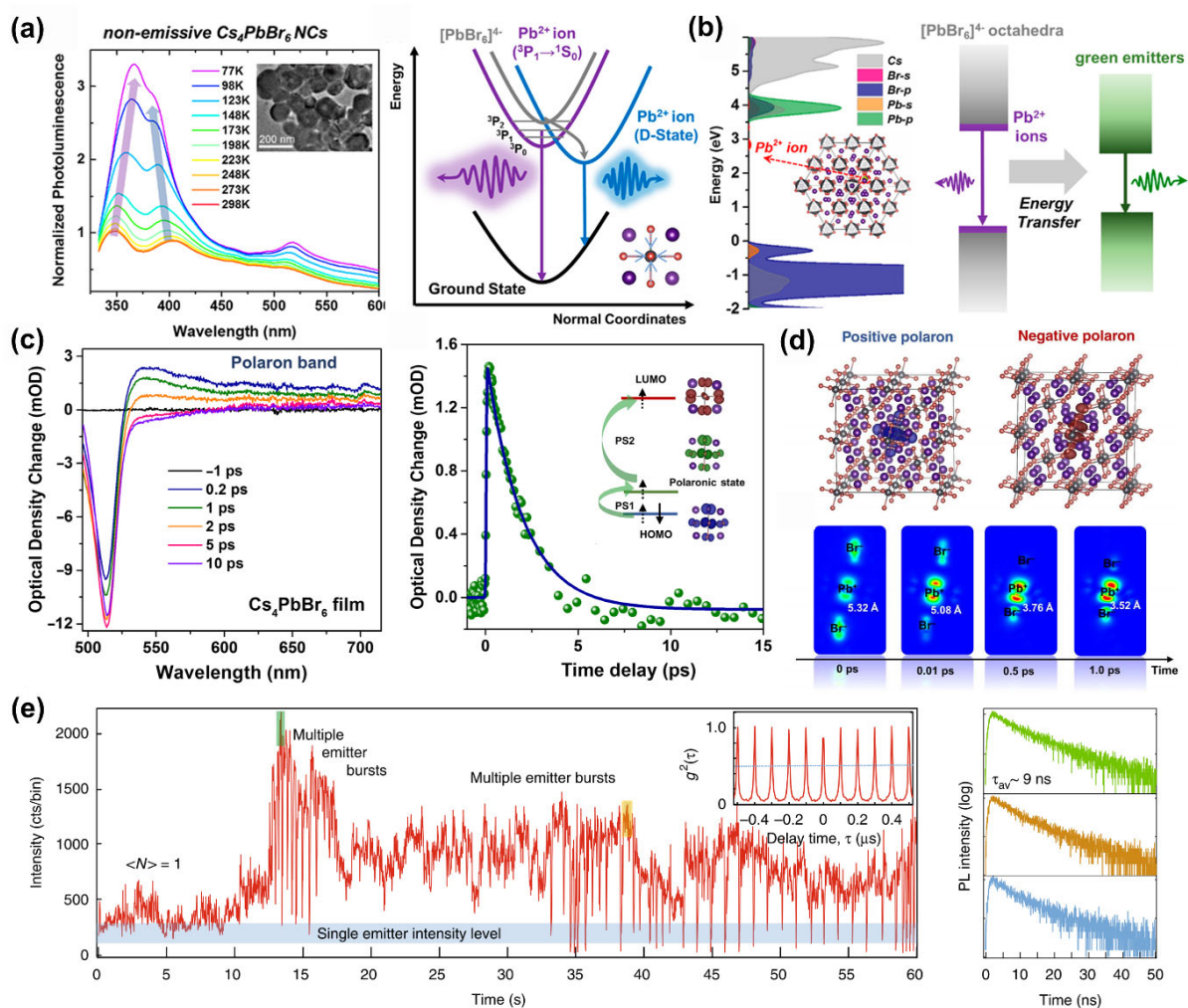
1 and partially and fully transformed NCs in toluene solutions. Reproduced from ref. ⁴⁴⁵. Copyright
2 2020 Royal Society of Chemistry.

3
4 Reversibly, Cs₄PbBr₆ NCs could be transformed back to CsPbBr₃ NCs through an insertion
5 reaction with PbBr₂.⁴³² As shown in Figure 38, this transformation would lead to the shape change
6 from the hexagonal to cubic structure, as well as the changes of spectral features, including
7 absorption, PL spectra and XRD patterns. The transformation from Cs₄PbBr₆ to CsPbBr₃ enabled
8 the preservation of CsPbBr₃ NCs size and crystallinity. Wu *et al.* reported the water-triggered
9 transformation from Cs₄PbX₆ to CsPbX₃ NCs with tunable optical properties and improved
10 stability in air.⁴⁴³ Such transformation occurred at the interface of water and a nonpolar solvent,
11 leaving the product of CsPbX₃ NCs in the organic solvent and the byproduct in the water. They
12 highlighted that the high solubility of CsX in water and the interface between nonpolar solvent and
13 water played important roles in the transformation process. In addition, the transformed CsPbBr₃
14 NCs showed better stability against moisture than those obtained through the hot-injection method.
15 Besides the phase transformation triggered by PbBr₂ or water, Palazon *et al.* showed that Cs₄PbBr₆
16 NCs can be transformed into CsPbBr₃ NCs either by thermal annealing or by reaction with prussian
17 blue.⁴⁴⁴ They also proposed that the use of prussian blue as an additive in 3D CsPbBr₃ films can
18 stabilize the 3D phase by preventing its transformation to other phases. In a recent work, Baranov
19 *et al.* were able to transform Cs₄PbBr₆ NCs to CsPbBr₃ NCs in a controlled way by reaction with
20 with poly(maleic anhydride-*alt*-1-octadecene) (PMAO).⁴⁴⁶ This polymer contains succinic
21 anhydride units that were able to react with the oleylamine ligands bound to the surface of the
22 Cs₄PbBr₆ nanocrystals, forming polysuccinamic acid, which was ultimately responsible for the
23 transformation of Cs₄PbBr₆ to CsPbBr₃. This reaction scheme is peculiar as the reaction was slow

1 and intermediate Cs₄PbBr₆-CsPbBr₃ heterostructures could be isolated for the first time. When
 2 analyzed under HRTEM, clear epitaxial interfaces were identified between the two domains in
 3 individual NCs.

4

5 3.2 OPTICAL FEATURES OF MOLECULAR-LIKE CSPbBr₃ NCs



6

7 **Figure 39.** (a) Temperature-dependent PL spectra of nonemissive (non-green emissive) Cs₄PbBr₆
 8 NCs and diagram of ³P₁ to ¹S₀ and D-state emissions from Pb²⁺ ions. Reproduced from Ref. ⁴⁴⁷.

9 Copyright 2017 American Chemical Society. (b) Projected density of states of Cs₄PbBr₆ supercell

10 after the replacement of a Cs⁺ with a Pb²⁺ ion and diagram of UV and visible emissions of Cs₄PbBr₆

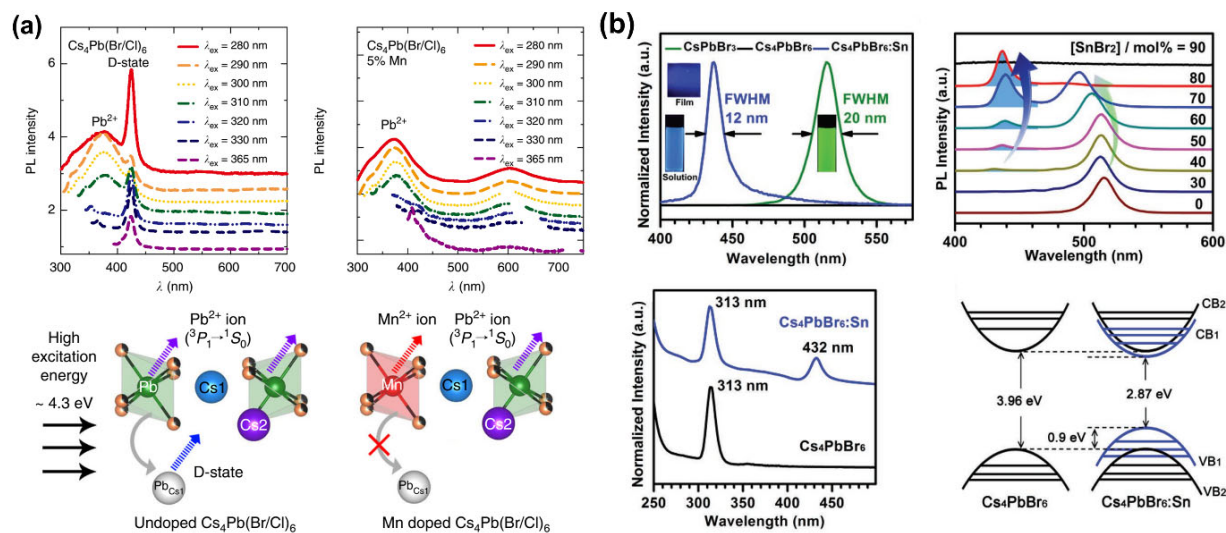
1 NCs. Reproduced from Ref. ⁴⁴⁷. Copyright 2017 American Chemical Society. (c) Transient
2 absorption spectra and photoexcitation kinetics probed at 600 nm of Cs₄PbBr₆ thin films.
3 Reproduced from Ref. ⁴⁴⁸. Copyright 2017 AAAS. (d) Charge density distributions for the
4 Cs₄PbBr₆ supercell with a positive/negative polaron located in the central octahedron and charge
5 density mapping of conduction band maximum (CBM) for the central octahedron at selected times.
6 Reproduced from Ref. ⁴⁴⁸. Copyright 2017 AAAS. (e) Blinking in individual Cs₄PbBr₆ NCs with
7 the emergence of multiple emitters. Reproduced from Ref. ³⁷⁶. Copyright 2019 Nature Publishing
8 Group.

9
10 The peculiar crystal structure of 0D inorganic perovskites with isolated lead halide octahedra
11 enables the study of the intrinsic properties of an individual octahedron, such as intrinsic Pb²⁺ ion
12 emission,⁴⁴⁷ large exciton binding energy and polaron formation energy,^{402, 448} as well as the
13 molecular-like blinking behavior.³⁷⁶ From temperature-dependent PL spectra, as given in Figure
14 39a, non-green emissive Cs₄PbBr₆ NCs showed spectral splitting feature in the UV range that were
15 originated from Pb²⁺ emissions.⁴⁴⁷ The high-energy UV emission (around 350 nm) in the non-
16 green emissive NCs was attributed to the allowed optical transition of Pb²⁺ ions (*i.e.*, ³P₁ to ¹S₀)
17 and the low-energy UV emission (around 400 nm) was assigned to the charge-transfer state
18 involved in the host lattice once a Cs⁺ ion was replaced by a Pb²⁺ ion (Figure 39b). In addition, the
19 energy transfer from Pb²⁺ ions to green luminescent centers occurred in the emissive Cs₄PbBr₆
20 NCs, in addition to the broadband UV emission.

21 Meanwhile Yin and co-workers underlined that Cs₄PbBr₆ behaves like a molecule by
22 demonstrating its low electrical conductivity and mobility, as well as large polaron binding
23 energy.⁴⁴⁸ As shown in Figure 39c, they observed a new positive broadband signal above 530 nm

1 (*i.e.*, polaron absorption) in the transient absorption spectra of the Cs₄PbBr₆ thin film and the
2 corresponding kinetics probed at 600 nm showed a lifetime of ~2 ps. This confirmed the generation
3 of small polarons with large binding energies and tight localization at individual [PbBr₆]⁴⁻
4 octahedra. The short lifetime of polaron state can be understood by *ab initio* molecular dynamics
5 calculations, showing the central octahedron recovered to the neutral state after 1.2 ps starting from
6 the initial polaronic state (Figure 39d). Thus, after photoexcitation, the structure deformation of
7 single octahedra leads to the formation of localized polarons with short lifetime and limited
8 transport in the Cs₄PbBr₆.

9 The molecular behavior of Cs₄PbBr₆ was further proved by the photon emission from
10 individual NCs.³⁷⁶ Cs₄PbBr₆ NCs showed a burst-like emission behavior with a uniform
11 distribution of PL lifetimes induced by increasing the excitation, and meanwhile exhibited a
12 photobrightening effect because of several emissive centers within the same NC (Figure 39e).
13 Actually, at lower excitation levels, both 3D and 0D perovskite NCs exhibited similar single
14 photon emission behavior, independent of their structural dimensionalities and NC size. Therefore,
15 the emission statistics of Cs₄PbBr₆ and CsPbBr₃ NCs were similar to those of individual molecular
16 fluorophores, which are different from the traditional semiconductor quantum dots.



1
2 **Figure 40.** (a) PL spectra of undoped Cs₄Pb(Br/Cl)₆ and Mn-doped Cs₄Pb(Br/Cl)₆ measured at
3 different excitation wavelengths and origin of Pb²⁺ emissions and D-state in Cs₄Pb(Br/Cl)₆ without
4 and with Mn²⁺-doping. Reproduced from Ref. ⁴⁴⁹. Copyright 2018 Nature Publishing Group. (b)
5 PL spectra of Cs₄PbBr₆ NCs, Sn-doped Cs₄PbBr₆ NCs, and CsPbBr₃ NCs, and UV-Vis absorption
6 spectra of pure and Sn-doped Cs₄PbBr₆ perovskite NCs, together with the schematic illustration of
7 the possible electronic dual-bandgap structure for the Cs₄PbBr₆ NCs before and after Sn²⁺-doping.
8 Reproduced from Ref. ⁴⁵⁰. Copyright 2019 Wiley-VCH.

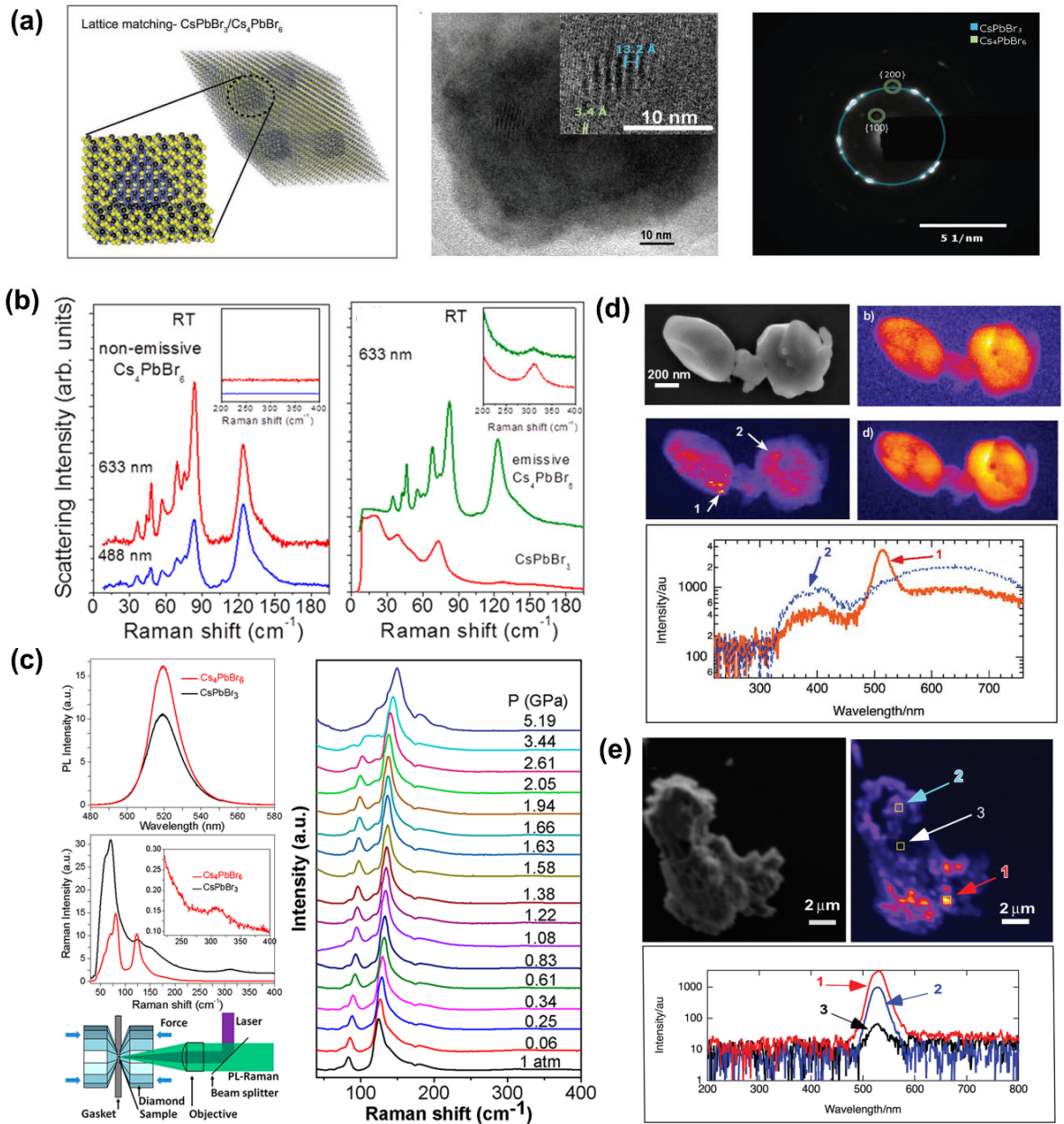
9
10 The intrinsic Pb²⁺ ion emissions of molecular-like 0D perovskites motivated several studies of
11 tuning the optical emissions of Cs₄PbBr₆ NCs. Arunkumar and co-workers studied the optical
12 behavior of Cs₄PbX₆ NCs through manganese (Mn²⁺) doping at Pb sites.⁴⁴⁹ They demonstrated
13 that the incorporation of Mn²⁺ dopants can stabilize Cs₄PbX₆ structure and suppress the formation
14 of CsPbX₃ impurities by the enhanced octahedral distortion. They also confirmed the incorporation
15 of Mn²⁺ in the 0D Cs₄PbX₆ lattice by the structural characterizations, PL spectra, and PL lifetime
16 (Figure 40a). Moreover, they achieved a high PLQY of Mn²⁺ emission in both colloidal (29%) and

1 solid (21%, powder) forms, and attributed the enhanced PLQY to the synergistic effect of
2 structure-induced spatial confinement of Cs_4PbX_6 and electronically decoupled PbX_6 octahedra.
3 Zou *et al.* proposed another method to tailor the bandgap of Cs_4PbBr_6 NCs to the blue spectral
4 region by changing the local coordination environment of isolated $[\text{PbBr}_6]^{4-}$ octahedra in the
5 Cs_4PbBr_6 through Sn^{2+} doping.⁴⁵⁰ Due to the unique Pb^{2+} -poor and Br^- -rich reaction environment,
6 the Sn^{2+} ions can be successfully incorporated into the Cs_4PbBr_6 NCs, giving rise to the coexisting
7 point defects of substitutional (Sn_{Pb}) and interstitial (Br_i) for an ultranarrow blue emission at ~ 437
8 nm (Figure 40b). They proposed an unusual electronic dual-bandgap structure, composed of the
9 new bandgap (2.87 eV) and original 0D bandgap (3.96 eV), to be at the origin of the ultranarrow
10 blue emission.

11

12

1 3.3 ORIGIN OF GREEN EMISSION IN Cs_4PbBr_6 NCs



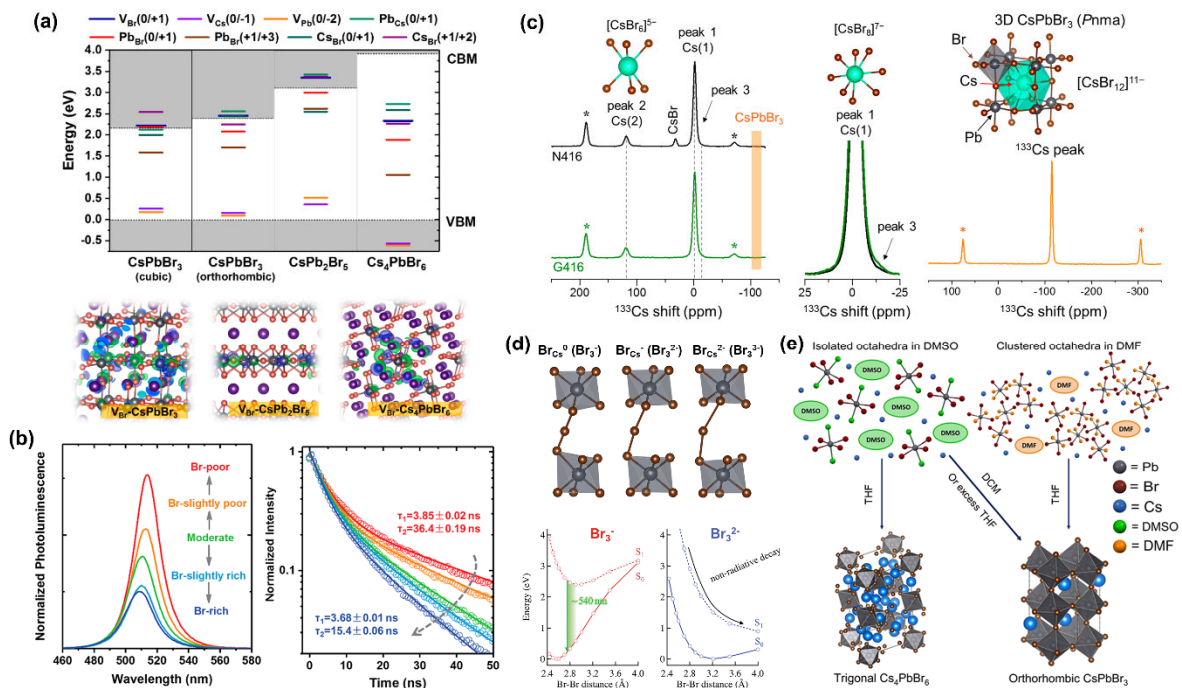
2

3 **Figure 41.** (a) Theoretical model of cubic perovskite embedded in each rhombic prism matrix
 4 together with a HRTEM image of a CsPbBr_3 -in- Cs_4PbBr_6 crystal. Reproduced from Ref. ⁴⁵¹.
 5 Copyright 2017 Wiley-VCH. (b) Raman spectra of CsPbBr_3 microcrystals, nonemissive and
 6 emissive Cs_4PbBr_6 at both 80 K and room temperature. Reproduced from Ref. ⁴⁵². Copyright 2019

1 American Chemical Society. (c) PL spectra, Raman spectra and diamond anvil cell for confocal
2 pressure Raman-PL and pressure evolution of Raman of emissive Cs₄PbBr₆. Reproduced from
3 Ref. ⁴⁵². Copyright 2019 American Chemical Society. (d) SEM micrograph of a particle aggregate
4 of Cs₄PbBr₆ with CL bandpass images. Reproduced with permission from Ref. ⁴⁵³. Copyright 2018
5 Royal Society of Chemistry. (e) SEM micrograph of Cs₄PbBr₆ aggregate with CL image and CL
6 spectra for three regions. Reproduced with permission from Ref. ⁴⁵³. Copyright 2018 Royal Society
7 of Chemistry.

8
9 Although the molecular-like quantum optoelectronic behavior of Cs₄PbBr₆ NCs is well studied,
10 the origin of their green emission is still not clear. Several emission mechanisms have been
11 proposed in the literature, including the embedded 3D CsPbBr₃ impurities, intrinsic point defects,
12 and 2D Cs₂PbBr₄ inclusion. First of all, Quan *et al.* confirmed the efficient green-emitting CsPbBr₃
13 NCs were embedded in air-stable Cs₄PbBr₆ microcrystals, *i.e.*, the coexistence of NCs and the
14 matrix, by powder XRD, high-resolution transmission electron microscopy (HRTEM) and
15 scanning electron microscope (SEM) imaging (Figure 41a).⁴⁵¹ They suggested the lattice matching
16 between the CsPbBr₃ NCs and the Cs₄PbBr₆ matrix contributed to improved passivation and such
17 spatial confinement can enhance the radiative rate of the NCs. Recently, Qin *et al.* also suggested
18 the presence of CsPbBr₃ impurities in Cs₄PbBr₆ by identifying the Raman difference between
19 emissive and nonemissive Cs₄PbBr₆. They found the Raman spectrum of emissive Cs₄PbBr₆ was
20 identical to that of nonemissive case, but it contains an additional Raman band at ~29 cm⁻¹ that
21 replicated the doublet at 28-30 cm⁻¹ of CsPbBr₃ (Figure 41b).⁴⁵² The concentration of CsPbBr₃ was
22 estimated to 0.2% in volume and this was below typical XRD sensitivity. They observed a fast
23 red-shifting, diminishing, and eventual disappearance feature of green emission by employing a

1 diamond anvil cell to probe the response of luminescence centers to hydrostatic pressure (Figure
 2 41c). This can help exclude the Br vacancies as the luminescent centers. Riesen *et al.* concluded
 3 that the green emission from Cs₄PbBr₆ is due to nanocrystalline CsPbBr₃ impurities by using
 4 cathodoluminescence (CL) imaging and energy dispersive X-ray (EDX) measurements.⁴⁵³ The CL
 5 imaging and spectroscopy showed the presence of small crystals embedded in/or between larger
 6 crystallites of Cs₄PbBr₆ which emitted around 520 nm (Figure 41d). EDX showed that the smaller
 7 crystal inclusions have a Pb:Br ratio that was approximately two times higher, confirming the
 8 CsPbBr₃ phase (Figure 41e).



9
 10 **Figure 42.** (a) Calculated defect charge-transition levels and charge density distributions of V_{Br}
 11 defect states for CsPbBr₃, CsPb₂Br₅, and Cs₄PbBr₆. (b) Normalized PL spectra and time-resolved
 12 PL spectra of Cs₄PbBr₆ NCs under different growth conditions. Reproduced from Ref. ⁴⁵⁴.
 13 Copyright 2018 American Chemical Society. (c) ¹³³Cs MAS NMR spectra and corresponding
 14 magnified spectra (25 to -25 ppm) of non-emissive and green-emissive Cs₄PbBr₆ obtained at 9.4

1 T and a spinning rate of 10 kHz at 300 K, together with ^{133}Cs MAS NMR spectra of CsPbBr_3
2 perovskite crystal. Reproduced from ref. ⁴⁵⁵. Copyright 2020 American Chemical Society. (d) The
3 local structure associated with point defect species in Cs_4PbBr_6 and relative potential energy
4 surfaces of ground state S_0 and first excited state S_1 as a function of the Br–Br distance for Br_3^-
5 and Br_3^{2-} . Reproduced with permission from ref. ⁴⁵⁶. Copyright 2019 Royal Society of Chemistry.
6 (e) Schematic diagram of the effect of the solvodynamic size and solvent-antisolvent pair on the
7 formed CsPbBr_3 and Cs_4PbBr_6 phases. Reproduced from ref. ⁴⁵⁷. Copyright 2019 American
8 Chemical Society.

9
10 Many other groups have argued that the green emission of Cs_4PbBr_6 is not from CsPbBr_3
11 impurities but an intrinsic property of Cs_4PbBr_6 because of *i*) absence of diffraction peak and
12 pattern of CsPbBr_3 , *ii*) failure of halogen exchange, and *iii*) no match of the emission peak for the
13 small-size CsPbBr_3 NCs. Yin *et al.* have demonstrated that bromide vacancy (V_{Br}) of Cs_4PbBr_6
14 has a low formation energy and a relevant defect level that contributed to the green emission.⁴⁵⁴
15 As shown in Figure 42a, in the Pb-rich/Br-poor condition, V_{Br} was the dominant defect and had a
16 transition level energy of ~ 2.3 eV located above the valence band maximum (VBM); while Pb-
17 and Cs-related vacancies showed a deep transition level (-0.5 eV below the VBM) and the other
18 antisites all had deep transition levels within the bandgap. To confirm the green emission from V_{Br}
19 point defects, they synthesized the Cs_4PbBr_6 NCs under different conditions by controlling the
20 HBr amount, and found the PL intensity increased when increasing the concentration of Br defects
21 and the highest PLQY was achieved in Br-deficient Cs_4PbBr_6 NCs (Figure 42b). Moreover, their
22 state-of-the-art characterizations including HRTEM further confirmed the purity of the 0D phase
23 of Br-deficient green-emissive Cs_4PbBr_6 NCs and also excluded the presence of CsPbBr_3 NCs

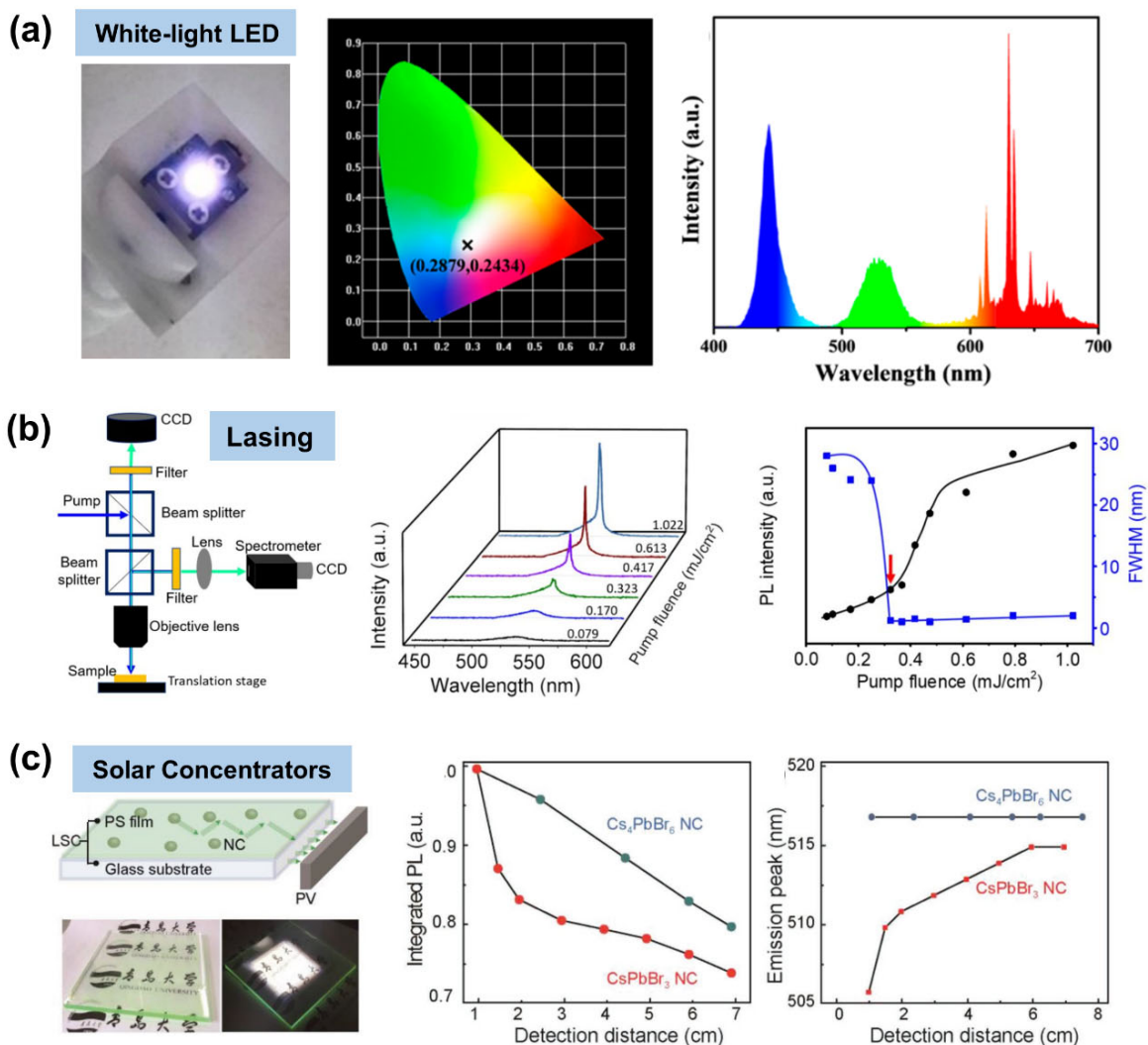
1 impurities. The theory concerning the inclusion of Br defects was recently supported by Cha and
2 co-workers based on the characteristic magnetic behavior of non-emissive and green-emissive
3 Cs₄PbBr₆ perovskite crystals.⁴⁵⁵ They demonstrated the presence of defects in green-emissive
4 Cs₄PbBr₆ and the extremely low concentration of a CsPbBr₃ phase in both non-emissive and green-
5 emissive crystals based on the analysis of ¹³³Cs magic-angle-spinning NMR spectra (Figure 44 c).

6 Jung and co-workers have a different theoretical view about defect properties of Cs₄PbBr₆.⁴⁵⁶
7 They showed that the Br_{Cs} defects led to the formation of molecular Br₃-type species that exhibited
8 a range of optical transitions in the visible range, and the green luminescence can be from the
9 emission of optically excited Br₃ to its ground state. Based on the analysis of the lowest-lying
10 electronic excitation energy as a function of the Br–Br distance (Figure 42d), they found Br₃[−] and
11 Br₃^{2−} provide S₁–S₀ energy differences in the range of green emission (~2.3 eV). They suggested
12 the presence of a radiative mechanism with visible-light emission in Br₃[−] molecular species that
13 could contribute to the green emission in Cs₄PbBr₆ upon tribromide defect formation.

14 Ray and co-workers proposed that a 2D Cs₂PbBr₄ inclusion may be responsible for the green
15 emission of Cs₄PbBr₆ NCs although they found no conclusive experimental evidence supporting
16 this claim.⁴⁵⁷ They found the solvodynamic size of the lead bromide species played a critical role
17 in determining the Cs-Pb-Br composition of the precipitated powders, *i.e.*, the smaller species
18 favored the precipitation of Cs₄PbBr₆ and larger species favored the formation of CsPbBr₃ under
19 the same experimental conditions (Figure 42d). Therefore, Cs₄PbBr₆ has a higher tendency to be
20 precipitated out from solutions with stronger coordinating solvents to Pb²⁺, lower absolute
21 concentration of the precursors, and higher CsBr/PbBr₂ ratios, as compared to 3D CsPbBr₃

1 counterpart. They concluded that 3D impurities might not be the only source of the emission and
 2 high PLQY and proposed an impurity of 2D Cs₂PbBr₄ may also contribute to the green emission.

3
 4 **3.4 OPTOELECTRONIC APPLICATIONS OF CS₄PbBr₆ MICROCRYSTALS AND**
 5 **NANOCRYSTALS**



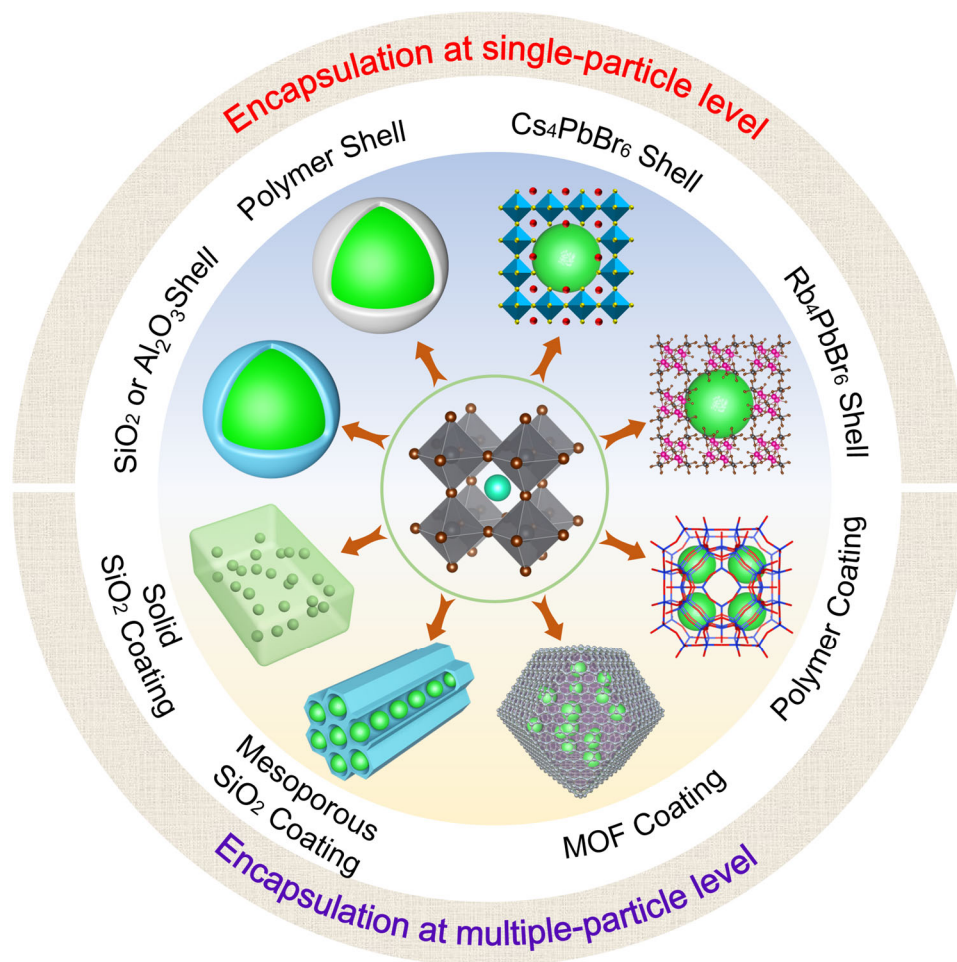
6
 7 **Figure 43.** (a) Photographs of LED devices fabricated with Cs₄PbBr₆ MCs and K₂SiF₆:Mn⁴⁺
 8 phosphor, color coordinate of the white-LEDs and electroluminescent spectra of the white-LED.
 9 Reproduced from Ref. ⁴⁵⁸. Copyright 2018 American Chemical Society. (b) Schematic of the

1 micro-PL setup for imaging and detection of the PL signal of an individual Cs₄PbBr₆ microcrystal
2 and evolution of the PL spectra with the pump fluence and dependence of the PL intensity and
3 FWHM on the pump fluence. Reproduced from Ref. ⁴⁵⁹. Copyright 2018 American Chemical
4 Society. (c) Scheme of an LSC and photographs of the LSC comprising perovskite NCs under
5 ambient and one sun illumination, and integrated PL intensity and emission peak positions as a
6 function of detection distance. Reproduced from Ref. ⁴⁶⁰. Copyright 2019 Wiley-VCH.

7
8 Despite the unclear origin of green emission in Cs₄PbBr₆ NCs, the high PL intensity and PLQY
9 of Cs₄PbBr₆ NCs make them interesting for the applications in the optoelectronic devices.⁴⁶¹ Bao
10 *et al.* reported a synthesis method to obtain highly stable Cs₄PbBr₆ microcrystals (MCs) using a
11 microfluidic system.⁴⁵⁸ They incorporated Cs₄PbBr₆ MCs with K₂SiF₆:Mn⁴⁺ phosphor onto InGaN
12 blue chips to fabricate the white light-emitting diodes (LEDs) (Figure 43a). The white-LED device
13 exhibited a wide color gamut of 119% of National Television Standards Committee (NTSC)
14 standard and a luminous efficiency of 13.91 lm/W. Sun *et al.* developed an antisolvent approach
15 to obtain the phase-pure Cs₄PbBr₆ MCs exhibiting intense PL centered at 518 nm with a PLQY of
16 ~30% and a large binding energy of 267 meV.⁴⁵⁹ They revealed the agreement between the PL
17 excitation spectrum and localized optical absorption of Pb²⁺ in isolated [PbBr₆]⁴⁻ octahedra, and
18 confirmed that the green emission was an intrinsic feature of Cs₄PbBr₆. Moreover, they
19 demonstrated the single- and multi-mode lasing resonances in individual Cs₄PbBr₆ MCs by optical
20 pumping, showing a high photostability even upon rather intense optical pumping (Figure 43b).
21 Cs₄PbBr₆ NCs can be used in luminescent solar concentrators (LSCs) (Figure 43c) absorber as
22 they meet the requirements of small absorption/emission spectral overlap, high PLQY, robust
23 stability and ease of synthesis. Zhao and co-workers fabricated semi-transparent large-area LSCs

1 using Cs₄PbBr₆ NCs and the optimized LSCs exhibited an external optical efficiency of 2.4% and
 2 a power conversion efficiency of 1.8% (100 cm²).⁴⁶⁰ These results suggest that 0D perovskite MCs
 3 and NCs are promising candidates for high-efficiency optoelectronic devices covering a similar
 4 application sphere as 3D perovskite NCs.

5 4. SURFACE COATING STRATEGIES FOR STABILITY IMPROVEMENT



6
 7 **Figure 44.** Schematic overview of different types of shell materials employed for coating on
 8 perovskite NCs to improve their stability toward heat, moisture, water and other environmental
 9 stresses.

10 Considering the intrinsic ionic nature,^{15, 462-463} the durability of MHP NCs against moisture,
 11 oxygen, light and high temperatures is still a significant challenge that has limited their further

1 development and practical applications. Over the years, significant studies have been devoted to
2 the encapsulation of perovskite NCs in various materials either in the form of core-shell NCs or
3 NCs in a matrix as illustrated in figure 44. The encapsulation process can be carried out by either
4 in situ synthesis or post-synthesis surface coating. Encapsulation by inert materials has proven to
5 be a feasible and effective approach to prevent the decomposition and enhance stability, enabling
6 them to survive under water/photo/thermal treatment.^{345, 464-468} It has been reported that CsPbX₃
7 NCs have a high defect-tolerance,²⁴ however, the surface traps that probably assist the nonradiative
8 process are still non-negligible.⁴⁶⁹ Besides surface passivation with molecular ligands, a suitable
9 encapsulation strategy (figure 44) can also efficiently remove or fix the quenching sites located on
10 the surface, and thus suppress the nonradiative recombination.³¹⁹ Hence, the encapsulation always
11 improves the photophysical properties of MHP NCs owing to the significant passivation effect.⁴⁷⁰⁻
12 ⁴⁷¹ In addition, encapsulation also protects against reactive oxygen species.⁴⁷² Furthermore, the
13 energy and charge transfer process within MHP NCs can also be tuned with semiconductor shells
14 on their surface. In some cases, brighter PL emission can be achieved by the introduction of wider-
15 gap semiconductors to fabricate type I composite. In this type, the foreign semiconductor shell has
16 a higher conduction band and a lower valence band compared to CsPbX₃, leading to confinement
17 of photo-generated carriers.^{376, 381, 473-476} On the contrary, PL quenching occurs in type II
18 heterostructure when the bandgap of CsPbX₃ NCs overlaps with another semiconductor, favoring
19 the charge diffusion, transfer, and finally separation.^{376, 477} Due to the distinctly different carrier
20 performance, these heterostructures with type I and type II can be applied in LEDs and
21 photocatalysis, respectively. Despite recent progress in the synthesis of perovskite NCs, further
22 advances in stability enhancement, surface passivation, and charge confinement/separation
23 endowed by encapsulation are still necessary for advancing the field perovskite NCs toward

1 commercial optoelectronic applications. Different strategies used for encapsulation of perovskite
2 NCs for enhancing their stability are discussed below. It should be noted that the conditions (e.g.
3 concentration, the physical state of NCs (colloidal dispersion or powder), temperature, solvent,
4 time, ligand density, shell thickness in case of core-shell NCs) used for the comparison of the
5 stability of perovskite NCs is different in different studies. Therefore, the discussion is mainly
6 limited to a specific example in each case.

7 **4.1 ENCAPSULATION AT MULTIPLE-PARTICLE LEVEL**

8 Despite the on-going intensive efforts and a plethora of conducted studies, metal halide
9 perovskite NCs (NCs) are still suffering from rather poor stability against many common factors
10 such as oxygen, humidity, light illumination, and heat. The identification of suitable encapsulation
11 of perovskite NCs is thus an ongoing task, and several types of protective materials have been
12 suggested, such as silica, organic polymers, metal oxides, metal salts, etc.

13 Silica coating of conventional semiconductor quantum dots (i.e, CdSe QDs) has become well
14 established and often used for MHP NCs as well, due to the non-toxic nature, mechanical
15 robustness, high thermal stability, and good optical transmission of this material.⁴⁷⁸⁻⁴⁷⁹ However,
16 as the conventional hydrolysis process to form SiO₂ shell needs some amount of water, this may
17 appear detrimental for the stability and optical properties of perovskites. Overall, the use of silica
18 encapsulation strategy for MHP NCs requires the right balance between the hydrolysis rate and
19 the ability to form compact and dense SiO₂ protective shells. There have been few attempts to
20 encapsulate MHP NCs in silica matrix using traditional precursors tetraethyl orthosilicate
21 (TEOS)³⁹⁶ and octadecyltrimethoxysilane (OTMS),⁴⁰⁶ while other precursors such as tetramethyl
22 orthosilicate (TMOS)⁴⁸⁰ and (3-aminopropyl)triethoxysilane (APTES)⁴⁶⁷ with higher hydrolysis
23 rate were employed to enable the faster formation of a SiO₂ protective layer under the assistance

1 of a trace amount of water, in which perovskite NCs are able to withstand.⁴⁸¹ The latter silicate
2 precursors enables to maintain the original high PLQY and narrow PL emission of both organic-
3 inorganic (methylammonium based) and all-inorganic (cesium based) lead halide perovskite NCs
4 for a longer time, so that the APTES shelled CsPb(Br/I)₃ NCs maintained 95% PLQY after 3
5 months of storage.

6 The incorporation of multiple perovskite NCs inside mesoporous silica spheres has been
7 demonstrated to be a good option to improve their thermal stability and photostability, with a final
8 aim to enhance the device performance.^{466, 482} HAADF-STEM was used to confirm the presence
9 of several CsPb₂Br₅ NCs in an individual mesoporous silica particle, as shown in Figure 45a. These
10 samples were used to fabricate white light-emitting devices (WLED).⁴⁸² Superhydrophobic
11 sponge-like silica aerogels acted as a scaffold to accommodate CH₃NH₃PbBr₃ NCs, and could well
12 preserve both the structure and optical properties of these perovskites due to their amorphous phase
13 and high optical transparency.⁴⁸³ This system was then demonstrated to serve as a sensitive
14 fluorescence SO₂ gas sensor with a reversible quench-and-recovery in the emission response.⁴⁸³

15 Some other silica-related compounds have been explored as well to protect lead halide
16 perovskite NCs from water and humid environment. Polyhedral oligomeric silsesquioxane (POSS)
17 with a cage-like structure and functional thiol group able to coordinate with the surface of CsPbBr₃
18 NCs (Figure 45b) was used as efficient encapsulating material able to protect these perovskites
19 from water. The encapsulated powdered samples kept their emission as a dispersion in water for
20 more than 10 weeks, as shown in Figure 48c, and also prevented mixed-anion (Br/I) perovskite

1 powders from ion exchange, thus enabling their use as light-emitting layers in down-conversion
2 WLEDs.⁴⁸⁴

3 For the conventional hydrolysis process to form a SiO₂ shell, the involved water will cause
4 irreversible damage to the CsPbX₃ NCs. On the other hand, the densification extent of SiO₂
5 produced by the hydrolysis process is not enough to prevent the penetration of water to the inner
6 CsPbX₃ NCs. To increase the densification extent of SiO₂ and improve the stability of CsPbX₃
7 NCs, high temperature annealing process can promote more densely cross-linked structure of SiO₂,
8 but the annealing temperature could not exceed 100 °C due to the severe surface oxidations or
9 fusing of CsPbX₃ NCs.⁴⁷ In view of this, Li *et al.* proposed a facile strategy to synthesize ceramic-
10 like stable and highly luminous CsPbBr₃ NC through template-confined solid-state synthesis and
11 in situ encapsulation based on the strategic disintegration of silicon molecular sieve (MS)
12 templates at high temperatures (Figure 45d)⁴⁸⁵. The synthesis process is a solid state reaction at
13 high temperature without organic solvents and organic ligands. Due to the encapsulation of dense
14 SiO₂ at high temperature (500~800 °C), the as prepared CsPbBr₃-SiO₂ powders exhibited
15 comparable operation stability as the commercial ceramic phosphors (Figure 45e-f). In addition,
16 high temperature solid-state reaction has been used for crystallizing CsPbX₃ NCs in glasses, and
17 the obtained CsPbX₃ NCs encapsulated with glasses present high PLQY and robust stabilities to
18 moisture, temperature, and UV light irradiation.⁴⁸⁶⁻⁴⁸⁸ In a recent work, Mai *et al.* have been able
19 to grown CsPbBr₃ NCs inside the pores of mesoporous silica using a molten salt approach at
20 temperatures as low as 350°C. The specific combination of salts enabled at the same time a high
21 PLQY and a sealing of the pores, such that the NCs were effectively isolated from the external

1 environment. A remarkable proof of the stability of these composites was given by the preservation
2 of their emission properties even if they were immersed in aqua regia for several weeks.

3 The encapsulation within an organic (especially, hydrophobic) polymer hosts is yet another
4 popular choice to improve the resistance of perovskite NCs towards harmful environments such
5 as moisture and oxygen. Zhang *et al.* demonstrated successful encapsulation of CsPbBr₃ NCs using
6 polyvinyl pyrrolidone (PVP), and used them as luminescent probes for intracellular imaging in an
7 aqueous environment, as illustrated in Figure 45g.⁴⁸⁹ In addition to PVP, a number of other
8 polymer matrices, including polystyrene (PS),⁴⁹⁰ polycarbonate (PC),⁴⁹¹ polyurethane (PU),⁴⁹²
9 polymethyl methacrylate (PMMA),⁷⁵ poly(laurylmethacrylate) (PLMA),⁴⁹³ and ethylene vinyl
10 acetate (EVA)⁴⁷³ were employed as protective coatings for perovskite NCs. The protection
11 strategies for perovskite NCs employing those different polymers can be classified into two major
12 categories: *in situ* fabrication from suitable precursors, and post-preparative encapsulation of pre-
13 synthesized perovskite nanoparticles (the previously mentioned POSS encapsulation technology⁴⁸⁴
14 belongs to the latter one, as shown in Figure 45b). Within the former strategy, Hintermayr *et al.*
15 used nanocavities formed by amphiphilic block-copolymer PS-*b*-P2VP (a combination of
16 hydrophilic P2VP part and hydrophobic PS) which provided a suitable space for the spontaneous
17 nucleation of perovskite precursors.⁴⁹⁴ Core/shell micelles serving as nanoreactors for the *in-situ*
18 formation of perovskite NCs were obtained upon the introduction of antisolvents such as toluene,
19 and were composed from the P2VP part as a core and the PS as an outer shell. However, the use
20 of the polymer-coated perovskite composites in LEDs may be problematic, as large applied

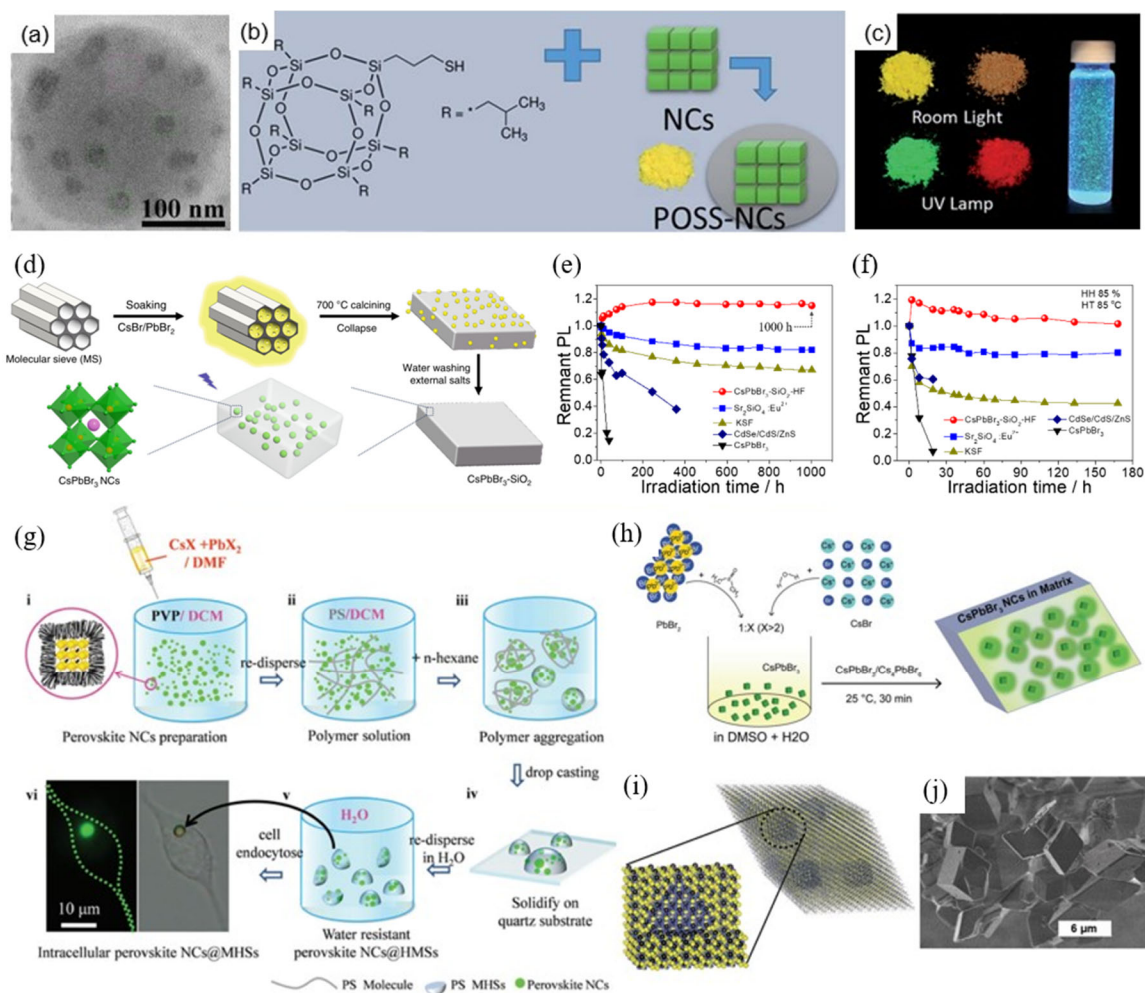
1 voltages and unavoidable heat generation during the device operation may induce polymer
2 degradation, and thus the emission quenching or undesirable shifts.

3 Capitalizing upon the previous experience with conventional semiconductor QDs,⁴⁹⁵⁻⁴⁹⁷ metal
4 oxides such as alumina (Al_2O_x), TiO_x , and ZnO have been recently applied to shelter perovskite
5 NCs. Atomic layer deposition and wet-chemical template method are two major fabrication routes
6 for metal oxide deposition,⁴⁹⁸⁻⁵⁰⁰ while the high temperature used in the annealing process may be
7 an issue resulting in undesirable decomposition of perovskite NCs. It has been reported that the
8 decomposition of CsPbBr_3 NCs could happen when porous TiO_2 matrix was annealed at just
9 85°C .^{477, 501} However, CsPbX_3 NCs synthesized by the template confined solid-synthesis in
10 mesoporous Al_2O_3 at 800°C show high PLQY and outstanding thermal stability beyond to 300
11 $^\circ\text{C}$.⁵⁰² Metal-organic frameworks (MOFs) composed of metal ions and bridging organic ligands
12 were also considered as a matrix able to protect and preserve the emission of perovskite NCs in
13 hostile environments.^{486, 503-505} The tunable size and shape of the pores in MOFs and the ability to
14 modify their surface through functional groups enabled their use as smart materials in anti-
15 counterfeiting applications.⁵⁰⁶⁻⁵⁰⁷ For instance, Zhang et al.⁵⁰⁸ demonstrated that the PL of
16 MAPbBr_3 perovskite NCs in the pores of MOFs can be reversibly switchable (quenched and
17 recovered) by treatment with water and MABr , and thus this process can be used for multiple
18 encryption and decryption of information.

19 Furthermore, metal halide salts have been shown to be able to serve as a protective matrix for
20 improving the chemical stability of perovskite NCs,⁵⁰⁹⁻⁵¹³ which has inspired from the original
21 work of Euchmüller and co-authors on protecting conventional QDs through the use of such kind
22 of salt matrices.⁵⁰⁹⁻⁵¹³ Dirin *et al.* reported a two-step synthesis, in which first nucleation followed
23 by a shelling process to deposit inorganic NaBr shells around multiple CsPbBr_3 NCs.⁵¹⁰ Perovskite

1 precursors firstly crystallized on the surface of micro-sized alkali halides, followed by a coating
2 process driven by surface reaction of amphiphilic Na and Br precursors in nonpolar solvents. A
3 series of other alkali halides including MgX_2 , CaX_2 , SrX_2 , BaX_2 , and ZnX_2 were tested as well to
4 validate the general applicability of this method.⁵¹⁰

5 The combinations of two different semiconductor materials to form core/shell heterostructures
6 have been widely demonstrated for different II-VI, IV-VI, and III-V QDs, where the trap states
7 could be removed and the stability improved.^{69,514} However, the synthetic strategies used for those
8 QDs were not easy to be translated towards lead halide perovskite NCs, eventually due to their
9 more dynamic surface and lower melting points. $CsPbX_3/ZnS$ QDs with a heterojunction-like
10 structure were reported, yet only a partial decoration of the surface of $CsPbX_3$ NCs with ZnS has
11 been achieved.⁵¹⁵ Cs_4PbX_6 is an insulating material with a wide bandgap of 3.9 eV,⁵¹⁶ and smaller
12 $CsPbBr_3$ NCs encapsulated inside a Cs_4PbBr_6 matrix were found to preserve high PLQY and thus
13 could be used as optical gain materials in lasers and as emissive layers in LEDs.^{477,517-518} Figure
14 45h illustrates a one-pot preparation of Cs_4PbBr_6 -in- $CsPbBr_3$ composites from suitable precursors
15 in a liquid environment, while Figure 45i shows lattice alignment of $CsPbBr_3$ NCs within the
16 Cs_4PbBr_6 matrix; well-faceted Cs_4PbBr_6 -in- $CsPbBr_3$ microprisms are visualized by SEM image in
17 Figure 45j.⁵¹⁷ More recently, Zeng's group demonstrated the use of the $CsPbX_3$ -in- Cs_4PbX_6
18 composites for X-ray sensing and imaging, with Cs_4PbBr_6 matrix providing a favorable
19 enhancement in the attenuation of X-rays.⁵¹⁹



1
2 **Figure 45.** (a) HAADF-STEM image of several CsPbBr₃ NCs embedded within a mesoporous
3 silica sphere. Reproduced with permission from Ref. ⁴⁸². Copyright 2017 Royal Chemical Society.
4 (b) The structure of thiolated polyhedral oligomeric silsesquioxane (POSS), and illustration of the
5 coating process of POSS on pre-synthesized perovskite NCs. (c) Photographs of POSS-coated
6 green-emitting CsPbBr₃ and red-emitting CsPb(Br/I)₃ powders under room light and UV light, and
7 a dispersion of green-emitting POSS-CsPbBr₃ NCs in water. (b, c) Reproduced with permission
8 from Ref. ⁴⁸⁴. Copyright 2016 Royal Chemical Society. (d) The schematic diagram of synthesis
9 CsPbBr₃ NCs into dense SiO₂ by high temperature solid state reaction. (e) Photostabilities of the
10 CsPbBr₃-SiO₂, ceramic Sr₂SiO₄:Eu²⁺ green phosphor, KSF red phosphor, colloidal CsPbBr₃ NCs

1 and CdSe/CdS/ZnS NCs under illumination, sealed with Norland-61 on the LED chips (20mA,
2 2.7V), (f) aged at 85°C and 85% humidity conditions on the LED chips (20mA, 2.7V). (d-f)
3 Reproduced with permission from Ref. 68. (g) Schematics of encapsulation of CsPbBr₃ NCs into
4 a PVP matrix resulting in water-resistant composites used for the intracellular imaging.
5 Reproduced with permission from Ref. ⁴⁸⁹. Copyright 2017 Wiley. (h) Schematics of one-pot
6 synthesis of CsPbBr₃-in-Cs₄PbBr₆ microcrystals from CsBr and PbBr₂ precursors, (i) crystal
7 structure model for composites synthesized in (h), with a Cs₄PbBr₆ microcrystal in a rhombic prism
8 shape hosting several CsPbBr₃ NCs, and (j) SEM image of CsPbBr₃-in-Cs₄PbBr₆ prism-shaped
9 microcrystals. Reproduced with permission from Ref. ⁵¹⁷. Copyright 2017 Wiley.

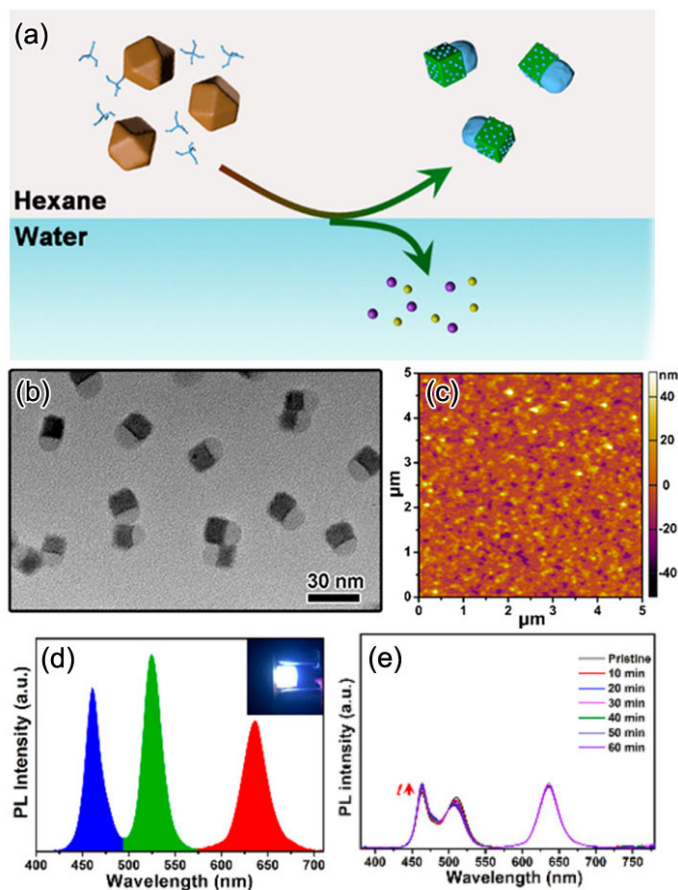
10

11 **4.2 ENCAPSULATION AT SINGLE-PARTICLE LEVEL**

12 From the afore-mentioned encapsulation strategies, a variety of materials including polymer,
13 SiO₂, and AlO_x have been employed to stabilize CsPbX₃ NCs resulting in impressive stability
14 improvement. The capsule-like structure endowed CsPbX₃ NCs enhanced optical properties
15 accompanied by exceptional stability. In these successful encapsulation examples, however, the
16 as-obtained products always had multiple particles in one shell, resulting in large particle size that
17 could reach up to tens of micrometers. In general, the CsPbX₃ NCs used in optoelectronic devices
18 are assembled in the form of a film, in which undesirable large particles would weaken the film
19 quality and consequently corresponding device performance. In addition to the poor uniformity in
20 film, micrometer-sized particles were unfavorable in many bio-related areas, such as cell uptake.
21 More importantly, the large particle size hampers their solution processability. The straightforward
22 solution for this problem is to shrink the size of the encapsulated CsPbX₃ product into the
23 nanoscale. Significant efforts have been devoted to exploring the encapsulation of CsPbX₃ NC at

1 single-particle level. Up to now, oxides and semiconductors have been employed in the fabrication
2 of CsPbX₃-based core/shell nanostructures with significantly improved optical properties and
3 stability.

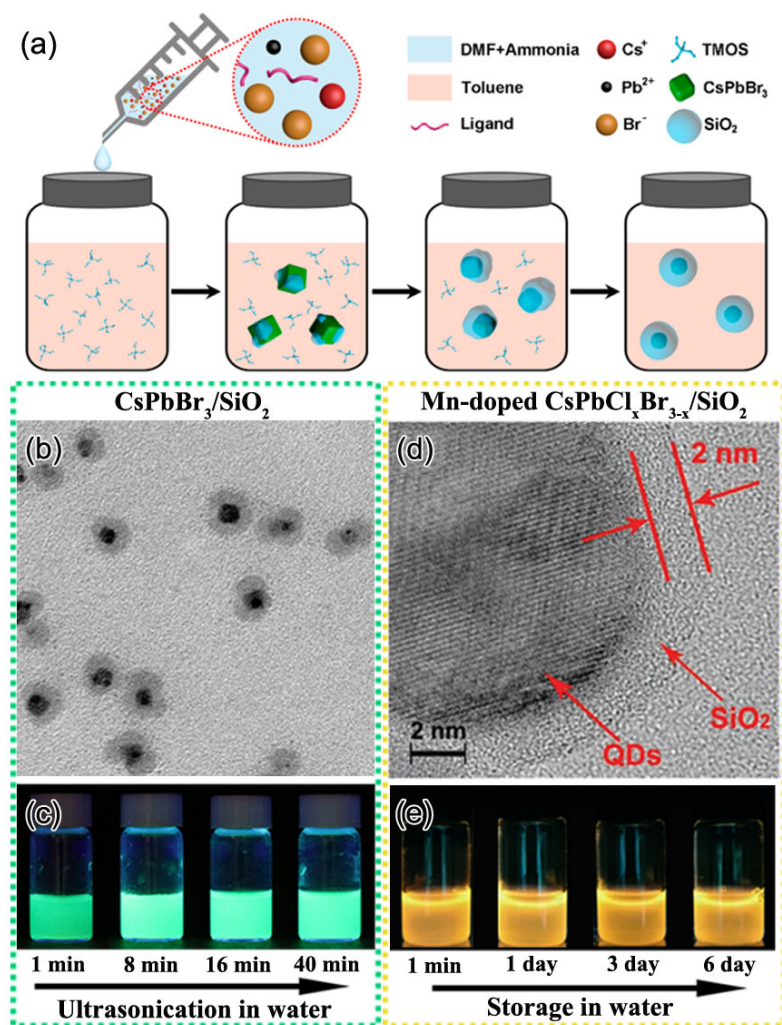
4 In 2017, Zhang et al.⁵²⁰ first developed a sol-gel method to produce monodispersed
5 CsPbX₃/SiO₂ Janus NCs at the oil-water interface. The simultaneous transformation Cs₄PbX₆
6 →CsPbX₃ and growth of SiO₂ at one side of CsPbX₃ NCs led to the formation of a unique Janus
7 structure, as shown in Figure 46a, b. As expected, the modification of SiO₂ ensured CsPbX₃ NCs
8 fewer surface traps and enhanced photophysical properties. More importantly, CsPbX₃/SiO₂ Janus
9 NCs could be fabricated into a high-quality film, which exhibited comparable smoothness and
10 uniformity to pristine CsPbX₃ NCs, as shown in Figure 46c. In addition, CsPbBr₃/SiO₂ Janus
11 nanoparticles could be employed as an emitting layer in a WLED, resulting in a significantly
12 improved photostability under continuous UV irradiation (Figure 46d, e).



1
 2 **Figure 46.** (a) Schematic illustration of the formation of CsPbX₃/SiO₂ Janus nanoparticles. (b)
 3 TEM image of CsPbBr₃/SiO₂ Janus NCs. (c) AFM image of the film fabricated from the
 4 CsPbBr₃/SiO₂ nanoparticles. (d) PL spectra of CsPbBr₃/SiO₂ based WLED device and (e) its
 5 corresponding time-dependent PL spectra. Inset in (d) shows an operating device. Reproduced
 6 with permission from Ref. ⁵²⁰. Copyright 2017 American Chemical Society.

7 In comparison with pristine CsPbX₃ NCs, the afore-mentioned CsPbX₃/SiO₂ Janus structure
 8 achieved great strides in their durability against water and irradiation. The long-term stability
 9 remains a challenge because of the partial coverage with oxides. The core/shell structure offers a
 10 more promising solution due to the complete encapsulation of CsPbX₃ NCs. SiO₂⁵²¹⁻⁵²² and
 11 Al₂O₃³⁰⁸ shells have been successfully coated on the CsPbX₃ NCs to produce core/shell
 12 nanostructures by using hydrolysis and atomic layer deposition (ALD), respectively. For example,

1 a modified supersaturated recrystallization approach has been developed to synthesis
2 CsPbBr₃/SiO₂ core/shell nanostructure, as shown in Figure 47a.⁵²¹ During the whole reaction, the
3 product quality was sensitive to multiple parameters, such as capping ligand type and density,
4 reaction temperature, silica precursor, and ammonia concentration. Therefore, the well-defined
5 core/shell structure could be realized only by carefully controlling the reaction conditions. As a
6 result, monodisperse core/shell nanoparticles with only one CsPbBr₃ core encapsulated in one SiO₂
7 shell was obtained (Figure 47b), which displayed outstanding stability against water under
8 ultrasonication treatment, as shown in Figure 47c. Later, a reverse microemulsion method was
9 devoted to the preparation of SiO₂ shell coated Mn-doped CsPbCl_xBr_{3-x} NCs by incorporation of
10 multibranching capping ligand trioctyl-phosphine oxide (TOPO).⁵²² One typical feature of this
11 product was its ultrathin SiO₂ shell, which ensured not only improved stability but also excellent
12 optical properties. Another method in the preparation of ultrathin inert shell was the colloidal ALD
13 reported by Loiudice et al.³⁰⁸ The resulting CsPbX₃/AlO_x core/shell nanoparticles preserved the
14 colloidal stability of CsPbX₃ NCs and controllable AlO_x shell from 1 to 6 nm. For inert shell
15 encapsulation, the product always exhibited improved photophysical features and enhanced
16 stability compared to naked CsPbX₃ NCs. However, the inert shell would weaken the electrical
17 properties, resulting in a poor performance in photoelectric devices such as solar cells and
18 electroluminescent LEDs. It may provide more opportunities in practical applications if one can
19 further reduce the inert shell thickness or employ other semiconductors to encapsulate CsPbX₃
20 NCs.



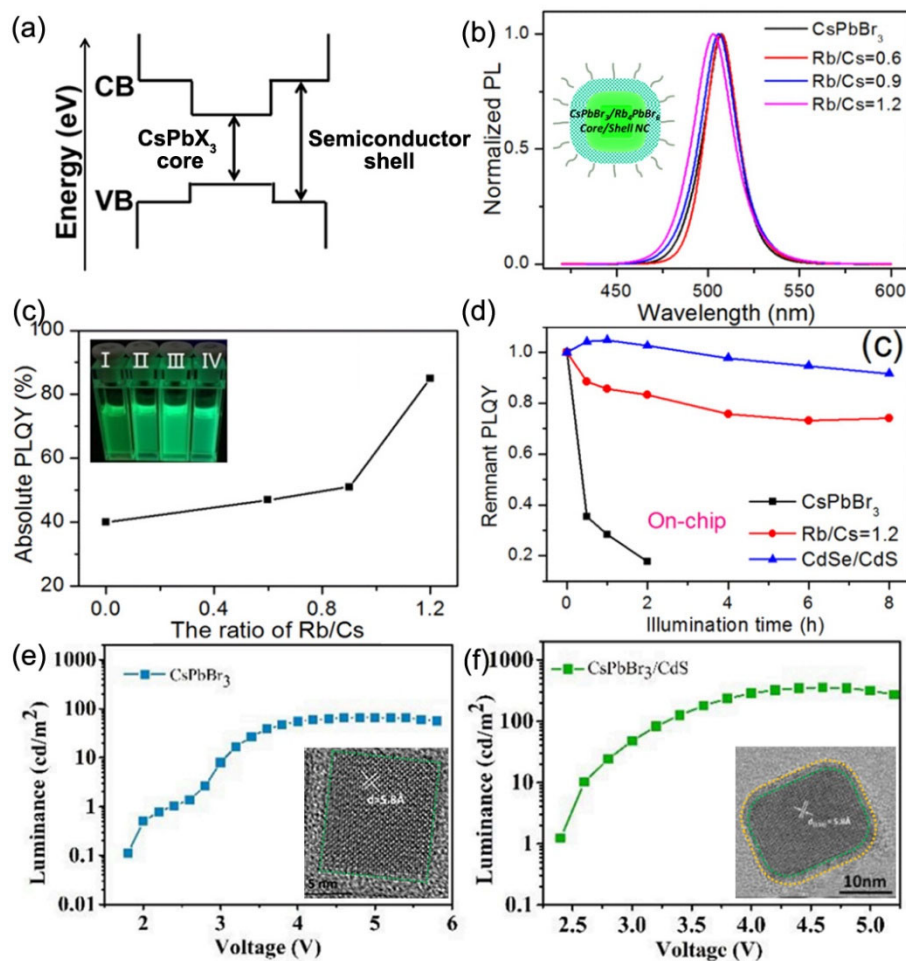
1
2 **Figure 47.** (a) The formation mechanism of CsPbBr₃/SiO₂ core/shell NCs. (b) TEM image and (c)
3 photographs of CsPbBr₃/SiO₂ NCs showing the durability against water under ultrasonication. (a-
4 c) Reproduced with permission from Ref. ⁵²¹, Copyright 2018 American Chemical Society. (d)
5 TEM image and (e) photographs of Mn-doped CsPbCl_xBr_{3-x}/SiO₂ core/shell nanoparticles against
6 water. (d, e) Reproduced with permission from Ref. ⁵²², Copyright 2019 Wiley.

7 Inspired by the core/shell structure in traditional II-VI (e.g., CdSe/ZnS) quantum dots,^{123, 523} a
8 variety of semiconductors have been devoted into the synthesis of CsPbX₃-based heterojunction.
9 In most cases, Cs₄PbX₆ is usually employed as the shell composition to enhance CsPbX₃
10 performance in photophysical characteristics and durability.^{381, 473-476} It may be ascribed to the

1 similar ternary crystal structure and identical $[\text{PbX}_6]^{4-}$ units in both CsPbX_3 and Cs_4PbX_6 , which
2 makes the corresponding dual-phase composite stable. In the bulk phase and multi-nanoparticle
3 coating, CsPbX_3 embedded in Cs_4PbX_6 host mostly achieve the enhancement in both PLQY and
4 stability compared to the pristine CsPbX_3 . Only limited investigations, however, have been
5 reported in the single-particle encapsulation. A seed-mediated approach has been established in
6 the synthesis of $\text{CsPbBr}_3/\text{Cs}_4\text{PbBr}_6$ core/shell NCs.⁵²⁴ In a typical process, additional cesium and
7 halide precursor was introduced into as-prepared CsPbBr_3 NC solution under certain conditions,
8 resulting in hexagonal Cs_4PbBr_6 shell formation on the CsPbBr_3 surface. The unique core/shell
9 heterostructure consisted of a core with narrow bandgap and a shell with a large bandgap would
10 contribute to type I band alignment, in which CB and VB of the core were located within those of
11 the shell (Figure 48a). Consequently, the excited carriers could be well confined within the CsPbX_3
12 core and gave rise to an enhanced recombination rate and PLQY. In parallel to Cs_4PbX_6 , also
13 CsPb_2X_5 , with its large bandgap, has been exploited in the fabrication of type I heterostructures,
14 this time containing a CsPbX_3 core and a CsPb_2X_5 shell, again with the purpose to optimize the
15 optical features.^{465, 525}

16 In addition to $\text{Cs}_x\text{Pb}_y\text{X}_z$ shell growth, Rb_4PbX_6 and II-VI semiconductor might be potential
17 passivation shell for CsPbX_3 NCs to fabricate type I or quasi-type I composite. For example, a
18 post-synthesis phase transformation $\text{CsPbBr}_3 \text{ NC} \rightarrow \text{CsPbBr}_3/\text{Rb}_4\text{PbBr}_6$ core/shell nanostructure
19 was presented by rubidium oleate triggering (also discussed in ion-exchange section).³¹⁹ By
20 controlling the Rb:Cs ratio in the precursor, Rb_4PbBr_6 shell with different thicknesses could be
21 realized, resulting in an obvious blue-shift in PL emission and increasing absolute PLQY, as shown
22 in Figure 48b, c. More importantly, the core/shell hybrid showed significantly enhanced
23 photostability after a long-term operation, which was comparable to the CdSe/CdS core/shell

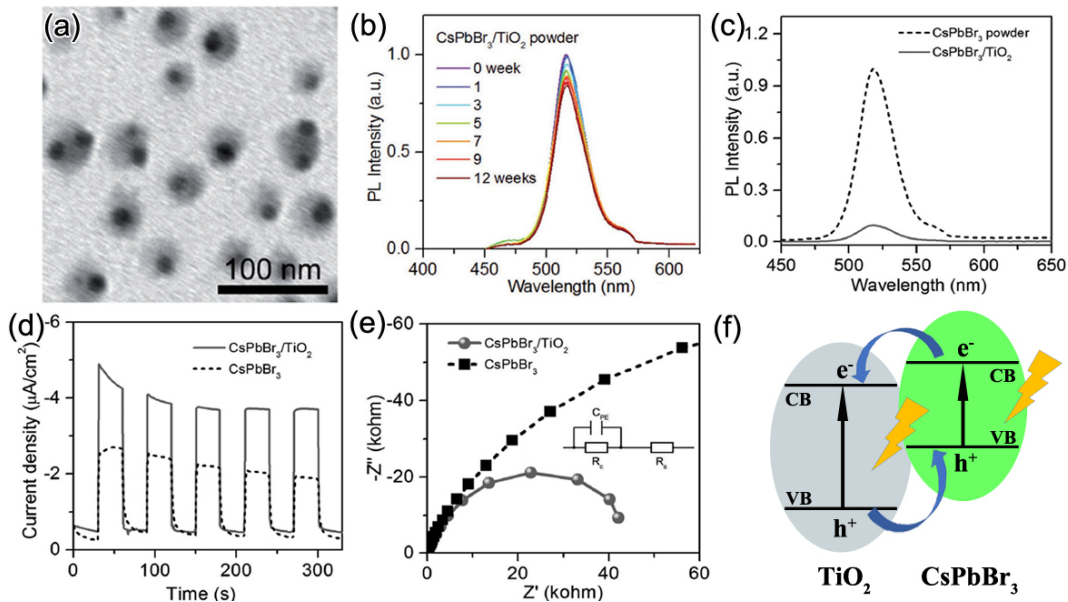
1 quantum dots (Figure 48d). Very recently, a II-VI semiconductor CdS shell was found to
 2 efficiently suppress the non-radiative recombination of CsPbX₃ NCs due to the type I alignment.⁵²⁶
 3 In addition, the CdS layer effectively passivates the surface traps, leading to a higher radiative
 4 recombination rate. Particularly, an inverted LED (ITO/ZnO:Mg/QDs/CBP(4,4'-Bis(N-
 5 carbazolyl)-1,1'-biphenyl)/MoO₃/Al) was fabricated based on the CsPbBr₃/CdS core/shell
 6 heterostructure. A maximum luminance of 354 cd/m² was acquired for CsPbBr₃/CdS NCs while
 7 that was only 65 cd/m² for pure CsPbBr₃ nanoparticles. The average EQE was 0.4% and 0.07%
 8 for the core/shell and naked samples, respectively. Though the overall performance of core/shell
 9 heterostructure is moderate, it sheds some light on the heading direction in the modification of
 10 CsPbX₃ NCs.



11

1 **Figure 48.** (a) Band alignment of type I composite with core/shell structure. (b) PL spectra, (c)
2 PLQY and (d) photostability of naked CsPbBr₃ and CsPbBr₃/Rb₄PbBr₆ core/shell NCs. Insets in
3 (c) show the images of CsPbBr₃ NCs with/without Rb treatment under 365 nm lamp, I: CsPbBr₃,
4 II: Rb/Cs=0.6, III: Rb/Cs=0.9, IV: Rb/Cs=1.2. (a-d) Reproduced with permission from Ref. ³¹⁹,
5 Copyright 2018 American Chemical Society. L-V curves of (e) CsPbBr₃ and (f) CsPbBr₃/CdS
6 core/shell NCs. Insets in (e) and (f) show TEM images of CsPbBr₃ and CsPbBr₃/CdS NC. (e, f)
7 Reproduced with permission from Ref. ⁵²⁷ Copyright 2019 Tang, Yang, Li, Chen, Hu and Qiu.

8
9 By tuning the composite component, one can easily adjust the energy or charger transfer
10 process.³⁷⁶ For example, type II composite could be fabricated by using TiO₂ shell to encapsulate
11 CsPbBr₃.⁴⁷⁷ Similar to inert shell coating, the resulting product exhibited a well-defined core/shell
12 nanostructure and excellent stability in water, as shown in Figure 49a, b. However, its PL emission
13 demonstrated an obviously quenching compared to naked CsPbBr₃ NCs (Figure 49c). Moreover,
14 photoelectrochemical studies including transient photocurrent responses and Nyquist plots
15 suggested an increased charge separation efficiency of CsPbBr₃ NCs upon TiO₂ shell
16 encapsulation (Figure 49d, e). In strong contrast to the afore-mentioned type I composite,
17 photoinduced charges were effectively separated and accumulated in TiO₂ and CsPbBr₃ part,
18 respectively, which might provide the opportunities for photocatalytic reactions.



1
2 **Figure 49.** (a) TEM image of CsPbBr₃/TiO₂ core/shell NCs. (b) The relative PL intensity of
3 CsPbBr₃/TiO₂ NCs in water. (c) PL spectra, (d) transient photocurrent responses and (e) Nyquist
4 plot of CsPbBr₃ and CsPbBr₃/TiO₂, respectively. (a-e) Reproduced with permission from Ref. ⁴⁷⁷,
5 Copyright 2017 Wiley. (f) Band alignment within this type II heterostructure.

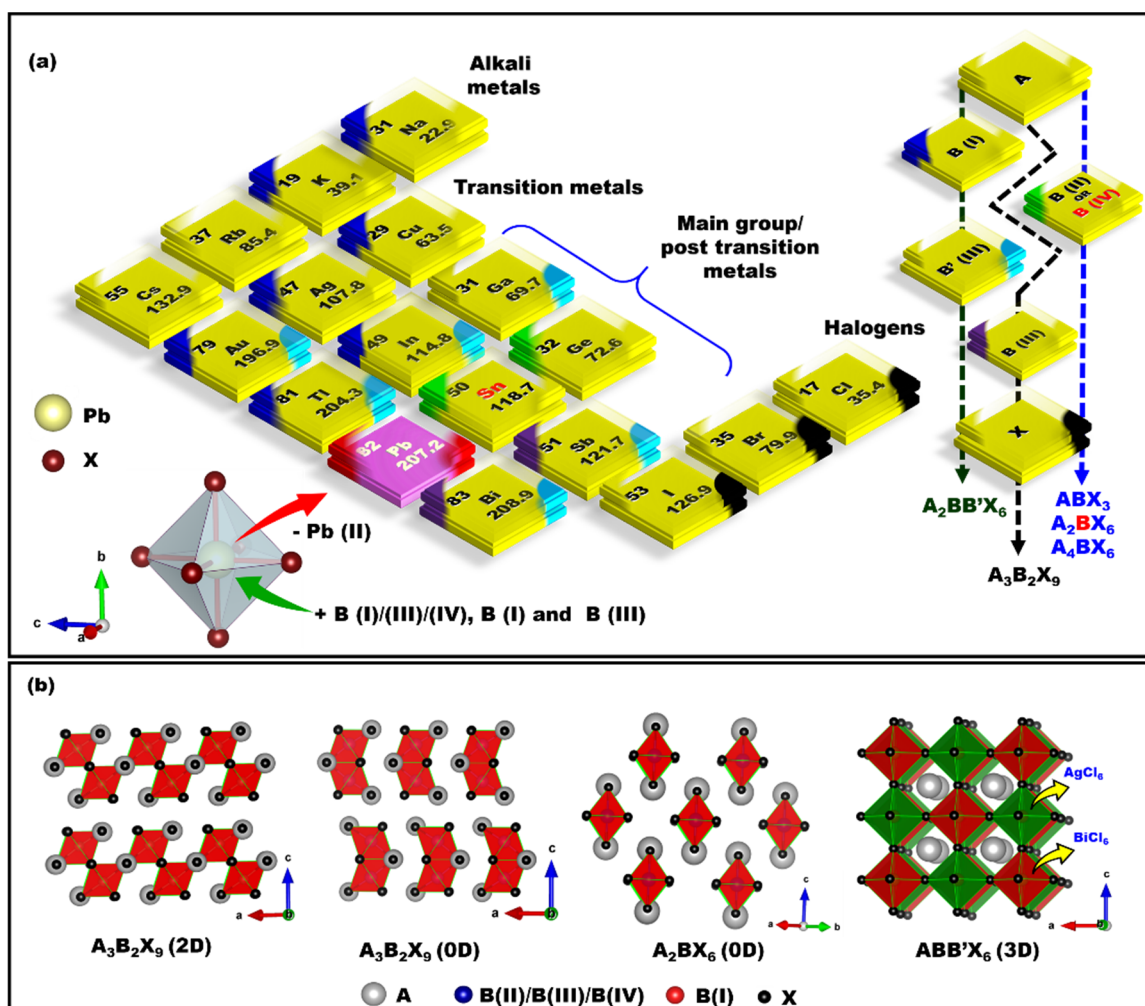
7 5. NANOCRYSTALS OF LEAD-FREE PEROVSKITE-INSPIRED MATERIALS

8 Despite rapid advancements in the synthesis, understanding and performance of Pb-based
9 perovskite NCs, the toxicity of Pb and the soluble nature of the Pb-based compounds in polar
10 solvents remain an issue for their widespread application. This is related to the fact that the lead
11 content in electronic products is restricted to 0.1 wt.% by the Regulation of Hazardous Substances.
12 This lead content restriction is as per the European Union guidelines and may vary by region.⁵²⁸
13 This practical consideration demands for novel, environmentally benign metal halide perovskites.
14 Furthermore, there is the fundamental question on whether we could identify alternative classes of
15 materials that could replicate the exceptional optoelectronic properties of the Pb-halide
16 perovskites. Both factors have motivated researchers across the globe to undertake extensive

1 theoretical and experimental work for designing Pb-free metal halide perovskites. In this sub-
2 section, we will highlight the major progress of the field, with emphasis on colloidal NC systems.
3 Readers may also refer to prior review articles on Pb-free perovskite NCs.^{109, 114, 529-534} In the
4 present article, we will capture the recent developments and insights into Pb-free metal halide
5 perovskite NCs. In addition to materials with perovskite crystal structures, we will also discuss
6 perovskite derivatives that are chemically or electronically analogous to MHPs, but do not have a
7 perovskite structure.

8 **5.1 LEAD-FREE PEROVSKITES AND THEIR DERIVATIVES: COLLOIDAL** 9 **SYNTHESIS AND OPTICAL PROPERTIES**

10 Figure 50a shows a selection of elements from the periodic table that are presently being
11 considered as substitutes for Pb(II). The color code specifies the B-site occupancy in composition
12 presented at the extreme right in Figure 50a. The crystal structures of representative generic
13 compositions for which colloidal NCs have already been prepared are given in Figure 50b.
14 Substituting Pb(II) with other group 14 elements (*e.g.*, Sn(II) and Ge(II)) maintains the perovskite
15 crystal structure (*i.e.*, ABX₃). On the other hand, substituting Pb(II) with an element from group
16 15 will result in materials with the A₃B₂X₉ stoichiometry, and these materials could either take on
17 a 2D or 0D crystal structure (Figure 50b). To maintain the cubic perovskite crystal structure, the
18 B-site in ABX₃ compounds could be alternately substituted for group 13 (*e.g.*, Ag(I)) and group
19 15 (*e.g.*, Bi(III)) elements. This results in double perovskite materials with the generic formula
20 A₂B(I)B'(III)X₆. One can go further and replace the B'-site with a tetravalent cation (*e.g.*, Sn⁴⁺ or
21 Ti⁴⁺). In order to maintain charge neutrality in a perovskite crystal structure, the B site would need
22 to be vacant. This, therefore, results in the vacancy-ordered double perovskites, with the generic
23 formula A₂BX₆.



1 **Figure 50.** (a) Combinations of elements from a part of periodic table forming possible Pb-free
 2 metal halide perovskite and their derivative structures. The triangular color code specifies the site
 3 occupancy as per the compositional formula presented in the extreme right. (b) Structural
 4 presentation of Pb-free metal halide perovskites and perovskite-derivatives showing network of
 5 octahedra in 3D, 2D and 0D directions.

6 **Sn and Ge-based Perovskite and Perovskite Derivative NCs.** The direct substitution of
 7 Pb(II) with an isovalent element to maintain the ABX₃ crystal structure has been one of the earliest
 8 manifestations of lead-free perovskite derivatives. Sn- and Ge-based perovskites have been
 9 successfully demonstrated in bulk thin films, both in hybrid and all-inorganic structures.⁵³⁵⁻⁵⁴¹
 10 Colloidal synthesis of CsSnX₃ NCs with different sizes and shapes has also been reported, along

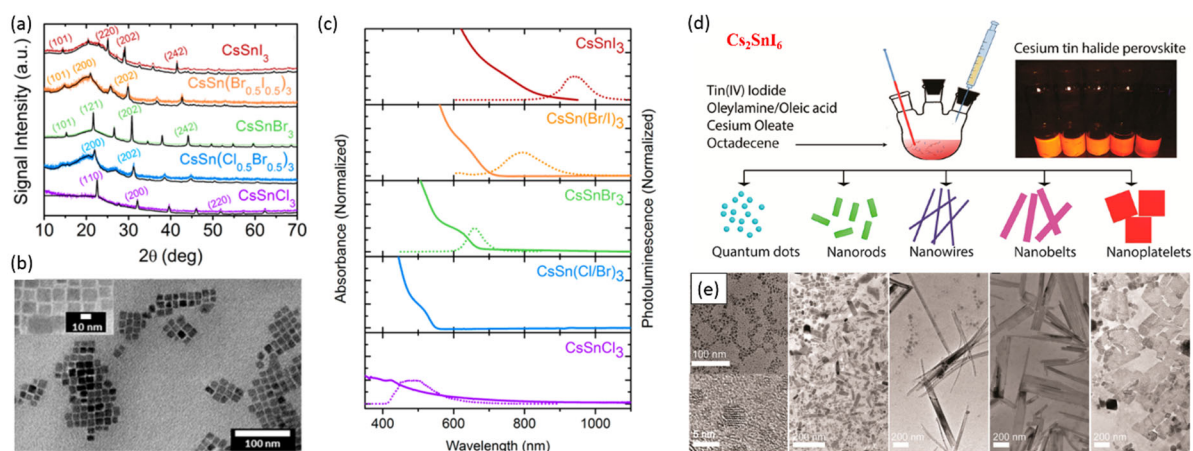
1 with the tuning of the optical properties.⁵⁴²⁻⁵⁴⁵ The bandgap of CsSnX₃ perovskite is lower
2 compared to the analogues Pb²⁺ based MHP mostly due to higher electronegativity of Sn ions
3 compared to Pb.^{542, 546} Huang *et. al.* showed that the relatively small bandgap changes from
4 CsSnCl₃ to CsSnI₃ are due to interatomic Sn *s* and Sn *p* character of the valence band maxima
5 (VBM) and the conduction band minima (CBM), respectively.⁵⁴⁷ This leads to high oscillator
6 strength in these direct bandgap perovskites where the photoluminescence peak was assigned to
7 acceptor bound excitons.⁵⁴⁷

8 The methods for synthesizing lead-free perovskite NCs are essentially the same as those used
9 for the synthesis of lead-halide NCs discussed in earlier sections. The first CsSnX₃ NCs were
10 reported by Jellicoe *et al.*, who prepared the colloidal NC solution by hot-injection (Figure 51a-
11 c).⁵⁴² The CsSnCl₃ NCs have a perovskite crystal structure with a cubic space group (Pm $\bar{3}$ m),
12 while the CsSnBr₃ and CsSnI₃ NCs have a lower symmetry orthorhombic (Pnma) phase (Figure
13 51a).⁵⁴² The synthesized CsSnX₃ nanocubes were nearly monodisperse, with a size of 10 nm, and
14 their bandgap could be easily tuned over the visible and near-infrared range by changing the halide
15 (X = Cl, Br and I) composition (Figure 51a & b). The CsSnX₃ NCs exhibit redshifted emission
16 (lower bandgap) compared to corresponding CsPbX₃ NCs with the same size and halide. Beyond
17 composition, the bandgap of CsSnX₃ NCs could also be tuned through their size and
18 dimensionality.^{542, 544} For instance, Yang and co-workers⁵⁴⁴ demonstrated the synthesis of strongly
19 quantum confined CsSnI₃ NPLs with blue-shifted PL (1.59 eV) compared to the PL in bulk (1.3
20 eV). Computations also predicted that CsSnI₃ NPLs synthesized under Sn-rich conditions would
21 have lower defect densities and higher stability.⁵⁴⁴ In general, 2D layered perovskites have been
22 reported to exhibit higher stability over their bulk counterparts.⁵⁴⁸ The high density of surface
23 ligands protects 2D layered perovskites or NPLs from air and moisture. It has been shown that Sn-

1 based colloidal 2D perovskite NPLs can be easily prepared at room temperature by ligand-assisted
2 nonsolvent crystallization method.²¹⁹

3 Despite successful shape-controlled synthesis of CsSnX₃ NCs, the stability of these NCs is
4 still a major concern. This is a consequence of the fact that, when these NCs are exposed to ambient
5 conditions, Sn²⁺ quickly oxidizes to Sn⁴⁺, forming a new composition, Cs₂SnX₆,⁵⁴² which has a
6 0D crystal structure, as shown in Figure 50.⁵⁴⁹⁻⁵⁵³ Several reports have indicated trioctyl phosphine
7 (TOP) ligands to be promising for stabilizing CsSnX₃ NCs. However, the transformation of Sn (II)
8 to Sn (IV) over time is inevitable.^{542, 544} The morphology of perovskite NCs can have an influence
9 on their stability. For instance, Wang et al.⁵⁵⁴ demonstrated that CsSnBr₃ cubic nanocages exhibit
10 improved stability under ambient conditions. These nanocages were synthesized by hot-injection
11 using stannous 2-ethylhexanoate (instead of TOP-SnBr₂) as the Sn precursor and MgBr₂ as the
12 bromide precursor. Importantly, the surface treatment of CsSnBr₃ nanocages with
13 perfluorooctanoic acid (PFOA) can significantly improve their stability against moisture, light and
14 oxygen. This was attributed to the strongly electronegative F-groups in PFOA suppressing the
15 oxidation of Sn²⁺ to Sn⁴⁺, whilst the bulky carbon chain prevented O₂ and H₂O access to the
16 perovskite through steric hindrance.⁵⁵⁴ The stability of Sn-perovskites could also be improved
17 through the formation of multi-cation alloying at A or B site.⁵⁵⁵⁻⁵⁵⁶ Several attempts have also been
18 made to improve the structural and environmental stability by only partially replacing Pb with
19 Sn.⁵⁵⁷⁻⁵⁵⁸ Such CsPb_xSn_{1-x}X₃ NCs can be obtained either through ion exchange or *via* direct
20 synthesis.^{556, 558} These CsPb_xSn_{1-x}X₃ NCs were found to be stable for months in ambient conditions
21 and have been successfully used in the fabrication of perovskite NC-based solar cells⁵⁵⁸ and
22 LEDs.⁵⁵⁹ However, NCs showed poor performance as compared to the polycrystalline films due
23 to the large number of grain boundaries and surface ligands which retard charge transport.⁵⁶⁰ The

1 environmental and thermal stability were also improved by mixing Cs with MA in the A-site (i.e.
 2 $\text{MA}_{0.5}\text{Cs}_{0.5}\text{Pb}_{1-x}\text{Sn}_x\text{Br}_3$) via the LARP approach.⁵⁶¹



3
 4 **Figure 51.** (a) XRD pattern of CsSnX_3 ($X = \text{Cl}, \text{Cl}_{0.5}\text{Br}_{0.5}, \text{Br}, \text{Br}_{0.5}\text{I}_{0.5}, \text{I}$) perovskite NCs
 5 synthesized by hot-injection method. (b) TEM images and (c) UV-Vis-NIR absorbance and PL
 6 spectra of CsSnX_3 NCs of different halide compositions. (d) Schematic illustration of the synthesis
 7 of Cs_2SnI_6 perovskite NCs by hot-injection approach (left panel) and photograph of the prepared
 8 colloidal solutions of Cs_2SnI_6 NCs under UV light (right panel). (e) Corresponding TEM images
 9 of the Cs_2SnI_6 NCs of different morphologies.

10 Although significant progress has been made toward the improvement of the phase stability
 11 of Sn-based perovskite NCs, it is still far from reaching the stability and optical quality of Pb-
 12 based perovskite NCs. On the other hand, groups have taken advantage of the improved stability
 13 of Sn (IV) over Sn (II) to synthesize stable and optically emissive Cs_2SnI_6 NCs.^{551, 562-563} These
 14 NCs can be prepared by conventional hot-injection using oleylamine and oleic acid as ligands.⁵⁵¹
 15 The shape of the Cs_2SnI_6 NCs are easily controllable from spherical dots to nanorods and
 16 nanowires, and nanobelts to nanoplatelets. In addition, these NCs can also be synthesized via hot-
 17 injection without the use of capping ligands, as demonstrated by Weiss and co-workers. In this

1 ligand-free approach, the size of the Cs_2SnI_6 NCs (from 12 ± 3 nm to 38 ± 4 nm) and thus their
2 bandgap is tunable by controlling the reaction temperature. Since these NCs are ligand-free, it is
3 easy to process them into high-quality thick NC films by simple drop casting, and these films could
4 be promising for optoelectronic applications.⁵⁶²

5 On the other hand, unlike Sn-perovskite NCs, only a few attempts have been made to
6 synthesize Ge-perovskite NCs.^{329, 564-565} In general, the synthesis of Ge-perovskite NCs needs to
7 be carried out under an inert atmosphere due to the ready oxidation of Ge(II) to Ge(IV). The
8 instability of Ge(II) is a critical limitation with this class of materials. It has been demonstrated
9 that monodisperse CsGeI_3 NCs can be prepared by hot-injection under an inert atmosphere.⁵⁶⁴
10 However the NCs are highly sensitive to electron beam irradiation and they initially transform into
11 CsI single crystals and eventually fragment into randomly oriented small debris. Besides, CsGeX_3
12 ($\text{X}=\text{Cl}$, Br and I) nanorods with tunable optical properties were prepared by solvothermal
13 synthesis, and the solar cells made of CsGeI_3 NCs exhibit PCE of 4.92%.³²⁹ Despite these few
14 studies, the shape-controlled synthesis and application of CsGeX_3 NCs are largely unexplored.
15 Further efforts are needed in this direction, because these NCs might be promising for solar cells
16 due to their low bandgap as compared to Sn- and Pb-based perovskites. Ge-based perovskites have
17 also been synthesized as quantum rods (QRs).³²⁹ The optical band edge of CsGeX_3 quantum rods
18 contains sharp absorption peak where the corresponding absorption onset shows a 90 nm red shift
19 from 565 to 655 nm while going from CsGeCl_3 to CsGeI_3 . The PL peak of these QRs tuned from
20 607 to 696 nm with a full width at half-maximum (FWHM) of about 25 nm.³²⁹

21 Beyond Ge-based perovskites, Eu^{2+} and Yb^{2+} have also been used in the B-site.⁵⁶⁶⁻⁵⁶⁷ CsEuCl_3
22 NCs exhibit strong excitonic absorption at around 350 nm, with a Stokes-shifted PL at 435 nm.
23 The PL peak has a narrow FWHM of 19 nm. Interestingly, in order to overcome the $\text{Eu}^{2+} \rightarrow \text{Eu}^{3+}$

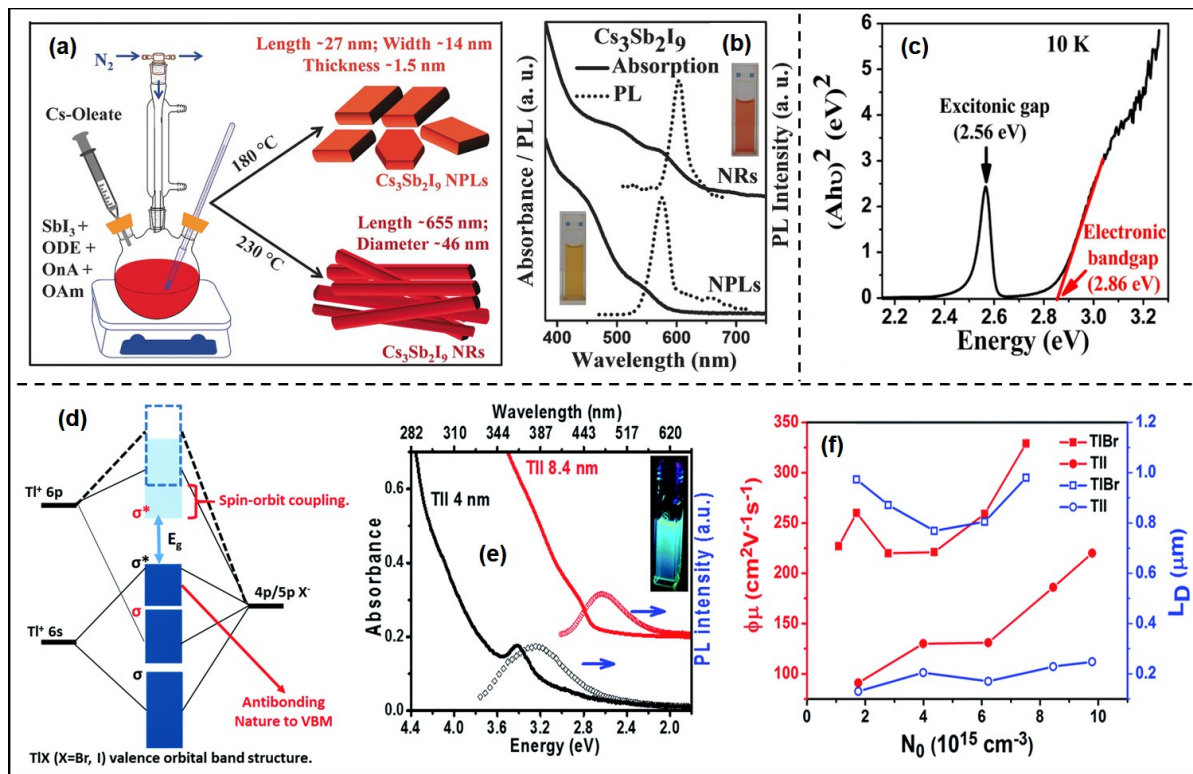
1 oxidation, EuCl_3 precursor was used and reduced to Eu^{2+} by oleylamine prior to the injection of
2 Cs-oleate.⁵⁶⁶ Moon *et al.* demonstrated the synthesis of monodisperse CsPbI_3 NCs by hot injection,
3 with a size of 10 ± 1 nm. These NCs have a low exciton binding energy of 33 meV, suggesting that
4 excitons are readily dissociated at room temperature. The PL peak is Stokes shifted by only 7 nm
5 to the absorption edge, and the PLQY is a high value of 58%. These materials achieved a high
6 photoresponsivity reaching $2.4 \times 10^3 \text{ A W}^{-1}$ in photodetectors.⁵⁶⁷

7 **Bi, Sb and Tl-based Perovskite-Derivative NCs.** Next we discuss materials with trivalent B-
8 site cations, namely, Bi(III) and Sb(III). The fact that both Bi(III) and Sb(III) have valence s^2
9 electrons, similar to Pb(II), encouraged researchers to explore Bi- and Sb-halide perovskite-
10 derivative NCs.^{530, 568-574} But bismuth and antimony are stable in the +3 oxidation state, whereas
11 lead forms a stable +2 oxidation state. So, two B(III) (B = Sb or Bi) cations replace three Pb(II)
12 ions in $\text{A}_3\text{Pb}_3\text{X}_9$ (or APbX_3), forming compounds with the general formula $\text{A}_3\text{B}_2\text{X}_9$ (Figure 50a).
13 Consequently, the 3D perovskite structure of APbX_3 is lost, resulting in compounds with a 2D
14 (*e.g.*, $\text{Rb}_3\text{Sb}_2\text{I}_9$) or 0D structure (*e.g.*, $\text{Cs}_3\text{Bi}_2\text{I}_9$).^{97, 575} The incorporation of smaller cations such as
15 Rb as the A-site cation in place of the Cs, the layered phase is favorable over the dimer phase, and
16 thus this favours the growth of 2D $\text{Rb}_3\text{Sb}_2\text{I}_9$ structures. For instance, Sargent and co-workers
17 reported the synthesis of $\text{Rb}_3\text{Sb}_2\text{I}_9$ nanoplatelets and single crystals. Interestingly, they found that
18 the nanoplatelets exhibit narrow emission (FWHM = 21 nm) with PL peak centred 512 nm, while
19 the single crystals exhibit broad emission (FWHM) = 75 nm) at 635 nm.⁵⁷⁵ There are multiple
20 reports of the synthesis of colloidal $\text{Cs}_2\text{Sb}_3\text{I}_3$ and $\text{Cs}_2\text{Sb}_3\text{Br}_3$ NCs.^{572, 576-577} Schematics in Figure
21 52a shows a typical hot-injection synthesis method for forming nanoplatelets and nanorods of
22 $\text{Cs}_3\text{Sb}_2\text{I}_9$ under different reaction conditions.⁵⁷² Figure 52b shows the corresponding UV-visible
23 absorption and photoluminescence (PL) spectra. Colloidal dispersion, band-edge emission and

1 quantum confinement effects are observed in Cs₃Sb₂I₉ NCs. Figure 52c shows the UV-visible
2 absorption spectra (Tauc plot) of Cs₃Sb₂I₉ NCs at 10 K.⁵⁷³ Owing to its 0D structure, Cs₃Bi₂I₉
3 shows a high exciton binding energy of ~300 meV, clearly separating the excitonic absorption
4 peak from the band edge. Reduction of structural dimensionality from 3D to 2D to 0D typically
5 decreases carrier mobility and increases bandgap. Therefore, Sb- and Bi-halide perovskite-
6 derivatives show inferior photovoltaic properties compared to Pb-halide perovskites. Instead one
7 can think of other applications such as light emitting diodes (LEDs) and surface enhanced Raman
8 spectroscopy using Cs₃Sb₂X₉ and Cs₃Bi₂X₉ NCs.⁵⁷⁷⁻⁵⁷⁹ However, further increases in PLQY by
9 optimizing the defect chemistry is required. Interestingly, Leng et al.⁵⁸⁰ reported that Cl-
10 passivation boost the blue photoluminescence of MA₃Bi₂Br₉ NCs upto a PLQY of 54.1%, which
11 is high compared to other lead-free perovskite or perovskite-derivative NCs. Similarly, high
12 PLQYs of 62% and 22% were reported for Cs₃Bi₂Cl₉ and Cs₃Bi₂Br₉, respectively, using the
13 mixture of octylammonium bromide and oleic acid as ligands.⁵⁸¹ These high PLQYs were
14 attributed to the effective passivation of surface traps through strong ligand binding. These
15 perovskite derivative NCs are therefore promising for further exploration.

16 We would like to mention here about another interesting class material, namely TIX (X = Br,
17 I). TIX does not have a perovskite crystal structure. However, (i) Tl(I) is isoelectronic with Pb(II)
18 with 6s² valence electrons, and (ii) the electronic structure of TIX is similar to that of CsPbX₃. The
19 electronic structure of TIX is similar to the Pb-halide perovskites, in which the valence band is
20 composed of cation 6s-halide 5 p orbitals, and the conduction band composed of cation 6s and
21 halide 5p orbitals (Figure 52d). This motivated Mir et al to synthesize colloidal TIX NCs.⁵⁸² Figure
22 52e compares optical absorption and emission of TII NCs with two different sizes. TIBr and TII
23 NCs emit UV-blue light with ~10% PLQY, which is reasonable compared to chloride-based

1 perovskites emitting in the UV-blue range. Notable carrier mobilities and carrier diffusion lengths
 2 (L_D) of TIBr (28.7 nm) and TII (8.4 nm) NCs estimated by terahertz spectroscopy are shown in
 3 Figure 52f. Suh high values of intrinsic carrier mobility, diffusion length, and PLQY suggest that
 4 TIX NCs can be a good optoelectronic material in the UV-blue region. On the other hand, it has to
 5 be noted that the Tl based compounds are highly toxic.⁵⁸³



6
 7 **Figure 52.** (a) Schematic showing colloidal synthesis of Cs₃Sb₂I₉ nanoplatelets (NPLs) and
 8 nanorods (NRs). ODE, OnA and OAm are abbreviated forms of 1-octadecene, octanoic acid and
 9 oleyl amine, respectively. (b) Optical absorption and emission spectra of colloidal Cs₃Sb₂I₉ NPLs
 10 and NRs. Photographs shown in inset are of colloidal Cs₃Sb₂I₉ NPLs (yellow) and NRs (red) under
 11 visible light. (c) Tauc plot of Cs₃Bi₂I₉ NCs obtained from optical absorption data measured at 10
 12 K. (d) Schematic illustration of the valence orbital band structure of TIX (X = Br and I). Dark blue
 13 color corresponds to bonding and antibonding orbitals formed by hybridization of p and s atomic

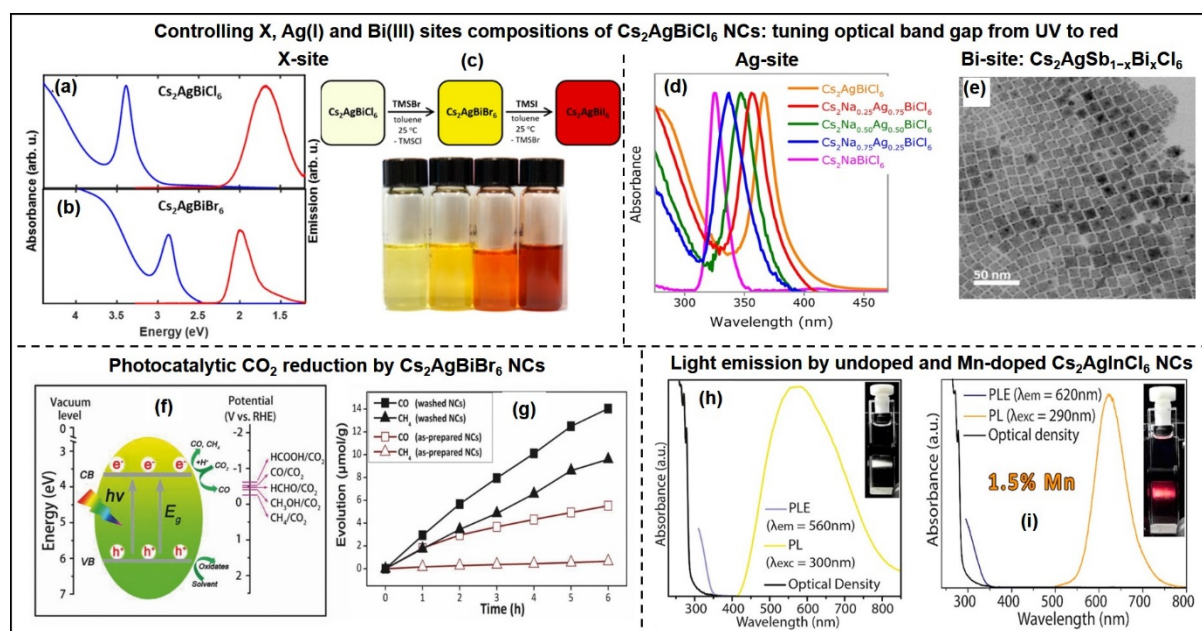
1 orbitals of Tl^+ and X^- . (e) Optical absorption and emission spectra of TII NCs. Photograph in the
2 inset shows colloidal dispersion of 8.4 nm TII NCs under 365 nm UV light. (f) The comparison of
3 effective carrier mobility ($\phi\mu$, red) and carrier diffusion length (L_D , blue) of films of TIBr (28.7
4 nm) and TII (8.4 nm) NCs, obtained by using terahertz spectroscopy. N_0 is carrier density obtained
5 at a given excitation fluence. Panels a and b adapted with permission from Ref. Copyright 2017
6 John Wiley and Sons. Panel c adapted with permission from Ref. Copyright 2018 American
7 Chemical Society. Panels d-f adapted with permission from Ref. Copyright 2017 Royal Society
8 of Chemistry.

9 **Cu-Based NCs.** Cu belongs to the group 11 and it is mostly existing in +2 or +1 oxidation
10 states, and this can be a potential alternative for Pb. In general, Cu-based metal halides mostly
11 crystallize in A_2CuX_4 or $A_3Cu_2X_5$ structures.^{46, 584-587} As a remark, there are no Cu- X_6 octahedra
12 in these structures. The interesting feature of these Cu-based NCs is that they exhibit relatively
13 high PLQYs. For instance, Cs_2CuX_4 NCs can be easily prepared at room temperature by LARP,
14 and the Cs_2CuCl_4 NCs obtained emit at 388 nm with 51.8% PLQY.⁵⁸⁴ In another study, Booker
15 et al.⁵⁸⁵ reported broad band green emission from Cs_2CuCl_4 NCs prepared by hot-injection, and
16 this is attributed to Cu-defect emission. The morphology of these NCs is tunable from dots to
17 platelets and rods by varying the ratio of coordinating solvents. Besides, the 0D $Cs_3Cu_2I_5$ NCs
18 synthesized by hot-injection exhibit intense emission at 445 nm with an absolute PLQY of ~87%,
19 and this makes them promising for deep-blue LEDs.⁴⁶ These colloidal $Cs_3Cu_2X_5$ ($X = I, Br/I, Br,$
20 $Br/Cl, Cl$) NCs can also be synthesized at room temperature through antisolvent precipitation and
21 the prepared $Cs_3Cu_2Cl_5$ NCs emit green PL with near-unity PLQY.⁵⁸⁶ In this case, the origin of
22 green PL is attributed to self-trapped exciton (STE) emission. However, further studies are needed
23 to understand the origin of green emission and high PLQY. Nevertheless, the higher thermal

1 stability due to its inorganic nature, eco-friendliness and high PLQY of these Cu-based NCs makes
2 them promising for lighting and display applications.

3 **Colloidal Double Perovskite NCs.** Another promising lead-free perovskite system is the
4 halide double perovskites (or elpasolites). These materials have the general formula
5 $A_2B(I)B'(III)X_6$ (see Figure 50). Charge neutrality is maintained by replacing two Pb(II) ions from
6 $A_2Pb_2X_6$ (ABX_3) with one B(I) and one B'(III) ions, forming compounds like $Cs_2AgBiCl_6$ and
7 $Cs_2AgInCl_6$. Colloidal syntheses of different double perovskite NCs have been reported.<sup>185, 544, 588-
8 598</sup> Figure 53a shows the UV-visible absorption and PL spectra of colloidal $Cs_2AgBiCl_6$ and
9 $Cs_2AgBiBr_6$ NCs. The PL is significantly red-shifted from the band-edge absorptions and
10 suggested to originate from defect and/or self-trapped excitons (STE).⁵⁹⁹⁻⁶⁰⁰ Composition driven
11 tuning of the bandgap of double perovskite NCs has been attempted by many groups. For example,
12 forming lower bandgap materials like Cs_2AgBiI_6 is highly desired for photovoltaics.
13 Unfortunately, Cs_2AgBiI_6 in the bulk form could not be prepared owing to their positive heat of
14 formation.⁶⁰¹ Interestingly, NCs of Cs_2AgBiI_6 can be prepared.^{185, 602} Therefore, NC synthesis
15 provides an addition handle to prepare compositions and phases of double perovskites, for which
16 the corresponding bulk counterparts do not exist. Creutz et al employed an anion exchange reaction
17 converting $Cs_2AgBiBr_6$ NCs to Cs_2AgBiI_6 NCs (Figure 53b).¹⁸⁵ In general, the anion exchange
18 reaction allowed them to control the X-site composition, and thereby tune the bandgap and color
19 of Cs_2AgBiX_6 NCs over a wide range, from 1.75 eV (Cs_2AgBiI_6) to 3.39 eV ($Cs_2AgBiCl_6$) (Figure
20 53c).¹⁸⁵ However, long term stability of red colored Cs_2AgBiI_6 NCs needs to be improved. In
21 another report, Lamba et al controlled the composition of B(I) site of $Cs_2(Na_xAg_{1-x})BiCl_6$ NCs to

- 1 tune the optical bandgap in the UV region (Figure 53d).⁵⁹² Likewise, the composition at the B'(III)
- 2 site also can be controlled forming $\text{Cs}_2\text{AgSb}_{1-x}\text{Bi}_x\text{Cl}_6$ NCs (Figure 53e).⁵⁹¹



- 3 **Figure 53.** UV-Vis absorption spectra (blue) measured at room temperature and PL spectra (red)
- 4 measured at 20 K for (a) Cs₂AgBiCl₆ NCs (NCs) and (b) Cs₂AgBiBr₆ NCs. (c) Scheme showing
- 5 halide exchange reactions using trimethylsilyl halide (TMSBr or TMSI) and photographs (left to
- 6 right) show colloidal dispersions of Cs₂AgBiBr₆, Cs₂AgBiBr_{5.2}I_{0.8}, Cs₂AgBiBr_{1.6}I_{4.4}, and
- 7 Cs₂AgBiI₆ NCs under visible white light. (d) UV-Vis absorption spectra of Na alloyed Cs₂AgBiCl₆
- 8 NCs showing shift towards higher energy with increasing Na. (e) Transmission electron
- 9 microscopy (TEM) image of Cs₂AgSb_{0.30}Bi_{0.70}Cl₆ NCs. (f) Schematic showing mechanism of
- 10 photocatalytic CO₂ reduction on the surface of Cs₂AgBiBr₆ NCs. (g) Plot of CO and CH₄ evolution
- 11 with respect to time upon photocatalytic CO₂ reduction using as-prepared (red) and washed (black)
- 12 Cs₂AgBiBr₆ NCs. UV-Visible absorption, PL and PL excitation (PLE) spectra of (h) undoped and
- 13 (i) Mn-doped Cs₂AgInCl₆ NCs. Photographs shown in inset of panels (h) and (i) correspond to
- 14 respective PL with 300 nm, Xe lamp excitation. Panels a-c adapted with permission from ref 28.
- 15 Copyright 2018 American Chemical Society. Panel d adapted with permission from ref 32.

1 Copyright 2019 American Chemical Society. Panel e adapted with permission from ref 31.
2 Copyright 2019 AIP Publishing. Panels f and g adapted with permission from ref 38. Copyright
3 2018 John Wiley and Sons. Panels h and i adapted with permission from ref 34. Copyright 2018
4 American Chemical Society.

5 Typical double perovskite NCs have a cube shape (Figure 53e), which is similar to that of
6 typical CsPbX_3 NCs. Most likely, appropriate surface chemistry will be required to prepare double
7 perovskite NCs of different shapes. Fine tuning of reaction conditions are often required to avoid
8 impurity phases like CsX , AgX and $\text{Cs}_3\text{Bi}_2\text{X}_9$.¹⁹⁸ Furthermore, NCs of double perovskites
9 containing Ag(I), *e.g.*, $\text{Cs}_2\text{AgSbCl}_6$ and $\text{Cs}_2\text{AgInCl}_6$, have a tendency to form small Ag NCs the
10 NCs.⁵⁸⁸

11 Double perovskite NCs of $\text{Cs}_2\text{AgBiX}_6$ ($X = \text{Cl}, \text{Br}$) and $\text{Cs}_2\text{AgInCl}_6$ are reasonably stable for
12 potential applications. Unfortunately, these NCs have wide bandgaps, hence they absorb only high
13 energy (>2.5 eV) photons, and are therefore not suitable for single junction solar cells. Zhou et al.
14 used $\text{Cs}_2\text{AgBiBr}_6$ NCs for the photocatalytic CO_2 reduction (see Figure 53f,g),⁵⁹⁷ demonstrating
15 photochemical conversion of CO_2 to solar fuels CO and CH_4 . In perspective, different double
16 perovskite NCs should be tested for such photocatalytic applications. Another potential application
17 of double perovskite NCs could be solid state lighting. Luo et al reported warm white light
18 emission with $\sim 86\%$ PLQY from bulk sample of Bi-doped $\text{Cs}_2(\text{Ag}_{0.6}\text{Na}_{0.4})\text{InCl}_6$,⁵²⁴ a result that
19 was recently confirmed by Li et al., who have fabricated white light emitting diodes based on Bi-
20 doped $\text{Cs}_2\text{Ag}_{0.7}\text{Na}_{0.3}\text{InCl}_6$ powders featuring a PLQY of 87.2% .⁶⁰³ The devices had a high stability
21 and high color rendering index.

22 Different reports on colloidal $\text{Cs}_2\text{AgInCl}_6$ and Bi-doped $\text{Cs}_2\text{AgInCl}_6$ NCs show similar broad
23 emission with white or yellow color.^{594, 599, 604} For example, Figure 53h shows white light emission

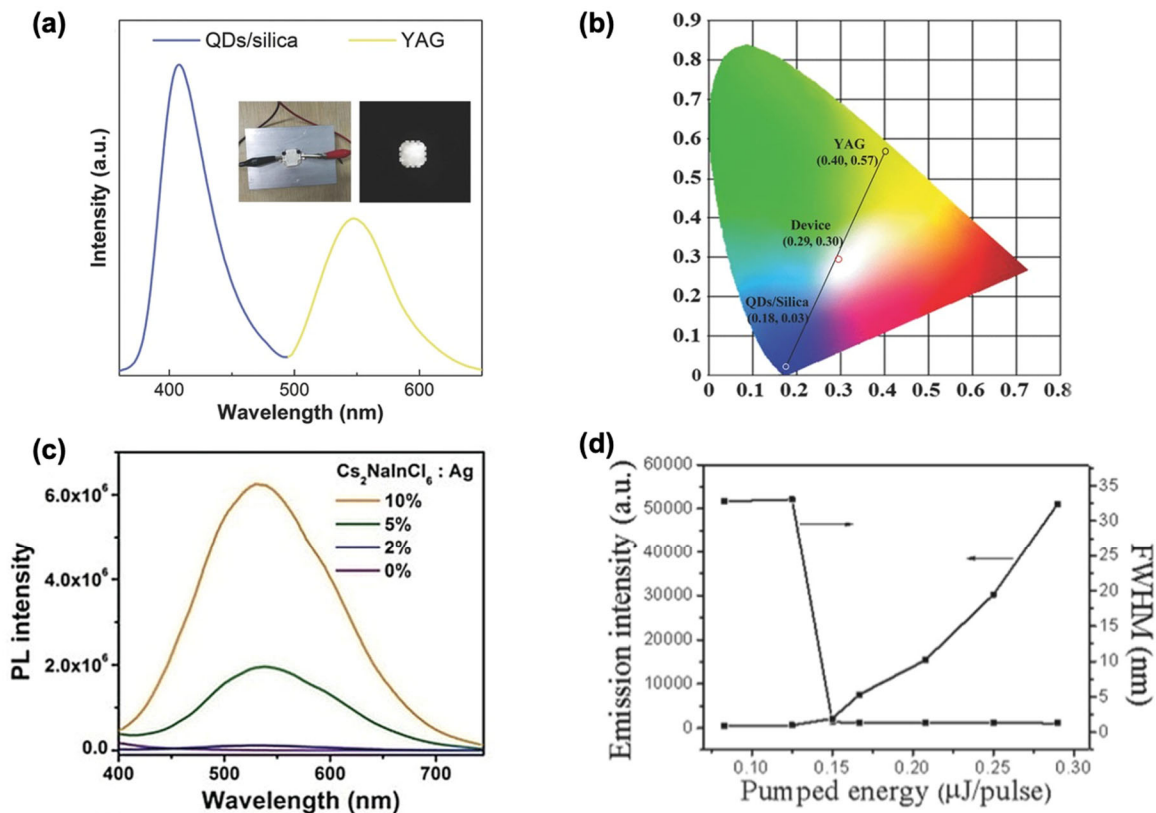
1 with a broad emission spectrum significantly red-shifted from the absorption and PL excitation
2 (PLE) data.⁵⁹⁴ Therefore, the PL from such double perovskite NCs will not suffer from the vexing
3 problems of self-absorption and Förster resonance energy transfer (FRET).⁶⁰⁵ The broad emission
4 has been assigned to STE,^{524, 604} but how it depends on different compositions is not yet well
5 understood. Yang et al.⁶⁰⁶ showed that the indirect bandgap can be tuned to a direct bandgap in
6 $\text{Cs}_2\text{AgIn}_x\text{Bi}_{1-x}\text{Cl}_6$ double perovskite NCs by increasing the In content. The direct bandgap double
7 perovskite NCs exhibit higher absorption cross section and the PLQY as compared to indirect
8 bandgap ($\text{Cs}_2\text{AgBiCl}_6$) NCs.

9 Another approach to impart visible and near infrared light emission is to dope luminescent
10 metal ions like Mn^{2+} and lanthanides like Yb^{3+} and Er^{3+} .⁶⁰⁷⁻⁶⁰⁸ Figure 53i shows the red colored
11 light emission from Mn-doped $\text{Cs}_2\text{AgInCl}_6$ NCs. Larger lanthanide ions require coordination
12 number ≥ 6 to incorporate into the lattice. Typical semiconductors like Si, GaAs, and CdSe have
13 coordination number = 4 for the metal ion, and are therefore not suitable for doping lanthanides.
14 Interestingly, both ABX_3 perovskites and $\text{AB}(\text{I})\text{B}'(\text{III})\text{X}_6$ double perovskites with B-site
15 coordination number = 6, can incorporate lanthanide ions.⁶⁰⁹ Yb^{3+} and Er^{3+} doped $\text{Cs}_2\text{AgInCl}_6$ NCs
16 with near infrared emission at ~ 990 nm due to quantum cutting and 1540 nm (low-loss optical
17 communication range) have been reported.^{593, 596} Yb has also been reported to directly substitute
18 Pb to form CsYbI_3 NCs with an emission wavelength 671 nm, and could be synthesized by hot-
19 injection.⁵⁶⁷

20 **5.2 LIGHT-EMISSION APPLICATIONS OF LEAD-FREE PEROVSKITE** 21 **NANOCRYSTALS**

22 For light-emission, lead-free perovskite-inspired materials have mostly been used in
23 applications involving optical excitation rather than charge injection. Namely, these applications

1 are phosphors for white-light emitters and gain media for optically-pumped lasers. For phosphors,
2 one approach has been to use a UV GaN LED to excite blue-emitting quantum dots and a yellow-
3 emitting phosphor to achieve white-light LEDs. Tang *et al.* used Cs₃Bi₂Br₉ colloidal quantum dots
4 as the blue-emitter (410 nm PL wavelength), and Y₃Al₅O₂ (YAG) as the yellow-emitter (broad PL
5 centered at 551 nm wavelength). The white-light LED had CIE coordinates of (0.29,0.30) and a
6 color temperature of 8477 K.⁵⁷⁸ (Figure 54a & b) Cs₃Bi₂Br₉ was advantageous because it forms a
7 passivating BiOBr layer in the presence of moisture. This increases the PLQY, but also improves
8 the stability of the quantum dots in the presence of moisture and acid. As a result, the Cs₃Bi₂Br₉
9 quantum dots could be mixed with tetraethyl orthosilicate (TEOS), which was hydrolyzed with
10 water and HBr to form silica. The resulting composite of quantum dots embedded in silica had
11 improved stability, with the 72% of the PL being retained after 16 of exposure to a UV lamp, and
12 75% of the PL being retained after 16 h heat stressing at 60 °C. ⁵⁷⁸Tang *et al.* also demonstrated
13 white-light LEDs using Cs₂SnCl₆ perovskites as the blue-emitter and Ba₂Sr₂SiO₄:Eu²⁺ and
14 GaAlSiN₃:Eu²⁺ as the yellow phosphors. Under excitation from a UV GaN LED, the white-light
15 LED had CIE coordinates of (0.36,0.37) and color temperature of 4486 K. The Cs₂SnCl₆:Bi
16 exhibited blue emission at 455 nm, with a PLQY of 78.9%, which was higher than Cs₃Bi₂Br₉ (10-
17 19% PLQY)^{578, 610}. The vacancy-ordered perovskite was also stable against moisture, due to the
18 formation of a protective BiOCl layer and due to the tin cation already being in the more stable +4
19 oxidation state.⁶¹⁰ Li *et al.* obtained lead-free blue-emitters with similarly high PLQYs of 32.8%
20 using Eu²⁺-doped CsBr NCs. By combining these NCs with YAG:Ce³⁺ with a UV-emitting GaN
21 LED, white emission with CIE coordinates of (0.32, 0.34) and color temperature of ~6300 K was
22 obtained.⁶¹¹



1
2 **Figure 54.** Applications of NCs of lead-free perovskite-inspired materials in light-emission
3 applications. (a) Electroluminescence spectra and (b) CIE coordinates of the $\text{Cs}_3\text{Bi}_2\text{Br}_9$ blue
4 phosphor and yellow YAG phosphor excited with a UV-emitting GaN LED, as well as the CIE
5 coordinates of the overall white-light LED. (c) PL spectra of $\text{Cs}_2\text{NaInCl}_6$ alloyed with Ag. (d)
6 Emission intensity and full-width at half maximum (FWHM) of CsSnI_3 quantum dots doped in a
7 cholesteric liquid crystal as a function of the pump energy. (a) and (b) reprinted with permission
8 from Ref. ⁵⁷⁸. Copyright 2017 John Wiley and Sons. (c) reprinted with permission from Ref. ⁶⁰⁴.
9 Copyright 2020 John Wiley and Sons. (d) reprinted with permission from Ref. ⁶¹². Copyright 2018
10 American Chemical Society.

11 Recently, it was demonstrated that white-light emission can be achieved using a phosphor
12 comprised solely of a double perovskite. Tang *et al.* demonstrated that powders of
13 $\text{Cs}_2(\text{Ag}_{0.6}\text{Na}_{0.4})\text{InCl}_6$ doped with 0.04% Bi luminesces broadly across 400 – 800 nm wavelength

1 (centered at 570 nm) with $86\pm 5\%$ PLQY, and 1000 h stability.⁵²⁴ The broad emission arises due
2 to the formation of a self-trapped exciton as a result of strong electron-phonon coupling and Jahn-
3 Teller distortion in the AgCl_6 octahedron. By pressing $\text{Cs}_2(\text{Ag}_{0.6}\text{Na}_{0.4})\text{InCl}_6$ powder onto a GaN
4 LED and encapsulating with silica, white-light emission was obtained through the blue emission
5 from the LED mixing with the broad emission from the double perovskite phosphor. The white-
6 light LED had CIE coordinates of (0.396, 0.448) and a color temperature of 4054 K, and stability
7 over 1000 h in air.⁵²⁴ Han *et al.* also produced a series of works showing broadband emission from
8 $\text{Cs}_2\text{AgIn}_x\text{Bi}_{1-x}\text{Cl}_6$, Ag-doped $\text{Cs}_2\text{NaInCl}_6$ and Mn-doped $\text{Cs}_2\text{NaIn}_{0.75}\text{Bi}_{0.25}\text{Cl}_6$ NCs.^{604, 606, 613}
9 $\text{Cs}_2\text{AgBiCl}_6$ has an indirect bandgap, with low PLQY. Alloying In into this system resulted in a
10 direct, but parity forbidden bandgap. With increasing In content, the PLQY was found to increase
11 up to 36.6% (with 90% In), along with an increase in broad emission centered at 570 nm
12 wavelength. This was attributed to the emission from the parity forbidden bandgap, which prevents
13 absorption but allows radiative recombination.⁶⁰⁶ $\text{Cs}_2\text{NaInCl}_6$ has a wide bandgap of 4.55 eV, but
14 almost no PL. Alloying with Ag resulted in an increased PLQY from a broad band sub-bandgap
15 emission, reaching up to 31.1% with 10% Ag. These results were attributed to a dark self-trapped
16 exciton being present in $\text{Cs}_2\text{NaInCl}_6$ that became bright with Ag alloying by breaking the parity-
17 forbidden transition in $\text{Cs}_2\text{NaInCl}_6$.⁶⁰⁴ (Figure 54c) The self-trapped exciton in $\text{Cs}_2\text{NaIn}_x\text{Bi}_{1-x}\text{Cl}_6$ is
18 also believed to be dark, with only blue PL due to free excitons. Broad band yellow emission was
19 obtained by doping with Mn^{2+} , which resulted in a PLQY of 44.6% being obtained. This broad
20 band transition was attributed to the dark self-trapped exciton transferring to the $^4\text{T}_1$ excited state
21 of Mn^{2+} and relaxing to give PL.⁶¹³ Recently, Lee et al have reported characteristic absorption
22 features in the Na/Bi³⁺ system. $\text{Cs}_2\text{NaBiCl}_6$ NCs and $\text{Cs}_2\text{NaBiBr}_6$ NCs showed sharp and discrete
23 single peaks assigned to the s-p transition ($6s^2 \rightarrow 6s^1 p^1$) from the $[\text{BiX}_6]^{3-}$ units within the crystal

1 lattice of elpasolite structures. Such discrete optical transition characteristics have not been
2 observed for Ag/M^{3+} DP or for $\text{Cs}_3\text{Bi}_2\text{X}_9$ materials.^{598, 614} A series of studies on Bi-doped $\text{Cs}_2\text{Na}_{1-x}\text{Ag}_x\text{InCl}_6$
3 and $\text{Cs}_2\text{Na}_{1-x}\text{Ag}_x\text{BiCl}_6$ NCs were recently reported in which the extent of Ag/Na
4 alloying was found to regulate the PLQY of the NCs.^{595, 615} Light emission in these materials was
5 identified to arise from recombination from carriers trapped in localized states. A combined
6 experimental and computation study showed that the extent of localization the holes (which were
7 found to be localized at AgCl_6 octahedra), was strongly dependent on the amount of Na^+ ions, that
8 is, on the average number of NaCl_6 octahedra surrounding each individual AgCl_6 octahedron. In
9 essence, the higher this number, the more likely is for the holes to stay localized, and the higher is
10 the PLQY. Also, the same authors found that, regardless of the type of ligands used in the synthesis
11 and of any post-synthesis ligand exchange that was attempted, the PLQY for these materials could
12 not be increased beyond 37%, against the 86% reported for the bulk.⁶¹⁶ Their conclusion, based
13 also on a series of experiments and calculations, was that unpassivated surface traps are most likely
14 responsible for the lower PLQY, and therefore these materials are much less surface tolerant than
15 the corresponding Pb-based halide perovskites.

16 Beyond the use of lead-free perovskite-inspired materials for phosphors, tin- and germanium-
17 based perovskites have been demonstrated as potential gain materials for optically-pumped lasing.
18 Sum *et al.* demonstrated amplified spontaneous emission (ASE) across the visible to near-infrared
19 (700 to 950 nm wavelength) from $\text{CsSnBr}_x\text{I}_{3-x}$ thin films.⁵⁵⁰ By reducing the trap density in the
20 thin films through the addition of SnF_2 during synthesis, the lasing threshold in CsSnI_3 was reduced
21 to a low value of $6 \mu\text{J cm}^{-2}$ (whereas lasing was not obtained in the films without SnF_2), and a
22 quality factor exceeding 500.⁵⁵⁰ Lee *et al.* synthesized CsSnI_3 quantum dots 3 – 5 nm in size, which
23 were doped into a cholesteric liquid crystal (CLC). The CsSnI_3 quantum dots acted as the gain

1 medium, and the CLC as the optical resonator. The lasing threshold was $\sim 0.8 \text{ mJ cm}^{-2} \text{ pulse}^{-1}$, but
2 the quality factor was ~ 2000 . The device was also air-stable, with the lasing emission intensity
3 decreasing only by 13% after 6 months of storage in air compared to the initial intensity.⁶¹² Hints
4 of amplified spontaneous emission was also found in $\text{CH}_3\text{NH}_3\text{Sn}_{0.5}\text{Ge}_{0.5}\text{I}_3$ by Nagane *et al.*⁶¹⁷, in
5 which the PL FWHM reduced from 75 nm to 40 nm when the excitation density was increased
6 from 10^{15} cm^{-3} to 10^{16} cm^{-3} . This 50% mixture of Sn and Ge was also found to give the lowest
7 Urbach energy (of 47 meV) across the Sn-Ge composition series.⁶¹⁷ Recently, Moon *et al.*⁵⁶⁷
8 reported the first synthesis of high quality cesium ytterbium triiodide (CsYbI_3) cubic perovskite
9 NCs with a PLQY of 58%. It was found that the CsYbI_3 NCs exhibit a high photoresponsivity (2.4
10 $\times 10^3 \text{ A W}^{-1}$) with an external quantum efficiency (EQE) of $5.8 \times 10^5\%$.

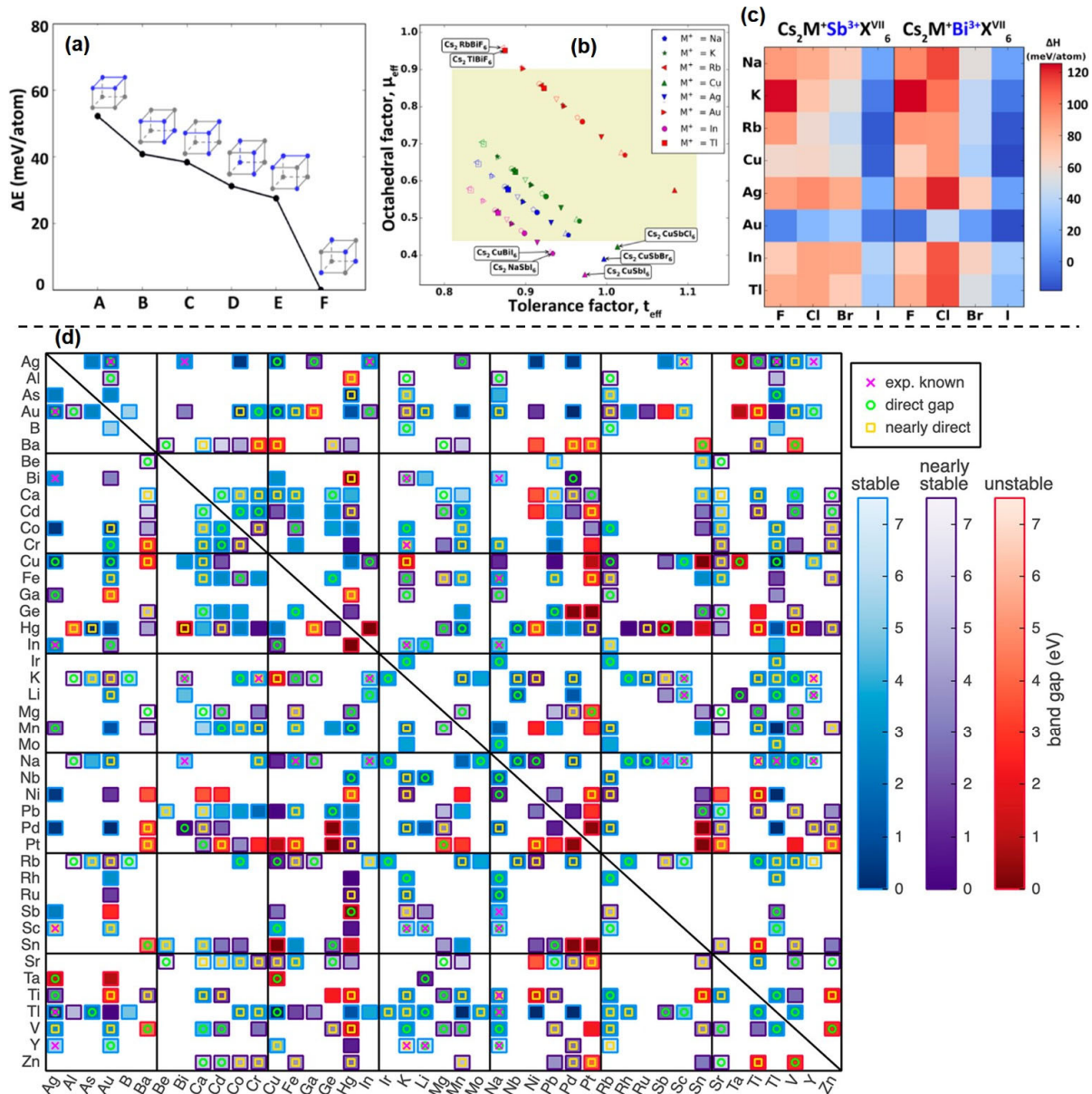
11

12 **5.3 DESIGNING NEW DOUBLE PEROVSKITE COMPOSITIONS**

13 The exploration of Pb-free materials is driven by theoretical predictions.⁶¹⁸⁻⁶²⁰ Based on the
14 above discussion, it appears that, (i) the optoelectronic properties of Pb-free perovskites are still
15 inferior compared to Pb-halide perovskites, and (ii) only a few double perovskite compositions
16 have been explored so far, while there are hundreds of possible compositions for metal halide
17 double perovskite that have yet to be explored.⁶²¹ The most important criteria when screening
18 materials based on computations are: (i) thermodynamic stability, (ii) bandgap (which should be
19 $< 2.5 \text{ eV}$, and (iii) effective masses of charge carriers (which should be < 1 electron mass).
20 Additional screening criteria include trap energy, along with the low toxicity and earth abundance
21 of the elements.

22 The stability of double perovskites strongly depends on the structural parameters.
23 $\text{A}_2\text{B}(\text{I})\text{B}'(\text{III})\text{X}_6$ has two kinds of octahedral motifs like $[\text{B}(\text{I})\text{X}_6]^{5-}$ and $[\text{B}(\text{III})\text{X}_6]^{3-}$. For example,

1 in $\text{Cs}_2\text{AgBiCl}_6$, the motifs are $[\text{AgX}_6]^{5-}$ and $[\text{BiX}_6]^{3-}$, and are represented by blue and gray dots
2 respectively in Figure 55a. In a crystal, the octahedral motifs can be arranged in six different ways
3 (A to F) as shown in Figure 55a. For $\text{Cs}_2\text{AgBiCl}_6$, it is found that the F-arrangement, i.e., with
4 $[\text{AgX}_6]^{5-}$ and $[\text{BiX}_6]^{3-}$ motifs being arranged alternatively, gives the thermodynamic stable state.
5 This thermodynamic stability of F-arrangement is at the basis of double perovskite structure shown
6 in Figure 50.



1 **Figure 55.** (a) Total energies for different arrangements $[AgX_6]^{5-}$ and $[BiX_6]^{3-}$ octahedral motifs
 2 calculated in a $2 \times 2 \times 2$ supercell of $Cs_2AgBiCl_6$. The energy for most stable configuration (F) is
 3 set at zero. (b) Evaluation of structural stability of different $Cs_2B(I)BiX_6$ and $Cs_2B(I)SbX_6$ with
 4 varying compositions for B(I) (indicated by M^+ in the figure) and X, on the basis of effective
 5 tolerance factor (t_{eff}) and octahedral factor (μ_{eff}) variables. The compositions present outside the
 6 inner square are unstable. Red, green, blue and brown colors correspond to F, Cl, Br and I
 7 respectively. The open and filled symbols specify Sb and Bi containing perovskites respectively.

1 (c) Thermodynamic stability of the double perovskite compositions calculated using
2 decomposition enthalpy (ΔH). Higher positive values of ΔH indicate more stable compositions.
3 (d) A map showing calculated thermodynamic stability, bandgap, and experimental existence for
4 a large number $\text{Cs}_2\text{BB}'\text{Cl}_6$ double perovskite compositions with different combinations of B and
5 B', shown along the axes. The map is mirrored across diagonal line because B and B' are treated
6 equivalently. Details of calculation and classification such as stable, nearly stable and unstable are
7 given in Ref.⁶²¹ Panels a-c adapted with permission from ref 54. Copyright 2017 American
8 Chemical Society. Panel d adapted with permission from ref 52. Copyright 2020 American
9 Chemical Society.

10

11 For ABX_3 perovskites, the structural stability can be described by the Goldschmidt tolerance
12 factor [$t = (r_A + r_X) / \sqrt{2(r_B + r_X)}$] and octahedral factor ($m = r_B / r_X$). These are defined using
13 the idealized solid-sphere model, where r_A , r_B and r_X are the ionic radii of A, B and X respectively.
14 It has been found empirically that for the formation of ABX_3 halide perovskites requires $0.81 < t$
15 < 1.11 and $0.44 < \mu < 0.90$.⁶²² For $\text{A}_2\text{B(I)B'(III)X}_6$ double perovskite, there are two B-site cations,
16 and therefore, $t_{eff} = (r_A + r_X) / \sqrt{2\{(r_B + r_{B'})/2 + r_X\}}$ and $m_{eff} = (r_B + r_{B'}) / 2r_X$. The shaded
17 region in Figure 55b empirically suggests the requirement of t_{eff} and m_{eff} to form stable double
18 perovskite of $\text{Cs}_2\text{B(I)BiX}_6$ and $\text{Cs}_2\text{B(I)SbX}_6$ with varying compositions for B(I) (indicated by M^+
19 in the figure) and X. Such crystallographic parameters provide the initial assessment regarding
20 the formability of a double perovskite composition. Furthermore, one can calculate the
21 decomposition enthalpy (ΔH) for double perovskites using DFT (Figure 55c). In the present
22 calculation,⁶²³ positive values of ΔH indicate thermodynamic stability. Particularly, samples with
23 $\Delta H > 20$ meV/atom are expected to be stable. Figure 55c shows that the iodide compositions show

1 poor thermodynamic stability, which also corroborates the fact that many iodide compositions
2 have χ that are too small and inhibit the formation of octahedral motifs. This instability of iodide
3 double perovskites has also been observed experimentally is most likely the main reason for the
4 absence of experimentally observed narrow (~ 2 eV) bandgap double perovskites. Fluoride based
5 double perovskites are also stable, but often not the preferred material for optoelectronics, since
6 the high electronegativity of fluoride is expected to yield wide bandgap insulating materials.
7 High stability and the possibility of reasonably narrow bandgap led Bartel *et al.* to screen 311
8 compositions of $\text{Cs}_2\text{B}(\text{I})\text{B}'(\text{III})\text{Cl}_6$.⁶²¹ The mapping of these compounds, showing their
9 thermodynamic stability, nature of the bandgap, and their whether they exist experimentally is
10 displayed in Figure 55d. They could identify about 47 nontoxic double perovskite compositions
11 with direct or nearly direct (within 100 meV) computed bandgaps between 1 and 3 eV. However,
12 many of these newer compositions need experimental verification.

13 **5.4 SUMMARY AND FUTURE OUTLOOK ON Pb-FREE MHP NCs**

14 Various colloidal Pb-free metal halide perovskite NCs like $\text{Cs}_3\text{B}_2\text{X}_9$ (B = Sb and Bi), CsBX_3 (B =
15 Sn and Ge), and Cs_4SnX_6 have prepared in recent years. CsSnX_3 and CsGeX_3 NCs are unstable.
16 By contrast $\text{Cs}_3\text{Sb}_2\text{X}_9$, $\text{Cs}_3\text{Bi}_2\text{X}_9$ and Cs_4SnX_6 NCs have improved stability, but charge transport
17 is restricted due to reduced structural dimensionality (2D or 0D) in these materials. Nevertheless,
18 these materials may find applications as stable blue phosphors, which can be used in combination
19 with yellow phosphors for white-light emission. Interestingly, non-perovskite TlX possesses
20 similar electronic structure to CsPbX_3 and have demonstrated promising optoelectronic properties
21 in the UV-blue region. But Tl compounds are highly toxic.

22 Despite reasonable progress in the synthesis of double perovskite NCs, a better understanding
23 of the origin of PL is required to tune the intensity, peak energy and shape of the broad PL, by fine

1 tuning the composition. Compositional fine tuning is also expected to suppress the effect of
2 reduction of Ag(I) to Ag(0) on the PL. Furthermore, doping with lanthanides (Yb^{3+} , Er^{3+} etc) can
3 provide intense near infrared emission, required for optical communication, infrared LEDs and
4 remote sensing. Exploring light emission properties of metal halide double perovskites and their
5 derivatives for real life application is an important future direction. However, an important
6 limitation of the double perovskites is their wide and/or indirect bandgap. Therefore, novel double
7 perovskite compositions need to be synthesized both in the bulk and nanocrystalline form. Recent
8 work also suggests that the bandgap could be reduced in alloys between compounds that form a
9 Type II alignment.²⁵⁰ We hope that, in near future, researchers will develop stable metal halide
10 double perovskite compositions with < 2 eV bandgap, along with good charge transport properties.
11 While looking for novel Pb-free perovskite semiconductors, compositions of chalcogenide
12 perovskites,⁶²⁴ mixed halide-chalcogenide perovskites⁶²⁵ and oxide perovskites⁶²⁶ provide
13 additional options.⁶²⁷

14 Finally, very little is reported on the use of perovskite derivative NCs in electrically-driven
15 applications, such as LEDs, although recent work on thin films motivates this effort. Of the handful
16 of examples of lead-free NC LEDs, recent reports of $\text{Cs}_3\text{Cu}_2\text{I}_5$ are some of the more promising.
17 1.12% EQE was achieved, with deep blue emission. The devices exhibited reasonable stability
18 with a half-life of more than 100 hours.⁴⁶ In addition, Shan *et al.* demonstrated LEDs from
19 $\text{Cs}_3\text{Sb}_2\text{Br}_9$ quantum dots, with electroluminescence at 408 nm (violet color) and an EQE of 0.2%.
20 $\text{Cs}_3\text{Sb}_2\text{Br}_9$ is a particularly suitable material for demonstration in LEDs given that they have a
21 PLQY of 51.2%, which is larger than other $\text{A}_3\text{B}_2\text{X}_9$ quantum dots. $\text{Cs}_3\text{Sb}_2\text{Br}_9$ is also stable against
22 heat, UV illumination, air and the presence of moisture, and the LEDs retained 90% of the initial
23 electroluminescence intensity after 6 h of operation at 7 V (~ 70 mA cm^{-2} current density).⁵⁶⁶ This

1 is an improvement over many Pb-based perovskite quantum dots (see Section 3). In thin films,
2 Rand *et al.* found that near-infrared LEDs with Pb-Sn perovskites had a two orders of magnitude
3 improvement in radiance when the films were grown with the addition of a bulky
4 organoammonium halide ligand to passivate the surface and reduce the grain size to better confine
5 carriers.⁶²⁸ NCs with carefully chosen ligands could therefore be worth investigation. Furthermore,
6 Rogach and co-workers recently demonstrated electroluminescence from self-trapped excitons in
7 thin films of a Ruddlesden-Popper $(C_{18}H_{35}NH_3)_2SnBr_4$ perovskite. This perovskite was
8 synthesized by hot-injection to form microplates, and self-trapping occurred in the $[SnBr_6]^{4-}$,
9 which are electronically isolated from neighboring Sn-Br layers by the long oleylamine cations.
10 Electroluminescence from the self-trapped exciton (centered at 625 nm wavelength) was obtained,
11 with 350 cd m^{-2} and 0.1% EQE achieved. The turn-on voltage was low, at 2.2 V, and it was
12 believed that electrons and holes were directly injected into the self-trapped states.⁶²⁸⁻⁶²⁹ This
13 motivates future efforts to i) understand the nature and behavior of the self-trapped exciton in the
14 quantum confined regime (i.e. in very small size NCs); ii) explore how to narrow the PL linewidth
15 (i.e. by varying the composition); iii) improve charge injection into the NCs and iv) to further
16 investigate other optical properties, such as anti-Stokes shifted PL.⁶³⁰⁻⁶³¹ Finally, the ambitious
17 goal would be to achieve white-light electroluminescence from self-trapped excitons in double
18 perovskites.

19

20 **6. DOPING (A and B-sites) OF MHP NCs**

21 Doping in metal halide perovskite NCs has been extensively studied to improve their optical
22 and electronic properties and structural stability by modifying the electronic structure or
23 introducing new pathways of energy and charge transfer. Both A- and B-site doping with various

1 mono-, di- and trivalent metal ions have been explored for this purpose. In general, A and B-site
2 doping can be achieved either by cation exchange or through in situ synthesis.^{108, 602, 632-633} Doping
3 through cation exchange is briefly introduced in section 2 (composition tuning by ion exchange).
4 In this section, we provide an extensive discussion regarding the recent progress made in A and
5 B-site doping methods and characterization of the new properties resulting from doping in metal
6 halide perovskite NCs. In particular, special attention is paid to the Mn²⁺- and lanthanide-doped
7 perovskite NCs, which have been widely studied over the years due to their interesting properties
8 and potential applications.

1 **6.1 B-SITE DOPING**

2 □□□□□□□□□□□□□□□□

3 Doping in metal halide perovskite NCs has been extensively studied to improve their optical
4 and electronic properties and structural stability by modifying the electronic structure or
5 introducing new pathways of energy and charge transfer. Both A- and B-site doping with various
6 mono-, di- and trivalent metal ions have been explored for this purpose. In general, A and B-site
7 doping can be achieved either by cation exchange or through in situ synthesis.^{108, 602, 632-633} Doping
8 through cation exchange is briefly introduced in section 2 (composition tuning by ion exchange).
9 In this section, we provide an extensive discussion regarding the recent progress made in A and
10 B-site doping methods and characterization of the new properties resulting from doping in metal
11 halide perovskite NCs. In particular, special attention is paid to the Mn²⁺- and lanthanide-doped
12 perovskite NCs, which have been widely studied over the years due to their interesting properties
13 and potential applications.

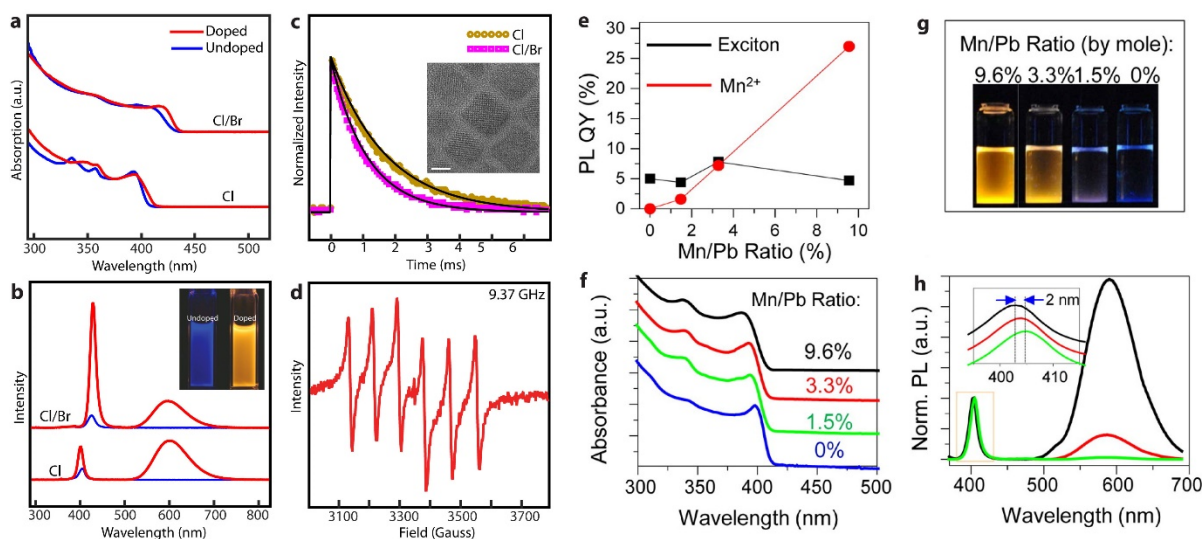
14 **6.1 Mn-DOPING OF PEROVSKITE NANOCRYSTALS**

15 Doping of semiconductor NCs with Mn²⁺ has been a topic of intensive research for many
16 decades, since it can introduce various new optical, electronic, and magnetic properties through
17 the interaction of exciton with dopants.⁶³⁴ For this reason, efforts in developing the Mn doping
18 methods in halide perovskite NCs have been a very active field in recent years. Currently, doping
19 of Mn in halide perovskite NCs has been demonstrated mostly in cesium lead halide NCs (CsPbX₃,
20 X=Cl, Br, I).

21 **Mn doping in CsPbCl₃ NCs:** The first successful Mn doping of metal halide perovskite NCs was
22 performed in CsPbCl₃ NCs of nanocube morphology, which was reported by two different groups
23 in 2016 (Son group and Klimov group).⁶³⁵⁻⁶³⁶ Mn doping in CsPbCl₃ NCs was achieved by adding

1 MnCl₂, an additional reactant as the source of Mn, under the typical hot injection synthesis
2 condition of CsPbCl₃ NCs. This resulted in doping of Mn at the level of < 1% to 10%, which
3 showed distinct Mn luminescence centered around 600 nm resulting from the sensitization of the
4 Mn ligand field transition. In this synthesis, MnCl₂ was the most effective precursor of Mn ions,
5 whereas many other organometallic precursors such as Mn(ac)₂, Mn(acac)₂, and Mn(oleate)₂ were
6 not effective as dopant precursors. However, extending the same approach to doping of Mn in
7 CsPbBr₃ NCs using MnBr₂ as the precursor of Mn was not successful, in contrast to the case of
8 MnCl₂ and CsPbCl₃ pair. On the other hand, when MnCl₂ and CsPbBr₃⁶³⁷ were used as the Mn
9 precursor and host NCs respectively, the resulting NCs were Cl/Br mixed-halide NCs doped with
10 Mn, indicating that the formation of Mn-Cl bond is preferred over that of the Mn-Br bond when
11 attempting doping using Mn halide as the precursor for Mn. Figure 56a-b shows the absorption
12 spectra of the undoped and Mn-doped CsPbCl₃ and CsPb(Cl/Br)₃ NCs synthesized using MnCl₂
13 as the Mn precursor at a doping concentration of <1% with corresponding photoluminescence
14 spectra. In these NCs, the characteristic Mn luminescence appearing near 600 nm indicates doping
15 of Mn²⁺ ions into perovskite NC hosts, which results from the energy transfer from the host to d-
16 d transition of Mn²⁺ ions. At low doping concentrations, the Mn luminescence exhibits nearly
17 single exponential decay, as expected from the relatively homogenous ligand field environment
18 and weak inter-dopant coupling. EPR data of Mn-doped CsPbCl₃ with <1 % doping also showed
19 the characteristic fine structure of Mn²⁺ expected from cubic lattice symmetry, confirming the
20 successful doping of Mn in the NC host.

1



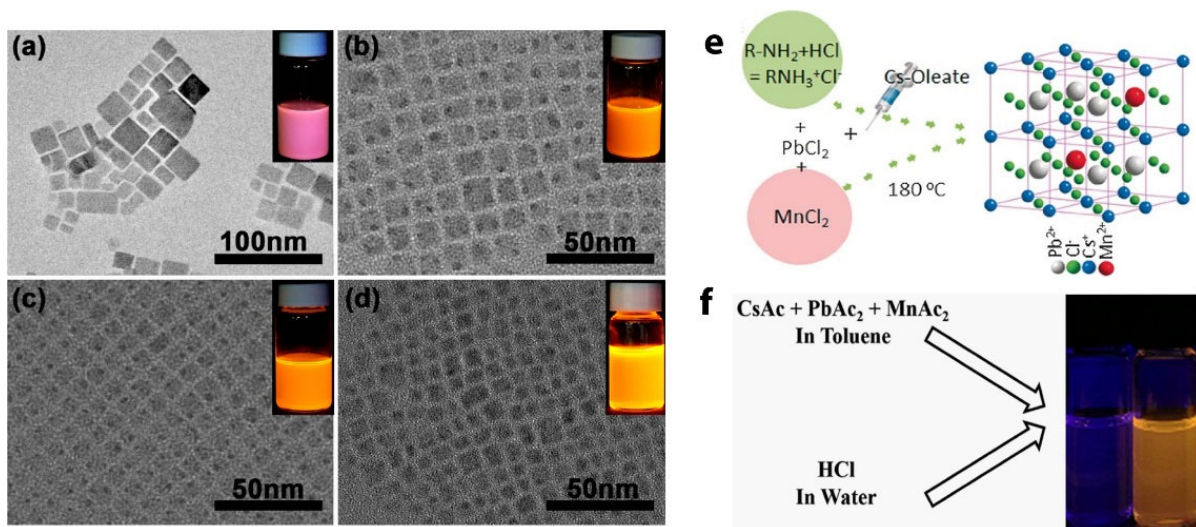
2 **Figure 56.** Synthesis and properties of Mn-doped CsPbCl₃ NCs. (a) Absorption and (b) PL spectra
 3 of Mn-doped CsPbCl₃ and CsPbCl_xBr_{3-x} NCs with those of undoped control samples. (c) Time-
 4 dependent PL decay of Mn phosphorescence. (d) EPR signal from Mn-doped CsPbCl₃ NCs.
 5 Images in (a-d) were taken with permission from Ref.⁶³⁵. (e) The dependence of exciton and Mn
 6 PLQY on dopant concentration. (f, h) Normalized absorption and (f) PL spectra (h) of Mn-doped
 7 CsPbCl₃ NCs of varying dopant concentration. Increased Mn-content is associated with a gradual
 8 blue-shift of both the band-edge peak in absorption and the intrinsic NC PL peak [expanded in the
 9 inset of panel d]; this can be attributed to the effects of alloying on the NC band structure. The
 10 Mn-emission peak grows in intensity with increasing Mn-content but does not shift. (g)
 11 Photograph of hexane solutions of Mn-doped CsPbCl₃ NCs of varying Mn-content illuminated by
 12 a UV lamp (365 nm). Solutions were diluted to exhibit the same optical density at 365 nm. Images
 13 in (e-h) were taken with permission from Ref.⁶³⁶.

14 In later studies on Mn doping in CsPbCl₃ NCs, additional efforts were made to increase the
 15 doping concentration. In principle, heavily-doped NCs should be called alloys rather than doped-
 16 NCs, because doping in NCs generally refers only to a few dopants per NCs.⁶³⁸ However, most

1 often heavily doped NCs also called doped- NCs.⁶³⁷ Herein, we have excluded the difference
2 between alloys and doped NCs for readers to avoid confusion. Exploration of these heavily doped
3 or alloy NCs were partially motivated by the desire to replace Pb with less toxic elements, and this
4 is important for practical applications of perovskite NCs. For example, Yang and coworkers
5 reported the Mn substitution ratio is up to 46% and a luminescence quantum yield of 56% in
6 CsPbCl₃, which was achieved by using the higher Mn:Pb ratio in the reactant mixture (Figure 57a-
7 d).⁶³⁷ Pradhan and coworkers reported another method of increasing the Mn doping concentration,
8 where the use of oleylammonium chloride as an additional reactant increased the efficiency of
9 doping (Figure 57e).⁶³⁹ In addition to the hot injection doping, room-temperature Mn doping
10 methods was also reported. Meijerink and coworkers reported Mn doping at room-temperature
11 using non-halide Mn precursors (Figure 57f).⁶⁴⁰ In their first report, they used metal acetate salts
12 as the precursor, which were converted to metal oleate complexes in the presence of ligands, and
13 then added HCl to protonate the carboxylate group, increasing the amount of monomer initiating
14 the formation of nanocubes. HCl also created a Cl-rich surface, supplying ample binding sites for
15 Mn²⁺ ions and facilitating Mn doping. Further coating of Mn-doped CsPbCl₃ with an additional
16 CsPbCl₃ shell improved the Mn luminescence quantum yield. Recently, Paul et al.⁶³³ reported that
17 the size distribution of CsPbCl₃ NCs significantly improves with slight doping of Mn²⁺ ions during
18 their synthesis by ultrasonication approach (Fig. 58a-b). This results in a prominent excitonic
19 resonance for Mn-doped CsPbCl₃ NCs as compared to pure CsPbCl₃ NCs. (the reader is directed
20 to the optical properties section for more details). Interestingly, it was observed that Mn doping
21 leads to the formation of Ruddlesden– Popper (R.P.) defects within the host NCs, in which
22 (Pb/Mn)-Cl atomic columns were shifted by half a unit cell at the border of the defect planes (Fig.
23 58c-e), thus inducing quantum confinement within the host NCs. This results in a gradual blue

1 shift of excitonic absorption and PL peaks. The authors attributed that the formation of such R.P.
 2 defects may be triggered by the size difference between Mn^{2+} (1.6 Å) and Pb^{2+} (2.38 Å) ions.

3

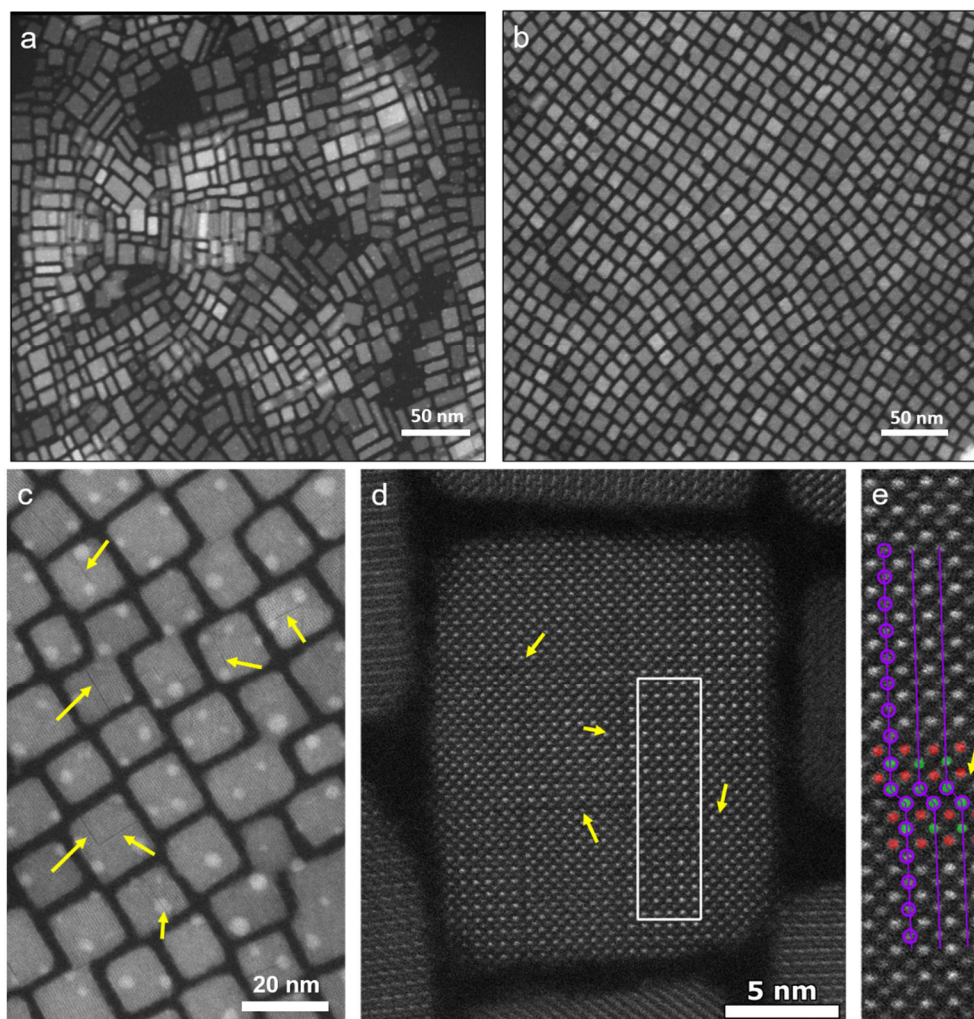


4

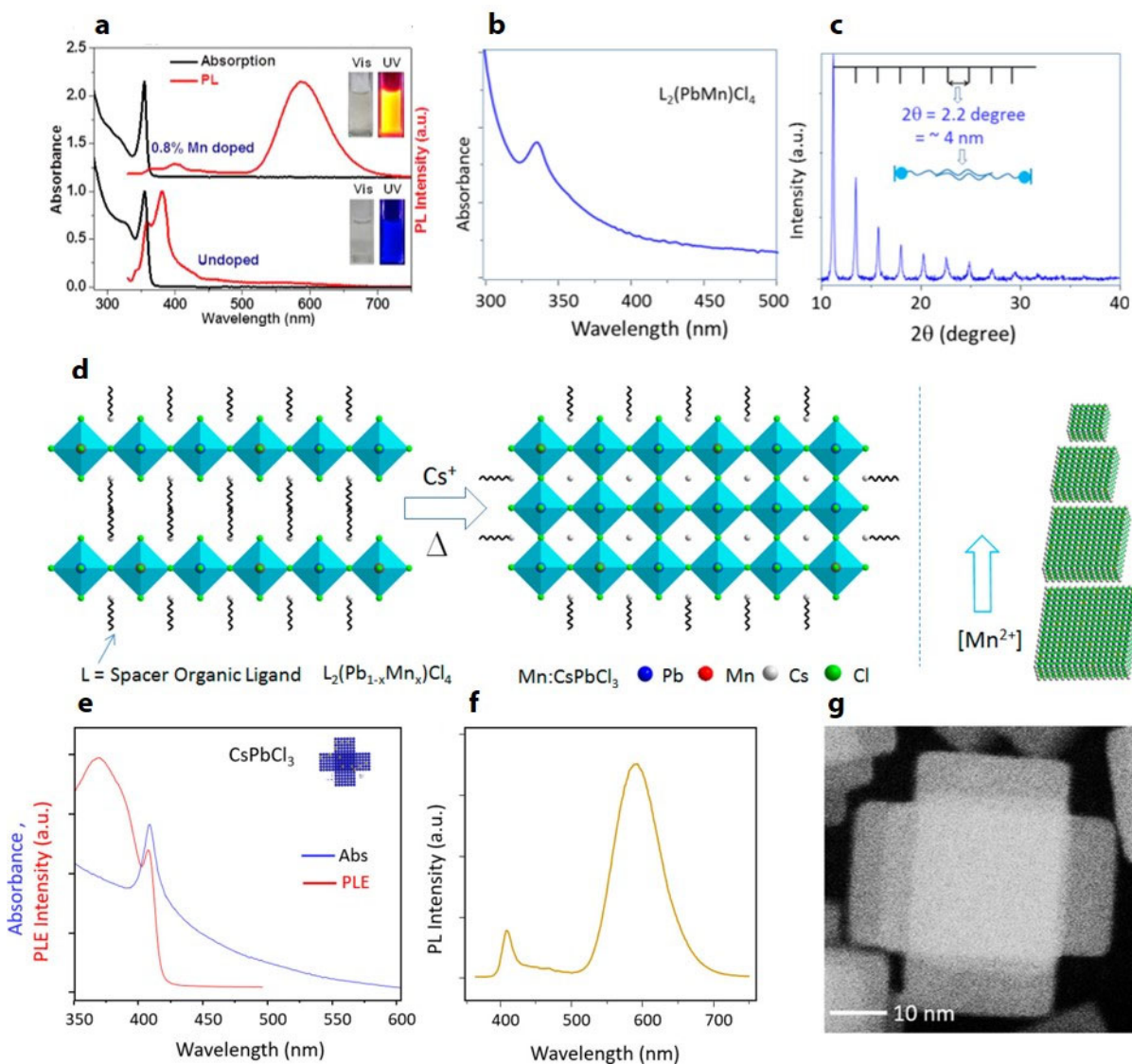
5 **Figure 57.** Heavy Mn doping in CsPbCl_3 NCs. (a-d) TEM images of the $\text{CsPb}_x\text{Mn}_{1-x}\text{Cl}_3$ NCs that
 6 are prepared with Pb-to-Mn molar feed ratios of 1:1.25 (a), 1:2.5 (b), 1:5 (c), and 1:10 (d) at 170
 7 °C. $x=0.02, 0.04, 0.10, 0.27$ respectively. Insets: Corresponding PL images excited by 365 nm UV
 8 light. Images in (a-d) were taken with permission from Ref.⁶³⁷. (e-f) Two additional methods of
 9 increasing Mn doping level in CsPbCl_3 NCs. Image in (e) was taken with permission from Ref.⁶³⁹.
 10 Image in (f) was taken with permission from Ref.⁶⁴⁰.

11 Although earlier studies focused on Mn doping in cube-shaped CsPbCl_3 NCs with very weak
 12 quantum confinement, more recent studies reported the synthesis of CsPbCl_3 NCs of different
 13 morphologies, such as nanoplatelets with strong confinement and branched structures. Nag and
 14 coworkers synthesized Mn-doped CsPbCl_3 nanoplatelets with the thickness of 2.2 nm, which
 15 imposes strong confinement along the thickness direction (Figure 59a).⁶⁴¹ Doping was achieved
 16 by modifying CsPbCl_3 nanoplatelets synthesis reported by Akkerman and coworkers,⁶⁴² where
 17 MnCl_2 was added additionally as the source of Mn. Pradhan and coworkers reported another

1 method of doping Mn in CsPbCl₃ nanoplatelets, which involves the initial synthesis of a Mn-doped
2 monolayer structure and subsequent formation of nanoplatelets by the addition of cesium oleate.⁶⁴³
3 They synthesized 5 nm-thick nanoplatelets with different lateral sizes (20–580 nm) that varied
4 with the concentration of Cs and Mn during the reaction (Figure 59b-d). Because quantum
5 confinement of the exciton in Mn-doped semiconductor NCs can enhance the exciton–dopant
6 interaction, which determines various magneto-optical properties, continued progress in the
7 synthesis of strongly confined Mn-doped perovskite NCs will be important for expanding their
8 applicability. In another study, Mn-doped CsPbCl₃ branched hexapods were synthesized using a
9 seeded growth approach.⁶⁴⁴ Cores were first formed under halide deficient condition. In the second
10 step, the reaction was enriched with halides to facilitate the arm growths. In the presence of Mn
11 precursor in the second step, the final product consisted of Mn-doped branched CsPbCl₃ NCs
12 (Figure 59e-g).⁶⁴⁴



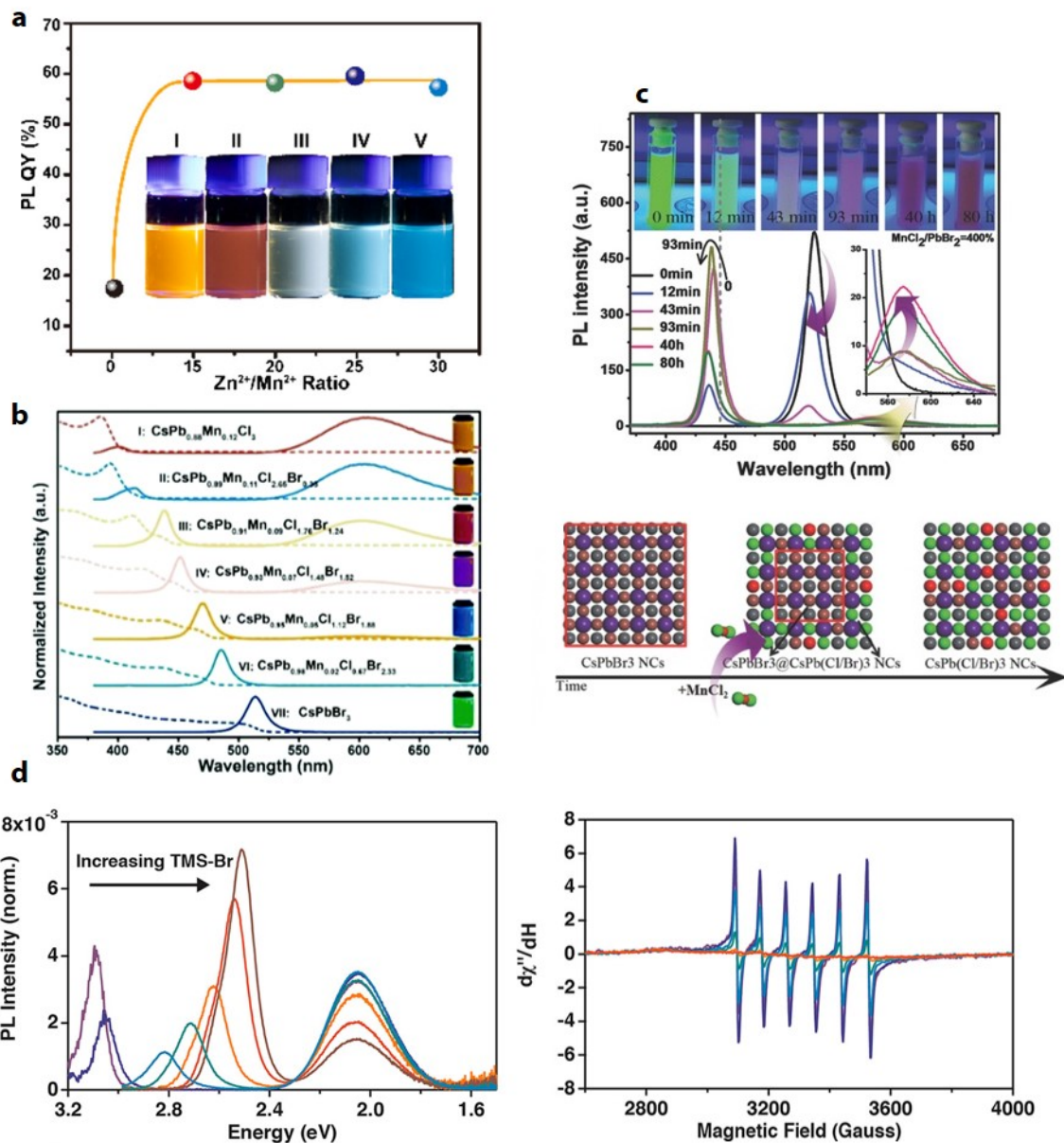
1
 2 **Figure 58.** Overview TEM images of (a) pure and (b,c) Mn^{2+} -doped CsPbCl_3 NCs (Mn to Pb feed
 3 ratio 3:1) As shown in (c), a large number of NCs have one or more line defects. f, g)
 4 Corresponding atomically resolved high-angle annular dark-field scanning transmission electron
 5 microscopy (HAADF-STEM) image showing R.P. defect planes (Pb/Mn-Cl=red, Cs=green). The
 6 lattices are shifted half of the unit cell at the grain boundaries. Figures 1, b, d, and e are reproduced
 7 with permission from Ref.⁶³³ Copyright 2020, Wiley-VCH.



1
2 **Figure 59.** Mn doping of anisotropic CsPbCl₃. (a) Absorption and PL spectra of undoped and 0.8
3 % Mn-doped CsPbCl₃ nanoplatelet. Image in (a) was taken with permission from Ref.⁶⁴¹ (b)
4 Absorption spectra of the layered perovskites. The peak at 334 nm is the typical characteristic of
5 the monolayered structures. (c) Powder X-ray diffraction pattern of the layered perovskites. The
6 interpeak spacing was 2.2° (2θ), which corresponds to ~4 nm. (d) Schematic presentation of
7 formation of doped perovskites from layered perovskites L₂(Pb_{1-x}Mn_x)Cl₄. L is *n*-butylammonium
8 and oleylammonium ions. The schematic shows Mn concentration in the reaction mixture to
9 control the size of Mn-doped platelets. With an increase in the amount of Mn in layered

1 perovskites, the surface area of the platelets decreases. Images in (b-d) were taken with permission
2 from Ref.⁶⁴³ (e) Absorption and PLE spectra of Mn-doped CsPbCl₃ hexapod nanostructures. PLE
3 was measured at Mn PL maxima. (f) PL spectra of Mn-doped CsPbCl₃ armed structures. Excitation
4 wavelength was 350 nm. (g) HRSTEM of Mn-doped CsPbCl₃ hexapod. Images in (e-g) were
5 taken with permission from Ref.⁶⁴⁴.

6 ***Mn doping in CsPbBr₃ NCs.*** Most of the work on Mn doping of CsPbX₃ NCs has focused on
7 CsPbCl₃ despite its less desirable optical properties than other halide systems (higher bandgap and
8 lower luminescence quantum yield). This is because doping of Mn is most favorable in CsPbCl₃
9 host and becomes increasingly more difficult for bromide and iodide perovskite NCs. Simply
10 extending the doping method used for producing Mn-doped CsPbCl₃ NCs described above did not
11 produce Mn-doped CsPbBr₃ NCs. It was hypothesized in the work by Klimov and coworkers that
12 direct hot injection synthesis of Mn-doped CsPbBr₃ using MnBr₂ was energetically unfavorable
13 owing to the large difference in bond energy between Pb–Br (249 kJ/mol) and Mn–Br (314 kJ/mol)
14 compared to that between Pb–Cl (301 kJ/mol) and Mn–Cl (338 kJ/mol).⁶³⁶ The authors argued
15 that the higher stability of the Mn–Br bond compared to the Pb–Br bond impeded the incorporation
16 of Mn²⁺ into the CsPbBr₃ lattice. Because of the difficulty of direct Mn doping in CsPbBr₃ NCs,
17 various post-synthesis doping methods were developed.



1
 2 **Figure 60.** Post-synthesis anion exchange of Mn-doped CsPbCl₃. (a) UV-visible optical
 3 absorption (dash line) and photoluminescence (PL) spectra (solid line) of
 4 Cs(Pb_xMn_{1-x})(Cl_yBr_{1-y})₃ NCs. Images were taken with permission from Ref.⁶⁴⁵ (b) PLQY and
 5 Mn²⁺ content of the initial and ion exchanged CsPb_{0.75}Cl₃:0.25Mn²⁺ NCs. The initial NCs have a
 6 low QY of 17.8%. After ion exchange, the QY of the samples sharply increases to 59.3% and
 7 maintains that level with the increasing ion exchange reaction time. The photographs of the pristine

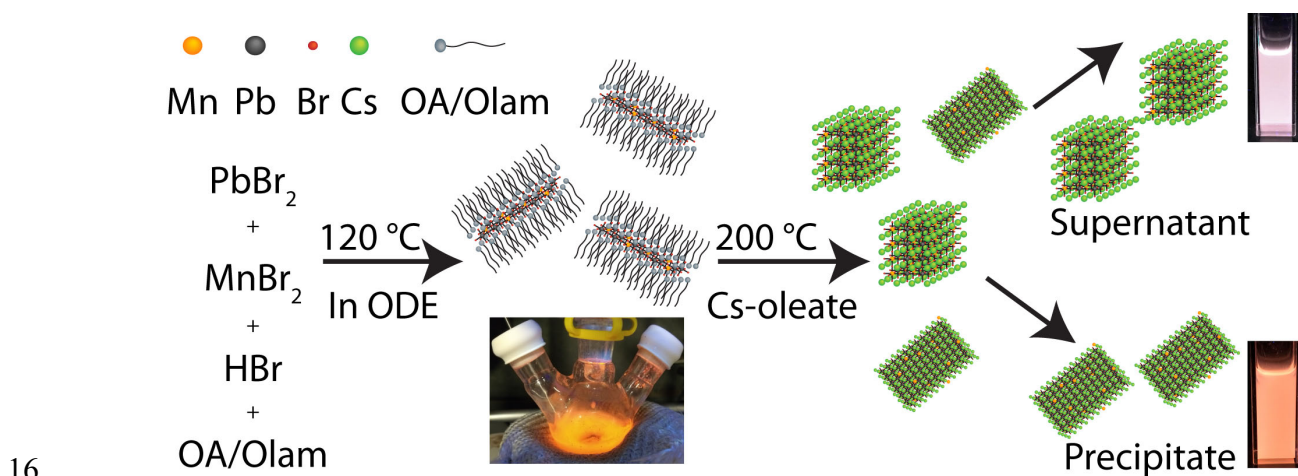
1 CsPb_{0.75}Cl₃:0.25Mn²⁺ NCs and ion exchanged NCs with different reaction times under 365 nm UV
2 lamp illumination. The color changes come from the decrease of the Mn²⁺ content. Images were
3 taken with permission from Ref.⁶⁴⁶ (c) Temporal evolution of PL spectra of CsPbBr₃ NCs after
4 adding the MnCl₂ precursor. The inset is the corresponding digital photograph at different times
5 under the irradiation of a 365 nm UV lamp. Sketch of the ion exchange process from pure
6 CsPbBr₃ NCs via adding MnCl₂ precursor. Images were taken with permission from Ref.⁶⁴⁷. (d)
7 PL spectra (left) and EPR spectra (right) of 1.1% Mn-doped CsPbCl₃ NCs in the EPR tube during
8 the course of an anion exchange reaction; note that Mn²⁺ PL is seen centered at ~610 nm at every
9 stage of the anion exchange reaction. The PL spectra are each normalized to their total integrated
10 PL intensity. A 365 nm diode was used for excitation. Each spectrum was taken at the same NC
11 concentration, and the NCs were never removed from the EPR tube over the entire experiment.
12 Images were taken with permission from Ref.⁶⁴⁸.

13 In an earlier attempt to dope Mn in CsPbBr₃ NCs by Zhang and coworkers, post-synthesis
14 halide exchange reaction was used, although it was only partially successful. For example, halide
15 exchange of Mn-doped CsPbCl₃ with Br⁻ using ZnBr₂ dissolved in the mixture of hexane and
16 oleylamine as the precursor resulted in not only the exchange of halide but also removal of doped
17 Mn²⁺ ions in the host NCs (Figure 60a).⁶⁴⁵ Cation exchange from Pb to Mn in CsPbBr₃ NCs using
18 MnCl₂ was also attempted (Figure 60b). However, this approach also suffered from the halide
19 exchange from Br⁻ to Cl⁻, forming Mn-doped CsPb(Cl/Br)₃ NCs with mostly Cl⁻ occupying the
20 anion sublattice.⁶⁴⁶ Cui and coworkers reported another post synthesis Mn doping method based
21 on halide exchange-driven cation exchange (Figure 60c).⁶⁴⁷ In this method, the addition of MnCl₂
22 solution dissolved in DMF to the colloidal solution of CsPbBr₃ NCs in toluene resulted in the
23 production of Mn-doped CsPb(Cl/Br)₃ NCs. Doping of Mn was facilitated by the halide exchange,

1 which was conjectured to be the result of simultaneous proceeding of opening up rigid halide
2 octahedron structure around Pb as well as the Pb-to-Mn cation exchange. However, the approach
3 has the same limitation of obtaining mixed halide phase after doping, since using MnBr_2 solution
4 did not result in Mn doping. Son and coworkers extended the halide exchange-driven cation
5 exchange approach as a method for Mn doping by combining photoinduced halide exchange.⁶⁴⁹ In
6 this method, halide was provided in situ via photoinduced reductive dissociation of the solvent
7 (CH_2Br_2) near the surface of the NCs, and a non-halide Mn salt was used as the Mn source. This
8 approach was able to dope Mn in small CsPbBr_3 NCs, however, intensity of the Mn-luminescence
9 was relatively low indicating the lower doping concentration.³³⁰

10 In Mn-doped $\text{CsPb}(\text{Cl}/\text{Br})_3$ NCs with mixed halide composition, the characteristic Mn
11 luminescence was still observed since the bandgap of the host NCs was still sufficiently high to
12 enable the sensitization of Mn transition. However, the Mn emission intensity decrease as the Br^-
13 content continued to increase in the mixed halide NCs. Initially, this was explained by a work from
14 Meijerink and coworker attributing the decrease in Mn emission to thermally assisted back energy
15 transfer from Mn to the host NCs, similar to Mn-doped CdSe.⁶⁵⁰ This point was argued by Gamelin
16 who showed the presence of the exciton emission at 4 K, whereas in Mn-doped CdSe the Mn
17 emission is only present due to the lack of any thermal back energy transfer. The mixed halide
18 perovskite showed a similar temperature dependent behavior to Mn-doped CsPbCl_3 which has too
19 great of an energy gap for thermally assisted back energy transfer.⁶⁵¹ Instead, Gamelin attributed
20 the change in PL properties from the clustering of Mn in the lattice as the anion is exchanged from
21 Cl to Br. They supported this by performing anion exchange from Mn-doped CsPbCl_3 to Mn-
22 doped $\text{CsPb}(\text{Cl}_{1-x}\text{Br}_x)_3$ with TMS-Br while showing the retention of Mn emission but the
23 disappearance of the EPR signal (Figure 60d).⁶⁴⁸

1 Another avenue towards post-synthesis doping of Mn was reported by Nag and coworkers,
 2 who used slightly different solvent conditions and were able to dope Mn in CsPbBr₃ NCs without
 3 concomitant halide exchange.⁶⁵² In this modified approach, Mn doping was achieved by using
 4 MnBr₂ dissolved in the mixture of toluene and acetone, where MnBr₂ and CsPbBr₃ can coexist
 5 due to moderately polar environment of the mixed solvent. It was conjectured that Mn doping
 6 under this condition takes advantage of dynamic nature of binding of a ligand to adsorb dopants
 7 on the surface of NCs and fast halide migration to incorporate dopants into the CsPbBr₃ NCs,
 8 although the detailed mechanism was not fully understood. Employing the same approach, they
 9 were able to synthesize Mn-doped CsPbBr₃ NCs with different morphologies, including nanocubes
 10 and nanoplatelets. In the case of nanoplatelets, sensitized Mn luminescence was observed due to
 11 the increased bandgap from the quantum confinement. Pradhan also employed a post synthetic
 12 method to dope CsPbBr₃ nanoplatelets by mixing them with MnBr₂ in a toluene solution. They
 13 also showed that the Mn luminescence was quenched upon dilution of the solution, which then
 14 regained Mn luminescence after solvent evaporation due to the changes in local halide
 15 concentration.⁶⁵³



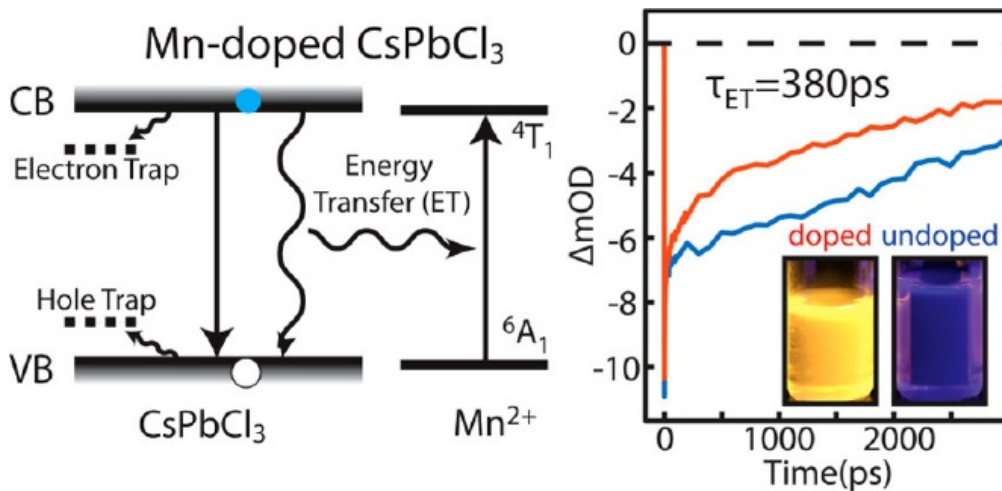
17 **Figure 61.** Mn doping in CsPbBr₃: Schematic representation of synthesis of Mn-Doped CsPbBr₃
 18 NCs. Image was taken with permission from Ref.⁶⁵⁴.

1 Although the earlier attempt to dope Mn in CsPbBr₃ NCs via one-pot hot injection synthesis
2 only resulted in a NC with enhanced stability but no visible Mn luminescence,⁶⁵⁵ Son and
3 coworkers developed a direct hot-injection method that produces Mn-doped CsPbBr₃ NCs via two-
4 step synthesis that exhibit Mn luminescence (Figure 61).⁶⁵⁴ In the first step of the synthesis, a Mn-
5 doped monolayer 2-dimensional (2D) structure is synthesized (L₂[Pb_xMn_{1-x}Br₄], where L is a
6 ligand) as an intermediate species. The presence of the intermediate 2D structure doped with Mn
7 was confirmed by small-angle X-ray diffraction, exhibiting the diffraction patterns of stacked 2D
8 layers with 4.1 nm interlayer spacing. Further confirmation for Mn doping within the 2D structure
9 came from the absorption spectrum and photoluminescence excitation spectrum at 620 nm where
10 Mn luminescence is observed. In the second step, the intermediate structure was converted to Mn-
11 doped CsPbBr₃ NCs by adding Cs-oleate at 200°C. Interestingly, the resulting product was a
12 mixture of Mn-doped CsPbBr₃ NCs with two different morphologies, i.e., nanocubes (6.5–8.5 nm)
13 and nanoplatelets (~2 nm in thickness), which were separated from each other via centrifugation.
14 Since both Mn-doped CsPbBr₃ NCs have sufficiently higher bandgap from the quantum
15 confinement, sensitized Mn luminescence was observed in this work.

16 **Mn doping in CsPbI₃ NCs.** Doping of Mn in CsPbI₃ NCs has also been reported by several
17 groups. Akkerman et al. reported the synthesis of Mn-doped CsPbI₃ using MnI₂ as an additional
18 reactant added to the hot injection synthesis conditions of CsPbI₃ NCs.⁶³⁸ Mn-doped CsPbI₃ NCs
19 with ~12 nm size were obtained from this synthesis. Unlike in Mn-doped CsPbCl₃ and CsPbBr₃
20 NCs, the bandgap of CsPbCl₃ NCs is smaller than the ligand field transition energy of Mn, which
21 prevents sensitization of the Mn luminescence. This also makes it more challenging to confirm
22 doping by spectroscopic techniques. On the other hand, the purpose of that work was to stabilize
23 the perovskite phase and prevent its transition to the δ-CsPbI₃ non-perovskite phase, as will be

1 discussed later in more detail. In another work, Nag and coworkers reported post-synthesis Mn
2 doping using MnI_2 dissolved in methyl acetates as the precursor of Mn. In their reaction, doping
3 was achieved at room temperature by mixing the solutions of $CsPbI_3$ NCs and MnI_2 .⁶³²

4 **Sensitized Mn luminescence and energy transfer dynamics.** So far, the most studied optical
5 properties of Mn-doped $CsPbX_3$ NCs are related to the sensitized Mn luminescence along with the
6 competitive dynamics between the radiative recombination of exciton and energy transfer to Mn.
7 The relative intensities of exciton and Mn-dopant emissions depend on various factors, including
8 the doping density, the relative energetics of host NC bandgap and the d-d transition of the Mn^{2+}
9 involved in the sensitization, degree of quantum confinement in the host NCs and temperature.
10 While a complete picture of the correlation between these variables and PL intensities has not yet
11 been reached, several recent studies have provided additional insights on the energy transfer
12 dynamics and microscopic mechanisms based on temperature-dependent transient absorption and
13 photoluminescence, as described below.



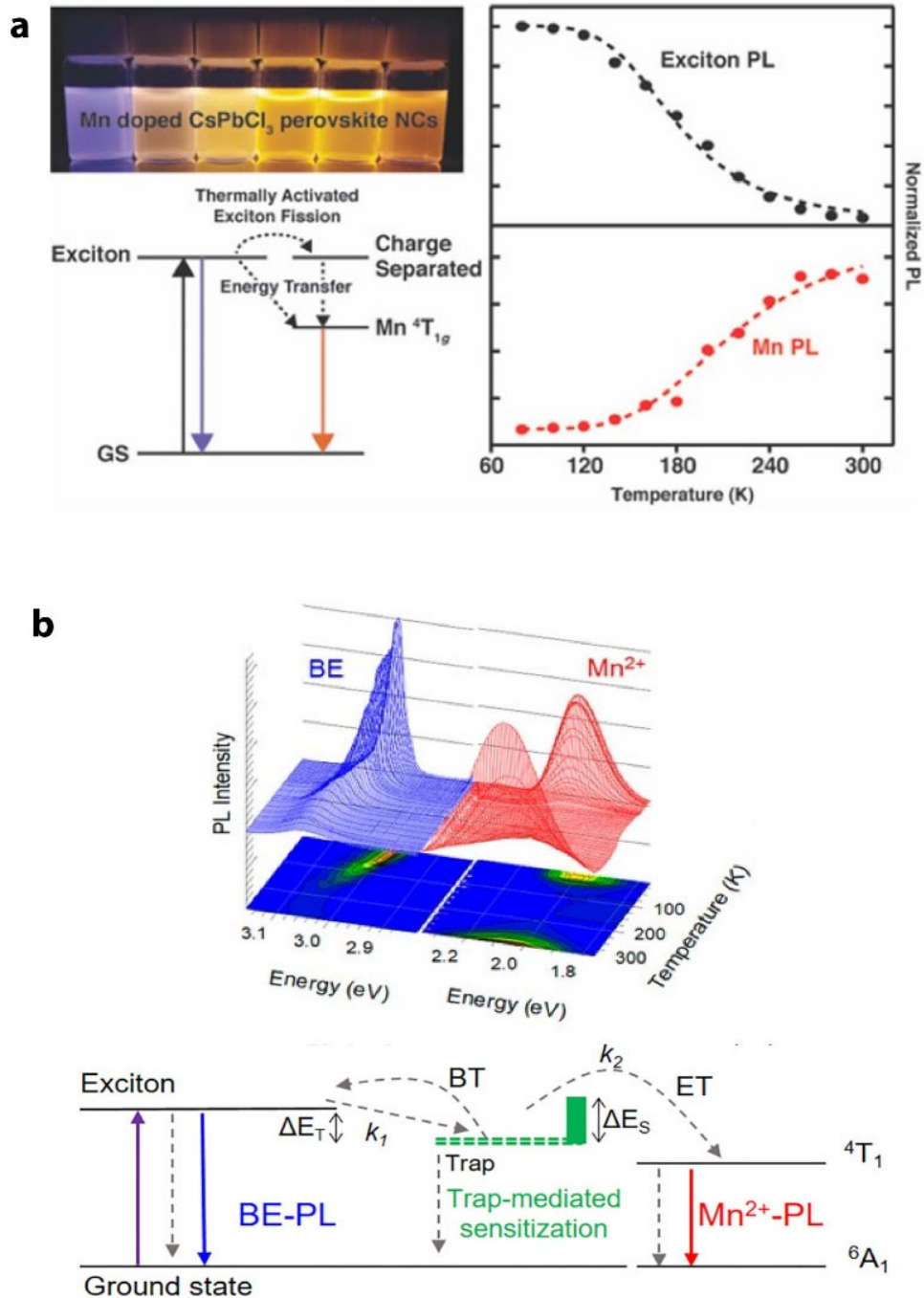
14
15 **Figure 62.** Dynamics of Mn doped $CsPbCl_3$: Scheme of exciton-to-dopant energy transfer in Mn-
16 doped $CsPbCl_3$ NCs and transient absorption data for doped and undoped $CsPbCl_3$. Images were
17 taken with permission from Ref.⁶⁵⁶.

1 For the Mn-doped CsPbX₃ NCs, Son and coworkers performed the first time-resolved
2 experiment to directly measure the rate of energy transfer instead of estimating it from the
3 luminescence quantum yield and relative intensities of luminescence from the host and Mn. In
4 their study, the energy transfer time (τ_{ET}) was obtained by a comparative analysis of the recovery
5 time of the bleach signal at the band edge in Mn-doped and undoped NCs using pump–probe
6 transient absorption spectroscopy. The energy transfer pathway that exists only in Mn-doped NCs
7 was manifested as an additional dynamic component in the bleach recovery of the exciton, as
8 shown in Figure 62. In Mn-doped CsPbCl₃ nanocubes with an edge length of 10 nm and a ~ 0.4%
9 doping concentration, τ_{ET} was determined to be ~380 ps.⁶⁵⁶ Compared to the τ_{ET} value of the
10 previously studied Mn-doped CdS/ZnS NCs after correcting for the difference in doping
11 concentration, the τ_{ET} in the Mn-doped CsPbCl₃ nanocubes is 2–5 times slower. The slower energy
12 transfer in CsPbCl₃ NCs compared to II-VI QDs was attributed to the intrinsically weaker
13 exchange interaction among excitons and *d* electrons of dopant in CsPbCl₃ NCs and the weaker
14 quantum confinement of the host NCs. Samanta and coworkers also performed transient absorption
15 spectroscopy in Mn-doped and undoped CsPbCl₃ NCs and made a similar observation.⁶⁵⁷ They
16 also observed the faster recovery of the bleach at the band edge in Mn-doped NCs reflecting the
17 energy transfer. So far, direct time-resolved studies have been limited to CsPbCl₃ NCs with weak
18 confinement. An indirect study on the rate of energy transfer based on relative intensities of exciton
19 and Mn PL was performed in CsPb(Cl/Br)₃ NCs as a function of the halide composition. In the
20 study by Meijerink and coworkers, the variation of $I_{\text{Mn}}/I_{\text{exc}}$ (ratio of Mn and exciton
21 photoluminescence intensity) with Br/Cl ratio in the host NCs was systematically studied.⁶⁵⁰ An
22 initial fast increase in the $I_{\text{Mn}}/I_{\text{exc}}$ with increasing Br⁻ content is followed by a decrease for higher
23 Br⁻ contents. The authors explained this observation by a reduced exciton decay rate and faster

1 exciton-to-Mn energy transfer upon Br⁻ substitution. Clearly, further investigation of other Mn-
2 doped CsPbX₃ NCs with different halide compositions and varying degrees of quantum
3 confinement is necessary to obtain a better picture of the coupling between the exciton and dopant
4 in this system.

5 A number of temperature-dependent studies on the intensity and lifetime of exciton and Mn
6 photoluminescence were performed by several groups, from which the involvement of charge-
7 separated state of exciton or trapped exciton in the energy transfer process was inferred. Gamelin
8 and coworkers measured the temperature-dependent exciton and Mn PL intensities in 80 -300K.⁶⁵¹
9 Exciton PL increased with decrease in temperature in this range whereas Mn PL exhibited the
10 opposite behavior. (Figure 63) To explain the observed temperature-dependent PL intensities, the
11 authors introduced a thermally activated charge-separated state that is longer-lived than the exciton
12 and that also participates in the energy transfer process. In this scheme, the temperature-dependent
13 competition between radiative recombination of exciton and formation of charge-separated state
14 ultimately determined the temperature-dependent competitive kinetics of exciton relaxation and
15 energy transfer. More recently, Brovelli and coworkers extended the range of temperature down
16 to 5K and studied the temperature-dependent branching between exciton recombination and
17 energy transfer.⁶⁵⁸ The noteworthy observation is the reappearance of Mn PL intensity below 70K
18 that increases with decrease in temperature, which contrasts to the trend at the higher temperatures.
19 To explain the more complex temperature dependence of the PL intensities, the authors proposed
20 a two-step process involving the initial localization of band-edge excitons in a shallow trap that
21 mediates the sensitization of the dopants and repopulates the band-edge by thermally activated
22 back-transfer. While this trap-mediated process was considered dominating above 70 K, the

- 1 authors suggested that the barrierless energy transfer directly from bandedge exciton to Mn occurs
- 2 below 70 K, which explains the reemergence of Mn PL at the lower temperatures.

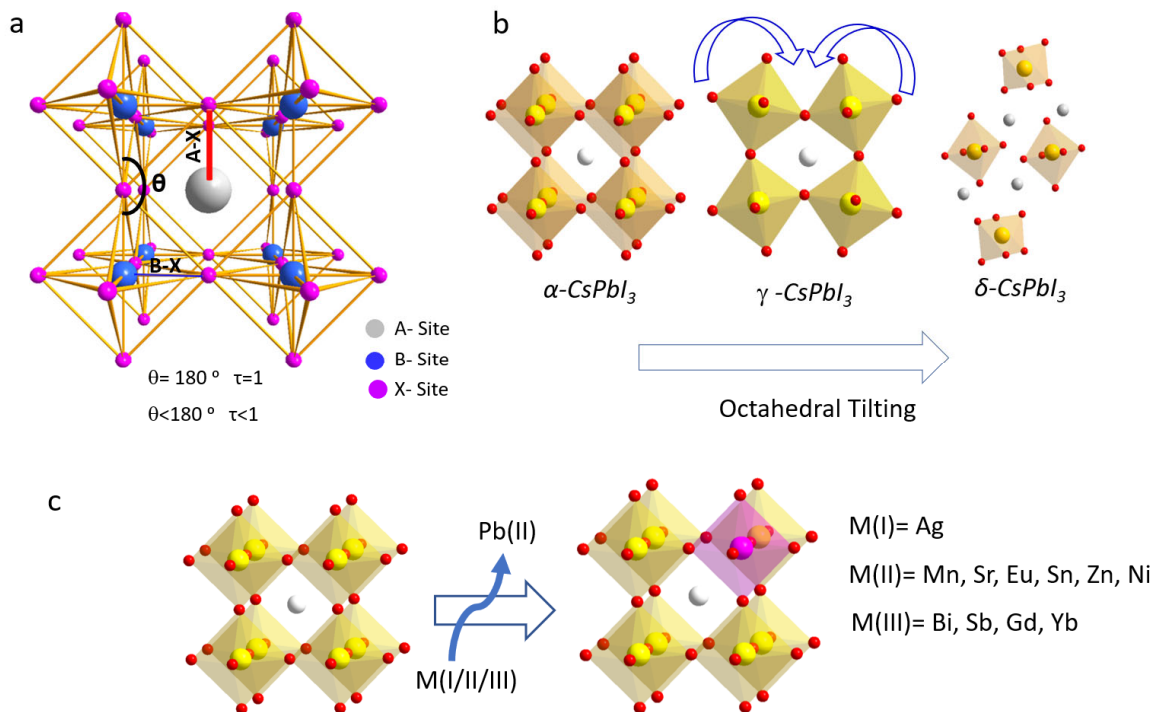


- 3
- 4 **Figure 63.** Temperature-dependent PL of Mn-doped CsPbCl₃ NCs. Temperature-dependent
- 5 exciton PL and Mn PL intensities in Mn-doped CsPbCl₃ NC films deposited on silicon substrates

1 with 2.4% Mn^{2+} , normalized at 80 K. Energy level diagram describing the energy transfer process
2 via thermally activated charge-separated state is also shown. Taken with permission from Ref.⁶⁵¹.
3 (b) 3D plot of PL spectra of the bandedge exciton (BE) and Mn luminescence from Mn-doped
4 CsPbCl_3 NCs. Bottom figure is the Jabloski diagram showing the energy transfer process through
5 intermediate shallow trap state. Taken with permission from Ref.⁶⁵⁸.

6 **B-site doping to stabilize red-emitting CsPbI_3 NCs**

7 Although this mode of predicting τ value from the ionic radii is most popular, it was initially
8 proposed for oxide and fluoride-based perovskites which were considered only the ionic
9 interactions. However, in comparison with fluoride, the polarizability of iodide induces covalent
10 character to the octahedra and the traditional calculation of τ does not clearly account for the
11 stability of the perovskite system. Palgrave and coworkers correlated different experimental result
12 to obtain the exact radii, and they found that the radii of Pb(II) in chloride, bromide, and iodide
13 are 0.99, 0.98, and 1.03 Å respectively, which remained significantly shorter than the Shannon
14 ionic radius (1.19 Å).⁶⁵⁹ Hence, they proposed a modified τ calculation with the experimentally
15 obtained radii values. After considering all these the calculated τ for CsPbI_3 is 0.89, which is on
16 the margin of the stable perovskite structure. There, the red emissive α - CsPbI_3 NCs degrade into
17 the yellow nonemitting δ - CsPbI_3 phase after few days of preparation.



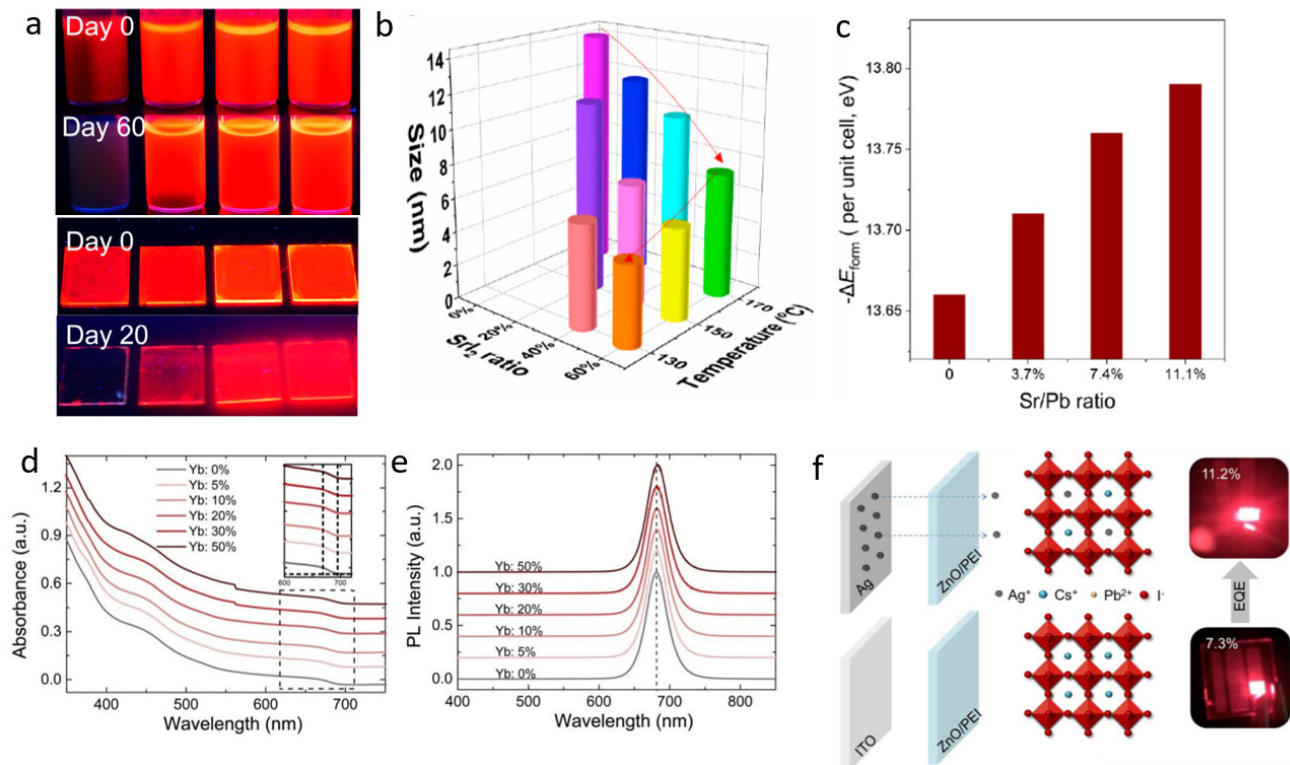
1
 2 **Figure 64.** (a) Schematic representation of a typical ABX₃ unit shell showing bond lengths, tilting
 3 angle (θ) and relationship of tilting angle (θ) with Goldschmidt tolerance factor (τ). Reproduced
 4 with permission from Ref.⁶⁶⁰ (b) Various ABX₃ unit cell with increasing tolerance factor. (c)
 5 Schematic illustration of B-site doping with various reported metal ions.

6
 7 It has been widely reported that the stability of the black perovskite phase of CsPbI₃ NCs can be
 8 significantly improved by doping or alloying them with a divalent cation of a smaller ionic radius
 9 than that of Pb²⁺ due to the increase of τ. A schematic of the B-site doping and the various dopant
 10 ions studied to date are illustrated in Figure 64c. For instance, Akkerman and coworkers have
 11 shown that alloying of α-CsPbI₃ NCs with Mn²⁺ leads to a remarkable enhancement in their
 12 stability while preserving the optical features and crystal structure of pristine CsPbI₃ NCs.⁶³⁸ The
 13 authors showed that the CsPb_xMn_{1-x}I₃ NCs were stable over a month in either colloidal solution or

1 thin films. The density functional calculations showed that the conduction and valence bands of
2 CsPbI₃ are influenced by both s and p orbitals of Pb and I respectively, while the Mn d-states
3 remained far below the conduction band. Hence, Mn²⁺ doping did not alter the bandgap or optical
4 features of the pristine NCs. Similarly, alloying CsPbI₃ NCs with Sn²⁺ also enhances their stability,
5 but in this case it does influence the bandgap of the NCs, hence their optical features.⁶⁶¹ As
6 discussed in earlier sections, CsSnI₃ is not stable because of the ease of oxidation of Sn²⁺ to Sn⁴⁺.
7 Interestingly, the alloyed CsSn_{1-x}Pb_xI₃ NCs remained stable for more than 150 days. CsSnI₃ and
8 CsPbI₃ have bandgaps of 1.3 eV and 1.75 eV, respectively, and their alloyed NCs possess
9 intermediate bandgap. These works suggest that the selection of proper B-site dopants remains
10 critical for preserving phase stability, but its influence on the optical properties of the NCs cannot
11 be ignored. In another work, Yao et al. demonstrated that alloying with Zn²⁺ reduces the non-
12 radiative decay rates by suppressing the defect states in CsPbI₃ NCs, and increases the radiative
13 decay rates by enhancing the exciton binding energy of the NCs.⁶⁶² Recently, Yao et al. reported
14 the use of Sr(II) as a dopant to stabilize cubic-CsPbI₃ NCs.⁶⁶³ As the ionic radius of Sr(II) is
15 smaller than that of Pb(II), its inclusion in CsPbI₃ NCs leads to the contraction of the crystal lattice,
16 and thus improves its phase stability. Figure 65a presents a digital image of the CsPbI₃ NC
17 suspensions and the corresponding films prepared under the addition of different percentages of
18 SrI₂ and, the colloidal solutions and films after 60 and 20 days of preparation, respectively. In
19 addition, the average size of the doped CsPbI₃ NCs was found to be dependent on the SrI₂ loading
20 at various temperatures (Figure 65b),⁶⁶³ in analogy with other reports in which the concentration
21 of halide ions in the synthesis is a key parameter for controlling the size of perovskite NCs.^{81 153}
22 To support the experimental findings on increased stability, the authors further computed the

1 formation energy of doped cubic CsPbI₃ NCs, and it increases with increasing the the Sr to Pb
2 ratios as shown in figure 65c.

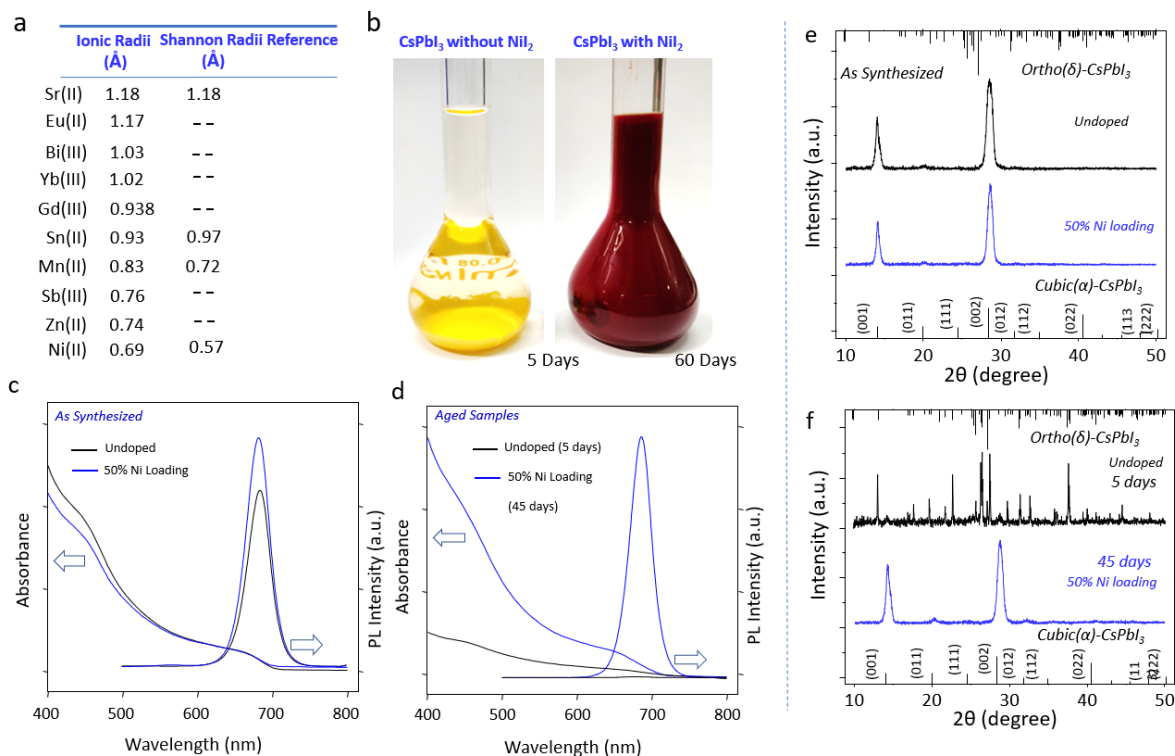
3 In addition to isovalent doping/alloying, the introduction of heterovalent ions (e.g. Yb(III),
4 Gd(III)and Sb(III)) ions was also explored to stabilize cubic-phase and preserve the red emission
5 of the CsPbI₃ NCs.⁶⁶⁴⁻⁶⁶⁶ Figure 65(d-e) present the absorbance and PL spectra of CsPbI₃ NCs with
6 various amounts of Yb(III) doping. From the band edge absorption spectra (Inset of Figure 65d),
7 the bandgap was found to be uncharged regardless of the level of doping. In addition, the authors
8 claimed that the PLQY increased from 75% to 86% with 20% Yb(III) doping, while it decreases
9 at higher emounts of doping. The authors attributed this enhancement to reduction in the density
10 of defects and trap states created by surface and lattice vacancies.⁶⁶⁴ In another work, Rogach and
11 co-workers found spontaneous Ag(I) doping in CsPbI₃ film when Ag film was used as an electrode
12 in place of ITO in an LED device.⁶⁶⁷ In addition, they claimed that the Ag (I) ions passivate the
13 CsPbI₃ NC surface, leading to the increase of external quantum efficiency (EQE) from 7.3% to
14 11.2 % using Ag electrode in the LED device (Figure 65f).



1
 2 **Figure 65.** (a) Digital image of films and NC suspension of CsPbI₃ NCs prepared with 0% SrI₂ at
 3 170 °C, 40% SrI₂ at 170 °C, 60% SrI₂ at 170 °C, 60% SrI₂ at 150 °C. (b) Plots showing the change
 4 of size of NCs with the amount of SrI₂ introduction at different temperatures. (c) Histogram
 5 showing change in formation energy with change in Sr to Pb ratios. These images (a-c) were
 6 obtained with permission from Ref. ⁶⁶³ (d) and (e) Absorption (d) and PL spectra (e) of CsPbI₃
 7 NCs synthesized at various loadings of Yb. Inset of (d) is the enlarged view of band edge of all
 8 absorption spectra. The spectra shows that the bandgap remains unaltered regardless of the amount
 9 of Yb doping. Figures d and e were reproduced from Ref. ⁶⁶⁴ (f) Films of CsPbI₃ NCs with and
 10 without Ag(I) and their respective lighting LEDs. Figure f is reproduced from Ref. ⁶⁶⁷

11 While analyzing the various reports on doping metal ions to achieve phase stabilization of red-
 12 emitting perovskite CsPbI₃, we found a correlation between temporal stability (either in solution
 13 or in the film) and size of the B-site (i.e. the Pb²⁺ site) dopant ions of CsPbI₃. A list of ions used

1 as dopants, along with the available values of the corresponding Shannon radii, is provided in
 2 Figure 68a. Among these, Ni(II) has the lowest Shannon radii, and it was found that CsPbI₃ NCs
 3 doped with this ion exhibited relatively longer stability.⁶⁶⁸ Photographs of the colloidal
 4 suspensions of Ni (II)-doped and undoped CsPbI₃ NCs are shown in figure 66b: the suspension
 5 containing undoped NCs turned yellow after five days, while the one containing the Ni(II) doped
 6 NCs preserved its red color even after 45 days of aging. Figure 66c&d present the absorption and
 7 PL spectra of suspensions of the undoped and Ni(II) doped NCs (as-synthesized and aged). Both
 8 suspensions are red-emitting soon after their synthesis. However, while the undoped sample
 9 becomes nonemissive after 5 days (Figure 66d), the Ni(II) doped sample emits strong red-emission
 10 even after 45 days. The phase change of the undoped sample after 5 days can be clearly seen in
 11 the powder X-ray measurements (figure 66 e& f).



12

1 **Figure 66.** (a) Table showing ionic and Shannon radii of various metal ions used for stabilizing
2 CsPbI₃ NCs. (b) Digital images of CsPbI₃ NCs dispersion having without and NiI₂ addition in
3 respective synthesis process. (c) and (d) Time dependent absorption and PL spectra of as
4 synthesized and aged CsPbI₃ NCs having with and without having NiI₂ incorporation. (e) and (f)
5 Powder X-ray diffractions of as synthesized and aged samples of with and without Ni incorporated
6 CsPbI₃ NCs. These images were obtained with permission from reference ⁶⁶⁸.

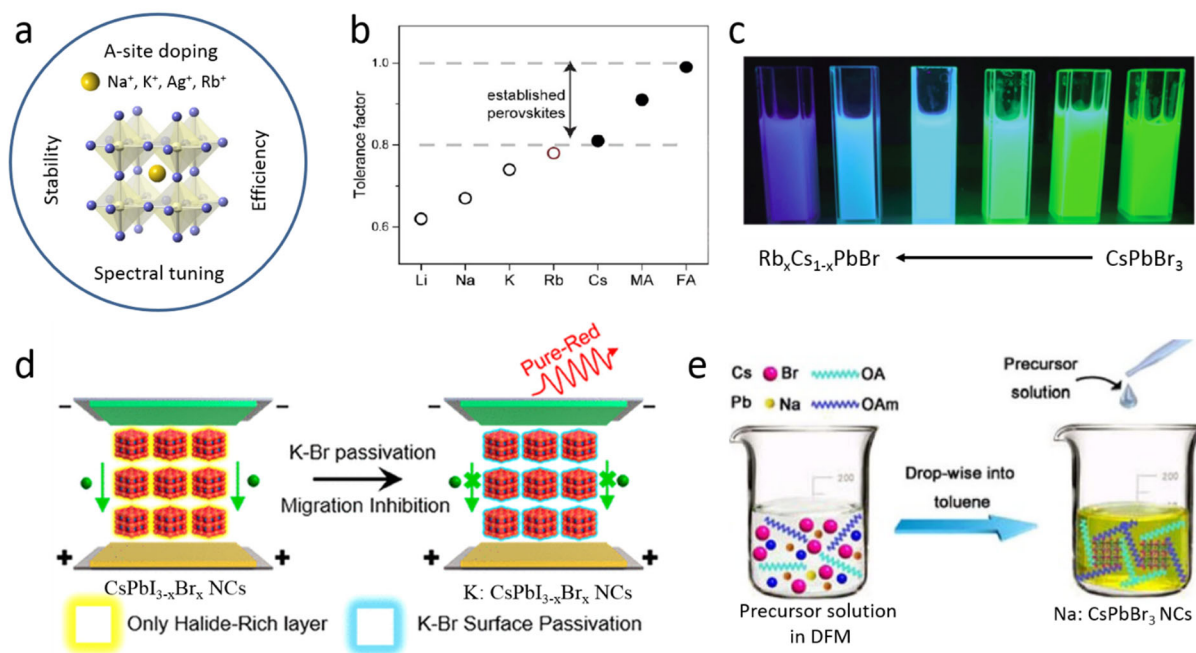
7 As discussed above, most reports suggest that the doping or alloying in CsPbI₃ NCs improves
8 the phase stability, and thus the optical quality and stability. It has also been claimed that the
9 doping removes nonradiative traps. In most cases, it was speculated that the divalent dopants
10 occupy Pb positions of the crystal lattice. In some reports, theoretical supports were also provided
11 for their experimental observations. However, there is no clear microscopic evidence for solid for
12 doping of B-site to date. On the other hand, in most studies, respective iodide precursors were
13 introduced for B-site doping, and this could lead to iodide rich condition in the synthesis. For
14 instance, Shen et al. promoted iodide rich condition in a typical CsPbI₃ NC synthesis using GeI₂
15 as an additional Iodide source. The authors claimed that the excess iodide in the reaction helped to
16 stabilize the CsPbI₃ NCs, however, unlike other bivalent metals Ge was not incorporated in the
17 NC lattice.⁶⁶⁹ A similar observation was reported by Jeong and coworkers using ZnI₂ as an
18 additional iodide precursor in the CsPbI₃ NC synthesis.⁴¹⁷ On the other hand, Imran et al.¹⁸⁰ and
19 Cai et al.¹⁷⁰ separately reported the use of non-halide Pb and Cs precursors in the perovskite NC
20 synthesis, in which the reaction was triggered by benzoyl iodide and trimethylsilyl Iodide as iodide
21 precursors, respectively. In both cases, stable CsPbI₃ NCs were prepared. These results put under
22 discussion the real need of doping in order to improve the stability of black-phase CsPbI₃ NCs and
23 opened many questions about replacing Pb(II) by mono-, di- and trivalent dopant ions. Hence, in-

1 depth experimental and theoretical studies are needed for better understanding and conclude the
2 role of dopants in the stabilization of black-phase, red-emitting CsPbI₃ NCs.

3

4 **6.2 APPARENT A-SITE DOPING**

5 In addition to the bivalent metal cation dopants discussed above, several monovalent cation
6 dopants such as Rb⁺, Na⁺, K⁺ and Ag⁺ are also being intensively investigated to enhance the
7 stability as well as photoluminescence efficiency of perovskite NCs (Figure 67a).^{602,670} It has been
8 claimed that these dopants occupy A-sites of perovskite NC lattice. The selection of dopants is
9 generally inspired from the previous research on perovskite solar cells, in which perovskite films
10 were doped with various monovalent cations to improve their power conversion efficiency and
11 stability.^{108, 602, 670-671} The phase stability of perovskites with specific monovalent cations depends
12 on their size and thus tolerance factor as discussed above.⁶⁷¹ For instance, Cs⁺, MA⁺, and FA⁺ ions
13 fit well into the A-site of the lead iodide perovskite structure (Cs⁺ “less” well than MA⁺, and FA⁺,
14 as discussed in the previous sections), while small metal ions such as Li⁺, Rb⁺, Na⁺, K⁺ cannot
15 stabilize the perovskite structure due a low tolerance factor (Figure 67b). Interestingly, doping
16 these small cations into perovskite NCs improves their optical properties and phase stability. Saliba
17 et al.⁶⁷¹ first showed the incorporation of small and oxidation-stable rubidium cation (Rb⁺) into
18 mixed cation perovskite (CsMAFA) films to create photoactive perovskite films with excellent
19 material properties. Remarkably, Rb incorporation does not alter the valence band position of the
20 host perovskite. They have showed that the Rb⁺ doping into perovskites leads to higher phase
21 stability and more reproducible power conversion efficiencies (PEC). Further studies revealed that
22 Rb⁺ incorporation can also enhances the performance of the corresponding light emitting diodes.⁶⁷²



1
 2 **Figure 67.** (a) Schematic illustration of perovskite cubic crystal structure with possible A-site
 3 dopants including Na⁺, K⁺, Ag⁺, Rb⁺. Through doping, enhanced stability and device efficiency,
 4 and spectral tuning has achieved. (b) Tolerance factor of APbI₃ perovskite for different A cations
 5 (A = Li, Na, K, Rb, Cs and MA and FA) (c) Schematic illustration of the synthesis of the Na⁺-
 6 doped CsPbBr₃ NCs by ligand-assisted reprecipitation approach. (d) Schematic illustration of
 7 doping K⁺ into CsPbI_{3-x}Br_x NCs by surface passivation for improving red photoluminescence. (e)
 8 Photograph of the colloidal solutions of Rb⁺ doped CsPbBr₃ perovskite NCs under UV light
 9 illumination.

10 Recently, the concept of Rb⁺ doping into bulk perovskites has been extended to perovskite
 11 NCs as well.^{606, 673-676} For instance, Wu et al.⁶⁰⁶ synthesized Rb⁺ doped CsPbBr₃ perovskite NCs
 12 with different ratios of Rb/Cs by the hot injection method. It was found that the bandgap gradually
 13 increases and thus the photoluminescence blue shifts with the increase of the Rb/Cs ratio (Figure
 14 67c). It is very interesting that the Rb_xCs_{1-x}PbBr₃ colloidal solution exhibit blue
 15 photoluminescence with increasing the Rb dopant concentrations. The authors attributed the

1 increase of bandgap to changes in the valence and conduction bands caused by the decrease of in-
2 plane Pb–Br–Pb band angle of the [PbBr₆] octahedron by the replacement of Cs⁺ with small Rb⁺
3 ions that does not fit well into perovskite lattice due to low tolerance factor.⁶⁰⁶ A similar blue shift
4 in photoluminescence was observed for Rb_xCs_{1-x}PbBrI₂ NCs with increasing ratio of Rb/Cs.⁶⁷⁷
5 Furthermore, Rb⁺ ions can also be doped into perovskite nanoplatelets of different thicknesses to
6 achieve tunable emission (green-sky blue-blue) with PLQY over 60%, as shown by Sargent and
7 co-workers.⁶⁷⁵ The fabrication of sky-blue and deep-blue LEDs has been demonstrated using these
8 mixed cation Rb_xCs_{1-x}PbBr₃ nanoplatelets, and they exhibit relatively high thermal stability and
9 operational stability. Despite these few studies, the position (surface or inside lattice) of Rb⁺ ions
10 in perovskite lattice is still unclear. Very recently, Etgar and co-workers⁶⁷³ performed EDS
11 analysis on atomically resolved HAAD-STEM images of Rb_xCs_{1-x}PbBr₃ NCs to understand the
12 position of Rb atoms in the lattice. They claimed that at medium dopant concentrations the Rb
13 atoms stays in the core region, while the Cs atoms are preferentially located in the shell region,
14 forming core–shell like structures. However, at high Rb dopant concentrations a phase separation
15 of Rb occurs within the perovskite NCs, because Rb atoms cannot form perovskite phase. In
16 contrast, Kubicki et al.⁶⁷⁸ performed ¹⁴N solid-state magic-angle spinning (MAS) NMR to probe
17 the compositions of mixed cation (Cs, Rb, K, MA, FA) perovskites and they found no signs of Rb
18 or K incorporation into the bulk perovskite lattice. From the X-ray photoelectron spectroscopy
19 (XPS) study, they found that the surface of perovskites has rubidium-rich phases, which can acts
20 as a passivation layer for the perovskites.

21 In addition, other alkali metal ions including K⁺ and Na⁺ are also gaining attention as potential
22 dopants for perovskite NCs for enhancement of their stability and photoluminescence efficiency.
23 For instance, Huang et al.⁶⁷⁹ reported a post-synthetic surface treatment of CsPbBr₃ perovskite

1 NCs with K-oleate to improve their PLQY and photostability. After K treatment, the NC films
2 retained their original photoluminescence intensity even after 150 h of illumination. However, it
3 is not clear whether the K just passivated the NC surface or it diffused into the perovskite lattice.
4 Similarly, CsPbI_{3-x}Br_x NCs were treated with K-oleate to enhance red photoluminescence, as
5 demonstrated by Yao and co-workers (Figure 67d).⁶⁸⁰ The addition of K-oleate led to the formation
6 of KBr on the CsPbI_{3-x}Br_x NC surface, which then passivated the NC surface effectively to obtain
7 PLQY over 90% (Figure 67d). More importantly, the K⁺ ions were able to protect the NC surface
8 from halide segregation, and the LED made using these NCs exhibited stable electroluminescence
9 and high brightness. On the other hand, Na⁺ ions were incorporated into colloidal CsPbBr₃ NCs
10 by ligand-assisted reprecipitation approach, as shown in Figure 67e.⁶⁸¹ It was found that the Na-
11 doped CsPbBr₃ NCs exhibit better color purity and higher PLQY. This was attributed to the
12 reduction of nonradiative trap centers in NCs by Na⁺ passivation. In addition, a gradual blue shift
13 in the emission peak was observed with an increasing Na⁺ dopant concentration similar to Rb
14 doped perovskite NCs. More importantly, the Na⁺-doped CsPbBr₃ NCs had enhanced stability
15 against ultraviolet light, heat, and moisture compared to pure CsPbBr₃ NCs, and thus the white
16 LEDs fabricated using these Na:CsPbBr₃ NCs as phosphors showed superior stability even under
17 continuous runs for over 500 h.⁶⁸¹ In another report, Chen et al.⁶⁸² demonstrated the in situ
18 incorporation of Na⁺ ions into CsPbBr₃ NCs prepared directly on a substrate by using NaBr
19 additive in the precursor solution. The authors claimed that the added NaBr passivates the NC
20 defects and also improves the conductivity of the films. More importantly, the green LEDs
21 fabricated using Na:CsPbBr₃ exhibited a maximum EQE of 17.4%, which is higher than the values
22 measured on the LEDs prepared using pure CsPbBr₃ NCs (EQE~12%).⁶⁸² Based on the above

1 discussed examples, it is clear that the doping perovskite NCs with smaller monovalent cations
2 improves their stability as well as PLQY, and thus the efficiency of LEDs. Despite these early
3 studies, the mechanism of doping is rather unclear and the question regarding the position of
4 dopants in the NCs (surface or inside crystal lattice) is yet to be explored. Addressing this question
5 requires a detailed analysis of atomically resolved HAAD-STEM images, but this is challenging,
6 as the amount of dopants is rather small and perovskite NCs are quite prone to damage induced by
7 electron beam irradiation. In addition, the relation between the concentration of dopants and the
8 emission efficiency is yet to be investigated in detail. It is likely that, in all investigated cases, there
9 is an optimum dopant concentration that maximizes the PLQY, past which any additional doping
10 may start actually degrading the emission efficiency.

11

12 **6.3 LANTHANIDE-DOPED PEROVSKITE NANOCRYSTALS**

13 Lanthanide ions are widely used as luminescence activators in inorganic materials.⁶⁸³⁻⁶⁸⁴ For
14 example, the spectral conversion phosphors in fluorescent lighting use lanthanides as activators to
15 emit visible photons following absorption of high-energy photons by the host material (either the
16 host lattice itself or an additional "sensitizer" impurity). Trivalent lanthanides (Ln^{3+}) are
17 particularly excellent in this role. The high shielding of their $4f$ valence orbitals results in sharp-
18 line f - f emission that is relatively insensitive to the crystalline field around the lanthanide.
19 Furthermore, white light of almost arbitrary color temperature can be generated by combining
20 several lanthanides.

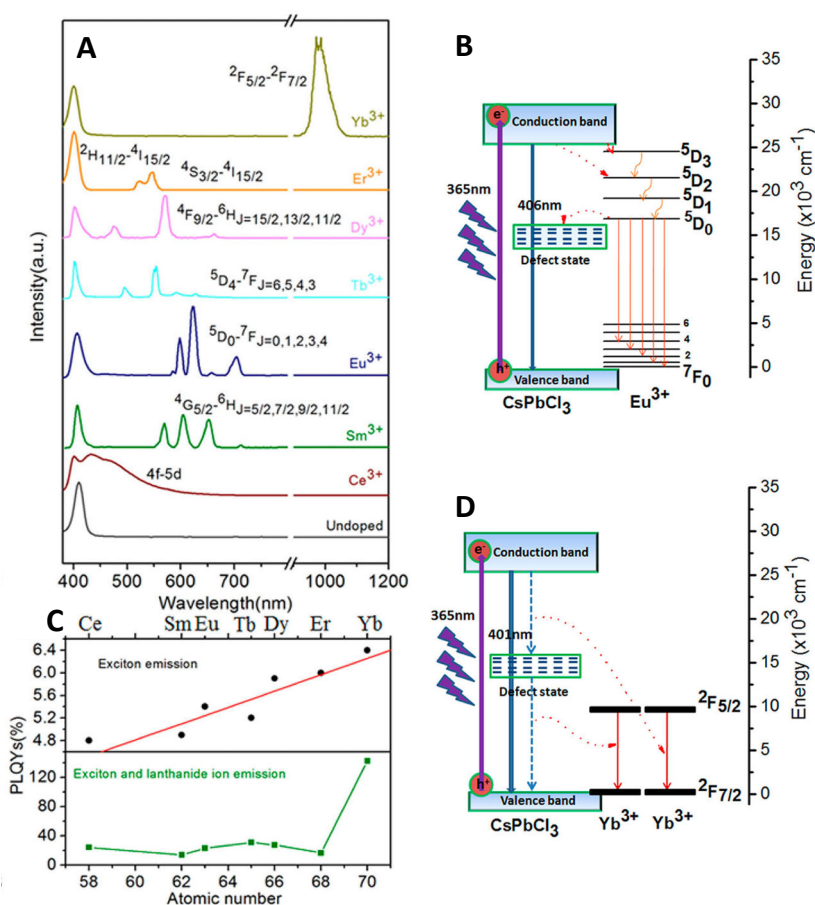
21 The f - f internal transitions of the lanthanides are parity forbidden and are only weakly coupled
22 to lattice vibrations that might relax this forbiddenness. Their radiative lifetimes are therefore often
23 extremely long (*e.g.*, milliseconds). In crystalline or amorphous matrices with only low-energy

1 vibrations, these ions frequently show very large photoluminescence quantum yields. In a minority
2 of cases, the optical spectroscopy of the lanthanides is dominated not by $f-f$ transitions but rather
3 by $f-d$ transitions. These specific cases include Ce^{3+} and divalent lanthanides, most commonly
4 Eu^{2+} . These $f-d$ transitions are parity allowed, and because of the much greater interaction of the
5 $5d$ orbitals with the surrounding environment, they are vibronically broadened and their energy is
6 more sensitive to the specific ligand-field environment.

7 In fluorescent lighting, the phosphor matrices are oxides (*e.g.*, Eu^{3+} -doped Y_2O_3 red phosphor)
8 that are robust under the very short wavelength excitation of the mercury gas discharge (254 nm),
9 and the materials need to absorb strongly at these short wavelengths. For other applications, greater
10 visible-light absorption is desirable. Lanthanide-doped perovskite NCs have recently begun
11 attracting broad attention as candidates for visible-light sensitized phosphors.^{135, 665, 685-702} In
12 contrast with the extensively studied Ln^{3+} -doped fluoride NCs used as upconversion phosphors
13 (*e.g.*, $Ln^{3+}:NaYF_4$, $Ln^{3+}:LaF_3$, *etc.*),⁷⁰³⁻⁷⁰⁵ Ln^{3+} emission in lead-halide perovskite NCs is generated
14 by direct excitation of the semiconductor band-to-band transitions, which have oscillator strengths
15 $\sim 10^5$ times greater than those of the Ln^{3+} $f-f$ transitions themselves. New materials with unique
16 spectral characteristics have been created by combining the energy-tunable light-harvesting
17 capabilities of metal-halide perovskite NCs with the excellent radiative properties of lanthanide
18 dopants. These materials have, in turn, opened new opportunities for unique applications in solar
19 spectral conversion and other related technologies.

20 The first reports of lanthanide-doped lead-halide perovskite NCs appeared in 2017, in which
21 the Song group surveyed a series of Ln^{3+} -doped $CsPbCl_3$ and anion-alloyed $CsPb(Cl_{1-x}Br_x)_3$ NCs
22 involving the entire series of trivalent lanthanide ions.^{135, 700} Figure 68a, the overview figure from
23 one of these studies, organized from top to bottom according to decreasing $4f$ electron count of the

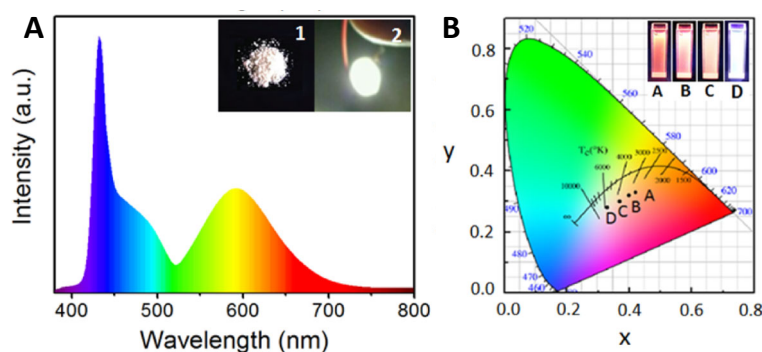
1 Ln^{3+} dopant in CsPbCl_3 NCs, and referenced to the undoped CsPbCl_3 spectrum. A few aspects of
 2 these data are notable. First, in each case (except Ce^{3+}), the PL spectrum shows both excitonic PL
 3 and the characteristic $f-f$ emission features of the lanthanide known from previous studies in
 4 analogous chloride host lattices. The Ce^{3+} -doped NCs showed broad emission near the perovskite
 5 bandgap, attributed to the well-known $f-d$ emission of this ion. For most cases, the sensitization
 6 scheme was considered to involve perovskite photoexcitation followed by nonradiative relaxation
 7 within the $4f$ manifold of excited states until a sizable energy gap was reached, at which point $f-f$
 8 emission is observed (Figure 68b).



9
 10 **Figure 68.** (A) Emission spectra of CsPbCl_3 NCs doped with different lanthanide ions. (B)
 11 Proposed energy level diagram for Eu^{3+} -doped CsPbCl_3 NCs showing a possible
 12 photoluminescence mechanism. (C) Photoluminescence quantum yields for excitonic (top) and

1 overall (exciton + Ln^{3+} , bottom) emission features. (D) Proposed energy-level diagram for Yb^{3+} -
2 doped CsPbCl_3 NCs showing a possible mechanism for quantum cutting *via* stepwise energy
3 transfer involving a deep (mid-gap) defect state. Adapted from Ref. ¹³⁵.

4 The observation of Ln^{3+} PL sensitized by semiconductor photoexcitation paves the way for
5 application of the various Ln^{3+} -doped NCs in numerous phosphor applications, including lighting
6 or display technologies, near-IR optics and telecommunications. For example, the Song group
7 subsequently demonstrated the use of CsPbCl_3 and $\text{CsPb}(\text{Cl}_{1-x}\text{Br}_x)_3$ NCs co-doped with pairs of
8 impurity ions, *e.g.*, $\text{Ce}^{3+}/\text{Mn}^{2+}$, $\text{Ce}^{3+}/\text{Eu}^{3+}$, $\text{Ce}^{3+}/\text{Sm}^{3+}$, $\text{Bi}^{3+}/\text{Eu}^{3+}$, and $\text{Bi}^{3+}/\text{Sm}^{3+}$, as spectral
9 converters for white-light generation.⁶⁹¹ Both ions in these pairs can be sensitized by the host NC,
10 and they function roughly independently of one another, such that color rendering can be optimized
11 by controlling the relative and absolute concentrations of each dopant (Figure 69). Particularly
12 efficient white-light emission was achieved with of $\text{Ce}^{3+}/\text{Mn}^{2+}$ co-doping of $\text{CsPb}(\text{Cl}_{0.6}\text{Br}_{0.4})_3$ NCs.
13 These NCs showed PLQYs of $\sim 75\%$, and luminous efficiencies as high as 51 lm/W with good
14 color rendering (~ 89) when pumped at 365 nm from a UV LED chip. These performances
15 demonstrate the lanthanide-doped perovskite NCs' potential as promising alternatives to undoped
16 NCs or other phosphors for lighting applications.



17
18 **Figure 69.** (A) Emission spectrum of a WLED based on 2.7% $\text{Ce}^{3+}/9.1\%$ Mn^{2+} -codoped
19 $\text{CsPb}(\text{Cl}_{0.6}\text{Br}_{0.4})_3$ nanocrystals pumped by an underlying UV diode. Inset #1 shows the powdered

1 phosphor composite made by mixing the NCs with polystyrene (PS), and Inset #2 shows a
2 photograph of the operating device prepared by depositing the phosphor composite onto a 365 nm
3 chip. (B) CIE chromaticity coordinate plot for WLEDs using $\text{Ce}^{3+}/\text{Mn}^{2+}$ co-doped $\text{CsPb}(\text{Cl}_{1-x}\text{Br}_x)_3$
4 NC phosphors [A(0.42, 0.33), B(0.39, 0.32), C(0.37, 0.30), and D(0.33, 0.29)]. The inset shows
5 photographs of the PL from colloidal 2.7% $\text{Ce}^{3+}/9.1\%$ Mn^{2+} -co-doped $\text{CsPb}(\text{Cl}_{1-x}\text{Br}_x)_3$ NCs with
6 different values of x under 365 nm excitation. Adapted from Ref.⁶⁹¹.

7 Figure 68c shows a notable feature of PLQY of various lanthanide-doped NCs. For each
8 dopant except Yb^{3+} , the PLQY was modest summing to a combined value of $\sim 25\%$ split between
9 the exciton and the visible lanthanide transitions. For Yb^{3+} , however, the PLQY appeared to exceed
10 100%, reaching a value of $\sim 127\%$ for the f - f transition and $\sim 20\%$ for the exciton in the NCs shown
11 in Figure 68a. PLQYs over 100% in Yb^{3+} -doped crystals are rare but not unknown.⁷⁰⁶⁻⁷⁰⁸ The
12 phenomenon, referred to as "quantum cutting", has generally involved participation of pairs of
13 Ln^{3+} ions with matched energy levels, such as one Pr^{3+} + two Yb^{3+} ions. In this case, it appears
14 that the process requires only Yb^{3+} and the semiconductor NC, involving the suggested stepwise
15 energy transfer shown in Figure 68d. Although the precise microscopic mechanism of quantum
16 cutting remains uncertain at this time, quantum cutting in Yb^{3+} -doped CsPbX_3 NCs has now been
17 observed in multiple laboratories and it represents a major new direction for doped NC science.

18 The Song group's synthesis of Ln^{3+} -doped CsPbX_3 NCs involved the injection of cation
19 precursors into organic solutions of anions at elevated temperatures ($> \sim 200$ °C), akin to popular
20 procedures for preparing undoped perovskite NCs. An alternative "inverted" approach involving
21 injection of trimethylsilyl halide (TMS-X) precursors into organic solutions of the cation
22 precursors was explored by the Gamelin group: they found that higher Yb^{3+} solubilities could be
23 achieved by this approach, and that the resulting NCs showed correspondingly improved

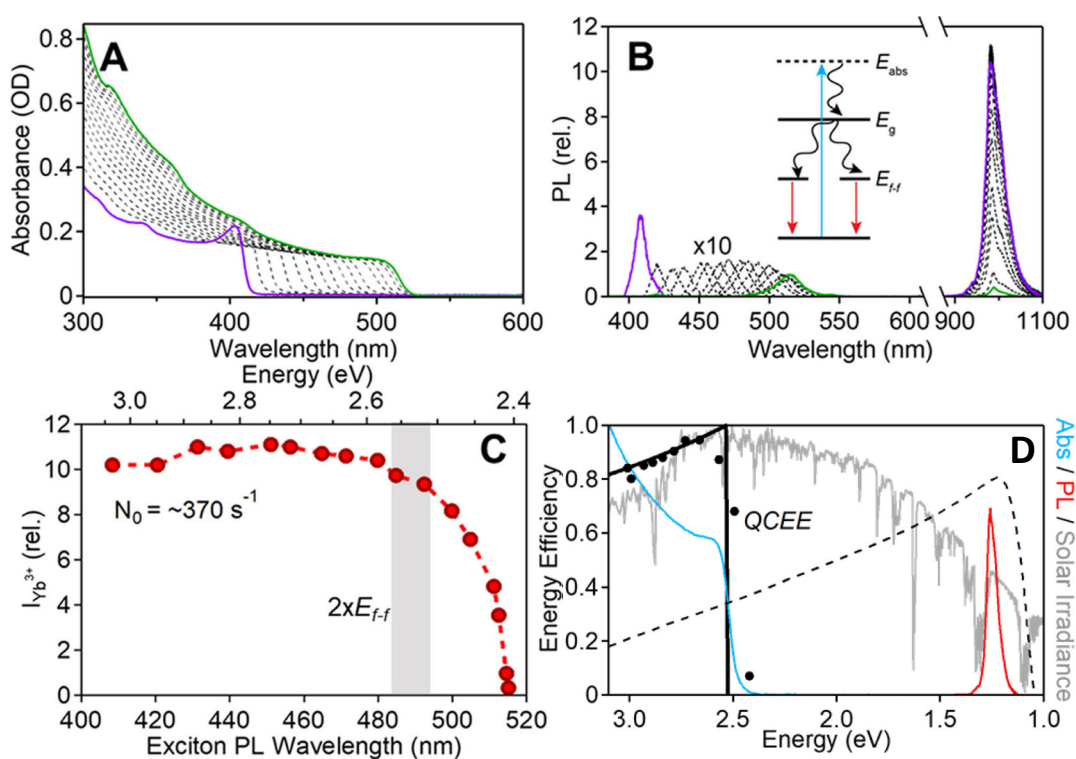
1 spectroscopic properties, specifically in the form of greater reduction of excitonic
2 photoluminescence and greater Yb^{3+} *f-f* PLQYs, now approaching 200%.⁶⁸⁸ Other methods for
3 doping Yb^{3+} into perovskite NCs have also been explored. The Nag group demonstrated post-
4 synthetic doping of Yb^{3+} into not just CsPbCl_3 NCs but also into nanoplatelets and into crystallites
5 of both CsPbBr_3 and CsPbI_3 composition.⁶⁸⁹ Yb^{3+} doping was achieved by an interesting post-
6 synthetic cation-exchange strategy, in which $\text{Yb}(\text{NO}_3)_3$ dissolved in a mixture of methyl
7 acetate:toluene is added to NC dispersions under continuous stirring for only 1 min, followed by
8 washing using MeOAc as the anti-solvent. The process is thus analogous to that recently explored
9 post-synthetic Mn^{2+} doping of lead-halide perovskite NCs,⁷⁰⁹⁻⁷¹⁰ but now involving Ln^{3+} ions. This
10 interesting chemistry reflects the extreme fluidity of the perovskite lattice, and the ability to drive
11 cation exchange reactions at room temperature. It is unclear whether these materials made by post-
12 synthetic cation exchange also show the very high PLQYs of those made at high temperature, but
13 future comparative studies could shed some insight into the participating defect structures if
14 temperature is an important contributor to their formation or stability.

15 The Gamelin group proposed a concerted rather than stepwise mechanism for the microscopic
16 quantum-cutting process.⁶⁸⁸ This group observed picosecond exciton depletion associated with
17 Yb^{3+} doping, which appeared too rapid for normal energy transfer to Ln^{3+} ions, and hence the
18 participation of a dopant-induced defect state was hypothesized. In this mechanism, energy is first
19 transferred to this defect state, where it subsequently bifurcates to excite two Yb^{3+} ions
20 simultaneously. The hypothesis of a participating shallow dopant-induced defect state is supported
21 by the observation of similar rapid exciton depletion as well as near-band-edge trap-state emission
22 when Yb^{3+} is replaced by spectroscopically innocent Ln^{3+} ions (*e.g.*, La^{3+}).⁶⁸⁸ Beyond this, the
23 microscopic details remain unclear. Because no mid-gap intermediate state is involved, the

1 excitations of the two Yb^{3+} ions must be correlated and this mechanism therefore predicts
2 correlated emission from these two Yb^{3+} ions, but such correlation remains to be demonstrated.
3 The Gamelin group also noted that the excess charge of Yb^{3+} requires compensation and speculated
4 that this compensation may be accomplished by substituting three Pb^{2+} ions with only two Yb^{3+}
5 ions, thereby creating a Pb^{2+} vacancy (V_{Pb}), by analogy to the well-known McPherson pair motif
6 in related metal-halide lattices.⁶⁸⁸ Computational work has suggested that a bent charge-neutral
7 $\text{Yb-Cl-V}_{\text{Pb}}\text{-Cl-Yb}$ defect cluster could indeed give rise to such a concerted energy transfer, and has
8 identified accumulation of charge density on neighboring Pb^{2+} ions as important in the microscopic
9 energy-transfer mechanism.⁶⁹⁵

10 A second important observation came from experiments using post-synthetic anion-exchange
11 chemistries to tune the bandgap of Yb^{3+} -doped perovskite NCs.⁶⁹⁸ Figure 70 summarizes the
12 results of one set of measurements that began with Yb^{3+} -doped CsPbCl_3 NCs. Figure 70a shows
13 that substoichiometric titrations of the reactive bromide precursor TMSBr narrowed the perovskite
14 bandgap, ultimately reaching ~ 515 nm at complete anion exchange to form Yb^{3+} -doped CsPbBr_3 .
15 Figure 70b plots the excitonic and Yb^{3+} PL spectra for each $\text{CsPb}(\text{Cl}_{1-x}\text{Br}_x)_3$ composition within
16 this series, and Figure 70c summarizes these results by plotting the Yb^{3+} PL intensity vs the exciton
17 PL wavelength. These data show that the Yb^{3+} PL intensity remains essentially constant with added
18 bromide until E_g reaches approximately 2 times the f - f energy (grey bar in Figure 70c), at which
19 point the PL drops precipitously. Further experiments showed that the PL recovered upon reverse
20 anion exchange, following much the same trajectory.⁶⁹⁸ These results verify the origin of this Yb^{3+}
21 PL as coming from a 2-for-1 quantum-cutting process. Moreover, these results demonstrate an
22 extremely high quantum-cutting *energy efficiency* (QCEE) of the sensitized PL process, quantified
23 as $QCEE = \frac{E_{\text{PL}}}{E_{\text{abs}}} \Phi \approx \frac{1.267 \text{ eV}}{E_{\text{abs}}} \Phi$. Figure 70d plots data from another experiment like that in Figure

1 70c, but now representing the data as the QCEE vs absorption threshold energy. This
 2 representation shows that experimental QCEEs exceeding 90% can be obtained, *i.e.*, only a very
 3 small portion of the energy from the absorbed photon is lost as heat, whereas the vast majority is
 4 re-emitted in the near-infrared. This value can be contrasted with the $\sim 25\%$ energy efficiency of a
 5 high-efficiency silicon heterojunction solar cell converting the same blue photon (dashed line in
 6 Figure 70d). These results have major significance for potential applications of these materials as
 7 spectral conversion layers in photovoltaics; in addition to demonstrating optimization of the
 8 bandgap for minimal thermalization loss, these results show that the emitted light is well matched
 9 to the absorption onset of red-sensitive Si photovoltaics (Figure 70d).



10
 11 **Figure 70.** (A) Absorption spectra of 7.7% Yb³⁺:CsPb(Cl_{1-x}Br_x)₃ NCs monitored during anion
 12 exchange from Yb³⁺:CsPbCl₃ (purple) to Yb³⁺:CsPbBr₃ (green). (B) PL spectra collected *in situ*
 13 during the reaction of panel A. PL spectra were measured using a constant NC excitation rate. The
 14 inset illustrates the quantum-cutting process. (C) Plot of the Yb³⁺ $^2F_{5/2} \rightarrow ^2F_{7/2}$ PL intensity vs the

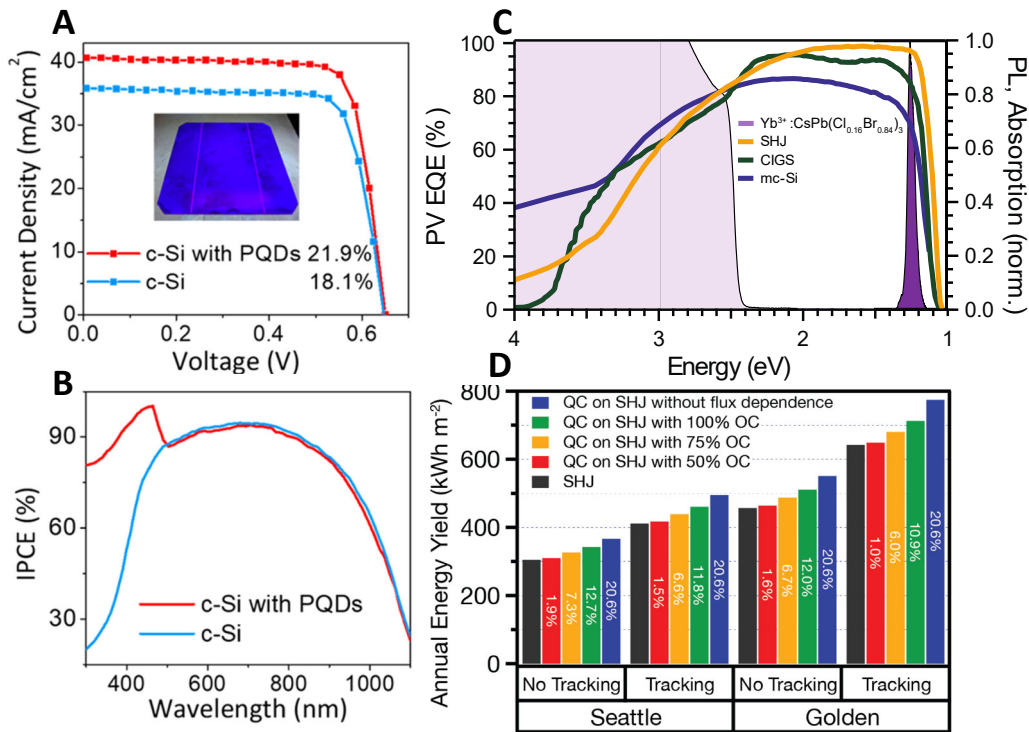
1 exciton PL wavelength, from the spectra in panel B. The gray shaded area marks approximately
2 twice the $\text{Yb}^{3+}({}^2\text{F}_{7/2} \rightarrow {}^2\text{F}_{5/2})$ absorption onset ($2xE_{f/f}$) estimated from the PL spectra, *i.e.*, the
3 anticipated energy threshold for quantum cutting in these materials below which energy
4 conservation cannot be maintained. (D) The data from a second experiment like panel C, plotted
5 as the quantum-cutting energy efficiency (QCEE) vs E_{abs} (black circles). The black curve plots the
6 idealized QCEE for bandgap-optimized $\text{Yb}^{3+}:\text{CsPb}(\text{Cl}_{1-x}\text{Br}_x)_3$ NCs ($x \sim 0.75$, solid black curve).
7 These NCs had a measured PLQY approaching 200%. For comparison, the energy-conversion
8 efficiency of a typical c-Si photovoltaic cell (dashed black), the AM1.5 solar spectral irradiance
9 (grey), and the absorption (blue) and PL spectra (red) of the $\text{Yb}^{3+}:\text{CsPb}(\text{Cl}_{1-x}\text{Br}_x)_3$ NCs are also
10 plotted. Adapted from Ref. ⁶⁹⁸.

11 To further advance the quantum-cutting properties, the Song group has developed a series of
12 bi- and tri-doped lead-halide perovskite NCs incorporating additional amounts of Pr^{3+} and Ce^{3+} ,
13 by analogy to more traditional quantum-cutting compositions.^{685, 700} Co-doping is achieved by hot
14 injection with subsequent anion exchange using PbX_2 to tune the energy gap. Pr^{3+} and Ce^{3+} both
15 possess excited states at energies close to the perovskite energy gap, and time-resolve PL
16 measurements showed participation of these ions, which dramatically slowed the arrival time of
17 the energy in the Yb^{3+} ions as detected by time-resolved PL.⁷⁰⁰ Maximum PLQYs of 173% were
18 reported for the optimized $\text{Yb}^{3+}, \text{Pr}^{3+}, \text{Ce}^{3+}$ tri-doped $\text{CsPb}(\text{Cl}_{0.33}\text{Br}_{0.66})_3$ NCs. These co-doped
19 materials may help to minimize the importance of uncontrolled traps as intermediate states in the
20 quantum-cutting process by instead routing energy through well-defined and well-controlled Ln^{3+}
21 intermediate states.

22 The Song group has made substantial progress in integrating Yb^{3+} -doped $\text{CsPb}(\text{Cl}_{1-x}\text{Br}_x)_3$ NCs
23 with both Si and CIGS photovoltaics.^{685, 700} Impressive gains in power conversion efficiencies have

1 been achieved simply by modifying the front surfaces of the PVs with doped perovskite NC
2 spectral conversion layers through a solution coating method. Layer thicknesses of ~230 nm were
3 found to allow the NCs to absorb most super-bandgap photons and downshift their energy *via*
4 quantum cutting to ~990 nm Yb³⁺ emission, without introducing too much light scattering at sub-
5 bandgap wavelengths that would interfere with transmission of those wavelengths to the
6 underlying photovoltaic. The lanthanide emission can then be absorbed by the underlying
7 photovoltaic cell. Figure 71A shows experimental $J-V$ data⁷⁰⁰ collected for a crystalline (*c*) Si PV
8 before and after coating with quantum-cutting NCs. An absolute increase of 3.1% (>20% rel.) is
9 observed in the power-conversion efficiency of this cell. Confirmation that this increase results
10 from spectral downshifting comes from the action spectrum of Figure 71B,⁷⁰⁰ which shows little
11 effect throughout the spectral response until the perovskite bandgap is reached, at which point the
12 incident power conversion efficiency increases sharply. These results demonstrate the promise of
13 these materials for making major improvements to photovoltaic efficiencies. The Gamelin group
14 has performed detailed balance calculations to assess the maximum thermodynamic efficiency
15 increases that can be anticipated from various photovoltaics types by taking advantage of this
16 quantum cutting, using the real spectroscopic characteristics of these new materials.⁶⁹⁶ Figure 71C
17 shows the spectral characteristics of the narrowest gap Yb³⁺:CsPb(Cl_{1-x}Br_x)₃ composition for
18 which quantum cutting is feasible, in comparison with the external quantum efficiency curves of
19 multicrystalline Si, CIGS, and silicon heterojunction (SHJ) cells. SHJ technology is very nearly
20 optimal for pairing with these quantum cutters because of its better red sensitivity. The calculations
21 considered various known loss processes, including power saturation⁶⁹⁷ of the quantum-cutting
22 luminescence and incomplete capture of emitted photons by the underlying cell, to project annual
23 energy yields for different implementations. Figure 71D summarizes these calculations, showing

1 that under all circumstances, sizable increases are anticipated. For example, a relative increase of
 2 7.3% is anticipated in the case where the PLQY = 200%, photon capture = 75%, and the real
 3 saturation response is included. These experimental and computational results indicate that
 4 substantial progress toward exceeding the Shockley-Queisser single-junction efficiency limit can
 5 be anticipated from this technology pending engineering advances.



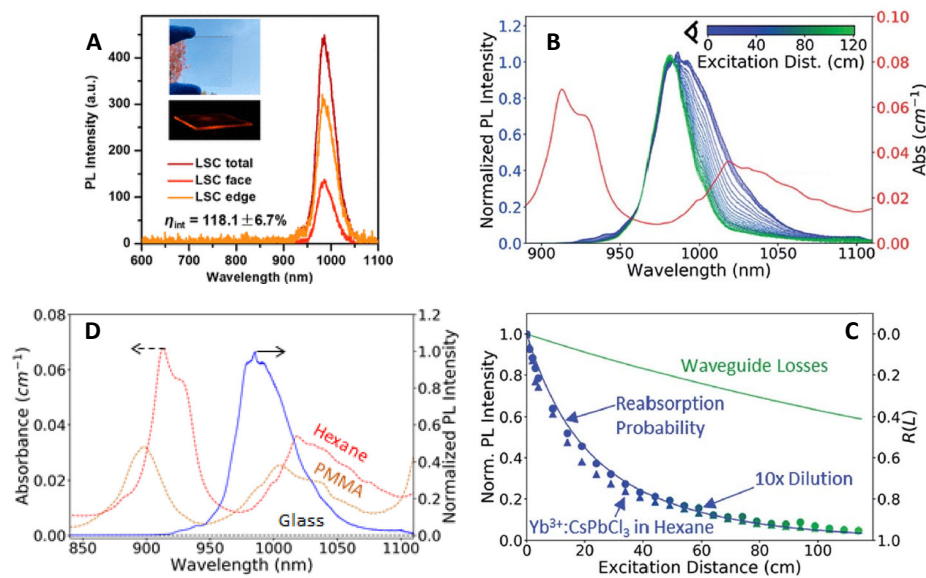
6
 7 **Figure 71.** (A) I–V curve of a single-crystal silicon solar cell with and without a coating of
 8 $\text{Yb}^{3+}(6\%)\text{-Pr}^{3+}(4\%)\text{-Ce}^{3+}(3\%)\text{-tridoped CsPb}(\text{Cl}_{0.33}\text{Br}_{0.67})_3$ NCs, showing an increase in power-
 9 conversion efficiency from 18.1% to 21.9% upon addition of the NCs. (B) IPCE (EQE) curves of
 10 a single-crystal silicon solar cell with and without a coating of $\text{Yb}^{3+}(6\%)\text{-Pr}^{3+}(4\%)\text{-Ce}^{3+}(3\%)\text{-}$
 11 tridoped $\text{CsPb}(\text{Cl}_{0.33}\text{Br}_{0.67})_3$ NCs, showing enhancement at short wavelengths where the NCs
 12 absorb. (C) The EQE characteristics of Si heterojunction (SHJ), CIGS, and multicrystalline-Si
 13 photovoltaics and the absorption and near-infrared (~ 1.26 eV) emission of $\text{Yb}^{3+}:\text{CsPb}(\text{Cl}_{0.16}\text{Br}_{0.84})_3$
 14 quantum cutters, showing the excellent match of the quantum-cutter absorption and

1 photoluminescence with the solar cell response curves, particularly for red-sensitive SHJ. **(D)** The
2 areal annual energy production yield of a $\text{Yb}^{3+}:\text{CsPb}(\text{Cl}_{1-x}\text{Br}_x)_3/\text{SHJ}$ QC/PV device with and
3 without 2-axis tracking mechanisms and for different efficiencies of optical coupling, including
4 the effects of flux-dependent PLQY. Relative percentage increases are labeled on each bar. Results
5 are presented for two geographic locations in the United States: Seattle, WA and Golden, CO.
6 Adapted from Ref. ⁷⁰⁰ (panels A, B) and Ref. ⁶⁹⁶ (panels C, D).

7 A second approach to harnessing the energy efficiency of these quantum-cutting NCs in solar
8 technologies is to integrate them into luminescent solar concentrators (LSCs). The first doped-NC
9 LSCs introduced used Mn-doped ZnSe as the active material, absorbing short-wavelength solar
10 photons and emitting from the internal Mn^{2+} *d-d* excited state.⁷¹¹ This work demonstrated that
11 doped nanocrystals excel at separating the tasks of photon absorption and photon emission,
12 yielding the lowest reabsorption losses of any spectral downshifter investigated to date.⁷¹² Mn^{2+}
13 emission occurs higher in energy than desired for this technology, however, and other copper-
14 containing luminescent NCs (*e.g.*, Cu^+ -doped quantum dots or CuInS_2) have the best overall solar
15 conversion efficiencies.⁷¹²⁻⁷¹⁶

16 Two studies have investigated using quantum-cutting $\text{Yb}^{3+}:\text{CsPb}(\text{Cl}_{1-x}\text{Br}_x)_3$ NCs in LSCs. The
17 Wu group has incorporated $\text{Yb}^{3+}:\text{CsPbCl}_3$ NCs into $5\text{ cm} \times 5\text{ cm}$ acrylic waveguides (Figure 72A)
18 and reported an internal optical efficiency (edge-emitted photons/absorbed solar photons) of 118%
19 for $\text{Yb}^{3+}:\text{CsPbCl}_3$ NCs in PMMA, extrapolating to estimate the performance of large-area
20 devices.⁶⁹⁴ The optical density of these devices was rather small (0.2 at the absorption edge),
21 possibly because of solubility limitations within the PMMA matrix. Moreover, the bandgap of
22 $\text{Yb}^{3+}:\text{CsPbCl}_3$ NCs is large, limiting absorption to only $\sim 3\%$ of the solar flux at AM1.5. The
23 external power conversion efficiency of the $5\text{ cm} \times 5\text{ cm}$ device was thus only 3.7%. Nonetheless,

- 1 the power of quantum cutting and lanthanide emission is evident, resulting in high PLQYs ($\sim 164\%$
- 2 for these NCs) and very low reabsorption of the emitted light by the same lanthanide $f-f$ transitions.



- 3
- 4 **Figure 72.** (A) Total (dark red), facial (light red), and edge (orange) emission spectra measured
- 5 from a $5 \text{ cm}^{-1} \times 5 \text{ cm}^{-1}$ LSC made using Yb³⁺-doped CsPbCl₃ NCs. The internal optical efficiency
- 6 (edge-emitted photons/absorbed solar photons) of this device was measured to be $118\% \pm 7\%$. The
- 7 top inset shows the high transparency of the LSC to visible light, and the bottom inset shows the
- 8 LSC's edge emission under UV illumination, collected with a 570 nm long-pass filter. The PLQY
- 9 of these NCs was measured to be $164 \pm 7\%$ prior to incorporation into the LSC. The optical density
- 10 of this LSC at the perovskite absorption edge is 0.2. (B) Normalized PL spectra of Yb³⁺:CsPbCl₃
- 11 NCs suspended in hexane with OD ~ 0.75 at 375 nm, obtained from a liquid 1D LSC experiment
- 12 at various excitation distances relative to the edge-mounted photodetector (inset). The red curve
- 13 shows the absorption spectrum of the hexane solvent. (C) Integrated normalized Yb³⁺:CsPbCl₃ NC
- 14 PL intensity plotted as a function of excitation distance away from the photodetector, for NCs in
- 15 hexane with OD ~ 0.75 (triangles) and OD ~ 0.075 (circles) at 375 nm. The blue trace is the
- 16 reabsorption probability predicted from a model. The green line is the experimental performance

1 limit of the 1D LSC waveguide itself. All PL data were collected with excitation at 375 nm, and
2 all data were collected at room temperature. (D) Absorption spectrum of hexane (red), a
3 representative PMMA sample (orange), and Schott optical-quality glass (black) overlaid with the
4 normalized PL spectrum of $\text{Yb}^{3+}:\text{CsPbCl}_3$ NCs (blue). Adapted from Ref. ⁶⁹⁴ (panel A) and Ref.
5 ⁶⁹⁵ (panels B-D).

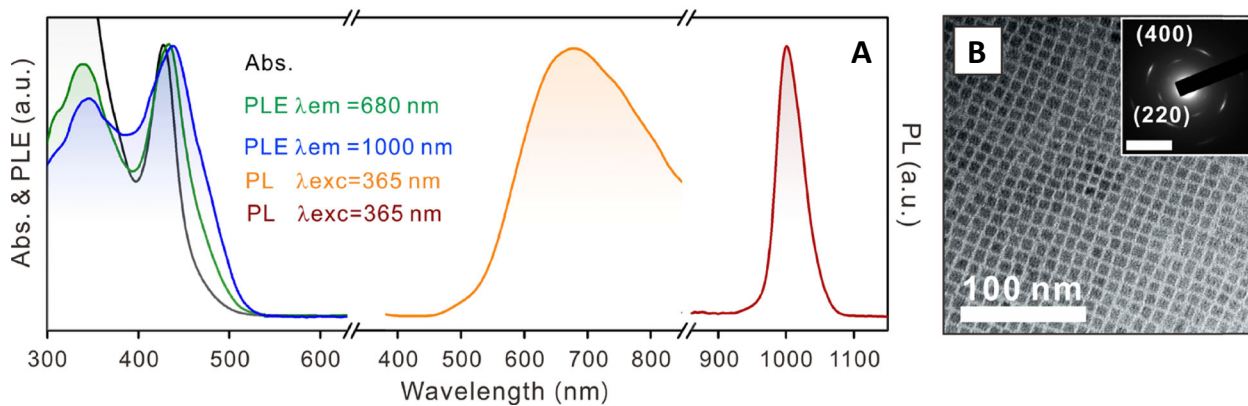
6 A key objective of LSCs is to concentrate photons harvested over large LSC facial areas onto
7 small PV areas. It is therefore critical to evaluate photon losses in large-scale waveguides, for
8 example on the scale of a building's windows, because many important loss mechanisms that do
9 not appear detrimental in short waveguides turn out to be problematic over larger distances. To
10 this end, the Gamelin group measured waveguiding within a 120 cm 1D LSC and found that
11 $\text{Yb}^{3+}:\text{CsPbCl}_3$ NC have negligible intrinsic attenuation losses over these very large waveguide
12 lengths, as expected from their strongly downshifted emission and the very small extinction
13 coefficients of the f - f transitions, but they also found severe attenuation of the f - f emission when
14 the waveguide contained C-H bonds (high-frequency vibrations).⁶⁹⁵ This result has very important
15 implications for any LSC work involving Yb^{3+} , because it precludes the use of popular acrylics as
16 the waveguide medium. This group demonstrated that the problem could be reduced or eliminated
17 by eliminating C-H vibrations within the waveguide medium. Implementation of this strategy in a
18 2D LSC will require additional waveguide innovations.

19 Beyond conventional 2D LSCs, this group further proposed and modeled a new "monolithic-
20 bilayer" LSC architecture that integrates quantum-cutting NCs with conventional LSC
21 chromophores in vertical series within the same waveguide.⁶⁹⁵ This architecture offers similar
22 advantages of tandem LSCs, but in a much simpler configuration. Modeling predicted that a
23 monolithic bilayer configuration could improve the performance of state-of-the-art CuInS_2 LSCs

1 by at least 19%, for example. Instead of summing voltages from the two layers of a tandem LSC,
2 however, the bilayer device sums the currents from each layer at the same voltage, allowing use
3 of only a single PV rather than two PVs with separate bandgaps. The bilayer approach also avoids
4 the challenge of current matching in tandem LSCs. Experimental demonstration of the device will
5 require C-H-free waveguides, as discussed above.

6 In related materials, lanthanide doping of lead-free metal-halide elpasolite (so-called "double
7 perovskite") NCs have yielded promising results that may point the way to convert these materials,
8 which generally show strong absorption but poor luminescence, into useful luminescent materials.
9 Three publications exploring Ln^{3+} doping of colloidal $\text{Cs}_2\text{AgInCl}_6$ NCs appeared within a few
10 months of one another.^{590, 593, 596} The Kim group synthesized colloidal $\text{Cs}_2\text{AgInCl}_6$ NCs doped with
11 Yb^{3+} , Er^{3+} , or both simultaneously, and they demonstrated that *f-f* emission from these lanthanides
12 can be generated by photoexcitation of the host NCs.⁵⁹³ The PLQYs in these NCs were noted to
13 be over an order of magnitude smaller than those of the $\text{Yb}^{3+}:\text{CsPb}(\text{Cl}_{1-x}\text{Br}_x)_3$ NCs, and the PL
14 excitation (PLE) spectra curiously did not reflect the absorption features of the materials. In
15 parallel, the Chen group studied Yb^{3+} doping of $\text{Cs}_2\text{AgBiCl}_6$ and $\text{Cs}_2\text{AgBiBr}_6$ NCs, showing that
16 both lattices can be used to host Yb^{3+} ions and sensitize their *f-f* luminescence.⁵⁹⁰ Figure 73
17 summarizes some key results from this study, showing the observation of both Yb^{3+} and broad trap
18 luminescence with UV photoexcitation of the $\text{Cs}_2\text{AgBiBr}_6$ NCs themselves when doped with a
19 few % Yb^{3+} . The PLE spectra track the absorption spectra, demonstrating conclusively the key
20 result of Yb^{3+} sensitization by the $\text{Cs}_2\text{AgInCl}_6$ NC host. The Nag group also examined Yb^{3+} doping
21 of colloidal $\text{Cs}_2\text{AgInCl}_6$ NCs.⁵⁹⁶ Their results highlighted that the sensitized Yb^{3+} PL is much
22 stronger than the weak, broad luminescence of the undoped NCs, and that it gets even weaker upon
23 introduction of Yb^{3+} . These observations show that Yb^{3+} competes with both nonradiative

1 recombination and trapping for the energy of the absorbed photon. Although the PLQY of all of
 2 these elpasolites were small (<10%), further synthetic advances with elpasolite NCs may help to
 3 boost this value by suppressing nonradiative decay in these materials. Notably, however, Yb³⁺
 4 doping into Cs₂AgInCl₆ and other elpasolite lattices can be achieved by isovalent substitution,
 5 meaning that it occurs without formation of the same kind of closely associated charge-
 6 compensating defect hypothesized to play a role in the quantum-cutting mechanism of the
 7 Yb³⁺:CsPb(Cl_{1-x}Br_x)₃ NCs. It is unclear whether such a defect level is actually necessary or merely
 8 incidental in those quantum-cutting compositions, and further development of luminescent Yb³⁺-
 9 doped elpasolite NCs could help to address this question. If quantum yields comparable to those
 10 found in Yb³⁺:CsPb(Cl_{1-x}Br_x)₃ NCs can ultimately be achieved in double perovskites, too, their
 11 lead-free compositions would be very attractive for large-scale solar applications.



12
 13 **Figure 73.** (A) Absorption, PL, and PLE spectra of 2.9% Yb³⁺-doped Cs₂AgBiBr₆ NCs. (B) TEM
 14 image of the Yb³⁺-doped Cs₂AgBiBr₆ NCs. Inset: SAED pattern for the same NCs (scale bar = 2
 15 nm⁻¹). Adapted from Ref.⁵⁹⁰.

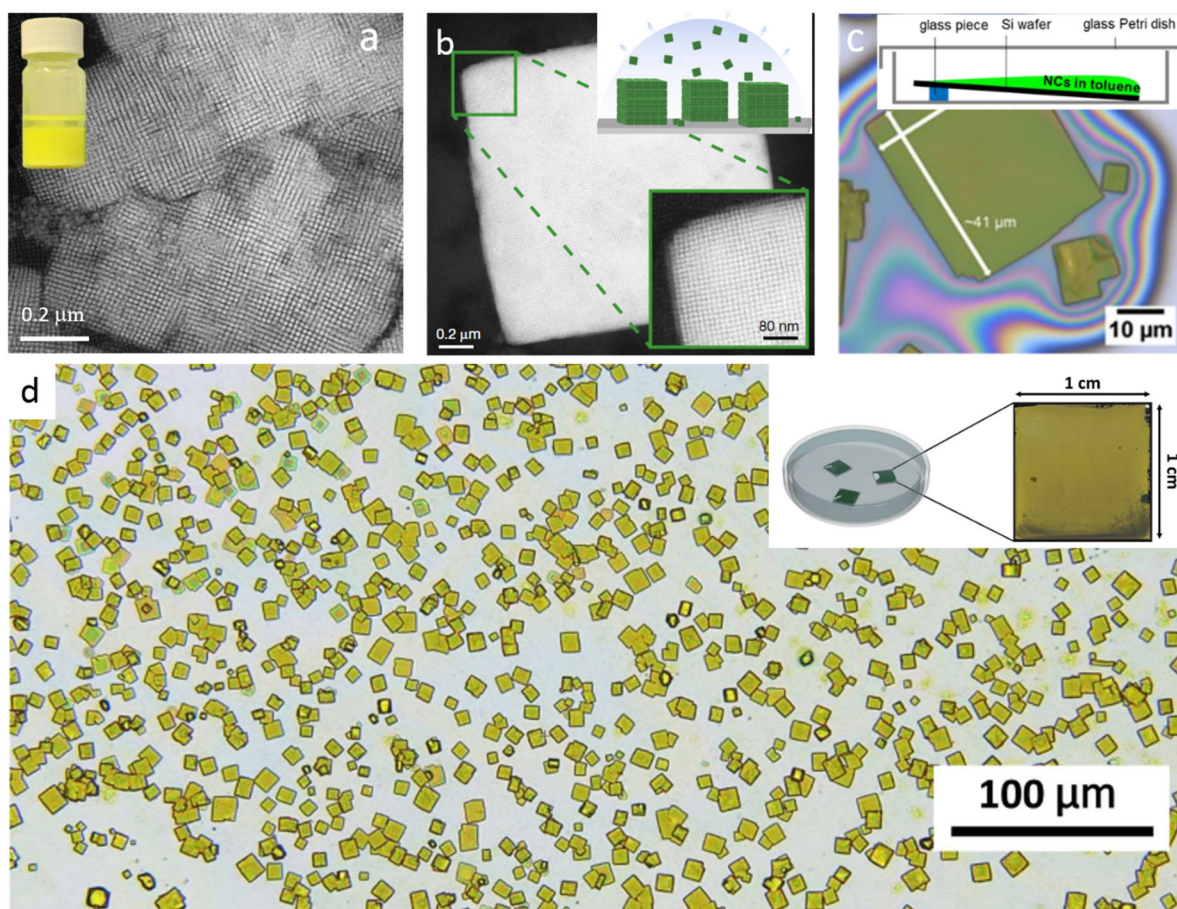
16
 17

1 7. SELF-ASSEMBLY

2 7.1 SELF-ASSEMBLY OF NANOCUBES

3 Over the last few decades, self-assembly of colloidal nano- and micro-particles into long-
4 range ordered superlattices (SLs) has been widely investigated on various material systems.⁷¹⁷⁻⁷²¹
5 Similar to atoms in crystals where the lattice defines the physical properties of the bulk compound,
6 the NCs in the SL could eventually determine new collective properties of the solid. This is a
7 crucial step for the integration of the colloidal nanostructures into devices. Uniform NCs can
8 assemble into 1D, 2D, and 3D architectures through the single component or binary (ternary) self-
9 assembly of larger and smaller particles.⁷¹⁷ The forces that drive NC self-assembly range from
10 hard- to soft-particle interactions. Taking advantage of previous knowledge gained on the self-
11 assembly of the conventional monodisperse colloidal NCs, a large variety of self-assembly
12 techniques have been reported over the years such as, evaporation-driven or destabilization-driven
13 approaches, spontaneous and template-assisted self-assembly.^{717, 719-720} Recently, these techniques
14 have been extended to self-assembly of the newly emerged halide perovskite NCs into highly
15 ordered SLs for exploration of their collective properties that can be very different from their
16 individual constituents.^{82-83, 111, 146, 164, 337, 653, 722-730} Near monodispersity of NCs and high shape
17 uniformity are important factors for obtaining long-range ordered NC SLs.^{720, 731-732} Fortunately,
18 these conditions are easily met for all-inorganic CsPbX₃ perovskite NCs as they are often prepared
19 with near monodispersity regardless of the synthesis method, as discussed in the synthesis
20 section.^{15, 54, 59, 135, 146} As a result, these perovskite nanocubes tend to self-assemble into 1D or 2D
21 SLs on a TEM grid upon solvent evaporation from a droplet of high concentrated colloidal
22 solution. First examples of CsPbBr₃ nanocube SLs date back to 2017, when 2D and 3D-assemblies
23 were obtained by the solvent evaporation method.^{111, 337, 722} In Ref.³³⁷ small superlattice domains

1 on TEM grids exhibit a simple cubic packing of the nanocubes with a lattice constant of ≈ 12.5 nm
2 and an interparticle separation of ≈ 2.3 nm. The SLs show a redshift of 15 nm compared to
3 individual NCs. Upon applying high-pressure perovskite NCs in the SLs fuse into each other and
4 the corresponding SLs transform into single-crystalline nanoplatelets. In Ref. ^{111, 722}, much larger
5 3D-aggregates were obtained on silicon substrates, and also exhibited a red-shifted PL peak at
6 room temperature.



7
8 **Figure 74.** HAAD-STEM image of CsPbBr₃ nanocube SLs obtained by spontaneous self-
9 assembly in solution (a) and by solvent evaporation (b). Reprinted with permission from Ref.⁸²⁻⁸³
10 Copyright John Wiley & Sons, Inc. 2018 and Nature Publishing Group 2018. (c) Optical
11 microscopy images of large (50 μm) CsPbBr₃ nanocube SLs prepared on top of a tilted Si wafer).

1 Reprinted with permission from Ref.¹⁴⁶ Copyright American Chemical Society 2018. (d) Large
2 area, nearly-uniform CsPbBr₃ nanocube SLs prepared on Si substrate by solvent drying in a closed
3 petri dish and the inset illustrates the experimental for self-assembly on a Si substrate in a Petri
4 dish (left panel) and an optical microscopy image of a Si substrate (right panel) covered with
5 densely-packed SLs. Reprinted with permission from Ref.⁷³³ Copyright American Chemical
6 Society 2019.

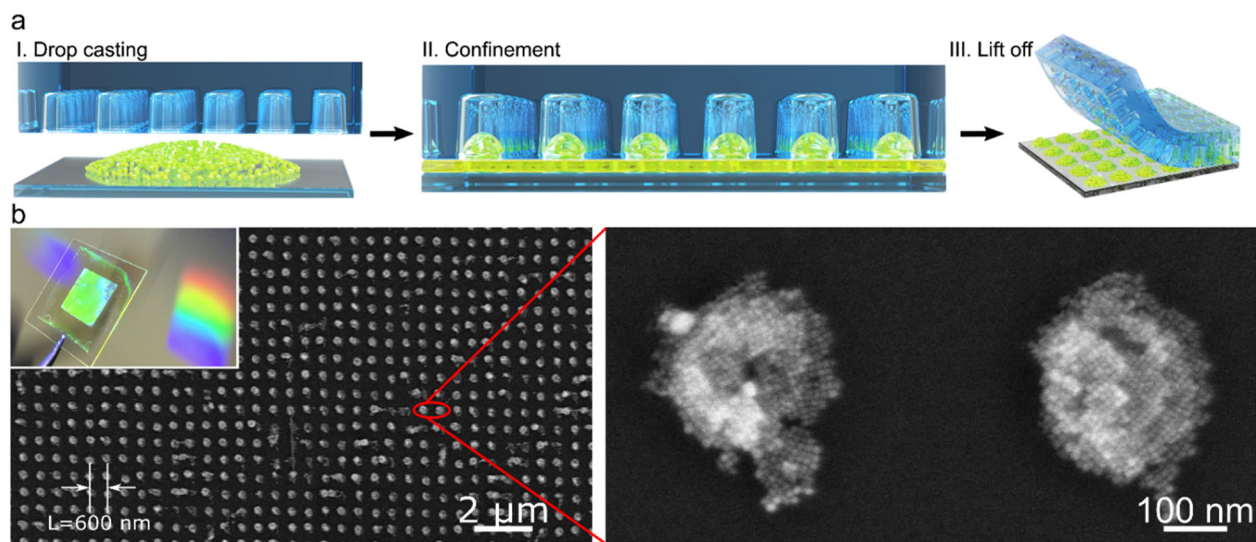
7
8 One of the interesting features of CsPbBr₃ nanocubes is that they spontaneously self-assemble
9 into SLs in a sufficiently concentrated colloidal solution, as shown by Tong et al. (Figure 74a).⁸²
10 The redshifted PL from SLs makes them better suited as pure-green emitters (ideal wavelength of
11 ca. 530nm), whereas individual nanocubes emit below 518nm. In Ref.⁸², the origin of the redshift
12 was attributed to the mini-band formation caused by the electronic coupling of nanocube subunits
13 in SLs. Interestingly, the colloidal SLs partially preserves their supercrystal morphology even after
14 halide exchange reaction, and thus their optical properties are easily tunable across the visible
15 wavelength range. However, spontaneous self-assembly has less control over the morphology and
16 size of the produced SLs. On the other hand, solvent drying techniques produce large area well-
17 defined square-shaped 3D CsPbBr₃ SLs, as first demonstrated by Kovalenko et al. (Figure 74b).⁸³
18 ¹¹¹ Interestingly, these SLs generate short, intense bursts of light—so-called superfluorescence -
19 upon light excitation due to coherent and cooperative emission of nanocubes in the SLs.⁸³ The
20 peak position of superfluorescence redshifted with more than 20-fold accelerated radiative decay
21 as compared to uncoupled nanocubes. Recently, a similar phenomenon has been reported in
22 CsPbBr₃ SLs by Xie and co-workers.⁷³⁴ They claimed that the stimulated emission of nanocube
23 assemblies in SLs is not limited by the traditional population-inversion condition. However, the

1 SLs reported in this work are not well defined regarding their morphology and the yield appears
2 to be low based on the given electron microscopy images.

3 Besides, several attempts have been made to optimize the solvent drying technique for
4 achieving large area cubic SLs with high yield.¹⁴⁶ One of the critical factors for obtaining SLs is
5 the size distribution and shape purity of the corresponding perovskite NC building blocks. In this
6 regard, Imran and co-workers¹⁴⁶ showed the fabrication of large cubic or rectangular 3D SLs (~50
7 μm lateral size) in very high yield using the shape-pure and nearly monodisperse CsPbBr_3
8 nanocubes prepared by using secondary aliphatic amines (Figure 74c). Such large size SLs have
9 been accomplished by evaporation of solvent from a colloidal solution on top of a tilted Si wafer
10 either inside a glovebox or at ambient conditions (inset of Figure 74c). Furthermore, large area,
11 nearly-uniform CsPbBr_3 NC SLs were prepared by slow solvent evaporation on a Si substrate
12 placed in a closed petri dish (Figure 74d), and the structural coherences of these SLs were revealed
13 by SL reflection peaks in wide-angle X-ray diffraction measurements.⁷³³ These are fingerprint
14 peaks to long-range order and high crystallinity of nanocubes and the angular separation if these
15 peaks are very sensitive to the periodicity of SL. It is very important to consider that the NCs of
16 SLs can coalesce into larger structures, and this can significantly effect their PL properties by
17 energy transfer process.⁷³⁵ could Despite significant progress toward the fabrication of high-
18 quality CsPbBr_3 nanocube 3D SLs, only a few studies published on the preparation of 2D and 1D
19 SLs.^{723, 725, 736} Very recently, Patra et al. demonstrated the preparation of ultra-smooth self-
20 assembled monolayer using CsPbBr_3 nanocubes functionalized with short-chain thiocyanate
21 ligands (SCN^-).⁷²⁵

22 Device applications of SLs will most likely require control over their dimensionality and
23 positioning on a given solid substrate. However, it is extremely difficult to fulfill these conditions

1 using the self-assembly techniques discussed above. Alternatively, template-assisted self-
2 assembly has been gaining significant attention to achieve these conditions.^{727, 737-738} However, the
3 packing of perovskite NCs in the assemblies patterned by this approach has yet to be investigated
4 in detail. Very recently, David et al.⁷²⁹ reported the fabrication of 2D perovskite photonic SLs
5 using pre-patterned PDMS templates. The height and lateral dimensions of the SLs were
6 controllable by the pre-designed PDMS template (Figure 75a-b). These photonic crystals exhibit
7 field enhancement at NIR excitation by light trapping mechanism. However, such self-assemblies
8 are not perfect as the SLs obtained by the slow solvent evaporation approach (Figure 75b).
9 Therefore, there is still plenty of room for the optimization of perovskite SLs obtained by the
10 template-assisted assembly. Despite rapid developments in the field of perovskite NCs, there is
11 still a lack of knowledge on the various NC assemblies such as free-standing SLs, binary and
12 ternary SLs.



13
14 **Figure 75.** (a) Schematic illustration of PDMS template assisted self-assembly CsPbBr₃
15 nanocubes into 2D photonic SLs. (b) Corresponding SEM images of 2D photonic CsPbBr₃ SLs
16 with lattice parameters of 600 nm (inset: Photograph of the CsPbBr₃ SL arrays on glass substrates

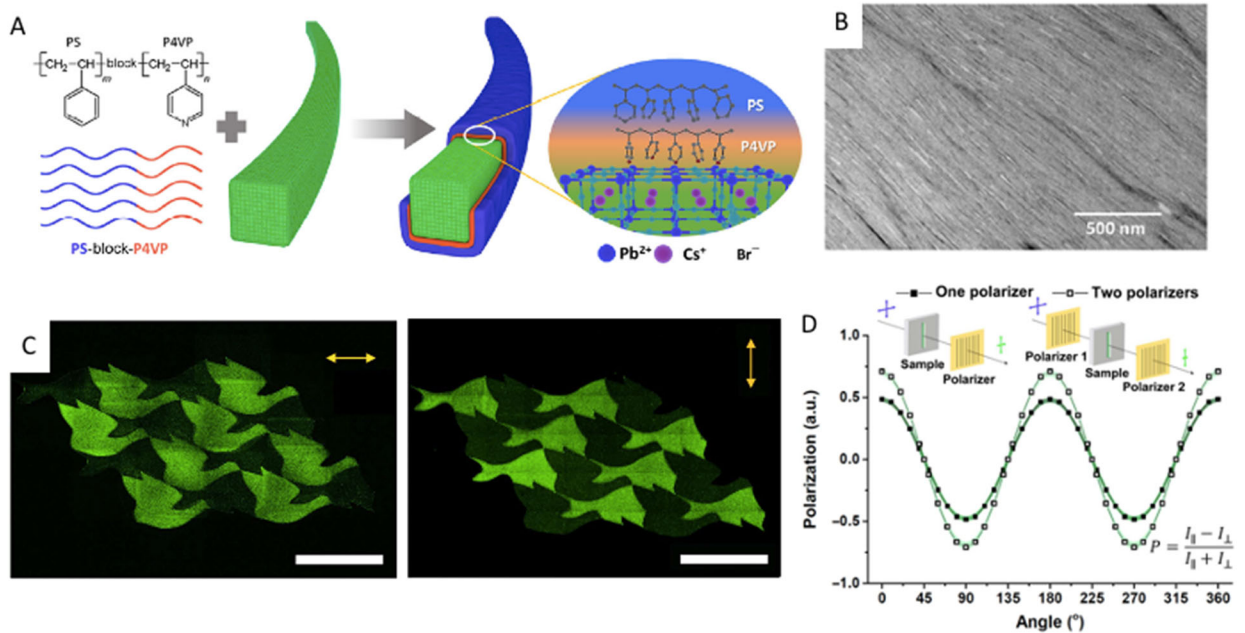
1 under white light illumination). Reprinted with permission from Ref.⁷²⁹ Copyright John Wiley &
2 Sons, Inc. 2020.

3 **7.2 SELF-ASSEMBLY OF ANISOTROPIC NCs**

4 In addition, self-assembly of other shapes including nanorods,⁶⁵³ nanowires,^{23, 739} and
5 nanoplatelets⁷²⁴ have also reported. For instance, Yang and co-workers⁷²⁴ reported the self-
6 assembly of 2D perovskite nanosheets by a layer-by-layer approach. Interestingly, the 2D
7 perovskite nanosheets SLs resemble Ruddlesden–Popper layered perovskite phase. This self-
8 assembly process is reversible as the SLs transform into individual building blocks upon
9 sonication. One-dimensional (1D) NWs show potential anisotropic optoelectronic properties
10 when they are highly oriented. It has been shown that oriented self-assemblies of perovskite NWs
11 were obtained at the air-liquid interface by Langmuir-Blodgett technique.^{23, 739} However, the ionic
12 nature of halide perovskites limits their stability at air-water assembly interface. To realize the
13 assembly of perovskite NWs with better stability against water, a core-shell type configuration has
14 been introduced by using the amphiphilic block copolymer such as polystyrene-block-poly-(4-
15 vinylpyridine) (PS-P4VP) (Figures 76A-B).⁷³⁹ The shelling polymer materials can not only
16 prevent the NW bundling, ensuring a better solution dispersion, but also improve the stability of
17 NWs against water, due to the blocking effect of hydrophobic polystyrene. For perovskite NWs,
18 the PLQY typically shows significant reduction due to their large surface-to-volume ratio
19 comparing with NCs, the polymer coating represents an effective strategy for the enhancement of
20 their absolute quantum efficiency due to the passivation effect. With a modified Langmuir-
21 Blodgett technique, the polymer-coated perovskite NWs were able to assemble into a uniform

1 monolayer with the uniaxial alignment at the air-liquid interface. The anisotropic polarized PL
 2 emission was detected at different angles from the oriented nanowire monolayers.

3 In addition to the conventional patterning method, a direct ink writing technique has been
 4 developed using the aligned cellulose fibrils embedded into a hydrogel matrix.⁷⁴⁰ This method can
 5 control the anisotropic alignment of nanocomposite with 3D architectures. The polymer-coated
 6 perovskite NW bundles were used as a printing nanocomposite ink.⁷⁴¹ It is possible to control the
 7 orientation of polymer-perovskite NW nanocomposites through the 3D printing technique, which
 8 influences their polarized PL emission (Figures 76 C-D). The polarization anisotropy in 3D printed
 9 perovskite nanowire composite could open new opportunities for optical device applications.



10
 11 **Figure 76.** (A) Schematic illustration of synthesis of block-co-polymer coated CsPbBr₃ nanowire
 12 with core-shell configurations. (B) Self-assembled nanowire monolayer from the Langmuir-
 13 Blodgett method.⁷³⁹ Copyright from Springer Nature. (C) Polarized emission from printed
 14 polymer-CsPbBr₃ nanowire composite with horizontal polarization (left) and vertical polarization

1 (right). Scale bars, 1 mm. (D) Polarized emission from printed perovskite as a function of different
2 angles⁷⁴¹. Copyright from American Association for the Advancement of Science.

3

4

1 **8. MORPHOLOGICAL AND STRUCTURAL CHARACTERIZATION**

2 As discussed in previous sections, the morphology and crystal structure of perovskite NCs play an
3 important role in their optical properties. This section is focused on the morphological and
4 structural characterization of perovskite NCs using electron microscopy and X-ray scattering
5 techniques, respectively. LHPs are very sensitive to electron beam illumination and they often tend
6 to degrade into metallic Pb. In particular, it is extremely difficult to obtain high-resolution electron
7 microscopy images. Therefore, electron microscopy images of perovskite NCs have to be acquired
8 with extreme care. We discussed the current challenges and recent advances in electron
9 microscopy studies on various kinds of perovskite NCs. On the other hand, various X-ray
10 scattering techniques have been used for the structural characterization of perovskite NCs and their
11 assemblies. We discussed the application of various X-ray scattering techniques on PeNCs,
12 ranging from common X-ray diffraction (XRD) measurements to advanced synchrotron-based in
13 situ measurements with 2D detectors. In particular, studies about phase-stability and degradation
14 are discussed. In addition, we discussed X-ray scattering studies used to investigate structure-
15 function correlations.

16 **8.1 ELECTRON MICROSCOPY**

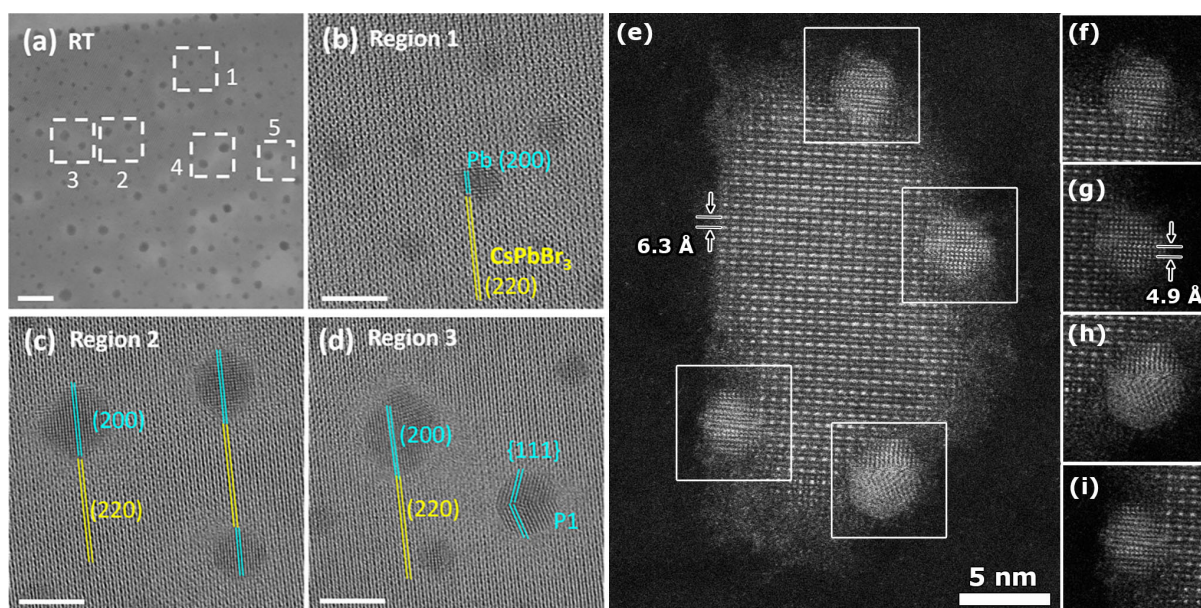
17 Aberration-corrected (scanning) transmission electron microscopy ((S)TEM) has become a
18 standard technique to investigate nanomaterials at the atomic level. With the development of C_s
19 (spherical aberration) and C_c (chromatic aberration) corrected microscopes, it has become feasible
20 to obtain structural information at the atomic scale, even using low acceleration voltages. Such
21 investigations allow us to correlate the (atomic) structure of nanomaterials with their chemical and
22 physical properties. The acquisition of atomically resolved (S)TEM images of halide perovskites
23 using conventional electron dose rates is however hindered by their sensitivity to the energetic

1 electron beam. Upon illumination, structural damage and/or phase transitions could occur, which
2 hampers a visualization/characterization of the initial (crystal) structure of the halide perovskite
3 NCs. Therefore, electron microscopy studies of halide perovskite NCs have to be performed with
4 extreme care.

5 **Degradation under the electron beam**

6 Illuminating halide perovskite NCs with an energetic electron beam results in the rapid
7 formation of high contrast particles, hampering the acquisition of an image at both nano and atomic
8 scale of halide perovskite NCs. Such behavior has been reported in multiple studies using either a
9 parallel beam in TEM mode (Figure 77a-d) or a focused electron probe in STEM (Figure 77e-i).
10 ^{17, 140, 742-747} Yu *et al.* performed comparative studies on lead halide perovskite nanostructures at
11 both low and high accelerating voltages in both TEM and STEM mode, which showed clear, rapid
12 formation of high contrast particles in all cases.⁷⁴⁷ Different claims have been made about the
13 nature of these nanometer-sized nanoparticles and the resulting structural deformations in the
14 perovskite NC.^{17, 743, 746-747} Recently, Dang *et al.* demonstrated that these particles consist of
15 metallic lead and that their nucleation mainly results from a radiolysis process.¹⁴⁰ It was shown
16 that at both low and high irradiation voltages desorption of halogen atoms from the surface of the
17 perovskites and reduction of Pb^{2+} ions to Pb^0 were induced by the interaction with the electron
18 beam. Subsequently, neighboring Pb^0 atoms diffused and aggregated into nanometer-sized,
19 spherical Pb particles. The formation of such metallic lead nanoparticles preferentially occurs at
20 the edges and corners of the perovskite NCs. Halide perovskite NCs with a high surface area-to-
21 volume ratio, such as thin nanowires and nanoplatelets, are therefore more susceptible to such
22 electron beam induced damage.¹⁴⁰ Next to the formation of metallic lead particles, degradation and
23 loss of crystallinity at the edges and/or corners of halide perovskite NCs are additional challenges

1 when investigating (thin) halide perovskite NCs. Both phenomena can be observed in movie S2
 2 (degradation of a CsPbBr₃ nanocube upon continuous scanning of the electron beam) and Figure
 3 S1 (A few selected high-resolution HAADF-STEM frames of movie S2), where the degradation
 4 of a single CsPbBr₃ nanocube is observed. This complicates the investigation of the surface
 5 termination of halide perovskite NCs since such degradation is (extremely) rapid depending on the
 6 thickness of the nanomaterial.

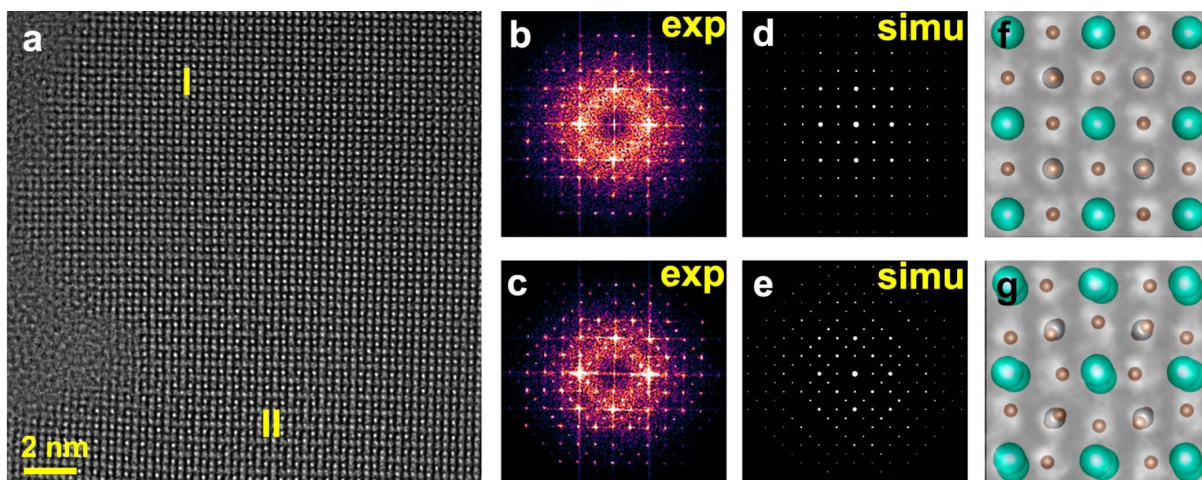


7
 8 **Figure 77.** (a-d) High resolution TEM analysis of the formation of metallic Pb particles on a 3 nm
 9 thick CsPbBr₃ nanosheet at room temperature: (a) overview image (scale bar: 20 nm) and (b-d)
 10 high resolution TEM images of three regions of interest in (a), which show the presence of Pb
 11 particles (scale bars: 5 nm). Reproduced with permission.¹⁴⁰ (e-i) High resolution HAADF-STEM
 12 image of a CsPbI₃ NC showing the presence of bright spherical particles mainly at the edge of the
 13 nanoparticle (f-i). These particles were identified as metallic Pb. Reproduced with permission.⁷⁴⁶

14 **The acquisition of atomically resolved images**

15 *All-inorganic halide perovskites NCs.* To overcome electron beam-induced sample degradation,
 16 aberration-corrected high resolution TEM,^{646, 748-750} low-dose in-line holography,⁷⁴⁷ and dose-

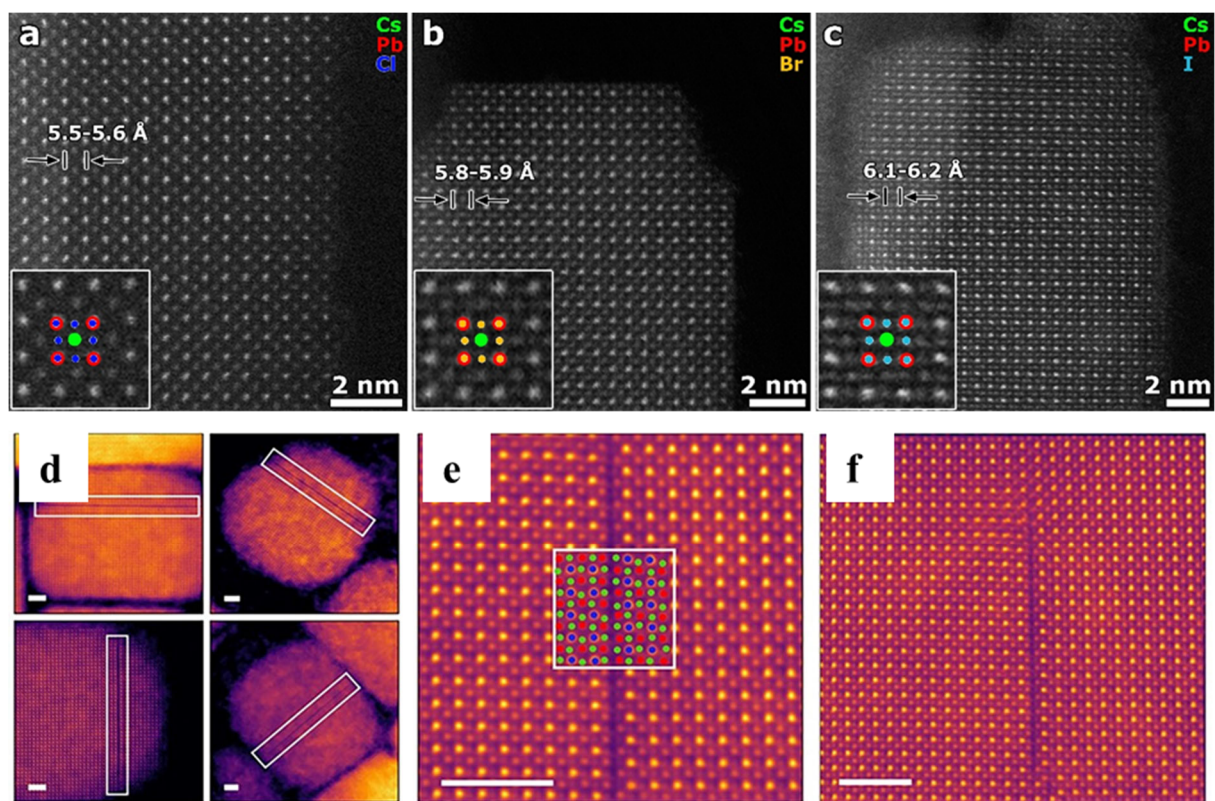
1 controlled aberration-corrected STEM imaging^{23, 75, 746-747, 751-752} have been successfully applied to
2 study all-inorganic lead halide perovskite nanomaterials at the atomic level. Yu *et al.* were the first
3 to visualize the pristine structure of ultrathin two-dimensional CsPbBr₃ perovskites by applying
4 low-dose in-line holography. Using this low-dose technique, a series of aberration-corrected high-
5 resolution TEM images were acquired and the phase information was extracted by reconstructing
6 the image series. The atomic structure of these two-dimensional CsPbBr₃ perovskites was
7 successfully studied before any electron beam-induced sample alterations had occurred. This study
8 revealed the coexistence of the high-temperature cubic and the low-temperature orthorhombic
9 phases in such CsPbBr₃ nanosheets. It must be pointed out that the two phases have a close
10 structural similarity, where only a small tilting of the PbBr₆ octahedra is necessary to transform
11 from the cubic phase into the orthorhombic phase. To distinguish between these two phases, high-
12 quality data with an optimal resolution are required. In addition, they also successfully acquired
13 single dose-controlled aberration-corrected high resolution TEM images using a negative C_s which
14 revealed this two-phase coexistence (Figure 78.a). The spatial resolution in these images is
15 sufficient to directly observe the octahedral tilting in the experimental images in Figures 78.f and
16 g, however the difference is more clearly observable in the Fourier transforms in Figures 78.b and
17 c.



1
2 **Figure 78.** Aberration-corrected high resolution TEM performed on CsPbBr₃ showing the
3 coexistence of the cubic and the orthorhombic phases. (b,c) Fourier transforms from region I (b)
4 and II (c), which are highlighted in image (a). (d,e) Simulated electron diffraction patterns of the
5 cubic (d) and the orthorhombic (e) CsPbBr₃ phase. (f,g) Enlarged images from region I (f) and II
6 (g). The cubic and orthorhombic structure models are overlaid on (f) and (g), respectively.
7 Reproduced with permission.⁷⁴⁷

8 Multiple aberration-corrected high resolution HAADF-STEM studies have been carried out to
9 investigate the crystal structure of all-inorganic lead halide perovskite NCs.^{23, 75, 746-747, 751-752} The
10 advantage of STEM imaging in comparison to TEM imaging is that the intensity in such an image
11 scales with the projected thickness of the NC and the average atomic number of the elements
12 present along the projection direction. This intensity-atomic number relation can be exploited to
13 identify atomic columns based on their composition if a significant atomic number difference is
14 present for the different elements. Thereby, the use of high resolution HAADF-STEM imaging
15 will enable a direct identification of the different atomic columns in the perovskite NC under
16 investigation (at a location of similar thickness), which is an advantage of using STEM in
17 comparison to the use of TEM. For example, for CsPbBr₃ perovskites with $Z_{\text{Pb}} = 82$, $Z_{\text{Cs}} = 55$,

1 $Z_{\text{Br}} = 35$ (Figure 79.b), this relation can be exploited to distinguish the different atomic columns
2 in the cubic [100] or orthorhombic [110] zone in a straightforward manner. In this orientation, the
3 bright atomic columns in the cubic [100] or orthorhombic [110] zone are mixed Pb-I columns with
4 an average atomic number of 58.5 due to the alternating nature of the presence of Pb and I atoms
5 in the column, which is heavier than the atomic number of Cs and Br. Subsequently, the Cs atomic
6 columns will appear brighter than the Br columns since Cs is heavier than Br, which have the
7 lowest intensity value. This intensity-atomic number relation (in combination with the knowledge
8 on the crystal structure) will also enable the elemental identification of CsPbBr₃ and CsPbI₃
9 perovskites (Figure 79.a and c, respectively). This powerful technique has been used to study
10 various all-inorganic halide perovskites. For example, Tong *et al.* revealed that CsPbBr₃ nanowires
11 were formed through oriented-attachment mechanism of initially formed CsPbBr₃ nanocubes by
12 imaging an intermediate nanowires.²³ Morrell *et al.* visualized the presence of
13 Ruddlesden–Popper planar defects in CsPbBr₃ NCs at the atomic level (Figure 79.d-f).⁷⁵²

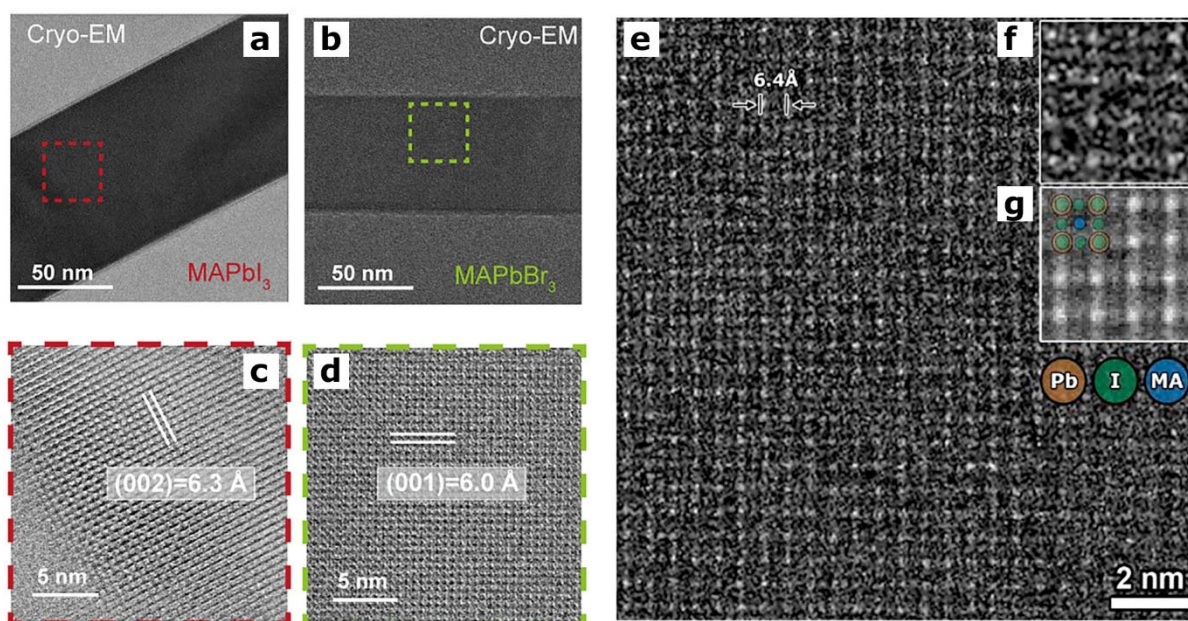


1
 2 **Figure 79.** High resolution HAADF-STEM images of a (a) CsPbCl₃, (b) CsPbBr₃ and (c) CsPbI₃
 3 perovskite nanowire. The different atomic columns are identified using the intensity-atomic
 4 number relation in HAADF-STEM imaging. Reproduced with permission.²³ (d) Overview
 5 HAADF-STEM images showing the presence of Ruddlesden–Popper planar defects (highlighted
 6 as rectangular boxes) in several CsPbBr₃ NCs. (e) Atomic resolution HAADF-STEM image of a
 7 Ruddlesden–Popper planar defect with an overlaid atomic model (blue: Pb, red: Cs and green: Br).
 8 (f) Atomic resolution HAADF-STEM image of a Ruddlesden–Popper planar defect extending
 9 only a few unit cells. The scale bars correspond to 3 nm. Reproduced with permission.⁷⁵²

10 *Organic-inorganic hybrid halide perovskite NCs.* The characterization of organic-inorganic hybrid
 11 halide perovskite NCs is even more challenging since these perovskites tend to degrade
 12 instantaneous upon electron beam illumination.^{17, 742} Recently, a few successful studies on
 13 methylammonium-based hybrid perovskites have been performed using low-dose high resolution

1 TEM⁷⁴⁶, cryogenic electron microscopy (cryo-EM)⁷⁵³, low-dose aberration-corrected HAADF-
2 STEM²⁹⁰ and integrated differential phase contrast STEM (iDPC-STEM)⁷⁵⁴. The first atomically
3 resolved HRTEM image of a CH₃NH₃PbBr₃ perovskite was collected using a Gatan K2 direct-
4 detection electron-counting camera by Zhang *et al.*⁷⁵⁵ The high detective quantum efficiency of a
5 direct-detection camera enables the investigation of highly beam sensitive materials as extremely
6 low-dose conditions can be applied. In this work, they revealed that the CH₃NH₃PbBr₃ crystals
7 consist of ordered nanometer-sized domains with off-centered CH₃NH₃ cations with an in-plane
8 and out-plane orientation, which provides direct evidence of the ferroelectric order in
9 CH₃NH₃PbBr₃. Cryo-EM is a technique which is often used to study the native state of a
10 material/specimen by rapidly freezing the material. This technique is mostly used in life sciences.
11 Recently, Li *et al.* preserved the native state of methylammonium-based hybrid perovskites by
12 plunge-freezing the sample in liquid nitrogen which enabled them to observe the atomic structure
13 of the native state of CH₃NH₃PbI₃ and CH₃NH₃PbBr₃ nanowires in Figures 80.c and d,
14 respectively.⁷⁵³ The high resolution cryo-TEM images were acquired at a temperature of -175°
15 using a direct detection camera in electron counting mode. The use of such cameras will be of key
16 importance to further progress in the study of these beam sensitive hybrid halide perovskites. In
17 addition to these low-dose HRTEM studies, the use of HAADF-STEM has also been proven
18 successful for the study of hybrid halide perovskites although it is often referred to as more
19 destructive when imaging halide perovskites. Debroye *et al.* were able to retrieve the native atomic
20 structure of CH₃NH₃PbI₃ NCs using low-dose aberration-corrected HAADF-STEM imaging in
21 combination with a template-matching procedure (Figure 80.e-g).²⁹⁰ The low-dose condition
22 resulted in the acquisition of a single HAADF-STEM image (Figure 80.e) with a very low signal-
23 to-noise ratio hampering the interpretability of the image. The template matching algorithm

1 statistically averaged a small part of the HAADF-STEM image resulting in an image with an
 2 improved signal-to-noise ratio. Such an algorithm searches throughout the image for specific
 3 regions which match the template (Figure 80.f). In this work, the perovskite lattice of a hybrid lead
 4 iodide perovskite was successfully observed in the final averaged template in Figure 80.g. This
 5 technique can only be used for an averaged observation of the crystal structure, local defects and/or
 6 the surface termination of the NC cannot be investigated using this averaging technique. The
 7 development of pixelated electron detectors has enabled another approach for low-dose high
 8 resolution STEM imaging using iDPC-STEM. A first iDPC-STEM attempt for the investigation
 9 of $\text{CH}_3\text{NH}_3\text{PbBr}_3$ perovskites was performed by Song *et al.*⁷⁵⁴



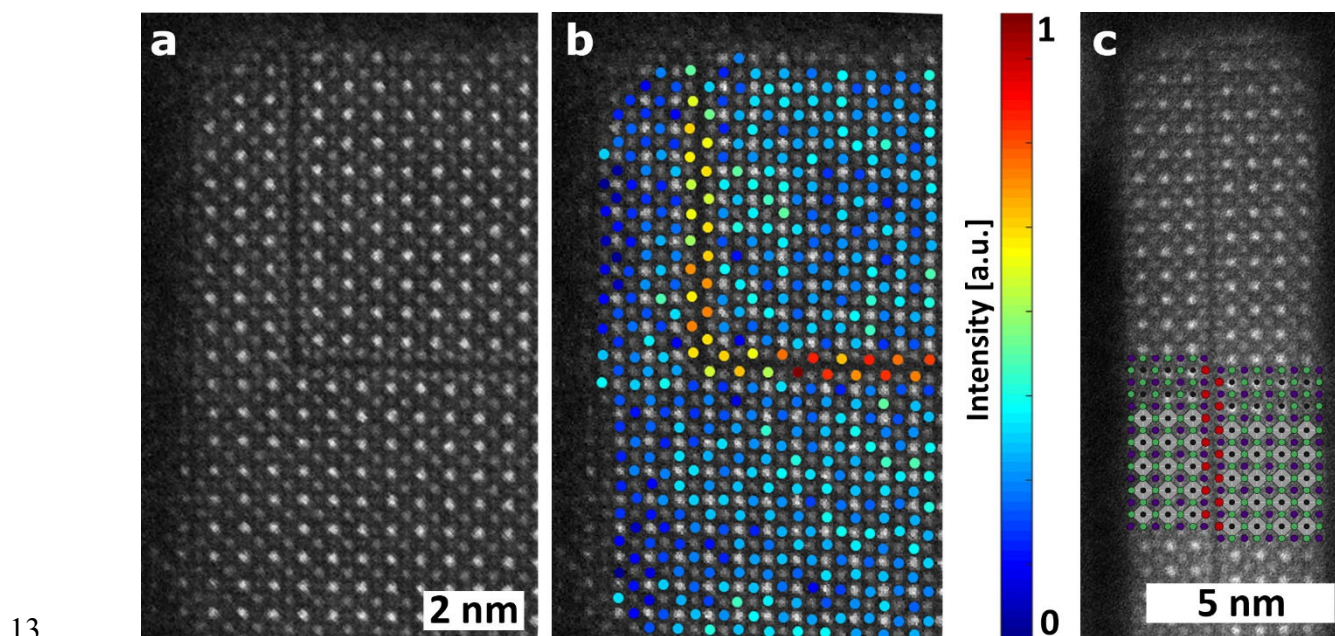
10
 11 **Figure 80.** (a-d) Cryo-EM investigation of $\text{CH}_3\text{NH}_3\text{PbI}_3$ and $\text{CH}_3\text{NH}_3\text{PbBr}_3$ nanowires. Overview
 12 cryo-EM images of both rods are visualized in (a) and (b). Atomically resolved TEM images
 13 capturing both the PbI_6 octahedra and the methylammonium molecules in $\text{CH}_3\text{NH}_3\text{PbI}_3$ (c) and
 14 $\text{CH}_3\text{NH}_3\text{PbBr}_3$ (d). Reproduced with permission.⁷⁵³ (e-g) Low-dose aberration-corrected HAADF-
 15 STEM imaging in combination with a template-matching procedure on a $\text{CH}_3\text{NH}_3\text{PbI}_3$ NC. The

1 atomic arrangement of the $\text{CH}_3\text{NH}_3\text{PbI}_3$ NC is clearly resolved in the averaged template (g) of the
2 low-dose HAADF-STEM image in (e), performed on the template image in (f). Reproduced with
3 permission.²⁹⁰

4 **Going beyond qualitative images**

5 Quantitative methods are emerging to retrieve additional in-depth information on halide
6 perovskite NCs such as the measurement of lattice parameters unit cell by unit cell. Such a
7 measurement will enable the unambiguous identification of the cubic and orthorhombic structure
8 of lead halide perovskite NCs, which differ approximately 0.05 Å in lattice parameter. This
9 requires the identification of the different atom types and a precise measurement of their atomic
10 column positions. In addition, the precise localization of the atom positions enables the
11 investigation of possible PbX_6 (X = Cl, Br, I) octahedral tilt, which is expected in the orthorhombic
12 phase. In principle, such an analysis can be performed both using aberration-corrected TEM and
13 STEM imaging. However, the identification of the atom types in each atom column in atomically
14 resolved TEM images is not straightforward, since the intensity in such images is not sensitive to
15 chemical information. In order to distinct between different atom types, a quantitative statistical
16 phase analysis needs to be carried out. In this manner, tilting of the PbX_6 octahedron was observed
17 in CsPbBr_3 nanosheets using in-line holography (Figure 80.f and g).⁷⁴⁷ In addition, a unit cell by
18 unit cell characterization of the lattice parameters showed that both the cubic and orthorhombic
19 phases exhibit a lattice expansion compared to their bulk counterpart, while still being able to
20 identify orthorhombic regions from cubic regions as they exhibit smaller lattice distances.⁷⁴⁷
21 Quantification of the atom positions in an atomically resolved STEM image of a CsPbX_3 (X=Cl,
22 Br, I) NC can be performed in a more straightforward manner, since the average atomic numbers
23 of the different atom columns are sufficiently large and the intensity in such images scales with

1 the atomic numbers of the present elements. Van der Stam *et al.* confirmed a lattice contraction
2 after a cation exchange in colloidal CsPbBr₃ NCs resulting in doped CsPb_{1-x}M_xBr₃ NCs (M= Sn²⁺,
3 Cd²⁺, and Zn²⁺; 0 < x ≤ 0.1).³²² Here, the lattice parameters are quantified using statistical
4 parameter estimation theory⁷⁵⁶⁻⁷⁵⁷ to retrieve the atom positions of each atom column. In addition,
5 the intensity-atomic number relation in HAADF-STEM imaging can be used to identify different
6 atom types in mixed halide perovskites. Akkerman *et al.* investigated all-inorganic Ruddlesden-
7 Popper double Cl-I and triple Cl-Br-I lead halide perovskite NCs and the position of the different
8 halides in the perovskite structure using quantitative high resolution HAADF-STEM imaging
9 (Figure 81).⁷⁵⁸ The intensities of the halide atom columns were calculated by fitting a Gaussian
10 function to each atom column (Figure 81.b). This work revealed that the small amount of iodide
11 clusters at the Ruddlesden-Popper planes. Up to date, quantitative (S)TEM techniques have only
12 been applied successfully to all-inorganic halide perovskite NCs.



14 **Figure 81.** (a) High resolution HAADF-STEM image of a CsPb(Cl:Br:I)₃ NC showing the
15 presence of plane shifts. (b) Calculated volume of the fitted Gaussian peaks of the halide columns

1 of the NC indicates increased intensity values of the halide columns around the
2 Ruddlesden–Popper planes, confirming an increased concentration of iodide ions at these
3 positions. (c) Ruddlesden–Popper plane shift model (Cs^+ = purple, Pb_2^+ = black, Cl^-/Br^- = blue,
4 I^- = red, and PbX_6 octahedra = gray) overlapping an HAADF-STEM image of a $\text{CsPb}(\text{Cl}:\text{Br}:\text{I})_3$
5 NC. Reproduced with permission.⁷⁵⁸

6 **Summary and outlook of electron microscopy studies on MHP NCs**

7 The previous sections have shown that halide perovskites have been studied successfully at
8 the atomic level using a range of techniques. Although these perovskites are very sensitive to the
9 electron beam, both the use of a parallel beam as a focused probe have been exploited. Most of
10 these studies dealt with beam damage and therefore often low-dose conditions are required to study
11 the native state of these halide perovskites. Recently, a few successful studies have been performed
12 on organic-inorganic hybrid halide perovskite NCs. The use of novel detectors with a high
13 detective quantum efficiency has played a big role in lowering the necessary dose needed to study
14 the native state of hybrid halide perovskites. Despite recent advances, there are still many
15 challenges in the electron microscopy characterization of perovskite NCs. For example,
16 quantitative determination and location of dopants in perovskite NCs is one of the main challenges
17 to be addressed for a better understanding of doped-perovskite NCs. It is well-known that LHPs
18 undergo phase changes at certain temperatures, and this has often studied by optical and X-ray
19 characterization. It would be very interesting to probe such phase changes at the atomic level with
20 in situ electron microscopy characterization at the single-particle level to obtain new insights.
21 Another important challenge is to apply 3D atomic imaging techniques to perovskite NCs to study
22 their crystal structures.

1 **8.2. X-RAY SCATTERING TECHNIQUES AND THEIR IMPACT ON THE STABILITY** 2 **AND DEGRADATION ANALYSIS OF PEROVSKITE NCs**

3 X-ray scattering is a powerful technique to investigate structures not only on atomic lengths scales
4 (angstroms, Å) but also on the mesoscale (nm). High time resolution is feasible, especially with
5 synchrotron radiation, and in situ investigations on many different NC systems are conceivable.
6 This approach gives insights into the kinetics as well as structure-function correlations. Especially
7 when coupled to other in-situ techniques, e.g. UV/VIS or photoluminescence (PL) measurements,
8 X-ray scattering is a versatile and fruitful technique for providing a quantitative understanding.

9 So far, X-ray scattering techniques have shown a high impact by analyzing the crystal structure of
10 perovskite NCs : Besides probing the inherent crystal structure (crystal lattice topography) the
11 ordering and alignment of perovskite NCs (superstructure) can be analyzed. Thus, X-ray scattering
12 techniques are a precise analysis tool for crystal and super-structure, crystal orientation, phase
13 identification and phase change tracking in perovskite NCs, which are used in different areas
14 ranging from photovoltaic and photo-detectors to LEDs.⁷⁵⁹⁻⁷⁶³

15 The focus of this section lies in the application of various X-ray scattering techniques on perovskite
16 NCs, ranging from common X-ray diffraction (XRD) measurements to advanced synchrotron-
17 based in situ measurements with 2D detectors. Especially studies about stability and degradation
18 will be mentioned, as well as studies about structure-function correlations. We aim to give also
19 insights into more advanced scattering techniques such as grazing-incidence small- and wide-angle
20 X-ray scattering (GISAXS and GIWAXS) and experimental setups that will help to improve
21 perovskite NC research and facilitate the road towards broader use of mentioned methods.

22 Fundamental understanding of the stability of perovskites is still one of the big challenges in the
23 field.^{110, 764-765} Thus, mechanisms of degradation have to be investigated in detail and, whenever

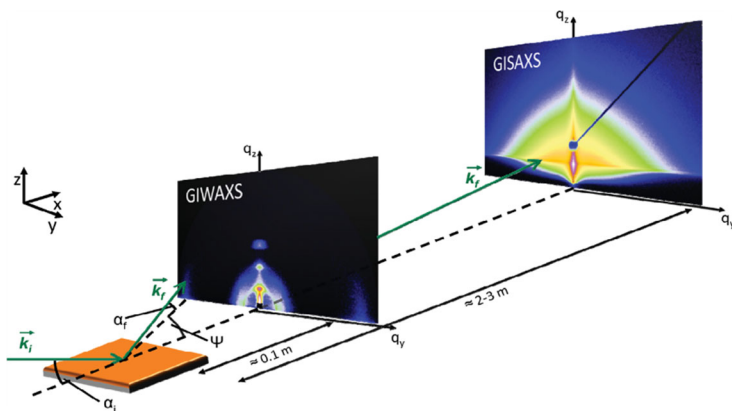
1 possible, with high time resolution. Investigations that capture processes in real time are commonly
2 referred to as in situ (in place) in contrast to ex situ (out of place) experiments, that only capture
3 the status after the time-dependent process. In situ experiments usually pose additional
4 experimental challenges, e.g. the necessity of high flux X-ray radiation (e.g. via synchrotron
5 access) and transportable experimental setups, detailed knowledge of reaction kinetics, as well as
6 considering damage induced by the high-intensity X-ray beam. In situ and operando studies have
7 already been used heavily on bulk and thin-film materials and offer many possibilities in
8 perovskite NC thin-film analysis including the elucidation of superstructural features.⁷⁶⁶⁻⁷⁷⁰

9 **Introduction to X-ray scattering methods used in the characterization of MHP NCs**

10 Elastic X-ray scattering is a non-destructive reciprocal space technique, i.e. it yields the Fourier
11 transform of the electron density of the probed material. This results in a diffraction pattern that
12 contains information about typical reciprocal distances in the sample, denoted \vec{G} . These distances
13 can be probed by X-ray scattering. Photons of wavelength λ impinge on the sample and are
14 scattered if they fulfill the Laue condition $\vec{k}_f - \vec{k}_i = \Delta\vec{k} = \vec{G}$, with incoming wavevector \vec{k}_i , final
15 wave vector \vec{k}_f and reciprocal lattice vector \vec{G} . Thus, the momentum change of the photon depends
16 on the structural lattice ordering of the sample. The momentum change q can be converted to a
17 real space distance d using the equation $q = 2\pi/d$. The scattering event results in a change in the
18 photon's trajectory which can be given as an angle 2θ using the Bragg equation $n\lambda = 2d \sin\theta$.
19 Diffraction peaks (reflexes) are indexed according to the diffractive planes that give rise to the
20 interference pattern. For indexing, Miller indices (hkl) are used. Further details about diffraction
21 techniques on functional material, e.g. perovskite LED and PV application, can be found in
22 literature.⁷⁷¹⁻⁷⁷³

1 In laboratories, X-ray diffraction (XRD) in Bragg-Brentano reflection geometry is well suited for
2 thin-film studies including perovskite NCs. Besides classical XRD measurements, with the use of
3 2D detectors, additional scattering methods have been established. Depending on the detector
4 placement, small- or wide-angle X-ray scattering (SAXS or WAXS) can be observed, which
5 corresponds to large and small distances probed, respectively. Whereas SAXS and WAXS are very
6 powerful for the analysis of volume samples, to study supported thin-films can be challenging. A
7 substantial contribution from the support can challenge the analysis of the thin-film. In such cases,
8 grazing-incidence small- and wide-angle X-ray scattering offer possibilities for structure analysis.
9 GISAXS and GIWAXS are performed in reflection geometry with a fixed grazing-incidence angle
10 ($\alpha_i \ll 1^\circ$). This offers the possibility to minimize substrate contributions to the scattering signal
11 by selecting an incidence angle below the critical angle of the substrate, thus preventing the
12 penetration of the incident beam into the substrate and/or subsequent layers. X-ray scattering is
13 not a local method like high-resolution real-space imaging and can probe an ensemble of small
14 crystallites, with the probe volume depending on the beam size. Especially when considering the
15 grazing-incidence geometry, the illuminated surface area can be rather large (order of mm^2). The
16 probed volume depends on the penetration depth, which is dependent on the X-ray wavelength and
17 the sample material.

18



1
 2 **Figure 82.** Schematic illustration of a typical GIXS setup with reference geometry. Photons with
 3 wavevector \vec{k}_i impinge on the sample under an incidence angle α_i . Scattered photons with
 4 wavevector \vec{k}_f leave the sample under an in-plane exit angle α_f and an out-of-plane exit angle Ψ .
 5 GIWAXS and GISAXS require different sample-detector-distances, typically in the range of
 6 around 100 mm and 2-3 m, respectively. Reproduced with permission.⁷⁷⁴ Copyright 2019,
 7 WILEY-VCH Verlag GmbH & Co. KGaA

8 A typical experimental GIXS setup is shown in figure 82.⁷⁷⁴ The reference coordinate system is
 9 commonly placed onto the sample surface, with z being normal to the surface, x along the beam
 10 direction and y perpendicular to the xz plane. When placing the 2D detector rather close to the
 11 sample (around 100 mm), GIWAXS patterns can be observed. GIWAXS probes the crystalline
 12 part of the sample and results in a 2D diffraction pattern on the detector. Questions that aim at
 13 texture or morphology analysis can only be partially answered by XRD, since only a small region
 14 around $q_r = \sqrt{q_x^2 + q_y^2} \approx 0$ is probed. In GIWAXS, however, a full 2D plane in q_r and q_z is
 15 recorded. The image on the detector is a result of the orientation sphere of the reciprocal lattice
 16 points cutting the Ewald's sphere. Unfortunately, the projection onto a 2D grid results in a range
 17 of missing q -values, because $q_x \neq 0$. The usual 2D representation in reciprocal space plots the
 18 momentum change q_r versus the momentum change in z -direction q_z . Thus, besides the classical

1 crystal structure, it can give information about the preferential orientation or texture of crystallites
2 on the sample. Diffraction peaks and rings are labelled in analogy to XRD patterns. From the width
3 of the Bragg diffraction peaks and rings the upper limit for crystallite size can be extracted using
4 the Debye-Scherrer equation.⁷⁷⁵ Bragg spots can arise for highly ordered systems with long-range
5 order, e.g. single crystals or ordered superlattice diffraction of NCs, due to distinct points in the
6 reciprocal lattice space of those systems. In contrast, missing preferential orientation of the
7 crystallites results in a powder scattering, which is identified from the ring shape of the intensity
8 maxima on the 2D detector.

9 When moving the 2D detector to larger distances on the order of 1-4 m, a GISAXS signal can be
10 recorded. GISAXS probes distances on the mesoscale (nm-regime) and is commonly used to
11 investigate the morphology, i.e. domain sizes and inter-domain distances of thin-films or
12 superstructures of NCs. Not only the crystalline parts of the sample contribute to the scattering,
13 since GISAXS probes the dispersion of the sample, which in turn is related to the scattering length
14 density (SLD). SLD is a material-specific property. Refraction inside the film leads to enhanced
15 out-coupling under the critical angle of the thin-film (so-called Yoneda peak). By analyzing this
16 material-sensitive Yoneda region by horizontal line cuts (in q_y direction), material-specific
17 structure information is accessible. For the analysis commonly the so-called distorted wave Born
18 approximation (DWBA) is combined with several approximations such as the effective interface
19 approximation (EIA) and the local monodisperse approximation (LMA). For more information the
20 reader is referred to the literature.⁷⁷⁶⁻⁷⁷⁷ In addition, GISAXS patterns of highly ordered systems
21 show Bragg peaks similar to GIWAXS, which, however, originate from a larger scale structure as
22 compared to GIWAXS.⁷⁷⁸⁻⁷⁸²

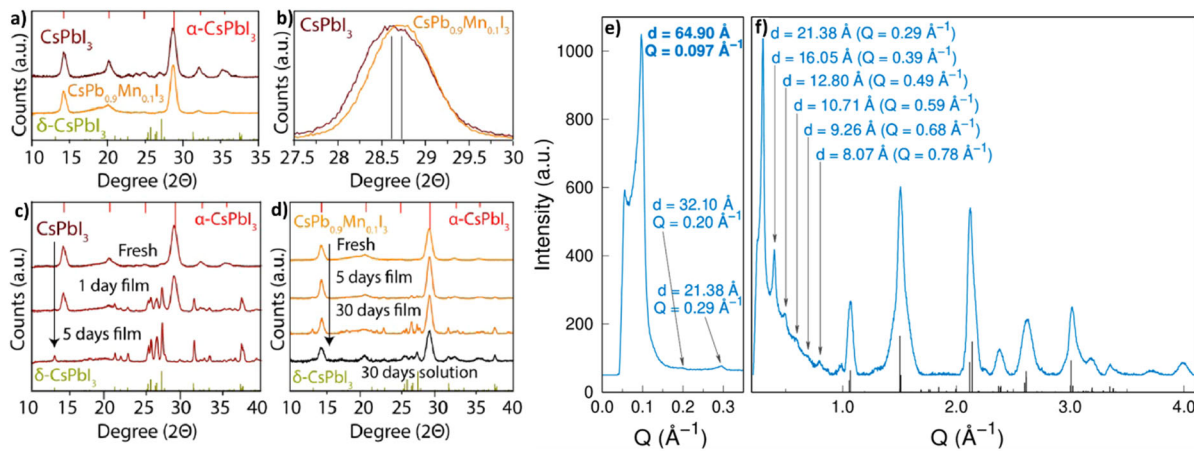
1 **1D X-Ray diffraction measurements**

2 Common XRD measurements with 1D detectors are probably the most frequently used X-ray
3 scattering technique and available in many laboratories at moderate cost. The collection of XRD
4 patterns can be a powerful and comparatively easy tool to identify and distinguish phases in a
5 sample. A complete measurement can often be conducted in less than one hour including sample
6 preparation and measurement set-up. Measurements of thin-films, e.g. when dealing with PeNCs
7 deposited on a substrate, are possible by using the Bragg-Brentano geometry.^{473, 783-785}
8 Straightforward studies employ *ex situ* XRD measurements. By comparing XRD patterns to
9 libraries, previous measurements, or literature, crystalline phases can be identified with a high
10 degree of certainty.^{473, 637, 760, 786-789} For example, Bertolotti et al used X-ray scattering techniques
11 to analyze the long sought after crystal structure of thin-films of CsPbBr₃ nanoplatelets (NPLs).²²⁰
12 The high asymmetry of NPLs favors narrow-band emission acting as nanowells with well-defined
13 dimensions and low variation, thus resulting in discrete bandgaps, which are very beneficial for
14 LED application. The crystal structure of NPLs is not easily accessible because of their quasi-2D
15 shape. In their study, a combination of low- and high-angle XRD and wide-angle X-ray total
16 scattering (WAXSTS) was used. The high-angle XRD region interestingly suggested an
17 orthorhombic crystal structure as shown in figure 83f. The result was confirmed via Debye
18 Scattering Equation (DSE) modeling.^{775, 790-791} Discriminating between different phases – even for
19 small crystallites like NPLs – is an important feature of X-ray scattering by accessing a statistically
20 relevant ensemble of crystallites. The low-angle region in XRD on the other hand, gives
21 information about large distances present in the structure. In this case, it revealed inter-platelet
22 distances as shown in figure 83e. The first peak appeared at $q = 4\pi \sin \theta / \lambda = 0.097\text{\AA}$ which

1 corresponds to a distance of $d_1 = 64.90 \text{ \AA}$. The high degree of long-range ordering was confirmed
 2 by the high number of harmonics towards higher 2θ -values marked with d_n in figure 83f.

3 Time-dependent XRD studies

4 To investigate kinetic changes, time-dependent XRD measurement protocols are well suited. This
 5 is especially useful for degradation studies that occur over many hours up to months, and the same
 6 measurement is repeated at certain intervals. Numerous stability related studies were done on
 7 perovskite NC systems and examined by time-dependent XRD studies.^{638, 785, 788, 792} For example,
 8 MAPbBr₃ perovskite NCs can be effectively stabilized by essential amino acids as identified by
 9 an unchanged XRD pattern over 6 months.⁷⁸⁶ CsPbBr₃ NCs for white LEDs showed higher
 10 resistance against heat and moisture-induced degradation by coating with alkyl phosphate⁷⁸⁷ and
 11 CsPbX₃ NC was effectively stabilized by a PMMA matrix as shown by time dependent XRD
 12 studies over several days in 80% rel. humidity.⁷⁹²



13
 14 **Figure 83.** (a) XRD patterns of CsPbI₃ and Mn-substituted phase. The calculated α - and δ -phase
 15 patterns are shown in red and green, respectively. (b) Zoom in of (a) to visualize the shift in Bragg
 16 peak position due to Mn-induced lattice parameter changes. (c-d) Time-dependent XRD patterns
 17 of CsPbI₃ and CsPb_{0.9}Mn_{0.1}I₃ over several days, showing the difference in degradation kinetics.

1 Reproduced with permission.^{638, 793} Copyright 2017, American Chemical Society. (e,f) Low and
2 high angle XRD pattern of CsPbBr₃ nanoplatelets. The first peak corresponds to a distance of the
3 NPs of 6.5 nm. Higher harmonics are also visible which confirms the high degree of long-range
4 order. The NPs have a thickness of around 3.5 nm as confirmed by TEM imaging. From the high
5 angle region, an orthorhombic structure could be determined. Reproduced with permission.²²⁰
6 Copyright 2019, American Chemical Society.

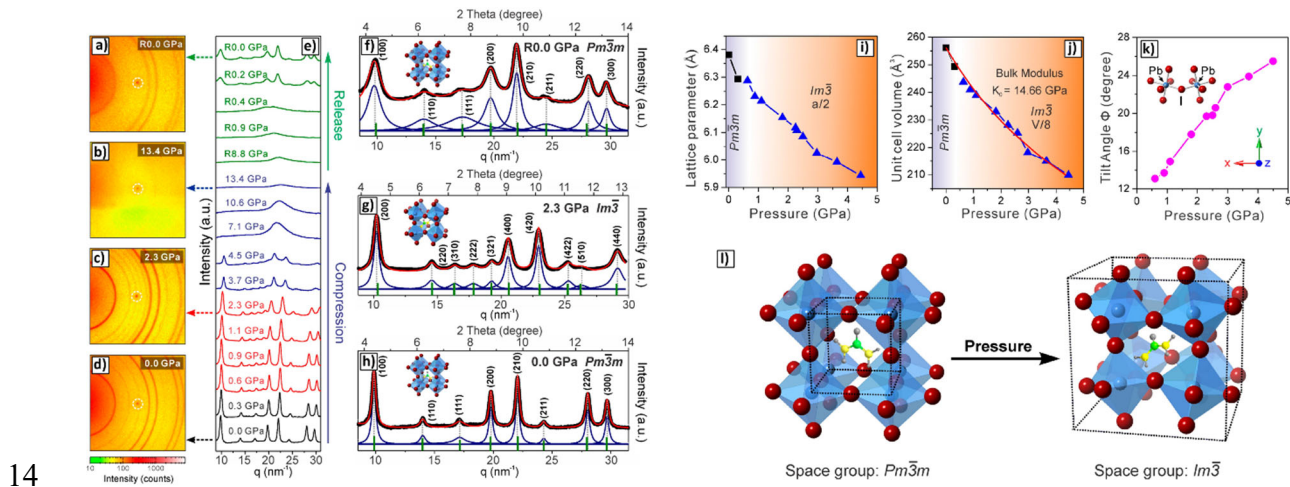
7
8 A different approach towards stabilizing CsPbI₃ was reported by Akkerman et al and confirmed
9 by time-dependent XRD measurements.⁶³⁸ It is well known that the stability of the cubic perovskite
10 α -phase is connected to the Goldschmidt tolerance factor and thus the stability can be tuned by site
11 occupation substitution.⁷⁹⁴ Pristine CsPbI₃ suffers from poor stability and is unstable in air. The
12 cubic α -phase decomposes rapidly (within days) into the yellow δ -phase and corresponding time-
13 dependent XRD data is shown in figure 83c-d. For obtaining stable cubic α -CsPbI₃, Pb was
14 partially replaced by Mn without significant changes to the crystal structure and, more importantly,
15 without inducing significant changes in PL, trPL and absorption properties of the material as was
16 shown by Liu et al.⁶³⁷ Klimov et al showed that Mn-doping can even be beneficial for its emission
17 properties.⁷⁹⁵ By adding MnI₂ to the precursor solution, alloying could be achieved by Akkerman
18 et al resulting in a cubic drop-cast CsPb_xMn_{1-x}I₃-phase. Meanwhile, the octahedral (Pb/Mn)O₆
19 geometry was preserved. The partial substitution of Pb with Mn led to a small reduction in unit
20 cell size and towards a more favorable Goldschmidt tolerance factor for a cubic system (see also
21 previous sections on doping/alloying of NCs). Thus, the structure factor of the crystallographic
22 unit cell changes, which resulted in a changed X-ray diffraction pattern. The decrease in unit cell
23 was verified by XRD measurements shown in figure 83b. CsPb_xMn_{1-x}I₃ showed increased stability

1 as proven by time-dependent XRD measurement over the course of 4 weeks. In figure 83d the
2 partial transition towards the orthorhombic delta phase can be seen starting on day 5 at around 25-
3 $28^\circ 2\theta$. As predicted by DFT calculations a lattice contraction of around 1 % was observed in XRD
4 (cf. figure 83b) for the chemical composition $\text{CsPb}_{0.91}\text{Mn}_{0.09}\text{I}_3$ resulting in decreased metal-iodine
5 bonds.

6 Challenging for PeNCs, especially for CsPbI_3 NCs, is the poor stability against illumination. Boote
7 et al followed the degradation of drop-cast CsPbX_3 NCs thin-films by time-dependent XRD for up
8 to 16 h under 1 sun irradiation and ambient conditions.⁷⁸⁸ They found that CsPbBr_3 was phase-
9 stable (orthorhombic γ -phase) under 1 sun illumination for up to 16 h and when heating up to 250
10 $^\circ\text{C}$. CsPbI_3 , however, was most volatile in the CsPbX_3 series as the non-luminescent yellow phase
11 appeared, as can be identified by decreasing Bragg diffraction intensity, which indicated
12 decomposition into a non-crystalline or amorphous phase.⁷⁸⁸ However, after some hours of
13 illumination and before the loss of crystallinity occurred, CsPbCl_3 and CsPbBr_3 showed an
14 increased intensity and decreased FWHM of the (100) and (200) reflexes. This led to the
15 conclusion of crystal growth and possibly oriented crystal growth with a changed preferential
16 orientation of the NCs. However, XRD by itself is only partly able to elucidate the texture of an
17 ensemble of crystallites. Preferential orientation is better probed by (GI)WAXS, which is
18 described below. CsPbI_3 thin-films washed with methyl acetate solution, for example, showed no
19 change in Bragg peak intensity and were stable under continuous illumination.^[24] XRD confirmed
20 the same phase and no observable crystallographic changes under illumination. This highlights the
21 importance of surface quality in perovskite NCs and their influence on the PeNCs stability.

22 XRD studies can also help to elucidate degradation mechanisms. It is known that CsPbBr_3
23 degrades to a yellow phase under illumination, which is accompanied by a strong PL-quenching,

1 thereby decreasing the EQE of an LED-device drastically. Huang et al carried out studies with
 2 different stress factors on the device, e.g. illumination, oxygen, humidity and temperature.⁷⁶⁰
 3 Illumination of 175 mW/cm² for 8 h led to a color change of the thin-film from green to yellow.
 4 The degradation was tracked using time-dependent XRD measurements. The cubic (100) and (200)
 5 Bragg reflexes of the perovskite NCs first broadened and then increased in intensity and sharpness.
 6 This indicated a crystal growth and thus was correlated with an observed PL red shift. Under higher
 7 illumination strength of 350 mW/cm² the degradation species PbO was identified via XRD after
 8 8h. The driving force of degradation was determined to be O₂ in combination with illumination
 9 strength and moisture, which seemed to support ion migration in crystal growth. Supported by
 10 XRD analysis, it was shown that under oxygen stress but no illumination no yellow phase and no
 11 PL loss occurred. Li et al showed by XRD analysis that cubic CsPbBr₃ NC-495 thin-films also
 12 degraded into PbCO₃ and PbO and Cs₄PbBr₆ under illumination in ambient conditions.⁷⁹⁶ Larger
 13 NC-520 thin-films did not decompose within 20 h of illumination.



14 **Figure 84.** (a-d) In situ GIWAXS patterns of FAPbI₃ NCs during compression and subsequent
 15 decompression with (e) corresponding pseudo-XRD pattern (radially integrated GIWAXS
 16 decompression with (e) corresponding pseudo-XRD pattern (radially integrated GIWAXS
 17 images). White circles represent noise. (f-h) Fitted and indexed pseudo-XRD patterns with

1 structure representation and corresponding calculated reflex positions. (i-k) Derived lattice
2 parameters, unit cell volume and octahedral tilt angle evolutions depending on pressure. (l)
3 Schematic representation of the structural changes occurring during pressure increase. The $[\text{PbI}_6]^{4-}$
4 -octahedron tilts along the cubic $[111]$ -direction. Reproduced with permission.⁷⁹⁷ Copyright 2018,
5 American Chemical Society.

6 **2D GIXS imaging: Applying advanced X-Ray scattering techniques**

7 When texture and morphology information about the sample are of critical interest, XRD can only
8 supply insufficient information, since it only provides information along $q_r \approx 0$. For texture
9 and/or morphology investigations, a larger q -space needs to be probed. As described above, small-
10 and wide-angle X-ray scattering onto a 2D detector can be the solution to this problem. Details
11 about those measurement techniques are described above.

12 For example, Zhu et al investigated the phase transitions of FAPbX_3 NCs, $x = \text{Cl, Br, I}$, by in situ
13 WAXS and UV/VIS measurements during the application of pressure in the range from 0 to 13.4
14 GPa.⁷⁹⁷ Pressure was applied by using a customized diamond anvil cell that enabled WAXS
15 measurements at a synchrotron at the same time. Radial integration of (GI)WAXS images lead to
16 a pseudo-XRD plot (signal intensity vs q) that can be indexed in analogy to XRD patterns. Indexing
17 the cut at ambient conditions showed a cubic space group ($Pm\bar{3}m$) and a lattice constant of $a =$
18 6.35 \AA . While increasing the pressure the WAXS pattern changed. First, additional Bragg rings
19 appeared as seen in figures **Figure 84a-d**, which was attributed to a different cubic phase ($Im\bar{3}$).
20 Corresponding pseudo-XRD patterns are shown in figure 84e. Further increase in pressure led to
21 increased tilting of the $[\text{PbI}_6]^{4-}$ -octahedron (cf. figures 84f-h) and increasing FWHM of the Bragg
22 rings. The latter usually indicates smaller crystallites or a loss in crystallinity. As expected, a
23 decrease in lattice parameters was observed (red-shifted q -values). Before the sample finally

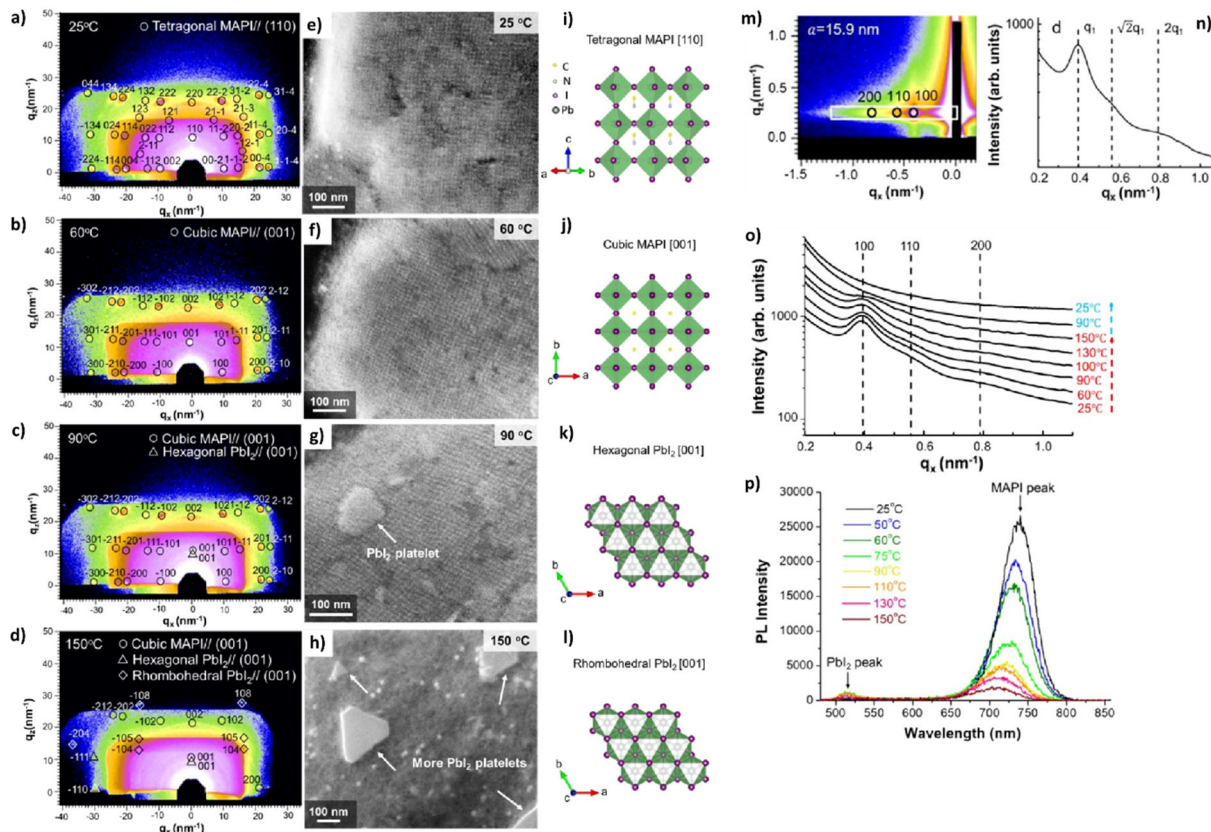
1 transformed into the amorphous state, degradation into the orthorhombic phase (*Pnma*) was
2 observed. The amorphous state was reversible when decreasing the pressure below 0.4 GPa. At
3 this point a fast reordering into the original cubic $Pm\bar{3}m$ -phase occurred. However, the Bragg rings
4 showed a broadening compared to the original sample at ambient conditions, indicating a slight
5 loss in crystallinity of the FAPbI₃ NC film. Often scanning electron microscopy (SEM) or
6 transmission electron microscopy (TEM) measurements are chosen to verify and improve the
7 structure model developed through X-ray scattering methods. Via TEM measurements it was
8 confirmed that no significant change in particle size and shape was induced by the pressure cycle.
9 The complete lattice parameter and unit cell volume evolution as deduced from WAXS analysis is
10 plotted in figures 84i-k. The corresponding tilt of the [PbI₆]⁴⁻-octahedron is shown in figure 84l.
11 In situ PL and UV/VIS measurements showed a pressure tunable bandgap between 1.44 and 2.17
12 eV. This WAXS study successfully correlated structural changes to optoelectronic properties that
13 might be vital for further research and the development of industrial production techniques. The
14 results may influence the fine-tuning of the bandgap for applications in optoelectronic devices like
15 PV or LEDs.

16 **Investigation of superstructures by advanced X-Ray scattering techniques**

17 Perovskite materials can be driven to self-assembly into 1D, 2D or 3D superlattices which has
18 given rise to focused research on targeted functionalization of low dimensional perovskites and
19 perovskite NC superlattice structures.^{194, 763, 772, 798-804} Improved strategies to control shape and size
20 have been found in recent years and targeted tuning is within reach.^{803, 805} As more methods for
21 self-assembly and directed superlattice growth of NCs become available also the need for more
22 detailed structural, superstructural and morphological characterization techniques arises. Long-
23 range ordering of the NCs leads to a scattering signal. However, depending on the magnitude of

1 the superlattice parameters, too long distances cannot be probed by conventional XRD. Long
2 distances, corresponding to exceedingly small diffraction angles of less than 2° 2θ are better
3 accessible by increasing the sample detector distance to several meters. (GI)SAXS is a suitable
4 tool to investigate superlattice ensembles revealing information in q_y and q_z direction.^{772-773, 799,}
5 ⁸⁰⁶

6 Horizontal line cuts can be performed on the 2D GISAXS data in the Yoneda region, which gives
7 information about the typical stacking distances present in the sample. From the q -ratio of those
8 peaks a first structure model can be derived, e.g. from the q -ratios $q : \sqrt{q} : 2q$ for a simple cubic
9 superlattice structure.^{193, 800, 807} Further information about GISAXS interpretation and
10 morphological modeling can be found above. Especially in combination with TEM/HRTEM and
11 FFT analysis of real-space imaging, (GI)SAXS can give precise information about superlattice
12 stacking, as explained above.¹⁹⁴ The interplay between superstructure and crystal structure
13 changes, and optoelectronic properties is of key interest for optoelectronic device research. The
14 combination of in situ (GI)WAXS and (GI)SAXS can be immensely powerful to track phase
15 transition and superlattice changes simultaneously. Real-space methods like SEM/TEM/STM can
16 be used complementary to reciprocal space imaging techniques and probe local areas and ensemble
17 information, respectively.⁸⁰⁸

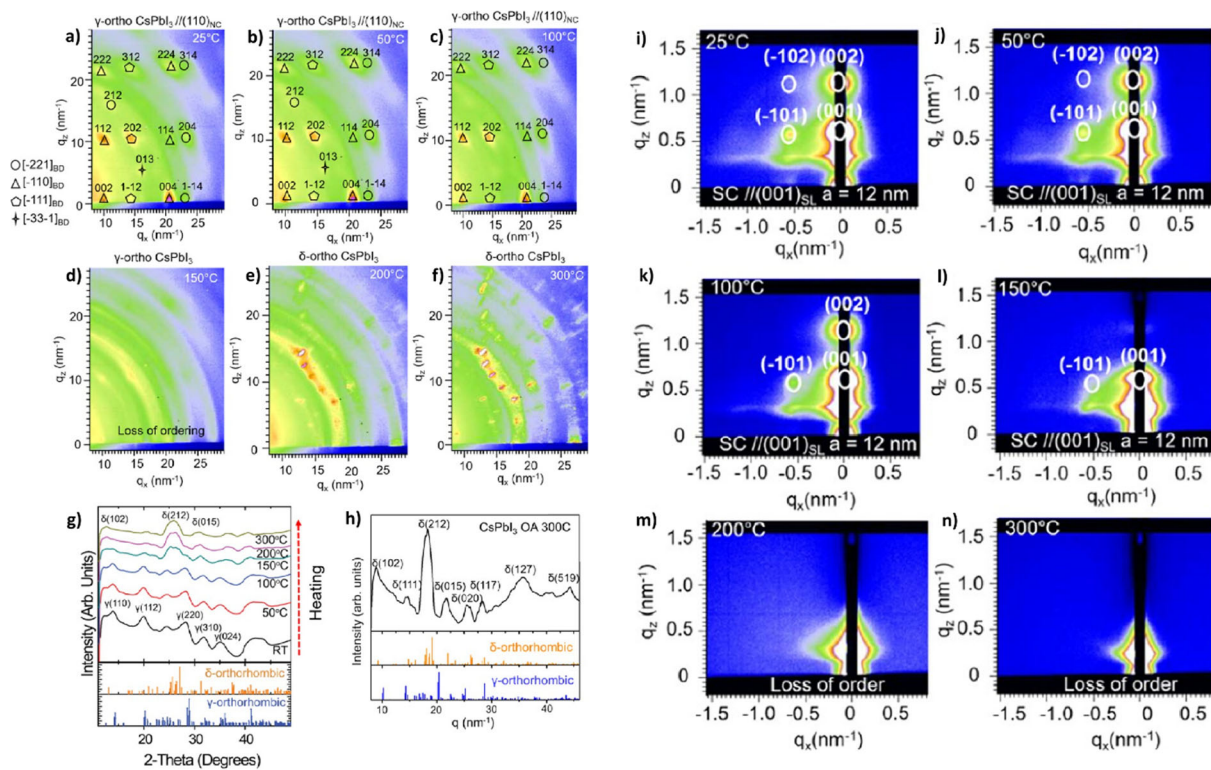


1
 2 **Figure 85.** (a-d) In situ GIWAXS images of MAPbI₃ NCs heated to 150 °C. The attenuation on
 3 the side is due to experimental restrictions. The pattern suggests high ordering with the tetragonal
 4 (110)-plane oriented parallel to the substrate. A phase transition from tetragonal to cubic is
 5 observed at around 60 °C. At higher temperatures hexagonal and also rhombohedral PbI₂ can be
 6 identified as a degradation product. (e-h) Corresponding SEM images and (i-l) corresponding
 7 derived structure representations. (m-n) GISAXS image and azimuthal cut to determine the cubic
 8 superstructure with a superlattice constant of 15.9 nm. The three largest distances are marked. (o)
 9 Horizontal GISAXS cuts (along q_x), showing a clear loss in ordering at around 150 °C. The
 10 diffraction peaks stem from a cubic superlattice. (p) PL emission spectra taken with an excitation
 11 wavelength of 442 nm. Reproduced with permission.¹⁶⁴ Copyright 2019, American Chemical
 12 Society.

1 For example, Zhang et al investigated the thermally induced crystal and superstructural
2 changes of luminescent cuboidal MAPbI₃ NCs by in situ GISAXS and GIWAXS imaging.¹⁶⁴ They
3 found that the chosen evaporation method formed MAPbI₃ NC films with an ordered superlattice.
4 In figure 85m a GISAXS image of MAPbI₃ NCs is shown which exhibits distinct in-plane features
5 that can be indexed to a cubic superlattice. A horizontal line cut (cf. figure 85n) shows a distinct
6 peak at around 0.4 nm⁻¹, which corresponds to a superlattice constant of around 15.9 nm. GISAXS
7 images were taken during the heating and cooling process and an evolution of cuts is shown in
8 figure 85o. Thereby the authors could show that the ordering of the lattice persists under elevated
9 temperatures until approximately 150°C. This agreed with steadily decreasing PL intensity as
10 shown in figure 85p. GIWAXS patterns (cf. figure 85a) were indexed to a tetragonal space group
11 with an orientation of mainly the (110) plane parallel to the substrate. Distinct Bragg spots were
12 visible in the GIWAXS pattern, which agreed with the high ordering of a superlattice. Upon
13 heating to 60 °C, a phase transition from tetragonal to cubic was observed. In situ GIWAXS
14 patterns, corresponding SEM images and schematic representations are found in figures 85a-d,
15 figures 85e-h and figures 85i-l, respectively. When reaching 90 °C, MAPbI₃ NCs started to
16 decompose and highly oriented hexagonal (001)-PbI₂ was found. At 150 °C rhombohedral PbI₂
17 ($R\bar{3}m$) was visible in the GIWAXS pattern as a degradation product and all superlattice ordering
18 was lost (cf. figures 85d,h,o). In this study, the scattering methods of in situ GIWAXS and
19 GISAXS were used in combination with real space SEM/TEM imaging to elucidate the exact
20 phase at varying temperatures, phase transition points, phase changes and preferential orientations
21 of MAPI NCs during thermally induced degradation. Thomas et al applied in situ GISAXS and
22 GIWAXS to investigate the heating response of all-inorganic cube-shaped CsPbI₃ NCs under
23 humid conditions in air.¹⁹³ The perovskite NCs were ligand-stabilized to improve their resistance

1 to moisture degradation by providing a hydrophobic shell. GIXS was used to investigate the
2 degradation and phase transitions as well as loss of superstructural ordering. Indexing of GIWAXS
3 patterns taken at RT showed the γ -orthorhombic phase ($Pbnm$) as shown in figures 86a,g. The
4 spot-like pattern indicated a high degree of ordering into a superlattice with γ -(110) and γ -(002)
5 being oriented parallel to the substrate. Often, indexing is tested for different space groups to
6 sufficiently explain the full diffraction pattern. In this case, indexing with a cubic phase left some
7 Bragg spots unexplained and therefore the γ -phase was favored. The black γ - or α -phase of $CsPbI_3$
8 is the optoelectronically interesting phase as opposed by the yellow δ -phase. In situ GIWAXS
9 imaging while heating γ - $CsPbI_3$ from RT to 300°C under 40% relative humidity, revealed the γ -
10 to- δ phase transition occurring at around 150°C (cf. figures 86a- h). GISAXS suggested a simple
11 cubic superstructure with a lattice spacing of 12 nm and (001)_{SL} orientation (cf. figures 86i-n). A
12 complete loss of the cubic superlattice ordering was observed at 200°C. Whether the phase
13 transition leads to a loss in superlattice ordering, or a loss in ordering makes a phase change more
14 favorable is difficult to tell. Thomas et al believe that the main driving force was the thermally
15 induced loss in surface capping ligands.

16



1
 2 **Figure 86.** (a-f) In situ GIWAXS images of CsPbI₃ NCs taken during heating from RT to 300 °C.
 3 Distinct Bragg spots indicate high ordering with the orthorhombic (110)-plane parallel to the
 4 substrate. (g-h) Pseudo-XRD patterns generated by azimuthal cuts to compare with calculated
 5 XRD-patterns of the γ - and δ -phase. Bragg peaks of interest are indexed to the corresponding
 6 phase. (i-n) In situ GISAXS images taken during the heating process. Clear long-range ordering
 7 of the NCs into a superstructure is visible. The loss of ordering starts at around 150 °C. Reproduced
 8 with permission.¹⁹³ Copyright 2019, American Chemical Society.

9
 10 GIXS can also be coupled to other in situ techniques like TEM, PL or UV/VIS, which can be a
 11 powerful approach to investigate degradation and structure-function relations. For example, Zhang
 12 et al from the Korgel group applied a combination of HRTEM/FFT and GISAXS/GIWAXS
 13 imaging to lead-free cubic Cs₂AgBiBr₆ perovskite NCs.¹⁹⁴ Disintegration of the superlattice was

1 observed around 200 °C and total loss of ordering of the cubic superlattice was reached at 250 °C.
2 Jurow et al used GISAXS to find correlation distances of 3.8 nm in q_z direction of CsPbBr₃ NCs
3 when tuning the transition dipole moment for improved optical characteristics.⁸⁰⁹

4 An interesting alternative to (GI)SAXS superlattice analysis is wide-angle parallel beam X-ray
5 scattering as done by Toso et al.⁸¹⁰ They used the fact that highly ordered CsPbBr₃ NCs form
6 superlattice scattering planes for previously diffracted X-rays that stem from scattering on crystal
7 lattice planes. This interference gives rise to equally spaced satellite peaks and its position is given
8 by $q_n = 2 \pi n / \Lambda$, with Λ being the average superlattice spacing. With this method, an average
9 spacing of $\Lambda \approx 12.2$ nm was found.

10 **X-Ray scattering on colloidal dispersions**

11 X-ray scattering is not limited to solid bulks or thin-film. Colloidal perovskite NCs in solution can
12 also be investigated by scattering techniques to give insight into the crystal structure and
13 morphology. Precursor engineering has been an important, though not very precise nor predictable
14 method to optimize perovskite materials.⁸¹¹ For example, Pratap et al investigated colloidal
15 perovskite precursor dispersion by GIWAXS and UV/VIS and found four stages of thin-film
16 formation: nanoparticles in solution, nanoparticle growth, formation of aggregates and complex
17 clusters, and fragmentation of large aggregates.⁸¹² Thus, the key steps in thin-film formation for
18 device fabrication could be looked at in detail using a combination of scattering techniques and
19 optical measurements. Van der Burgt et al used transmission SAXS to monitor the formation of
20 perovskite supraparticles in solution (inside a quartz capillary) and was able to prove that the
21 addition of methyl acetate triggered the formation of supraparticles over the course of several
22 days.⁸⁰⁰

23

1 **Summary and Outlook of X-Ray scattering characterization of MHP NCs**

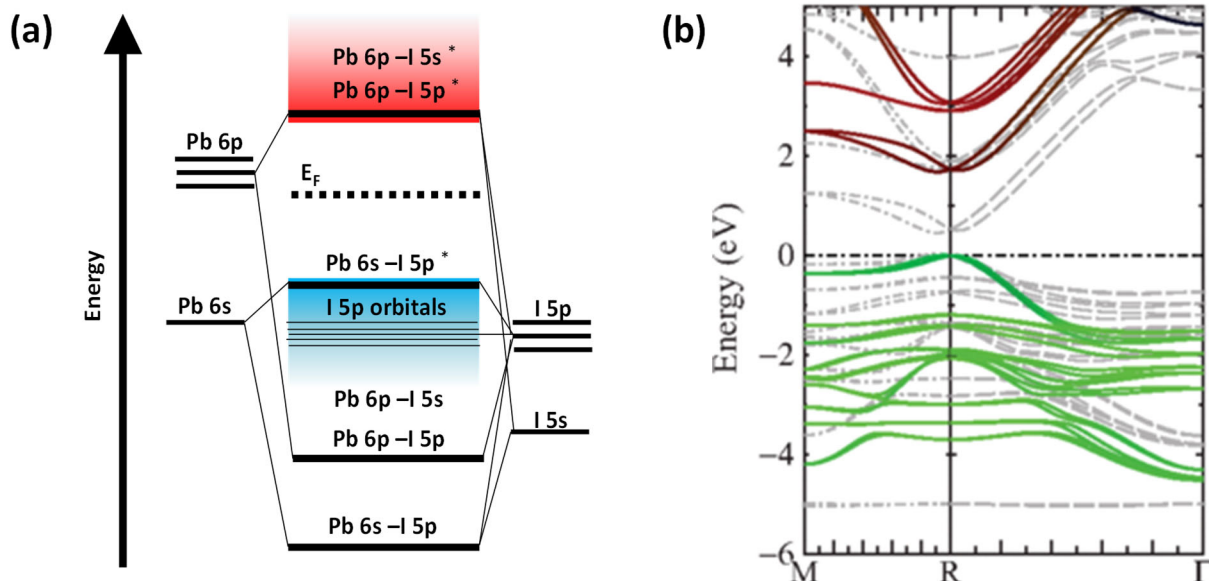
2 X-ray scattering techniques are incredibly useful for analyzing crystal structure, degradation
3 induced phase changes, preferential orientation, crystallinity, morphology and superstructure of
4 perovskite NCs. As advanced scattering techniques become better understood and availability
5 increases, more and more focus is put on in situ GIXS measurements. Grazing-incidence geometry
6 allows for analyzing statistically relevant sample volumes. With small and wide-angle X-ray
7 scattering (SAXS and WAXS), methods are available to probe length scales from the crystal- to
8 the mesoscale. X-ray scattering can be coupled to additional in situ compatible measurements, e.g.
9 PL, trPL or UV/VIS. Thereby, a wide-ranging toolbox of techniques is available that allows for
10 flexible and focused investigations of structure-function correlation - especially in the field of PV
11 and LED, where optoelectronic properties are of key interest and often heavily influenced by
12 structure.^{761, 813-814} X-ray scattering techniques are constantly improved and especially image
13 processing and simulation of 2D scattering images from advanced scattering techniques will
14 become increasingly available.⁸¹⁵⁻⁸¹⁸ In situ investigations on deposition techniques well fitted for
15 industrial purposes, e.g. roll-to-roll processing, and coupling to advanced experiments for
16 degradation and formation investigations might well be in the focus of future research. However,
17 also more easily accessible X-ray diffraction routinely available at many groups can be greatly
18 beneficial for perovskite NC studies. XRD measurements can be used to provide phase
19 information, phase purity, lattice parameters and can give hints for superstructural arrangements
20 and crystallinity. Thereby, X-ray scattering techniques will help perovskite NC systems to gain
21 even more attention from the scientific community and become increasingly promising for
22 industrial applications.^{804, 819-820}

1 9. OPTICAL PROPERTIES

2 9.1 LINEAR ABSORPTION AND PHOTOLUMINESCENCE

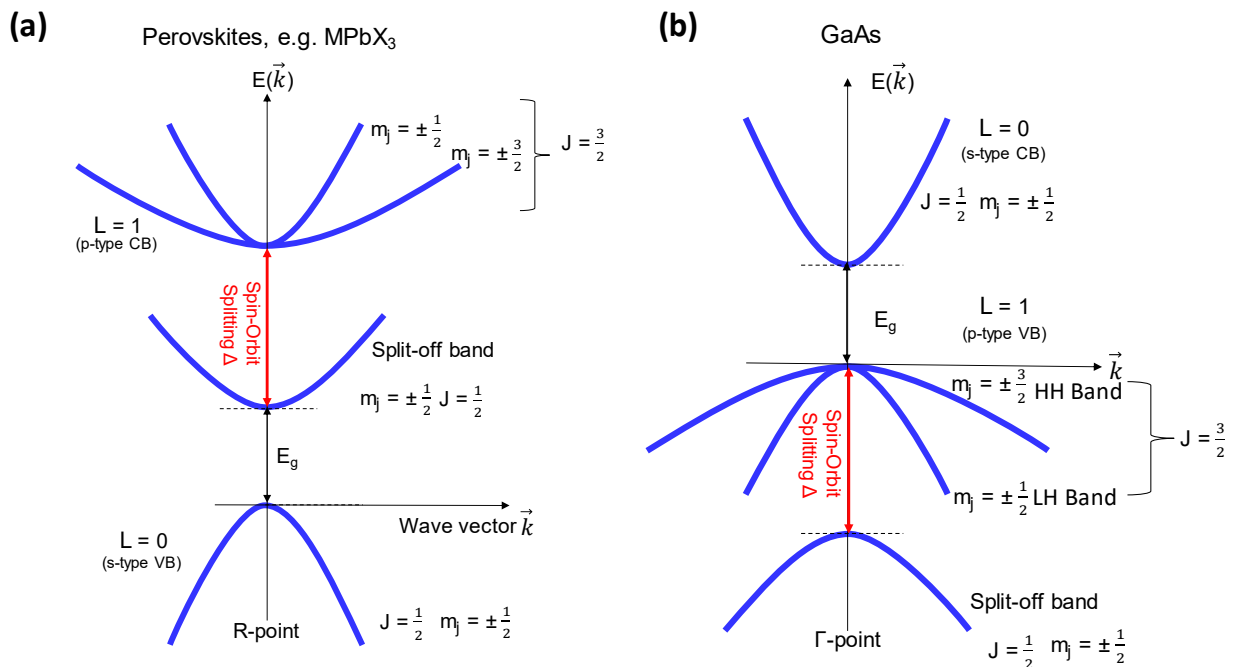
3 MHPs have been known for their intriguing optical and electronic properties that are appealing
4 for low-cost, high-performance optoelectronic devices. These include tunable photoluminescence
5 across the entire visible spectrum, high color purity, multicolor chromism, high absorption
6 coefficients, high photoluminescence quantum yield (PLQY), and long charge carrier diffusion
7 lengths.^{14, 821-823} The band gap of MHPs is easily tunable over UV-Vis-near IR wavelengths by
8 varying the halide compositions ($X = \text{I}^-, \text{Br}^-, \text{Cl}^-$).^{15, 329, 824-829} They have been intensely explored in
9 solar energy and light harvesting applications. MHPs based colloidal NCs exhibit high PLQY
10 compared to classical, core-only quantum dots, suggesting the significant reduction of non-
11 radiative loss pathways prevalent in the corresponding bulk MHPs films. In the previous sections,
12 we reviewed the shape and composition-controlled synthesis of perovskite NCs. In this section,
13 we focus on their optical properties. We start by briefly reviewing the optical properties of bulk
14 MHPs and then review how they change when the size of the crystals decreases to the nanoscale.
15 We further discuss the phenomena which manifest themselves only in NCs, such as quantum
16 confinement. As discussed in other sections, the advances in the synthesis enable the preparation
17 of MHP NCs with highly controlled size, shape and surface properties. These NCs provide a very
18 convenient platform to study the optical properties of MHPs which are not specific only to
19 nanoscale. In this context, we review how the NCs can be used to reveal insights into the optical,
20 spin and electronic properties of bulk MHPs.

1 **Electronic band structure:** In lead based MHP, the conduction band consists of σ -antibonding
2 Pb $6p$ orbitals and halide np orbitals, hence possesses a p -type character. (**Figure 87a**). The
3 electronic configuration of Pb (II) is $6s^26p^0$, and it is np^6 for halides (where $n=3$ to 5 from Cl to
4 I).⁸³⁰⁻⁸³¹ The valence band in MHP is made of σ -antibonding Pb $6s$ and halide np orbitals,
5 conferring the band a partial s -type character. In effect, the transition from the valence to the
6 conduction band is dipole allowed.⁸³² **Figure 87b** shows the calculated electronic band structure
7 of the 3D MAPbI₃ perovskites under quasiparticle self-consistent GW approximation (QSGW).⁸³³
8 The color of the bands corresponds to their orbital characters where green, red and blue depicts I
9 $5p$, Pb $6p$, and Pb $6s$ orbitals, respectively. M and R points are the zone-boundary points close to
10 $(1/2,1/2,0)$ and $(1/2,1/2,1/2)$, respectively. MAPbI₃ has a direct bandgap with the conduction band
11 minima (CBM) and valence band maxima (VBM) lying at the R point of the Brillouin zone. The
12 VBM and CBM are shifted slightly from R as a consequence of spin-orbit coupling (SOC). As
13 lead and iodine are heavy elements, SOC is large in MHPs and has significant effect in their optical
14 and electronic properties. Even *et al* reported that the exclusion of SOC severely underestimates
15 the bandgap calculation in MHPs.⁸³⁴ Importantly, the SOC strongly influences the width of the
16 band gap. Specifically, the optical band gaps in MAPbI₃ and MAPbBr₃ shrink by 0.5 eV and 0.8
17 eV, respectively when SOC is taken into account as compared to the bandgap calculation without
18 considering SOC.⁸³⁴ Due to its p -type character, the conduction band is affected strongly due to
19 SOC while the valence band remains nearly unaffected. This leads to two-fold degenerate split-off
20 (SO) states representing the CBM in the lead based MHPs (**Figure 88a**).⁸³⁴



1
 2 **Figure 87.** (a) Electronic bands formation in case of MAPbI₃ perovskites due to hybridization of
 3 Pb and I orbitals. Schematic is drawn according to Ref⁸³⁰. (b) Calculated energy- band diagram of
 4 the 3D CH₃NH₃PbI₃ perovskites under quasiparticle self-consistent GW approximation. Adapted
 5 with permission from Ref⁸³³

1 The electronic band structure of MHP is inverted compared to the classical semiconductor such as
 2 GaAs (**Figure 88b**). In GaAs the CBM and VBM lie at the Γ point of the Brillouin zone where the
 3 CB is s type with orbital angular momentum $L=0$ and the VB is p type with $L=1$. The VB in GaAs
 4 consists of heavy hole (HH) band and light hole (LH) band with total spin angular momentum
 5 $J=3/2$ and magnetic quantum number $m_j=\pm 3/2$ for HH and $\pm 1/2$ for LH, respectively. The split
 6 off band with $J=1/2$ lies below the LH band separated by the spin orbit coupling induced splitting
 7 (Δ). In case of MHP, the VB is s type whereas the CB is p type where the split off band ($J=1/2$)
 8 represents the CB. Importantly, the valence and the conduction bands in MAPbI₃ have high energy
 9 dispersion in k -space which gives rise to small hole and electron effective masses. The small carrier
 10 effective masses are consistent with high mobilities and long carrier diffusion lengths in this
 11 material.⁸³³

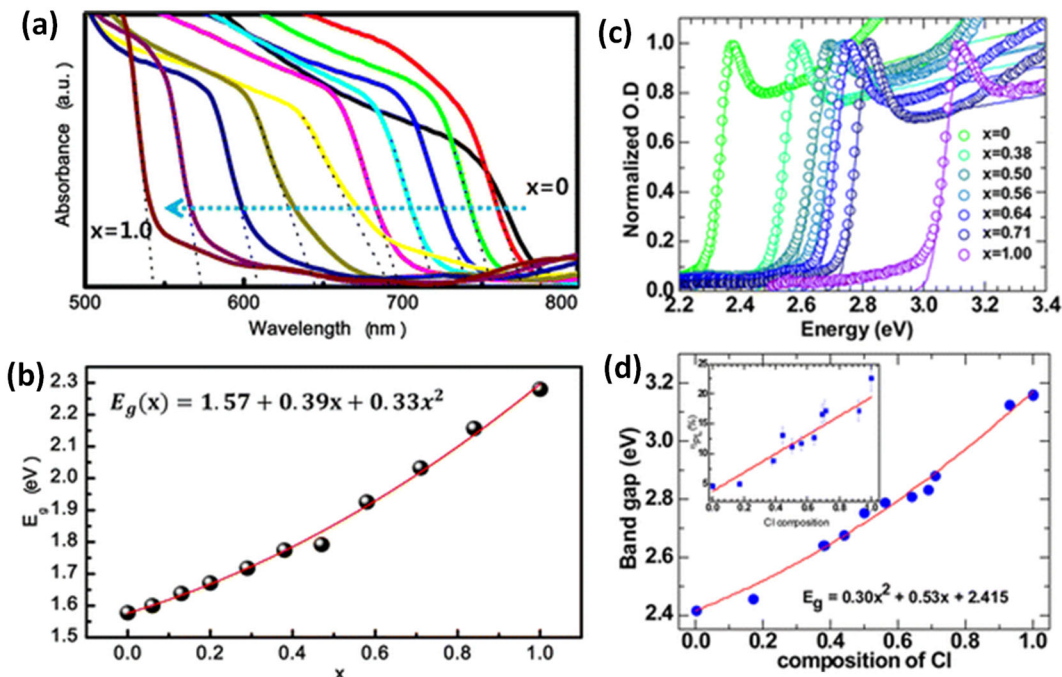


12
 13 **Figure 88.** Schematic representation of the electronic band structure of (a) lead based MHP and
 14 (b) GaAs. The VB of GaAs consists of heavy hole (HH) and light hole (LH) bands, along with a

1 split off band. On the contrary, MHP has an inverted band structure with the split off band being
2 the CB.

3 **Optical band gap:** Since the upper valence bands in MHPs are dominated by the halide p
4 orbitals (Figure 87b) with only minor contributions from anti-bonding Pb $6s^2$ orbitals, the valence
5 band position becomes sensitive to the choice of halide ions. The bandgap increases from I to Br
6 to Cl based MHPs. The increase in bandgap is predominately driven by the downshift of valence
7 band while the conduction band upshift is less pronounced.⁸³¹ Noh *et al.* showed optical bandgap
8 tuning in mixed halide MAPb(I_{1-x}Br_x)₃ perovskites by changing the compositions of I and Br
9 ions.⁸³⁵ **Figure 89a** shows the corresponding experimental absorption spectra of mp-
10 TiO₂/MAPb(I_{1-x}Br_x)₃ ($0 \leq x \leq 1$). The absorption onsets of mp-TiO₂/MAPb(I_{1-x}Br_x)₃ vary from
11 786 nm (1.58 eV) to 544 nm (2.28 eV), resulting in wide color tunability. The estimated bandgaps
12 from the absorption onsets, were observed to follow a quadratic relationship with halide
13 compositions (**Figure 89b**). The absorption spectra increases sharply at the optical band edge
14 consistent with a direct bandgap with allowed transitions. While in the iodide, the excitonic
15 contribution is not much pronounced, it becomes prominent at the optical band edge when moving
16 from I to Br to Cl based MHPs (**Figure 89c**). Kumawat *et. al* calculated the bandgap in MAPb(Br₁₋
17 _xCl_x)₃ by considering the effect of excitonic contribution at the band edge using the Sommerfeld
18 model. The bandgap increases from 2.4 eV for MAPbBr₃ to 3.1 eV for MAPbCl₃.⁸²⁸ Similar to the
19 case of I-Br based mixed halide MHPs, the bandgap tuning in Br-Cl based MHPs varies in a
20 quadratic fashion with the Cl composition (**Figure 89d**). Similar to MA- based MHPs, FA- and
21 Cs-based LHPs also exhibit similar trends of bandgap tuning with the change in halide
22 compositions.

1 It is important to note that A-site cations such as MA, FA, or Cs, do not contribute to the
 2 electronic bandgap directly but can still influence the crystal structure *via* rotation of Pb-X-Pb
 3 bond angles and thus, indirectly modify the bandgap.⁸³⁶⁻⁸³⁸ Beyond lead-based systems, there has
 4 been extensive work on MHPs based on Sn and Ge, as well as halide double perovskites and other
 5 perovskite-inspired materials (refer to Section 5). The band gap of CsSnX₃ perovskite is lower
 6 compared to the Pb²⁺ analogues due to higher electronegativity of Sn ions compared to Pb.⁸³⁹⁻⁸⁴⁰
 7 Huang *et. al.* showed that there is relatively small amount of change in the bandgap from CsSnCl₃
 8 to CsSnI₃ compared to Pb based MHP, due to interatomic Sn *s* and Sn *p* character of the VBM and
 9 CBM.⁵⁴⁷ Unlike Pb²⁺ based MHP, lead free double perovskites (DP) with stoichiometric formula
 10 (A₂B^IB^{III}X₆),^{524, 841-843} show weak photoluminescence due to indirect bandgap or parity forbidden
 11 direct transitions. Using density functional theory (DFT) calculations, Meng *et. al.* showed out of
 12 nine possible DP, six of them show parity forbidden direct band gap transitions.⁸⁴²



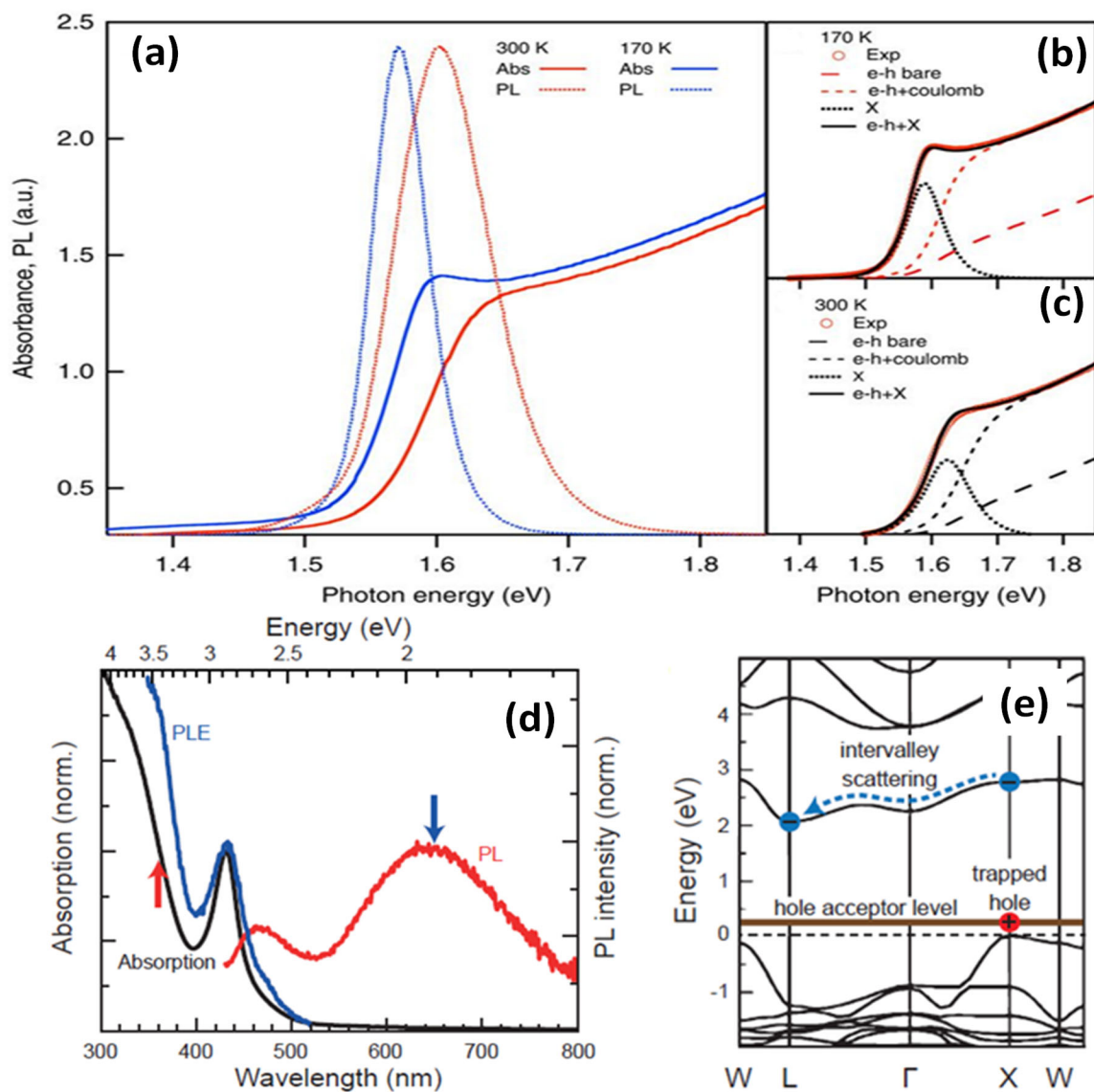
13

1 **Figure 89.** (a) Absorption spectra of FTO/bl-TiO₂/mp-TiO₂/ MAPb(I_{1-x}Br_x)₃/Au cells, the
2 bandgap shifts toward lower wavelengths with increasing Br substitution. (b) The composition
3 dependent bandgap follows a quadratic relationship with respect to Br concentration (x). Adapted
4 with permission from Ref⁸³⁵ (c) Absorption spectra of MAPb(Br_{1-x}Cl_x)₃ bulk thin films where x
5 varies from 0 (MAPbBr₃) to 1 (in case of MAPbCl₃). The circles correspond to the experimental
6 data whereas the solid lines are simulated absorption spectra using Sommerfeld model, considering
7 the enhancement in the absorption coefficient by taking into account for the coulomb field of the
8 exciton. (d) Quadratic behavior of the band gap with Cl composition in case of MAPb(Br_{1-x}Cl_x)₃
9 thin films. Adapted with permission from Ref.⁸²⁸

10 **Bandgap excitation:** As observed in Figure 89c, the excitonic transitions at the band gap in MHPs
11 imply considerable Coulomb interactions between the electrons and holes. Therefore, the
12 absorption coefficient does not simply follow the square root dependence as in case of free
13 electrons and holes. Instead, there is an additional contribution from Sommerfeld enhancement
14 above the band edge and excitonic transitions below. Therefore, it is appropriate to deconvolute
15 excitonic vs continuum transition probabilities.^{828, 844} In case of bulk MHPs, Saba *et al* first used
16 the Elliot theory of Wannier-Mott excitons to model the measured absorption spectra.⁸⁴⁵ **Figure**
17 **90a** shows the linear absorption and emission spectra of MAPbI₃ thin films at 300 K and 170 K,
18 respectively, as measured by Saba *et al.*⁸⁴⁵ The excitonic vs. continuum contributions have been
19 separated out using Elliot model. It was noticed that at lower temperatures the excitonic
20 contribution increases in MHPs (**Figure 90b-4c**).

21 Similarly to Pb²⁺ based MHP, the optical bandedge of lead-free double perovskites is also
22 dominated by sharp absorption resonance (**Figure 90d**).⁸⁴³ This optical resonance has been
23 assigned to self-trapped exciton in case of Cs₂AgInCl₆.⁵²⁴ In case of Cs₂AgBiBr₆ double

1 perovskites, Dey *et. al.* explained the origin of this sharp optical resonance with the help of the
2 electronic band structure (**Figure 90e**).⁸⁴³ It was demonstrated that it is unlikely that the high
3 effective mass electron along with the low effective mass hole at the direct bandgap could lead to
4 a bound state with strong binding energy, because the reduced mass of the electron-hole pair would
5 have been small in such case. Considering, the effect of hole trapping by Ag vacancies, they
6 concluded that the bound hole along with the high effective mass electron could lead to a defect
7 bound exciton at the direct band gap. Consequently, the high energy PL emission close to the
8 optical resonance (**Figure 90d**) was assigned to the radiative recombination of these direct bound
9 excitons due to their giant oscillator strength. This was corroborated by theoretical calculations in
10 which using ground- and excited-state *ab-initio* methods, Maurizia *et. al.* showed that the first
11 absorption peak in Cs₂AgBiBr₆ and Cs₂In₂X₆ is consistent with bound excitons.⁸⁴⁶



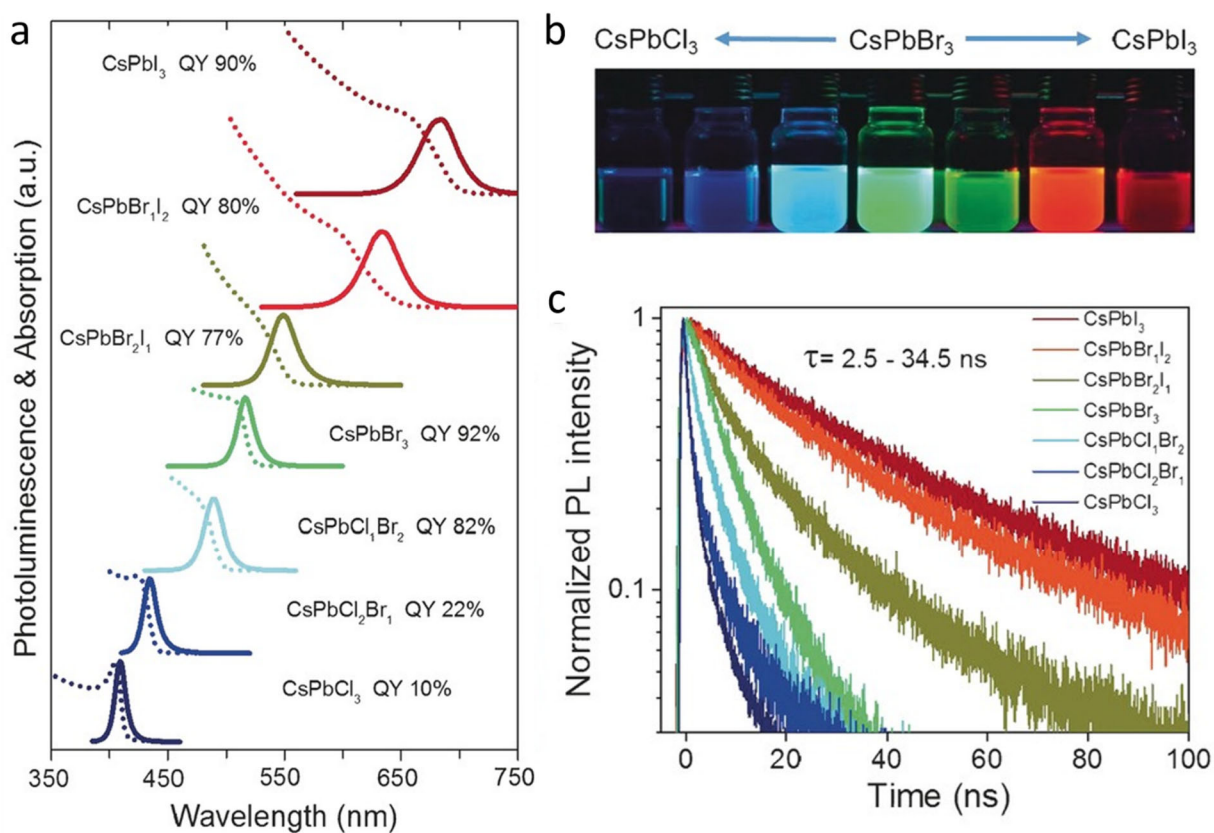
1
 2 **Figure 90.** (a) Absorption (continuous line) and PL(dashed line) spectra in MAPbI₃ films, recorded
 3 at 300 and 170 K. Elliot fits to the experimental absorption spectra at (b) 170 and (c) 300 K,
 4 respectively. Excitonic and band-to-band oscillator strengths contributions calculated by taking
 5 into account Coulomb interaction according to Elliott's theory of Wannier excitons are shown in
 6 (b) and (c). The excitonic contribution is enhanced at low temperature. Adapted with permission
 7 from Ref.⁸⁴⁴ (d) Linear absorption, PL, and PLE (detected at 650 nm) spectra of DP NCs dispersed
 8 in toluene. (e) Electronic band structure of Cs₂AgBiBr₆ double perovskite. The blue and red circles

1 represent electron and trapped hole where the brown solid line indicates hole acceptor level.

2 Adapted with permission from Ref⁸⁴³

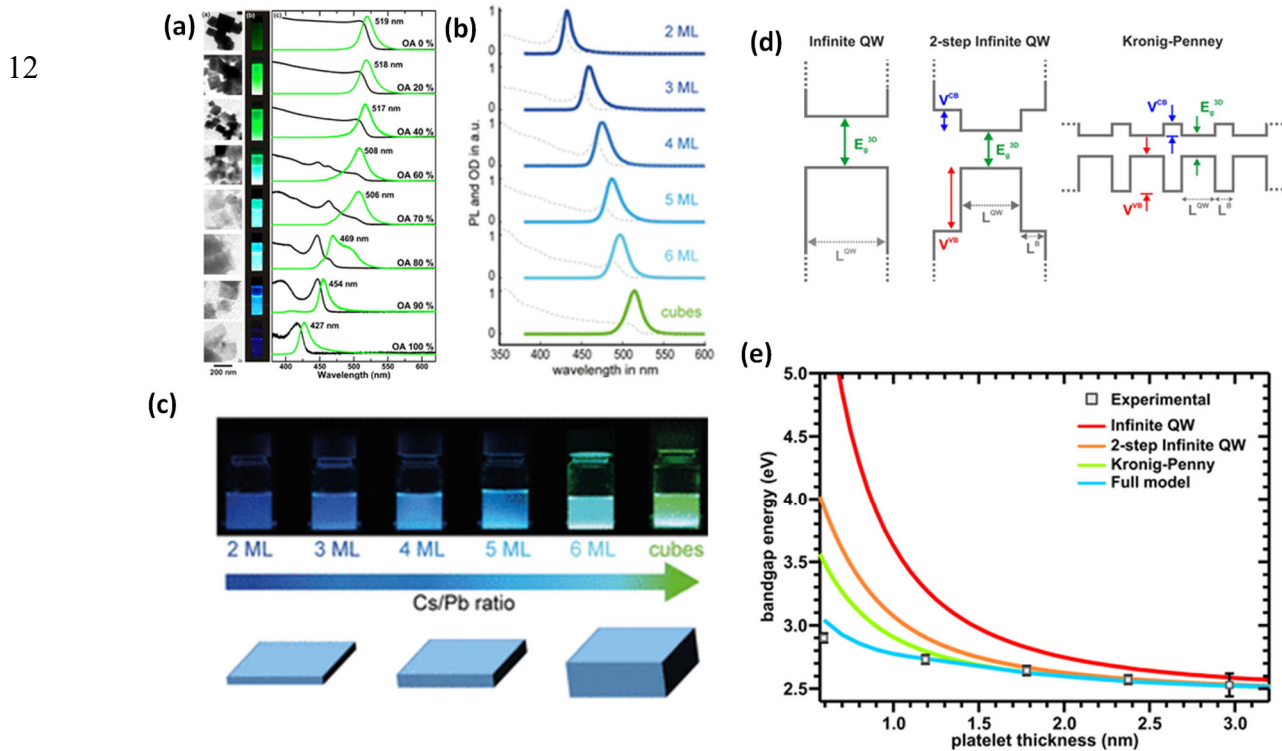
3 Bulk MHPs typically exhibit weak photoluminescence quantum yield (PLQY) limiting
4 their light-emitting applications. Crucially, this property is radically changed when moving from
5 bulk to nanocrystals underscoring the effect of the crystal size and interface composition on the
6 optical properties of MHP. Specifically, it has been shown that reducing the crystal size to
7 nanoscale leads to a significant improvement in PLQY.^{15, 26, 30, 59, 173} Since the first report of highly
8 luminescent (PLQY~ 80%) green emissive MAPbBr₃ colloidal crystals,²⁶ significant research
9 efforts have been devoted to the development of colloidal MHP NCs made of different cation and
10 anion compositions with improved optical properties regarding their stability, PL tunability, PLQY
11 (discussed in previous sections). Similar to their bulk counterparts, the optical bandgap and PL
12 emission in colloidal MHP NCs is easily tunable across the visible region of electromagnetic
13 spectrum by varying the halide composition.^{15, 59} For example, colloidal CsPbX₃ NCs synthesized
14 by ultrasonication approach exhibit extremely high PLQYs and tunable emission between 400-
15 680 nm by just varying the halide composition (Figure 91a-b). Br- and I-based MHP NCs exhibit
16 near-unity PLQY under optimized synthesis conditions, while the Cl-based MHPs exhibit lower
17 PLQY.^{15, 59} The low PLQY of Cl-based perovskites has been attributed to the halide vacancies
18 acting as non-radiative traps. PL decay gets faster going from iodide *via* bromide to chloride based
19 CPbX₃ perovskite NCs (Figure 91c). The faster PL decay time and low PLQY in case of Cl-based
20 NCs suggest that they exhibit higher non-radiative rates as compared to the iodide and bromine
21 based NCs. Nevertheless, it has been shown recently, PLQY in these perovskites can also be
22 dramatically improved to near unity by doping with metal halides such as CuCl₂, MgCl₂.⁸⁴⁷⁻⁸⁴⁸ The
23 origin of the high PLQYs of the colloidal MHPs with respect to the bulk material is still an

1 intensively investigated subject.^{150, 849} It is postulated that the increased surface to volume ratio
 2 and effective surface passivation with ligand molecules, and thereby a removal of surface traps,
 3 causes the increased PLQY of colloidal MHP NCs as compared to their bulk counterparts. A recent
 4 study suggested that increased oscillator strength in MHP NCs results in enhanced PLQY when
 5 their morphology is tuned from bulk-to-nano scales.⁸⁴⁹



6
 7 **Figure 91.** (a) Linear absorption and PL spectra and the corresponding PLQYs of CsPbX₃ NCs of
 8 different halide compositions synthesized by ultrasonication approach. (b) Photograph of the
 9 corresponding colloidal dispersions in hexane under UV light. (c) PL decay traces of the
 10 corresponding NCs. Adapted with permission from the Ref.⁵⁹

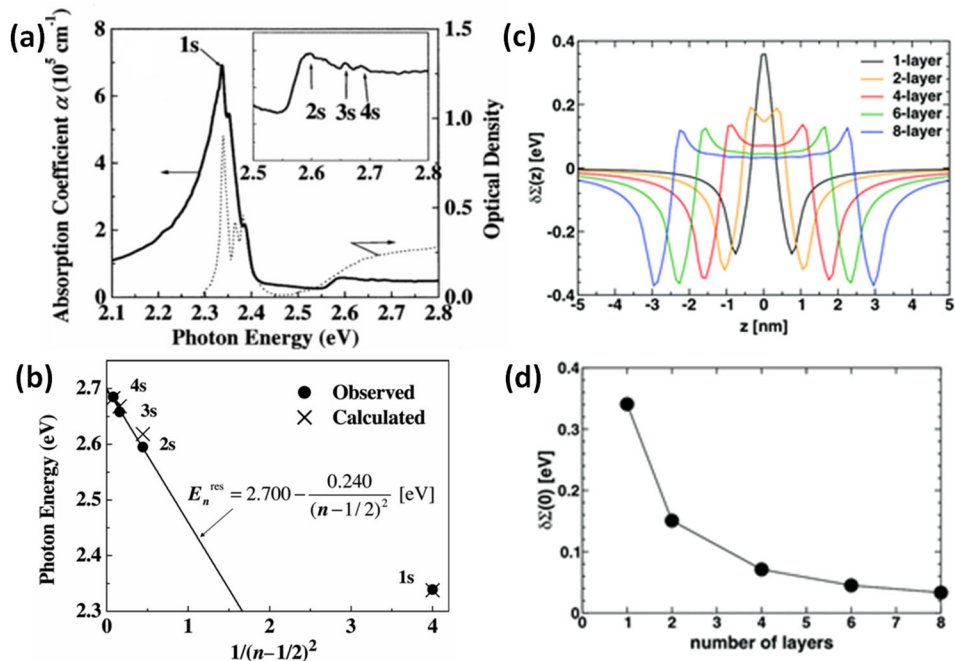
1 **Quantum-confinement effect on optical band gap:** Another important consequence of the
 2 reduction in size of the MHP crystals is the manifestation of quantum confinement effects. Three
 3 size ranges may be delimited: (i) when the size is much larger than the exciton Bohr radius ($d \gg$
 4 a_B), so that the confinement effects are negligible, (ii) weak confinement regime when the size is
 5 comparable with the exciton Bohr radius, and (iii) strong confinement regime when the exciton
 6 Bohr radius is larger than the NC ($a_B \gg d$). Interestingly, the average size distribution of typical
 7 colloidal MHP NCs is $\sim 10 \pm 1$ nm which falls under the weak confinement regime where the effect
 8 on the band gap is small. Nonetheless, in the strong confinement regime provides a means to
 9 effectively tune the band gap in MHP^{17, 62, 139, 850-852}. In the strong quantum confinement regime,
 10 the electron and the hole should be viewed as independent particles and their confinement energies
 11 needs to be calculated first before taking into account their Coulomb interaction.⁸⁵³



1 **Figure 92.** (a) TEM images, pictures of NPLs solutions, linear absorption and PL spectra of
2 MAPbBr₃ NPLs, respectively. Adapted with permission from Ref¹⁷. (b) Linear absorption and PL
3 spectra of CsPbBr₃ NPLs with varying thicknesses. (c) Pictures of CsPbBr₃ NPLs and cubes
4 dispersed in Hexane under UV-light exposure. The emission wavelength red shifts with increase
5 in monolayer (ML) thickness. Panels (b) and (c) are adapted with permission from Ref⁶² (d)
6 Quantum well models used to reproduce the experimental spectra as shown in c. (e) Calculation
7 of the energy of perovskite nanoplatelets as a function of platelet thickness (solid lines) and the
8 experimentally determined values (gray squares). Panels (d) and (e) were adapted with permission
9 from Ref¹⁷.

10 Colloidal 2D perovskite nanoplatelets (NPLs) have been greatly explored to understand the
11 quantum confinement effects in MHPs (refer to nanoplatelets section for detailed discussion). In
12 the pioneering work by Sichert *et. al.* they first demonstrated and modelled the quantum size effect
13 in 2D MHP NPLs based on MAPbBr₃ perovskites (**Figure 92a**).¹⁷ Later, Bohn *et. al.* showed
14 precise control over the thickness of CsPbBr₃ perovskite NPLs by varying it, from 2 to 6
15 monolayers (**Figure 92b**). The colloidal NPLs exhibit sharp optical transitions at the band edge due
16 to strong quantum confinement effect. Hence, in 2D perovskite NPLs the exciton binding energy
17 enhanced compared to 3D nanocubes.^{17, 62} The exciton binding energy in CsPbBr₃ increases from
18 30 meV to 280 meV when their dimension changes from 3D nanocubes to 2D NPLs with 2
19 monolayer thickness (**Figure 92c**).⁶²

1 Sichert *et al.* demonstrated that the simple consideration of an infinite quantum well model
2 (**Figure 92d**), overestimates the quantization energy compared to the experimentally determined
3 values under the assumption of infinite confinement energy.¹⁷ They successfully modeled the
4 bandgap energies for NPLs with mono layer numbers (n) =3, 4, 5, under the approximation of a
5 one-band effective-mass Kronig-Penny model. They observed for thinner NPLs (**Figure 92e**) such
6 as n=2 and n=1 where the exciton binding is very high, the discrepancies between theory and
7 experiment is quite large.¹⁷ In case of bulk perovskites with low dielectric constant, Coulomb
8 screening dominates, leading to a reduction of the exciton binding energy. In case of extremely
9 thin NPLs most of the electric field lines between electron and hole are outside of the platelets
10 where the dielectric constant is low compared to the semiconductor platelets, this minimizes the
11 Coulomb screening and thus, enhances the exciton binding energy, accounting for the results
12 obtained for extremely thin platelets.¹⁷



1 **Figure 93.** (a) Solid line shows the optical absorption spectrum of a $(\text{C}_6\text{H}_{13}\text{NH}_3)_2\text{PbI}_4$ single crystal
2 at 5 K obtained from the Kramers-Kronig transformation of its reflection spectrum. The inset
3 shows the expansion around 2.6 eV. Dotted line shows the optical absorption spectrum of
4 $(\text{C}_6\text{H}_{13}\text{NH}_3)_2\text{PbI}_4$ polycrystalline film measured at 5 K. (b) Resonance energies of Wannier-series
5 excitons in $(\text{C}_6\text{H}_{13}\text{NH}_3)_2\text{PbI}_4$ as a function of $1/(\text{N}-1/2)^2$. Closed circles and crosses represent the
6 observed and calculated energies of the excitons, respectively. The solid line shows the fitting
7 based on a simple two dimensional Wannier exciton model. Adapted with permission from Ref⁸⁵⁴
8 (c) Self-energy profile $\delta\Sigma(z)$ for slabs of $\text{CH}_3\text{NH}_3\text{PbI}_3$. (d) Self-energy taken at the slab centre
9 $\delta\Sigma(0)$. Adapted with permission from Ref⁸⁵⁵

10

11 **Effect of dielectric confinement on low dimensional MHPs:** When charge carriers are confined
12 in low dimensional multi-layer halide perovskites, their self-energy could be further enhanced by
13 the surrounding polarizability of perovskite lattice arising due to dielectric inhomogeneity.⁸⁵⁵⁻⁸⁵⁷
14 This effect influences the electron-hole interaction energy, thus giving rise to a strong exciton
15 resonance (**Figure 93a**). In case of $(\text{C}_6\text{H}_{13}\text{NH}_3)_2\text{PbI}_4$ crystals⁸⁵⁴ and for bromide compounds
16 $(\text{C}_4\text{H}_9\text{NH}_3)_2\text{PbBr}_4$ and $(\text{C}_6\text{H}_5\text{C}_2\text{H}_4\text{NH}_3)_2\text{PbBr}_4$,⁸⁵⁸ it was shown that the exciton resonance spectra
17 deviated from the well-known 2D-hydrogen-like series due to the dielectric confinement effect
18 (**Figure 93b**). Saponi *et. al.* calculated the self-energy profile for MAPbI_3 nanoplatelets (**Figure**
19 **93c**).⁸⁵⁵ The self-energy is equivalent to one-particle electrostatic potential profile acting on a
20 charge carrier in layered hetero-structures and calculated by solving the inhomogeneous Poisson
21 equation. The self-energy value is higher at the center of the slab for lower thicknesses due to
22 dielectric confinement effects (**Figure 93d**).⁸⁵⁵

23

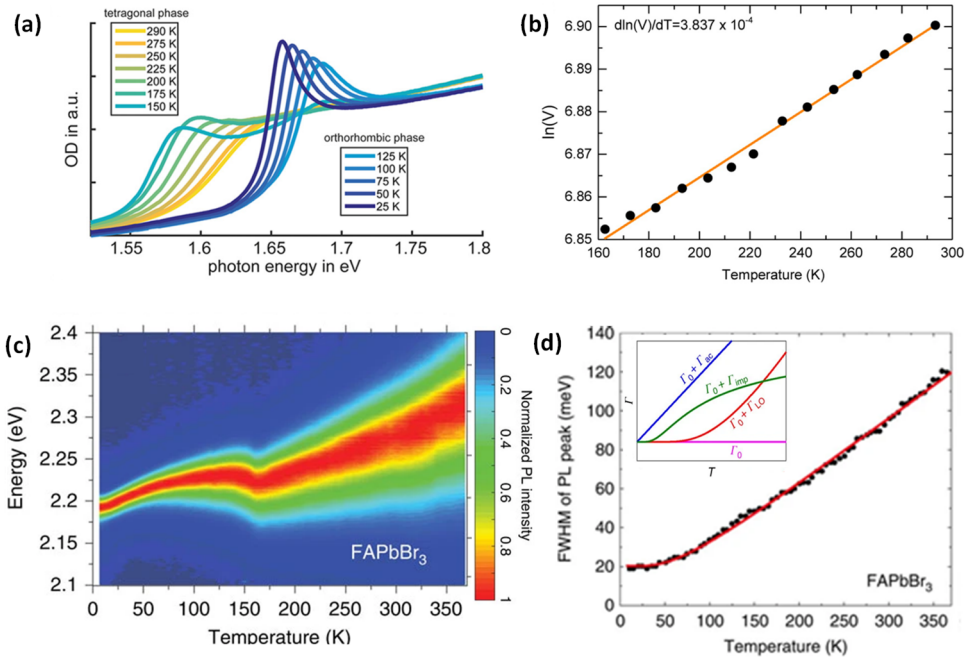
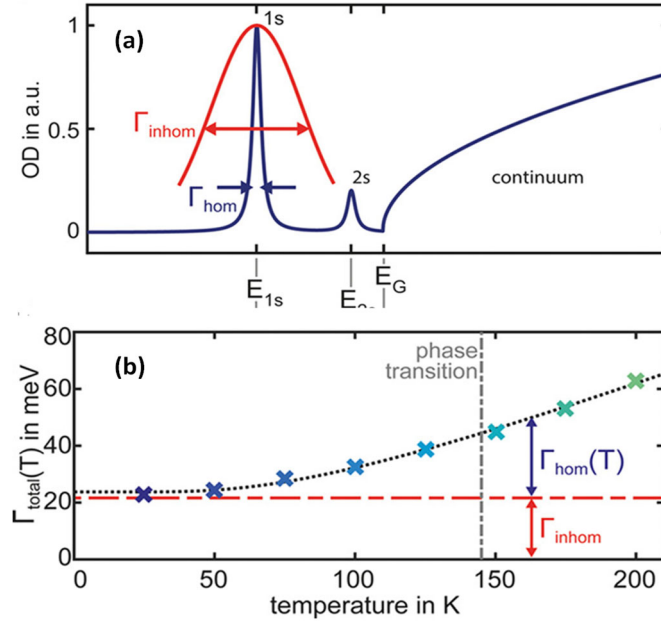


Figure 94. (a) Temperature dependent absorption spectra on $\text{CH}_3\text{NH}_3\text{PbI}_3$ nanoplatelets for temperatures 25 K to 290 K. The $1s$ exciton transition is prominent at low temperature. Adapted with permission from Ref⁸⁵⁹ (b) $\ln(V)$ of volume of $\text{CH}_3\text{NH}_3\text{PbI}_3$ in tetragonal phase as a function of temperature. Solid line is a linear fit representing positive coefficient of thermal expansion. Adapted with permission from Ref⁸⁶⁰ (c) Colour plot for the normalized steady state PL spectra of FAPbBr_3 thin film between temperature range 10 K to 370 K (d) corresponding FWHM of the steady state PL spectra. Panels (c) and (d) are adapted with permission from Ref⁸⁶¹

1 **Effect of temperature on optical transitions:** Unlike most conventional semiconductors (*e.g.*,
2 GaAs, GaN or Si), MHP shows a blue shift in the bandgap with increasing temperature (**Figure**
3 **94a**).^{844, 860-862} MAPbI₃ undergoes a phase transition from the tetragonal to the orthorhombic phase
4 at temperatures below 163 K.^{859-860, 862} In both phases the bandgap increases with increasing
5 temperature due to a large coefficient of thermal expansion, which results in a positive temperature
6 coefficient of the bandgap (**Figure 94b**).⁸⁶⁰ Singh *et. al.* showed that in case of MAPbI₃, lattice
7 dilation plays a more significant role compared to electron-phonon coupling.⁸⁶³ They determined
8 the volume expansion coefficient of CH₃NH₃PbI₃ to be $(1.35 \pm 0.014) \times 10^{-4} \text{ K}^{-1}$ which is 50 times
9 higher than crystalline Si. In contrast to MAPbI₃ and MAPbBr₃, MAPbCl₃ shows a decrease in the
10 bandgap with increasing temperature because electron-phonon coupling dominates over the effects
11 of lattice dilation.⁸⁶⁴ In MHP, electron-phonon coupling is found to be very strong, in which
12 Fröhlich interactions between carriers and optical phonons are the dominant source of electron–
13 phonon coupling.^{861 865} In case of defect halide perovskites single crystals, such as Cs₃Bi₂I₉,
14 Cs₃Sb₂I₉, Rb₃Bi₂I₉ the emission process has been explained with self-trapped excitons which arise
15 due to strong electron-phonon coupling inducing the formation of small polarons.⁸⁶⁶

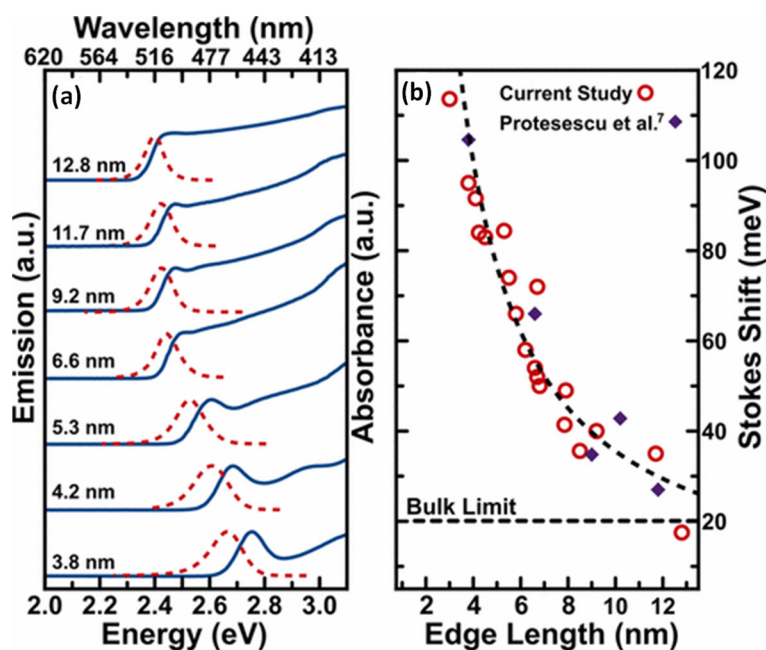


1
2 **Figure 95.** (a) Schematic of the absorption spectrum of one single bulk-like NPL where the
3 homogeneous broadening of the Lorentzian-shaped excitonic peaks is given by Γ_{homo} (dark blue).
4 The excitonic levels (1s, 2s) and the continuum onset are well separated and easily distinguishable.
5 (b) Total exciton line broadening of the 1s exciton state $\Gamma_{\text{total}} (= \Gamma_{\text{homo}} + \Gamma_{\text{inhomo}})$ as a function of
6 temperature T (< 200 K) where the dotted line represents the fitting of the theoretical model
7 considering LO phonons. The Γ_{homo} has been calculated using the exciton dephasing time (T_2) as,
8 $\Gamma_{\text{homo}} = 2 \hbar / T_2$. Adapted with permission from Ref⁸⁵⁹.

1 In MHP, charge carrier scattering with longitudinal optical (LO) phonons has been shown
2 to cause the broadening of the excitonic absorption⁸⁵⁹ and photoluminescence peaks (**Figure**
3 **94d**).⁸⁶¹ In general, impurities or (in the case of NCs) polydispersity can cause the exciton
4 linewidth to further broaden inhomogeneously (Γ_{inhomo}) as shown in **Figure 95a**.⁸⁵⁹ Γ_{inhomo} is a
5 temperature independent quantity whereas Γ_{homo} depends on temperature (**Figure 95b**). Bohn *et.*
6 *al.* determined the homogeneous line broadening in case of MAPbI₃ nanoplatelets using
7 temperature dependent transient four wave mixing (FWM).⁸⁵⁹ They determined an exciton
8 dephasing time (T_2) $\sim 800 \pm 20$ fs for the $1s$ exciton in MAPbI₃ nanoplatelets at 25 K, giving rise
9 to $\Gamma_{\text{homo}} = 2\hbar/T_2 = 1.7 \pm 0.1$ meV and $\Gamma_{\text{inhomo}} = 22 \pm 1$ meV.⁸⁵⁹

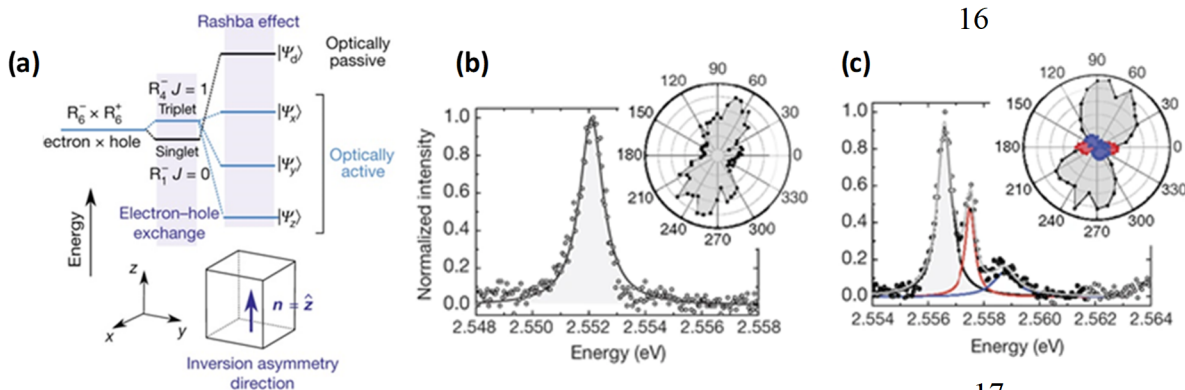
10 **Stokes Shift:** Quantum confined (QC) MHP NCs exhibit blue shifted emission compared to
11 their 3D bulk counterparts. For instance, strongly quantum confined CsPbBr₃ NCs emit blue
12 photoluminescence, while their 3D counterparts emit green photoluminescence. Brennan *et. al.*
13 synthesized CsPbBr₃ nanocubes with size distribution ranging from 13 nm to 4 nm.⁸⁵¹ They found
14 that the Stokes shift for CsPbBr₃ nanocubes increased with increasing quantum confinement (or
15 decreasing size).⁸⁵¹ The Stokes shift was found to decrease from 82 to 20 meV for the CsPbBr₃
16 nanocubes as the size increased from 4 to 13 nm (**Figure 96a-b**). The size dependent Stokes shift
17 has been explained by the confinement of the hole state.⁸⁵¹ For double perovskites, vacancy-
18 ordered halide perovskites, and inorganic zero dimensional tin halide perovskites
19 Cs_{4-x}A_xSn(Br_{1-y}I_y)₆ (A=Rb, K; $x \leq 1$, $y \leq 1$), the long lived emission was strongly Stokes-shifted and
20 have been assigned to the formation of self-trapped excitons.^{569, 867-868}

1 Similarly to the bandgap width, the Stokes shift for MAPbBr₃ and CsPbBr₃ single crystals
 2 has been found to be highly temperature dependent.⁶⁶² Guo *et. al.* observed that between 60 K to
 3 300 K, the luminescence Stokes shifts for MAPbBr₃ and CsPbBr₃ single crystals increased with
 4 increasing temperature. However below 50K, the luminescence Stokes shift weakly depended on
 5 temperature and decreased as the temperature increased.⁶⁶² This temperature dependent Stokes
 6 shift was explained in terms of a classical Debye-like relaxation process of the dielectric response
 7 function originating from the anharmonicity of the LO (longitudinal-optical) phonons at about 160
 8 cm⁻¹ in the lead bromide sub-lattice.



9
 10 **Figure 96.** (a) CsPbBr₃ NCs ensemble absorption (solid blue lines) and emission (dashed red lines,
 11 $E_{exc} = 3.543$ eV, $\lambda_{exc} = 350$ nm) spectra for a series of varying sizes. All absorption/emission
 12 spectral pairs offset for clarity. (b) Corresponding size-dependent Stokes shifts and those extracted
 13 from existing literature. Adapted with permission from Ref⁸⁵¹

1 **Exciton fine structure:** Excitons are the central emitting species in the semiconductor
 2 nanostructures that appear as additional (sometimes sharp) optical transitions at the optical band
 3 edge.⁸⁶⁹⁻⁸⁷¹The degeneracies of the lowest exciton states are broken by strong exchange
 4 interactions, spin-orbit coupling, intrinsic crystal field; nanostructures shape anisotropy giving rise
 5 to the multiple splitting of the lowest exciton states known as exciton fine structure.^{870, 872-875} In
 6 almost all bulk III-V semiconductors hetero-structures, II-VI core-shell colloidal nanostructures,
 7 the lowest available exciton states are found to be optically inactive known as dark exciton.⁸⁷⁶⁻⁸⁷⁸
 8 In case of bulk semiconductor the splitting between the bright (optically active) and the dark
 9 (optically inactive) exciton is very small, generally less than the thermal energy even at cryogenic
 10 temperature. Hence, the photoluminescence decay is not strongly affected by temperature.⁸⁶⁹⁻
 11 ⁸⁷⁰Nevertheless, the energy separation between them is increased up to tens of meV in case of
 12 semiconductor nanostructures where the photoluminescence decay is prolonged at low
 13 temperature due to acoustic phonon mediated relaxation of the bright exciton to the dark exciton
 14 states.^{876, 878-880}

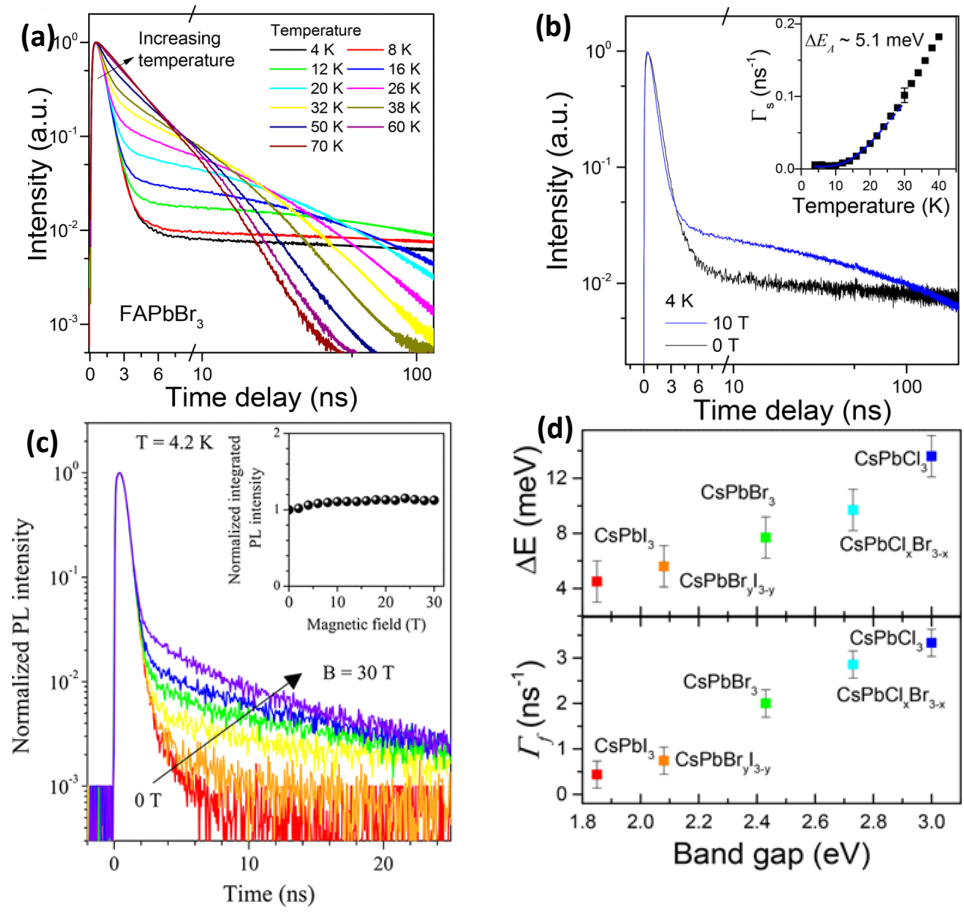


18

1 **Figure 97.** (a) Fine structure of the band-edge exciton considering short-range electron–hole
2 exchange (middle) and then including the Rashba effect (right) under orthorhombic symmetry. The
3 latter splits the exciton into three bright states with transition dipoles oriented along the
4 orthorhombic symmetry axes (labelled x , y and z) and a higher-energy dark state (labelled ‘d’).
5 The energetic order of the three lowest sublevels is determined by the orthorhombic distortion.
6 Photoluminescence spectra from individual NCs showing (b) one and (c) three photoluminescence
7 peaks. Adapted with permission from Ref⁸⁸¹.

8 In almost all MHPs, it is observed that the photoluminescence decay becomes faster at low
9 temperature where the photoluminescence quantum yield still remains high.⁸⁸¹⁻⁸⁸² The explanation
10 of the high radiative recombination in Pb^{2+} halide perovskites at low temperature was proposed by
11 Becker *et. al.*⁸⁸¹ They claimed the lowest exciton state as the bright triplet state for CsPbX_3 ($X=\text{Br}$,
12 Cl , I) crystals structure arising due to combination of strong spin-orbit coupling with Rashba-
13 effect.⁸⁸³ According to them,⁸⁸¹ if only short-range electron-hole exchange interaction is taken into
14 account then the singlet state lies below the triplet state, making the lowest available exciton state
15 dark (**Figure 97a**). They showed that inclusion of Rashba effect leads to the alteration of the bright
16 and dark exciton levels in CsPbX_3 NCs. If the effective Rashba field is parallel to one of the
17 orthorhombic symmetry axes of the CsPbX_3 NCs the bright triplet exciton states split into three
18 linearly polarized sub-levels (**Figure 97b-c**).⁸⁸¹In a detailed study by Efros *et. al.* they
19 demonstrated that the ground state of the perovskite nanostructure is indeed optically inactive
20 (dark) like any other classical semiconductor quantum dots, if only exchange interaction has been
21 considered.⁸⁸³ However, the experimentally observed bright exciton level order in tetragonal
22 CsPbBr_3 NCs can be explained including the contribution of the Rashba effect, which supports the
23 theory by Becker *et. al.*⁸⁸¹ Moreover, it was shown that the bright–dark state positions could be

1 reversed in low dimensional nanostructures, which, consequently, possess a dark exciton ground
 2 state.⁸⁸³ Opposite experimental observations were found in case of CsPbBr₃, FAPbBr₃ and FAPbI₃
 3 nanocrystals.^{819, 884-885}

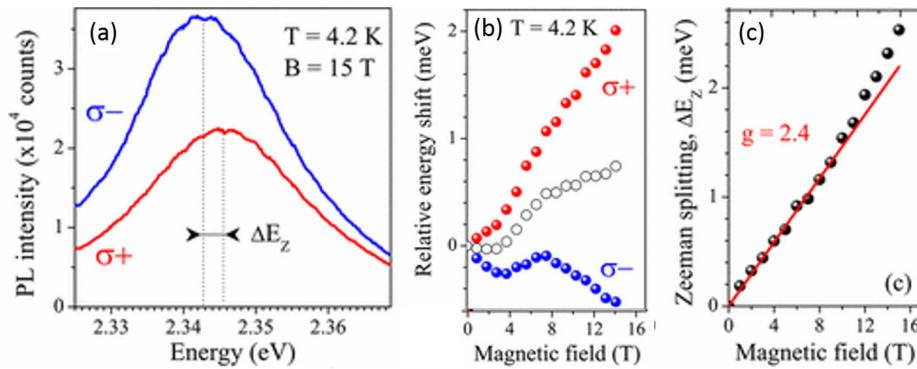


16 **Figure 98.** (a) Temperature dependent PL decay traces in FAPbBr₃ NCs. (b) PL decay curves
 17 recorded from FAPbBr₃ nanocrystals at 4 K with and without an applied external magnetic field
 18 of 10 T, respectively. Inset shows the temperature-dependent relaxation rate of the slow decay
 19 component analyzed with the three-level model yielding a bright dark energy splitting of 5.1 meV.
 20 (c) PL decay recorded at cryogenic temperature for CsPbBr₃ nanocrystals at varying magnetic
 21 fields. The inset shows the integrated PL intensity with respect to magnetic field. (d) Anion
 22 composition dependence of the bright – dark energy splitting (ΔE) and the decay rate of the fast

1 component (Γ). The values are plotted vs. the bandgaps of different nanocrystals at room
2 temperature. Adapted with permission from Ref^{819, 884}.

3 **Figure 98a** shows the temperature dependent PL decay in FAPbBr₃ nanocrystals. At 4 K,
4 PL decay is bi-exponential with a dominant fast decay component, followed by a slow component.
5 With rise in temperature the slow components grows gradually and becomes more prominent at
6 higher temperature. Similar observation was also noticed in case of CsPbX₃ nanocrystals.^{819, 884}
7 ⁸⁸⁶ The first component is assigned to the radiative decay of the bright exciton whereas the slow
8 component is assigned to the dark exciton decay, the rate of which is increases at higher
9 temperature as shown in **Figure 98b** inset.⁸⁸⁴ The lengthening of the dark exciton relaxation rate
10 at higher temperature is due to thermal activation.^{819, 884} **Figure 98b** also shows that under the
11 application of an external magnetic field of 10T, the amplitude of the slow decay component
12 enhances which is due to dark exciton states mixing with the bright exciton states resulting into
13 the brightening of the dark excitons.^{819, 878, 884} Similar observation was also noticed by Biadala *et.*
14 *al.*⁸¹⁹ in CsPbBr₃ nanocrystals as shown in **Figure 98c** where with increase in magnetic field, the
15 amplitude of the slow component enhances due to magnetic field induced brightening of the dark
16 exciton states. Using three level model for bright and dark excitons Chen *et. al.*⁸⁸⁴ determined the
17 energy splitting (ΔE) between the bright and dark exciton states as depicted in **Figure 98d**. ΔE
18 increases while going from CsPbI₃ to CsPbCl₃. It doesn't only depend on anion composition but
19 also on A site cation composition.⁸⁸⁴ It has been also demonstrated that external dopant like Mn²⁺
20 is able to manipulate the dark and bright exciton mixing.⁸⁸⁶ In case of CsPbCl₃ nanocrystals a
21 similar brightening of the dark exciton states has been observed upon Mn²⁺ doping.⁸⁸⁶ The
22 amplitude of the slow decay component at the cryogenic temperature was enhanced 5-10 times in
23 Mn²⁺ CsPbCl₃ nanocrystals as compared to the undoped CsPbCl₃ nanocrystals.⁸⁸⁶

1 A direct observation of dark exciton emission in FAPbBr₃ nanocrystals has been reported
 2 by Lounis *et al.*⁸⁸⁵ Using magneto-optical studies at cryogenic temperature, they observed a low
 3 energy zero phonon line appears at 2 to 2.8 meV below the zero phonon line of bright triplet state
 4 at 7T which has been ascribed to dark singlet exciton state resulting due to the mixing of dark
 5 states with neighboring bright states. Similar to Chen *et al.* they also observed magnetic field
 6 induced brightening of the dark singlet state at low temperature.⁸⁸⁵



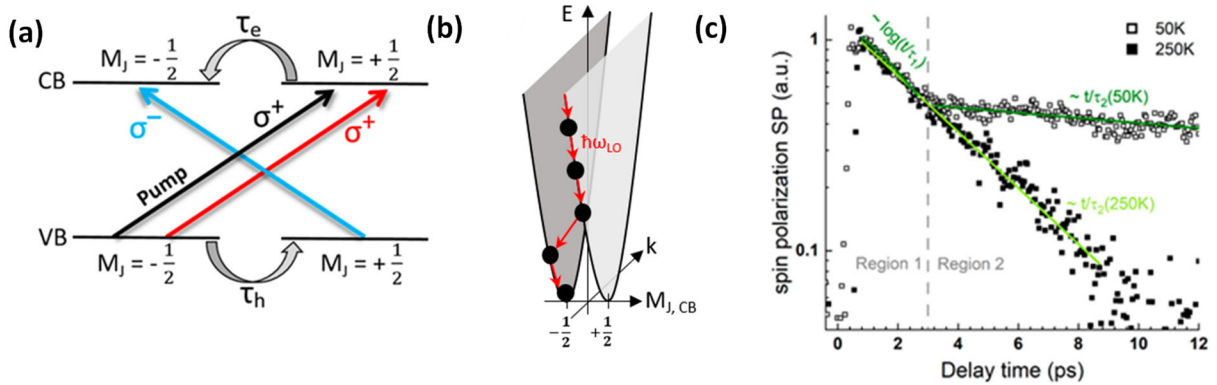
7
 8
 9
 10
 11
 12 **Figure 99.** (a) Time integrated polarization-resolved PL spectra of CsPbBr₃ NCs at B = 15 T and
 13 T = 4.2 K. The spectra are split by the Zeeman splitting, ΔE_Z. (b) Magnetic field dependence of
 14 the relative spectral positions of σ⁻ (open blue circles) and σ⁺ (red circles) components. Open
 15 circles show the shift of the center-of-gravity of the two polarized components, corresponding to
 16 the exciton shift without contribution of the Zeeman splitting. (c) Zeeman splitting of emission
 17 line. Red line is a linear fit with |g| = 2.4. Adapted with permission from Ref⁸¹⁹

1 At cryogenic temperature, the bright excitons can further split into narrow spectral lines.⁸⁸¹,
2 ⁸⁸⁷⁻⁸⁸⁸ Xiao *et. al.* had shown in CsPbI₃ nanocrystals the bright exciton split into two linear
3 orthogonal polarized emission with energy separation of few hundred μeV .⁸⁸⁸ They also showed
4 that in photo-charged CsPbI₃ nanocrystal the doublet emission of bright exciton switched to a
5 single emission peak due to elimination of electron-hole exchange interaction.⁸⁸⁸ In case of
6 CsPbBr₃ nanocrystals Lounis *et. al.* found two different kind of fine structure splitting of bright
7 exciton for orthorhombic and tetragonal phases.⁸⁸⁷ Under application of external magnetic field of
8 15 T Biadala *et. al.* observed the bright exciton emission from CsPbBr₃ nanocrystals, to be
9 circularly polarized where the left handed circularly polarized light was more intense compared to
10 right handed circularly polarized light (**Figure 99a-b**).⁸¹⁹ With increase in magnetic field the
11 splitting between two opposite circularly polarized light enhances due to increased amount of
12 Zeeman splitting from which they could determine the exciton g factor for CsPbBr₃ nanocrystals
13 to be 2.4 with electron and hole g factors +2.18 and -0.22, respectively (**Figure 99c**).⁸¹⁹

14 **Spin polarization of optically generated carriers:** The exciton spin that determines the
15 singlet/triplet dark/bright character of the states plays a critical role in controlling the optical
16 transitions in semiconductor NCs. For instance, a spin flip may cause a transition from an optically
17 active (bright) to a passive (dark) state. Therefore, selective excitation of exciton spin is an
18 effective approach to tune the optical properties of NCs.

19 Spin dynamics of particular spin states of photoexcited carriers could be studied using helicity-
20 dependent time-resolved differential transmission spectroscopy (DTS) by employing circularly
21 polarized light for pump and probe.⁸⁸⁹ The helicity of the circular polarization can be controlled
22 by the rotation of the azimuthal angle of the optical axis of a quarter wave plate ($\lambda/4$) with respect
23 to the linear polarization axis of the pump/probe beam. The detector view conventions for positive

1 helicity: σ^+ = left handed circular polarization; negative helicity: σ^- = right handed circular
 2 polarization. **Figure 100a** schematically illustrates the possible optical transitions induced by the
 3 circularly polarized resonant optical pumping at the bandgap of Pb^{2+} based MHP. Under σ^+
 4 excitation, the electron flips from the $M_{J,\text{VB}} = -1/2$ state into the $M_{J,\text{CB}} = +1/2$ state because of the
 5 conservation of angular momentum in an optical transition. Then, the conduction band electron
 6 can undergo an intra-band M_J spin-flip from $M_{J,\text{CB}} = +1/2$ to $M_{J,\text{CB}} = -1/2$ at a rate of $1/\tau_e$. Similarly,
 7 the holes in the VB can undergo spin-flip from $M_{J,\text{VB}} = -1/2$ to $M_{J,\text{VB}} = +1/2$ at a rate $1/\tau_h$.

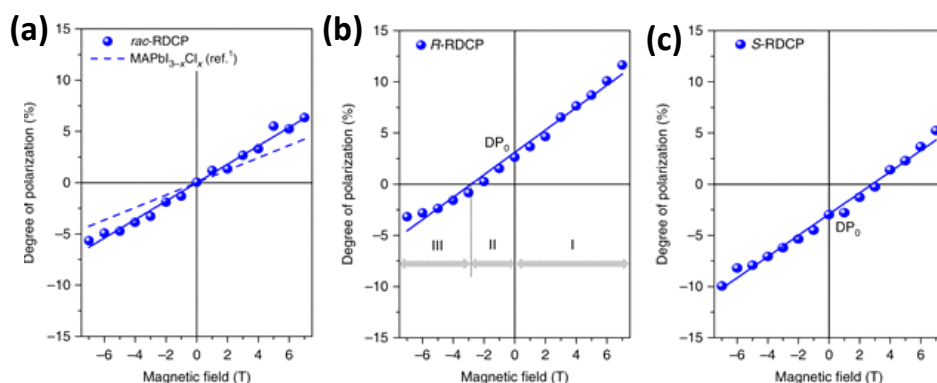


8
 9 **Figure 100.** (a) Spin-dependent optical transitions between valence and conduction band states
 10 induced by circularly polarized pump and probe beams with similar and opposite helicities. (b)
 11 Electron spin relaxation process in CB due to LO phonon scattering process. (c) Temperature
 12 dependent SP in CsPbI_3 NCs. At 50 K an additional spin relaxation channel appears due to exciton
 13 spin flip. Adapted with permission from Ref⁸⁹⁰

14 Strohmer *et. al* have reported spin relaxation processes of free charge carriers in CsPbI_3 nanocubes
 15 using circularly polarized differential transmission spectroscopy. They observed that the spin-
 16 polarization (SP_{max}) $[(\Delta T/T)_{\sigma^+\sigma^+} - (\Delta T/T)_{\sigma^+\sigma^-}]$ decreases dramatically for above bandgap excitation,
 17 and is almost 70 % smaller at 2.32 eV compared to SP_{max} detected at 1.92 eV.⁸⁹⁰ The spin
 18 polarization of the photo-excited charge carriers diminishes during thermalization and cooling

1 down to the band edge by emitting longitudinal optical (LO) phonons (**Figure 100b**). In this
2 context, Strohmair *et al.* emphasized the dominant contribution from LO phonons *via* the Elliott-
3 Yafet spin relaxation mechanism in case of free carriers in CsPbI₃ NCs due to strong Fröhlich
4 interaction present in MHPs.⁸⁹⁰ At low temperature the spin relaxation time increases and an
5 additional fast relaxation channel appears due to excitonic processes becoming prominent. The
6 faster spin relaxation channel at low temperature occurs *via* Coulomb mediated exchange
7 interaction according to the Bir-Aronov-Pikus (BAP) model (**Figure 100c**).^{890 891} Spin-dynamics
8 has also been studied in polycrystalline MAPbI₃ thin films using helicity-dependent time-resolved
9 transient absorption spectroscopy. The spin relaxation times of the photo-excited free charge
10 carriers have been found to be in the range of a few picoseconds, and the spin-depolarization was
11 attributed to the Elliott-Yafet (EY) mechanism.⁸⁹² In the case of 2D layered (C₆H₅C₂H₄NH₃)₂PbI₄,
12 the observed exciton spin-relaxation time was even on the shorter time scales. Due to the fact that
13 the exciton binding energy in 2D layered perovskites is relatively high (~180 meV), the spin-
14 relaxation mechanism is usually controlled *via* Coulomb exchange interaction and is described by
15 BAP model.⁸⁹¹ By using pump-probe Kerr rotation, Belykh *et al.* measured that the charge carrier
16 spin relaxation in CsPbBr₃ perovskite crystals is in the nanosecond regime.⁵¹⁰ They assigned the
17 long-lasting spin relaxation time to hyperfine interaction between localized charge carriers and the
18 nuclei spins. Li *et al.* have observed decrease in spin lifetime with decrease in size CsPbBr₃ and
19 CsPbI₃ QDs. In case of CsPbI₃ QDs, the spin relaxation time decreased from 3.2 to 1.9 ps for the
20 QD size reduction from 8.3 to 4.2 nm while it decreased from 1.9 to 1.2 ps for CsPbBr₃ QDs with
21 size decreasing from 7.5 to 3.5 nm. Elliot-Yafet spin relaxation mechanism was postulated to be
22 absent in case of CsPbBr₃ QDs where electron-hole exchange interaction, surface scattering, and
23 spin-spin interaction have been held responsible as probable spin relaxation channel.⁸⁹³

1 Furthermore, spin-polarization has also been induced externally in MHPs using chiral ligands or
 2 by doping with transition metal ions.^{509, 886} For example, Long *et al.* were able to achieve 3% spin-
 3 polarized photoluminescence from the reduced dimensional chiral perovskites at zero applied
 4 magnetic field due to the different emission rates of right and left handed circularly polarized
 5 light.⁵⁰⁹ To achieve the same magnitude of spin-polarized photoluminescence from achiral
 6 perovskite an external magnetic field of 5 T is needed, as shown in **Figure 101**.

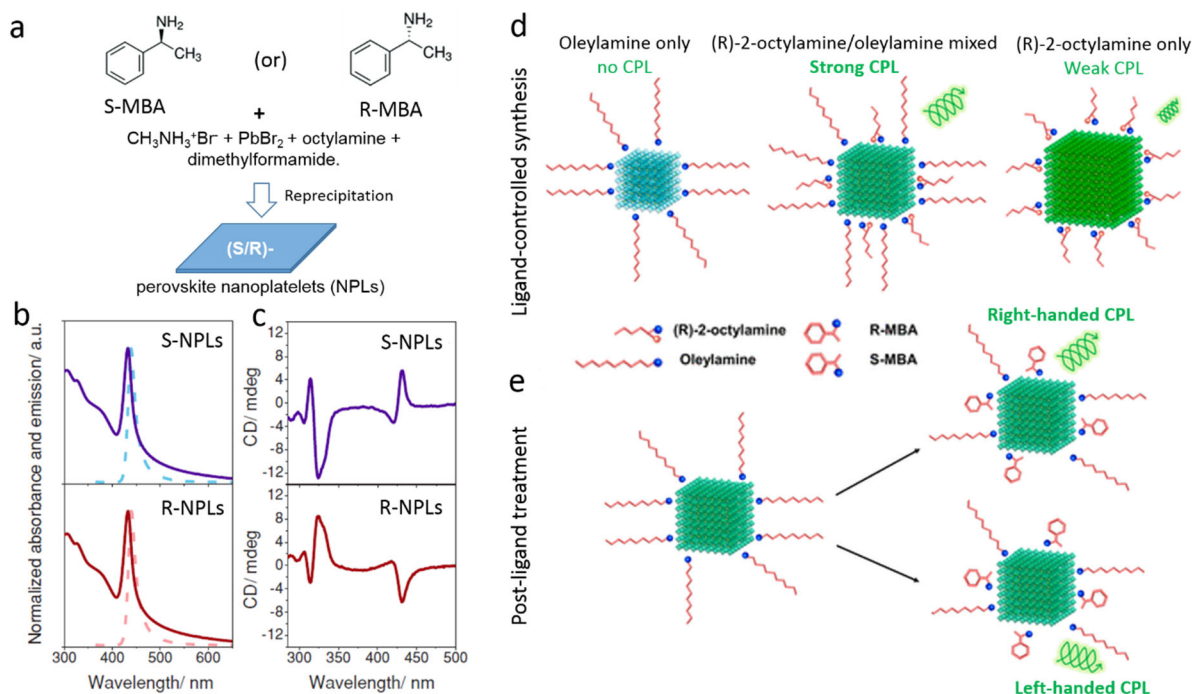


7
 8 **Figure 101.** Degree of photoluminescence polarization for *rac*-RDCP (a), *R*-RDCP (b) and *S*-
 9 RDCP (c) with magnetic field varied from -7 T to 7 T. The graph of *R*-RDCP is divided into three
 10 regions: I, II and III. At $B = 0$ (no external magnetic field), there is a degree of polarization (DP_0)
 11 for *R*-RDCP. When a positive magnetic field is applied, the degree of polarization increases with
 12 the magnetic field (region I). In region II, as a negative magnetic field is applied, the degree of
 13 polarization decreases accordingly until it is zero. As a stronger negative magnetic field is applied,
 14 the degree of polarization changes sign from positive to negative (region III). Opposite phenomena
 15 are observed for *S*-RDCP. Adapted with permission from Ref⁵⁰⁹

16 9.2. CHIRAL PEROVSKITE NCs

17 Thanks to the flexible chemical composition and surface chemistry of perovskite NCs, which
 18 enables the introduction of new functions and properties through surface ligands. Recently, there

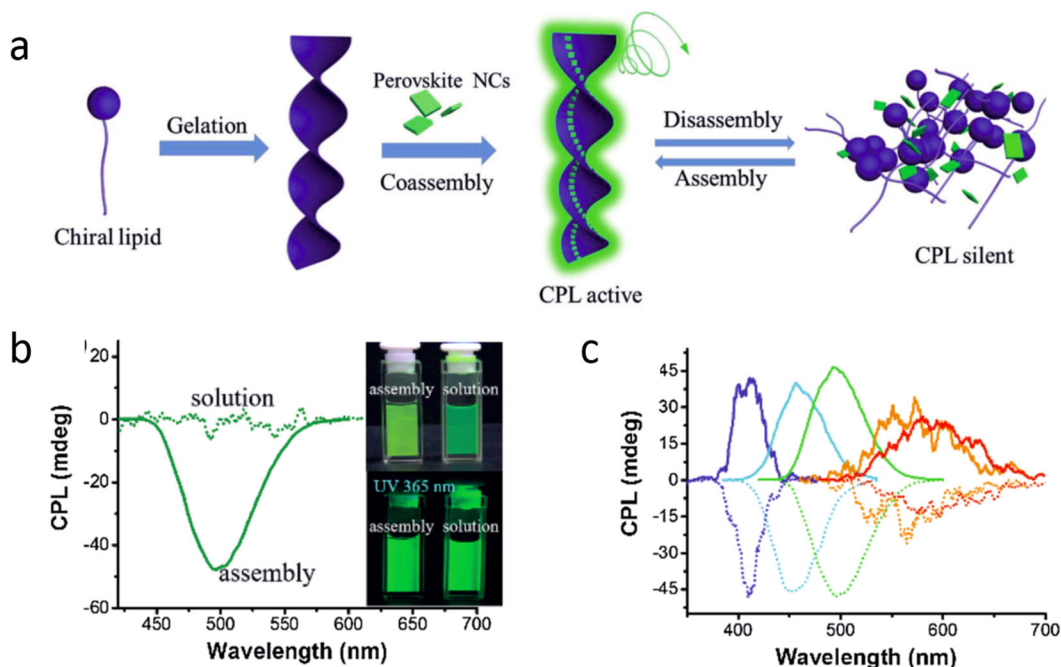
1 has been a growing research attention regarding the introduction of chiral function into halide
2 perovskites by their integration with chiral ligands.^{568, 724, 894-911} The concept of chirality or
3 handedness refers to the functional property of chiral materials/molecules that are not
4 superimposable with their mirror images, and these are called enantiomers (*(R)*-(-) (right) and *(S)*-
5 (+) (left)).⁹¹² The unique property of chiral molecules is their ability to rotate the plane of linearly
6 polarized light differently depending on the respective enantiomer. The reason for this so-called
7 Optical Rotation (OR) lies in the circular birefringence, i.e. the refractive index is different for
8 right and left circularly polarized light. With linearly polarized light depicted as a superposition
9 of two circularly polarized waves (clockwise and counter-clockwise), the polarization of light is
10 rotated when passing through a chiral medium. Chiral molecules play a crucial role in many
11 biological processes, real life systems and electronic devices.⁹¹³ In general, most small chiral
12 molecules exhibit optical activity in the ultraviolet region of the light spectrum. However,
13 interestingly, it has been shown that such molecules can confer chirality in colloidal metallic or
14 semiconductor NCs that show optical activity in the visible to near-IR region by means of surface
15 functionalization. Over the last few decades, a significant amount of research work has been done
16 regarding the fabrication and application of chiral plasmonic, and semiconductor NCs. Recently,
17 these concepts have been extended to newly emerged perovskites for a variety of applications,
18 including ferroelectrics, chiroptoelectronics and chiro-spintronics. Readers may also refer to two
19 latest review articles on chiral perovskites.^{724, 911}



1
 2 **Figure 102.** (a) Schematic representation of the synthesis of chiral organic-inorganic hybrid
 3 perovskite NPLs by reprecipitation in the presence of chiral ligands (S-MBA and R-MBA). (b, c)
 4 UV-visible absorption (solid line) and PL (dotted line) (b), and the corresponding CD spectra (c)
 5 of the enantiomeric NPLs obtained with S-MBA and R-MBA ligands. Panels (b) and (c) are adapted
 6 from Ref.⁹⁰⁰ (d, e) Schematic illustration of the synthesis of FAPbBr₃ nanocubes in the presence
 7 of the chiral ligand (R)-2-octylamine (d) and post-synthetic surface treatment of FAPbBr₃
 8 nanocubes with chiral ligands (R-, S-MBA.Br) (e). Panels (d) and (e) are adapted from Ref.⁸⁹⁵

9 The initial studies on chiral perovskites were mainly focused on 1D single crystals, 2D layered
 10 systems and bulk thin films.^{724, 894, 896, 898, 903, 907-908, 910-911, 914} In 2003, Billing et al⁸⁹⁸ were the first
 11 to report the synthesis of organic-inorganic hybrid 1D perovskite single crystals (((S)-
 12 $\text{C}_6\text{H}_5\text{C}_2\text{H}_4\text{NH}_3$)[PbBr_3]) by in situ incorporation of a chiral amine (1-phenyl-ethyl-ammonium
 13 (PEA), also called methylbenzylammonium (MBA)) as the counterion. However, their chiral
 14 properties were not investigated. After being out of limelight for a few years, chiral perovskites

1 have regained attention after the chiroptical study of (S-MBA)₂PbI₄ and (R-MBA)₂PbI₄ 2D layered
2 perovskite films by Moon and co-workers in 2017.⁹⁰⁸ These perovskite enantiomers were achieved
3 through the incorporation of the respective chiral organic molecule (S-MBA and R-MBA) into the
4 layered lead-iodide framework. They exhibit oppositely signed circular dichroism (CD) signals at
5 their excitonic transitions, while the chiral molecules alone do not show any CD signal at these
6 wavelengths. After these findings, chiral 2D layered perovskite films and single crystals have been
7 significantly explored regarding their synthesis and applications.^{724, 894, 896, 903, 907, 909-911, 915} For
8 instance, Chen et. al.⁹¹⁰ and Wang et al.⁹⁰³ independently demonstrated the fabrication of flexible
9 photodetectors using chiral 2D perovskites for efficient detection of circularly polarized (CP) light.
10 The principle of these CP light photodetectors is the generation of different photocurrents for
11 different circular polarization states of detected photons. Furthermore, chiral 2D perovskites are
12 being studied for exploring circularly polarized photoluminescence (CPP)^{894, 896} and
13 ferroelectricity⁹¹⁶. Recently, these concepts have been extended to colloidal perovskite NCs. They
14 can be excellent candidates as CP light sources for optoelectronic applications owing to their high
15 PLQY and easily tunable emission color. However, unlike chiral 2D layered perovskites, only a
16 few studies have been reported on colloidal chiral perovskite NCs.



1
 2 **Figure 103.** (a) Schematic illustration showing the gelation of chiral lipids into helical structure
 3 followed by co-assembly of perovskite NCs along the helical gel to obtain chiral assemblies that
 4 emit circularly polarized luminescence (CPL). (b) CPL spectra of chiral gel induced CsPbBr₃
 5 assemblies and the disassembled CsPbBr₃ colloidal solution, with the latter obtained by dispersing
 6 the gel-perovskite NC assemblies in chlorobenzene solution. The inset shows the photographs of
 7 the colloidal solutions containing perovskite NC assemblies and individual NCs (disassembled)
 8 under room light (top) and UV light (bottom, 365 nm) illumination. (c) CPL spectra of chiral gel
 9 induced CsPbX₃ NC assemblies of different halide composition. Adapted with permission from
 10 Ref.⁹⁰¹

11 Generally, there are three different synthetic approaches to obtain colloidal chiral perovskite
 12 NCs: 1) in situ incorporation of chiral ligands during the synthesis (figure 102)^{895, 900, 905} (similar
 13 to the case of chiral 2D layered perovskites), 2) post-synthetic surface treatment with chiral
 14 molecules⁸⁹⁵ or chiral assemblies (figures 102, 103), 3) synthesis of helical perovskite NCs (not
 15 yet achieved). Figure 102b summarizes the first two (in situ and post-synthetic) strategies one can

1 use to synthesize chiral perovskite NCs. In this regard, Waldeck and co-workers⁹⁰⁰ demonstrated
2 the in situ incorporation of chiral molecules (S-MBA and R-MBA) onto hybrid perovskite NPLs
3 synthesized by the reprecipitation method (figure 102a). In this case, the chiral MBA cation
4 molecules were introduced along with achiral octylamine as ligands into the precursor solution.
5 The injection of precursor solution into toluene leads to the formation of chiral hybrid perovskite
6 NPLs, which exhibit sharp excitonic absorption and emission features that are consistent with
7 quantum-confined NPLs (figure 102b). The NPLs (S-,R-NPLs) obtained with the two enantiomer
8 ligands (S-, R- MBA) exhibit mirror-image like CD spectra with peaks at their excitonic absorption
9 (figure 102c), where the ligand molecules alone do not show any CD signal. . The authors take
10 this as a clear indication for the ligands imprinting their chirality onto the NPLs electronic structure.
11 In addition, the CD peaks observed at higher energy (~300–350 nm) were assigned to the charge
12 transfer bands between the chiral ligands and the NPL surface (Figure 102c). Very recently, this in
13 situ synthesis of chiral perovskite NCs has been extended to CsPbBr₃⁹⁰⁵ and FAPbBr₃⁸⁹⁵ NCs using
14 the short chiral ligand α -octylamine (figure 102d). The partial replacement of oleylamine with (R)-
15 2-octylamine during the synthesis of FAPbBr₃ NCs results in monodisperse chiral perovskite NCs
16 that emit CPL with a luminescence dissymmetry (*g*-) factor of 6.8×10^{-2} , which is the highest
17 among reported perovskite materials.

18 Besides these direct synthetic strategies, post-synthetic treatments have also been used to
19 induce chirality in perovskite NCs by two different approaches. Firstly, the surface of pre-
20 synthesized perovskite NCs can be modified with chiral ligands through ligand exchange (figure
21 102d) .⁸⁹⁵ For instance, Luther and co-workers demonstrated the post-synthetic ligand exchange
22 on FAPbBr₃ NCs with chiral ligands (S-,R-MBA), which induces CPL with an average
23 dissymmetry *g*-factor of $\pm 1.18 \times 10^{-2}$. The second post-synthetic approach is the supramolecular

1 self-assembly of NCs into helical structures.^{901, 917} Previously this approach has been extensively
2 used to induce chirality in plasmonic NCs using biomolecules such as DNA, DNA origami, and
3 supramolecular fibers.⁹¹⁷⁻⁹¹⁹ Recently, Shi et al.⁹⁰¹ demonstrated the supramolecular self-assembly
4 of CsPbX₃ (X=Cl, Br and I) into chiral assemblies that emit CPL by mixing chiral organogels
5 made of lipids (N,N'-bis(octadecyl)-l-glutamic diamide (LGAm) and its enantiomer (DGAm))
6 with perovskite NCs in hexane (figure 103a). In this approach, chiral assemblies were obtained by
7 simple mixing of chiral organogels made of lipid (N,N'-bis(octadecyl)-l-glutamic diamide
8 (LGAm) and its enantiomer (DGAm)) molecules with perovskite NCs in hexane (figure 103a).
9 The shape of the emission spectra remains unchanged with a slight red-shift after self-assembly.
10 However, interestingly, the perovskite NC assemblies exhibit CPL with a dissymmetry *g*-factor up
11 to 10⁻³, while disassembled gels do not show CPL (figure 103b). The disassembled gels were
12 obtained by dissolving the DGAm-CsPbBr₃ hybrid assemblies in chlorobenzene. The wavelength
13 of the CPL peak is easily tunable across the visible spectrum of light by varying the halide
14 composition (figure 103c). Furthermore, it has been shown that these chiral assemblies could be
15 incorporated into polymer film to obtain flexible CPL devices. Despite these interesting reports,
16 the study of chiral perovskite NCs is still in the beginning stage. There are many questions yet to
17 be addressed regarding colloidal chiral perovskite NCs. For instance, the mechanism of chiral
18 induction via surface ligands on 3D perovskite NCs is still unclear. In addition, the number of
19 chiral ligands used so far to modify the surface of perovskite NCs are limited because many chiral
20 molecules are not miscible in non-polar solvents. Furthermore, perovskite NCs with helical

1 morphology have yet to be achieved. More importantly, the application of chiral perovskite NCs
2 in optoelectronic and spintronic applications need to be explored.

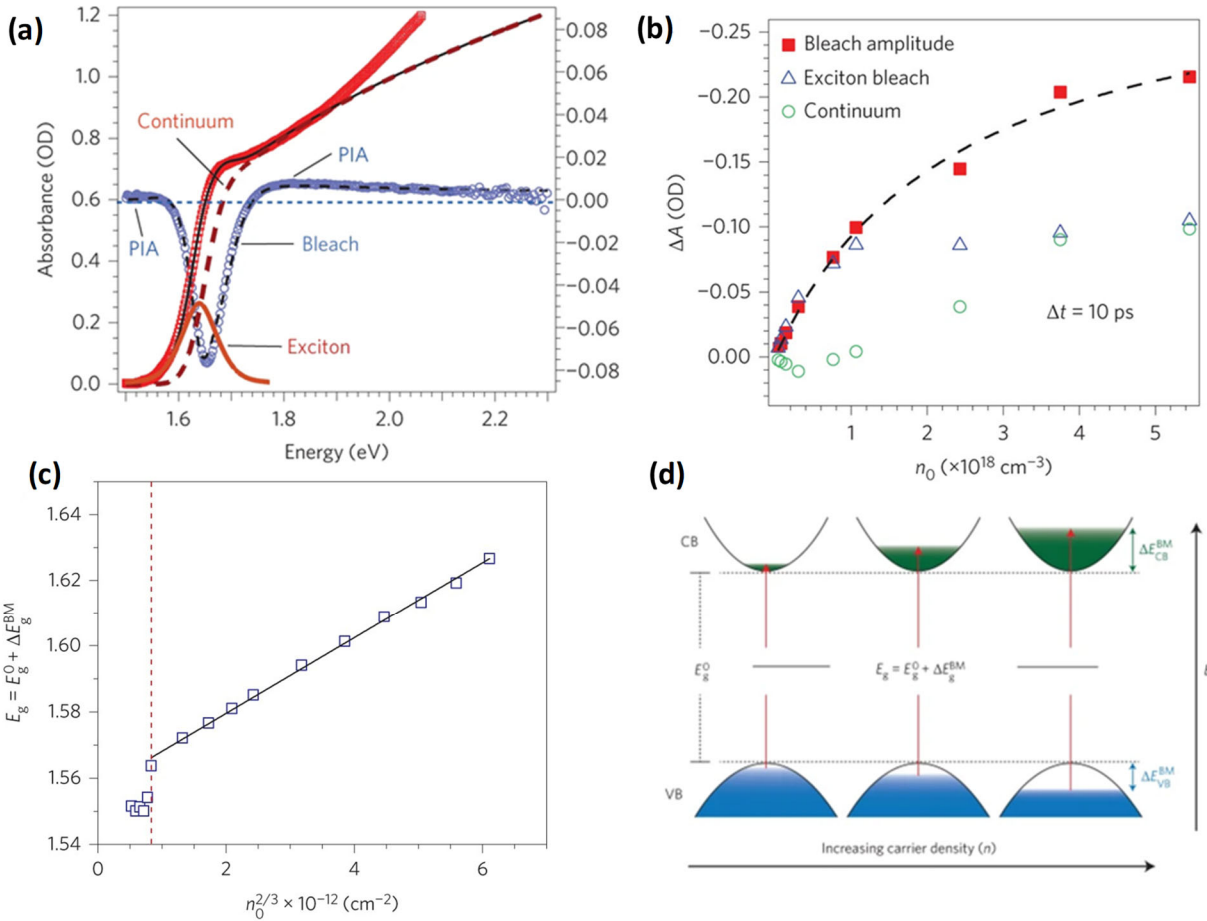
3

4 **9.3. CHARGE CARRIER DYNAMICS**

5 Understanding the fate of the photo excited charge carriers in a semiconducting material is of
6 fundamental importance for the development of efficient optoelectronic devices. Photoexcitation
7 produces electron- hole pairs whose energy relaxation pathways depend on a variety of
8 conditions.^{10 920-921} Followed by initial carrier thermalization, the hot charge carrier loses its energy
9 by emitting optical phonons and successively relaxes down to the electronic band edge. The charge
10 carriers then either radiatively decay to produce light or recombine nonradiatively. The following
11 sections, discuss various such energy relaxation dynamics in MHP under ultrafast photo-
12 excitation.

13 Figure 104a represents a typical steady state linear absorption spectrum (red squares) and
14 a transient absorption (TA) spectrum (blue circles) of a planar MAPbI₃ perovskite thin film. The
15 absorption spectrum of MAPbI₃ shows a steep rise at the absorption onset (at 1.6 eV). According
16 to the Elliot model (Figure 90b-c), both excitonic and band-to-band continuum transitions
17 contribute to the optical band gap in MHPs. This is shown by the representative TA spectrum
18 ($\hbar\omega_{\text{pump}} = 1.82$ eV) at a pump–probe delay of 10 ps. It has two general features: a sharp photo
19 bleach (PB) and a broad photo-induced absorption (PIA).⁹²² The PB signal peaking at ~ 1.65 eV
20 has been attributed to both band filling and free carrier induced bleaching of the exciton transition.
21 The PIA has been related to several factors such as hot carrier (HC) cooling, polaron formation
22 and free carrier absorption.⁹²² With increase in the excitation fluence, the amplitude of the PB
23 signal ($-\Delta A$) increases in a nonlinear fashion (**Figure 104b**). The spectral position was found to

1 depend on the initial carrier density n_0 . Manser *et al.* reported a carrier density dependent blue shift
 2 and broadening of the PB signal in MAPbI₃ thin films due to the Burstein–Moss shift (**Figure**
 3 **104c**).⁹²³ When the photo generated carriers fill the electronic band edge states (valence and
 4 conduction band), the effective bandgap shifts towards higher-energy due to Pauli-blocking.
 5 (**Figure 104d**).

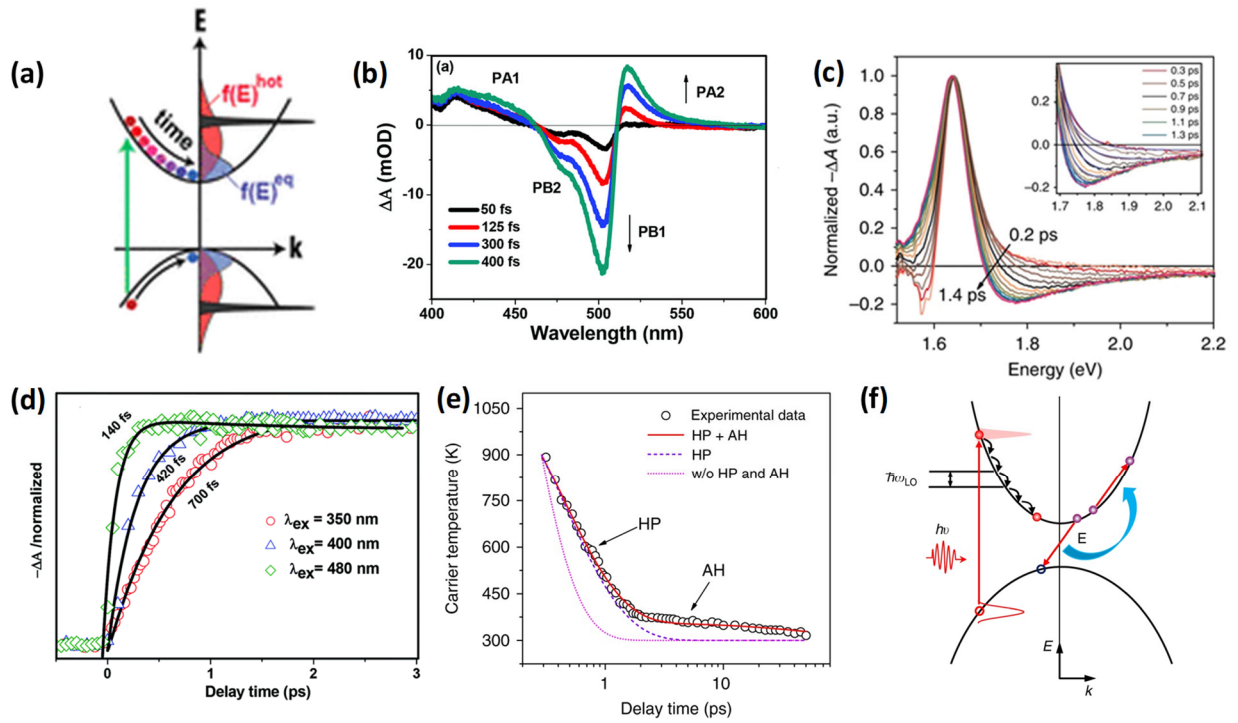


6
 7 **Figure 104.** (a) Steady-state (red squares) and transient absorption (TA) (blue circles) spectra of a
 8 typical MAPbI₃ perovskite thin film. Black line: modelled band edge absorption. Red dashed line:
 9 continuum contribution. Red line: exciton contribution. Adapted with permission from Ref.⁹²² (b)
 10 ΔA at $h\omega_{\text{probe}} = 1.65$ eV as a function of the initial charge carrier density n_0 . Blue triangles: exciton
 11 contribution. Green circles: continuum band contribution. Adapted with permission from Ref.⁹²²

1 (c) Modulation of the intrinsic bandgap of MAPbI₃ according to the Burstein–Moss model. The
2 vertical dashed line marks the onset of bandgap broadening. The solid line is a linear fit to the data
3 after the onset. The linear trend indicates an agreement with band filling by free charge carriers.
4 Adapted with permission from Ref.⁹²³ (d) Schematic representation of the Burstein–Moss effect
5 showing the contribution from both, electrons in the conduction band (CB) and holes in the valence
6 band (VB) due to their similar effective masses. Adapted with permission from Ref.⁹²³
7 *Hot carrier relaxation dynamics:* When excited by photons with energy higher than the band-gap
8 energy, the charge carriers (electrons and holes) are produced in states much above the band edge
9 states with a non-equilibrium distribution in energy. These ‘hot carriers’ thermalize through
10 carrier-carrier scattering processes within 1 ps. The subsequent process is called “carrier cooling”,
11 in which the quasi-equilibrated HCs (at temperature higher than the lattice temperature and
12 governed by the Fermi-Dirac distribution) dissipate their excess energy as heat *via* phonon
13 emission and come to the band edge states (**Figure 105a**).^{515, 924}

14 The overall hot carrier (HC) cooling process can be probed by using ultrafast transient
15 absorption (TA) and photoluminescence (PL) measurement techniques. **Figure 105b** shows the
16 TA spectra of CsPbBr₃ NCs for short (0.05–0.4 ps) time scales, where the TA spectra comprise
17 off positive differential absorption (ΔA) bands PA1, PA2 and a strong negative photo bleach signal
18 due to carrier-filling effect of the band edge states.⁹²⁵ The formation kinetics of this bleach signal
19 (PB1) delivers a carrier cooling time (τ_c).⁹²⁵⁻⁹²⁶ The time dependence of the recovery of the
20 secondary weak bleach signal (PB2) (**Figure 105b**) matches with the formation kinetics of PB1.
21 The lower energy absorption band (PA2), which is related to the HC cooling, has been recently
22 attributed to polaron formation.⁹²⁷⁻⁹³⁰ Another approach to probing HC cooling is by measuring
23 the carrier temperature by fitting the high energy tail of the TA spectra to a Maxwell-Boltzmann

1 (M-B) distribution (**Figure 105c**).^{515, 922} However, the exact estimation of the individual
 2 contributions of hot holes and hot electrons to the carrier cooling time is difficult as the excess
 3 energy is almost equally distributed between the hot electrons and hot holes. As the energy of HC
 4 depends on the energy provided in excess of the bandgap energy, τ_C directly correlates with the
 5 excitation energy. The higher the excitation energy is, the longer is the hot carrier cooling time. In
 6 case of CsPbBr₃ NCs, Mondal *et. al.* reported an increase in τ_C from 140 to 700 fs, as the excitation
 7 wavelength was changed from 480 to 350 nm (**Figure 105d**).⁹²⁵



8
 9 **Figure 105.** (a) Thermalization and relaxation schemes of the photoexcited electrons and holes.
 10 The initial δ -like distribution of the electrons and holes changes to an equilibrium distribution in
 11 two stages. Adapted with permission from Ref. ⁹³¹ (b) Time-dependent evolution of the TA
 12 spectrum ($\lambda_{ex} = 350$ nm) of CsPbBr₃ NCs in the early time window (0.05 – 0.4 ps). Adapted with
 13 permission from Ref. ⁹²⁵ (c) Normalized TA spectra with variable delays from 0.2 ps to 1.4 ps with
 14 the inset showing the high energy tails fitted to the M-B distribution for extraction of the HC

1 temperature. Adapted with permission from Ref. ⁵¹⁵ (d) Formation kinetics of the PB1 band
2 (representing HC cooling time) of CsPbBr₃ NCs as a function of the excitation wavelengths.
3 Adapted with permission from Ref. ⁹²⁵ (e) HC cooling dynamics in a MAPbI₃ thin film following
4 photoexcitation at 2.48 eV with a carrier density n_0 of $10.4 \times 10^{18} \text{ cm}^{-3}$ at RT. Black circles: HC
5 temperature extracted from TA spectra. The lines show the calculated HC cooling dynamics for
6 $\tau_h = 0.6$ ps: with a hot-phonon (HP) effect only (violet dashed line); with both HP and Auger
7 heating (AH) effects (bright red line); and without HP and AH effects (magenta line). Adapted
8 with permission from Ref. ⁵¹⁵ (f) Schematic of the hot electron relaxation process. Auger heating,
9 which contributes to further deceleration of hot electron cooling, is also shown. The same
10 processes apply to the hot holes but are omitted for clarity. Adapted with permission from Ref. ⁵¹⁵

11
12 The HC cooling dynamics also depends on the excitation fluence and cannot be explained
13 by the hot phonon effect alone.^{924, 932-933} For all APbBr₃ NCs (A= Cs, MA and FA), HC cooling
14 slows down with an increase in excitation fluence.⁹³⁴ At high excitation fluence, the carrier-carrier
15 interactions come into the picture due to high carrier densities and this can cause re-excitation of
16 the hot charge carriers (called “Auger heating”) and slows down the overall HC cooling process.
17 Fu *et al.* reported that at carrier densities above 10^{19} cm^{-3} , the HC cooling dynamics is governed
18 by the combined effect of hot-phonon and Auger heating.⁹³⁵ **Figure 105e** shows the HC cooling
19 dynamics in MAPbI₃ when photo-excited at 2.48 eV at room temperature with an initial carrier
20 density of $1 \times 10^{19} \text{ cm}^{-3}$. Two gradients are clearly visible, indicating the presence of two distinct
21 HC cooling mechanisms which are the hot phonon effect and the Auger effect. There are two
22 distinct types of Auger recombination processes : the intraband and the interband Auger
23 recombination among which the later process (also called Auger heating) causes a non-radiative

1 transfer of the electron-hole recombination energy to a third electron (or hole), resulting in the
2 excitation of the third carrier to higher energy level (**Figure 105f**). As the Auger lifetime (τ_{Aug}) is
3 dependent on the volume (V) of the NCs ($\tau_{\text{Aug}} \sim V^{1/2}$), the HC cooling time at high excitation
4 fluence is expected to be dependent on the NCs' volume.⁹²⁴ Indeed, an increase in the HC cooling
5 time from 12 to 27 ps has been observed with increasing the size of the NCs from 4.9 to 11.6
6 nm.⁹²⁴

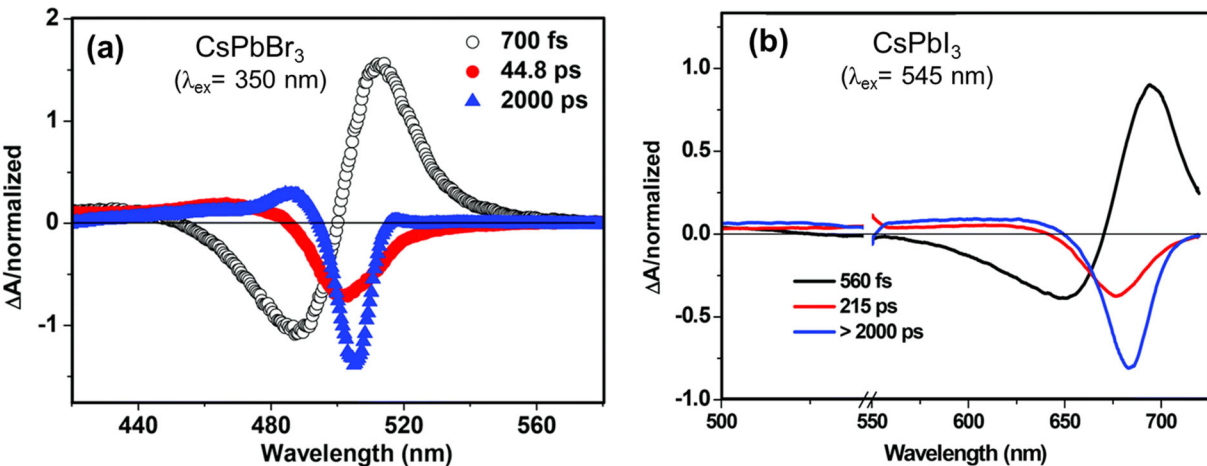
7 In CsPbX₃ (X= Br and I) NCs, τ_c (for the same amount of excess energy) decreases while
8 going from iodide based NCs to bromide based NCs: CsPbI₃ (580 fs) > CsPb(Br/I)₃ (380 fs) >
9 CsPbBr₃ (310 fs).⁹²⁶ As the halide's orbitals mainly contribute to the valence band of the NCs, this
10 HC cooling time seems to represent the effective hot hole cooling dynamics rather than the hot
11 electron cooling.⁹²⁶ The HC cooling time is also influenced by the A site cation composition in
12 MHP NCs where it was observed that τ_c decreases from Cs to FA based NCs: CsPbBr₃ (390 fs) >
13 MAPbBr₃ (270 ps) > FAPbBr₃ (210 fs).⁹³⁴ A faster τ_c in hybrid perovskites (FAPbBr₃ and
14 MAPbBr₃) compared to the Cs-based MHP is attributed to a stronger carrier-phonon coupling
15 facilitated by the vibrational modes of the organic cations.^{934, 936-937} The role of molecular
16 vibrations in HC relaxation is confirmed by the ability to slow down the cooling process at lower
17 temperatures for FAPbBr₃, while no/a less strong effect is observed for CsPbBr₃ NCs.⁹³⁸ The
18 dependence of the HC cooling on the B site cation was studied by a partial replacement (60%) of
19 Pb with Sn and found to slow down the HC cooling time of MAPbI₃ from 0.3 ps to 93 ps.⁹³⁹ A
20 very slow HC cooling in FASnI₃ thin films was reported to give rise to hot PL.⁹⁴⁰ However, as an
21 opposite trend (a faster HC cooling dynamics upon partial Sn substitution in CsPbBr₃ NCs) is also
22 reported recently,⁹⁴¹ more studies are needed to understand the exact role of 'Sn' on HC cooling
23 dynamics in Sn-doped lead-halide perovskite NCs.

1 In quantum confined systems, the HC cooling time depends on the size of the NCs. For
2 example, HC cooling dynamics become faster (from 700 fs to 500 fs) when the size of MAPbBr₃
3 NCs is increased from ~4.9 to 11.3 nm.⁹²⁴ A slower HC cooling in smaller NCs is attributed to the
4 intrinsic phonon bottleneck effect due to the availability of fewer phonon modes.^{924, 942}
5 Interestingly, a small change in HC cooling time of CsPbBr₃ NCs on varying the edge length from
6 2.6 to 6.2 nm indicates the absence of any hot phonon bottleneck in this class of NCs.⁹⁴³ The effect
7 of dimensionality on HC cooling dynamics was also investigated. The HC cooling was reported to
8 be much faster in 2D MAPbI₃ NPLs compared to quasi-3D system⁹³¹ due to the low dielectric
9 screening and high surface-to-volume ratio of the 2D NPLs. An increase in HC cooling time from
10 260 fs to 720 fs for A₂PbI₄ on changing the organic spacers from C₆H₅C₂H₄NH₃⁺ ($\epsilon = 3.3$) to
11 HOC₂H₄NH₃⁺ ($\epsilon = 37$) is a reflection of the influence of dielectric screening on HC cooling
12 dynamics, too.⁹⁴⁴ A slowdown of HC cooling due to the formation of large polarons at low
13 excitation fluence has also been reported very recently.^{927, 945,21}

14 **Carrier trapping and recombination dynamics in MHPs:** Radiative recombination of the
15 charge carriers is one of the most important pathways in direct bandgap semiconductors that
16 determines its utility in optoelectronic devices. Radiative recombination is slow compared to
17 exciton dephasing, spin-relaxation, HC cooling time and is commonly observed on the ps-ns time
18 scale. If indeed the perovskites were perfectly defect tolerant,⁹⁴⁶⁻⁹⁴⁷ the radiative recombination
19 would have been the only route for the relaxation of the charge carriers. However, multi-
20 exponential PL decay dynamics of most perovskites NCs even at low excitation fluence suggests
21 the existence of sub-bandgap energy levels arising from various defects that act as trap centres.^{101,}
22 ⁹⁴⁸⁻⁹⁵³ These trapped carriers can return to the conduction or valence band and recombine
23 radiatively, if the de-trapping process is effective such as in case of shallow defects.^{954 882}This

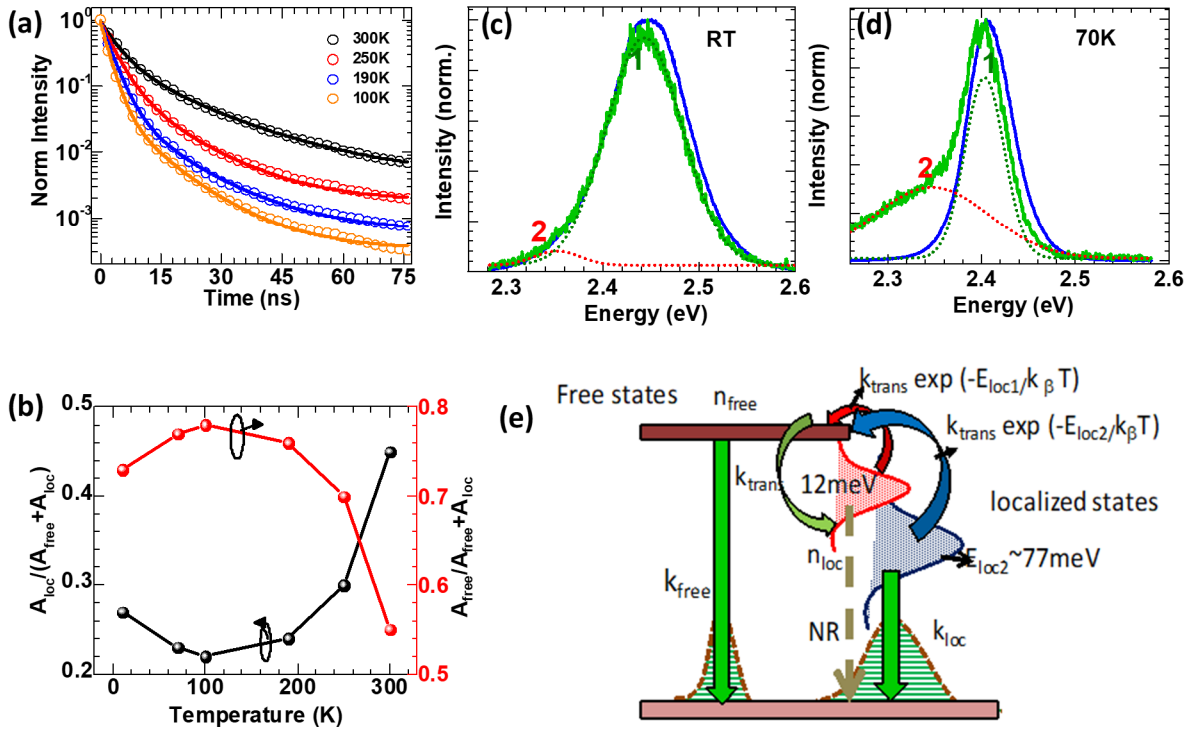
1 process is responsible for an additional longer decay component in the PL decay profile.⁹⁵⁵⁻⁹⁵⁶
2 However, when the separation between the trap state and band edge is large, as in case of deep
3 traps, the charge carriers relax nonradiatively.⁹⁵⁴ For smaller NCs, which have a high surface to
4 volume ratio, “surface trapping” can also facilitate nonradiative recombination of the charge
5 carriers resulting in lowering of the PL efficiency and acceleration of the PL decay dynamics.

6 While the time constants for the radiative processes are most commonly estimated from
7 the PL-decay profiles measured using the time correlated single photon counting (TCSPC)
8 technique, the nonradiative recombination processes are much faster and require ultrafast TA and
9 PL measurements. Most often, the temporal profile of the photo bleach recovery signal (in TA
10 measurements) contains a fast component due to carrier trapping in addition to the long component
11 due to radiative recombination. The bleach recovery kinetics of CsPbBr₃ NCs consists of two
12 components (~45 ps and ~2 ns) (**Figure 106**) in which the former has been assigned to electron
13 trapping.⁹²⁵

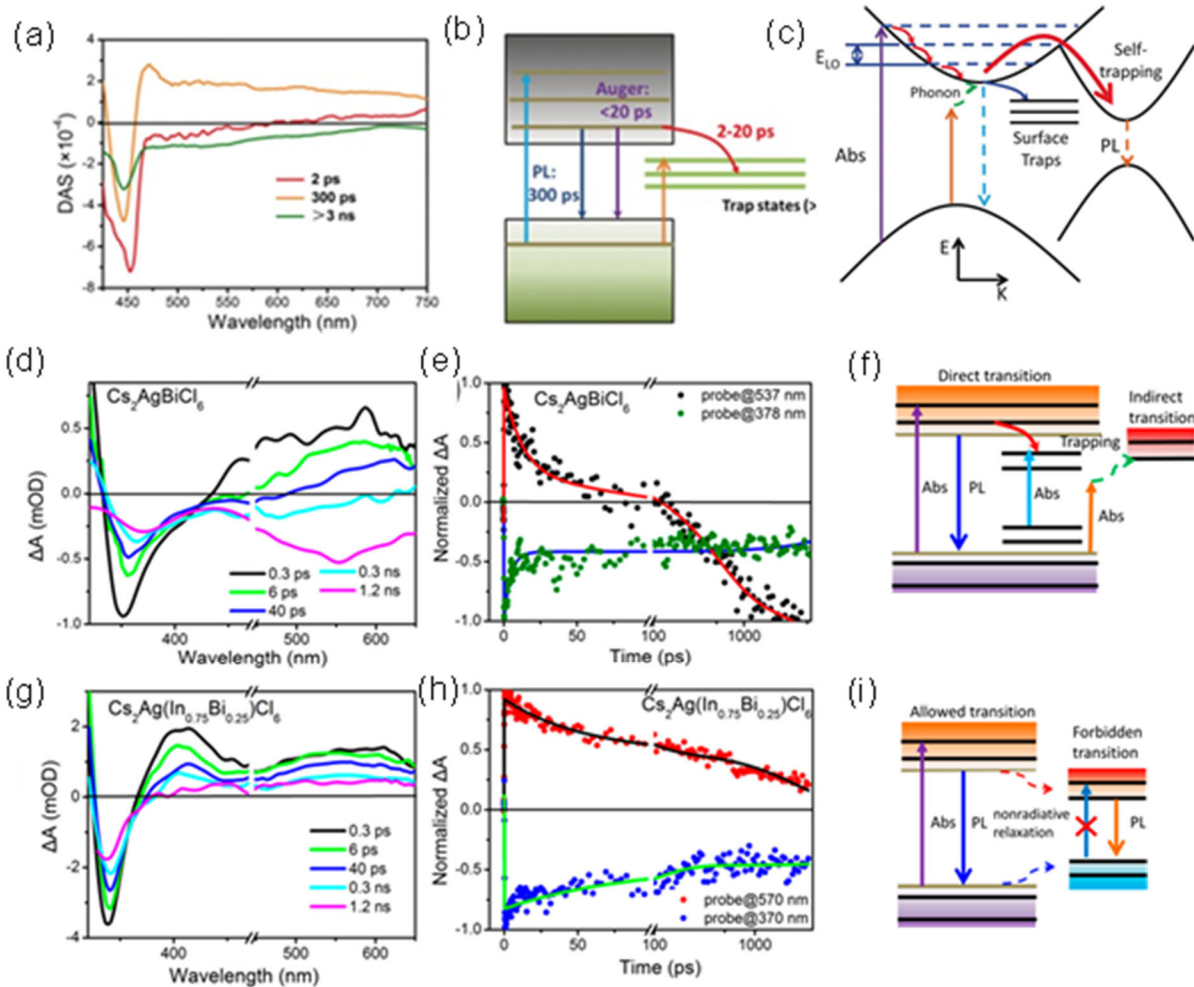


14
15 **Figure 106.** Decay associated TA spectra of (a) CsPbBr₃ and (b) CsPbI₃ NCs. Adapted with
16 permission from Ref. ⁹²⁵

1 In case of CsPbI₃, carrier trapping time is estimated as ~ (215-400) ps.^{925, 957-958} A recent
2 theoretical study shows that halide vacancies in the NCs are the major contributor to the defect
3 energy levels, which are shallow in nature for CsPbBr₃ and CsPbI₃, but deep in case of CsPbCl₃.^{152,}
4 ⁹⁵⁹ The high trap density in large bandgap CsPbCl₃ NCs accounts for its weak luminescence(PLQY
5 <10%) and TA studies show multiple carrier trapping channels with time constants ranging from
6 3 to 64 ps,^{151, 848, 960-961 847} Dey *et al.* have studied the temperature dependent time resolved PL
7 dynamics in case of CsPbBr₃ NCs, where they observed the PL decay getting faster when lowering
8 the temperature.⁸⁸² Additionally, a low energy PL peak appeared at low temperature for the long
9 time delays. (**Figure 107a-d**). Both effects can be attributed to the presence of defect states. While
10 at room temperature the detrapping process is efficient slowing down the PL decay, emission from
11 these localized states becomes significant at low temperatures as evident in the formation of the
12 additional low energy PL peak (**Figure 107e**).⁸⁸² Very recently, trapping of the hot charge carriers
13 in states within the band itself is reported for APbBr₃ NCs.^{191, 962-963}



1
 2 **Figure 107.** (a) Temperature dependent PL decay in CsPbBr₃ NCs. (b) Relative weight
 3 contributions of the free vs. localized states in controlling the PL dynamics at different
 4 temperatures. Time resolved PL spectra (PL1 at t=0 and PL2 at t=32 ns) at room temperature (c)
 5 and at low temperature (d) for CsPbBr₃ NCs. (e) Schematic of the model depicting interactions
 6 between free and localized states. Adapted with permission from Ref. ⁸⁸²



1
 2 **Figure 108.** (a) Decay associated spectra of $\text{Cs}_3\text{Bi}_2\text{X}_9$ NCs. (b) Model illustrating several
 3 photoinduced processes in $\text{Cs}_3\text{Bi}_2\text{X}_9$ NCs. Adapted with permission from Ref. ⁹⁶⁴. Copyright
 4 (2017) John Wiley & Sons. (c) Schematic illustration of the carrier dynamics of the
 5 $\text{Cs}_2\text{AgSb}_{0.25}\text{Bi}_{0.75}\text{Br}_6$ double perovskites. Adapted with permission from Ref. ⁹⁶⁵ Copyright (2019)
 6 John Wiley & Sons. Respective transient absorption spectra, kinetics and schematic model explain
 7 the carrier relaxation pathways of (d-f) $\text{Cs}_2\text{AgBiCl}_6$ and (g-i) $\text{Cs}_2\text{AgIn}_{0.75}\text{Bi}_{0.25}\text{Cl}_6$ NCs. Adapted
 8 with permission from Ref. ⁹⁶⁶. Copyright (2018) American Chemical Society.

9 Lead-free perovskite NCs, which are recently receiving increasing attention due to their
 10 non-toxic nature,⁹⁶⁴⁻⁹⁶⁷ possess a very low PLQY and are so far less explored. For $\text{Cs}_3\text{Bi}_2\text{X}_9$ ($\text{X} =$

1 Cl, Br, I) NCs, the estimated time constant for carrier trapping, band edge radiative recombination
2 and trapped charge carrier relaxation are 2-20 ps, ~300 ps and > 3 ns, respectively. (Figure
3 108a,b).⁹⁶⁴ Bleach recovery kinetics of Cs₂AgSb_{0.25}Bi_{0.75}Br₆ NCs reveal three components which
4 have been attributed to self-trapping of the charge carriers (1-2ps), surface trapping (50-100ps) and
5 geminate recombination (>5ns).⁹⁶⁵ TA spectra of Cs₂AgBiCl₆ and Cs₂AgIn_{0.75}Bi_{0.25}Cl₆ show two-
6 component ground state bleach recovery with time constants of ~100 ps due to carrier trapping
7 and >2 ns due to radiative recombination.⁹⁶⁶ In the former case, the trapping contribution is,
8 however, larger and an additional strong bleach signal due to sub bandgap trap state absorption or
9 indirect bandgap transition is observed (**Figure 108d**). Recently, in case of Cs₂AgBiBr₆ NCs, Dey
10 *et al.* showed that the PL originates from defect related bound excitons at the Γ -point
11 corresponding to the direct band transition, *via* trapping of holes occurring on a time scale of
12 hundreds fs.⁸⁴³ The PL measurements on the ps time scale using a streak camera revealed that the
13 PL maximum, which is originally close to the excitonic resonance, shifts by more than 1eV
14 towards longer wavelength/lower energy within tens ps. This has been attributed to intervalley
15 scattering. Whereas the emission from the direct bound excitons decays fast, the indirect emission
16 showed a slow recombination.⁸⁴³ More experimental studies in combination with theoretical
17 calculations are needed for a clear understanding of the underlying photo-physical processes in
18 these systems. Readers interested in carrier dynamics of lead free perovskites may go through the
19 accounts of Yang and Han.⁹⁶⁸

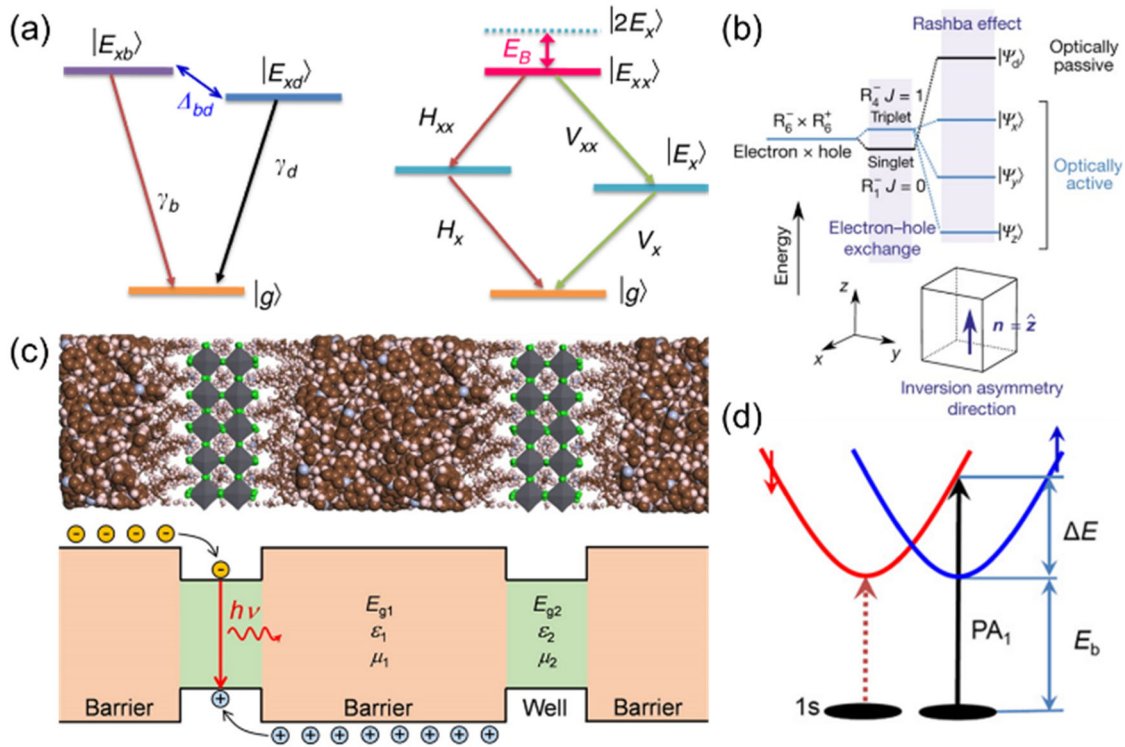
20 **Exciton recombination:** In bulk and NC LHPs, both excitons and free carriers contribute to
21 the radiative recombination.⁹²³ The populations of excitons and free carriers are determined by the
22 initial exciton concentration and the exciton binding energy (E_B). Excitons in bulk LHPs possess
23 a very small E_B but the η_{PL} is typically lower than 10%.⁹⁶⁹ On the other hand, the quantum and

1 dielectric confinement effects in LHP NCs increase E_B and the η_{PL} can approach unity at relatively
2 low excitation density. While, upon increasing the exciton concentration, the Auger recombination
3 pathway, including biexcitons and trions,⁹⁷⁰⁻⁹⁷² and trap-assisted non-radiative recombination,⁹⁷³
4 come into play. Therefore, it is obvious that the suppression of nonradiative recombination losses
5 is essential to realize the optoelectronic applications of LHPs.

6 It has been suggested that 2D LHPs possess a very high E_B that results in a low nonradiative
7 recombination rate. This is due to (i) a relatively low density of intrinsic defects (owing to high
8 defect formation energy), (ii) the presence of distinct polaronic effects, and (iii) the Rashba
9 splitting induced bright triplet excitons (**Figure 109a,b**).⁹⁷⁴⁻⁹⁷⁵ More specifically, a high carrier
10 recombination rate can be achieved by increasing the overlap between hole and electron wave
11 functions by quantum confinement, enhancing the exciton localization (the Frenkel-like
12 excitons).⁹⁷⁶⁻⁹⁷⁷ Indeed, the enhancement of E_B plays a crucial role in high-performance light
13 emitting devices. E_B can be increased by more than one order of magnitude from ~ 10 meV in 3D
14 bulk LHPs⁹⁷⁸⁻⁹⁸⁰ to >150 meV in 2D LHPs^{976, 979, 981-983} due to dielectric confinement effect (**Figure**
15 **109c**).^{979, 984-985} In the quasi-2D perovskites, $(BA)_2(MA)_{n-1}Pb_n I_{3n+1}$, one can increase E_B up to 470
16 meV.⁹⁸⁶

17 Strong spin-orbit coupling (SOC) and inversion asymmetry have been observed in inorganic
18 $CsPbX_3$ LHP NCs.¹⁵⁰ It has been proposed that these systems also exhibit a high degree of Rashba
19 splitting in the excited state energy levels, which alters the degeneracy of triplet excited states and
20 the order of energy sublevels, thereby yielding a bright triplet state as the lowest energy state.¹⁵⁰
21 This is distinct from most quantum emitters, including organic fluorophores and inorganic
22 quantum dots, in which the lowest excited states correspond to the dark triplets.¹⁵⁰ It is noteworthy

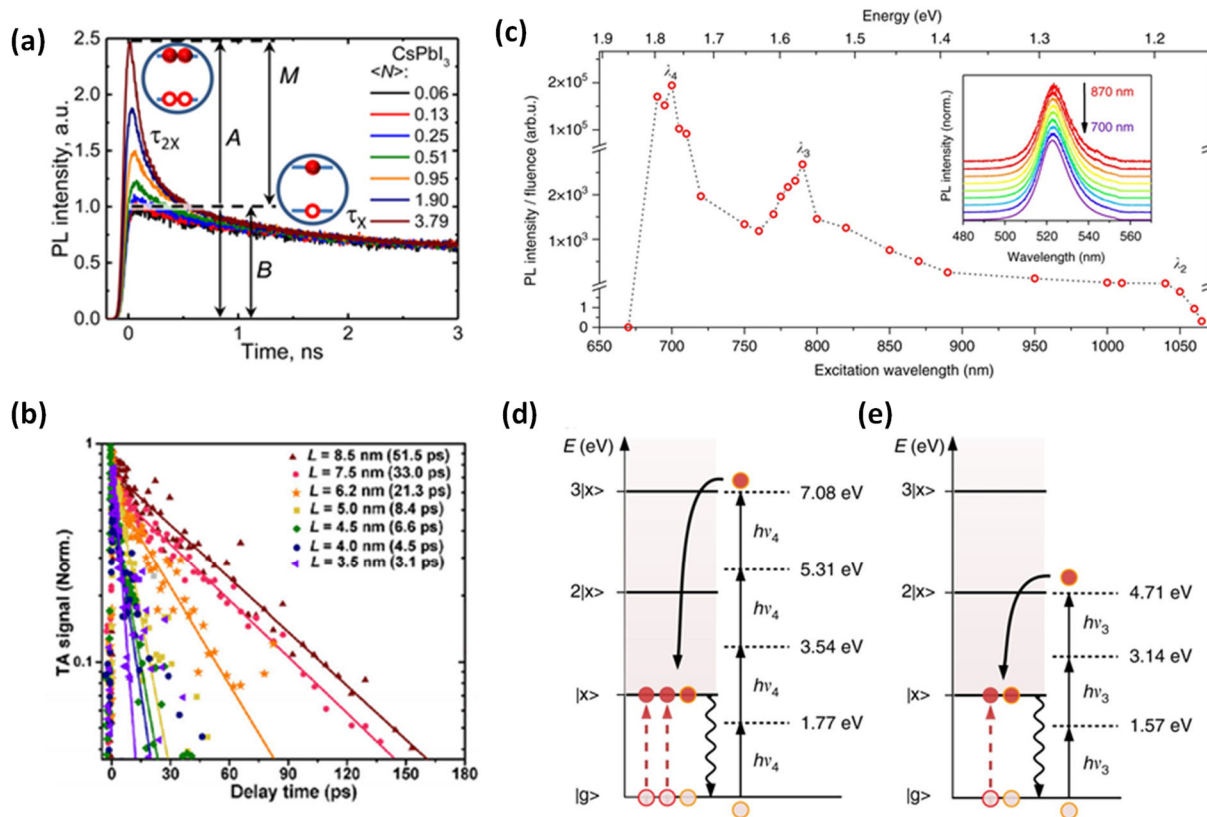
1 that recent experimental observations have suggested that the Rashba splitting effect becomes
 2 more pronounced in 2D quantum well and quasi-2D LHPs (**Figure 109d**).⁹⁸⁷



3
 4 **Figure 109.** Excitonic characteristics in the lead halide perovskites (LHPs). (a) Schematic
 5 illustration of charge carrier recombination, including exciton and biexciton transitions, in the 2D
 6 CsPbBr₃ perovskites. Adapted with permission from Ref.⁹⁷⁵ (b) Schematic band structure
 7 demonstrating short-range electron-hole exchange and Rashba effect in 3D-orthorhombic
 8 CsPbBr₃ NCs. Adapted with permission from Ref.¹⁵⁰ (c) Schematic (bottom) and molecular model
 9 (top) of the dielectric quantum wells formed between low dielectric constant, k , (barriers) and 2D
 10 MAPbBr₃ perovskites (wells), illustrating excitonic recombination to enhance E_B in the wells.
 11 Adapted with permission from Ref.²²¹ (d) Schematic band diagram depicting Rashba splitting in
 12 that occur due to SOC in the 2D (C₆H₅C₂H₄NH₃)₂PbI₄. Adapted with permission from Ref.⁹⁸⁷

13
 14 **Multielectron Dynamics**

1 When the excess energy available to a HC is high enough, it can generate a second exciton by
2 transferring this energy. Generation of multiple excitons by absorption of a single photon can
3 enhance the power conversion efficiency (PCE) of single-junction photovoltaics. In bulk
4 semiconductors, the carrier multiplication efficiency is usually low due to rapid intra-band
5 relaxation processes. However, in the nanoscale regime, multiexciton generation is more efficient
6 with a minimal energy loss. For example, generation of seven excitons is documented for PbSe
7 QDs upon excitation with a photon energy of $7.8E_g$, indicating an energy loss of only $\sim 10\%$.⁹⁸⁸
8 Multiexcitons can also be generated by using high fluence of the excitation laser pulse. Even
9 though the solar flux density is not high enough to produce multiple excitons, studies on
10 multiexciton dynamics are commonly performed using high photon flux.^{928, 949, 989-991} However,
11 as the multiexciton dynamics is independent of the method of generation, the results of these
12 studies can be applied to improve solar cell applications. Klimov and co-workers studied
13 multiexciton dynamics in CsPbI₃ NCs by monitoring the PL kinetics as a function of the pump
14 fluence.⁹²⁸ The appearance of a new fast decay component at higher laser fluences (**Figure 110a**)
15 indicates the formation of multiexcitons. The generation of a large number of charge carriers in
16 spatially confined NCs enhances the carrier-carrier interaction, which leads to Auger
17 recombination, an additional nonradiative channel for the relaxation of the charge carriers. As both
18 VB- and the CB-edge states of the perovskite NCs, can accommodate a maximum of two charge
19 carriers (2-fold degeneracy), multiexciton generation in these systems is limited to biexcitons.⁹²⁸
20 As the carrier-carrier interaction is enhanced in a confined condition, the volume (V) of the NCs
21 influences the biexciton lifetime of a system.



1
2 **Figure 110.** (a) Pump-fluence-dependent PL dynamics of CsPbI₃. At early time, a short-lived PL
3 component due to biexcitons (denoted as τ_{2x}) emerges at higher pump intensities. A and B denote
4 the amplitudes of the total PL signal and its single-exciton component, respectively while $M=A -$
5 B denotes the amplitude of the multiexciton signal. Adapted with permission from Ref.⁹²⁸.
6 Copyright (2016) American Chemical Society. (b) Variation in biexciton lifetime with varying
7 sizes of CsPbBr₃ NCs. Adapted with permission from Ref.⁹⁹². Tsinghua University Press and
8 Springer-Verlag GmbH Germany, part of Springer Nature 2018. (c) Nonlinear absorption-induced
9 PL in CsPbBr₃ NCs as a function of the below-band-gap excitation wavelength. The dashed line
10 is a guide to the eye. The inset shows the normalized PL spectra for excitation wavelengths varying
11 from 870 to 700 nm. Energy diagram of the resonances between multi photon excitation and multi
12 exciton generation in CsPbBr₃ NCs. Photo-excitation at $3E_x$ (d) and $2E_x$ (e) and subsequent

1 generation of three (d) and two (e) excitons via multiple photon excitation processes with photons
2 of energies $h\nu_4$ and $h\nu_3$, respectively. Panels (c-e) are adapted with permission from Ref. ⁹⁹³
3
4 Systematic studies of the volume dependence of the Auger lifetime of a series of NCs
5 (FAPbBr₃ and CsPbBr₃) with varying sizes from a strongly regime to a weakly confined regime,
6 confirm the decrease in the biexciton lifetime with decrease in NC volume (Figure 110b).^{938, 992}
7 The volume scaling of the biexciton lifetime (τ_{xx}) is usually represented as: $\tau_{xx} = \gamma V$, where γ is the
8 scaling factor, whose value is found to be an order of magnitude lower for FAPbBr₃ (0.068 ± 0.005
9 ps/nm³) and CsPbBr₃ (0.085 ± 0.001 ps/nm³) compared to CdSe or PbSe QDs (for which $\gamma \approx 1$
10 ps/nm³).⁹³⁸ However, the reason for this large variation is not yet clear. A high multiexciton
11 efficiency and low multiexciton generation threshold are advantageous from the practical utility
12 point of view, and in this context, intermediate-confined FAPbI₃ NCs appear to be the best choice.
13 Multiexciton generation with a threshold of $2.25E_g$ and an efficiency of 75% has been
14 demonstrated for this system.⁹⁹⁴ Even for CsPbI₃, a carrier multiplication efficiency of 98% is
15 reported for $E_{exc} \geq 2E_g$.⁹⁹⁵ The biexciton lifetime of the pure CsPbX₃ NCs varies with the halide
16 composition as CsPbI₃ (90-115 ps) > CsPbBr₃ (40-74 ps) > CsPbCl₃ (~20 ps).^{928-929, 989, 996-999}
17 Systems with higher biexciton lifetime are of great interest as they provide a longer period for the
18 extraction of biexcitons prior to nonradiative Auger recombination. Mondal *et al.* have shown that
19 the biexciton lifetime of CsPbI₃ can be almost doubled by doping a small amount of chloride or
20 formamidinium ion into the system.⁹⁹⁸ Eperon *et al.* found a longer biexciton lifetime (198-227
21 ps) in hybrid perovskite NCs, FAPbBr₃ and MAPbI₃, compared to all-inorganic, CsPbBr₃ NCs (74
22 ps).⁹⁹⁷ The effect of dimensionality of the perovskite NCs on the biexciton lifetime has also been
23 studied using CsPbBr₃ nanoplates (NPLs) and nanorods (NRs) of different lateral areas and rod

1 lengths, respectively.⁹⁰⁴ A linear correlation is found between the biexciton Auger lifetime and the
2 NPL lateral area and the NR length, which is related to exciton collision frequency. Reduced Auger
3 probability per collision in 2D materials (NPIs) explains the longer biexciton lifetime of it
4 compared to in 1D NRs.

5 Another possible non-radiative loss channel is the formation of a trion, which is a localized
6 center containing three charged particles. A positively charged trion consists of two holes and one
7 electron and a negatively charged one comprises two electrons and a hole. These species are
8 formed on photoexcitation of a NC, which already contains a trapped electron or hole. Since the
9 formation of trions requires re-excitation of the same NC, it can be avoided by performing the
10 measurements under vigorously stirring, such that each photon is absorbed by a fresh NC sample.
11 As the trions influence the PL behavior of the NCs (e.g. contributed to PL intermittency), it is
12 important to understand the trion dynamics and several studies have been dedicated to this.^{27, 1000-}
13 ¹⁰⁰¹ A trion lifetime of 235 ps has been estimated by comparing the normalized bleach/PL kinetics
14 of static and stirred CsPbI₃ colloidal NCs.⁹²⁸ Kanemitsu and co-workers estimated the lifetime of
15 a biexciton and a trion in CsPbBr₃ NCs to be 39 and 190 ps, respectively, by performing pump
16 fluence dependent TA measurements.¹⁰⁰² Wu and co-workers determined a trion lifetime of
17 220±50 ps for CsPbBr₃ NCs through carrier doping using double pump-probe spectroscopy.¹⁰⁰³ In
18 another study, negative trions were generated in FAPbBr₃ NCs using strong hole acceptors like
19 CuSCN and their lifetime was estimated (~600 ps).¹⁰⁰⁴ Considering that the trions are generally
20 formed due to surface trapping of an electron or a hole, post-synthetic surface treatments can
21 suppress the trion recombination process.^{962, 1005} Additional information on this topic can be found
22 in a recent review.¹⁰⁰⁶

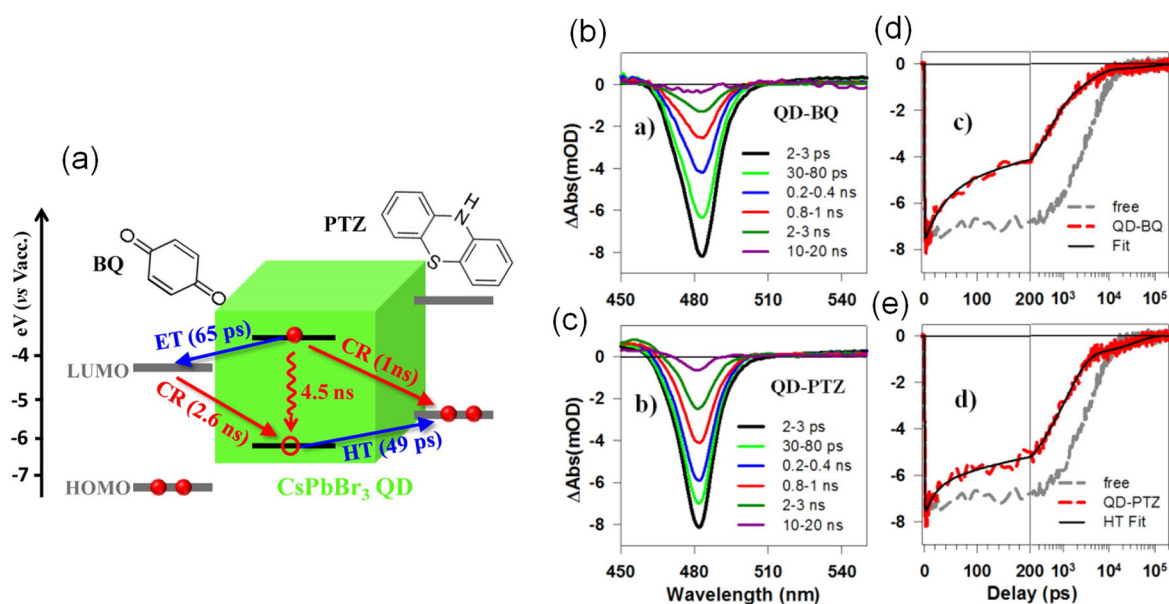
1 Non-radiative multi-exciton annihilation processes can be avoided by below bandgap multi-
2 photon excitation and generation processes.⁹⁹³ Manzi *et al.* observed the PL centered at 523 nm
3 from CsPbBr₃ NCs assembly for a wide range of below bandgap non-linear excitations (**Figure**
4 **110 c**).⁹⁹³ They noticed that the spectral shape of the emitted PL remained unchanged while the
5 emission intensity highly depended on the excitation wavelength. PL can be observed starting at
6 an excitation wavelength around $\lambda_2 = 1030$ nm (photon energy $h\nu_2 = 1.20$ eV $\approx 0.50 E_g$). The PL
7 intensity then increases towards lower excitation energies in a non- monotonic fashion. Two
8 distinct peaks, located at an excitation wavelength of $\lambda_3 = 790$ nm and $\lambda_4 = 700$ nm (corresponding
9 to the photon energies $h\nu_3 = 1.57$ eV $\approx 0.66 E_g$ and $h\nu_4 = 1.77$ eV $\approx 0.75 E_g$, respectively), have
10 been found with the PL intensity being several orders of magnitude higher (10^3 and 10^5 ,
11 respectively) than the signal detected in the vicinity of λ_2 . These particular energies (at λ_3 and λ_4)
12 perfectly match the multiples of the exciton energy $h\nu_x$, suggesting a multiple photon absorption
13 and a subsequent resonant generation of multiple excitons. A schematic representation of the
14 combined multi photon excitation and multi exciton generation processes in CsPbBr₃ NCs system
15 is shown in **Figure 110 d** and **e**. For the excitation wavelength λ_4 , the NCs assembly undergoes a
16 4-photon absorption and reaches an energy level resonant with $3E_x = 7.10$ eV. Likewise, for the
17 excitation wavelength λ_3 , a 3-photon absorption process occurred giving rise to photo generated
18 excitons with an energy resonant with $2E_x = 4.73$ eV.

19 **Charge transfer dynamics**

20 Our discussion so far has been restricted to different intrinsic relaxation processes of the
21 photogenerated charge carriers in perovskites. However, for applications like in solar cells, these
22 photoactive materials are sandwiched between carrier harvesters. It is thus necessary to have an
23 understanding of how charge transfer dynamics (at the donor-acceptor interface) competes with

1 the dynamics of intra-system relaxation processes. In this section, we highlight some of the charge
2 transfer studies on various perovskite NCs with a variety of carrier acceptors.

3 **Single electron/hole transfer:** Lian and co-workers investigated the electron and hole transfer
4 dynamics from CsPbBr₃ NCs to traditional electron and hole acceptors, benzoquinone (BQ) and
5 phenothiazine (PTZ), respectively (Figure 111a), by monitoring the bleach recovery kinetics of
6 the NCs in presence and absence of the acceptors in ultrafast TA measurements.¹⁰⁰⁷



7
8 **Figure 111.** (a) Schematic energy level diagram of CsPbBr₃ NCs-BQ/-PTZ complexes and
9 possible charge separation and recombination pathways. (b,c) TA spectra NCs-BQ and NCs-PTZ
10 complexes at indicated time delays after 400 nm excitation. (d,e) Corresponding accelerated bleach
11 recovery kinetics as compared with the free NCs (gray dashed line). Permission to be obtained
12 Ref.¹⁰⁰⁷. Copyright (2015) American Chemical Society.

13
14 The bleach recovery kinetics of the CsPbBr₃ NCs is accelerated in presence of BQ/PTZ due
15 to charge transfer from the perovskites (111b-e). Subsequently, several molecular acceptors such

1 as fullerene, ferrocene, tetracyanoethylene, anthraquinones, 1-aminopyrene etc. were used with a
 2 variety of perovskites. The time constants for charge transfer between different pairs are
 3 summarized in Table 2.^{998, 1008-1017}
 4 **Table 2:** Charge transfer dynamics between various pairs of perovskites NCs and molecular
 5 acceptors investigated through transient absorption measurements (unless otherwise mentioned).

System	Carrier Acceptor	Carrier Transfer Time (ps)	Reference
Electron Transfer			
CsPbBr ₃	Benzoquinone	65±5 (Half-life)	1007
	Benzoquinone†	20-50	1018
	Rhodamine-B	600	1003
	Anthraquinone	30	1009
	C60	190	1009
CsPbI ₃	Rhodamine-B	40.6-872	1019
	C60	18-45	998
Hole Transfer			
CsPbBr ₃	Phenothiazine	49 ± 6 (Half-life)	34
	Phenothiazine†	137-166	1018
	4,5- dibromofluorescein	1-1.25	1016
	1-aminopyrene	~120	1013

	TIPS-Pc#	~5	1015
	4-mercaptophenol	~14.1±3	1020
CsPbCl _x Br _{3-x}	Tetracene carboxylic acid	7.6 ± 0.2	1021
CsPbI ₃	1-aminopyrene	~170	1013

1 †Through Terahertz (THz) measurements, #Triisopropylsilylethynyl pentacene carboxylic
2 acid,

3 The electronic coupling of the QD and acceptor orbitals influences both charge separation
4 (CS) and charge recombination (CR) dynamics.¹⁰¹⁹ It is shown that ~99% photogenerated
5 electrons can be transferred from CsPbI₃ NCs to TiO₂, with a size-dependent rate ranging from
6 1.30×10^{10} to 2.10×10^{10} s⁻¹.⁹⁵⁷ Kamat and co-workers investigated electron transfer between
7 CsPbBr₃ NCs and several metal oxides such as TiO₂, SnO₂ and ZnO.¹⁰²² Formation of a long-lived
8 (~μs to ms) species is observed in CsPbBr₃/ methyl viologen²⁺ system.¹⁰²³ A long-lived (5.1 ± 0.3
9 μs) charge separated state for CsPbCl_xBr_{3-x} perovskite-tetracene complex is also reported.¹⁰²¹
10 Electron and hole transfer from CsPbBr₃ nanoplatelets (NPLs) to BQ and PTZ with a time constant
11 of 10-25 ps and a half-life time >100 ns of the charge-separated state in NPLs-PTZ is also
12 reported.¹⁰²⁴ To examine the dependence of the charge transfer dynamics on the morphology of
13 the perovskite NCs, Ahmed *et al.* studied electron transfer between tetracyanoethylene and the
14 nano-spheres, -plates and -cubes of MAPbBr₃.¹⁰¹⁰ Electron transfer from photoexcited CsPbBr₃
15 NCs to CdSe QDs and hole transfer from photoexcited CdSe to perovskites were studied.¹⁰²⁵
16 Charge transfer between CsPbBr₃ NCs and CdSe QDs and NPLs is also examined.¹⁰²⁶ The electron
17 transfer from CsPbBr₃ to 2D NPLs is found to be faster as compared to the QDs due to larger
18 surface area and greater density of states in 2D materials. There are also a few studies on charge

1 transfer dynamics between photoexcited non-perovskite semiconductors and perovskite NCs.¹⁰²⁷⁻
2 ¹⁰²⁹ Yao *et al.* studied the charge transfer and exciton diffusion process in bilayer and blend
3 structures of CsPbBr₃/PCBM interfaces.¹⁰³⁰ By varying the thickness of the CsPbBr₃ NC film on
4 top of the PCBM layer in the bi-layer heterostructure, they determined an exciton diffusion length
5 of 290 ± 28 nm for CsPbBr₃ assembly. They concluded that the diffusion process in such cases is
6 followed by an ultrafast exciton dissociation (within 200 fs) at the CsPbBr₃/PCBM interface. Even
7 an overall faster charge transfer process was observed by them in the blend structures which
8 revealed an effective charge extraction from the active layer resulting in a high photosensitivity.
9 ¹⁰³⁰

10 **Triplet energy transfer:** As the band-edge excitonic states of the perovskites possess both singlet
11 and triplet characters,¹⁰³¹ recent studies focused as well on harvesting the triplet exciton. The triplet
12 exciton can be used for sensitization of molecular triplets that generates possibilities like room
13 temperature phosphorescence, triplet-triplet annihilation mediated photon upconversion, etc.^{150,}
14 ^{510, 1032-1036} Several polyaromatic hydrocarbons with appropriate band alignment have been
15 investigated in this regard.¹⁰³⁷ It is interesting to note the enhancement of triplet energy transfer
16 (TET) efficiency with a decrease in NC size. For strongly quantum confined (edge length of ~ 3.5
17 nm) CsPbBr₃ NCs, the TET efficiency is found to be as high as $\sim 99\%$, but for 11.2 nm sized NCs
18 no TET is observed.¹⁰³⁷ This is because for quantum confined NCs, the electron and hole wave-
19 functions spread beyond the NCs surface that enhances the orbital overlap between surface-
20 adsorbed triplet acceptors and the NCs. While direct observation of the formation of molecular

1 triplets confirms TET, a recent study suggests that the mechanism can vary from system to
2 system.¹⁰³⁸

3 ***Multielectron extraction:*** Extraction of multielectrons prior to Auger recombination is an important
4 process, which can push up power conversion efficiency (PCE) of the solar cells by manifolds.
5 While extensive studies on harvesting multielectrons from the metal chalcogenide quantum dots
6 have been made,¹⁰³⁹⁻¹⁰⁴⁰ there are only a few similar studies with the perovskite NCs. Wu and co-
7 workers demonstrated tetracene-assisted dissociation of up to 5.6 excitons per NC from
8 CsPbCl_xBr_{3-x} NCs.¹⁰²¹ Multielectron extraction from CsPbI_{3-y}Cl_y using C₆₀ has also been
9 successfully achieved.⁹⁹⁸ In a recent study, it was shown that out of 14 excitons generated under
10 high excitation fluence in CsPbBr₃ NCs, approximately five electrons get transferred to surface-
11 bound anthraquinones.¹⁰¹² As discussed earlier, Manzi *et. al.* showed efficient multi-electron
12 generation also takes place for below bandgap excitation in the case of CsPbBr₃ NCs.⁹⁹³ While
13 this topic holds promises for further advancements, clearly it is in the early stages of development.

14 ***Hot carrier transfer:*** Extraction of hot charge carriers is a challenging task due to their rapid
15 relaxation to the band edge states. Only a few reports of HC extraction from perovskites are so far
16 available.^{924, 1018, 1041-1043} In an early work, transfer of hot electron and hot hole from CsPbBr₃ NCs
17 to BQ and PTZ was established by monitoring the photoinduced change in conductivity in time-
18 resolved THz transmission.¹⁰¹⁸ Sum and co-workers showed transfer of hot electrons from
19 MAPbBr₃ to 4,7-diphenyl-1,10-phenanthroline (Bphen)⁹²⁴ from the sharp drop in bleach amplitude
20 at early time in presence of the latter. The hot electron extraction efficiency is estimated to be
21 ~83% for ~0.6 eV excess energy and this efficiency progressively decreases with lowering of the
22 excess energy. Hot hole extraction from MAPbI₃ to spiro-OMeTAD has also been
23 demonstrated.¹⁰⁴² More studies on this important but challenging task are needed.

1 9.4 SUMMARY AND OUTLOOK OF OPTICAL PROPERTIES AND CHARGE 2 CARRIER DYNAMICS

3 In conclusions, in this section we have tried to review the fundamental optical properties in MHPs
4 covering a broad range of topics. Though still, the stability of MHP nanocrystals is a major issue
5 which needs further improvement from their chemistry point of view for their future
6 commercialization, it is also absolutely necessary to have understanding of their fundamental
7 optical properties for their ultimate employment in the optoelectronic devices. One of the major
8 ongoing debate in the field of MHP nanostructures, is to understand the exciton fine structures
9 which governs the radiative vs nonradiative rates significantly and it is essential for their light
10 emitting applications. Though initially it was believed that the lowest exciton state is bright in case
11 of MHP NCs, in later investigations it is found to be opposite in many cases. As the transition
12 metal ion doping in MHP is a quickly emerging topic, it demands more in depth understanding of
13 the crystal field induced splitting of bright vs dark excitonic states. Hence, a significant amount of
14 research needs to be done in this direction. Besides the lead based MHP, many new lead free MHP
15 such as double perovskites, 0D MHP, are emerging as potential semiconducting material for white
16 light generation from self-trapped excitons. The self-trapped exciton formation process in such
17 materials is still not understood. Self-trapping process is highly non-linear and strongly related
18 with electron-phonon coupling.⁸⁷⁶ Hence, a considerable amount of research should be performed
19 in this direction to understand the phonon dynamics in such material system to unravel small
20 polaron formations kinetics and the relevant photophysics of these systems. Hot carrier cooling in
21 MHP is also not fully understood where many theories like large polaron formation,¹⁰⁴⁴ acoustic
22 to optical phonon up-conversion¹⁰⁴⁵ have been proposed so far. Recently it is shown by atomistic
23 simulation that lattice vibrations is important in understanding the hot carrier cooling process in

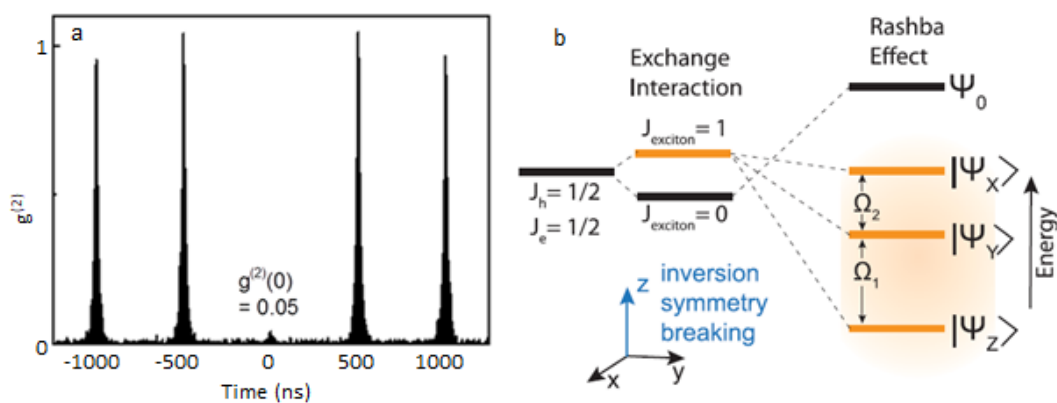
1 case of MHP.¹⁰⁴⁶ Thus, it is also crucial to understand the role of electron-phonon coupling for hot
2 carrier's extraction at the MHP/organic interfaces for the realization of hot carrier solar cells.
3 Therefore, further research needs to be carried out in this direction. Multi-excitonic processes such
4 as multi photon generation processes are important to increase power conversion efficiencies of
5 solar cells by harvesting below bandgap photons and to minimize above bandgap excitation
6 induced multi excitonic annihilation processes such as Auger heating. This non-radiative process
7 becomes dominant at high excitation densities and thus, plays an important role in the non-
8 radiative process in case of high current driven LEDs and lasers. To get better understanding of
9 those processes and how they control the efficiency of Perovskite LEDs, such processes need to
10 be monitored in detail in operational devices. The recent findings of ultrafast spin relaxation
11 dynamics in case of MHP NCs may become beneficial for MHP based spintronics such as spin
12 LEDs and spin lasers. Chirally functionalized MHP shows room temperature circular dichroism⁵⁰⁹
13 where a detailed understanding of the spin-dependent chirality transfer process in the photo-
14 excited carriers needs more investigations.

15 **10. OPTICAL STUDIES OF QUANTUM DOTS AND NANO- AND MICROCRYSTALS** 16 **AT THE SINGLE PARTICLE LEVEL**

17 **10.1 PHOTOLUMINESCENCE BLINKING IN MHP SINGLE NCs**

18 MHP NCs show properties similar to the conventional QDs based on cadmium or lead
19 chalcogenides, such as broad absorption of light in the UV-Vis-NIR region, size-tuneable
20 absorption and emission, and narrowband, bright photoluminescence (PL). Like conventional
21 QDs, MHP NCs show stochastic fluctuations of PL intensity, also called PL intermittency or
22 blinking. PL blinking varies with size, morphology and composition of the MHP NCs, the nature
23 and density of defects, intensity and energy of incident light and the degeneracy of band-edge

1 states. Quantum emitters are further characterized by the emission of a single photon within their
 2 PL lifetime. Recent studies show that the band-edge states of MHP NCs become nondegenerate
 3 due to the mixing of electron and hole states, exchange interactions of excitons and the Rashba
 4 effect.^{25, 150} While the highest lying band-edge singlet state in MHP NCs is optically inactive due
 5 to inversion symmetry breaking of perovskite crystals, multiphoton emission from the low lying
 6 nondegenerate triplet states can occur.¹⁵⁰ Hence, although single MHP NCs can be spatially
 7 isolated and studied, the exclusion of entangled photons from closely spaced band-edge triplet
 8 states (Ω_1 and Ω_2 , Figure 112b) becomes necessary. Conversely, excellent antibunching (temporal
 9 separation) of photons from single MHP NCs at room temperature suggests that the degeneracy of
 10 the band-edge states increases with an increase in temperature, resulting in the maintenance of
 11 single-photon emission. Despite the complexity of the band-edge states and entangled photons,
 12 which are resolved at temperatures as low as 3.6 K,¹⁵⁰ we focus in this section on the blinking
 13 behavior of single MHP NCs by referring to the intrinsic defects or traps, photoionization and
 14 biexciton generation.



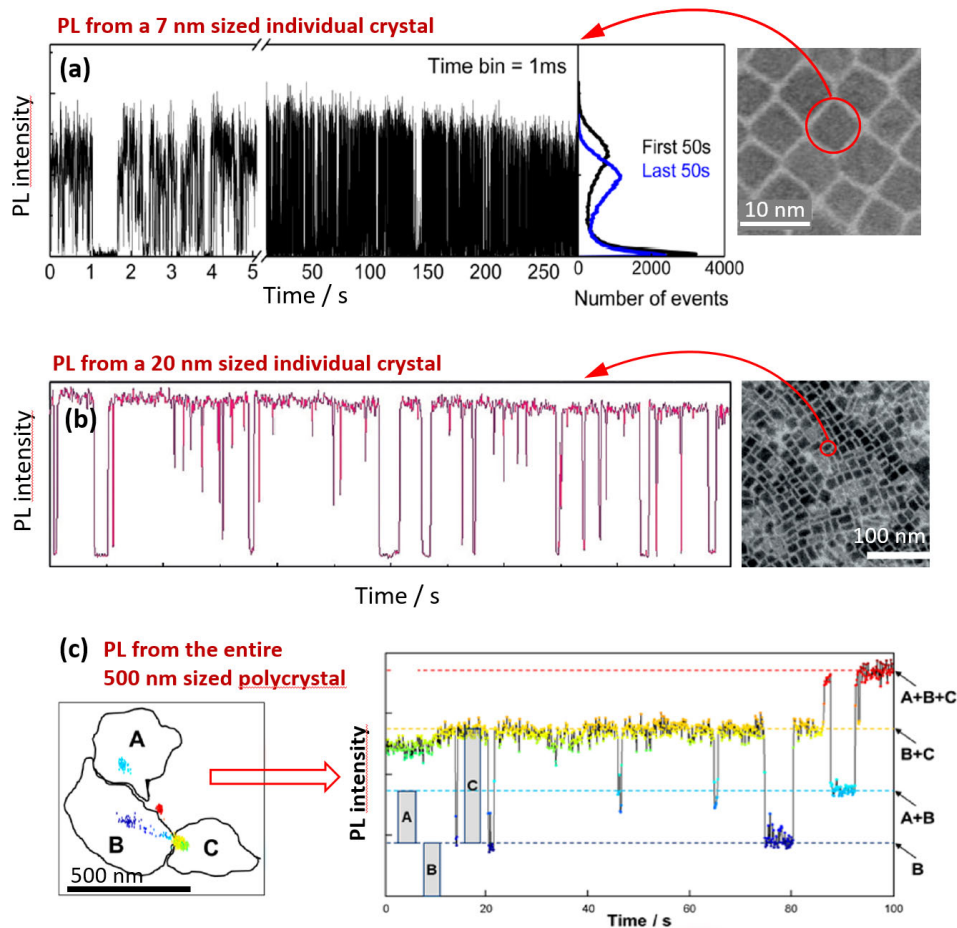
20

21 **Figure 112.** (a) Photon coincidence histogram of a CsPbI₃ MHP QD under pulsed excitation. The
 22 low value of coincidence (0.05) at time-zero represents single photon emission. Reprinted with
 23 permission from Ref.¹⁰⁴⁷. Copyright 2015, American Chemical Society. (b) Splitting of exciton

1 fine structure in a MHP QD after the breaking of the inversion symmetry of a CsPbBr₃ QD owing
2 to the Rashba effect, where J_e and J_h are the total angular momentum of electron and hole, Ψ_0 is
3 optically inactive singlet state, and $|\Psi_{x,y,z}\rangle$ are emissive triplet states. Reprinted with permission
4 from Ref. ²⁵copyright 2019, American Association for the Advancement of Science.

5 The strong quantum confinement regime in NCs which is smaller than the exciton Bohr radius
6 (<10 nm for MHPs), plays an important role in PL blinking.¹⁵ Hence, quantum size effects should
7 be precisely considered during the analysis of single MHP's PL. Differences in the MHP QD
8 blinking behavior when compared to nano- and microcrystals are depicted in Figure 113,¹⁰⁴⁷⁻¹⁰⁴⁹
9 the multi-state blinking of MHP nano- and microcrystals attributed to multiple emissive sites that
10 are governed by metastable nonradiative recombination centers will be discussed in the next
11 section. MHP NCs show, besides the distinct ON and OFF blinking behaviour, also intermediate
12 PL levels, similar to GREY states of conventional QDs.¹⁰⁵⁰

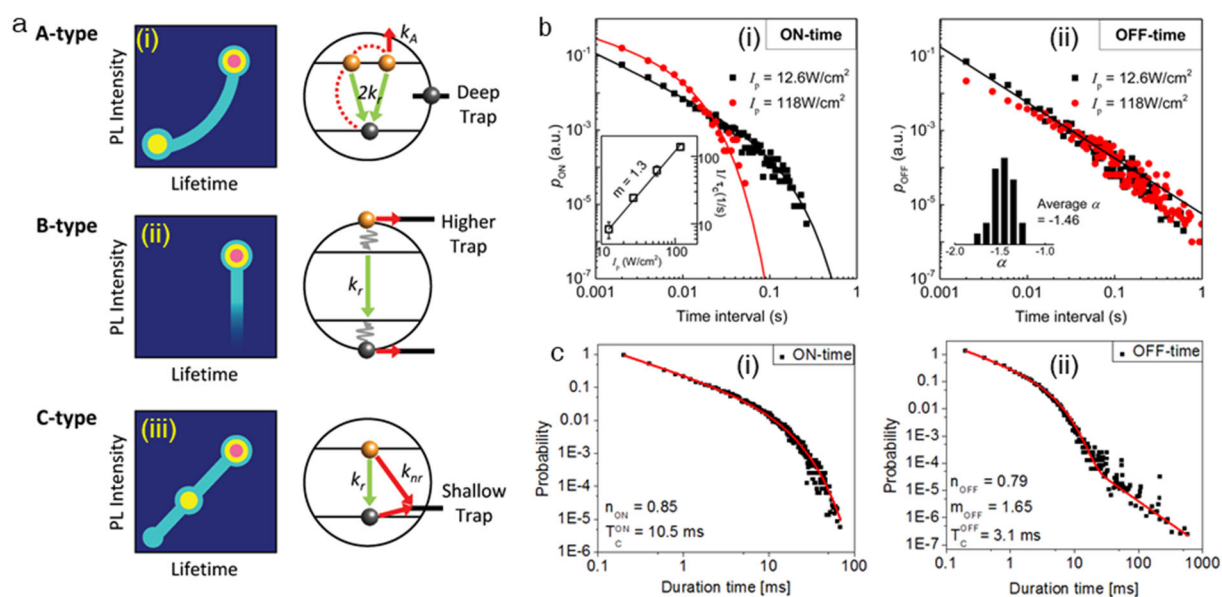
13



1
 2 **Figure 113.** Single particle PL intensity vs. time of perovskite crystals with different sizes. (a)
 3 CsPbI₃ NCs with a size of 7 nm. Reprinted with permission from Ref. ¹⁰⁴⁷ Copyright 2015,
 4 American Chemical Society. (b) MAPbI₃ nanocrystals with a size of 20 nm. Reprinted with
 5 permission from Ref. ¹⁰⁴⁸ Copyright 2019, Wiley-VCH Verlag GmbH & Co. KGaA, Weinheim.
 6 (c) MAPbI₃ polycrystals with a size of 500 nm, where A, B and C are three parts of the crystal.
 7 Reprinted with permission from Ref. ¹⁰⁴⁹ Copyright 2017, American Chemical Society.

8 **Blinking mechanism.** The ON and OFF periods during QD PL blinking correspond to the neutral
 9 and charged states with random switches between the states due to (dis)charging. Like
 10 conventional QDs, the blinking of MHP NCs can be assigned to type-A and type-B
 11 mechanisms,^{1050 1051} with random QD charging and discharging the key features of type-A blinking

1 (Figure 114a(i)), and the activation and deactivation of trap or defect states in type-B blinking
 2 (Figure 114a(ii)). In type-A, PL lifetimes are changing with PL intensity (the smaller intensity, the
 3 shorter the lifetime). In type-B, PL lifetime is not changing upon blinking. In addition, there are
 4 differences in the distributions of the ON- and OFF-times. For type-A blinking, the distributions
 5 of the ON- and OFF-times follow the exponential power-law function, $p_{\text{ON/OFF}} \propto t^\alpha \exp(-t/t_c)$,
 6 where t_c is the truncation time and α is the power-law coefficient. In contrast, in type-B blinking,
 7 the distributions of the ON- and OFF- times fit with the linear power-law function, $p_{\text{ON/OFF}} \propto t^\alpha$.



8
 9 **Figure 114.** (a) Schemes correlating PL intensity and PL lifetime with the mechanisms of charge
 10 carrier dynamics for (i) type-A, (ii) type-B and (iii) type-C blinking. Reprinted with permission
 11 from Ref. ¹⁰⁵². Copyright 2019, Wiley-VCH Verlag GmbH & Co. KGaA, Weinheim. (b) Power-
 12 law functions showing type-A blinking of CsPbI₃ NCs at two excitation pulse intensities.
 13 Reprinted with permission from Ref. ¹⁰⁴⁷ Copyright 2015, American Chemical Society. (c) Power-

1 law functions of FAPbBr₃ NCs showing both type-A and type-B blinking. Reprinted with
2 permission from Ref.¹⁰⁵³. Copyright 2018, American Chemical Society.

3 Photoactivation of MHP QD surface defects or deep traps can produce a trion. In this scenario,
4 after photoexcitation a charge is transferred to the crystal shell, leaving behind a net charge with
5 the opposite sign. Upon additional photoexcitation, the core of the QD will then contain three
6 charges (trion state). Subsequently, excited electron-hole pairs will recombine nonradiatively by
7 transferring their excitation energy to the extra charge via an Auger process instead of emitting a
8 photon. Hence, one observes type-A blinking through repeated nonradiative Auger recombination,
9 charge neutralization and radiative relaxation. For example, Park *et al.* have shown strong photon
10 antibunching and type-A blinking in CsPbI₃ NCs;¹⁰⁴⁷ Figure 114b shows the ON- and OFF-time
11 distributions associated to type-A blinking. Certain MHP NCs show both type-A and type-B
12 blinking in tandem, as was shown for CsPbI₃ QD by Yuan *et al.*¹⁰⁵⁰ and FAPbBr₃ QD by Trinh *et*
13 *al.*¹⁰⁵³ For example, the OFF-time distribution of FAPbBr₃ NCs follows an exponential behavior
14 initially, which is the characteristic of type-A blinking [Figure 114c(ii)]. After the truncation time,
15 a linear behavior is followed, which is characteristic of type-B blinking.¹⁰⁵³ Type-A blinking of
16 these NCs obeys the exponential nature of ON- and OFF-time distributions. The ON-time duration
17 cut-off for FAPbBr₃ NCs decreases with increasing excitation light intensity and saturates at $\langle N \rangle$
18 ≈ 1 ; whereas, OFF-time distribution does not show such behaviour. The switching from ON to
19 OFF states takes place through either type-A or type-B pathway. However, MHP NCs turned OFF
20 by ionization continues to be OFF until neutralized. In addition to type-A and type-B blinking,
21 Kim *et al.* explained their MAPbBr₃ QD blinking using a type-C model (Figure 114a(iii)).¹⁰⁵²
22 Type-C blinking is associated with shallow traps common to NCs. The proximity of the traps to

1 the band-edge, restricts the charge carrier trapping time and the rates of radiative and nonradiative
2 recombination processes become comparable in type-C blinking.

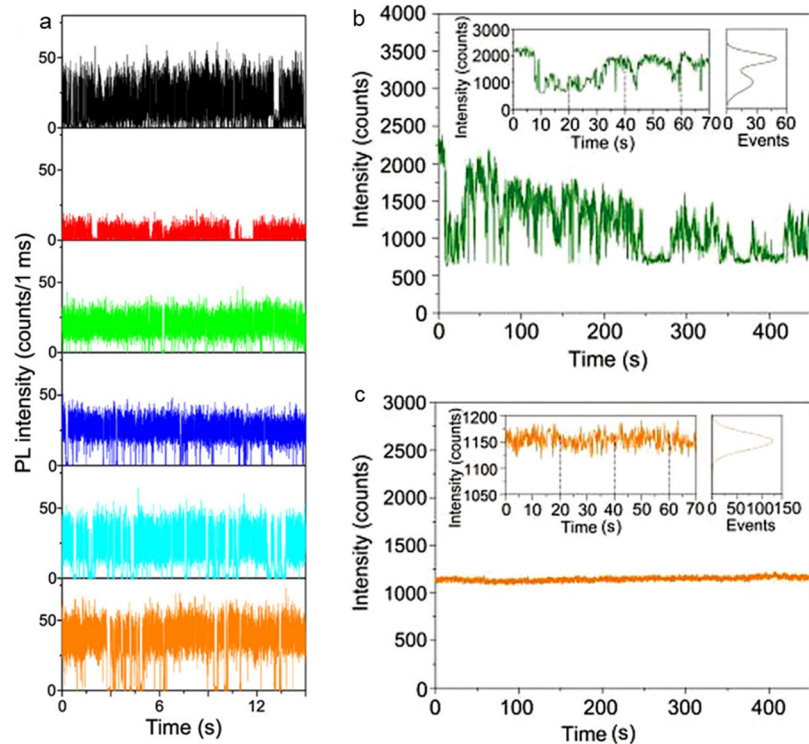
3 Trion and multiple exciton states, common to MHP NCs excited with high intensity/energy
4 light, affect the PL quantum efficiency and induce frequent ON/OFF events in the PL trajectories.
5 Like conventional QDs, biexcitons are generated in MHP NCs by mainly two mechanisms, (i) the
6 absorption of two photons with an energy equal or higher than the bandgap energy (E_g) or (ii) the
7 absorption of a photon with an energy equal or higher than $2E_g$. The biexciton can emit two photons
8 by first going to the single exciton state and then to the ground state. The second-order correlation
9 function depends on the PLQYs of the biexciton (Q_{XX}) and single exciton (Q_X) states. Under low
10 intensities of excitation, $g^{(2)}(0) \approx \frac{Q_{XX}}{Q_X}$ takes values close to zero, which is proportional to the ratio
11 of the biexciton (τ_{XX}) and single exciton (τ_X) lifetimes and the ratio (β) of the corresponding
12 radiative rates.^{1047, 1054} Thus, the above equation can be rewritten as $g^2(0) = \beta \frac{\tau_{XX}}{\tau_X}$. Generally, if
13 the statistics are scaled quadratically with radiative rates and the multiplicity of excitons, the value
14 of β can be 4.

15 PL intensity transients of NCs show multiple intensity levels, which can be explained by the
16 activation and deactivation of multiple recombination centres (MRC model).¹⁰⁵⁵⁻¹⁰⁵⁶ Li *et al.*
17 described the relation of PL blinking to MRC and bright biexcitons.¹⁰⁵⁴ The activation and
18 deactivation of MRCs govern the nonradiative recombination rate in a QD. This rate increases
19 with an increase in the number of activated MRC, and as a result, the PL intensity and lifetime
20 decrease. To account for the changes in PL lifetime and blinking at different intensities of
21 excitation light, Li *et al.* recorded the single MHP QD behavior at $\langle N \rangle = 0.02, 0.2$ and 2 . The PL
22 blinking at $\langle N \rangle = 0.2$ shows more frequent OFF states when compared with the blinking at $\langle N \rangle$
23 $= 0.02$. The blinking of an MHP QD shows the flickering effect at higher intensities of excitation

1 light, suggesting switching between the bright and dim states. PL blinking at $\langle N \rangle = 2$ is explained
2 based on the activation and deactivation of MRCs and the charging and discharging of the trion
3 state.

4 Apart from MRC, blinking due to nonradiative Auger recombination is correlated to the
5 particle size. For example, the energy levels of larger MHP NCs are perturbed by the delocalization
6 of the hole state throughout a QD.¹⁰⁵² An increase in ON-time distribution with an increase in QD
7 size suggests a low trapping rate and high de-trapping rate for larger MHP NCs. These rates can
8 be extracted from the power-law coefficients of ON- and OFF-time distributions. The trapping and
9 de-trapping rates depend on (i) photoionization of NCs, (ii) charge tunneling from a NC to the trap
10 state, and (iii) trapping time of electrons and holes. The nonradiative Auger recombination of trions
11 becomes fast if an MHP NC is photoionized by trapping, which can be analyzed from the OFF-
12 time distribution and PL lifetime. The trapping and de-trapping time of electrons and holes also
13 affect the recombination rates; nonradiative recombination of the hole in short-lived trapped state
14 decreases the PL intensity and lifetime.

15 **Blinking suppression.** The blinking behavior of MHP NCs may also depend upon the halide ion
16 and A/B-site cation, halide vacancies and surface defects.^{962, 1000, 1057} For example, with the
17 exchange of bromide to iodide in CsPbBr₃ NCs, Yoshimura *et al.* revealed a considerable increase
18 in the ON-time (Figure 115a),¹⁰⁵⁸ which should be attributed to not only the exchange of halide
19 ions but also the filling of halide vacancies. Also, blinking can be suppressed by the passivation
20 of surface defects using shells. For example, Tang *et al.* demonstrated the suppression of the trap-
21 assisted blinking in CsPbBr₃ NCs by the preparation of CdS shells (Figure 115b, c).¹⁰⁵⁹ Here
22 blinking suppression is assigned to the passivation of deep electron or hole traps at the interface
23 between MHP QD core and CdS shell.



1
 2 **Figure 115.** (a) PL intensity transients of a CsPbBr₃ QD as a function of the bromide to iodide
 3 exchange reaction before (black), during (red, green, blue, cyan) and after (orange) the addition of
 4 PbI₂ dissolved in a mixture of oleic acid and oleyl amine. Reprinted with permission from Ref.¹⁰⁵⁸
 5 Copyright 2020, American Chemical Society. (b,c) PL blinking of CsPbBr₃ MHP NCs (b) without,
 6 and (c) with a CdS shell. Reprinted with permission from Ref.¹⁰⁵⁹. Copyright 2019, Wiley-VCH
 7 Verlag GmbH & Co. KGaA, Weinheim.

8 Although blinking of MHP NCs with different A-site cations is independently investigated by
 9 many groups, systematic single-molecule studies correlating the composition of A-site cation and
 10 blinking, are required to understand the role of A-site cation on blinking. Any differences in the
 11 blinking behavior due to differences in the composition at the A-site should be correlated with the
 12 dipole moment. Organic cations such as methylammonium (MA⁺) and formamidinium (FA⁺) ions
 13 are dipolar, whereas Cs⁺ is unipolar. When compared with Cs⁺ and FA⁺, the higher dipole moment
 14 of MA⁺ and its rapid motion within the lattice create a polaronic screen of the charge carriers. As

1 a result, the exciton-exciton interactions are suppressed in MAPbX₃. MA⁺ is also more susceptible
2 to the fluctuations in the external charge and local current than Cs⁺ and FA⁺. Thus, the energy
3 states in MAPbX₃ or CsPbX₃ can be modified by the quantum-confined Stark effect.¹⁰⁶⁰
4 Nonetheless, the exact relationship between blinking and A-site cation in an MHP QD is yet to be
5 verified.

6

7 **10.2 PHOTOLUMINESCENCE BLINKING IN MHP SINGLE NANO- AND** 8 **MICROCRYSTALS**

9 As outlined in the previous section, photoluminescence blinking on time scales up to seconds or
10 minutes is an established phenomenon for single quantum systems such as molecules and classical
11 QDs. Hence, the observation of blinking in larger MHP nano- and microcrystals was surprising,
12 necessitating physical explanations beyond the mechanistic picture of blinking in quantum
13 systems. In recent years, unravelling the underlying processes of blinking has become a topic of
14 intense research. Even though full understanding of the physical picture is still absent, several key
15 experiments have been carried out and yielded important information for the research on the origin
16 of blinking. Moreover, blinking in spatially extended objects offers the unique opportunity to
17 spatially resolve the intensity fluctuations and correlate them with the material's morphology.

18 **Pioneering work and general picture.** The first studies on blinking in MHPs emerged in 2015
19 and focused on larger sized MAPbI₃ nanocrystals (NCs) and microcrystals (μCs)^{742, 1061} whereas
20 MHP QD blinking was reported only a few months later.¹⁰⁴⁷ With their observation of blinking in
21 2-3 μm long MAPbI₃ microrods, Zhu *et al.* reported for the first time PL intermittency of MHP
22 crystals larger than the diffraction limit of light. Tian *et al.*¹⁰⁶¹ carried out more extensive research
23 on the blinking phenomenon itself using polycrystalline MHP NCs. They suggested that the

1 intensity fluctuations in such polycrystalline NCs are controlled by chemical or structural defects
2 that trap free charges.¹⁰⁶¹ Due to their ability to quench the PL across surprisingly large volumes
3 of MHP NCs and even μ Cs, Merdasa et al.¹⁰⁴⁹ later termed these presumable defects “supertraps”.
4 There is a clear analogy to large organic systems like conjugated polymers and aggregates, as in
5 both cases the excited states are not delocalized over the whole volume ($100 \times 100 \times 100 \text{ nm}^3$ or
6 larger), however, the excitations are very mobile and can travel over almost the entire system and
7 potentially undergo nonradiative decay via an active quencher.

8 Conceptually, this idea is similar to the model of multiple recombination centers (MRC)
9 proposed by Frantsuzov and Marcus.¹⁰⁵⁵⁻¹⁰⁵⁶ Originally, this model was invoked to explain the
10 power law distribution of switching times in QDs, which were inconsistent with the commonly
11 accepted model of trap-assisted Auger recombination. As illustrated in Figure 116, the main idea
12 is that the nonradiative rate fluctuates due to the ON/OFF switching of one or several metastable
13 defects, leading to a time-dependent luminescence yield

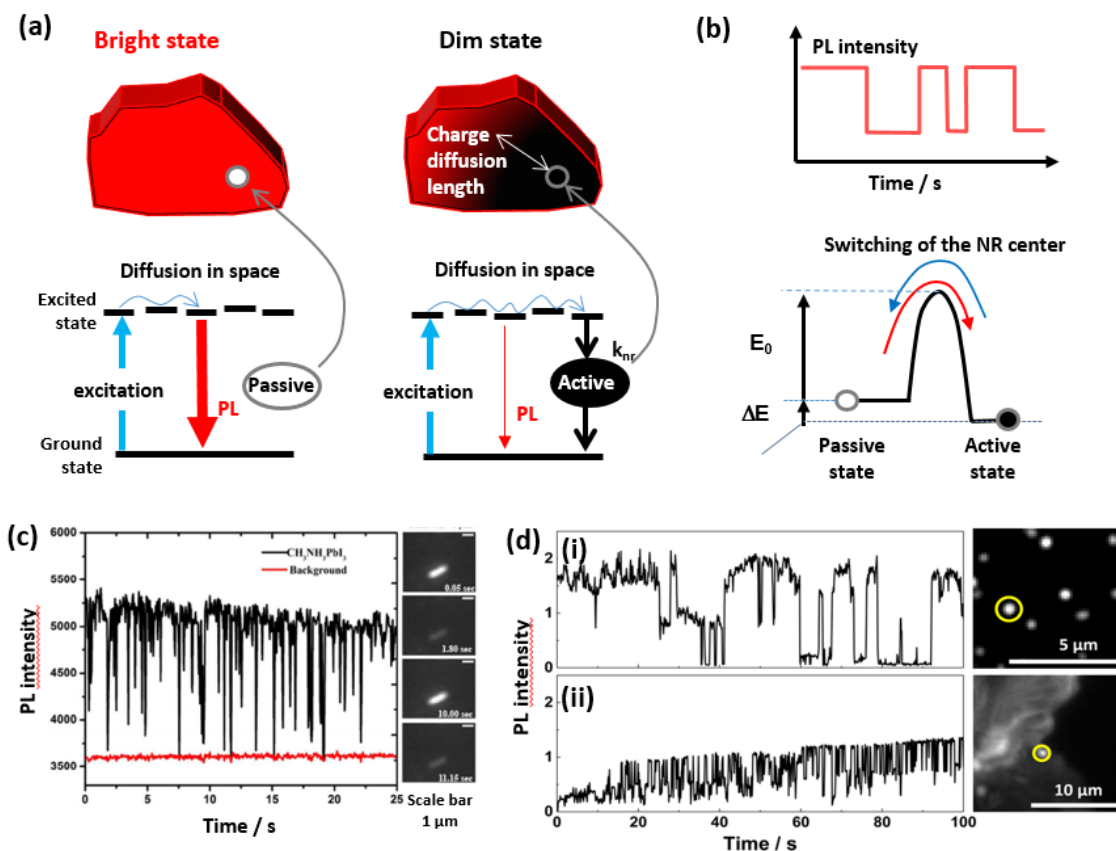
$$\Phi(t) = \frac{k_r}{k_r + \sum_i k_{nr,i}(t)} \quad (1)$$

14 where k_r denotes the radiative decay rate and $k_{nr,i}$ is the time-dependent nonradiative rate
15 provided by an active defect. In larger crystals it is important to consider that Φ may also have
16 some spatial dependence due to the spatial distribution of nonradiative recombination (NR) centers
17 and the potentially limited diffusion of photoexcited carriers towards these centers.

18 Tian *et al.*¹⁰⁶¹ estimated the “quenching volume” of their polycrystalline MAPbI₃ NCs to be $>$
19 10^{-16} cm^3 and the concentration of quenchers to be $< 10^{16} \text{ cm}^{-3}$. From the saturation of blinking at
20 high excitation power, the authors also estimated the capacity of the quenchers, *i.e.*, the maximum
21 nonradiative recombination rate, to be 10^8 s^{-1} , corresponding to the quenching of one electron-hole

1 pair per 10 ns. Later, similar estimates yielded quencher concentrations of $1.6 \times 10^{16} \text{ cm}^{-3}$ in the
2 study of Gerhard *et al.*¹⁰⁶² Hence, even for defect-rich polycrystalline MHPs of several hundred
3 of nanometers in size, there is only a relatively small number of metastable quenchers per
4 crystal.¹⁰⁶²⁻¹⁰⁶³ Note that the defect concentration is highly dependent on the synthesis procedure
5 and the crystallinity of the formed MHP crystals, which is reflected in the variety of numbers
6 reported here.

7 Similar to small NCs, Yuan *et al.*¹⁰⁶⁴ encountered power-law distributions of the active and
8 passive time periods exceeding two orders of magnitude upon blinking of large-sized MAPbI₃
9 NCs. Moreover, Yuan *et al.*²¹ as well as Merdasa *et al.*¹⁰⁴⁹ confirmed the time fluctuations of the
10 nonradiative rate by correlating the appearance of intermediate PL intensity levels in the blinking
11 transient to faster PL decay. This is similar to the so-called C-type blinking, using the terminology
12 in the field of QD spectroscopy (Figure 114). Faster PL decay in connection with a lower PL
13 intensity is expected when the PL yield is modulated by a fluctuating nonradiative rate according
14 to equation (1).



1
2 **Figure 116.** (a) Schematic illustration of the mechanism of a NR center in an MHP crystal and
3 corresponding energy diagram schemes showing the sub-bandgap state formed by the defect.
4 When passivated, the charge carriers freely diffuse until they recombine radiatively (Bright state).
5 When the NR center gets activated, a charge carrier can be ‘trapped’ by the center due the typical
6 long charge carrier diffusion lengths in MHPs, experiencing a trap-assisted nonradiative
7 recombination (Dim state). (b) A typical recorded PL transient and corresponding energy diagram
8 illustrating the energy barrier for ‘on/off’ switching of the NR center. (c-d) Pioneering blinking
9 experiments showing PL intensity time traces for (c) a single MAPbI₃ microrod ($\lambda_{\text{exc}} = 540$ nm,
10 $\lambda_{\text{PL}} = 700$ nm).⁷⁴² Reprinted with permission from Ref. ⁷⁴² Copyright 2015, American Chemical
11 Society. (d) (i) a MAPbI₃ nanocrystal and (ii) a bright dot located on the top of a polycrystalline

1 MAPbI₃ crystal.¹⁰⁶¹ Reprinted with permission from Ref. ¹⁰⁶¹ Copyright 2015, American Chemical
2 Society.

3 After introducing these NR centers, we would like to reiterate why the blinking in MHP nano-
4 and microcrystals must have different underlying mechanisms to blinking in MHP NCs. As
5 outlined in the first section of this review, PL blinking is commonly ascribed to the Auger process
6 in colloidal QDs with sizes in the range of 2 to 7 nm. After the creation of a trion, subsequently
7 excited electron-hole pairs will recombine nonradiatively by transferring their excitation energy to
8 the extra charge via an Auger process, instead of emitting a photon. This ‘dark’ state of the crystal
9 lasts until the MHP QD turns back to the neutral state by recapturing the charge. Switching of the
10 QD between the charged state and the neutral state can take several seconds and the process can
11 therefore be easily framed.

12 For the Auger process to occur the charges must be confined in a very small volume on the
13 order of 100 nm³, which corresponds to a charge concentration of 10¹⁹ cm⁻³. This is exactly the
14 regime of carrier concentrations when charge recombination in a bulk semiconductor is dominated
15 by the Auger process. In MHP crystals with dimensions on the order of 100 nm length or larger,
16 the carrier concentrations are orders of magnitude lower (10¹³ to 10¹⁶ cm⁻³). Even if the crystals
17 become charged, the extra charges do not increase the carrier concentration close to the Auger
18 regime. Reaching sufficiently high carrier densities is possible by choosing appropriate excitation
19 conditions (> 100 W cm⁻²), however, this would not lead to ‘digital’ switching of the nonradiative
20 rate, because the process is masked by the high number of other recombination events. Therefore,
21 a much larger volume requires a different mechanism to explain PL blinking. Moreover, the
22 absence of the photon antibunching effect in MHP sub-micrometer-sized crystals recently
23 demonstrated by Eremchev *et al.*¹⁰⁶⁵ rejects the simple Auger-based blinking mechanism. An

1 alternative mechanism mechanism is trapping by a strong NR center which is metastable and
2 works at any excitation condition as long as the trap is not saturated. The only requirement is that
3 the charge carrier should be able to diffuse over of the whole volume of the crystal to reach the
4 center.

5 **Origin of metastable defects.** The idea of metastable NR centers has become the basis of the
6 current understanding of PL fluctuations in MHP NCs. However, the chemical origin of the
7 underlying defects has not yet been unraveled. It is important to note that the blinking phenomenon
8 is not restricted to prototypical MAPbI₃, but rather seems to occur in a wide variety of MHP
9 compositions and morphologies.

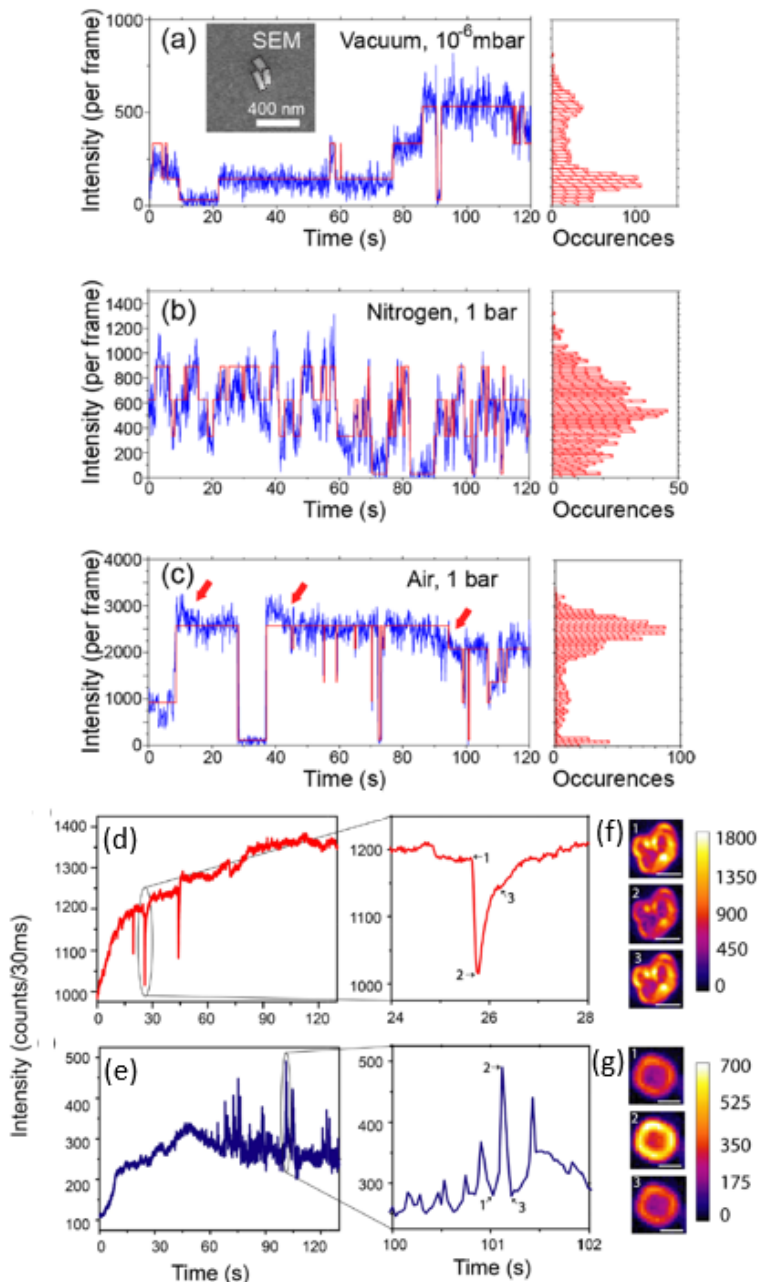
10 Wen *et al.*¹⁰⁶⁶ reported blinking in local regions of a polycrystalline film comprised of
11 MAPbBr₃ NCs, whereas intermittency in isolated NCs was suppressed. In this early work the
12 authors assigned the dim intervals to enhanced Auger recombination at interfaces between NCs in
13 the film where charge carriers get accumulated in analogy to blinking of aggregates of QDs.^{1047,}
14 ^{1050, 1052-1053} However, as we have discussed before, Auger recombination cannot be the primary
15 origin of blinking in large crystals because of their size. Freppon *et al.*¹⁰⁶⁷ studied the PL
16 intermittency in pure MAPbI₃ and MAPbBr₃ NCs, as well as in NCs with mixed halide
17 composition. The PL in the pure components was stable, while the mixed compounds showed
18 pronounced blinking behavior, most likely due to (light-induced) iodide-rich and bromide-rich
19 phase segregation. Tachikawa *et al.*¹⁰⁶⁸ on the other hand reported blinking for individual
20 MAPbBr₃ NCs, which was accompanied by light induced PL enhancement. Halder *et al.*¹⁰⁶⁹
21 observed blinking in both pure and SCN⁻ doped MAPbI₃ NCs, and Li *et al.*¹⁰⁷⁰ demonstrated PL
22 intermittency behavior in individual grains of mixed halide MAPbI_{3-x}Cl_x films. The above-
23 mentioned studies confirm that the blinking phenomenon occurs in a plethora of MHP systems,

1 which indicates that it is a general feature of MHP semiconductors related to the presence of a
2 small number of metastable NR centers per grain/crystal¹⁰⁶³ rather than an effect, which is limited
3 to certain material compositions or morphologies.

4 A very informative approach to comprehend the origin of metastable defects is the study of
5 blinking in different atmospheric conditions, as they provide different reactive environments for
6 trap formation and annihilation, in particular at the crystal surface. Yuan *et al.*¹⁰⁶⁴ investigated the
7 environmental dependence of blinking in single-crystalline MAPbI₃ nanorods and found
8 pronounced differences in the blinking behavior under vacuum, nitrogen and ambient air (Figure
9 117). From this they concluded that most of the defects causing PL blinking must be located close
10 to crystal surface. As potential candidates for the metastable defects they proposed under-
11 coordinated Pb ions and MA vacancies. For the formation of the latter species, they argued that
12 vacuum could promote detachment of MA due to its low boiling point, whereas the presence of
13 oxygen, light and moderate humidity enable chemical reactions that promote passivation of surface
14 defects. Passivation of defects under these atmospheric conditions has also been reported by Tian
15 *et al.*,¹⁰⁷¹ Tachikawa *et al.*¹⁰⁶⁸ and Merdasa *et al.*¹⁰⁴⁹ who found an increase of the overall PL
16 intensity and connected this to the emergence of blinking. Although, it is important to realize that
17 fast diffusion of gases like oxygen through MHP crystals does not allow to assign the effect of
18 atmosphere to surface modification only. The influence of surface defects on the PL are consistent
19 with surface passivation studies leading to a significant improvement of the luminescence yield
20 and optical stability.^{1068, 1072-1073} However, note that not all metastable defects were passivated,
21 potentially because some of them are inherent structural defects, as pointed out by Yuan *et al.*¹⁰⁷²

22 Detailed studies on the influence of the ambient atmosphere on MAPbBr₃ μ Cs were also
23 carried out by Halder *et al.*¹⁰⁷⁴ In particular, they investigated the effect of high humidity and

1 observed a lower PLQY in humid atmosphere and the appearance of strong variations of PL
2 intensity looking like PL flickering. This process was found to be accelerated in presence of
3 oxygen. Upon the removal of moisture, the flickering disappeared, accompanied by a considerable
4 enhancement in the overall PL intensity. It is important to note that the change in PL was usually
5 gradual rather than abrupt, thus it cannot be explained by activation/de-activation of just one
6 quencher. In this work, the slow PL flickering was assigned to a concerted phenomenon caused by
7 several defects. Such defects may be induced via interaction with the environment, for example
8 transient chemical changes to the surface layer due to local fluctuations of humidity. So far, all
9 these are pure speculation and further studies are needed to understand the nature of such large
10 scale, gradual fluctuations. It is interesting to note that the emergence of PL flickering observed
11 by Halder *et al.* was connected to an overall reduction of the PL intensity due to the humidity
12 effect, whereas in the other reports mentioned above,^{1049, 1068, 1071} PL blinking appeared after light-
13 induced PL enhancement. This is a strong indication that the flickering phenomenon observed by
14 Halder *et al.* under high humidity has a different origin from “real” blinking related to individual
15 luminescence quenchers, which becomes more pronounced after PL enhancement potentially due
16 to light-induced defect curing, which increases the diffusion length and with this the quenching
17 volume of individual metastable quenchers.



1
 2 **Figure 117.** Effect of environmental conditions on PL blinking time traces of MAPbI₃ nanorods
 3 (a) under vacuum, (b) in nitrogen under ambient pressure, (c) in air under ambient pressure. The
 4 inset shows the scanning electron micrograph of the cluster of three perovskite nanorods. The red
 5 lines are a guide for the eye.¹⁰⁶⁴ Reprinted with permission from Ref. ¹⁰⁶⁴. Copyright 2016,
 6 American Chemical Society. (d-g) Slow, gradual PL flickering of MAPbBr₃ microcrystals under

1 different humidity conditions. PL intensity time traces showing exceptional (d) sudden dim states
2 under low humidity conditions (35–70% RH) and (e) sudden bright states under high humidity
3 conditions (75–90% RH). (f, g) PL images of the particular microcrystals from (d, e) respectively,
4 at timing 1, 2, and 3. Scale bar = 1 μm .¹⁰⁷⁴ Reprinted with permission from Ref. ¹⁰⁷⁴. Copyright
5 2016, American Chemical Society.

6 Variation of the experimental conditions can also be employed to study whether blinking is a
7 photo- or thermally-activated process. Tian *et al.*¹⁰⁶¹ and Yuan *et al.*¹⁰⁶⁴ studied the influence of
8 optical power on the blinking characteristics. Both found a strong reduction of the relative blinking
9 amplitudes, which was interpreted as a saturation of the metastable nonradiative center (trap
10 filling) and an overall reduction of blinking events with increasing excitation power. Photo-
11 activation, however, would become apparent as an increase of the switching dynamics. Hence, in
12 recent studies there is no evidence for photo-activation of the switching process. However, trap
13 filling effects could mask the photo-activation phenomenon and more suitable model systems, *e.g.*,
14 smaller crystals, are needed to clarify this point.

15 By investigating the influence of temperature on luminescence blinking, Gerhard *et al.*¹⁰⁶²
16 provided a detailed view on the underlying mechanism of blinking in MAPbI₃ NCs. After
17 decreasing the temperature from 295 to 77 K, an increased time-averaged PL intensity by 1 to 2
18 orders of magnitude was observed as well as a substantial reduction in the relative magnitude of
19 blinking below 200 K. Both the observed temperature dependent PL intensity and the blinking
20 dynamics were very specific from crystal to crystal and often fully repeatable in consecutive
21 cooling-heating cycles. It was proposed that this peculiar behavior comes from the presence of
22 several quenchers per crystal having potential barriers between active and passive states. Using a
23 simple model, the activation energies of the switching of individual quenchers were found to be

1 broadly distributed from 0.2 to 0.8 eV. This range matches the range of reported energy barriers
2 for ion migration in perovskites. Therefore, it is likely that the random switching is caused by
3 diffusing ions which can passivate or activate a NR center, whose energetic position is determined
4 by the local environment.

5 Even though the above-mentioned studies revealed important insights into the processes that
6 drive luminescence blinking, the nature of the underlying defects has not yet been defined. It is
7 important to note that most MHPs possess defect levels close to the band edges. Therefore, it is
8 unlikely that they act as strong luminescence quenchers. However, as pointed out by Merdasa *et*
9 *al.*¹⁰⁴⁹, one should consider that the defects could also be complexes comprised of *e.g.* an electron
10 donor and an electron accepting species. This way, electrons and holes are efficiently trapped in
11 close proximity and their spatial overlap leads to fast nonradiative recombination. Additionally,
12 this hypothesis seems to explain the relatively low estimated concentration of metastable NR
13 centers.

14 **Super-resolution methods to unravel the spatial distribution of NR centers.** The fact that
15 blinking in MHPs occurs in spatially extended objects offers the opportunity to obtain information
16 about the location of quenchers and emissive sites. In this context, a particular powerful approach
17 is the combination of electron microscopy with super-resolution fluorescence microscopy,^{1049, 1064,}
18 ¹⁰⁷² which allows for the direct correlation between the morphology of the material and the local
19 emissive properties.

20 In their study on monocrystalline MAPbI₃ NCs, Yuan *et al.*¹⁰⁶⁴ recorded SEM images and
21 employed a localization algorithm to track the center of the profile emission in the course of
22 blinking. Interestingly, they found no change in the emission localization position upon blinking
23 of single crystals. In contrast, for polycrystalline MHP NCs, Tian *et al.*¹⁰⁶¹ observed a clear

1 correlation between the PL intensity fluctuations and shifts in the emission location. In the first
2 case carrier diffusion through the whole crystal is very efficient and the extent of luminescence
3 quenching is only limited by the capacity of the metastable defect. As a consequence, the PL of
4 the crystal is spatially homogeneously quenched. In the second case charge carrier diffusion plays
5 a crucial role such that quenching in some regions of the objects is more efficient than in other
6 regions, leading to shifts of the emission location in the course of blinking. The existence of both
7 quenching regimes was first pointed out by Merdasa *et al.*¹⁰⁴⁹, who presented an extensive study
8 on PL blinking in polycrystalline MAPbI₃ μ Cs (Figure 118a-c), as well as monocrystalline
9 microrods up to 10 μ m in length. The authors demonstrated experimentally clear examples of the
10 diffusion-limited and the NR center capacity-limited blinking regimes, as illustrated schematically
11 in Figure 118f. It was found that high-capacity NR centers, also termed “supertraps”, are most
12 efficient in structurally homogeneous and large MAPbI₃ crystals where carrier diffusion is
13 efficient, which may pose limitations on the efficiency of perovskite-based devices. Furthermore,
14 as can be found in Figure 118f, they have elaborated a scheme considering the high-capacity NR
15 center or supertrap as a donor–acceptor pair.

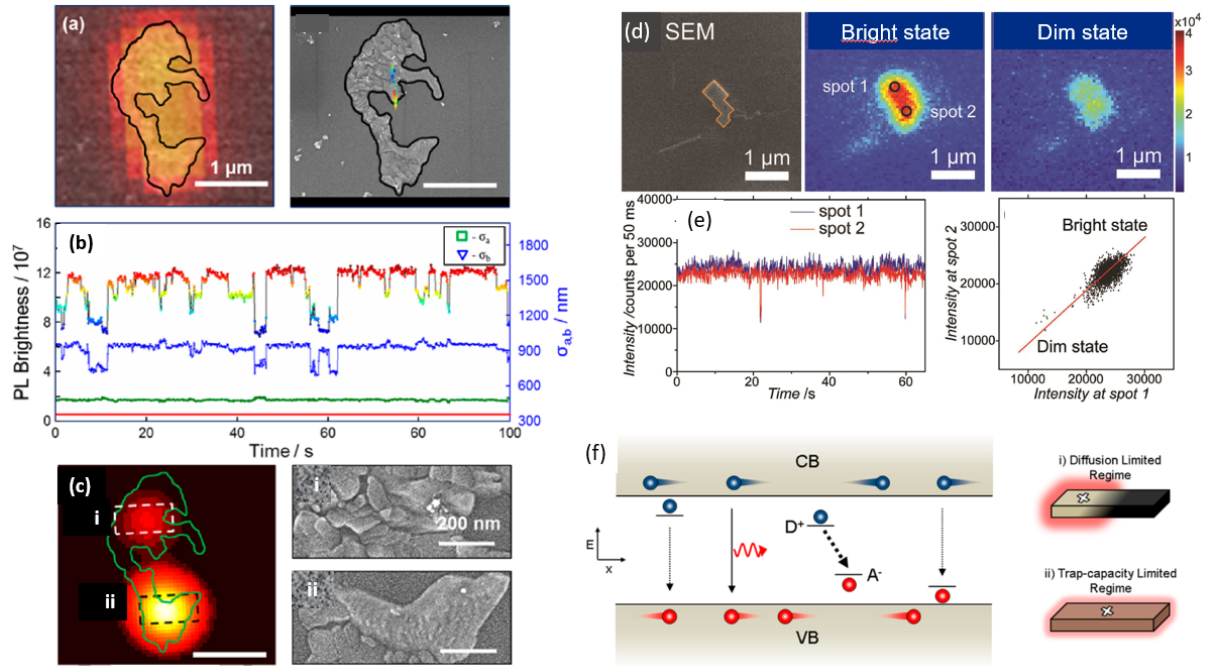
16 Sharma *et al.*¹⁰⁷⁵ demonstrated electroluminescence blinking in aggregated CsPbBr₃ NCs, but
17 noted the absence of blinking when the material was photo-excited. By employing a super-
18 resolution technique, they found that the electroluminescence was emitted from only a few distinct
19 spots in each aggregate. They attributed this to the fact that in case of electroluminescence, only a
20 few of the agglomerated NCs are emissive due to funneling of the injected charges to the lowest
21 energy levels. PL on the other hand resulted from collective excitation of the overall aggregates,
22 hence, no fluctuations of individual nanocrystals became apparent. Their work further exemplifies
23 that a key requirement to observe blinking is a high interconnectivity between the emissive entities,

1 or, in other words, efficient diffusion of a major fraction of the emissive population towards the
2 quenching defect.

3 Beside localization of the emission position, other techniques borrowed from the toolkit of
4 super-resolution methods have been employed to study the blinking dynamics. Tian *et al.*¹⁰⁷¹
5 utilized a differential super-resolution technique to spatially map the regions characterized by
6 intense PL blinking in a polycrystalline MAPbI₃ film and found that the emission predominantly
7 stems from very localized sites of less than 100 nm in size. It was hypothesized that an emitting
8 site can be either a small crystallite free from quenchers or a spatially localized state in a large
9 crystal with increased radiative recombination probability. Merdasa *et al.*¹⁰⁴⁹ employed super-
10 resolution optical fluctuation imaging (SOFI) to detect local regions with strong and frequent
11 blinking in polycrystalline MAPbI₃ NCs. As depicted in Figure 118d-e, Yuan *et al.*¹⁰⁷² used a
12 differential imaging approach similar to that of Tian *et al.*, from which they determined a
13 heterogeneous distribution of fluctuating quenchers in mono- and polycrystalline objects
14 comprised of MAPbI₃. Interestingly, the authors demonstrated that even a micrometer-sized
15 polycrystal comprised of several well-defined cubic sub-micrometer crystals can generate one
16 common PL blinking time trace which is not limited by diffusion.

17 The combination of SEM with super-resolution fluorescence allowed furthermore to directly
18 correlate the location of the NR center to a specific blinking volume, allowing to precisely define
19 the density of NR center. As such, Merdasa *et al.*¹⁰⁴⁹ estimated a 10⁹ s⁻¹ recombination rate
20 introduced by a single quencher (supertrap) and Yuan *et al.*¹⁰⁷² obtained quencher densities of 8.5
21 × 10¹³, and 1.3 × 10¹⁴ cm⁻³ for monocrystalline and polycrystalline NCs, respectively. The
22 discrepancies in the reported defect concentrations highlight once more the importance of the
23 material quality. Additionally, the crystal morphology and size may play a role. For smaller

1 crystals, defects with a smaller capacity cause detectable PL blinking, while in larger crystals their
 2 influence can be suppressed because they get saturated at the same excitation power due to larger
 3 number of electron-hole pair generated in the crystal.



4
 5 **Figure 118.** (a) PL emission profile of a large MAPbI₃ polycrystal with its contour shown by the
 6 black line (left) and the emission localizations indicated on the corresponding SEM image (right).
 7 (b) PL intensity transient and time dependence of the Gaussian widths ($\sigma_{a,b}$) indicating a fluctuating
 8 asymmetric emission profile. The red horizontal line at 360 nm is the σ_{PSF} of the microscope for λ
 9 = 760 nm. (c) SOFI image showing two well-separated spots (left) and their corresponding zoomed
 10 in SEM images (right).¹⁰⁴⁹ Reprinted with permission from Ref. ¹⁰⁴⁹ Copyright 2017, American
 11 Chemical Society. (d) SEM image of a polycrystalline MAPbI₃ NC with a volume of about $9 \times$
 12 10^6 nm^3 and the PL images in its bright state and dim state, respectively. (e) PL intensity time
 13 traces recorded at the two ends of the crystal (left) and scatter plot of the PL intensities at both
 14 ends showing a strong correlation (right).¹⁰⁷² Reprinted with permission from Ref. ¹⁰⁷². Copyright

1 2018, Wiley-VCH Verlag GmbH & Co. KGaA, Weinheim. (f) Schematic illustration of a high-
2 capacity NR center (supertrap) as a donor–acceptor pair. Left: Energy diagram schemes showing
3 the sub-bandgap states formed by the defects. In case of an ionized donor (D^+) and acceptor (A^-),
4 the high-capacity NR center is created and efficient nonradiative recombination occurs (thick
5 dashed line). In case they are separated in space, nonradiative recombination is inefficient (thin
6 dashed lines). Radiative recombination occurs across the bandgap (solid line). Right: The different
7 operational regimes of the high-capacity NR center as affected by its location (white crosses).¹⁰⁴⁹
8 Reprinted with permission from Ref. ¹⁰⁴⁹. Copyright 2017, American Chemical Society.

9

10 **10.3 ELECTRON-PHONON COUPLING IN SINGLE NCs**

11 The intrinsic (photo)physical properties of MHP semiconductors are strongly related to the
12 coupling of excited electronic and vibrational states.⁹²¹ The vibrational modes in MHPs can be
13 generally split into two branches:¹⁰⁷⁶⁻¹⁰⁷⁷ a low energy band ($20\text{--}200\text{ cm}^{-1}$) dominated by the
14 inorganic $[\text{PbX}_6]^{4-}$ sublattice, along with the high-energy vibrations of the organic components
15 ($200\text{--}3300\text{ cm}^{-1}$). In all-inorganic systems, like the CsPbX_3 perovskites, the high-energy branch
16 is missing. Following the absorption of above bandgap light,¹⁰⁷⁸ the thermalization, transport and
17 recombination of photo-generated carriers will depend on the underlying electron-phonon
18 interactions. For instance, stronger electron–phonon scattering in lead-based $[\text{PbX}_6]^{4-}$ octahedra
19 directly reduces carrier mobility and increases the PL emission Stokes shift and linewidth (*i.e.*,
20 color purity). At relatively low temperatures (below $\sim 50\text{ K}$), scattering from low-energy acoustic
21 phonons is dominant, while closer to room temperature (RT) Fröhlich coupling with high-energy
22 longitudinal optical (LO) phonons ($E_{\text{LO}} = \hbar\omega_{\text{LO}}$) is the principal scattering mechanism in polar
23 MHPs.

1 Analysis of the PL FWHM between 0 K and RT has become routine for gauging the strength
2 of electron-phonon coupling within MHPs and comparing its magnitude across different
3 compositions.¹⁰⁷⁹⁻¹⁰⁸⁰ The temperature-dependent excitonic linewidth of band-to-band
4 recombination within semiconductors^{1079, 1081-1082}; is related to the carrier-phonon coupling by

$$5 \quad \Gamma(T) = \Gamma_0 + \gamma_{ac}T + \gamma_{LO} \frac{1}{e^{E_{LO}/k_B T} - 1}. \quad (2)$$

6 The first term (Γ_0) represents the intrinsic low-temperature FWHM, while the second and the
7 third terms (Γ_{ac} and Γ_{LO}) describe acoustic and LO-phonon (Fröhlich) scattering contributions,
8 respectively, with coupling strengths γ_{ac} and γ_{LO} . Below 75 K, the linear Γ_{ac} component
9 dominates due to low-energy acoustic phonons. The LO phonon population requires more thermal
10 energy to become impactful, being governed by Bose–Einstein statistics, with k_B being the
11 Boltzmann constant.

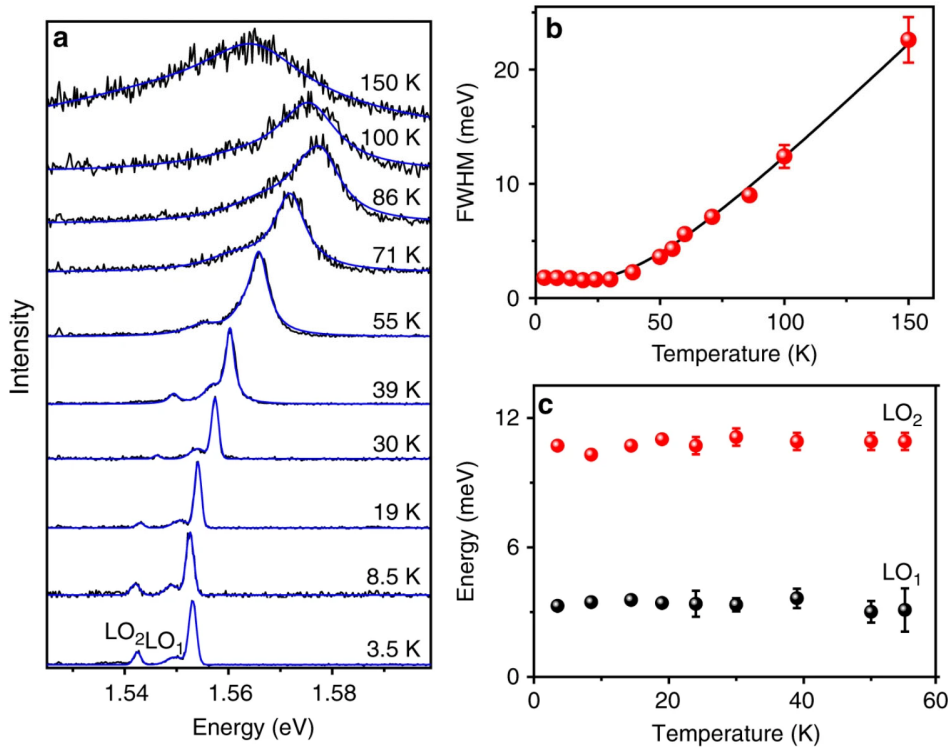
12 Studying single MHP NCs also allows one to investigate electron-phonon interactions beyond
13 the bulk approximation. In the absence of strong thermal broadening close to 0 K, electron-phonon
14 coupling in MHP NCs can manifest additional satellite peaks in the high-resolution PL spectrum,
15 appearing as low-energy phonon replicas.¹⁰⁸³⁻¹⁰⁸⁴ These additional peaks correspond to weak
16 phonon-assisted transitions and are redshifted relative to the central zero-phonon PL (ZPL)
17 emission. The relative intensity of phonon replicas between different NCs of different sizes will
18 vary.¹⁰⁸⁵ Whereas low-temperature PL spectroscopic studies are widely adopted to probe electron-
19 phonon interactions in MHPs, relatively few studies have focused on single MHP NCs. At the
20 nanoscale, perovskite crystals tend to exhibit higher phase stability, preferring to occupy the
21 desired perovskite structure,³ allowing more complete low-temperature optical studies.
22 Furthermore, for micro-PL studies on single MHP NCs, the emission FWHM is substantially

1 reduced^{1083, 1086-1089} (≤ 1 meV) compared to ensemble NC studies, better revealing fine energetic
2 structure.

3 **Temperature dependent PL.** In Figure 119a Lounis *et al.*¹⁰⁸³ examine the thermal evolution of
4 the exciton-phonon coupling phenomena in individual FAPbI₃ NCs. Interestingly, below 30 K,
5 they found negligible thermal broadening in the ZPL emission from a single FAPbI₃ NC (Figure
6 119b), which suggests a weak electron-acoustic phonon interaction. An upper limit of $\gamma_{ac} \sim 5$
7 $\mu\text{eV}\cdot\text{K}^{-1}$ is extracted from equation (2) from their temperature-dependent broadening, which is
8 found to be over one order of magnitude smaller than that previously reported for bulk FAPbI₃.¹⁰⁷⁹
9 Thus, using a single optical phonon mode is enough to reproduce the thermal-induced broadening
10 evolution in Figure 119b (parameters: $\Gamma_0 = 1.5$ meV, $\gamma_{ac} = 0$ meV, $\gamma_{LO} = 27$ meV and $E_{LO} =$
11 10.7 meV). While the optical phonon energy appears to be softened in the NC, the γ_{LO} broadening
12 coefficient derived is in agreement with measurements on bulk FAPbI₃.¹⁰⁷⁹ Due to the location of
13 the A-site cation within the charged octahedral cavity formed by the BX₃ sublattice, MHP NCs
14 exhibit a soft ionic structure which endow them with so-called “crystal–liquid duality”.¹⁰⁹⁰ More
15 specifically, this glass character arises from the crystalline-like response of coherent band transport
16 and a liquid-like response in the dielectric function. Hence, Fu *et al.*^{1083, 1091} assign the derived
17 smaller γ_{ac} value to the phonon glass character of the soft perovskite lattice and the larger bulk
18 values to extrinsic influences (counterintuitive to expected confinement effects¹⁰⁹¹), rather than
19 intrinsic electron–phonon interactions.

20 Below roughly 60 K, the appearance of additional phonon replicas are also resolved in the
21 single FAPbI₃ NC¹⁰⁸³ PL spectrum, assigned to different bundles of separated low-energy lattice
22 modes (Figure 119c). On the basis of theoretical predictions and low-temperature vibrational
23 studies of APbI₃-based systems, they assign these phonon replicas to different bundles modes

1 which are seen to be thermally stable in Figure 118c. Up to three additional satellites were resolved
 2 during their survey¹⁰⁸³, being governed by different bending and stretching modes of the PbI₆
 3 network and motion of the organic FA cation, and by their mutual couplings.



4
 5 **Figure 119.** Temperature-dependent PL (a) spectral evolution and (b) zero-phonon PL (ZPL)
 6 linewidth (FWHM) of a single FAPbI₃ NC. The black line is a fitting curve made using equation
 7 (2), taking into account only the low temperature linewidth ($\Gamma_0 = 1.5$ meV) and Fröhlich coupling
 8 contributions ($E_{LO} = 10.7$ meV). Broadening due to acoustic phonon scattering is found to be
 9 negligible. (c) LO₁ and LO₂ phonon energies as a function of temperature from 3.5 K to 55 K,
 10 recovered from (a).¹⁰⁸³ Reprinted with permission from Ref. ¹⁰⁸³. Copyright 2018, Springer Nature.

11 Through PL studies of individual all-inorganic CsPbBr₃ microwires at cryogenic temperatures
 12 (77 to 300 K), Zhao *et al.*¹⁰⁹² revealed the electron-phonon interactions arising in wires ranging
 13 from 0.5 to 5 μm thick and up to hundreds of microns long. They found that the PL spectrum

1 exhibited a dominant green (527 nm) triplet exciton emission with an additional low-energy
2 shoulder (~540 nm) which became better resolved at lower temperatures, due to a replica emission.
3 Fitting the thermal-induced broadening of the ZPL emission down to 77 K in the single CsPbBr₃
4 microwires, they extracted an LO-phonon coupling constant of $\gamma_{LO} = 66 \text{ meV}^{1092}$ using a
5 thermally-stable phonon energy¹⁰⁸¹ of $E_{LO} = 19 \text{ meV}$, as derived from the single crystal Raman
6 scattering spectrum. This value is comparable to other bulk lead bromine-based perovskites¹⁰⁷⁹
7 and confirms the preservation of strong Fröhlich interactions in their single CsPbBr₃ microwires,
8 arising from relatively weak confinement effects, *i.e.*, due to the relatively large NC dimensions.

9 Rainò *et al.*¹⁰⁸⁶ reported one of the first low-temperature PL studies of single MHP NCs,
10 examining individual all-inorganic CsPbX₃ (X = Cl/Br) perovskites. Beyond the interesting
11 blinking phenomena exhibited by the NCs, spectra measured from a single particle using
12 sufficiently high optical excitations contained an additional low-energy peak, arising from a
13 charged excitonic emission. Measured at what they define as intermediate excitation power,¹⁰⁸⁶
14 the charged exciton line of some NCs became 2–3 times narrower than the principle exciton line,
15 suggesting that the excitonic transition might have reduced electron–phonon coupling. At the
16 single FAPbBr₃ NC-level, Pffingsten *et al.*¹⁰⁸⁷ examined exciton–phonon interactions via
17 temperature- and polarization-dependent PL measurements. Near 0 K, pronounced satellite PL
18 peaks appear shifted relative to the ZPL band due to the TO₁, TO₂, and TO₃/LO₁ phonon bands,
19 by energies of 4.3, 8.6, and 13.2 meV, respectively. Through their survey of multiple individual
20 NCs, some extra replica peaks sometimes appeared, redshifted by higher energies (18.3 and 37.2
21 meV) relative to the ZPL.¹⁰⁸⁷ Based on the expected low-energy vibrational modes of the PbBr₆
22 octahedra, they attribute these additional emission peaks to coupling of charge carriers to liberation
23 modes of the FA⁺ cations. Fitting the temperature dependent FWHM of the ZPL with equation (2),

1 Pfingsten *et al.*¹⁰⁸⁷ also inferred a negligible contribution from acoustic phonon coupling ($\gamma_{ac} < 0.1$
2 meV) and identified thermal-induced broadening to principally arise via an optical phonon
3 coupling constant (γ_{LO}) of roughly 32 meV. Notably again, the optical phonon contribution is
4 recorded here to be relatively low compared to other bulk Br-based MHP counterparts.¹⁰⁷⁹

5 Employing low-temperature (down to 5 K) polarized PL studies of CsPbBr₃ single NCs (~7
6 nm), Ramade *et al.*¹⁰⁸⁸ also found that the temperature-dependent PL linewidth is mainly governed
7 by the Fröhlich term ($\gamma_{LO} = 42 \pm 15$ meV), being consistent with the polar nature of the bulk lead
8 halide perovskite.¹⁰⁷⁹ Within this regime (*i.e.*, NCs exhibiting bandgaps of 2.46 - 2.62 eV), they
9 found no correlation of the crystal size, for NCs in the order of the Bohr diameter, with the PL
10 broadening due to acoustic phonon coupling. Liu *et al.*¹⁰⁸⁹ reported single-dot PL measurements
11 of MAPbI₃ NCs (~7 nm) down to 5 K, realizing the narrowest ZPL linewidth of ~0.6 meV ever
12 managed in the archetypal perovskite system. They also noted a sharp satellite peak redshifted by
13 ~4 meV in low-temperature spectra, which varied in relative amplitude between dot-to-dot,
14 inferring variation in their exciton-phonon coupling strengths.

15

16 **10.4 SUMMARY AND OUTLOOK FOR SINGLE PARTICLE STUDIES OF MHP NCs**

17 Photoluminescence blinking of MHP NCs hampers the application of these bright luminescent
18 crystals in quantum optical devices. Spectrally and temporally correlated single photon counting
19 through single-molecule microscopy and spectroscopy have been helpful for the classification of
20 the emitting states and the blinking mechanisms. Although single NCs emit entangled photons
21 with slightly different energies from the band-edge triplet states which become nondegenerate
22 when cooled significantly, the degree of degeneracy increases with temperature and the second-
23 order single-photon correlation function minimizes at room temperature. Thus, the blinking

1 mechanism of MHP NCs is dissected at room temperature. Photo-charging followed by
2 nonradiative Auger recombination is the primary mechanism of blinking in metal halide perovskite
3 NCs and metal chalcogenides. Here, blinking is due to the random switching of a NC between
4 nonradiative and radiative cycles by charging and discharging. Also, MHP NCs show blinking due
5 to trap-assisted nonradiative carrier recombination involving surface traps, deep traps and shallow
6 traps, governed by ion vacancies, interstitial sites and anti-sites. Hence, post-synthetic chemical
7 modification of MHP NCs allows for blinking suppression. Nonblinking MHP NCs for
8 applications in nanophotonic quantum devices can be developed by optimizing the energy and
9 intensity of excitation light, the nature and density of trap states, the size of quantum dots and the
10 chemical composition of cations, halide ions, ligands and shells.

11 The growing number of studies related to PL intermittency in MHPs indicates that the
12 phenomenon is an intrinsic feature of this material class rather than an effect related to specific
13 processing conditions or a specific environment. Furthermore, it is important to note that blinking
14 in crystals with sizes beyond quantum confinement up to several micrometers goes mechanistically
15 beyond the physics and chemistry of single quantum systems. A consistent explanation for
16 blinking in MHP nano- and microcrystals can be given by the presence of metastable nonradiative
17 centres. Metastability of defect states is in fact reflected in many phenomena observed in MHPs
18 and related devices, for example PL enhancement and suppression, ion migration, self-healing
19 after photodegradation, dropping and recovery of solar cell efficiencies¹⁰⁹³ and the sensitivity of
20 these processes to light illumination, atmospheric constituents and temperature. Thus, it is
21 plausible that PL blinking is another manifestation of the metastable character of incorporated
22 defect states. Except for PL blinking, however, all defect-related phenomena are ensemble
23 observations, where contributions of individual defects are averaged out. This averaging is

1 unavoidable because of the very large number of individual species in the volume, which can be
2 described by the concentration n . Now, let us hypothetically decrease the volume of the sample to
3 $1/n$. Following Poissonian statistics, a crystal of this volume should contain on average 1 NR center
4 and its metastability becomes apparent as discrete blinking. To investigate this individual defect,
5 methods of luminescence microscopy and in particular techniques inspired by super-resolution
6 methods and single molecule spectroscopy are ideal tools. The resolution of optical microscopy is
7 about 500 nm which is equal to the typical grain size in polycrystalline films. Moreover, isolated
8 crystals of sizes from 10 to 1000 nm can be readily investigated as model systems representing
9 individual constituents of a perovskite film. Studying individual defects incorporated in these
10 objects allows us to rationalize fundamental properties behind solar cells and other devices.

11 Furthermore, correlating PL and electron microscopy allows estimating the quenching volume
12 and defect concentration. Taking the inverse of the concentration, we obtain the cube-shaped
13 volume containing only one defect to range from $10^{-10} - 10^{-17} \text{ cm}^3$, giving cube side lengths from
14 $4.6 \mu\text{m}$ to 21 nm. Grain sizes in MHP films vary over the same range, hence, a number on the
15 order of one defect per grain appears reasonable. This estimation is nicely supported by the long
16 list of experiments discussed above where strong PL fluctuations have been reported for MHP
17 crystals of very different sizes up to micrometers. Note that in order to observe blinking, it is not
18 necessary to have exactly one defect per crystal. Additionally, defects with the strongest quenching
19 capacity will be more visible in case of many defects contributing. Increasing the number of
20 defects, however, will make the blinking transients more complex and eventually reduce the
21 overall modulation of the luminescence yield, such that a number much higher than one appears
22 unfeasible. Despite the uncertainty in determining the actual concentration of metastable
23 quenchers, the current stage of experimental work indicates that there is a high variety in densities.

1 Likewise, literature is filled with very divergent estimations of the defect state concentrations in
2 MHPs based on distinct techniques, ranging from 10^{10} to 10^{17} cm^{-3} , which may be related to
3 diversity from poly- to monocrystalline crystals, different detection techniques and different
4 methods of data analysis. However, we note that it is a remaining open question whether blinking
5 studies and other methods are actually sensitive to the same type of defects, whether or whether
6 not being (high-capacity) NR centers.

7 Despite a growing number of studies related to blinking in MHPs, several questions regarding
8 the phenomenon of blinking in MHP NCs and μCs remain open. These include in particular the
9 nature of the metastable quenchers and the mechanism of their activation and de-activation. It has
10 also not yet been studied whether the switching process can be activated by light. Better
11 understanding of the origin of blinking can open pathways to passivate the quenchers permanently,
12 which will be beneficial for the performance of MHP devices. Another interesting question is
13 which fraction of the defect states in MHPs is metastable. The defect concentrations estimated
14 from blinking experiments yield defect concentrations similar to the range reported from other
15 methods, suggesting that the defects probed in blinking experiments are actually representative for
16 a high fraction and maybe even all of the defects in the material. Furthermore, micro-
17 photoluminescence studies on individual MHP NCs reveal high-resolution information on the
18 nature and extent of charge carrier-phonon coupling in these systems, which are not averaged out
19 by bulk measurements. Much deeper understanding of these photophysical processes can direct
20 material development ensuring optimized charge dynamics with the aim to further design high-
21 performance MHP NC-based optoelectronic devices.

22

1 11. APPLICATIONS

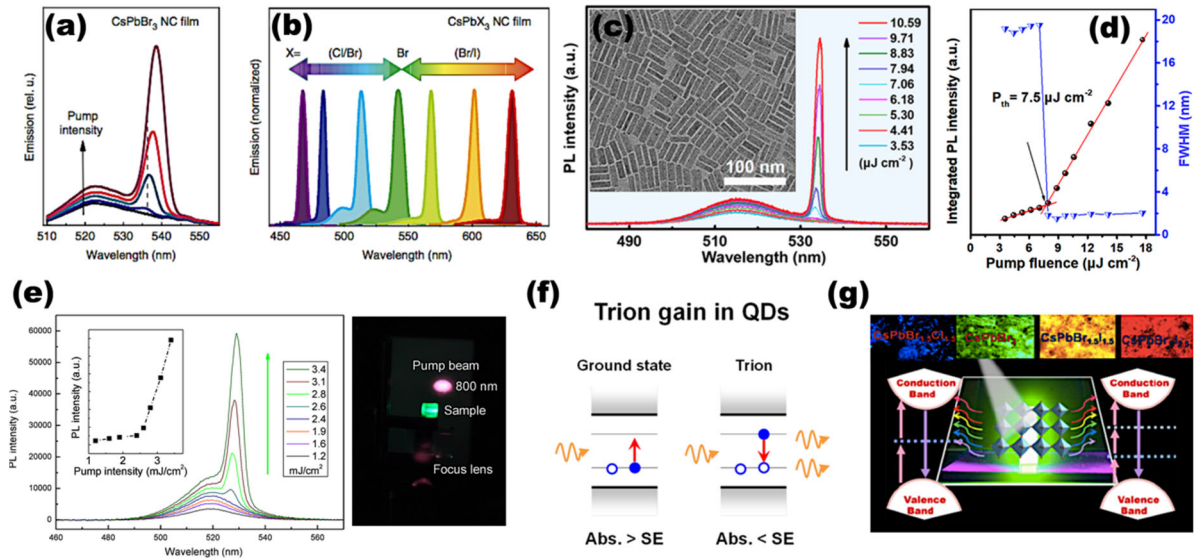
2 11.1 LASERS

3 Since the first observation of stimulated emission (SE) and lasing from colloidal perovskite
4 quantum dots (Perovskite NCs), there has been a surge in research activities in developing high-
5 performance Perovskite NCs-based lasers because the Perovskite NCs feature the advantages of
6 both the colloidal quantum dots (QDs) and halide perovskites for optical gain media, such as the
7 facile solution processability, bandgap tunability, large absorption cross-section and defect-
8 tolerant nature.^{7, 29, 1094-1104} In general, there are two kinds of halide perovskite nanocrystals, that
9 is, the organic-inorganic hybrid halide perovskites NCs (OHPNs) and the all-inorganic cesium
10 halide perovskites NCs (IHPNs). The IHPNs manifest better stability against moisture and oxygen
11 than OHPNs since the organic compounds tend to dissociate when exposed to ambient
12 environments. Until now, both the IHPNs and OHPNs have shown favorable optical gain
13 performance and were used in a variety of laser devices, including random lasers,^{487, 1105}
14 whispering-gallery-mode (WGM) lasers,¹¹⁰⁶ distributed feedback (DFB) lasers,¹¹⁰⁷⁻¹¹⁰⁹ vertical
15 cavity surface emitting lasers (VCSELs)^{888, 1100, 1110-1111} and even high-resolution large-area laser
16 arrays with multicolor outputs¹¹¹²⁻¹¹¹³ have been fabricated in the past few years.

17 In this section, we will discuss the optical gain in Perovskite NCs including the SE behavior
18 under one- and multi-photon pumping as well as the optical gain mechanism. Afterwards, the
19 recent progress in laser devices developed from Perovskite NCs will be presented. Finally, we will
20 discuss the current challenges and perspective on the development of lasers based on Perovskite
21 NCs. We believe that the Pe-QD based lasers will become an important complement to epitaxial
22 semiconductor lasers in the near future.

23

1 Optical gain in MHP NCs



2
3 **Figure 120.** (a) Pump intensity dependence of the emission in a CsPbBr₃ NC film (pumping
4 intensity range was 3-25 mJ cm⁻²). (b) Spectral emission-tunability of ASE via modulating
5 constituents in a CsPbBr₃ NC film. Reprinted with permission from Ref.¹⁰⁹⁶ (c) Pump fluence-
6 dependent emission of CsPbBr₃ perovskite nanorods with uniform surface, inset: the typical TEM
7 images of low-defect CsPbBr₃ nanorods. (d) Integrated PL intensity and line widths of CsPbBr₃
8 nanorods as a function of pump fluences. Reprinted with permission from Ref.¹¹¹⁴ (e) Two-photon
9 pumped PL spectra from CsPbBr₃ nanocrystals at varied pump intensities, inset right (e):
10 photograph of the stripe pumping configuration adopted to pump the CsPbBr₃ NCs with an 800
11 nm laser beam with the pulse width of 100 fs and repetition rate of 1000 Hz. Reprinted with
12 permission from Ref.¹⁰⁹⁷ (f) Mechanism for trion gain in singly charged NCs with doubly
13 degenerate band edge states. Reprinted with permission from Ref.¹¹¹⁵ (g) Two-photon fluorescent
14 microscope images of different CsPbX₃ Pe-NCs as well as the simple illustration of two-, and
15 three-photon excited PL. Reprinted with permission from Ref.¹¹¹⁶

16

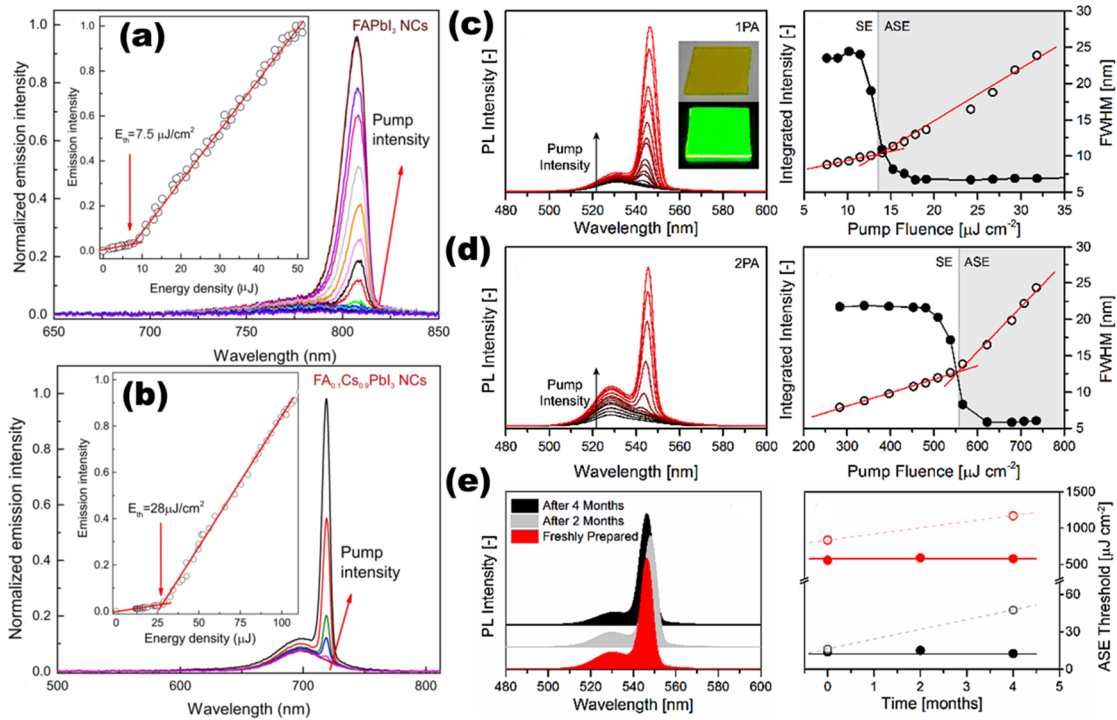
1 In 2014, the first SE behavior was demonstrated in solution-processed $\text{CH}_3\text{NH}_3\text{PbX}_3$ ($X = \text{Cl}$,
2 Br and I) perovskites thin films, indicating that the halide perovskites are not only excellent
3 photovoltaic materials, but also promising gain media for lasing.^{178, 1117-1119} Soon afterwards, the
4 favorable optical gain properties of IHPNs were reported by Yakunin et al. and Wang et al. nearly
5 simultaneously in 2015.^{29, 1096} Both the groups demonstrated robust SE under either femtosecond
6 or nanosecond pulsed excitation from the close-packed thin films of CsPbX_3 IHPNs, where the
7 thresholds were found to be orders-of-magnitude lower than those of the traditional CdSe-based
8 NCs. The low SE threshold can be attributed to the large absorption cross-section and the moderate
9 non-radiative recombination loss (e.g., minor carrier trapping and the relatively slow Auger
10 recombination rate).^{29, 1100} Leveraging on the variable stripe length technique, the modal gain in
11 CsPbBr_3 nanocrystals was determined to be as high as $\sim 450 \text{ cm}^{-1}$. Moreover, the SE spectrum can
12 be easily tuned from blue, green to red region by adjusting the composition and sizes of IHPNs.
13 (Figure 120a and b).^{29, 1096} Later, using the intermediate monomer reservoir synthetic strategy,
14 Yang *et al.* fabricated rod shaped IHPNs. Thanks to surface-ligand passivation, the perovskite
15 nanorods showed a high PL QY of up to 90% and enhanced stability in aqueous environments and
16 at high temperature, exhibiting an extremely high gain of 980 cm^{-1} and a low SE threshold of 7.5
17 $\mu\text{J cm}^{-2}$ under nanosecond laser pumping, as shown in Figure 120c.^{1114, 1120} Besides the close-
18 packed films of IHPNs, SE from the liquid solution of CsPbBr_3 nanocrystals has also been reported
19 recently. The SE threshold was estimated to be $105 \mu\text{J cm}^{-2}$ and photostability tests exhibited
20 steady SE intensities for more than three hours under the pump of a constant femtosecond pulsed
21 laser beam ($>10^7$ shots).¹¹²¹ The superior gain properties of these IHPNs hold great potential for
22 developing novel miniaturized laser devices.

1 Regarding the gain mechanism in IHPNs, Wang *et al.* performed comprehensive steady-state
2 and time-resolved PL measurements and revealed that the optical gain might come from the
3 radiative recombination of biexcitons.²⁹ Lately, through two-dimensional electronic spectroscopy,
4 Xiao *et al.* reported that the SE threshold in CsPbBr₃ nanocrystals is largely determined by the
5 competition between SE from biexcitons and excited-state absorption from single exciton to
6 biexciton states.¹¹²² In other words, the optical gain in CsPbBr₃ nanocrystals was again confirmed
7 to originate from biexcitons. The lower photon energy from biexciton recombination than single
8 exciton transition as well as the relatively larger biexciton binding energy from nanocrystals makes
9 IHPNs attractive candidates as optical gain media because red-shifted SE peak could effectively
10 reduce the reabsorption loss in an inhomogeneous NC entropy. In addition, trion-based optical
11 gain in colloidal CsPbBr₃ nanocrystals has been proposed by Wang *et al.* in 2018.¹¹¹⁵ Through
12 surface treatment with excess PbBr₂, the trion lifetime of CsPbBr₃ NCs film has been prolonged.
13 At the same time, ultralow SE pump threshold of 1.2 μJ cm⁻² (the average number of excitons per
14 nanocrystal $\langle N \rangle = 0.62$, which is close to the theoretical threshold value of $\langle N \rangle_{\text{th}} = 0.58$ for trion-
15 based gain) has been observed, indicating the participation of trions in optical gain. The schematic
16 illustration of trion gain in NCs is shown in Figure 120f. Furthermore, single exciton
17 recombination induced SE with threshold of 8-12 μJ cm⁻² in CsPbX₃ (X = Br, I) nanocrystals has
18 also been reported.¹¹²³ The single-exciton gain mechanism is plausibly more favorable for the low
19 optical losses, where the nonradiative exciton-exciton annihilation (Auger recombination) can be
20 efficiently eliminated, but the reabsorption loss may be an issue. Until now, the gain mechanism
21 in Pe-NCs remains an open question, and more comprehensive spectroscopic studies correlated
22 with theoretical calculations are required to reach a consensus. Nevertheless, the mechanisms of
23 stimulated emission and lasing depend on the electronic structure of the particular material because

1 different optical processes may compete with each other. There is no universal description of the
2 mechanism for inhomogeneous NC entropy.

3 SE induced by two-photon and even high-order multi-photon absorption in Perovskite NCs
4 has also been extensively demonstrated in recent years, which highlights the potential of these
5 materials for nonlinear photonics and devices.^{896, 1097, 1116, 1124-1127} Multi-photon absorption is a vital
6 branch of nonlinear optics, which features long excitation wavelengths and nonlinear excitation
7 intensity dependence on the fluorescence. Hence, it brings about the advantages of deeper
8 penetration depth, higher damage threshold, higher image contrast and less scattering effects.¹¹²⁷
9 Wang *et al.* found that the CsPbBr₃ nanocrystals exhibit strong nonlinear absorption and derived
10 a two-photon absorption (2PA) cross-section (σ_2) as high as $\sim 1.2 \times 10^5$ GM (1 GM = 10^{-50} cm⁴ s)
11 at 800 nm for the 9 nm-sized CsPbBr₃ NCs.¹⁰⁹⁷ It is worth mentioning that the 2PA cross-section
12 of various dye molecules are in the range of 10^{-10} - 10^3 GM.¹¹²⁸ the Furthermore, it was demonstrated
13 that these close-packed thin films of CsPbBr₃ nanocrystals possessed low threshold of frequency-
14 upconverted SE pumped by simultaneous two-photon absorption (800 nm, threshold ~ 2.5 mJ
15 cm⁻²) and three-photon absorption (3PA) (1200 nm, threshold ~ 5.2 mJ cm⁻²) (Figure 120e) and
16 the photostability of SE under two-photon pumping was practically favorable. Moreover, $\langle N \rangle$ can
17 be calculated with the equation $\langle N \rangle = f^2 \sigma_2 / \tau$,¹⁰⁹⁷ where f is the pump fluence (photons cm⁻²) and τ
18 is the pulse linewidth, the $\langle N \rangle$ at SE threshold is estimated to be ~ 1.2 , which indicates that the SE
19 in Pe-NCs arises from the biexciton recombination. Soon afterwards, the two-photon-pumped laser
20 with favorable stability based on CsPbBr₃ nanocrystals was demonstrated in the work by Xu *et*
21 *al.*¹¹⁰⁶ Figure 120g displays two-photon fluorescent images of CsPbX₃ Perovskite NCs with
22 different halide stoichiometry under 800 nm and 1064 nm excitation. It is noted that the progress

1 in nonlinear optically pumped SE and lasing from Perovskite NCs may offer new possibilities in
 2 the development of next-generation multiphoton imaging techniques.^{7, 1097, 1129}



3
 4 **Figure 121.** Emission spectra of (a) FAPbI₃ and (b) FA_{0.1}Cs_{0.9}PbI₃ NCs film pumped by pulsed
 5 laser with duration of 100 fs, indicating the SE behavior with ultralow thresholds. The insets show
 6 the integrated PL intensity as a function of energy density. Reprinted with permission from Ref.¹¹³⁰
 7 Excited steady-state PL emission spectra of BnOH-modified MAPbBr₃ NCs under (c) one- and
 8 (d) two-photon absorption. (w) Consistency of steady-state PL and stimulated emission peak
 9 position and the corresponding ASE threshold of different month(s) old BnOH-modified
 10 MAPbBr₃ NCs samples stored under ambient conditions. Reprinted with permission from Ref.¹¹³¹

11
 12 Apart from the IHPNs, the OHPNs also exhibit SE with fairly low thresholds and the
 13 photostability was improved by surface ligand engineering and chemical treatment. In 2017,
 14 Protesescu *et al.* synthesized monodisperse, nearly cubic FAPbI₃ and FA_{0.1}Cs_{0.9}PbI₃ with average

1 sizes of 10-15 nm, which extends the emission spectra into the near-infrared (near-IR) range (*e.g.*
2 780 nm for FAPbI₃ NCs).¹¹³⁰ The SE threshold of 7.5 μJ cm⁻² of FAPbI₃ was among the lowest
3 values of the red-to-near-IR emitting perovskites (5-10 μJ cm⁻²).^{1096, 1132-1134} Figure 121a and 121b
4 separately show the emission spectra of FAPbI₃ and FA_{0.1}Cs_{0.9}PbI₃ NCs films pumped by a pulsed
5 laser with pulse width of 100 fs, indicating the SE behavior with ultralow thresholds.^{1130, 1135} The
6 integrated PL emission intensity as a function of pump energy is plotted in Figure 121a and 121b,
7 separately. It is highlighted that surface engineering can serve as an effective strategy to improve
8 the active layer stability despite that the active media are made of organic-inorganic hybrid
9 components.^{1125, 1135} The robust FAPbI₃ NCs exhibiting low-threshold SE behavior manifest
10 improved ambient thermodynamic and chemical stability over pristine CsPbI₃ analogues,¹¹³⁶⁻¹¹³⁷
11 making them suitable for light-emitting applications, including lasers in the red region. Also, it
12 was demonstrated that FAPbBr₃ NCs show low SE threshold and highly stable SE intensity
13 insensitive with temperature during continuous laser pulse under both two- and one-photon
14 excitations, benefiting from large two-photon absorption coefficient (0.76 cm GW⁻¹) and high
15 optical net gain (480 cm⁻¹).¹¹³⁸ The WGM lasing from these FAPbBr₃ NCs under two-photon
16 excitation has been achieved by inserting FAPbBr₃ into a microresonator.¹¹³⁸ Also in 2017
17 Veldhuis et al. reported the high-yield synthesis of luminescent MAPbBr₃ NCs through direct
18 precipitation of the chemical precursors in a benzyl alcohol (BnOH)-toluene phase, where the
19 BnOH can steer the passivating ligands and maintain the ligand binding motifs on the NCs surface,
20 resulting in improved structural stability and optoelectronic properties.¹¹³¹ They revealed ultralow
21 SE thresholds (13.9 ± 1.3 μJ cm⁻² under one-photon (400 nm) absorption, Figure 121c; 569.7 ± 6
22 μJ cm⁻² at two-photon (800nm) absorption, Figure 121d, respectively), high-stability under

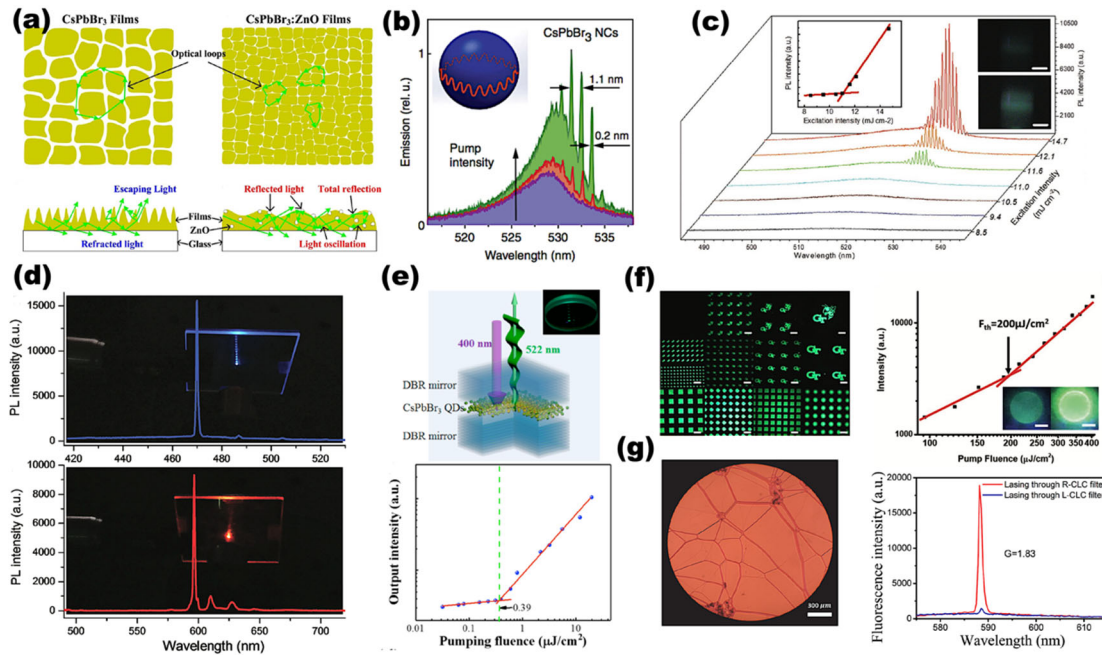
1 ambient storage and measurement conditions (Figure 121e), as well as outstanding optical modal
2 gain coefficient (520 cm^{-1}) through the detailed ultrafast spectroscopic studies.

3

4 **Laser Devices Developed From MHPs**

5 A suitable feedback mechanism combined with a gain material is the key to realize a laser
6 device, in which the light can be amplified in certain resonating frequencies.^{1124,1125} In this regard,
7 a variety of high-quality optical resonators were employed aiming at realizing desirable coherent
8 light output based on Perovskite NCs.

9 Random lasers are the simplest laser configuration where the optical feedback is offered by
10 the constructive interference of the scattered light in the disordered system.^{1124, 1139} In year 2017,
11 random lasing was demonstrated in the perovskite $\text{CsPbBr}_3:\text{ZnO}$ films. The ZnO nanoparticles are
12 found to be able to improve the lasing performance thanks to the shortened optical loops and
13 increased light oscillation as shown in Figure 122a. In this way, the SE thresholds of $\text{CsPbBr}_3:\text{ZnO}$
14 films were significantly reduced under both 1PA and 2PA.¹¹⁴⁰ Leveraging on the similar strategy,
15 ultralow threshold random lasing was achieved by depositing MAPbBr_3 NCs on a heterostructures
16 of 3D graphene-sheathed SiC nanowalls.¹¹⁴¹ Strong scattering of emitted photons and highly
17 confined photons by leachy vertical graphene networks provide the effectively optical feedback to
18 achieve random lasing. Moreover, the lasing threshold can be further lowered by the combined
19 effect of the improved scattering cross-section and plasmonic field enhancement of extra Ag/SiO₂
20 particles.



1
 2 **Figure 122.** Different laser devices based on Perovskite NCs. (a) The shortened optical loops and
 3 increased light oscillation in the perovskite CsPbBr₃:ZnO films for random lasing. Reprinted with
 4 permission from Ref.¹¹⁴⁰ (b) WGM lasing in a microsphere resonator of 15 mm in diameter,
 5 covered by a film of CsPbBr₃ nanocrystals. Reprinted with permission from Ref.¹⁰⁹⁶ (c) WGM
 6 lasing from CsPbBr₃ nanocrystals infiltrated into a capillary tube with inner diameter of $\approx 50 \mu\text{m}$.
 7 Reprinted with permission from Ref.²⁹ (d) Blue and red lasing spectra of VCSELs from
 8 CsPb(Br/Cl)₃ and CsPb(I/Br)₃ IHPNs under pump intensity of 38.2 and 30.5 $\mu\text{J cm}^{-2}$, respectively.
 9 Reprinted with permission from Ref.¹¹⁰⁰ (e) Schematic of CsPbBr₃ NCs-based VCSELs setup with
 10 ultralow lasing threshold (0.39 $\mu\text{J cm}^{-2}$). Reprinted with permission from Ref.¹¹⁴² (f) Different
 11 arrays of CsPbBr₃ nanocrystals patterns and lasing in arrays of micro-disk lasers. Reprinted with

1 permission from Ref.¹¹¹² (g) Single mode lasing action in CsSnI₃-doped with CLC cavities.
2 Reprinted with permission from Ref.⁶¹²

3
4 Silica microspheres can naturally serve as WGM cavities. Yakunin *et al.* coated the ILHPs onto
5 silica spheres and achieved the WGM microlaser (Figure 122b, inset), in which the light
6 propagation was total internally reflected around the circular cavity edges.^{1096, 1124} WGM lasing
7 could also be developed by infiltrating the gain media into a capillary tube.¹¹⁴³⁻¹¹⁴⁴ In this way,
8 Wang et al. coated a thin film of CsPbBr₃ nanocrystals onto the inner wall of a capillary tube and
9 realized the high-quality WGM lasers with a high-quality factor (Q-factor) of ~ 2000 (Figure
10 122c)²⁹. The occurrence of evenly-spaced spikes and super-linear increase of the integrated PL
11 intensity versus pump fluence (inset in Figure 122c, left) confirmed the development of lasing
12 action, and the longitudinal optical modes could be well-assigned according to the WGM
13 model.¹¹⁴⁴⁻¹¹⁴⁶ Recently, by embedding the CsPbBr₃-SiO₂ spheres into a microtubule, the
14 frequency up-converted WGM lasing over 140 min with a low lasing threshold of 430 $\mu\text{J cm}^{-2}$ has
15 been successfully achieved under two-photon excitation. Combining the effect of natural micro-
16 ring resonator of SiO₂ and high gain of CsPbBr₃ NCs, it provides a promising strategy to realize
17 and frequency up-converted lasing devices with low threshold.¹¹⁴⁷

18 DFB lasers are made by an active waveguide, where the refractive index along the light
19 propagation direction at the wavelengths satisfying the Bragg condition. The feedback for lasing
20 distributed along the active materials comes from partial reflection at varied refractive index.¹¹²⁵
21 In year of 2016, DFB lasers based on MAPbI₃ perovskites with threshold at optical pump
22 intensities of 5 kW cm^{-2} for durations up to ~ 25 ns at repetition rates exceeding 2 MHz has been
23 reported. It highlighted that the short pulsed current drive to minimize threshold will be an effective

1 strategy in a Perovskite NCs based laser diode.¹¹⁰⁷ Immediately after, highly green luminescent
2 MAPbBr₃ perovskites are used to produce stable DFB lasers emitting at 550 nm, with a low
3 threshold of 6 μJ cm⁻² have been demonstrated. These DFB lasers were able to support multiple
4 polarizations and could be switched between transverse magnetic and transverse electric mode
5 operation through tuning of the distributed feedback grating period.¹¹⁰⁸

6 Additionally, VCSELs, basically constructed by cladding an active layer into two parallel
7 reflecting mirrors, have been demonstrated based on Perovskite NCs. In year 2017, Wang et al.
8 sandwiched the CsPbX₃ nanocrystals between two distributed Bragg mirrors (DBRs) to achieve
9 high-performance VCSELs, showing low threshold (9 μJ cm⁻²), directional output (beam
10 divergence of ~3.6°), and favorable stability.¹¹⁰⁰ Blue-emitting CsPb(Br/Cl)₃ IHPNs and red-
11 emitting CsPb(I/Br)₃ IHPNs were similarly inserted into the DBR resonators to obtain the VCSELs
12 across the full visible region (Figure 122d), which offered a new strategy to fulfil single-source
13 pumped white lasers. In the same year, VCSELs based on CsPbBr₃ NCs with ultralow lasing
14 threshold (0.39 μJ cm⁻², Figure 122e) have also been reported. The schematic of the CsPbBr₃ NCs
15 VCSELs is shown in Figure 122e. This hybrid-integrated perovskite laser exhibits superior long-
16 term stability and stable device operation over 5 h or 1.8 × 10⁷ optical pulse excitations at ambient
17 conditions, demonstrating the potential in practical coherent light-emitting applications.¹¹⁴²

18 Moreover, duplicable and scalable micro-laser array have been realized from CsPbX₃ NCs
19 relying on a novel orthogonal lithography approach, which is promising for integrated photonic
20 applications.¹¹¹² In that work, Lin *et al.* fabricated large-area high-resolution arrays of micro-disk
21 lasers and multicolor (binary and ternary emission) pixels (Figure 122f). The newly developed

1 orthogonal lithography method preserves the high optical gain performance of CsPbBr₃ NCs film
2 and is the key to achieve the WGM lasing action.¹¹¹²⁻¹¹¹³

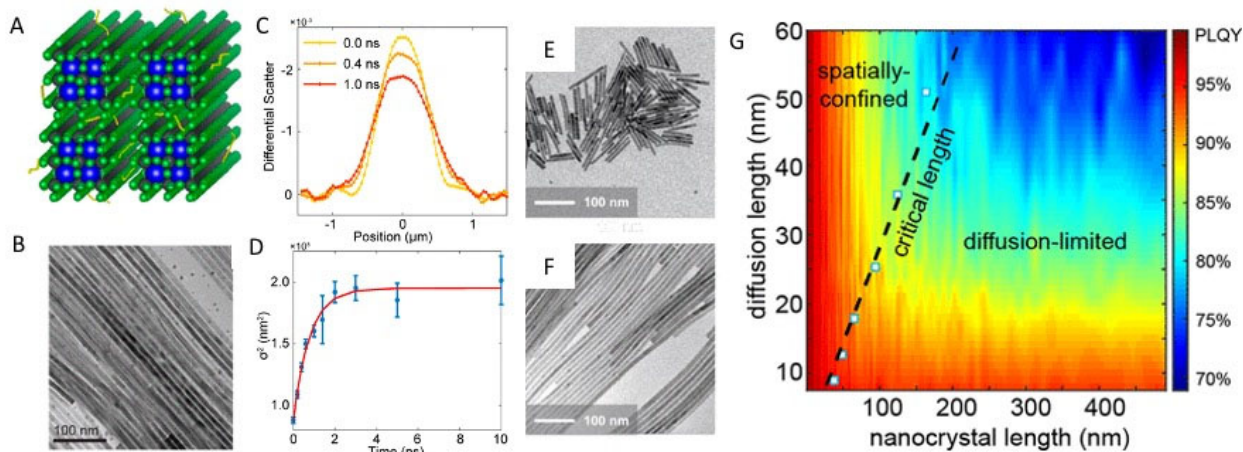
3 Besides, dynamically tunable lasing action have been realized by doping CsSnI₃ NCs into
4 cholesteric liquid crystal (CLC) reflectors, demonstrating the progress in achieving the
5 wavelength-tunable and single mode lasers (Figure 122g).⁶¹² The similar approach was employed
6 by Stranks *et al.* to obtain robust and stable SE under 5 ns pumping at 532 nm (a minimum
7 threshold of only 7.6 μJ cm⁻²), where the MAPbI₃ NCs thin film was sandwiched within a cavity
8 composed of two 50 nm-thick polymethylmethacrylate (PMMA) layers and a thin CLC film (~7
9 μm) coupled with a metal back-reflector.¹¹⁴⁸ The employment of flexible CLC reflectors provides
10 a pivotal step toward “mirror-less” single-mode lasers with wavelength-tunability on flexible
11 substrates, which could be exploited in applications such as flexible displays and military
12 identification.

13 **MHP nanowire lasers**

14 Despite the fact that the carrier dynamics in perovskite NCs has been extensively studied in 0D
15 quantum dots systems, studies on the 1D geometry of perovskite NWs also demonstrate an
16 important role on the modification of electronic state, carrier trapping and exciton decay
17 mechanisms. Carrier diffusion in one-dimension CsPbBr₃ NWs with 10 nm lateral widths were
18 directly visualized from stroboSCAT (stroboscopic interferometric scattering microscopy)
19 measurements (Figure 123A-D)¹¹⁴⁹. The rapid diffusion of excitons found along the NWs with less
20 trap densities. The qualitative study using ultrafast transient microscopy showed the anisotropy
21 splitting of band edge exciton in nanowires due to dielectric confinement in one-dimension¹¹⁴⁹.

22 To demonstrate the charge carrier behaviors in a more controllable system, high-quality, single
23 crystalline 1D CsPbX₃ NWs with aspect ratios varying from 1 to 1000 were used to construct a

1 model platform to investigate the optical scaling laws of NCs (Figure 123E-G)²⁵³. NW surface
 2 ligands with tunable Lewis acidity offer control over the nonradiative rate of the perovskite NWs.
 3 The steady-state PLQY and time-resolved PL lifetime measurements have provided valuable
 4 information on the impact of nanowire aspect ratio on excitonic dynamics within the wire. The
 5 scaling laws derived from this model system are not only a phenomenological observation but
 6 unravelled the carrier dynamics of these microscopic systems in a quantitative and interpretable
 7 manner. Monte Carlo simulations with an exciton-diffusion-defect-encounter random walk model
 8 extracted an exciton diffusivity of $0.4 \text{ cm}^2/\text{s}$, and together with the scaling behaviors, revealed
 9 materials dimensionality as a hidden constraint on the carrier recombination kinetics. In addition,
 10 Janker *et. al.*, employed the spatiotemporal dynamics of electrons and holes in aligned CsPbI₃ NW
 11 bundles using acousto-optoelectric spectroscopy¹¹⁵⁰.



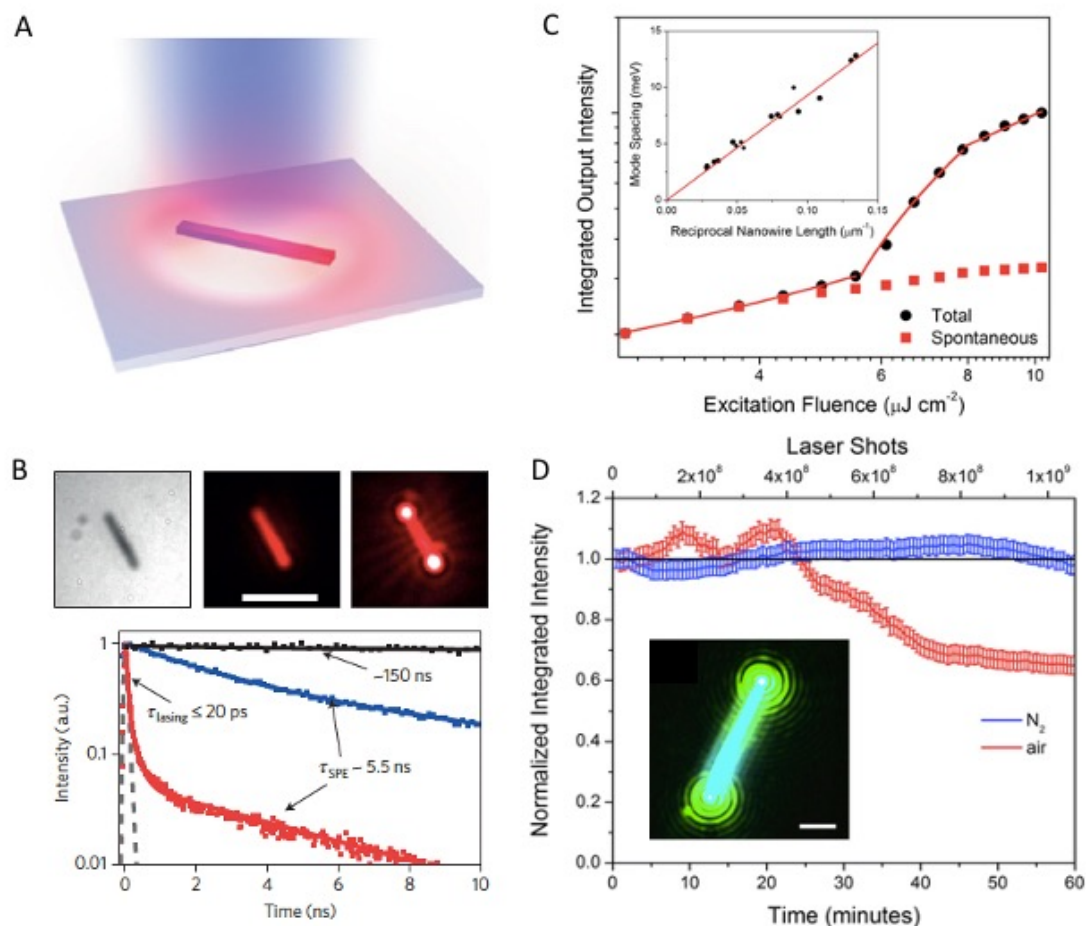
12
 13 **Figure 123.** A) Schematic diagram and B) SEM image of perovskite nanowire bundle. C, D)
 14 Diffusion profile of energy along the longitudinal axis of the nanowires¹¹⁴⁹. E, F) TEM images of
 15 CsPbBr₃ nanowires with different aspect ratios. G) 2D counter plot as an illustration of the optical

1 scaling law of PLQY as a function of NC length in both the spatially confined regime and the
2 diffusion limited regime²⁵³. Copyright 2020 American Chemical Society.

3
4 NW lasers are ideal candidates for miniaturized light sources, providing both the optical gain
5 medium and the resonant laser cavity that can potentially allow their facile integration into circuits.
6 The perovskite NWs that were synthesized from colloidal methods are too thin to be effectively
7 supporting the photonic lasing modes. A low-temperature, solution-phase growth of single
8 crystalline CsPbX₃ NWs with a few hundred nm in width and micron length scale, led to the Fabry-
9 Pérot mode lasing behavior with a low lasing threshold, high maximum quality factor, and the
10 wavelength tunability from blue to near-IR regions of the visible spectrum (Figure 124)^{258, 260, 1151-}
11 ¹¹⁵³. The confined exciton-polaritons in perovskite NWs and the composition dependent Rabi
12 splitting has been studied using high-quality in-plane aligned CsPbX₃ (X=Cl, Br, I) NWs that were
13 grown on the M-plane sapphire substrates¹¹⁵⁴. The corresponding energy-wavevector dispersion
14 relation of the lasing mode well agreed with the exciton-polariton model, and the Rabi splitting
15 was extracted as $\sim 210 \pm 13$, 146 ± 9 , and 103 ± 5 meV in CsPbCl₃, CsPbBr₃ and CsPbI₃ nanowires.
16 Moreover, the lasing from CsPbBr₃ NWs has been maintained for over one hour of constant, pulsed
17 excitation in both nitrogen and ambient atmospheres (Figure 124D)²⁶⁰. This represents
18 unprecedented stability for inorganic perovskite NWs and demonstrates the viability of the robust,
19 all inorganic compositions for photonic integrated circuits that require highly stable miniaturized
20 light sources. In addition to the inorganic perovskite NWs for lasing, organic-inorganic hybrid
21 CH₃NH₃PbX₃ NWs have been grown from vapor phase synthesis and equally show excellent
22 optical properties with adequate gain and efficient optical feedback.¹¹⁵⁵ The surface plasmon effect
23 in CH₃NH₃PbBr₃/SiO₂/Ag cavity can further enhance the strong exciton-photon interactions in

1 perovskite NWs.¹¹⁵⁶ The exciton-photon coupling strength can be enhanced by ~35 %, and this is
2 t attributed to the localized excitation field redistribution from surface plasmon effect.

3 The origin of the lasing in halide perovskite nanowires is still a controversial topic. In addition
4 to the lasing mechanism involving exciton-polaritons as mentioned above, X. Zhu, *et. al.*, have
5 proposed that under pulsed excitation density, the excitation power would exceed the exciton Mott
6 density, and as a result, lasing in CsPbBr₃ nanowires was originated from the stimulated emission
7 of a nondegenerate electron-hole plasma rather than exciton-polaritons¹¹⁵⁷. The changes in laser
8 gain profile and refractive index that leads to the lasing mode distribution of nanowires strongly
9 depends on excitation density and pulse duration time. Especially, the high intrinsic PL quantum
10 efficiency is crucial for advancing their application as light-emitting sources. It has been
11 demonstrated that the quantum efficiency of single crystalline CsPbBr₃ nanowires can be improved
12 by 3 orders of magnitude upon exposure to the oxygen molecule²⁶⁵. The oxygen can passivate the
13 perovskite surface defects originated from lead rich surface, therefore greatly reduces the
14 nonradiative recombination rate.



1
 2 **Figure 124.** A) Schematic diagram of perovskite nanowire pumped by a laser. B) Optical images
 3 of a single nanowire with and without laser excitation, and corresponding transient PL decay
 4 kinetics at certain excitation intensity¹¹⁵¹. Copyright from the Nature Publishing Group. C)
 5 Integrated output intensity from CsPbBr₃ nanowire as a function of increasing excitation fluence,
 6 D) Stability test of lasing from CsPbBr₃ nanowire in both air and N₂ environment²⁶⁰. Copyright
 7 National Academy of Sciences of the United States of America.

8
 9 **Summary and future outlook on MHP lasers**

10 Perovskite NCs, including organic-inorganic hybrid and all-inorganic perovskite NCs, are
 11 emerging as a new class of cost-effective and wavelength-tunable lasing materials. Although

1 tremendous progress has been made in developing solution-processed lasers from Perovskite NCs,
2 especially in terms of understanding the fundamental physics and improving the device
3 performance, there remain challenges with regard to developing practical and commercially
4 available lasers utilizing the Perovskite NCs. Firstly, these Perovskite NCs are severely affected
5 by chemical and environmental factors (*e.g.*, oxygen, moisture, heat, and continuous light
6 illumination) instabilities.¹¹⁵⁸⁻¹¹⁶⁰ Li *et al.* developed an amination-mediated nucleation strategy
7 and demonstrated significantly improved SE stability of Perovskite NCs.¹¹⁶¹ In another case, Yuan
8 *et al.* fabricated the CsPbBr₃ nanocrystals in glass matrix through in-situ crystallization synthesis,
9 which not only protected the nanocrystals from the ambient conditions, but also hindered the
10 aggregation of Perovskite NCs.⁴⁸⁷ In 2017, Wang *et al.* demonstrated the insertion of CsPbBr₃ NCs
11 into a wider-band-gap Cs₄PbBr₆ matrix through low-temperature solution-phase synthesis method.
12 It was found that the thermal stability of IHPNs is enhanced, and robust high-temperature
13 perovskite lasers could be realized.¹¹⁴⁰ However, most of the strategies are only applicable for the
14 pure, green emitting CsPbBr₃ NCs, while the stability of blue-emitting and red-emitting Perovskite
15 NCs is lagging behind. Secondly, most of the progress made on perovskite NCs lasers¹¹⁶²⁻¹¹⁶⁵ has
16 focused on lead-containing compounds, which are toxic and their use may be restricted in the
17 future. As a result, studying non-toxic NCs and developing heavy metal-free perovskite NCs for
18 laser media will probably be an irreversible trend.¹¹⁶⁶ For example, air-stable lead-free ordered
19 double perovskites NCs (chemical formula: A₂MM'X₆, where A is monovalent cations Cs⁺,
20 CH₃NH₃⁺, M is +1 cations Ag⁺, Au⁺, Cu⁺, M' is +3 cations Bi³⁺, Sb³⁺, Pd⁴⁺, and X is the halogen
21 anion Cl⁻, Br⁻, I⁻) have been recently synthesized (see dedicated sections in this review), and they
22 may open the door to lead-free perovskite lasers in the near future.⁹¹⁶ Thirdly, to date, only
23 optically-pumped lasing has been demonstrated in Perovskite NCs, whereas electrical pumping is

1 more practically desired.^{1163, 1166} Despite significant progress in optically pumped lasers and
2 electrically driven light-emitting diodes have been demonstrated, there is still a long way to go
3 towards the electrical pumped Perovskite-NC lasers. In particular, the following issues have to be
4 addressed to achieve lasing in NCs by electrical pumping. First, the Auger recombination, which
5 generally limits the electrically-driven lasing in perovskite NCs lasing because the carriers are
6 injected into Perovskite NCs one-by-one.¹¹⁶⁷ So, this nonradiative Auger recombination has to be
7 suppressed by electron-hole wavefunction engineering and other new strategies. Second, the
8 organic ligands used for the passivation of perovskite NC surfaces generally exhibit poor electrical
9 conductivity, hampering the carrier injection and transport.^{1096, 1165} Therefore, it is imperative to
10 find ways to achieve efficient injection of charge carriers into the perovskite NC layer. The
11 methods include the modification of the NC surface and the reduction of the thickness of the
12 emitting layer.

13

14 **11.2 LIGHT-EMITTING DEVICES**

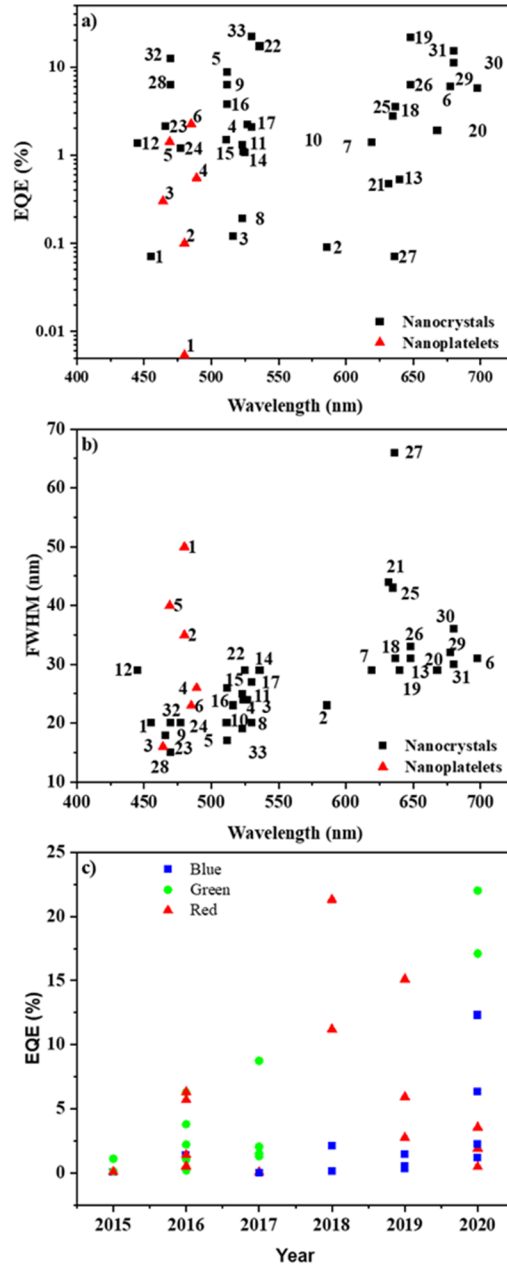
15 Light-emitting diodes (LEDs) based on lead-halide perovskites (LHPs) emerged more than a
16 decade ago. However, there was no electroluminescence (EL) reported at that time because of the
17 weak light emission from LHPs.¹¹⁶⁸⁻¹¹⁷⁰ However, in the past few years, there have been significant
18 developments and LHPs have returned to the spotlight, not only as highly efficient photon
19 absorbers in solar cells, but also as efficient photon emitters in LEDs.^{31, 1171-1172} Remarkably, the
20 external quantum efficiencies (EQEs) of LHP-LEDs reached the same level as organic LEDs and
21 colloidal cadmium selenide (CdSe) quantum dot (QD) LEDs of over 20% in just 5 years.^{425, 1173-}
22 ¹¹⁷⁴ Generally, the whole LHP-LED with a total thickness of hundreds of nanometers is deposited
23 onto a transparent substrate coated with an indium tin oxide electrode, and functional films are

1 also required for facilitating charge carrier injection into the LHP layer from external electrodes.^{31,}
2 ^{425, 1173-1174} Because the LHP emitter and other functional layers are deposited by solution
3 processing, the device structures of most LHP-LEDs are simple.^{31, 425, 1173-1174} By changing the
4 halide anion from chloride to iodide, the emission wavelength of LHPs can be tuned across the
5 whole visible range (refer to Section 3).^{15, 82, 1175-1177} Moreover, nanostructured emitters are
6 effective for confining charge carriers in the LHP layer and achieve highly efficient radiative
7 recombination. These nanostructured emitters include 3D nanocrystals, quasi-2D nanoplatelets,
8 and multilayer quantum wells.^{23, 227, 405, 986, 1173, 1178-1179} Apart from high EQEs, LHP-LEDs achieve
9 narrow emission peaks with high color purity.^{80, 425, 1175, 1180} LHP-LEDs are therefore a natural
10 candidate for potential applications in full color information displays. So far, bromide- and iodide-
11 based green and near-infrared LHP-LEDs have achieved record EQEs of over 20%. However, the
12 development of blue LHP-LEDs lags behind.^{405, 425, 1173-1174, 1181-1182} The synthesis of a wide variety
13 of LHP emitters and their deposition in films can be conducted simply and quickly, even in ambient
14 atmosphere, which is another advantage compared to their counterparts, such as CdSe QDs.^{15, 80,}
15 ^{1180, 1183} As a new kind of soft semiconductor emitter, the similarity in the processing LHPs and
16 OLEDs/QD-LEDs suggests that LHPs may be compatible with the booming OLED/QD-LED
17 industry.^{1173-1174, 1179} However, LHP emitters and the resulting LEDs are still limited by the toxicity
18 of the lead ions and rapid degradation under operation condition, and efforts to develop lead-free
19 alternatives are discussed in Section 7.^{112, 973, 1176, 1184 524, 1185-1188} Details of the fundamental
20 properties of LHPs (*e.g.*, bandgap tunability, defect tolerance and carrier dynamics) are covered in
21 earlier sections, particularly Section 13 on optical properties.

22

1 **Classification of Perovskite Light-Emitters**

2 Although the first perovskite LEDs to operate at room temperature used bulk 3D perovskite thin
3 films, the EQEs reached up to only $\sim 1\%$.³¹ An important challenge was the low exciton binding
4 energy of a few meV in the films,⁹⁷⁸ necessitating the spatial confinement of charges to increase
5 the fraction of injected carriers that radiatively recombine.¹¹⁸⁹ While this was initially achieved by
6 creating a quantum well (by sandwiching the emitter between two injectors that each block one of
7 the carriers),³¹ a more effective strategy was to create a multi-quantum well structure through thin
8 films comprised of mixtures of perovskites with different dimensionality (3D, 2D and quasi-
9 2D).⁴⁰⁵ This has led to near-infrared perovskite LEDs with $>20\%$ EQE.¹¹⁷⁴ But controlling the
10 phase-purity and distribution of phases in these multi-dimensional perovskite thin films remains
11 challenging.¹¹⁸⁹ An important alternative to thin films for improving the spatial confinement of
12 charge-carriers is through nanostructured perovskites. These include colloidal nanocubes,
13 nanoplatelets (NPLs), NCs embedded in 3D perovskite matrices and perovskite-polymer
14 composites (Figure 125). Nanostructured perovskites have the advantages of higher exciton
15 binding energy, bandgap tunability, and the ability to passivate the surfaces to achieve high PLQYs
16 near unity.¹¹⁸³ Details of the synthesis and optical properties of nanocubes and NPLs are given in
17 Section 2, while 0D nonperovskites and NCs embedded in these nonperovskites are discussed in
18 detail in Section 5. The discussion below focuses on the application of these materials in LEDs.



1

2 **Figure 125.** (a) EQE and (b) PL FWHM vs. emission wavelength for different emitters and
 3 structures. The number labelled in the figure matches the label number in table 3 and the

- 1 corresponding references are shown in table 3 c) The development of red, green and blue PeLEDs
- 2 over the last 5years.

Labels in Figure.125	Emitting Materials	EL Peak Centre (nm)	EQE (%)	FWHM (nm)	Reference
1	$\text{CsPbBr}_x\text{Cl}_{3-x}$	455	0.07	20	28
2	$\text{CsPbBr}_x\text{I}_{3-x}$	586	0.09	23	28
3	CsPbBr_3	516	0.12	23	28
4	$\text{CsPbBr}_3/\text{CsPb}_2\text{Br}_5$	527	2.21	24	1159
5	CsPbBr_3	512	8.73	17	192
6	CsPbI_3	698	5.7	31	1160
7	$\text{CsPbBr}_{0.75}\text{I}_{2.25}$	619	1.4	29	1160
8	CsPbBr_3	523	0.19	19	1160
9	CsPbBr_3	512	6.27	20	186
10	$\text{CsPbBr}_3:\text{Mn}$	511	1.49	20	1190
11	$\text{MA}_{0.8}\text{Cs}_{0.2}\text{PbBr}_3$	523	1.3	25	1191
12	$\text{MAPb}(\text{BrCl})_3$	445	1.37	29	1192
13	MAPbI_3	640	0.53	29	1192
14	MAPbBr_3	525	1.06	29	1192
15	MAPbBr_3	524	1.1	24	142
16	MAPbBr_3	512	3.8	26	1193
17	FAPbBr_3	530	2.05	27	424
18	$\text{CsPbI}_{3-x}\text{Br}_x$	637	3.55	31	1194
19	$\text{CsPbBr}_{0.6}\text{I}_{2.4}$	648	21.3	31	1173
20	CsPbI_3	668	1.9	29	1195

21	$\text{CsPbBr}_x\text{I}_{3-x}$	632	0.47	44	1195
22	FAPbBr_3	536	17.1	29	1196
23	$\text{CsMnyPb}_{1-y}\text{Br}_x\text{I}_{1-x}$	466	2.12	17.9	1197
24	$\text{CsPbBr}_x\text{Cl}_{3-x}$	477	1.19	20	1198
25	$\text{MAPbBr}_x\text{I}_{3-x}$	635	2.75	43	1199
26	$\text{CsPbBr}_x\text{I}_{3-x}$	648	6.3	33	1200
27	$\text{CsPbBr}_x\text{I}_{3-x}$	636	0.071	66	1201
28	$\text{CsPbBr}_x\text{Cl}_{3-x}$	470	6.3	15	1202
29	Sr-CspbI_3	678	5.92	32	663
30	Ag-CspbI_3	680	11.2	36	667
31	$\text{CsPb}_{0.64}\text{Zn}_{0.36}\text{I}_3$	680	15.1	30	1203
32	CsPbBr_3	470	12.3	20	1204
33	CsPbBr_3	530	22	20	1204
1	CsPbBr_3 NPL	480	0.0054	50	1205
2	CsPbBr_3 NPL	480	0.1	35	227
3	CsPbBr_3 NPL	464	0.3	16	1206
4	CsPbBr_3 NPL	489	0.55	26	1206
5	CsPbBr_3 NPL	469	1.42	40	1207

1 Table 3. EQE and FWHM of EL of Perovskite Nanocrystals and Nanoplatelets Light Emitting
2 Diodes

3

4

1 **Nanocrystal emitters:** Efficient performance has been achieved in perovskite NC LEDs emitting
2 across the entire visible wavelength range. The morphology of the NCs is shown in Figure 126a.
3 Two critical strategies that have enabled this result are surface passivation and the use of dopants.

4 An important source of non-radiative recombination is due to uncoordinated Pb^{2+} at the surface
5 of NCs. In red-emitting CsPbI_3 NCs, the uncoordinated Pb^{2+} ions were passivated by introducing
6 excess iodine to the surface. This was achieved by using excess trimethylsilyl iodine as the iodine
7 source during synthesis, which resulted in the surface I/Pb ratio reaching 4.4. Through surface
8 passivation, the PLQY of the colloidal NCs in solution approached unity, and the device reached
9 1.8% EQE.¹¹⁶² Surface passivation can also be achieved post-synthesis. For example, Pan *et al.*
10 introduced 2,2'-iminodibenzoic acid to CsPbI_3 NCs, leading to the a peak EQE increase from
11 2.26% to 5.02%. The improvement in performance was attributed to the bidentate ligands binding
12 firmly to the PbI_2 -rich surface of the NCs and reducing the density of surface traps.¹²⁰⁸ Potassium
13 halides have also been found to be effective surface passivation agents, and were used by Yang *et*
14 *al.* to passivate the surface of $\text{CsPbI}_{3-x}\text{Br}_x$ NCs to suppress phase-separation into iodide- and
15 bromide-rich regions, and this stabilized the PL spectra over time, as shown in Figure 126b. In
16 doing so, they achieved electroluminescence at 637 nm wavelength, which is required for pure-
17 red emission for displays, and increased the EQE from 1.89% (pristine NCs) to 3.55% (KBr-
18 passivated NCs) as shown in Figure. 126c.¹¹⁹⁴

19 An important challenge with CsPbI_3 is that the cubic perovskite phase (the α -phase) is metastable
20 at room temperature, due to the small size of the Cs^+ cation, which leads to the Goldschmidt
21 tolerance factor being below the range for cubic perovskites (refer to the Introduction).⁵² The
22 room-temperature orthorhombic phase has a wider bandgap and undesirable optoelectronic
23 properties.¹¹⁹⁵ An approach to stabilize the α -phase at room temperature is to partially replace

1 Pb^{2+} cations with smaller cations (*e.g.*, Sr^{2+} , Ag^+ and Zn^{2+}), in order to increase the tolerance factor.
2 LEDs made from these perovskites emitted at 678 – 690 nm, with EQEs ranging from 5.92% (Sr
3 doping) to 15.1% (Zn doping).^{1203, 1209-1210} Another successful approach was iodide anion-
4 exchange in CsPbBr_3 NCs. For example, Mathews and co-workers used FAI in water as the iodide
5 source for ion exchange. Water was used because it is not miscible with the toluene solvent for the
6 colloidal CsPbBr_3 quantum dots, therefore preventing ligand desorption. By tuning the
7 concentration of FAI in the aqueous solution, either mixed Br/I or pure I-based NCs were achieved,
8 with EL wavelengths ranging from 630 nm to 670 nm (pure iodide) and high PLQYs >74%.
9 However, the EQEs only reached up to 1.9% for CsPbI_3 NCs.¹¹⁹⁵ Kido *et al.* achieved much higher
10 EQEs, reaching 21.3%, through anion exchange using iodide-containing ligands. Starting with
11 CsPbBr_3 NCs, oleylammonium iodide (OAM-I) was used for halide exchange to form CsPbI_3 by
12 adding the ligand to the colloidal solution. In this halide-exchange process, the surface anion
13 vacancy concentration was significantly reduced from a starting Br/Pb ratio of 2.78 to a final I/Pb
14 ratio of 3.00. This, in part, accounts for the PLQY increase from 38% for CsPbBr_3 to 80% for
15 CsPbI_3 . Although the EQE of the CsPbI_3 LEDs matched their bulk thin film counterparts, the
16 device stability was limited, with the performance halving after only 5 min at 1.25 mA cm⁻² current
17 density.¹¹⁷³

18 Surface engineering has also been important for improving the performance of green emitters
19 (510 – 530 nm wavelength). Successful strategies include: 1) eliminating labile OLA (oleylamine)
20 from the synthesis (EQE=0.32%),³⁶² 2) treating NCs with ammonium thiocyanate
21 (EQE=1.2%),¹²¹¹ 3) employing octylphosphonic acid post-synthesis (EQE=7.74%),¹²¹² 4) using
22 didodecyldimethylammonium (DDA) ligand during synthesis (EQE=9.80%),¹²¹³ and 5) triple-
23 ligand surface treatment (EQE=11.6%).¹²¹⁴ Combining these organic ligands with inorganic

1 passivation agents has also been shown to be effective in improving EQE. The addition of ZnBr₂
2 to DDA-Br-capped NCs resulted in the improvement of the EQE of the green LEDs from 10.7%
3 to 16.48%.³²⁴ Introducing excess FABr to the precursor solution was also found to be effective,
4 with PLQYs increasing from 62% to 74% in films, and device EQEs increasing from 1.5% to
5 17.1%, as the FABr/PbBr₂ molar ratio was increased from 1:1 to 2.2:1.¹²¹⁵ XPS measurements
6 indicated that there was a reduction in the concentration of bromide and formamidinium vacancies,
7 which may be due to these being filled by the excess FABr. There was also a lower surface ligand
8 density, which may have resulted in improved charge transport between the NCs. The operational
9 stability was also improved from 52 s (control (FABr/PbBr₂ molar ratio 1:1)) to 1080 s
10 (FABr/PbBr₂ molar ratio 2.2:1), due to the suppression of non-radiative recombination as the
11 excess FABr passivated the surface defects. However, it was found that this was not due to any
12 improvements in thermal stability, which was found to be unaffected by the addition of FABr from
13 thermogravimetric analysis.¹²¹⁵ Indeed, Sargent *et al.* found that a limitation of ligand exchange is
14 that the process results in the removal of surface bromide anions, which results in lower PLQYs.
15 They showed that this could be overcome by mixing the NC solution with a saturated solution of
16 isopropylammonium bromide in DMF or NaBr in DMF after multiple reprecipitation steps to heal
17 the surface bromide vacancies. As a result, their 4 nm and 7 nm CsPbBr₃ NCs exhibited near-unity
18 PLQYs after ligand exchange, resulting in blue LEDs with 12.2% EQE (480 nm wavelength).¹²⁰⁴
19 Beyond these surface treatments, Zheng *et al.* decorate nickel oxide on the CsPbBr₃ NC surface
20 through adsorption and a sequential oxidation treatment. This resulted in EQE increasing from
21 0.7% to 16.8% with a drop in turn-on voltage from 5.6 V to 2.8 V.¹²¹⁶

22 There has also been increased recent focus on blue-emitting perovskites: it is a fact that the
23 EQEs of these devices currently limit the development of perovskite-based displays and solid-

1 state white lighting. A key challenge is the low PLQYs of Cl-based perovskite emitters. Recent
2 efforts to address this limitation include passivation with K^+ , Cl^- (from $CuCl_2$), Ni^{2+} and Mn
3 ions.^{847, 1181, 1197} Yang *et al.* recognized that a challenge with using oleic acid and oleylamine (the
4 most common ligands) in the synthesis of perovskite NCs is that the protonation process between
5 the acid and amine (i.e. the surface bound ammonium ion giving back the proton to the surface
6 bound carboxylate ion) can result in ligand desorption and the formation of surface defects.¹¹⁸¹
7 The introduction of K^+ (through K_2CO_3) was found to passivate surface defects and also reduce
8 the density of organic ligands required on the surface (as found from Fourier-transform infrared
9 spectroscopy), which improved charge transport between NCs in films. It is thought that K^+ bound
10 to halide ions on the NC surface can passivate dangling bonds. As a result, the PLQY of the
11 colloidal NCs increased from 9.50% (no K^+) to 38.4% with 8% K^+ , which correlated with increases
12 in the EQE from 0.23% (no K^+) to 0.82% (8% K^+).¹¹⁸¹ But the highest EQE was achieved with 4%
13 K^+ (1.19% EQE) due to improved surface morphology, for which the emission wavelength was
14 476 nm.¹¹⁸¹ With surface passivation, the LT_{50} also improved by 2.6 times up to 4.5 min with an
15 applied bias of 4 V. Further improvements in EQE were achieved by replacing the TPBi electron
16 injector with PO-T2T, which has higher mobility that is better matched with the poly-TPD hole
17 injector. By also adding a layer of poly(9-vinylcarbazole) between the poly-TPD and emitter, the
18 EQE reached a peak of 1.93%.¹¹⁸¹

19 De *et al.* demonstrated that the addition of $CuCl_2 \cdot 2H_2O$ to the reaction mixture during the
20 synthesis of $CsPbCl_3$ by hot injection, led to an increase of the PLQY of $CsPbCl_3$ NCs from 0.5%
21 (no doping) to 60% (1% Cu doping) at 400 nm wavelength (violet). It was also found that with Cu
22 doping, the NCs became halide-rich rather than halide-deficient, and the improvement in PLQY is
23 attributed to the reduction in the density of anion vacancies on the surface.⁸⁴⁷ Bi *et al.* reported

1 improvements in PLQY in mixed Cl-Br NCs emitting in the 430-460 nm range, which reached
2 92% and 98%, respectively, after incorporating CuCl₂. Improvements in the air-stability of the
3 NCs were also seen, but the effect on device performance was not reported.¹²¹⁷

4 Congreve *et al.* also demonstrated improvements in the PLQY and, consequently, the EQE of
5 blue-emitting CsPbBr_{1-x}Cl_x NCs through Mn doping (by hot-injection synthesis). The PLQY
6 improved from 9% (no Mn) to 28% (with 0.19% Mn). This correlated with improvements in the
7 EQE from 0.50% to 2.12% at an emission wavelength of 466 nm. The emission FWHM was also
8 narrow (18 nm). The high-performance blue LEDs were used to excite red and green perovskite
9 nanocrystal downconverters, resulting in CIE coordinates of (0.311, 0.326), close to the values for
10 true white emission. The white-light LED was calculated to have an EQE of 0.25%. Despite the
11 promising device performance, the stability was limited, with the devices degrading within
12 seconds to minutes. Another important challenge is the Mn content, which needed to be controlled
13 very carefully. Having Mn content above 0.2% resulted in a reduction in the PLQY and a longer-
14 wavelength emission from the Mn ion center increasing in intensity significantly.¹¹⁹⁷ More
15 recently, Bakr and Liao *et al.* reported the passivation of Cl⁻ vacancies using *n*-dodecylammonium
16 thiocyanate (DAT). The thiocyanate component is a ‘pseudohalide’ capable of filling halide
17 vacancies but has the important advantage of not shifting the emission peak (unlike the use of
18 organic halides). DAT was introduced to CsPb(Br_xCl_{1-x})₃ quantum dots post-synthesis because the
19 long-chain dodecylammonium component of DAT enabled it to dissolve in toluene, the same
20 solvent of the quantum dots. After post-treatment, the PLQY of the quantum dots increased from
21 83% (as-synthesized) to 100% (post-treatment), whereas the PL peak remained at the same
22 wavelength (468 nm). The EQE improved from 3.5% (without treatment) to 6.3% (with DAT
23 treatment), with an electroluminescence wavelength of 470 nm. DAT treatment also resulted in an

1 improvement in device stability from 17 s (without treatment) to 99 s (with DAT treatment), and
2 this was attributed to reduced ion migration due to a reduced concentration of Cl⁻ vacancies.⁴⁸

3 ***NPI Emitters:*** In addition to being grown as symmetrical, three-dimensional NCs, LHPs can
4 also be synthesized as 2D nanoplatelets (NPLs). the common morphology of nanoplatelets can be
5 seen in Figure 126 d). The thickness of these NPLs can be finely tuned from one monolayer
6 (approximately 0.6 nm) to several monolayers. These perovskite NPLs exhibit quantum
7 confinement when the thickness is smaller than the Bohr radius (typically 2–3 nm),⁴⁸ enabling a
8 blue-shift in the emission. This is currently simpler and more reproducible than growing perovskite
9 NCs smaller than 3 nm.^{62, 103} Perovskite NPLs have therefore gained significant attention for blue-
10 emission applications, by allowing pure-bromide perovskites to emit at between 400 nm and 475
11 nm wavelength.⁶² In 3D perovskite NCs larger than the Bohr radius, achieving these blue emission
12 wavelengths requires using Cl-based or mixed chloride-bromide perovskites.¹⁰³ An important
13 limitation is that Cl vacancies form deep traps that result in low PLQYs.^{103, 1197} Although these
14 limitations could be addressed through passivation, bromide-based perovskite nanoplatelets are an
15 important alternative. However, nanoplatelets have a higher surface area to volume ratio, and
16 exhibit pronounced surface defects. Originally, this limited the PLQYs to low values of 20% or
17 less.^{48, 219} However, Bohn, Tong, *et al.* demonstrated that the PLQYs can be substantially increased
18 up to 75% through surface passivation by adding PbBr₂ complexed with organic ligands to the
19 colloidal solution.⁶² Wu *et al.* also demonstrated that surface Br vacancies could be passivated by
20 using HBr, resulting in PLQYs up to 96% at a PL wavelength of ~460 nm,⁴¹⁸ which is suitable for
21 blue-emitters in ultra-high definition displays.^{524, 1218}

22 The use of passivation in bromide-based perovskite nanoplatelets has led to improved
23 performance with significantly improved color-purity. An early report of perovskite nanoplatelet

1 LEDs used MAPbBr₃ and MAPbI₃ nanoplatelets complexed with long-chain butylammonium
2 ligands. These nanoplatelets were denoted L₂[MAPbX₃]_{n-1}PbX₄, where X is the halide (either Br⁻
3 or I⁻), L the butylammonium ligand,¹²⁰⁵ and *n* the number of monolayers. It is noted that other
4 groups would refer to these as simply MAPbX₃ nanoplatelets.^{62, 418} However, the Br-based
5 perovskites contained a mixture of nanoplatelets with different thicknesses, with
6 electroluminescence from *n* = 2, 3 and 4 layers. The EQEs were all well below 0.01%.¹²⁰⁵ Yang *et*
7 *al.* subsequently developed a hot-injection approach to synthesize monodisperse CsPbBr₃
8 nanoplatelets using the long-chain oleylamine, oleic acid and octadecene as the ligands. By
9 controlling the reaction temperature, they were able to fine-tune the number of monolayers in the
10 nanoplatelets, with fewer layers obtained at lower reaction temperatures. Using a reaction
11 temperature of 180 °C, CsPbBr₃ nanoplatelets with a thickness of 3.1 nm were obtained, which
12 gave EL in LEDs at 480 nm. In both the PL and EL spectra, only one emission peak was obtained,
13 and according to TEM analysis there was a narrow distribution in the nanoplatelet thicknesses.
14 The performance of the LEDs reached 0.1%, with a maximum luminance of 25 cd m⁻².²²⁷ Through
15 passivation of the CsPbBr₃ nanoplatelets using HBr, Wu *et al.* achieved an improvement in EQE
16 to 0.124%, with 62 cd m⁻² luminance. This was made possible by using thinner nanoplatelets with
17 bluer emission at 463 nm. Color-pure emission was also achieved, with the FWHM of the EL peak
18 being only 12 nm. As such, the CIE coordinates (0.157, 0.045) fulfilled the requirements for ultra-
19 high definition displays.⁴¹⁸ However, the EQE falls well below the near-unity PLQY. Hoye, Lai,
20 *et al.* investigated the limiting factors in CsPbBr₃ perovskite nanoplatelet LEDs. They found that
21 when using PEDOT:PSS as the hole-injector, there was significant non-radiative decay, leading to
22 the PLQYs of the nanoplatelets nearly halving. By adding a poly(triarylamine) layer between
23 PEDOT:PSS and the nanoplatelet, non-radiative recombination was reduced, as found from time-

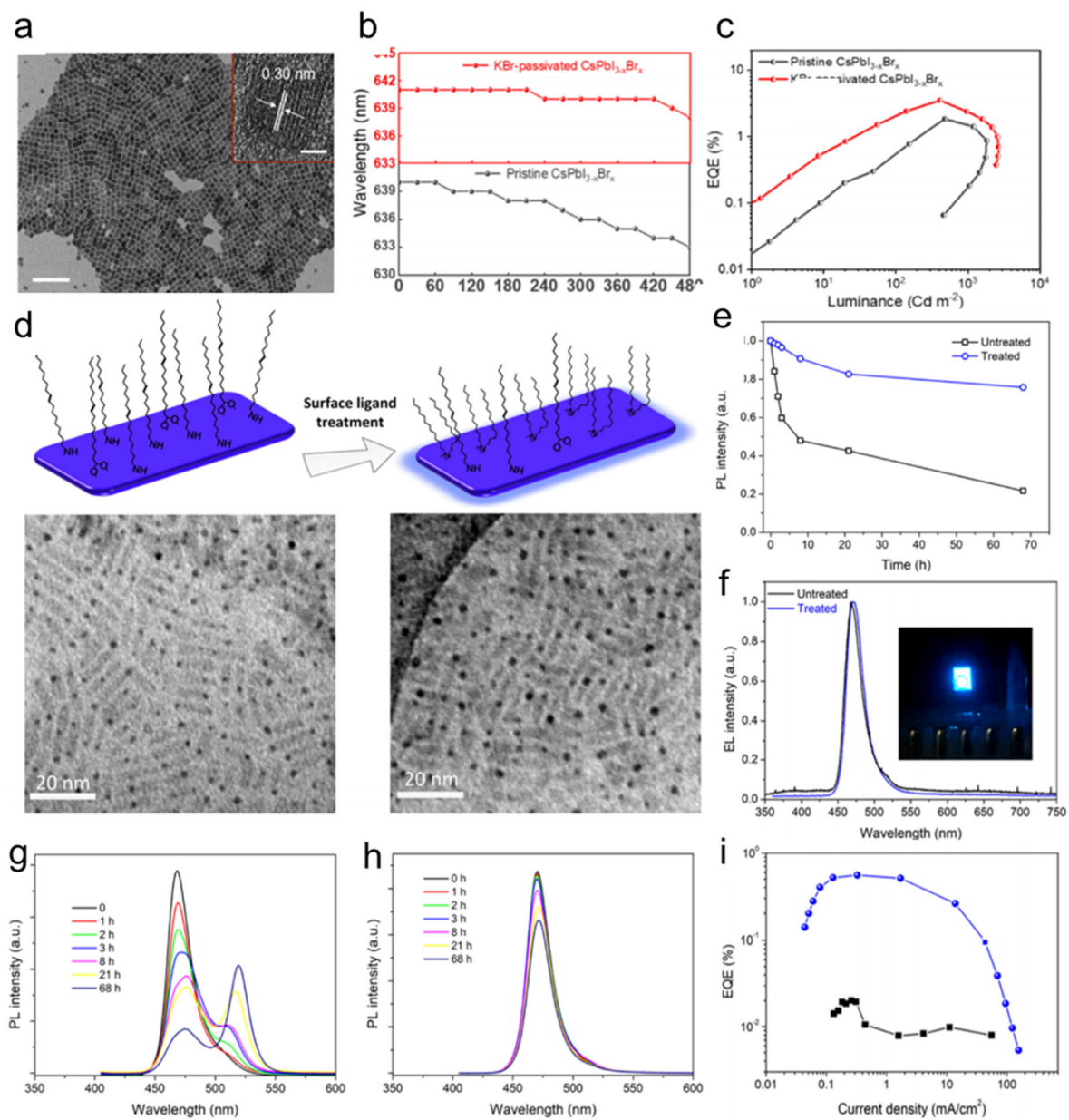
1 resolved PL measurements. This led to an improvement in the EQEs by two orders of magnitude,
2 from 0.007% to 0.3%, with 40 cd m⁻² luminance for blue emitters (464 nm EL wavelength).¹²⁰⁶
3 Similar results were obtained from sky-blue emitters (490 nm wavelength). Further improvements
4 in EQE for the sky-blue emitters were achieved by adding PbBr₂ complexed with oleylamine and
5 oleic acid for surface passivation, as previously detailed by Bohn, Tong, *et al.*⁶² However, it was
6 found that only a small amount (10 vol.%) could be added to the nanoplatelet solution to improve
7 the LED performance of the sky-blue emitters (from 0.24% to 0.55%).¹²⁰⁶ Further increases in the
8 volume of the PbBr₂-ligand passivating agent led to a reduction in performance. By contrast, Bohn,
9 Tong, *et al.* redispersed all of their purified perovskite nanoplatelets into a solution of PbBr₂-ligand
10 in order to achieve the maximum improvement in PLQY.⁶² It was also found that adding PbBr₂-
11 ligand to the blue-emitters led to no improvement in performance. While the reason behind the
12 limitation in the amount of passivating agent that could be added is unknown, possibilities include
13 the formation of an insulating shell around the nanoplatelets that make charge-injection
14 challenging.

15 Another approach used to passivate surface defects in CsPbBr₃ perovskite nanoplatelets was to
16 use soft Lewis bases. Zhang *et al.* used di-dodecyl dimethyl ammonium bromide (DDAB) to
17 partially replace the original oleylamine ligands through liquid-phase ligand exchange of the
18 colloidal nanoplatelets. The replacement of shorter DDAB ligand and the corresponding TEM
19 images before and after the ligand treatment can be seen in Figure 126d. This increased the PLQY
20 of blue-emitting perovskite nanoplatelets from 45.1% to 69.4%, with a consequent increase in the
21 device EQEs by an order of magnitude to 0.56%. Further improvements in EQE to 1.42% (shown
22 in Figure 126i) were achieved by adding a layer of CBP between the poly-TPD hole-injector and
23 nanoplatelets. The role of the CBP was attributed to a reduction in the hole injection barrier, owing

1 to the higher HOMO level of 6 eV. Furthermore, the stability of the LEDs also improved, with the
2 time for the EL to reach half the peak value increasing from 15 s to 42 s at a constant current of 1
3 mA cm⁻². Also, the PL stability was improved over time after ligand treatment, as shown in Figure
4 126 e,h,g.¹²⁰⁷ While short, these lifetimes are among the longest for blue perovskite nanoplatelets
5 reported to date. Nevertheless, they are shorter than those achieved by sky-blue emitting perovskite
6 thin films,¹²¹⁹ and significant improvements in device operation stability are needed before the
7 nanoplatelet devices can be used commercially. It is believed that these effects are due to the
8 DDAB ligands binding to surface bromide vacancies (XPS showed an increase in the Br/Pb ratio
9 after adding DDAB), as well as to exposed lead cations on the surface.¹²⁰⁷

10 An important challenge in the early development of perovskite nanoplatelet LEDs was a poor
11 knowledge of the exact band positions.¹⁰³ This was recently addressed through the use of Kelvin
12 probe to measurements of the work function, and through X-ray photoemission spectroscopy to
13 measure the valence band to Fermi level offset of blue and sky-blue emitting CsPbBr₃
14 nanoplatelets. According to these measurements, both emitters have deep ionization potentials of
15 6.8 eV (blue) and 6.5 eV (sky-blue). As a result, conventional hole-injectors would give rise to a
16 large hole-injection barrier, whereas conventional electron-injecting materials would have a lower
17 electron affinity or LUMO than the conduction band minimum of the nanoplatelets (3.8-3.9 eV).
18 This was found to result in significant charge imbalance, which limits the EQEs of the devices,
19 and indicates that future efforts need to focus on developing higher hole-injection level
20 materials.¹²⁰⁶ Another alternative is to change the ligands to tune the band positions. Zhang *et al.*
21 showed that partially substituting oleylamine for DDAB resulted in a reduction of the ionization
22 potential of CsPbBr₃ nanoplatelets from 7.1 eV to 6.8 eV. Nevertheless, the hole-injection level
23 remained deep.¹²⁰⁷

1 Beyond CsPbBr₃, perovskite nanoplatelets using both Pb²⁺ and Sn²⁺ cations, and with halides
2 ranging from I⁻ to Br⁻ to Cl⁻ have been grown, demonstrating PL emission wavelengths that can be
3 tuned from 690 nm to 400 nm, although it should be noted that Cl-based nanoplatelets were not
4 emissive.²¹⁹ There is therefore potential to use perovskite nanoplates beyond solely blue emission
5 (as it is in the cases that have been discussed previously), although there has been less focus on
6 device development, since green, red and near-infrared emitting thin films and NCs have already
7 reached >20% EQE. Nevertheless, the ability of perovskite nanoplatelets to blue-shift the emission
8 of pure-halide materials may be advantageous in avoiding phase-segregation and broadening of
9 PL peaks that could be observed in mixed halide perovskite thin films. But further work is needed
10 to improve the purity of iodide-based perovskite nanoplatelets, with recent examples
11 demonstrating broad PL FWHMs (50 nm at 650 nm wavelength) or multiple emission peaks.⁵⁵



1
2 **Figure 126.** a) TEM image of KBr-passivated CsPbI_{3-x}Br_x NCs. The inset shows the corresponding
3 HRTEM image. Scale bars: 100 and 5 nm, respectively. b) PL peak position as a function of
4 irradiation time for pristine and KBr passivated CsPbBr_{3-x}I_x NC films. The ensemble films were
5 continuously excited by a laser emitting at 365 nm with a power density of 100 mWcm⁻² c) EQEs
6 of LEDs based on prepared pristine and KBr passivated CsPbI_{3-x}Br_x NCs at different luminance.
7 a)-c) are reproduced from Ref. ¹¹⁹⁴ Copyright 2020 American Chemical Society d) TEM images

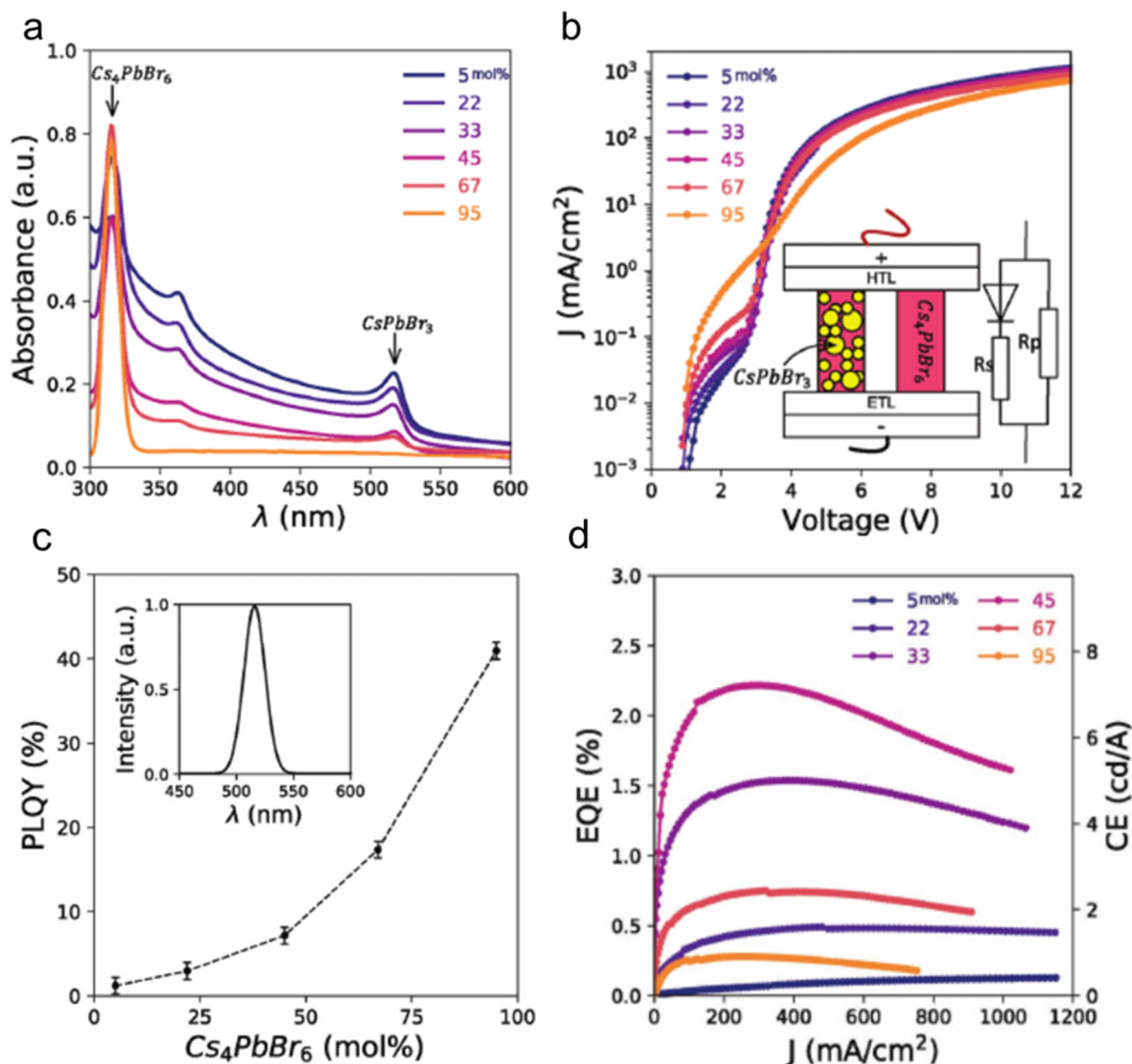
1 of untreated and treated CsPbBr₃ NPLs. e) Remnant PL intensity of treated and untreated NPLs. f)
2) EL spectra of the untreated and treated CsPbBr₃ NPL-based LEDs. Inset: a photograph of a
3 working treated CsPbBr₃ NPL-based LED at a driving voltage of 5 V. Recorded PL spectra of g)
4 untreated and h) treated CsPbBr₃ NPL/toluene solutions. i) external quantum efficiency–current
5 density curves of the untreated and treated CsPbBr₃ NPL-based LEDs. d)-i) are reproduced from
6 Ref. ¹²⁰⁷ Copyright 2019 American Chemical Society.

7
8 ***NCs embedded in 3D matrices:*** 3D NCs embedded within a matrix of a lower dimensionality
9 perovskite have been demonstrated, as discussed in Section 5. This enables charges to be more
10 effectively confined in the 3D NCs, while having a well-controlled structure. An example that has
11 gained attention recently is CsPbBr₃ embedded within a matrix of Cs₄PbBr₆,¹²²⁰ which is a wide
12 bandgap 0D non-perovskite. The absorbance due to Cs₄PbBr₆ is shown in Figure 127 a. This
13 composite structure has been shown to result in significantly improved PLQY. For example, Lian
14 *et al.* found that CsPbBr₃ grown by thermal evaporation has a PLQY of 1.2%, whereas 5 mol.%
15 CsPbBr₃ embedded in Cs₄PbBr₆ has a PLQY of 40% (Figure 127c). This has been attributed to
16 spatial confinement of charges, as well as the passivation of surface defects.¹²²⁰ In devices, this
17 correlated with a significant improvement in device performance, from 0.13% for CsPbBr₃ LEDs
18 to 2.5% for the composite devices with 55 mol.% CsPbBr₃ (Figure 127d, a sketch of the device
19 structure and device current density at different composite ratio are shown in Figure 127b).¹²²⁰
20 Similar improvements in performance were also observed by Shin *et al.*, from 0.0062% EQE for
21 CsPbBr₃ to 0.36% for the composite, which was consistent with the improvement in the PLQY to
22 55% for the composite. Optical modelling found the outcoupling of these devices to be similar, at
23 between 9-12%, and the calculated internal quantum efficiencies were 0.072% and 2.9%

1 respectively. From this, it was calculated that the injection efficiency was lower for the composite,
2 in agreement with the wide bandgap of the Cs₄PbBr₆ host.¹²²¹ Both Lian *et al.* and Shin *et al.* grew
3 the composite films through the evaporation of CsBr and PbBr₂ in alternate layers and adjusting
4 the ratio of the thicknesses of each layer. But Shin *et al.* reported that a limitation with this
5 technique is that CsPbBr₃ formed in the Cs₄PbBr₆ is not stable and is affected by exposure to
6 moisture. Indeed, they reported that the as-grown film (that was nominally Cs₄PbBr₆) was
7 originally yellow-colored CsPbBr₃ that became transparent Cs₄PbBr₆ with embedded CsPbBr₃
8 after 15 min in ambient air. After several days in air, the film had completely become Cs₄PbBr₆
9 and no green emission was observed.¹²²¹ This therefore shows the limitation of Cs₄PbBr₆/CsPbBr₃
10 composites prepared by the sequential deposition approach, even though Lian *et al.* reported that
11 the composite was more stable under operation than CsPbBr₃.¹²²⁰

12 Composites comprised of PbS quantum dots heteroepitaxially incorporated in perovskite
13 matrices have also been demonstrated with success.¹²²² These structures are particularly
14 advantageous for devices emitting in the near-infrared at wavelengths (900–1560 nm) longer than
15 achievable with pure lead perovskite emitters.¹²²³ Such long wavelength emitters are important for
16 applications in night vision, biomedical imaging, optical communications and computing,¹²²⁴ and
17 the ability to achieve these devices using low-cost solution-based methods could be significantly
18 advantageous over the epitaxial structures currently used.¹²²³ PbS can form heteroepitaxially in
19 MAPbI₃ lattices because they have strong structural affinity and similar Pb-Pb bond distances
20 (5.97 Å for PbS, 6.26 Å for MAPbI₃) that are within 4.6% of each other.¹²²² Further improvements
21 in lattice matching could be achieved by alloying I with Br in the perovskite due to reductions in
22 the lattice parameter of the perovskite.¹²²⁴ Theoretical considerations also showed that it is possible
23 for PbS/MAPbI₃ interfaces to form without defects. HR-TEM measurements showed a well-

1 defined orientation between PbS and MAPbI₃. The growth of the MAPbI₃ matrix around the PbS
2 quantum dots was achieved by exchanging the organic ligands for short halide ligands. By mixing
3 with PbI₂ dissolved in butylamine, the PbI₂ formed a complex with the halide species on the
4 quantum dot surface. This complex was deposited onto a surface by spin-coating, followed by
5 soaking in a solution of methylammonium iodide in isopropanol, thus forming the MAPbI₃ matrix.
6 Changing the ratio of PbI₂ and quantum dot in the precursor changed the final content of the
7 quantum dots in the matrix from 0.2 to 29%.¹²²² Spectroscopic measurements showed that the
8 efficiency of carrier transfer to the PbS was up to 80%.¹²²² Demonstrations of near-infrared LEDs
9 achieved EQEs up to 5.2% at 1390 nm emission wavelength, which was significantly higher than
10 the PbS quantum dot only control (0.03%).¹²²⁴ Further improvements in performance were
11 achieved by embedding PbS quantum dots in a 2D perovskite matrix, with phenethylamine used
12 as the stabilizing agent bound to the PbS quantum dots. This was mixed into the solution containing
13 the inorganic precursors (CsBr, PbBr₂), which was spin-coated, with toluene dripped as the anti-
14 solvent. GISAXS measurements showed that this resulted in quantum dots that were regularly and
15 evenly spaced (on average 4.4 nm apart). Spectroscopic measurements showed that the exciton
16 transfer efficiency from perovskite to quantum dot was 82% at 1533 nm emission wavelength,
17 with LEDs achieving 3.5% EQE. For 1300 nm emission wavelength, the EQE was 6%, but the
18 highest EQE was achieved for 986 nm emission, with a peak value of 8.08%. The increases in
19 EQE with shorter wavelength were due to increased PLQY in the quantum dots.¹²²³ These devices
20 also demonstrated improved stability compared to earlier quantum dot in perovskite versions, with
21 the EL intensity reaching half the peak value after 1 h of operation.¹²²³



1
 2 **Figure 127.** a) Absorbance of CsPbBr₃|Cs₄PbBr₆ composite with different CsBr and PbBr₂
 3 precursors ratios. b) Current density for devices based on the composite perovskites with different
 4 Cs₄PbBr₆ molar percentages. Inset: schematic showing two types of current conducting channels
 5 (CsPbBr₃-rich zone and Cs₄PbBr₆-rich zone) through the perovskite layer in LED devices. The
 6 former channel could form a typical LED structure with a series resistor, whereas the latter one
 7 would serve as a shunt resistor due to the lack of emitter. c) The PLQY of composite films
 8 increased with an increased percentage of Cs₄PbBr₆. (Inset: photoluminescence spectrum of

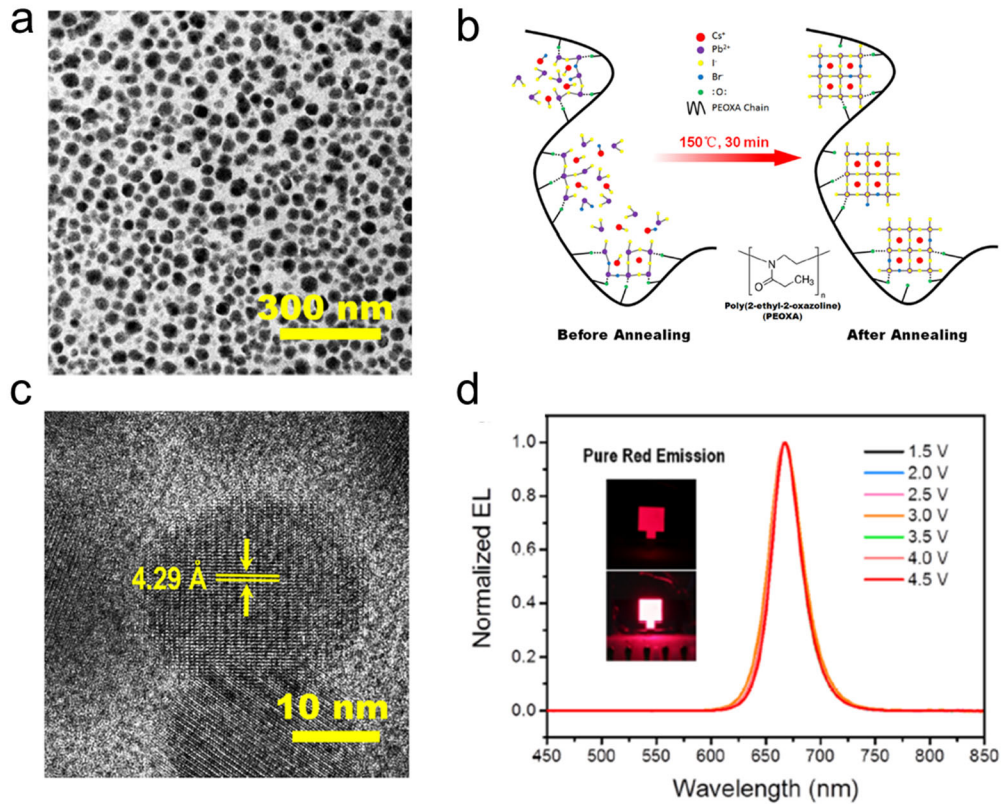
1 composite films showing sharp peak near 516 nm with FWHM = 20 nm.) d) EQE for devices with
2 respect to Cs₄PbBr₆ molar percentage. Reproduced from Ref. ¹²²⁰

3

4 **NC-Polymer Composites:** Perovskite nanocrystal – polymer composites have been explored as
5 a means to improve the stability of the NCs.^{21, 301, 1184, 1225} Xin *et al.* demonstrated blends of
6 CsPbBr₃ NCs with the poly(methyl-methacrylate (PMMA), polystyrene (PS) and poly(butyl
7 methacrylate) (PBMA). These composites were able to maintain their quantum yield in air for
8 more than a month.³⁰¹ Wang *et al.* also reported a swelling-deswelling microencapsulation strategy
9 to fabricate MAPbBr₃ NC/polymer composite films which were stable against moisture and heat.²¹
10 Perovskite-polymer composites have also been shown to result in reduced non-radiative
11 recombination and improved device performance. Zhao *et al.* demonstrated this with perovskite
12 thin films. They embedded a 2D/3D bulk perovskite into an insulating polymer matrix, resulting
13 in near-infrared LEDs with EQEs reaching 20.1%.¹¹⁷⁴ The polymer component suppressed non-
14 radiative recombination at the interfaces between the perovskite emissive layer and charge
15 transport layers. Li *et al.* demonstrated improved performance in perovskite LEDs using perovskite
16 NC/polymer composites. They fabricated a composite of MAPbBr₃ NCs and an aromatic
17 polyimide precursor (PIP). By adding the PIP polymer matrix, the EQE was increased by two
18 orders of magnitude compared with pristine MAPbBr₃ NCs in a thin film, giving an EQE of
19 1.2%.¹²²⁶ Cai *et al.* blended CsPb(Br,I)₃ NCs in different ratios with the polymer poly(2-ethyl-2-
20 oxazoline). The TEM images are shown in Fig. 128a, c. This resulted in improved EQEs in pure-
21 red LEDs from 1.04% (0 wt.% polymer) to 6.55% (45 wt.% polymer).¹²²⁷ The enhancement of
22 EQE and stability are attributed to strong interactions between the functional group in the polymer
23 matrix and the Pb²⁺ in NCs, which facilitates homogeneous distribution of NCs and increases the

1 PLQY (Fig. 128b). The EL spectra is stable under different operational voltage as shown in Fig
2 128d. In addition to homogenous distribution of NCs, Raino *et al.* suggested the improvement of
3 spectra stability is due to that the high hydrophobicity and efficient molecular packing of the
4 polymer matrix with the long-chain NC surface ligands are the key factors for protecting the NCs
5 against environmental damage.¹²²⁸ The polymer matrix also provides excess nucleation sites
6 during the NC recrystallization process, which leads to more uniform NC distributions in the films,
7 resulting in a higher PLQY in thin films of the composite.¹²²⁷ Another promising application of
8 the perovskite NC/polymer composite is as downconverters. Through excitation with commercial
9 blue LEDs, these downconverters efficiently produce sharp green and red photoluminescence,
10 which is important for display applications.^{295, 1229} Start-up companies are beginning to explore
11 the commercial potential of perovskite NC/polymer composite phosphors.¹²³⁰ However, devices
12 are still limited by the thermal stability of the composite materials. For example, LEDs using
13 MAPbBr₃ NCs/Polyvinylidene fluoride composites undergo thermally-induced degradation when
14 temperature exceeds 70 °C.²⁹⁵

1



2 **Figure 128.** a) TEM of CsPbBr_{0.6}I_{2.4} film with 45% PEOXA. b) Schematic diagram of polymer-
3 induced in situ perovskite nanocrystal formation process. c) High-resolution TEM image of
4 crystals; the repeated distance of 4.29 Å indicates the (110) plane of CsPbBr_{0.6}I_{2.4} lattice. d) EL-
5 spectrum stability of the CsPbBr_{0.6}I_{2.4} LED with 45% PEOXA. The inset is the photos of a light-
6 up LED at voltage biases of 1.5 V (top) and 3.0 V (bottom). Reproduced from Ref. ¹²²⁷

7

8 **Optical features of perovskite light emitters**

9 **Highly Efficient Light Emission:** The emergence of LHP NC systems as a new class of light-
10 emitting materials may offer new technology opportunities, as reflected by the enormous
11 enhancement of photoluminescence quantum yield in the past five years. The defect-mediate
12 nonradiative losses in the bulk LHPs are often considerable, but in the NC systems, strategies

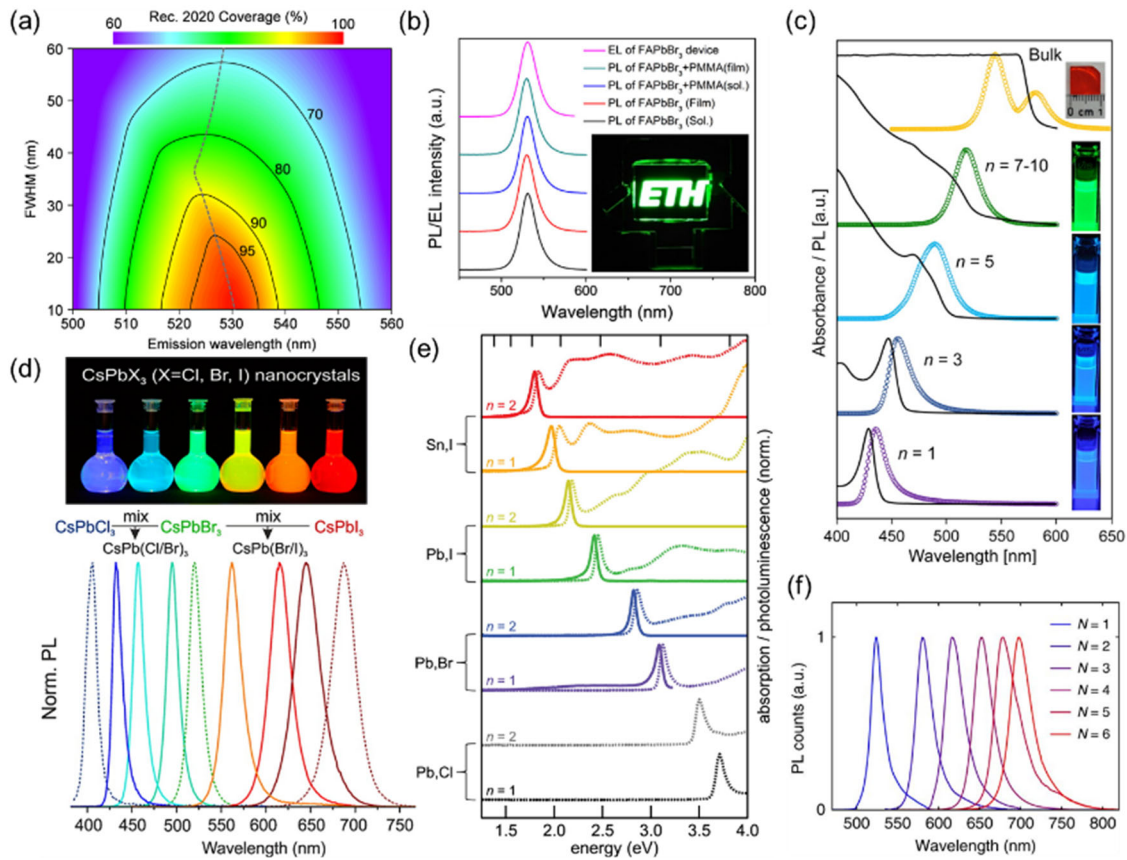
1 including composition engineering, ligand passivation, quantum and dielectric confinement, and
2 post-treatments of LHP thin films and NCs, have shown promise. For example, Hassan et al. first
3 achieved a η_{PL} of >93% in cubic MAPbI₃ NCs synthesized by the ligand assisted reprecipitation
4 (LARP) technique.¹²³¹ In the mixed-cation NCs, e.g., FA_{0.5}MA_{0.5}PbBr₃, near-unity η_{PL} was also
5 achieved.¹²³² Pan et al. synthesized highly luminescent red CsPbI₃ NCs with η_{PL} of >95% using
6 bidentate 2,2'-iminodibenzoic acid as ligands to passivate NC surfaces.¹⁷⁵ Near-unity η_{PL} was also
7 reported in CsPbI₃ NCs,¹²³³ as well as other CsPbX₃,⁸⁰ by stabilizing the cubic phase using
8 trioctylphosphine lead iodide precursor and passivating the surface with alkylammonium ligands
9 using the hot injection (HI) methods. New strategies, such as selective chemical etching¹²³⁴ and
10 spray pyrolysis synthesis,¹²³⁵ were also reported to significantly enhance η_{PL} to near unity.

11 In quantum confined LHP NC systems, η_{PL} enhancement generally requires more efforts. For
12 example, the quasi-2D PEA₂A_{1.5}Pb_{2.5}Br_{8.5} NCs, where A = MA and Cs, exhibit a high η_{PL} of
13 88%.¹¹⁷⁸ In the 2D (RNH₃)₂[MAPbBr₃]₃PbBr₄ nanoplatelet system, where R is an alkyl chain, η_{PL}
14 in the assembled superlattices can reach 90%,¹²³⁶ hypothetically due to a special aggregation-
15 induced emission (AIE) mechanism. An important merit for 2D material-based emitters is that the
16 exciton transition dipole moments (TDMs) can be aligned parallel to the surface plane, guiding
17 the emission perpendicular to the out-of-plane direction, which greatly enhances the light
18 outcoupling efficiency in LEDs.^{1232, 1237} Recent advances in 2D CsPbBr₃ and MAPbBr₃ NCs have
19 shown that one can obtain a high degree of in-plane TDM ratio in their superlattices, showing
20 promise for future photonic devices.¹²³⁸⁻¹²³⁹

21 **Narrow Emission Band:** Bright and narrowband fluorophores as primary colors emitting at pure
22 red (R), green (G), and blue (B) wavelength regions are critical to enable next-generation displays
23 with extremely high chromaticity. The emergence of LHP NC-based LEDs is mainly driven by

1 their intrinsically narrowband emission, whose full width at half maximum (FWHM) ranges from
2 9 to 42 nm, from B to R.^{24, 105, 1240} Notably, an extremely narrow FWHM of 11 nm had been
3 reported in the layer-controlled 2D CsPbBr₃ NC solutions.⁶² In LEDs, the FWHM of 14.7 nm has
4 been realized using the mixed anion CsPbBr₃/Cl₃ NCs with appropriate ligand engineering.¹²⁴¹
5 Sim et al. reported bright EL based on CsPbX₃, giving narrow FWHMs of 16, 16, and 40 nm for
6 B, G, R primaries, respectively.¹²⁴² A report demonstrated that the PL FWHM decreased from 36
7 to 32 nm when the CsPbI₃ NCs were encapsulated by varying the amount of ammonium
8 thiocyanate.¹²⁴³ Zhang and co-workers achieved a very narrow EL FWHM of 33 nm for the R
9 primary at 648 nm using the CsPb(Br/I)₃ NCs.¹²⁰⁰ By crosslinking the CsPbI₃ perovskite NCs with
10 trimethylaluminum, the FWHM further reduced to 31 nm for the R primary.¹¹⁶⁰ In the NIR
11 wavelength region, by modulating the anion and cation compositions, the EL FWHM was reported
12 to as low as 27 nm in the Cs_xFA_{1-x}Pb(Br_{1-y}I_y)₃ NCs, optimized by an automated microfluidic
13 platform.¹²⁴⁴

14 Although narrowband emission can be realized in the green-emitting CsPbBr₃ NCs, the Rec.
15 2020 gamut area only covers 90% of the recommendation (Rec.) 2020 standard, the newly defined
16 color gamut for next-generation displays, because the emission peaks at < 520 nm.⁵³ By using the
17 colloidal 2D FAPbBr₃ NCs with a FWHM of 22.8 nm peaking at 529 nm, a coverage of >98%
18 Rec. 2020 has been reported (Figure 129a,b).¹²⁴⁵⁻¹²⁴⁶ We consider that the perovskite NC emitters
19 would be the most promising candidate reaching 100% of the Rec. 2020 color gamut among all
20 semiconductor systems.



1
2 **Figure 129.** Fundamental characteristics of lead halide perovskites (LHPs). (a) Calculated Rec.
3 2020 color gamut coverage in CIE 1931 color space as a function of FWHM and emission
4 wavelength for the green emitter. (b) PL and EL spectra of FAPbBr₃ NCs that achieved Rec. 2020
5 gamut area coverage >97%. (c) Absorption and tunable PL spectra of 3D-bulk single crystal and
6 colloidal solution of 2D MAPbBr₃ NCs with precise layer control between n = 7–10 and n = 1. (d)
7 Tunable PL spectra in the colloidal CsPbX₃, where X = Cl, Br, and I, NCs using fast anion
8 exchange either from bromide to iodide (red-shift) or bromide to chloride (blue-shift). (e)

1 Absorbance and highly tunable PL spectra of 2D LHPs by varying the B-site cations, Pb and Sn,
2 and anions, Cl, Br, and I. (f) Tunable PL spectra in the layered quazi-2D perovskite NCs.

3
4 ***Tunable Emissive Spectra:*** The emission spectra and corresponding optical bandgaps in the
5 LHPs are continuously tunable over the entire visible spectral region from 400 to 780 nm. A few
6 strategies, including stoichiometric mixing and quantum confinement were utilized to tune the
7 optical bandgap of the perovskite NCs, as amply discussed in previous sections. For example,
8 Nedelcu et al. demonstrated emission wavelength tunability in the CsPbX₃ NCs by fast anion
9 exchange at 40 °C (Figure 129d).³⁰² The NCs exhibit η_{PL} of 10 - 80% and FWHM of 12 - 40 nm.
10 A similar approach was reported by the Manna group by exchanging bromide anions using iodide
11 and chloride precursors.⁵⁸ Similar approaches were also carried out in the MAPbX₃ and FAPbX₃
12 systems.^{30, 166} For the RP phase quazi-2D NPs the PL emission can also be tuned between 464 and
13 675 nm, yielding corresponding EL devices emitting at 465, 487, 506, 513, 615, 649, 654, and 681
14 nm (Figure 129f).²³ Note that although the anion exchange enables viable bandgap tunability, the
15 high η_{PL} of the mother NCs is not always preserved.³⁰² Moreover, the solubility of chloride
16 precursors in the common polar solvents is generally low, making it more difficult to prepare blue
17 emitters.⁹⁸⁴ The emission spectra can also be modulated by temperature (temperature-dependent
18 PL studies have mainly been used to investigate the excitonic properties of LHPs).

19 One-dimensional quantum confinement by controlling the lattice layer number in 2D NPs is
20 another attractive approach to enable emission blueshift.^{17, 19, 743, 979, 1231, 1247} Note that the 2D NPs
21 are different from the RPPs, which are quasi-2D phases comprised of stacked 2D layers.
22 Considerable efforts have been made in the 2D MAPbX₃, CsPbX₃ systems using the ligand assisted
23 reprecipitation (LARP), non-solvent crystallization, and hot injection technique.^{219, 1248} For

1 example, the Tisdale group identified the colloidal 2D MAPbBr₃ perovskites with layer numbers
2 (*n*) of 4, 5, and 6 emitting at 475, 490, and 504 nm, respectively.²⁰ By gradually varying the
3 octylammonium (OA) ligand concentration between 100 and 0%, the colloidal 2D MAPbBr₃ NCs
4 were isolated giving emission between 427 and 519 nm for *n* = 1 to ∞.¹⁷ The Tisdale group also
5 demonstrated thin layers of *n* = 1 and 2 using the non-solvent crystallization method (Figure
6 129e).²¹⁹ The Shih group reported high η_{PL} of up to 90% in the 2D NC solutions of *n* = 1, 3, 5, and
7 7, yielding stable room-temperature EL at 436, 456, 489, and 517 nm, respectively (Figure
8 129c).⁹⁸⁴

9

10 **Electrical Features of Nanocrystal Perovskite Light Emitters**

11 *Charge carrier dynamics.* While there has been tremendous progress in the performance of
12 perovskite NC LEDs, future improvements will require a more in-depth understanding of the
13 intrinsic photophysics of these materials, and also how charge carriers are transported across
14 interfaces within the devices. The recombination rate of free carriers can be described by Eq. 1:¹²⁴⁹⁻
15 ¹²⁵¹

$$16 \quad \frac{dn(t)}{dt} = -k_1n - k_2n^2 - k_3n^3 \quad (1)$$

17 where *t* is time, *n* is charge carrier density, *k*₁ is recombination rate of exciton recombination or
18 trap-related recombination, *k*₂ is the bimolecular recombination rate of free charge carriers, and
19 *k*₃ is the Auger (multi charge carrier) recombination rate. By comparing the charge carrier
20 dynamics of polycrystalline perovskite bulk thin films and perovskite nanocrystal films using
21 steady-state and transient photoluminescence spectroscopy, Kim *et al.* and other researchers found
22 out that both exciton recombination and bimolecular recombination occur in bulk thin films, while

1 exciton recombination is dominant in nanocrystal thin films.^{30, 1179, 1251-1252} Further details on the
2 physics of hot carrier relaxation and exciton recombination are given in Section 9.3.

3 As the main radiative recombination of perovskite NCs is due to exciton recombination, it is
4 important to understand the source of band-edge exciton generation inside NCs. During
5 photoexcitation, photons with energy higher than the band-gap will create hot carriers. The
6 interactions between carriers (carrier-carrier interactions) and the surrounding lattice (carrier-
7 phonon interactions) play an important role in hot carrier cooling process in perovskite NCs which
8 generate band-edge excitons or cold carriers.^{935, 1253} The radiative recombination of these single
9 band-edge excitons is the main contribution of photon generation in a perovskite nanocrystal light-
10 emitting diode. Another pathway to create band-edge excitons is through biexciton or multiexciton
11 generation processes. When the incident photon energy is higher than $2hn$ during the photo-
12 excitation process, the excess energy of the generated hot carriers can create additional
13 excitons.¹²⁵⁴ Then, the bi/multiexcitons will recombine non-radiatively through an Auger process
14 and form band-edge excitons.¹²⁵⁵⁻¹²⁵⁶ The hot carrier cooling rate can be influenced by several
15 factors including excitation energy¹²⁵⁶, halide compositions⁹²⁶ and types of cations.¹²¹⁷ Refer to
16 Section 13 for more details on this topic.

17 Carrier trapping will also influence the carrier dynamics in perovskite NCs for light-emitting
18 applications. It occurs when the band-edge excitons do not recombine radiatively and instead
19 migrate to a trap state which is close to the band edge.^{22, 1256} As perovskite NCs still suffer from
20 a broadening in the photoluminescence peak, it is important to understand what gives rise to this
21 effect.¹²⁵⁷⁻¹²⁵⁸ Wehrenfennig *et al.* suggested that the homogeneous PL broadening could be
22 increased through phonon creation and annihilation which would generate side peaks, or through
23 polaronic effects where the photogenerated electron-hole pair is strongly coupled to the

1 surrounding lattice, causing a geometric lattice relaxation and a Stokes-shifted emission from the
2 absorption edge.¹²⁵⁸ A typical Stokes shift for CsPbBr₃ NCs with effective edge length between 4
3 and 13nm ranges from 20-80 meV.⁸⁵¹ Brennan *et al.* reported that the size-dependent Stokes shift
4 is intrinsic to the NC electronic structure and independent from extrinsic influences such as
5 solvents and impurities.⁸⁵¹ Another factor which can influence the band structure and hence the
6 Stokes shift is temperature. Naghadeh *et al.* reported that the PL spectra will exhibit a blue shift
7 for small NCs (~3.1nm) with decreasing temperature from 300 K to 20 K, while exhibiting a red
8 shift with decreasing temperature for medium-sized (5.1 nm) and large (9.2 nm) NCs. The size of
9 NC will also influence the carrier dynamics as the PL lifetime increases with temperature for larger
10 NCs, and it remains the same for the small and medium-sized NCs.¹²⁵⁹

11 The majority of investigations into perovskite NC carrier dynamics are performed on solutions
12 or thin films under photoexcitation. But future insights into the carrier dynamics of the NCs under
13 electrical excitation are also needed. Sharma *et al.* recently demonstrated that the NCs aggregates
14 in the thin film did not blink in PL but showed strong blinking in EL. This is because that all NCs
15 can be photoexcited spontaneously and emit photons during the photoluminescence process.
16 However, only a small fraction of the NCs within the aggregates can undergo electroluminescence,
17 the majorities remain dark permanently, resulting in blinking.¹⁰⁷⁵ By investigating CsPbBr₃ NCs
18 system (~16±5nm), they reported that the selective EL process is due to charge migration and
19 selective recombination. During the electroluminescence process, the injected charges will migrate
20 to larger NCs that have smaller bandgaps. As a result, the larger NCs function as traps where the
21 charges migrating over other NCs get accumulated and recombined. It shows that under
22 comparable excitation rates, the intrinsic ELQY is only 36% that of the PLQY.¹⁰⁷⁵ During
23 photoluminescence, simultaneous emissions can occur on all NCs after photoexcitation and

1 exciton recombination. However, when injecting carriers, only a larger nanocrystal will emit as it
2 acts as a trap center due to its lower bandgap energy.

3 ***Role of Contact Layers and Charge Balance:*** Charge balance and the charge injection barrier
4 are two parameters that are strongly linked together because they are determined by the position
5 of the perovskite bands relative to the band positions of the materials for injecting electrons and
6 holes. The most common organic and inorganic charge injection materials are detailed in several
7 reviews, *e.g.*, Ref. ^{662, 1260-1262}. From these, it is evident that the most common charge injectors enable
8 efficient electron injection over the full range of perovskite electron affinities (down to 3.1 eV for
9 MAPbCl₃),^{1260, 1263} but hole-injection is more challenging. While the hole-injection level for
10 typical materials is up to 5.4 eV (for TFB and poly-TPD),¹²⁶⁰ the perovskite ionization potential
11 can reach values as high as 6.8 eV for blue-emitting CsPbBr₃ perovskite nanoplatelets.¹²⁰⁶ Green-
12 emitting perovskites also have higher ionization potentials (*e.g.*, 5.9 eV for MAPbBr₃).¹²⁶⁰ Higher
13 hole-injection levels have been achieved through modifications in common organic materials. For
14 example, PEDOT:PSS has been mixed with MoO_x to increase the work function from 5.20 eV to
15 5.62 eV.^{1221, 1264} As another example, Nafion perfluorinated ionomer (PFI) has been used to modify
16 the surface of TFB. The surface dipole from PFI gives rise to band bending of the TFB beneath to
17 a higher work function, resulting in an improvement in the performance of blue-emitting CsPbBr₃-
18 *x*Cl_{*x*} NCs.¹²⁶⁵ Similarly, Chiba *et al.* also reported using Nafion blending with PEDOT:PSS to
19 modify the workfunction of PEDOT:PSS, as shown in Figure. 130b.¹⁹²

20 Charge balance is measured by constructing two single-carrier devices from the same perovskite
21 emitter. One device has hole-injecting and hole-selective contacts on both sides (*e.g.*,
22 ITO/PEDOT:PSS/perovskite/MoO_x/Au). The other has electron-injecting and electron-selective
23 contact which have deep ionization potentials or HOMO levels to block holes (*e.g.*,

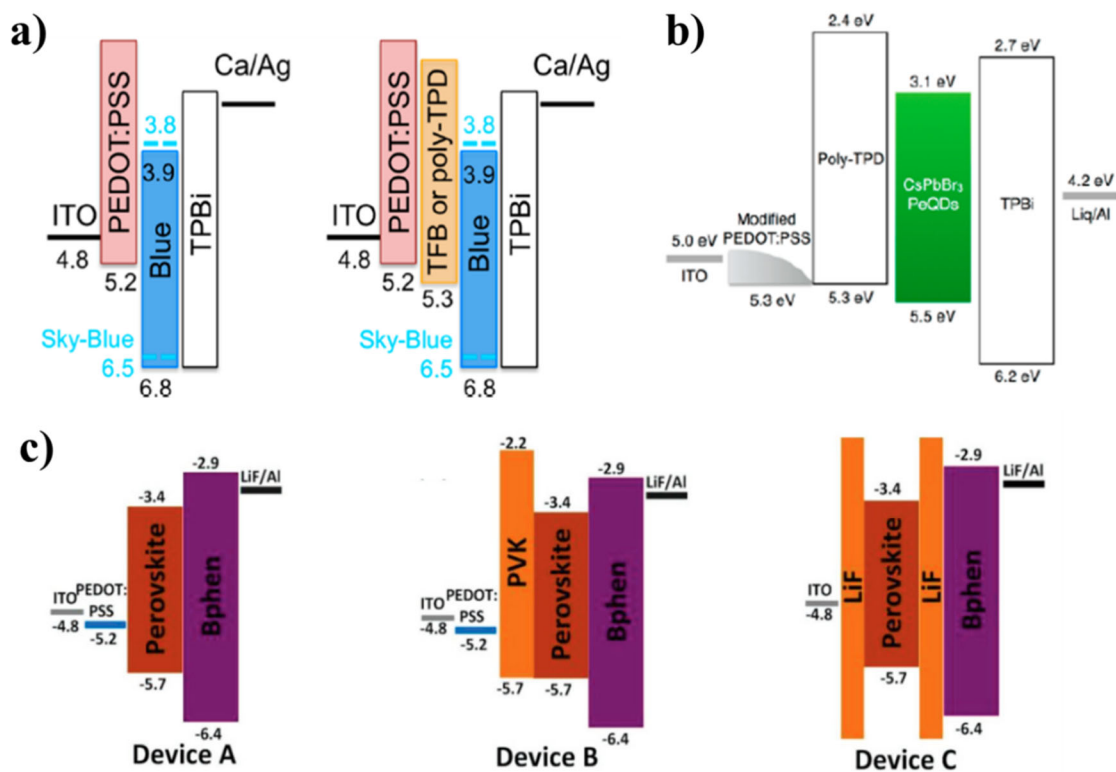
1 ITO/ZnO/PEI/perovskite/TPBi/Ca/Ag). By controlling the polarity of the applied bias, hole or
2 electron injection from each of the injecting layers is measured, and the current densities for
3 electrons and holes are compared. Unbalanced current densities would result in the recombination
4 zone being close to the electrode with the less efficient injection. For example, a higher electron
5 current density would imply that the recombination of injected electrons and holes occur at hole-
6 injector interface. In such cases, it is important to ensure that the electron affinity or LUMO of the
7 hole-injector is sufficiently low to confine carriers within the active layers in order to avoid
8 parasitic emission from the injecting layer itself.

9 The size of the injection barriers can be measured from the device itself through
10 electroabsorption spectroscopy,¹²⁶⁶ or is determined through photoemission spectroscopy
11 measurements of the individual layers. Details and best practices of the latter approach are given
12 in Ref. ¹²⁶⁷. It should be emphasized that owing to strong spin-orbit coupling, perovskites often
13 have significant tailing in the density of states at the valence band maximum, and accurately
14 determining the valence band to Fermi level offset would require fitting the density of states to the
15 valence spectrum rather than through simple linear fits.^{1206, 1268} Another approach to measure the
16 work function is to perform Kelvin probe measurements, which has the advantage of measuring
17 the work function of the layers under ambient conditions that may be more representative of the
18 films in devices. Details on best practices on Kelvin probe measurements on perovskites are given
19 in Ref. ¹²⁶⁹.

20 Careful choice of the charge-injection layers is necessary not only to minimize injection
21 barriers and control charge-balance, but also to minimize non-radiative recombination at the
22 interfaces. PEDOT:PSS is one of the most common hole-injection materials deposited beneath the
23 perovskite active layer,⁶⁶² but has in many cases it been shown to give high rates of non-radiative

1 recombination with both bulk 3D perovskites and perovskite nanoplatelets,^{1206, 1270} leading to
2 lower external PLQYs and fast PL decay. This is due to the semi-metallic nature of PEDOT:PSS
3 and high density of defect states that would occur at the interface.¹²⁷⁰ The effects of non-radiative
4 recombination at the interface with PEDOT:PSS has been addressed through the use of
5 poly(triarylamine) interlayers between PEDOT:PSS and perovskite. For example, the use of TFB
6 or poly-TPD resulted in an increase in the PL decay time of blue-emitting CsPbBr₃ perovskite
7 nanoplatelet thin films deposited on top, which led to the device EQE improving by two orders of
8 magnitude, as shown in Figure. 130a.¹²⁰⁶ Similarly, it has been found that adding a 20 nm layer of
9 poly-TPD between PEDOT:PSS and MAPbI₃ in solar cells resulted in a significant reduction in
10 leakage current, along with an increase in the open-circuit voltage.¹²⁷⁰

11 Work on reducing interface recombination has also focused on passivating the perovskite
12 itself, though this has to date largely been demonstrated in photovoltaic systems. This includes the
13 use of surface passivating species such as alkali metal halide additives and generation of 2D/3D
14 surfaces that significantly reduce non-radiative recombination at the interfaces.¹²⁷¹⁻¹²⁷³ Another
15 important consideration for the device performance is the charge leakage, which refers to the
16 escape of holes and electrons from the perovskite layer to the charge transport layer. To solve the
17 leakage issue, Wu et al proposed an LiF double insulating structure shown in Figure.130c¹²⁷⁴. The
18 sandwiched FAPbBr₃ perovskites are protected by LiF layers to avoid leakage, which increases
19 the EQE to 5.53% device C, compared to devices A and B which is 0.174%.



1
 2 **Figure 130.** Band structure illustration of perovskite LEDs with different interfacial layers. a) Blue
 3 and sky-blue emitting perovskite NPI LEDs with or without an interfacial layer of TFB or poly-
 4 TPD. Reproduced from Ref. ¹²⁰⁶ b) HTL modification: Energy diagram for modified hole injection
 5 layer (Nafion blending PEDOT:PSS). Reproduced from Ref ¹⁹². c) Comparison of devices with
 6 different interfacial layers Device A: PEDOT:PSS/Perovskite/Bphen; Device B: PEDOT:PSS
 7 /PVK/ Perovskite/ Bphen; Device C: LiF/Perovskite/LiF/Bphen. Reproduced from Ref ¹²⁷⁴

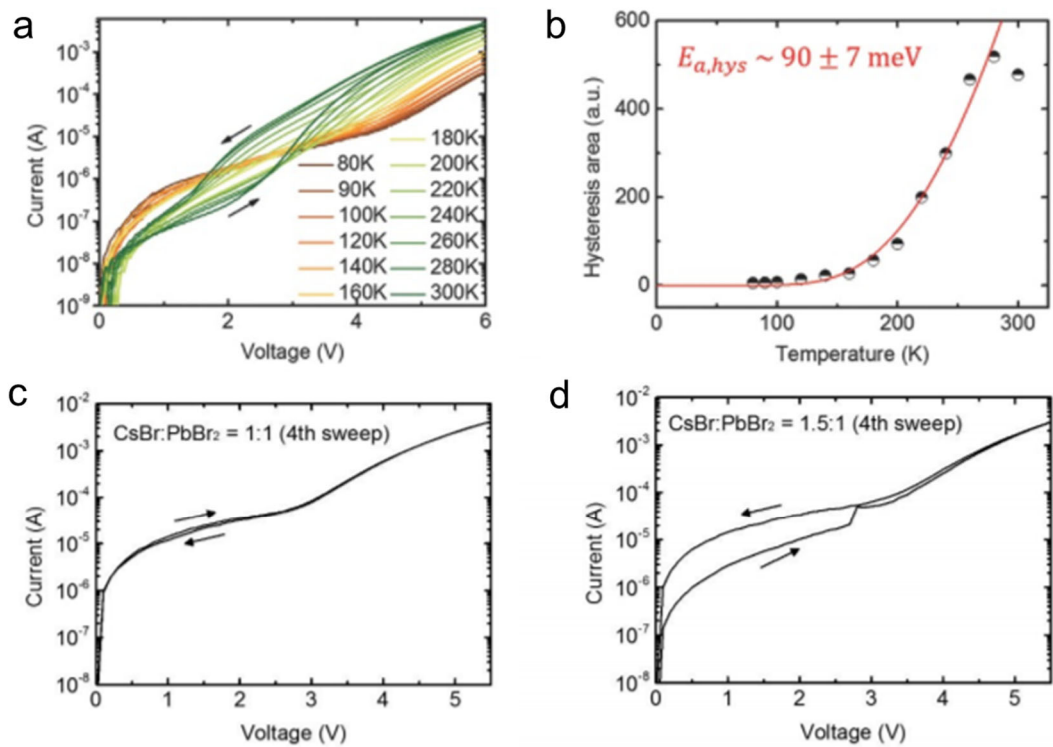
8
 9 **Ion Conductance and Hysteresis:** Typically, perovskite LEDs are only measured in one voltage
 10 direction. In many cases, this is due to the device degrading towards the higher voltage end of the
 11 measurement. But measurements of the forward and reverse sweep of non-degraded perovskite
 12 LEDs have shown hysteresis to be present,³¹ similar to observations made in perovskite solar cells.

1 In photovoltaics, hysteresis is attributed to ion migration, owing to the high density of halide ions
2 and vacancies present in the perovskite material.

3 Changing the distribution of ions at the interface impacts charge collection (in a solar cell) or
4 injection (in an LED); in certain configurations, this may be more favorable, but typically, this
5 creates unwanted barriers to charge movement at the interfaces.¹²⁷⁵ Furthermore, these interfacial
6 halides and vacancies may also lead to non-radiative recombination sites as the very ions or defects
7 themselves may introduce trap states in the bandgap, particularly at surfaces.¹²⁷⁶ We note that such
8 ion migration effects can also be seen as an opportunity, as demonstrated by light-emitting
9 electrochemical cells,^{1277,1278} in which the devices are designed such that the local distribution of
10 ions allows for favorable injection and emission properties. However, achieving control over the
11 ionic movement will be critical for its practical use.

12 Work by Cho *et al.* on CsPbBr₃ thin film LEDs showed that the degree of current hysteresis
13 increased exponentially with temperature, following an Arrhenius relationship that had an
14 activation energy of 90±7 meV. This is close to the reported activation energy for halide anion
15 migration in MAPbBr₃ and it was proposed that the migration of Br⁻ accounts for the current
16 hysteresis observed at different temperatures (Figure. 131a,b). When the ratio of CsBr:PbBr₂ was
17 increased from 1:1 to 1.5:1 in the precursor solution, the current hysteresis from the resultant films
18 became worse (Figure. 131c,d), possibly due to an increase in trap density. With higher
19 CsBr:PbBr₂ ratio, the hysteresis increased up to 4th sweep compared with low CsBr:PbBr₂ ratio.¹²⁷⁹
20 Chen *et al.* also found that ions migrated with the application of an electric field of 0.3 V m⁻¹
21 vertically in a MAPbBr₃ microplatelet, enabling the formation of a *p-i-n* junction, which could be
22 frozen in place by rapidly cooling to -193 °C. This operated as an LED, with negligible current
23 hysteresis at -193 °C, but significant hysteresis at ambient temperature, which is again consistent

1 with ion migration giving rise to the observed hysteresis.¹²⁸⁰ Such ion migrations results in halide
2 segregation in LHP NCs with mixed halide composition. Under photoirradiation or with an applied
3 bias, mixed halide perovskites present a main limitation due to the segregation of the mixed phase
4 into two phases, as was first reported by Hoke et al.¹²⁸¹ For example, in the ensemble film of
5 CsPbBr_{1.2}I_{1.8} NCs, laser excitation causes a blue shift from 630 to 520 nm in the PL peak that can
6 revert back in the dark. Interestingly, for an isolated single CsPbBr_{1.2}I_{1.8} NC, the PL is also blue-
7 shifted upon laser excitation but never returns back in the dark, revealing the fact that the presence
8 of adjacent NCs is crucial to channel the migration of iodide ions.¹²⁸² Furthermore, Zhang *et al.*
9 also observed blue-shifted PL when the NCs were electrically biased in the dark without the
10 injection of excited-state charge carriers. This finding suggests that the local electric field breaks
11 the iodide bonds that triggers the ion migration process.¹²⁸² Gualdrón-Reyes et al. found that such
12 segregation is a size-dependent phenomena and is minimized in thin films of smaller size NCs.¹²⁸³
13 Similarly, the spectral instability of the PeLEDs is observed under varying bias when mixed Cl/Br
14 halide is used for blue EL. Wang et al. reported EL red shift as function of Cl content caused by
15 strong electrical field.¹²⁸⁴ It was found that the deeper blue device appeared to be more subjected
16 to the field-induced phase separation.



1
 2 **Figure 131.** a) Temperature-dependent current–voltage characteristics of the CsPbBr₃ PeLED
 3 showing current hysteresis. b) Plot of hysteresis area versus T with a nonlinear fitting based on
 4 Arrhenius equation. c) Hysteresis behavior of a CsPbBr₃ PeLED with CsBr:PbBr₂ = 1:1 (based on
 5 Buf-HIL) at room temperature with 4 sweeps. d) Hysteresis behavior of a CsPbBr₃ PeLED with
 6 CsBr:PbBr₂ = 1:1.5 (based on Buf-HIL) at room temperature with 4 sweeps. Reproduced from
 7 Ref. ¹²⁷⁹

8
 9 **LEDs Exploiting Lead-Halide Perovskite Emitters**

10 By virtue of superior features in light generations and electrical characteristics, lead-halide
 11 perovskites (LHPs), especially the NCs, were supposed to be new generation soft light emitters in
 12 flexible thin film light-emitting diodes (LEDs).^{324, 425, 524, 1185} Besides the cost advantage endowed
 13 by cheap raw materials, facile synthesis of emitters and solution processing film deposition, LHP-

1 LEDs also demonstrate high luminous efficiency, high colour purity and ultra-wide colour gamut
2 for prospective full color display, white lighting, and other applications.^{173, 425, 524, 1180, 1182, 1235} Thus
3 far, some impressive achievements have been reported in the few years, including a high external
4 quantum efficiency (EQE) level over 20%, ultrahigh brightness level over 100 000 cd m⁻², a good
5 flexibility, a facile device fabrication, but an incongruous operation stability.^{324, 425, 1173, 1223, 1252,}
6 ¹²⁸⁵ Because of the environment-friendly consideration of lead component, some lead-free metal
7 halide perovskite emitters were also developed and great progresses, e.g. high colour rendering
8 index over 90, were achieved.⁵²⁴ However, limited by a high quality film deposition, these emitters
9 are more compatible with inorganic LEDs as phosphors.^{524, 1212} This section mainly concentrates
10 onto the LEDs exploiting LHP emitters.

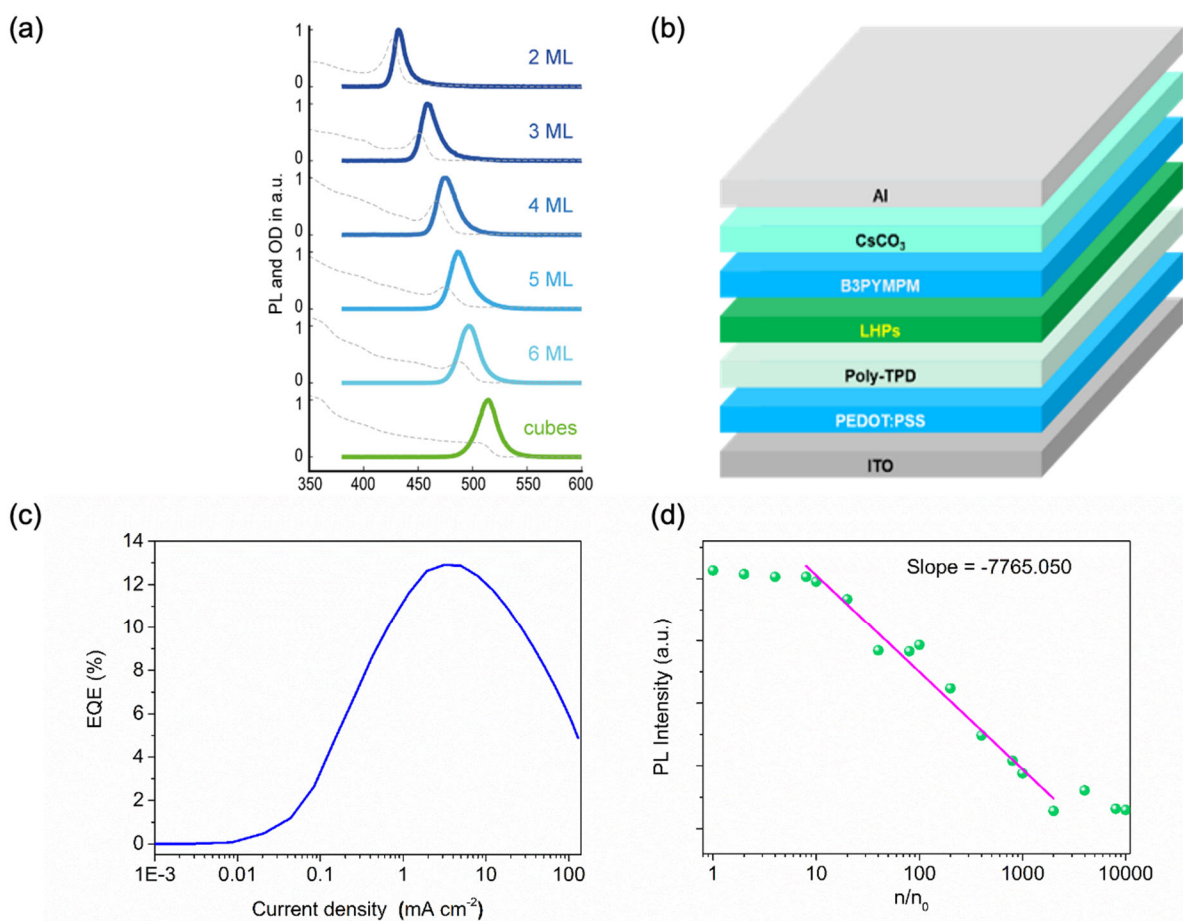
11 **Classifications:** Like other solution processed thin film devices, such as QD-LEDs and polymer
12 solar cells, the device structures of most LHP-LEDs are simple, and their primary difference are
13 the emitters. Thus, the classification of LHP-LEDs is mainly based on the colors, dimensions, film
14 deposition technologies and other features of LHP emitters.

15 **Color of LHP Emitters:** Normally, the electroluminescence (EL) spectra of LHP-LEDs are
16 almost same with the photoluminescence (PL) spectra of adopted LHP emitters, with bandgap
17 being predominately determined by the halogen species.^{1233, 1268, 1286} For the LHPs with single
18 halogen species, three discrete and narrow emissive bands with a width of around 20-30 nm go
19 across the whole visible range, which means almost the whole colour gamut is covered.^{15, 1287-1288}
20 However, except the green bromine-based LHPs, the near-ultraviolet chlorine-based and near-
21 infrared iodine-based LHPs are too extreme for most application of LEDs.^{80, 1194, 1284} Using alloyed
22 halogen species, the emissive band of the resulting LHPs can be tuned across the whole visible
23 range, correspondingly, their colour gamut is also extended.^{80, 1180, 1194, 1284} However, compared to

1 the single halogen specie LHP-LEDs, the EL spectra of LHP-LEDs based on alloyed halogen
2 specie LHP emitters demonstrate an irreversible shift because of the migration of halogen anions
3 and vacancies under an applied electric field.^{1160, 1173, 1201, 1251, 1282} To date, LEDs using single
4 halogen specie emitters, especially the APbBr₃ green ones, still dominate the development of LHP-
5 LEDs by virtue of high EQEs over 20% and high device operation stability.^{425, 1174} As the last piece
6 of LHP-LED jigsaw in the prospective full color display applications, the progress of blue LHP-
7 LEDs is still lagging behind the red and green ones, because of a low luminous efficiency and poor
8 stability of chloride-based blue LHP emitters.^{1160, 1180-1181} Alternatively, APbBr₃ nanoplatelets
9 (NPLs) and other nanostructures with a strong quantum confinement are held in great consideration
10 as prospective blue emitters in LHP-LEDs.^{227, 984, 1178, 1219, 1289}

11 ***Dimension of LHP Emitters:*** Because of a low exciton binding energy (around dozens of meV),
12 most excitons generated by photon excitation or electrically driven in bulky LHPs would dissociate
13 into free charge carriers, leading to a low efficient radiative recombination.^{978, 980, 1242, 1290-1291} Also,
14 trap-assisted non-radiative recombination in polycrystalline LHPs with high density of defects
15 additionally competes with the radiative processes.^{1290, 1292-1294} Nanocrystalline LHP grains with
16 dimension less than 10 nm, e.g., quantum dots, quantum well and NPLs, confine charge carriers in
17 a small volume, and this enhances exciton binding energy to hundreds of meV and facilitates
18 exciton radiative recombination.^{62, 1290-1291, 1295} Moreover, the surface defects of nanocrystalline
19 LHPs can be passivated effectively using long chain molecule ligands. Quasi-2D LHP NPLs with
20 a strong quantum confinement shift the emission toward high energy even by 200 meV compared
21 to their 3D NCs counterparts.^{62, 1295} By varying the number of [PbX₆]⁴⁻ octahedral layers in these
22 APbBr₃ NPLs, their emission color can be adjusted from green to deep-blue, providing an
23 alternative pathway for blue LHP-LEDs (Figure 132a).^{17, 227, 418, 1206} Synthesis approaches have

1 achieved a level of control such that NPLs narrow thickness distributions and characterized by
 2 narrow emission spectra, can be prepared.^{62, 227, 418, 983, 1206} The presence of long alkyl chain spacers,
 3 confers also excellent stability against ambient moisture but on the other hand it blocks the
 4 injection of charge carriers into the NPLs.^{50, 1296-1298}



5
 6 **Figure 132.** (a) PL (solid) and absorption (dashed) spectra of CsPbBr₃ colloidal nanoplatelet with
 7 different thicknesses. (b) The scheme structure of LHP-LED. (c) EQE-current density
 8 characteristics of LHP-LEDs. (d) The PL intensity dependence of MAPbBr₃ film on electron
 9 number, and n₀ is the density of electron injected when the current density is 1.0 × 10⁻² mA cm⁻².
 10 Reproduced from Ref⁶². Copyright © 2018 American Chemical Society.

11

1 ***Deposition of LHP Emitter Films:*** The emissive films of most LHP-LEDs are deposited by
2 solution processing, especially the organic-inorganic hybrid ones, which mainly includes ex-situ
3 deposition using a prepared nanocrystalline LHP colloidal solution and in-situ deposition using
4 precursor solution.^{425, 1173-1174, 1178-1179} For the former, the synthesized high quality nanocrystalline
5 LHP, e.g. NPIs, is dispersed into a low polarity solvent, e.g., toluene or tetrahydrofuran, to form a
6 uniform colloidal solution for subsequent film deposition.^{1173-1174, 1179} Normally, the concentration
7 of these colloidal solutions must be high enough to deposit a continuous and uniform LHP film.
8 In the meanwhile, to get a good charge carrier transport of the deposited LHP film, the amount of
9 insulating long chain ligands is kept at a low level, although leads to a poor stability of these
10 colloidal solution, especially the NPI because of their propensity of self-assembly into stacks.^{62,}
11 ¹²³⁶ By changing the preferred orientation of LHP-NPIs into random or using a semi-conductive
12 molecular spacer, the emission from the resulting LEDs can be improved.^{1296, 1299} For the latter, all
13 precursors are resolved in a polar solvent, e.g., dimethylformamide (DMF) or dimethyl sulfoxide
14 (DMSO), to form a uniform solution for film deposition.^{418, 1178, 1227} Generally, an antisolvent
15 crystallization treatment using a low polarity solvent, e.g., toluene, or solution is adopted during
16 the film deposition.^{405, 1178, 1182, 1300} Moreover, an annealing post-treatment of the deposited LHP
17 film is also required to enhance the quality of LHP films.^{405, 1178, 1182, 1300} Besides solution
18 processing, inorganic CsPbX₃ film can also be deposited by vacuum thermal evaporation.
19 However, in this case the polycrystalline film that is obtained has high density of defects, without
20 an effective spatial confinement of excitons and charge carriers, and exhibits a much lower
21 emissive efficiency compared to the solution processed films prepared with surface passivated
22 nanoscale emitters.¹³⁰¹⁻¹³⁰⁴

1 **Device Structures and Fabrications:** The guideline of device structure design and fabrication
2 of LHP-LEDs are developed within the framework originating from OLEDs and limited by the
3 deposition of emissive layer, thus the device structures of most LHP-LEDs are simple. Normally,
4 an LHP-LED contains multilayer thin films with a total thickness of around 100-200 nm
5 sandwiched by two planar electrodes. Like other soft emitters, except rigid ITO glass, LHPs also
6 demonstrate a good compatibility with flexible substrates.

7 **Device Structures:** To avoid the near field quenching caused by electrode, in most LHP-LEDs
8 a conductive poly(3,4-ethylenedioxythiophene)-polystyrene sulfonate (PEDOT:PSS) film is
9 selected as a spacer, which also can enhance hole injection from ITO anode (Figure 132(b) and
10 Fig. 133a,b).^{425, 1173, 1178-1179} In principle, the metallic PEDOT:PSS film is also regarded as an
11 exciton quencher because of its highly electrical conductivity and interfacial defects.^{1173, 1305}
12 Therefore, an organic semiconductor film, e.g., poly(4-butylphenyldiphenylamine) (poly-TPD),
13 with low density of charge carriers is adopted as a buffer layer to eliminate the exciton quenching
14 caused by PEDOT:PSS.^{324, 1173} Moreover, this organic hole transport film is supposed to enhance
15 hole injection into the recombination zone because there is a large mismatch between the deep
16 valance band of LHPs and the Fermi level of PEDOT:PSS.^{324, 1173, 1178, 1216}

17 To get a high EQE, a balanced charge carrier injection into the recombination zone is essential.
18 In LHPs, holes and electrons have comparable mobilities, which helps to achieve a balanced charge
19 carrier in LHP-LEDs.^{13, 1179, 1306} With consideration of the high conductivity of PEDOT:PSS,
20 therefore, a high mobility/conductivity electron injection/transport layer, e.g. 2,2',2''-(1,3,5-
21 Benzinetriyl)-tris(1-phenyl-1-H-benzimidazole) (TPBi), is required to ensure a balanced charge
22 carrier injected into the LHP layer.^{324, 1173, 1178-1179} For the cathode, a thermal evaporating deposited
23 aluminium film with a buffer layer, e.g., lithium fluoride or caesium carbonate, is a popular

1 choice.^{324, 1173, 1178-1179} Additionally, ITO can also work as cathode to in an inverted structure
2 device.^{1174, 1307-1309} Correspondingly, some functional layers were also required for a balanced
3 charge carrier injection. Normally, a n-type semiconductor film, e.g., zinc oxide nanocrystals, can
4 be selected as matched electron transport layer.^{1174, 1307-1309} Drawing inspiration from the
5 PEDOT:PSS/poly-TPD combination used in normal structure devices, a polymer film, e.g.,
6 polyethyleneimine ethoxylated, is required to modify ZnO nanocrystal film before the deposition
7 of LHPs.^{1174, 1307-1309}

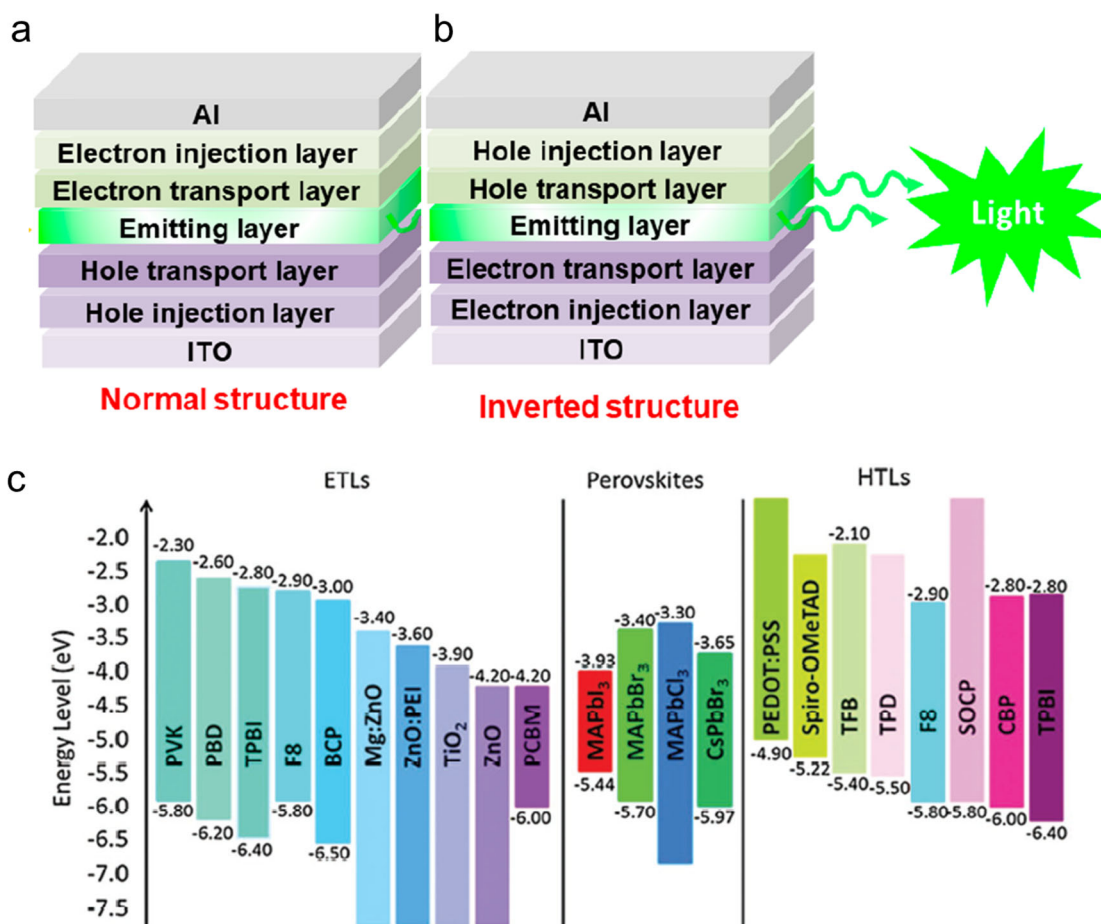
8 Without the limitation of solution processing deposition, in principle, an LHP-LED with more
9 advanced device structure can be achieved using vacuum thermal evaporating deposition. Even in
10 most solution processed LHP-LEDs, the deposition of metal electrode and other organic functional
11 layers still need a vacuum thermal evaporation. Especially, using current solution processing
12 technology, it is almost impossible to get a large-scale uniform emissive film with fine structure
13 pattern for a LED display.

14 ***Device Fabrication:*** Generally, the solution processing deposition used for LHP films in LHP-
15 LEDs includes spin-cast, ink-jet printing and slot-die coating technologies.^{1179, 1310-1311} As far, spin-
16 cast is the most popular technology used for the solution processing film deposition in various soft
17 material LED fabrication, including LHP-LEDs, QLEDs, and polymer LEDs.

18 At a practical level, for solution processing film deposition, the compatibility of film deposition
19 plays a critical role in fabricating a successful LHP-LED. Normally, it is required that the surface
20 energy of the deposited film must be higher than that of the solution used for subsequent film
21 deposition. To increase the surface energy of polymer film, a charging treatment of oxygen plasma
22 can be adopted. This however leads to the formation of surface defects that would increase the
23 non-radiative recombination of emitters. Moreover, the deposited films are required to be highly

1 passivated to withstand the solution processing of subsequent LHP film deposition. For example,
2 with an annealing post-treatment, the passivation of poly-TPD and ZnO nanocrystal film are
3 improved against subsequent solution processing on them.^{324, 1173-1174, 1178, 1216, 1307-1309} Because of
4 their ionic crystal structure, LHPs are sensitive to high dielectric constant environment. For this
5 reason, any processing of highly polar solvents onto LHPs are excluded from device
6 fabrication.^{1173, 1312-1313} Other functional layers, including top electrode, can also be deposited
7 using solution processing deposition, however, their device reliability is not as good as the thermal
8 evaporated ones.

9 For inorganic CsPbX₃ LHPs, the films can also be deposited by a co-evaporation of two
10 precursors CsX and PbX₂ or CsPbX₃ in a high vacuum chamber.¹³⁰¹⁻¹³⁰⁴ The whole device, except
11 some solution processing functional layers, e.g., PEDOT:PSS, can be deposited in a single run
12 without breaking the vacuum, which is helpful to eliminate any potential negative influence caused
13 by the atmosphere in the glovebox. In principle, the uniformity of LHP film and the reliability of
14 resulting LEDs fabricated using the vacuum thermal evaporating are higher than those of the
15 corresponding devices fabricated using solution processing technologies, especially in large scale
16 film deposition. Commonly used electron transport layers and hole transport layers are summarised
17 in Figure. 133 c) with their corresponding energy levels.⁴⁰



1
 2 **Figure 133.** Device structures of perovskite LEDs. (a) Normal structure; (b) Inverted structure.
 3 Reproduced from Ref. ¹³¹⁴ Energy level alignment of various materials used as perovskites, ETLs,
 4 and HTLs in the reported HPLEDs. Reproduced with permission from Ref.⁴⁰ Copyright 2017,
 5 Elsevier B.V.

6
 7 **Luminous Efficiency Drop:** A high EQE means a maximized output of photon number with
 8 respect to a minimized input of electrons number injected into devices, mainly including three
 9 factors for LHP-LEDs:

1 $EQE = E_{in} \cdot E_{eh} \cdot E_{rad} \cdot E_{out}$ (2)

2 In the expression above, E_{in} is the charge carrier balance factor in the recombination zone, and
3 these injected charge carriers will form excitons with a possibility of E_{eh} . The factor E_{rad} depicts
4 the fraction of the intrinsic radiative efficiency of emitters, normally, which is equivalent to the
5 PLQY of LHP emissive film. Though the emission of LHPs originates from exciton radiation, due
6 to a strong spin-orbit coupling caused by heavy lead atoms, this electron transition obeys the
7 conservation of total momenta rather than spin statistics.¹⁵⁰ The last E_{out} determines the photon
8 extraction efficiency of the device, which is dependent on the device structure and can be defined
9 as $1/(2n^2)$ (n is the refractive index of films).

10 If all charge carriers injected through electrode flow into the recombination zone, the E_{in} will be
11 unity. EQE loss related to E_{in} is caused by leakage currents which depends on device structure and
12 quality. In a low-quality device containing a large number of pinholes and trap states, the injected
13 charge carriers would flow across the device via this bypass instead of being injected into the
14 recombination zone. Due to an effective spatial confinement of nanocrystalline LHP domains, the
15 charge carriers injected into the recombination zone will meet each other with a high possibility
16 E_{eh} and form stable excitons. In a high driving current density level, the injected charge carriers
17 would pass through the device without recombination as an overflow current, resulting in a drop
18 in E_{eh} and EQE , which can be supposed to be another origin of leakage current.¹¹⁷⁹

19 The factor E_{rad} plays a dominating role in determining EQE of LHP-LEDs. At a low excitation
20 intensity level, a trap-mediated non-radiative process dominates the exciton recombination, which
21 is consistent with the low initial value of luminous efficiency, thus a high quality LHP emissive
22 film with a low density of defect is essential.^{1179, 1315-1318} By increasing the excitation intensity, the
23 exciton radiative recombination will dominate the trap-mediate process.^{1179, 1315, 1317-1318} A further

1 increase of excitation intensity will result in a multi-exciton Auger non-radiative process and
2 luminous efficiency droop (Figure 132c).^{1179, 1315, 1317-1318} In the electrically driven devices, the
3 injected charge carriers, especially the excess ones caused by imbalanced injection, will increase
4 the probability of Auger non-radiative recombination even at a low driving current density level
5 (Figure 132d).^{1179, 1319}

6 For almost of all planar multilayer structure LEDs, including OLEDs and QLEDs, most
7 generated photons will be trapped inside devices by waveguide mode and substrate mode, only
8 around 15%-20% photons can be outcoupled because of the refractive index mismatch among
9 functional layers, glass substrate and air.^{1179, 1320} Like to OLEDs, E_{out} can be enhanced using
10 periodic nano- or micro-structures, e.g., micro lens array in this kind of multilayer planner structure
11 LEDs.¹³²¹ Moreover, because of the overlap between absorption and luminescence spectra, which
12 means an equivalently prolonged lifetime of excitons, the photons trapped inside device should
13 have more chance to escape before annihilation by a recycling process.¹²⁴⁹

14 In working state of LHP-LEDs, one more factor that can result in EQE drop is the degradation
15 of LHPs emitters caused by a considerable ion migration, which can be facilitated by applied
16 electrical field and evidenced by a hysteresis dependence between driving current density and
17 driving voltage in almost all electrooptic applications based on LHPs.^{1041, 1322}

18 **Stability of LHP-LEDs:** Device operation stability is a very important consideration when
19 evaluating a LED at a practical level, and achieving a good stability is still a severe challenge for
20 LHP-LEDs.^{117, 1041, 1184, 1201} Whilst LHP-based LEDs have a similar device structure to QLEDs the
21 degradation is faster, and the degradation pathways may relate to the perovskite itself. In general,
22 the degradation mechanisms of perovskite LEDs are divided into four categories: (a) Ion
23 migration, (b) interactions with surrounding moisture and oxygen. (c) electrochemical reactions

1 and (d) interfacial reactions.¹³²³ Ion migration of halide ions in PeLED is intrinsically a defect
2 migration process which is strongly related to perovskite surface chemistry and defects.¹⁵² It leads
3 to defect creation (e.g. Frenkel defects), halide vacancy migration and lattice distortion which are
4 detrimental to spectral stability and material stability. Halide ion migration can occur both within
5 the perovskite emitting layer¹³²⁴⁻¹³²⁵ and across the organic transport layers.¹³²⁶⁻¹³²⁷ In addition,
6 LHPs are sensitive to moisture, thus high quality encapsulation is required for protecting the device
7 against the environment.^{117, 1041, 1184, 1188, 1201} The heterostructure of 2D LHP-NPIs and matrix-
8 dispersed nanoscale LHPs can suppress ion migration effectively and provide additional protection
9 for LHP emitters against environmental moisture.^{418, 1174, 1300, 1328} Moreover, as current-driven
10 devices, the structural instability induced by mechanical stress is also a severe challenge for LHP
11 emitters because of their ultralow thermal conductivity and Joule heating generated by devices
12 under operation.¹³²⁹⁻¹³³² Electroluminescence spectral stability is another challenge for colloidal
13 perovskite LEDs, especially for deep blue (~465nm) and pure-red (~625nm) emitters.¹³³³ The
14 instability of the EL spectra is primarily due to the halide segregation. Apart from ion migration,
15 electrochemical reactions between migrated perovskite and electrodes is another degradation
16 pathway during device operation. Yuan *et al* showed in bulk thin film MAPbI₃ under electrical
17 bias, the perovskite can react with electrodes to form I₂ gas and PbI₂ which make the degradation
18 irreversible.¹³³⁴ The interaction between the perovskite layer and transport layers can take place
19 without external electrical bias, for example, the acidic nature of PEDOT:PSS layer can cause
20 reactions with ITO over time upon direct contact, and the etched Sn and In ions can diffuse into
21 perovskite layers and act as traps.¹³³⁵ To suppress ion migration (halide segregation) and
22 interfacial interactions, there are many methods that have been reported, such as compositional
23 engineering, dimensional engineering, and defect passivation at NC surface and at interfaces

1 between emitting layers and transport layers.⁵⁰ However, currently there is no individual strategy
2 can passivate all defects and prohibit device instability, it is crucial to understand and utilize
3 multiple strategies to further improve the stability of PeLEDs.

4 **Summary and outlook of perovskite LEDs**

5 LHP-LEDs have achieved incredible progresses in past few years, which excellent features,
6 including highly efficient light emission, high color purity, ultrawide color gamut, low cost of raw
7 materials and fabrications as well as good compatibility with existing OLEDs/QD-LEDs
8 manufacturing technologies. In recent years, OLEDs, QD-LEDs, micro-LEDs and other screenless
9 display technologies are competing with each other. Especially, the great similarity between LHP-
10 LEDs and CdSe QD-LEDs from device fabrication procedures to output features in working state
11 suggests a strong exclusiveness as prospective applications.

12 However, before evolving into practical products, LHP-LEDs need to overcome some critical
13 bottlenecks, such as the concern of the toxic lead atoms, poor operation stability and large-scale
14 panel fabrications, which has been attracting great attentions and some impressive progresses have
15 been achieved thus far. Until now, the performances have been achieved by the LEDs with non-
16 lead perovskite emitters still close to nothing compared to the lead counterparts, and as divertive
17 species with formula of $A_2BB'X_6$ some characters of non-lead perovskites are different from the
18 classical LHPs ABX_3 . The operation stability of LHP-LEDs is a complicated issue because the
19 device contains multilayer thin films and resulting heterogeneous interfaces. The extrinsic factors,
20 including oxygen, moisture and others caused by ambient environment, can be fixed by following
21 the well-established programmes developed by OLEDs. The degradation of LHP emitters should
22 be intrinsic among all possible factors, especially, which can be accelerated by applied electrical
23 current and field in LEDs. The large scale panel manufacturing is not an exclusive problem of

1 LHP-LEDs, which also challenges for other solution processing LEDs, such as QD-LEDs and
2 polymer LEDs. A nanoscale uniformity of all functional films contained in the LHP-LEDs is
3 essential, because the pinhole and any other non-uniform morphology will lead to a highly deviated
4 distribution of electric current flow and resulting brightness. A LHP-LED demo with spot size of
5 square millimetres can be fabricated simply by using spin-cast. However, when the spot area is
6 increased to square centimetres level and even larger size, the deposition of such a large area film
7 with a nanoscale uniformity is almost impossible by using current technologies, including spin-
8 cast, inkjet printing and others.

9 Thus far, most works on LHP-LEDs have focussed on the enhancement of characteristic
10 parameters, especially EQEs, at the technical level, however, the understanding of such
11 enhancements are chained to the framework borrowed from OLEDs and QD-LEDs to a great
12 extent. And, actually, the performance enhancements of LHP-LEDs seem to have plateaued in the
13 past years. Therefore, more fundamental work on LHP-LEDs is required for a better understanding
14 of the working mechanism of such a new generation LEDs. This would provide a guideline for the
15 device works at the technical level and trigger a breakthrough in the device performance
16 improvement in the future. For example, the above-mentioned stability issue of LHP-LEDs,
17 though the same LHP emitters demonstrate a great stability under optical excitation, even in
18 ambient atmosphere.

19

20 **11.3 PHOTODETECTORS AND FIELD-EFFECT TRANSISTORS**

21 Photodetectors convert light signals to electrical signals, which is critical for a diverse range of
22 applications, such as sensors and optical communication devices.¹³³⁶ Lead-halide perovskites are
23 promising materials for photodetectors with high figure-of-merit (*e.g.*, responsivity and temporal

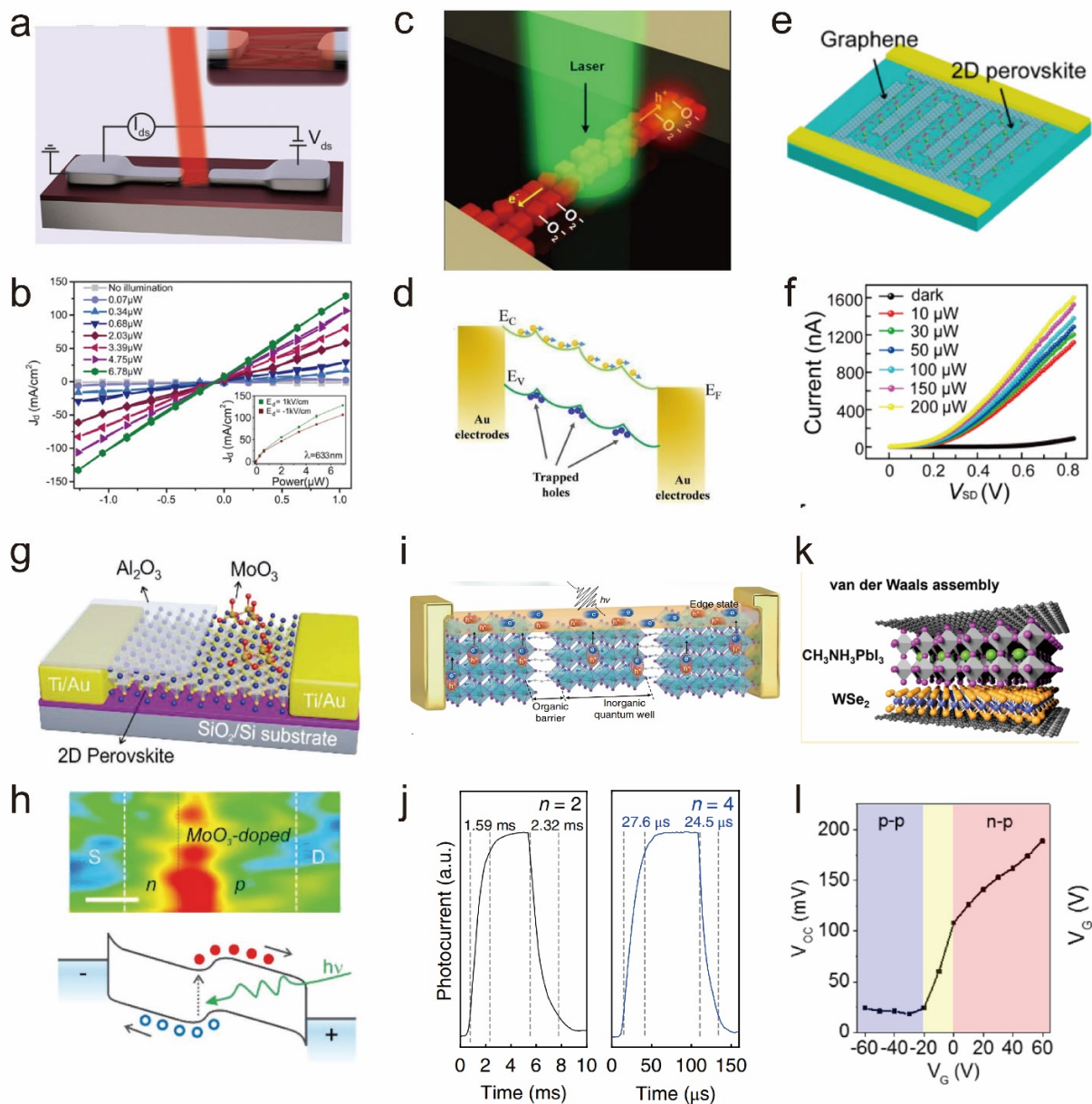
1 response) owing to their strong optical absorption, high quantum efficiency and ultra-long carrier
2 diffusion length.^{1078, 1337-1338} The first perovskite photodetectors reported were based on
3 polycrystalline film, which indicates highest photo-responsivity of $\sim 3.5 \text{ A W}^{-1}$ at 365 nm in the
4 range of visible to the near-infrared region.¹³³⁹ However, owing to polycrystalline structure,
5 numerous crystal boundaries and defects exist in the perovskite film, which would serve as
6 recombination and scattering centres in carrier dynamics, limiting the performance of the
7 perovskite-based photodetectors.¹³³⁹⁻¹³⁴⁰ Low-dimensional perovskite nanocrystals including
8 nanocubes, nanowires or nanorods (1D), and nanosheets (2D) have recently been developed and
9 tested high-performance photodetectors. In particular, it has been demonstrated that lower defect
10 density can be achieved than in their 3D counterparts, such as through surface passivation.

11 Fully inorganic CsPbX_3 QD based photodetectors have achieved high on/off ratio photocurrent
12 ratios of over 10^5 , thereby enabling effective switching.¹³⁴¹ In order to increase the performance
13 of the inorganic perovskite NC photodetectors, Kwak *et al* and Wang *et al* introduced conductive
14 graphene as charge transport pathways to enhance charge transfer, reaching a responsivity over \sim
15 10^8 A W^{-1} .^{249, 1342} However, in general, perovskite NCs are coordinated with long-chain organic
16 ligands, which could hinder charge transport and therefore lead to slow photoresponses ($> 1 \text{ s}$).
17 With regard to fast carrier dynamics, it is crucially important to optimize ligand molecular and
18 device configuration. In this framework, conductive nanonets made of carbon nanotubes (CNTs)
19 in CsPbBr_3 QD/CNT composites were used to improve charge extraction and transport, by which
20 fast-response photodetectors with rise time of 0.016 ms have been achieved.¹³⁴³

21 Up to now, there have only been a few reports of MAPbI_3 -based photodetectors due to the
22 limited stability of MAPbI_3 .⁵⁰¹ However, 1D solid hybrid organic-inorganic perovskite NCs
23 remain attractive as efficient carrier transport pathways in photodetectors. Figures 134a,b present

1 the perovskite photodetectors based on solution processed 1D MAPbI₃ NWs with a responsivity
2 of 5 mA W⁻¹ and a response time of ~ 0.3 ms.¹³⁴⁴ However, the defects and grain boundaries in
3 MAPbI₃ NWs lead to scattering effects which significantly reduces the responsivity. The defect
4 density in MAPbI₃ NWs was reduced by surface passivation through OA soaking treatment.¹³⁴⁵
5 As a result, larger responsivities (4.95 A W⁻¹) and a shorter response times (< 0.5 ms) were
6 achieved. To further enhance the photodetector performance, Deng *et al* developed a blade solution
7 casting method to increase the crystallinity of MAPbI₃ NW.¹³⁴⁶ As the blade moves against the
8 MAPbI₃ solution on the substrate, MAPbI₃ precipitates out at the triple-phase (solid-liquid-solvent
9 vapour) interface upon solvent evaporation and continues to self-organise to form 1D NWs along
10 the direction the blade moves in. The as-fabricated MAPbI₃ NW photodetector possesses a high
11 responsivity over 13 A W⁻¹ due to the high perovskite crystal quality. Therefore, well-controlled
12 gas-liquid-solid triple-phase contact within pre-patterned substrates could be a key factor to
13 produce large-scale high-quality NW crystals and practical perovskite NW photodetectors. Feng
14 *et al.* developed a template-assisted method for the production of well-aligned single crystal
15 CsPbBr₃ NW arrays, which enabled a surprisingly high responsivity of ~1400 A W⁻¹.¹³⁴⁷ Dai *et al.*
16 introduced an oxygen-related hole trapping state on the surface of the NCs, causing surface band
17 bending, which results in an internal electric field that can spatially separate the photogenerated
18 electron-hole pair, thereby suppressing the carrier recombination, as shown in Figures 134c,d.
19 Additionally, polarized light detection can be achieved in the photodetectors based on the strict
20 alignment of CsPbBr₃ NW arrays along the [100] orientation.¹³⁴⁷ All these pioneering works would
21 pave the way for the realization of additional functionality in the perovskite NW photodetectors.

22



1
2
3 **Figure 134.** Photodetectors and field-effect transistors based on perovskite NCs. (a) Schematic
4 diagram of 1D MAPbI₃ wire photodetectors, and (b) *I-V* curve of the MAPbI₃ wire photodetectors
5 under irradiation with laser wavelength of 633 nm.¹³⁴⁴ (c) Schematic diagram of 1D aligned
6 CsPbX₃ NCs photodetectors, and (d) Schematics of carrier dynamic in perovskite 1D NCs
7 photodetectors under illumination.¹³⁴⁸ (e) Schematic diagram of 2D perovskite/graphene

1 photodetectors, and (f) I - V curve of the 2D $(\text{C}_4\text{H}_9\text{NH}_3)_2\text{PbBr}_4$ /graphene heterostructure
2 photodetectors in the dark and under various illumination intensities with a 470 nm laser
3 irradiation.¹³⁴⁹ (g) Schematic MoO_3 -doped 2D perovskite nanosheet photodetector, and (h)
4 Photogenerated current mapping in Source-Drain channel and schematic band diagram under $V_d =$
5 $+ 1$ V under irradiation.¹³⁵⁰ (i) Schematic diagram carrier dynamics in the single-crystalline (101)-
6 oriented layered perovskite photodetector, and (j) photo-response of 1D layered perovskites array
7 with $n=2$ and 4.¹³⁵¹ (k) Schematic of $\text{CH}_3\text{NH}_3\text{PbI}_3/\text{WSe}_2$ heterojunction field transistor, and (l)
8 The V_g - V_{OC} curve extracted from source and drain channel in $\text{CH}_3\text{NH}_3\text{PbI}_3/\text{WSe}_2$ heterojunction
9 at 77 K.¹³⁵²

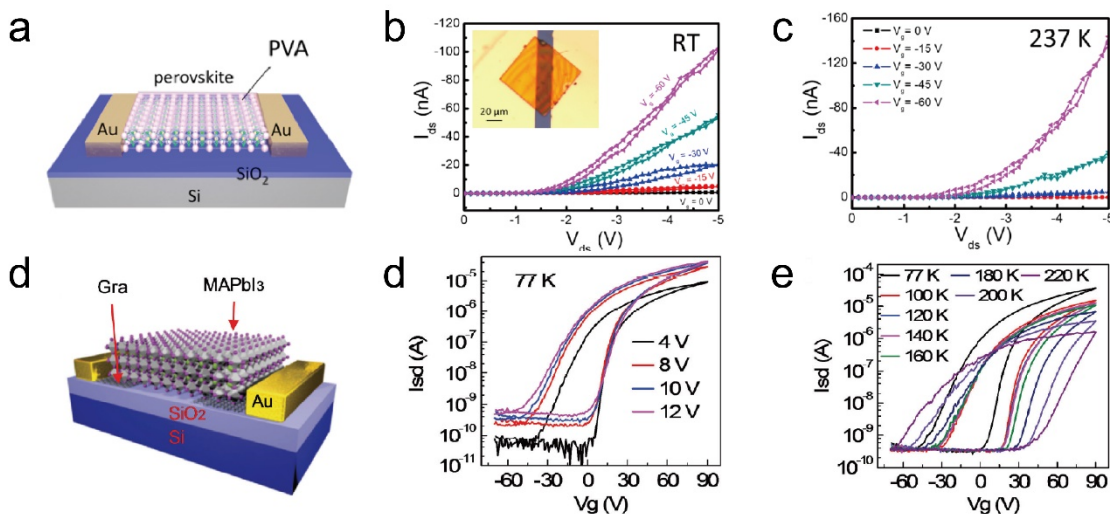
10

11 High quality 2D perovskite NCs have been considered to be effective photoactive media for high
12 performance photodetectors due to their large surface area to volume ratio and potential integration
13 with other 2D materials and conventional silicon circuits.¹³⁵³ Essentially, there are two major
14 working principles for photodetectors based on 2D perovskite NCs, *i.e.*, photoconductive and
15 photovoltaic effects. A typical structure for perovskite photoconductors involves the perovskite
16 sandwiched between two gold electrodes. 2D perovskite photoconductors typically deliver a
17 responsivity of 22 A W^{-1} under visible laser illumination, which is superior to those
18 photodetectors based on 3D perovskite films.¹³⁵⁴ The integration of 2D perovskites with other 2D
19 conductive materials can be an efficient approach to improve photodetector performance. In
20 particular, heterostructure photodetectors consisting of 2D perovskite $(\text{C}_4\text{H}_9\text{NH}_3)_2\text{PbBr}_4$ and
21 interdigitated graphene electrodes were demonstrated, as shown in Figures 134e,f, in which
22 graphene would be favorable for transporting photocarriers and improving stability in air.¹³⁴⁹ This
23 device gives a high responsivity of 2100 A W^{-1} .¹³⁴⁹ For devices operating based on the photovoltaic

1 effect, one or more junctions are normally required. In this regard, Ou *et al* fabricated a lateral
2 junction by partially doping the n-type pristine perovskite nanosheet.¹³⁵⁰ A large depletion region
3 with a few micrometers width formed in which a lateral built-in electric field facilitates the
4 separation and transport of photogenerated carriers. As a result, these photodetectors have a
5 responsivity of $\sim 1.42 \text{ A W}^{-1}$ and an EQE of $\sim 3.93\%$ at zero bias, much higher than those of the
6 pristine 2D perovskite device. A single-crystalline 2D Ruddlesden–Popper perovskite nanowire
7 with a pure (101) crystallographic orientation has been used to fabricate ultrasensitive
8 photodetectors, as shown by Figure 134i.¹³⁵¹ The organic layers act as insulating barriers which
9 significantly reduce the dark current, whereas exposed crystalline perovskite layers function as
10 charge conductive pathway for exciton dissociation, free-carrier conduction and charge injection,
11 therefore giving an averaged responsivity of over 10^4 A W^{-1} and a detectivity of over 7×10^{15} jones.
12 Apart from using dopants, the combination of 2D perovskites with other 2D semiconductors could
13 also create a built-in electric field to form a *p-i-n* junction.^{1352, 1355} A graphene/WSe₂/2D
14 MAPbI₃/graphene device was assembled to work as a photodetector with ultrahigh on/off
15 photocurrent ratios ($> 10^6$) under negative bias.

16 Beyond photodetectors, the unique gate-modulated features due to the ambipolar nature of 2D
17 perovskites under different biases underpin their great promise for transistors. The reported
18 mobilities of hybrid perovskite film-based transistors are mostly below $1 \text{ cm}^2 \text{ V}^{-1} \text{ s}^{-1}$, which are
19 much lower than their high intrinsic mobility $\sim 200 \text{ cm}^2 \text{ V}^{-1} \text{ s}^{-1}$ due to unavoidable ion migration
20 at room temperature.¹³⁵⁶⁻¹³⁶⁰ In this regard, these results would suggest that perovskite NCs with
21 lower ion vacancy and grain boundary densities are promising for achieving improved
22 performance. As shown in Figure 135a-c, Huo *et. al.* developed high-quality ultrathin boundary-
23 free CsPbBr₃ platelets by using van der Waals epitaxy and dry transfer processes, yielding FET

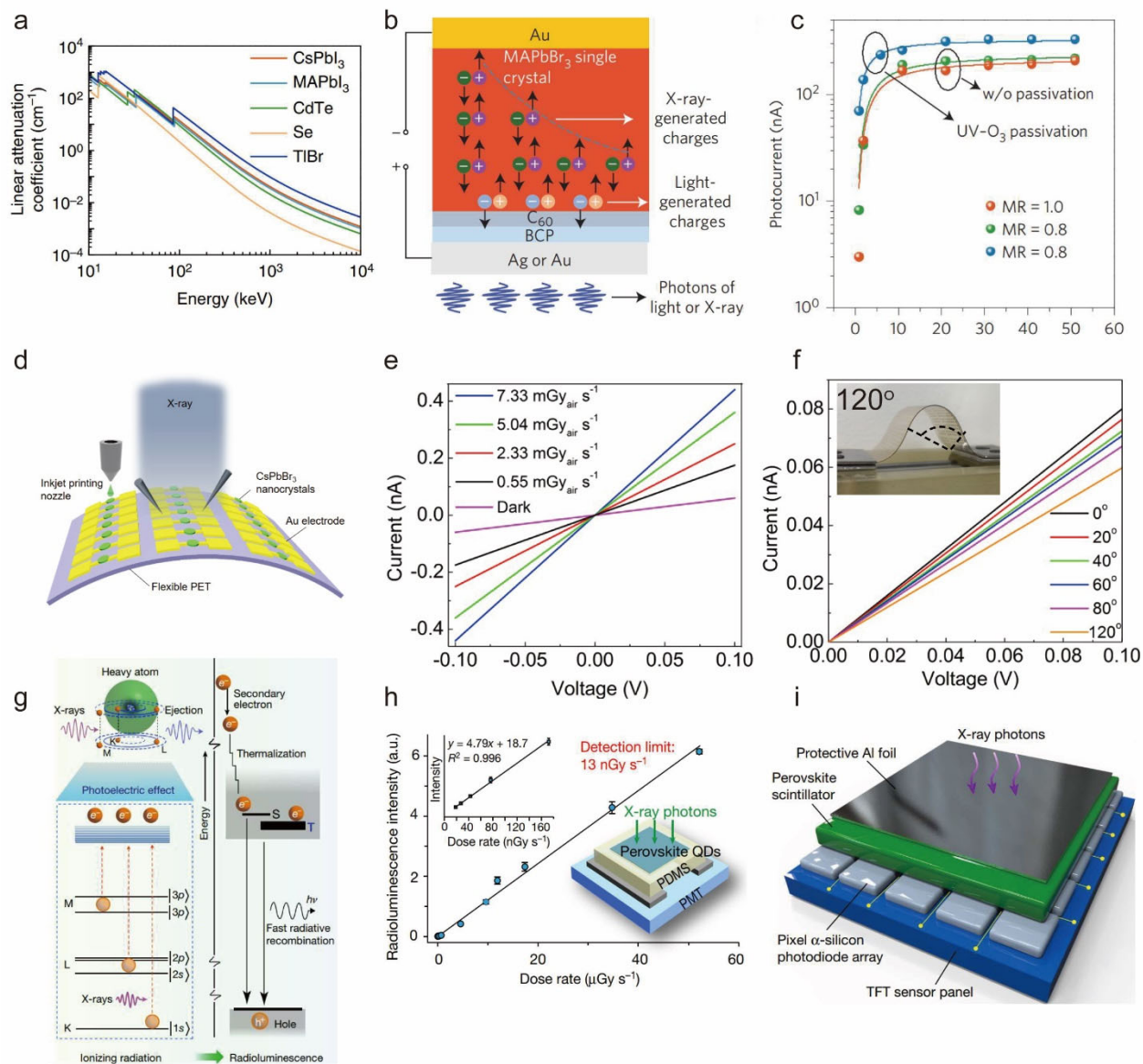
1 hole mobilities of 0.32 and $1.04 \text{ cm}^2 \text{ V}^{-1} \text{ s}^{-1}$ at room temperature and 273 K , respectively.¹³⁶¹ Yu
 2 *et. al.* further enhanced surface adhesion between thin single crystal MAPbX₃ and pre-patterned
 3 FET substrates to reduce surface contamination, reaching record electron and hole mobilities of
 4 1.5 and $4.7 \text{ cm}^2 \text{ V}^{-1} \text{ s}^{-1}$ at room temperature, respectively. Moreover, Duan *et al.* systematically
 5 investigated transport properties of the high-quality perovskite materials with van der Waals
 6 contacts such as graphene and gold.^{1352, 1362-1364} As shown in Figure 135d-e, Li *et. al.* demonstrated
 7 temperature-dependent transfer characteristics of graphene-contact MAPbI₃ microplate based
 8 FETs with estimated electron mobilities of $4 \text{ cm}^2 \text{ V}^{-1} \text{ s}^{-1}$ at 77 K .¹³⁶⁴ However, by achieving
 9 atomically flat contacts, the as-fabricated CsPbBr₃ FETs showed hall mobilities $> 2,000 \text{ cm}^2 \text{ V}^{-1}$
 10 s^{-1} at 80 K and ultralow bimolecular recombination coefficients of $3.5 \times 10^{-15} \text{ cm}^3 \text{ s}^{-1}$.¹³⁶²
 11 Improving contacts with electrode and dielectric layers in FETs would be effective strategies to
 12 increase the performance of the perovskite NC-based FETs. However, exploration of perovskite
 13 NCs with lower ion vacancy densities will be essential for achieving practical FETs.¹³⁶⁵



14
 15 **Figure 135.** Perovskite NC based FETs. (a) Schematic illustration of CsPbBr₃-based FETs
 16 fabricated by using dry transfer method. Output characteristics of the as-fabricated CsPbBr₃ FETs
 17 under gate voltages in the range from -60 - 0 V at (b) room temperature and (c) 237 K .¹³⁶¹ (d)

1 Schematic illustration of the graphene-contact MAPbI₃ microplate-based FETs. (d) Transfer
2 characteristics of the as-fabricated MAPbI₃ FETs under different gate voltages from 4-12 V at 77
3 K. (e) Transfer characteristics of the as-fabricated MAPbI₃ FETs under source-drain bias of 10 V
4 at different temperatures from 77-220 K. ¹³⁶⁴

5
6 Beyond visible photodetectors and FETs, metal-halide perovskites are also promising candidates
7 for the detection of high-energy ionizing radiation, such as X-rays and gamma-rays. Radiation
8 detectors with high sensitivities and small lowest detectable dose rates can potentially be achieved
9 with low cost due to the solution processability of the metal-halide perovskites and their high-Z
10 elements.¹³⁶⁶⁻¹³⁶⁸ For X-ray detectors, the ability to control charge carrier movement is key to their
11 functionality. Charge generation, transport and separation all must occur in the perovskite
12 nanocrystals sequentially upon X-ray irradiation.¹³⁶⁹⁻¹³⁷⁰ In particular, favorable optoelectronic
13 properties, such as strong absorption, tunable bandgap, long carrier diffusion length and large bulk
14 resistivity in lead halide perovskite NCs also contribute to improved sensitivity.¹³⁷¹ Figure 136a
15 shows the linear X-ray attenuation coefficient of different materials, suggesting that the perovskite
16 materials are superior over current commercial materials for multiple solid-state applications.¹³⁷⁰



1
2 **Figure 136.** High-energy ionizing radiation detectors based on perovskite NCs. (a) Linear
3 attenuation coefficient of MAPbI_3 , MAPbBr_3 , CdTe , Se , and TlBr in the 10-10000 KeV energy
4 range.¹³⁷⁰ (b) Schematic configuration of the cross-section view of single crystal X-ray detector.
5 (c) Photocurrent of MAPbBr_3 single-crystal devices with different molar ratios and surface
6 passivation procedure versus electrical bias.¹³⁷² (d) Schematic diagram of the flexible X-ray
7 detector arrays based on inkjet-printed CsPbBr_3 NCs on PET substrate. (e) Dark current and
8 photocurrent of the CsPbBr_3 NCs X-ray detectors under different X-ray dose rates with 0.1V bias

1 voltage. (f) I - V curves of the CsPbBr₃ NCs X-ray detectors at various bending angles with the X-
2 ray irradiation of 7.33 mGy_{air} s⁻¹ and 0.1 V bias voltage.³⁷⁶ (g) Hypothesis of working principle of
3 a CsPbBr₃ NCs based X-ray scintillation. In general, photoelectric ionization, thermalization and
4 fast radiative recombination take place upon X-ray illumination in lead halide perovskite NCs. (h)
5 Radioluminescence intensity of a CsPbBr₃-based scintillator versus dose rate The inset in top left
6 presents radioluminescence profiles in the low dose rate range. (i) Schematic illustration of a
7 prototype CsPbBr₃ NCs-based flat-panel X-ray imaging system.¹³⁷³

8
9 In general, X-ray detectors could be classified as semiconductor-based direct and scintillator-
10 based indirect devices. Solution-processed MAPbI₃ films were first used for X-ray detection by
11 directly recording photogenerated current in both photovoltaic and photoconductive devices.¹³⁷⁴
12 Owing to the heavy Z elements (Pb and I), high X-ray sensitivity and ($\sim 25 \mu\text{C mGy}_{\text{air}}^{-1} \text{cm}^{-3}$) and
13 responsivity (1.9×10^4 carriers/photon) were demonstrated, which is superior to amorphous a-Se
14 based X-ray detectors. Similar to visible photodetectors, the performance of X-ray detectors could
15 be dramatically improved by interfacial engineering.¹³⁷⁵ As shown in Figure 136b and c, by using
16 surface defect passivation processes, Wei *et al.* developed a hard X-ray detector using high-quality
17 single crystal MAPbBr₃, which would enhance charge extraction efficiency and therefore yield a
18 high sensitivity ($\sim 80 \mu\text{C Gy}_{\text{air}}^{-1} \text{cm}^{-2}$) and a lowest detectable dose rate ($\sim 0.5 \mu\text{C mGy}_{\text{air}} \text{s}^{-1}$) at
19 near zero bias.¹³⁷² The as-fabricated MAPbBr₃ X-ray detectors provide not only a four times higher
20 X-ray sensitivity but also ~ 100 -fold reduction in the lowest detectable dose rate than a-Se based
21 X-ray detectors.¹³⁷² Moreover, the record-high X-ray sensitivity could be further promoted up to
22 $\sim 50000 \mu\text{C Gy}_{\text{air}}^{-1} \text{cm}^{-2}$ in thick hot-pressed CsPbBr₃ quasi-particle film with same crystal
23 orientation and thickness of several hundreds of micrometers.¹³⁶⁸ Alternatively, interface

1 engineering would be suggested as an effective way to minimize the dark current upon X-ray
2 irradiation. Park and co-workers demonstrated a spin-cast MAPbI₃-based X-ray detector
3 comprised of polyimide(PI)-MAPbI₃ layer as the hole-transporting pathway and PI-MAPbBr₃ as
4 hole-blocking pathway, producing broad X-ray absorption range and a large sensitivity over 10
5 $\mu\text{C mGy}_{\text{air}}^{-1} \text{cm}^{-2}$.¹³⁷⁶ Strategically, low-cost patterning perovskite NCs on flat or flexible
6 substrates is of great importance for scale production of printable and flexible perovskite-based X-
7 ray detectors. As shown in Figure 136b. Liu *et al.* demonstrated flexible soft X-ray detectors array
8 based on CsPbBr₃ NCs film by using inkjet printing.³⁷⁶ Apart from a reasonably high sensitivity at
9 low X-ray dose rate ($\sim 17.2 \mu\text{C mGy}_{\text{air}} \text{s}^{-1}$, see Figure 136e), the as-fabricated perovskite flexible
10 devices only lose 25% electrical signal at bending angle over 120° (see Figure 136f) and sacrifice
11 only 12% current after 200 bending circles.

12 Perovskite NC scintillators have also emerged as commercially competitive indirect converters
13 for nondestructive X-ray detectors.^{1367, 1377} Chen *et al* demonstrated fully-inorganic perovskite NC
14 based scintillators for X-ray imaging.¹³⁷³ Due to highly emissive triplet excited states, fast radiative
15 recombination and high quantum efficiency from CsPbBr₃ NCs, the as-fabricated scintillators have
16 a rapid response time of $\sim 46 \text{ ns}$ and a low X-ray detection limit of 13 nGy s^{-1} (~ 400 times lower
17 than typical X-ray diagnostics), as indicated in Figure 136g and h.¹³⁷³ The as-fabricated prototype
18 CsPbBr₃ NCs-based flat-panel X-ray imaging system is desired for dynamic real-time X-ray
19 imaging when exposed to a low X-ray dose of $15 \mu\text{Gy}$, as shown by Figure 136i. In addition, very
20 recent reports indicated that embedding emissive CsPbBr₃ NCs in host matrices such as Cs₄PbBr₆
21 and plastic waveguides is a very effective approach to produce stable and low optical loss
22 scintillators for X-ray detectors.¹³⁷⁸⁻¹³⁷⁹ Moreover, lead-free perovskites have also been used in the
23 fabrication of X-ray detectors.^{902, 1380} For example, $(\text{C}_8\text{H}_{17}\text{NH}_3)_2\text{SnBr}_4$ 2D layered perovskites

1 with absolute near-unity PLQY and a large Stokes shift , have been applied in scintillators for
2 green X-ray imaging applications.¹³⁸⁰ In another work, Zhu *et. al.*¹¹⁸¹ have demonstrated the
3 scintillators based $\text{Cs}_2\text{Ag}_{0.6}\text{Na}_{0.4}\text{In}_{0.85}\text{Bi}_{0.15}\text{Cl}_6$ (PL lifetime: $1.3 \mu\text{s}$) with enhanced light yield of
4 $39,000 \pm 7000$ photons/MeV as compared to that of perovskite colloidal CsPbBr_3 materials,
5 however, the lead free perovskite materials in general suffer from long decay time, which are
6 required further material optimization. More importantly, most reported the reported lead-free
7 based X-ray detectors are based on bulk single crystals or 2D layered perovskites while the
8 corresponding NC based devices are yet to be realized. In summary, the field of perovskite-based
9 visible light and X-ray detectors is a very fast-moving research area toward the realization of
10 various applications including integrated optoelectronic devices, sensing and medical radiography.
11 Among all, scintillator-based indirect strategy is more promising in low-cost X-ray imaging system
12 by combing current CMOS system and facile preparation methods.

13 **Summary and outlook on perovskite photodetectors**

14 Owing to their strong attenuation of visible and high-energy photons, high photoluminescence
15 quantum yields and ambipolar charge transport, lead-halide perovskites have been demonstrated
16 as promising photodetectors, FETs and X-ray/gamma-ray detectors. Among these applications, it
17 has been shown that nanostructuring has delivered benefits in terms of performance or
18 compatibility with flexible substrates. In photodetectors, perovskite nanocrystals has demonstrated
19 improved performance over 3D perovskite thin films through ^{surface} passivation to reduce non-
20 radiative recombination. On/off ratios exceeding 10^5 have been achieved in photodetectors based
21 on CsPbX_3 NCs. Blending with conducting graphene or CNTs led to high responsivities of 10^8 A
22 W^{-1} and fast response times of 0.016 ms by improving carrier extraction. Furthermore, by
23 synthesizing CsPbBr_3 NWs that are well aligned, responsivities as high as $\sim 1400 \text{ A W}^{-1}$ have been

1 achieved, as well as polarized light detection. Future improvements in performance will depend
2 on careful control over the interfaces between the perovskite and contacts, as well as control over
3 the distribution of organic ligands, which could reduce dark current but could also increase
4 response times if placed inappropriately such that they reduce charge extraction.

5 The ambipolar nature of charge transport in lead-halide perovskites has been taken advantage of
6 in FET applications. A key challenge is ion migration in perovskites, which modulates the field-
7 effect mobility to well below the intrinsic mobility. Grain boundary density, as well as interfaces
8 with contacts play an important role. Future work should focus on improved contact and dielectric
9 layers, as well as synthesis routes to reduce the density of vacancies to reduce ion migration.

10 Finally, the high average atomic number in lead-halide perovskites allows them to strongly
11 attenuate X-ray and gamma rays, and improved performance over industry-standard amorphous
12 selenium has been demonstrated. Although full attenuation requires the use of thick single crystals,
13 NC-based perovskites has been shown to demonstrate reasonable performance as solid-state X-ray
14 detectors, but with the added advantage of being solution processable on flexible substrates.
15 CsPbBr₃ NCs have also been shown to be effective X-ray scintillators, owing to the high quantum
16 efficiency, fast radiative recombination and highly emissive triplet excited states.

17

1 **11.4 PEROVSKITE NANOCRYSTAL SOLAR CELLS**

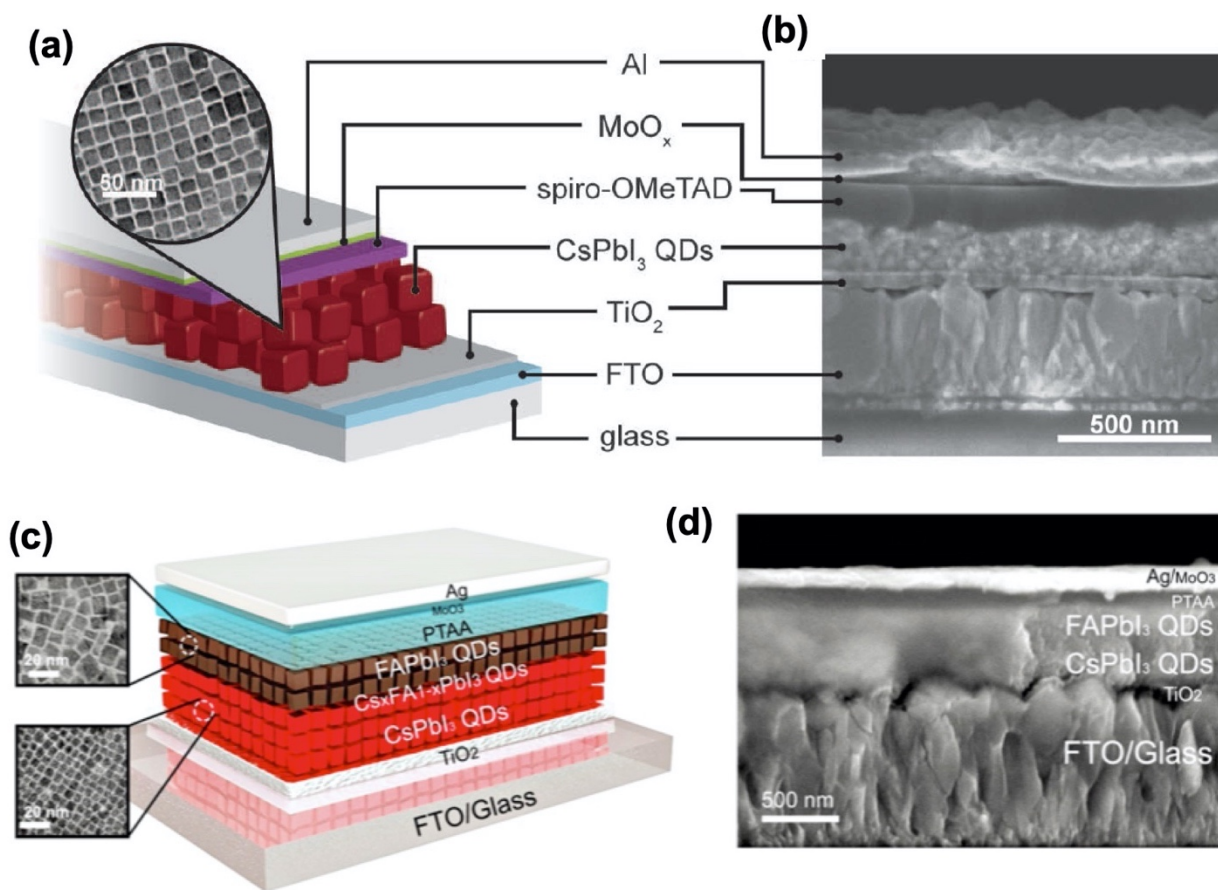
2 **Lead-Halide Perovskite NCs**

3 Lead-halide perovskites have brought about a revolution in thin film photovoltaics. In a similar
4 manner, lead-halide perovskite NCs have very recently also brought about a revolution in quantum
5 dot (QD) solar cells.^{90, 115, 187, 1381-1387} Perovskite NCs can utilize surface energy for improving
6 phase stability, have different, but also low cost solution-based fabrication processes, and enable
7 a platform to better understand and engineer the properties of MHPs, such as through molecular
8 surface/grain passivation, achieving higher PLQY, formation of perovskite heterojunctions, etc.⁹⁰
9 Quantum confinement effects, while perhaps less pronounced than in the Pb chalcogenides, are
10 still prevalent in Pb halide perovskites which have similar Bohr radii as Cd chalcogenides. Thus
11 perovskite NCs with relatively large diameters (>10 nm) are best characterized as in the
12 intermediate confinement regime.¹³⁸⁸⁻¹³⁸⁹

13 An interesting aspect of halide perovskite NCs is the role the surface energy plays in the
14 stabilization of certain crystalline phases that are not stable in their bulk counterparts at room
15 temperature. Perhaps a reason why researchers have broadly overlooked halide perovskites as a
16 semiconductor system for the past 80 years is the limited number of A-site cations needed stabilize
17 Pb-halides as a perovskite. Cs⁺ is typically too small to promote CsPbI₃ into the octahedral corner-
18 sharing perovskite phase, and thus a slightly larger but uncommon organic cation, such as
19 methylammonium, is required to achieve the tolerance factor needed to achieve the perovskite
20 structure. For the interest of single junction solar cells, a bandgap as close as possible to 1.3 eV is
21 preferred in order to maximize the potential efficiency as predicted by the Shockley-Queisser
22 analysis.¹³⁹⁰ Thus CsPbI₃, MAPbI₃ and FAPbI₃,¹³⁹¹ are the most common conventional perovskite
23 structures of which CsPbI₃ and FAPbI₃ are especially interesting. The former by the inorganic

1 nature with higher temperature stability and the later also presenting higher stability than MAPbI₃,
2 and the narrowest bandgap of 3D iodine perovskites. As stated above, pure composition CsPbI₃
3 and FAPbI₃ suffer from cations either too small or too large to preserve the stability of the
4 photoactive perovskite black phase, converting into the less photoactive yellow phase at room
5 temperature in bulk materials.^{187, 1391-1392} However, by reducing the perovskite size to <20 nm, the
6 contribution of the surface energy (namely tensile strain) can influence the stability of the phase,
7 promoting the formation of the black perovskite phase of CsPbI₃ and FAPbI₃.^{187, 1393-1394} Ironically,
8 at the nanoscale, MAPbI₃ (with the most ideal A-site cation radius for bulk compounds) has the
9 lowest stability.¹³⁹⁵ There are phase related nuances of perovskite NCs where the transitions among
10 the α , γ , and δ perovskite phase can be size, composition, and temperature dependent.^{1389, 1396}

11 Beyond phase stabilization of the building blocks needed for perovskite QD solar cells, the next
12 challenge is preparing QD films thick enough to absorb incident light, whilst simultaneously
13 having sufficient transport properties to harvest the photogenerated charges. Low polarity solvents
14 such as methyl acetate (MeOAc) or ethyl acetate (EtOAc)^{187, 1397} preserve the stability while
15 removing or replacing surface ligands¹³⁹⁸ and have permitted the first report on perovskite NC
16 solar cells which showed power conversion efficiencies (PCEs) exceeding 10%.¹⁸⁷ Here, a layer
17 of few hundred nm of CsPbI₃ NCs were sandwiched between TiO₂ and spiro-OMeTAD, which act
18 as electron and hole selective contacts respectively, see Figure 137a,b. It was found that the CsPbI₃
19 NC-based solar cell devices showed improved operational stability as well as tolerance to higher
20 relative humidity levels.



1
 2 **Figure 137.** (a) Schematic of a perovskite QD solar cell with halide perovskite NCs as the light
 3 absorber and (b) the corresponding SEM image of an exposed cross-section. Reproduced with
 4 permission from Ref. ¹⁸⁷ Copyright AAAS. (c) Schematic of a perovskite QD solar cell employing
 5 two compositions which have been shown to form a charge separating heterostructures¹³⁹⁹ and (d)
 6 the corresponding cross sectional SEM image. Reproduced with permission from Ref. ¹⁴⁰⁰
 7 Copyright American Chemical Society.

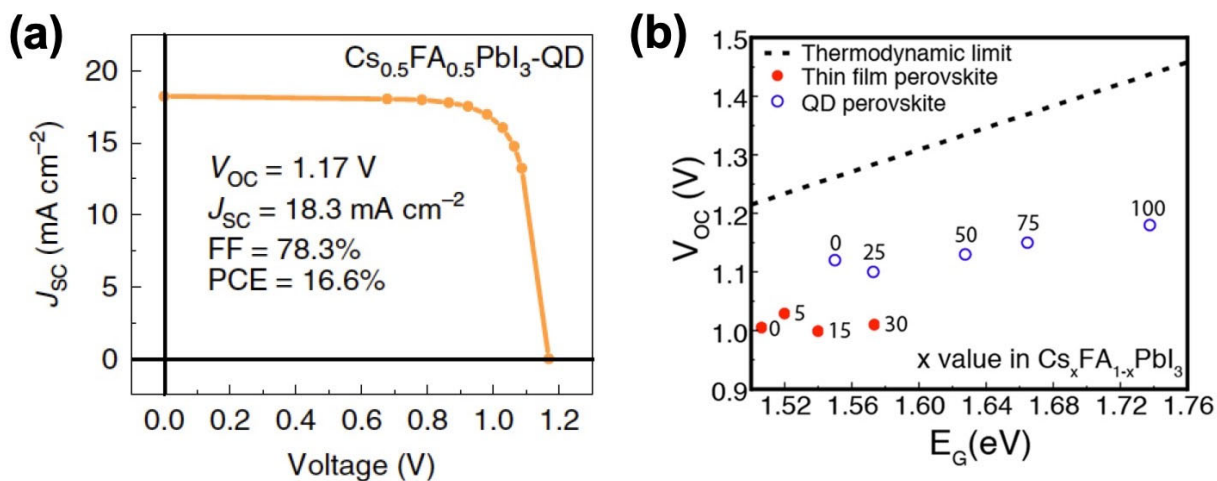
8
 9 The high crystallinity of colloiddally grown perovskite NCs reduces non-radiative recombination
 10 pathways, reflected by an enhancement in the PLQY, especially if the surface states of NCs are
 11 properly passivated.¹⁴⁰¹⁻¹⁴⁰² This property is especially attractive for the development of
 12 photocatalytic systems,^{45, 1403} optoelectronic devices¹⁴⁰⁴ and also for photovoltaic applications.¹³⁸⁷

1 The increase in PLQY to values higher than 80%, in conventional NCs, has been a process that
2 has required a couple of decades of research.¹⁴⁰² In contrast, immediately following the first report
3 of perovskite NCs⁶⁸ were reports with PLQY beyond 80%^{15, 26} and soon after reports of NCs with
4 PLQYs near unity.¹⁴⁰⁵ Low non-radiative recombination is necessary for photovoltaic devices with
5 high open circuit voltage, V_{oc} .¹⁴⁰⁶ Because of this, halide perovskite QD solar cells presents
6 outstanding V_{oc} , with several reports showing values greater than 1.25 V with up to 90% of the
7 thermodynamically limited V_{oc} demonstrated.^{195, 1407-1409}

8 While low non-radiative recombination ensures a high V_{oc} , achieving high efficiencies also
9 require good transport properties of the photogenerated charges, along with an absorber layer thick
10 enough to harvest all available incident light. A critical component fundamental for eliminating
11 non-radiative recombination in colloidal NCs in general and of perovskite NCs in particular is the
12 passivation of the NC surfaces with organic capping ligands. However, these organic ligands
13 hinder charge transport. Therefore, a balance is required for proper passivation, such that the
14 spacing between NCs is short, such that electron hopping can still occur. In Pb chalcogenide QD
15 solar cells, transport properties are actively studied using a wide variety of ligand exchange
16 strategies with many ligand head group options.^{1401, 1410-1411} Perovskite NCs often have multiple
17 ligand types (cationic and anionic species) which may be handled individually.¹³⁹⁷⁻¹³⁹⁸
18 Nevertheless, it is anticipated that with more work on designing better ligand motifs for halide
19 NCs, as demonstrated for other NCs systems, perovskite QD solar cell performance may greatly
20 increase.

21 $FAPbI_3$ is *a priori* more appealing for photovoltaic applications than $CsPbI_3$ due to a narrower
22 bandgap.¹⁴¹² However, due to transport limitations, the performance of perovskite QD solar cells
23 based on $FAPbI_3$ NCs has not exceeded the efficiency of $CsPbI_3$ NCs. Nevertheless, the

1 combination of CsPbI₃ with FAPbI₃ and/or Cs_xFA_{1-x}PbI₃ NCs in charge separating
 2 heterostructures, see Figure 137c,d, has enabled the PCE of perovskite QD solar cells to exceed
 3 15%.¹³⁹⁹⁻¹⁴⁰⁰ Cells based on mixed cation NCs has also shown better performance than analogous
 4 devices but based on single cation NCs.^{195, 1413} Cs_xFA_{1-x}Pb(I_{1-x}Br_x)₃ based perovskite QD solar
 5 cells with bandgaps larger than 1.8 eV exhibit V_{oc} values nearly 100 mV higher than those of the
 6 solar cells based on CsPb(I_{1-x}Br_x)₃ NCs.¹⁹⁵ The current PCE record of QD solar cells of 16.6%,
 7 was obtained with devices using Cs_xFA_{1-x}PbI₃ NCs as a light harvesting material, see Figure
 8 138a.¹⁴¹³ In this achievement, the synthesis of the NCs with excess oleic acid ligand is reported to
 9 play a key role. In additon, it was demonstrated that the Cs_xFA_{1-x}PbI₃ NCs-based solar cell
 10 devices exhibit significantly enhanced photostability compared with their thin-film counterparts,
 11 and they retain 94% of the original PCE under continuous solar illumination for 600 h.



12
 13 **Figure 138.** (a) Current-voltage characteristics of the current world record QD solar cell; the
 14 device is based in Cs_xFA_{1-x}PbI₃ NCs. Reproduced with permission from Ref. ¹⁴¹³ Copyright
 15 Springer-Nature. (b) Comparison between V_{oc} obtained for perovskite QD solar cells, standard

1 thin film solar cell and the maximum thermodynamic limit. NCs. Reproduced with permission
2 from Ref. ¹⁴¹⁴ Copyright American Chemical Society.

3
4 Halide perovskite NCs may also be attractive for the development of multijunction solar cells as
5 the wide gap component. However, there has not been a compelling demonstration published yet.
6 First, the NCs offer bandgap control by quantum confinement effects in addition to composition.
7 The versatility of halide perovskites allows the bandgap to be easily tuned through the halide
8 composition.^{835,1415} In bulk thin films, halide phase segregation is readily observed in mixed halide
9 perovskites under illumination^{1281, 1416-1417} or when electrical bias is applied,¹⁴¹⁸ limiting bandgap
10 stability in mixed perovskites. But due to size constraints, phase segregation is suppressed in
11 mixed halide perovskites NCs in comparison with thin films.^{1416, 1419-1420} This may lead to more
12 opportunities for achieving higher voltages in devices with bandgap in the 1.8-2.0 eV range.
13 Presently, perovskite QD solar cells often exhibit higher V_{oc} than bulk perovskites of similar
14 bandgap and composition, in the range of 1.55-1.77 eV, see Figure 138b.¹⁴¹⁴ However, there are
15 several key limitations of perovskite QD solar cells at this stage. One area is the development of
16 greater versatility in terms of carrier selective contacts, such as being able to construct the cell in
17 a *p-i-n* geometry instead of an *n-i-p* structure, or using contacts with lower thermal budgets for
18 processing on other subcells. Another challenge is that increasing the bandgap by quantum
19 confinement or by introducing bromine has yet to produce a high efficiency solar cell with larger
20 V_{oc} due to reductions in the lifetime. Likely a breakthrough in ligand exchange for improved
21 passivation or more complex compositions that yield longer lifetimes and higher bandgaps could
22 be the key to realizing this potential in multijunction cells using high voltage perovskite NCs.

1 The fact that perovskite QD solar cells have now demonstrated >16% PCE is exciting in its own
2 right, however just having this distinct solar cell platform can enable us to learn more about metal
3 halide perovskites in general. The high surface area to volume ratio enables studies of surface
4 passivation, which could carry over to other areas in halide perovskite science. NCs can act as
5 seeds for the nucleation of larger crystals. At this moment it is not clearly known if both kinds of
6 devices fully share the same working principles or if there are significant differences in effective
7 carrier concentrations, junction characteristics, *etc.* Recent studies point to similar optoelectronic
8 behavior as the impedance spectroscopy analysis highlights.¹⁴²¹ Furthermore, several groups have
9 demonstrated improved characteristics in devices using heterojunctions containing a thin film layer
10 and a QD layer.^{1395, 1422-1423} For these reasons, perovskite QD solar cells offer us many more
11 opportunities with high potential.

12 **Lead-Free Perovskite NCs**

13 As discussed in Section 5, there has been extensive work in developing lead-free analogues to
14 LHP nanocrystals. Beyond lighting applications, these materials have also been investigated for
15 photovoltaics. For example, tin halide perovskite solar cells have achieved high photocurrents as
16 it has a low bandgap, high absorption coefficient and a symmetric perovskite crystal structure with
17 disperse bands.¹⁴²⁴⁻¹⁴²⁵ The highest efficiency currently reported of bulk Sn based perovskite solar
18 cell is reported by Jokar *et al.* using a mixed cation (guanidinium (GA⁺), formamidinium (FA⁺),
19 tin triiodide perovskite with ethylenediammonium diiodide (EDAI₂) as an additive. The PCE of
20 the device is 9.6% with a J_{sc} of 21.2 mA cm⁻².¹⁴²⁶ Sn-based perovskite quantum dot solar cells
21 have achieved comparable PCEs. For example, CH₃NH₃SnBr_{3-x}I_x NC solar cells using mesoscopic
22 TiO₂ anode has a PCE of 8.79%, V_{oc} of 0.758 V, J_{sc} of 17.06 mA cm⁻², and FF of 68.1%.¹⁴²⁷ Tin-
23 based perovskite quantum rods (QRs) have also been synthesized and investigated for

1 photovoltaics. Chen *et al.* reported a CsSnX₃ QR solar cell with a PCE of 12.96% for CsSnI₃. They
2 also reported CsSnBr₃ and CsSnCl₃ QRs with 10.46% for and 9.66% efficiency, respectively.⁵⁴⁵
3 Similar work has also been reported by Chen *et al.* for CsGeX₃ QRs with a peak PCE of 4.92%.³²⁹
4 The bottleneck for tin halide perovskite NC solar cells are low open circuit voltages. The average
5 V_{oc} of Sn-based perovskite solar cells is around 0.5V, which is significantly below their bandgap
6 of 1.2-1.4eV ^{1424, 1428} This is due to the facile and undesirable oxidation from Sn²⁺ to Sn⁴⁺, which
7 leads to *p*-type doping and an increase in the dark current density and photocarrier recombination.
8 ¹⁴²⁸⁻¹⁴²⁹ The PCEs of Sn-based perovskite solar cells are currently well below their Shockley-
9 Queisser limit of 33%. ¹⁴²⁸ Unlike lead-based perovskites, tin-based perovskites do not have
10 inactive lone-pair which could provide oxidative resistivity. As a result, tin-based perovskites are
11 extremely sensitive to oxidation induced self-doping, which leads to perovskite degradation. The
12 future challenges include stabilizing the tin oxidation state to improve the defect-tolerant
13 properties of Sn-based perovskite and solar cell performance. Apart from methods like partial
14 substitution, additive engineering and addition of deoxidizer, ¹³⁸² developing low dimensional
15 structures, such as quantum dots, could be another approach to stabilize Sn-based perovskites, as
16 NCs have less intrinsic defects caused by large surface-to-volume ratios and automatic elimination
17 of volume defects.

18 Apart from isovalent substitution of lead, other lead-free perovskite NC solar cells have been
19 investigated, including A₂B(I)B(III)X₆ double perovskite NCs, 0D A₃B(III)₂X₉ and 0D A₂B(IV)X₆
20 perovskite-inspired materials.^{95, 368, 1430} Cho *et al.* recently reported a Cs₂AgBiBr₆ double
21 perovskite NC solar cell using semiconductor oxides such as TiO₂ or ZnO as the ETL. By
22 depositing multiple layers (20 deposition cycles, 225nm) of the QD film, the device achieved an
23 open-circuit voltage of 0.92 V. Although this is similar to the V_{oc} of LHP solar cells, it is well

1 below the ~ 2.1 eV bandgap of $\text{Cs}_2\text{AgBiBr}_6$. Furthermore, the efficiency was only 0.13%. The low
2 PCE cannot be further improved by simply increasing the thickness of the absorber layer as the
3 material can only absorb light with wavelength below 550nm due to the wide bandgap.¹⁴³¹ Also,
4 the low fill factor (32%) indicated the QD films to have high series resistance.^{368, 1432} Vacancy-
5 ordered double perovskite $\text{A}_2\text{B(IV)X}_6$ is considered a 0D perovskite-inspired materials due to the
6 absence of connectivity between BX_6 octahedra.³⁶⁸ Many $\text{A}_2\text{B(IV)X}_6$ compounds have been
7 investigated for potential photovoltaic applications, including MA_2SnI_6 ¹⁴³³, Cs_2TiBr_6 ¹⁴³⁴
8 (champion efficiency of 3.3%) and Cs_2PdBr_6 ¹⁴³⁰. However, there are no reported quantum dots
9 solar cell for these materials yet. Recently, Zhou *et al.* successfully synthesized Cs_2PdBr_6 NCs
10 with single unit cell thickness and high stability.¹⁴³⁰ The nanocrystals demonstrated a measured
11 photocurrent density of $1.2 \mu\text{A cm}^{-2}$ under an applied potential of 0.65 $\text{V}_{\text{Ag}/\text{AgCl}}$ with simulated
12 solar light (AM 1.5G, $150 \text{ mW}/\text{cm}^2$). Comparing with lead-free perovskite thin film, nanocrystals.
13 It would be interesting to see if the development of $\text{A}_2\text{B(IV)X}_6$ nanocrystal materials can further
14 improve the performance of the solar cell, such as using 0D Cs_2TiBr_6 , as low-dimension quantum
15 dots have larger surface to volume ratio and less volume defects. In general, comparing with lead
16 halide perovskite quantum dots solar cell, the research of lead-free perovskite nanocrystal solar
17 cell is still at the beginning stage. There is a strong incentive to synthesis high quality nanocrystal
18 materials and fabricating more efficient lead-free quantum dots for solar cells applications, even
19 though the current PCE of the cell remains low. The motivation would be it has been shown that
20 NCs can stabilize thermodynamically unstable phase.¹⁴³⁵ For example, the bulk perovskite cubic
21 $\alpha\text{-CsPbI}_3$ black phase is unstable under room temperature, the phase become metastable in the
22 form of nanocrystals, and can survive for days in solution.¹⁸⁷

1 **Conclusions and Outlook**

2 Currently, one of the main challenges for lead-free perovskite-inspired NCs is to achieve high
3 efficiency and stability simultaneously. Sn-based NC solar cells have achieved the highest
4 efficiencies among these materials, but the materials still suffer from instability issues. By contrast,
5 stable materials such as bismuth-based (Bi) and antimony-based (Sb) double perovskites
6 nanocrystals, have low power conversion efficiency (less than 5%). The degradation mechanism
7 has been discussed previously in the LED section. Although surface ligands are expected to
8 stabilize the metal stable phase of perovskites, they are often removed either by washing or
9 annealing for improving the charge transport across the films. Therefore, it is still unclear on the
10 required density of ligands on the NC surface for their phase stability. Currently, extensive studies
11 have been made on improving the stability of solar cells made with perovskite bulk thin films.¹⁴³⁶⁻
12 ¹⁴³⁸ By following a similar logic, more works are required on quantum dot-based solar cells, such
13 as utilizing compositional engineering or using doped NCs to understand their stability.
14 Furthermore, the candidates for solving the toxicity of lead-based perovskite should not be limited
15 to perovskites materials, other perovskite-inspired materials such as chalcogenide NCs should also
16 be explored, and these materials are detailed in Ref¹⁴³⁹.

17

18 **11.5 PHOTOCATALYSIS USING PEROVSKITE NCs**

19 Chemical fuels have significantly higher energy storage capacity than the batteries due to the
20 very high specific energy of the former, which can be released by combustion.^{1440,1441} Harvesting
21 the energy from chemical fuels through the use of solar radiation can enable the clean and efficient
22 storage or renewable solar energy.¹⁴⁴² The common chemical fuels generated are hydrogen and
23 oxygen (from water splitting), or methane (from CO₂ reduction).^{1443,1444} Photons in the UV and

1 visible wavelength regions have sufficient energy to drive these photochemical reactions.¹⁴⁴⁵
2 Owing to their large specific surface area, nanocrystals offer the possibility to both absorb solar
3 radiation and drive the desired solar fuel generating reaction without any external bias.^{1446,1447} The
4 attractive optical properties of halide perovskite nanocrystals (for example, high absorption
5 coefficients in the UV-visible region, a tunable bandgap, and high PLQY) make them suitable
6 candidates for solar-driven photocatalytic applications. While recent progress in the halide
7 perovskite NCs leads to successful use in different optoelectronic fields, their use in the field of
8 photocatalysis remains a challenge due to their instability in aqueous media.¹⁴⁴⁸⁻¹⁴⁴⁹ Here, we will
9 provide the current development of perovskite NCs towards photocatalytic dye degradation, H₂
10 evolution as well as CO₂ reduction. First, we will discuss the photocatalytic activity of the Pb-
11 based and Pb-free perovskite NCs, followed by photocatalytic activity of halide perovskite-based
12 heterostructures.

13 **Photocatalysis with Pb-based perovskites**

14 Most of the developed wastewater treatment strategies primarily separate only organic
15 contaminants from water. However, it is necessary to convert these contaminants to non-toxic
16 substances. The outstanding optoelectronic properties of lead-halide perovskites, *e.g.*, CsPbBr₃
17 NCs can be used for the photocatalytic degradation of organic pollutants and convert them to non-
18 toxic substances. The photocatalytic degradation of a common organic pollutant 2-
19 mercaptobenzothiazole (MBT) in the presence of CsPbBr₃ NCs has been investigated
20 systematically.¹⁴⁰³ MBT is a poorly biodegradable heterocyclic organic compound which causes
21 severe toxicity in the aqueous solution. As has been shown in Figure. 139a, the PL intensity of
22 CsPbBr₃ NCs reduces drastically in the presence of MBT. The energy level alignment between
23 CsPbBr₃ NCs and MBT suggests a photoinduced hole transfer from the perovskite NCs to MBT,

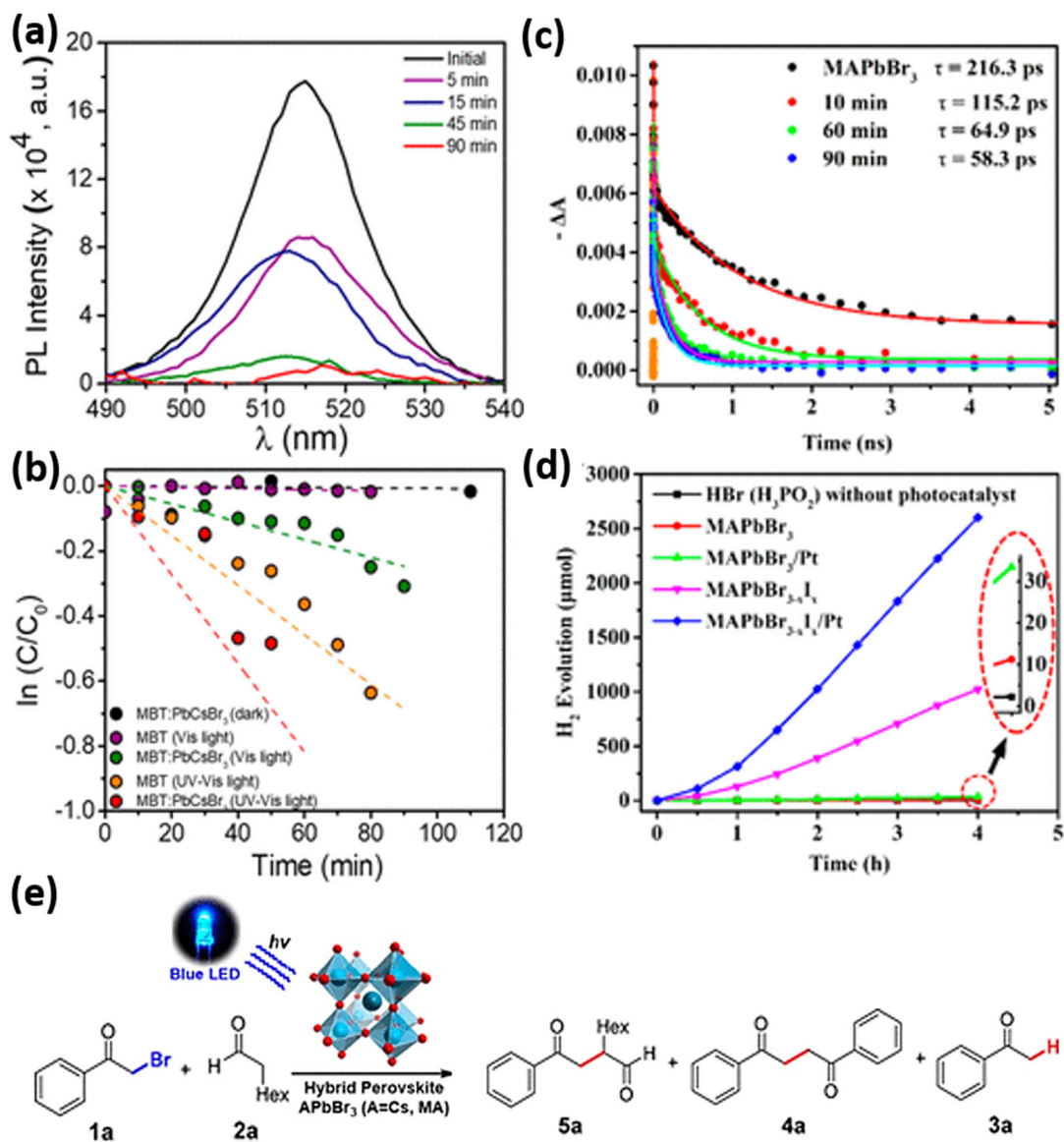
1 which results in PL quenching. This leads to the oxidation of MBT in the presence of lead-halide
2 perovskite NCs and results complete degradation of the pollutants. Time-resolved PL
3 measurements further support the hole transfer phenomenon.¹¹ To unambiguously determine the
4 role of lead-halide perovskite NCs in MBT photodegradation, several control experiments were
5 carried out and shown as relative concentration of the contaminant with time in Figure. 139b. It is
6 evident from the experiments that in the absence of the perovskite NCs, only UV light is effective
7 for the degradation of MBT. However, in the presence of the CsPbBr₃ NCs, significantly faster
8 photodegradation of MBT takes place under both visible and UV irradiation. The photodegradation
9 rate constant for MBT has been calculated from the linear plot of $\ln(C/C_0)$ vs. t , assuming a
10 pseudo-first order reaction (Figure. 139b). The calculated rate constant suggests although in the
11 presence of UV irradiation the photo degradation rate of MBT doubled with CsPbBr₃ NCs,
12 however, in the presence of visible irradiation the rate becomes six-fold faster with CsPbBr₃ NCs.
13 The zero response towards photo degradation of MBT in the presence of CsPbBr₃ NCs in the dark
14 eliminates the possibility of any competing mechanism.

15 Employing light-assisted halide exchange method in aqueous HBr/HI solution, mixed halide
16 MAPbBr_{3-x}I_x perovskite has been synthesized from pristine MAPbBr₃ which processes a bandgap-
17 funnel structure.¹⁴²³ Such a structure results in an iodine-concentration gradient within the
18 perovskite, where the iodine concentration increases gradually from the core to the surface of the
19 NC. This enhances the charge transport properties towards the surface, which is beneficial for
20 photocatalytic reactions at the surface of the perovskites. The photogenerated electron-holes thus
21 can migrate towards the surface through such bandgap-funnelled perovskite and can initiate the
22 photocatalytic reaction. To understand the charge carrier dynamics induced by the halide-exchange
23 reaction, ultrafast transient absorption (TA) spectroscopy has been performed. The TA spectrum

1 of pristine MAPbBr₃ shows a ground state bleach at 526 nm due to photoinduced phase-space
2 filling from electrons and holes.¹⁴²³ However, the 90-min iodine exchange perovskite sample
3 shows only a 10-nm red shift in the bleach signal, suggesting the TA spectrum is dominated by
4 Br-ions in the MAPbBr_{3-x}I_x. In other words, the bromide ions inside the particle are only partially
5 replaced by the iodide ions which supports the bandgap-funnel structure. However, on comparing
6 the ground state bleach recovery kinetics of MAPbBr₃ and MAPbBr_{3-x}I_x at different time of ion-
7 exchange reaction (Figure. 139c) reveals significantly faster bleach recovery signal for longer time
8 iodide-exchange perovskites. This indicates on increasing iodine content at the surface (at longer
9 time ion-exchange reaction), charge transport towards surface increases significantly due to the
10 bandgap-funnel effect, which results in faster recovery of the bromide-rich photobleach signal. To
11 corroborate the enhanced charge transport property towards better photocatalytic performance in
12 the bandgap-funnel MAPbBr_{3-x}I_x perovskite, photocatalytic H₂ evolution reaction has been
13 performed under visible light irradiation. The pristine MAPbBr₃ shows poor photocatalytic H₂
14 evolution performance (2.8 mmol/h) which improves to 8.4 mmol/h after loading on Pt (Figure
15 139d). Surprisingly, after introducing the bandgap-funnelled MAPbBr_{3-x}I_x perovskite, the activity
16 increases significantly to 255.3 mmol/h. Expectedly, on loading with Pt, a further 2.5 fold (651.2
17 mmol/h) enhancement was observed as a result of efficient separation of the photogenerated
18 electron-hole.

19 Yan *et al.* demonstrated the first C–C bond coupling organic reactions using APbBr₃ (A= Cs or
20 MA) as photocatalysts.¹⁴⁵⁰ As shown in Figure. 139e, under visible light ($\lambda = 450$ nm) irradiation,
21 APbBr₃ NCs can selectively produce several products, including dehalogenated acetophenone **3a**
22 (yield 76%), sp³ C-coupling product **4a** (8%), and α -alkylation product **5a** (7%). In addition, the
23 broad reaction scope of this important organic transformation, especially the tolerance of

1 sophisticated bio-relevant functional groups, indicates the feasibility of employing halide
2 perovskites for photo-driven pharmaceutical molecule synthesis. In another work,¹⁴⁵¹ they further
3 demonstrated the halide perovskites NCs can catalyze a series of organic reactions, such as C–C
4 bond formations via C–H activation, C–N bond formations via N-heterocyclizations and C–O bond
5 formations via aryl-esterifications. In this work, the impacts of reaction conditions (e.g., the size
6 of NCs, solvent types, acid/base, and air tolerance, etc.) on the performance of CsPbX₃ (X = Cl,
7 Br, I) NCs were systematically investigated, which provide important guidance for expanding the
8 application of halide perovskite-driven organic reactions. Another remarkable example of the use
9 of perovskites in photocatalysis is that of CsPbBr₃ nanoparticles as photosensitizers for a
10 demanding photoredox catalytic homo- and cross-coupling of alkyl bromides at room temperature
11 by merely using visible light and an electron donor, as demonstrated by Pérez-Prieto and co-
12 workers.³⁶⁴ The building of a high concentration of the generated radical anions in the NC surface
13 eventually facilitated the exergonic C–C bond formation, thus demonstrating the cooperative
14 action between the nanoparticle surface and the organic capping.



1
2 **Figure 139.** (a) PL spectra of CsPbBr₃ NCs in the absence and presence of 2-
3 mercaptobenzothiazole (MBT), under 100 mW cm⁻² irradiation with UV filter. (b) Relative
4 change in MBT concentration (without and with CsPbBr₃) with time under visible and UV-visible
5 light. (c) Bleach recovery kinetics of MAPbBr₃ (0 min) and MAPbBr_{3-x}I_x at different time (10
6 to 90 min) of ion-exchange reaction as observed from transient-absorption spectroscopy. (d)
7 Photocatalytic activity of the H₂ evolution without and with different photocatalysts (MAPbBr₃,
8 MAPbBr₃/Pt, MAPbBr_{3-x}I_x, and MAPbBr_{3-x}I_x/Pt). (e) APbBr₃ (A= Cs or MA) NCs for

1 photocatalytic α -alkylation of aldehydes. Figures a and b are reproduced with permission from
2 Ref.¹⁴⁰³ Copyright 2019, Journal of the American Chemical Society. Figures c and d are
3 reproduced with permission from Ref.¹⁴²³ Copyright 20198, Journal of the American Chemical
4 Society. Figure e reproduced with permission from Ref.¹⁴⁵⁰ Copyright 2019 American Chemical
5 Society.

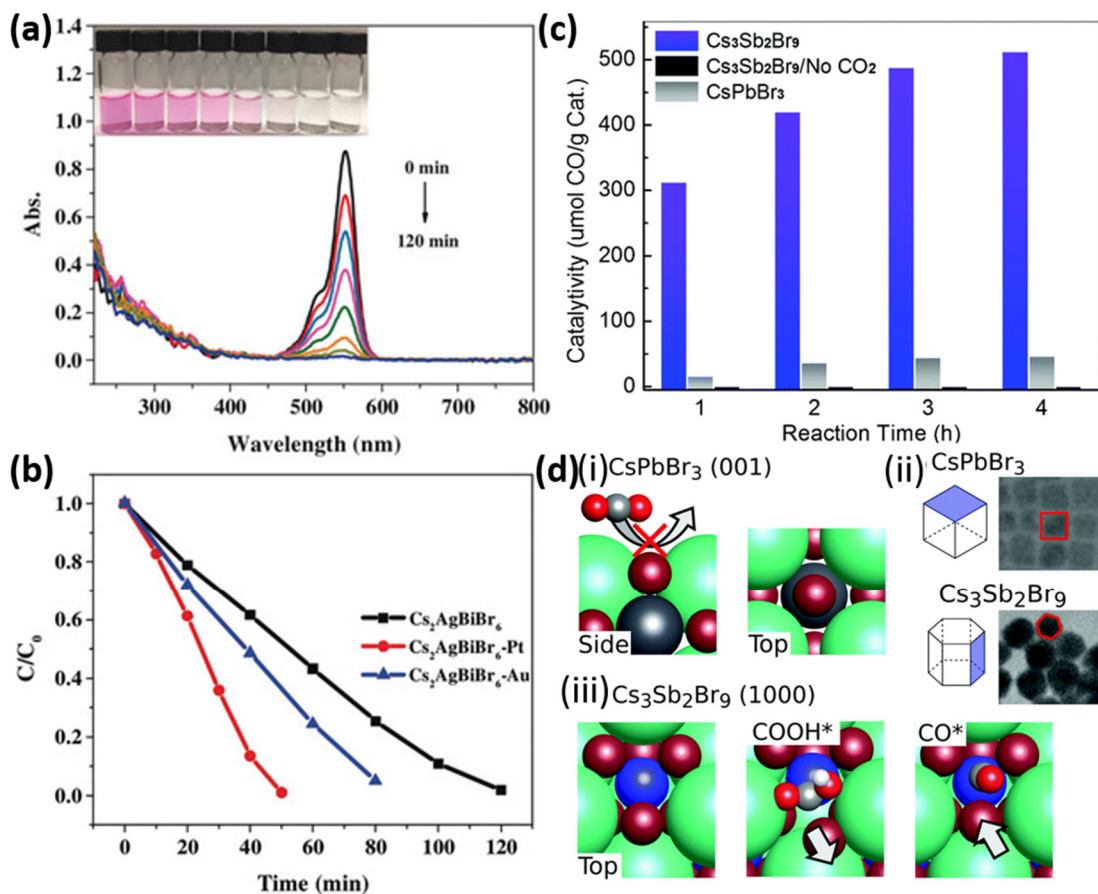
6

7 **Photocatalysis using Pb-free perovskites**

8 While lead-halide perovskites demonstrate significant potential towards different optoelectronic
9 properties including photocatalysis, the toxic nature of Pb limits its large scale application.
10 Furthermore, other metal centers (e.g. Bi, Sb) than Pb may allow higher activity and better
11 selectivity towards photocatalysis. An alcohol-based Pb-free Cs₂AgBiBr₆ double perovskite has
12 been developed recently which shows a great promise towards dye degradation under visible light
13 irradiation with high chemical stability.¹⁴⁵² Cs₂AgBiBr₆ has been studied for photocatalytic
14 degradation of Rhodamine B (RhB), a common organic contaminant, under visible light irradiation
15 (Figure. 140a) which shows up to 98% degradation of the dye upon a continuous irradiation for 120
16 minutes. The photocatalytic activity of Cs₂AgBiBr₆ was enhanced after depositing Au and Pt on
17 the surface (Figure. 140b), which improves the charge transport efficiency and has been verified
18 using steady-state and time-resolved PL quenching measurements.

19 Although the photocatalytic activity of lead-free double perovskites is promising, the stability
20 of this material remains challenging. In this respect, lead-free Cs₃Sb₂X₉ and Cs₃Bi₂X₉ defect-
21 ordered perovskites are promising and have greater thermal stability.^{572, 1453} The photocatalytic
22 activity of Cs₃Sb₂Br₉ perovskite for CO₂ reduction reaction has been explored recently.¹⁴⁵⁴ Unlike
23 the commonly used solvent ethyl acetate or acetonitrile, in this work high boiling-point octadecene

1 was chosen due to its larger CO₂ solubility. Figure. 140c compares the photocatalytic activity
2 towards CO₂ reduction of Cs₃Sb₂Br₉ and CsPbBr₃ perovskite NCs. Over the course of 4 h
3 irradiation, CsPbBr₃ NCs produces 50 mmol/g CO which is higher than previous reports. This has
4 been attributed to increased CO₂ solubility as well as reduced degradation of perovskite NCs in
5 octadecene compared to commonly used acetonitrile or ethyl acetate for photocatalytic reactions.
6 Surprisingly, the activity of Cs₃Sb₂Br₉ NCs to CO₂ reduction is more than 10-fold higher,
7 producing a total of 510 mmol/g CO after 4 h irradiation (Figure. 140c). The control experiments
8 in the absence of CO₂ shows no CO production which confirms the result of CO generation is not
9 from the degradation of ligands or solvent. The activity of both the catalysts was found to be
10 reduced over the multiple reaction cycles. However, the Cs₃Sb₂Br₉ NCs still showed a 5 to 10-fold
11 larger activity than Pb-based CsPbBr₃ NCs. Density functional theory (DFT) calculations were
12 performed to unravel the underlying cause for such enhanced activity in Cs₃Sb₂Br₉ NCs.¹⁴⁵⁴ No
13 intermediate COOH* bound states were observed on the CsPbBr₃ NC (001) surface from the
14 calculations. This is because Pb atom is completely isolated from the surface by the Cs and Br
15 atoms, as shown in Figure. 140d (i) which restrict to form any direct interaction with COOH*. The
16 (1000) and (0001) surface of Cs₃Sb₂Br₉ NCs, however, have high exposure due to the hexagonal
17 structure (Figure. 140d (ii)). Here the Sb atom is only partially shielded by 3 Br atoms (Figure.
18 140d (iii)). A Sb-C bound state is observed in the DFT calculation for both (1000) and (0001)
19 surface for COOH* where one of the ionic Br ions displaces slightly to allow the formation of the
20 Sb-COOH* bond. The smaller size of CO* allows the shifted Br to return to its initial position
21 during the evolution of CO. Thus, DFT calculations show that the mechanism for the enhanced
22 photocatalytic activity of Cs₃Sb₂Br₉ NCs is due to the effective binding sites on the (1000) and
23 (0001) surfaces for COOH* and CO* intermediates.



1
 2 **Figure 140.** a) UV-vis absorption spectra of Rhodamine B in the presence of $\text{Cs}_2\text{AgBiBr}_6$ at
 3 different irradiation times (between 0 to 120 min). (Inset: digital photographs of the corresponding
 4 photocatalyst at different irradiation times). (b) C/C_0 plot as a function of irradiation time for
 5 photodegradation of RhB in the presence of $\text{Cs}_2\text{AgBiBr}_6$, $\text{Cs}_2\text{AgBiBr}_6\text{-Pt}$ and $\text{Cs}_2\text{AgBiBr}_6\text{-Au}$.
 6 Reproduced with permission from Ref.¹⁴⁵² Copyright 2019, Wiley-VCH. (c) Photocatalytic
 7 activity towards production of CO by $\text{Cs}_3\text{Sb}_2\text{Br}_9$ NCs, as compared to CsPbBr_3 NCs. (d) (i)
 8 Inaccessibility of Pb-atoms as shown in CsPbBr_3 (001) surface. (ii) TEM image showing cubic
 9 CsPbBr_3 and hexagonal $\text{Cs}_3\text{Sb}_2\text{Br}_9$ NCs, along with the planes of (001) for CsPbBr_3 and (1000)
 10 for $\text{Cs}_3\text{Sb}_2\text{Br}_9$. (iii) Reactivity of highly exposed $\text{Cs}_3\text{Sb}_2\text{Br}_9$ NCs (1000) surface via partial

1 displacement of one of the Br atoms. Reproduced with permission from Ref.¹⁴⁵⁴ Copyright 2020,
2 Royal Society of Chemistry.

3

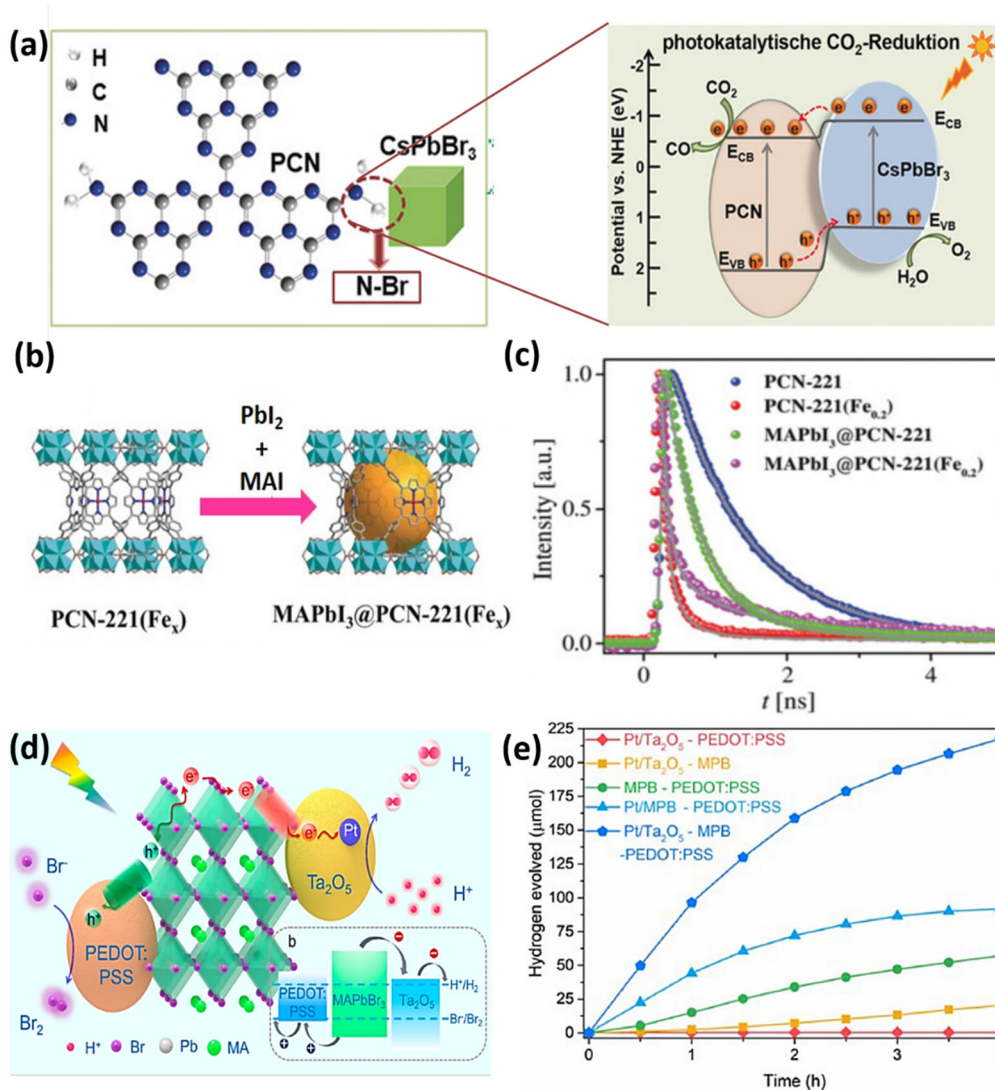
4 **Photocatalytic activity of perovskite-based heterostructures**

5 The high absorption coefficient, defect-tolerance and tunable band positions of halide
6 perovskites are strongly beneficial for photocatalysis. In addition to efficient charge separation and
7 transfer, photocatalysts also require a high density of active sites, good stability and recyclability.
8 Generally, it is difficult to satisfy all these requirements for a single-component halide perovskite
9 photocatalyst. Owing to the synergistic properties induced by the interactions among different
10 components, heterostructures of diverse functional materials into a single system with precise
11 design is a commonly employed strategy to enhance the performance of semiconductors.¹⁴⁵⁵
12 Halide perovskite-based heterostructures have therefore demonstrated improved performance. For
13 instance, based on a facile self-assembly method, Ou *et al.*¹⁴⁵⁶ prepared CsPbBr₃ NCs anchored
14 on porous g-C₃N₄ nanosheet heterojunctions for CO₂ photoreduction. The intimate interface
15 interaction enable by N–Br chemical bonding as well as the matched band alignment between
16 CsPbBr₃ and g-C₃N₄ semiconductors effectively facilitate the separation and transport of
17 photogenerated carriers (Figure. 141a). As a result, the optimal CsPbBr₃/g-C₃N₄ heterojunction
18 exhibits enhanced stability and CO production compared to CsPbBr₃ NCs and g-C₃N₄ alone.

19 Metal organic frameworks (MOFs) are also promising CO₂ catalysts due to their porous
20 crystalline framework offering a large specific surface area and highly active metal centers for
21 selective CO₂ absorption/activation. Recently, Wu *et al.*¹⁴⁵⁷ prepared Fe-based MOF coated
22 MAPbI₃ perovskites, (*i.e.*, MAPbI₃@PCN-221(Fe_x)) via a sequential deposition method (Figure.
23 141b). TRPL measurements in Figure. 141c suggest that the electron transfer from MAPbI₃ to Fe-

1 based MOFs reaction sites greatly promotes efficient charge separation. The MAPbI₃@PCN-
2 221(Fe_x) can serve as efficient photocatalysts for CO₂ reduction with the highest yield of 19.5 μmol
3 g⁻¹ h⁻¹ for solar fuel production (CH₄+CO). In addition to MOFs, other porous materials such as
4 silica matrixes,¹⁴⁵⁸ TiO₂¹⁴¹² and graphene³⁸ have also been employed as support to stabilize and
5 disperse halide perovskite, thus tuning their photocatalytic performance.

6 As shown in Figure. 141d, a multicomponent halide perovskite-based hybrid consisting of
7 MAPbBr₃ modified with Pt/Ta₂O₅ as electron transport layers and poly(3,4-ethylenedioxy-
8 thiophene) polystyrene sulfonate as hole transport layers were reported by Li *et al.*¹⁴⁵⁹ The
9 photocatalytic H₂ evolution rate of this novel catalyst reached 105 μmol h⁻¹, which was drastically
10 increased about 52 fold over the pristine MAPbBr₃ (Figure. 141e). However, the photoactivity of
11 this system decreased gradually with prolonged reaction times, indicating poor stability of the
12 reaction. Sá and co-workers developed a photocatalytic reaction system that employed CsPbBr₃ as
13 the light-absorber and Ru@TiO₂ nanoparticles (NPs) as proton reductant catalyst.¹⁴⁶⁰ Stable H₂
14 production was observed, which suggest that this reaction system can be a feasible platform for
15 fundamental investigations on halide perovskites photoactivity and stability.



1
 2 **Figure 141.** a) Schematic illustrations for the interfacial interaction and band alignment within
 3 CsPbBr₃ NCs/g-C₃N₄ heterojunction. Reproduced with permission from Ref. ¹⁴⁵⁶. Copyright 2018
 4 John Wiley and Sons. b) Schematic illustration for the synthesis of MAPbI₃@PCN-221(Fe_x). c)
 5 TRPL decays of different samples. Reproduced with permission from Ref. ¹⁴⁵⁷. Copyright 2018
 6 John Wiley and Sons. d) Schematic illustration of the mechanism of photocatalytic HER over
 7 Pt/Ta₂O₅-MAPbBr₃-PEDOT:PSS heterojunction. e) Comparison of the H₂ evolution activities of
 8 Pt/Ta₂O₅-PEDOT:PSS, Pt/Ta₂O₅-MAPbBr₃, Pt/MAPbBr₃-PEDOT:PSS, MAPbBr₃-

1 PEDOT:PSS, and Pt/Ta₂O₅-MAPbBr₃-PEDOT:PSS. Reproduced with permission from Ref. ¹⁴⁵⁹.
2 Copyright 2018 American Chemical Society.

3

4 **Summary and outlook on perovskite photocatalysis**

5 Inspired by these pioneering works, various halide perovskite materials with tunable size,
6 morphology and crystal structure have been prepared by a range of methods. These halide
7 perovskites can also be incorporated with metal nanostructures,¹⁴³⁵ semiconductors¹⁴⁶¹ and carbon-
8 based materials¹⁴⁶²⁻¹⁴⁶³ to form heterojunction photocatalysts. Recent advances of halide
9 perovskite in photocatalysis fields show that these materials can be used to drive H₂ evolution,
10 CO₂ reduction, degradation of organic pollutants and selective organic synthesis. Thus, it may be
11 concluded that the renaissance of halide perovskites in the photovoltaic and optoelectronic fields
12 has also sparked considerable interest in their photocatalytic applications. Currently, the highest
13 CO₂-to-solar fuel (CO + CH₄) production rate has reached 431 μmol g⁻¹ h⁻¹ with transition metal
14 Ni complex modified-CsPbBr₃,¹⁴⁶⁴ and the maximum H₂ generation rate of 7.3 mmol g⁻¹ h⁻¹ was
15 gained with BP/MAPbI₃ heterojunctions.¹⁴⁶¹ Despite the exciting progress, the field is still at its
16 infancy and there is great room for the design of target reaction systems, enhancing the stability
17 and efficiency, and eliminating toxicity of the halide systems for solar-to-chemical energy
18 conversion.

19 The future development of halide perovskite-based photocatalysts can be divided into the
20 following aspects:

21 1. The reaction type and scope of metal halide perovskites can be expanded by fine-tuning the
22 structural composition which may lead to efficient manipulation of the bandgap and alignment.
23 For example, doping Sn in the B-site of MAPbI₃ lead to reduction in the bandgap which may lead

1 to enhanced light absorption. Such engineering may lead to achieve some novel photocatalysts
2 with improved charge transfer efficiency.

3 2. The photocatalytic performance of metal halide perovskites can be improved by structural
4 engineering towards stability, reactivity and selectivity e.g. by ligand engineering, doping, surface
5 modification with co-catalysts, surface passivation layers. This may result in increasing stability
6 as well as enhanced reactivity and boost in the photocatalytic performance. For example, the
7 stability can be enhanced by using bulky organic ligands (e.g. butylamine) which may reduce the
8 dimension of 3D-perovskite to 2D-perovskite. The diffusion length can be enhanced in MAPbI₃
9 by A-site (X-site) doping of MA (I) with FA (Br) and suppress electron-hole recombination, leads
10 to increased reactivity. For selective charge-extraction, several electron and hole transporting
11 materials (e.g. GO, MOF etc.) can be used in combination with the perovskite, as discussed above.

12 3. Furthermore, development of efficient eco-friendly Pb-free metal halide perovskites by
13 replacing Pb with other transition metals (e.g. Sn, Sb, Bi, Ag etc.) is necessary, though the Pb-free
14 perovskites suffer from reduced activity. Thus, development of such Pb-free photocatalysts should
15 occur in combination with several improving strategies.

16

1 **OVERALL SUMMARY AND OUTLOOK**

2 Over the last few years, perovskite NCs have quickly emerged as an important class of
3 semiconductors. Research into perovskite NCs has been sparked not only because of their
4 intriguing fundamental optical and electronic properties, but also by their appeal in many
5 semiconductor-based technologies. This review has covered most of the lines of research that are
6 being carried on perovskite NCs. Most of these lines of research only started a few years ago, and
7 range from synthesis to self-assembly and characterization, through to applications. Tremendous
8 research progress has been made in these various research areas in a short span of time, yet there
9 are many open questions and challenges to be addressed to move the field forward.

10

11 **SHAPE/COMPOSITION-CONTROLLED SYNTHESIS AND SELF-ASSEMBLY OF** 12 **MHP NCs**

13 A wide range of synthetic methods have been developed for the preparation of perovskite NCs
14 on a large scale using different precursors and ligands. Various morphologies include nanocubes,
15 nanoplatelets (NPLs), nanowires (NWs), and nanorods (NRs). The size and shape of the perovskite
16 NCs is usually controllable by the reaction temperature, the ratio of acid-base ligands, precursor
17 ratio (A to B), the alkyl chain length of the ligands, and the thermodynamic equilibrium of the
18 reaction.^{19, 48, 62, 148, 153} However, the level of shape control in MHP NCs is far from what has been
19 achieved for metal nanoparticles and classical colloidal quantum dots. Most of the synthesis
20 methods reported for MHP NCs generally yield nanocubes or cuboid morphologies.^{36, 53} The
21 crystallization of perovskite NCs is an extremely fast process, which makes it difficult to probe
22 their growth mechanisms. Therefore, it is still challenging to understand the nucleation and growth
23 processes of perovskite NCs for a precise control of their morphology. An approach that could be

1 used to slow-down the reaction speed is by using precursors that react at a lower rate. In general,
2 fast nucleation and growth result in isotropic NCs, while slow growth processes lead to anisotropic
3 colloidal NCs. This is indeed the case for metal NPs. However, in the case of perovskite NCs, it is
4 still unclear how 2D nanoplatelets are formed from an isotropic crystal lattice and homogeneous
5 reaction environment. It is most likely that the symmetry breaks as soon as nucleation occurs and
6 the NCs grow into 2D shapes rather than 3D. Another possibility is that the ligands could bind to
7 specific facets of the nucleus more strongly than others and restrict growth, resulting in growth
8 being anisotropic. To prove these speculations, in-depth studies on growth mechanisms are needed.
9 On the other hand, it has been revealed that the formation of perovskite NWs occurs through the
10 oriented-attachment of nanocubes rather than a seed-mediated growth process.^{23, 188, 243, 1465}
11 Although this is well understood for thick (10-12 nm thickness) nanowires, the growth mechanism
12 of ultrathin (2-3 nm) NWs is still unclear. Despite decent progress in inorganic perovskite NWs,
13 controlling their length scales is still challenging. One possible way to better control the shape of
14 perovskite NCs is to further elaborate on the use of pre-formed, sub-nm perovskite clusters, as
15 those developed by Peng *et al.* and employed for the synthesis of perovskite NCs of different
16 shapes.²⁶⁵ These clusters are expected to be less reactive than the direct metal and halide
17 precursors, and are already capped by ligands, providing at the same time all what is needed for
18 the synthesis of NCs, and preventing a massive nucleation of NCs.

19 Also, the level of control over the shape and polydispersity achieved in inorganic perovskite
20 NCs has not been realized in OIHP NCs. In fact, researchers have paid more attention toward
21 inorganic perovskite NCs due to their higher stability and shape-purity as compared to OIHP NCs.
22 Despite the poor stability caused by the organic component, thin films of OIHPs have been shown

1 to be potential candidates for photovoltaics. Therefore, it would be interesting to pay more
2 attention to OIHP NCs in the future and compare their properties with inorganic perovskite NC.

3 One of the most interesting properties of perovskite NCs is their tunable PL by the constituted
4 halide composition. Halide ion exchange in perovskites is relatively easy and it takes place at room
5 temperature due to spontaneous halide ion migration, and has been applied to LHP NCs of different
6 morphologies to tune their emission color. However, spontaneous halide exchange is a problem
7 for the fabrication of white LEDs based on all-perovskite NCs. A few reports demonstrate the
8 prevention of halide exchange between perovskite NCs of different halide components, but then
9 the surface coatings used for preventing halide exchange can be a problematic for charge carrier
10 transport. Therefore, this issue needs further attention in the future. In addition, cation exchange
11 reactions have also been applied to obtain mixed cation perovskite NCs with distinct optical
12 properties as compared to either all-inorganic or OIHP NCs. However, this has been mostly
13 applied to nanocubes. It would be important to determine if the anisotropic NCs such as NPLs,
14 NWs and NRs retain their shape after cation exchange. More importantly, the mechanism of cation
15 exchange is not yet well understood. There is still an open question regarding whether the addition
16 of cations can lead to re-nucleation or to an actual, topotactic replacement of the original cations
17 of the crystal lattice. There is also a considerable work to be done on the transformations involving
18 cesium halide nanocrystals and their interconversions.¹⁴⁶⁶ In this list, we consider CsX, Cs₄PbX₆,
19 the perovskite phase of CsPbX₃, and CsPb₂Br₅. It has been recently shown, by Toso *et al.* that
20 there is a common thread linking all these materials, that is, the Cs⁺ cation substructure: this
21 substructure is expanded/contracted and/or twisted when one material of this class converts into
22 another material of the same class, but it is not destroyed. This helps to rationalize the observation
23 of hepitaxial interfaces (some in nanocrystals, other in bulk films), for example CsBr/CsPbBr₃,

1 Cs₄PbBr₆/CsPbBr₃, and CsPbBr₃/CsPb₂Br₅, in which there is a continuity of the Cs⁺
2 substructure across the interface. This mechanism of preservation of the large “A” cation might be
3 more general and expandable to a broad series of metal halides, paving the way to the study of
4 many possible transformations in perovskite and perovskite related materials.

5 The soft and highly dynamic nature of the perovskite crystal lattice results in liquid-like
6 properties. This property makes the aggregated perovskite NCs perfectly single-crystalline. For
7 instance, it has been shown that CsPbBr₃ nanocubes and NPLs can transform into single-crystalline
8 NWs and nanobelts, respectively.^{23,245} Similarly, it has been often observed that the nanocubes on
9 TEM grids connect with their neighboring nanocubes either side-by-side or corner-to-corner.³³⁵
10 Very interestingly, most connected NCs appear to be single crystalline, suggesting the liquid
11 crystalline behavior of the lattice. However, it is still unclear how the lattice restructures at the
12 connected joints. Further investigation will be required through high-resolution electron
13 microscopy into what happens at the connected joints of the NCs.²³

14

15 **SURFACE CHEMISTRY AND SURFACE PASSIVATION/COATING OF MHP NCs**

16 There has been significant progress in the understanding of the surface chemistry of perovskite
17 NCs through NMR studies, which were aimed to explore how the ligands could bind and stabilize
18 the NC surface. It has often been stated that the ligands control the growth process, but we have
19 only limited knowledge of how the ligands control the nucleation and growth of perovskite NCs.
20 The studies suggest that bidentate and tridentate ligands are more suited to stabilizing the NC
21 surface compared to the routinely used OLA/OA system. However, the chemistry behind ligand
22 coordination to the NC surface remains unclear. It has been stated that the ligands are weakly
23 bound to the surface of perovskite NCs and that this binding is highly dynamic due to the ionic

1 character of such binding. The ligands are easy to detach from the NC surface during washing with
2 polar solvents, and this creates surface defects, which affects their PLQY. A large number of
3 studies have been focused on surface passivation of LHP NCs using various ligand molecules and
4 metal halides to recover their PLQY. However, we know very little about the surface passivation
5 mechanism at the atomic level. It is still unclear whether the ligand molecules alone can passivate
6 the surface or if metal halides are compulsory to fill Pb and halide vacancies. More importantly, it
7 is worth mentioning that there are differences in the trap energies and the interactions of ligands
8 with perovskites of different halide compositions. Therefore, we cannot generalize the surface
9 passivation mechanism for all halides. Until now, most reported studies into surface passivation
10 have focused on the CsPbBr₃ NC system to improve their PLQY to near unity.

11 One of the important problems associated with perovskite NCs is their instability in water. To
12 address this issue, LHP NCs have been coated with various shell materials such as bulky organic
13 ligands, TiO₂, SiO₂, Al₂O₃, and block copolymers. However, these shells affect charge transport
14 in corresponding optoelectronic devices. Therefore, more research efforts are needed to find
15 conductive shells for perovskite NCs to improve their stability in water, but without affecting
16 charge transport.

17 **FEATURE PROSPECTS OF 0D NONPEROVSKITES N Cs.**

18 Section 3 summarizes the recent developments in the synthesis, phase transformation, and optical
19 features of Cs₄PbBr₆ NCs, particularly focusing on the material's molecular behavior, the origin
20 of green emission, and optoelectronic applications. However, there are still many challenges and
21 opportunities lie ahead for exploring these class of materials in optoelectronics. Here we share a
22 few future prospects for the advancement of fundamental understanding of Cs₄PbBr₆ NCs as well
23 as the development of new 0D NCs, which would facilitate their applications.

1 1. Although different synthesis methods have been developed for Cs₄PbX₆ NCs, other 0D A₄PbX₆
2 NCs, like Rb₄PbBr₆, have not yet been reported. Thus, there is a large scope for the development
3 of synthesis methods that allow precise control over the size and phase of 0D NCs with different
4 A-site cations, and for uncovering the relationship between A-site cations and the optical
5 properties of A₄PbX₆ NCs.

6 2. The origin of green emission in Cs₄PbBr₆ NCs is still under debate. It is attributed to the presence
7 of 3D CsPbBr₃ impurities as well as defect-related emission. Therefore, sophisticated synthesis
8 and characterization methods are needed to identify their emissive centers. For example, to confirm
9 the role of defect-induced emission, low-dose HRTEM and data processing methods can be used
10 to image the point defects in Cs₄PbBr₆ nanoplates of thickness less than 2 nm.

11 3. Developing lead-free 0D NCs for optoelectronic applications is another important research
12 direction regarding this class of materials. For instance, Cs₄SnBr₆ NCs were recently synthesized,
13 and they exhibit the characteristic green emission with enhanced air stability in the form of both
14 colloidal suspensions and thin films.¹⁴⁶⁷ Furthermore, it was demonstrated that the lead-free Cu(I)-
15 based 0D NCs (*i.e.*, Cs₃Cu₂X₅) display efficient luminescence and improved stability compared to
16 that of Pb-based 0D NCs.¹⁴⁶⁸⁻¹⁴⁶⁹

17 4. Like Pb-free perovskite NCs, stability is also a major concern for Pb-free 0D NCs. To address
18 the issue related to oxidation of Sn(II)- and Cu(I)-based 0D NCs, core/shell strategy can be used.
19 Theoretical studies have predicted that A₄SnX₆/A₄PbX₆ core/shell type NCs exhibit type-I energy
20 level alignment for promoting the energy transfer from shell to the core and thus boosting the
21 emission of A₄SnX₆ core.¹⁴⁷⁰ However, new innovations in synthesis methods are required to
22 realize 0D core/shell NCs.

23

1 **OUTSTANDING QUESTIONS INTO THE DOPING OF MHP NCs**

2 Recently, there has been an explosion of research into the doping of perovskites with various
3 metal ions, with the aim of improving stability, improving PLQY, and tuning the emission
4 wavelength. Despite great progress into the doping of perovskite NCs, there are still a number of
5 transition and inner transition metals that remain unexplored. With new dopants, new optical and
6 magnetic properties may be achieved. While B-site doping is largely explored, there should be
7 more focus on A-site doping and on the influence on the stability and properties of the NCs. One
8 of the important and open questions in the doping of perovskites is the exact location of the dopant
9 sites in perovskite NCs. In most studies, it has been speculated that the dopants occupy the A-site
10 or B-site regardless of their sizes. However, one should know that if the size of the dopant ion is
11 too different from that of the cations of the host matrix, there may be phase segregation or the
12 dopants destabilize the perovskite crystal structure. It is still remains unexplored whether the
13 dopants are substitutional in the crystal lattice or they simply stay on the surface of the crystal
14 lattice.

15 **Pb-FREE PEROVSKITE NCs**

16 Beyond lead-containing perovskite nanocrystals, a wide range of lead-free alternatives have
17 been explored. These are termed perovskite-inspired materials (PIMs) because the main
18 motivation is to find materials that could replicate the exceptional optoelectronic properties of the
19 lead-halide perovskites. PIMs include halide perovskites based on Sn and Ge (ABX_3), Cu-based
20 materials, Sb- and Bi-based defect-ordered perovskites ($A_3B_2X_9$), double perovskites
21 ($A_2B(I)B(III)X_6$) and vacancy-ordered double perovskites ($A_2B(IV)X_6$). The synthesis routes are
22 similar to those for lead-halide perovskites. Although the performances (such as PLQY,
23 narrowness of the PL linewidth) of these materials have not matched the lead-based perovskites,

1 they have given rise to unique applications. These include blue phosphors (namely with $A_3B_2X_9$
2 compounds), which lead to white-light emission when combined with conventional yellow
3 phosphors. Other materials (namely double perovskites) have demonstrated promise as white-light
4 phosphors. This emission is attributed to self-trapped excitons. The key advantage of these
5 phosphors is that the materials demonstrate improved ambient and thermal stability over lead-
6 halide perovskites. However, it is currently rare to find examples of lead-free NCs used in
7 electrically-driven applications. Promising results have so far been obtained from $Cs_3Cu_2I_5$ and
8 $Cs_3Sb_2Br_9$ NC LEDs, and there has also been the demonstrations of direct injection into self-
9 trapped excitons in tin-based perovskites. Further work on improving the properties of lead-free
10 NCs and developing these materials for electrically-driven applications is still needed.

11

12 **MORPHOLOGICAL AND STRUCTURAL CHARACTERIZATION**

13 The characterization of perovskite NCs by TEM and X-ray scattering techniques is important
14 for understanding their structure-property relationships. Perovskites are highly sensitive to the high
15 energy electron beam, which can lead to structural damage or phase transitions. NCs are
16 particularly susceptible because Pb degradation products preferentially form at edges and corners.
17 In particular, OIHP NCs are very difficult to characterize by high-resolution TEM because of the
18 rapid degradation of the organic component. Using instruments with higher sensitivity has enabled
19 reduced dosing of perovskites during characterization. As an example, this made it possible for
20 $MAPbBr_3$ NCs to be measured with atomic resolution by TEM. However, unlike metal NPs,
21 electron microscopy has not been utilized with its full potential in the characterization of
22 perovskite NCs due to its beam sensitivity issue. Therefore, there are many open questions to be
23 addressed by electron microscopy. For example, it has been proposed that perovskites undergo

1 phase changes at certain temperatures, and to probing such phase changes at the atomic level with
2 in situ characterization at the single-particle level will provide important insights. Another
3 important question to be addressed is the 3D atomic imaging of perovskite NCs and this can solve
4 the issues associated with the crystallinity of perovskite NCs. In addition, electron microscopy
5 could play an important role in identifying the location of dopants in doped perovskite NCs. On
6 the author hand, X-ray scattering techniques have been used extensively to characterize the
7 crystallinity of bulk and NC perovskites. X-rays have previously been used to study the nucleation
8 and growth mechanism of metal NCs. Extending such studies to perovskite NCs would improve
9 the understanding of their growth process. In addition, small-angle X-ray scattering techniques
10 could help us unfold the assembly of ligand molecules on the surface of perovskite NCs.

11 **OPTICAL PROPERTIES**

12 Perovskites have become popular for their interesting properties. Unlike classical QDs,
13 perovskite NCs exhibit extremely high PLQY without having any shell on their surface. This is
14 attributed to the shallow character of the defect-related energy states, which enables defect
15 tolerance, that is, low non-radiative recombination rates despite high densities of defects.
16 However, recent studies have shown that the surface traps generated by the detachment of ligands
17 and surface atoms from perovskite NCs can have a drastic effect on their PLQY. It appears
18 therefore that the nature of surface traps is not yet fully understood. The energy and nature of the
19 traps created by the detached ligands need to be measured, especially since the traps created may
20 not follow thermodynamic predictions. In addition, the role of ligands on the optical properties of
21 perovskite NCs has not been investigated in detail. In particular, ligands can significantly influence
22 the optical properties of thinner nanostructures such as NPLs and ultrathin NWs. One of the ongoing
23 debates about light emission in LHP NCs is the exciton fine structure, which governs the radiative

1 vs nonradiative recombination rates significantly. Although initially it was believed that the lowest
2 exciton state of LHP NCs is bright, while the highest exciton state is dark, later investigations
3 suggested the opposite. As transition metal ion doping in LHP NCs has been gaining increasing
4 attention, more in-depth understanding is needed on how the crystal field resulting from doping
5 induces the splitting of bright vs dark excitonic states. On the other hand, 0D non-perovskites, and
6 Pb-free perovskites are emerging as potential semiconducting materials for white light generation
7 from self-trapped excitons. However, the formation of self-trapped excitons and the photophysics
8 in such materials is still not well understood. Very recently, chiral perovskite NCs have been
9 receiving significant attention due to their polarized emission. In most cases, chirality in
10 perovskites is induced by chiral ligands. However, the origin of the induced chirality in perovskites
11 is still under debate. Several mechanisms, such as chiral molecules-induced symmetry breaking in
12 the crystal lattice, dipolar interactions between chiral molecules and perovskites, and spin-orbit
13 coupling, have been proposed for the origin of chirality, and these need further in-depth
14 investigations in the future.

15 Another important phenomenon of MHP NCs that requires further understanding is
16 photoluminescence intermittency, which is also known as ‘blinking’. This limits the application of
17 these materials in quantum optical devices. Single-particle investigations of MHP NCs suggest
18 that this effect is intrinsic to the materials themselves, rather than the effect of the processing route,
19 and it has been found that blinking occurs not only in quantum-confined systems but also in
20 microcrystals. Several mechanisms have been put forward to explain how blinking occurs. These
21 include the effects of photo-charging and Auger recombination, or the effects of non-radiative
22 recombination centers that could be meta-stable. However, further work is needed to understand
23 how meta-stable defects could be activated/de-activated, and whether light could play a role. The

1 density of these meta-stable defects also needs to be more reliably measured. Besides blinking,
2 single-particle investigations have also shown that electron-phonon coupling in MHP NCs affects
3 the emission spectra, leading to extra PL peaks. However, there is debate in the literature as to the
4 degree of coupling between electrons and optical vs. acoustic phonons. Furthermore understanding
5 into these phenomena could lead to insights into how charge transport could be improved.

6

7 **APPLICATIONS**

8 MHP NCs have gained significant attention for applications involving optical emission and
9 absorption. These include lasing, in which MHP NCs could lead to cost-effective solid-state lasers
10 with emissions wavelengths that can be easily tuned. Here, we foresee three key challenges.
11 Firstly, the MHP NCs are unstable to heat and environmental stress, and require encapsulation
12 strategies (*e.g.*, NCs embedded in a glass matrix or in a Cs₄PbBr₆ matrix). Secondly, most work
13 has been on Pb-based materials, and non-toxic alternatives that are air-stable needed to be
14 developed. These include double perovskites, but the PLQY in many lead-free alternatives have
15 not matched the near-unity values the Pb-based NCs can be routinely obtained (as discussed
16 above). Thirdly, lasing in MHPs has only been achieved through optical pumping. Electrical
17 pumping has been elusive, due to Auger recombination at high injection rates and the the long-
18 chain ligands used with NCs.

19 On the other hand, electrically-driven spontaneous emission from MHP NCs has been achieved,
20 and efficient LEDs based on lead-halide perovskite NCs been demonstrated, with EQEs exceeding
21 20% after only 5 years of development. Perovskite LEDs also have the advantages of high color-
22 purity, ultrawide color gamut, potential for low materials and fabrication costs, as well as
23 compatibility with the existing manufacturing technology for OLEDs/QD-LEDs. Thus far, most

1 efforts have focused on improving the EQEs of perovskite LEDs. But it is also important to
2 develop an understanding behind these improvements in performance, which will be important for
3 rationally achieving further increases in efficiency. It will also be important to scale-up perovskite
4 LEDs from the mm-level to large-area displays with nanometer-level uniformity in terms of NC
5 size and emission wavelength. The stability of perovskite LEDs needs to be improved, particularly
6 under operation. Furthermore, the development of perovskite LEDs has been focused on green,
7 red and near-infrared emitters, which have achieved the highest EQEs (of >20%). More recently,
8 there have been significant efforts to develop blue emitters, owing to their importance for full-
9 color displays, but both the EQE and stability lag behind their green and near-infrared counterparts.
10 Beyond these challenges, it will also be important to replicate the high performance of lead-halide
11 perovskites in lead-free alternatives. Currently, this is challenging because Sn- and Ge-based
12 perovskites are less stable than the Pb-based perovskites, and many of other materials that have
13 been proposed as alternatives have indirect bandgaps and low PLQYs.

14 MHPs are promising for photodetectors and radiation detectors due to their high optical
15 absorption coefficients, high Z numbers (ensuring strong attenuation of radiation) and long diffusion
16 lengths. In photodetectors, NCs with reduced defect density have been achieved, leading to devices
17 with high on/off ratios for the photocurrent exceeding 10^5 . Nanostructured perovskites have also
18 been realized in 1D and 2D structures and combined with carbon nanotubes or 2D materials to
19 demonstrate enhanced performance. In radiation detectors, NCs have shown promise for X-ray
20 scintillators, which rapid response times and low X-ray detection limits demonstrated.

21 Furthermore, perovskites have been explored for FETs, where the ambipolar nature of charge
22 transport could offer unique opportunities. However, one the important challenges to overcome is

1 the low field-effect mobility, which arises in part from ion migration. Passivating surface defects
2 in NCs may aid in addressing this.

3 Perovskite NCs have also demonstrated significant promise in solar cells, with PCEs >16%
4 achieved, which represents the highest efficiencies for any QD-based solar cell. NCs offer the
5 advantage of stabilizing metastable phases, such as the alpha phase of CsPbI₃, which led to >10%-
6 efficient devices. NCs in particular offer the important advantage of high PLQYs, which result in
7 low non-radiative losses. The open-circuit voltages of NC perovskite solar cells have therefore
8 been closer to the radiative limits than bulk thin film perovskites. The NCs are also amenable to
9 alloying, and the most efficient NC perovskite solar cells use a mixture of Cs and FA in the A-site,
10 which leads to a smaller bandgap than pure Cs-based perovskites. Finally, perovskite NCs have
11 just started to receive significant attention as photosensitizers in photocatalysis. Perovskite
12 photocatalysis has already been demonstrated for H₂ evolution, CO₂ reduction, the degradation of
13 organic pollutants and selective organic synthesis. However, the field is still young and there is
14 are still many possibilities that remain to be explored. Some of the challenges include enhancing
15 stability and performance, as well as developing more effective encapsulation strategies.

16

1 AUTHOR INFORMATION

2 **Corresponding Authors**

3 **Robert LZ Hoye**- *Department of Materials, Imperial College London, Exhibition Road, London*
4 *SW7 2AZ, UK; Email: r.hoye@imperial.ac.uk*

5
6 **Lakshminarayana Polavarapu**- *Materials Chemistry and Physics group, CINBIO, Universidade*
7 *de Vigo, Departamento de Química Física, Campus Universitario As Lagoas, Marcosende, 36310*
8 *Vigo, Spain; Chair for Photonics and Optoelectronics, Nano-Institute Munich, Department of*
9 *Physics, Ludwig-Maximilians-Universität (LMU), Königinstrasse 10, 80539 Munich, Germany;*
10 *Email: lakshmi@uvigo.es; l.polavarapu@lmu.de*

11

12 **Author Contributions**

13 L. P. initiated and coordinated the review. L.P., R.L.Z.H., and L. M. edited the manuscript. The
14 manuscript was written through contributions of all authors. L. P. contributed to the introduction;
15 L. P., H. Z. and M. V. K. contributed to the general synthesis methods; L. P. contributed to the
16 synthesis of nanocubes; B. A. K. and Y. Z. contributed purification of nanocubes; W. A. T. and S.
17 K. A. contributed synthesis of nanoplatelets; P. Y., L. N. Q., and M. G. contributed synthesis and
18 self-assembly of nanowires; L. P., H. Zhong, and X. G. W. contributed *in-situ* synthesis; L. M., R.
19 K. and P. V. K. contributed synthesis by ion exchnage; R. K. and L. P. contributed post-synthetic
20 shape transformations; J. P. P, R. E. G., H. Zeng, X. L., J. Z., and K. X. contributed surface
21 chemistry and post-synthetic surface passivation; O. M. B., O. F. M. and J. Y. contributed synthesis
22 of 0D nonperovskites; Q. Z., M. C., A. L. R., Y. L., and L. L. contributed surface coating strategies;
23 D. H. S., D. R. G., L. P., N. P., and An. D. contributed synthesis by doping; A. N., A. S. K.,
24 R.L.Z.H., J. S., and L.P. contributed synthesis of Pb-free NCs; L. P., and M. Y. B. contributed self-
25 assembly into superlattices; L. P. J. F. and I. V. contributed chiral perovskite NCs; Am. D., J. K.

1 S., J. F., A. S., and Ap. D. contributed linear optical properties, charge carrier dynamics and charge
2 transfer studies; E. D., J. H., M. B. J. R., J. A. S., V. B., L. C., I. G. S., and M. G. contributed single
3 particle studies; E. B. and S. B. contributed electron microscopy characterization; P. M. B. and M.
4 A. S. contributed X-ray scattering characterization; H. S., H. Zeng, and Y. W. contributed lasing in
5 perovskite NCs; H. V. D., Y. F., R.L.Z.H., J. Y., S. D. S, J. S., C. J. S., and S. K. contributed LEDs
6 section; Q. B. and Z. W. contributed photodetectors and FETs; T. D., Y. Y., and C. H. contributed
7 photocatalysis section; J. M. L. and I. M. S. contributed solar cell section. All authors read the
8 manuscript and have given approval to the final version of the manuscript.

9 **Notes**

10 Any additional relevant notes should be placed here.

11 **ACKNOWLEDGMENTS**

12 L. P. acknowledge support from the Spanish Ministerio de Ciencia e Innovación through Ramón
13 y Cajal grant (RYC2018-026103-I). A.D., T.D., I.V., J.K.S., J. F., and L.P. acknowledge financial
14 support by the Bavarian State Ministry of Science, Research, and Arts through the grant “Solar
15 Technologies go Hybrid (SolTech)” and by the Deutsche Forschungsgemeinschaft (DFG, German
16 Research Foundation) under Germany’s Excellence Strategy—EXC 2089/1—390776260 (“e-
17 conversion”). J.F. L.P. and V.D acknowledge support by LMU's 'Singapore Initiative' funded
18 within the German Excellence Strategy. H. Zeng. acknowledges the support of NSFC (61874054,
19 51902160), the Natural Science Foundation of Jiangsu Province (BK20180489), Young Elite
20 Scientists Sponsorship Program by CAST (2018QNRC001), Fundamental Research Funds for the
21 Central Universities (30918011208), and the National Natural Science Funds for Distinguished
22 Young Scholars (61725402). B.A.K. and Y.Z. acknowledge funding of this work by the Robert A.
23 Welch Foundation (grant no. F-1464). H. S acknowledges the support of Ministry of Education

1 Singapore through the Academic Research Fund under Projects MOE Tier 1, RG 189/17 and RG
2 RG95/19 as well as Tier 2 MOE2016-T2-1-054. H.V.D. and Y.F. gratefully acknowledge TUBA
3 and support in part from NRF-NRFI2016-08 and A*STAR SERC Pharos 52 73 00025. Y. W. thank
4 the support by the Natural Science Foundation of Jiangsu Province (BK20190446) and NSFC
5 (11904172). J.P.P. and R. E.G. acknowledges the support of Ministerio de Economía, Industria y
6 Competitividad (CTQ2017-82711-P and MDM-2015-0538, partially cofinanced with Fondo
7 Europeo de Desarrollo Regional and Agencia Estatal de Investigación) and Generalitat Valenciana
8 (IDIFEDER/2018/064 and PROMETEO/2018/138, partially cofinanced with Fondo Europeo de
9 Desarrollo Regional). E. D. and J. H. acknowledge financial support from the Research Foundation
10 - Flanders (FWO Grant Numbers G.0B39.15, G.0B49.15, G.0962.13, G098319N and ZW15_09-
11 GOH6316), the Research Foundation - Flanders postdoctoral fellowships to J.A.S. and E.D. (FWO
12 Grant Numbers 12Y7218N and 12O3719N, respectively), the KU Leuven Research Fund
13 (C14/15/053 and C19/19/079), the Flemish government through long term structural funding
14 Methusalem (CASAS2, Meth/15/04), the Hercules foundation (HER/11/14), the Swedish
15 Research Council (VR 2016-04433), Knut and Alice Wallenberg foundation (KAW 2016.0059),
16 MEXT JSPS Grant-in-Aid for Scientific Research B (19H02550) and Specially Promoted
17 Research (18H05205). R.L.Z.H. acknowledges support from the Royal Academy of Engineering
18 through the Research Fellowship scheme (No.: RF\201718\1701) and Downing College
19 Cambridge through the Kim and Juliana Silverman Research Fellowship. M.G. acknowledges a
20 Wenner-Gren fellowship (UPD2017-0223) and L. C. acknowledges a JICA fellowship. A.S
21 acknowledges the J.C. Bose Fellowship of the Science and Engineering Research Board (SERB),
22 A.L.R acknowledges the Croucher Foundation of Hong Kong. J.M.L. acknowledges support from
23 the U.S. Department of Energy, Office of Basic Energy Sciences through the Energy Frontier

1 Research Center, Center for Hybrid Organic Inorganic Semiconductors for Energy (CHOISE).
2 S.K.H. and W.A.T. were supported by the U.S. Department of Energy, Office of Science, Basic
3 Energy Sciences under award number DE-SC0019345. A.L.R acknowledges the Croucher
4 Foundation of Hong Kong, and the National Science Foundation of China / Research Grant
5 Council of Hong Kong project N_CityU108/1. JZZ is grateful to financial support from the US
6 NSF (CHE-1904547). A.D, T.D acknowledge post-doctoral research fellowship support from
7 Alexander von Humboldt foundation.

1 **ABBREVIATIONS**

2

3	0D	Zero-dimensional
4	1D	One-dimensional
5	2D	Two-dimensional
6	3D	Three-dimensional
7	2PA	Two-photon absorption
8	3PA	Three-photon absorption
9	APTES	(3-aminopropyl) triethoxysilane
10	APTMS	(3-Aminopropyl)trimethoxysilane
11	BE	Band-edge exciton
12	CBM	Conduction band minimum
13	CIE	Commission Internationale de l'éclairage
14	CIGS	Copper indium gallium diselenide
15	CLC	Cholesteric liquid crystal
16	CPP	Circularly polarized photoluminescence
17	Cryo-EM	Cryogenic electron microscopy
18	DDAB	didodecyldimethylammonium bromide
19	DFB	Distributed feedback
20	DFT	Density functional theory
21	DMF	N,N-Dimethylformamide
22	DMSO	Dimethylsulfoxide

1	DOS	Density of states
2	DOSY	Diffusion ordered spectroscopy
3	DTS	Differential transmission spectroscopy
4	DWBA	Distorted wave Born approximation
5	EIA	Effective interface approximation
6	EQE	External quantum efficiency
7	FA	Formamidinium
8	FETs	Field-Effect Transistors
9	FTIR	Fourier-transform infrared
10	FWHM	Full Width at Half Maximum
11	GISAXS	Grazing Incidence Small X-ray scattering
12	GIWAXS	Grazing incidence wide angle X-ray scattering
13	HAAD-STEM	High-angle annular dark-field imaging-Scanning transmission electron
14	microscopy	
15	HI	Hot Injection
16	iDPC-STEM	Integrated differential phase contrast STEM
17	IHPNs	All-inorganic cesium halide perovskites nanocrystals
18	LARP	Ligand-assisted Reprecipitation
19	LEDs	Light-Emitting Diodes
20	LHPs	Lead Halide Perovskites
21	LMA	Local monodisperse approximation
22	LO	Longitude-Optical

1	LSCs	Luminescent Solar Concentrators
2	MA	Methylammonium
3	MAPI	Methylammonium lead iodide (CH ₃ NH ₃ PbI ₃)
4	MBA	Methylbenzylammonium
5	MBT	Mercaptobenzothiazole
6	MeOAc	Methyl Acetate
7	MPHs	Metal Halide Perovskites
8	NCs	Nanocrystals
9	NMR	Nuclear magnetic resonance
10	NOESY	Nuclear Overhauser effect spectroscopy
11	NPIs	Nanoplatelets
12	NRs	Nanorods
13	NSs	Nanosheets
14	NWs	Nanowires
15	OA	Oleic Acid
16	ODE	Octadecene
17	OHPNs	Organic-inorganic hybrid halide perovskites nanocrystals
18	OIH	Organic-inorganic hybrid
19	OIHP	Organic-inorganic hybrid Perovskites
20	OLA	Oleylamine
21	OTMS	Octadecyltrimethoxysilane
22	PCE	Power Conversion Efficiency

1	PEA	Amine 1-phenyl-ethyl-ammonium
2	PL	Photoluminescence
3	PLQYs	Photoluminescence Quantum Yields
4	PMMA	Poly(methyl methacrylate)
5	PMSCs	Perovskite magic sized clusters
6	POSS	Polyhedral oligomeric silsesquioxane
7	PS	Polystyrene
8	PVP	Polyvinyl pyrrolidone
9	PVs	Photovoltaics
10	QCEE	Quantum-cutting energy efficiency
11	QDs	Quantum Dots
12	RT	Room temperature
13	SHJ	Silicon heterojunction
14	SLD	Scattering length density
15	SLs	Superlattices
16	SOC	Spin-orbit coupling
17	TA	Transient Absorption
18	TEM	Transmission electron microscopy
19	TEOS	Tetraethyl orthosilicate
20	TMOS	Tetramethyl orthosilicate
21	TOP	Trioctylphosphine
22	TOPO	Trioctylphosphine oxide

1	VBM	Valence band maximum
2	VCSELs	Vertical cavity surface emitting lasers
3	WGM	Whispering-gallery-mode
4	WLEDs	White Light-Emitting Diodes
5	XRD	X-ray diffraction
6	XPS	X-ray photoelectron spectroscopy

7

8 REFERENCES

- 9 1. Wells, H. L., Über die Cäsium- und Kalium-Bleihalogenide. *Zeitschrift für anorganische*
10 *Chemie* **1893**, 3 (1), 195-210.
- 11 2. Dieter, W., Das Perowskitesystem $\text{CH}_3\text{NH}_3 [\text{Pb}, \text{Sn}_{1-n}\text{X}_3]$ ($\text{X} = \text{Cl}, \text{Br}, \text{I}$) / The Perovskite
12 System $\text{CH}_3\text{NH}_3[\text{PbnSn}_{1-n}\text{X}_3]$ ($\text{X} = \text{Cl}, \text{Br}, \text{I}$). *Z. Naturforsch. B* **1979**, 34 (7), 939-941.
- 13 3. Dieter, W., $\text{CH}_3\text{NH}_3\text{PbX}_3$, ein Pb(II)-System mit kubischer Perowskitstruktur /
14 $\text{CH}_3\text{NH}_3\text{PbX}_3$, a Pb(II)-System with Cubic Perovskite Structure. *Z. Naturforsch. B* **1978**, 33 (12),
15 1443-1445.
- 16 4. Dieter, W., $\text{CH}_3\text{NH}_3\text{SnBr}_x\text{I}_{3-x}$ ($x = 0-3$), ein Sn(II)-System mit kubischer Perowskitstruktur
17 / $\text{CH}_3\text{NH}_3\text{SnBr}_x\text{I}_{3-x}$ ($x = 0-3$), a Sn(II)-System with Cubic Perovskite Structure. *Z. Naturforsch.*
18 *B* **1978**, 33 (8), 862-865.
- 19 5. Mitzi, D. B.; Chondroudis, K.; Kagan, C. R., Organic-inorganic electronics. *IBM J. Res.*
20 *Dev.* **2001**, 45 (1), 29-45.
- 21 6. Mitzi, D. B.; Feild, C. A.; Harrison, W. T. A.; Guloy, A. M., Conducting tin halides with a
22 layered organic-based perovskite structure. *Nature* **1994**, 369 (6480), 467-469.
- 23 7. Kojima, A.; Teshima, K.; Shirai, Y.; Miyasaka, T., Organometal Halide Perovskites as
24 Visible-Light Sensitizers for Photovoltaic Cells. *J. Am. Chem. Soc.* **2009**, 131 (17), 6050-6051.
- 25 8. Kim, H.-S.; Lee, C.-R.; Im, J.-H.; Lee, K.-B.; Moehl, T.; Marchioro, A.; Moon, S.-J.;
26 Humphry-Baker, R.; Yum, J.-H.; Moser, J. E.; Grätzel, M.; Park, N.-G., Lead Iodide Perovskite
27 Sensitized All-Solid-State Submicron Thin Film Mesoscopic Solar Cell with Efficiency
28 Exceeding 9%. *Sci. Rep.* **2012**, 2 (1), 591.
- 29 9. Lee, M. M.; Teuscher, J.; Miyasaka, T.; Murakami, T. N.; Snaith, H. J., Efficient Hybrid
30 Solar Cells Based on Meso-Superstructured Organometal Halide Perovskites. *Science* **2012**, 338
31 (6107), 643-647.
- 32 10. Manser, J. S.; Christians, J. A.; Kamat, P. V., Intriguing Optoelectronic Properties of Metal
33 Halide Perovskites. *Chem. Rev.* **2016**, 116 (21), 12956-13008.
- 34 11. Xing, G.; Mathews, N.; Sun, S.; Lim, S. S.; Lam, Y. M.; Grätzel, M.; Mhaisalkar, S.; Sum,
35 T. C., Long-Range Balanced Electron- and Hole-Transport Lengths in Organic-Inorganic
36 $\text{CH}_3\text{NH}_3\text{PbI}_3$. *Science* **2013**, 342 (6156), 344-347.

- 1 12. Cao, D. H.; Stoumpos, C. C.; Farha, O. K.; Hupp, J. T.; Kanatzidis, M. G., 2D Homologous
2 Perovskites as Light-Absorbing Materials for Solar Cell Applications. *J. Am. Chem. Soc.* **2015**,
3 *137* (24), 7843-50.
- 4 13. Xing, G.; Mathews, N.; Sun, S.; Lim, S. S.; Lam, Y. M.; Gratzel, M.; Mhaisalkar, S.; Sum,
5 T. C., Long-range balanced electron- and hole-transport lengths in organic-inorganic
6 CH₃NH₃PbI₃. *Science* **2013**, *342* (6156), 344-7.
- 7 14. Stranks, S. D.; Eperon, G. E.; Grancini, G.; Menelaou, C.; Alcocer, M. J.; Leijtens, T.; Herz,
8 L. M.; Petrozza, A.; Snaith, H. J., Electron-hole diffusion lengths exceeding 1 micrometer in an
9 organometal trihalide perovskite absorber. *Science* **2013**, *342* (6156), 341-344.
- 10 15. Protesescu, L.; Yakunin, S.; Bodnarchuk, M. I.; Krieg, F.; Caputo, R.; Hendon, C. H.; Yang,
11 R. X.; Walsh, A.; Kovalenko, M. V., Nanocrystals of Cesium Lead Halide Perovskites (CsPbX₃,
12 X = Cl, Br, and I): Novel Optoelectronic Materials Showing Bright Emission with Wide Color
13 Gamut. *Nano Lett.* **2015**, *15* (6), 3692-3696.
- 14 16. de Quilletes, D. W.; Vorpahl, S. M.; Stranks, S. D.; Nagaoka, H.; Eperon, G. E.; Ziffer, M.
15 E.; Snaith, H. J.; Ginger, D. S., Impact of microstructure on local carrier lifetime in perovskite
16 solar cells. *Science* **2015**, *348* (6235), 683-686.
- 17 17. Sichert, J. A.; Tong, Y.; Mutz, N.; Vollmer, M.; Fischer, S.; Milowska, K. Z.; García
18 Cortadella, R.; Nickel, B.; Cardenas-Daw, C.; Stolarczyk, J. K.; Urban, A. S.; Feldmann, J.,
19 Quantum Size Effect in Organometal Halide Perovskite Nanoplatelets. *Nano Lett.* **2015**, *15* (10),
20 6521-6527.
- 21 18. Dou, L.; Wong, A. B.; Yu, Y.; Lai, M.; Kornienko, N.; Eaton, S. W.; Fu, A.; Bischak, C. G.;
22 Ma, J.; Ding, T.; Ginsberg, N. S.; Wang, L.-W.; Alivisatos, A. P.; Yang, P., Atomically thin two-
23 dimensional organic-inorganic hybrid perovskites. *Science* **2015**, *349* (6255), 1518-1521.
- 24 19. Bekenstein, Y.; Koscher, B. A.; Eaton, S. W.; Yang, P.; Alivisatos, A. P., Highly
25 Luminescent Colloidal Nanoplates of Perovskite Cesium Lead Halide and Their Oriented
26 Assemblies. *J. Am. Chem. Soc.* **2015**, *137* (51), 16008-16011.
- 27 20. Tyagi, P.; Arveson, S. M.; Tisdale, W. A., Colloidal Organohalide Perovskite Nanoplatelets
28 Exhibiting Quantum Confinement. *J. Phys. Chem. Lett.* **2015**, *6* (10), 1911-1916.
- 29 21. Zhu, H.; Miyata, K.; Fu, Y.; Wang, J.; Joshi, P. P.; Niesner, D.; Williams, K. W.; Jin, S.;
30 Zhu, X.-Y., Screening in Crystalline Liquids Protects Energetic Carriers in Hybrid Perovskites.
31 *Science* **2016**, *353*, 1409-1413.
- 32 22. Kovalenko, M. V.; Protesescu, L.; Bodnarchuk, M. I., Properties and potential optoelectronic
33 applications of lead halide perovskite nanocrystals. *Science* **2017**, *358* (6364), 745-750.
- 34 23. Tong, Y.; Bohn, B. J.; Bladt, E.; Wang, K.; Müller-Buschbaum, P.; Bals, S.; Urban, A. S.;
35 Polavarapu, L.; Feldmann, J., From Precursor Powders to CsPbX₃ Perovskite Nanowires: One-
36 Pot Synthesis, Growth Mechanism, and Oriented Self-Assembly. *Angew. Chem. Int. Ed.* **2017**,
37 *56* (44), 13887-13892.
- 38 24. Akkerman, Q. A.; Rainò, G.; Kovalenko, M. V.; Manna, L., Genesis, challenges and
39 opportunities for colloidal lead halide perovskite nanocrystals. *Nat. Mater.* **2018**, *17* (5), 394-
40 405.
- 41 25. Utzat, H.; Sun, W.; Kaplan, A. E. K.; Krieg, F.; Ginterseder, M.; Spokoyny, B.; Klein, N. D.;
42 Shulenberger, K. E.; Perkinson, C. F.; Kovalenko, M. V.; Bawendi, M. G., Coherent single-
43 photon emission from colloidal lead halide perovskite quantum dots. *Science* **2019**, *363* (6431),
44 1068-1072.

- 1 26. Gonzalez-Carrero, S.; Galian, R. E.; Pérez-Prieto, J., Maximizing the emissive properties of
2 CH₃NH₃PbBr₃ perovskite nanoparticles. *J. Mater. Chem. A* **2015**, *3* (17), 9187-9193.
- 3 27. Park, Y.-S.; Guo, S.; Makarov, N. S.; Klimov, V. I., Room Temperature Single-Photon
4 Emission from Individual Perovskite Quantum Dots. *ACS Nano* **2015**, *9*, 10386-10396.
- 5 28. Song, J.; Li, J.; Li, X.; Xu, L.; Dong, Y.; Zeng, H., Quantum Dot Light-Emitting Diodes
6 Based on Inorganic Perovskite Cesium Lead Halides (CsPbX₃). *Adv. Mater.* **2015**, *27* (44),
7 7162-7167.
- 8 29. Wang, Y.; Li, X.; Song, J.; Xiao, L.; Zeng, H.; Sun, H., All - inorganic colloidal perovskite
9 quantum dots: a new class of lasing materials with favorable characteristics. *Adv. Mater.* **2015**,
10 *27* (44), 7101-7108.
- 11 30. Zhang, F.; Zhong, H.; Chen, C.; Wu, X.-g.; Hu, X.; Huang, H.; Han, J.; Zou, B.; Dong, Y.,
12 Brightly Luminescent and Color-Tunable Colloidal CH₃NH₃PbX₃ (X = Br, I, Cl) Quantum
13 Dots: Potential Alternatives for Display Technology. *ACS Nano* **2015**, *9* (4), 4533-4542.
- 14 31. Tan, Z. K.; Moghaddam, R. S.; Lai, M. L.; Docampo, P.; Higler, R.; Deschler, F.; Price, M.;
15 Sadhanala, A.; Pazos, L. M.; Credgington, D.; Hanusch, F.; Bein, T.; Snaith, H. J.; Friend, R. H.,
16 Bright light-emitting diodes based on organometal halide perovskite. *Nat. Nanotech.* **2014**, *9* (9),
17 687-92.
- 18 32. Green, M. A.; Ho-Baillie, A.; Snaith, H. J., The emergence of perovskite solar cells. *Nat.*
19 *Photonics* **2014**, *8* (7), 506-514.
- 20 33. Park, N.-G., Perovskite solar cells: an emerging photovoltaic technology. *Mater. Today*
21 **2015**, *18* (2), 65-72.
- 22 34. Zhu, H.; Fu, Y.; Meng, F.; Wu, X.; Gong, Z.; Ding, Q.; Gustafsson, M. V.; Trinh, M. T.; Jin,
23 S.; Zhu, X. Y., Lead halide perovskite nanowire lasers with low lasing thresholds and high
24 quality factors. *Nat. Mater.* **2015**, *14* (6), 636-642.
- 25 35. Jung, H. S.; Park, N.-G., Perovskite Solar Cells: From Materials to Devices. *Small* **2015**, *11*
26 (1), 10-25.
- 27 36. Huang, H.; Polavarapu, L.; Sichert, J. A.; Susha, A. S.; Urban, A. S.; Rogach, A. L.,
28 Colloidal lead halide perovskite nanocrystals: synthesis, optical properties and applications. *NPG*
29 *Asia Mater.* **2016**, *8* (11), e328-e328.
- 30 37. Ramasamy, P.; Lim, D.-H.; Kim, B.; Lee, S.-H.; Lee, M.-S.; Lee, J.-S., All-inorganic cesium
31 lead halide perovskite nanocrystals for photodetector applications. *Chem. Commun.* **2016**, *52*
32 (10), 2067-2070.
- 33 38. Xu, Y.-F.; Yang, M.-Z.; Chen, B.-X.; Wang, X.-D.; Chen, H.-Y.; Kuang, D.-B.; Su, C.-Y., A
34 CsPbBr₃ Perovskite Quantum Dot/Graphene Oxide Composite for Photocatalytic CO₂
35 Reduction. *J. Am. Chem. Soc.* **2017**, *139* (16), 5660-5663.
- 36 39. Lin, Y.-H.; Pattanasattayavong, P.; Anthopoulos, T. D., Metal-Halide Perovskite Transistors
37 for Printed Electronics: Challenges and Opportunities. *Adv. Mater.* **2017**, *29* (46), 1702838.
- 38 40. Van Le, Q.; Jang, H. W.; Kim, S. Y., Recent Advances toward High-Efficiency Halide
39 Perovskite Light-Emitting Diodes: Review and Perspective. *Small Methods* **2018**, *2* (10),
40 1700419.
- 41 41. Wei, Y.; Cheng, Z.; Lin, J., An overview on enhancing the stability of lead halide perovskite
42 quantum dots and their applications in phosphor-converted LEDs. *Chem. Soc. Rev.* **2019**, *48* (1),
43 310-350.

- 1 42. Chen, J.; Dong, C.; Idriss, H.; Mohammed, O. F.; Bakr, O. M., Metal Halide Perovskites for
2 Solar-to-Chemical Fuel Conversion. *Adv. Energy Mater.* **2020**, *10* (13), 1902433.
- 3 43. Dong, H.; Zhang, C.; Liu, X.; Yao, J.; Zhao, Y. S., Materials chemistry and engineering in
4 metal halide perovskite lasers. *Chem. Soc. Rev.* **2020**, *49* (3), 951-982.
- 5 44. Liu, S.; Guan, Y.; Sheng, Y.; Hu, Y.; Rong, Y.; Mei, A.; Han, H., A Review on Additives
6 for Halide Perovskite Solar Cells. *Adv. Energy Mater.* **2020**, *10* (13), 1902492.
- 7 45. Huang, H.; Pradhan, B.; Hofkens, J.; Roeffaers, M. B. J.; Steele, J. A., Solar-Driven Metal
8 Halide Perovskite Photocatalysis: Design, Stability, and Performance. *ACS Energy Lett.* **2020**, *5*
9 (4), 1107-1123.
- 10 46. Senanayak, S. P.; Abdi-Jalebi, M.; Kamboj, V. S.; Carey, R.; Shivanna, R.; Tian, T.;
11 Schweicher, G.; Wang, J.; Giesbrecht, N.; Di Nuzzo, D.; Beere, H. E.; Docampo, P.; Ritchie, D.
12 A.; Fairen-Jimenez, D.; Friend, R. H.; Sirringhaus, H., A general approach for hysteresis-free,
13 operationally stable metal halide perovskite field-effect transistors. *Sci. Adv.* **2020**, *6* (15),
14 eaaz4948.
- 15 47. Zhang, C.; Kuang, D.-B.; Wu, W.-Q., A Review of Diverse Halide Perovskite Morphologies
16 for Efficient Optoelectronic Applications. *Small Methods* **2020**, *4* (2), 1900662.
- 17 48. Weidman, M. C.; Goodman, A. J.; Tisdale, W. A., Colloidal Halide Perovskite
18 Nanoplatelets: An Exciting New Class of Semiconductor Nanomaterials. *Chem. Mater.* **2017**, *29*
19 (12), 5019-5030.
- 20 49. Akkerman, Q. A.; Motti, S. G.; Srimath Kandada, A. R.; Mosconi, E.; D'Innocenzo, V.;
21 Bertoni, G.; Marras, S.; Kamino, B. A.; Miranda, L.; De Angelis, F.; Petrozza, A.; Prato, M.;
22 Manna, L., Solution Synthesis Approach to Colloidal Cesium Lead Halide Perovskite
23 Nanoplatelets with Monolayer-Level Thickness Control. *J. Am. Chem. Soc.* **2016**, *138* (3), 1010-
24 6.
- 25 50. Soe, C. M. M.; Nagabhushana, G. P.; Shivaramaiah, R.; Tsai, H.; Nie, W.; Blancon, J.-C.;
26 Melkonyan, F.; Cao, D. H.; Traoré, B.; Pedesseau, L.; Kepenekian, M.; Katan, C.; Even, J.;
27 Marks, T. J.; Navrotsky, A.; Mohite, A. D.; Stoumpos, C. C.; Kanatzidis, M. G., Structural and
28 thermodynamic limits of layer thickness in 2D halide perovskites. *Proc. Natl. Acad. Sci. U.S.A*
29 **2019**, *116* (1), 58-66.
- 30 51. Zhang, F.; Lu, H.; Tong, J.; Berry, J. J.; Beard, M. C.; Zhu, K., Advances in two-
31 dimensional organic-inorganic hybrid perovskites. *Energy Environ. Sci.* **2020**, *13* (4), 1154-
32 1186.
- 33 52. Travis, W.; Glover, E. N. K.; Bronstein, H.; Scanlon, D. O.; Palgrave, R. G., On the
34 application of the tolerance factor to inorganic and hybrid halide perovskites: a revised system.
35 *Chem. Sci.* **2016**, *7* (7), 4548-4556.
- 36 53. Shamsi, J.; Urban, A. S.; Imran, M.; De Trizio, L.; Manna, L., Metal Halide Perovskite
37 Nanocrystals: Synthesis, Post-Synthesis Modifications, and Their Optical Properties. *Chem. Rev.*
38 **2019**, *119* (5), 3296-3348.
- 39 54. Li, X.; Wu, Y.; Zhang, S.; Cai, B.; Gu, Y.; Song, J.; Zeng, H., CsPbX₃ Quantum Dots for
40 Lighting and Displays: Room-Temperature Synthesis, Photoluminescence Superiorities,
41 Underlying Origins and White Light-Emitting Diodes. *Adv. Funct. Mater.* **2016**, *26* (15), 2435-
42 2445.

- 1 55. Huang, H.; Li, Y.; Tong, Y.; Yao, E.-P.; Feil, M. W.; Richter, A. F.; Döblinger, M.; Rogach,
2 A. L.; Feldmann, J.; Polavarapu, L., Spontaneous Crystallization of Perovskite Nanocrystals in
3 Nonpolar Organic Solvents: A Versatile Approach for their Shape-Controlled Synthesis. *Angew.*
4 *Chem. Int. Ed.* **2019**, *58* (46), 16558-16562.
- 5 56. Nedelcu, G.; Protesescu, L.; Yakunin, S.; Bodnarchuk, M. I.; Grotevent, M. J.; Kovalenko,
6 M. V., Fast Anion-Exchange in Highly Luminescent Nanocrystals of Cesium Lead Halide
7 Perovskites (CsPbX₃, X = Cl, Br, I). *Nano Lett.* **2015**, *15* (8), 5635-5640.
- 8 57. Zhang, D. D.; Yang, Y. M.; Bekenstein, Y.; Yu, Y.; Gibson, N. A.; Wong, A. B.; Eaton, S.
9 W.; Kornienko, N.; Kong, Q.; Lai, M. L.; Alivisatos, A. P.; Leone, S. R.; Yang, P. D., Synthesis
10 of Composition Tunable and Highly Luminescent Cesium Lead Halide Nanowires through
11 Anion-Exchange Reactions. *J. Am. Chem. Soc.* **2016**, *138* (23), 7236-7239.
- 12 58. Akkerman, Q. A.; D'Innocenzo, V.; Accornero, S.; Scarpellini, A.; Petrozza, A.; Prato, M.;
13 Manna, L., Tuning the Optical Properties of Cesium Lead Halide Perovskite Nanocrystals by
14 Anion Exchange Reactions. *J. Am. Chem. Soc.* **2015**, *137* (32), 10276-10281.
- 15 59. Tong, Y.; Bladt, E.; Aygüler, M. F.; Manzi, A.; Milowska, K. Z.; Hintermayr, V. A.;
16 Docampo, P.; Bals, S.; Urban, A. S.; Polavarapu, L.; Feldmann, J., Highly Luminescent Cesium
17 Lead Halide Perovskite Nanocrystals with Tunable Composition and Thickness by
18 Ultrasonication. *Angew. Chem. Int. Ed.* **2016**, *55* (44), 13887-13892.
- 19 60. Murray, C. B.; Norris, D. J.; Bawendi, M. G., Synthesis and characterization of nearly
20 monodisperse CdE (E = sulfur, selenium, tellurium) semiconductor nanocrystallites. *J. Am.*
21 *Chem. Soc.* **1993**, *115* (19), 8706-8715.
- 22 61. Zorman, B.; Ramakrishna, M. V.; Friesner, R. A., Quantum Confinement Effects in CdSe
23 Quantum Dots. *J. Phys. Chem.* **1995**, *99* (19), 7649-7653.
- 24 62. Bohn, B. J.; Tong, Y.; Gramlich, M.; Lai, M. L.; Döblinger, M.; Wang, K.; Hoyer, R. L. Z.;
25 Müller-Buschbaum, P.; Stranks, S. D.; Urban, A. S.; Polavarapu, L.; Feldmann, J., Boosting
26 Tunable Blue Luminescence of Halide Perovskite Nanoplatelets through Postsynthetic Surface
27 Trap Repair. *Nano Lett.* **2018**, *18* (8), 5231-5238.
- 28 63. Zheng, Y.; Niu, T.; Ran, X.; Qiu, J.; Li, B.; Xia, Y.; Chen, Y.; Huang, W., Unique
29 characteristics of 2D Ruddlesden–Popper (2DRP) perovskite for future photovoltaic application.
30 *J. Mater. Chem. A* **2019**, *7* (23), 13860-13872.
- 31 64. Wang, F.; Bai, S.; Tress, W.; Hagfeldt, A.; Gao, F., Defects engineering for high-
32 performance perovskite solar cells. *npj Flex. Electron.* **2018**, *2* (1), 22.
- 33 65. Uratani, H.; Yamashita, K., Charge Carrier Trapping at Surface Defects of Perovskite Solar
34 Cell Absorbers: A First-Principles Study. *J. Phys. Chem. Lett.* **2017**, *8* (4), 742-746.
- 35 66. Papavassiliou, G. C.; Pagona, G.; Karousis, N.; Mousdis, G. A.; Koutselas, I.;
36 Vassilakopoulou, A., Nanocrystalline/microcrystalline materials based on lead-halide units. *J.*
37 *Mater. Chem.* **2012**, *22* (17), 8271-8280.
- 38 67. Papavassiliou, G. C.; Pagona, G.; Mousdis, G. A.; Karousis, N., Enhanced phosphorescence
39 from nanocrystalline/microcrystalline materials based on (CH₃NH₃)(1-naphthylmethyl
40 ammonium)2Pb2Cl7 and similar compounds. *Chem. Phys. Lett.* **2013**, *570*, 80-84.
- 41 68. Schmidt, L. C.; Pertegás, A.; González-Carrero, S.; Malinkiewicz, O.; Agouram, S.;
42 Mínguez Espallargas, G.; Bolink, H. J.; Galian, R. E.; Pérez-Prieto, J., Nontemplate Synthesis of
43 CH₃NH₃PbBr₃ Perovskite Nanoparticles. *J. Am. Chem. Soc.* **2014**, *136* (3), 850-853.

- 1 69. Talapin, D. V.; Mekis, I.; Götzinger, S.; Kornowski, A.; Benson, O.; Weller, H.,
2 CdSe/CdS/ZnS and CdSe/ZnSe/ZnS Core–Shell–Shell Nanocrystals. *J. Phys. Chem. B* **2004**,
3 *108* (49), 18826-18831.
- 4 70. Protesescu, L.; Yakunin, S.; Bodnarchuk, M. I.; Bertolotti, F.; Masciocchi, N.; Guagliardi,
5 A.; Kovalenko, M. V., Monodisperse Formamidinium Lead Bromide Nanocrystals with Bright
6 and Stable Green Photoluminescence. *J. Am. Chem. Soc.* **2016**, *138* (43), 14202-14205.
- 7 71. Protesescu, L.; Yakunin, S.; Kumar, S.; Bär, J.; Bertolotti, F.; Masciocchi, N.; Guagliardi,
8 A.; Grotevent, M.; Shorubalko, I.; Bodnarchuk, M. I.; Shih, C.-J.; Kovalenko, M. V.,
9 Dismantling the “Red Wall” of Colloidal Perovskites: Highly Luminescent Formamidinium and
10 Formamidinium–Cesium Lead Iodide Nanocrystals. *ACS Nano* **2017**, *11* (3), 3119-3134.
- 11 72. Hudait, B.; Dutta, S. K.; Pradhan, N., Isotropic CsPbBr₃ Perovskite Nanocrystals beyond
12 Nanocubes: Growth and Optical Properties. *ACS Energy Lett.* **2020**, *5* (2), 650-656.
- 13 73. Bera, S.; Behera, R. K.; Pradhan, N., α -Halo Ketone for Polyhedral Perovskite Nanocrystals:
14 Evolutions, Shape Conversions, Ligand Chemistry, and Self-Assembly. *J. Am. Chem. Soc.* **2020**,
15 *142* (49), 20865-20874.
- 16 74. Peng, L.; Dutta, S. K.; Mondal, D.; Hudait, B.; Shyamal, S.; Xie, R.; Mahadevan, P.;
17 Pradhan, N., Arm Growth and Facet Modulation in Perovskite Nanocrystals. *J. Am. Chem. Soc.*
18 **2019**, *141* (40), 16160-16168.
- 19 75. Tong, Y.; Fu, M.; Bladt, E.; Huang, H.; Richter, A. F.; Wang, K.; Müller-Buschbaum, P.;
20 Bals, S.; Tamarat, P.; Lounis, B.; Feldmann, J.; Polavarapu, L., Chemical Cutting of Perovskite
21 Nanowires into Single-Photon Emissive Low-Aspect-Ratio CsPbX₃ (X=Cl, Br, I) Nanorods.
22 *Angew. Chem. Int. Ed.* **2018**, *57* (49), 16094-16098.
- 23 76. Imran, M.; Di Stasio, F.; Dang, Z. Y.; Canale, C.; Khan, A. H.; Shamsi, J.; Brescia, R.;
24 Prato, M.; Manna, L., Colloidal Synthesis of Strongly Fluorescent CsPbBr₃ Nanowires with
25 Width Tunable down to the Quantum Confinement Regime. *Chem. Mater.* **2016**, *28* (18), 6450-
26 6454.
- 27 77. Zhang, D.; Eaton, S. W.; Yu, Y.; Dou, L.; Yang, P., Solution-Phase Synthesis of Cesium
28 Lead Halide Perovskite Nanowires. *J. Am. Chem. Soc.* **2015**, *137* (29), 9230-9233.
- 29 78. Zhang, D. D.; Yu, Y.; Bekenstein, Y.; Wong, A. B.; Alivisatos, A. P.; Yang, P. D., Ultrathin
30 Colloidal Cesium Lead Halide Perovskite Nanowires. *J. Am. Chem. Soc.* **2016**, *138* (40), 13155-
31 13158.
- 32 79. Zhong, Q.; Cao, M.; Xu, Y.; Li, P.; Zhang, Y.; Hu, H.; Yang, D.; Xu, Y.; Wang, L.; Li, Y.;
33 Zhang, X.; Zhang, Q., L-Type Ligand-Assisted Acid-Free Synthesis of CsPbBr₃ Nanocrystals
34 with Near-Unity Photoluminescence Quantum Yield and High Stability. *Nano Lett.* **2019**, *19* (6),
35 4151-4157.
- 36 80. Dutta, A.; Behera, R. K.; Pal, P.; Baitalik, S.; Pradhan, N., Near-Unity Photoluminescence
37 Quantum Efficiency for All CsPbX₃ (X=Cl, Br, and I) Perovskite Nanocrystals: A Generic
38 Synthesis Approach. *Angew. Chem. Int. Ed.* **2019**, *58* (17), 5552-5556.
- 39 81. Dutta, A.; Dutta, S. K.; Das Adhikari, S.; Pradhan, N., Tuning the Size of CsPbBr₃
40 Nanocrystals: All at One Constant Temperature. *ACS Energy Lett.* **2018**, *3* (2), 329-334.
- 41 82. Tong, Y.; Yao, E.-P.; Manzi, A.; Bladt, E.; Wang, K.; Döblinger, M.; Bals, S.; Müller-
42 Buschbaum, P.; Urban, A. S.; Polavarapu, L.; Feldmann, J., Spontaneous Self-Assembly of
43 Perovskite Nanocrystals into Electronically Coupled Supercrystals: Toward Filling the Green
44 Gap. *Adv. Mater.* **2018**, *30* (29), 1801117.

- 1 83. Rainò, G.; Becker, M. A.; Bodnarchuk, M. I.; Mahrt, R. F.; Kovalenko, M. V.; Stöferle, T.,
2 Superfluorescence from lead halide perovskite quantum dot superlattices. *Nature* **2018**, *563*
3 (7733), 671-675.
- 4 84. Baranov, D.; Toso, S.; Imran, M.; Manna, L., Investigation into the Photoluminescence Red
5 Shift in Cesium Lead Bromide Nanocrystal Superlattices. *J. Phys. Chem. Lett.* **2019**, *10* (3), 655-
6 660.
- 7 85. De Roo, J.; Ibáñez, M.; Geiregat, P.; Nedelcu, G.; Walravens, W.; Maes, J.; Martins, J. C.;
8 Van Driessche, I.; Kovalenko, M. V.; Hens, Z., Highly Dynamic Ligand Binding and Light
9 Absorption Coefficient of Cesium Lead Bromide Perovskite Nanocrystals. *ACS Nano* **2016**, *10*
10 (2), 2071-2081.
- 11 86. Yang, D.; Li, X.; Zeng, H., Surface Chemistry of All Inorganic Halide Perovskite
12 Nanocrystals: Passivation Mechanism and Stability. *Adv. Mater. Interfaces* **2018**, *5* (8), 1701662.
- 13 87. Behera, R. K.; Das Adhikari, S.; Dutta, S. K.; Dutta, A.; Pradhan, N., Blue-Emitting
14 CsPbCl₃ Nanocrystals: Impact of Surface Passivation for Unprecedented Enhancement and Loss
15 of Optical Emission. *J. Phys. Chem. Lett.* **2018**, *9* (23), 6884-6891.
- 16 88. Koscher, B. A.; Swabeck, J. K.; Bronstein, N. D.; Alivisatos, A. P., Essentially Trap-Free
17 CsPbBr₃ Colloidal Nanocrystals by Postsynthetic Thiocyanate Surface Treatment. *J. Am. Chem.*
18 *Soc.* **2017**, *139* (19), 6566-6569.
- 19 89. Chen, J.; Du, W.; Shi, J.; Li, M.; Wang, Y.; Zhang, Q.; Liu, X., Perovskite quantum dot
20 lasers. *InfoMat* **2020**, *2* (1), 170-183.
- 21 90. Yuan, J.; Hazarika, A.; Zhao, Q.; Ling, X.; Moot, T.; Ma, W.; Luther, J. M., Metal Halide
22 Perovskites in Quantum Dot Solar Cells: Progress and Prospects. *Joule* **2020**, *4* (6), 1160-1185.
- 23 91. Wang, Y.; Yuan, J.; Zhang, X.; Ling, X.; Larson, B. W.; Zhao, Q.; Yang, Y.; Shi, Y.; Luther,
24 J. M.; Ma, W., Surface Ligand Management Aided by a Secondary Amine Enables Increased
25 Synthesis Yield of CsPbI₃ Perovskite Quantum Dots and High Photovoltaic Performance. *Adv.*
26 *Mater.* **2020**, *32* (32), 2000449.
- 27 92. Zhang, Y.; Liu, J.; Wang, Z.; Xue, Y.; Ou, Q.; Polavarapu, L.; Zheng, J.; Qi, X.; Bao, Q.,
28 Synthesis, properties, and optical applications of low-dimensional perovskites. *Chem. Commun.*
29 **2016**, *52* (94), 13637-13655.
- 30 93. Liu, X.; Yu, D.; Song, X.; Zeng, H., Metal Halide Perovskites: Synthesis, Ion Migration, and
31 Application in Field-Effect Transistors. *Small* **2018**, *14* (36), 1801460.
- 32 94. Chang, S.; Bai, Z.; Zhong, H., In Situ Fabricated Perovskite Nanocrystals: A Revolution in
33 Optical Materials. *Adv. Opt. Mater.* **2018**, *6* (18), 1800380.
- 34 95. Park, B.-W.; Philippe, B.; Zhang, X.; Rensmo, H.; Boschloo, G.; Johansson, E. M. J.,
35 Bismuth Based Hybrid Perovskites A₃Bi₂I₉ (A: Methylammonium or Cesium) for Solar Cell
36 Application. *Adv. Mater.* **2015**, *27* (43), 6806-6813.
- 37 96. Rieger, S.; Bohn, B. J.; Döblinger, M.; Richter, A. F.; Tong, Y.; Wang, K.; Müller-
38 Buschbaum, P.; Polavarapu, L.; Leppert, L.; Stolarczyk, J. K.; Feldmann, J., Excitons and
39 narrow bands determine the optical properties of cesium bismuth halides. *Phys. Rev. B* **2019**, *100*
40 (20), 201404.

- 1 97. Correa-Baena, J.-P.; Nienhaus, L.; Kurchin, R. C.; Shin, S. S.; Wieghold, S.; Putri Hartono,
2 N. T.; Layurova, M.; Klein, N. D.; Poindexter, J. R.; Polizzotti, A.; Sun, S.; Bawendi, M. G.;
3 Buonassisi, T., A-Site Cation in Inorganic A3Sb2I9 Perovskite Influences Structural
4 Dimensionality, Exciton Binding Energy, and Solar Cell Performance. *Chem. Mater.* **2018**, *30*
5 (11), 3734-3742.
- 6 98. Huang, H.; Bodnarchuk, M. I.; Kershaw, S. V.; Kovalenko, M. V.; Rogach, A. L., Lead
7 Halide Perovskite Nanocrystals in the Research Spotlight: Stability and Defect Tolerance. *ACS*
8 *Energy Lett.* **2017**, *2* (9), 2071-2083.
- 9 99. Polavarapu, L.; Zhang, Q.; Krahne, R., Nanoscale & Nanoscale Advances joint themed
10 collection on halide perovskite nanocrystals. *Nanoscale* **2019**, *11* (18), 8648-8650.
- 11 100. Saidaminov, M. I.; Mohammed, O. F.; Bakr, O. M., Low-Dimensional-Networked Metal
12 Halide Perovskites: The Next Big Thing. *ACS Energy Lett.* **2017**, *2* (4), 889-896.
- 13 101. Seth, S.; Ahmed, T.; De, A.; Samanta, A., Tackling the Defects, Stability, and
14 Photoluminescence of CsPbX₃ Perovskite Nanocrystals. *ACS Energy Lett.* **2019**, *4*, 1610-1618.
- 15 102. Swarnkar, A.; Ravi, V. K.; Nag, A., Beyond Colloidal Cesium Lead Halide Perovskite
16 Nanocrystals: Analogous Metal Halides and Doping. *ACS Energy Lett.* **2017**, *2* (5), 1089-1098.
- 17 103. Wu, Y.; Li, X.; Zeng, H., Highly Luminescent and Stable Halide Perovskite
18 Nanocrystals. *ACS Energy Lett.* **2019**, *4* (3), 673-681.
- 19 104. Bera, S.; Pradhan, N., Perovskite Nanocrystal Heterostructures: Synthesis, Optical
20 Properties, and Applications. *ACS Energy Lett.* **2020**, *5* (9), 2858-2872.
- 21 105. He, X.; Qiu, Y.; Yang, S., Fully-Inorganic Trihalide Perovskite Nanocrystals: A New
22 Research Frontier of Optoelectronic Materials. *Adv. Mater.* **2017**, *29* (32), 1700775.
- 23 106. Huang, J.; Lai, M.; Lin, J.; Yang, P., Rich Chemistry in Inorganic Halide Perovskite
24 Nanostructures. *Adv. Mater.* **2018**, *30* (48), 1802856.
- 25 107. Jeong, B.; Han, H.; Park, C., Micro- and Nanopatterning of Halide Perovskites Where
26 Crystal Engineering for Emerging Photoelectronics Meets Integrated Device Array Technology.
27 *Adv. Mater.* *n/a* (n/a), 2000597.
- 28 108. Zhang, X.; Li, L.; Sun, Z.; Luo, J., Rational chemical doping of metal halide perovskites.
29 *Chem. Soc. Rev.* **2019**, *48* (2), 517-539.
- 30 109. Ghosh, S.; Pradhan, B., Lead-Free Metal Halide Perovskite Nanocrystals: Challenges,
31 Applications, and Future Aspects. *ChemNanoMat* **2019**, *5* (3), 300-312.
- 32 110. Luo, B.; Naghadeh, S. B.; Zhang, J. Z., Lead Halide Perovskite Nanocrystals: Stability,
33 Surface Passivation, and Structural Control. *ChemNanoMat* **2017**, *3* (7), 456-465.
- 34 111. Kovalenko, M. V.; Bodnarchuk, M. I., Lead Halide Perovskite Nanocrystals: From
35 Discovery to Self-assembly and Applications. *CHIMIA International Journal for Chemistry*
36 **2017**, *71* (7-8), 461-470.
- 37 112. Yan, F.; Tan, S. T.; Li, X.; Demir, H. V., Light Generation in Lead Halide Perovskite
38 Nanocrystals: LEDs, Color Converters, Lasers, and Other Applications. *Small* **2019**, *15* (47),
39 1902079.
- 40 113. Dong, Y.; Zhao, Y.; Zhang, S.; Dai, Y.; Liu, L.; Li, Y.; Chen, Q., Recent advances
41 toward practical use of halide perovskite nanocrystals. *J. Mater. Chem. A* **2018**, *6* (44), 21729-
42 21746.

- 1 114. Ravi, V. K.; Singhal, N.; Nag, A., Initiation and future prospects of colloidal metal
2 halide double-perovskite nanocrystals: Cs₂AgBiX₆ (X = Cl, Br, I). *J. Mater. Chem. A* **2018**, *6*
3 (44), 21666-21675.
- 4 115. Que, M.; Zhu, L.; Guo, Y.; Que, W.; Yun, S., Toward perovskite nanocrystalline solar
5 cells: progress and potential. *J. Mater. Chem. C* **2020**, *8* (16), 5321-5334.
- 6 116. Kaur, G.; Ghosh, H. N., Hot Carrier Relaxation in CsPbBr₃-Based Perovskites: A
7 Polaron Perspective. *J. Phys. Chem. Lett.* **2020**, *11* (20), 8765-8776.
- 8 117. Huang, H.; Bodnarchuk, M. I.; Kershaw, S. V.; Kovalenko, M. V.; Rogach, A. L., Lead
9 Halide Perovskite Nanocrystals in the Research Spotlight: Stability and Defect Tolerance. *ACS*
10 *Energy Letters* **2017**, *2* (9), 2071-2083.
- 11 118. Zhang, Q.; Yin, Y., All-Inorganic Metal Halide Perovskite Nanocrystals: Opportunities
12 and Challenges. *ACS Central Sci.* **2018**, *4* (6), 668-679.
- 13 119. Li, Z.; Peng, X., Size/Shape-Controlled Synthesis of Colloidal CdSe Quantum Disks:
14 Ligand and Temperature Effects. *J. Am. Chem. Soc.* **2011**, *133* (17), 6578-6586.
- 15 120. Brus, L., Electronic wave functions in semiconductor clusters: experiment and theory. *J.*
16 *Phys. Chem.* **1986**, *90* (12), 2555-2560.
- 17 121. Brus, L. E., A simple model for the ionization potential, electron affinity, and aqueous
18 redox potentials of small semiconductor crystallites. *J. Chem. Phys.* **1983**, *79* (11), 5566-5571.
- 19 122. Murphy, J. E.; Beard, M. C.; Norman, A. G.; Ahrenkiel, S. P.; Johnson, J. C.; Yu, P.;
20 Mičić, O. I.; Ellingson, R. J.; Nozik, A. J., PbTe Colloidal Nanocrystals: Synthesis,
21 Characterization, and Multiple Exciton Generation. *J. Am. Chem. Soc.* **2006**, *128* (10), 3241-
22 3247.
- 23 123. Talapin, D. V.; Rogach, A. L.; Kornowski, A.; Haase, M.; Weller, H., Highly
24 Luminescent Monodisperse CdSe and CdSe/ZnS Nanocrystals Synthesized in a
25 Hexadecylamine–Trioctylphosphine Oxide–Trioctylphosphine Mixture. *Nano Lett.* **2001**, *1* (4),
26 207-211.
- 27 124. Steigerwald, M. L.; Brus, L. E., Semiconductor crystallites: a class of large molecules.
28 *Acc. Chem. Res.* **1990**, *23* (6), 183-188.
- 29 125. Gao, M.-R.; Xu, Y.-F.; Jiang, J.; Yu, S.-H., Nanostructured metal chalcogenides:
30 synthesis, modification, and applications in energy conversion and storage devices. *Chem. Soc.*
31 *Rev.* **2013**, *42* (7), 2986-3017.
- 32 126. Nikl, M.; Nitsch, K.; Polák, K.; Mihókova, E.; Zazubovich, S.; Pazzi, G. P.; Fabeni, P.;
33 Salvini, L.; Aceves, R.; Barbosa-Flores, M.; Salas, R. P.; Gurioli, M.; Scacco, A., Quantum size
34 effect in the excitonic luminescence of CsPbX₃-like quantum dots in CsX (X = Cl, Br) single
35 crystal host. *J. Lumin.* **1997**, *72-74*, 377-379.
- 36 127. Nikl, M.; Nitsch, K.; Polak, K.; Pazzi, G. P.; Fabeni, P.; Citrin, D. S.; Gurioli, M.,
37 Optical properties of the Pb²⁺-based aggregated phase in a CsCl host crystal: Quantum-
38 confinement effects. *Phys. Rev. B* **1995**, *51* (8), 5192-5199.
- 39 128. Ishihara, T.; Takahashi, J.; Goto, T., Optical properties due to electronic transitions in
40 two-dimensional semiconductors (C_nH_{2n+1}NH₃)₂PbI₄. *Phys. Rev. B* **1990**, *42* (17), 11099-
41 11107.
- 42 129. Koutselas, I. B.; Ducasse, L.; Papavassiliou, G. C., Electronic properties of three- and
43 low-dimensional semiconducting materials with Pb halide and Sn halide units. *J. Condens.*
44 *Matter Phys.* **1996**, *8* (9), 1217-1227.

- 1 130. Im, J.-H.; Lee, C.-R.; Lee, J.-W.; Park, S.-W.; Park, N.-G., 6.5% efficient perovskite
2 quantum-dot-sensitized solar cell. *Nanoscale* **2011**, *3* (10), 4088-4093.
- 3 131. Ishihara, T.; Takahashi, J.; Goto, T., Exciton state in two-dimensional perovskite
4 semiconductor (C₁₀H₂₁NH₃)₂PbI₄. *Solid State Commun.* **1989**, *69* (9), 933-936.
- 5 132. Protesescu, L.; Yakunin, S.; Nazarenko, O.; Dirin, D. N.; Kovalenko, M. V., Low-Cost
6 Synthesis of Highly Luminescent Colloidal Lead Halide Perovskite Nanocrystals by Wet Ball
7 Milling. *ACS Appl. Nano Mater.* **2018**, *1* (3), 1300-1308.
- 8 133. Hintermayr, V. A.; Richter, A. F.; Ehrat, F.; Döblinger, M.; Vanderlinden, W.; Sichert, J.
9 A.; Tong, Y.; Polavarapu, L.; Feldmann, J.; Urban, A. S., Tuning the Optical Properties of
10 Perovskite Nanoplatelets through Composition and Thickness by Ligand-Assisted Exfoliation.
11 **2016**, *28* (43), 9478-9485.
- 12 134. Pan, Q.; Hu, H.; Zou, Y.; Chen, M.; Wu, L.; Yang, D.; Yuan, X.; Fan, J.; Sun, B.;
13 Zhang, Q., Microwave-assisted synthesis of high-quality “all-inorganic” CsPbX₃ (X = Cl, Br, I)
14 perovskite nanocrystals and their application in light emitting diodes. *J. Mater. Chem. C* **2017**, *5*
15 (42), 10947-10954.
- 16 135. Chen, M.; Zou, Y.; Wu, L.; Pan, Q.; Yang, D.; Hu, H.; Tan, Y.; Zhong, Q.; Xu, Y.; Liu,
17 H.; Sun, B.; Zhang, Q., Solvothermal Synthesis of High-Quality All-Inorganic Cesium Lead
18 Halide Perovskite Nanocrystals: From Nanocube to Ultrathin Nanowire. *Adv. Funct. Mater.*
19 **2017**, *27* (23), 1701121.
- 20 136. Debuigne, F.; Jeunieu, L.; Wiame, M.; B.Nagy, J., Synthesis of Organic Nanoparticles
21 in Different W/O Microemulsions. *Langmuir* **2000**, *16* (20), 7605-7611.
- 22 137. Fu, H.-B.; Yao, J.-N., Size Effects on the Optical Properties of Organic Nanoparticles. *J.*
23 *Am. Chem. Soc.* **2001**, *123* (7), 1434-1439.
- 24 138. Horn, D.; Rieger, J., Organic Nanoparticles in the Aqueous Phase—Theory, Experiment,
25 and Use. *Angew. Chem. Int. Ed.* **2001**, *40* (23), 4330-4361.
- 26 139. Huang, H.; Susha, A. S.; Kershaw, S. V.; Hung, T. F.; Rogach, A. L., Control of
27 Emission Color of High Quantum Yield CH₃NH₃PbBr₃ Perovskite Quantum Dots by
28 Precipitation Temperature. *Adv. Sci.* **2015**, *2* (9), 1500194.
- 29 140. Dang, Z.; Shamsi, J.; Palazon, F.; Imran, M.; Akkerman, Q. A.; Park, S.; Bertoni, G.;
30 Prato, M.; Brescia, R.; Manna, L., In Situ Transmission Electron Microscopy Study of Electron
31 Beam-Induced Transformations in Colloidal Cesium Lead Halide Perovskite Nanocrystals. *ACS*
32 *Nano* **2017**, *11* (2), 2124-2132.
- 33 141. Li, Y.-F.; Chou, S.-Y.; Huang, P.; Xiao, C.; Liu, X.; Xie, Y.; Zhao, F.; Huang, Y.; Feng,
34 J.; Zhong, H.; Sun, H.-B.; Pei, Q., Stretchable Organometal-Halide-Perovskite Quantum-Dot
35 Light-Emitting Diodes. *Adv. Mater.* **2019**, *31* (22), 1807516.
- 36 142. Huang, H.; Zhao, F.; Liu, L.; Zhang, F.; Wu, X.-g.; Shi, L.; Zou, B.; Pei, Q.; Zhong, H.,
37 Emulsion Synthesis of Size-Tunable CH₃NH₃PbBr₃ Quantum Dots: An Alternative Route
38 toward Efficient Light-Emitting Diodes. *ACS Appl. Mater. Interfaces* **2015**, *7* (51), 28128-28133.
- 39 143. Shamsi, J.; Urban, A. S.; Imran, M.; De Trizio, L.; Manna, L., Metal Halide Perovskite
40 Nanocrystals: Synthesis, Post-Synthesis Modifications, and Their Optical Properties. *Chemical*
41 *Reviews* **2019**, *119* (5), 3296-3348.

- 1 144. Li, X.; Wu, Y.; Zhang, S.; Cai, B.; Gu, Y.; Song, J.; Zeng, H., CsPbX₃ Quantum Dots
2 for Lighting and Displays: Room-Temperature Synthesis, Photoluminescence Superiorities,
3 Underlying Origins and White Light-Emitting Diodes. *Advanced Functional Materials* **2016**, *26*
4 (15), 2435-2445.
- 5 145. Lu, M.; Zhang, Y.; Wang, S.; Guo, J.; Yu, W. W.; Rogach, A. L., Metal Halide
6 Perovskite Light-Emitting Devices: Promising Technology for Next-Generation Displays. *Adv.*
7 *Funct. Mater.* **2019**, *29* (30), 1902008.
- 8 146. Imran, M.; Ijaz, P.; Baranov, D.; Goldoni, L.; Petralanda, U.; Akkerman, Q.; Abdelhady,
9 A. L.; Prato, M.; Bianchini, P.; Infante, I.; Manna, L., Shape-Pure, Nearly Monodispersed
10 CsPbBr₃ Nanocubes Prepared Using Secondary Aliphatic Amines. *Nano Lett.* **2018**, *18* (12),
11 7822-7831.
- 12 147. Lignos, I.; Stavrakis, S.; Nedelcu, G.; Protesescu, L.; deMello, A. J.; Kovalenko, M. V.,
13 Synthesis of Cesium Lead Halide Perovskite Nanocrystals in a Droplet-Based Microfluidic
14 Platform: Fast Parametric Space Mapping. *Nano Lett.* **2016**, *16* (3), 1869-1877.
- 15 148. Almeida, G.; Goldoni, L.; Akkerman, Q.; Dang, Z.; Khan, A. H.; Marras, S.; Moreels, I.;
16 Manna, L., Role of Acid-Base Equilibria in the Size, Shape, and Phase Control of Cesium Lead
17 Bromide Nanocrystals. *ACS Nano* **2018**, *12* (2), 1704-1711.
- 18 149. Cottingham, P.; Brutchey, R. L., On the crystal structure of colloiddally prepared
19 CsPbBr₃ quantum dots. *Chem. Commun.* **2016**, *52* (30), 5246-5249.
- 20 150. Becker, M. A.; Vaxenburg, R.; Nedelcu, G.; Sercel, P. C.; Shabaev, A.; Mehl, M. J.;
21 Michopoulos, J. G.; Lambrakos, S. G.; Bernstein, N.; Lyons, J. L.; Stöferle, T.; Mahrt, R. F.;
22 Kovalenko, M. V.; Norris, D. J.; Rainò, G.; Efros, A. L., Bright triplet excitons in caesium lead
23 halide perovskites. *Nature* **2018**, *553* (7687), 189-193.
- 24 151. Mondal, N.; De, A.; Samanta, A., Achieving Near-Unity Photoluminescence Efficiency
25 for Blue-Violet-Emitting Perovskite Nanocrystals. *ACS Energy Lett.* **2019**, *4* (1), 32-39.
- 26 152. Ye, J.; Byranvand, M. M.; Martínez, C. O.; Hoye, R. L.; Saliba, M.; Polavarapu, L.,
27 Defect Passivation in Lead-Halide Perovskite Nanocrystals and Thin Films: Toward Efficient
28 LEDs and Solar cells. *Angew. Chem. Int. Ed.* **2021**, *n/a* (n/a), DOI:10.1002/anie.202102360.
- 29 153. Dong, Y.; Qiao, T.; Kim, D.; Parobek, D.; Rossi, D.; Son, D. H., Precise Control of
30 Quantum Confinement in Cesium Lead Halide Perovskite Quantum Dots via Thermodynamic
31 Equilibrium. *Nano Lett.* **2018**, *18* (6), 3716-3722.
- 32 154. Rossi, D.; Wang, H.; Dong, Y.; Qiao, T.; Qian, X.; Son, D. H., Light-Induced Activation
33 of Forbidden Exciton Transition in Strongly Confined Perovskite Quantum Dots. *ACS Nano*
34 **2018**, *12* (12), 12436-12443.
- 35 155. Cheng, O. H.-C.; Qiao, T.; Sheldon, M.; Son, D. H., Size- and temperature-dependent
36 photoluminescence spectra of strongly confined CsPbBr₃ quantum dots. *Nanoscale* **2020**, *12*
37 (24), 13113-13118.
- 38 156. Li, Y.; Luo, X.; Liu, Y.; Lu, X.; Wu, K., Size- and Composition-Dependent Exciton Spin
39 Relaxation in Lead Halide Perovskite Quantum Dots. *ACS Energy Lett.* **2020**, *5* (5), 1701-1708.
- 40 157. Rossi, D.; Liu, X.; Lee, Y.; Khurana, M.; Puthenpurayil, J.; Kim, K.; Akimov, A. V.;
41 Cheon, J.; Son, D. H., Intense Dark Exciton Emission from Strongly Quantum Confined
42 CsPbBr₃ Nanocrystals. *Nano Letters* **2020**.

- 1 158. Forde, A.; Fagan, J. A.; Schaller, R. D.; Thomas, S. A.; Brown, S. L.; Kurtti, M. B.;
2 Petersen, R. J.; Kilin, D. S.; Hobbie, E. K., Brightly Luminescent CsPbBr₃ Nanocrystals through
3 Ultracentrifugation. *J. Phys. Chem. Lett.* **2020**, 7133-7140.
- 4 159. Li, Y.; Huang, H.; Xiong, Y.; Richter, A. F.; Kershaw, S. V.; Feldmann, J.; Rogach, A.
5 L., Using Polar Alcohols for the Direct Synthesis of Cesium Lead Halide Perovskite Nanorods
6 with Anisotropic Emission. *ACS Nano* **2019**, 13 (7), 8237-8245.
- 7 160. Zhai, W.; Lin, J.; Li, Q.; Zheng, K.; Huang, Y.; Yao, Y.; He, X.; Li, L.; Yu, C.; Liu, C.;
8 Fang, Y.; Liu, Z.; Tang, C., Solvothermal Synthesis of Ultrathin Cesium Lead Halide Perovskite
9 Nanoplatelets with Tunable Lateral Sizes and Their Reversible Transformation into Cs₄PbBr₆
10 Nanocrystals. *Chem. Mater.* **2018**, 30 (11), 3714-3721.
- 11 161. Ahmed, G. H.; Yin, J.; Bose, R.; Sinatra, L.; Alarousu, E.; Yengel, E.; AlYami, N. M.;
12 Saidaminov, M. I.; Zhang, Y.; Hedhili, M. N.; Bakr, O. M.; Brédas, J.-L.; Mohammed, O. F.,
13 Pyridine-Induced Dimensionality Change in Hybrid Perovskite Nanocrystals. *Chem. Mater.*
14 **2017**, 29 (10), 4393-4400.
- 15 162. Vybornyi, O.; Yakunin, S.; Kovalenko, M. V., Polar-solvent-free colloidal synthesis of
16 highly luminescent alkylammonium lead halide perovskite nanocrystals. *Nanoscale* **2016**, 8 (12),
17 6278-6283.
- 18 163. Levchuk, I.; Osvet, A.; Tang, X.; Brandl, M.; Perea, J. D.; Hoegl, F.; Matt, G. J.; Hock,
19 R.; Batentschuk, M.; Brabec, C. J., Brightly Luminescent and Color-Tunable Formamidinium
20 Lead Halide Perovskite FAPbX₃ (X = Cl, Br, I) Colloidal Nanocrystals. *Nano Lett.* **2017**, 17 (5),
21 2765-2770.
- 22 164. Zhang, Y.; Thomas, C. J.; Guillaussier, A.; Smilgies, D.-M.; Korgel, B. A., Thermal
23 Phase Transitions in Superlattice Assemblies of Cuboidal CH₃NH₃PbI₃ Nanocrystals Followed
24 by Grazing Incidence X-ray Scattering. *J. Phys. Chem. C* **2019**, 123 (28), 17555-17565.
- 25 165. Imran, M.; Ijaz, P.; Goldoni, L.; Maggioni, D.; Petralanda, U.; Prato, M.; Almeida, G.;
26 Infante, I.; Manna, L., Simultaneous Cationic and Anionic Ligand Exchange For Colloidally
27 Stable CsPbBr₃ Nanocrystals. *ACS Energy Lett.* **2019**, 4 (4), 819-824.
- 28 166. Minh, D. N.; Kim, J.; Hyon, J.; Sim, J. H.; Sowlih, H. H.; Seo, C.; Nam, J.; Eom, S.;
29 Suk, S.; Lee, S.; Kim, E.; Kang, Y., Room-Temperature Synthesis of Widely Tunable
30 Formamidinium Lead Halide Perovskite Nanocrystals. *Chem. Mater.* **2017**, 29 (13), 5713-5719.
- 31 167. Koczkur, K. M.; Mourdikoudis, S.; Polavarapu, L.; Skrabalak, S. E.,
32 Polyvinylpyrrolidone (PVP) in nanoparticle synthesis. *Dalton Trans.* **2015**, 44 (41), 17883-
33 17905.
- 34 168. Ling, D.; Hackett, M. J.; Hyeon, T., Surface ligands in synthesis, modification, assembly
35 and biomedical applications of nanoparticles. *Nano Today* **2014**, 9 (4), 457-477.
- 36 169. Zhang, B.; Goldoni, L.; Lambruschini, C.; Moni, L.; Imran, M.; Pianetti, A.; Pinchetti,
37 V.; Brovelli, S.; De Trizio, L.; Manna, L., Stable and Size Tunable CsPbBr₃ Nanocrystals
38 Synthesized with Oleylphosphonic Acid. *Nano Lett.* **2020**.
- 39 170. Cai, Y.; Wang, H.; Li, Y.; Wang, L.; Lv, Y.; Yang, X.; Xie, R.-J., Trimethylsilyl Iodine-
40 Mediated Synthesis of Highly Bright Red-Emitting CsPbI₃ Perovskite Quantum Dots with
41 Significantly Improved Stability. *Chem. Mater.* **2019**, 31 (3), 881-889.
- 42 171. Wu, L.; Zhong, Q.; Yang, D.; Chen, M.; Hu, H.; Pan, Q.; Liu, H.; Cao, M.; Xu, Y.; Sun,
43 B.; Zhang, Q., Improving the Stability and Size Tunability of Cesium Lead Halide Perovskite
44 Nanocrystals Using Trioctylphosphine Oxide as the Capping Ligand. *Langmuir* **2017**, 33 (44),
45 12689-12696.

- 1 172. Krieg, F.; Ong, Q. K.; Burian, M.; Rainò, G.; Naumenko, D.; Amenitsch, H.; Süess, A.;
2 Grotevent, M. J.; Krumeich, F.; Bodnarchuk, M. I.; Shorubalko, I.; Stellacci, F.; Kovalenko, M.
3 V., Stable Ultraconcentrated and Ultradilute Colloids of CsPbX₃ (X = Cl, Br) Nanocrystals
4 Using Natural Lecithin as a Capping Ligand. *J. Am. Chem. Soc.* **2019**, *141* (50), 19839-19849.
- 5 173. Liu, F.; Zhang, Y.; Ding, C.; Kobayashi, S.; Izuishi, T.; Nakazawa, N.; Toyoda, T.;
6 Ohta, T.; Hayase, S.; Minemoto, T.; Yoshino, K.; Dai, S.; Shen, Q., Highly Luminescent Phase-
7 Stable CsPbI₃ Perovskite Quantum Dots Achieving Near 100% Absolute Photoluminescence
8 Quantum Yield. *ACS Nano* **2017**, *11* (10), 10373-10383.
- 9 174. Krieg, F.; Ochsenein, S. T.; Yakunin, S.; ten Brinck, S.; Aellen, P.; Süess, A.; Clerc,
10 B.; Guggisberg, D.; Nazarenko, O.; Shynkarenko, Y.; Kumar, S.; Shih, C.-J.; Infante, I.;
11 Kovalenko, M. V., Colloidal CsPbX₃ (X = Cl, Br, I) Nanocrystals 2.0: Zwitterionic Capping
12 Ligands for Improved Durability and Stability. *ACS Energy Lett.* **2018**, *3* (3), 641-646.
- 13 175. Pan, J.; Shang, Y.; Yin, J.; De Bastiani, M.; Peng, W.; Dursun, I.; Sinatra, L.; El-Zohry,
14 A. M.; Hedhili, M. N.; Emwas, A.-H.; Mohammed, O. F.; Ning, Z.; Bakr, O. M., Bidentate
15 Ligand-Passivated CsPbI₃ Perovskite Nanocrystals for Stable Near-Unity Photoluminescence
16 Quantum Yield and Efficient Red Light-Emitting Diodes. *J. Am. Chem. Soc.* **2018**, *140* (2), 562-
17 565.
- 18 176. Wang, S.; Du, L.; Jin, Z.; Xin, Y.; Mattoussi, H., Enhanced Stabilization and Easy Phase
19 Transfer of CsPbBr₃ Perovskite Quantum Dots Promoted by High-Affinity Polyzwitterionic
20 Ligands. *J. Am. Chem. Soc.* **2020**, *142* (29), 12669-12680.
- 21 177. Yoo, D.; Woo, J. Y.; Kim, Y.; Kim, S. W.; Wei, S.-H.; Jeong, S.; Kim, Y.-H., Origin of
22 the Stability and Transition from Anionic to Cationic Surface Ligand Passivation of All-
23 Inorganic Cesium Lead Halide Perovskite Nanocrystals. *J. Phys. Chem. Lett.* **2020**, *11* (3), 652-
24 658.
- 25 178. Sun, S.; Yuan, D.; Xu, Y.; Wang, A.; Deng, Z., Ligand-Mediated Synthesis of Shape-
26 Controlled Cesium Lead Halide Perovskite Nanocrystals via Reprecipitation Process at Room
27 Temperature. *ACS Nano* **2016**, *10* (3), 3648-3657.
- 28 179. Pan, A.; He, B.; Fan, X.; Liu, Z.; Urban, J. J.; Alivisatos, A. P.; He, L.; Liu, Y., Insight
29 into the Ligand-Mediated Synthesis of Colloidal CsPbBr₃ Perovskite Nanocrystals: The Role of
30 Organic Acid, Base, and Cesium Precursors. *ACS Nano* **2016**, *10* (8), 7943-7954.
- 31 180. Imran, M.; Caligiuri, V.; Wang, M.; Goldoni, L.; Prato, M.; Krahne, R.; De Trizio, L.;
32 Manna, L., Benzoyl Halides as Alternative Precursors for the Colloidal Synthesis of Lead-Based
33 Halide Perovskite Nanocrystals. *J. Am. Chem. Soc.* **2018**, *140* (7), 2656-2664.
- 34 181. Almeida, G.; Ashton, O. J.; Goldoni, L.; Maggioni, D.; Petralanda, U.; Mishra, N.;
35 Akkerman, Q. A.; Infante, I.; Snaith, H. J.; Manna, L., The Phosphine Oxide Route toward Lead
36 Halide Perovskite Nanocrystals. *J. Am. Chem. Soc.* **2018**, *140* (44), 14878-14886.
- 37 182. Akkerman, Q. A.; Martínez-Sarti, L.; Goldoni, L.; Imran, M.; Baranov, D.; Bolink, H. J.;
38 Palazon, F.; Manna, L., Molecular Iodine for a General Synthesis of Binary and Ternary
39 Inorganic and Hybrid Organic-Inorganic Iodide Nanocrystals. *Chem. Mater.* **2018**, *30* (19),
40 6915-6921.
- 41 183. Ashton, O. J.; Marshall, A. R.; Warby, J. H.; Wenger, B.; Snaith, H. J., A Phosphine
42 Oxide Route to Formamidinium Lead Tribromide Nanoparticles. *Chem. Mater.* **2020**, *32* (17),
43 7172-7180.

- 1 184. Paul, S.; Samanta, A., N-Bromosuccinimide as Bromide Precursor for Direct Synthesis
2 of Stable and Highly Luminescent Green-Emitting Perovskite Nanocrystals. *ACS Energy Lett.*
3 **2020**, *5* (1), 64-69.
- 4 185. Creutz, S. E.; Crites, E. N.; De Siena, M. C.; Gamelin, D. R., Colloidal Nanocrystals of
5 Lead-Free Double-Perovskite (Elpasolite) Semiconductors: Synthesis and Anion Exchange To
6 Access New Materials. *Nano Lett.* **2018**, *18* (2), 1118-1123.
- 7 186. Li, J.; Xu, L.; Wang, T.; Song, J.; Chen, J.; Xue, J.; Dong, Y.; Cai, B.; Shan, Q.; Han,
8 B.; Zeng, H., 50-Fold EQE Improvement up to 6.27% of Solution-Processed All-Inorganic
9 Perovskite CsPbBr₃ QLEDs via Surface Ligand Density Control. *Adv. Mater.* **2017**, *29* (5),
10 1603885.
- 11 187. Swarnkar, A.; Marshall, A. R.; Sanehira, E. M.; Chernomordik, B. D.; Moore, D. T.;
12 Christians, J. A.; Chakrabarti, T.; Luther, J. M., Quantum dot-induced phase stabilization of α -
13 CsPbI₃ perovskite for high-efficiency photovoltaics. *Science* **2016**, *354* (6308), 92-
14 95.
- 15 188. Sun, J. K.; Huang, S.; Liu, X. Z.; Xu, Q.; Zhang, Q. H.; Jiang, W. J.; Xue, D. J.; Xu, J.
16 C.; Ma, J. Y.; Ding, J.; Ge, Q. Q.; Gu, L.; Fang, X. H.; Zhong, H. Z.; Hu, J. S.; Wan, L. J., Polar
17 Solvent Induced Lattice Distortion of Cubic CsPbI₃ Nanocubes and Hierarchical Self-Assembly
18 into Orthorhombic Single-Crystalline Nanowires. *J. Am. Chem. Soc.* **2018**, *140* (37), 11705-
19 11715.
- 20 189. Zhang, Y.; Siegler, T. D.; Thomas, C. J.; Abney, M. K.; Shah, T.; De Gorostiza, A.;
21 Greene, R. M.; Korgel, B. A., A “Tips and Tricks” Practical Guide to the Synthesis of Metal
22 Halide Perovskite Nanocrystals. *Chem. Mater.* **2020**, *32* (13), 5410-5423.
- 23 190. Wang, L.; Williams, N. E.; Malachosky, E. W.; Otto, J. P.; Hayes, D.; Wood, R. E.;
24 Guyot-Sionnest, P.; Engel, G. S., Scalable Ligand-Mediated Transport Synthesis of Organic-
25 Inorganic Hybrid Perovskite Nanocrystals with Resolved Electronic Structure and Ultrafast
26 Dynamics. *ACS Nano* **2017**, *11* (3), 2689-2696.
- 27 191. Jiang, Y.; Qin, C.; Cui, M.; He, T.; Liu, K.; Huang, Y.; Luo, M.; Zhang, L.; Xu, H.; Li,
28 S.; Wei, J.; Liu, Z.; Wang, H.; Kim, G.-H.; Yuan, M.; Chen, J., Spectra stable blue perovskite
29 light-emitting diodes. *Nat. Commun.* **2019**, *10* (1), 1868.
- 30 192. Chiba, T.; Hoshi, K.; Pu, Y.-J.; Takeda, Y.; Hayashi, Y.; Ohisa, S.; Kawata, S.; Kido, J.,
31 High-Efficiency Perovskite Quantum-Dot Light-Emitting Devices by Effective Washing Process
32 and Interfacial Energy Level Alignment. *ACS Appl. Mater. Interfaces* **2017**, *9* (21), 18054-
33 18060.
- 34 193. Thomas, C. J.; Zhang, Y.; Guillaussier, A.; Bdeir, K.; Aly, O. F.; Kim, H. G.; Noh, J.;
35 Reimnitz, L. C.; Li, J.; Deepak, F. L.; Smilgies, D.-M.; Milliron, D. J.; Korgel, B. A., Thermal
36 Stability of the Black Perovskite Phase in Cesium Lead Iodide Nanocrystals Under Humid
37 Conditions. *Chem. Mater.* **2019**, *31* (23), 9750-9758.
- 38 194. Zhong, Q.; Cao, M.; Xu, Y.; Li, P.; Zhang, Y.; Hu, H.; Yang, D.; Xu, Y.; Wang, L.; Li,
39 Y.; Zhang, X.; Zhang, Q., L-Type Ligand-Assisted Acid-Free Synthesis of CsPbBr₃
40 Nanocrystals with Near-Unity Photoluminescence Quantum Yield and High Stability. *Nano*
41 *Letters* **2019**, *19* (6), 4151-4157.
- 42 195. Suri, M.; Hazarika, A.; Larson, B. W.; Zhao, Q.; Vallés-Pelarda, M.; Siegler, T. D.;
43 Abney, M. K.; Ferguson, A. J.; Korgel, B. A.; Luther, J. M., Enhanced Open-Circuit Voltage of
44 Wide-Bandgap Perovskite Photovoltaics by Using Alloyed (FA_{1-x}Cs_x)Pb(I_{1-x}Br_x)₃ Quantum
45 Dots. *ACS Energy Lett.* **2019**, *4* (8), 1954-1960.

- 1 196. Nenon, D. P.; Pressler, K.; Kang, J.; Koscher, B. A.; Olshansky, J. H.; Osowiecki, W. T.;
2 Koc, M. A.; Wang, L.-W.; Alivisatos, A. P., Design Principles for Trap-Free CsPbX₃
3 Nanocrystals: Enumerating and Eliminating Surface Halide Vacancies with Softer Lewis Bases.
4 *J. Am. Chem. Soc.* **2018**, *140* (50), 17760-17772.
- 5 197. Bodnarchuk, M. I.; Boehme, S. C.; ten Brinck, S.; Bernasconi, C.; Shynkarenko, Y.;
6 Krieg, F.; Widmer, R.; Aeschlimann, B.; Günther, D.; Kovalenko, M. V.; Infante, I.,
7 Rationalizing and Controlling the Surface Structure and Electronic Passivation of Cesium Lead
8 Halide Nanocrystals. *ACS Energy Lett.* **2019**, *4* (1), 63-74.
- 9 198. Bekenstein, Y.; Dahl, J. C.; Huang, J.; Osowiecki, W. T.; Swabeck, J. K.; Chan, E. M.;
10 Yang, P.; Alivisatos, A. P., The Making and Breaking of Lead-Free Double Perovskite
11 Nanocrystals of Cesium Silver–Bismuth Halide Compositions. *Nano Lett.* **2018**, *18* (6), 3502-
12 3508.
- 13 199. Li, X.; Wu, Y.; Zhang, S.; Cai, B.; Gu, Y.; Song, J.; Zeng, H., CsPbX₃ quantum dots for
14 lighting and displays: room - temperature synthesis, photoluminescence superiorities, underlying
15 origins and white light - emitting diodes. *Advanced Functional Materials* **2016**, *26* (15), 2435-
16 2445.
- 17 200. Almeida, G.; Goldoni, L.; Akkerman, Q.; Dang, Z.; Khan, A. H.; Marras, S.; Moreels, I.;
18 Manna, L., Role of Acid–Base Equilibria in the Size, Shape, and Phase Control of Cesium Lead
19 Bromide Nanocrystals. *ACS Nano* **2018**, *12* (2), 1704-1711.
- 20 201. Imran, M.; Caligiuri, V.; Wang, M.; Goldoni, L.; Prato, M.; Krahne, R.; De Trizio, L.;
21 Manna, L., Benzoyl Halides as Alternative Precursors for the Colloidal Synthesis of Lead-Based
22 Halide Perovskite Nanocrystals. *Journal of the American Chemical Society* **2018**, *140* (7), 2656-
23 2664.
- 24 202. Krieg, F.; Ochsenein, S. T.; Yakunin, S.; ten Brinck, S.; Aellen, P.; Süess, A.; Clerc,
25 B.; Guggisberg, D.; Nazarenko, O.; Shynkarenko, Y.; Kumar, S.; Shih, C.-J.; Infante, I.;
26 Kovalenko, M. V., Colloidal CsPbX₃ (X = Cl, Br, I) Nanocrystals 2.0: Zwitterionic Capping
27 Ligands for Improved Durability and Stability. *ACS Energy Letters* **2018**, *3* (3), 641-646.
- 28 203. Pan, J.; Shang, Y.; Yin, J.; De Bastiani, M.; Peng, W.; Dursun, I.; Sinatra, L.; El-Zohry,
29 A. M.; Hedhili, M. N.; Emwas, A.-H.; Mohammed, O. F.; Ning, Z.; Bakr, O. M., Bidentate
30 Ligand-Passivated CsPbI₃ Perovskite Nanocrystals for Stable Near-Unity Photoluminescence
31 Quantum Yield and Efficient Red Light-Emitting Diodes. *Journal of the American Chemical*
32 *Society* **2018**, *140* (2), 562-565.
- 33 204. Fan, Q.; Biesold-McGee, G. V.; Ma, J.; Xu, Q.; Pan, S.; Peng, J.; Lin, Z., Lead-Free
34 Halide Perovskite Nanocrystals: Crystal Structures, Synthesis, Stabilities, and Optical Properties.
35 *Angewandte Chemie International Edition* **2020**, *59* (3), 1030-1046.
- 36 205. Mitzi, D. B., Synthesis, structure, and properties of organic - inorganic perovskites and
37 related materials. *Prog. Inorg. Chem.* **1999**, *48*, 1-121.
- 38 206. Mitzi, D. B.; Wang, S.; Feild, C. A.; Chess, C. A.; Guloy, A. M., Conducting Layered
39 Organic-Inorganic Halides Containing (110)-Oriented Perovskite Sheets. *Science* **1995**, *267*
40 (5203), 1473-1476.
- 41 207. Ishihara, T.; Hong, X.; Ding, J.; Nurmikko, A. V., Dielectric Confinement Effect For
42 Exciton and Biexciton States in PbI₄-Based 2-Dimensional Semiconductor Structures. *Surf. Sci.*
43 **1992**, *267*, 323-326.

- 1 208. Koutselas, I.; Ducasse, L.; Papavassiliou, G. C., Electronic properties of three- and low-
2 dimensional semiconducting materials with Pb halide and Sn halide units. *J. Phys.: Condens.*
3 *Matter* **1996**, *8* (9), 1217.
- 4 209. Ishihara, T.; Takahashi, J.; Goto, T., Exciton state in two-dimensional perovskite
5 semiconductor (C₁₀H₂₁NH₃)₂PbI₄. *Solid State Commun.* **1989**, *69* (9), 933-936.
- 6 210. Stoumpos, C. C.; Cao, D. H.; Clark, D. J.; Young, J.; Rondinelli, J. M.; Jang, J. I.; Hupp,
7 J. T.; Kanatzidis, M. G., Ruddlesden–Popper hybrid lead iodide perovskite 2D homologous
8 semiconductors. *Chem. Mater.* **2016**, *28* (8), 2852-2867.
- 9 211. Soe, C. M. M.; Nagabhushana, G.; Shivaramaiah, R.; Tsai, H.; Nie, W.; Blancon, J.-C.;
10 Melkonyan, F.; Cao, D. H.; Traoré, B.; Pedesseau, L.; Kepenekian, M.; Katan, C.; Even, J.;
11 Marks, T. J.; Navrotsky, A.; Mohite, A. D.; Stoumpos, C. C.; Kanatzidis, M. G., Structural and
12 thermodynamic limits of layer thickness in 2D halide perovskites. *Proc. Natl. Acad. Sci. U.S.A.*
13 **2019**, *116* (1), 58-66.
- 14 212. Nagabhushana, G. P.; Shivaramaiah, R.; Navrotsky, A., Direct calorimetric verification
15 of thermodynamic instability of lead halide hybrid perovskites. *Proc. Natl. Acad. Sci. U.S.A.*
16 **2016**, *113* (28), 7717-21.
- 17 213. Ciccioli, A.; Latini, A., Thermodynamics and the Intrinsic Stability of Lead Halide
18 Perovskites CH₃NH₃PbX₃. *J. Phys. Chem. Lett.* **2018**, *9* (13), 3756-3765.
- 19 214. Tyagi, P.; Arveson, S. M.; Tisdale, W. A., Colloidal Organohalide Perovskite
20 Nanoplatelets Exhibiting Quantum Confinement. *J. Phys. Chem. Lett.* **2015**, *6* (10), 1911-6.
- 21 215. Riedinger, A.; Ott, F. D.; Mule, A.; Mazzotti, S.; Knusel, P. N.; Kress, S. J. P.; Prins, F.;
22 Erwin, S. C.; Norris, D. J., An intrinsic growth instability in isotropic materials leads to quasi-
23 two-dimensional nanoplatelets. *Nat. Mater.* **2017**, *16* (7), 743-748.
- 24 216. Burlakov, V. M.; Hassan, Y.; Danaie, M.; Snaith, H. J.; Goriely, A., Competitive
25 Nucleation Mechanism for CsPbBr₃ Perovskite Nanoplatelet Growth. *J. Phys. Chem. Lett.* **2020**,
26 *11* (16), 6535-6543.
- 27 217. Paritmongkol, W.; Dahod, N. S.; Stollmann, A.; Mao, N.; Settens, C.; Zheng, S.-L.;
28 Tisdale, W. A., Synthetic Variation and Structural Trends in Layered Two-Dimensional
29 Alkylammonium Lead Halide Perovskites. *Chem. Mater.* **2019**, *31* (15), 5592-5607.
- 30 218. Stoumpos, C. C.; Soe, C. M. M.; Tsai, H.; Nie, W.; Blancon, J.-C.; Cao, D. H.; Liu, F.;
31 Traoré, B.; Katan, C.; Even, J.; Mohite, A. D.; Kanatzidis, M. G., High Members of the 2D
32 Ruddlesden–Popper Halide Perovskites: Synthesis, Optical Properties, and Solar Cells of (CH₃
33 (CH₂)₃NH₃)₂(CH₃NH₃)₄Pb₅I₁₆. *Chem* **2017**, *2* (3), 427-440.
- 34 219. Weidman, M. C.; Seitz, M.; Stranks, S. D.; Tisdale, W. A., Highly Tunable Colloidal
35 Perovskite Nanoplatelets through Variable Cation, Metal, and Halide Composition. *ACS Nano*
36 **2016**, *10* (8), 7830-7839.
- 37 220. Bertolotti, F.; Nedelcu, G.; Vivani, A.; Cervellino, A.; Masciocchi, N.; Guagliardi, A.;
38 Kovalenko, M. V., Crystal Structure, Morphology, and Surface Termination of Cyan-Emissive,
39 Six-Monolayers-Thick CsPbBr₃ Nanoplatelets from X-ray Total Scattering. *ACS Nano* **2019**, *13*
40 (12), 14294-14307.
- 41 221. Kumar, S.; Jagielski, J.; Yakunin, S.; Rice, P.; Chiu, Y.-C.; Wang, M.; Nedelcu, G.;
42 Kim, Y.; Lin, S.; Santos, E. J.; Kovalenko, M. V.; Shih, C.-J., Efficient blue electroluminescence
43 using quantum-confined two-dimensional perovskites. *ACS Nano* **2016**, *10* (10), 9720-9729.

- 1 222. Zhao, J.; Cao, S.; Li, Z.; Ma, N., Amino Acid-Mediated Synthesis of CsPbBr₃
2 Perovskite Nanoplatelets with Tunable Thickness and Optical Properties. *Chem. Mater.* **2018**, *30*
3 (19), 6737-6743.
- 4 223. Zhao, H.; Wei, L.; Zeng, P.; Liu, M., Formation of highly uniform thinly-wrapped
5 CsPbX₃@silicone nanocrystals via self-hydrolysis: suppressed anion exchange and superior
6 stability in polar solvents. *Journal of Materials Chemistry C* **2019**, *7* (32), 9813-9819.
- 7 224. Shamsi, J.; Kubicki, D.; Anaya, M.; Liu, Y.; Ji, K.; Frohna, K.; Grey, C. P.; Friend, R.
8 H.; Stranks, S. D., Stable Hexylphosphonate-Capped Blue-Emitting Quantum-Confined
9 CsPbBr₃ Nanoplatelets. *ACS Energy Lett.* **2020**, *5* (6), 1900-1907.
- 10 225. Bonato, L. G.; Moral, R. F.; Nagamine, G.; Alo, A.; Germino, J. C.; da Silva, D. S.;
11 Almeida, D. B.; Zagonel, L. F.; Galembeck, F.; Padilha, L. A.; Nogueira, A. F., Revealing the
12 Role of Tin(IV) Halides in the Anisotropic Growth of CsPbX₃ Perovskite Nanoplates. *Angew.*
13 *Chem.* **2020**.
- 14 226. Huang, H.; Li, Y.; Tong, Y.; Yao, E. P.; Feil, M. W.; Richter, A. F.; Doblinger, M.;
15 Rogach, A. L.; Feldmann, J.; Polavarapu, L., Spontaneous Crystallization of Perovskite
16 Nanocrystals in Nonpolar Organic Solvents: A Versatile Approach for their Shape-Controlled
17 Synthesis. *Angew. Chem.* **2019**, *58* (46), 16558-16562.
- 18 227. Yang, D.; Zou, Y.; Li, P.; Liu, Q.; Wu, L.; Hu, H.; Xu, Y.; Sun, B.; Zhang, Q.; Lee, S.-
19 T., Large-scale synthesis of ultrathin cesium lead bromide perovskite nanoplates with precisely
20 tunable dimensions and their application in blue light-emitting diodes. *Nano Energy* **2018**, *47*,
21 235-242.
- 22 228. Shamsi, J.; Dang, Z.; Bianchini, P.; Canale, C.; Di Stasio, F.; Brescia, R.; Prato, M.;
23 Manna, L., Colloidal synthesis of quantum confined single crystal CsPbBr₃ nanosheets with
24 lateral size control up to the micrometer range. *J. Am. Chem. Soc.* **2016**, *138* (23), 7240-7243.
- 25 229. Han, D.; Imran, M.; Zhang, M.; Chang, S.; Wu, X.-g.; Zhang, X.; Tang, J.; Wang, M.;
26 Ali, S.; Li, X.; Yu, G.; Han, J.; Wang, L.; Zou, B.; Zhong, H., Efficient Light-Emitting Diodes
27 Based on in Situ Fabricated FAPbBr₃ Nanocrystals: The Enhancing Role of the Ligand-Assisted
28 Reprecipitation Process. *ACS Nano* **2018**, *12* (8), 8808-8816.
- 29 230. Yuan, Z.; Shu, Y.; Xin, Y.; Ma, B., Highly luminescent nanoscale quasi-2D layered lead
30 bromide perovskites with tunable emissions. *Chem. Commun.* **2016**, *52* (20), 3887-90.
- 31 231. Wei, M.; de Arquer, F. P. G.; Walters, G.; Yang, Z.; Quan, L. N.; Kim, Y.; Sabatini, R.;
32 Quintero-Bermudez, R.; Gao, L.; Fan, J. Z.; Fan, F.; Gold-Parker, A.; Toney, M. F.; Sargent, E.
33 H., Ultrafast narrowband exciton routing within layered perovskite nanoplatelets enables low-
34 loss luminescent solar concentrators. *Nat. Energy* **2019**, *4* (3), 197-205.
- 35 232. Jagielski, J.; Kumar, S.; Yu, W.-Y.; Shih, C.-J., Layer-controlled two-dimensional
36 perovskites: synthesis and optoelectronics. *J. Mater. Chem. C* **2017**, *5* (23), 5610-5627.
- 37 233. Huang, S.; Li, Z.; Wang, B.; Zhu, N.; Zhang, C.; Kong, L.; Zhang, Q.; Shan, A.; Li, L.,
38 Morphology Evolution and Degradation of CsPbBr₃ Nanocrystals under Blue Light-Emitting
39 Diode Illumination. *ACS Appl. Mater. Interfaces* **2017**, *9* (8), 7249-7258.
- 40 234. Mehetor, S. K.; Ghosh, H.; Pradhan, N., Acid-Amine Equilibria for Formation and
41 Long-Range Self-Organization of Ultrathin CsPbBr₃ Perovskite Platelets. *J. Phys. Chem. Lett.*
42 **2019**, *10* (6), 1300-1305.

- 1 235. Wu, Y.; Wei, C.; Li, X.; Li, Y.; Qiu, S.; Shen, W.; Cai, B.; Sun, Z.; Yang, D.; Deng, Z.;
2 Zeng, H., In Situ Passivation of PbBr₆ Octahedra toward Blue Luminescent CsPbBr₃
3 Nanoplatelets with Near 100% Absolute Quantum Yield. *ACS Energy Lett.* **2018**, *3* (9), 2030-
4 2037.
- 5 236. DeCrescent, R. A.; Venkatesan, N. R.; Dahlman, C. J.; Kennard, R. M.; Chabinyk, M.
6 L.; Schuller, J. A., Optical Constants and Effective-Medium Origins of Large Optical
7 Anisotropies in Layered Hybrid Organic/Inorganic Perovskites. *ACS Nano* **2019**, *13* (9), 10745-
8 10753.
- 9 237. Jurow, M. J.; Morgenstern, T.; Eisler, C.; Kang, J.; Penzo, E.; Do, M. Q.; Engelmayer,
10 M.; Osowiecki, W. T.; Bekenstein, Y.; Tassone, C. J.; Wang, L.-W.; Alivisatos, A. P.; Brutting,
11 W.; Liu, Y., Manipulating the Transition Dipole Moment of CsPbBr₃ Perovskite Nanocrystals
12 for Superior Optical Properties. *Nano Lett.* **2019**, *19* (4), 2489-2496.
- 13 238. Zhou, S.; Zhu, Y.; Zhong, J.; Tian, F.; Huang, H.; Chen, J.; Chen, D., Chlorine-additive-
14 promoted incorporation of Mn²⁺ dopants into CsPbCl₃ perovskite nanocrystals. *Nanoscale*
15 **2019**, *11* (26), 12465-12470.
- 16 239. Nistal, A.; Garcia, E.; Pérez -Coll, D.; Prieto, C.; Belmonte, M.; Osendi, M. I.; Miranzo,
17 P., Low percolation threshold in highly conducting graphene nanoplatelets/glass composite
18 coatings. *Carbon* **2018**, *139*, 556-563.
- 19 240. Tong, Y.; Ehrat, F.; Vanderlinden, W.; Cardenas-Daw, C.; Stolarczyk, J. K.; Polavarapu,
20 L.; Urban, A. S., Dilution-Induced Formation of Hybrid Perovskite Nanoplatelets. *ACS Nano*
21 **2016**, *10* (12), 10936-10944.
- 22 241. Sun, S.; Yuan, D.; Xu, Y.; Wang, A.; Deng, Z., Ligand-Mediated Synthesis of Shape-
23 Controlled Cesium Lead Halide Perovskite Nanocrystals via Reprecipitation Process at Room
24 Temperature. *ACS Nano* **2016**, *10* (3), 3648-57.
- 25 242. Cho, J.; Choi, Y.-H.; O'Loughlin, T. E.; De Jesus, L.; Banerjee, S., Ligand-Mediated
26 Modulation of Layer Thicknesses of Perovskite Methylammonium Lead Bromide Nanoplatelets.
27 *Chem. Mater.* **2016**, *28* (19), 6909-6916.
- 28 243. Seth, S.; Samanta, A., A Facile Methodology for Engineering the Morphology of
29 CsPbX₃ Perovskite Nanocrystals under Ambient Condition. *Sci. Rep.* **2016**, *6*, 37693.
- 30 244. Pan, A.; He, B.; Fan, X.; Liu, Z.; Urban, J. J.; Alivisatos, A. P.; He, L.; Liu, Y., Insight
31 into the Ligand-Mediated Synthesis of Colloidal CsPbBr₃ Perovskite Nanocrystals: The Role of
32 Organic Acid, Base, and Cesium Precursors. *ACS Nano* **2016**, *10* (8), 7943-54.
- 33 245. Shamsi, J.; Rastogi, P.; Caligiuri, V.; Abdelhady, A. L.; Spirito, D.; Manna, L.; Krahne,
34 R., Bright-Emitting Perovskite Films by Large-Scale Synthesis and Photoinduced Solid-State
35 Transformation of CsPbBr₃ Nanoplatelets. *ACS Nano* **2017**, *11* (10), 10206-10213.
- 36 246. Wang, Y.; Li, X.; Sreejith, S.; Cao, F.; Wang, Z.; Stuparu, M. C.; Zeng, H.; Sun, H.,
37 Photon Driven Transformation of Cesium Lead Halide Perovskites from Few-Monolayer
38 Nanoplatelets to Bulk Phase. *Adv. Mater.* **2016**, *28* (48), 10637-10643.
- 39 247. Tong, Y.; Bladt, E.; Ayguler, M. F.; Manzi, A.; Milowska, K. Z.; Hintermayr, V. A.;
40 Docampo, P.; Bals, S.; Urban, A. S.; Polavarapu, L.; Feldmann, J., Highly Luminescent Cesium
41 Lead Halide Perovskite Nanocrystals with Tunable Composition and Thickness by
42 Ultrasonication. *Angew. Chem.* **2016**, *55* (44), 13887-13892.

- 1 248. Hintermayr, V. A.; Richter, A. F.; Ehrat, F.; Döblinger, M.; Vanderlinden, W.; Sichert, J.
2 A.; Tong, Y.; Polavarapu, L.; Feldmann, J.; Urban, A. S., Tuning the Optical Properties of
3 Perovskite Nanoplatelets through Composition and Thickness by Ligand - Assisted Exfoliation.
4 *Adv. Mater.* **2016**, *28* (43), 9478-9485.
- 5 249. Dou, L. T.; Wong, A. B.; Yu, Y.; Lai, M. L.; Kornienko, N.; Eaton, S. W.; Fu, A.;
6 Bischak, C. G.; Ma, J.; Ding, T. N.; Ginsberg, N. S.; Wang, L. W.; Alivisatos, A. P.; Yang, P. D.,
7 Atomically thin two-dimensional organic-inorganic hybrid perovskites. *Science* **2015**, *349*
8 (6255), 1518-1521.
- 9 250. Dahlman, C. J.; Venkatesan, N. R.; Corona, P. T.; Kennard, R. M.; Mao, L.; Smith, N.
10 C.; Zhang, J.; Seshadri, R.; Helgeson, M. E.; Chabinyk, M. L., Structural Evolution of Layered
11 Hybrid Lead Iodide Perovskites in Colloidal Dispersions. *ACS Nano* **2020**, *14* (9), 11294-11308.
- 12 251. Mir, W. J.; Jagadeeswararao, M.; Das, S.; Nag, A., Colloidal Mn-Doped Cesium Lead
13 Halide Perovskite Nanoplatelets. *ACS Energy Lett.* **2017**, *2* (3), 537-543.
- 14 252. Zhang, D. D.; Eaton, S. W.; Yu, Y.; Dou, L. T.; Yang, P. D., Solution-Phase Synthesis
15 of Cesium Lead Halide Perovskite Nanowires. *J. Am. Chem. Soc.* **2015**, *137* (29), 9230-9233.
- 16 253. Gao, M. Y.; Liu, H.; Yu, S.; Louisia, S.; Zhang, Y.; Nenon, D. P.; Alivisatos, A. P.;
17 Yang, P. D., Scaling Laws of Exciton Recombination Kinetics in Low Dimensional Halide
18 Perovskite Nanostructures. *J. Am. Chem. Soc.* **2020**, *142* (19), 8871-8879.
- 19 254. Lai, M.; Kong, Q.; Bischak, C. G.; Yu, Y.; Dou, L.; Eaton, S. W.; Ginsberg, N. S.;
20 Yang, P., Structural, optical, and electrical properties of phase-controlled cesium lead iodide
21 nanowires. *Nano Res.* **2017**, *10* (4), 1107-1114.
- 22 255. Akkerman, Q. A.; D'Innocenzo, V.; Accornero, S.; Scarpellini, A.; Petrozza, A.; Prato,
23 M.; Manna, L., Tuning the Optical Properties of Cesium Lead Halide Perovskite Nanocrystals by
24 Anion Exchange Reactions. *J. Am. Chem. Soc.* **2015**, *137* (32), 10276-10281.
- 25 256. Wong, A. B.; Lai, M. L.; Eaton, S. W.; Yu, Y.; Lin, E.; Dou, L.; Fu, A.; Yang, P. D.,
26 Growth and Anion Exchange Conversion of CH₃NH₃PbX₃ Nanorod Arrays for Light-Emitting
27 Diodes. *Nano Lett.* **2015**, *15* (8), 5519-5524.
- 28 257. Lai, M. L.; Kong, Q.; Bischak, C. G.; Yu, Y.; Dou, L. T.; Eaton, S. W.; Ginsberg, N. S.;
29 Yang, P. D., Structural, optical, and electrical properties of phase-controlled cesium lead iodide
30 nanowires. *Nano Res.* **2017**, *10* (4), 1107-1114.
- 31 258. Fu, Y. P.; Zhu, H. M.; Schrader, A. W.; Liang, D.; Ding, Q.; Joshi, P.; Hwang, L.; Zhu,
32 X. Y.; Jin, S., Nanowire Lasers of Formamidinium Lead Halide Perovskites and Their Stabilized
33 Alloys with Improved Stability. *Nano Lett.* **2016**, *16* (2), 1000-1008.
- 34 259. Lei, T.; Lai, M. L.; Kong, Q.; Lu, D. Y.; Lee, W.; Dou, L. T.; Wu, V.; Yu, Y.; Yang, P.
35 D., Electrical and Optical Tunability in All-Inorganic Halide Perovskite Alloy Nanowires. *Nano*
36 *Lett.* **2018**, *18* (6), 3538-3542.
- 37 260. Eaton, S. W.; Lai, M. L.; Gibson, N. A.; Wong, A. B.; Dou, L. T.; Ma, J.; Wang, L. W.;
38 Leone, S. R.; Yang, P. D., Lasing in robust cesium lead halide perovskite nanowires. *Proc. Natl.*
39 *Acad. Sci. U.S.A* **2016**, *113* (8), 1993-1998.
- 40 261. Dai, J.; Fu, Y. P.; Manger, L. H.; Rea, M. T.; Hwang, L.; Goldsmith, R. H.; Jin, S.,
41 Carrier Decay Properties of Mixed Cation Formamidinium-Methylammonium Lead Iodide
42 Perovskite [HC(NH₂)₂](1-X)[CH₃NH₃](x)PbI₃ Nanorods. *J. Phys. Chem. Lett.* **2016**, *7* (24),
43 5036-5043.

- 1 262. Chen, J.; Fu, Y. P.; Samad, L.; Dang, L. N.; Zhao, Y. Z.; Shen, S. H.; Guo, L. J.; Jin, S.,
2 Vapor-Phase Epitaxial Growth of Aligned Nanowire Networks of Cesium Lead Halide
3 Perovskites (CsPbX₃, X = Cl, Br, I). *Nano Lett.* **2017**, *17* (1), 460-466.
- 4 263. Zhou, H.; Yuan, S. P.; Wang, X. X.; Xu, T.; Wang, X.; Li, H. L.; Zheng, W. H.; Fang,
5 P.; Li, Y. Y.; Sun, L. T.; Pan, A. L., Vapor Growth and Tunable Lasing of Band Gap Engineered
6 Cesium Lead Halide Perovskite Micro/Nanorods with Triangular Cross Section. *ACS Nano*
7 **2017**, *11* (2), 1189-1195.
- 8 264. Wang, Y. P.; Sun, X.; Shivanna, R.; Yang, Y. B.; Chen, Z. Z.; Guo, Y. W.; Wang, G. C.;
9 Wertz, E.; Deschler, F.; Cai, Z. H.; Zhou, H.; Lu, T. M.; Shi, J., Photon Transport in One-
10 Dimensional Incommensurately Epitaxial CsPbX₃ Arrays. *Nano Lett.* **2016**, *16* (12), 7974-7981.
- 11 265. Peng, L.; Dutta, A.; Xie, R.; Yang, W.; Pradhan, N., Dot-Wire-Platelet-Cube: Step
12 Growth and Structural Transformations in CsPbBr₃ Perovskite Nanocrystals. *ACS Energy Lett.*
13 **2018**, *3* (8), 2014-2020.
- 14 266. Shoaib, M.; Zhang, X.; Wang, X.; Zhou, H.; Xu, T.; Wang, X.; Hu, X.; Liu, H.; Fan, X.;
15 Zheng, W.; Yang, T.; Yang, S.; Zhang, Q.; Zhu, X.; Sun, L.; Pan, A., Directional Growth of
16 Ultralong CsPbBr₃ Perovskite Nanowires for High-Performance Photodetectors. *J. Am. Chem.*
17 *Soc.* **2017**, *139* (44), 15592-15595.
- 18 267. Oksenberg, E.; Sanders, E.; Popovitz-Biro, R.; Houben, L.; Joselevich, E., Surface-
19 Guided CsPbBr₃ Perovskite Nanowires on Flat and Faceted Sapphire with Size-Dependent
20 Photoluminescence and Fast Photoconductive Response. *Nano Lett.* **2018**, *18* (1), 424-433.
- 21 268. Dou, L.; Lai, M. L.; Kley, C. S.; Yang, Y. M.; Bischak, C. G.; Zhang, D. D.; Eaton, S.
22 W.; Ginsberg, N. S.; Yang, P. D., Spatially resolved multicolor CsPbX₃ nanowire
23 heterojunctions via anion exchange. *Proc. Natl. Acad. Sci. U.S.A* **2017**, *114* (28), 7216-7221.
- 24 269. Kong, Q.; Obliger, A.; Lai, M.; Gao, M.; Limmer, D. T.; Yang, P., Solid-State Ionic
25 Rectification in Perovskite Nanowire Heterostructures. *Nano Lett.* **2020**.
- 26 270. Nah, S.; Spokoyny, B.; Stoumpos, C.; Soe, C. M. M.; Kanatzidis, M.; Harel, E.,
27 Spatially segregated free-carrier and exciton populations in individual lead halide perovskite
28 grains. *Nat. Photonics* **2017**, *11* (5), 285-+.
- 29 271. deQuilettes, D. W.; Vorpahl, S. M.; Stranks, S. D.; Nagaoka, H.; Eperon, G. E.; Ziffer,
30 M. E.; Snaith, H. J.; Ginger, D. S., Impact of microstructure on local carrier lifetime in
31 perovskite solar cells. *Science* **2015**, *348* (6235), 683-686.
- 32 272. Lai, M. L.; Obliger, A.; Lu, D.; Kley, C. S.; Bischak, C. G.; Kong, Q.; Lei, T.; Dou, L.
33 T.; Ginsberg, N. S.; Limmer, D. T.; Yang, P. D., Intrinsic anion diffusivity in lead halide
34 perovskites is facilitated by a soft lattice. *Proc. Natl. Acad. Sci. U.S.A* **2018**, *115* (47), 11929-
35 11934.
- 36 273. Pan, D.; Fu, Y.; Chen, J.; Czech, K. J.; Wright, J. C.; Jin, S., Visualization and Studies of
37 Ion-Diffusion Kinetics in Cesium Lead Bromide Perovskite Nanowires. *Nano Lett.* **2018**, *18* (3),
38 1807-1813.
- 39 274. Bischak, C. G.; Lai, M.; Lu, D.; Fan, Z.; David, P.; Dong, D.; Chen, H.; Etman, A. S.;
40 Lei, T.; Sun, J., Liquid-like interfaces mediate structural phase transitions in lead halide
41 perovskites. *arXiv preprint arXiv:1907.13509* **2019**.
- 42 275. Kong, Q.; Lee, W.; Lai, M. L.; Bischak, C. G.; Gao, G. P.; Wong, A. B.; Lei, T.; Yu, Y.;
43 Wang, L. W.; Ginsberg, N. S.; Yang, P. D., Phase-transition-induced p-n junction in single
44 halide perovskite nanowire. *Proc. Natl. Acad. Sci. U.S.A* **2018**, *115* (36), 8889-8894.

- 1 276. Lee, W.; Li, H. S.; Wong, A. B.; Zhang, D. D.; Lai, M. L.; Yu, Y.; Kong, Q.; Lin, E.;
2 Urban, J. J.; Grossman, J. C.; Yang, P. D., Ultralow thermal conductivity in all-inorganic halide
3 perovskites. *Proc. Natl. Acad. Sci. U.S.A* **2017**, *114* (33), 8693-8697.
- 4 277. Wang, Y.; Lin, R.; Zhu, P.; Zheng, Q.; Wang, Q.; Li, D.; Zhu, J., Cation Dynamics
5 Governed Thermal Properties of Lead Halide Perovskite Nanowires. *Nano Lett* **2018**, *18* (5),
6 2772-2779.
- 7 278. Wang, Y.; Lin, R.; Zhu, P.; Zheng, Q.; Wang, Q.; Li, D.; Zhu, J., Cation Dynamics
8 Governed Thermal Properties of Lead Halide Perovskite Nanowires. *Nano Lett.* **2018**, *18* (5),
9 2772-2779.
- 10 279. Zhu, P.; Gu, S.; Shen, X.; Xu, N.; Tan, Y.; Zhuang, S.; Deng, Y.; Lu, Z.; Wang, Z.; Zhu,
11 J., Direct Conversion of Perovskite Thin Films into Nanowires with Kinetic Control for Flexible
12 Optoelectronic Devices. *Nano Lett.* **2016**, *16* (2), 871-876.
- 13 280. Zhang, X.; Chen, S.; Wang, X.; Pan, A., Controlled Synthesis and Photonics
14 Applications of Metal Halide Perovskite Nanowires. *Small Methods* **2019**, *3* (1), 1800294.
- 15 281. Gao, L.; Zeng, K.; Guo, J.; Ge, C.; Du, J.; Zhao, Y.; Chen, C.; Deng, H.; He, Y.; Song,
16 H.; Niu, G.; Tang, J., Passivated Single-Crystalline CH₃NH₃PbI₃ Nanowire Photodetector with
17 High Detectivity and Polarization Sensitivity. *Nano Lett.* **2016**, *16* (12), 7446-7454.
- 18 282. Singh, R.; Suranagi, S. R.; Yang, S. J.; Cho, K., Enhancing the power conversion
19 efficiency of perovskite solar cells via the controlled growth of perovskite nanowires. *Nano*
20 *Energy* **2018**, *51*, 192-198.
- 21 283. Wang, S.; Yan, S.; Wang, M.; Chang, L.; Wang, J.; Wang, Z., Construction of nanowire
22 CH₃NH₃PbI₃-based solar cells with 17.62% efficiency by solvent etching technique. *Solar*
23 *Energy Materials and Solar Cells* **2017**, *167*, 173-177.
- 24 284. Horváth, E.; Spina, M.; Szekrényes, Z.; Kamarás, K.; Gaal, R.; Gachet, D.; Forró, L.,
25 Nanowires of Methylammonium Lead Iodide (CH₃NH₃PbI₃) Prepared by Low Temperature
26 Solution-Mediated Crystallization. *Nano Lett.* **2014**, *14* (12), 6761-6766.
- 27 285. Petrov, A. A.; Pellet, N.; Seo, J.-Y.; Belich, N. A.; Kovalev, D. Y.; Shevelkov, A. V.;
28 Goodilin, E. A.; Zakeeruddin, S. M.; Tarasov, A. B.; Graetzel, M., New Insight into the
29 Formation of Hybrid Perovskite Nanowires via Structure Directing Adducts. *Chem. Mater.* **2017**,
30 *29* (2), 587-594.
- 31 286. Spina, M.; Bonvin, E.; Sienkiewicz, A.; Náfrádi, B.; Forró, L.; Horváth, E., Controlled
32 growth of CH₃NH₃PbI₃ nanowires in arrays of open nanofluidic channels. *Sci. Rep.* **2016**, *6* (1),
33 19834.
- 34 287. Ashley, M. J.; O'Brien, M. N.; Hedderick, K. R.; Mason, J. A.; Ross, M. B.; Mirkin, C.
35 A., Templated Synthesis of Uniform Perovskite Nanowire Arrays. *J. Am. Chem. Soc.* **2016**, *138*
36 (32), 10096-10099.
- 37 288. Xing, J.; Liu, X. F.; Zhang, Q.; Ha, S. T.; Yuan, Y. W.; Shen, C.; Sum, T. C.; Xiong, Q.,
38 Vapor Phase Synthesis of Organometal Halide Perovskite Nanowires for Tunable Room-
39 Temperature Nanolasers. *Nano Lett.* **2015**, *15* (7), 4571-4577.
- 40 289. Zhang, F.; Chen, C.; Kershaw, S. V.; Xiao, C.; Han, J.; Zou, B.; Wu, X.; Chang, S.;
41 Dong, Y.; Rogach, A. L.; Zhong, H., Ligand-Controlled Formation and Photoluminescence
42 Properties of CH₃NH₃PbBr₃ Nanocubes and Nanowires. *ChemNanoMat* **2017**, *3* (5), 303-310.

- 1 290. Debroye, E.; Yuan, H.; Bladt, E.; Baekelant, W.; Van der Auweraer, M.; Hofkens, J.;
2 Bals, S.; Roeffaers, M. B. J., Facile Morphology-Controlled Synthesis of Organolead Iodide
3 Perovskite Nanocrystals Using Binary Capping Agents. *ChemNanoMat* **2017**, *3* (4), 223-227.
- 4 291. Xuan, T.; Yang, X.; Lou, S.; Huang, J.; Liu, Y.; Yu, J.; Li, H.; Wong, K.-L.; Wang, C.;
5 Wang, J., Highly stable CsPbBr₃ quantum dots coated with alkyl phosphate for white light-
6 emitting diodes. *Nanoscale* **2017**, *9* (40), 15286-15290.
- 7 292. Liu, L. C.; Risbud, S. H., Quantum - dot size - distribution analysis and precipitation
8 stages in semiconductor doped glasses. *J. Appl. Phys.* **1990**, *68* (1), 28-32.
- 9 293. Xu, K.; Liu, C.; Chung, W. J.; Heo, J., Optical properties of CdSe quantum dots in
10 silicate glasses. *Journal of Non-Crystalline Solids* **2010**, *356* (44), 2299-2301.
- 11 294. Nagabhushana, G. P.; Shivaramaiah, R.; Navrotsky, A., Direct calorimetric verification
12 of thermodynamic instability of lead halide hybrid perovskites. *PANS* **2016**.
- 13 295. Zhou, Q.; Bai, Z.; Lu, W.-g.; Wang, Y.; Zou, B.; Zhong, H., In Situ Fabrication of
14 Halide Perovskite Nanocrystal-Embedded Polymer Composite Films with Enhanced
15 Photoluminescence for Display Backlights. *Adv. Mater.* **2016**, *28* (41), 9163-9168.
- 16 296. Kojima, A.; Ikegami, M.; Teshima, K.; Miyasaka, T., Highly Luminescent Lead
17 Bromide Perovskite Nanoparticles Synthesized with Porous Alumina Media. *Chem. Lett.* **2012**,
18 *41* (4), 397-399.
- 19 297. Liu, S.; He, M.; Di, X.; Li, P.; Xiang, W.; Liang, X., Precipitation and tunable emission
20 of cesium lead halide perovskites (CsPbX₃, X = Br, I) QDs in borosilicate glass. *Ceram. Int.*
21 **2018**, *44* (4), 4496-4499.
- 22 298. Shen, L.; Zhang, Z.; Zhao, Y.; Yang, H.; Yuan, L.; Chen, Y.; Xiang, W.; Liang, X.,
23 Synthesis and optical properties of novel mixed-metal cation CsPb_{1-x}Ti_xBr₃-based perovskite
24 glasses for W-LED. *J. Am. Ceram. Soc.* **2020**, *103* (1), 382-390.
- 25 299. Huang, X.; Guo, Q.; Yang, D.; Xiao, X.; Liu, X.; Xia, Z.; Fan, F.; Qiu, J.; Dong, G.,
26 Reversible 3D laser printing of perovskite quantum dots inside a transparent medium. *Nat.*
27 *Photonics* **2020**, *14* (2), 82-88.
- 28 300. Zhang, Q.; Wang, B.; Zheng, W.; Kong, L.; Wan, Q.; Zhang, C.; Li, Z.; Cao, X.; Liu,
29 M.; Li, L., Ceramic-like stable CsPbBr₃ nanocrystals encapsulated in silica derived from
30 molecular sieve templates. *Nat. Commun.* **2020**, *11* (1), 31.
- 31 301. Xin, Y.; Zhao, H.; Zhang, J., Highly Stable and Luminescent Perovskite-Polymer
32 Composites from a Convenient and Universal Strategy. *ACS Appl. Mater. Interfaces* **2018**, *10*
33 (5), 4971-4980.
- 34 302. Nedelcu, G.; Protesescu, L.; Yakunin, S.; Bodnarchuk, M. I.; Grotevent, M. J.;
35 Kovalenko, M. V., Fast Anion-Exchange in Highly Luminescent Nanocrystals of Cesium Lead
36 Halide Perovskites (CsPbX₃, X = Cl, Br, I). *Nano Lett.* **2015**, *15* (8), 5635-5640.
- 37 303. Kang, S.-M.; Park, B.; Raju, G. S. R.; Baek, S.; Hussain, S. K.; Kwak, C. H.; Han, Y.-
38 K.; Yu, J. S.; Kim, S.-W.; Huh, Y. S., Generation of cesium lead halide perovskite nanocrystals
39 via a serially-integrated microreactor system: Sequential anion exchange reaction. *Chem. Eng. J.*
40 **2020**, *384*, 123316.
- 41 304. Koscher, B. A.; Bronstein, N. D.; Olshansky, J. H.; Bekenstein, Y.; Alivisatos, A. P.,
42 Surface- vs Diffusion-Limited Mechanisms of Anion Exchange in CsPbBr₃ Nanocrystal Cubes
43 Revealed through Kinetic Studies. *J. Am. Chem. Soc.* **2016**, *138* (37), 12065-12068.

- 1 305. Zhang, Y.; Lu, D.; Gao, M.; Lai, M.; Lin, J.; Lei, T.; Lin, Z.; Quan, L. N.; Yang, P.,
2 Quantitative imaging of anion exchange kinetics in halide perovskites. *Proc. Natl. Acad. Sci.*
3 *U.S.A* **2019**, *116* (26), 12648.
- 4 306. Wang, D.; Cavin, J.; Yin, B.; Thind, A. S.; Borisevich, A. Y.; Mishra, R.; Sadtler, B.,
5 Role of Solid-State Miscibility during Anion Exchange in Cesium Lead Halide Nanocrystals
6 Probed by Single-Particle Fluorescence. *J. Phys. Chem. Lett.* **2020**, *11* (3), 952-959.
- 7 307. Haque, A.; Ravi, V. K.; Shanker, G. S.; Sarkar, I.; Nag, A.; Santra, P. K., Internal
8 Heterostructure of Anion-Exchanged Cesium Lead Halide Nanocubes. *J. Phys. Chem. C* **2018**,
9 *122* (25), 13399-13406.
- 10 308. Loiudice, A.; Strach, M.; Saris, S.; Chernyshov, D.; Buonsanti, R., Universal Oxide
11 Shell Growth Enables in Situ Structural Studies of Perovskite Nanocrystals during the Anion
12 Exchange Reaction. *J. Am. Chem. Soc.* **2019**, *141* (20), 8254-8263.
- 13 309. Hoffman, J. B.; Schleper, A. L.; Kamat, P. V., Transformation of Sintered CsPbBr₃
14 Nanocrystals to Cubic CsPbI₃ and Gradient CsPbBr_xI_{3-x} through Halide Exchange. *J. Am.*
15 *Chem. Soc.* **2016**, *138* (27), 8603-8611.
- 16 310. Elmelund, T.; Scheidt, R. A.; Seger, B.; Kamat, P. V., Bidirectional Halide Ion
17 Exchange in Paired Lead Halide Perovskite Films with Thermal Activation. *ACS Energy Lett.*
18 **2019**, *4* (8), 1961-1969.
- 19 311. Scheidt, R. A.; Kamat, P. V., Temperature-driven anion migration in gradient halide
20 perovskites. *J. Chem. Phys.* **2019**, *151* (13), 134703.
- 21 312. Ravi, V. K.; Scheidt, R. A.; DuBose, J.; Kamat, P. V., Hierarchical Arrays of Cesium
22 Lead Halide Perovskite Nanocrystals through Electrophoretic Deposition. *J. Am. Chem. Soc.*
23 **2018**, *140* (28), 8887-8894.
- 24 313. Ravi, V. K.; Scheidt, R. A.; Nag, A.; Kuno, M.; Kamat, P. V., To Exchange or Not to
25 Exchange. Suppressing Anion Exchange in Cesium Lead Halide Perovskites with PbSO₄-Oleate
26 Capping. *ACS Energy Lett.* **2018**, *3* (4), 1049-1055.
- 27 314. Zhao, H.; Wei, L.; Zeng, P.; Liu, M., Formation of highly uniform thinly-wrapped
28 CsPbX₃@silicone nanocrystals via self-hydrolysis: suppressed anion exchange and superior
29 stability in polar solvents. *J. Mater. Chem. C* **2019**, *7* (32), 9813-9819.
- 30 315. Palazon, F.; Akkerman, Q. A.; Prato, M.; Manna, L., X-ray Lithography on Perovskite
31 Nanocrystals Films: From Patterning with Anion-Exchange Reactions to Enhanced Stability in
32 Air and Water. *ACS Nano* **2016**, *10* (1), 1224-1230.
- 33 316. Xiao, X.; Dai, J.; Fang, Y.; Zhao, J.; Zheng, X.; Tang, S.; Rudd, P. N.; Zeng, X. C.;
34 Huang, J., Suppressed Ion Migration along the In-Plane Direction in Layered Perovskites. *ACS*
35 *Energy Lett.* **2018**, *3* (3), 684-688.
- 36 317. Rivest, J. B.; Jain, P. K., Cation exchange on the nanoscale: an emerging technique for
37 new material synthesis, device fabrication, and chemical sensing. *Chem. Soc. Rev.* **2013**, *42* (1),
38 89-96.
- 39 318. Xie, Y.-M.; Yu, B.; Ma, C.; Xu, X.; Cheng, Y.; Yuan, S.; Wang, Z.-K.; Chandran, H. T.;
40 Lee, C.-S.; Liao, L.-S.; Tsang, S.-W., Direct observation of cation-exchange in liquid-to-solid
41 phase transformation in FA_{1-x}MA_xPbI₃ based perovskite solar cells. *J. Mater. Chem. A* **2018**, *6*
42 (19), 9081-9088.

- 1 319. Wang, B.; Zhang, C.; Huang, S.; Li, Z.; Kong, L.; Jin, L.; Wang, J.; Wu, K.; Li, L.,
2 Postsynthesis Phase Transformation for CsPbBr₃/Rb₄PbBr₆ Core/Shell Nanocrystals with
3 Exceptional Photostability. *ACS Appl. Mater. Interfaces* **2018**, *10* (27), 23303-23310.
- 4 320. Wei, J.; Huang, F.; Wang, S.; Zhou, L.; Jin, P.; Xin, Y.; Cai, Z.; Yin, Z.; Pang, Q.;
5 Zhang, J. Z., Highly Stable Hybrid Perovskite Solar Cells Modified with Polyethylenimine via
6 Ionic Bonding. *ChemNanoMat* **2018**, *4* (7), 649-655.
- 7 321. Lau, C. F. J.; Wang, Z.; Sakai, N.; Zheng, J.; Liao, C. H.; Green, M.; Huang, S.; Snaith,
8 H. J.; Ho-Baillie, A., Fabrication of Efficient and Stable CsPbI₃ Perovskite Solar Cells through
9 Cation Exchange Process. *Adv. Energy Mater.* **2019**, *9* (36), 1901685.
- 10 322. van der Stam, W.; Geuchies, J. J.; Altantzis, T.; van den Bos, K. H. W.; Meeldijk, J. D.;
11 Van Aert, S.; Bals, S.; Vanmaekelbergh, D.; de Mello Donega, C., Highly Emissive Divalent-
12 Ion-Doped Colloidal CsPb_{1-x}M_xBr₃ Perovskite Nanocrystals through Cation Exchange. *J. Am.*
13 *Chem. Soc.* **2017**, *139* (11), 4087-4097.
- 14 323. Roman, B. J.; Otto, J.; Galik, C.; Downing, R.; Sheldon, M., Au Exchange or Au
15 Deposition: Dual Reaction Pathways in Au–CsPbBr₃ Heterostructure Nanoparticles. *Nano Lett.*
16 **2017**, *17* (9), 5561-5566.
- 17 324. Song, J.; Fang, T.; Li, J.; Xu, L.; Zhang, F.; Han, B.; Shan, Q.; Zeng, H., Organic–
18 Inorganic Hybrid Passivation Enables Perovskite QLEDs with an EQE of 16.48%. *Advanced*
19 *Materials* **2018**, *30* (50), 1805409.
- 20 325. Eames, C.; Frost, J. M.; Barnes, P. R. F.; O'Regan, B. C.; Walsh, A.; Islam, M. S., Ionic
21 transport in hybrid lead iodide perovskite solar cells. *Nat. Commun.* **2015**, *6* (1), 7497.
- 22 326. Gao, D.; Qiao, B.; Xu, Z.; Song, D.; Song, P.; Liang, Z.; Shen, Z.; Cao, J.; Zhang, J.;
23 Zhao, S., Postsynthetic, Reversible Cation Exchange between Pb²⁺ and Mn²⁺ in Cesium Lead
24 Chloride Perovskite Nanocrystals. *J. Phys. Chem. C* **2017**, *121* (37), 20387-20395.
- 25 327. Fang, G.; Chen, D.; Zhou, S.; Chen, X.; Lei, L.; Zhong, J.; Ji, Z., Reverse synthesis of
26 CsPb_xMn_{1-x}(Cl/Br)₃ perovskite quantum dots from CsMnCl₃ precursors through cation
27 exchange. *J. Mater. Chem. C* **2018**, *6* (22), 5908-5915.
- 28 328. Eperon, G. E.; Ginger, D. S., B-Site Metal Cation Exchange in Halide Perovskites. *ACS*
29 *Energy Lett.* **2017**, *2* (5), 1190-1196.
- 30 329. Chen, L.-J., Synthesis and optical properties of lead-free cesium germanium halide
31 perovskite quantum rods. *RSC Adv.* **2018**, *8* (33), 18396-18399.
- 32 330. Qiao, T.; Parobek, D.; Dong, Y.; Ha, E.; Son, D. H., Photoinduced Mn doping in cesium
33 lead halide perovskite nanocrystals. *Nanoscale* **2019**, *11* (12), 5247-5253.
- 34 331. Shapiro, A.; Heindl, M. W.; Horani, F.; Dahan, M.-H.; Tang, J.; Amouyal, Y.; Lifshitz,
35 E., Significance of Ni Doping in CsPbX₃ Nanocrystals via Postsynthesis Cation–Anion
36 Coexchange. *J. Phys. Chem. C* **2019**, *123* (40), 24979-24987.
- 37 332. Yuan, X.; Hou, X.; Li, J.; Qu, C.; Zhang, W.; Zhao, J.; Li, H., Thermal degradation of
38 luminescence in inorganic perovskite CsPbBr₃ nanocrystals. *Phys. Chem. Chem. Phys.* **2017**, *19*
39 (13), 8934-8940.
- 40 333. Pradhan, B.; Mushtaq, A.; Roy, D.; Sain, S.; Das, B.; Ghorai, U. K.; Pal, S. K.; Acharya,
41 S., Postsynthesis Spontaneous Coalescence of Mixed-Halide Perovskite Nanocubes into Phase-
42 Stable Single-Crystalline Uniform Luminescent Nanowires. *J. Phys. Chem. Lett.* **2019**, *10* (8),
43 1805-1812.

- 1 334. Pan, J.; Li, X.; Gong, X.; Yin, J.; Zhou, D.; Sinatra, L.; Huang, R.; Liu, J.; Chen, J.;
2 Dursun, I.; El-Zohry, A. M.; Saidaminov, M. I.; Sun, H.-T.; Mohammed, O. F.; Ye, C.; Sargent,
3 E. H.; Bakr, O. M., Halogen Vacancies Enable Ligand-Assisted Self-Assembly of Perovskite
4 Quantum Dots into Nanowires. *Angew. Chem. Int. Ed.* **2019**, *58* (45), 16077-16081.
- 5 335. Dang, Z.; Dhanabalan, B.; Castelli, A.; Dhall, R.; Bustillo, K. C.; Marchelli, D.; Spirito,
6 D.; Petralanda, U.; Shamsi, J.; Manna, L.; Krahne, R.; Arciniegas, M. P., Temperature-Driven
7 Transformation of CsPbBr₃ Nanoplatelets into Mosaic Nanotiles in Solution through Self-
8 Assembly. *Nano Lett.* **2020**, *20*, 1808–1818.
- 9 336. Hudait, B.; Dutta, S. K.; Patra, A.; Nasipuri, D.; Pradhan, N., Facets Directed
10 Connecting Perovskite Nanocrystals. *J. Am. Chem. Soc.* **2020**, *142* (15), 7207-7217.
- 11 337. Nagaoka, Y.; Hills-Kimball, K.; Tan, R.; Li, R.; Wang, Z.; Chen, O., Nanocube
12 Superlattices of Cesium Lead Bromide Perovskites and Pressure-Induced Phase Transformations
13 at Atomic and Mesoscale Levels. *Adv. Mater.* **2017**, *29* (18), 1606666.
- 14 338. Fanizza, E.; Cascella, F.; Altamura, D.; Giannini, C.; Panniello, A.; Triggiani, L.;
15 Panzarea, F.; Depalo, N.; Grisorio, R.; Suranna, G. P.; Agostiano, A.; Curri, M. L.; Striccoli, M.,
16 Post-synthesis phase and shape evolution of CsPbBr₃ colloidal nanocrystals: The role of ligands.
17 *Nano Res.* **2019**, *12* (5), 1155-1166.
- 18 339. Hintermayr, V. A.; Richter, A. F.; Ehrat, F.; Döblinger, M.; Vanderlinden, W.; Sichert, J.
19 A.; Tong, Y.; Polavarapu, L.; Feldmann, J.; Urban, A. S., Tuning the Optical Properties of
20 Perovskite Nanoplatelets through Composition and Thickness by Ligand-Assisted Exfoliation.
21 *Adv. Mater.* **2016**, *28* (43), 9478-9485.
- 22 340. Liu, L.; Huang, S.; Pan, L.; Shi, L.-J.; Zou, B.; Deng, L.; Zhong, H., Colloidal Synthesis
23 of CH₃NH₃PbBr₃ Nanoplatelets with Polarized Emission through Self-Organization. *Angew.*
24 *Chem. Int. Ed.* **2017**, *56* (7), 1780-1783.
- 25 341. Xu, S.; Ziegler, J.; Nann, T., Rapid synthesis of highly luminescent InP and InP/ZnS
26 nanocrystals. *J. Mater. Chem.* **2008**, *18* (23), 2653-2656.
- 27 342. Gao, Y.; Peng, X., Photogenerated Excitons in Plain Core CdSe Nanocrystals with Unity
28 Radiative Decay in Single Channel: The Effects of Surface and Ligands. *J. Am. Chem. Soc.*
29 **2015**, *137* (12), 4230-4235.
- 30 343. Pu, C.; Qin, H.; Gao, Y.; Zhou, J.; Wang, P.; Peng, X., Synthetic Control of Exciton
31 Behavior in Colloidal Quantum Dots. *J. Am. Chem. Soc.* **2017**, *139* (9), 3302-3311.
- 32 344. Pu, C.; Peng, X., To Battle Surface Traps on CdSe/CdS Core/Shell Nanocrystals: Shell
33 Isolation versus Surface Treatment. *J. Am. Chem. Soc.* **2016**, *138* (26), 8134-8142.
- 34 345. Dirin, D. N.; Protesescu, L.; Trummer, D.; Kochetygov, I. V.; Yakunin, S.; Krumeich,
35 F.; Stadie, N. P.; Kovalenko, M. V., Harnessing Defect-Tolerance at the Nanoscale: Highly
36 Luminescent Lead Halide Perovskite Nanocrystals in Mesoporous Silica Matrixes. *Nano Lett.*
37 **2016**, *16* (9), 5866-5874.
- 38 346. González-Carrero, S.; Martínez-Sarti, L.; Sessolo, M.; Galian, R. E.; Pérez-Prieto, J.,
39 Highly photoluminescent, dense solid films from organic-capped CH₃NH₃PbBr₃ perovskite
40 colloids. *J. Mater. Chem. C* **2018**, *6* (25), 6771-6777.
- 41 347. Kang, J.; Wang, L.-W., High Defect Tolerance in Lead Halide Perovskite CsPbBr₃. *J.*
42 *Phys. Chem. Lett.* **2017**, *8* (2), 489-493.

- 1 348. Di Stasio, F.; Christodoulou, S.; Huo, N.; Konstantatos, G., Near-Unity
2 Photoluminescence Quantum Yield in CsPbBr₃ Nanocrystal Solid-State Films via Postsynthesis
3 Treatment with Lead Bromide. *Chem. Mater.* **2017**, *29* (18), 7663-7667.
- 4 349. Raquel Eugenia, G.; Julia, P.-P., Synergism at the Nanoscale: Photoactive
5 Semiconductor Nanoparticles and their Organic Ligands. In *Research Perspectives on*
6 *Functional Micro- and Nanoscale Coatings*, IGI Global: Hershey, PA, USA, 2016; pp 42-77.
- 7 350. Pan, J.; Quan, L. N.; Zhao, Y.; Peng, W.; Murali, B.; Sarmah, S. P.; Yuan, M.; Sinatra,
8 L.; Alyami, N. M.; Liu, J.; Yassitepe, E.; Yang, Z.; Voznyy, O.; Comin, R.; Hedhili, M. N.;
9 Mohammed, O. F.; Lu, Z. H.; Kim, D. H.; Sargent, E. H.; Bakr, O. M., Highly Efficient
10 Perovskite-Quantum-Dot Light-Emitting Diodes by Surface Engineering. **2016**, *28* (39), 8718-
11 8725.
- 12 351. Vickers, E. T.; Graham, T. A.; Chowdhury, A. H.; Bahrami, B.; Dreskin, B. W.; Lindley,
13 S.; Naghadeh, S. B.; Qiao, Q.; Zhang, J. Z., Improving Charge Carrier Delocalization in
14 Perovskite Quantum Dots by Surface Passivation with Conductive Aromatic Ligands. *ACS*
15 *Energy Lett.* **2018**, *3* (12), 2931-2939.
- 16 352. Anderson, N. C.; Hendricks, M. P.; Choi, J. J.; Owen, J. S., Ligand Exchange and the
17 Stoichiometry of Metal Chalcogenide Nanocrystals: Spectroscopic Observation of Facile Metal-
18 Carboxylate Displacement and Binding. *J. Am. Chem. Soc.* **2013**, *135* (49), 18536-18548.
- 19 353. De Roo, J.; Yazdani, N.; Drijvers, E.; Lauria, A.; Maes, J.; Owen, J. S.; Van Driessche,
20 I.; Niederberger, M.; Wood, V.; Martins, J. C.; Infante, I.; Hens, Z., Probing Solvent-Ligand
21 Interactions in Colloidal Nanocrystals by the NMR Line Broadening. *Chem. Mater.* **2018**, *30*
22 (15), 5485-5492.
- 23 354. Moreels, I.; Fritzinger, B.; Martins, J. C.; Hens, Z., Surface Chemistry of Colloidal PbSe
24 Nanocrystals. *J. Am. Chem. Soc.* **2008**, *130* (45), 15081-15086.
- 25 355. Green, M. L. H., A new approach to the formal classification of covalent compounds of
26 the elements. *J. Organomet. Chem.* **1995**, *500* (1), 127-148.
- 27 356. Green, M. L. H.; Parkin, G., Application of the Covalent Bond Classification Method for
28 the Teaching of Inorganic Chemistry. *J. Chem. Educ.* **2014**, *91* (6), 807-816.
- 29 357. Gonzalez-Carrero, S.; Francés-Soriano, L.; González-Béjar, M.; Agouram, S.; Galian, R.
30 E.; Pérez-Prieto, J., The Luminescence of CH₃NH₃PbBr₃ Perovskite Nanoparticles Crests the
31 Summit and Their Photostability under Wet Conditions is Enhanced. **2016**, *12* (38), 5245-5250.
- 32 358. Huang, H.; Raith, J.; Kershaw, S. V.; Kalytchuk, S.; Tomanec, O.; Jing, L.; Susha, A. S.;
33 Zboril, R.; Rogach, A. L., Growth mechanism of strongly emitting CH₃NH₃PbBr₃ perovskite
34 nanocrystals with a tunable bandgap. *Nat. Commun.* **2017**, *8* (1), 996.
- 35 359. McCleverty, J. A., Meyer T. J. (eds). in *Comprehensive Coordination Chemistry II:*
36 *From Biology to Nanotechnology* 2nd edn (Elsevier, 2004)
- 37 360. Luo, B.; Pu, Y.-C.; Lindley, S. A.; Yang, Y.; Lu, L.; Li, Y.; Li, X.; Zhang, J. Z.,
38 Organolead Halide Perovskite Nanocrystals: Branched Capping Ligands Control Crystal Size
39 and Stability. **2016**, *55* (31), 8864-8868.
- 40 361. Jancik Prochazkova, A.; Salinas, Y.; Yumusak, C.; Brüggemann, O.; Weiter, M.;
41 Sariciftci, N. S.; Krajcovic, J.; Kovalenko, A., Cyclic Peptide Stabilized Lead Halide Perovskite
42 Nanoparticles. *Sci. Rep.* **2019**, *9* (1), 12966.

- 1 362. Yassitepe, E.; Yang, Z.; Voznyy, O.; Kim, Y.; Walters, G.; Castañeda, J. A.;
2 Kanjanaboos, P.; Yuan, M.; Gong, X.; Fan, F.; Pan, J.; Hoogland, S.; Comin, R.; Bakr, O. M.;
3 Padilha, L. A.; Nogueira, A. F.; Sargent, E. H., Amine-Free Synthesis of Cesium Lead Halide
4 Perovskite Quantum Dots for Efficient Light-Emitting Diodes. *Adv. Funct. Mater.* **2016**, *26* (47),
5 8757-8763.
- 6 363. Lu, H.; Zhu, X.; Miller, C.; Martin, J. S.; Chen, X.; Miller, E. M.; Yan, Y.; Beard, M. C.,
7 Enhanced photoredox activity of CsPbBr₃ nanocrystals by quantitative colloidal ligand
8 exchange. *J. Chem. Phys.* **2019**, *151* (20), 204305.
- 9 364. Rosa-Pardo, I.; Casadevall, C.; Schmidt, L.; Claros, M.; Galian, R. E.; Lloret-Fillol, J.;
10 Pérez-Prieto, J., The synergy between the CsPbBr₃ nanoparticle surface and the organic ligand
11 becomes manifest in a demanding carbon–carbon coupling reaction. *Chem. Commun.* **2020**, *56*
12 (37), 5026-5029.
- 13 365. Ruan, L.; Shen, W.; Wang, A.; Xiang, A.; Deng, Z., Alkyl-Thiol Ligand-Induced Shape-
14 and Crystalline Phase-Controlled Synthesis of Stable Perovskite-Related CsPb₂Br₅ Nanocrystals
15 at Room Temperature. *J. Phys. Chem. Lett.* **2017**, *8* (16), 3853-3860.
- 16 366. Ravi, V. K.; Santra, P. K.; Joshi, N.; Chugh, J.; Singh, S. K.; Rensmo, H.; Ghosh, P.;
17 Nag, A., Origin of the Substitution Mechanism for the Binding of Organic Ligands on the
18 Surface of CsPbBr₃ Perovskite Nanocubes. *J. Phys. Chem. Lett.* **2017**, *8* (20), 4988-4994.
- 19 367. Zhang, B.; Goldoni, L.; Zito, J.; Dang, Z.; Almeida, G.; Zaccaria, F.; de Wit, J.; Infante,
20 I.; De Trizio, L.; Manna, L., Alkyl Phosphonic Acids Deliver CsPbBr₃ Nanocrystals with High
21 Photoluminescence Quantum Yield and Truncated Octahedron Shape. *Chem. Mater.* **2019**, *31*
22 (21), 9140-9147.
- 23 368. Yang, D.; Li, X.; Zhou, W.; Zhang, S.; Meng, C.; Wu, Y.; Wang, Y.; Zeng, H., CsPbBr₃
24 Quantum Dots 2.0: Benzenesulfonic Acid Equivalent Ligand Awakens Complete Purification.
25 *Adv. Mater.* **2019**, *31* (30), 1900767.
- 26 369. Huang, S.; Wang, B.; Zhang, Q.; Li, Z.; Shan, A.; Li, L., Postsynthesis Potassium-
27 Modification Method to Improve Stability of CsPbBr₃ Perovskite Nanocrystals. **2018**, *6* (6),
28 1701106.
- 29 370. Sun, C.; Zhang, Y.; Ruan, C.; Yin, C.; Wang, X.; Wang, Y.; Yu, W. W., Efficient and
30 stable white LEDs with silica - coated inorganic perovskite quantum dots. *Advanced Materials*
31 **2016**, *28* (45), 10088-10094.
- 32 371. Gonzalez-Carrero, S.; Bareño, L.; Debroye, E.; Martin, C.; Bondia, P.; Flors, C.; Galian,
33 R. E.; Hofkens, J.; Pérez-Prieto, J., Linear assembly of lead bromide-based nanoparticles inside
34 lead(ii) polymers prepared by mixing the precursors of both the nanoparticle and the polymer.
35 *Chem. Commun.* **2019**, *55* (20), 2968-2971.
- 36 372. Zhang, J. Z., A “Cocktail” Approach to Effective Surface Passivation of Multiple
37 Surface Defects of Metal Halide Perovskites Using a Combination of Ligands. *J. Phys. Chem.*
38 *Lett.* **2019**, *10* (17), 5055-5063.
- 39 373. Wang, S.; Zhou, L.; Huang, F.; Xin, Y.; Jin, P.; Ma, Q.; Pang, Q.; Chen, Y.; Zhang, J.
40 Z., Hybrid organic–inorganic lead bromide perovskite supercrystals self-assembled with l-
41 cysteine and their good luminescence properties. *J. Mater. Chem. C* **2018**, *6* (41), 10994-11001.
- 42 374. Hu, Y.; Zhang, X.; Yang, C.; Li, J.; Wang, L., Fe²⁺ doped in CsPbCl₃ perovskite
43 nanocrystals: impact on the luminescence and magnetic properties. *RSC Adv.* **2019**, *9* (57),
44 33017-33022.

- 1 375. Wang, F.; Geng, W.; Zhou, Y.; Fang, H. H.; Tong, C. J.; Loi, M. A.; Liu, L. M.; Zhao,
2 N., Phenylalkylamine Passivation of Organolead Halide Perovskites Enabling High-Efficiency
3 and Air-Stable Photovoltaic Cells. *Adv. Mater.* **2016**, *28* (45), 9986-9992.
- 4 376. Zhang, Y. H.; Guo, T. L.; Yang, H. Z.; Bose, R.; Liu, L. M.; Yin, J.; Han, Y.; Bakr, O.
5 M.; Mohammed, O. F.; Malko, A. V., Emergence of multiple fluorophores in individual cesium
6 lead bromide nanocrystals. *Nat. Commun.* **2019**, *10*.
- 7 377. Xu, K.; Vickers, E. T.; Rao, L.; Lindley, S. A.; Allen, A. C.; Luo, B.; Li, X.; Zhang, J.
8 Z., Synergistic Surface Passivation of CH₃NH₃PbBr₃ Perovskite Quantum Dots with
9 Phosphonic Acid and (3-Aminopropyl)triethoxysilane. *Chem. Eur. J.* **2019**, *25*, 5014-5021.
- 10 378. Zhang, F.; Huang, S.; Wang, P.; Chen, X.; Zhao, S.; Dong, Y.; Zhong, H., Colloidal
11 Synthesis of Air-Stable CH₃NH₃PbI₃ Quantum Dots by Gaining Chemical Insight into the
12 Solvent Effects. *Chem. Mater.* **2017**, *29* (8), 3793-3799.
- 13 379. Wei, J.; Huang, F.; Wang, S.; Zhou, L.; Xin, Y.; Jin, P.; Cai, Z.; Yin, Z.; Pang, Q.;
14 Zhang, J. Z., Highly stable and efficient hybrid perovskite solar cells improved with conductive
15 polyanilines. *Mater. Res. Bull.* **2018**, *106*, 35-39.
- 16 380. Luo, B.; Naghadeh, S. B.; Allen, A. L.; Li, X.; Zhang, J. Z., Peptide-Passivated Lead
17 Halide Perovskite Nanocrystals Based on Synergistic Effect between Amino and Carboxylic
18 Functional Groups. *Adv. Funct. Mater.* **2017**, *27* (6), 1604018.
- 19 381. Wang, Y.; Yu, D.; Wang, Z.; Li, X.; Chen, X.; Nalla, V.; Zeng, H.; Sun, H., Solution-
20 Grown CsPbBr₃/Cs₄PbBr₆ Perovskite Nanocomposites: Toward Temperature-Insensitive
21 Optical Gain. *Small* **2017**, *13* (34), 1701587.
- 22 382. Li, Z. J.; Hofman, E.; Li, J.; Davis, A. H.; Tung, C. H.; Wu, L. Z.; Zheng, W.,
23 Photoelectrochemically Active and Environmentally Stable CsPbBr₃/TiO₂ Core/Shell
24 Nanocrystals. *Advanced Functional Materials* **2018**, *28* (1), 1704288.
- 25 383. Inglezakis, V. J.; Loizidou, M. D.; Grigoropoulou, H. P., Ion exchange of Pb²⁺, Cu²⁺,
26 Fe³⁺, and Cr³⁺ on natural clinoptilolite: selectivity determination and influence of acidity on
27 metal uptake. *J. Coll. Interf. Sci.* **2003**, *261* (1), 49-54.
- 28 384. Li, C.; Yin, J.; Chen, R.; Lv, X.; Feng, X.; Wu, Y.; Cao, J., Monoammonium Porphyrin
29 for Blade-Coating Stable Large-Area Perovskite Solar Cells with >18% Efficiency. *J. Am. Chem.*
30 *Soc.* **2019**, *141* (15), 6345-6351.
- 31 385. Yang, W.; Gao, F.; Qiu, Y.; Liu, W.; Xu, H.; Yang, L.; Liu, Y., CsPbBr₃ - Quantum -
32 Dots/Polystyrene@Silica Hybrid Microsphere Structures with Significantly Improved Stability
33 for White LEDs. *Advanced Optical Materials* **2019**, 1900546.
- 34 386. Dai, J.; Xi, J.; Li, L.; Zhao, J.; Shi, Y.; Zhang, W.; Ran, C.; Jiao, B.; Hou, X.; Duan, X.;
35 Wu, Z., Charge Transport between Coupling Colloidal Perovskite Quantum Dots Assisted by
36 Functional Conjugated Ligands. *Angew. Chem. Int. Ed.* **2018**, *57* (20), 5754-5758.
- 37 387. Zhang, Z.; Li, X.; Xia, X.; Wang, Z.; Huang, Z.; Lei, B.; Gao, Y., High-Quality
38 (CH₃NH₃)₃Bi₂I₉ Film-Based Solar Cells: Pushing Efficiency up to 1.64. *J. Phys. Chem. Lett.*
39 **2017**, *8* (17), 4300-4307.
- 40 388. Zhang, J. Z., A "Cocktail" Approach to Effective Surface Passivation of Multiple
41 Surface Defects of Metal Halide Perovskites Using a Combination of Ligands. *J. Phys. Chem.*
42 *Lett.* **2019**, 5055-5063.

- 1 389. Li, X.; Dar, M. I.; Yi, C.; Luo, J.; Tschumi, M.; Zakeeruddin, S. M.; Nazeeruddin, M.
2 K.; Han, H.; Gratzel, M., Improved performance and stability of perovskite solar cells by crystal
3 crosslinking with alkylphosphonic acid omega-ammonium chlorides. *Nat. Chem.* **2015**, *7* (9),
4 703-711.
- 5 390. De Roo, J.; Ibanez, M.; Geiregat, P.; Nedelcu, G.; Walravens, W.; Maes, J.; Martins, J.
6 C.; Van Driessche, I.; Kovalenko, M. V.; Hens, Z., Highly Dynamic Ligand Binding and Light
7 Absorption Coefficient of Cesium Lead Bromide Perovskite Nanocrystals. *ACS Nano* **2016**, *10*
8 (2), 2071-2081.
- 9 391. Rao, L.; Ding, X.; Du, X.; Liang, G.; Tang, Y.; Tang, K.; Zhang, J. Z., Ultrasonication-
10 assisted synthesis of CsPbBr₃ and Cs₄PbBr₆ perovskite nanocrystals and their reversible
11 transformation. *Beilstein J. Nanotechnol.* **2019**, *10*, 666-676.
- 12 392. Zhu, J.; Zhu, Y.; Huang, J.; Gong, Y.; Shen, J.; Li, C., Synthesis of CsPbBr₃ perovskite
13 nanocrystals with the sole ligand of protonated (3-aminopropyl)triethoxysilane. *J. Mater. Chem.*
14 *C* **2019**, *7* (24), 7201-7206.
- 15 393. Luo, B.; Pu, Y. C.; Lindley, S. A.; Yang, Y.; Lu, L.; Li, Y.; Li, X.; Zhang, J. Z.,
16 Organolead Halide Perovskite Nanocrystals: Branched Capping Ligands Control Crystal Size
17 and Stability. *Angew. Chem. Int. Ed.* **2016**, *55* (31), 8864-8.
- 18 394. Abdelmageed, G.; Sully, H. R.; Bonabi Naghadeh, S.; El-Hag Ali, A.; Carter, S. A.;
19 Zhang, J. Z., Improved Stability of Organometal Halide Perovskite Films and Solar Cells toward
20 Humidity via Surface Passivation with Oleic Acid. *ACS Appl. Energy Mater.* **2018**, *1* (2), 387-
21 392.
- 22 395. Zhong, Y.; Munir, R.; Balawi, A. H.; Sheikh, A. D.; Yu, L.; Tang, M.-C.; Hu, H.;
23 Laquai, F.; Amassian, A., Mesostructured Fullerene Electrodes for Highly Efficient n-i-p
24 Perovskite Solar Cells. *ACS Energy Lett.* **2016**, *1* (5), 1049-1056.
- 25 396. Dong, H.; Xi, J.; Zuo, L.; Li, J.; Yang, Y.; Wang, D.; Yu, Y.; Ma, L.; Ran, C.; Gao, W.;
26 Jiao, B.; Xu, J.; Lei, T.; Wei, F.; Yuan, F.; Zhang, L.; Shi, Y.; Hou, X.; Wu, Z., Conjugated
27 Molecules "Bridge" : Functional Ligand toward Highly Efficient and Long - Term Stable
28 Perovskite Solar Cell. *Adv. Funct. Mater.* **2019**, *29* (17), 1808119.
- 29 397. Vickers, E. T.; Xu, K.; Dreskin, B. W.; Graham, T. A.; Li, X.; Zhang, J. Z., Ligand
30 Dependent Growth and Optical Properties of Hybrid Organo-metal Halide Perovskite Magic
31 Sized Clusters. *J. Phys. Chem. C* **2019**, *123* (30), 18746-18752.
- 32 398. Nevers, D. R.; Williamson, C. B.; Savitzky, B. H.; Hadar, I.; Banin, U.; Kourkoutis, L.
33 F.; Hanrath, T.; Robinson, R. D., Mesophase Formation Stabilizes High-Purity Magic-Sized
34 Clusters. *J. Am. Chem. Soc.* **2018**, *140* (10), 3652-3662.
- 35 399. Evans, C. M.; Love, A. M.; Weiss, E. A., Surfactant-controlled polymerization of
36 semiconductor clusters to quantum dots through competing step-growth and living chain-growth
37 mechanisms. *J. Am. Chem. Soc.* **2012**, *134* (41), 17298-17305.
- 38 400. Yu, K., CdSe magic-sized nuclei, magic-sized nanoclusters and regular nanocrystals:
39 monomer effects on nucleation and growth. *Adv. Mater.* **2012**, *24* (8), 1123-1132.
- 40 401. Peng, L.; Geng, J.; Ai, L.; Zhang, Y.; Xie, R.; Yang, W., Room temperature synthesis of
41 ultra-small, near-unity single-sized lead halide perovskite quantum dots with wide color emission
42 tunability, high color purity and high brightness. *Nanotechnology* **2016**, *27* (33), 335604.

- 1 402. Xu, Y.; Zhang, Q.; Lv, L.; Han, W.; Wu, G.; Yang, D.; Dong, A., Synthesis of ultrasmall
2 CsPbBr₃ nanoclusters and their transformation to highly deep-blue-emitting nanoribbons at room
3 temperature. *Nanoscale* **2017**, *9* (44), 17248-17253.
- 4 403. Zheng, W.; Li, Z.; Zhang, C.; Wang, B.; Zhang, Q.; Wan, Q.; Kong, L.; Li, L.,
5 Stabilizing perovskite nanocrystals by controlling protective surface ligands density. *Nano Res.*
6 **2019**, *12* (6), 1461-1465.
- 7 404. Quarta, D.; Imran, M.; Capodilupo, A.-L.; Petralanda, U.; van Beek, B.; De Angelis, F.;
8 Manna, L.; Infante, I.; De Trizio, L.; Giansante, C., Stable Ligand Coordination at the Surface of
9 Colloidal CsPbBr₃ Nanocrystals. *J. Phys. Chem. Lett.* **2019**, *10* (13), 3715-3726.
- 10 405. Wang, N.; Cheng, L.; Ge, R.; Zhang, S.; Miao, Y.; Zou, W.; Yi, C.; Sun, Y.; Cao, Y.;
11 Yang, R.; Wei, Y.; Guo, Q.; Ke, Y.; Yu, M.; Jin, Y.; Liu, Y.; Ding, Q.; Di, D.; Yang, L.; Xing,
12 G.; Tian, H.; Jin, C.; Gao, F.; Friend, R. H.; Wang, J.; Huang, W., Perovskite light-emitting
13 diodes based on solution-processed self-organized multiple quantum wells. *Nat. Photonics* **2016**,
14 *10* (11), 699-704.
- 15 406. Yang, W.; Gao, F.; Qiu, Y.; Liu, W.; Xu, H.; Yang, L.; Liu, Y., CsPbBr₃ - Quantum -
16 Dots/Polystyrene@Silica Hybrid Microsphere Structures with Significantly Improved Stability
17 for White LEDs. *Adv. Opt. Mater.* **2019**, 1900546.
- 18 407. Gautier, R.; Paris, M.; Massuyeau, F., Exciton Self-Trapping in Hybrid Lead Halides:
19 Role of Halogen. *J. Am. Chem. Soc.* **2019**, *141* (32), 12619-12623.
- 20 408. Pan, J.; Quan, L. N.; Zhao, Y.; Peng, W.; Murali, B.; Sarmah, S. P.; Yuan, M.; Sinatra,
21 L.; Alyami, N. M.; Liu, J.; Yassitepe, E.; Yang, Z.; Voznyy, O.; Comin, R.; Hedhili, M. N.;
22 Mohammed, O. F.; Lu, Z. H.; Kim, D. H.; Sargent, E. H.; Bakr, O. M., Highly Efficient
23 Perovskite-Quantum-Dot Light-Emitting Diodes by Surface Engineering. *Advanced Materials*
24 **2016**, *28* (39), 8718-8725.
- 25 409. Pan, J.; Sarmah, S. P.; Murali, B.; Dursun, I.; Peng, W.; Parida, M. R.; Liu, J.; Sinatra,
26 L.; Alyami, N.; Zhao, C.; Alarousu, E.; Ng, T. K.; Ooi, B. S.; Bakr, O. M.; Mohammed, O. F.,
27 Air-Stable Surface-Passivated Perovskite Quantum Dots for Ultra-Robust, Single- and Two-
28 Photon-Induced Amplified Spontaneous Emission. *J. Phys. Chem. Lett.* **2015**, *6* (24), 5027-5033.
- 29 410. Ahmed, T.; Seth, S.; Samanta, A., Boosting the Photoluminescence of CsPbX₃ (X = Cl,
30 Br, I) Perovskite Nanocrystals Covering a Wide Wavelength Range by Postsynthetic Treatment
31 with Tetrafluoroborate Salts. *Chem. Mater.* **2018**, *30* (11), 3633-3637.
- 32 411. Wang, Y.; Li, X.; Sreejith, S.; Cao, F.; Wang, Z.; Stuparu, M. C.; Zeng, H.; Sun, H.,
33 Photon Driven Transformation of Cesium Lead Halide Perovskites from Few-Monolayer
34 Nanoplatelets to Bulk Phase. *Advanced Materials* **2016**, *28* (48), 10637-10643.
- 35 412. Ahmed, G. H.; El-Demellawi, J. K.; Yin, J.; Pan, J.; Velusamy, D. B.; Hedhili, M. N.;
36 Alarousu, E.; Bakr, O. M.; Alshareef, H. N.; Mohammed, O. F., Giant Photoluminescence
37 Enhancement in CsPbCl₃ Perovskite Nanocrystals by Simultaneous Dual-Surface Passivation.
38 *ACS Energy Lett.* **2018**, *3* (10), 2301-2307.
- 39 413. Xie, R.; Rutherford, M.; Peng, X., Formation of High-Quality I-III-VI Semiconductor
40 Nanocrystals by Tuning Relative Reactivity of Cationic Precursors. *J. Am. Chem. Soc.* **2009**, *131*
41 (15), 5691-5697.
- 42 414. Li, L. S.; Pradhan, N.; Wang, Y.; Peng, X., High Quality ZnSe and ZnS Nanocrystals
43 Formed by Activating Zinc Carboxylate Precursors. *Nano Lett.* **2004**, *4* (11), 2261-2264.

- 1 415. Li, Z.; Ji, Y.; Xie, R.; Grisham, S. Y.; Peng, X., Correlation of CdS Nanocrystal
2 Formation with Elemental Sulfur Activation and Its Implication in Synthetic Development. *J.*
3 *Am. Chem. Soc.* **2011**, *133* (43), 17248-17256.
- 4 416. Liu, P.; Chen, W.; Wang, W.; Xu, B.; Wu, D.; Hao, J.; Cao, W.; Fang, F.; Li, Y.; Zeng,
5 Y.; Pan, R.; Chen, S.; Cao, W.; Sun, X. W.; Wang, K., Halide-Rich Synthesized Cesium Lead
6 Bromide Perovskite Nanocrystals for Light-Emitting Diodes with Improved Performance. *Chem.*
7 *Mater.* **2017**, *29* (12), 5168-5173.
- 8 417. Woo, J. Y.; Kim, Y.; Bae, J.; Kim, T. G.; Kim, J. W.; Lee, D. C.; Jeong, S., Highly
9 Stable Cesium Lead Halide Perovskite Nanocrystals through in Situ Lead Halide Inorganic
10 Passivation. *Chem. Mater.* **2017**, *29* (17), 7088-7092.
- 11 418. Wu, Y.; Wei, C.; Li, X.; Li, Y.; Qiu, S.; Shen, W.; Cai, B.; Sun, Z.; Yang, D.; Deng, Z.;
12 Zeng, H., In Situ Passivation of PbBr₆⁴⁻ Octahedra toward Blue Luminescent CsPbBr₃
13 Nanoplatelets with Near 100% Absolute Quantum Yield. *ACS Energy Letters* **2018**, *3* (9), 2030-
14 2037.
- 15 419. Yong, Z.-J.; Guo, S.-Q.; Ma, J.-P.; Zhang, J.-Y.; Li, Z.-Y.; Chen, Y.-M.; Zhang, B.-B.;
16 Zhou, Y.; Shu, J.; Gu, J.-L.; Zheng, L.-R.; Bakr, O. M.; Sun, H.-T., Doping-Enhanced Short-
17 Range Order of Perovskite Nanocrystals for Near-Unity Violet Luminescence Quantum Yield. *J.*
18 *Am. Chem. Soc.* **2018**, *140* (31), 9942-9951.
- 19 420. Yang, J.-N.; Song, Y.; Yao, J.-S.; Wang, K.-H.; Wang, J.-J.; Zhu, B.-S.; Yao, M.-M.;
20 Rahman, S. U.; Lan, Y.-F.; Fan, F.-J.; Yao, H.-B., Potassium-Bromide Surface Passivation on
21 CsPbI_{3-x}Br_x Nanocrystals for Efficient and Stable Pure Red Perovskite Light Emitting Diodes.
22 *J. Am. Chem. Soc.* **2020**.
- 23 421. Wu, H.; Zhang, Y.; Lu, M.; Zhang, X.; Sun, C.; Zhang, T.; Colvin, V. L.; Yu, W. W.,
24 Surface ligand modification of cesium lead bromide nanocrystals for improved light-emitting
25 performance. *Nanoscale* **2018**, *10* (9), 4173-4178.
- 26 422. Dutta, A.; Behera, R. K.; Pal, P.; Baitalik, S.; Pradhan, N., Near-Unity
27 Photoluminescence Quantum Efficiency for All CsPbX₃ (X=Cl, Br, and I) Perovskite
28 Nanocrystals: A Generic Synthesis Approach. *Angewandte Chemie* **2019**, *131* (17), 5608-5612.
- 29 423. Luo, C.; Li, W.; Xiong, D.; Fu, J.; Yang, W., Surface pre-optimization of a mixed halide
30 perovskite toward high photoluminescence quantum yield in the blue spectrum range. *Nanoscale*
31 **2019**, *11* (32), 15206-15215.
- 32 424. Kim, Y.-H.; Lee, G.-H.; Kim, Y.-T.; Wolf, C.; Yun, H. J.; Kwon, W.; Park, C. G.; Lee,
33 T. W., High efficiency perovskite light-emitting diodes of ligand-engineered colloidal
34 formamidinium lead bromide nanoparticles. *Nano Energy* **2017**, *38*, 51-58.
- 35 425. Lin, K.; Xing, J.; Quan, L. N.; de Arquer, F. P. G.; Gong, X.; Lu, J.; Xie, L.; Zhao, W.;
36 Zhang, D.; Yan, C.; Li, W.; Liu, X.; Lu, Y.; Kirman, J.; Sargent, E. H.; Xiong, Q.; Wei, Z.,
37 Perovskite light-emitting diodes with external quantum efficiency exceeding 20 per cent. *Nature*
38 **2018**, *562* (7726), 245-248.
- 39 426. Lu, M.; Guo, J.; Sun, S.; Lu, P.; Zhang, X.; Shi, Z.; Yu, W. W.; Zhang, Y., Surface
40 ligand engineering-assisted CsPbI₃ quantum dots enable bright and efficient red light-emitting
41 diodes with a top-emitting structure. *Chem. Eng. J.* **2021**, *404*, 126563.
- 42 427. Park, J. H.; Lee, A.-y.; Yu, J. C.; Nam, Y. S.; Choi, Y.; Park, J.; Song, M. H., Surface
43 Ligand Engineering for Efficient Perovskite Nanocrystal-Based Light-Emitting Diodes. *ACS*
44 *Appl. Mater. Interfaces* **2019**, *11* (8), 8428-8435.

- 1 428. Yan, W.; Shen, J.; Zhu, Y.; Gong, Y.; Zhu, J.; Wen, Z.; Li, C., CsPbBr₃ quantum dots
2 photodetectors boosting carrier transport via molecular engineering strategy. *Nano Res.* **2021**,
3 429. Hassan, Y.; Park, J. H.; Crawford, M. L.; Sadhanala, A.; Lee, J.; Sadighian, J. C.;
4 Mosconi, E.; Shivanna, R.; Radicchi, E.; Jeong, M.; Yang, C.; Choi, H.; Park, S. H.; Song, M.
5 H.; De Angelis, F.; Wong, C. Y.; Friend, R. H.; Lee, B. R.; Snaith, H. J., Ligand-engineered
6 bandgap stability in mixed-halide perovskite LEDs. *Nature* **2021**, 591 (7848), 72-77.
- 7 430. Han, B.; Yuan, S.; Fang, T.; Zhang, F.; Shi, Z.; Song, J., Novel Lewis Base Cyclam
8 Self-Passivation of Perovskites without an Anti-Solvent Process for Efficient Light-Emitting
9 Diodes. *ACS Appl. Mater. Interfaces* **2020**, 12 (12), 14224-14232.
- 10 431. Saidaminov, M. I.; Almutlaq, J.; Sarmah, S.; Dursun, I.; Zhumekenov, A. A.; Begum,
11 R.; Pan, J.; Cho, N.; Mohammed, O. F.; Bakr, O. M., Pure Cs₄PbBr₆: Highly Luminescent Zero
12 Dimensional Perovskite Solids. *ACS Energy Lett.* **2016**, 1 (4), 840-845.
- 13 432. Akkerman, Q. A.; Park, S.; Radicchi, E.; Nunzi, F.; Mosconi, E.; De Angelis, F.;
14 Brescia, R.; Rastogi, P.; Prato, M.; Manna, L., Nearly Monodisperse Insulator Cs₄PbX₆ (X = Cl,
15 Br, I) Nanocrystals, Their Mixed Halide Compositions, and Their Transformation into CsPbX₃
16 Nanocrystals. *Nano Lett.* **2017**, 17 (3), 1924-1930.
- 17 433. Seth, S.; Samanta, A., Fluorescent Phase-Pure Zero-Dimensional Perovskite-Related
18 Cs₄PbBr₆ Microdisks: Synthesis and Single-Particle Imaging Study. *J. Phys. Chem. Lett.* **2017**,
19 8 (18), 4461-4467.
- 20 434. Mohammed, O. F., Outstanding Challenges of Zero-Dimensional Perovskite Materials.
21 *J. Phys. Chem. Lett.* **2019**, 10 (19), 5886-5888.
- 22 435. Thumu, U.; Piotrowski, M.; Owens-Baird, B.; Kolen'ko, Y. V., Zero-dimensional cesium
23 lead halide perovskites: Phase transformations, hybrid structures, and applications. *J Solid State*
24 *Chem* **2019**, 271, 361-377.
- 25 436. Udayabhaskararao, T.; Houben, L.; Cohen, H.; Menahem, M.; Pinkas, I.; Avram, L.;
26 Wolf, T.; Teitelboim, A.; Leskes, M.; Yaffe, O.; Oron, D.; Kazes, M., A Mechanistic Study of
27 Phase Transformation in Perovskite Nanocrystals Driven by Ligand Passivation. *Chem. Mater.*
28 **2018**, 30 (1), 84-93.
- 29 437. Yang, H. Z.; Zhang, Y. H.; Pan, J.; Yin, J.; Bakr, O. M.; Mohammed, O. F., Room-
30 Temperature Engineering of All-Inorganic Perovskite Nanocrystals with Different
31 Dimensionalities. *Chem. Mater.* **2017**, 29 (21), 8978-8982.
- 32 438. Zhang, Y.; Sinatra, L.; Alarousu, E.; Yin, J.; El-Zohry, A. M.; Bakr, O. M.; Mohammed,
33 O. F., Ligand-Free Nanocrystals of Highly Emissive Cs₄PbBr₆ Perovskite. *J. Phys. Chem. C*
34 **2018**, 122 (11), 6493-6498.
- 35 439. Hui, J.; Jiang, Y. N.; Gokcinar, O. O.; Tang, J. B.; Yu, Q. Y.; Zhang, M.; Yu, K.,
36 Unveiling the Two-Step Formation Pathway of Cs₄PbBr₆ Nanocrystals. *Chem. Mater.* **2020**, 32
37 (11), 4574-4583.
- 38 440. Jia, C.; Li, H.; Meng, X.; Li, H., CsPbX₃/Cs₄PbX₆ core/shell perovskite nanocrystals.
39 *Chemical Communications* **2018**, 54, 6300-6303.
- 40 441. Liu, Z. K.; Bekenstein, Y.; Ye, X. C.; Nguyen, S. C.; Swabeck, J.; Zhang, D. D.; Lee, S.
41 T.; Yang, P. D.; Ma, W. L.; Alivisatos, A. P., Ligand Mediated Transformation of Cesium Lead
42 Bromide Perovskite Nanocrystals to Lead Depleted Cs₄PbBr₆ Nanocrystals. *J. Am. Chem. Soc.*
43 **2017**, 139 (15), 5309-5312.

- 1 442. Palazon, F.; Almeida, G.; Akkerman, Q. A.; De Trizio, L.; Dang, Z. Y.; Prato, M.;
2 Manna, L., Changing the Dimensionality of Cesium Lead Bromide Nanocrystals by Reversible
3 Postsynthesis Transformations with Amines. *Chem. Mater.* **2017**, *29* (10), 4167-4171.
- 4 443. Wu, L. Z.; Hu, H. C.; Xu, Y.; Jiang, S.; Chen, M.; Zhong, Q. X.; Yang, D.; Liu, Q. P.;
5 Zhao, Y.; Sun, B. Q.; Zhang, Q.; Yin, Y. D., From Nonluminescent Cs₄PbX₆ (X = Cl, Br, I)
6 Nanocrystals to Highly Luminescent CsPbX₃ Nanocrystals: Water-Triggered Transformation
7 through a CsX-Stripping Mechanism. *Nano Lett.* **2017**, *17* (9), 5799-5804.
- 8 444. Palazon, F.; Urso, C.; De Trizio, L.; Akkerman, Q.; Marras, S.; Locardi, F.; Nelli, I.;
9 Ferretti, M.; Prato, M.; Manna, L., Postsynthesis Transformation of Insulating Cs₄PbBr₆
10 Nanocrystals into Bright Perovskite CsPbBr₃ through Physical and Chemical Extraction of CsBr.
11 *ACS Energy Lett.* **2017**, *2* (10), 2445-2448.
- 12 445. Baranov, D.; Caputo, G.; Goldoni, L.; Dang, Z. Y.; Scarfiello, R. S.; De Trizio, L.;
13 Portone, A.; Fabbri, F.; Camposeo, A.; Pisignano, D.; Manna, L., Transforming colloidal
14 Cs₄PbBr₆ nanocrystals with poly(maleic anhydride-alt-1-octadecene) into stable CsPbBr₃
15 perovskite emitters through intermediate heterostructures. *Chem. Sci.* **2020**, *11* (15), 3986-3995.
- 16 446. Baranov, D.; Caputo, G.; Goldoni, L.; Dang, Z.; Scarfiello, R.; De Trizio, L.; Portone,
17 A.; Fabbri, F.; Camposeo, A.; Pisignano, D.; Manna, L., Transforming colloidal Cs₄PbBr₆
18 nanocrystals with poly(maleic anhydride-alt-1-octadecene) into stable CsPbBr₃ perovskite
19 emitters through intermediate heterostructures. *Chem Sci* **2020**, *11* (15), 3986-3995.
- 20 447. Yin, J.; Zhang, Y. H.; Bruno, A.; Soci, C.; Bakr, O. M.; Bredas, J. L.; Mohammed, O. F.,
21 Intrinsic Lead Ion Emissions in Zero-Dimensional Cs₄PbBr₆ Nanocrystals. *ACS Energy Lett.*
22 **2017**, *2* (12), 2805-2811.
- 23 448. Yin, J.; Maity, P.; De Bastiani, M.; Dursun, I.; Bakr, O. M.; Bredas, J. L.; Mohammed,
24 O. F., Molecular behavior of zero-dimensional perovskites. *Sci. Adv.* **2017**, *3* (12), e1701793.
- 25 449. Arunkumar, P.; Cho, H. B.; Gil, K. H.; Unithrattil, S.; Kim, Y. H.; Im, W. B. B., Probing
26 molecule-like isolated octahedra via-phase stabilization of zero-dimensional cesium lead halide
27 nanocrystals. *Nat. Commun.* **2018**, *9*, 4691.
- 28 450. Zou, S. H.; Liu, C. P.; Li, R. F.; Jiang, F. L.; Chen, X. Y.; Liu, Y. S.; Hong, M. C., From
29 Nonluminescent to Blue-Emitting Cs₄PbBr₆ Nanocrystals: Tailoring the Insulator Bandgap of
30 0D Perovskite through Sn Cation Doping. *Adv. Mater.* **2019**, *31* (24), 1900606.
- 31 451. Quan, L. N.; Quintero-Bermudez, R.; Voznyy, O.; Walters, G.; Jain, A.; Fan, J. Z.;
32 Zheng, X. L.; Yang, Z. Y.; Sargent, E. H., Highly Emissive Green Perovskite Nanocrystals in a
33 Solid State Crystalline Matrix. *Adv. Mater.* **2017**, *29* (21), 1605945.
- 34 452. Qin, Z. J.; Dai, S. Y.; Hadjiev, V. G.; Wang, C.; Xie, L. X.; Ni, Y. Z.; Wu, C. Z.; Yang,
35 G.; Chen, S.; Deng, L. Z.; Yu, Q. K.; Feng, G. Y.; Wang, Z. M. M.; Bao, J. M., Revealing the
36 Origin of Luminescence Center in 0D Cs₄PbBr₆ Perovskite. *Chem. Mater.* **2019**, *31* (21), 9098-
37 9104.
- 38 453. Riesen, N.; Lockrey, M.; Badek, K.; Riesen, H., On the origins of the green
39 luminescence in the "zero-dimensional perovskite" Cs₄PbBr₆: conclusive results from
40 cathodoluminescence imaging. *Nanoscale* **2019**, *11* (9), 3925-3932.
- 41 454. Yin, J.; Yang, H.; Song, K.; El-Zohry, A. M.; Han, Y.; Bakr, O. M.; Bredas, J. L.;
42 Mohammed, O. F., Point Defects and Green Emission in Zero-Dimensional Perovskites. *J. Phys.*
43 *Chem. Lett.* **2018**, *9* (18), 5490-5495.

- 1 455. Cha, J. H.; Lee, H. J.; Kim, S. H.; Ko, K. C.; Suh, B. J.; Han, O. H.; Jung, D. Y.,
2 Superparamagnetism of Green Emissive Cs₄PbBr₆ Zero-Dimensional Perovskite Crystals. *Acs*
3 *Energy Lett* **2020**, *5* (7), 2208-2216.
- 4 456. Jung, Y. K.; Calbo, J.; Park, J. S.; Whalley, L. D.; Kim, S.; Walsh, A., Intrinsic doping
5 limit and defect-assisted luminescence in Cs₄PbBr₆. *J. Mater. Chem. A* **2019**, *7* (35), 20254-
6 20261.
- 7 457. Ray, A.; Maggioni, D.; Baranov, D.; Dang, Z. Y.; Prato, M.; Akkerman, Q. A.; Goldoni,
8 L.; Caneva, E.; Manna, L.; Abdelhady, A. L., Green-Emitting Powders of Zero-Dimensional
9 Cs₄PbBr₆: Delineating the Intricacies of the Synthesis and the Origin of Photoluminescence.
10 *Chem. Mater.* **2019**, *31* (18), 7761-7769.
- 11 458. Bao, Z.; Wang, H. C.; Jiang, Z. F.; Chung, R. J.; Liu, R. S., Continuous Synthesis of
12 Highly Stable Cs₄PbBr₆ Perovskite Microcrystals by a Microfluidic System and Their
13 Application in White-Light-Emitting Diodes. *Inorg Chem* **2018**, *57* (21), 13071-13074.
- 14 459. Sun, X.; Gao, Z.; Liu, Y.; Wang, Z.; Wang, X.; Zhang, W.; Xu, B.; Meng, X., Lasing
15 from zero-dimensional perovskite and optical imaging applications. *ACS Photonics* **2019**, *6* (12),
16 3290-3297.
- 17 460. Zhao, H. G.; Sun, R. J.; Wang, Z. F.; Fu, K. F.; Hu, X.; Zhang, Y. H., Zero-Dimensional
18 Perovskite Nanocrystals for Efficient Luminescent Solar Concentrators. *Adv. Funct. Mater.*
19 **2019**, *29* (30), 1902262.
- 20 461. Seth, S.; Samanta, A., Photoluminescence of Zero-Dimensional Perovskites and
21 Perovskite-Related Materials. *J. Phys. Chem. Lett.* **2018**, *9* (1), 176-183.
- 22 462. Wu, L.; Hu, H.; Xu, Y.; Jiang, S.; Chen, M.; Zhong, Q.; Yang, D.; Liu, Q.; Zhao, Y.;
23 Sun, B., From Nonluminescent Cs₄PbX₆ (X= Cl, Br, I) Nanocrystals to Highly Luminescent
24 CsPbX₃ Nanocrystals: Water-Triggered Transformation through a CsX-Stripping Mechanism.
25 *Nano Lett.* **2017**, *17* (9), 5799-5804.
- 26 463. Pan, A.; Jurow, M. J.; Qiu, F.; Yang, J.; Ren, B.; Urban, J. J.; He, L.; Liu, Y., Nanorod
27 Suprastructures from a Ternary Graphene Oxide–Polymer–CsPbX₃ Perovskite Nanocrystal
28 Composite That Display High Environmental Stability. *Nano Lett.* **2017**, *17* (11), 6759-6765.
- 29 464. Zhang, H.; Wang, X.; Liao, Q.; Xu, Z.; Li, H.; Zheng, L.; Fu, H., Embedding Perovskite
30 Nanocrystals into a Polymer Matrix for Tunable Luminescence Probes in Cell Imaging. *Adv.*
31 *Funct. Mater.* **2017**, *27* (7), 1604382.
- 32 465. Yoon, H. C.; Lee, H.; Kang, H.; Oh, J. H.; Do, Y. R., Highly efficient wide-color-gamut
33 QD-emissive LCDs using red and green perovskite core/shell QDs. *J. Mater. Chem. C* **2018**, *6*
34 (47), 13023-13033.
- 35 466. Wang, H.-C.; Lin, S.-Y.; Tang, A.-C.; Singh, B. P.; Tong, H.-C.; Chen, C.-Y.; Lee, Y.-
36 C.; Tsai, T.-L.; Liu, R.-S., Mesoporous Silica Particles Integrated with All-Inorganic CsPbBr₃
37 Perovskite Quantum-Dot Nanocomposites (MP-PQDs) with High Stability and Wide Color
38 Gamut Used for Backlight Display. *Angew. Chem. Int. Ed.* **2016**, *55* (28), 7924-7929.
- 39 467. Sun, C.; Zhang, Y.; Ruan, C.; Yin, C.; Wang, X.; Wang, Y.; Yu, W. W., Efficient and
40 stable white LEDs with silica - coated inorganic perovskite quantum dots. *Adv. Mater.* **2016**, *28*
41 (45), 10088-10094.
- 42 468. Li, Z.; Kong, L.; Huang, S.; Li, L., Highly Luminescent and Ultrastable CsPbBr₃
43 Perovskite Quantum Dots Incorporated into a Silica/Alumina Monolith. *Angew. Chem. Int. Ed.*
44 **2017**, *56* (28), 8134-8138.

- 1 469. Koscher, B. A.; Swabeck, J. K.; Bronstein, N. D.; Alivisatos, A. P., Essentially trap-free
2 CsPbBr₃ colloidal nanocrystals by postsynthetic thiocyanate surface treatment. *J Am Chem Soc*
3 **2017**, *139* (19), 6566-6569.
- 4 470. Xu, K.; Lin, C. C.; Xie, X.; Meijerink, A., Efficient and Stable Luminescence from
5 Mn²⁺ in Core and Core-Isocrystalline Shell CsPbCl₃ Perovskite Nanocrystals. *Chem. Mater.*
6 **2017**, *29* (10), 4265-4272.
- 7 471. Wang, S.; Bi, C.; Yuan, J.; Zhang, L.; Tian, J., Original Core-Shell Structure of Cubic
8 CsPbBr₃@Amorphous CsPbBr_x Perovskite Quantum Dots with a High Blue Photoluminescence
9 Quantum Yield of over 80%. *ACS Energy Letters* **2018**, *3* (1), 245-251.
- 10 472. Moot, T.; Dikova, D. R.; Hazarika, A.; Schloemer, T. H.; Habisreutinger, S. N.; Leick,
11 N.; Dunfield, S. P.; Rosales, B. A.; Harvey, S. P.; Pfeilsticker, J. R.; Teeter, G.; Wheeler, L. M.;
12 Larson, B. W.; Luther, J. M., Beyond Strain: Controlling the Surface Chemistry of CsPbI₃
13 Nanocrystal Films for Improved Stability against Ambient Reactive Oxygen Species. *Chem.*
14 *Mater.* **2020**, *32* (18), 7850-7860.
- 15 473. Xuan, T.; Lou, S.; Huang, J.; Cao, L.; Yang, X.; Li, H.; Wang, J., Monodisperse and
16 brightly luminescent CsPbBr₃/Cs₄PbBr₆ perovskite composite nanocrystals. *Nanoscale* **2018**,
17 *10* (21), 9840-9844.
- 18 474. Xu, J.; Huang, W.; Li, P.; Onken, D. R.; Dun, C.; Guo, Y.; Ucer, K. B.; Lu, C.; Wang,
19 H.; Geyer, S. M., Imbedded Nanocrystals of CsPbBr₃ in Cs₄PbBr₆: Kinetics, Enhanced
20 Oscillator Strength, and Application in Light - Emitting Diodes. *Adv. Mater.* **2017**, *29* (43),
21 1703703.
- 22 475. Chen, X.; Zhang, F.; Ge, Y.; Shi, L.; Huang, S.; Tang, J.; Lv, Z.; Zhang, L.; Zou, B.;
23 Zhong, H., Centimeter - Sized Cs₄PbBr₆ Crystals with Embedded CsPbBr₃ Nanocrystals
24 Showing Superior Photoluminescence: Nonstoichiometry Induced Transformation and Light -
25 Emitting Applications. *Adv. Funct. Mater.* **2018**, *28* (16), 1706567.
- 26 476. Quan, L. N.; Quintero-Bermudez, R.; Voznyy, O.; Walters, G.; Jain, A.; Fan, J. Z.;
27 Zheng, X.; Yang, Z.; Sargent, E. H., Highly Emissive Green Perovskite Nanocrystals in a Solid
28 State Crystalline Matrix. *Adv. Mater.* **2017**, *29* (21), 1605945.
- 29 477. Li, Z. J.; Hofman, E.; Li, J.; Davis, A. H.; Tung, C. H.; Wu, L. Z.; Zheng, W.,
30 Photoelectrochemically Active and Environmentally Stable CsPbBr₃/TiO₂ Core/Shell
31 Nanocrystals. *Adv. Funct. Mater.* **2018**, *28* (1), 1704288.
- 32 478. Selvan, S. T.; Tan, T. T.; Ying, J. Y., Robust, Non-Cytotoxic, Silica-Coated CdSe
33 Quantum Dots with Efficient Photoluminescence. *Adv. Mater.* **2005**, *17* (13), 1620-1625.
- 34 479. Zhang, T.; Stilwell, J. L.; Gerion, D.; Ding, L.; Elboudwarej, O.; Cooke, P. A.; Gray, J.
35 W.; Alivisatos, A. P.; Chen, F. F., Cellular effect of high doses of silica-coated quantum dot
36 profiled with high throughput gene expression analysis and high content cellomics
37 measurements. *Nano Lett.* **2006**, *6* (4), 800-808.
- 38 480. Huang, S.; Li, Z.; Kong, L.; Zhu, N.; Shan, A.; Li, L., Enhancing the Stability of
39 CH₃NH₃PbBr₃ Quantum Dots by Embedding in Silica Spheres Derived from Tetramethyl
40 Orthosilicate in "Waterless" Toluene. *J. Am. Chem. Soc.* **2016**, *138* (18), 5749-5752.
- 41 481. Zhang, X.; Bai, X.; Wu, H.; Zhang, X.; Sun, C.; Zhang, Y.; Zhang, W.; Zheng, W.; Yu,
42 W. W.; Rogach, A. L., Water-Assisted Size and Shape Control of CsPbBr₃ Perovskite
43 Nanocrystals. *Angew. Chem. Int. Ed.* **2018**, *57* (13), 3337-3342.

- 1 482. Shao, G.; Zhao, Y.; Yu, Y.; Yang, H.; Liu, X.; Zhang, Y.; Xiang, W.; Liang, X., Bright
2 emission and high photoluminescence CsPb₂Br₅ NCs encapsulated in mesoporous silica with
3 ultrahigh stability and excellent optical properties for white light-emitting diodes. *J. Mater.*
4 *Chem. C* **2019**, 7 (43), 13585-13593.
- 5 483. You, X.; Wu, J.; Chi, Y., Superhydrophobic Silica Aerogels Encapsulated Fluorescent
6 Perovskite Quantum Dots for Reversible Sensing of SO₂ in a 3D-Printed Gas Cell. *Anal. Chem.*
7 **2019**, 91 (8), 5058-5066.
- 8 484. Huang, H.; Chen, B.; Wang, Z.; Hung, T. F.; Susha, A. S.; Zhong, H.; Rogach, A. L.,
9 Water Resistant CsPbX₃ Nanocrystals Coated with Polyhedral Oligomeric Silsesquioxane and
10 Their Use as Solid State Luminophores in All-Perovskite White Light-Emitting Devices. *Chem.*
11 *Sci.* **2016**, 7 (9), 5699-5703.
- 12 485. Zhang, Q.; Wang, B.; Zheng, W.; Kong, L.; Wan, Q.; Zhang, C.; Li, Z.; Cao, X.; Liu,
13 M.; Li, L., Ceramic-like stable CsPbBr₃ nanocrystals encapsulated in silica derived from
14 molecular sieve templates. *Nat. Commun.* **2020**, 11 (1), 1-9.
- 15 486. Ye, Y.; Zhang, W.; Zhao, Z.; Wang, J.; Liu, C.; Deng, Z.; Zhao, X.; Han, J., Highly
16 luminescent cesium lead halide perovskite nanocrystals stabilized in glasses for light - emitting
17 applications. *Adv. Opt. Mater.* **2019**, 7 (9), 1801663.
- 18 487. Yuan, S.; Chen, D.; Li, X.; Zhong, J.; Xu, X., In situ crystallization synthesis of
19 CsPbBr₃ perovskite quantum dot-embedded glasses with improved stability for solid-state
20 lighting and random upconverted lasing. *ACS Appl. Mater. Interfaces* **2018**, 10 (22), 18918-
21 18926.
- 22 488. Di, X.; Hu, Z.; Jiang, J.; He, M.; Zhou, L.; Xiang, W.; Liang, X., Use of long-term stable
23 CsPbBr₃ perovskite quantum dots in phospho-silicate glass for highly efficient white LEDs.
24 *Chem. Commun.* **2017**, 53 (80), 11068-11071.
- 25 489. Zhang, H.; Wang, X.; Liao, Q.; Xu, Z.; Li, H.; Zheng, L.; Fu, H., Embedding Perovskite
26 Nanocrystals into a Polymer Matrix for Tunable Luminescence Probes in Cell Imaging. *Adv.*
27 *Mater.* **2017**, 27 (7), 1604382.
- 28 490. Chen, K.; Schunemann, S.; Tuysuz, H., Preparation of Waterproof Organometal Halide
29 Perovskite Photonic Crystal Beads. *Angew. Chem. Int. Ed.* **2017**, 56 (23), 6548-6552.
- 30 491. Long, Z.; Wang, Y.; Fu, Q.; Ouyang, J.; He, L.; Na, N., Accelerated crystallization and
31 encapsulation for the synthesis of water- and oxygen-resistant perovskite nanoparticles in micro-
32 droplets. *Nanoscale* **2019**, 11 (23), 11093-11098.
- 33 492. Shi, J.; Ge, W.; Gao, W.; Xu, M.; Zhu, J.; Li, Y., Enhanced Thermal Stability of Halide
34 Perovskite CsPbX₃ Nanocrystals by a Facile TPU Encapsulation. *Adv. Opt. Mater.* **2019**,
35 1901516.
- 36 493. Raja, S. N.; Bekenstein, Y.; Koc, M. A.; Fischer, S.; Zhang, D.; Lin, L.; Ritchie, R. O.;
37 Yang, P.; Alivisatos, A. P., Encapsulation of Perovskite Nanocrystals into Macroscale Polymer
38 Matrices: Enhanced Stability and Polarization. *ACS Appl. Mater. Interfaces* **2016**, 8 (51), 35523-
39 35533.
- 40 494. Hintermayr, V. A.; Lampe, C.; Low, M.; Roemer, J.; Vanderlinden, W.; Gramlich, M.;
41 Bohm, A. X.; Sattler, C.; Nickel, B.; Lohmuller, T.; Urban, A. S., Polymer Nanoreactors Shield
42 Perovskite Nanocrystals from Degradation. *Nano Lett.* **2019**, 19 (8), 4928-4933.

- 1 495. Yin, B.; Sadtler, B.; Berezin, M. Y.; Thimsen, E., Quantum dots protected from
2 oxidative attack using alumina shells synthesized by atomic layer deposition. *Chem. Commun.*
3 **2016**, 52 (74), 11127-11130.
- 4 496. Liu, Y.; Gibbs, M.; Perkins, C. L.; Tolentino, J.; Zarghami, M. H.; Bustamante, J., Jr.;
5 Law, M., Robust, functional nanocrystal solids by infilling with atomic layer deposition. *Nano*
6 *Lett.* **2011**, 11 (12), 5349-5355.
- 7 497. Pourret, A.; Guyot-Sionnest, P.; Elam, J. W., Atomic Layer Deposition of ZnO in
8 Quantum Dot Thin Films. *Adv. Mater.* **2009**, 21 (2), 232-235.
- 9 498. Loiudice, A.; Saris, S.; Oveisi, E.; Alexander, D. T. L.; Buonsanti, R., CsPbBr₃
10 QD/AlO_x Inorganic Nanocomposites with Exceptional Stability in Water, Light, and Heat.
11 *Angew. Chem. Int. Ed.* **2017**, 56 (36), 10696-10701.
- 12 499. Guo, T.; Bose, R.; Zhou, X.; Gartstein, Y. N.; Yang, H.; Kwon, S.; Kim, M. J.; Lutfullin,
13 M.; Sinatra, L.; Gereige, I.; Al-Saggaf, A.; Bakr, O. M.; Mohammed, O. F.; Malko, A. V.,
14 Delayed Photoluminescence and Modified Blinking Statistics in Alumina-Encapsulated Zero-
15 Dimensional Inorganic Perovskite Nanocrystals. *J. Phys. Chem. Lett.* **2019**, 10 (21), 6780-6787.
- 16 500. Buonsanti, R.; Loiudice, A.; Niemann, V.; Dona, S.; Saris, S., Optimizing the Atomic
17 Layer Deposition of Alumina on Perovskite Nanocrystal Films by Using O₂ as a Molecular
18 Probe. *ChemRxiv* **2019**, 10.26434/chemrxiv.9991919.v1.
- 19 501. Zheng, Z.; Zhuge, F.; Wang, Y.; Zhang, J.; Gan, L.; Zhou, X.; Li, H.; Zhai, T.,
20 Decorating Perovskite Quantum Dots in TiO₂Nanotubes Array for Broadband Response
21 Photodetector. *Adv. Funct. Mater.* **2017**, 27 (43), 1703115.
- 22 502. Wang, B.; Zhang, C.; Zheng, W.; Zhang, Q.; Bao, Z.; Kong, L.; Li, L., Large-Scale
23 Synthesis of Highly Luminescent Perovskite Nanocrystals by Template-Assisted Solid-State
24 Reaction at 800° C. *Chem. Mater.* **2019**, 32 (1), 308-314.
- 25 503. Zhang, D.; Xu, Y.; Liu, Q.; Xia, Z., Encapsulation of CH₃NH₃PbBr₃ Perovskite
26 Quantum Dots in MOF-5 Microcrystals as a Stable Platform for Temperature and Aqueous
27 Heavy Metal Ion Detection. *Inorg Chem* **2018**, 57 (8), 4613-4619.
- 28 504. Ren, J. J.; Li, T. R.; Zhou, X. P.; Dong, X.; Shorokhov, A. V.; Semenov, M. B.;
29 Krevchik, V. D.; Wang, Y. H., Encapsulating all-inorganic perovskite quantum dots into
30 mesoporous metal organic frameworks with significantly enhanced stability for optoelectronic
31 applications. *Chem. Eng. J.* **2019**, 358, 30-39.
- 32 505. Wu, L. Y.; Mu, Y. F.; Guo, X. X.; Zhang, W.; Zhang, Z. M.; Zhang, M.; Lu, T. B.,
33 Encapsulating Perovskite Quantum Dots in Iron-Based Metal-Organic Frameworks (MOFs) for
34 Efficient Photocatalytic CO₂ Reduction. *Angew. Chem. Int. Ed.* **2019**, 58 (28), 9491-9495.
- 35 506. Zhang, C.; Wang, B.; Li, W.; Huang, S.; Kong, L.; Li, Z.; Li, L., Conversion of invisible
36 metal-organic frameworks to luminescent perovskite nanocrystals for confidential information
37 encryption and decryption. *Nat. Commun.* **2017**, 8 (1), 1138.
- 38 507. Zhang, D.; Zhou, W.; Liu, Q.; Xia, Z., CH₃NH₃PbBr₃ Perovskite Nanocrystals
39 Encapsulated in Lanthanide Metal-Organic Frameworks as a Photoluminescence Converter for
40 Anti-Counterfeiting. *ACS Appl. Mater. Interfaces* **2018**, 10 (33), 27875-27884.
- 41 508. Zhang, D.; Zhou, W.; Liu, Q.; Xia, Z., CH₃NH₃PbBr₃ Perovskite Nanocrystals
42 Encapsulated in Lanthanide Metal-Organic Frameworks as a Photoluminescence Converter for
43 Anti-Counterfeiting. *ACS Appl. Mater. Interfaces* **2018**, 10 (33), 27875-27884.

- 1 509. Long, G.; Jiang, C.; Sabatini, R.; Yang, Z.; Wei, M.; Quan, L. N.; Liang, Q.; Rasmita,
2 A.; Askerka, M.; Walters, G., Spin control in reduced-dimensional chiral perovskites. *Nat.*
3 *Photonics* **2018**, *12* (9), 528-533.
- 4 510. Belykh, V. V.; Yakovlev, D. R.; Glazov, M. M.; Grigoryev, P. S.; Hussain, M.; Rautert,
5 J.; Dirin, D. N.; Kovalenko, M. V.; Bayer, M., Coherent spin dynamics of electrons and holes in
6 CsPbBr₃ perovskite crystals. *Nat. Commun.* **2019**, *10* (1), 673.
- 7 511. Müller, M.; Kaiser, M.; Stachowski, G. M.; Resch-Genger, U.; Gaponik, N.;
8 Eychemüller, A., Photoluminescence Quantum Yield and Matrix-Induced Luminescence
9 Enhancement of Colloidal Quantum Dots Embedded in Ionic Crystals. *Chem. Mater.* **2014**, *26*
10 (10), 3231-3237.
- 11 512. Adam, M.; Tietze, R.; Gaponik, N.; Eychemüller, A., QD-Salt Mixed Crystals: the
12 Influence of Salt-Type, Free-Stabilizer, and pH. *Zeitschrift für Physikalische Chemie* **2015**, *229*
13 (1-2), 109-118.
- 14 513. Benad, A.; Guhrenz, C.; Bauer, C.; Eichler, F.; Adam, M.; Ziegler, C.; Gaponik, N.;
15 Eychemüller, A., Cold Flow as Versatile Approach for Stable and Highly Luminescent Quantum
16 Dot-Salt Composites. *ACS Appl. Mater. Interfaces* **2016**, *8* (33), 21570-21575.
- 17 514. Rogach, A. L., *Semiconductor Nanocrystal Quantum Dots: Synthesis, Assembly,*
18 *Spectroscopy and Applications*. Springer, Verlag Wien: 2008.
- 19 515. Fu, J.; Xu, Q.; Han, G.; BoWu; Huan, C. H. A.; Leek, M. L.; Sum, T. C., Hot Carrier
20 Cooling Mechanisms in Halide Perovskites. *Nat. Commun.* **2017**, *8*, 1300.
- 21 516. Akkerman, Q. A.; Abdelhady, A. L.; Manna, L., Zero-Dimensional Cesium Lead
22 Halides: History, Properties, and Challenges. *J. Phys. Chem. Lett.* **2018**, *9* (9), 2326-2337.
- 23 517. Quan, L. N.; Quintero-Bermudez, R.; Voznyy, O.; Walters, G.; Jain, A.; Fan, J. Z.;
24 Zheng, X.; Yang, Z.; Sargent, E. H., Highly Emissive Green Perovskite Nanocrystals in a Solid
25 State Crystalline Matrix. *Adv Mater* **2017**, *29* (21), 1605945.
- 26 518. Wang, Y.; Yu, D.; Wang, Z.; Li, X.; Chen, X.; Nalla, V.; Zeng, H.; Sun, H., Solution-
27 Grown CsPbBr₃/Cs₄PbBr₆ Perovskite Nanocomposites: Toward Temperature-Insensitive
28 Optical Gain. *Small* **2017**, *13* (34).
- 29 519. Cao, F.; Yu, D.; Ma, W.; Xu, X.; Cai, B.; Yang, Y. M.; Liu, S.; He, L.; Ke, Y.; Lan, S.;
30 Choy, K. L.; Zeng, H., Shining Emitter in a Stable Host: Design of Halide Perovskite
31 Scintillators for X-ray Imaging from Commercial Concept. *ACS Nano* **2019**,
32 doi.org/10.1021/acsnano.9b06114.
- 33 520. Hu, H.; Wu, L.; Tan, Y.; Zhong, Q.; Chen, M.; Qiu, Y.; Yang, D.; Sun, B.; Zhang, Q.;
34 Yin, Y., Interfacial Synthesis of Highly Stable CsPbX₃/Oxide Janus Nanoparticles. *J. Am. Chem.*
35 *Soc.* **2018**, *140* (1), 406-412.
- 36 521. Zhong, Q.; Cao, M.; Hu, H.; Yang, D.; Chen, M.; Li, P.; Wu, L.; Zhang, Q., One-Pot
37 Synthesis of Highly Stable CsPbBr₃@SiO₂ Core-Shell Nanoparticles. *ACS Nano* **2018**, *12*,
38 8579-8587.
- 39 522. Tang, X.; Chen, W.; Liu, Z.; Du, J.; Yao, Z.; Huang, Y.; Chen, C.; Yang, Z.; Shi, T.; Hu,
40 W.; Zang, Z.; Chen, Y.; Leng, Y., Ultrathin, Core-Shell Structured SiO₂ Coated Mn²⁺-Doped
41 Perovskite Quantum Dots for Bright White Light-Emitting Diodes. *Small* **2019**, *15* (19),
42 1900484.

- 1 523. Dabbousi, B. O.; Rodriguez-Viejo, J.; Mikulec, F. V.; Heine, J. R.; Mattoussi, H.; Ober,
2 R.; Jensen, K. F.; Bawendi, M. G., (CdSe)ZnS Core-Shell Quantum Dots: Synthesis and
3 Characterization of a Size Series of Highly Luminescent Nanocrystallites. *J. Phys. Chem. B*
4 **1997**, *101* (46), 9463-9475.
- 5 524. Luo, J.; Wang, X.; Li, S.; Liu, J.; Guo, Y.; Niu, G.; Yao, L.; Fu, Y.; Gao, L.; Dong, Q.;
6 Zhao, C.; Leng, M.; Ma, F.; Liang, W.; Wang, L.; Jin, S.; Han, J.; Zhang, L.; Etheridge, J.;
7 Wang, J.; Yan, Y.; Sargent, E. H.; Tang, J., Efficient and stable emission of warm-white light
8 from lead-free halide double perovskites. *Nature* **2018**, *563* (7732), 541-545.
- 9 525. Qiao, B.; Song, P.; Cao, J.; Zhao, S.; Shen, Z.; Di, G.; Liang, Z.; Xu, Z.; Song, D.; Xu,
10 X., Water-resistant, monodispersed and stably luminescent CsPbBr₃/CsPb₂Br₅ core-shell-like
11 structure lead halide perovskite nanocrystals. *Nanotechnology* **2017**, *28* (44), 445602.
- 12 526. Tang, X.; Yang, J.; Li, S.; Chen, W.; Hu, Z.; Qiu, J., CsPbBr₃/CdS Core/Shell Structure
13 Quantum Dots for Inverted Light-Emitting Diodes Application. *Front. Chem.* **2019**, *7* (499).
- 14 527. Tang, X.; Yang, J.; Li, S.; Chen, W.; Hu, Z.; Qiu, J., CsPbBr₃/CdS Core/Shell Structure
15 Quantum Dots for Inverted Light-Emitting Diodes Application. *Front. Chem.* **2019**, *7*, 499.
- 16 528. Eorpach, A. t., Official Journal of the European Union, L 281. **2017**.
- 17 529. Swarnkar, A.; Ravi, V. K.; Nag, A., Beyond Colloidal Cesium Lead Halide Perovskite
18 Nanocrystals: Analogous Metal Halides and Doping. *ACS Energy Letters* **2017**, *2* (5), 1089-
19 1098.
- 20 530. Sun, J.; Yang, J.; Lee, J. I.; Cho, J. H.; Kang, M. S., Lead-Free Perovskite Nanocrystals
21 for Light-Emitting Devices. *J. Phys. Chem. Lett.* **2018**, *9* (7), 1573-1583.
- 22 531. Khalfin, S.; Bekenstein, Y., Advances in lead-free double perovskite nanocrystals,
23 engineering band-gaps and enhancing stability through composition tunability. *Nanoscale* **2019**,
24 *11* (18), 8665-8679.
- 25 532. Fan, Q.; Biesold-McGee, G. V.; Ma, J.; Xu, Q.; Pan, S.; Peng, J.; Lin, Z., Lead-Free
26 Halide Perovskite Nanocrystals: Crystal Structures, Synthesis, Stabilities, and Optical Properties.
27 *Angew. Chem. Int. Ed.* **2020**, *59* (3), 1030-1046.
- 28 533. Zhu, D.; Zito, J.; Pinchetti, V.; Dang, Z.; Olivati, A.; Pasquale, L.; Tang, A.; Zaffalon,
29 M. L.; Meinardi, F.; Infante, I.; De Trizio, L.; Manna, L.; Brovelli, S., Compositional Tuning of
30 Carrier Dynamics in Cs₂Na_{1-x}Ag_xBiCl₆ Double-Perovskite Nanocrystals. *ACS Energy Letters*
31 **2020**, *5* (6), 1840-1847.
- 32 534. Xia, Z.; Liu, Y.; Nag, A.; Manna, L., Lead-Free Double Perovskite Cs₂AgInCl₆. *Angew.*
33 *Chem. Int. Ed. n/a* (n/a).
- 34 535. Zhang, B.; Wang, M.; Ghini, M.; Melcherts, A. E. M.; Zito, J.; Goldoni, L.; Infante, I.;
35 Guizzardi, M.; Scotognella, F.; Kriegel, I.; De Trizio, L.; Manna, L., Colloidal Bi-Doped
36 Cs₂Ag_{1-x}Na_xInCl₆ Nanocrystals: Undercoordinated Surface Cl Ions Limit their Light Emission
37 Efficiency. *ACS Materials Letters* **2020**, 1442-1449.
- 38 536. Zhu, P.; Chen, C.; Gu, S.; Lin, R.; Zhu, J., CsSnI₃ Solar Cells via an Evaporation-
39 Assisted Solution Method. *Solar RRL* **2018**, *2* (4), 1700224.
- 40 537. Chen, M.; Ju, M.-G.; Garces, H. F.; Carl, A. D.; Ono, L. K.; Hawash, Z.; Zhang, Y.;
41 Shen, T.; Qi, Y.; Grimm, R. L.; Pacifici, D.; Zeng, X. C.; Zhou, Y.; Padture, N. P., Highly stable
42 and efficient all-inorganic lead-free perovskite solar cells with native-oxide passivation. *Nat.*
43 *Commun.* **2019**, *10* (1), 16.

- 1 538. Sabba, D.; Mulmudi, H. K.; Prabhakar, R. R.; Krishnamoorthy, T.; Baikie, T.; Boix, P.
2 P.; Mhaisalkar, S.; Mathews, N., Impact of Anionic Br⁻ Substitution on Open Circuit Voltage in
3 Lead Free Perovskite (CsSnI_{3-x}Br_x) Solar Cells. *J. Phys. Chem. C* **2015**, *119* (4), 1763-1767.
- 4 539. Ke, W.; Stoumpos, C. C.; Zhu, M.; Mao, L.; Spanopoulos, I.; Liu, J.; Kontsevoi, O. Y.;
5 Chen, M.; Sarma, D.; Zhang, Y.; Wasielewski, M. R.; Kanatzidis, M. G., Enhanced photovoltaic
6 performance and stability with a new type of hollow 3D perovskite $\{en\}FASn_{3}$.
7 *Sci. Adv.* **2017**, *3* (8), e1701293.
- 8 540. Krishnamoorthy, T.; Ding, H.; Yan, C.; Leong, W. L.; Baikie, T.; Zhang, Z.; Sherburne,
9 M.; Li, S.; Asta, M.; Mathews, N.; Mhaisalkar, S. G., Lead-free germanium iodide perovskite
10 materials for photovoltaic applications. *J. Mater. Chem. A* **2015**, *3* (47), 23829-23832.
- 11 541. Ju, M.-G.; Dai, J.; Ma, L.; Zeng, X. C., Lead-Free Mixed Tin and Germanium
12 Perovskites for Photovoltaic Application. *J. Am. Chem. Soc.* **2017**, *139* (23), 8038-8043.
- 13 542. Jellicoe, T. C.; Richter, J. M.; Glass, H. F. J.; Tabachnyk, M.; Brady, R.; Dutton, S. E.;
14 Rao, A.; Friend, R. H.; Credgington, D.; Greenham, N. C.; Böhm, M. L., Synthesis and Optical
15 Properties of Lead-Free Cesium Tin Halide Perovskite Nanocrystals. *J. Am. Chem. Soc.* **2016**,
16 *138* (9), 2941-2944.
- 17 543. Hu, M.; Ge, C.; Yu, J.; Feng, J., Mechanical and Optical Properties of Cs₄BX₆ (B = Pb,
18 Sn; X = Cl, Br, I) Zero-Dimension Perovskites. *J. Phys. Chem. C* **2017**, *121* (48), 27053-27058.
- 19 544. Wong, A. B.; Bekenstein, Y.; Kang, J.; Kley, C. S.; Kim, D.; Gibson, N. A.; Zhang, D.;
20 Yu, Y.; Leone, S. R.; Wang, L.-W.; Alivisatos, A. P.; Yang, P., Strongly Quantum Confined
21 Colloidal Cesium Tin Iodide Perovskite Nanoplates: Lessons for Reducing Defect Density and
22 Improving Stability. *Nano Lett.* **2018**, *18* (3), 2060-2066.
- 23 545. Chen, L.-J.; Lee, C.-R.; Chuang, Y.-J.; Wu, Z.-H.; Chen, C., Synthesis and Optical
24 Properties of Lead-Free Cesium Tin Halide Perovskite Quantum Rods with High-Performance
25 Solar Cell Application. *J. Phys. Chem. Lett.* **2016**, *7* (24), 5028-5035.
- 26 546. Hao, F.; Stoumpos, C. C.; Cao, D. H.; Chang, R. P. H.; Kanatzidis, M. G., Lead-free
27 solid-state organic-inorganic halide perovskite solar cells. *Nat. Photonics* **2014**, *8* (6), 489-494.
- 28 547. Huang, L.-y.; Lambrecht, W. R. L., Electronic band structure, phonons, and exciton
29 binding energies of halide perovskites CsSnCl₃, CsSnBr₃, and CsSnI₃.
30 *Physical Review B* **2013**, *88* (16), 165203.
- 31 548. Yan, J.; Qiu, W.; Wu, G.; Heremans, P.; Chen, H., Recent progress in 2D/quasi-2D
32 layered metal halide perovskites for solar cells. *J. Mater. Chem. A* **2018**, *6* (24), 11063-11077.
- 33 549. Chung, I.; Song, J.-H.; Im, J.; Androulakis, J.; Malliakas, C. D.; Li, H.; Freeman, A. J.;
34 Kenney, J. T.; Kanatzidis, M. G., CsSnI₃: Semiconductor or Metal? High Electrical Conductivity
35 and Strong Near-Infrared Photoluminescence from a Single Material. High Hole Mobility and
36 Phase-Transitions. *J. Am. Chem. Soc.* **2012**, *134* (20), 8579-8587.
- 37 550. Xing, G.; Kumar, M. H.; Chong, W. K.; Liu, X.; Cai, Y.; Ding, H.; Asta, M.; Grätzel,
38 M.; Mhaisalkar, S.; Mathews, N.; Sum, T. C., Solution-Processed Tin-Based Perovskite for
39 Near-Infrared Lasing. *Adv. Mater.* **2016**, *28* (37), 8191-8196.
- 40 551. Wang, A.; Yan, X.; Zhang, M.; Sun, S.; Yang, M.; Shen, W.; Pan, X.; Wang, P.; Deng,
41 Z., Controlled Synthesis of Lead-Free and Stable Perovskite Derivative Cs₂SnI₆ Nanocrystals
42 via a Facile Hot-Injection Process. *Chem. Mater.* **2016**, *28* (22), 8132-8140.

- 1 552. Tan, L.; Wang, W.; Li, Q.; Luo, Z.; Zou, C.; Tang, M.; Zhang, L.; He, J.; Quan, Z.,
2 Colloidal syntheses of zero-dimensional Cs₄SnX₆ (X = Br, I) nanocrystals with high emission
3 efficiencies. *Chem. Commun.* **2020**, *56* (3), 387-390.
- 4 553. Chiara, R.; Ciftci, Y. O.; Queloz, V. I. E.; Nazeeruddin, M. K.; Grancini, G.; Malavasi,
5 L., Green-Emitting Lead-Free Cs₄SnBr₆ Zero-Dimensional Perovskite Nanocrystals with
6 Improved Air Stability. *J. Phys. Chem. Lett.* **2020**, *11* (3), 618-623.
- 7 554. Wang, A.; Guo, Y.; Muhammad, F.; Deng, Z., Controlled Synthesis of Lead-Free
8 Cesium Tin Halide Perovskite Cubic Nanocages with High Stability. *Chem. Mater.* **2017**, *29*
9 (15), 6493-6501.
- 10 555. Wang, C.; Zhang, Y.; Wang, A.; Wang, Q.; Tang, H.; Shen, W.; Li, Z.; Deng, Z.,
11 Controlled Synthesis of Composition Tunable Formamidinium Cesium Double Cation Lead
12 Halide Perovskite Nanowires and Nanosheets with Improved Stability. *Chem. Mater.* **2017**, *29*
13 (5), 2157-2166.
- 14 556. Liu, F.; Zhang, Y.; Ding, C.; Kawabata, K.; Yoshihara, Y.; Toyoda, T.; Hayase, S.;
15 Minemoto, T.; Wang, R.; Shen, Q., Trioctylphosphine Oxide Acts as Alkahest for SnX₂/PbX₂:
16 A General Synthetic Route to Perovskite ASn_xPb_{1-x}X₃ (A = Cs, FA, MA; X = Cl, Br, I)
17 Quantum Dots. *Chem. Mater.* **2020**, *32* (3), 1089-1100.
- 18 557. Vitoreti, A. B. F.; Agouram, S.; Solis de la Fuente, M.; Muñoz-Sanjosé, V.; Schiavon,
19 M. A.; Mora-Seró, I., Study of the Partial Substitution of Pb by Sn in Cs–Pb–Sn–Br Nanocrystals
20 Owing to Obtaining Stable Nanoparticles with Excellent Optical Properties. *J. Phys. Chem. C*
21 **2018**, *122* (25), 14222-14231.
- 22 558. Liu, F.; Ding, C.; Zhang, Y.; Ripolles, T. S.; Kamisaka, T.; Toyoda, T.; Hayase, S.;
23 Minemoto, T.; Yoshino, K.; Dai, S.; Yanagida, M.; Noguchi, H.; Shen, Q., Colloidal Synthesis
24 of Air-Stable Alloyed CsSn_{1-x}Pb_xI₃ Perovskite Nanocrystals for Use in Solar Cells. *J. Am.*
25 *Chem. Soc.* **2017**, *139* (46), 16708-16719.
- 26 559. Deng, J.; Wang, H.; Xun, J.; Wang, J.; Yang, X.; Shen, W.; Li, M.; He, R., Room-
27 temperature synthesis of excellent-performance CsPb_{1-x}Sn_xBr₃ perovskite quantum dots and
28 application in light emitting diodes. *Materials & Design* **2020**, *185*, 108246.
- 29 560. Palmstrom, A. F.; Eperon, G. E.; Leijtens, T.; Prasanna, R.; Habisreutinger, S. N.;
30 Nemeth, W.; Gaubing, E. A.; Dunfield, S. P.; Reese, M.; Nanayakkara, S.; Moot, T.; Werner, J.;
31 Liu, J.; To, B.; Christensen, S. T.; McGehee, M. D.; van Hest, M. F. A. M.; Luther, J. M.; Berry,
32 J. J.; Moore, D. T., Enabling Flexible All-Perovskite Tandem Solar Cells. *Joule* **2019**, *3* (9),
33 2193-2204.
- 34 561. Selvarajan, P.; Kundu, K.; Sathish, C. I.; Umapathy, S.; Vinu, A., Enriched
35 Photophysical Properties and Thermal Stability of Tin(II) Substituted Lead-Based Perovskite
36 Nanocrystals with Mixed Organic–Inorganic Cations. *J. Phys. Chem. C* **2020**, *124* (17), 9611-
37 9621.
- 38 562. Dolzhenkov, D. S.; Wang, C.; Xu, Y.; Kanatzidis, M. G.; Weiss, E. A., Ligand-Free,
39 Quantum-Confined Cs₂SnI₆ Perovskite Nanocrystals. *Chem. Mater.* **2017**, *29* (18), 7901-7907.
- 40 563. Ghosh, S.; Paul, S.; De, S. K., Control Synthesis of Air-Stable Morphology Tunable Pb-
41 Free Cs₂SnI₆ Perovskite Nanoparticles and Their Photodetection Properties. *Part. Part. Syst.*
42 *Char.* **2018**, *35* (9), 1800199.
- 43 564. Wu, X.; Song, W.; Li, Q.; Zhao, X.; He, D.; Quan, Z., Synthesis of Lead-free CsGeI₃
44 Perovskite Colloidal Nanocrystals and Electron Beam-induced Transformations. *Chem. Asian J.*
45 **2018**, *13* (13), 1654-1659.

- 1 565. Men, L.; Rosales, B. A.; Gentry, N. E.; Cady, S. D.; Vela, J., Lead-Free Semiconductors:
2 Soft Chemistry, Dimensionality Control, and Manganese-Doping of Germanium Halide
3 Perovskites. *ChemNanoMat* **2019**, *5* (3), 334-339.
- 4 566. Ma, Z.; Shi, Z.; Yang, D.; Zhang, F.; Li, S.; Wang, L.; Wu, D.; Zhang, Y.; Na, G.;
5 Zhang, L.; Li, X.; Zhang, Y.; Shan, C., Electrically-Driven Violet Light-Emitting Devices Based
6 on Highly Stable Lead-Free Perovskite Cs₃Sb₂Br₉ Quantum Dots. *ACS Energy Lett.* **2020**, *5* (2),
7 385-394.
- 8 567. Moon, B. J.; Kim, S. J.; Lee, S.; Lee, A.; Lee, H.; Lee, D. S.; Kim, T.-W.; Lee, S.-K.;
9 Bae, S.; Lee, S. H., Rare-Earth-Element-Ytterbium-Substituted Lead-Free Inorganic Perovskite
10 Nanocrystals for Optoelectronic Applications. *Adv. Mater.* **2019**, *31* (33), 1901716.
- 11 568. He, T.; Li, J.; Li, X.; Ren, C.; Luo, Y.; Zhao, F.; Chen, R.; Lin, X.; Zhang, J.,
12 Spectroscopic studies of chiral perovskite nanocrystals. *Appl. Phys. Lett.* **2017**, *111* (15), 151102.
- 13 569. McCall, K. M.; Stoumpos, C. C.; Kostina, S. S.; Kanatzidis, M. G.; Wessels, B. W.,
14 Strong Electron-Phonon Coupling and Self-Trapped Excitons in the Defect Halide Perovskites
15 A₃M₂I₉ (A = Cs, Rb; M = Bi, Sb). *Chem. Mater.* **2017**, *29* (9), 4129-4145.
- 16 570. Zuo, C.; Ding, L., Lead-free Perovskite Materials (NH₄)₃Sb₂I_xBr_{9-x}. *Angew. Chem. Int.*
17 *Ed.* **2017**, *56* (23), 6528-6532.
- 18 571. Yang, B.; Chen, J.; Hong, F.; Mao, X.; Zheng, K.; Yang, S.; Li, Y.; Pullerits, T.; Deng,
19 W.; Han, K., Lead-Free, Air-Stable All-Inorganic Cesium Bismuth Halide Perovskite
20 Nanocrystals. *Angew. Chem. Int. Ed.* **2017**, *56* (41), 12471-12475.
- 21 572. Pal, J.; Manna, S.; Mondal, A.; Das, S.; Adarsh, K. V.; Nag, A., Colloidal Synthesis and
22 Photophysics of M₃Sb₂I₉ (M=Cs and Rb) Nanocrystals: Lead-Free Perovskites. *Angew. Chem.*
23 *Int. Ed.* **2017**, *56* (45), 14187-14191.
- 24 573. Pal, J.; Bhunia, A.; Chakraborty, S.; Manna, S.; Das, S.; Dewan, A.; Datta, S.; Nag, A.,
25 Synthesis and Optical Properties of Colloidal M₃Bi₂I₉ (M = Cs, Rb) Perovskite Nanocrystals. *J.*
26 *Phys. Chem. C* **2018**, *122* (19), 10643-10649.
- 27 574. Cai, T.; Shi, W.; Hwang, S.; Kobbekaduwa, K.; Nagaoka, Y.; Yang, H.; Hills-Kimball,
28 K.; Zhu, H.; Wang, J.; Wang, Z.; Liu, Y.; Su, D.; Gao, J.; Chen, O., Lead-Free Cs₄CuSb₂Cl₁₂
29 Layered Double Perovskite Nanocrystals. *J. Am. Chem. Soc.* **2020**.
- 30 575. Johnston, A.; Dinic, F.; Todorović, P.; Chen, B.; Sagar, L. K.; Saidaminov, M. I.;
31 Hoogland, S.; Voznyy, O.; Sargent, E. H., Narrow Emission from Rb₃Sb₂I₉ Nanoparticles. *Adv.*
32 *Opt. Mater.* **2020**, *8* (1), 1901606.
- 33 576. Pradhan, B.; Kumar, G. S.; Sain, S.; Dalui, A.; Ghorai, U. K.; Pradhan, S. K.; Acharya,
34 S., Size Tunable Cesium Antimony Chloride Perovskite Nanowires and Nanorods. *Chem. Mater.*
35 **2018**, *30* (6), 2135-2142.
- 36 577. Liu, F.; Ding, C.; Zhang, Y.; Ripolles, T. S.; Kamisaka, T.; Toyoda, T.; Hayase, S.;
37 Minemoto, T.; Yoshino, K.; Dai, S., Colloidal Synthesis of Air-Stable Alloyed CsSn_{1-x}Pb_xI₃
38 Perovskite Nanocrystals for Use in Solar Cells. *Journal of the American Chemical Society* **2017**,
39 *139* (46), 16708-16719.
- 40 578. Leng, M.; Yang, Y.; Zeng, K.; Chen, Z.; Tan, Z.; Li, S.; Li, J.; Xu, B.; Li, D.;
41 Hautzinger, M. P.; Fu, Y.; Zhai, T.; Xu, L.; Niu, G.; Jin, S.; Tang, J., All-Inorganic Bismuth-
42 Based Perovskite Quantum Dots with Bright Blue Photoluminescence and Excellent Stability.
43 *Adv. Funct. Mater.* **2018**, *28* (1), 1704446.

- 1 579. Paternò, G. M.; Mishra, N.; Barker, A. J.; Dang, Z.; Lanzani, G.; Manna, L.; Petrozza,
2 A., Broadband Defects Emission and Enhanced Ligand Raman Scattering in 0D Cs₃Bi₂I₉
3 Colloidal Nanocrystals. *Adv. Funct. Mater.* **2019**, *29* (21), 1805299.
- 4 580. Leng, M.; Yang, Y.; Chen, Z.; Gao, W.; Zhang, J.; Niu, G.; Li, D.; Song, H.; Zhang, J.;
5 Jin, S.; Tang, J., Surface Passivation of Bismuth-Based Perovskite Variant Quantum Dots To
6 Achieve Efficient Blue Emission. *Nano Lett.* **2018**, *18* (9), 6076-6083.
- 7 581. Lou, Y.; Fang, M.; Chen, J.; Zhao, Y., Formation of highly luminescent cesium bismuth
8 halide perovskite quantum dots tuned by anion exchange. *Chem. Commun.* **2018**, *54* (30), 3779-
9 3782.
- 10 582. Mir, W. J.; Warankar, A.; Acharya, A.; Das, S.; Mandal, P.; Nag, A., Colloidal thallium
11 halide nanocrystals with reasonable luminescence, carrier mobility and diffusion length. *Chem.*
12 *Sci.* **2017**, *8* (6), 4602-4611.
- 13 583. Galván-Arzate, S.; Santamaría, A., Thallium toxicity. *Toxic. Lett.* **1998**, *99* (1), 1-13.
- 14 584. Yang, P.; Liu, G.; Liu, B.; Liu, X.; Lou, Y.; Chen, J.; Zhao, Y., All-inorganic Cs₂CuX₄
15 (X = Cl, Br, and Br/I) perovskite quantum dots with blue-green luminescence. *Chem. Commun.*
16 **2018**, *54* (82), 11638-11641.
- 17 585. Booker, E. P.; Griffiths, J. T.; Eyre, L.; Ducati, C.; Greenham, N. C.; Davis, N. J. L. K.,
18 Synthesis, Characterization, and Morphological Control of Cs₂CuCl₄ Nanocrystals. *J. Phys.*
19 *Chem. C* **2019**, *123* (27), 16951-16956.
- 20 586. Li, Y.; Vashishtha, P.; Zhou, Z.; Li, Z.; Shivarudraiah, S. B.; Ma, C.; Liu, J.; Wong, K.
21 S.; Su, H.; Halpert, J. E., Room Temperature Synthesis of Stable, Printable Cs₃Cu₂X₅ (X = I,
22 Br/I, Br, Br/Cl, Cl) Colloidal Nanocrystals with Near-Unity Quantum Yield Green Emitters (X =
23 Cl). *Chem. Mater.* **2020**.
- 24 587. Luo, Z.; Li, Q.; Zhang, L.; Wu, X.; Tan, L.; Zou, C.; Liu, Y.; Quan, Z., 0D Cs₃Cu₂X₅
25 (X = I, Br, and Cl) Nanocrystals: Colloidal Syntheses and Optical Properties. *Small* **2020**, *16* (3),
26 1905226.
- 27 588. Dahl, J. C.; Osowiecki, W. T.; Cai, Y.; Swabeck, J. K.; Bekenstein, Y.; Asta, M.; Chan,
28 E. M.; Alivisatos, A. P., Probing the Stability and Band Gaps of Cs₂AgInCl₆ and Cs₂AgSbCl₆
29 Lead-Free Double Perovskite Nanocrystals. *Chem. Mater.* **2019**, *31* (9), 3134-3143.
- 30 589. Han, P.; Zhang, X.; Luo, C.; Zhou, W.; Yang, S.; Zhao, J.; Deng, W.; Han, K.,
31 Manganese-Doped, Lead-Free Double Perovskite Nanocrystals for Bright Orange-Red Emission.
32 *ACS Central Sci.* **2020**.
- 33 590. Chen, N.; Cai, T.; Li, W.; Hills-Kimball, K.; Yang, H.; Que, M.; Nagaoka, Y.; Liu, Z.;
34 Yang, D.; Dong, A.; Xu, C.-Y.; Zia, R.; Chen, O., Yb- and Mn-Doped Lead-Free Double
35 Perovskite Cs₂AgBiX₆ (X = Cl-, Br-) Nanocrystals. *ACS Appl. Mater. Interfaces* **2019**, *11* (18),
36 16855-16863.
- 37 591. Kshirsagar, A. S.; Nag, A., Synthesis and optical properties of colloidal
38 Cs₂AgSb_{1-x}Bi_xCl₆ double perovskite nanocrystals. *J. Chem. Phys.* **2019**, *151* (16), 161101.
- 39 592. Lamba, R. S.; Basera, P.; Bhattacharya, S.; Sapra, S., Band Gap Engineering in
40 Cs₂(Na_xAg_{1-x})BiCl₆ Double Perovskite Nanocrystals. *J. Phys. Chem. Lett.* **2019**, *10* (17), 5173-
41 5181.
- 42 593. Lee, W.; Hong, S.; Kim, S., Colloidal Synthesis of Lead-Free Silver-Indium Double-
43 Perovskite Cs₂AgInCl₆ Nanocrystals and Their Doping with Lanthanide Ions. *J. Phys. Chem. C*
44 **2019**, *123* (4), 2665-2672.

- 1 594. Locardi, F.; Cirignano, M.; Baranov, D.; Dang, Z.; Prato, M.; Drago, F.; Ferretti, M.;
2 Pinchetti, V.; Fanciulli, M.; Brovelli, S.; De Trizio, L.; Manna, L., Colloidal Synthesis of Double
3 Perovskite Cs₂AgInCl₆ and Mn-Doped Cs₂AgInCl₆ Nanocrystals. *J. Am. Chem. Soc.* **2018**, *140*
4 (40), 12989-12995.
- 5 595. Locardi, F.; Sartori, E.; Buha, J.; Zito, J.; Prato, M.; Pinchetti, V.; Zaffalon, M. L.;
6 Ferretti, M.; Brovelli, S.; Infante, I.; De Trizio, L.; Manna, L., Emissive Bi-Doped Double
7 Perovskite Cs₂Ag_{1-x}Na_xInCl₆ Nanocrystals. *ACS Energy Lett.* **2019**, *4* (8), 1976-1982.
- 8 596. Mahor, Y.; Mir, W. J.; Nag, A., Synthesis and Near-Infrared Emission of Yb-Doped
9 Cs₂AgInCl₆ Double Perovskite Microcrystals and Nanocrystals. *J. Phys. Chem. C* **2019**, *123*
10 (25), 15787-15793.
- 11 597. Zhou, L.; Xu, Y.-F.; Chen, B.-X.; Kuang, D.-B.; Su, C.-Y., Synthesis and Photocatalytic
12 Application of Stable Lead-Free Cs₂AgBiBr₆ Perovskite Nanocrystals. *Small* **2018**, *14* (11),
13 1703762.
- 14 598. Lee, W.; Choi, D.; Kim, S., Colloidal Synthesis of Shape-Controlled Cs₂NaBiX₆ (X =
15 Cl, Br) Double Perovskite Nanocrystals: Discrete Optical Transition by Non-Bonding Characters
16 and Energy Transfer to Mn Dopants. *Chem. Mater.* **2020**.
- 17 599. Liu, Y.; Jing, Y.; Zhao, J.; Liu, Q.; Xia, Z., Design Optimization of Lead-Free
18 Perovskite Cs₂AgInCl₆:Bi Nanocrystals with 11.4% Photoluminescence Quantum Yield. *Chem.*
19 *Mater.* **2019**, *31* (9), 3333-3339.
- 20 600. Yang, B.; Hong, F.; Chen, J.; Tang, Y.; Yang, L.; Sang, Y.; Xia, X.; Guo, J.; He, H.;
21 Yang, S.; Deng, W.; Han, K., Colloidal Synthesis and Charge-Carrier Dynamics of
22 Cs₂AgSb_{1-y}Bi_yX₆ (X: Br, Cl; 0 ≤ y ≤ 1) Double Perovskite Nanocrystals. *Angew. Chem. Int. Ed.*
23 **2019**, *58* (8), 2278-2283.
- 24 601. Savory, C. N.; Walsh, A.; Scanlon, D. O., Can Pb-Free Halide Double Perovskites
25 Support High-Efficiency Solar Cells? *ACS Energy Lett.* **2016**, *1* (5), 949-955.
- 26 602. Zhou, Y.; Chen, J.; Bakr, O. M.; Sun, H.-T., Metal-Doped Lead Halide Perovskites:
27 Synthesis, Properties, and Optoelectronic Applications. *Chem. Mater.* **2018**, *30* (19), 6589-6613.
- 28 603. Li, S.; Shi, Z.; Zhang, F.; Wang, L.; Ma, Z.; Wu, D.; Yang, D.; Chen, X.; Tian, Y.;
29 Zhang, Y.; Shan, C.; Li, X., Ultrastable Lead-Free Double Perovskite Warm-White Light-
30 Emitting Devices with a Lifetime above 1000 Hours. *ACS Appl. Mater. Interfaces* **2020**, *12* (41),
31 46330-46339.
- 32 604. Han, P.; Mao, X.; Yang, S.; Zhang, F.; Yang, B.; Wei, D.; Deng, W.; Han, K., Lead-Free
33 Sodium-Indium Double Perovskite Nanocrystals through Doping Silver Cations for Bright
34 Yellow Emission. *Angew. Chem. Int. Ed.* **2019**, *58* (48), 17231-17235.
- 35 605. Swarnkar, A.; Chulliyil, R.; Ravi, V. K.; Irfanullah, M.; Chowdhury, A.; Nag, A.,
36 Colloidal CsPbBr₃ Perovskite Nanocrystals: Luminescence beyond Traditional Quantum Dots.
37 *Angew. Chem. Int. Ed.* **2015**, *54* (51), 15424-15428.
- 38 606. Wu, H.; Yang, Y.; Zhou, D.; Li, K.; Yu, J.; Han, J.; Li, Z.; Long, Z.; Ma, J.; Qiu, J., Rb⁺
39 cations enable the change of luminescence properties in perovskite (Rb_xCs_{1-x}PbBr₃) quantum
40 dots. *Nanoscale* **2018**, *10* (7), 3429-3437.
- 41 607. K, N. N.; Nag, A., Synthesis and luminescence of Mn-doped Cs₂AgInCl₆ double
42 perovskites. *Chem. Commun.* **2018**, *54* (41), 5205-5208.

- 1 608. Arfin, H.; Kaur, J.; Sheikh, T.; Chakraborty, S.; Nag, A., Bi³⁺-Er³⁺ and Bi³⁺-Yb³⁺
2 Codoped Cs₂AgInCl₆ Double Perovskite Near Infrared Emitters. *Angew. Chem. Int. Ed.* **2020**,
3 10.1002/anie.202002721.
- 4 609. Mir, W. J.; Sheikh, T.; Arfin, H.; Xia, Z.; Nag, A., Lanthanide doping in metal halide
5 perovskite nanocrystals: spectral shifting, quantum cutting and optoelectronic applications. *NPG*
6 *Asia Mater.* **2020**, *12* (1), 9.
- 7 610. Tan, Z.; Li, J.; Zhang, C.; Li, Z.; Hu, Q.; Xiao, Z.; Kamiya, T.; Hosono, H.; Niu, G.;
8 Lifshitz, E.; Cheng, Y.; Tang, J., Highly Efficient Blue-Emitting Bi-Doped Cs₂SnCl₆ Perovskite
9 Variant: Photoluminescence Induced by Impurity Doping. *Adv. Funct. Mater.* **2018**, *28* (29),
10 1801131.
- 11 611. Yang, Z.; Jiang, Z.; Liu, X.; Zhou, X.; Zhang, J.; Li, W., Bright Blue Light-Emitting
12 Doped Cesium Bromide Nanocrystals: Alternatives of Lead-Free Perovskite Nanocrystals for
13 White LEDs. *Adv. Opt. Mater.* **2019**, *7* (10), 1900108.
- 14 612. Chen, L.-J.; Dai, J.-H.; Lin, J.-D.; Mo, T.-S.; Lin, H.-P.; Yeh, H.-C.; Chuang, Y.-C.;
15 Jiang, S.-A.; Lee, C.-R., Wavelength-Tunable and Highly Stable Perovskite-Quantum-Dot-
16 Doped Lasers with Liquid Crystal Lasing Cavities. *ACS Appl. Mater. Interfaces* **2018**, *10* (39),
17 33307-33315.
- 18 613. Han, P.; Zhang, X.; Luo, C.; Zhou, W.; Yang, S.; Zhao, J.; Deng, W.; Han, K.,
19 Manganese-Doped, Lead-Free Double Perovskite Nanocrystals for Bright Orange-Red Emission.
20 *ACS Central Science* **2020**, *6* (4), 566-572.
- 21 614. Zhao, X.-G.; Yang, D.; Ren, J.-C.; Sun, Y.; Xiao, Z.; Zhang, L., Rational Design of
22 Halide Double Perovskites for Optoelectronic Applications. *Joule* **2018**, *2* (9), 1662-1673.
- 23 615. Zhu, D.; Zito, J.; Pinchetti, V.; Dang, Z.; Olivati, A.; Pasquale, L.; Tang, A.; Zaffalon,
24 M. L.; Meinardi, F.; Infante, I.; De Trizio, L.; Manna, L.; Brovelli, S., Compositional Tuning of
25 Carrier Dynamics in Cs₂Na_{1-x}Ag_xBiCl₆ Double-Perovskite Nanocrystals. *ACS Energy Lett.*
26 **2020**, *5* (6), 1840-1847.
- 27 616. Zhang, B.; Wang, M.; Ghini, M.; Melcherts, A. E. M.; Zito, J.; Goldoni, L.; Infante, I.;
28 Guizzardi, M.; Scotognella, F.; Kriegel, I.; De Trizio, L.; Manna, L., Colloidal Bi-Doped
29 Cs₂Ag_{1-x}NaxInCl₆ Nanocrystals: Undercoordinated Surface Cl Ions Limit their Light Emission
30 Efficiency. *ACS Mater. Lett.* **2020**, 1442-1449.
- 31 617. Nagane, S.; Ghosh, D.; Hoye, R. L. Z.; Zhao, B.; Ahmad, S.; Walker, A. B.; Islam, M.
32 S.; Ogale, S.; Sadhanala, A., Lead-Free Perovskite Semiconductors Based on Germanium-Tin
33 Solid Solutions: Structural and Optoelectronic Properties. *J. Phys. Chem. C* **2018**, *122* (11),
34 5940-5947.
- 35 618. Zhao, X.-G.; Yang, D.; Sun, Y.; Li, T.; Zhang, L.; Yu, L.; Zunger, A., Cu-In Halide
36 Perovskite Solar Absorbers. *J. Am. Chem. Soc.* **2017**, *139* (19), 6718-6725.
- 37 619. Sun, Q.; Yin, W.-J., Thermodynamic Stability Trend of Cubic Perovskites. *J. Am. Chem.*
38 *Soc.* **2017**, *139* (42), 14905-14908.
- 39 620. Jiang, J.; Onwudinanti, C. K.; Hatton, R. A.; Bobbert, P. A.; Tao, S., Stabilizing Lead-
40 Free All-Inorganic Tin Halide Perovskites by Ion Exchange. *J. Phys. Chem. C* **2018**, *122* (31),
41 17660-17667.
- 42 621. Bartel, C. J.; Clary, J. M.; Sutton, C.; Vigil-Fowler, D.; Goldsmith, B. R.; Holder, A. M.;
43 Musgrave, C. B., Inorganic Halide Double Perovskites with Optoelectronic Properties Modulated
44 by Sublattice Mixing. *J. Am. Chem. Soc.* **2020**, *142* (11), 5135-5145.

- 1 622. Li, C.; Lu, X.; Ding, W.; Feng, L.; Gao, Y.; Guo, Z., Formability of ABX₃ (X = F, Cl,
2 Br, I) halide perovskites. *Acta Crystallogr., Sect. B* **2008**, *64* (6), 702-707.
- 3 623. Zhao, X.-G.; Yang, J.-H.; Fu, Y.; Yang, D.; Xu, Q.; Yu, L.; Wei, S.-H.; Zhang, L.,
4 Design of Lead-Free Inorganic Halide Perovskites for Solar Cells via Cation-Transmutation. *J.*
5 *Am. Chem. Soc.* **2017**, *139* (7), 2630-2638.
- 6 624. Swarnkar, A.; Mir, W. J.; Chakraborty, R.; Jagadeeswararao, M.; Sheikh, T.; Nag, A.,
7 Are Chalcogenide Perovskites an Emerging Class of Semiconductors for Optoelectronic
8 Properties and Solar Cell? *Chem. Mater.* **2019**, *31* (3), 565-575.
- 9 625. Hong, F.; Saparov, B.; Meng, W.; Xiao, Z.; Mitzi, D. B.; Yan, Y., Viability of Lead-Free
10 Perovskites with Mixed Chalcogen and Halogen Anions for Photovoltaic Applications. *J. Phys.*
11 *Chem. C* **2016**, *120* (12), 6435-6441.
- 12 626. Sun, Q.; Wang, J.; Yin, W.-J.; Yan, Y., Bandgap Engineering of Stable Lead-Free Oxide
13 Double Perovskites for Photovoltaics. *Adv. Mater.* **2018**, *30* (15), 1705901.
- 14 627. Holzapfel, N. P.; Majher, J. D.; Strom, T. A.; Moore, C. E.; Woodward, P. M., Cs₄Cd_{1-x}
15 Mn_xBi₂Cl₁₂—A Vacancy-Ordered Halide Perovskite Phosphor with High-Efficiency Orange-
16 Red Emission. *Chem. Mater.* **2020**, *32* (8), 3510-3516.
- 17 628. Qiu, W.; Xiao, Z.; Roh, K.; Noel, N. K.; Shapiro, A.; Heremans, P.; Rand, B. P., Mixed
18 Lead–Tin Halide Perovskites for Efficient and Wavelength-Tunable Near-Infrared Light-
19 Emitting Diodes. *Adv. Mater.* **2019**, *31* (3), 1806105.
- 20 629. Zhang, X.; Wang, C.; Zhang, Y.; Zhang, X.; Wang, S.; Lu, M.; Cui, H.; Kershaw, S. V.;
21 Yu, W. W.; Rogach, A. L., Bright Orange Electroluminescence from Lead-Free Two-
22 Dimensional Perovskites. *ACS Energy Lett.* **2019**, *4* (1), 242-248.
- 23 630. Creason, T. D.; Yangui, A.; Roccanova, R.; Strom, A.; Du, M.-H.; Saparov, B.,
24 Rb₂CuX₃ (X = Cl, Br): 1D All-Inorganic Copper Halides with Ultrabright Blue Emission and
25 Up-Conversion Photoluminescence. *Adv. Opt. Mater.* **2020**, *8* (2), 1901338.
- 26 631. Yamada, T.; Aharen, T.; Kanemitsu, Y., Up-converted photoluminescence from
27 CH₃NH₃PbI₃ perovskite semiconductors: Implications for laser cooling. *Phys. Rev. Mater.*
28 **2019**, *3* (2), 024601.
- 29 632. Mir, W. J.; Swarnkar, A.; Nag, A., Postsynthesis Mn-doping in CsPbI₃ nanocrystals to
30 stabilize the black perovskite phase. *Nanoscale* **2019**, *11* (10), 4278-4286.
- 31 633. Paul, S.; Bladt, E.; Richter, A. F.; Döblinger, M.; Tong, Y.; Huang, H.; Dey, A.; Bals,
32 S.; Debnath, T.; Polavarapu, L.; Feldmann, J., Manganese-Doping-Induced Quantum
33 Confinement within Host Perovskite Nanocrystals through Ruddlesden–Popper Defects. *Angew.*
34 *Chem. Int. Ed.* **2020**, *59* (17), 6794-6799.
- 35 634. Pradhan, N., Mn-Doped Semiconductor Nanocrystals: 25 Years and Beyond. *J. Phys.*
36 *Chem. Lett.* **2019**, *10* (10), 2574-2577.
- 37 635. Parobek, D.; Roman, B. J.; Dong, Y.; Jin, H.; Lee, E.; Sheldon, M.; Son, D. H., Exciton-
38 to-Dopant Energy Transfer in Mn-Doped Cesium Lead Halide Perovskite Nanocrystals. *Nano*
39 *Lett.* **2016**, *16* (12), 7376-7380.
- 40 636. Liu, W.; Lin, Q.; Li, H.; Wu, K.; Robel, I.; Pietryga, J. M.; Klimov, V. I., Mn²⁺-Doped
41 Lead Halide Perovskite Nanocrystals with Dual-Color Emission Controlled by Halide Content. *J.*
42 *Am. Chem. Soc.* **2016**, *138* (45), 14954-14961.

- 1 637. Liu, H.; Wu, Z.; Shao, J.; Yao, D.; Gao, H.; Liu, Y.; Yu, W.; Zhang, H.; Yang, B.,
2 CsPb_xMn_{1-x}Cl₃ Perovskite Quantum Dots with High Mn Substitution Ratio. *ACS Nano* **2017**, *11*
3 (2), 2239-2247.
- 4 638. Akkerman, Q. A.; Meggiolaro, D.; Dang, Z.; De Angelis, F.; Manna, L., Fluorescent
5 Alloy CsPb_xMn_{1-x}I₃ Perovskite Nanocrystals with High Structural and Optical Stability. *ACS*
6 *Energy Lett.* **2017**, *2* (9), 2183-2186.
- 7 639. Pradhan, N.; Das Adhikari, S.; Dutta, S. K.; Dutta, A.; Guria, A. K., Chemically
8 Tailoring the Dopant Emission in Mn doped CsPbCl₃ Perovskite Nanocrystals. *Angew. Chem.*
9 *Int. Ed.* **2017**.
- 10 640. Xu, K.; Lin, C. C.; Xie, X.; Meijerink, A., Efficient and Stable Luminescence from Mn²⁺
11 in Core and Core-Isocrystalline Shell CsPbCl₃ Perovskite Nanocrystals. *Chem. Mater.* **2017**, *29*
12 (10), 4265-4272.
- 13 641. Mir, W. J.; Jagadeeswararao, M.; Das, S.; Nag, A., Colloidal Mn-Doped Cesium Lead
14 Halide Perovskite Nanoplatelets. *ACS Energy Lett.* **2017**, *2* (3), 537-543.
- 15 642. Akkerman, Q. A.; Motti, S. G.; Kandada, A. R. S.; Mosconi, E.; D'Innocenzo, V.;
16 Bertoni, G.; Marras, S.; Kamino, B. A.; Miranda, L.; De Angelis, F., Solution synthesis approach
17 to colloidal cesium lead halide perovskite nanoplatelets with monolayer-level thickness control.
18 *J. Am. Chem. Soc.* **2016**, *138* (3), 1010-1016.
- 19 643. Das Adhikari, S.; Dutta, A.; Dutta, S. K.; Pradhan, N., Layered Perovskites L₂(Pb₁₋
20 _xMn_x)Cl₄ to Mn-Doped CsPbCl₃ Perovskite Platelets. *ACS Energy Lett.* **2018**, *3* (6), 1247-1253.
- 21 644. Dutta, S. K.; Pradhan, N., Coupled Halide-deficient and Halide-rich Reaction System for
22 Doping in Perovskite Armed Nanostructures. *J. Phys. Chem. Lett.* **2019**, *10* (21), 6788-6793.
- 23 645. Li, F.; Xia, Z.; Pan, C.; Gong, Y.; Gu, L.; Liu, Q.; Zhang, J. Z., High Br- Content
24 CsPb(ClyBr_{1-y})₃ Perovskite Nanocrystals with Strong Mn²⁺ Emission through Diverse
25 Cation/Anion Exchange Engineering. *ACS Appl. Mater. Interfaces* **2018**, *10* (14), 11739-11746.
- 26 646. Li, F.; Xia, Z.; Gong, Y.; Gu, L.; Liu, Q., Optical properties of Mn²⁺ doped cesium lead
27 halide perovskite nanocrystals via a cation-anion co-substitution exchange reaction. *J. Mater.*
28 *Chem. C* **2017**, *5* (36), 9281-9287.
- 29 647. Huang, G.; Wang, C.; Xu, S.; Zong, S.; Lu, J.; Wang, Z.; Lu, C.; Cui, Y., Postsynthetic
30 Doping of MnCl₂ Molecules into Preformed CsPbBr₃ Perovskite Nanocrystals via a Halide
31 Exchange-Driven Cation Exchange. *Adv. Mater.* **2017**, *29* (29), 1700095.
- 32 648. De Siena, M. C.; Sommer, D. E.; Creutz, S. E.; Dunham, S. T.; Gamelin, D. R., Spinodal
33 Decomposition During Anion Exchange in Colloidal Mn²⁺-Doped CsPbX₃ (X = Cl, Br)
34 Perovskite Nanocrystals. *Chem. Mater.* **2019**, *31* (18), 7711-7722.
- 35 649. Parobek, D.; Dong, Y.; Qiao, T.; Rossi, D.; Son, D. H., Photoinduced anion exchange in
36 cesium lead halide perovskite nanocrystals. *J. Am. Chem. Soc.* **2017**, *139* (12), 4358-4361.
- 37 650. Xu, K.; Meijerink, A., Tuning Exciton-Mn²⁺ Energy Transfer in Mixed Halide
38 Perovskite Nanocrystals. *Chem. Mater.* **2018**, *30* (15), 5346-5352.
- 39 651. Yuan, X.; Ji, S.; De Siena, M. C.; Fei, L.; Zhao, Z.; Wang, Y.; Li, H.; Zhao, J.; Gamelin,
40 D. R., Photoluminescence Temperature Dependence, Dynamics, and Quantum Efficiencies in
41 Mn²⁺-Doped CsPbCl₃ Perovskite Nanocrystals with Varied Dopant Concentration. *Chem.*
42 *Mater.* **2017**, *29* (18), 8003-8011.

- 1 652. Mir, W. J.; Mahor, Y.; Lohar, A.; Jagadeeswararao, M.; Das, S.; Mahamuni, S.; Nag, A.,
2 Postsynthesis Doping of Mn and Yb into CsPbX₃ (X = Cl, Br, or I) Perovskite Nanocrystals for
3 Downconversion Emission. *Chem. Mater.* **2018**, *30* (22), 8170-8178.
- 4 653. Mehetor, S. K.; Ghosh, H.; Pradhan, N., Blue-Emitting CsPbBr₃ Perovskite Quantum
5 Rods and Their Wide-Area 2D Self-Assembly. *ACS Energy Lett.* **2019**, *4* (6), 1437-1442.
- 6 654. Parobek, D.; Dong, Y.; Qiao, T.; Son, D. H., Direct Hot-Injection Synthesis of Mn-
7 Doped CsPbBr₃ Nanocrystals. *Chem. Mater.* **2018**, *30* (9), 2939-2944.
- 8 655. Zou, S.; Liu, Y.; Li, J.; Liu, C.; Feng, R.; Jiang, F.; Li, Y.; Song, J.; Zeng, H.; Hong, M.;
9 Chen, X., Stabilizing Cesium Lead Halide Perovskite Lattice through Mn(II) Substitution for
10 Air-Stable Light-Emitting Diodes. *J. Am. Chem. Soc.* **2017**, *139* (33), 11443-11450.
- 11 656. Rossi, D.; Parobek, D.; Dong, Y.; Son, D. H., Dynamics of exciton–mn energy transfer
12 in mn-doped cspbcl₃ perovskite nanocrystals. *J. Phys. Chem. C* **2017**, *121* (32), 17143-17149.
- 13 657. De, A.; Mondal, N.; Samanta, A., Luminescence tuning and exciton dynamics of Mn-
14 doped CsPbCl₃ nanocrystals. *Nanoscale* **2017**, *9* (43), 16722-16727.
- 15 658. Pinchetti, V.; Anand, A.; Akkerman, Q. A.; Sciacca, D.; Lorenzon, M.; Meinardi, F.;
16 Fanciulli, M.; Manna, L.; Brovelli, S., Trap-Mediated Two-Step Sensitization of Manganese
17 Dopants in Perovskite Nanocrystals. *ACS Energy Lett.* **2019**, *4* (1), 85-93.
- 18 659. Travis, W.; Glover, E.; Bronstein, H.; Scanlon, D.; Palgrave, R., On the application of
19 the tolerance factor to inorganic and hybrid halide perovskites: a revised system. *Chem Sci* **2016**,
20 *7* (7), 4548-4556.
- 21 660. Dutta, A.; Pradhan, N., Phase-Stable Red-Emitting CsPbI₃ Nanocrystals: Successes and
22 Challenges. *ACS Energy Lett.* **2019**, *4* (3), 709-719.
- 23 661. Liu, F.; Ding, C.; Zhang, Y.; Ripolles, T. S.; Kamisaka, T.; Toyoda, T.; Hayase, S.;
24 Minemoto, T.; Yoshino, K.; Dai, S., Colloidal Synthesis of Air-Stable Alloyed CsSn_{1-x}Pb_xI₃
25 Perovskite Nanocrystals for Use in Solar Cells. *J. Am. Chem. Soc.* **2017**, *139* (46), 16708-16719.
- 26 662. Guo, Y.; Yaffe, O.; Hull, T. D.; Owen, J. S.; Reichman, D. R.; Brus, L. E., Dynamic
27 emission Stokes shift and liquid-like dielectric solvation of band edge carriers in lead-halide
28 perovskites. *Nat. Commun.* **2019**, *10* (1), 1175.
- 29 663. Yao, J.-S.; Ge, J.; Wang, K.-H.; Zhang, G.; Zhu, B.-S.; Chen, C.; Zhang, Q.; Luo, Y.;
30 Yu, S.-H.; Yao, H.-B., Few-Nanometer-Sized α -CsPbI₃ Quantum Dots Enabled by Strontium
31 Substitution and Iodide Passivation for Efficient Red-Light Emitting Diodes. *J. Am. Chem. Soc.*
32 **2019**, *141* (5), 2069-2079.
- 33 664. Shi, J.; Li, F.; Yuan, J.; Ling, X.; Zhou, S.; Qian, Y.; Ma, W., Efficient and stable
34 CsPbI₃ perovskite quantum dots enabled by in situ ytterbium doping for photovoltaic
35 applications. *J. Mater. Chem. A* **2019**, *7* (36), 20936-20944.
- 36 665. Guvenc, C. M.; Yalcinkaya, Y.; Ozen, S.; Sahin, H.; Demir, M. M., Gd³⁺-Doped α -
37 CsPbI₃ Nanocrystals with Better Phase Stability and Optical Properties. *J. Phys. Chem. C* **2019**,
38 *123* (40), 24865-24872.
- 39 666. Bera, S.; Ghosh, D.; Dutta, A.; Bhattacharyya, S.; Chakraborty, S.; Pradhan, N.,
40 Limiting Heterovalent B-Site Doping in CsPbI₃ Nanocrystals: Phase and Optical Stability. *ACS*
41 *Energy Lett.* **2019**, *4* (6), 1364-1369.

- 1 667. Lu, M.; Zhang, X.; Bai, X.; Wu, H.; Shen, X.; Zhang, Y.; Zhang, W.; Zheng, W.; Song,
2 H.; Yu, W. W.; Rogach, A. L., Spontaneous Silver Doping and Surface Passivation of CsPbI₃
3 Perovskite Active Layer Enable Light-Emitting Devices with an External Quantum Efficiency of
4 11.2%. *Acs Energy Lett* **2018**, *3* (7), 1571-1577.
- 5 668. Behera, R. K.; Dutta, A.; Ghosh, D.; Bera, S.; Bhattacharyya, S.; Pradhan, N., Doping
6 the Smallest Shannon Radii Transition Metal Ion Ni(II) for Stabilizing α -CsPbI₃ Perovskite
7 Nanocrystals. *J. Phys. Chem. Lett.* **2019**, *10* (24), 7916-7921.
- 8 669. Liu, F.; Ding, C.; Zhang, Y.; Kamisaka, T.; Zhao, Q.; Luther, J. M.; Toyoda, T.; Hayase,
9 S.; Minemoto, T.; Yoshino, K., GeI₂ additive for high optoelectronic quality CsPbI₃ quantum
10 dots and their application in photovoltaic devices. *Chem. Mater.* **2019**, *31* (3), 798-807.
- 11 670. Xu, L.; Yuan, S.; Zeng, H.; Song, J., A comprehensive review of doping in perovskite
12 nanocrystals/quantum dots: evolution of structure, electronics, optics, and light-emitting diodes.
13 *Mater. Today Nano* **2019**, *6*, 100036.
- 14 671. Saliba, M.; Matsui, T.; Domanski, K.; Seo, J.-Y.; Ummadisingu, A.; Zakeeruddin, S. M.;
15 Correa-Baena, J.-P.; Tress, W. R.; Abate, A.; Hagfeldt, A.; Grätzel, M., Incorporation of
16 rubidium cations into perovskite solar cells improves photovoltaic performance. *Science* **2016**,
17 *354* (6309), 206-209.
- 18 672. Shi, Y.; Xi, J.; Lei, T.; Yuan, F.; Dai, J.; Ran, C.; Dong, H.; Jiao, B.; Hou, X.; Wu, Z.,
19 Rubidium Doping for Enhanced Performance of Highly Efficient Formamidinium-Based
20 Perovskite Light-Emitting Diodes. *ACS Appl. Mater. Interfaces* **2018**, *10* (11), 9849-9857.
- 21 673. Binyamin, T.; Pedesseau, L.; Remennik, S.; Sawahreh, A.; Even, J.; Etgar, L., Fully
22 Inorganic Mixed Cation Lead Halide Perovskite Nanoparticles: A Study at the Atomic Level.
23 *Chem. Mater.* **2019**.
- 24 674. Xiao, J.-W.; Liang, Y.; Zhang, S.; Zhao, Y.; Li, Y.; Chen, Q., Stabilizing RbPbBr₃
25 Perovskite Nanocrystals through Cs⁺ Substitution. *Chem. Eur. J.* **2019**, *25* (10), 2597-2603.
- 26 675. Todorović, P.; Ma, D.; Chen, B.; Quintero-Bermudez, R.; Saidaminov, M. I.; Dong, Y.;
27 Lu, Z.-H.; Sargent, E. H., Spectrally Tunable and Stable Electroluminescence Enabled by
28 Rubidium Doping of CsPbBr₃ Nanocrystals. *Adv. Opt. Mater.* **2019**, *7* (24), 1901440.
- 29 676. Amgar, D.; Binyamin, T.; Uvarov, V.; Etgar, L., Near ultra-violet to mid-visible band
30 gap tuning of mixed cation RbxCs_{1-x}PbX₃ (X = Cl or Br) perovskite nanoparticles. *Nanoscale*
31 **2018**, *10* (13), 6060-6068.
- 32 677. Lin, Y.-H.; Qiu, Z.-H.; Wang, S.-H.; Zhang, X.-H.; Wu, S.-F., All-inorganic RbxCs_{1-x}
33 PbBrI₂ perovskite nanocrystals with wavelength-tunable properties for red light-emitting.
34 *Inorg. Chem. Commun.* **2019**, *103*, 47-52.
- 35 678. Kubicki, D. J.; Prochowicz, D.; Hofstetter, A.; Zakeeruddin, S. M.; Grätzel, M.; Emsley,
36 L., Phase Segregation in Cs-, Rb- and K-Doped Mixed-Cation (MA)_x(FA)_{1-x}PbI₃ Hybrid
37 Perovskites from Solid-State NMR. *J. Am. Chem. Soc* **2017**, *139* (40), 14173-14180.
- 38 679. Huang, S.; Wang, B.; Zhang, Q.; Li, Z.; Shan, A.; Li, L., Postsynthesis Potassium-
39 Modification Method to Improve Stability of CsPbBr₃ Perovskite Nanocrystals. *Adv. Opt. Mater*
40 **2018**, *6* (6), 1701106.
- 41 680. Yang, D.; Löhner, F. C.; Körstgens, V.; Schreiber, A.; Cao, B.; Bernstorff, S.; Müller -
42 Buschbaum, P., In Operando GISAXS and GIWAXS Stability Study of Organic Solar Cells
43 Based on PffBT4T - 2OD:PC
44 71

- 1 BM with and without Solvent Additive. *Advanced Science* **2020**.
- 2 681. Li, S.; Shi, Z.; Zhang, F.; Wang, L.; Ma, Z.; Yang, D.; Yao, Z.; Wu, D.; Xu, T.-T.; Tian,
3 Y.; Zhang, Y.; Shan, C.; Li, X. J., Sodium Doping-Enhanced Emission Efficiency and Stability
4 of CsPbBr₃ Nanocrystals for White Light-Emitting Devices. *Chem. Mater.* **2019**, *31* (11), 3917-
5 3928.
- 6 682. Chen, H.; Fan, L.; Zhang, R.; Liu, W.; Zhang, Q.; Guo, R.; Zhuang, S.; Wang, L.,
7 Sodium Ion Modifying In Situ Fabricated CsPbBr₃ Nanoparticles for Efficient Perovskite Light
8 Emitting Diodes. *Adv. Opt. Mater.* **2019**, *7* (21), 1900747.
- 9 683. Ronda, C.; (Ed.), *Luminescence: From Theory to Applications*. Wiley-VCH: Weinheim,
10 2008.
- 11 684. Blasse, G.; Grabmaier, B. C., *Luminescent Materials*. Springer-Verlag, Berlin, Germany:
12 1994.
- 13 685. Zhou, D.; Liu, D.; Pan, G.; Chen, X.; Li, D.; Xu, W.; Bai, X.; Song, H., Cerium and
14 Ytterbium Codoped Halide Perovskite Quantum Dots: A Novel and Efficient Downconverter for
15 Improving the Performance of Silicon Solar Cells. *Adv. Mater.* **2017**, *29* (42), 1704149.
- 16 686. Yao, J.-S.; Ge, J.; Han, B.-N.; Wang, K.-H.; Yao, H.-B.; Yu, H.-L.; Li, J.-H.; Zhu, B.-S.;
17 Song, J.-Z.; Chen, C.; Zhang, Q.; Zeng, H.-B.; Luo, Y.; Yu, S.-H., Ce³⁺-Doping to Modulate
18 Photoluminescence Kinetics for Efficient CsPbBr₃ Nanocrystals Based Light-Emitting Diodes.
19 *J. Am. Chem. Soc.* **2018**, *140*, 3626–3634.
- 20 687. Li, Q.; Liu, Y.; Chen, P.; Hou, J.; Sun, Y.; Zhao, G.; Zhang, N.; Zou, J.; Xu, J.; Fang,
21 Y.; Dai, N., Excitonic Luminescence Engineering in Tervalent-Europium-Doped Cesium Lead
22 Halide Perovskite Nanocrystals and Their Temperature-Dependent Energy Transfer Emission
23 Properties. *J. Phys. Chem. C* **2018**, *122*, 29044–29050.
- 24 688. Milstein, T.; Kroupa, D. M.; Gamelin, D. R., Picosecond Quantum Cutting Generates
25 Photoluminescence Quantum Yields Over 100% in Ytterbium-Doped CsPbCl₃ Nanocrystals.
26 *Nano Lett.* **2018**, *18* (6), 3792–3799.
- 27 689. Mir, W. J.; Mahor, Y.; Lohar, A.; Jagadeeswararao, M.; Das, S.; Mahamuni, S.; Nag, A.,
28 Postsynthesis Doping of Mn and Yb into CsPbX₃ (X = Cl, Br, or I) Perovskite Nanocrystals for
29 Downconversion Emission. *Chem. Mater.* **2018**, *30*, 8170–8178.
- 30 690. Zheng, W.; Huang, P.; Gong, Z.; Tu, D.; Xu, J.; Zou, Q.; Li, R.; You, W.; Bünzli, J.-C.
31 G.; Chen, X., Near-infrared-triggered photon upconversion tuning in all-inorganic cesium lead
32 halide perovskite quantum dots. *Nat. Commun.* **2018**, *9*, 3462.
- 33 691. Pan, G.; Bai, X.; Xu, W.; Chen, X.; Zhou, D.; Zhu, J.; Shao, H.; Zhai, Y.; Dong, B.; Xu,
34 L.; Song, H., Impurity Ions Codoped Cesium Lead Halide Perovskite Nanocrystals with Bright
35 White Light Emission toward Ultraviolet–White Light-Emitting Diode. *ACS Appl. Mater.*
36 *Interfaces* **2018**, *10*, 39040–39048.
- 37 692. Zhang, X.; Zhang, Y.; Zhang, X.; Yin, W.; Wang, Y.; Wang, H.; Lu, M.; Li, Z.; Gu, Z.;
38 Yu, W. W., Yb³⁺ and Yb³⁺/Er³⁺ doping for near-infrared emission and improved stability of
39 CsPbCl₃ nanocrystals. *J. Mater. Chem. C* **2018**, *6*, 10101-10105.
- 40 693. Zhou, L.; Liu, T.; Zheng, J.; Yu, K.; Yang, F.; Wang, N.; Zuo, Y.; Liu, Z.; Xue, C.; Li,
41 C.; Cheng, B.; Wang, Q., Dual-Emission and Two Charge-Transfer States in Ytterbium-doped
42 Cesium Lead Halide Perovskite Solid Nanocrystals. *J. Phys. Chem. C* **2018**, *122*, 26825–26834.

- 1 694. Luo, X.; Ding, T.; Liu, X.; Liu, Y.; Wu, K., Quantum-Cutting Luminescent Solar
2 Concentrators Using Ytterbium-Doped Perovskite Nanocrystals. *Nano Lett.* **2019**, *19* (1), 338-
3 341.
- 4 695. Cohen, T. A.; Milstein, T. J.; Kroupa, D. M.; MacKenzie, J. D.; Luscombe, C. K.;
5 Gamelin, D. R., Quantum-cutting Yb³⁺-doped perovskite nanocrystals for monolithic bilayer
6 luminescent solar concentrators. *J. Mater. Chem. A* **2019**, *7* (15), 9279-9288.
- 7 696. Crane, M. J.; Kroupa, D. M.; Gamelin, D. R., Detailed-balance analysis of
8 Yb³⁺:CsPb(Cl_{1-x}Br_x)₃ quantum-cutting layers for high-efficiency photovoltaics under real-
9 world conditions. *Energy Environ. Sci.* **2019**, *12* (8), 2486-2495.
- 10 697. Erickson, C. S.; Crane, M. J.; Milstein, T. J.; Gamelin, D. R., Photoluminescence
11 Saturation in Quantum-Cutting Yb³⁺-Doped CsPb(Cl_{1-x}Br_x)₃ Perovskite Nanocrystals:
12 Implications for Solar Downconversion. *J. Phys. Chem. C* **2019**, *123* (19), 12474-12484.
- 13 698. Milstein, T. J.; Kluherz, K. T.; Kroupa, D. M.; Erickson, C. S.; De Yoreo, J. J.; Gamelin,
14 D. R., Anion Exchange and the Quantum-Cutting Energy Threshold in Ytterbium-Doped
15 CsPb(Cl_{1-x}Br_x)₃ Perovskite Nanocrystals. *Nano Lett.* **2019**, *19* (3), 1931-1937.
- 16 699. Ma, J.-P.; Chen, Y.-M.; Zhang, L.-M.; Guo, S.-Q.; Liu, J.-D.; Li, H.; Ye, B.-J.; Li, Z.-Y.;
17 Zhou, Y.; Zhang, B.-B.; Bakr, O. M.; Zhang, J.-Y.; Sun, H.-T., Insights into the local structure of
18 dopants, doping efficiency, and luminescence properties of lanthanide-doped CsPbCl₃
19 perovskite nanocrystals. *J. Mater. Chem. C* **2019**, *7* (10), 3037-3048.
- 20 700. Zhou, D.; Sun, R.; Xu, W.; Ding, N.; Li, D.; Chen, X.; Pan, G.; Bai, X.; Song, H.,
21 Impact of Host Composition, Codoping, or Tridoping on Quantum-Cutting Emission of
22 Ytterbium in Halide Perovskite Quantum Dots and Solar Cell Applications. *Nano Lett.* **2019**, *19*
23 (10), 6904-6913.
- 24 701. Luo, B.; Li, F.; Xu, K.; Guo, Y.; Liu, Y.; Xia, Z.; Zhang, J. Z., B-Site doped lead halide
25 perovskites: synthesis, band engineering, photophysics, and light emission applications. *J. Mater.*
26 *Chem. C* **2019**, *7* (10), 2781-2808.
- 27 702. Mir, W. J.; Sheikh, T.; Arfin, H.; Xia, Z.; Nag, A., Lanthanide doping in metal halide
28 perovskite nanocrystals: spectral shifting, quantum cutting and optoelectronic applications. *NPG*
29 *Asia Materials* **2020**, *12*, 9.
- 30 703. Heer, S.; Koempe, K.; Güdel, H.-U.; Haase, M., Highly efficient multicolour
31 upconversion emission in transparent colloids of lanthanide-doped NaYF₄ nanocrystals. *Adv.*
32 *Mater.* **2004**, *16*, 2102-2105.
- 33 704. Wang, F.; Liu, X., Recent advances in the chemistry of lanthanide-doped upconversion
34 nanocrystals. *Chem. Soc. Rev.* **2009**, *38*, 976-989
- 35 705. Haase, M.; Schäfer, H., Upconverting Nanoparticles. *Angew. Chem.* **2011**, *50*, 5808-
36 5829.
- 37 706. Wegh, R. T.; Donker, H.; Oskam, K. D.; Meijerink, A., Visible Quantum Cutting in
38 LiGdF₄:Eu³⁺ through Downconversion. *Science* **1999**, *283*, 663-666.
- 39 707. van der Ende, B. M.; Aarts, L.; Meijerink, A., Lanthanide ions as spectral converters for
40 solar cells. *Phys. Chem. Chem. Phys.* **2009**, *11* (47), 11081-11095.
- 41 708. Liu, T.-C.; Zhang, G.; Qiao, X.; Wang, J.; Seo, H. J.; Tsai, D.-P.; Liu, R.-S., Near-
42 Infrared Quantum Cutting Platform in Thermally Stable Phosphate Phosphors for Solar Cells.
43 *Inorg Chem* **2013**, *52* (13), 7352-7357.

- 1 709. Huang, G.; Wang, C.; Xu, S.; Zong, S.; Lu, J.; Wang, Z.; Lu, C.; Cui, Y., Postsynthetic
2 Doping of MnCl₂ Molecules into Preformed CsPbBr₃ Perovskite Nanocrystals via a Halide
3 Exchange - Driven Cation Exchange. *Adv. Mater.* **2017**, *29*, 1700095.
- 4 710. Chen, D.; Zhou, S.; Fang, G.; Chen, X.; Zhong, J., Fast Room-Temperature Cation
5 Exchange Synthesis of Mn-Doped CsPbCl₃ Nanocrystals Driven by Dynamic Halogen
6 Exchange. *ACS Appl. Mater. Interfaces* **2018**, *10* (46), 39872-39878.
- 7 711. Erickson, C. S.; Bradshaw, L. R.; McDowall, S.; Gilbertson, J. D.; Gamelin, D. R.;
8 Patrick, D. L., Zero-Reabsorption Doped-Nanocrystal Luminescent Solar Concentrators. *ACS*
9 *Nano* **2014**, *8* (4), 3461-3467.
- 10 712. Bradshaw, L. R.; Knowles, K. E.; McDowall, S.; Gamelin, D. R., Nanocrystals for
11 Luminescent Solar Concentrators. *Nano Lett.* **2015**, *15* (2), 1315-1323.
- 12 713. Knowles, K. E.; Kilburn, T. B.; Alzate, D. G.; McDowall, S.; Gamelin, D. R., Bright
13 CuInS₂/CdS nanocrystal phosphors for high-gain full-spectrum luminescent solar concentrators.
14 *Chem. Commun.* **2015**, *51* (44), 9129-9132.
- 15 714. Meinardi, F.; McDaniel, H.; Carulli, F.; Colombo, A.; Velizhanin, K. A.; Makarov, N.
16 S.; Simonutti, R.; Klimov, V. I.; Brovelli, S., Highly efficient large-area colourless luminescent
17 solar concentrators using heavy-metal-free colloidal quantum dots. *Nat. Nanotech.* **2015**, *10* (10),
18 878-885.
- 19 715. Sumner, R.; Eiselt, S.; Kilburn, T. B.; Erickson, C.; Carlson, B.; Gamelin, D. R.;
20 McDowall, S.; Patrick, D. L., Analysis of Optical Losses in High-Efficiency CuInS₂-Based
21 Nanocrystal Luminescent Solar Concentrators: Balancing Absorption versus Scattering. *J. Phys.*
22 *Chem. C* **2017**, *121* (6), 3252-3260.
- 23 716. Bergren, M. R.; Makarov, N. S.; Ramasamy, K.; Jackson, A.; Guglielmetti, R.;
24 McDaniel, H., High-Performance CuInS₂ Quantum Dot Laminated Glass Luminescent Solar
25 Concentrators for Windows. *ACS Energy Lett.* **2018**, 520-525.
- 26 717. Boles, M. A.; Engel, M.; Talapin, D. V., Self-Assembly of Colloidal Nanocrystals: From
27 Intricate Structures to Functional Materials. *Chem. Rev.* **2016**, *116* (18), 11220-11289.
- 28 718. Weller, H., Synthesis and self-assembly of colloidal nanoparticles *Philos. Trans. A*
29 *Math. Phys. Eng. Sci.* **2003**, *361* (1803), 229-240.
- 30 719. Shevchenko, E. V.; Talapin, D. V.; Kotov, N. A.; O'Brien, S.; Murray, C. B., Structural
31 diversity in binary nanoparticle superlattices. *Nature* **2006**, *439* (7072), 55-59.
- 32 720. García-Lojo, D.; Núñez-Sánchez, S.; Gómez-Graña, S.; Grzelczak, M.; Pastoriza-Santos,
33 I.; Pérez-Juste, J.; Liz-Marzán, L. M., Plasmonic Supercrystals. *Acc. Chem. Res.* **2019**, *52* (7),
34 1855-1864.
- 35 721. Redl, F. X.; Cho, K. S.; Murray, C. B.; O'Brien, S., Three-dimensional binary
36 superlattices of magnetic nanocrystals and semiconductor quantum dots. *Nature* **2003**, *423*
37 (6943), 968-971.
- 38 722. Kovalenko, M. V.; Protesescu, L.; Bodnarchuk, M. I., Properties and potential
39 optoelectronic applications of lead halide perovskite nanocrystals. **2017**, *358* (6364), 745-750.
- 40 723. Soetan, N.; Erwin, W. R.; Tonigan, A. M.; Walker, D. G.; Bardhan, R., Solvent-Assisted
41 Self-Assembly of CsPbBr₃ Perovskite Nanocrystals into One-Dimensional Superlattice. *J. Phys.*
42 *Chem. C* **2017**, *121* (33), 18186-18194.

- 1 724. Liu, Y.; Siron, M.; Lu, D.; Yang, J.; dos Reis, R.; Cui, F.; Gao, M.; Lai, M.; Lin, J.;
2 Kong, Q.; Lei, T.; Kang, J.; Jin, J.; Ciston, J.; Yang, P., Self-Assembly of Two-Dimensional
3 Perovskite Nanosheet Building Blocks into Ordered Ruddlesden–Popper Perovskite Phase. *J.*
4 *Am. Chem. Soc.* **2019**, *141* (33), 13028-13032.
- 5 725. Patra, B. K.; Agrawal, H.; Zheng, J.-Y.; Zha, X.; Travesset, A.; Garnett, E. C., Close-
6 Packed Ultrasoother Self-assembled Monolayer of CsPbBr₃ Perovskite Nanocubes. *ACS Appl.*
7 *Mater. Interfaces* **2020**, *12* (28), 31764–31769.
- 8 726. van der Burgt, J. S.; Geuchies, J. J.; van der Meer, B.; Vanrompay, H.; Zanaga, D.;
9 Zhang, Y.; Albrecht, W.; Petukhov, A. V.; Filion, L.; Bals, S.; Swart, I.; Vanmaekelbergh, D.,
10 Cuboidal Supraparticles Self-Assembled from Cubic CsPbBr₃ Perovskite Nanocrystals. *J. Phys.*
11 *Chem. C* **2018**, *122* (27), 15706-15712.
- 12 727. Xin, B.; Pak, Y.; Mitra, S.; Almalawi, D.; Alwadai, N.; Zhang, Y.; Roqan, I. S., Self-
13 Patterned CsPbBr₃ Nanocrystals for High-Performance Optoelectronics. *ACS Appl. Mater.*
14 *Interfaces* **2019**, *11* (5), 5223-5231.
- 15 728. Wang, K.-H.; Yang, J.-N.; Ni, Q.-K.; Yao, H.-B.; Yu, S.-H., Metal Halide Perovskite
16 Supercrystals: Gold–Bromide Complex Triggered Assembly of CsPbBr₃ Nanocubes. *Langmuir*
17 **2018**, *34* (2), 595-602.
- 18 729. Vila-Liarte, D.; Feil, M. W.; Manzi, A.; Garcia-Pomar, J. L.; Huang, H.; Döblinger, M.;
19 Liz-Marzán, L. M.; Feldmann, J.; Polavarapu, L.; Mihi, A., Templated-assembly of CsPbBr₃
20 perovskite nanocrystals into 2D photonic supercrystals with amplified spontaneous emission.
21 *Angew. Chem. Int. Ed.* **2020**, *59* (40), 17750-17756.
- 22 730. Krieg, F.; Sercel, P. C.; Burian, M.; Andrusiv, H.; Bodnarchuk, M. I.; Stöferle, T.;
23 Mahrt, R. F.; Naumenko, D.; Amenitsch, H.; Rainò, G.; Kovalenko, M. V., Monodisperse Long-
24 Chain Sulfobetaine-Capped CsPbBr₃ Nanocrystals and Their Superfluorescent Assemblies. *ACS*
25 *Central Sci.* **2021**, *7* (1), 135-144.
- 26 731. Prasad, B. L. V.; Sorensen, C. M.; Klabunde, K. J., Gold nanoparticle superlattices.
27 *Chem. Soc. Rev.* **2008**, *37* (9), 1871-1883.
- 28 732. Motte, L.; Billoudet, F.; Lacaze, E.; Pileni, M.-P., Self-organization of size-selected,
29 nanoparticles into three-dimensional superlattices. *Adv. Mater.* **1996**, *8* (12), 1018-1020.
- 30 733. Toso, S.; Baranov, D.; Giannini, C.; Marras, S.; Manna, L., Wide-Angle X-ray
31 Diffraction Evidence of Structural Coherence in CsPbBr₃ Nanocrystal Superlattices. *ACS Mater.*
32 *Lett.* **2019**, *1* (2), 272-276.
- 33 734. Zhou, C.; Zhong, Y.; Dong, H.; Zheng, W.; Tan, J.; Jie, Q.; Pan, A.; Zhang, L.; Xie, W.,
34 Cooperative excitonic quantum ensemble in perovskite-assembly superlattice microcavities. *Nat.*
35 *Commun.* **2020**, *11* (1), 329.
- 36 735. Baranov, D.; Fieramosca, A.; Yang, R. X.; Polimeno, L.; Lerario, G.; Toso, S.;
37 Giansante, C.; Giorgi, M. D.; Tan, L. Z.; Sanvitto, D.; Manna, L., Aging of Self-Assembled Lead
38 Halide Perovskite Nanocrystal Superlattices: Effects on Photoluminescence and Energy Transfer.
39 *ACS Nano* **2021**, *15* (1), 650-664.
- 40 736. Pan, A.; Jurow, M.; Zhao, Y.; Qiu, F.; Liu, Y.; Yang, J.; Urban, J. J.; He, L.; Liu, Y.,
41 Templated self-assembly of one-dimensional CsPbX₃ perovskite nanocrystal superlattices.
42 *Nanoscale* **2017**, *9* (45), 17688-17693.
- 43 737. Wang, K.; Xing, G.; Song, Q.; Xiao, S., Micro- and Nanostructured Lead Halide
44 Perovskites: From Materials to Integrations and Devices. *Adv. Mater.* **2021**, *33* (6).

- 1 738. Lin, C. H.; Zeng, Q.; Lafalce, E.; Yu, S.; Smith, M. J.; Yoon, Y. J.; Chang, Y.; Jiang, Y.;
2 Lin, Z.; Vardeny, Z. V.; Tsukruk, V. V., Large-Area Lasing and Multicolor Perovskite Quantum
3 Dot Patterns. *Adv. Opt. Mater.* **2018**, *6* (16), 1800474.
- 4 739. Liu, H.; Siron, M.; Gao, M.; Lu, D.; Bekenstein, Y.; Zhang, D.; Dou, L.; Alivisatos, A.
5 P.; Yang, P., Lead halide perovskite nanowires stabilized by block copolymers for Langmuir-
6 Blodgett assembly. *Nano Res.* **2020**, *13* (5), 1453-1458.
- 7 740. Gladman, A. S.; Matsumoto, E. A.; Nuzzo, R. G.; Mahadevan, L.; Lewis, J. A.,
8 Biomimetic 4D printing. *Nat. Mater.* **2016**, *15* (4), 413-+.
- 9 741. Zhou, N. J.; Bekenstein, Y.; Eisler, C. N.; Zhang, D. D.; Schwartzberg, A. M.; Yang, P.
10 D.; Alivisatos, A. P.; Lewis, J. A., Perovskite nanowire-block copolymer composites with
11 digitally programmable polarization anisotropy. *Sci. Adv.* **2019**, *5* (5).
- 12 742. Zhu, F.; Men, L.; Guo, Y.; Zhu, Q.; Bhattacharjee, U.; Goodwin, P. M.; Petrich, J. W.;
13 Smith, E. A.; Vela, J., Shape Evolution and Single Particle Luminescence of Organometal Halide
14 Perovskite Nanocrystals. *ACS Nano* **2015**, *9* (3), 2948-2959.
- 15 743. Akkerman, Q. A.; Motti, S. G.; Srimath Kandada, A. R.; Mosconi, E.; D'Innocenzo, V.;
16 Bertoni, G.; Marras, S.; Kamino, B. A.; Miranda, L.; De Angelis, F.; Petrozza, A.; Prato, M.;
17 Manna, L., Solution Synthesis Approach to Colloidal Cesium Lead Halide Perovskite
18 Nanoplatelets with Monolayer-Level Thickness Control. *J. Am. Chem. Soc.* **2016**, *138* (3), 1010-
19 1016.
- 20 744. Shamsi, J.; Dang, Z.; Bianchini, P.; Canale, C.; Di Stasio, F.; Brescia, R.; Prato, M.;
21 Manna, L., Colloidal Synthesis of Quantum Confined Single Crystal CsPbBr₃ Nanosheets with
22 Lateral Size Control up to the Micrometer Range. *Journal of the American Chemical Society*
23 **2016**, *138* (23), 7240-7243.
- 24 745. Imran, M.; Di Stasio, F.; Dang, Z.; Canale, C.; Khan, A. H.; Shamsi, J.; Brescia, R.;
25 Prato, M.; Manna, L., Colloidal Synthesis of Strongly Fluorescent CsPbBr₃ Nanowires with
26 Width Tunable down to the Quantum Confinement Regime. *Chem Mater* **2016**, *28* (18), 6450-
27 6454.
- 28 746. Tong, Y.; Bladt, E.; Aygüler, M. F.; Manzi, A.; Milowska, K. Z.; Hintermayr, V. A.;
29 Docampo, P.; Bals, S.; Urban, A. S.; Polavarapu, L.; Feldmann, J., Highly Luminescent Cesium
30 Lead Halide Perovskite Nanocrystals with Tunable Composition and Thickness by
31 Ultrasonication. *Angewandte Chemie International Edition* **2016**, *55* (44), 13887-13892.
- 32 747. Yu, Y.; Zhang, D.; Kisielowski, C.; Dou, L.; Kornienko, N.; Bekenstein, Y.; Wong, A.
33 B.; Alivisatos, A. P.; Yang, P., Atomic Resolution Imaging of Halide Perovskites. *Nano Lett.*
34 **2016**, *16* (12), 7530-7535.
- 35 748. Dang, Z.; Shamsi, J.; Akkerman, Q. A.; Imran, M.; Bertoni, G.; Brescia, R.; Manna, L.,
36 Low-Temperature Electron Beam-Induced Transformations of Cesium Lead Halide Perovskite
37 Nanocrystals. *ACS Omega* **2017**, *2* (9), 5660-5665.
- 38 749. Udayabhaskararao, T.; Houben, L.; Cohen, H.; Menahem, M.; Pinkas, I.; Avram, L.;
39 Wolf, T.; Teitelboim, A.; Leskes, M.; Yaffe, O.; Oron, D.; Kazes, M., A Mechanistic Study of
40 Phase Transformation in Perovskite Nanocrystals Driven by Ligand Passivation. *Chemistry of*
41 *Materials* **2018**, *30* (1), 84-93.
- 42 750. Brennan, M. C.; Kuno, M.; Rouvimov, S., Crystal Structure of Individual CsPbBr₃
43 Perovskite Nanocubes. *Inorg Chem* **2019**, *58* (2), 1555-1560.

- 1 751. Yu, Y.; Zhang, D.; Yang, P., Ruddlesden–Popper Phase in Two-Dimensional Inorganic
2 Halide Perovskites: A Plausible Model and the Supporting Observations. *Nano Lett.* **2017**, *17*
3 (9), 5489-5494.
- 4 752. Morrell, M. V.; He, X.; Luo, G.; Thind, A. S.; White, T. A.; Hachtel, J. A.; Borisevich,
5 A. Y.; Idrobo, J.-C.; Mishra, R.; Xing, Y., Significantly Enhanced Emission Stability of CsPbBr₃
6 Nanocrystals via Chemically Induced Fusion Growth for Optoelectronic Devices. *ACS Appl.*
7 *Nano Mater.* **2018**, *1* (11), 6091-6098.
- 8 753. Li, Y.; Zhou, W.; Li, Y.; Huang, W.; Zhang, Z.; Chen, G.; Wang, H.; Wu, G.-H.;
9 Rolston, N.; Vila, R.; Chiu, W.; Cui, Y., Unravelling Degradation Mechanisms and Atomic
10 Structure of Organic-Inorganic Halide Perovskites by Cryo-EM. *Joule* **2019**, *3* (11), 2854-2866.
- 11 754. Song, K.; Liu, L.; Zhang, D.; Hautzinger, M. P.; Jin, S.; Han, Y., Atomic-Resolution
12 Imaging of Halide Perovskites Using Electron Microscopy. *Adv. Energy Mater.* **2020**, *10* (26),
13 1904006.
- 14 755. Zhang, D.; Zhu, Y.; Liu, L.; Ying, X.; Hsiung, C.-E.; Sougrat, R.; Li, K.; Han, Y.,
15 Atomic-resolution transmission electron microscopy of electron beam-sensitive crystalline
16 materials. *Science* **2018**, *359* (6376), 675-679.
- 17 756. Van Aert, S.; Verbeeck, J.; Erni, R.; Bals, S.; Luysberg, M.; Dyck, D. V.; Tendeloo, G.
18 V., Quantitative atomic resolution mapping using high-angle annular dark field scanning
19 transmission electron microscopy. *Ultramicroscopy* **2009**, *109* (10), 1236-1244.
- 20 757. De Backer, A.; van den Bos, K. H. W.; Van den Broek, W.; Sijbers, J.; Van Aert, S.,
21 StatSTEM: An efficient approach for accurate and precise model-based quantification of atomic
22 resolution electron microscopy images. *Ultramicroscopy* **2016**, *171*, 104-116.
- 23 758. Akkerman, Q. A.; Bladt, E.; Petralanda, U.; Dang, Z.; Sartori, E.; Baranov, D.;
24 Abdelhady, A. L.; Infante, I.; Bals, S.; Manna, L., Fully Inorganic Ruddlesden–Popper Double
25 Cl–I and Triple Cl–Br–I Lead Halide Perovskite Nanocrystals. *Chem. Mater.* **2019**, *31* (6), 2182-
26 2190.
- 27 759. Polavarapu, L.; Nickel, B.; Feldmann, J.; Urban, A. S., Advances in Quantum-Confined
28 Perovskite Nanocrystals for Optoelectronics. *Advanced Energy Materials* **2017**, *7* (16).
- 29 760. Huang, S.; Li, Z.; Wang, B.; Zhu, N.; Zhang, C.; Kong, L.; Zhang, Q.; Shan, A.; Li, L.,
30 Morphology Evolution and Degradation of CsPbBr₃ Nanocrystals under Blue Light-Emitting
31 Diode Illumination. *ACS Appl Mater Interfaces* **2017**, *9* (8), 7249-7258.
- 32 761. Pan, J.; Quan, L. N.; Zhao, Y.; Peng, W.; Murali, B.; Sarmah, S. P.; Yuan, M.; Sinatra,
33 L.; Alyami, N. M.; Liu, J.; Yassitepe, E.; Yang, Z.; Voznyy, O.; Comin, R.; Hedhili, M. N.;
34 Mohammed, O. F.; Lu, Z. H.; Kim, D. H.; Sargent, E. H.; Bakr, O. M., Highly Efficient
35 Perovskite-Quantum-Dot Light-Emitting Diodes by Surface Engineering. *Adv. Mater.* **2016**, *28*
36 (39), 8718-8725.
- 37 762. Yuan, M.; Quan, L. N.; Comin, R.; Walters, G.; Sabatini, R.; Voznyy, O.; Hoogland, S.;
38 Zhao, Y.; Beauregard, E. M.; Kanjanaboos, P.; Lu, Z.; Kim, D. H.; Sargent, E. H., Perovskite
39 energy funnels for efficient light-emitting diodes. *Nat. Nanotech.* **2016**, *11* (10), 872-877.
- 40 763. Konstantatos, G.; Sargent, E. H., Nanostructured materials for photon detection. *Nat.*
41 *Nanotech.* **2010**, *5* (6), 391-400.
- 42 764. Petrus, M. L.; Schlipf, J.; Li, C.; Gujar, T. P.; Giesbrecht, N.; Müller-Buschbaum, P.;
43 Thelakkat, M.; Bein, T.; Hüttner, S.; Docampo, P., Capturing the Sun: A Review of the
44 Challenges and Perspectives of Perovskite Solar Cells. *Adv. Energy Mater.* **2017**, *7* (16).

- 1 765. Yang, D.; Li, X.; Zeng, H., Surface Chemistry of All Inorganic Halide Perovskite
2 Nanocrystals: Passivation Mechanism and Stability. *Advanced Materials Interfaces* **2018**, *5* (8).
- 3 766. Mundt, L. E.; Schelhas, L. T., Structural Evolution During Perovskite Crystal Formation
4 and Degradation: In Situ and Operando X - Ray Diffraction Studies. *Adv. Energy Mater.* **2019**.
- 5 767. Alsari, M.; Bikondoa, O.; Bishop, J.; Abdi-Jalebi, M.; Y. Ozer, L.; Hampton, M.;
6 Thompson, P.; T. Hörantner, M.; Mahesh, S.; Greenland, C.; Macdonald, J. E.; Palmisano, G.;
7 Snaith, H. J.; Lidzey, D. G.; Stranks, S. D.; Friend, R. H.; Lilliu, S., In situ simultaneous
8 photovoltaic and structural evolution of perovskite solar cells during film formation. *Energy*
9 *Environ. Sci.* **2018**, *11* (2), 383-393.
- 10 768. Fransishyn, K. M.; Kundu, S.; Kelly, T. L., Elucidating the Failure Mechanisms of
11 Perovskite Solar Cells in Humid Environments Using In Situ Grazing-Incidence Wide-Angle X-
12 ray Scattering. *ACS Energy Lett.* **2018**, *3* (9), 2127-2133.
- 13 769. Bhaway, S. M.; Qiang, Z.; Xia, Y.; Xia, X.; Lee, B.; Yager, K. G.; Zhang, L.; Kisslinger,
14 K.; Chen, Y. M.; Liu, K.; Zhu, Y.; Vogt, B. D., Operando Grazing Incidence Small-Angle X-ray
15 Scattering/X-ray Diffraction of Model Ordered Mesoporous Lithium-Ion Battery Anodes. *ACS*
16 *Nano* **2017**, *11* (2), 1443-1454.
- 17 770. Yang, D.; Löhner, F. C.; Körstgens, V.; Schreiber, A.; Cao, B.; Bernstorff, S.; Müller -
18 Buschbaum, P., In Operando GISAXS and GIWAXS Stability Study of Organic Solar Cells
19 Based on PffBT4T - 2OD:PC
20 71
21 BM with and without Solvent Additive. *Adv. Sci.* **2020**.
- 22 771. Schlipf, J.; Müller-Buschbaum, P., Structure of Organometal Halide Perovskite Films as
23 Determined with Grazing-Incidence X-Ray Scattering Methods. *Adv. Energy Mater.* **2017**, *7*
24 (16).
- 25 772. Boles, M. A.; Engel, M.; Talapin, D. V., Self-Assembly of Colloidal Nanocrystals: From
26 Intricate Structures to Functional Materials. *Chem Rev* **2016**, *116* (18), 11220-89.
- 27 773. Li, T.; Senesi, A. J.; Lee, B., Small Angle X-ray Scattering for Nanoparticle Research.
28 *Chem. Rev.* **2016**, *116* (18), 11128-80.
- 29 774. Muller-Buschbaum, P., The active layer morphology of organic solar cells probed with
30 grazing incidence scattering techniques. *Adv. Mater.* **2014**, *26* (46), 7692-709.
- 31 775. Tsybulya, S.; Yatsenko, D., X-ray diffraction analysis of ultradisperse systems: The
32 Debye formula. *J. Struct. Chem.* **2012**, *53* (1), 150-165.
- 33 776. Müller-Buschbaum, P., A basic introduction to grazing incidence small-angle X-ray
34 scattering. In *Applications of synchrotron light to scattering and diffraction in materials and life*
35 *sciences*, Springer: 2009; pp 61-89.
- 36 777. Müller-Buschbaum, P., Structure determination in thin film geometry using grazing
37 incidence small-angle scattering. In *Poly. Surf. Interfaces*, Springer: 2008; pp 17-46.
- 38 778. Putnam, C. D.; Hammel, M.; Hura, G. L.; Tainer, J. A., X-ray solution scattering
39 (SAXS) combined with crystallography and computation: defining accurate macromolecular
40 structures, conformations and assemblies in solution. *Q Rev Biophys* **2007**, *40* (3), 191-285.
- 41 779. Hexemer, A.; Muller-Buschbaum, P., Advanced grazing-incidence techniques for
42 modern soft-matter materials analysis. *IUCrJ* **2015**, *2* (Pt 1), 106-25.

- 1 780. Muller-Buschbaum, P., Grazing incidence small-angle X-ray scattering: an advanced
2 scattering technique for the investigation of nanostructured polymer films. *Anal. Bioanal. Chem.*
3 **2003**, 376 (1), 3-10.
- 4 781. Gordon, T. R.; Diroll, B. T.; Paik, T.; Doan-Nguyen, V. V. T.; Gaulding, E. A.; Murray,
5 C. B., Characterization of Shape and Monodispersity of Anisotropic Nanocrystals through
6 Atomistic X-ray Scattering Simulation. *Chem. Mater.* **2015**, 27 (7), 2502-2506.
- 7 782. Yager, K. G.; Zhang, Y.; Lu, F.; Gang, O., Periodic lattices of arbitrary nano-objects:
8 modeling and applications for self-assembled systems. *J. Appl. Crystallogr.* **2013**, 47 (1), 118-
9 129.
- 10 783. Brentano, J., Focussing method of crystal powder analysis by X-rays. *Proc. Phys. Soc.*
11 (*London*) **1924**, 37, 184.
- 12 784. Tong, Y.; Yao, E. P.; Manzi, A.; Bladt, E.; Wang, K.; Doblinger, M.; Bals, S.; Muller-
13 Buschbaum, P.; Urban, A. S.; Polavarapu, L.; Feldmann, J., Spontaneous Self-Assembly of
14 Perovskite Nanocrystals into Electronically Coupled Supercrystals: Toward Filling the Green
15 Gap. *Adv. Mater.* **2018**, e1801117.
- 16 785. Yuan, X.; Hou, X.; Li, J.; Qu, C.; Zhang, W.; Zhao, J.; Li, H., Thermal degradation of
17 luminescence in inorganic perovskite CsPbBr₃ nanocrystals. *Phys. Chem. Chem. Phys.* **2017**, 19
18 (13), 8934-8940.
- 19 786. Sharma, A. K.; Bansal, P.; Nim, G. K.; Kar, P., Essential Amino Acid-Enabled Lead
20 Bromide Perovskite Nanocrystals with High Stability. *Part. Part. Syst. Char.* **2019**, 36 (12).
- 21 787. Xuan, T.; Yang, X.; Lou, S.; Huang, J.; Liu, Y.; Yu, J.; Li, H.; Wong, K. L.; Wang, C.;
22 Wang, J., Highly stable CsPbBr₃ quantum dots coated with alkyl phosphate for white light-
23 emitting diodes. *Nanoscale* **2017**, 9 (40), 15286-15290.
- 24 788. Boote, B. W.; Andaraarachchi, H. P.; Rosales, B. A.; Blome-Fernandez, R.; Zhu, F.;
25 Reichert, M. D.; Santra, K.; Li, J.; Petrich, J. W.; Vela, J.; Smith, E. A., Unveiling the Photo- and
26 Thermal-Stability of Cesium Lead Halide Perovskite Nanocrystals. *Chemphyschem* **2019**, 20
27 (20), 2647-2656.
- 28 789. Soetan, N.; Erwin, W. R.; Tonigan, A. M.; Walker, D. G.; Bardhan, R., Solvent-Assisted
29 Self-Assembly of CsPbBr₃ Perovskite Nanocrystals into One-Dimensional Superlattice. *J. Phys.*
30 *Chem. C* **2017**, 121 (33), 18186-18194.
- 31 790. Tiensuu, V. H.; Ergun, S.; Alexander, L. E., X - Ray Diffraction from Small
32 Crystallites. *J. Appl. Phys.* **1964**, 35 (6), 1718-1720.
- 33 791. Kumpf, C.; Neder, R. B.; Niederdraenk, F.; Luczak, P.; Stahl, A.; Scheuermann, M.;
34 Joshi, S.; Kulkarni, S. K.; Barglik-Chory, C.; Heske, C.; Umbach, E., Structure determination of
35 CdS and ZnS nanoparticles: direct modeling of synchrotron-radiation diffraction data. *J. Chem.*
36 *Phys.* **2005**, 123 (22), 224707.
- 37 792. Yu, J. C.; Lee, A.-Y.; Kim, D. B.; Jung, E. D.; Kim, D. W.; Song, M. H., Enhancing the
38 Performance and Stability of Perovskite Nanocrystal Light-Emitting Diodes with a Polymer
39 Matrix. *Adv. Mater. Technol.* **2017**, 2 (6).
- 40 793. Akkerman, Q. A.; Meggiolaro, D.; Dang, Z.; De Angelis, F.; Manna, L., Fluorescent
41 Alloy CsPb_xMn_{1-x}I₃ Perovskite Nanocrystals with High Structural and Optical Stability. *ACS*
42 *Energy Lett.* **2017**, 2 (9), 2183-2186.
- 43 794. Goldschmidt, V. M., Die Gesetze der Krystallochemie. *Naturwissenschaften* **1926**, 14
44 (21), 477-485.

- 1 795. Liu, W.; Lin, Q.; Li, H.; Wu, K.; Robel, I.; Pietryga, J. M.; Klimov, V. I., Mn(2+)-
2 Doped Lead Halide Perovskite Nanocrystals with Dual-Color Emission Controlled by Halide
3 Content. *J. Am. Chem. Soc.* **2016**, *138* (45), 14954-14961.
- 4 796. Li, J.; Wang, L.; Yuan, X.; Bo, B.; Li, H.; Zhao, J.; Gao, X., Ultraviolet light induced
5 degradation of luminescence in CsPbBr₃ perovskite nanocrystals. *Mater. Res. Bull.* **2018**, *102*,
6 86-91.
- 7 797. Zhu, H.; Cai, T.; Que, M.; Song, J. P.; Rubenstein, B. M.; Wang, Z.; Chen, O., Pressure-
8 Induced Phase Transformation and Band-Gap Engineering of Formamidinium Lead Iodide
9 Perovskite Nanocrystals. *J. Phys. Chem. Lett.* **2018**, *9* (15), 4199-4205.
- 10 798. Quan, L. N.; Yuan, M.; Comin, R.; Voznyy, O.; Beauregard, E. M.; Hoogland, S.; Buin,
11 A.; Kirmani, A. R.; Zhao, K.; Amassian, A.; Kim, D. H.; Sargent, E. H., Ligand-Stabilized
12 Reduced-Dimensionality Perovskites. *J. Am. Chem. Soc.* **2016**, *138* (8), 2649-55.
- 13 799. Chen, W.; Tang, H.; Li, N.; Scheel, M. A.; Xie, Y.; Li, D.; Korstgens, V.; Schwartzkopf,
14 M.; Roth, S. V.; Wang, K.; Sun, X. W.; Muller-Buschbaum, P., Colloidal PbS quantum dot
15 stacking kinetics during deposition via printing. *Nanoscale Horiz.* **2020**, *5* (5), 880-885.
- 16 800. van der Burgt, J. S.; Geuchies, J. J.; van der Meer, B.; Vanrompay, H.; Zanaga, D.;
17 Zhang, Y.; Albrecht, W.; Petukhov, A. V.; Filion, L.; Bals, S.; Swart, I.; Vanmaekelbergh, D.,
18 Cuboidal Supraparticles Self-Assembled from Cubic CsPbBr₃ Perovskite Nanocrystals. *J Phys*
19 *Chem C Nanomater Interfaces* **2018**, *122* (27), 15706-15712.
- 20 801. De Caro, L.; Scattarella, F.; Altamura, D.; Arciniegas, M. P.; Siliqi, D.; Manna, L.;
21 Giannini, C., X-ray ptychographic mode of self-assembled CdSe/CdS octapod-shaped
22 nanocrystals in thick polymers. *J. Appl. Crystallogr.* **2020**, *53* (Pt 3), 741-747.
- 23 802. Sasaki, E.; Dragoman, R. M.; Mantri, S.; Dirin, D. N.; Kovalenko, M. V.; Hilvert, D.,
24 Self-Assembly of Proteinaceous Shells around Positively Charged Gold Nanomaterials Enhances
25 Colloidal Stability in High-Ionic-Strength Buffers. *ChemBiochem* **2020**, *21* (1-2), 74-79.
- 26 803. Dang, Z.; Dhanabalan, B.; Castelli, A.; Dhall, R.; Bustillo, K. C.; Marchelli, D.; Spirito,
27 D.; Petralanda, U.; Shamsi, J.; Manna, L.; Krahne, R.; Arciniegas, M. P., Temperature-Driven
28 Transformation of CsPbBr₃ Nanoplatelets into Mosaic Nanotiles in Solution through Self-
29 Assembly. *Nano Lett.* **2020**, *20* (3), 1808-1818.
- 30 804. Liao, Y.; Liu, H.; Zhou, W.; Yang, D.; Shang, Y.; Shi, Z.; Li, B.; Jiang, X.; Zhang, L.;
31 Quan, L. N.; Quintero-Bermudez, R.; Sutherland, B. R.; Mi, Q.; Sargent, E. H.; Ning, Z., Highly
32 Oriented Low-Dimensional Tin Halide Perovskites with Enhanced Stability and Photovoltaic
33 Performance. *J. Am. Chem. Soc.* **2017**, *139* (19), 6693-6699.
- 34 805. Tao, A. R.; Habas, S.; Yang, P., Shape Control of Colloidal Metal Nanocrystals. *Small*
35 **2008**, *4* (3), 310-325.
- 36 806. Chen, W.; Zhong, J.; Li, J.; Saxena, N.; Kreuzer, L. P.; Liu, H.; Song, L.; Su, B.; Yang,
37 D.; Wang, K.; Schlipf, J.; Korstgens, V.; He, T.; Wang, K.; Muller-Buschbaum, P., Structure and
38 Charge Carrier Dynamics in Colloidal PbS Quantum Dot Solids. *J. Phys. Chem. Lett.* **2019**, *10*
39 (9), 2058-2065.
- 40 807. Bekenstein, Y.; Dahl, J. C.; Huang, J.; Osowiecki, W. T.; Swabeck, J. K.; Chan, E. M.;
41 Yang, P.; Alivisatos, A. P., The Making and Breaking of Lead-Free Double Perovskite
42 Nanocrystals of Cesium Silver-Bismuth Halide Compositions. *Nano Lett.* **2018**, *18* (6), 3502-
43 3508.
- 44 808. Chen, J.; Ye, X.; Murray, C. B., Systematic electron crystallographic studies of self-
45 assembled binary nanocrystal superlattices. *ACS nano* **2010**, *4* (4), 2374-2381.

- 1 809. Jurow, M. J.; Morgenstern, T.; Eisler, C.; Kang, J.; Penzo, E.; Do, M.; Engelmayer, M.;
2 Osowiecki, W. T.; Bekenstein, Y.; Tassone, C.; Wang, L. W.; Alivisatos, A. P.; Brutting, W.;
3 Liu, Y., Manipulating the Transition Dipole Moment of CsPbBr₃ Perovskite Nanocrystals for
4 Superior Optical Properties. *Nano Lett.* **2019**, *19* (4), 2489-2496.
- 5 810. Wang, Y.; Liu, Y. H.; Zhang, Y.; Kowalski, P. J.; Rohrs, H. W.; Buhro, W. E.,
6 Preparation of primary amine derivatives of the magic-size nanocluster (CdSe)₁₃. *Inorg Chem*
7 **2013**, *52* (6), 2933-8.
- 8 811. Li, B.; Binks, D.; Cao, G.; Tian, J., Engineering Halide Perovskite Crystals through
9 Precursor Chemistry. *Small* **2019**, *15* (47), e1903613.
- 10 812. Pratap, S.; Keller, E.; Muller-Buschbaum, P., Emergence of lead halide perovskite
11 colloidal dispersions through aggregation and fragmentation: insights from the nanoscale to the
12 mesoscale. *Nanoscale* **2019**, *11* (8), 3495-3499.
- 13 813. Ban, M.; Zou, Y.; Rivett, J. P. H.; Yang, Y.; Thomas, T. H.; Tan, Y.; Song, T.; Gao, X.;
14 Credgington, D.; Deschler, F.; Sirringhaus, H.; Sun, B., Solution-processed perovskite light
15 emitting diodes with efficiency exceeding 15% through additive-controlled nanostructure
16 tailoring. *Nat Commun* **2018**, *9* (1), 3892.
- 17 814. Davis, N. J.; de la Pena, F. J.; Tabachnyk, M.; Richter, J. M.; Lamboll, R. D.; Booker, E.
18 P.; Wisnivesky Rocca Rivarola, F.; Griffiths, J. T.; Ducati, C.; Menke, S. M.; Deschler, F.;
19 Greenham, N. C., Photon Reabsorption in Mixed CsPbCl₃:CsPbI₃ Perovskite Nanocrystal Films
20 for Light-Emitting Diodes. *J. Phys. Chem. C* **2017**, *121* (7), 3790-3796.
- 21 815. Pospelov, G.; Van Herck, W.; Burle, J.; Carmona Loaiza, J. M.; Durniak, C.; Fisher, J.
22 M.; Ganeva, M.; Yurov, D.; Wuttke, J., BornAgain: software for simulating and fitting grazing-
23 incidence small-angle scattering. *J. Appl. Crystallogr.* **2020**, *53* (Pt 1), 262-276.
- 24 816. Jiang, Z., GIXSGUI: a MATLAB toolbox for grazing-incidence X-ray scattering data
25 visualization and reduction, and indexing of buried three-dimensional periodic nanostructured
26 films. *J. Appl. Crystallogr.* **2015**, *48* (3), 917-926.
- 27 817. Benecke, G.; Wagermaier, W.; Li, C.; Schwartzkopf, M.; Flucke, G.; Hoerth, R.; Zizak,
28 I.; Burghammer, M.; Metwalli, E.; Muller-Buschbaum, P.; Trebbin, M.; Forster, S.; Paris, O.;
29 Roth, S. V.; Fratzl, P., A customizable software for fast reduction and analysis of large X-ray
30 scattering data sets: applications of the new DPDAK package to small-angle X-ray scattering and
31 grazing-incidence small-angle X-ray scattering. *J. Appl. Crystallogr.* **2014**, *47* (Pt 5), 1797-1803.
- 32 818. Hammersley, A. P., FIT2D: a multi-purpose data reduction, analysis and visualization
33 program. *J. Appl. Crystallogr.* **2016**, *49* (2), 646-652.
- 34 819. Canneson, D.; Shornikova, E. V.; Yakovlev, D. R.; Rogge, T.; Mitioglu, A. A.;
35 Ballottin, M. V.; Christianen, P. C.; Lhuillier, E.; Bayer, M.; Biadala, L., Negatively charged and
36 dark excitons in CsPbBr₃ perovskite nanocrystals revealed by high magnetic fields. *Nano Lett.*
37 **2017**, *17* (10), 6177-6183.
- 38 820. Rong, Y.; Hu, Y.; Mei, A.; Tan, H.; Saidaminov, M. I.; Seok, S. I.; McGehee, M. D.;
39 Sargent, E. H.; Han, H., Challenges for commercializing perovskite solar cells. *Science* **2018**,
40 *361* (6408).
- 41 821. Stranks, S. D.; Burlakov, V. M.; Leijtens, T.; Ball, J. M.; Goriely, A.; Snaith, H. J.,
42 Recombination kinetics in organic-inorganic perovskites: excitons, free charge, and subgap
43 states. *Phys. Rev. Appl.* **2014**, *2* (3), 034007.
- 44 822. Walsh, A.; Zunger, A., Instilling defect tolerance in new compounds. *Nat. Mater.* **2017**,
45 *16* (10), 964-967.

- 1 823. Rosales, B. A.; Mundt, L. E.; Allen, T. G.; Moore, D. T.; Prince, K. J.; Wolden, C. A.;
2 Rumbles, G.; Schelhas, L. T.; Wheeler, L. M., Reversible multicolor chromism in layered
3 formamidinium metal halide perovskites. *Nat. Commun.* **2020**, *11* (1), 5234.
- 4 824. Noh, J. H.; Im, S. H.; Heo, J. H.; Mandal, T. N.; Seok, S. I., Chemical management for
5 colorful, efficient, and stable inorganic–organic hybrid nanostructured solar cells. *Nano Lett.*
6 **2013**, *13* (4), 1764-1769.
- 7 825. Eperon, G. E.; Stranks, S. D.; Menelaou, C.; Johnston, M. B.; Herz, L. M.; Snaith, H. J.,
8 Formamidinium lead trihalide: a broadly tunable perovskite for efficient planar heterojunction
9 solar cells. *Energy Environ. Sci.* **2014**, *7* (3), 982-988.
- 10 826. Tan, Z.-K.; Moghaddam, R. S.; Lai, M. L.; Docampo, P.; Higler, R.; Deschler, F.; Price,
11 M.; Sadhanala, A.; Pazos, L. M.; Credginton, D., Bright light-emitting diodes based on
12 organometal halide perovskite. *Nat. Nanotech.* **2014**, *9* (9), 687-692.
- 13 827. Sadhanala, A.; Deschler, F.; Thomas, T. H.; Dutton, S. E.; Goedel, K. C.; Hanusch, F.
14 C.; Lai, M. L.; Steiner, U.; Bein, T.; Docampo, P., Preparation of single-phase films of
15 CH₃NH₃Pb(I_{1-x}Br_x)₃ with sharp optical band edges. *J. Phys. Chem. Lett.* **2014**, *5* (15),
16 2501-2505.
- 17 828. Kumawat, N. K.; Dey, A.; Kumar, A.; Gopinathan, S. P.; Narasimhan, K. L.; Kabra, D.,
18 Band Gap Tuning of CH₃NH₃Pb(Br_{1-x}Cl_x)₃ Hybrid Perovskite for Blue Electroluminescence.
19 *ACS Appl. Mater. Interfaces* **2015**, *7* (24), 13119-13124.
- 20 829. Coduri, M.; Strobel, T. A.; Szafranski, M.; Katrusiak, A.; Mahata, A.; Cova, F.; Bonomi,
21 S.; Mosconi, E.; De Angelis, F.; Malavasi, L., Band Gap Engineering in MASnBr₃ and CsSnBr₃
22 Perovskites: Mechanistic Insights through the Application of Pressure. *J. Phys. Chem. Lett.* **2019**,
23 *10* (23), 7398-7405.
- 24 830. Umebayashi, T.; Asai, K.; Kondo, T.; Nakao, A., Electronic structures of lead iodide
25 based low-dimensional crystals. *Phys. Rev. B* **2003**, *67* (15), 155405.
- 26 831. Butler, K. T.; Frost, J. M.; Walsh, A., Band alignment of the hybrid halide perovskites
27 CH₃NH₃PbCl₃, CH₃NH₃PbBr₃ and CH₃NH₃PbI₃. *Materials Horizons* **2015**, *2* (2), 228-231.
- 28 832. Payne, D. J.; Egdell, R. G.; Walsh, A.; Watson, G. W.; Guo, J.; Glans, P. A.; Learmonth,
29 T.; Smith, K. E., Electronic Origins of Structural Distortions in Post-Transition Metal Oxides:
30 Experimental and Theoretical Evidence for a Revision of the Lone Pair Model. *Phys. Rev. Lett.*
31 **2006**, *96* (15), 157403.
- 32 833. Brivio, F.; Butler, K. T.; Walsh, A.; van Schilfgaarde, M., Relativistic quasiparticle self-
33 consistent electronic structure of hybrid halide perovskite photovoltaic absorbers. *Phys. Rev. B*
34 **2014**, *89* (15), 155204.
- 35 834. Even, J.; Pedesseau, L.; Jancu, J.-M.; Katan, C., Importance of Spin–Orbit Coupling in
36 Hybrid Organic/Inorganic Perovskites for Photovoltaic Applications. *J. Phys. Chem. Lett.* **2013**,
37 *4* (17), 2999-3005.
- 38 835. Noh, J. H.; Im, S. H.; Heo, J. H.; Mandal, T. N.; Seok, S. I., Chemical management for
39 colorful, efficient, and stable inorganic–organic hybrid nanostructured solar cells. *Nano letters*
40 **2013**, *13* (4), 1764-1769.
- 41 836. Filip, M. R.; Eperon, G. E.; Snaith, H. J.; Giustino, F., Steric engineering of metal-halide
42 perovskites with tunable optical band gaps. *Nat. Commun.* **2014**, *5* (1), 5757.

- 1 837. Brivio, F.; Walker, A. B.; Walsh, A., Structural and electronic properties of hybrid
2 perovskites for high-efficiency thin-film photovoltaics from first-principles. *APL Mater.* **2013**, *1*
3 (4), 042111.
- 4 838. Borriello, I.; Cantele, G.; Ninno, D., Ab initio investigation of hybrid organic-inorganic
5 perovskites based on tin halides. *Phys. Rev. B* **2008**, *77* (23), 235214.
- 6 839. Jellicoe, T. C.; Richter, J. M.; Glass, H. F. J.; Tabachnyk, M.; Brady, R.; Dutton, S. E.;
7 Rao, A.; Friend, R. H.; Credgington, D.; Greenham, N. C.; Böhm, M. L., Synthesis and Optical
8 Properties of Lead-Free Cesium Tin Halide Perovskite Nanocrystals. *Journal of the American*
9 *Chemical Society* **2016**, *138* (9), 2941-2944.
- 10 840. Hao, F.; Stoumpos, C. C.; Cao, D. H.; Chang, R. P. H.; Kanatzidis, M. G., Lead-free
11 solid-state organic-inorganic halide perovskite solar cells. *Nature Photonics* **2014**, *8* (6), 489-
12 494.
- 13 841. Creutz, S. E.; Crites, E. N.; De Siena, M. C.; Gamelin, D. R., Colloidal nanocrystals of
14 lead-free double-perovskite (elpasolite) semiconductors: synthesis and anion exchange to access
15 new materials. *Nano Lett.* **2018**, *18* (2), 1118-1123.
- 16 842. Meng, W.; Wang, X.; Xiao, Z.; Wang, J.; Mitzi, D. B.; Yan, Y., Parity-forbidden
17 transitions and their impact on the optical absorption properties of lead-free metal halide
18 perovskites and double perovskites. *J. Phys. Chem. Lett.* **2017**, *8* (13), 2999-3007.
- 19 843. Dey, A.; Richter, A. F.; Debnath, T.; Huang, H.; Polavarapu, L.; Feldmann, J., Transfer
20 of Direct to Indirect Bound Excitons by Electron Intervalley Scattering in Cs₂AgBiBr₆ Double
21 Perovskite Nanocrystals. *ACS Nano* **2020**.
- 22 844. Saba, M.; Cadelano, M.; Marongiu, D.; Chen, F.; Sarritzu, V.; Sestu, N.; Figus, C.;
23 Aresti, M.; Piras, R.; Geddo Lehmann, A.; Cannas, C.; Musinu, A.; Quochi, F.; Mura, A.;
24 Bongiovanni, G., Correlated electron-hole plasma in organometal perovskites. *Nat. Commun.*
25 **2014**, *5* (1), 5049.
- 26 845. Saba, M.; Cadelano, M.; Marongiu, D.; Chen, F.; Sarritzu, V.; Sestu, N.; Figus, C.;
27 Aresti, M.; Piras, R.; Geddo Lehmann, A.; Cannas, C.; Musinu, A.; Quochi, F.; Mura, A.;
28 Bongiovanni, G., Correlated electron-hole plasma in organometal perovskites. *Nature*
29 *Communications* **2014**, *5* (1), 5049.
- 30 846. Palummo, M.; Berrios, E.; Varsano, D.; Giorgi, G., Optical Excitations of Lead-free
31 Double Perovskites by Ab-initio Excited-State Methods. *ACS Energy Letters* **2020**, *5* (2), 457-
32 463.
- 33 847. De, A.; Das, S.; Mondal, N.; Samanta, A., Highly Luminescent Violet- and Blue-
34 Emitting Stable Perovskite Nanocrystals. *ACS Mater. Lett.* **2019**, *1*, 116-122.
- 35 848. Das, S.; De, A.; Samanta, A., Ambient Condition Mg²⁺-Doping Producing Highly
36 Luminescent Green- and Violet-Emitting Perovskite Nanocrystals with Reduced Toxicity and
37 Enhanced Stability. *J. Phys. Chem. Lett.* **2020**, *11*, 1178-1188.
- 38 849. Droseros, N.; Longo, G.; Brauer, J. C.; Sessolo, M.; Bolink, H. J.; Banerji, N., Origin of
39 the Enhanced Photoluminescence Quantum Yield in MAPbBr₃ Perovskite with Reduced Crystal
40 Size. *ACS Energy Lett.* **2018**, *3* (6), 1458-1466.
- 41 850. Dong, Y.; Qiao, T.; Kim, D.; Parobek, D.; Rossi, D.; Son, D. H., Precise Control of
42 Quantum Confinement in Cesium Lead Halide Perovskite Quantum Dots via Thermodynamic
43 Equilibrium. *Nano Letters* **2018**, *18* (6), 3716-3722.

- 1 851. Brennan, M. C.; Herr, J. E.; Nguyen-Beck, T. S.; Zinna, J.; Draguta, S.; Rouvimov, S.;
2 Parkhill, J.; Kuno, M., Origin of the Size-Dependent Stokes Shift in CsPbBr₃ Perovskite
3 Nanocrystals. *J. Am. Chem. Soc.* **2017**, *139* (35), 12201-12208.
- 4 852. Blancon, J.-C.; Tsai, H.; Nie, W.; Stoumpos, C. C.; Pedesseau, L.; Katan, C.;
5 Kepenekian, M.; Soe, C. M. M.; Appavoo, K.; Sfeir, M. Y.; Tretiak, S.; Ajayan, P. M.;
6 Kanatzidis, M. G.; Even, J.; Crochet, J. J.; Mohite, A. D., Extremely efficient internal exciton
7 dissociation through edge states in layered 2D perovskites. *Science* **2017**, *355* (6331), 1288-
8 1292.
- 9 853. Efros, A. L., Excitons in quantum-well structures. *SOVIET PHYSICS*
10 *SEMICONDUCTORS-USSR* **1986**, *20* (7), 808-812.
- 11 854. Tanaka, K.; Takahashi, T.; Kondo, T.; Umebayashi, T.; Asai, K.; Ema, K., Image charge
12 effect on two-dimensional excitons in an inorganic-organic quantum-well crystal. *Phys. Rev. B*
13 **2005**, *71* (4), 045312.
- 14 855. Saponi, D.; Kepenekian, M.; Pedesseau, L.; Katan, C.; Even, J., Quantum confinement
15 and dielectric profiles of colloidal nanoplatelets of halide inorganic and hybrid organic-inorganic
16 perovskites. *Nanoscale* **2016**, *8* (12), 6369-6378.
- 17 856. Katan, C.; Mercier, N.; Even, J., Quantum and dielectric confinement effects in lower-
18 dimensional hybrid perovskite semiconductors. *Chem. rev.* **2019**, *119* (5), 3140-3192.
- 19 857. Chakraborty, R.; Nag, A., Correlation of Dielectric Confinement and Excitonic Binding
20 Energy in 2D Layered Hybrid Perovskites Using Temperature Dependent Photoluminescence. *J.*
21 *Phys. Chem. C* **2020**, *124* (29), 16177-16185.
- 22 858. Takagi, H.; Kunugita, H.; Ema, K., Influence of the image charge effect on excitonic
23 energy structure in organic-inorganic multiple quantum well crystals. *Phys. Rev. B* **2013**, *87* (12),
24 125421.
- 25 859. Bohn, B. J.; Simon, T.; Gramlich, M.; Richter, A. F.; Polavarapu, L.; Urban, A. S.;
26 Feldmann, J., Dephasing and Quantum Beating of Excitons in Methylammonium Lead Iodide
27 Perovskite Nanoplatelets. *ACS Photonics* **2017**, *5* (2), 648-654.
- 28 860. Singh, S.; Li, C.; Panzer, F.; Narasimhan, K.; Graeser, A.; Gujar, T. P.; Köhler, A.;
29 Thelakkat, M.; Huettner, S.; Kabra, D., Effect of thermal and structural disorder on the electronic
30 structure of hybrid perovskite semiconductor CH₃NH₃PbI₃. *J. Phys. Chem. Lett.* **2016**, *7* (15),
31 3014-3021.
- 32 861. Wright, A. D.; Verdi, C.; Milot, R. L.; Eperon, G. E.; Perez-Osorio, M. A.; Snaith, H. J.;
33 Giustino, F.; Johnston, M. B.; Herz, L. M., Electron-phonon coupling in hybrid lead halide
34 perovskites. *Nat. Commun.* **2016**, *7*.
- 35 862. Wehrenfennig, C.; Eperon, G. E.; Johnston, M. B.; Snaith, H. J.; Herz, L. M., High
36 charge carrier mobilities and lifetimes in organolead trihalide perovskites. *Adv. Mater.* **2014**, *26*
37 (10), 1584-1589.
- 38 863. Singh, S.; Li, C.; Panzer, F.; Narasimhan, K. L.; Graeser, A.; Gujar, T. P.; Köhler, A.;
39 Thelakkat, M.; Huettner, S.; Kabra, D., Effect of Thermal and Structural Disorder on the
40 Electronic Structure of Hybrid Perovskite Semiconductor CH₃NH₃PbI₃. *The Journal of*
41 *Physical Chemistry Letters* **2016**, *7* (15), 3014-3021.

- 1 864. Saxena, R.; Kangsabanik, J.; Kumar, A.; Shahee, A.; Singh, S.; Jain, N.; Ghorui, S.;
2 Kumar, V.; Mahajan, A. V.; Alam, A.; Kabra, D., Contrasting temperature dependence of the
3 band gap in $\{\mathrm{CH}\}_3\{\mathrm{NH}\}_3\mathrm{Pb}\{\mathrm{X}\}_3$
4 $(\mathrm{X}=\mathrm{I}, \mathrm{Br}, \mathrm{Cl})$: Insight from lattice dilation and electron-
5 phonon coupling. *Physical Review B* **2020**, *102* (8), 081201.
- 6 865. Steele, J. A.; Puech, P.; Keshavarz, M.; Yang, R.; Banerjee, S.; Debroye, E.; Kim, C.
7 W.; Yuan, H.; Heo, N. H.; Vanacken, J., Giant electron–phonon coupling and deep conduction
8 band resonance in metal halide double perovskite. *ACS nano* **2018**, *12* (8), 8081-8090.
- 9 866. McCall, K. M.; Stoumpos, C. C.; Kostina, S. S.; Kanatzidis, M. G.; Wessels, B. W.,
10 Strong electron–phonon coupling and self-trapped excitons in the defect halide perovskites
11 $\mathrm{A}_3\mathrm{M}_2\mathrm{I}_9$ (A= Cs, Rb; M= Bi, Sb). *Chemistry of Materials* **2017**, *29* (9), 4129-4145.
- 12 867. Zelewski, S.; Urban, J.; Surrente, A.; Maude, D.; Kuc, A.; Schade, L.; Johnson, R.;
13 Dollmann, M.; Nayak, P.; Snaith, H., Revealing the nature of photoluminescence emission in the
14 metal-halide double perovskite $\mathrm{Cs}_2\mathrm{AgBiBr}_6$. *J. Mater. Chem. A* **2019**, *7* (27), 8350-8356.
- 15 868. Benin, B. M.; Dirin, D. N.; Morad, V.; Wörle, M.; Yakunin, S.; Rainò, G.; Nazarenko,
16 O.; Fischer, M.; Infante, I.; Kovalenko, M. V., Highly Emissive Self-Trapped Excitons in Fully
17 Inorganic Zero-Dimensional Tin Halides. *Angew. Chem. Int. Ed.* **2018**, *57* (35), 11329-11333.
- 18 869. Knox, R. S., Theory of Excitons. *Solid State Phys.* **1963**, *5*.
- 19 870. Kusrayev, Y. G.; Zakharchenya, B.; Karczewski, G.; Wojtowicz, T.; Kossut, J., Fine
20 structure of exciton levels in $\mathrm{CdTe}/\mathrm{CdMgTe}$ quantum wells. *Solid State Commun.* **1997**, *104* (8),
21 465-468.
- 22 871. Chamarro, M.; Gourdon, C.; Lavallard, P.; Lublinskaya, O.; Ekimov, A., Enhancement
23 of electron-hole exchange interaction in CdSe nanocrystals: A quantum confinement effect.
24 *Phys. Rev. B* **1996**, *53* (3), 1336.
- 25 872. Bayer, M.; Ortner, G.; Stern, O.; Kuther, A.; Gorbunov, A.; Forchel, A.; Hawrylak, P.;
26 Fafard, S.; Hinzer, K.; Reinecke, T., Fine structure of neutral and charged excitons in self-
27 assembled $\mathrm{In}(\mathrm{Ga})\mathrm{As}/(\mathrm{Al})\mathrm{GaAs}$ quantum dots. *Phys. Rev. B* **2002**, *65* (19), 195315.
- 28 873. Sercel, P. C.; Lyons, J. L.; Wickramaratne, D.; Vaxenburg, R.; Bernstein, N.; Efros, A.
29 L., Exciton fine structure in perovskite nanocrystals. *Nano Lett.* **2019**, *19* (6), 4068-4077.
- 30 874. Efros, A. L.; Rosen, M.; Kuno, M.; Nirmal, M.; Norris, D. J.; Bawendi, M., Band-edge
31 exciton in quantum dots of semiconductors with a degenerate valence band: Dark and bright
32 exciton states. *Phys. Rev. B* **1996**, *54* (7), 4843.
- 33 875. Korkusinski, M.; Voznyy, O.; Hawrylak, P., Fine structure and size dependence of
34 exciton and biexciton optical spectra in CdSe nanocrystals. *Phys. Rev. B* **2010**, *82* (24), 245304.
- 35 876. Korkusinski, M.; Hawrylak, P., Atomistic theory of emission from dark excitons in self-
36 assembled quantum dots. *Phys. Rev. B* **2013**, *87* (11), 115310.
- 37 877. Smoleński, T.; Kazimierzczuk, T.; Goryca, M.; Jakubczyk, T.; Wojnar, P.; Golnik, A.;
38 Kossacki, P., In-plane radiative recombination channel of a dark exciton in self-assembled
39 quantum dots. *Phys. Rev. B* **2012**, *86* (24), 241305.
- 40 878. Nirmal, M.; Norris, D. J.; Kuno, M.; Bawendi, M. G.; Efros, A. L.; Rosen, M.,
41 Observation of the "dark exciton" in CdSe quantum dots. *Phys. Rev. Lett.* **1995**, *75* (20), 3728.
- 42 879. Biadala, L.; Liu, F.; Tessier, M. D.; Yakovlev, D. R.; Dubertret, B.; Bayer, M.,
43 Recombination dynamics of band edge excitons in quasi-two-dimensional CdSe nanoplatelets.
44 *Nano Lett.* **2014**, *14* (3), 1134-1139.

- 1 880. Biadala, L.; Siebers, B.; Beyazit, Y.; Tessier, M. I. D.; Dupont, D.; Hens, Z.; Yakovlev,
2 D. R.; Bayer, M., Band-edge exciton fine structure and recombination dynamics in InP/ZnS
3 colloidal nanocrystals. *ACS nano* **2016**, *10* (3), 3356-3364.
- 4 881. Becker, M. A.; Vaxenburg, R.; Nedelcu, G.; Sercel, P. C.; Shabaev, A.; Mehl, M. J.;
5 Michopoulos, J. G.; Lambrakos, S. G.; Bernstein, N.; Lyons, J. L., Bright triplet excitons in
6 caesium lead halide perovskites. *Nature* **2018**, *553* (7687), 189-193.
- 7 882. Dey, A.; Rathod, P.; Kabra, D., Role of Localized States in Photoluminescence
8 Dynamics of High Optical Gain CsPbBr₃ Nanocrystals. *Adv. Opt. Mater.* **2018**, *6* (11), 1800109.
- 9 883. Sercel, P. C.; Lyons, J. L.; Wickramaratne, D.; Vaxenburg, R.; Bernstein, N.; Efros, A.
10 L., Exciton Fine Structure in Perovskite Nanocrystals. *Nano Letters* **2019**, *19* (6), 4068-4077.
- 11 884. Chen, L.; Li, B.; Zhang, C.; Huang, X.; Wang, X.; Xiao, M., Composition-Dependent
12 Energy Splitting between Bright and Dark Excitons in Lead Halide Perovskite Nanocrystals.
13 *Nano Lett.* **2018**, *18* (3), 2074-2080.
- 14 885. Tamarat, P.; Bodnarchuk, M. I.; Trebbia, J.-B.; Erni, R.; Kovalenko, M. V.; Even, J.;
15 Lounis, B., The ground exciton state of formamidinium lead bromide perovskite nanocrystals is a
16 singlet dark state. *Nat. Mater.* **2019**, *1*.
- 17 886. Xu, K.; Vliem, J. F.; Meijerink, A., Long-Lived Dark Exciton Emission in Mn-Doped
18 CsPbCl₃ Perovskite Nanocrystals. *J. Phys. Chem. C* **2019**, *123* (1), 979-984.
- 19 887. Fu, M.; Tamarat, P.; Huang, H.; Even, J.; Rogach, A. L.; Lounis, B., Neutral and
20 Charged Exciton Fine Structure in Single Lead Halide Perovskite Nanocrystals Revealed by
21 Magneto-optical Spectroscopy. *Nano Lett.* **2017**, *17* (5), 2895-2901.
- 22 888. Yin, C.; Chen, L.; Song, N.; Lv, Y.; Hu, F.; Sun, C.; Yu, W. W.; Zhang, C.; Wang, X.;
23 Zhang, Y.; Xiao, M., Bright-Exciton Fine-Structure Splittings in Single Perovskite Nanocrystals.
24 *Phys. Rev. Lett.* **2017**, *119* (2), 026401.
- 25 889. Bar-Ad, S.; Bar-Joseph, I., Exciton spin dynamics in GaAs heterostructures. *Phys. Rev.*
26 *Lett.* **1992**, *68* (3), 349-352.
- 27 890. Strohmair, S.; Dey, A.; Tong, Y.; Polavarapu, L.; Bohn, B. J.; Feldmann, J., Spin
28 Polarization Dynamics of Free Charge Carriers in CsPbI₃ Nanocrystals. *Nano Lett.* **2020**, *20* (7),
29 4724-4730.
- 30 891. Modern Problems in Condensed Matter Sciences. In *Optical Orientation*, Meier, F.;
31 Zakharchenya, B. P., Eds. North-Holland Physics Publishing (Elsevier Science Publishers B.V):
32 Amsterdam, The Netherlands, 1984; pp 73-105.
- 33 892. Giovanni, D.; Ma, H.; Chua, J.; Grätzel, M.; Ramesh, R.; Mhaisalkar, S.; Mathews, N.;
34 Sum, T. C., Highly Spin-Polarized Carrier Dynamics and Ultralarge Photoinduced Magnetization
35 in CH₃NH₃PbI₃ Perovskite Thin Films. *Nano Lett.* **2015**, *15* (3), 1553-1558.
- 36 893. Li, Y.; Luo, X.; Liu, Y.; Lu, X.; Wu, K., Size- and Composition-Dependent Exciton Spin
37 Relaxation in Lead Halide Perovskite Quantum Dots. *ACS Energy Letters* **2020**, *5* (5), 1701-
38 1708.
- 39 894. Di Nuzzo, D.; Cui, L.; Greenfield, J. L.; Zhao, B.; Friend, R. H.; Meskers, S. C. J.,
40 Circularly Polarized Photoluminescence from Chiral Perovskite Thin Films at Room
41 Temperature. *ACS Nano* **2020**, *14* (6), 7610-7616.

- 1 895. Kim, Y.-H.; Zhai, Y.; Gauldin, E. A.; Habisreutinger, S. N.; Moot, T.; Rosales, B. A.;
2 Lu, H.; Hazarika, A.; Brunecky, R.; Wheeler, L. M.; Berry, J. J.; Beard, M. C.; Luther, J. M.,
3 Strategies to Achieve High Circularly Polarized Luminescence from Colloidal Organic–
4 Inorganic Hybrid Perovskite Nanocrystals. *ACS Nano* **2020**.
- 5 896. Krishnakanth, K.; Seth, S.; Samanta, A.; Rao, S. V., Broadband ultrafast nonlinear
6 optical studies revealing exciting multi-photon absorption coefficients in phase pure zero-
7 dimensional Cs₄PbBr₆ perovskite films. *Nanoscale* **2019**, *11* (3), 945-954.
- 8 897. Wang, J.; Fang, C.; Ma, J.; Wang, S.; Jin, L.; Li, W.; Li, D., Aqueous Synthesis of Low-
9 Dimensional Lead Halide Perovskites for Room-Temperature Circularly Polarized Light
10 Emission and Detection. *ACS Nano* **2019**, *13* (8), 9473-9481.
- 11 898. Billing, D. G.; Lemmerer, A., Bis[(S)-[beta]-phenethylammonium]
12 tribromoplumbate(II). *Acta Crystallogr., Sect. E* **2003**, *59* (6), m381-m383.
- 13 899. Wang, C.-T.; Chen, K.; Xu, P.; Yeung, F.; Kwok, H.-S.; Li, G., Fully Chiral Light
14 Emission from CsPbX₃ Perovskite Nanocrystals Enabled by Cholesteric Superstructure Stacks.
15 *Adv. Funct. Mater.* **2019**, *29* (35), 1903155.
- 16 900. Georgieva, Z. N.; Bloom, B. P.; Ghosh, S.; Waldeck, D. H., Imprinting Chirality onto
17 the Electronic States of Colloidal Perovskite Nanoplatelets. *Adv. Mater.* **2018**, *30* (23), 1800097.
- 18 901. Shi, Y.; Duan, P.; Huo, S.; Li, Y.; Liu, M., Endowing Perovskite Nanocrystals with
19 Circularly Polarized Luminescence. *Adv. Mater.* **2018**, *30* (12), 1705011.
- 20 902. Steele, J. A.; Pan, W.; Martin, C.; Keshavarz, M.; Debroye, E.; Yuan, H.; Banerjee, S.;
21 Fron, E.; Jonckheere, D.; Kim, C. W.; Baekelant, W.; Niu, G.; Tang, J.; Vanacken, J.; Van der
22 Auweraer, M.; Hofkens, J.; Roeffaers, M. B. J., Photophysical Pathways in Highly Sensitive
23 Cs₂AgBiBr₆ Double-Perovskite Single-Crystal X-Ray Detectors. *Adv. Mater.* **2018**, *30* (46),
24 1804450.
- 25 903. Wang, L.; Xue, Y.; Cui, M.; Huang, Y.; Xu, H.; Qin, C.; Yang, J.; Dai, H.; Yuan, M., A
26 Chiral Reduced-Dimension Perovskite for an Efficient Flexible Circularly Polarized Light
27 Photodetector. *Angew. Chem. Int. Ed.* **2020**, *59* (16), 6442-6450.
- 28 904. Miao, J.; Zhang, F., Recent progress on highly sensitive perovskite photodetectors. *J.*
29 *Mater. Chem. C* **2019**, *7* (7), 1741-1791.
- 30 905. Chen, W.; Zhang, S.; Zhou, M.; Zhao, T.; Qin, X.; Liu, X.; Liu, M.; Duan, P., Two-
31 Photon Absorption-Based Upconverted Circularly Polarized Luminescence Generated in Chiral
32 Perovskite Nanocrystals. *J. Phys. Chem. Lett.* **2019**, *10* (12), 3290-3295.
- 33 906. Dang, Y.; Liu, X.; Sun, Y.; Song, J.; Hu, W.; Tao, X., Bulk Chiral Halide Perovskite
34 Single Crystals for Active Circular Dichroism and Circularly Polarized Luminescence. *J. Phys.*
35 *Chem. Lett.* **2020**, *11* (5), 1689-1696.
- 36 907. Ahn, J.; Ma, S.; Kim, J.-Y.; Kyhm, J.; Yang, W.; Lim, J. A.; Kotov, N. A.; Moon, J.,
37 Chiral 2D Organic Inorganic Hybrid Perovskite with Circular Dichroism Tunable Over Wide
38 Wavelength Range. *J. Am. Chem. Soc.* **2020**, *142* (9), 4206-4212.
- 39 908. Ahn, J.; Lee, E.; Tan, J.; Yang, W.; Kim, B.; Moon, J., A new class of chiral
40 semiconductors: chiral-organic-molecule-incorporating organic–inorganic hybrid perovskites.
41 *Mater. Horiz.* **2017**, *4* (5), 851-856.
- 42 909. Yuan, C.; Li, X.; Semin, S.; Feng, Y.; Rasing, T.; Xu, J., Chiral Lead Halide Perovskite
43 Nanowires for Second-Order Nonlinear Optics. *Nano Lett.* **2018**, *18* (9), 5411-5417.

- 1 910. Chen, C.; Gao, L.; Gao, W.; Ge, C.; Du, X.; Li, Z.; Yang, Y.; Niu, G.; Tang, J.,
2 Circularly polarized light detection using chiral hybrid perovskite. *Nat. Commun.* **2019**, *10* (1),
3 1927.
- 4 911. Long, G.; Sabatini, R.; Saidaminov, M. I.; Lakhwani, G.; Rasmita, A.; Liu, X.; Sargent,
5 E. H.; Gao, W., Chiral-perovskite optoelectronics. *Nat. Rev. Mater.* **2020**, *5* (6), 423-439.
- 6 912. Cahn, R. S.; Ingold, C.; Prelog, V., Specification of Molecular Chirality. *Angew. Chem.*
7 *Int. Ed.* **1966**, *5* (4), 385-415.
- 8 913. Gal, J., Molecular Chirality in Chemistry and Biology: Historical Milestones. *Helvetica*
9 *Chimica Acta* **2013**, *96* (9), 1617-1657.
- 10 914. Long, G.; Jiang, C.; Sabatini, R.; Yang, Z.; Wei, M.; Quan, L. N.; Liang, Q.; Rasmita,
11 A.; Askerka, M.; Walters, G.; Gong, X.; Xing, J.; Wen, X.; Quintero-Bermudez, R.; Yuan, H.;
12 Xing, G.; Wang, X. R.; Song, D.; Voznyy, O.; Zhang, M.; Hoogland, S.; Gao, W.; Xiong, Q.;
13 Sargent, E. H., Spin control in reduced-dimensional chiral perovskites. *Nat. Photonics* **2018**, *12*
14 (9), 528-533.
- 15 915. Lu, H.; Xiao, C.; Song, R.; Li, T.; Maughan, A. E.; Levin, A.; Brunecky, R.; Berry, J. J.;
16 Mitzi, D. B.; Blum, V.; Beard, M. C., Highly Distorted Chiral Two-Dimensional Tin Iodide
17 Perovskites for Spin Polarized Charge Transport. *J. Am. Chem. Soc.* **2020**, *142* (30), 13030-
18 13040.
- 19 916. Yang, B.; Hong, F.; Chen, J.; Tang, Y.; Yang, L.; Sang, Y.; Xia, X.; Guo, J.; He, H.;
20 Yang, S., Colloidal Synthesis and Charge - Carrier Dynamics of Cs₂AgSb_{1-y}BiyX₆ (X: Br, Cl;
21 0 ≤ y ≤ 1) Double Perovskite Nanocrystals. *Angew. Chem. Int. Ed.* **2019**, *58* (8), 2278-2283.
- 22 917. Schreiber, R.; Luong, N.; Fan, Z.; Kuzyk, A.; Nickels, P. C.; Zhang, T.; Smith, D. M.;
23 Yurke, B.; Kuang, W.; Govorov, A. O.; Liedl, T., Chiral plasmonic DNA nanostructures with
24 switchable circular dichroism. *Nat. Commun.* **2013**, *4* (1), 2948.
- 25 918. Zhou, C.; Duan, X.; Liu, N., DNA-Nanotechnology-Enabled Chiral Plasmonics: From
26 Static to Dynamic. *Acc. Chem. Res.* **2017**, *50* (12), 2906-2914.
- 27 919. Shen, X.; Song, C.; Wang, J.; Shi, D.; Wang, Z.; Liu, N.; Ding, B., Rolling Up Gold
28 Nanoparticle-Dressed DNA Origami into Three-Dimensional Plasmonic Chiral Nanostructures.
29 *J. Am. Chem. Soc.* **2012**, *134* (1), 146-149.
- 30 920. Herz, L. M., Charge-Carrier Dynamics in Organic-Inorganic Metal Halide Perovskites.
31 *Ann. Rev. Phys. Chem.* **2016**, *67* (1), 65-89.
- 32 921. Herz, L. M., Charge-Carrier Mobilities in Metal Halide Perovskites: Fundamental
33 Mechanisms and Limits. *ACS Energy Letters* **2017**, *2* (7), 1539-1548.
- 34 922. Yang, Y.; Ostrowski, D. P.; France, R. M.; Zhu, K.; Lagemaat, J. v. d.; Luther, J. M.;
35 Beard, M. C., Observation of a Hot-phonon Bottleneck in Lead-iodide Perovskites. *Nat.*
36 *Photonics* **2016**, *10*, 53-59.
- 37 923. Manser, J. S.; Kamat, P. V., Band filling with free charge carriers in organometal halide
38 perovskites. *Nat. Photonics* **2014**, *8* (9), 737-743.
- 39 924. Zhai, Y.; Baniya, S.; Zhang, C.; Li, J.; Haney, P.; Sheng, C.-X.; Ehrenfreund, E.;
40 Vardeny, Z. V., Giant Rashba splitting in 2D organic-inorganic halide perovskites measured by
41 transient spectroscopies. *Science Advances* **2017**, *3* (7), e1700704.
- 42 925. Mondal, N.; Samanta, A., Complete Ultrafast Charge Carrier Dynamics in Photo-excited
43 All-inorganic Perovskite Nanocrystals (CsPbX₃). *Nanoscale* **2017**, *9*, 1878-1885.

- 1 926. Chung, H.; Jung, S. I.; Kim, H. J.; Cha, W.; Sim, E.; Kim, D.; KyuKoh, W.; Kim, J.,
2 Composition-Dependent Hot Carrier Relaxation Dynamics in Cesium Lead Halide (CsPbX₃, X =
3 Br and I) Perovskite Nanocrystals. *Angew. Chem. Int. Ed.* **2017**, *56*, 4160-4164.
- 4 927. Miyata, K.; Meggiolaro, D.; Trinh, M. T.; Joshi, P. P.; Mosconi, E.; Jones, S. C.;
5 Angelis, F. D.; Zhu, X.-Y., Large Polarons in Lead Halide Perovskites. *Sci. Adv.* **2017**, *3*,
6 e1701217.
- 7 928. Makarov, N. S.; Guo, S.; Isaienko, O.; Liu, W.; Robel, I. n.; Klimov, V. I., Spectral and
8 Dynamical Properties of Single Excitons, Biexcitons, and Trions in Cesium–Lead-Halide
9 Perovskite Quantum Dots. *Nano Lett.* **2016**, *16*, 2349-2362.
- 10 929. Aneesh, J.; Swarnkar, A.; Ravi, V. K.; Sharma, R.; Nag, A.; Adarsh, K. V., Ultrafast
11 Exciton Dynamics in Colloidal CsPbBr₃ Perovskite Nanocrystals: Biexciton Effect and Auger
12 Recombination. *J. Phys. Chem. C* **2017**, *121*, 4734-4739.
- 13 930. Rossi, D.; Wang, H.; Dong, Y.; Qiao, T.; Qian, X.; Son, D. H., Light-Induced Activation
14 of Forbidden Exciton Transition in Strongly Confined Perovskite Quantum Dots. *ACS Nano*
15 **2018**, *12*, 12436-12443.
- 16 931. Hintermayr, V. A.; Polavarapu, L.; Urban, A. S.; Feldmann, J., Accelerated Carrier
17 Relaxation through Reduced Coulomb Screening in TwoDimensional Halide Perovskite
18 Nanoplatelets. *ACS Nano* **2018**, *12*, 10151-10158.
- 19 932. Shen, Q.; Ripolles, T. S.; Even, J.; Ogomi, Y.; Koji Nishinaka; Izuishi, T.; Nakazawa,
20 N.; Zhang, Y.; Ding, C.; Liu, F.; Toyoda, T.; Yoshino, K.; Minemoto, T.; Katayama, K.; Hayase,
21 S., Slow Hot Carrier Cooling in Cesium Lead Iodide Perovskites. *Appl. Phys. Lett.* **2017**, *111*,
22 153903.
- 23 933. Diroll, B. T.; Schaller, R. D., Intraband Cooling in All-Inorganic and Hybrid Organic–
24 Inorganic Perovskite Nanocrystals. *Adv. Funct. Mater.* **2019**, *29*, 1901725.
- 25 934. Chen, J.; Messing, M. E.; Zheng, K.; Pullerits, T., Cation-Dependent Hot Carrier
26 Cooling in Halide Perovskite Nanocrystals. *J. Am. Chem. Soc.* **2019**, *141*, 3532-3540.
- 27 935. Fu, J.; Xu, Q.; Han, G.; Wu, B.; Huan, C. H. A.; Leek, M. L.; Sum, T. C., Hot carrier
28 cooling mechanisms in halide perovskites. *Nat. Commun.* **2017**, *8* (1), 1300.
- 29 936. Hopper, T. R.; Gorodetsky, A.; Frost, J. M.; Müller, C.; Lovrincic, R.; Bakulin, A. A.,
30 Ultrafast Intraband Spectroscopy of Hot Carrier Cooling in Lead-Halide Perovskites. *ACS*
31 *Energy Lett.* **2018**, *3*, 2199-2205.
- 32 937. Madjet, M. E.; Berdiyrov, G. R.; El-Mellouhi, F.; Alharbi, F. H.; Akimov, A. V.; Kais,
33 S., Cation Effect on Hot Carrier Cooling in Halide Perovskite Materials. *J. Phys. Chem. Lett.*
34 **2017**, *8*, 4439-4445.
- 35 938. Li, Y.; Ding, T.; Luo, X.; Tian, Y.; Lu, X.; Wu, K., Synthesis and Spectroscopy of
36 Monodispersed, Quantum-Confined FAPbBr₃ Perovskite Nanocrystals. *Chem. Mater.* **2020**, *32*,
37 549-556.
- 38 939. Verma, S. D.; Gu, Q.; Sadhanala, A.; Venugopalan, V.; Rao, A., Slow Carrier Cooling in
39 Hybrid Pb–Sn Halide Perovskites. *ACS Energy Lett.* **2019**, *4*, 736-740.
- 40 940. Fang, H.-H.; Adjokatse, S.; Shao, S.; Even, J.; Loi, M. A., Long-lived Hot-carrier Light
41 Emission and Large Blue Shift in Formamidinium Tin Triiodide Perovskites. *Nat. Commun.*
42 **2018**, *9*, 243.

- 1 941. Liu, F.; Zhang, Y.; Ding, C.; Kawabata, K.; Yoshihara, Y.; Toyoda, T.; Hayase, S.;
2 Minemoto, T.; Wang, R.; Shen, Q., Trioctylphosphine Oxide Acts as Alkahest for SnX₂/PbX₂: A
3 General Synthetic Route to Perovskite ASn_xPb_{1-x}X₃ (A = Cs, FA, MA; X = Cl, Br, I) Quantum
4 Dots. *Chem. Mater.* **2020**, DOI: 10.1021/acs.chemmater.9b03918.
- 5 942. Li, M.; Fu, J.; Xu, Q.; Sum, T. C., Slow Hot-Carrier Cooling in Halide Perovskites:
6 Prospects for Hot-Carrier Solar Cells. *Adv. Mater.* **2019**, *31*, 1802486.
- 7 943. Li, Y.; Lai, R.; Luo, X.; Liu, X.; Ding, T.; Lu, X.; Wu, K., On the Absence of a Phonon
8 Bottleneck in Strongly Confined CsPbBr₃ Perovskite Nanocrystals. *Chem. Sci.* **2019**, *10*, 5983-
9 5989.
- 10 944. Yin, J.; Maity, P.; Naphade, R.; Cheng, B.; He, J.-H.; Bakr, O. M.; das, J.-L. B.;
11 Mohammed, O. F., Tuning Hot Carrier Cooling Dynamics by Dielectric Confinement in Two-
12 Dimensional Hybrid Perovskite Crystals. *ACS Nano* **2019**, *13*, 12621-12629.
- 13 945. Kaur, G.; Babu, K. J.; Ghorai, N.; Goswami, T.; Maiti, S.; Ghosh, H. N., Polaron-
14 Mediated Slow Carrier Cooling in a Type-1 3D/0D CsPbBr₃@Cs₄PbBr₆ Core-Shell Perovskite
15 System. *J. Phys. Chem. Lett.* **2019**, *10*, 5302-5311.
- 16 946. Kovalenko, M. V.; Protesescu, L.; Bodnarchuk, M. I., Properties and Potential
17 Optoelectronic Applications of Lead Halide Perovskite Nanocrystals. *Science* **2017**, *358*, 745-
18 750.
- 19 947. Brandt, R. E.; Poindexter, J. R.; Gorai, P.; Kurchin, R. C.; Hoye, R. L. Z.; Nienhaus, L.;
20 Wilson, M. W. B.; Polizzotti, J. A.; Sereika, R.; Žaltauskas, R.; Lee, L. C.; MacManus-Driscoll,
21 J. L.; Bawendi, M.; Stevanovic, V.; Buonassisi, T., Searching for “Defect-Tolerant” Photovoltaic
22 Materials: Combined Theoretical and Experimental Screening. *Chem. Mater.* **2017**, *29*, 4667-
23 4674.
- 24 948. deQuilettes, D. W.; Frohna, K.; Emin, D.; Kirchartz, T.; Bulovic, V.; Ginger, D. S.;
25 Stranks, S. D., Charge-Carrier Recombination in Halide Perovskites Focus Review. *Chem. Rev.*
26 **2019**, *119*, 11007-11019.
- 27 949. Mondal, N.; De, A.; Das, S.; Paul, S.; Samanta, A., Ultrafast Carrier Dynamics of Metal
28 Halide Perovskite Nanocrystals and Perovskite Composites. *Nanoscale* **2019**, *11*, 9796-9818.
- 29 950. Zheng, X.; Hou, Y.; Sun, H.-T.; Mohammed, O. F.; Sargent, E. H.; Bakr, O. M.,
30 Reducing Defects in Halide Perovskite Nanocrystals for Light Emitting Applications. *J. Phys.*
31 *Chem. Lett.* **2019**, *10*, 2629-2640.
- 32 951. Ball, J. M.; Petrozza, A., Defects in perovskite-halides and their effects in solar cells.
33 *Nat. Mater.* **2016**, *1*, 16149.
- 34 952. Jin, H.; Debroye, E.; Keshavarz, M.; Scheblykin, I. G.; Roeyfaers, M. B. J.; Hofkens, J.;
35 Steele, J. A., It’s a Trap! On the Nature of Localised States and Charge Trapping in Lead
36 Halide Perovskites. *Mater. Horiz* **2019**, DOI: 10.1039/c9mh00500e.
- 37 953. Saxena, R.; Kumar, A.; Jain, N.; Kumawat, N. K.; Narasimhan, K. L.; Kabra, D.,
38 Photophysical Model for Non-Exponential Relaxation Dynamics in Hybrid Perovskite
39 Semiconductors. *J. Phys. Chem. C* **2018**, *122* (2), 1119-1124.
- 40 954. Wang, S.; Du, L.; Jin, Z.; Xin, Y.; Mattoussi, H., Enhanced Stabilization and Easy Phase
41 Transfer of CsPbBr₃ Perovskite Quantum Dots Promoted by High-Affinity Polyzwitterionic
42 Ligands. *Journal of the American Chemical Society* **2020**, *142* (29), 12669-12680.

- 1 955. Chirvony, V. S.; Gonzalez-Carrero, S.; Suarez, I.; Galian, R. E.; Sessolo, M.; Bolink, H.
2 J.; Martínez-Pastor, J. P.; Perez-Prieto, J., Delayed Luminescence in Lead Halide Perovskite
3 Nanocrystals. *J. Phys. Chem. C* **2017**, *121*, 13381-13390.
- 4 956. Wang, Y.; Zhi, M.; Chan, Y., Delayed Exciton Formation Involving Energetically
5 Shallow Trap States in Colloidal CsPbBr₃ Quantum Dots. *J. Phys. Chem. C* **2017**, *121*, 28498-
6 28505.
- 7 957. Liu, F.; Zhang, Y.; Ding, C.; Toyoda, T.; Ogomi, Y.; Ripolles, T. S.; Hayase, S.;
8 Minemoto, T.; Yoshino, K.; Dai, S.; Shen, Q., Ultrafast Electron Injection from Photoexcited
9 Perovskite CsPbI₃ QDs into TiO₂ Nanoparticles with Injection Efficiency near 99%. *J. Phys.*
10 *Chem. Lett.* **2018**, *9*, 294-297.
- 11 958. Liu, F.; Zhang, Y.; Ding, C.; Kobayashi, S.; Izuishi, T.; Nakazawa, N.; Toyoda, T.;
12 Ohta, T.; Hayase, S.; Minemoto, T.; Yoshino, K.; Dai, S.; Shen, Q., Highly Luminescent Phase-
13 Stable CsPbI₃ Perovskite Quantum Dots Achieving Near 100% Absolute Photoluminescence
14 Quantum Yield. *ACS Nano* **2017**, *11*, 10373-10383.
- 15 959. Nenon, D. P.; Pressler, K.; Kang, J.; Koscher, B. A.; Olshansky, J. H.; Osowiecki, W. T.;
16 Koc, M. A.; Wang, L.-W.; Alivisatos, A. P., Design Principles for Trap-Free CsPbX₃
17 Nanocrystals: Enumerating and Eliminating Surface Halide Vacancies with Softer Lewis Bases.
18 *J. Am. Chem. Soc.* *2018*, *140*, 17760–17772 **2018**, *140*, 17760-17772.
- 19 960. Rossi, D.; Parobek, D.; Dong, Y.; Son, D. H., Dynamics of Exciton–Mn Energy
20 Transfer in Mn-Doped CsPbCl₃ Perovskite Nanocrystals. *J. Phys. Chem. C* **2017**, *121*, 17143-
21 17149.
- 22 961. Lai, R.; Wu, K., Picosecond Electron Trapping Limits the Emissivity of CsPbCl₃
23 Perovskite Nanocrystals. *J. Chem. Phys.* **2019**, *151*, 194701.
- 24 962. Ahmed, T.; Seth, S.; Samanta, A., Mechanistic Investigation of the Defect Activity
25 Contributing to the Photoluminescence Blinking of CsPbBr₃ Perovskite Nanocrystals. *ACS Nano*
26 **2019**, *13*, 13537-13544.
- 27 963. Mandal, S.; Mukherjee, S.; De, C. K.; Roy, D.; Swarnali Ghosh; Mandal, P. K., Extent
28 of Shallow/Deep Trap States beyond the Conduction Band Minimum in Defect-Tolerant
29 CsPbBr₃ Perovskite Quantum Dot: Control over the Degree of Charge Carrier Recombination. *J.*
30 *Phys. Chem. Lett.* **2020**, *11*, 1702-1707.
- 31 964. Yang, B.; Chen, J.; Hong, F.; Mao, X.; Zheng, K.; Yang, S.; Yajuan Li; Pullerits, T.;
32 Deng, W.; Han, K., Lead-Free, Air-Stable All-Inorganic Cesium Bismuth Halide Perovskite
33 Nanocrystals. *Angew. Chem. Int. Ed.* **2017**, *56*, 12471-12475.
- 34 965. Yang, B.; Hong, F.; Chen, J.; Tang, Y.; Yang, L.; Sang, Y.; Xia, X.; Guo, J.; He, H.;
35 Yang, S.; Deng, W.; Han, K., Colloidal Synthesis and Charge-Carrier Dynamics of Cs₂AgSb₁₋
36 _yBi_yX₆ (X: Br, Cl; 0 ≤ y ≤ 1) Double Perovskite Nanocrystals. *Angew. Chem. Int. Ed.* **2019**, *58*,
37 2278-2283.
- 38 966. Yang, B.; Mao, X.; Hong, F.; Meng, W.; Tang, Y.; Xia, X.; Yang, S.; Deng, W.; Han,
39 K., Lead-Free Direct Band Gap Double-Perovskite Nanocrystals with Bright Dual-Color
40 Emission. *J. Am. Chem. Soc.* **2018**, *140*, 17001-17006.
- 41 967. Pal, J.; Manna, S.; Mondal, A.; Das, S.; Adarsh, K. V.; Nag, A., Colloidal Synthesis and
42 Photophysics of M₃Sb₂I₉ (M = Cs and Rb) Nanocrystals :Lead-Free Perovskites. *Angew. Chem.*
43 *Int. Ed.* **2017**, *56*, 14187-14191.
- 44 968. Yang, B.; Han, K., Charge-Carrier Dynamics of Lead-Free Halide Perovskite
45 Nanocrystals. *Acc. Chem. Res.* **2019**, *52*, 3188-3198.

- 1 969. Woo, H. C.; Choi, J. W.; Shin, J.; Chin, S.-H.; Ann, M. H.; Lee, C.-L., Temperature-
2 Dependent Photoluminescence of CH₃NH₃PbBr₃ Perovskite Quantum Dots and Bulk
3 Counterparts. *J. Phys. Chem. Lett.* **2018**, *9* (14), 4066-4074.
- 4 970. Makarov, N. S.; Guo, S.; Isaienko, O.; Liu, W.; Robel, I.; Klimov, V. I., Spectral and
5 Dynamical Properties of Single Excitons, Biexcitons, and Trions in Cesium–Lead-Halide
6 Perovskite Quantum Dots. *Nano Lett.* **2016**, *16* (4), 2349-2362.
- 7 971. Eperon, G. E.; Jedlicka, E.; Ginger, D. S., Biexciton Auger Recombination Differs in
8 Hybrid and Inorganic Halide Perovskite Quantum Dots. *J. Phys. Chem. Lett.* **2018**, *9* (1), 104-
9 109.
- 10 972. Klimov, V. I., Spectral and Dynamical Properties of Multiexcitons in Semiconductor
11 Nanocrystals. *Ann. Rev. Phys. Chem.* **2007**, *58* (1), 635-673.
- 12 973. Yang, B.; Han, K., Charge-Carrier Dynamics of Lead-Free Halide Perovskite
13 Nanocrystals. *Accounts of Chemical Research* **2019**, *52* (11), 3188-3198.
- 14 974. Egger, D. A.; Bera, A.; Cahen, D.; Hodes, G.; Kirchartz, T.; Kronik, L.; Lovrincic, R.;
15 Rappe, A. M.; Reichman, D. R.; Yaffe, O., What Remains Unexplained about the Properties of
16 Halide Perovskites? *Adv. Mater.* **2018**, *30* (20), 1800691.
- 17 975. Chen, J.; Zhang, Q.; Shi, J.; Zhang, S.; Du, W.; Mi, Y.; Shang, Q.; Liu, P.; Sui, X.; Wu,
18 X.; Wang, R.; Peng, B.; Zhong, H.; Xing, G.; Qiu, X.; Sum, T. C.; Liu, X., Room temperature
19 continuous-wave excited biexciton emission in perovskite nanoplatelets via plasmonic nonlinear
20 fano resonance. *Commun. Physics* **2019**, *2* (1), 80.
- 21 976. Straus, D. B.; Kagan, C. R., Electrons, Excitons, and Phonons in Two-Dimensional
22 Hybrid Perovskites: Connecting Structural, Optical, and Electronic Properties. *J. Phys. Chem.*
23 *Lett.* **2018**, *9* (6), 1434-1447.
- 24 977. Jiang, Y.; Wang, X.; Pan, A., Properties of Excitons and Photogenerated Charge Carriers
25 in Metal Halide Perovskites. *Adv. Mater.* **2019**, *31* (47), 1806671.
- 26 978. Miyata, A.; Mitioglu, A.; Plochocka, P.; Portugall, O.; Wang, J. T.-W.; Stranks, S. D.;
27 Snaith, H. J.; Nicholas, R. J., Direct measurement of the exciton binding energy and effective
28 masses for charge carriers in organic–inorganic tri-halide perovskites. *Nat. Phys.* **2015**, *11* (7),
29 582-587.
- 30 979. Kumagai, M.; Takagahara, T., Excitonic and nonlinear-optical properties of dielectric
31 quantum-well structures. *Phys. Rev. B* **1989**, *40* (18), 12359-12381.
- 32 980. Yang, Y.; Yang, M.; Li, Z.; Crisp, R.; Zhu, K.; Beard, M. C., Comparison of
33 Recombination Dynamics in CH₃NH₃PbBr₃ and CH₃NH₃PbI₃ Perovskite Films: Influence of
34 Exciton Binding Energy. *J. Phys. Chem. Lett.* **2015**, *6* (23), 4688-4692.
- 35 981. Hong, X.; Ishihara, T.; Nurmikko, A. V., Dielectric confinement effect on excitons in
36 $\{\text{PbI}\}_4$ -based layered semiconductors. *Physical Review B* **1992**, *45* (12), 6961-
37 6964.
- 38 982. Ishihara, T.; Hong, X.; Ding, J.; Nurmikko, A. V., Dielectric confinement effect for
39 exciton and biexciton states in PbI₄-based two-dimensional semiconductor structures. *Surf. Sci.*
40 **1992**, *267* (1), 323-326.
- 41 983. Li, J.; Luo, L.; Huang, H.; Ma, C.; Ye, Z.; Zeng, J.; He, H., 2D Behaviors of Excitons in
42 Cesium Lead Halide Perovskite Nanoplatelets. *J. Phys. Chem. Lett.* **2017**, *8* (6), 1161-1168.

- 1 984. Kumar, S.; Jagielski, J.; Yakunin, S.; Rice, P.; Chiu, Y. C.; Wang, M.; Nedelcu, G.;
2 Kim, Y.; Lin, S.; Santos, E. J. G.; Kovalenko, M. V.; Shih, C. J., Efficient Blue
3 Electroluminescence Using Quantum-Confined Two-Dimensional Perovskites. *ACS Nano* **2016**,
4 *10* (10), 9720-9729.
- 5 985. Kumar, S.; Jagielski, J.; Kallikounis, N.; Kim, Y.-H.; Wolf, C.; Jenny, F.; Tian, T.;
6 Hofer, C. J.; Chiu, Y.-C.; Stark, W. J.; Lee, T.-W.; Shih, C.-J., Ultrapure Green Light-Emitting
7 Diodes Using Two-Dimensional Formamidinium Perovskites: Achieving Recommendation 2020
8 Color Coordinates. *Nano Lett.* **2017**, *17* (9), 5277-5284.
- 9 986. Blancon, J. C.; Stier, A. V.; Tsai, H.; Nie, W.; Stoumpos, C. C.; Traoré, B.; Pedesseau,
10 L.; Kepenekian, M.; Katsutani, F.; Noe, G. T.; Kono, J.; Tretiak, S.; Crooker, S. A.; Katan, C.;
11 Kanatzidis, M. G.; Crochet, J. J.; Even, J.; Mohite, A. D., Scaling law for excitons in 2D
12 perovskite quantum wells. *Nat. Commun.* **2018**, *9* (1), 2254.
- 13 987. Zhai, Y.; Baniya, S.; Zhang, C.; Li, J.; Haney, P.; Sheng, C.-X.; Ehrenfreund, E.;
14 Vardeny, Z. V., Giant Rashba splitting in 2D organic-inorganic halide perovskites measured by
15 transient spectroscopies. *Sci. Adv.* **2017**, *3* (7), e1700704.
- 16 988. Schaller, R. D.; Sykora, M.; Pietryga, J. M.; Klimov, V. I., Seven Excitons at a Cost of
17 One: Redefining the Limits for Conversion Efficiency of Photons into Charge Carriers. *Nano*
18 *Lett.* **2006**, *6*, 424-429.
- 19 989. Castañeda, J. A.; Nagamine, G.; Yassitepe, E.; Bonato, L. G.; Voznyy, O.; Hoogland, S.;
20 Nogueira, A. F.; Sargent, E. H.; Cruz, C. H. B.; Padilha, L. A., Efficient Biexciton Interaction in
21 Perovskite Quantum Dots Under Weak and Strong Confinement. *ACS Nano* **2016**, *10*, 8603-
22 8609.
- 23 990. Soetan, N.; Puretzky, A.; Reid, K.; Boulesbaa, A.; Zarick, H. F.; Hunt, A.; Rose, O.;
24 Rosenthal, S.; Geohegan, D. B.; Bardhan, R., Ultrafast Spectral Dynamics of CsPb(Br_xCl_{1-x})₃
25 Mixed-Halide Nanocrystals. *ACS Photonics* **2018**, *5*, 3575-3583.
- 26 991. Mondal, A.; Aneesh, J.; Ravi, V. K.; Sharma, R.; Mir, W. J.; Beard, M. C.; Nag, A.;
27 Adarsh, K. V., Ultrafast Exciton Many-Body Interactions and Hot-Phonon Bottleneck in
28 Colloidal Cesium Lead Halide Perovskite Nanocrystals. *Phys. Rev. B* **2018**, *98*, 115418.
- 29 992. Li, Y.; Ding, T.; Luo, X.; Chen, Z.; Liu, X.; Lu, X.; Wu, K., Biexciton Auger
30 Recombination in Mono-dispersed, Qntum-confined CsPbBr₃ Povskite Nanocrystals Obeys
31 Universal Volume-scaling. *Nano Res.* **2019**, *12*, 619-623.
- 32 993. Manzi, A.; Tong, Y.; Feucht, J.; Yao, E.-P.; Polavarapu, L.; Urban, A. S.; Feldmann, J.,
33 Resonantly enhanced multiple exciton generation through below-band-gap multi-photon
34 absorption in perovskite nanocrystals. *Nat. Commun.* **2018**, *9* (1), 1518.
- 35 994. Li, M.; Begum, R.; Fu, J.; Xu, Q.; Koh, T. M.; Veldhuis, S. A.; Grätzel, M.; Mathews,
36 N.; Mhaisalkar, S.; Sum, T. C., Low Threshold and Efficient Multiple Exciton Generation in
37 Halide Perovskite Nanocrystals. *Nat. Commun.* **2018**, *9*, 4197.
- 38 995. Weerd, C. d.; Gomez, L.; Capretti, A.; Lebrun, D. M.; Matsubara, E.; Lin, J.; Ashida,
39 M.; Spoor, F. C. M.; Siebbeles, L. D. A.; Houtepen, A. J.; Suenaga, K.; Fujiwara, Y.;
40 Gregorkiewicz, T., Efficient Carrier Multiplication in CsPbI₃ Perovskite Nanocrystals. *Nat.*
41 *Commun.* **2018**, *9*, 4199.
- 42 996. Ahumada-Lazo, R.; Alanis, J. A.; Parkinson, P.; Binks, D. J.; Hardman, S. J. O.;
43 Griffiths, J. T.; Rivarola, F. W. R.; Humphrey, C. J.; Ducati, C.; Davis, N. J. L. K., Emission
44 Properties and Ultrafast Carrier Dynamics of CsPbCl₃ Perovskite Nanocrystals. *J. Phys. Chem. C*
45 **2019**, *123*, 2651-2657.

- 1 997. Eperon, G. E.; Jedlicka, E.; Ginger, D. S., Biexciton Auger Recombination Differs in
2 Hybrid and Inorganic Halide Perovskite Quantum Dots. *J. Phys. Chem. Lett.* **2018**, *9*, 104-109.
- 3 998. Mondal, N.; De, A.; Samanta, A., Biexciton Generation and Dissociation Dynamics in
4 Formamidinium Chloride-Doped Cesium Lead Iodide Perovskite Nanocrystals. *J. Phys.*
5 *Chem. Lett.* **2018**, *9*, 3673-3679.
- 6 999. Jong, E. M. L. D. d.; Yamashita, G.; Gomez, L.; Ashida, M.; Fujiwara, Y.;
7 Gregorkiewicz, T., Multiexciton Lifetime in All-Inorganic CsPbBr₃ Perovskite Nanocrystals. *J.*
8 *Phys. Chem. C* **2017**, *121*, 1941-1947.
- 9 1000. Seth, S.; Ahmed, T.; Samanta, A., Photoluminescence Flickering and Blinking of Single
10 CsPbBr₃ Perovskite Nanocrystals: Revealing Explicit Carrier Recombination Dynamics. *J. Phys.*
11 *Chem. Lett.* **2018**, *9*, 7007-7014.
- 12 1001. Yarita, N.; Tahara, H.; Saruyama, M.; Kawawaki, T.; Sato, R.; Teranishi, T.; Kanemitsu,
13 Y., Impact of Postsynthetic Surface Modification on Photoluminescence Intermittency in
14 Formamidinium Lead Bromide Perovskite Nanocrystals. *J. Phys. Chem. Lett.* **2017**, *8*, 6041-
15 6047.
- 16 1002. Yarita, N.; Tahara, H.; Ihara, T.; Kawawaki, T.; Sato, R.; Saruyama, M.; Teranishi, T.;
17 Kanemitsu, Y., Dynamics of Charged Excitons and Biexcitons in CsPbBr₃ Perovskite
18 Nanocrystals Revealed by Femtosecond Transient-Absorption and Single-Dot Luminescence
19 Spectroscopy. *J. Phys. Chem. Lett.* **2017**, *8* (7), 1413-1418.
- 20 1003. Wang, J.; Ding, T.; Leng, J.; Jin, S.; Wu, K., “Intact”Carrier Doping by
21 Pump–Pump–Probe Spectroscopy in Combination with Interfacial Charge Transfer: A Case
22 Study of CsPbBr₃ Nanocrystals. *J. Phys. Chem. Lett.* **2018**, *9*, 3372-3377.
- 23 1004. Yarita, N.; Aharen, T.; Tahara, H.; Saruyama, M.; Kawawaki, T.; Sato, R.; Teranishi, T.;
24 Kanemitsu, Y., Observation of Positive and Negative Trions in Organic-inorganic Hybrid
25 Perovskite Nanocrystals. *Phys. Rev. Mater.* **2018**, *2*, 116003.
- 26 1005. Nakahara, S.; Tahara, H.; Yumoto, G.; Kawawaki, T.; Saruyama, M.; Sato, R.;
27 Teranishi, T.; Kanemitsu, Y., Suppression of Trion Formation in CsPbBr₃ Perovskite
28 Nanocrystals by Postsynthetic Surface Modification
29 *J. Phys. Chem. C* **2018**, *122*, 22188-22193.
- 30 1006. Kanemitsu, Y., Trion Dynamics in Lead Halide Perovskite Nanocrystals. *J. Chem. Phys.*
31 **2019**, *151*, 170902.
- 32 1007. Wu, K.; Liang, G.; Shang, Q.; Ren, Y.; Kong, D.; Lian, T., Ultrafast Interfacial Electron
33 and Hole Transfer from CsPbBr₃ Perovskite Quantum Dots. *J. Am. Chem. Soc.* **2015**, *137* (40),
34 12792-12795.
- 35 1008. Nair, V. C.; Muthu, C.; Rogach, A. L.; Kohara, R.; Biju, V., Channeling Exciton
36 Migration into Electron Transfer in Formamidinium Lead Bromide Perovskite
37 Nanocrystal/Fullerene Composites. *Angew. Chem. Int. Ed.* **2017**, *56*, 1214-1218.
- 38 1009. Mandal, S.; George, L.; Tkachenko, N. V., Charge Transfer Dynamics in CsPbBr₃
39 Perovskite Quantum Dots–Anthraquinone/Fullerene (C60) Hybrids. *Nanoscale* **2019**, *11*, 862-
40 869.
- 41 1010. Ahmed, G. H.; Liu, J.; Parida, M. R.; Murali, B.; Bose, R.; AlYami, N. M.; Hedhili, M.
42 N.; Peng, W.; Pan, J.; Besong, T. M. D.; Bakr, O. M.; Mohammed, O. F., Shape-Tunable Charge
43 Carrier Dynamics at the Interfaces between Perovskite Nanocrystals and Molecular Acceptors *J.*
44 *Phys. Chem. Lett.* **2016**, *7*, 3913-3919.

- 1 1011. Zhang, Y.-X.; Wang, H.-Y.; Zhang, Z.-Y.; Zhang, Y.; Sun, C.; Yue, Y.-Y.; Wang, L.;
2 Chen, Q.-D.; Sun, H.-B., Photoluminescence Quenching of Inorganic Cesium Lead Halides
3 Perovskite Quantum Dots. *Phys. Chem. Chem. Phys.* **2017**, *19*, 1920-1926.
- 4 1012. Mandal, S.; Tkachenko, N. V., Multiphoton Excitation of CsPbBr₃ Perovskite Quantum
5 Dots (PQDs): How Many Electrons Can One PQD Donate to Multiple Molecular Acceptors? *J.*
6 *Phys. Chem. Lett.* **2019**, *10*, 2775-2781.
- 7 1013. De, A.; Mondal, N.; Samanta, A., Hole Transfer Dynamics from Photoexcited Cesium
8 Lead Halide Perovskite Nanocrystals: 1-Aminopyrene as Hole Acceptor. *J. Phys. Chem. C* **2018**,
9 *122*, 13617-13623.
- 10 1014. DuBose, J. T.; Kamat, P. V., Probing Perovskite Photocatalysis. Interfacial Electron
11 Transfer between CsPbBr₃ and Ferrocene Redox Couple. *J. Phys. Chem. Lett.* **2019**, *10*, 6074-
12 6080.
- 13 1015. Lu, H.; Chen, X.; Anthony, J. E.; Johnson, J. C.; Beard, M. C., Sensitizing Singlet
14 Fission with Perovskite Nanocrystals. *J. Am. Chem. Soc.* **2019**, *141*, 4919-4927.
- 15 1016. Maity, P.; Dana, J.; Ghosh, H. N., Multiple Charge Transfer Dynamics in Colloidal
16 CsPbBr₃ Perovskite Quantum Dots Sensitized Molecular Adsorbate. *J. Phys. Chem. C* **2016**, *120*,
17 18348-18354.
- 18 1017. Begum, R.; Parida, M. R.; Abdelhady, A. L.; Murali, B.; Alyami, N. M.; Ahmed, G. H.;
19 Hedhili, M. N.; Bakr, O. M.; Mohammed, O. F., Engineering Interfacial Charge Transfer in
20 CsPbBr₃ Perovskite Nanocrystals by Heterovalent Doping. *J. Am. Chem. Soc.* **2017**, *139*, 731-
21 737.
- 22 1018. Sarkar, S.; Ravi, V. K.; Banerjee, S.; Yettapu, G. R.; Markad, G. B.; Nag, A.; Mandal,
23 P., Terahertz Spectroscopic Probe of Hot Electron and Hole Transfer from Colloidal CsPbBr₃
24 Perovskite Nanocrystals. *Nano Lett.* **2017**, *17*, 5402-5407.
- 25 1019. Shang, Q.; Kaledin, A. L.; Li, Q.; Lian, T., Size Dependent Charge Separation and
26 Recombination in CsPbI₃ Perovskite Quantum Dots. *J. Chem. Phys.* **2019**, *151*, 074705.
- 27 1020. De, A.; Das, S.; Samanta, A., Hot Hole Transfer Dynamics from CsPbBr₃ Perovskite
28 Nanocrystals. *ACS Energy Lett.* **2020**, *5* (7), 2246-2252.
- 29 1021. Luo, X.; Liang, G.; Wang, J.; Liu, X.; Wu, K., Picosecond Multi-hole Transfer and
30 Microsecond Charge-separated States at the Perovskite Nanocrystal/Tetracene Interface. *Chem.*
31 *Sci.* **2019**, *10*, 2459-2464.
- 32 1022. Scheidt, R. A.; Kerns, E.; Kamat, P. V., Interfacial Charge Transfer between Excited
33 CsPbBr₃ Nanocrystals and TiO₂: Charge Injection versus Photodegradation. *J. Phys. Chem. Lett.*
34 **2018**, *9* (20), 5962-5969.
- 35 1023. Kobosko, S. M.; DuBose, J. T.; Kamat, P. V., Perovskite Photocatalysis. Methyl
36 Viologen Induces Unusually Long-Lived Charge Carrier Separation in CsPbBr₃ Nanocrystals.
37 *ACS Energy Lett.* **2020**, *5*, 221-223.
- 38 1024. Li, Q.; Lian, T., Ultrafast Charge Separation in Two-Dimensional CsPbBr₃ Perovskite
39 Nanoplatelets. *J. Phys. Chem. Lett.* **2019**, *10* (3), 566-573.
- 40 1025. Dana, J.; Maity, P.; Jana, B.; Maiti, S.; Ghosh, H. N., Concurrent Ultrafast Electron- and
41 Hole-Transfer Dynamics in CsPbBr₃ Perovskite and Quantum Dots. *ACS Omega* **2018**, *3*, 2706-
42 2714.

- 1 1026. Brumberg, A.; Diroll, B. T.; Nedelcu, G.; Sykes, M. E.; Liu, Y.; Harvey, S. M.;
2 Wasielewski, M. R.; Kovalenko, M. V.; Schaller, R. D., Material Dimensionality Effects on
3 Electron Transfer Rates Between CsPbBr₃ and CdSe Nanoparticles. *Nano Lett.* **2018**, *18*, 4771-
4 4776.
- 5 1027. Quintero-Bermudez, R.; Sabatini, R. P.; Lejay, M.; Voznyy, O.; Sargent, E. H., Small-
6 Band-Offset Perovskite Shells Increase Auger Lifetime in Quantum Dot Solids. *ACS Nano* **2017**,
7 *11*, 12378-12384.
- 8 1028. Galar, P.; PiotrPiatkowski; Ngo, T. T.; Gutiérrez, M.; IvánMora-Seró; Douhal, A.,
9 Perovskite-quantum Qots Interface: Deciphering its Ultrafast Charge Carrier Dynamics. *Nano*
10 *Energy* **2018**, *49*, 471-480.
- 11 1029. Mondal, N.; De, A.; Samanta, A., All-inorganic Perovskite Nanocrystal Assisted
12 Extraction of Hot Electrons and Biexcitons from Photoexcited CdTe Quantum Dots. *Nanoscale*
13 **2018**, *10*, 639-645.
- 14 1030. Yao, E.-P.; Bohn, B. J.; Tong, Y.; Huang, H.; Polavarapu, L.; Feldmann, J., Exciton
15 Diffusion Lengths and Dissociation Rates in CsPbBr₃ Nanocrystal–Fullerene Composites:
16 Layer-by-Layer versus Blend Structures. *Adv. Opt. Mater.* **2019**, *7* (8), 1801776.
- 17 1031. VanOrman, Z. A.; Bieber, A. S.; Wieghold, S.; Nienhaus, L., A Perspective on Triplet
18 Fusion Upconversion: Triplet Sensitizers Beyond Quantum Dots. *MRS Commun.* **2019**, *9*, 924-
19 935.
- 20 1032. He, S.; Luo, X.; Liu, X.; Li, Y.; Wu, K., Visible-to-Ultraviolet Upconversion Efficiency
21 above 10% Sensitized by Quantum-Confined Perovskite Nanocrystals. *J. Phys. Chem. Lett.*
22 **2019**, *10*, 5036-5040.
- 23 1033. Mase, K.; Okumura, K.; Yanai, N.; Kimizuka, N., Triplet Sensitization by Perovskite
24 Nanocrystals for Photon Upconversion. *Chem. Commun.* **2017**, *53*, 8261-8264.
- 25 1034. Okumura, K.; Yanai, N.; Kimizuka, N., Visible-to-UV Photon Upconversion Sensitized
26 by Lead Halide Perovskite Nanocrystals. *Chem. Lett.* **2019**, *48*, 1347-1350.
- 27 1035. Nienhaus, L.; Correa-Baena, J.-P.; Wieghold, S.; Einzinger, M.; Lin, T.-A.;
28 Shulenberger, K. E.; Klein, N. D.; Wu, M.; Bulović, V.; Buonassisi, T.; Baldo, M. A.; Bawendi,
29 M. G., Triplet-Sensitization by Lead Halide Perovskite Thin Films for Near-Infrared-toVisible
30 Upconversion. *ACS Energy Lett.* **2019**, *4*, 888-595.
- 31 1036. Hu, H.; Meier, F.; Zhao, D.; Abe, Y.; Gao, Y.; Chen, B.; Salim, T.; Chia, E. E. M.; Qiao,
32 X.; Deibel, C.; Lam, Y. M., Efficient Room-Temperature Phosphorescence from Organic-
33 Inorganic Hybrid Perovskites by Molecular Engineering. *Adv. Mater.* **2018**, *30*, 1707621.
- 34 1037. Luo, X.; Lai, R.; Li, Y.; Han, Y.; Liang, G.; Liu, X.; Ding, T.; Wang, J.; Wu, K., Triplet
35 Energy Transfer from CsPbBr₃ Nanocrystals Enabled by Quantum Confinement. *J. Am. Chem.*
36 *Soc.* **2019**, *141*, 4186-4190.
- 37 1038. Luo, X.; Han, Y.; Chen, Z.; Li, Y.; Liang, G.; Liu, X.; Ding, T.; Nie, C.; Wang, M.;
38 Castellano, F. N.; W, K., Mechanisms of Triplet Energy Transfer Across the Inorganic
39 Nanocrystal/Organic Molecule Interface. *Nat. Commun.* **2020**, *11*, 28.
- 40 1039. Matylitsky, V. V.; Dworak, L.; Breus, V. V.; Basche', T.; Wachtveitl, J., Ultrafast
41 Charge Separation in Multiexcited CdSe Quantum Dots Mediated by Adsorbed Electron
42 Acceptors. *J. Am. Chem. Soc.* **2009**, *131*, 2424-2425.

- 1 1040. Huang, J.; Huang, Z.; Yang, Y.; Zhu, H.; Lian, T., Multiple Exciton Dissociation in
2 CdSe Quantum Dots by Ultrafast Electron Transfer to Adsorbed Methylene Blue. *J. Am. Chem.*
3 *Soc.* **2010**, *132*, 4858–4864.
- 4 1041. Lim, S. S.; Giovanni, D.; Zhang, Q.; Solanki, A.; Jamaludin, N. F.; Lim, J. W. M.;
5 Mathews, N.; Mhaisalkar, S.; Pshenichnikov, M. S.; Sum, T. C., Hot Carrier Extraction in
6 CH₃NH₃PbI₃ Unveiled by Pump-Push-Probe Spectroscopy. *Sci. Adv.* **2019**, *5*, eaax3620.
- 7 1042. Dursun, I.; Maity, P.; Jun Yin; Turedi, B.; Zhumeckenov, A. A.; Lee, K. J.; Mohammed,
8 O. F.; Bakr, O. M., Why are Hot Holes Easier to Extract than Hot Electrons from
9 Methylammonium Lead Iodide Perovskite? *Adv. Energy Mater.* **2019**, *9*, 1900084.
- 10 1043. Shen, Q.; Ripolles, T. S.; Even, J.; Zhang, Y.; Ding, C.; Liu, F.; Izuishi, T.; Nakazawa,
11 N.; Toyoda, T.; Ogomi, Y.; Hayase, S., Ultrafast Selective Extraction of Hot Holes from Cesium
12 Lead Iodide Perovskite films. *J. Energy Chem.* **2018**, doi.org/10.1016/j.jechem.2018.01.006.
- 13 1044. Evans, T. J. S.; Miyata, K.; Joshi, P. P.; Maehrlein, S.; Liu, F.; Zhu, X. Y., Competition
14 Between Hot-Electron Cooling and Large Polaron Screening in CsPbBr₃ Perovskite Single
15 Crystals. *J. Phys. Chem. C* **2018**, *122* (25), 13724-13730.
- 16 1045. Yang, J.; Wen, X.; Xia, H.; Sheng, R.; Ma, Q.; Kim, J.; Tapping, P.; Harada, T.; Kee, T.
17 W.; Huang, F.; Cheng, Y.-B.; Green, M.; Ho-Baillie, A.; Huang, S.; Shrestha, S.; Patterson, R.;
18 Conibeer, G., Acoustic-optical phonon up-conversion and hot-phonon bottleneck in lead-halide
19 perovskites. *Nat. Commun.* **2017**, *8* (1), 14120.
- 20 1046. Boehme, S. C.; Brinck, S. t.; Maes, J.; Yazdani, N.; Zapata, F.; Chen, K.; Wood, V.;
21 Hodgkiss, J. M.; Hens, Z.; Geiregat, P.; Infante, I., Phonon-Mediated and Weakly Size-
22 Dependent Electron and Hole Cooling in CsPbBr₃ Nanocrystals Revealed by Atomistic
23 Simulations and Ultrafast Spectroscopy. *Nano Lett.* **2020**, *20* (3), 1819-1829.
- 24 1047. Park, Y.-S.; Guo, S.; Makarov, N. S.; Klimov, V. I., Room Temperature Single-Photon
25 Emission from Individual Perovskite Quantum Dots. *ACS Nano* **2015**, *9* (10), 10386-10393.
- 26 1048. Chouhan, L.; Ghimire, S.; Biju, V., Blinking Beats Bleaching: The Control of
27 Superoxide Generation by Photo-ionized Perovskite Nanocrystals. *Angew. Chem. Int. Ed.* **2019**,
28 *58* (15), 4875-4879.
- 29 1049. Merdasa, A.; Tian, Y.; Camacho, R.; Dobrovolsky, A.; Debroye, E.; Unger, E. L.;
30 Hofkens, J.; Sundström, V.; Scheblykin, I. G., “Supertrap” at Work: Extremely Efficient
31 Nonradiative Recombination Channels in MAPbI₃ Perovskites Revealed by Luminescence
32 Super-Resolution Imaging and Spectroscopy. *ACS Nano* **2017**, *11* (6), 5391-5404.
- 33 1050. Yuan, G.; Ritchie, C.; Ritter, M.; Murphy, S.; Gómez, D. E.; Mulvaney, P., The
34 Degradation and Blinking of Single CsPbI₃ Perovskite Quantum Dots. *J. Phys. Chem. C* **2018**,
35 *122* (25), 13407-13415.
- 36 1051. Galland, C.; Ghosh, Y.; Steinbrück, A.; Sykora, M.; Hollingsworth, J. A.; Klimov, V. I.;
37 Htoon, H., Two types of luminescence blinking revealed by spectroelectrochemistry of single
38 quantum dots. *Nature* **2011**, *479* (7372), 203-207.
- 39 1052. Kim, T.; Jung, S. I.; Ham, S.; Chung, H.; Kim, D., Elucidation of Photoluminescence
40 Blinking Mechanism and Multiexciton Dynamics in Hybrid Organic–Inorganic Perovskite
41 Quantum Dots. *Small* **2019**, *15* (33), 1900355.
- 42 1053. Trinh, C. T.; Minh, D. N.; Ahn, K. J.; Kang, Y.; Lee, K.-G., Organic–Inorganic
43 FAPbBr₃ Perovskite Quantum Dots as a Quantum Light Source: Single-Photon Emission and
44 Blinking Behaviors. *ACS Photonics* **2018**, *5* (12), 4937-4943.

- 1 1054. Li, B.; Huang, H.; Zhang, G.; Yang, C.; Guo, W.; Chen, R.; Qin, C.; Gao, Y.; Biju, V.
2 P.; Rogach, A. L.; Xiao, L.; Jia, S., Excitons and Biexciton Dynamics in Single CsPbBr₃
3 Perovskite Quantum Dots. *J. Phys. Chem. Lett.* **2018**, *9* (24), 6934-6940.
- 4 1055. Frantsuzov, P. A.; Marcus, R. A., Explanation of quantum dot blinking without the long-
5 lived trap hypothesis. *Phys. Rev. B* **2005**, *72* (15), 155321.
- 6 1056. Frantsuzov, P. A.; Volkán-Kacsó, S.; Jankó, B., Model of Fluorescence Intermittency of
7 Single Colloidal Semiconductor Quantum Dots Using Multiple Recombination Centers. *Phys.*
8 *Rev. Lett.* **2009**, *103* (20), 207402.
- 9 1057. Seth, S.; Mondal, N.; Patra, S.; Samanta, A., Fluorescence Blinking and Photoactivation
10 of All-Inorganic Perovskite Nanocrystals CsPbBr₃ and CsPbBr₂I. *J. Phys. Chem. Lett.* **2016**, *7*
11 (2), 266-271.
- 12 1058. Yoshimura, H.; Yamauchi, M.; Masuo, S., In Situ Observation of Emission Behavior
13 during Anion-Exchange Reaction of a Cesium Lead Halide Perovskite Nanocrystal at the Single-
14 Nanocrystal Level. *J. Phys. Chem. Lett.* **2020**, *11* (2), 530-535.
- 15 1059. Tang, X.; Yang, J.; Li, S.; Liu, Z.; Hu, Z.; Hao, J.; Du, J.; Leng, Y.; Qin, H.; Lin, X.;
16 Lin, Y.; Tian, Y.; Zhou, M.; Xiong, Q., Single Halide Perovskite/Semiconductor Core/Shell
17 Quantum Dots with Ultrastability and Nonblinking Properties. *Adv. Sci.* **2019**, *6* (18), 1900412.
- 18 1060. Sharma, D. K.; Hirata, S.; Biju, V.; Vacha, M., Stark Effect and Environment-Induced
19 Modulation of Emission in Single Halide Perovskite Nanocrystals. *ACS Nano* **2019**, *13* (1), 624-
20 632.
- 21 1061. Tian, Y.; Merdasa, A.; Peter, M.; Abdellah, M.; Zheng, K.; Ponseca, C. S.; Pullerits, T.;
22 Yartsev, A.; Sundström, V.; Scheblykin, I. G., Giant Photoluminescence Blinking of Perovskite
23 Nanocrystals Reveals Single-Trap Control of Luminescence. *Nano Lett.* **2015**, *15* (3), 1603-
24 1608.
- 25 1062. Gerhard, M.; Louis, B.; Camacho, R.; Merdasa, A.; Li, J.; Kiligaridis, A.; Dobrovolsky,
26 A.; Hofkens, J.; Scheblykin, I. G., Microscopic insight into non-radiative decay in perovskite
27 semiconductors from temperature-dependent luminescence blinking. *Nat. Commun.* **2019**, *10* (1),
28 1698.
- 29 1063. Scheblykin, I. G., Small Number of Defects per Nanostructure Leads to “Digital”
30 Quenching of Photoluminescence: The Case of Metal Halide Perovskites. *Adv. Energy Mater.*
31 **2020**, *10* (46), 2001724.
- 32 1064. Yuan, H.; Debroye, E.; Caliendo, G.; Janssen, K. P. F.; van Loon, J.; Kirschhock, C. E.
33 A.; Martens, J. A.; Hofkens, J.; Roeffaers, M. B. J., Photoluminescence Blinking of Single-
34 Crystal Methylammonium Lead Iodide Perovskite Nanorods Induced by Surface Traps. *ACS*
35 *Omega* **2016**, *1* (1), 148-159.
- 36 1065. Eremchev, I. Y.; Tarasevich, A. O.; Li, J.; Naumov, A. V.; Scheblykin, I. G., Lack of
37 Photon Antibunching Supports Supertrap Model of Photoluminescence Blinking in Perovskite
38 Sub-Micrometer Crystals. *Adv. Opt. Mater.* **2021**, *9* (3), 2001596.
- 39 1066. Wen, X.; Ho-Baillie, A.; Huang, S.; Sheng, R.; Chen, S.; Ko, H.-c.; Green, M. A.,
40 Mobile Charge-Induced Fluorescence Intermittency in Methylammonium Lead Bromide
41 Perovskite. *Nano Lett.* **2015**, *15* (7), 4644-4649.
- 42 1067. Freppon, D. J.; Men, L.; Burkhov, S. J.; Petrich, J. W.; Vela, J.; Smith, E. A.,
43 Photophysical properties of wavelength-tunable methylammonium lead halide perovskite
44 nanocrystals. *J. Mater. Chem. C* **2017**, *5* (1), 118-126.

- 1 1068. Tachikawa, T.; Karimata, I.; Kobori, Y., Surface Charge Trapping in Organolead Halide
2 Perovskites Explored by Single-Particle Photoluminescence Imaging. *J. Phys. Chem. Lett.* **2015**,
3 6 (16), 3195-3201.
- 4 1069. Halder, A.; Chulliyil, R.; Subbiah, A. S.; Khan, T.; Chattoraj, S.; Chowdhury, A.;
5 Sarkar, S. K., Pseudohalide (SCN⁻)-Doped MAPbI₃ Perovskites: A Few Surprises. *J. Phys.*
6 *Chem. Lett.* **2015**, 6 (17), 3483-3489.
- 7 1070. Li, C.; Zhong, Y.; Luna, C. A.; Unger, T.; Deichsel, K.; Gräser, A.; Köhler, J.; Köhler,
8 A.; Hildner, R.; Huettner, S., Emission Enhancement and Intermittency in Polycrystalline
9 Organolead Halide Perovskite Films. *Molecules* **2016**, 21 (8).
- 10 1071. Tian, Y.; Merdasa, A.; Unger, E.; Abdellah, M.; Zheng, K.; McKibbin, S.; Mikkelsen,
11 A.; Pullerits, T.; Yartsev, A.; Sundström, V.; Scheblykin, I. G., Enhanced Organo-Metal Halide
12 Perovskite Photoluminescence from Nanosized Defect-Free Crystallites and Emitting Sites. *J.*
13 *Phys. Chem. Lett.* **2015**, 6 (20), 4171-4177.
- 14 1072. Yuan, H.; Debroye, E.; Bladt, E.; Lu, G.; Keshavarz, M.; Janssen, K. P. F.; Roeffaers,
15 M. B. J.; Bals, S.; Sargent, E. H.; Hofkens, J., Imaging Heterogeneously Distributed Photo-
16 Active Traps in Perovskite Single Crystals. *Adv. Mater.* **2018**, 30 (13), 1705494.
- 17 1073. Lee, S.; Park, J. H.; Lee, B. R.; Jung, E. D.; Yu, J. C.; Di Nuzzo, D.; Friend, R. H.; Song,
18 M. H., Amine-Based Passivating Materials for Enhanced Optical Properties and Performance of
19 Organic-Inorganic Perovskites in Light-Emitting Diodes. *J. Phys. Chem. Lett.* **2017**, 8 (8), 1784-
20 1792.
- 21 1074. Halder, A.; Pathoor, N.; Chowdhury, A.; Sarkar, S. K., Photoluminescence Flickering of
22 Micron-Sized Crystals of Methylammonium Lead Bromide: Effect of Ambience and Light
23 Exposure. *J. Phys. Chem. C* **2018**, 122 (27), 15133-15139.
- 24 1075. Sharma, D. K.; Hirata, S.; Vacha, M., Single-particle electroluminescence of CsPbBr₃
25 perovskite nanocrystals reveals particle-selective recombination and blinking as key efficiency
26 factors. *Nat. Commun.* **2019**, 10 (1), 4499.
- 27 1076. Pérez-Osorio, M. A.; Milot, R. L.; Filip, M. R.; Patel, J. B.; Herz, L. M.; Johnston, M.
28 B.; Giustino, F., Vibrational Properties of the Organic-Inorganic Halide Perovskite
29 CH₃NH₃PbI₃ from Theory and Experiment: Factor Group Analysis, First-Principles
30 Calculations, and Low-Temperature Infrared Spectra. *J. Phys. Chem. C* **2015**, 119 (46), 25703-
31 25718.
- 32 1077. Brivio, F.; Frost, J. M.; Skelton, J. M.; Jackson, A. J.; Weber, O. J.; Weller, M. T.; Goñi,
33 A. R.; Leguy, A. M. A.; Barnes, P. R. F.; Walsh, A., Lattice dynamics and vibrational spectra of
34 the orthorhombic, tetragonal, and cubic phases of methylammonium lead iodide. *Phys. Rev. B*
35 **2015**, 92 (14), 144308.
- 36 1078. Clinckemalie, L.; Valli, D.; Roeffaers, M. B. J.; Hofkens, J.; Pradhan, B.; Debroye, E.,
37 Challenges and Opportunities for CsPbBr₃ Perovskites in Low- and High-Energy Radiation
38 Detection. *ACS Energy Lett.* **2021**, 1290-1314.
- 39 1079. Wright, A. D.; Verdi, C.; Milot, R. L.; Eperon, G. E.; Pérez-Osorio, M. A.; Snaith, H. J.;
40 Giustino, F.; Johnston, M. B.; Herz, L. M., Electron-phonon coupling in hybrid lead halide
41 perovskites. *Nat. Commun.* **2016**, 7 (1), 11755.

- 1 1080. Keshavarz, M.; Debroye, E.; Ottesen, M.; Martin, C.; Zhang, H.; Fron, E.; Küchler, R.;
2 Steele, J. A.; Bremholm, M.; Van de Vondel, J.; Wang, H. I.; Bonn, M.; Roeffaers, M. B. J.;
3 Wiedmann, S.; Hofkens, J., Tuning the Structural and Optoelectronic Properties of Cs₂AgBiBr₆
4 Double-Perovskite Single Crystals through Alkali-Metal Substitution. *Adv. Mater.* **2020**, *32* (40),
5 2001878.
- 6 1081. Steele, J. A.; Puech, P.; Monserrat, B.; Wu, B.; Yang, R. X.; Kirchartz, T.; Yuan, H.;
7 Fleury, G.; Giovanni, D.; Fron, E.; Keshavarz, M.; Debroye, E.; Zhou, G.; Sum, T. C.; Walsh,
8 A.; Hofkens, J.; Roeffaers, M. B. J., Role of Electron–Phonon Coupling in the Thermal
9 Evolution of Bulk Rashba-Like Spin-Split Lead Halide Perovskites Exhibiting Dual-Band
10 Photoluminescence. *ACS Energy Lett.* **2019**, *4* (9), 2205-2212.
- 11 1082. Steele, J. A.; Puech, P.; Keshavarz, M.; Yang, R.; Banerjee, S.; Debroye, E.; Kim, C.
12 W.; Yuan, H.; Heo, N. H.; Vanacken, J.; Walsh, A.; Hofkens, J.; Roeffaers, M. B. J., Giant
13 Electron-Phonon Coupling and Deep Conduction Band Resonance in Metal Halide Double
14 Perovskite. *ACS Nano* **2018**, *12* (8), 8081-8090.
- 15 1083. Fu, M.; Tamarat, P.; Trebbia, J.-B.; Bodnarchuk, M. I.; Kovalenko, M. V.; Even, J.;
16 Lounis, B., Unraveling exciton–phonon coupling in individual FAPbI₃ nanocrystals emitting
17 near-infrared single photons. *Nat. Commun.* **2018**, *9* (1), 3318.
- 18 1084. Becker, M. A.; Scarpelli, L.; Nedelcu, G.; Rainò, G.; Masia, F.; Borri, P.; Stöferle, T.;
19 Kovalenko, M. V.; Langbein, W.; Mahrt, R. F., Long Exciton Dephasing Time and Coherent
20 Phonon Coupling in CsPbBr₂Cl Perovskite Nanocrystals. *Nano Lett.* **2018**, *18* (12), 7546-7551.
- 21 1085. Sychugov, I.; Juhasz, R.; Valenta, J.; Linnros, J., Narrow luminescence linewidth of a
22 silicon quantum dot. *Phys. Rev. Lett.* **2005**, *94* (8), 087405.
- 23 1086. Rainò, G.; Nedelcu, G.; Protesescu, L.; Bodnarchuk, M. I.; Kovalenko, M. V.; Mahrt, R.
24 F.; Stöferle, T., Single Cesium Lead Halide Perovskite Nanocrystals at Low Temperature: Fast
25 Single-Photon Emission, Reduced Blinking, and Exciton Fine Structure. *ACS Nano* **2016**, *10* (2),
26 2485-2490.
- 27 1087. Pfingsten, O.; Klein, J.; Protesescu, L.; Bodnarchuk, M. I.; Kovalenko, M. V.; Bacher,
28 G., Phonon Interaction and Phase Transition in Single Formamidinium Lead Bromide Quantum
29 Dots. *Nano Lett.* **2018**, *18* (7), 4440-4446.
- 30 1088. Ramade, J.; Andriambarijaona, L. M.; Steinmetz, V.; Goubet, N.; Legrand, L.;
31 Barisien, T.; Bernardot, F.; Testelin, C.; Lhuillier, E.; Bramati, A.; Chamarro, M., Exciton-
32 phonon coupling in a CsPbBr₃ single nanocrystal. *Appl. Phys. Lett.* **2018**, *112* (7), 072104.
- 33 1089. Liu, L.; Pevero, F.; Zhang, F.; Zhong, H.; Sychugov, I., Cation effect on excitons in
34 perovskite nanocrystals from single-dot photoluminescence of
35 $\text{C}_{\text{H}_3\text{N}_3\text{PbI}_3}$. *Physical Review B* **2019**, *100* (19), 195430.
- 36
37 1090. Miyata, K.; Atallah, T. L.; Zhu, X.-Y., Lead halide perovskites: Crystal-liquid duality,
38 phonon glass electron crystals, and large polaron formation. *Sci. Adv.* **2017**, *3* (10), e1701469.
- 39 1091. Scamarcio, G.; Spagnolo, V.; Ventrucci, G.; Lugará, M.; Righini, G. C., Size dependence
40 of electron–LO-phonon coupling in semiconductor nanocrystals. *Phys. Rev. B* **1996**, *53* (16),
41 R10489-R10492.
- 42 1092. Zhao, Z.; Zhong, M.; Zhou, W.; Peng, Y.; Yin, Y.; Tang, D.; Zou, B., Simultaneous
43 Triplet Exciton–Phonon and Exciton–Photon Photoluminescence in the Individual Weak
44 Confinement CsPbBr₃ Micro/Nanowires. *J. Phys. Chem. C* **2019**, *123* (41), 25349-25358.

- 1 1093. Nie, W.; Blancon, J.-C.; Neukirch, A. J.; Appavoo, K.; Tsai, H.; Chhowalla, M.; Alam,
2 M. A.; Sfeir, M. Y.; Katan, C.; Even, J.; Tretiak, S.; Crochet, J. J.; Gupta, G.; Mohite, A. D.,
3 Light-activated photocurrent degradation and self-healing in perovskite solar cells. *Nat.*
4 *Commun.* **2016**, *7* (1), 11574.
- 5 1094. Petruska, M. A.; Malko, A. V.; Voyles, P. M.; Klimov, V. I., High - performance,
6 quantum dot nanocomposites for nonlinear optical and optical gain applications. *Adv. Mater.*
7 **2003**, *15* (7 - 8), 610-613.
- 8 1095. Mi, Y.; Zhong, Y.; Zhang, Q.; Liu, X., Continuous - Wave Pumped Perovskite Lasers.
9 *Adv. Opt. Mater.* **2019**, 1900544.
- 10 1096. Yakunin, S.; Protesescu, L.; Krieg, F.; Bodnarchuk, M. I.; Nedelcu, G.; Humer, M.; De
11 Luca, G.; Fiebig, M.; Heiss, W.; Kovalenko, M. V., Low-threshold amplified spontaneous
12 emission and lasing from colloidal nanocrystals of caesium lead halide perovskites. *Nat.*
13 *Commun.* **2015**, *6*, 8056.
- 14 1097. Wang, Y.; Li, X.; Zhao, X.; Xiao, L.; Zeng, H.; Sun, H., Nonlinear absorption and low-
15 threshold multiphoton pumped stimulated emission from all-inorganic perovskite nanocrystals.
16 *Nano Lett.* **2015**, *16* (1), 448-453.
- 17 1098. Eisler, H.-J.; Sundar, V. C.; Bawendi, M. G.; Walsh, M.; Smith, H. I.; Klimov, V.,
18 Color-selective semiconductor nanocrystal laser. *Appl. Phys. Lett.* **2002**, *80* (24), 4614-4616.
- 19 1099. Dai, X.; Deng, Y.; Peng, X.; Jin, Y., Quantum - dot light - emitting diodes for large -
20 area displays: towards the dawn of commercialization. *Adv. Mater.* **2017**, *29* (14), 1607022.
- 21 1100. Wang, Y.; Li, X.; Nalla, V.; Zeng, H.; Sun, H., Solution - processed low threshold
22 vertical cavity surface emitting lasers from all - inorganic perovskite nanocrystals. *Adv. Funct.*
23 *Mater.* **2017**, *27* (13), 1605088.
- 24 1101. Kambhampati, P., Hot exciton relaxation dynamics in semiconductor quantum dots:
25 radiationless transitions on the nanoscale. *J. Phys. Chem. C* **2011**, *115* (45), 22089-22109.
- 26 1102. She, C.; Fedin, I.; Dolzhenkov, D. S.; Demortière, A.; Schaller, R. D.; Pelton, M.;
27 Talapin, D. V., Low-threshold stimulated emission using colloidal quantum wells. *Nano Lett.*
28 **2014**, *14* (5), 2772-2777.
- 29 1103. Grim, J. Q.; Christodoulou, S.; Di Stasio, F.; Krahn, R.; Cingolani, R.; Manna, L.;
30 Moreels, I., Continuous-wave biexciton lasing at room temperature using solution-processed
31 quantum wells. *Nat. Nanotech.* **2014**, *9* (11), 891.
- 32 1104. García-Santamaría, F.; Chen, Y.; Vela, J.; Schaller, R. D.; Hollingsworth, J. A.; Klimov,
33 V. I., Suppressed auger recombination in “giant” nanocrystals boosts optical gain performance.
34 *Nano Lett.* **2009**, *9* (10), 3482-3488.
- 35 1105. Shi, Z.-F.; Sun, X.-G.; Wu, D.; Xu, T.-T.; Tian, Y.-T.; Zhang, Y.-T.; Li, X.-J.; Du, G.-
36 T., Near-infrared random lasing realized in a perovskite CH₃NH₃PbI₃ thin film. *J. Mater.*
37 *Chem. C* **2016**, *4* (36), 8373-8379.
- 38 1106. Xu, Y.; Chen, Q.; Zhang, C.; Wang, R.; Wu, H.; Zhang, X.; Xing, G.; Yu, W. W.; Wang,
39 X.; Zhang, Y., Two-photon-pumped perovskite semiconductor nanocrystal lasers. *J. Am. Chem.*
40 *Soc.* **2016**, *138* (11), 3761-3768.
- 41 1107. Jia, Y.; Kerner, R. A.; Grede, A. J.; Brigeman, A. N.; Rand, B. P.; Giebink, N. C.,
42 Diode-pumped organo-lead halide perovskite lasing in a metal-clad distributed feedback
43 resonator. *Nano Lett.* **2016**, *16* (7), 4624-4629.

- 1 1108. Harwell, J. R.; Whitworth, G. L.; Turnbull, G. A.; Samuel, I. D. W., Green perovskite
2 distributed feedback lasers. *Sci. Rep.* **2017**, *7* (1), 11727.
- 3 1109. Mathies, F.; Brenner, P.; Hernandez-Sosa, G.; Howard, I. A.; Paetzold, U. W.; Lemmer,
4 U., Inkjet-printed perovskite distributed feedback lasers. *Opt. express* **2018**, *26* (2), A144-A152.
- 5 1110. Tian, C.; Zhao, S.; Zhai, W.; Ge, C.; Ran, G., Low-threshold room-temperature
6 continuous-wave optical lasing of single-crystalline perovskite in a distributed reflector
7 microcavity. *RSC Adv.* **2019**, *9* (62), 35984-35989.
- 8 1111. Chen, S.; Zhang, C.; Lee, J.; Han, J.; Nurmikko, A., High - Q, Low - Threshold
9 Monolithic Perovskite Thin - Film Vertical - Cavity Lasers. *Adv. Mater.* **2017**, *29* (16),
10 1604781.
- 11 1112. Lin, C. H.; Zeng, Q.; Lafalce, E.; Yu, S.; Smith, M. J.; Yoon, Y. J.; Chang, Y.; Jiang, Y.;
12 Lin, Z.; Vardeny, Z. V., Large - Area Lasing and Multicolor Perovskite Quantum Dot Patterns.
13 *Adv. Opt. Mater.* **2018**, *6* (16), 1800474.
- 14 1113. Bar-On, O.; Brenner, P.; Lemmer, U.; Scheuer, J. In *Perovskite Micro Laser arrays*
15 *using Scalable Lithography: Towards Integrated Perovskite Photonics*, CLEO: Science and
16 Innovations, Optical Society of America: 2019; p SF2J. 2.
- 17 1114. Wang, S.; Yu, J.; Zhang, M.; Chen, D.; Li, C.; Chen, R.; Jia, G.; Rogach, A. L.; Yang,
18 X., Stable, Strongly Emitting Cesium Lead Bromide Perovskite Nanorods with High Optical
19 Gain Enabled by an Intermediate Monomer Reservoir Synthetic Strategy. *Nano Lett.* **2019**, *19*
20 (9), 6315-6322.
- 21 1115. Wang, Y.; Zhi, M.; Chang, Y.-Q.; Zhang, J.-P.; Chan, Y., Stable, ultralow threshold
22 amplified spontaneous emission from CsPbBr₃ nanoparticles exhibiting trion gain. *Nano Lett.*
23 **2018**, *18* (8), 4976-4984.
- 24 1116. Pramanik, A.; Gates, K.; Gao, Y.; Begum, S.; Chandra Ray, P., Several Orders-of-
25 Magnitude Enhancement of Multiphoton Absorption Property for CsPbX₃ Perovskite Quantum
26 Dots by Manipulating Halide Stoichiometry. *J. Phys. Chem. C* **2019**, *123* (8), 5150-5156.
- 27 1117. Wei, S.; Yang, Y.; Kang, X.; Wang, L.; Huang, L.; Pan, D., Room-temperature and
28 gram-scale synthesis of CsPbX₃ (X= Cl, Br, I) perovskite nanocrystals with 50–85%
29 photoluminescence quantum yields. *Chemical Communications* **2016**, *52* (45), 7265-7268.
- 30 1118. Li, X.; Wu, Y.; Zhang, S.; Cai, B.; Gu, Y.; Song, J.; Zeng, H., CsPbX₃ quantum dots for
31 lighting and displays: room - temperature synthesis, photoluminescence superiorities, underlying
32 origins and white light - emitting diodes. *Adv. Funct. Mater.* **2016**, *26* (15), 2435-2445.
- 33 1119. Xing, G.; Mathews, N.; Lim, S. S.; Yantara, N.; Liu, X.; Sabba, D.; Grätzel, M.;
34 Mhaisalkar, S.; Sum, T. C., Low-temperature solution-processed wavelength-tunable perovskites
35 for lasing. *Nat. Mater.* **2014**, *13* (5), 476.
- 36 1120. Balena, A.; Perulli, A.; Fernandez, M.; De Giorgi, M. L.; Nedelcu, G.; Kovalenko, M.
37 V.; Anni, M., Temperature Dependence of the Amplified Spontaneous Emission from CsPbBr₃
38 Nanocrystal Thin Films. *J. Phys. Chem. C* **2018**, *122* (10), 5813-5819.
- 39 1121. Tan, M. J.; Wang, Y.; Chan, Y., Solution-based green amplified spontaneous emission
40 from colloidal perovskite nanocrystals exhibiting high stability. *Appl. Phys. Lett.* **2019**, *114* (18),
41 183101.
- 42 1122. Zhao, W.; Qin, Z.; Zhang, C.; Wang, G.; Huang, X.; Li, B.; Dai, X.; Xiao, M., Optical
43 Gain from Biexcitons in CsPbBr₃ Nanocrystals Revealed by Two-dimensional Electronic
44 Spectroscopy. *J. Phys. Chem. Lett.* **2019**, *10* (6), 1251-1258.

- 1 1123. Navarro-Arenas, J.; Suárez, I.; Chirvony, V. S.; Gualdrón-Reyes, A. F.; Mora-Seró, I.;
2 Martínez-Pastor, J., Single-Exciton Amplified Spontaneous Emission in Thin Films of CsPbX₃
3 (X= Br, I) Perovskite Nanocrystals. *J. Phys. Chem. Lett.* **2019**, *10* (20), 6389-6398.
- 4 1124. Stylianakis, M. M.; Maksudov, T.; Panagiotopoulos, A.; Kakavelakis, G.; Petridis, K.,
5 Inorganic and hybrid perovskite based laser devices: A Review. *Materials* **2019**, *12* (6), 859.
- 6 1125. De Giorgi, M. L.; Anni, M., Amplified Spontaneous Emission and Lasing in Lead
7 Halide Perovskites: State of the Art and Perspectives. *Appl. Sci.* **2019**, *9* (21), 4591.
- 8 1126. Nagamine, G.; Rocha, J. O.; Bonato, L. G.; Nogueira, A. F.; Zaharieva, Z.; Watt, A. A.;
9 de Brito Cruz, C. H.; Padilha, L. A., Two-Photon Absorption and Two-Photon-Induced Gain in
10 Perovskite Quantum Dots. *J. Phys. Chem. Lett.* **2018**, *9* (12), 3478-3484.
- 11 1127. Wang, Y.; Yang, X.; He, T.; Gao, Y.; Demir, H. V.; Sun, X.; Sun, H., Near resonant and
12 nonresonant third-order optical nonlinearities of colloidal InP/ZnS quantum dots. *Appl. Phys.*
13 *Lett.* **2013**, *102* (2), 021917.
- 14 1128. He, G. S.; Tan, L.-S.; Zheng, Q.; Prasad, P. N., Multiphoton Absorbing Materials:
15 Molecular Designs, Characterizations, and Applications. *Chem. Rev.* **2008**, *108* (4), 1245-1330.
- 16 1129. Jasieniak, J. J.; Fortunati, I.; Gardin, S.; Signorini, R.; Bozio, R.; Martucci, A.;
17 Mulvaney, P., Highly Efficient Amplified Stimulated Emission from CdSe - CdS - ZnS
18 Quantum Dot Doped Waveguides with Two - Photon Infrared Optical Pumping. *Adv. Mater.*
19 **2008**, *20* (1), 69-73.
- 20 1130. Protesescu, L.; Yakunin, S.; Kumar, S.; Bär, J.; Bertolotti, F.; Masciocchi, N.;
21 Guagliardi, A.; Grotevent, M.; Shorubalko, I.; Bodnarchuk, M. I., Dismantling the “red wall” of
22 colloidal perovskites: highly luminescent formamidinium and formamidinium–cesium lead
23 iodide nanocrystals. *ACS nano* **2017**, *11* (3), 3119-3134.
- 24 1131. Veldhuis, S. A.; Tay, Y. K. E.; Bruno, A.; Dintakurti, S. S.; Bhaumik, S.; Muduli, S. K.;
25 Li, M.; Mathews, N.; Sum, T. C.; Mhaisalkar, S. G., Benzyl alcohol-treated CH₃NH₃PbBr₃
26 nanocrystals exhibiting high luminescence, stability, and ultralow amplified spontaneous
27 emission thresholds. *Nano Lett.* **2017**, *17* (12), 7424-7432.
- 28 1132. Dou, L.; Wong, A. B.; Yu, Y.; Lai, M.; Kornienko, N.; Eaton, S. W.; Fu, A.; Bischak, C.
29 G.; Ma, J.; Ding, T., Atomically thin two-dimensional organic-inorganic hybrid perovskites.
30 *Science* **2015**, *349* (6255), 1518-1521.
- 31 1133. Xing, G.; Kumar, M. H.; Chong, W. K.; Liu, X.; Cai, Y.; Ding, H.; Asta, M.; Grätzel,
32 M.; Mhaisalkar, S.; Mathews, N., Solution - Processed Tin - Based Perovskite for Near -
33 Infrared Lasing. *Adv. Mater.* **2016**, *28* (37), 8191-8196.
- 34 1134. She, C.; Fedin, I.; Dolzhenkov, D. S.; Dahlberg, P. D.; Engel, G. S.; Schaller, R. D.;
35 Talapin, D. V., Red, yellow, green, and blue amplified spontaneous emission and lasing using
36 colloidal CdSe nanoplatelets. *ACS nano* **2015**, *9* (10), 9475-9485.
- 37 1135. Yuan, F.; Wu, Z.; Dong, H.; Xi, J.; Xi, K.; Divitini, G.; Jiao, B.; Hou, X.; Wang, S.;
38 Gong, Q., High stability and ultralow threshold amplified spontaneous emission from
39 formamidinium lead halide perovskite films. *J. Phys. Chem. C* **2017**, *121* (28), 15318-15325.
- 40 1136. Trots, D.; Myagkota, S., High-temperature structural evolution of caesium and rubidium
41 triiodoplumbates. *J. Phys. Chem. Solids* **2008**, *69* (10), 2520-2526.
- 42 1137. Stoumpos, C. C.; Malliakas, C. D.; Kanatzidis, M. G., Semiconducting tin and lead
43 iodide perovskites with organic cations: phase transitions, high mobilities, and near-infrared
44 photoluminescent properties. *Inorg Chem* **2013**, *52* (15), 9019-9038.

- 1 1138. Liu, Z.; Hu, Z.; Zhang, Z.; Du, J.; Yang, J.; Tang, X.; Liu, W.; Leng, Y., Two-Photon
2 Pumped Amplified Spontaneous Emission and Lasing from Formamidinium Lead Bromine
3 Nanocrystals. *ACS Photonics* **2019**.
- 4 1139. Dhanker, R.; Brigeman, A.; Larsen, A.; Stewart, R.; Asbury, J. B.; Giebink, N. C.,
5 Random lasing in organo-lead halide perovskite microcrystal networks. *Appl. Phys. Lett.* **2014**,
6 *105* (15), 151112.
- 7 1140. Wang, Y.; Yu, D.; Wang, Z.; Li, X.; Chen, X.; Nalla, V.; Zeng, H.; Sun, H., Solution -
8 Grown CsPbBr₃/Cs₄PbBr₆ Perovskite Nanocomposites: Toward Temperature - Insensitive
9 Optical Gain. *Small* **2017**, *13* (34), 1701587.
- 10 1141. Roy, P. K.; Haider, G.; Lin, H. I.; Liao, Y. M.; Lu, C. H.; Chen, K. H.; Chen, L. C.;
11 Shih, W. H.; Liang, C. T.; Chen, Y. F., Multicolor Ultralow - Threshold Random Laser Assisted
12 by Vertical - Graphene Network. *Adv. Opt. Mater.* **2018**, *6* (16), 1800382.
- 13 1142. Huang, C.-Y.; Zou, C.; Mao, C.; Corp, K. L.; Yao, Y.-C.; Lee, Y.-J.; Schlenker, C. W.;
14 Jen, A. K.; Lin, L. Y., CsPbBr₃ perovskite quantum dot vertical cavity lasers with low threshold
15 and high stability. *Acs Photonics* **2017**, *4* (9), 2281-2289.
- 16 1143. Malko, A.; Mikhailovsky, A.; Petruska, M.; Hollingsworth, J.; Htoon, H.; Bawendi, M.;
17 Klimov, V. I., From amplified spontaneous emission to microring lasing using nanocrystal
18 quantum dot solids. *Appl. Phys. Lett.* **2002**, *81* (7), 1303-1305.
- 19 1144. Kazes, M.; Lewis, D. Y.; Ebenstein, Y.; Mokari, T.; Banin, U., Lasing from
20 semiconductor quantum rods in a cylindrical microcavity. *Adv. Mater.* **2002**, *14* (4), 317-321.
- 21 1145. Tang, B.; Dong, H.; Sun, L.; Zheng, W.; Wang, Q.; Sun, F.; Jiang, X.; Pan, A.; Zhang,
22 L., Single-mode lasers based on cesium lead halide perovskite submicron spheres. *ACS nano*
23 **2017**, *11* (11), 10681-10688.
- 24 1146. Kurahashi, N.; Nguyen, V.-C.; Sasaki, F.; Yanagi, H., Whispering gallery mode lasing in
25 lead halide perovskite crystals grown in microcapillary. *Appl. Phys. Lett.* **2018**, *113* (1), 011107.
- 26 1147. Liu, Z.; Hu, Z.; Shi, T.; Du, J.; Yang, J.; Zhang, Z.; Tang, X.; Leng, Y., Stable and
27 enhanced frequency up-converted lasing from CsPbBr₃ quantum dots embedded in silica
28 sphere. *Opt. express* **2019**, *27* (7), 9459-9466.
- 29 1148. Stranks, S. D.; Wood, S. M.; Wojciechowski, K.; Deschler, F.; Saliba, M.; Khandelwal,
30 H.; Patel, J. B.; Elston, S. J.; Herz, L. M.; Johnston, M. B., Enhanced amplified spontaneous
31 emission in perovskites using a flexible cholesteric liquid crystal reflector. *Nano Lett.* **2015**, *15*
32 (8), 4935-4941.
- 33 1149. Folie, B. D.; Tan, J. A.; Huang, J. M.; Sercel, P. C.; Delor, M.; Lai, M. L.; Lyons, J. L.;
34 Bernstein, N.; Efros, A. L.; Yang, P. D.; Ginsberg, N. S., Effect of Anisotropic Confinement on
35 Electronic Structure and Dynamics of Band Edge Excitons in Inorganic Perovskite Nanowires. *J*
36 *Phys Chem A* **2020**, *124* (9), 1867-1876.
- 37 1150. Janker, L.; Tong, Y.; Polavarapu, L.; Feldmann, J.; Urban, A. S.; Krenner, H. J., Real-
38 Time Electron and Hole Transport Dynamics in Halide Perovskite Nanowires. *Nano Lett.* **2019**,
39 *19* (12), 8701-8707.
- 40 1151. Zhu, H. M.; Fu, Y. P.; Meng, F.; Wu, X. X.; Gong, Z. Z.; Ding, Q.; Gustafsson, M. V.;
41 Trinh, M. T.; Jin, S.; Zhu, X. Y., Lead halide perovskite nanowire lasers with low lasing
42 thresholds and high quality factors. *Nat. Mater.* **2015**, *14* (6), 636-U115.

- 1 1152. Fu, Y. P.; Zhu, H. M.; Stoumpos, C. C.; Ding, Q.; Wang, J.; Kanatzidis, M. G.; Zhu, X.
2 Y.; Jin, S., Broad Wavelength Tunable Robust Lasing from Single-Crystal Nanowires of Cesium
3 Lead Halide Perovskites (CsPbX_3 , $X = \text{Cl, Br, I}$). *ACS Nano* **2016**, *10* (8), 7963-7972.
- 4 1153. Park, K.; Lee, J. W.; Kim, J. D.; Han, N. S.; Jang, D. M.; Jeong, S.; Park, J.; Song, J. K.,
5 Light-Matter Interactions in Cesium Lead Halide Perovskite Nanowire Lasers. *J. Phys. Chem.*
6 *Lett.* **2016**, *7* (18), 3703-10.
- 7 1154. Wang, X.; Shoaib, M.; Wang, X.; Zhang, X.; He, M.; Luo, Z.; Zheng, W.; Li, H.; Yang,
8 T.; Zhu, X.; Ma, L.; Pan, A., High-Quality In-Plane Aligned CsPbX_3 Perovskite Nanowire
9 Lasers with Composition-Dependent Strong Exciton-Photon Coupling. *ACS Nano* **2018**, *12* (6),
10 6170-6178.
- 11 1155. Xing, J.; Liu, X. F.; Zhang, Q.; Ha, S. T.; Yuan, Y. W.; Shen, C.; Sum, T. C.; Xiong, Q.,
12 Vapor Phase Synthesis of Organometal Halide Perovskite Nanowires for Tunable Room-
13 Temperature Nanolasers. *Nano Lett.* **2015**, *15* (7), 4571-7.
- 14 1156. Shang, Q.; Zhang, S.; Liu, Z.; Chen, J.; Yang, P.; Li, C.; Li, W.; Zhang, Y.; Xiong, Q.;
15 Liu, X.; Zhang, Q., Surface Plasmon Enhanced Strong Exciton-Photon Coupling in Hybrid
16 Inorganic-Organic Perovskite Nanowires. *Nano Lett.* **2018**, *18* (6), 3335-3343.
- 17 1157. Schlaus, A. P.; Spencer, M. S.; Miyata, K.; Liu, F.; Wang, X. X.; Datta, I.; Lipson, M.;
18 Pan, A. L.; Zhu, X. Y., How lasing happens in CsPbBr_3 perovskite nanowires. *Nat. Commun.*
19 **2019**, *10*, 265.
- 20 1158. Huang, H.; Chen, B.; Wang, Z.; Hung, T. F.; Susha, A. S.; Zhong, H.; Rogach, A. L.,
21 Water resistant CsPbX_3 nanocrystals coated with polyhedral oligomeric silsesquioxane and their
22 use as solid state luminophores in all-perovskite white light-emitting devices. *Chemical science*
23 **2016**, *7* (9), 5699-5703.
- 24 1159. Zhang, X.; Lin, H.; Huang, H.; Reckmeier, C.; Zhang, Y.; Choy, W. C.; Rogach, A. L.,
25 Enhancing the brightness of cesium lead halide perovskite nanocrystal based green light-emitting
26 devices through the interface engineering with perfluorinated ionomer. *Nano Lett.* **2016**, *16* (2),
27 1415-1420.
- 28 1160. Chen, J.; Liu, D.; Al-Marri, M. J.; Nuuttila, L.; Lehtivuori, H.; Zheng, K., Photo-stability
29 of CsPbBr_3 perovskite quantum dots for optoelectronic application. *Sci. China Mater.* **2016**, *59*
30 (9), 719-727.
- 31 1161. Li, X.; Wang, Y.; Sun, H.; Zeng, H., Amino - Mediated Anchoring Perovskite Quantum
32 Dots for Stable and Low - Threshold Random Lasing. *Adv. Mater.* **2017**, *29* (36), 1701185.
- 33 1162. Xie, Y. C.; Haoran, W.; Ye, L.; Le, W.; Ying, L.; Xuyong, Y.; Rong, J., Trimethylsilyl
34 Iodine-Mediated Synthesis of Highly Bright Red-Emitting CsPbI_3 Perovskite Quantum Dots
35 with Significantly Improved Stability. **2019**.
- 36 1163. Chen, J.; Du, W.; Shi, J.; Li, M.; Wang, Y.; Zhang, Q.; Liu, X., Perovskite quantum dot
37 lasers. *InfoMat* **2019**.
- 38 1164. Jia, Y.; Kerner, R. A.; Grede, A. J.; Rand, B. P.; Giebink, N. C., Continuous-wave lasing
39 in an organic-inorganic lead halide perovskite semiconductor. *Nat. Photonics* **2017**, *11* (12),
40 784.
- 41 1165. Evans, T. J.; Schlaus, A.; Fu, Y.; Zhong, X.; Atallah, T. L.; Spencer, M. S.; Brus, L. E.;
42 Jin, S.; Zhu, X. Y., Continuous - wave lasing in cesium lead bromide perovskite nanowires. *Adv.*
43 *Opt. Mater.* **2018**, *6* (2), 1700982.

- 1 1166. Wang, Y.; Sun, H., Advances and prospects of lasers developed from colloidal
2 semiconductor nanostructures. *Prog. Quantum Electron.* **2018**, *60*, 1-29.
- 3 1167. Pietryga, J. M.; Park, Y.-S.; Lim, J.; Fidler, A. F.; Bae, W. K.; Brovelli, S.; Klimov, V.
4 I., Spectroscopic and Device Aspects of Nanocrystal Quantum Dots. *Chem. Rev.* **2016**, *116* (18),
5 10513-10622.
- 6 1168. Hong, X.; Ishihara, T.; Nurmikko, A. V., Photoconductivity and electroluminescence in
7 lead iodide based natural quantum well structures. *Solid State Commun.* **1992**, *84* (6), 657-661.
- 8 1169. Hattori, T.; Taira, T.; Era, M.; Tsutsui, T.; Saito, S., Highly efficient
9 electroluminescence from a heterostructure device combined with emissive layered-perovskite
10 and an electron-transporting organic compound. *Chem. Phys. Lett.* **1996**, *254* (1-2), 103-108.
- 11 1170. Chondroudis, K.; Mitzi, D. B., Electroluminescence from an Organic-Inorganic
12 Perovskite Incorporating a Quaterthiophene Dye within Lead Halide Perovskite Layers. *Chem.*
13 *Mater.* **1999**, *11* (11), 3028-3030.
- 14 1171. Kim, H. S.; Lee, C. R.; Im, J. H.; Lee, K. B.; Moehl, T.; Marchioro, A.; Moon, S. J.;
15 Humphry-Baker, R.; Yum, J. H.; Moser, J. E.; Grätzel, M.; Park, N. G., Lead iodide perovskite
16 sensitized all-solid-state submicron thin film mesoscopic solar cell with efficiency exceeding
17 9%. *Sci Rep* **2012**, *2*, 591.
- 18 1172. Heo, J. H.; Im, S. H.; Noh, J. H.; Mandal, T. N.; Lim, C.-S.; Chang, J. A.; Lee, Y. H.;
19 Kim, H.-j.; Sarkar, A.; Nazeeruddin, M. K.; Grätzel, M.; Seok, S. I., Efficient inorganic-organic
20 hybrid heterojunction solar cells containing perovskite compound and polymeric hole
21 conductors. *Nat. Photonics* **2013**, *7* (6), 486-491.
- 22 1173. Chiba, T.; Hayashi, Y.; Ebe, H.; Hoshi, K.; Sato, J.; Sato, S.; Pu, Y.-J.; Ohisa, S.; Kido,
23 J., Anion-exchange red perovskite quantum dots with ammonium iodine salts for highly efficient
24 light-emitting devices. *Nat. Photonics* **2018**, *12* (11), 681-687.
- 25 1174. Zhao, B.; Bai, S.; Kim, V.; Lamboll, R.; Shivanna, R.; Auras, F.; Richter, J. M.; Yang,
26 L.; Dai, L.; Alsari, M.; She, X.-J.; Liang, L.; Zhang, J.; Lilliu, S.; Gao, P.; Snaith, H. J.; Wang,
27 J.; Greenham, N. C.; Friend, R. H.; Di, D., High-efficiency perovskite-polymer bulk
28 heterostructure light-emitting diodes. *Nat. Photonics* **2018**, *12* (12), 783-789.
- 29 1175. Li, X.; Wu, Y.; Zhang, S.; Cai, B.; Gu, Y.; Song, J.; Zeng, H., CsPbX₃Quantum Dots for
30 Lighting and Displays: Room-Temperature Synthesis, Photoluminescence Superiorities,
31 Underlying Origins and White Light-Emitting Diodes. *Advanced Functional Materials* **2016**, *26*
32 (15), 2435-2445.
- 33 1176. Tress, W., Metal Halide Perovskites as Mixed Electronic-Ionic Conductors: Challenges
34 and Opportunities-From Hysteresis to Memristivity. *J. Phys. Chem. Lett.* **2017**, *8* (13), 3106-
35 3114.
- 36 1177. Govinda, S.; Kore, B. P.; Bokdam, M.; Mahale, P.; Kumar, A.; Pal, S.; Bhattacharyya,
37 B.; Lahnsteiner, J.; Kresse, G.; Franchini, C.; Pandey, A.; Sarma, D. D., Behavior of
38 Methylammonium Dipoles in MAPbX₃ (X = Br and I). *J. Phys. Chem. Lett.* **2017**, *8* (17), 4113-
39 4121.
- 40 1178. Xing, J.; Zhao, Y.; Askerka, M.; Quan, L. N.; Gong, X.; Zhao, W.; Zhao, J.; Tan, H.;
41 Long, G.; Gao, L.; Yang, Z.; Voznyy, O.; Tang, J.; Lu, Z.-H.; Xiong, Q.; Sargent, E. H., Color-
42 stable highly luminescent sky-blue perovskite light-emitting diodes. *Nat. Commun.* **2018**, *9* (1),
43 3541.

- 1 1179. Yan, F.; Xing, J.; Xing, G.; Quan, L.; Tan, S. T.; Zhao, J.; Su, R.; Zhang, L.; Chen, S.;
2 Zhao, Y.; Huan, A.; Sargent, E. H.; Xiong, Q.; Demir, H. V., Highly Efficient Visible Colloidal
3 Lead-Halide Perovskite Nanocrystal Light-Emitting Diodes. *Nano Lett.* **2018**, *18* (5), 3157-3164.
- 4 1180. Xing, J.; Yan, F.; Zhao, Y.; Chen, S.; Yu, H.; Zhang, Q.; Zeng, R.; Demir, H. V.; Sun,
5 X.; Huan, A.; Xiong, Q., High-Efficiency Light-Emitting Diodes of Organometal Halide
6 Perovskite Amorphous Nanoparticles. *ACS Nano* **2016**, *10* (7), 6623-30.
- 7 1181. Zhu, W.; Ma, W.; Su, Y.; Chen, Z.; Chen, X.; Ma, Y.; Bai, L.; Xiao, W.; Liu, T.; Zhu,
8 H.; Liu, X.; Liu, H.; Liu, X.; Yang, Y., Low-dose real-time X-ray imaging with nontoxic double
9 perovskite scintillators. *Light: Sci. Appl.* **2020**, *9* (1), 112.
- 10 1182. Tong, J.; Wu, J.; Shen, W.; Zhang, Y.; Liu, Y.; Zhang, T.; Nie, S.; Deng, Z., Direct Hot-
11 Injection Synthesis of Lead Halide Perovskite Nanocubes in Acrylic Monomers for Ultrastable
12 and Bright Nanocrystal-Polymer Composite Films. *ACS Applied Materials & Interfaces* **2019**,
13 *11* (9), 9317-9325.
- 14 1183. Shamsi, J.; Urban, A. S.; Imran, M.; De Trizio, L.; Manna, L., Metal Halide Perovskite
15 Nanocrystals: Synthesis, Post-Synthesis Modifications, and Their Optical Properties. *Chem Rev*
16 **2019**, *119* (5), 3296-3348.
- 17 1184. Raja, S. N.; Bekenstein, Y.; Koc, M. A.; Fischer, S.; Zhang, D.; Lin, L.; Ritchie, R. O.;
18 Yang, P.; Alivisatos, A. P., Encapsulation of Perovskite Nanocrystals into Macroscale Polymer
19 Matrices: Enhanced Stability and Polarization. *ACS Applied Materials & Interfaces* **2016**, *8* (51),
20 35523-35533.
- 21 1185. Yan, F.; Demir, H. V., LEDs using halide perovskite nanocrystal emitters. *Nanoscale*
22 **2019**, *11* (24), 11402-11412.
- 23 1186. Kim, G. Y.; Senocrate, A.; Yang, T. Y.; Gregori, G.; Gratzel, M.; Maier, J., Large
24 tunable photoeffect on ion conduction in halide perovskites and implications for
25 photodecomposition. *Nat. Mater.* **2018**, *17* (5), 445-449.
- 26 1187. Shan, X.; Li, J.; Chen, M.; Geske, T.; Bade, S. G. R.; Yu, Z., Junction Propagation in
27 Organometal Halide Perovskite-Polymer Composite Thin Films. *J. Phys. Chem. Lett.* **2017**, *8*
28 (11), 2412-2419.
- 29 1188. Kim, S.; Bae, S.; Lee, S. W.; Cho, K.; Lee, K. D.; Kim, H.; Park, S.; Kwon, G.; Ahn, S.
30 W.; Lee, H. M.; Kang, Y.; Lee, H. S.; Kim, D., Relationship between ion migration and
31 interfacial degradation of CH₃NH₃PbI₃ perovskite solar cells under thermal conditions. *Sci.*
32 *Rep.* **2017**, *7* (1), 1200.
- 33 1189. Fakharuddin, A.; Shabbir, U.; Qiu, W.; Iqbal, T.; Sultan, M.; Heremans, P.; Schmidt-
34 Mende, L., Inorganic and Layered Perovskites for Optoelectronic Devices. *Adv. Mater.* **2019**, *31*
35 (47), e1807095.
- 36 1190. Zou, S.; Liu, Y.; Li, J.; Liu, C.; Feng, R.; Jiang, F.; Li, Y.; Song, J.; Zeng, H.; Hong, M.;
37 Chen, X., Stabilizing Cesium Lead Halide Perovskite Lattice through Mn(II) Substitution for
38 Air-Stable Light-Emitting Diodes. *Journal of the American Chemical Society* **2017**, *139* (33),
39 11443-11450.
- 40 1191. Xu, B.; Wang, W.; Zhang, X.; Cao, W.; Wu, D.; Liu, S.; Dai, H.; Chen, S.; Wang, K.;
41 Sun, X., Bright and efficient light-emitting diodes based on MA/Cs double cation perovskite
42 nanocrystals. *J. Mater. Chem. C* **2017**, *5* (25), 6123-6128.
- 43 1192. Deng, W.; Xu, X.; Zhang, X.; Zhang, Y.; Jin, X.; Wang, L.; Lee, S.-T.; Jie, J.,
44 Organometal Halide Perovskite Quantum Dot Light-Emitting Diodes. *Adv. Funct. Mater.* **2016**,
45 *26* (26), 4797-4802.

- 1 1193. Xing, J.; Yan, F.; Zhao, Y.; Chen, S.; Yu, H.; Zhang, Q.; Zeng, R.; Demir, H. V.; Sun,
2 X.; Huan, A.; Xiong, Q., High-Efficiency Light-Emitting Diodes of Organometal Halide
3 Perovskite Amorphous Nanoparticles. *ACS Nano* **2016**, *10* (7), 6623-6630.
- 4 1194. Yang, J. N.; Song, Y.; Yao, J. S.; Wang, K. H.; Wang, J. J.; Zhu, B. S.; Yao, M. M.;
5 Rahman, S. U.; Lan, Y. F.; Fan, F. J.; Yao, H. B., Potassium Bromide Surface Passivation on
6 CsPbI₃-xBr_x Nanocrystals for Efficient and Stable Pure Red Perovskite Light-Emitting Diodes.
7 *J. Am. Chem. Soc.* **2020**, *142* (6), 2956-2967.
- 8 1195. Begum, R.; Chin, X. Y.; Damodaran, B.; Hooper, T. J. N.; Mhaisalkar, S.; Mathews, N.,
9 Cesium Lead Halide Perovskite Nanocrystals Prepared by Anion Exchange for Light-Emitting
10 Diodes. *ACS Appl. Nano Mater.* **2020**, *3* (2), 1766-1774.
- 11 1196. Chen, H.; Fan, L.; Zhang, R.; Bao, C.; Zhao, H.; Xiang, W.; Liu, W.; Niu, G.; Guo, R.;
12 Zhang, L.; Wang, L., High-Efficiency Formamidinium Lead Bromide Perovskite Nanocrystal-
13 Based Light-Emitting Diodes Fabricated via a Surface Defect Self-Passivation Strategy. *Adv.*
14 *Opt. Mater.* **2020**, *8* (6), 1901390.
- 15 1197. Hou, S.; Gangishetty, M. K.; Quan, Q.; Congreve, D. N., Efficient Blue and White
16 Perovskite Light-Emitting Diodes via Manganese Doping. *Joule* **2018**, *2* (11), 2421-2433.
- 17 1198. Yang, F.; Chen, H.; Zhang, R.; Liu, X.; Zhang, W.; Zhang, J.; Gao, F.; Wang, L.,
18 Efficient and Spectrally Stable Blue Perovskite Light - Emitting Diodes Based on Potassium
19 Passivated Nanocrystals. *Adv. Funct. Mater.* **2020**, *30* (10).
- 20 1199. Hassan, Y.; Ashton, O. J.; Park, J. H.; Li, G.; Sakai, N.; Wenger, B.; Haghighirad, A.-A.;
21 Noel, N. K.; Song, M. H.; Lee, B. R.; Friend, R. H.; Snaith, H. J., Facile Synthesis of Stable and
22 Highly Luminescent Methylammonium Lead Halide Nanocrystals for Efficient Light Emitting
23 Devices. *J. Am. Chem. Soc.* **2019**, *141* (3), 1269-1279.
- 24 1200. Zhang, X.; Sun, C.; Zhang, Y.; Wu, H.; Ji, C.; Chuai, Y.; Wang, P.; Wen, S.; Zhang, C.;
25 Yu, W. W., Bright Perovskite Nanocrystal Films for Efficient Light-Emitting Devices. *J. Phys.*
26 *Chem. Lett.* **2016**, *7* (22), 4602-4610.
- 27 1201. Vashishtha, P.; Halpert, J. E., Field-Driven Ion Migration and Color Instability in Red-
28 Emitting Mixed Halide Perovskite Nanocrystal Light-Emitting Diodes. *Chem. Mater.* **2017**, *29*
29 (14), 5965-5973.
- 30 1202. Zheng, X.; Yuan, S.; Liu, J.; Yin, J.; Yuan, F.; Shen, W.-S.; Yao, K.; Wei, M.; Zhou, C.;
31 Song, K.; Zhang, B.-B.; Lin, Y.; Hedhili, M. N.; Wehbe, N.; Han, Y.; Sun, H.-T.; Lu, Z.-H.;
32 Anthopoulos, T. D.; Mohammed, O. F.; Sargent, E. H.; Liao, L.-S.; Bakr, O. M., Chlorine
33 Vacancy Passivation in Mixed Halide Perovskite Quantum Dots by Organic Pseudohalides
34 Enables Efficient Rec. 2020 Blue Light-Emitting Diodes. *ACS Energy Lett.* **2020**, *5* (3), 793-798.
- 35 1203. Shen, X.; Zhang, Y.; Kershaw, S. V.; Li, T.; Wang, C.; Zhang, X.; Wang, W.; Li, D.;
36 Wang, Y.; Lu, M.; Zhang, L.; Sun, C.; Zhao, D.; Qin, G.; Bai, X.; Yu, W. W.; Rogach, A. L.,
37 Zn-Alloyed CsPbI₃ Nanocrystals for Highly Efficient Perovskite Light-Emitting Devices. *Nano*
38 *Lett.* **2019**, *19* (3), 1552-1559.
- 39 1204. Dong, Y.; Wang, Y.-K.; Yuan, F.; Johnston, A.; Liu, Y.; Ma, D.; Choi, M.-J.; Chen, B.;
40 Chekini, M.; Baek, S.-W.; Sagar, L. K.; Fan, J.; Hou, Y.; Wu, M.; Lee, S.; Sun, B.; Hoogland, S.;
41 Quintero-Bermudez, R.; Ebe, H.; Todorovic, P.; Dinic, F.; Li, P.; Kung, H. T.; Saidaminov, M.
42 I.; Kumacheva, E.; Spiecker, E.; Liao, L.-S.; Voznyy, O.; Lu, Z.-H.; Sargent, E. H., Bipolar-shell
43 resurfacing for blue LEDs based on strongly confined perovskite quantum dots. *Nat. Nanotech.*
44 **2020**.

- 1 1205. Congreve, D. N.; Weidman, M. C.; Seitz, M.; Paritmongkol, W.; Dahod, N. S.; Tisdale,
2 W. A., Tunable Light-Emitting Diodes Utilizing Quantum-Confined Layered Perovskite
3 Emitters. *ACS Photonics* **2017**, *4* (3), 476-481.
- 4 1206. Hoye, R. L. Z.; Lai, M.-L.; Anaya, M.; Tong, Y.; Gałkowski, K.; Doherty, T.; Li, W.;
5 Huq, T. N.; Mackowski, S.; Polavarapu, L.; Feldmann, J.; MacManus-Driscoll, J. L.; Friend, R.
6 H.; Urban, A. S.; Stranks, S. D., Identifying and Reducing Interfacial Losses to Enhance Color-
7 Pure Electroluminescence in Blue-Emitting Perovskite Nanoplatelet Light-Emitting Diodes. *ACS*
8 *Energy Lett.* **2019**, *4* (5), 1181-1188.
- 9 1207. Zhang, C.; Wan, Q.; Wang, B.; Zheng, W.; Liu, M.; Zhang, Q.; Kong, L.; Li, L., Surface
10 Ligand Engineering toward Brightly Luminescent and Stable Cesium Lead Halide Perovskite
11 Nanoplatelets for Efficient Blue-Light-Emitting Diodes. *J. Phys. Chem. C* **2019**, *123* (43),
12 26161-26169.
- 13 1208. Pan, J.; Shang, Y.; Yin, J.; De Bastiani, M.; Peng, W.; Dursun, I.; Sinatra, L.; El-Zohry,
14 A. M.; Hedhili, M. N.; Emwas, A. H.; Mohammed, O. F.; Ning, Z.; Bakr, O. M., Bidentate
15 Ligand-Passivated CsPbI₃ Perovskite Nanocrystals for Stable Near-Unity Photoluminescence
16 Quantum Yield and Efficient Red Light-Emitting Diodes. *J. Am. Chem. Soc.* **2018**, *140* (2), 562-
17 565.
- 18 1209. Yao, J.-S. Y.; Jing, G.; Kun-Hua, W.; Guozhen, Z.; Bai-Sheng, Z.; Chen, C.; Qun, Z.;
19 Yi, L.; Shu-Hong, Y.; Hong, B., Few-Nanometer-Sized α -CsPbI₃ Quantum Dots Enabled by
20 Strontium Substitution and Iodide Passivation for Efficient Red-Light Emitting Diodes. **2019**.
- 21 1210. Rogach, M. L.; Xiaoyu, Z.; Xue, B.; Hua, W.; Xinyu, S.; Yu, Z.; Wei, Z.; Weitao, Z.;
22 Hongwei, S.; William, W. Y.; Andrey, L., Spontaneous Silver Doping and Surface Passivation of
23 CsPbI₃ Perovskite Active Layer Enable Light-Emitting Devices with an External Quantum
24 Efficiency of 11.2%. **2018**.
- 25 1211. Chen, F.; Boopathi, K. M.; Imran, M.; Lauciello, S.; Salerno, M., Thiocyanate-Treated
26 Perovskite-Nanocrystal-Based Light-Emitting Diodes with Insight in Efficiency Roll-Off.
27 *Materials* **2020**, *13* (2), 367.
- 28 1212. Brown, A. A. M.; Hooper, T. J. N.; Veldhuis, S. A.; Chin, X. Y.; Bruno, A.; Vashishtha,
29 P.; Tey, J. N.; Jiang, L.; Damodaran, B.; Pu, S. H.; Mhaisalkar, S. G.; Mathews, N., Self-
30 assembly of a robust hydrogen-bonded octylphosphonate network on cesium lead bromide
31 perovskite nanocrystals for light-emitting diodes. *Nanoscale* **2019**, *11* (25), 12370-12380.
- 32 1213. Shynkarenko, Y.; Bodnarchuk, M. I.; Bernasconi, C.; Berezovska, Y.; Verteletskyi, V.;
33 Ochsenein, S. T.; Kovalenko, M. V., Direct Synthesis of Quaternary Alkylammonium-Capped
34 Perovskite Nanocrystals for Efficient Blue and Green Light-Emitting Diodes. *ACS Energy Lett.*
35 **2019**, *4* (11), 2703-2711.
- 36 1214. Song, J.; Li, J.; Xu, L.; Li, J.; Zhang, F.; Han, B.; Shan, Q.; Zeng, H., Room-
37 Temperature Triple-Ligand Surface Engineering Synergistically Boosts Ink Stability,
38 Recombination Dynamics, and Charge Injection toward EQE-11.6% Perovskite QLEDs.
39 *Advanced Materials* **2018**, *30* (30), 1800764.
- 40 1215. Chen, H.; Fan, L.; Zhang, R.; Bao, C.; Zhao, H.; Xiang, W.; Liu, W.; Niu, G.; Guo, R.;
41 Zhang, L.; Wang, L., High - Efficiency Formamidinium Lead Bromide Perovskite
42 Nanocrystal - Based Light - Emitting Diodes Fabricated via a Surface Defect Self - Passivation
43 Strategy. *Adv. Opt. Mater.* **2020**, *8* (6).

- 1 1216. Zheng, W.; Wan, Q.; Zhang, Q.; Liu, M.; Zhang, C.; Wang, B.; Kong, L.; Li, L., High-
2 efficiency perovskite nanocrystal light-emitting diodes via decorating NiOx on the nanocrystal
3 surface. *Nanoscale* **2020**, *12* (16), 8711-8719.
- 4 1217. Liu, J.; Shabbir, B.; Wang, C.; Wan, T.; Ou, Q.; Yu, P.; Tadich, A.; Jiao, X.; Chu, D.;
5 Qi, D.; Li, D.; Kan, R.; Huang, Y.; Dong, Y.; Jasieniak, J.; Zhang, Y.; Bao, Q., Flexible,
6 Printable Soft-X-Ray Detectors Based on All-Inorganic Perovskite Quantum Dots. *Adv. Mater.*
7 **2019**, *31* (30), 1901644.
- 8 1218. brweb, BT.2020 : Parameter values for ultra-high definition television systems for
9 production and international programme exchange. **2020**.
- 10 1219. Jin, Y.; Wang, Z.-K.; Yuan, S.; Wang, Q.; Qin, C.; Wang, K.-L.; Dong, C.; Li, M.; Liu,
11 Y.; Liao, L.-S., Synergistic Effect of Dual Ligands on Stable Blue Quasi-2D Perovskite Light-
12 Emitting Diodes. *Adv. Funct. Mater.* **2020**, *30* (6), 1908339.
- 13 1220. Lian, X.; Wang, X.; Ling, Y.; Lochner, E.; Tan, L.; Zhou, Y.; Ma, B.; Hanson, K.; Gao,
14 H., Light Emitting Diodes Based on Inorganic Composite Halide Perovskites. *Adv. Funct. Mater.*
15 **2019**, *29* (5), 1807345.
- 16 1221. Shin, M.; Nam, S.-W.; Sadhanala, A.; Shivanna, R.; Anaya, M.; Jiménez-Solano, A.;
17 Yoon, H.; Jeon, S.; Stranks, S. D.; Hoye, R. L. Z.; Shin, B., Understanding the Origin of
18 Ultrasharp Sub-bandgap Luminescence from Zero-Dimensional Inorganic Perovskite Cs4PbBr6.
19 *ACS Appl. Energy Mater.* **2020**, *3* (1), 192-199.
- 20 1222. Ning, Z.; Gong, X.; Comin, R.; Walters, G.; Fan, F.; Voznyy, O.; Yassitepe, E.; Buin,
21 A.; Hoogland, S.; Sargent, E. H., Quantum-dot-in-perovskite solids. *Nature* **2015**, *523* (7560),
22 324-328.
- 23 1223. Gao, L.; Quan, L. N.; García de Arquer, F. P.; Zhao, Y.; Munir, R.; Proppe, A.;
24 Quintero-Bermudez, R.; Zou, C.; Yang, Z.; Saidaminov, M. I.; Voznyy, O.; Kinger, S.; Lu, Z.;
25 Kelley, S. O.; Amassian, A.; Tang, J.; Sargent, E. H., Efficient near-infrared light-emitting
26 diodes based on quantum dots in layered perovskite. *Nat. Photonics* **2020**, *14* (4), 227-233.
- 27 1224. Gong, X.; Yang, Z.; Walters, G.; Comin, R.; Ning, Z.; Beauregard, E.; Adinolfi, V.;
28 Voznyy, O.; Sargent, E. H., Highly efficient quantum dot near-infrared light-emitting diodes.
29 *Nat. Photonics* **2016**, *10* (4), 253-257.
- 30 1225. Tong, J.; Wu, J.; Shen, W.; Zhang, Y.; Liu, Y.; Zhang, T.; Nie, S.; Deng, Z., Direct Hot-
31 Injection Synthesis of Lead Halide Perovskite Nanocubes in Acrylic Monomers for Ultrastable
32 and Bright Nanocrystal-Polymer Composite Films. *ACS Appl. Mater. Interfaces* **2019**, *11* (9),
33 9317-9325.
- 34 1226. Li, G.; Tan, Z.-K.; Di, D.; Lai, M. L.; Jiang, L.; Lim, J. H.-W.; Friend, R. H.; Greenham,
35 N. C., Efficient Light-Emitting Diodes Based on Nanocrystalline Perovskite in a Dielectric
36 Polymer Matrix. *Nano Lett.* **2015**, *15* (4), 2640-2644.
- 37 1227. Cai, W.; Chen, Z.; Li, Z.; Yan, L.; Zhang, D.; Liu, L.; Xu, Q.-h.; Ma, Y.; Huang, F.; Yip,
38 H.-L.; Cao, Y., Polymer-Assisted In Situ Growth of All-Inorganic Perovskite Nanocrystal Film
39 for Efficient and Stable Pure-Red Light-Emitting Devices. *ACS Appl. Mater. Interfaces* **2018**, *10*
40 (49), 42564-42572.
- 41 1228. Rainò, G.; Landuyt, A.; Krieg, F.; Bernasconi, C.; Ochsenbein, S. T.; Dirin, D. N.;
42 Bodnarchuk, M. I.; Kovalenko, M. V., Underestimated Effect of a Polymer Matrix on the Light
43 Emission of Single CsPbBr3 Nanocrystals. *Nano Lett.* **2019**, *19* (6), 3648-3653.

- 1 1229. Yoon, H. C.; Do, Y. R., Stable and Efficient Green Perovskite Nanocrystal–Polysilazane
2 Films for White LEDs Using an Electrospray Deposition Process. *ACS Appl. Mater. Interfaces*
3 **2019**, *11* (25), 22510-22520.
- 4 1230. MAKE SCREEN TIME A TREAT FOR YOUR EYES EVERY TIME.
5 <https://nanolumi.com/>.
- 6 1231. Hassan, Y.; Song, Y.; Pensack, R. D.; Abdelrahman, A. I.; Kobayashi, Y.; Winnik, M.
7 A.; Scholes, G. D., Structure-Tuned Lead Halide Perovskite Nanocrystals. *Adv. Mater.* **2016**, *28*
8 (3), 566-573.
- 9 1232. Kumar, S.; Jagielski, J.; Marcato, T.; Solari, S. F.; Shih, C.-J., Understanding the Ligand
10 Effects on Photophysical, Optical, and Electroluminescent Characteristics of Hybrid Lead Halide
11 Perovskite Nanocrystal Solids. *J. Phys. Chem. Lett.* **2019**, *10* (24), 7560-7567.
- 12 1233. Philippe, B.; Jacobsson, T. J.; Correa-Baena, J.-P.; Jena, N. K.; Banerjee, A.;
13 Chakraborty, S.; Cappel, U. B.; Ahuja, R.; Hagfeldt, A.; Odellius, M.; Rensmo, H., Valence
14 Level Character in a Mixed Perovskite Material and Determination of the Valence Band
15 Maximum from Photoelectron Spectroscopy: Variation with Photon Energy. *J. Phys. Chem. C*
16 **2017**, *121* (48), 26655-26666.
- 17 1234. Koscher, B. A.; Nett, Z.; Alivisatos, A. P., The Underlying Chemical Mechanism of
18 Selective Chemical Etching in CsPbBr₃ Nanocrystals for Reliably Accessing Near-Unity
19 Emitters. *ACS Nano* **2019**, *13* (10), 11825-11833.
- 20 1235. Dai, S.-W.; Hsu, B.-W.; Chen, C.-Y.; Lee, C.-A.; Liu, H.-Y.; Wang, H.-F.; Huang, Y.-
21 C.; Wu, T.-L.; Manikandan, A.; Ho, R.-M.; Tsao, C.-S.; Cheng, C.-H.; Chueh, Y.-L.; Lin, H.-W.,
22 Perovskite Quantum Dots with Near Unity Solution and Neat-Film Photoluminescent Quantum
23 Yield by Novel Spray Synthesis. *Adv. Mater.* **2018**, *30* (7), 1705532.
- 24 1236. Jagielski, J.; Kumar, S.; Wang, M.; Scullion, D.; Lawrence, R.; Li, Y.-T.; Yakunin, S.;
25 Tian, T.; Kovalenko, M. V.; Chiu, Y.-C.; Santos, E. J. G.; Lin, S.; Shih, C.-J., Aggregation-
26 induced emission in lamellar solids of colloidal perovskite quantum wells. *Sci. Adv.* **2017**, *3* (12),
27 eaaq0208.
- 28 1237. Schuller, J. A.; Karaveli, S.; Schiros, T.; He, K.; Yang, S.; Kymissis, I.; Shan, J.; Zia, R.,
29 Orientation of luminescent excitons in layered nanomaterials. *Nat. Nanotech.* **2013**, *8* (4), 271-
30 276.
- 31 1238. Jurow, M. J.; Morgenstern, T.; Eisler, C.; Kang, J.; Penzo, E.; Do, M.; Engelmayer, M.;
32 Osowiecki, W. T.; Bekenstein, Y.; Tassone, C.; Wang, L.-W.; Alivisatos, A. P.; Brütting, W.;
33 Liu, Y., Manipulating the Transition Dipole Moment of CsPbBr₃ Perovskite Nanocrystals for
34 Superior Optical Properties. *Nano Lett.* **2019**, *19* (4), 2489-2496.
- 35 1239. Jagielski, J.; Solari, S. F.; Jordan, L.; Scullion, D.; Blulle, B.; Li, Y. T.; Krumeich, F.;
36 Chiu, Y. C.; Ruhstaller, B.; Santos, E. J. G.; Shih, C. J., Scalable photonic sources using two-
37 dimensional lead halide perovskite superlattices. *Nat. Commun.* **2020**, *11* (1), 387.
- 38 1240. Akkerman, Q. A.; Park, S.; Radicchi, E.; Nunzi, F.; Mosconi, E.; De Angelis, F.;
39 Brescia, R.; Rastogi, P.; Prato, M.; Manna, L., Nearly Monodisperse Insulator Cs₄PbX₆ (X = Cl,
40 Br, I) Nanocrystals, Their Mixed Halide Compositions, and Their Transformation into CsPbX₃
41 Nanocrystals. *Nano Letters* **2017**, *17* (3), 1924-1930.
- 42 1241. Zhang, B.-B.; Yuan, S.; Ma, J.-P.; Zhou, Y.; Hou, J.; Chen, X.; Zheng, W.; Shen, H.;
43 Wang, X.-C.; Sun, B.; Bakr, O. M.; Liao, L.-S.; Sun, H.-T., General Mild Reaction Creates
44 Highly Luminescent Organic-Ligand-Lacking Halide Perovskite Nanocrystals for Efficient
45 Light-Emitting Diodes. *J. Am. Chem. Soc.* **2019**, *141* (38), 15423-15432.

- 1 1242. Sim, K.; Jun, T.; Bang, J.; Kamioka, H.; Kim, J.; Hiramatsu, H.; Hosono, H.,
2 Performance boosting strategy for perovskite light-emitting diodes. *Appl. Phys. Rev.* **2019**, *6* (3),
3 031402.
- 4 1243. Lu, M.; Guo, J.; Lu, P.; Zhang, L.; Zhang, Y.; Dai, Q.; Hu, Y.; Colvin, V. L.; Yu, W.
5 W., Ammonium Thiocyanate-Passivated CsPbI₃ Perovskite Nanocrystals for Efficient Red
6 Light-Emitting Diodes. *J. Phys. Chem. C* **2019**, *123* (37), 22787-22792.
- 7 1244. Lignos, I.; Morad, V.; Shynkarenko, Y.; Bernasconi, C.; Maceiczky, R. M.; Protesescu,
8 L.; Bertolotti, F.; Kumar, S.; Ochsenbein, S. T.; Masciocchi, N.; Guagliardi, A.; Shih, C.-J.;
9 Bodnarchuk, M. I.; deMello, A. J.; Kovalenko, M. V., Exploration of Near-Infrared-Emissive
10 Colloidal Multinary Lead Halide Perovskite Nanocrystals Using an Automated Microfluidic
11 Platform. *ACS Nano* **2018**, *12* (6), 5504-5517.
- 12 1245. Solari, S. F.; Kumar, S.; Jagielski, J.; Shih, C.-J., Monochromatic LEDs based on
13 perovskite quantum dots: Opportunities and challenges. *J. Soc. Inf. Display* **2019**, *27* (11), 667-
14 678.
- 15 1246. Kumar, S.; Jagielski, J.; Tian, T.; Kallikounis, N.; Lee, W.-C.; Shih, C.-J., Mixing
16 Entropy-Induced Layering Polydispersity Enabling Efficient and Stable Perovskite Nanocrystal
17 Light-Emitting Diodes. *ACS Energy Lett.* **2019**, *4* (1), 118-125.
- 18 1247. Quan, L. N.; Yuan, M.; Comin, R.; Voznyy, O.; Beauregard, E. M.; Hoogland, S.; Buin,
19 A.; Kirmani, A. R.; Zhao, K.; Amassian, A.; Kim, D. H.; Sargent, E. H., Ligand-Stabilized
20 Reduced-Dimensionality Perovskites. *Journal of the American Chemical Society* **2016**, *138* (8),
21 2649-2655.
- 22 1248. Jagielski, J.; Kumar, S.; Yu, W.-Y.; Shih, C.-J., Layer-controlled two-dimensional
23 perovskites: synthesis and optoelectronics. *Journal of Materials Chemistry C* **2017**, *5* (23), 5610-
24 5627.
- 25 1249. Richter, J. M.; Abdi-Jalebi, M.; Sadhanala, A.; Tabachnyk, M.; Rivett, J. P. H.; Pazos-
26 Outón, L. M.; Gödel, K. C.; Price, M.; Deschler, F.; Friend, R. H., Enhancing photoluminescence
27 yields in lead halide perovskites by photon recycling and light out-coupling. *Nat. Commun.*
28 **2016**, *7* (1), 13941.
- 29 1250. Xing, G.; Wu, B.; Wu, X.; Li, M.; Du, B.; Wei, Q.; Guo, J.; Yeow, E. K. L.; Sum, T. C.;
30 Huang, W., Transcending the slow bimolecular recombination in lead-halide perovskites for
31 electroluminescence. *Nat. Commun.* **2017**, *8* (1), 14558.
- 32 1251. Kim, Y.-H.; Wolf, C.; Kim, H.; Lee, T.-W., Charge carrier recombination and ion
33 migration in metal-halide perovskite nanoparticle films for efficient light-emitting diodes. *Nano*
34 *Energy* **2018**, *52*, 329-335.
- 35 1252. Kim, Y.-H.; Wolf, C.; Kim, Y.-T.; Cho, H.; Kwon, W.; Do, S.; Sadhanala, A.; Park, C.
36 G.; Rhee, S.-W.; Im, S. H.; Friend, R. H.; Lee, T.-W., Highly Efficient Light-Emitting Diodes of
37 Colloidal Metal-Halide Perovskite Nanocrystals beyond Quantum Size. *ACS Nano* **2017**, *11* (7),
38 6586-6593.
- 39 1253. Hopper, T. R.; Gorodetsky, A.; Jeong, A.; Krieg, F.; Bodnarchuk, M. I.; Maimaris, M.;
40 Chaplain, M.; Macdonald, T. J.; Huang, X.; Lovrincic, R.; Kovalenko, M. V.; Bakulin, A. A.,
41 Hot Carrier Dynamics in Perovskite Nanocrystal Solids: Role of the Cold Carriers,
42 Nanoconfinement, and the Surface. *Nano Lett.* **2020**, *20* (4), 2271-2278.
- 43 1254. Mondal, N.; De, A.; Samanta, A., Biexciton Generation and Dissociation Dynamics in
44 Formamidinium- and Chloride-Doped Cesium Lead Iodide Perovskite Nanocrystals. *J. Phys.*
45 *Chem. Lett.* **2018**, *9* (13), 3673-3679.

- 1 1255. Schaller, R. D.; Klimov, V. I., High Efficiency Carrier Multiplication in PbSe
2 Nanocrystals: Implications for Solar Energy Conversion. *Phys. Rev. Lett.* **2004**, *92* (18), 186601.
- 3 1256. Mondal, N.; De, A.; Das, S.; Paul, S.; Samanta, A., Ultrafast carrier dynamics of metal
4 halide perovskite nanocrystals and perovskite-composites. *Nanoscale* **2019**, *11* (20), 9796-9818.
- 5 1257. Zhang, J.; He, J.; Yang, L.; Gan, Z., Photoluminescent Spectral Broadening of Lead
6 Halide Perovskite Nanocrystals Investigated by Emission Wavelength Dependent Lifetime.
7 *Molecules* **2020**, *25* (5), 1151.
- 8 1258. Wehrenfennig, C.; Liu, M.; Snaith, H. J.; Johnston, M. B.; Herz, L. M., Homogeneous
9 Emission Line Broadening in the Organo Lead Halide Perovskite CH₃NH₃PbI_{3-x}Cl_x. *J. Phys.*
10 *Chem. Lett.* **2014**, *5* (8), 1300-1306.
- 11 1259. Naghadeh, S. B.; Sarang, S.; Brewer, A.; Allen, A. L.; Chiu, Y.-H.; Hsu, Y.-J.; Wu, J.-
12 Y.; Ghosh, S.; Zhang, J. Z., Size and temperature dependence of photoluminescence of hybrid
13 perovskite nanocrystals. *J. Chem. Phys.* **2019**, *151* (15), 154705.
- 14 1260. Kim, Y.-H.; Cho, H.; Lee, T.-W., Metal halide perovskite light emitters. *Proc. Natl.*
15 *Acad. Sci. U.S.A* **2016**, *113* (42), 11694-11702.
- 16 1261. Gan, J.; He, J.; Hoyer, R. L. Z.; Mavlonov, A.; Raziq, F.; MacManus-Driscoll, J. L.; Wu,
17 X.; Li, S.; Zu, X.; Zhan, Y.; Zhang, X.; Qiao, L., α -CsPbI₃ Colloidal Quantum Dots: Synthesis,
18 Photodynamics, and Photovoltaic Applications. *ACS Energy Lett.* **2019**, *4* (6), 1308-1320.
- 19 1262. Quan, L. N.; Rand, B. P.; Friend, R. H.; Mhaisalkar, S. G.; Lee, T.-W.; Sargent, E. H.,
20 Perovskites for Next-Generation Optical Sources. *Chem. Rev.* **2019**, *119* (12), 7444-7477.
- 21 1263. Hoyer, R. L. Z.; Chua, M. R.; Musselman, K. P.; Li, G.; Lai, M.-L.; Tan, Z.-K.;
22 Greenham, N. C.; MacManus-Driscoll, J. L.; Friend, R. H.; Credgington, D., Enhanced
23 Performance in Fluorene-Free Organometal Halide Perovskite Light-Emitting Diodes using
24 Tunable, Low Electron Affinity Oxide Electron Injectors. *Adv. Mater.* **2015**, *27* (8), 1414-1419.
- 25 1264. Qiu, W.; Hadipour, A.; Müller, R.; Conings, B.; Boyen, H.-G.; Heremans, P.; Froyen, L.,
26 Ultrathin Ammonium Heptamolybdate Films as Efficient Room-Temperature Hole Transport
27 Layers for Organic Solar Cells. *ACS Appl. Mater. Interfaces* **2014**, *6* (18), 16335-16343.
- 28 1265. Gangishetty, M. K.; Hou, S.; Quan, Q.; Congreve, D. N., Reducing Architecture
29 Limitations for Efficient Blue Perovskite Light-Emitting Diodes. *Adv. Mater.* **2018**, *30* (20),
30 1706226.
- 31 1266. Hoyer, R. L. Z.; Musselman, K. P.; Chua, M. R.; Sadhanala, A.; Raninga, R. D.;
32 MacManus-Driscoll, J. L.; Friend, R. H.; Credgington, D., Bright and efficient blue polymer
33 light emitting diodes with reduced operating voltages processed entirely at low-temperature. *J.*
34 *Mater. Chem. C* **2015**, *3* (36), 9327-9336.
- 35 1267. Brandt, R. E.; Poindexter, J. R.; Gorai, P.; Kurchin, R. C.; Hoyer, R. L. Z.; Nienhaus, L.;
36 Wilson, M. W. B.; Polizzotti, J. A.; Sereika, R.; Žaltauskas, R.; Lee, L. C.; MacManus-Driscoll,
37 J. L.; Bawendi, M.; Stevanović, V.; Buonassisi, T., Searching for “Defect-Tolerant” Photovoltaic
38 Materials: Combined Theoretical and Experimental Screening. *Chemistry of Materials* **2017**, *29*
39 (11), 4667-4674.
- 40 1268. Endres, J.; Egger, D. A.; Kulbak, M.; Kerner, R. A.; Zhao, L.; Silver, S. H.; Hodes, G.;
41 Rand, B. P.; Cahen, D.; Kronik, L.; Kahn, A., Valence and Conduction Band Densities of States
42 of Metal Halide Perovskites: A Combined Experimental–Theoretical Study. *J. Phys. Chem. Lett.*
43 **2016**, *7* (14), 2722-2729.

- 1 1269. Zhang, F.; Silver, S. H.; Noel, N. K.; Ullrich, F.; Rand, B. P.; Kahn, A., Ultraviolet
2 Photoemission Spectroscopy and Kelvin Probe Measurements on Metal Halide Perovskites:
3 Advantages and Pitfalls. *Adv. Energy Mater.* **2020**, n/a (n/a), 1903252.
- 4 1270. Tvingstedt, K.; Gil-Escrig, L.; Momblona, C.; Rieder, P.; Kiermasch, D.; Sessolo, M.;
5 Baumann, A.; Bolink, H. J.; Dyakonov, V., Removing Leakage and Surface Recombination in
6 Planar Perovskite Solar Cells. *ACS Energy Lett.* **2017**, 2 (2), 424-430.
- 7 1271. Abdi-Jalebi, M.; Andaji-Garmaroudi, Z.; Cacovich, S.; Stavrakas, C.; Philippe, B.;
8 Richter, J. M.; Alsari, M.; Booker, E. P.; Hutter, E. M.; Pearson, A. J.; Lilliu, S.; Savenije, T. J.;
9 Rensmo, H.; Divitini, G.; Ducati, C.; Friend, R. H.; Stranks, S. D., Maximizing and stabilizing
10 luminescence from halide perovskites with potassium passivation. *Nature* **2018**, 555 (7697), 497-
11 501.
- 12 1272. Wang, L.; Moghe, D.; Hafezian, S.; Chen, P.; Young, M.; Elinski, M.; Martinu, L.;
13 Kéna-Cohen, S.; Lunt, R. R., Alkali Metal Halide Salts as Interface Additives to Fabricate
14 Hysteresis-Free Hybrid Perovskite-Based Photovoltaic Devices. *ACS Appl. Mater. Interfaces*
15 **2016**, 8 (35), 23086-23094.
- 16 1273. Jiang, Q.; Zhao, Y.; Zhang, X.; Yang, X.; Chen, Y.; Chu, Z.; Ye, Q.; Li, X.; Yin, Z.;
17 You, J., Surface passivation of perovskite film for efficient solar cells. *Nat. Photonics* **2019**, 13
18 (7), 460-466.
- 19 1274. Shi, Y.; Wu, W.; Dong, H.; Li, G.; Xi, K.; Divitini, G.; Ran, C.; Yuan, F.; Zhang, M.;
20 Jiao, B.; Hou, X.; Wu, Z., A Strategy for Architecture Design of Crystalline Perovskite Light-
21 Emitting Diodes with High Performance. *Adv. Mater.* **2018**, 30 (25), 1800251.
- 22 1275. Snaith, H. J.; Abate, A.; Ball, J. M.; Eperon, G. E.; Leijtens, T.; Noel, N. K.; Stranks, S.
23 D.; Wang, J. T.-W.; Wojciechowski, K.; Zhang, W., Anomalous Hysteresis in Perovskite Solar
24 Cells. *J. Phys. Chem. Lett.* **2014**, 5 (9), 1511-1515.
- 25 1276. van Reenen, S.; Kemerink, M.; Snaith, H. J., Modeling Anomalous Hysteresis in
26 Perovskite Solar Cells. *J. Phys. Chem. Lett.* **2015**, 6 (19), 3808-3814.
- 27 1277. Aygüler, M. F.; Weber, M. D.; Puscher, B. M. D.; Medina, D. D.; Docampo, P.; Costa,
28 R. D., Light-Emitting Electrochemical Cells Based on Hybrid Lead Halide Perovskite
29 Nanoparticles. *J. Phys. Chem. C* **2015**, 119 (21), 12047-12054.
- 30 1278. Puscher, B. M. D.; Aygüler, M. F.; Docampo, P.; Costa, R. D., Unveiling the Dynamic
31 Processes in Hybrid Lead Bromide Perovskite Nanoparticle Thin Film Devices. *Adv. Energy*
32 *Mater.* **2017**, 7 (15), 1602283.
- 33 1279. Cho, H.; Wolf, C.; Kim, J. S.; Yun, H. J.; Bae, J. S.; Kim, H.; Heo, J.-M.; Ahn, S.; Lee,
34 T.-W., High-Efficiency Solution-Processed Inorganic Metal Halide Perovskite Light-Emitting
35 Diodes. *Adv. Mater.* **2017**, 29 (31), 1700579.
- 36 1280. Chen, M.; Shan, X.; Geske, T.; Li, J.; Yu, Z., Manipulating Ion Migration for Highly
37 Stable Light-Emitting Diodes with Single-Crystalline Organometal Halide Perovskite
38 Microplatelets. *ACS Nano* **2017**, 11 (6), 6312-6318.
- 39 1281. Hoke, E. T.; Slotcavage, D. J.; Dohner, E. R.; Bowring, A. R.; Karunadasa, H. I.;
40 McGehee, M. D., Reversible photo-induced trap formation in mixed-halide hybrid perovskites
41 for photovoltaics. *Chem. Sci.* **2015**, 6 (1), 613-617.
- 42 1282. Zhang, H.; Fu, X.; Tang, Y.; Wang, H.; Zhang, C.; Yu, W. W.; Wang, X.; Zhang, Y.;
43 Xiao, M., Phase segregation due to ion migration in all-inorganic mixed-halide perovskite
44 nanocrystals. *Nat. Commun.* **2019**, 10 (1), 1088.

- 1 1283. Gualdrón-Reyes, A. F.; Yoon, S. J.; Barea, E. M.; Agouram, S.; Muñoz-Sanjosé, V.;
2 Meléndez, Á. M.; Niño-Gómez, M. E.; Mora-Seró, I., Controlling the Phase Segregation in
3 Mixed Halide Perovskites through Nanocrystal Size. *ACS Energy Lett.* **2019**, *4* (1), 54-62.
- 4 1284. Wang, K.-H.; Peng, Y.; Ge, J.; Jiang, S.; Zhu, B.-S.; Yao, J.; Yin, Y.-C.; Yang, J.-N.;
5 Zhang, Q.; Yao, H.-B., Efficient and Color-Tunable Quasi-2D CsPbBr_xCl_{3-x} Perovskite Blue
6 Light-Emitting Diodes. *ACS Photonics* **2019**, *6* (3), 667-676.
- 7 1285. Xu, H.; Wang, X.; Li, Y.; Cai, L.; Tan, Y.; Zhang, G.; Wang, Y.; Li, R.; Liang, D.;
8 Song, T.; Sun, B., Prominent Heat Dissipation in Perovskite Light-Emitting Diodes with
9 Reduced Efficiency Droop for Silicon-Based Display. *J. Phys. Chem. Lett.* **2020**, *11* (9), 3689-
10 3698.
- 11 1286. Meloni, S.; Palermo, G.; Ashari-Astani, N.; Grätzel, M.; Rothlisberger, U., Valence and
12 conduction band tuning in halide perovskites for solar cell applications. *J. Mater. Chem. A* **2016**,
13 *4* (41), 15997-16002.
- 14 1287. Yoon, H. C.; Lee, H.; Kang, H.; Oh, J. H.; Do, Y. R., Highly efficient wide-color-gamut
15 QD-emissive LCDs using red and green perovskite core/shell QDs. *Journal of Materials*
16 *Chemistry C* **2018**, *6* (47), 13023-13033.
- 17 1288. Ko, Y. H.; Jalalah, M.; Lee, S. J.; Park, J. G., Super Ultra-High Resolution Liquid-
18 Crystal-Display Using Perovskite Quantum-Dot Functional Color-Filters. *Sci. Rep.* **2018**, *8* (1),
19 12881.
- 20 1289. Worku, M.; Tian, Y.; Zhou, C.; Lin, H.; Chaaban, M.; Xu, L. J.; He, Q.; Beery, D.;
21 Zhou, Y.; Lin, X.; Su, Y. F.; Xin, Y.; Ma, B., Hollow metal halide perovskite nanocrystals with
22 efficient blue emissions. *Sci. Adv.* **2020**, *6* (17), eaaz5961.
- 23 1290. Johnston, M. B.; Herz, L. M., Hybrid Perovskites for Photovoltaics: Charge-Carrier
24 Recombination, Diffusion, and Radiative Efficiencies. *Acc Chem Res* **2016**, *49* (1), 146-54.
- 25 1291. Ambrosio, F.; Wiktor, J.; De Angelis, F.; Pasquarello, A., Origin of low electron-hole
26 recombination rate in metal halide perovskites. *Energy Environ. Sci.* **2018**, *11* (1), 101-105.
- 27 1292. Wolff, C. M.; Caprioglio, P.; Stolterfoht, M.; Neher, D., Nonradiative Recombination in
28 Perovskite Solar Cells: The Role of Interfaces. *Adv. Mater.* **2019**, *31* (52), e1902762.
- 29 1293. Yang, M.; Zeng, Y.; Li, Z.; Kim, D. H.; Jiang, C. S.; van de Lagemaat, J.; Zhu, K., Do
30 grain boundaries dominate non-radiative recombination in CH₃NH₃PbI₃ perovskite thin films?
31 *Phys. Chem. Chem. Phys.* **2017**, *19* (7), 5043-5050.
- 32 1294. Luo, D.; Su, R.; Zhang, W.; Gong, Q.; Zhu, R., Minimizing non-radiative recombination
33 losses in perovskite solar cells. *Nat. Rev. Mater.* **2019**, *5* (1), 44-60.
- 34 1295. Zheng, K.; Zhu, Q.; Abdellah, M.; Messing, M. E.; Zhang, W.; Generalov, A.; Niu, Y.;
35 Ribaud, L.; Canton, S. E.; Pullerits, T., Exciton Binding Energy and the Nature of Emissive
36 States in Organometal Halide Perovskites. *J. Phys. Chem. Lett.* **2015**, *6* (15), 2969-75.
- 37 1296. Lee, H. D.; Kim, H.; Cho, H.; Cha, W.; Hong, Y.; Kim, Y. H.; Sadhanala, A.;
38 Venugopalan, V.; Kim, J. S.; Choi, J. W.; Lee, C. L.; Kim, D.; Yang, H.; Friend, R. H.; Lee, T.
39 W., Efficient Ruddlesden-Popper Perovskite Light - Emitting Diodes with Randomly Oriented
40 Nanocrystals. *Adv. Funct. Mater.* **2019**.
- 41 1297. Wang, K.; Wu, C.; Jiang, Y.; Yang, D.; Wang, K.; Priya, S., Distinct conducting layer
42 edge states in two-dimensional (2D) halide perovskite. *Sci. Adv.* **2019**, *5* (7), eaau3241.
- 43 1298. Zheng, K.; Pullerits, T., Two Dimensions Are Better for Perovskites. *J. Phys. Chem.*
44 *Lett.* **2019**, *10* (19), 5881-5885.

- 1 1299. Yang, X.; Zhang, X.; Deng, J.; Chu, Z.; Jiang, Q.; Meng, J.; Wang, P.; Zhang, L.; Yin,
2 Z.; You, J., Efficient green light-emitting diodes based on quasi-two-dimensional composition
3 and phase engineered perovskite with surface passivation. *Nat. Commun.* **2018**, *9* (1), 570.
- 4 1300. Jiang, Y.; Qin, C.; Cui, M.; He, T.; Liu, K.; Huang, Y.; Luo, M.; Zhang, L.; Xu, H.; Li,
5 S.; Wei, J.; Liu, Z.; Wang, H.; Kim, G. H.; Yuan, M.; Chen, J., Spectra stable blue perovskite
6 light-emitting diodes. *Nat. Commun.* **2019**, *10* (1), 1868.
- 7 1301. Li, J.; Du, P.; Li, S.; Liu, J.; Zhu, M.; Tan, Z.; Hu, M.; Luo, J.; Guo, D.; Ma, L.; Nie, Z.;
8 Ma, Y.; Gao, L.; Niu, G.; Tang, J., High - Throughput Combinatorial Optimizations of
9 Perovskite Light - Emitting Diodes Based on All - Vacuum Deposition. *Adv. Funct. Mater.*
10 **2019**, *29* (51).
- 11 1302. Hu, Y.; Wang, Q.; Shi, Y.-L.; Li, M.; Zhang, L.; Wang, Z.-K.; Liao, L.-S., Vacuum-
12 evaporated all-inorganic cesium lead bromine perovskites for high-performance light-emitting
13 diodes. *J. Mater. Chem. C* **2017**, *5* (32), 8144-8149.
- 14 1303. Xie, S.; Osherov, A.; Bulović, V., All-vacuum-deposited inorganic cesium lead halide
15 perovskite light-emitting diodes. *APL Mater.* **2020**, *8* (5).
- 16 1304. Ni, Z.; Bao, C.; Liu, Y.; Jiang, Q.; Wu, W. Q.; Chen, S.; Dai, X.; Chen, B.; Hartweg, B.;
17 Yu, Z.; Holman, Z.; Huang, J., Resolving spatial and energetic distributions of trap states in
18 metal halide perovskite solar cells. *Science* **2020**, *367* (6484), 1352-1358.
- 19 1305. Abbaszadeh, D.; Wetzelaer, G. A. H.; Nicolai, H. T.; Blom, P. W. M., Exciton
20 quenching at PEDOT:PSS anode in polymer blue-light-emitting diodes. *J. Appl. Phys.* **2014**, *116*
21 (22).
- 22 1306. Chen, Y.; Peng, J.; Su, D.; Chen, X.; Liang, Z., Efficient and balanced charge transport
23 revealed in planar perovskite solar cells. *ACS Appl. Mater. Interfaces* **2015**, *7* (8), 4471-5.
- 24 1307. Shang, Y.; Liao, Y.; Wei, Q.; Wang, Z.; Xiang, B.; Ke, Y.; Liu, W.; Ning, Z., Highly
25 stable hybrid perovskite light-emitting diodes based on Dion-Jacobson structure. *Sci. Adv.* **2019**,
26 *5* (8), eaaw8072.
- 27 1308. Yuan, Z.; Miao, Y.; Hu, Z.; Xu, W.; Kuang, C.; Pan, K.; Liu, P.; Lai, J.; Sun, B.; Wang,
28 J.; Bai, S.; Gao, F., Unveiling the synergistic effect of precursor stoichiometry and interfacial
29 reactions for perovskite light-emitting diodes. *Nat. Commun.* **2019**, *10* (1), 2818.
- 30 1309. Zhang, L.; Yang, X.; Jiang, Q.; Wang, P.; Yin, Z.; Zhang, X.; Tan, H.; Yang, Y. M.;
31 Wei, M.; Sutherland, B. R.; Sargent, E. H.; You, J., Ultra-bright and highly efficient inorganic
32 based perovskite light-emitting diodes. *Nat. Commun.* **2017**, *8*, 15640.
- 33 1310. Whitaker, J. B.; Kim, D. H.; Larson, Bryon W.; Zhang, F.; Berry, J. J.; van Hest, M. F.
34 A. M.; Zhu, K., Scalable slot-die coating of high performance perovskite solar cells. *Sustain.*
35 *Energy & Fuels* **2018**, *2* (11), 2442-2449.
- 36 1311. Yang, P.; Zhang, L.; Kang, D. J.; Strahl, R.; Kraus, T., High - Resolution Inkjet Printing
37 of Quantum Dot Light - Emitting Microdiode Arrays. *Adv. Opt. Mater.* **2019**, *8* (1).
- 38 1312. Hoshi, K.; Chiba, T.; Sato, J.; Hayashi, Y.; Takahashi, Y.; Ebe, H.; Ohisa, S.; Kido, J.,
39 Purification of Perovskite Quantum Dots Using Low-Dielectric-Constant Washing Solvent
40 "Diglyme" for Highly Efficient Light-Emitting Devices. *ACS Appl. Mater. Interfaces* **2018**, *10*
41 (29), 24607-24612.
- 42 1313. Hamill, J. C.; Schwartz, J.; Loo, Y.-L., Influence of Solvent Coordination on Hybrid
43 Organic-Inorganic Perovskite Formation. *ACS Energy Lett.* **2017**, *3* (1), 92-97.

- 1 1314. Xiao, P.; Huang, J.; Yan, D.; Luo, D.; Yuan, J.; Liu, B.; Liang, D., Emergence of
2 Nanoplatelet Light-Emitting Diodes. *Materials* **2018**, *11* (8).
- 3 1315. Stranks, S. D., Nonradiative Losses in Metal Halide Perovskites. *ACS Energy Lett.* **2017**,
4 *2* (7), 1515-1525.
- 5 1316. Zhang, Z. Y.; Wang, H. Y.; Zhang, Y. X.; Hao, Y. W.; Sun, C.; Zhang, Y.; Gao, B. R.;
6 Chen, Q. D.; Sun, H. B., The Role of Trap-assisted Recombination in Luminescent Properties of
7 Organometal Halide CH₃NH₃PbBr₃ Perovskite Films and Quantum Dots. *Sci. Rep.* **2016**, *6*,
8 27286.
- 9 1317. Mariano, F.; Creti, A.; Carbone, L.; Genco, A.; D'Agostino, S.; Carallo, S.; Montagna,
10 G.; Lomascolo, M.; Mazzeo, M., The enhancement of excitonic emission crossing Saha
11 equilibrium in trap passivated CH₃NH₃PbBr₃ perovskite. *Commun. Phys.* **2020**, *3* (1).
- 12 1318. Zou, W.; Li, R.; Zhang, S.; Liu, Y.; Wang, N.; Cao, Y.; Miao, Y.; Xu, M.; Guo, Q.; Di,
13 D.; Zhang, L.; Yi, C.; Gao, F.; Friend, R. H.; Wang, J.; Huang, W., Minimising efficiency roll-
14 off in high-brightness perovskite light-emitting diodes. *Nat. Commun.* **2018**, *9* (1), 608.
- 15 1319. Wu, W.; Zhang, Y.; Liang, T.; Fan, J., Carrier accumulation enhanced Auger
16 recombination and inner self-heating-induced spectrum fluctuation in CsPbBr₃ perovskite
17 nanocrystal light-emitting devices. *Appl. Phys. Lett.* **2019**, *115* (24).
- 18 1320. Jung, Y. J.; Cho, S. Y.; Jung, J. W.; Kim, S. Y.; Lee, J. H., Influence of indium-tin-oxide
19 and emitting-layer thicknesses on light outcoupling of perovskite light-emitting diodes. *Nano*
20 *Converg* **2019**, *6* (1), 26.
- 21 1321. Shen, Y.; Cheng, L. P.; Li, Y. Q.; Li, W.; Chen, J. D.; Lee, S. T.; Tang, J. X., High-
22 Efficiency Perovskite Light-Emitting Diodes with Synergetic Outcoupling Enhancement. *Adv.*
23 *Mater.* **2019**, *31* (24), e1901517.
- 24 1322. Wu, T.; Ahmadi, M.; Hu, B., Giant current amplification induced by ion migration in
25 perovskite single crystal photodetectors. *J. Mater. Chem. C* **2018**, *6* (30), 8042-8050.
- 26 1323. Dong, Q.; Lei, L.; Mendes, J.; So, F., Operational stability of perovskite light emitting
27 diodes. *Journal of Physics: Materials* **2020**, *3* (1), 012002.
- 28 1324. Li, C.; Guerrero, A.; Huettner, S.; Bisquert, J., Unravelling the role of vacancies in lead
29 halide perovskite through electrical switching of photoluminescence. *Nature Communications*
30 **2018**, *9* (1), 5113.
- 31 1325. Xu, B.; Wang, W.; Zhang, X.; Liu, H.; Zhang, Y.; Mei, G.; Chen, S.; Wang, K.; Wang,
32 L.; Sun, X. W., Electric Bias Induced Degradation in Organic-Inorganic Hybrid Perovskite
33 Light-Emitting Diodes. *Scientific Reports* **2018**, *8* (1), 15799.
- 34 1326. Rivkin, B.; Fassel, P.; Sun, Q.; Taylor, A. D.; Chen, Z.; Vaynzof, Y., Effect of Ion
35 Migration-Induced Electrode Degradation on the Operational Stability of Perovskite Solar Cells.
36 *ACS Omega* **2018**, *3* (8), 10042-10047.
- 37 1327. Li, J.; Dong, Q.; Li, N.; Wang, L., Direct Evidence of Ion Diffusion for the Silver-
38 Electrode-Induced Thermal Degradation of Inverted Perovskite Solar Cells. *Advanced Energy*
39 *Materials* **2017**, *7* (14), 1602922.
- 40 1328. Li, Z.; Chen, Z.; Yang, Y.; Xue, Q.; Yip, H. L.; Cao, Y., Modulation of recombination
41 zone position for quasi-two-dimensional blue perovskite light-emitting diodes with efficiency
42 exceeding 5. *Nat. Commun.* **2019**, *10* (1), 1027.

- 1 1329. Adil Afroz, M.; Ghimire, N.; Reza, K. M.; Bahrami, B.; Bobba, R. S.; Gurung, A.;
2 Chowdhury, A. H.; Iyer, P. K.; Qiao, Q., Thermal Stability and Performance Enhancement of
3 Perovskite Solar Cells Through Oxalic Acid-Induced Perovskite Formation. *ACS Appl. Energy*
4 *Mater.* **2020**, 3 (3), 2432-2439.
- 5 1330. Heiderhoff, R.; Haeger, T.; Pourdavoud, N.; Hu, T.; Al-Khafaji, M.; Mayer, A.; Chen,
6 Y.; Scheer, H.-C.; Riedl, T., Thermal Conductivity of Methylammonium Lead Halide Perovskite
7 Single Crystals and Thin Films: A Comparative Study. *J. Phys. Chem. C* **2017**, 121 (51), 28306-
8 28311.
- 9 1331. Ge, C.; Hu, M.; Wu, P.; Tan, Q.; Chen, Z.; Wang, Y.; Shi, J.; Feng, J., Ultralow Thermal
10 Conductivity and Ultrahigh Thermal Expansion of Single-Crystal Organic-Inorganic Hybrid
11 Perovskite CH₃NH₃PbX₃ (X = Cl, Br, I). *J. Phys. Chem. C* **2018**, 122 (28), 15973-15978.
- 12 1332. Eaton, S. W.; Lai, M.; Gibson, N. A.; Wong, A. B.; Dou, L.; Ma, J.; Wang, L. W.;
13 Leone, S. R.; Yang, P., Lasing in robust cesium lead halide perovskite nanowires. *Proc. Natl.*
14 *Acad. Sci. U.S.A* **2016**, 113 (8), 1993-8.
- 15 1333. Gao, F.; Zhao, Y.; Zhang, X.; You, J., Recent Progresses on Defect Passivation toward
16 Efficient Perovskite Solar Cells. *Advanced Energy Materials* **2020**, 10 (13), 1902650.
- 17 1334. Yuan, Y.; Wang, Q.; Shao, Y.; Lu, H.; Li, T.; Gruverman, A.; Huang, J., Electric-Field-
18 Driven Reversible Conversion Between Methylammonium Lead Triiodide Perovskites and Lead
19 Iodide at Elevated Temperatures. *Advanced Energy Materials* **2016**, 6 (2), 1501803.
- 20 1335. Wong, K. W.; Yip, H. L.; Luo, Y.; Wong, K. Y.; Lau, W. M.; Low, K. H.; Chow, H. F.;
21 Gao, Z. Q.; Yeung, W. L.; Chang, C. C., Blocking reactions between indium-tin oxide and poly
22 (3,4-ethylene dioxythiophene):poly(styrene sulphonate) with a self-assembly monolayer. *Applied*
23 *Physics Letters* **2002**, 80 (15), 2788-2790.
- 24 1336. Wang, H.; Kim, D. H., Perovskite-based photodetectors: materials and devices. *Chem.*
25 *Soc. Rev.* **2017**, 46 (17), 5204-5236.
- 26 1337. Ahmadi, M.; Wu, T.; Hu, B., A Review on Organic-Inorganic Halide Perovskite
27 Photodetectors: Device Engineering and Fundamental Physics. *Adv. Mater.* **2017**, 29 (41).
- 28 1338. Jing, H.; Peng, R.; Ma, R.-M.; He, J.; Zhou, Y.; Yang, Z.; Li, C.-Y.; Liu, Y.; Guo, X.;
29 Zhu, Y.; Wang, D.; Su, J.; Sun, C.; Bao, W.; Wang, M., Flexible Ultrathin Single-Crystalline
30 Perovskite Photodetector. *Nano Lett.* **2020**, 20 (10), 7144-7151.
- 31 1339. Hu, X.; Zhang, X. D.; Liang, L.; Bao, J.; Li, S.; Yang, W. L.; Xie, Y., High-Performance
32 Flexible Broadband Photodetector Based on Organolead Halide Perovskite. *Adv. Funct. Mater.*
33 **2014**, 24 (46), 7373-7380.
- 34 1340. Xia, H. R.; Li, J.; Sun, W. T.; Peng, L. M., Organohalide lead perovskite based
35 photodetectors with much enhanced performance. *Chem. Commun.* **2014**, 50 (89), 13695-7.
- 36 1341. Ramasamy, P.; Lim, D. H.; Kim, B.; Lee, S. H.; Lee, M. S.; Lee, J. S., All-inorganic
37 cesium lead halide perovskite nanocrystals for photodetector applications. *Chem. Commun.*
38 **2016**, 52 (10), 2067-70.
- 39 1342. Kwak, D.-H.; Lim, D.-H.; Ra, H.-S.; Ramasamy, P.; Lee, J.-S., High performance hybrid
40 graphene-CsPbBr₃-xI_x perovskite nanocrystal photodetector. *RSC Adv.* **2016**, 6 (69), 65252-
41 65256.
- 42 1343. Li, X.; Yu, D.; Chen, J.; Wang, Y.; Cao, F.; Wei, Y.; Wu, Y.; Wang, L.; Zhu, Y.; Sun,
43 Z.; Ji, J.; Shen, Y.; Sun, H.; Zeng, H., Constructing Fast Carrier Tracks into Flexible Perovskite
44 Photodetectors To Greatly Improve Responsivity. *ACS Nano* **2017**, 11 (2), 2015-2023.

- 1 1344. Horvath, E.; Spina, M.; Szekrenyes, Z.; Kamaras, K.; Gaal, R.; Gachet, D.; Forro, L.,
2 Nanowires of methylammonium lead iodide (CH₃NH₃PbI₃) prepared by low temperature
3 solution-mediated crystallization. *Nano Lett.* **2014**, *14* (12), 6761-6.
- 4 1345. Gao, L.; Zeng, K.; Guo, J.; Ge, C.; Du, J.; Zhao, Y.; Chen, C.; Deng, H.; He, Y.; Song,
5 H.; Niu, G.; Tang, J., Passivated Single-Crystalline CH₃NH₃PbI₃ Nanowire Photodetector with
6 High Detectivity and Polarization Sensitivity. *Nano Lett.* **2016**, *16* (12), 7446-7454.
- 7 1346. Deng, W.; Zhang, X.; Huang, L.; Xu, X.; Wang, L.; Wang, J.; Shang, Q.; Lee, S. T.; Jie,
8 J., Aligned Single-Crystalline Perovskite Microwire Arrays for High-Performance Flexible
9 Image Sensors with Long-Term Stability. *Adv. Mater.* **2016**, *28* (11), 2201-8.
- 10 1347. Feng, J.; Yan, X.; Liu, Y.; Gao, H.; Wu, Y.; Su, B.; Jiang, L., Crystallographically
11 Aligned Perovskite Structures for High-Performance Polarization-Sensitive Photodetectors. *Adv.*
12 *Mater.* **2017**, *29* (16).
- 13 1348. Dai, Z.; Ou, Q.; Wang, C.; Si, G.; Shabbir, B.; Zheng, C.; Wang, Z.; Zhang, Y.; Huang,
14 Y.; Dong, Y.; Jasieniak, J. J.; Su, B.; Bao, Q., Capillary-bridge mediated assembly of aligned
15 perovskite quantum dots for high-performance photodetectors. *J. Mater. Chem. C* **2019**, *7* (20),
16 5954-5961.
- 17 1349. Tan, Z.; Wu, Y.; Hong, H.; Yin, J.; Zhang, J.; Lin, L.; Wang, M.; Sun, X.; Sun, L.;
18 Huang, Y.; Liu, K.; Liu, Z.; Peng, H., Two-Dimensional (C₄H₉NH₃)₂PbBr₄ Perovskite Crystals
19 for High-Performance Photodetector. *J. Am. Chem. Soc.* **2016**, *138* (51), 16612-16615.
- 20 1350. Ou, Q.; Zhang, Y.; Wang, Z.; Yuwono, J. A.; Wang, R.; Dai, Z.; Li, W.; Zheng, C.; Xu,
21 Z. Q.; Qi, X.; Duhm, S.; Medhekar, N. V.; Zhang, H.; Bao, Q., Strong Depletion in Hybrid
22 Perovskite p-n Junctions Induced by Local Electronic Doping. *Adv. Mater.* **2018**, *30* (15),
23 e1705792.
- 24 1351. Feng, J.; Gong, C.; Gao, H.; Wen, W.; Gong, Y.; Jiang, X.; Zhang, B.; Wu, Y.; Wu, Y.;
25 Fu, H.; Jiang, L.; Zhang, X., Single-crystalline layered metal-halide perovskite nanowires for
26 ultrasensitive photodetectors. *Nat. Electron.* **2018**, *1* (7), 404-410.
- 27 1352. Cheng, H. C.; Wang, G.; Li, D.; He, Q.; Yin, A.; Liu, Y.; Wu, H.; Ding, M.; Huang, Y.;
28 Duan, X., van der Waals Heterojunction Devices Based on Organohalide Perovskites and Two-
29 Dimensional Materials. *Nano Lett.* **2016**, *16* (1), 367-73.
- 30 1353. Qi, X.; Zhang, Y.; Ou, Q.; Ha, S. T.; Qiu, C. W.; Zhang, H.; Cheng, Y. B.; Xiong, Q.;
31 Bao, Q., Photonics and Optoelectronics of 2D Metal-Halide Perovskites. *Small* **2018**, e1800682.
- 32 1354. Liu, J.; Xue, Y.; Wang, Z.; Xu, Z.-Q.; Zheng, C.; Weber, B.; Song, J.; Wang, Y.; Lu, Y.;
33 Zhang, Y.; Bao, Q., Two-Dimensional CH₃NH₃PbI₃ Perovskite: Synthesis and Optoelectronic
34 Application. *ACS Nano* **2016**, *10* (3), 3536-3542.
- 35 1355. Kang, D. H.; Pae, S. R.; Shim, J.; Yoo, G.; Jeon, J.; Leem, J. W.; Yu, J. S.; Lee, S.; Shin,
36 B.; Park, J. H., An Ultrahigh-Performance Photodetector based on a Perovskite-Transition-
37 Metal-Dichalcogenide Hybrid Structure. *Adv. Mater.* **2016**, *28* (35), 7799-806.
- 38 1356. Wehrenfennig, C.; Liu, M.; Snaith, H. J.; Johnston, M. B.; Herz, L. M., Charge-carrier
39 dynamics in vapour-deposited films of the organolead halide perovskite CH₃NH₃PbI₃-xCl_x.
40 *Energy Environ. Sci.* **2014**, *7* (7), 2269-2275.
- 41 1357. Li, F.; Ma, C.; Wang, H.; Hu, W.; Yu, W.; Sheikh, A. D.; Wu, T., Ambipolar solution-
42 processed hybrid perovskite phototransistors. *Nat. Commun.* **2015**, *6*, 8238.

- 1 1358. Ngai, J. H. L.; Ho, J. K. W.; Chan, R. K. H.; Cheung, S. H.; Leung, L. M.; So, S. K.,
2 Growth, characterization, and thin film transistor application of CH₃NH₃PbI₃ perovskite on
3 polymeric gate dielectric layers. *RSC Adv.* **2017**, *7* (78), 49353-49360.
- 4 1359. Zeidell, A. M.; Tyznik, C.; Jennings, L.; Zhang, C.; Lee, H.; Guthold, M.; Vardeny, Z.
5 V.; Jurchescu, O. D., Enhanced Charge Transport in Hybrid Perovskite Field-Effect Transistors
6 via Microstructure Control. *Adv. Electron. Mater.* **2018**, *4* (12), 1800316.
- 7 1360. Ward, J. W.; Smith, H. L.; Zeidell, A.; Diemer, P. J.; Baker, S. R.; Lee, H.; Payne, M.
8 M.; Anthony, J. E.; Guthold, M.; Jurchescu, O. D., Solution-Processed Organic and Halide
9 Perovskite Transistors on Hydrophobic Surfaces. *ACS Appl. Mater. Interfaces* **2017**, *9* (21),
10 18120-18126.
- 11 1361. Huo, C.; Liu, X.; Song, X.; Wang, Z.; Zeng, H., Field-Effect Transistors Based on van-
12 der-Waals-Grown and Dry-Transferred All-Inorganic Perovskite Ultrathin Platelets. *J. Phys.*
13 *Chem. Lett.* **2017**, *8* (19), 4785-4792.
- 14 1362. Wang, Y.; Wan, Z.; Qian, Q.; Liu, Y.; Kang, Z.; Fan, Z.; Wang, P.; Wang, Y.; Li, C.;
15 Jia, C.; Lin, Z.; Guo, J.; Shakir, I.; Goorsky, M.; Duan, X.; Zhang, Y.; Huang, Y.; Duan, X.,
16 Probing photoelectrical transport in lead halide perovskites with van der Waals contacts. *Nat.*
17 *Nanotech.* **2020**.
- 18 1363. Wang, G.; Li, D.; Cheng, H.-C.; Li, Y.; Chen, C.-Y.; Yin, A.; Zhao, Z.; Lin, Z.; Wu, H.;
19 He, Q.; Ding, M.; Liu, Y.; Huang, Y.; Duan, X., Wafer-scale growth of large arrays of perovskite
20 microplate crystals for functional electronics and optoelectronics. *Sci. Adv.* **2015**, *1* (9),
21 e1500613.
- 22 1364. Li, D.; Cheng, H. C.; Wang, Y.; Zhao, Z.; Wang, G.; Wu, H.; He, Q.; Huang, Y.; Duan,
23 X., The Effect of Thermal Annealing on Charge Transport in Organolead Halide Perovskite
24 Microplate Field-Effect Transistors. *Adv. Mater.* **2017**, *29* (4).
- 25 1365. Liang, Y.; Li, F.; Zheng, R., Low - Dimensional Hybrid Perovskites for Field - Effect
26 Transistors with Improved Stability: Progress and Challenges. *Adv. Electron. Mater.* **2020**.
- 27 1366. Sytnyk, M.; Deumel, S.; Tedde, S. F.; Matt, G. J.; Heiss, W., A perspective on the bright
28 future of metal halide perovskites for X-ray detection. *Appl. Phys. Lett.* **2019**, *115* (19).
- 29 1367. Heo, J. H.; Shin, D. H.; Park, J. K.; Kim, D. H.; Lee, S. J.; Im, S. H., High-Performance
30 Next-Generation Perovskite Nanocrystal Scintillator for Nondestructive X-Ray Imaging. *Adv.*
31 *Mater.* **2018**, e1801743.
- 32 1368. Pan, W.; Yang, B.; Niu, G.; Xue, K. H.; Du, X.; Yin, L.; Zhang, M.; Wu, H.; Miao, X.
33 S.; Tang, J., Hot-Pressed CsPbBr₃ Quasi-Monocrystalline Film for Sensitive Direct X-ray
34 Detection. *Adv. Mater.* **2019**, *31* (44), e1904405.
- 35 1369. Yakunin, S.; Dirin, D. N.; Shynkarenko, Y.; Morad, V.; Cherniukh, I.; Nazarenko, O.;
36 Kreil, D.; Nauser, T.; Kovalenko, M. V., Detection of gamma photons using solution-grown
37 single crystals of hybrid lead halide perovskites. *Nat. Photonics* **2016**, *10* (9), 585-589.
- 38 1370. Wei, H.; Huang, J., Halide lead perovskites for ionizing radiation detection. *Nat.*
39 *Commun.* **2019**, *10* (1), 1066.
- 40 1371. Stoumpos, C. C.; Malliakas, C. D.; Peters, J. A.; Liu, Z.; Sebastian, M.; Im, J.; Chasapis,
41 T. C.; Wibowo, A. C.; Chung, D. Y.; Freeman, A. J.; Wessels, B. W.; Kanatzidis, M. G., Crystal
42 Growth of the Perovskite Semiconductor CsPbBr₃: A New Material for High-Energy Radiation
43 Detection. *Cryst. Growth Des.* **2013**, *13* (7), 2722-2727.

- 1 1372. Wei, H.; Fang, Y.; Mulligan, P.; Chuirazzi, W.; Fang, H.-H.; Wang, C.; Ecker, B. R.;
2 Gao, Y.; Loi, M. A.; Cao, L.; Huang, J., Sensitive X-ray detectors made of methylammonium
3 lead tribromide perovskite single crystals. *Nat. Photonics* **2016**, *10* (5), 333-339.
- 4 1373. Chen, Q.; Wu, J.; Ou, X.; Huang, B.; Almutlaq, J.; Zhumekenov, A. A.; Guan, X.; Han,
5 S.; Liang, L.; Yi, Z.; Li, J.; Xie, X.; Wang, Y.; Li, Y.; Fan, D.; Teh, D. B. L.; All, A. H.;
6 Mohammed, O. F.; Bakr, O. M.; Wu, T.; Bettinelli, M.; Yang, H.; Huang, W.; Liu, X., All-
7 inorganic perovskite nanocrystal scintillators. *Nature* **2018**, *561* (7721), 88-93.
- 8 1374. Yakunin, S.; Sytnyk, M.; Kriegner, D.; Shrestha, S.; Richter, M.; Matt, G. J.; Azimi, H.;
9 Brabec, C. J.; Stangl, J.; Kovalenko, M. V.; Heiss, W., Detection of X-ray photons by solution-
10 processed organic-inorganic perovskites. *Nat. Photonics* **2015**, *9* (7), 444-449.
- 11 1375. Wei, W.; Zhang, Y.; Xu, Q.; Wei, H.; Fang, Y.; Wang, Q.; Deng, Y.; Li, T.; Gruverman,
12 A.; Cao, L.; Huang, J., Monolithic integration of hybrid perovskite single crystals with
13 heterogenous substrate for highly sensitive X-ray imaging. *Nat. Photonics* **2017**, *11* (5), 315-321.
- 14 1376. Kim, Y. C.; Kim, K. H.; Son, D. Y.; Jeong, D. N.; Seo, J. Y.; Choi, Y. S.; Han, I. T.;
15 Lee, S. Y.; Park, N. G., Printable organometallic perovskite enables large-area, low-dose X-ray
16 imaging. *Nature* **2017**, *550* (7674), 87-91.
- 17 1377. Maddalena, F.; Tjahjana, L.; Xie, A.; Arramel; Zeng, S.; Wang, H.; Coquet, P.;
18 Drozdowski, W.; Dujardin, C.; Dang, C.; Birowosuto, M., Inorganic, Organic, and Perovskite
19 Halides with Nanotechnology for High-Light Yield X- and γ -ray Scintillators. *Crystals* **2019**, *9*
20 (2).
- 21 1378. Cao, F.; Yu, D.; Ma, W.; Xu, X.; Cai, B.; Yang, Y. M.; Liu, S.; He, L.; Ke, Y.; Lan, S.;
22 Choy, K. L.; Zeng, H., Shining Emitter in a Stable Host: Design of Halide Perovskite
23 Scintillators for X-ray Imaging from Commercial Concept. *ACS Nano* **2020**, *14* (5), 5183-5193.
- 24 1379. Gandini, M.; Villa, I.; Beretta, M.; Gotti, C.; Imran, M.; Carulli, F.; Fantuzzi, E.; Sassi,
25 M.; Zaffalon, M.; Brofferio, C.; Manna, L.; Beverina, L.; Vedda, A.; Fasoli, M.; Gironi, L.;
26 Brovelli, S., Efficient, fast and reabsorption-free perovskite nanocrystal-based sensitized plastic
27 scintillators. *Nat. Nanotech.* **2020**, *15* (6), 462-468.
- 28 1380. Cao, J.; Guo, Z.; Zhu, S.; Fu, Y.; Zhang, H.; Wang, Q.; Gu, Z., Preparation of Lead-free
29 Two-Dimensional-Layered (C₈H₁₇NH₃)₂SnBr₄ Perovskite Scintillators and Their Application
30 in X-ray Imaging. *ACS Appl. Mater. Interfaces* **2020**, *12* (17), 19797-19804.
- 31 1381. Wang, A.; Jin, Z.; Cheng, M.; Hao, F.; Ding, L., Advances in perovskite quantum-dot
32 solar cells. *J. Energy Chem.* **2021**, *52*, 351-353.
- 33 1382. Yao, H.; Zhou, F.; Li, Z.; Ci, Z.; Ding, L.; Jin, Z., Strategies for Improving the Stability
34 of Tin-Based Perovskite (ASnX₃) Solar Cells. *Adv. Sci.* **2020**, *7* (10), 1903540.
- 35 1383. Li, F.; Zhou, S.; Yuan, J.; Qin, C.; Yang, Y.; Shi, J.; Ling, X.; Li, Y.; Ma, W., Perovskite
36 Quantum Dot Solar Cells with 15.6% Efficiency and Improved Stability Enabled by an α -
37 CsPbI₃/FAPbI₃ Bilayer Structure. *ACS Energy Lett.* **2019**, *4* (11), 2571-2578.
- 38 1384. Hao, M.; Bai, Y.; Zeiske, S.; Ren, L.; Liu, J.; Yuan, Y.; Zarrabi, N.; Cheng, N.;
39 Ghasemi, M.; Chen, P.; Lyu, M.; He, D.; Yun, J.-H.; Du, Y.; Wang, Y.; Ding, S.; Armin, A.;
40 Meredith, P.; Liu, G.; Cheng, H.-M.; Wang, L., Ligand-assisted cation-exchange engineering for
41 high-efficiency colloidal Cs_{1-x}FaxPbI₃ quantum dot solar cells with reduced phase
42 segregation. *Nat. Energy* **2020**, *5* (1), 79-88.
- 43 1385. Liu, C.; Zeng, Q.; Zhao, Y.; Yu, Y.; Yang, M.; Gao, H.; Wei, H.; Yang, B., Surface
44 Ligands Management for Efficient CsPbBr₂ Perovskite Nanocrystal Solar Cells. *Solar RRL*
45 **2020**, *4* (5), 2000102.

- 1 1386. Khan, J.; Zhang, X.; Yuan, J.; Wang, Y.; Shi, G.; Patterson, R.; Shi, J.; Ling, X.; Hu, L.;
2 Wu, T.; Dai, S.; Ma, W., Tuning the Surface-Passivating Ligand Anchoring Position Enables
3 Phase Robustness in CsPbI₃ Perovskite Quantum Dot Solar Cells. *ACS Energy Lett.* **2020**, *5*
4 (10), 3322-3329.
- 5 1387. Tan, L.; Wang, W.; Li, Q.; Luo, Z.; Zou, C.; Tang, M.; Zhang, L.; He, J.; Quan, Z.,
6 Colloidal syntheses of zero-dimensional Cs₄SnX₆ (X = Br, I) nanocrystals with high emission
7 efficiencies. *Chemical Communications* **2020**, *56* (3), 387-390.
- 8 1388. Alivisatos, A. P., Semiconductor Clusters, Nanocrystals, and Quantum Dots. *Science*
9 **1996**, *271*, 933-937.
- 10 1389. Zhao, Q.; Hazarika, A.; Schelhas, L. T.; Liu, J.; Gauding, E. A.; Li, G.; Zhang, M.;
11 Toney, M. F.; Serce, P. C.; Luther, J. M., Size-Dependent Lattice Structure and Confinement
12 Properties in CsPbI₃ Perovskite Nanocrystals: Negative Surface Energy for Stabilization. *ACS*
13 *Energy Lett.* **2020**, *5* (1), 238-247.
- 14 1390. Shockley, W.; Queisser, H. J., Detailed Balance Limit of Efficiency of p - n Junction
15 Solar Cells. *J. Appl. Phys.* **1961**, *32* (3), 510-519.
- 16 1391. Gholipour, S.; Ali, A. M.; Correa-Baena, J.-P.; Turren-Cruz, S.-H.; Tajabadi, F.; Tress,
17 W.; Taghavinia, N.; Grätzel, M.; Abate, A.; De Angelis, F.; Gaggioli, C. A.; Mosconi, E.;
18 Hagfeldt, A.; Saliba, M., Globularity-Selected Large Molecules for a New Generation of
19 Multication Perovskites. *Adv. Mater.* **2017**, *29* (38), 1702005.
- 20 1392. Koh, T. M.; Fu, K.; Fang, Y.; Chen, S.; Sum, T. C.; Mathews, N.; Mhaisalkar, S. G.;
21 Boix, P. P.; Baikie, T., Formamidinium-Containing Metal-Halide: An Alternative Material for
22 Near-IR Absorption Perovskite Solar Cells. *J. Phys. Chem. C* **2014**, *118* (30), 16458-16462.
- 23 1393. Kong, X.; Shayan, K.; Hua, S.; Strauf, S.; Lee, S. S., Complete Suppression of
24 Detrimental Polymorph Transitions in All-Inorganic Perovskites via Nanoconfinement. *ACS*
25 *Appl. Energy Mater.* **2019**, *2* (4), 2948-2955.
- 26 1394. Masi, S.; Gualdrón Reyes, A. F.; Mora-Seró, I., Stabilization of Black Perovskite Phase
27 in FAPbI₃ and CsPbI₃. *ACS Energy Lett.* **2020**.
- 28 1395. Sidhik, S.; Esparza, D.; Martínez-Benítez, A.; Lopez-Luke, T.; Carriles, R.; Mora-Sero,
29 I.; de la Rosa, E., Enhanced Photovoltaic Performance of Mesoscopic Perovskite Solar Cells by
30 Controlling the Interaction between CH₃NH₃PbI₃ Films and CsPbX₃ Perovskite Nanoparticles.
31 *J. Phys. Chem. C* **2017**, *121* (8), 4239-4245.
- 32 1396. Vigil, J. A.; Hazarika, A.; Luther, J. M.; Toney, M. F., FA_xCs_{1-x}PbI₃ Nanocrystals:
33 Tuning Crystal Symmetry by A-Site Cation Composition. *ACS Energy Letters* **2020**, 2475-2482.
- 34 1397. Sanhira, E. M.; Marshall, A. R.; Christians, J. A.; Harvey, S. P.; Ciesielski, P. N.;
35 Wheeler, L. M.; Schulz, P.; Lin, L. Y.; Beard, M. C.; Luther, J. M., Enhanced mobility CsPbI₃
36 quantum dot arrays for record-efficiency, high-voltage photovoltaic cells. *Sci. Adv.* **2017**, *3* (10).
- 37 1398. Wheeler, L. M.; Sanhira, E. M.; Marshall, A. R.; Schulz, P.; Suri, M.; Anderson, N. C.;
38 Christians, J. A.; Nordlund, D.; Sokaras, D.; Kroll, T.; Harvey, S. P.; Berry, J. J.; Lin, L. Y.;
39 Luther, J. M., Targeted Ligand-Exchange Chemistry on Cesium Lead Halide Perovskite
40 Quantum Dots for High-Efficiency Photovoltaics. *J. Am. Chem. Soc.* **2018**, *140* (33), 10504-
41 10513.

- 1 1399. Zhao, Q.; Hazarika, A.; Chen, X.; Harvey, S. P.; Larson, B. W.; Teeter, G. R.; Liu, J.;
2 Song, T.; Xiao, C.; Shaw, L.; Zhang, M.; Li, G.; Beard, M. C.; Luther, J. M., High efficiency
3 perovskite quantum dot solar cells with charge separating heterostructure. *Nat. Commun.* **2019**,
4 *10* (1), 2842.
- 5 1400. Li, F.; Zhou, S.; Yuan, J.; Qin, C.; Yang, Y.; Shi, J.; Ling, X.; Li, Y.; Ma, W., Perovskite
6 Quantum Dot Solar Cells with 15.6% Efficiency and Improved Stability Enabled by an α -
7 CsPbI₃/FAPbI₃ Bilayer Structure. *ACS Energy Letters* **2019**, *4* (11), 2571-2578.
- 8 1401. Carey, G. H.; Abdelhady, A. L.; Ning, Z.; Thon, S. M.; Bakr, O. M.; Sargent, E. H.,
9 Colloidal Quantum Dot Solar Cells. *Chem. Rev.* **2015**.
- 10 1402. Owen, J.; Brus, L., Chemical Synthesis and Luminescence Applications of Colloidal
11 Semiconductor Quantum Dots. *J. Am. Chem. Soc.* **2017**, *139* (32), 10939-10943.
- 12 1403. Cardenas-Morcoso, D.; Gualdrón-Reyes, A. F.; Ferreira Vitoreti, A. B.; García-Tecedor,
13 M.; Yoon, S. J.; Solis de la Fuente, M.; Mora-Seró, I.; Gimenez, S., Photocatalytic and
14 Photoelectrochemical Degradation of Organic Compounds with All-Inorganic Metal Halide
15 Perovskite Quantum Dots. *J. Phys. Chem. Lett.* **2019**, *10* (3), 630-636.
- 16 1404. Fakharuddin, A.; Shabbir, U.; Qiu, W.; Iqbal, T.; Sultan, M.; Heremans, P.; Schmidt-
17 Mende, L., Inorganic and Layered Perovskites for Optoelectronic Devices. *Advanced Materials*
18 **2019**, *0* (0), 1807095.
- 19 1405. Yan, J.; Qiu, W.; Wu, G.; Heremans, P.; Chen, H., Recent progress in 2D/quasi-2D
20 layered metal halide perovskites for solar cells. *Journal of Materials Chemistry A* **2018**, *6* (24),
21 11063-11077.
- 22 1406. Tress, W.; Marinova, N.; Inganäs, O.; Nazeeruddin, M. K.; Zakeeruddin, S. M.;
23 Graetzel, M., Predicting the Open-Circuit Voltage of CH₃NH₃PbI₃ Perovskite Solar Cells Using
24 Electroluminescence and Photovoltaic Quantum Efficiency Spectra: the Role of Radiative and
25 Non-Radiative Recombination. *Adv. Energy Mater.* **2015**, *5* (3), 1400812.
- 26 1407. Yuan, J.; Ling, X.; Yang, D.; Li, F.; Zhou, S.; Shi, J.; Qian, Y.; Hu, J.; Sun, Y.; Yang,
27 Y.; Gao, X.; Duhm, S.; Zhang, Q.; Ma, W., Band-Aligned Polymeric Hole Transport Materials
28 for Extremely Low Energy Loss α -CsPbI₃ Perovskite Nanocrystal Solar Cells. *Joule* **2018**.
- 29 1408. Christodoulou, S.; Di Stasio, F.; Pradhan, S.; Stavrinadis, A.; Konstantatos, G., High-
30 Open-Circuit-Voltage Solar Cells Based on Bright Mixed-Halide CsPbBr₂I₂ Perovskite
31 Nanocrystals Synthesized under Ambient Air Conditions. *J. Phys. Chem. C* **2018**, *122* (14),
32 7621-7626.
- 33 1409. Akkerman, Q. A.; Gandini, M.; Di Stasio, F.; Rastogi, P.; Palazon, F.; Bertoni, G.; Ball,
34 J. M.; Prato, M.; Petrozza, A.; Manna, L., Strongly emissive perovskite nanocrystal inks for
35 high-voltage solar cells. *Nat. Energy* **2016**, *2* (2), 16194.
- 36 1410. Lin, Q.; Yun, H. J.; Liu, W.; Song, H.-J.; Makarov, N. S.; Isaienko, O.; Nakotte, T.;
37 Chen, G.; Luo, H.; Klimov, V. I.; Pietryga, J. M., Phase-Transfer Ligand Exchange of Lead
38 Chalcogenide Quantum Dots for Direct Deposition of Thick, Highly Conductive Films. *J. Am.*
39 *Chem. Soc.* **2017**, *139* (19), 6644-6653.
- 40 1411. Shrestha, A.; Batmunkh, M.; Tricoli, A.; Qiao, S. Z.; Dai, S., Near-Infrared Active Lead
41 Chalcogenide Quantum Dots: Preparation, Post-Synthesis Ligand Exchange, and Applications in
42 Solar Cells. *Angew. Chem. Int. Ed.* **2019**, *58* (16), 5202-5224.
- 43 1412. Xu, Y.-F.; Wang, X.-D.; Liao, J.-F.; Chen, B.-X.; Chen, H.-Y.; Kuang, D.-B.,
44 Amorphous-TiO₂-Encapsulated CsPbBr₃ Nanocrystal Composite Photocatalyst with Enhanced
45 Charge Separation and CO₂ Fixation. *Adv. Mater. Interfaces* **2018**, *5* (22), 1801015.

- 1 1413. Hao, M.; Bai, Y.; Zeiske, S.; Ren, L.; Liu, J.; Yuan, Y.; Zarrabi, N.; Cheng, N.;
2 Ghasemi, M.; Chen, P.; Lyu, M.; He, D.; Yun, J.-H.; Du, Y.; Wang, Y.; Ding, S.; Armin, A.;
3 Meredith, P.; Liu, G.; Cheng, H.-M.; Wang, L., Ligand-assisted cation-exchange engineering for
4 high-efficiency colloidal Cs_{1-x}FaxPbI₃ quantum dot solar cells with reduced phase
5 segregation. *Nature Energy* **2020**, *5* (1), 79-88.
- 6 1414. Hazarika, A.; Zhao, Q.; Gaulding, E. A.; Christians, J. A.; Dou, B.; Marshall, A. R.;
7 Moot, T.; Berry, J. J.; Johnson, J. C.; Luther, J. M., Perovskite Quantum Dot Photovoltaic
8 Materials beyond the Reach of Thin Films: Full-Range Tuning of A-Site Cation Composition.
9 *ACS Nano* **2018**, *12* (10), 10327-10337.
- 10 1415. Suarez, B.; Gonzalez-Pedro, V.; Ripolles, T. S.; Sanchez, R. S.; Otero, L.; Mora-Sero, I.,
11 Recombination Study of Combined Halides (Cl, Br, I) Perovskite Solar Cells. *J. Phys. Chem.*
12 *Lett.* **2014**, *5* (10), 1628-1635.
- 13 1416. Gualdrón-Reyes, A. F.; Yoon, S. J.; Mora-Seró, I., Recent insights for achieving mixed
14 halide perovskites without halide segregation. *Curr. Opin. Electrochem.* **2018**.
- 15 1417. Unger, E. L.; Kegelmann, L.; Suchan, K.; Sorell, D.; Korte, L.; Albrecht, S., Roadmap
16 and roadblocks for the band gap tunability of metal halide perovskites. *J. Mater. Chem. A* **2017**,
17 *5* (23), 11401-11409.
- 18 1418. Braly, I. L.; Stoddard, R. J.; Rajagopal, A.; Uhl, A. R.; Katahara, J. K.; Jen, A. K. Y.;
19 Hillhouse, H. W., Current-Induced Phase Segregation in Mixed Halide Hybrid Perovskites and
20 its Impact on Two-Terminal Tandem Solar Cell Design. *ACS Energy Lett.* **2017**, *2* (8), 1841-
21 1847.
- 22 1419. Draguta, S.; Sharia, O.; Yoon, S. J.; Brennan, M. C.; Morozov, Y. V.; Manser, J. S.;
23 Kamat, P. V.; Schneider, W. F.; Kuno, M., Rationalizing the Light-induced Phase Separation of
24 Mixed Halide Organic-inorganic Perovskites. *Nat. Commun.* **2017**, *8* (1), 200.
- 25 1420. Gualdrón-Reyes, A. F.; Yoon, S. J.; Barea, E. M.; Agouram, S.; Muñoz-Sanjosé, V.;
26 Meléndez, Á. M.; Niño-Gómez, M. E.; Mora-Seró, I., Controlling the Phase Segregation in
27 Mixed Halide Perovskites through Nanocrystal Size. *ACS Energy Letters* **2019**, *4*, 54-62.
- 28 1421. Zolfaghari, Z.; Hassanabadi, E.; Pitarch-Tena, D.; Yoon, S. J.; Shariatnia, Z.; van de
29 Lagemaat, J.; Luther, J. M.; Mora-Seró, I., Operation Mechanism of Perovskite Quantum Dot
30 Solar Cells Probed by Impedance Spectroscopy. *ACS Energy Lett.* **2019**, *4* (1), 251-258.
- 31 1422. Que, M.; Dai, Z.; Yang, H.; Zhu, H.; Zong, Y.; Que, W.; Padture, N. P.; Zhou, Y.; Chen,
32 O., Quantum-Dot-Induced Cesium-Rich Surface Imparts Enhanced Stability to Formamidinium
33 Lead Iodide Perovskite Solar Cells. *ACS Energy Lett.* **2019**, *4* (8), 1970-1975.
- 34 1423. Liu, C.; Hu, M.; Zhou, X.; Wu, J.; Zhang, L.; Kong, W.; Li, X.; Zhao, X.; Dai, S.; Xu,
35 B.; Cheng, C., Efficiency and stability enhancement of perovskite solar cells by introducing
36 CsPbI₃ quantum dots as an interface engineering layer. *NPG Asia Mater.* **2018**, *10* (6), 552-561.
- 37 1424. Siddiqui, H., Lead-free perovskite quantum structures towards the efficient solar cell.
38 *Mater. Lett.* **2019**, *249*, 99-103.
- 39 1425. Ke, W.; Kanatzidis, M. G., Prospects for low-toxicity lead-free perovskite solar cells.
40 *Nat. Commun.* **2019**, *10* (1), 965.
- 41 1426. Jokar, E.; Chien, C.-H.; Tsai, C.-M.; Fathi, A.; Diao, E. W.-G., Robust Tin-Based
42 Perovskite Solar Cells with Hybrid Organic Cations to Attain Efficiency Approaching 10%.
43 *Advanced Materials* **2019**, *31* (2), 1804835.

- 1 1427. Xu, H.; Yuan, H.; Duan, J.; Zhao, Y.; Jiao, Z.; Tang, Q., Lead-free CH₃NH₃SnBr_{3-x}I_x
2 perovskite quantum dots for mesoscopic solar cell applications. *Electrochimica Acta* **2018**, *282*,
3 807-812.
- 4 1428. Hasan, S. A. U.; Lee, D. S.; Im, S. H.; Hong, K.-H., Present Status and Research
5 Prospects of Tin-based Perovskite Solar Cells. *Solar RRL* **2020**, *4* (2), 1900310.
- 6 1429. Xiao, Z.; Song, Z.; Yan, Y., From Lead Halide Perovskites to Lead-Free Metal Halide
7 Perovskites and Perovskite Derivatives. *Adv. Mater.* **2019**, *31* (47), 1803792.
- 8 1430. Zhou, L.; Liao, J.-F.; Huang, Z.-G.; Wang, X.-D.; Xu, Y.-F.; Chen, H.-Y.; Kuang, D.-B.;
9 Su, C.-Y., All-Inorganic Lead-Free Cs₂PdX₆ (X = Br, I) Perovskite Nanocrystals with Single
10 Unit Cell Thickness and High Stability. *ACS Energy Lett.* **2018**, *3* (10), 2613-2619.
- 11 1431. Kung, P.-K.; Li, M.-H.; Lin, P.-Y.; Jhang, J.-Y.; Pantaler, M.; Lupascu, D. C.; Grancini,
12 G.; Chen, P., Lead - Free Double Perovskites for Perovskite Solar Cells. *Solar RRL* **2019**, *4* (2).
- 13 1432. Cho, J.; DuBose, J. T.; Kamat, P. V., Charge Injection from Excited Cs₂AgBiBr₆
14 Quantum Dots into Semiconductor Oxides. *Chem. Mater.* **2020**, *32* (1), 510-517.
- 15 1433. Funabiki, F.; Toda, Y.; Hosono, H., Optical and Electrical Properties of Perovskite
16 Variant (CH₃NH₃)₂SnI₆. *J. Phys. Chem. C* **2018**, *122* (20), 10749-10754.
- 17 1434. Chen, M.; Ju, M.-G.; Carl, A. D.; Zong, Y.; Grimm, R. L.; Gu, J.; Zeng, X. C.; Zhou, Y.;
18 Padture, N. P., Cesium Titanium(IV) Bromide Thin Films Based Stable Lead-free Perovskite
19 Solar Cells. *Joule* **2018**, *2* (3), 558-570.
- 20 1435. Wu, C.; Zhang, Q.; Liu, Y.; Luo, W.; Guo, X.; Huang, Z.; Ting, H.; Sun, W.; Zhong, X.;
21 Wei, S.; Wang, S.; Chen, Z.; Xiao, L., The Dawn of Lead-Free Perovskite Solar Cell: Highly
22 Stable Double Perovskite Cs₂AgBiBr₆ Film. *Adv. Sci.* **2018**, *5* (3), 1700759.
- 23 1436. Wali, Q.; Iftikhar, F. J.; Khan, M. E.; Ullah, A.; Iqbal, Y.; Jose, R., Advances in stability
24 of perovskite solar cells. *Organic Electronics* **2020**, *78*, 105590.
- 25 1437. Sidhik, S.; Rosiles Pérez, C.; Serrano Estrada, M. A.; López-Luke, T.; Torres, A.; De la
26 Rosa, E., Improving the stability of perovskite solar cells under harsh environmental conditions.
27 *Solar Energy* **2020**, *202*, 438-445.
- 28 1438. Li, N.; Niu, X.; Chen, Q.; Zhou, H., Towards commercialization: the operational
29 stability of perovskite solar cells. *Chemical Society Reviews* **2020**, *49* (22), 8235-8286.
- 30 1439. Huang, Y.-T.; Kavanagh, S. R.; Scanlon, D. O.; Walsh, A.; Hoye, R. L. Z., Perovskite-
31 Inspired Materials for Photovoltaics -- From Design to Devices. **2020**.
- 32 1440. Tarascon, J. M.; Armand, M., Issues and challenges facing rechargeable lithium
33 batteries. *Nature* **2001**, *414* (6861), 359-367.
- 34 1441. Bruce, P. G.; Freunberger, S. A.; Hardwick, L. J.; Tarascon, J.-M., Erratum: Li-O₂ and
35 Li-S batteries with high energy storage. *Nat. Mater.* **2012**, *11* (2), 172-172.
- 36 1442. Lewis, N. S.; Nocera, D. G., Powering the planet: Chemical challenges in solar energy
37 utilization. *Proc. Natl. Acad. Sci. U.S.A* **2006**, *103* (43), 15729-15735.
- 38 1443. Nahar, S.; Zain, M. F. M.; Kadhun, A. A. H.; Hasan, H. A.; Hasan, M. R., Advances in
39 Photocatalytic CO₂ Reduction with Water: A Review. *Materials* **2017**, *10* (6), 629.
- 40 1444. Maeda, K.; Domen, K., Photocatalytic Water Splitting: Recent Progress and Future
41 Challenges. *J. Phys. Chem. Lett.* **2010**, *1* (18), 2655-2661.
- 42 1445. Stolarczyk, J. K.; Bhattacharyya, S.; Polavarapu, L.; Feldmann, J., Challenges and
43 Prospects in Solar Water Splitting and CO₂ Reduction with Inorganic and Hybrid
44 Nanostructures. *ACS Catal.* **2018**, *8* (4), 3602-3635.

- 1 1446. Chen, X.; Shen, S.; Guo, L.; Mao, S. S., Semiconductor-based Photocatalytic Hydrogen
2 Generation. *Chem. Rev.* **2010**, *110* (11), 6503-6570.
- 3 1447. Kubacka, A.; Fernández-García, M.; Colón, G., Advanced Nanoarchitectures for Solar
4 Photocatalytic Applications. *Chem. Rev.* **2012**, *112* (3), 1555-1614.
- 5 1448. Huynh, K. A.; Nguyen, D. L. T.; Nguyen, V.-H.; Vo, D.-V. N.; Trinh, Q. T.; Nguyen, T.
6 P.; Kim, S. Y.; Le, Q. V., Halide perovskite photocatalysis: progress and perspectives. *J. Chem.*
7 *Technol. Biot. n/a* (n/a).
- 8 1449. Park, S.; Chang, W. J.; Lee, C. W.; Park, S.; Ahn, H.-Y.; Nam, K. T., Photocatalytic
9 hydrogen generation from hydriodic acid using methylammonium lead iodide in dynamic
10 equilibrium with aqueous solution. *Nat. Energy* **2016**, *2* (1), 16185.
- 11 1450. Zhu, X.; Lin, Y.; Sun, Y.; Beard, M. C.; Yan, Y., Lead-Halide Perovskites for
12 Photocatalytic α -Alkylation of Aldehydes. *J. Am. Chem. Soc.* **2019**, *141* (2), 733-738.
- 13 1451. Zhu, X.; Lin, Y.; San Martin, J.; Sun, Y.; Zhu, D.; Yan, Y., Lead halide perovskites for
14 photocatalytic organic synthesis. *Nat. Commun.* **2019**, *10* (1), 2843.
- 15 1452. Zhang, Z.; Liang, Y.; Huang, H.; Liu, X.; Li, Q.; Chen, L.; Xu, D., Stable and Highly
16 Efficient Photocatalysis with Lead-Free Double-Perovskite of Cs₂AgBiBr₆. *Angew. Chem. Int.*
17 *Ed.* **2019**, *58* (22), 7263-7267.
- 18 1453. Leng, M.; Chen, Z.; Yang, Y.; Li, Z.; Zeng, K.; Li, K.; Niu, G.; He, Y.; Zhou, Q.; Tang,
19 J., Lead-Free, Blue Emitting Bismuth Halide Perovskite Quantum Dots. *Angew. Chem. Int. Ed.*
20 **2016**, *55* (48), 15012-15016.
- 21 1454. Lu, C.; Itanze, D. S.; Aragon, A. G.; Ma, X.; Li, H.; Ucer, K. B.; Hewitt, C.; Carroll, D.
22 L.; Williams, R. T.; Qiu, Y.; Geyer, S. M., Synthesis of lead-free Cs₃Sb₂Br₉ perovskite
23 alternative nanocrystals with enhanced photocatalytic CO₂ reduction activity. *Nanoscale* **2020**,
24 *12* (5), 2987-2991.
- 25 1455. Han, C.; Tang, Z.-R.; Liu, J.; Jin, S.; Xu, Y.-J., Efficient photoredox conversion of
26 alcohol to aldehyde and H₂ by heterointerface engineering of bimetal–semiconductor hybrids.
27 *Chem. Sci.* **2019**, *10* (12), 3514-3522.
- 28 1456. Ou, M.; Tu, W.; Yin, S.; Xing, W.; Wu, S.; Wang, H.; Wan, S.; Zhong, Q.; Xu, R.,
29 Amino-Assisted Anchoring of CsPbBr₃ Perovskite Quantum Dots on Porous g-C₃N₄ for
30 Enhanced Photocatalytic CO₂ Reduction. *Angew. Chem.* **2018**, *57* (41), 13570-13574.
- 31 1457. Wu, L.-Y.; Mu, Y.-F.; Guo, X.-X.; Zhang, W.; Zhang, Z.-M.; Zhang, M.; Lu, T.-B.,
32 Encapsulating Perovskite Quantum Dots in Iron-Based Metal–Organic Frameworks (MOFs) for
33 Efficient Photocatalytic CO₂ Reduction. *Angew. Chem.* **2019**, *58* (28), 9491-9495.
- 34 1458. Dai, Y.; Poidevin, C.; Ochoa-Hernández, C.; Auer, A. A.; Tüysüz, H., A Supported
35 Bismuth Halide Perovskite Photocatalyst for Selective Aliphatic and Aromatic C–H Bond
36 Activation. *Angew. Chem. Int. Ed.* **2020**, *59* (14), 5788-5796.
- 37 1459. Wang, H.; Wang, X.; Chen, R.; Zhang, H.; Wang, X.; Wang, J.; Zhang, J.; Mu, L.; Wu,
38 K.; Fan, F.; Zong, X.; Li, C., Promoting Photocatalytic H₂ Evolution on Organic–Inorganic
39 Hybrid Perovskite Nanocrystals by Simultaneous Dual-Charge Transportation Modulation. *ACS*
40 *Energy Lett.* **2019**, *4* (1), 40-47.
- 41 1460. Pavliuk, M. V.; Abdellah, M.; Sá, J., Hydrogen evolution with CsPbBr₃ perovskite
42 nanocrystals under visible light in solution. *Mater. Today Commun.* **2018**, *16*, 90-96.

- 1 1461. Li, R.; Li, X.; Wu, J.; Lv, X.; Zheng, Y.-Z.; Zhao, Z.; Ding, X.; Tao, X.; Chen, J.-F.,
2 Few-layer black phosphorus-on-MAPbI₃ for superb visible-light photocatalytic hydrogen
3 evolution from HI splitting. *Appl. Catal. B* **2019**, *259*, 118075.
- 4 1462. Wang, Q.; Yu, S.; Qin, W.; Wu, X., Isopropanol-assisted synthesis of highly stable
5 MAPbBr₃/p-g-C₃N₄ intergrowth composite photocatalysts and their interfacial charge carrier
6 dynamics. *Nanoscale Adv.* **2020**, *2* (1), 274-285.
- 7 1463. Pan, A.; Ma, X.; Huang, S.; Wu, Y.; Jia, M.; Shi, Y.; Liu, Y.; Wangyang, P.; He, L.; Liu,
8 Y., CsPbBr₃ Perovskite Nanocrystal Grown on MXene Nanosheets for Enhanced Photoelectric
9 Detection and Photocatalytic CO₂ Reduction. *J. Phys. Chem. Lett.* **2019**, *10* (21), 6590-6597.
- 10 1464. Chen, Z.; Hu, Y.; Wang, J.; Shen, Q.; Zhang, Y.; Ding, C.; Bai, Y.; Jiang, G.; Li, Z.;
11 Gaponik, N., Boosting Photocatalytic CO₂ Reduction on CsPbBr₃ Perovskite Nanocrystals by
12 Immobilizing Metal Complexes. *Chem. Mater.* **2020**, *32* (4), 1517-1525.
- 13 1465. Liu, J.; Song, K.; Shin, Y.; Liu, X.; Chen, J.; Yao, K. X.; Pan, J.; Yang, C.; Yin, J.; Xu,
14 L.-J.; Yang, H.; El-Zohry, A. M.; Xin, B.; Mitra, S.; Hedhili, M. N.; Roqan, I. S.; Mohammed,
15 O. F.; Han, Y.; Bakr, O. M., Light-Induced Self-Assembly of Cubic CsPbBr₃ Perovskite
16 Nanocrystals into Nanowires. *Chem. Mater.* **2019**, *31* (17), 6642-6649.
- 17 1466. Toso, S.; Baranov, D.; Manna, L., Hidden in Plain Sight: The Overlooked Influence of
18 the Cs⁺ Substructure on Transformations in Cesium Lead Halide Nanocrystals. *ACS Energy Lett.*
19 **2020**, 3409-3414.
- 20 1467. Benin, B. M.; Dirin, D. N.; Morad, V.; Worle, M.; Yakunin, S.; Raino, G.; Nazarenko,
21 O.; Fischer, M.; Infante, I.; Kovalenko, M. V., Highly Emissive Self-Trapped Excitons in Fully
22 Inorganic Zero-Dimensional Tin Halides. *Angew Chem Int Edit* **2018**, *57* (35), 11329-11333.
- 23 1468. Cheng, P. F.; Sun, L.; Feng, L.; Yang, S. Q.; Yang, Y.; Zheng, D. Y.; Zhao, Y.; Sang, Y.
24 B.; Zhang, R. L.; Wei, D. H.; Deng, W. Q.; Han, K. L., Colloidal Synthesis and Optical
25 Properties of All-Inorganic Low-Dimensional Cesium Copper Halide Nanocrystals. *Angew*
26 *Chem Int Edit* **2019**, *58* (45), 16087-16091.
- 27 1469. Li, Y. Y.; Vashishtha, P.; Zhou, Z. C.; Li, Z.; Shivarudraiah, S. B.; Ma, C.; Liu, J. K.;
28 Wong, K. S.; Su, H. B.; Halpert, J. E., Room Temperature Synthesis of Stable, Printable
29 Cs₃Cu₂X₅ (X = I, Br/I, Br, Br/Cl, Cl) Colloidal Nanocrystals with Near-Unity Quantum Yield
30 Green Emitters (X = Cl). *Chem. Mater.* **2020**, *32* (13), 5515-5524.
- 31 1470. Yin, J.; Bredas, J. L.; Bakr, O. M.; Mohammed, O. F., Boosting Self-Trapped Emissions
32 in Zero-Dimensional Perovskite Heterostructures. *Chem. Mater.* **2020**, *32* (12), 5036-5043.
- 33